THIESEL 2014

Thermo-and fluid dynamic processes in **direct injection** engines

September 9th-12th · 2014 · Valencia (Spain)

ORGANISED BY: **CMT-MOTORES TÉRMICOS** · Universitat Politècnica de València (Spain)

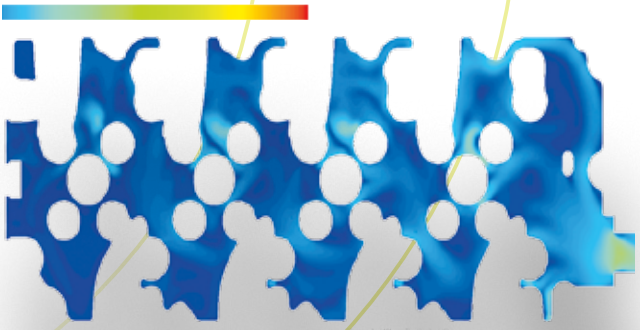

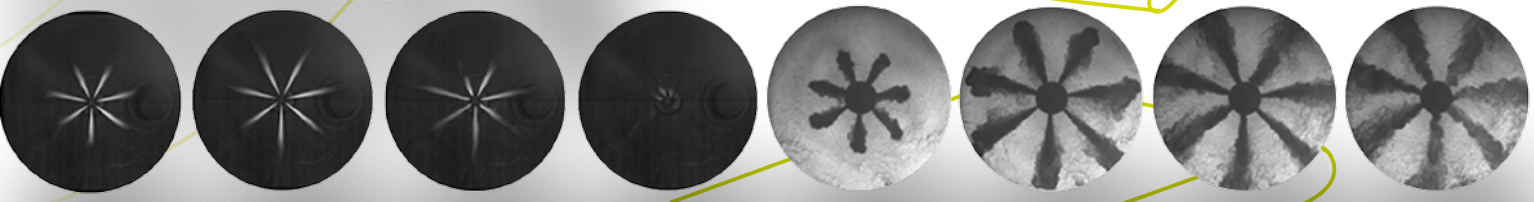

UNIVERSITAT POLITÈCNICA DE VALÈNCIA

cmt motores térmicos

Colección Congresos UPV

The contents of this publication have been approved by the Congress Scientific Committee and in accordance to the procedure set out in http://www.cmt.upv.es/Thiesel.aspx

First edition, 2014 (electronic version)

www.lalibreria.upv.es / Ref.: 6182_01_01_01

ISBN: 978-84-9048-268-1 (electronic version)

Air Quality: Technologies for a Diesel Engine More and More Environmentally Friendly

P.Macaudière

PSA Peugeot-Citroën Group. DPMO/CSCT/SYFM. Centre Technique de Vélizy. Route de Gizy. 78140 Vélizy Villacoublay. France

E-mail: pierre.macaudiere@mpsa.com

Abstract. OEMs development teams are involved for a long time to address the two major environmental challenges linked to transport, climate change and air quality. They have introduced several original technologies for both gasoline or Diesel Engines in order to reduce fuel consumption (thus CO_2 emissions) or pollutants emissions such as nitrogen oxides (NOx), Carbon monoxide (CO) or particulate matter (PM and PN).

It is important to first remind that a Diesel HDi engines emit around 15% less CO_2 than an equivalent gasoline one, and will remain an important brick to reach the 95 g of CO_2 per km required by the European Commission by 2020.

The objective of this presentation is to expose the most recent after treatment technologies to reduce the two air pollutants linked to Diesel, Particulate matter and NOx. It is also to explain approaches and strategies which begin more than 10 years ago and that aim at putting Diesel engine with emission level similar to gasoline engine while keeping its CO_2 advantage:

- The introduction, as a world premiere by PSA Peugeot Citroën, of the Diesel Particulate filter, that drastically reduces particulate matter in mass (PM) and in number (PN) by a factor of more than 99%, whatever the size (from 10 nanometers to several hundreds of nanometers) and whatever the driving conditions (cold start, traffic jam, city or highway)
- The development of NOx elimination systems, with for example the generalization of urea (AdBlue®) based SCR starting end 2013 to reduce NOx by at least 56% for Euro6 engines compared to Euro5 ones, with a DeNOx efficiency that could reach up to 90% depending on the driving conditions

To finish, we will also expose that the new after treatment architectures using SCR are already able to meet the new constraints such as the more dynamic homologation driving cycle (WLTP) and the measurement of pollutant emissions in real driving conditions (so call RDE test). This will however require that a dense and structured AdBlue® pump distribution network be developed with an easy access for automotive drivers, as it was done for trucks several years ago.

Fuel heating in high pressure diesel nozzles

G. Strotos[1,a], P. Koukouvinis[1,b], A. Theodorakakos[1,c] , M. Gavaises[1,d] , L. Wang[2,e] , J. Li[2,f] , R. M. McDavid[3,g]

[1]School of Engineering and Mathematical Sciences, City University London, Northampton Square, EC1V 0HB, London, UK .
[2] Caterpillar Fuel Systems, Peoria, Illinois, US
[3] Caterpillar Engines, Peterborough, UK

[a] George.Strotos.1@city.ac.uk (corresponding author)
[b] Foivos.Koukouvinis.1@city.ac.uk
[c] Andreas.Theodorakakos.1@city.ac.uk
[d] M.Gavaises@city.ac.uk
[e] WANG_LIFENG@cat.com
[f] Li_Jason_Z@cat.com
[g] McDavid_Robert_M@cat.com

Abstract. Properties variation resulting from fuel pressurisation and friction induced heating affect the estimation of the mass flow rate and the temperature of the fuel injected from high pressure Diesel nozzles. In this paper, the Navier-Stokes equations are solved along with the energy equation to predict the in-nozzle temperature field, coupled with an iterative algorithm which converts enthalpy to temperature and updates the physical properties of the fuel at each computational cell; the latter are assumed to be function of local pressure and temperature. The model predictions are compared against those obtained from a zero-dimensional model based on the 1st law of thermodynamics, which also accounts for the effect of variable properties. The effect of increasing the injection pressure up to 3000bar is also investigated. The influence of the cavitating phase on the temperature distribution is also quantified. Results indicate a significant variation of the temperature field as the inlet pressure is increased.

1. Introduction

Cavitation phenomena are known to affect the injection performance and nozzle durability [Arcoumanis et al. 2000]. Several experimental studies which emulate the real operating conditions (due to difficulty in real-time measurements) have been published such as [Badock et al. 1999], [Chaves et al. 1995; Soteriou et al. 2000; Blessing et al. 2003; Andriotis et al. 2008], while advanced experimental techniques [Lai et al. 2011] may provide new information in nozzle cavitation. Additionally, high injection pressures reaching 3000bar are needed for more efficient IC engines. Computational methodologies have a strong potential in understanding the nature of cavitation under real operating conditions. Several methodologies have been proposed such as treating the cavitating fluid as a single mixture [Chen & Heister 1995], the two-fluid method in which conservation equations are solved for both phases separately [Alajbegovic et al. 1999], bubble based cavitation models [Yuan & Schnerr 2001], modified VOF methodologies [Schnerr & Sauer 2001; Singhal et al. 2001], models which account for compressibility effects [Ando et al. 2011; Fuster & Colonius 2011; Jamaluddin et al. 2011; Zeravcic et al. 2011], homogeneous equilibrium models which estimate the cavitation growth by using a barotropic equation [Payri et al. 2012; Salvador et al. 2013], as also Eulerian-Lagrangian models which implement the Rayleigh-Plesset equation [Keller & Miksis 1980; Brennen 1995; Hilgenfeldt et al. 1998]. The challenging task of quantifying the effect of needle motion in fuel injectors has attracted interest and various computational techniques have been used to simulate the needle movement [Payri et al. 2009; Margot et al. 2010; He et al. 2013]. Due to the small timescales involved with the whole phenomenon, the majority of the aforementioned studies are based on the assumption of isothermal flow, but under extreme pressurisation conditions, the flow is characterized by strong friction forces which induce fuel heating and this may even lead to fuel boiling.

The present work aims to shed light on the thermal phenomena occurring in high pressure Diesel nozzles by solving the energy equation and including the heating induced by friction forces. The Eu-

lerian-Lagrangian model used is based on the CFD code developed by [Giannadakis et al. 2008]; this work is an extension of [Giannadakis et al. 2009] and [Theodorakakos et al. 2014], quantifying the effect of the motion of the injector's needle valve; thus the mathematical model will not be repeated here. Briefly, the Navier-Stokes equations are solved along with the energy equation to obtain the temperature field and update the fuel properties, while the turbulence is modeled with the widely used k-ε model. In the following sections, the simulation cases and the results obtained are presented, while the most important conclusions are summarised at the end.

2. Simulation Cases

A 60^o sector of a 6-hole tapered nozzle with 0.175mm hole diameter has been used in the present investigation, applying symmetry boundary conditions at the cross sections. The unstructured grid used consists of approximately one millions cells; it was proved that a grid independent solution is achieved after contacting numerical experiments. Details of the nozzle geometry along with the boundary conditions used and grid details are presented in Fig. 1. The computational technique adopted for the simulation of needle motion uses three pairs of "base grids" (with identical number of cells for each pair) at various needle lifts and any grid at intermediate lift positions is obtained by linear interpolation between the "base grids". Overlapping regions exist between each pair of "base grids" and grid remapping is used to switch from one pair to the other.

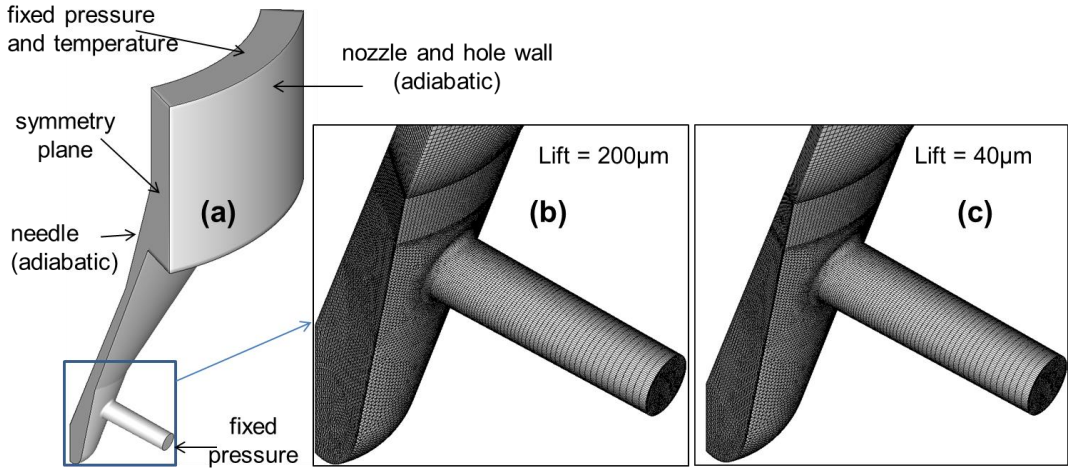

Fig. 1: Nozzle geometry and grid details. (a) computational domain and boundary conditions, (b) grid detail at 200μm lift, (c) grid detail at 40μm lift

A wide range of fixed needle lift positions (varying from 5 up to 200μm) and transient simulations with a moving needle have been examined; these cases are listed in Table 1. In both cases of fixed and moving needle the effect of single-phase and two-phase flow was examined focusing on the cavitation in the region of the hole. The operating conditions include two inlet pressures (2000 and 3000bar) with fixed pressure at the nozzle's exit equal to 60bar, as also fixed inlet temperature at 353K (80^oC). The initial temperature distribution for the fuel was assumed to be uniform and equal to the inlet temperature; this assumption may not reflect the actual initial condition for the fuel and it will be further examined in future work. The solid boundaries were assumed to be adiabatic since their temperature is not generally known. The fluid properties were assumed to be dependent on pressure and temperature according to the relationships given in [Kolev 2002] for the so-called "summer-diesel"; for the purposes of the present work, they have been extrapolated up to 3000bar and 400^oC.

Table 1: Simulation Cases

Lift [μm]	Inlet pressure (bar)	phases
5, 20, 40, 80, 200	2000, 3000	single
20, 40, 80, 200	2000, 3000	two
Moving lift	2000, 3000	single
Moving lift	2000, 3000	two

3. Results and discussion

3.1 Steady lift simulations

The present model is validated against a 0-D thermodynamic model since there is a lack of experimental data for the fuel heating in Diesel nozzles. According to the 1st law of thermodynamics, under fixed needle lift conditions (i.e no work exchange) without energy exchange with the surroundings (i.e adiabatic wall), the pressure difference (Δp) in a variable cross section duct between the nozzle's inlet and exit is converted to liquid kinetic energy and liquid heating when a given flow rate is assumed. In the case of variable fuel properties, the fuel depressurisation tends to suppress the fuel heating and in this case an iterative procedure is required. Fuel depressurisation maybe the dominant mechanism in low friction cases and may even lead to fuel subcooling. The mass flow rate injected from the nozzle ($\dot{m}$) is expressed in dimensionless form through the definition of the discharge coefficient Cd in equation (1) and it is calculated by using the inlet density (ρ_{in}) which is fixed:

$$Cd = \frac{\dot{m}}{\rho_{in} A_{out} U_{ref}}, \quad U_{ref} = \sqrt{\frac{2\Delta p}{\rho_{in}\left(1-\left(A_{out}/A_{in}\right)^2\right)}} \tag{1}$$

where A_{in} and A_{out} are the inlet and outlet surface areas respectively and U_{ref} is the reference velocity (Bernoulli velocity).

In Fig. 2 the fuel heating (i.e. the average fuel temperature at outlet, minus the average fuel temperature at inlet) for the cases of steady lift simulations is presented. These include the cases with inlet pressure 2000 and 3000 bar as also the cases with single and two phase flow. The theoretic heating based of the 0-D model is also presented. As seen, the cases involving a single phase flow are in good agreement with the theoretic values covering a wide range of discharge coefficient (Cd) as the needle lift is varied. Increasing the inlet pressure results in more fuel heating while low friction flows (i.e high Cd) exhibit subcooling due to depressurization. It is interesting to note that the effect of two-phase flow is to reduce the discharge coefficient (two-phase flow points are shifted to the left) since the flow is partially blocked by the presence of cavitation, while slightly less heating is observed; this is attributed to the reduction of friction forces in cavitating flows [Payri et al. 2012], [Javier López et al. 2012]

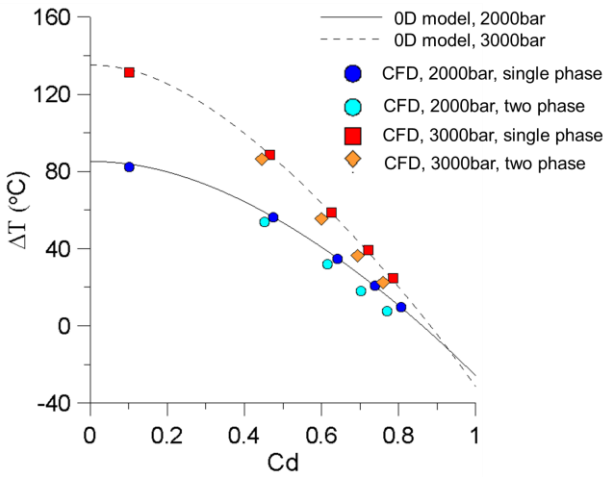

Fig. 2: Effect of discharge coefficient (Cd) on steady state fuel heating for two inlet pressures

3.2 Moving Lift simulations

Moving needle simulations which resemble a realistic injection event are examined in this section. In these cases the lift law plays important role, due to the timescales involved. Generally an injection event has a small duration and the flow may not reach a quasi-steady state, while the closing phase is usually much shorter than the opening phase. As a result, different behaviour of the fuel heating is observed in the opening and closing phase. In Fig. 3a the lift law is presented along with the fuel heating for two inlet pressures (2000 and 3000bar); both single-phase and two-phase flow simulations are presented. In Fig. 3b the fuel heating and the nozzle's discharge coefficient are presented for the case of 2000bar inlet pressure. The nozzle's discharge coefficient shown in Fig. 3b varies at low lifts, while it approaches an asymptotic value for lifts higher than 80μm. Furthermore, at lifts lower than 80μm the amount of liquid injected in the opening and the closing phases is different. This hysteresis is ought to the presence of the sac volume. In the opening phase mass is accumulated to the nozzle's sac volume, while in the closing phase the already accumulated mass is pushed from the downwards needle motion towards the nozzle hole. Thus, a higher flow rate is observed in the closing phase.

Regarding the fuel heating, the fuel is abruptly heated in the opening phase reaching its maximum value at 20μm and then the fuel is gradually cooled tending to reach the steady state heating predicted from the constant lift simulations. During the needle's closing phase, the fuel starts to heat-up again but lower values are predicted compared to those of the opening phase. This is attributed to the fact that closing is faster than opening and the flow has not enough time to reach a "steady" state. In Fig. 3a the fuel heating for the two inlet pressures simulated is also presented. It is obvious that increasing inlet pressure results in more heating. The effect of cavitation on the mean liquid temperature becomes appreciable for needle lift values exceeding 40μm.

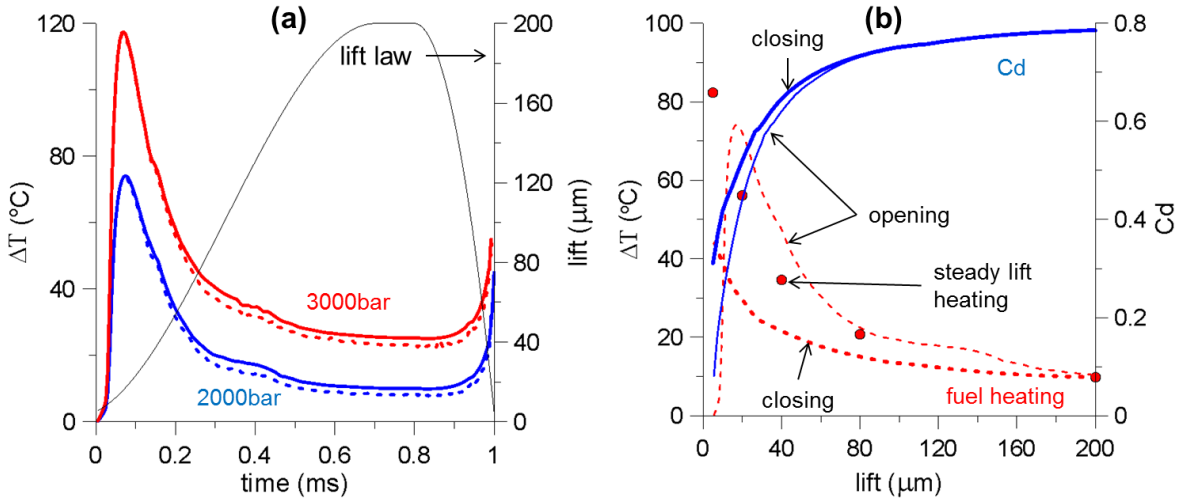

Fig. 3: (a) Lift law and fuel heating versus time for two inlet pressures (dashed lines refer to two-phase flow). (b) fuel heating and discharge coefficient versus lift (2000bar inlet pressure, single phase)

3.3 Flow field regimes

Focusing our interest on the temperature field, the case of full lift (200μm) is presented. For this lift, no differences were observed between the steady state and the transient simulations. On the other hand, inlet pressure has an important effect in the internal temperature field. In Fig. 4a,b the temperature field for the cases of single phase flow with 2000 and 3000bar inlet pressure respectively is presented. The maximum temperature is observed at the upper part of the hole inlet due to the strong velocity gradients in this region and increases with increasing inlet pressure. It is interesting to observe that in the case of 2000bar inlet pressure there is a subcooled liquid core which vanishes towards the nozzle exit. This behaviour is not observed in the case with 3000bar inlet pressure. Additional numerical simulations for a wider range of inlet pressures have shown that the subcooling region decreases with increasing inlet pressure. The effect of two phase flow is presented in Fig. 4c as the difference between the temperature field of single phase flow and two phase flow (T_{single}-T_{two}) for the case of 200bar inlet pressure. As seen, the differences between the cases involving single-phase and two-phase flow, are generally small and limited to the region in which bubbles are present; in this region the temperature difference may reach 25K.

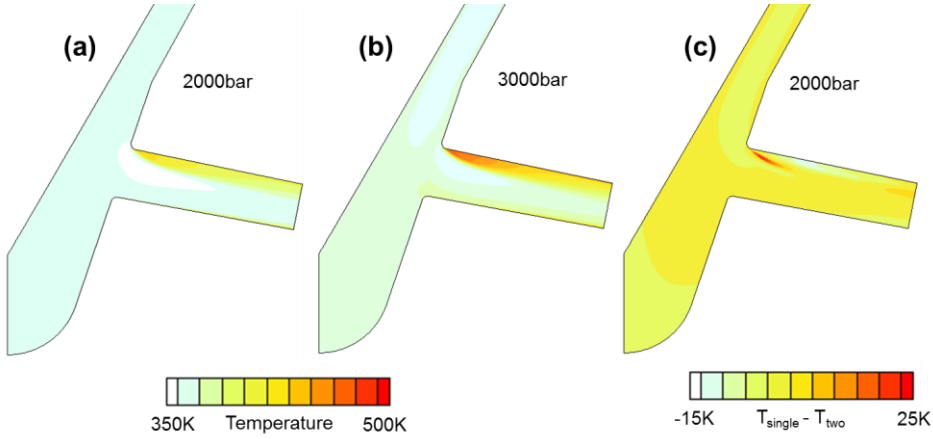

Fig. 4: Temperature field of single-phase flow at 200μm lift. (a) 2000bar, (b) 3000bar. In (c) the difference between the temperature field of single phase flow (T_{single}) minus the two phase flow field (T_{two}) is presented

A different behaviour between opening and closing phase is observed when lower needle lifts are examined, since the motion of the needle (either upwards or downwards) affects both the velocity and the temperature field. The differences between the opening and the closing phase become more evident when the lift is low and tend to vanish near the full lift, while the temperature "history" (i.e. the temperature field at the previous time-step) plays a role. Contrary to the case of steady lift, the temperature field in moving needle lift simulations does not reach a quasi-steady state. A comparison between these approaches is presented in Fig. 5 for the case of 40μm needle lift, 2000bar inlet pressure and single phase flow. In the fixed needle lift simulation (Fig. 5a), the sac volume is occupied with relatively hot fuel (in the order of 380K), while the maximum heating (approximately 450K) is observed at the hole inlet. In transient simulations and under the assumption of uniform initial fuel temperature equal to the inlet temperature, the sac volume during opening is gradually filled with a warmer fluid (compared to the inlet temperature) as it flows through the needle seat passage (Fig. 5b). As the lift increases, the friction forces in the needle seat passage become smaller and the fuel is heated less. When the full lift is reached, the sac volume contains fuel with temperature equal to the inlet temperature. At the start of the closing phase (Fig. 5c) the nozzle's sac volume is occupied with fuel having temperature equal to the feed temperature. Progressively, it is heated up as the needle returns back to its seat position. In the injection hole the thermal boundary layer during the closing phase is thinner than during opening, since higher velocities are predicted in the closing phase due to the downward motion of the needle.

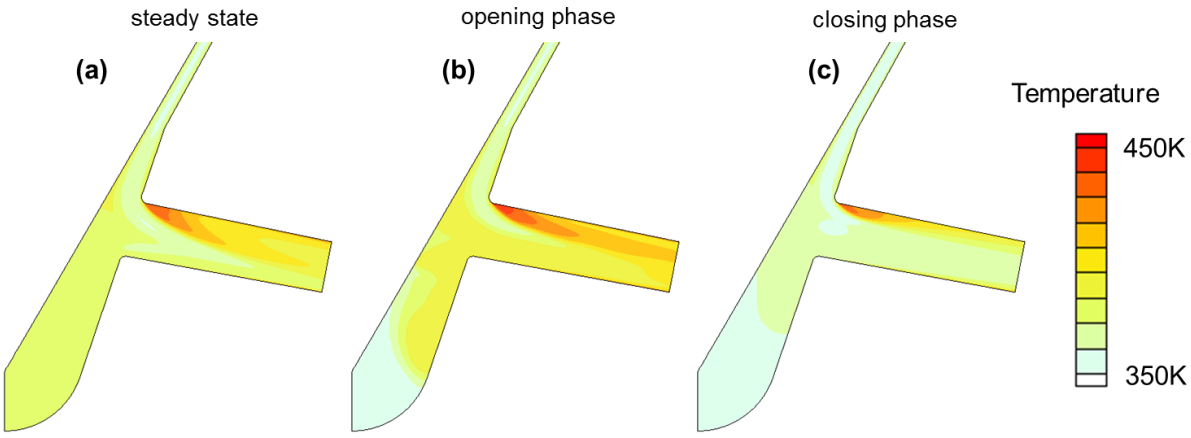

Fig. 5: Temperature field for the case of 2000bar inlet pressure and single phase flow at 40μm lift. (a) steady state solution, (b) opening phase and (c) closing phase

4. Conclusions

The thermal phenomena appearing in the flow inside a high pressure Diesel injector nozzle have been studied with a CFD model. The model includes variable fuel properties as a function of pressure and temperature. Results for the mean fuel exit temperature predicted by the CFD model have been compared against those obtained from a 0-D thermodynamic model for the cases of 2000bar and 3000bar inlet pressure, showing good agreement. A significant temperature increase is predicted with increasing injection pressure. Following the fixed needle lift simulations, the case of moving needle has been examined shedding light on the differences observed in opening and closing phase respectively. The temperature field is affected by the needle motion, while two-phase flow simulations show decreased mass flow rate and reduced fuel heating.

Acknowledgements

The research leading to these results has received funding from the People Programme (IAPP Marie Curie Actions) of the European Union's Seventh Framework Programme FP7/2007-2013/ under REA grant agreement n. 324313.

References

Alajbegovic, A., Grogger, H. A. and Philipp, H. (1999). *Calculation of Transient Cavitation in Nozzle Using the Two-Fluid Model*. Proc. 12th ILASS, Indianapolis, Indiana, USA.

Ando, K., Colonius, T. and Brennen, C. (2011). "Numerical simulation of shock propagation in a polydisperse bubbly liquid." *International Journal of Multiphase Flow*, **37**: 596–608.

Andriotis, A., Gavaises, M. and C., A. (2008). "Vortex flow and cavitation in diesel injector nozzles." *Journal of Fluid Mechanics*, **610**: 195–215.

Arcoumanis, C., Badami, M., Flora, H. and Gavaises, M. (2000). "Cavitation in Real-Size Multi-Hole Diesel Injector Nozzles." *SAE Paper 2000-01-1249*.

Badock, C., Wirth, R., Fath, A. and Leipertz, A. (1999). "Investigation of cavitation in real size diesel injection nozzles." *International Journal of Heat and Fluid Flow*, **20**(5): 538-544.

Blessing, M., König, G., Krüger, C., Michels, U. and Schwarz, V. (2003). "Analysis of Flow and Cavitation Phenomena in Diesel Injection Nozzles and its Effect on Spray and Mixture Formation." *SAE Paper 2003-01-1358*.

Brennen, C. E. (1995). *Cavitation and Bubble Dynamics*. New York; Oxford, Oxford University Press.

Chaves, H., Knapp, M., Kubitzek, A. and Obermeier, F. (1995). "Experimental Study of Cavitation in the Nozzle Hole of Diesel Injectors Using Transparent Nozzles." *SAE Paper 950290*.

Chen, Y. L. and Heister, S. D. (1995). "Two-Phase Modeling of Cavitated Flows." *Computers & Fluids*, **24**(7): 799-809.

Fuster, D. and Colonius, T. (2011). "Modelling bubble clusters in compressible liquids." *Journal of Fluid Mechanics*, **1**: 1–38.

Giannadakis, E., Gavaises, M. and Arcoumanis, C. (2008). "Modelling of cavitation in diesel injector nozzles." *Journal of Fluid Mechanics*, **616**(1): 153–193.

Giannadakis, E., Gavaises, M. and Theodorakakos, A. (2009). "The influence of variable fuel properties in high-pressure diesel injectors." *SAE Paper 2009-01-0832*.

He, Z., Zhong, W., Wang, Q., Jiang, Z. and Fu, Y. (2013). "An investigation of transient nature of the cavitating flow in injector nozzles." *Applied Thermal Engineering*, **54**(1): 56-64.

Hilgenfeldt, S., Brenner, M. P., Grossmann, S. and Lohse, D. (1998). "Analysis of rayleigh-plesset dynamics for sonoluminescing bubbles." *Journal of Fluid Mechanics*, **365**: 171–204.

Jamaluddin, A., Ball, G., Turangan, C. and Leighton, T. (2011). "The collapse of single bubbles and approximation of the far-field acoustic emissions for cavitation induced by shock wave lithotripsy." *Journal of Fluid Mechanics*, **677**: 305–341.

Javier López, J., Salvador, F. J., de la Garza, O. A. and Arrègle, J. (2012). "A comprehensive study on the effect of cavitation on injection velocity in diesel nozzles." *Energy Conversion and Management*, **64**(0): 415-423.

Keller, J. and Miksis, M. (1980). "Bubble oscillations of large amplitude." *Journal of the Acoustical Society of America*, **68**(2): 628–633.

Kolev, N. (2002). *Multiphase Flow Dynamics 3: Turbulence, Gas Absorption and Release, Diesel Fuel Properties*, Springer.

Lai, M.-C., Zheng, Y., Xie, X.-B., Moon, S., Liu, Z., Gao, J., Zhang, X., Fezzaa, K., Wang, J. and Shi, J. (2011). "Characterization of the near-field spray and internal flow of single-hole and multi-hole sac nozzles using phase contrast x-ray imaging and cfd." *SAE Transactions Journal of Engines*, **4**(1): 703–719.

Margot, X., Hoyas, S., Fajardo, P. and Patouna, S. (2010). "A moving mesh generation strategy for solving an injector internal flow problem." *Mathematical and Computer Modelling*, **52**(7-8): 1143-1150.

Payri, F., Margot, X., Patouna, S., Ravet, F. and Funk, M. (2009). "A CFD Study of the Effect of the Needle Movement on the Cavitation Pattern of Diesel Injectors." *SAE Technical Paper*, **2009-24-0025**.

Payri, F., Payri, R., Salvador, F. J. and Martínez-López, J. (2012). "A contribution to the understanding of cavitation effects in Diesel injector nozzles through a combined experimental and computational investigation." *Computers & Fluids*, **58**(0): 88-101.

Salvador, F. J., Martínez-López, J., Romero, J. V. and Roselló, M. D. (2013). "Computational study of the cavitation phenomenon and its interaction with the turbulence developed in diesel injector nozzles by Large Eddy Simulation (LES)." *Mathematical and Computer Modelling*, **57**(7–8): 1656-1662.

Schnerr, G. H. and Sauer, J. (2001). *Physical and Numerical Modeling of Unsteady Cavitation Dynamics*. Proc. ICMF 2001, Fourth International Conference on Multiphase Flows, New Orleans, USA.

Singhal, A. K., Athavale, M. M., Li, H. Y. and Jiang, Y. (2001). *Mathematical basis and validation of the full cavitation model*. Proc. of FEDSM'01 - 2001 ASME Fluid Engineering Division Summer Meeting, New Orleans, Louisiana, USA.

Soteriou, C., Andrews, R., Smith, M., Torres, N. and Sankhalpara, S. (2000). "The flow patterns and sprays of variable orifice nozzle geometries for diesel injection." *SAE Paper 2000-01-0943*.

Theodorakakos, A., Mitroglou, N., Strotos, G., Atkin, C. and Gavaises, M. (2014). "Friction-induced heating in nozzle hole micro-channels under extreme fuel pressurisation." *FUEL*, **123**: 143-150.

Yuan, W. and Schnerr, G. H. (2001). *Cavitation in Injection Nozzles - Effect of Injection Pressure Fluctuations*. Proc. CAV2001, Fourth International Symposium on Cavitation, Pasadena, California, USA.

Zeravcic, Z., Lohse, D. and Saarloos, W. (2011). "Collective oscillations in bubble clouds." *Journal of Fluid Mechanics*, **680**: 114–149.

Visualization Analysis of Relationship between Vortex Flow and Cavitation Behavior in Diesel Nozzle

H. Watanabe[1], M. Nishikori[1], T. Hayashi[2], M. Suzuki[2], N. Kakehashi[2] and M. Ikemoto[3]

[1]NIPPON SOKEN, INC., Nishio, Aichi, Japan.

E-mail: hiroki_i_watanabe@soken1.denso.co.jp
Telephone: +(81) 563 55 1824
Fax: +(81) 563 55 1839

[2]DENSO CORPORATION, Kariya, Aichi, Japan

[3]TOYOTA MOTOR CORPORATION, Susono, Shizuoka, Japan

Abstract. In diesel engines for passenger cars, the spray and combustion characteristics are one of the important factors for determining the exhaust and engine performances. These characteristics are affected by the internal flow, the film-type and string-type cavitations in the diesel nozzle. Specifically, the string-type cavitation correlates well with the spray cone angle and the string-type cavitation behavior destabilizes the spray formation and combustion. The string-type cavitation is influenced by the vortex flow in the nozzle sac. Therefore, it is important to clarify the effect of nozzle and needle shapes on the vortex flow for further development of the diesel injector. This study investigates the effect of needle tip shape on a vortex flow, string-type cavitation and the spray characteristics. This was realized by comparison of the three needle shapes which were chosen in order to control the vortex flow in nozzle sac. A real-size transparent nozzle technique was used to investigate the relationship between the vortex flow and cavitation behavior in the diesel nozzle. This technique allows a spray characteristic to be observed concurrently with the inner flow as well. In addition, the visualized vortex flow was analyzed in detail by the micro PIV method and computational fluid dynamics (CFD).

Notation (optional)

Re	*Reynolds number.*
u	*Flow velocity inside the nozzle hole (m/s).*
v	*Dynamic viscosity (m^2/s).*
CN	*Cavitation number.*
α	*Angle of the needle tip (degree).*
t	*String-type cavitation thickness.*
L_f	*Spray tip penetration (mm).*
a_f	*Spray cone angle (degree).*
ASOI	*After start of injection (ms).*
MS	*Mini-sac.*

1. Introduction

Clean and high efficiency combustion is required to achieve the fuel consumption and exhaust gas regulations in the future. In the diesel engines, common rail fuel injection system has been widely employed for achieving high efficiency and low emission. In the common rail system, injector is an important part in determining the engine performance and exhaust gas. The fuel spray injected from the nozzle hole is momentarily burned in-cylinder. Therefore combustion of the diesel engine is largely affected by the process of fuel atomization and distribution in the combustion chamber. The principal characteristics of fuel spray that govern the diesel combustion are droplet size, spray tip penetration, spray cone angle and variation during a single injection. These characteristics are largely affected by

the internal flow of the nozzle. Therefore, many studies have focused on internal flow and spray formations. These studies have indicated that the spray characteristics are markedly influenced by cavitation generated in the nozzle hole. However, direct observation between the seat and nozzle hole of the diesel is difficult due to the high-speed flow in a narrow space. In order to resolve this issue, some studies have attempted to replicate and visualize the flow characteristics with enlarged transparent nozzles [8, 10, 11]. These flow visualizations are conducted by adjusting the Reynolds number in the large-scale nozzle to that of the real-size nozzle with alternative fluid, thereby allowing researchers to perform more detailed analysis. Recently, there have been some efforts to make flow visualization with real-size nozzles to clarify the relationship between the flow characteristics and combustion [1, 2, 4, 12]. By this technique, a few studies have defined that the variation of the spray cone angle is caused by an unstable string-type cavitation behavior during fuel injection [5]. As a result, it is important in further development of the nozzles that a methods for controlling the string-type cavitation are studied.

The string-type cavitation is influenced by the flow velocity in the nozzle hole and the vortex flow in the nozzle sac of which scale and strength is changed with needle-lift. In order to control the spray characteristics, previous studies have reported the string-type cavitation in the nozzle hole is controlled by nozzle geometries such as the inlet roundness, conical shape factor of the injection hole and shape of the nozzle sac [3, 9]. On the other hand, effect of the vortex flow in the sac, the string-type cavitation and spray characteristics have not been elucidated clearly. Moreover, a method of controlling the vortex flow has not also been clarified yet. Only a few studies have investigated the vortex flow in the sac. Internal flow of mini-sac (MS) nozzle concerning the needle-lift was reported as follows [6]:

- In the low needle-lift, a large vortex flow is generated by the swirling flow structure in the nozzle sac, which originates from the attached flow on the tip of the needle surface.
- In high needle-lift, the vortex flow disappears or downscales in the nozzle sac.

These results indicate that the attached flow on the needle surface has an important role in the formation of the vortex flow in low needle-lift. Thus, optimization for flow channel geometry by the needle shape is one method to control the vortex flow in the nozzle under the low needle-lift.

This study investigates the effect of needle tip shape on a vortex flow, string-type cavitation and the spray characteristics. This was realized by comparison of the three needle shapes which were chosen in order to control the vortex flow in nozzle sac. A real-size transparent nozzle technique was used to investigate the relationship between the vortex flow and cavitation behavior in the diesel nozzle. This technique allows a spray characteristic to be observed concurrently with the inner flow as well. In addition, the visualized vortex flow was analyzed in detail by the micro PIV method and computational fluid dynamics (CFD).

2. Experimental apparatus

2.1 Needle geometries

Figure 1 shows the internal flow of the common type MS nozzles which were presented in the past study [5, 6]. As mentioned previously, the velocity vector shows that large vortex flow form in the nozzle sac. In order to investigate the correlation between the vortex flow and the string-type cavitation, the scale and strength of the vortex flow was controlled by an angle of the needle tip α was changed.

Figure 2 shows needle geometries in this experiment. These needles have different angle of the needle tip (α=90 degree, 70 degree and 30 degree). In Fig. 2 (a), the needle with the angle α=90 degree is the common type in the MS nozzles. The needle with the angle α=70 degree, presented in Figure 2 (b), could cause smaller and weaker vortex flow than α=90 degree. The needle with the angle α=30 degree eliminated the space of forming the vortex in the sac so that the vortex flow in the sac could disappear.

However, sac volume of the nozzle was changed by a geometric restriction, and so the spray formation might be influenced by raising the sac pressure.

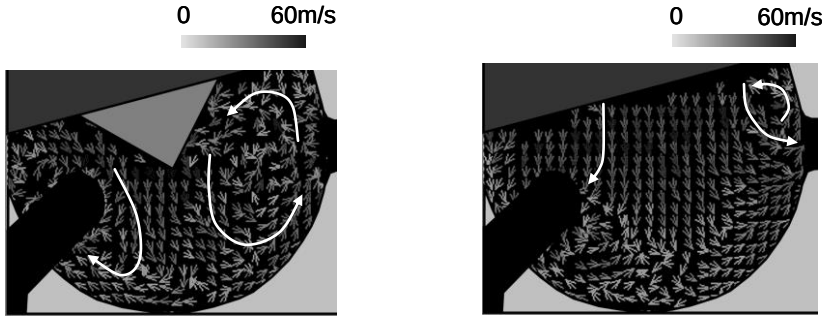

(a) micro PIV in low needle-lift (0.3ms after start of injection)

(b) micro PIV in high needle-lift (1.0ms after start of injection)

Fig. 1. Internal flow of the MS nozzle [5, 6] (P_{inj}=50MPa, t_{inj}=1.0ms)

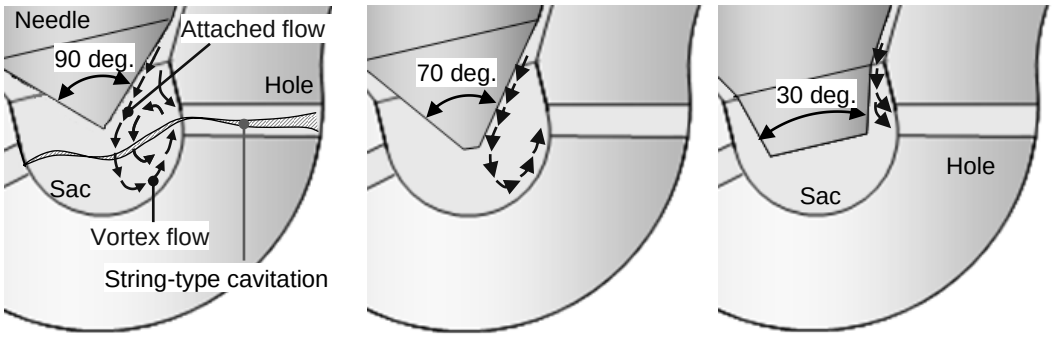

Sac volume 0.4mm³

(a) Angle of needle tip: α =90 degree

Sac volume 0.3mm³

(b) α =70 degree

Sac volume 0.2mm³

(c) α = 30 degree

Fig. 2. Needle geometry in the experiment

2.2 Real-size transparent nozzle and visualization system

2.2.1 Transparent nozzle

The transparent nozzle, as shown in Fig. 3, is made of acrylic resin which has a refractive index similar to that of the diesel fuel. In order to evaluate the internal flow and cavitation generated in the actual MS nozzle, geometry of the sac and hole of the transparent portion is made to be the same as the original nozzle.

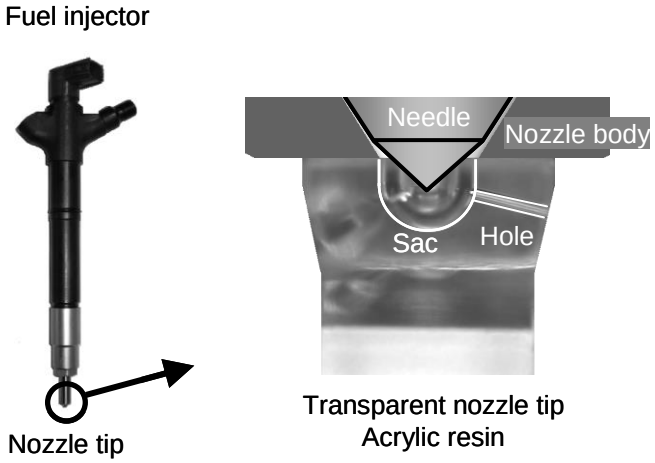

Fig. 3. Optically visible MS nozzle

2.2.2 Visualization system and text conditions

Figure 4 shows the visualization system that was used for the observation of internal flow and cavitation in the transparent nozzle. A shadowgraph technique was introduced to observe cavitation in the nozzle and the spray formation process during fuel injection. Two types of high-speed camera were used for visualization. One was Photron FASTCMA SA1.1 (resolution: 320x128 pixels, frame rate: 0.1Mfps) for obtaining the cavitation and spray combustion images with a metal-halide lamp. Another one was Shimadzu HPV-2A (resolution: 312x260 pixels, frame rate: 1Mfps) with a strobe light, (Sugawara ESD-VF2M-U2) for capturing a detailed visualization of the nozzle and micro-PIV method. In the micro-PIV method, the tracer particle (average diameter is 10μm and relative density is 2.0g/cm^3) is added to the fuel. In order to perform a series of investigation under an injection environment that approximates the high density condition, pressure chamber was used to create atmosphere of density: 15kg/m^3. The pressure chamber was filled with argon gas which is an inert gas. Figure 5 (a) shows a typical captured image of the internal nozzle and fuel spray. Since the refractive index of transparent nozzle made of acrylic resin (1.49) is close to diesel fuel (1.46), light is able to permeate the interior of the nozzle sac filled with fuel. On the other hand, cavitation (gaseous phase) can be observed as a dark shadow since the refractive index of the gaseous phase is different from that of acrylic resin. Figure 5 (b) shows the evaluated spray cone angle and spray tip penetration. The profile of the fuel spray, which was visualized by Mie-scattered light using metal-halide lamp, can be observed as a white mist. The spray cone angle was calculated based on the straight-line distance between the spray width measured 10 mm away from the nozzle hole outlet and the nozzle hole outlet itself.

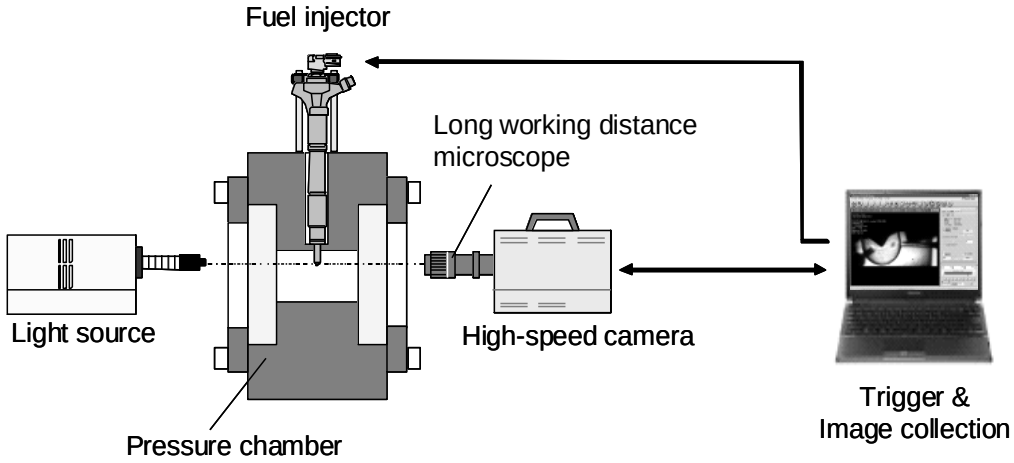

Fig. 4. Experimental apparatus

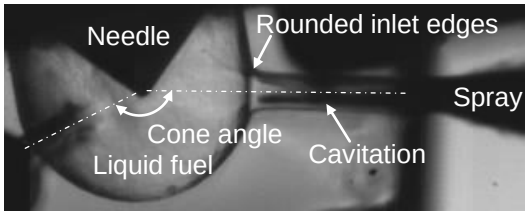

(a) Internal nozzle and spray near the nozzle

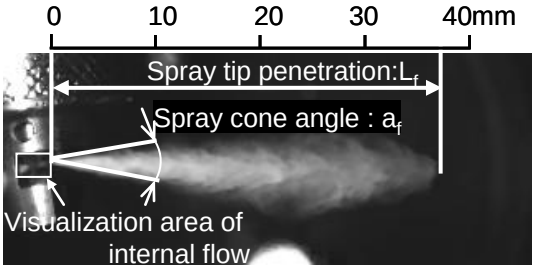

(b) Outer shape of fuel spray

Fig. 5. Example of the visualization images

In this study, a Denso third generation piezo injector was used to control the nozzle needle. Table 1 and 2 indicate the nozzle specifications and the test conditions. The Reynolds number shown in Table 2 is defined as equation Re=du/ν, where d is the representative length (nozzle hole diameter). The cavitation number is defined as equation CN=$(P_a-P_v)/(P_{inj}-P_a)$, where P_a is the ambient pressure, P_v is the vapor pressure, and P_{inj} is the injection pressure.

Table 1. Specifications of the test nozzle

Hole number	n [-]	3
Hole diameter	d [mm]	ϕ0.14
Hole length	L [mm]	0.8
Inlet roundness of hole	R [mm]	0.03
Cone angle	a [deg.]	155

Table 2. Test conditions

Ambient temperature	T_a [K]	293
Ambient pressure	P_a [MPa]	1.0 (Ar gas)
Ambient density	ρ [kg/m^3]	15
Vapor pressure	P_v [MPa]	4.0
Injection pressure	P_{inj} [MPa]	50
Reynolds number	Re [-]	11914
Cavitation number	CN [-]	0.020

2.3 Numerical simulation methods

The commercial CFD code FIRE ver. 2008 (AVL) was used for the calculation of the nozzle internal flow. Figure 6 shows the computational grid of the 3-hole MS nozzle for the simulation. By taking into account the geometric periodicity, only one third of the whole internal flow area of the nozzle was chosen as a computational domain. The measured transient needle-lift and inlet pressure are applied for the computational model. The RANS scheme with standard K-ε model is introduced to describe the turbulent flow in the nozzle and spray chamber. The assumed fluid is composed of three constituents, i.e., liquid / gas phase fuel and air. The cavitation bubble behavior is simulated by the linearized Rayleigh model.

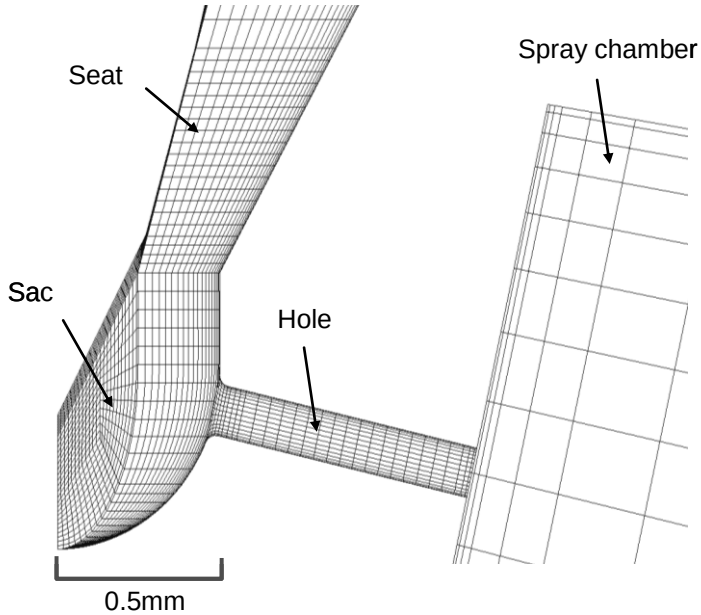

Fig. 6. Computational grid for the simulation of the nozzle flow

3 Results and discussion

3.1 Visualization of the vortex flow behavior

In order to elucidate the changing of the vortex flow by the needle geometries, the internal flow was visualized and analyzed by micro-PIV and CFD. Figure 7 (a) shows the velocity vector in the nozzle sac by micro-PIV and Figure 7 (b) shows the velocity vector and stream line by CFD at 0.2ms after start of injection (ASOI) when the needle-lift was low. In nozzle with α=90 degree needle, the large vortex was formed in the sac. Then, in the nozzle with α=70 degree needle, the vortex scale was smaller than the nozzle with α=90 degree needle, because the attached flow on the needle surface flowed near the nozzle hole and the fuel flow did not path at the bottom of the sac. Moreover, the low speed flow in the vortex near the nozzle hole, presented in micro-PIV and CFD, suggests that the vortex in the nozzle sac was weak in α=70 degree. Finally, in the nozzle withα=30 degree needle, the vortex flow in the sac did not exist near the nozzle hole. The fuel in the sac was observed to directly flow into nozzle hole.

These results show that the vortex flow near the nozzle hole in the sac was suppressed by setting small angle of the needle tip. In addition, the internal flow in the sac directly streamed into the injection hole.

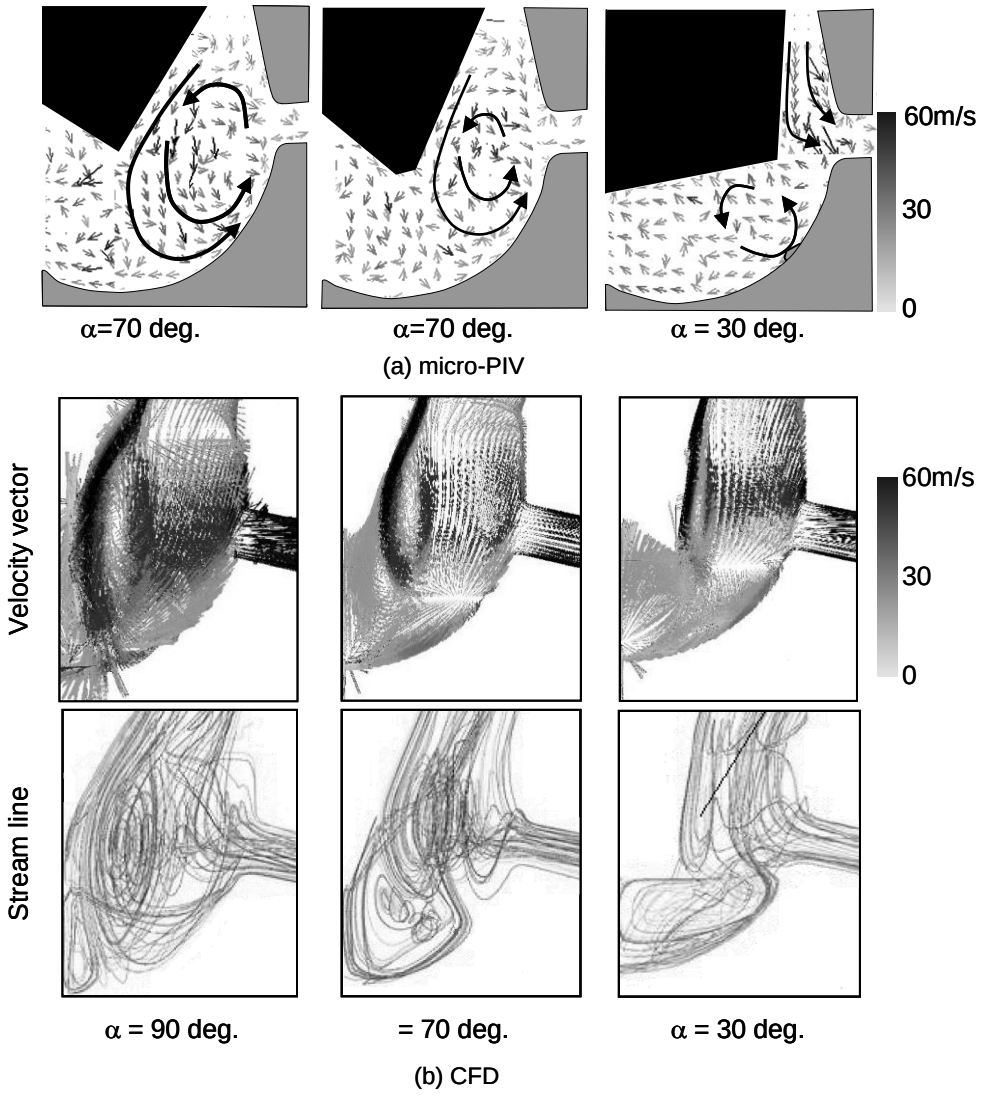

Fig. 7. Internal Flow by micro PIV and CFD at 0.2ms after start of injection (ASOI)

3.2 Relationship between the vortex flow and string-type cavitation behavior

Relationship between the vortex flow and string-type cavitation behavior was investigated. Figure 8 shows the evaluated string-type cavitation thickness and occurrence of the cavitation in the nozzle sac. The string-type cavitation thickness was a normalized number that was calculated as a rate of thickness to the nozzle hole diameter *d* at the hole outlet. Figure 9 shows the string-type cavitation thickness, occurrence of the cavitation in the sac and needle-lift during the injection.

When the cavitation was connected in the sac, the string-type cavitation thickness *t/d* was large. There was a good correlation between the connection of the cavitation in the nozzle sac and the string-type cavitation behavior. In α=90 degree, the connection of the cavitation in the nozzle sac was frequently and the string-type cavitation thickness was large during the rise of the needle. In α=70 degree, the cavitation was observed in nozzle sac. In α=70 degree, the cavitation was observed in the nozzle sac. However, the occurrence frequency of the cavitation in the nozzle sac was less than α=90 degree. Moreover, the string-type cavitation thickness was smaller as well. Finally, the string-type cavitation thickness of α=30 degree needle without the occurrence of the cavitation in the nozzle sac was small during the fuel injection.

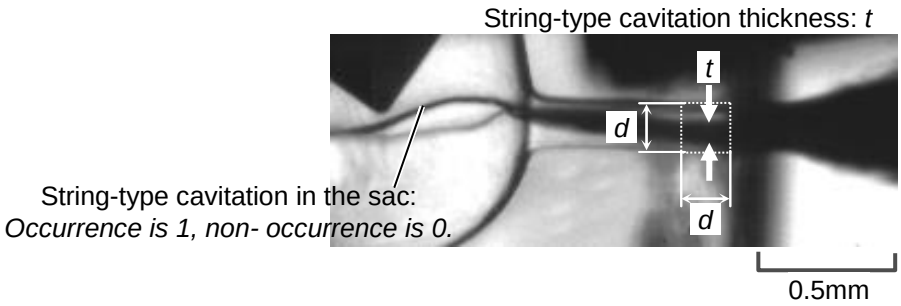

Fig. 8. Definition of cavitation profile

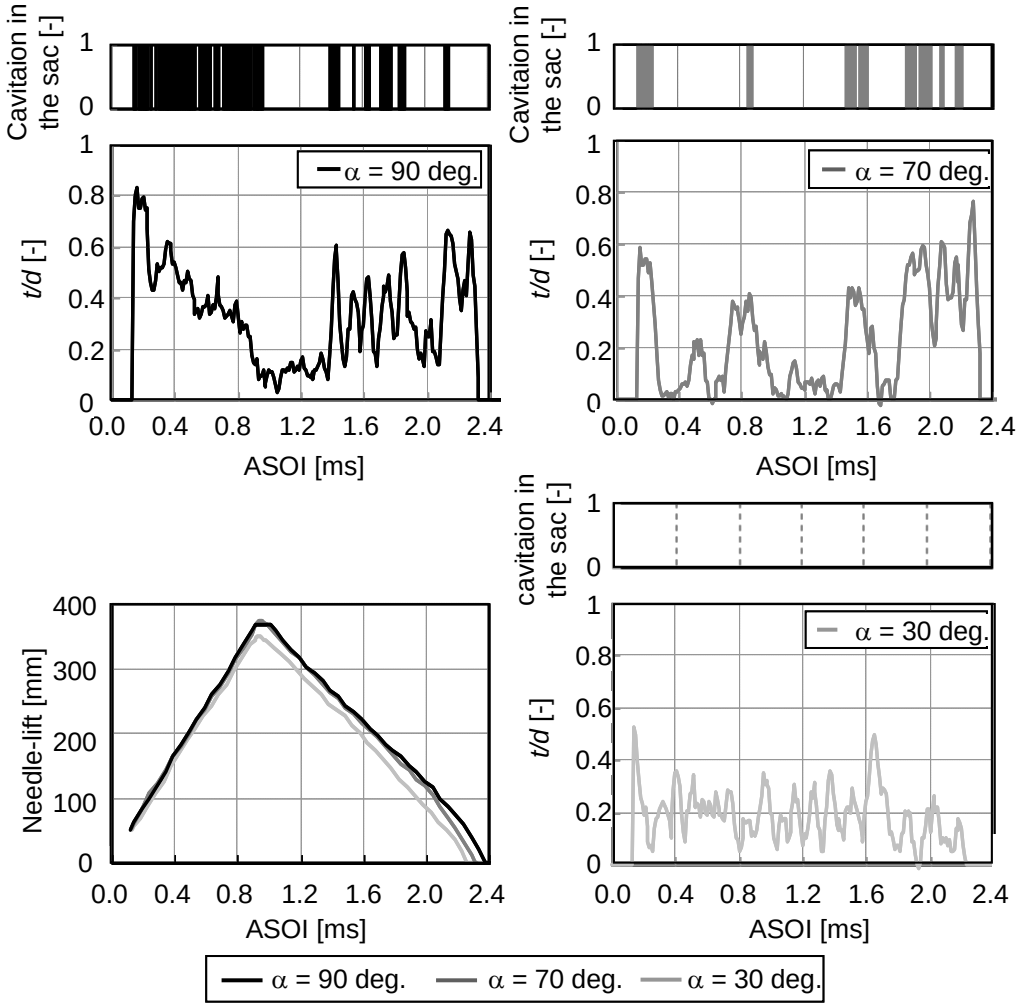

Fig. 9. Cavitation characteristics

The weak vortex flow with the small angle of needle tip decreased the occurrence frequency of the cavitation in nozzle sac and the string-type cavitation thickness in nozzle hole. These results are suggested that the weak vortex flow unable to connect the string-type cavitation in the nozzle hole and another hole is not able to develop the string-type cavitation originating from swirling flow of the nozzle hole which has been mentioned the past study [5, 6]. Thus, the vortex affect the string-type cavitation through the strength of the swirling flow in nozzle sac.

3.3 Effect of vortex flow on spray formation

Finally, the effect of the vortex flow in nozzle sac on the spray formation was confirmed. Figure 10 shows the visualization images of the internal nozzle and the spray. In nozzle with α=90 degree needle, when the string-type cavitation formed clearly, a large spray cone angle was observed at 0.3ms ASOI. Then, in the nozzle with α=70 degree needle which the string-type cavitation was weak, the spray cone angle was smaller than α=90 degree at 0.3ms ASOI. In contrast, the spray cone angle of nozzle with α=30 degree needle was small during the injection. These three types nozzle had a variation of the spray cone angle during 0.3ms ASOI to 0.8ms ASOI.

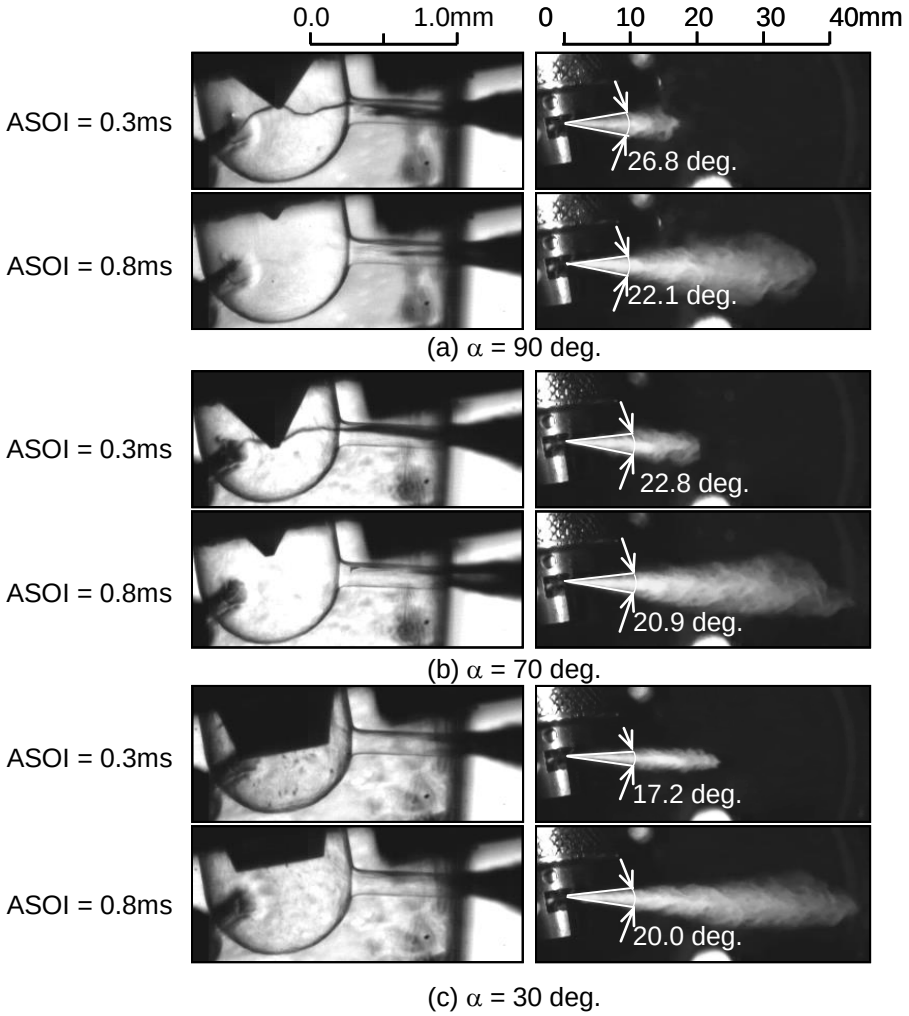

Fig. 10. Cavitation and spray for a variation of the needle shape

Figure 11 shows the rate of injection, string-type cavitation thickness, spray cone angle, and spray tip penetration from the start injection to 1.0ms ASOI. The rate of injection was calculated as equation (1), where q is a rate of injection with a single hole, F is a colliding force on a force sensor of the spray with the single hole, C is flow coefficient, A is cross-section area of the nozzle hole outlet, and ρ_f is density of the fuel [7]. When the string-type cavitation formed with high probability during 0.15ms to 0.30ms ASOI, the rate of injection of α=90 degree needle decrease. The rate of injection was influenced by the string-type cavitation. Next, the spray cone angle in proportion as the string-type cavitation thickness was changed during the fuel injection. Moreover, the maximum of the spray cone angle with each needle shape was decreased as well. Then, the spray tip penetration was strong in inverse proportion to the string-type cavitation. These results suggest that the string-type cavitation thickness shows the strength of radial direction velocity in nozzle hole. Because the strong radial direction velocity is able to raise the spray tip penetration and decrease the spray cone angle.

The small angle of the needle tip is caused for small spray cone angle, large spray tip penetration and stable rate of injection due to small string-type cavitation thickness. These results show that the spray characteristics are affected by the string-type cavitation: therefore, the vortex flow in nozzle sac affected the spray characteristics through the string-type cavitation behavior.

$$q = \sqrt{\frac{F \cdot C \cdot A}{\rho_f}} \qquad (1)$$

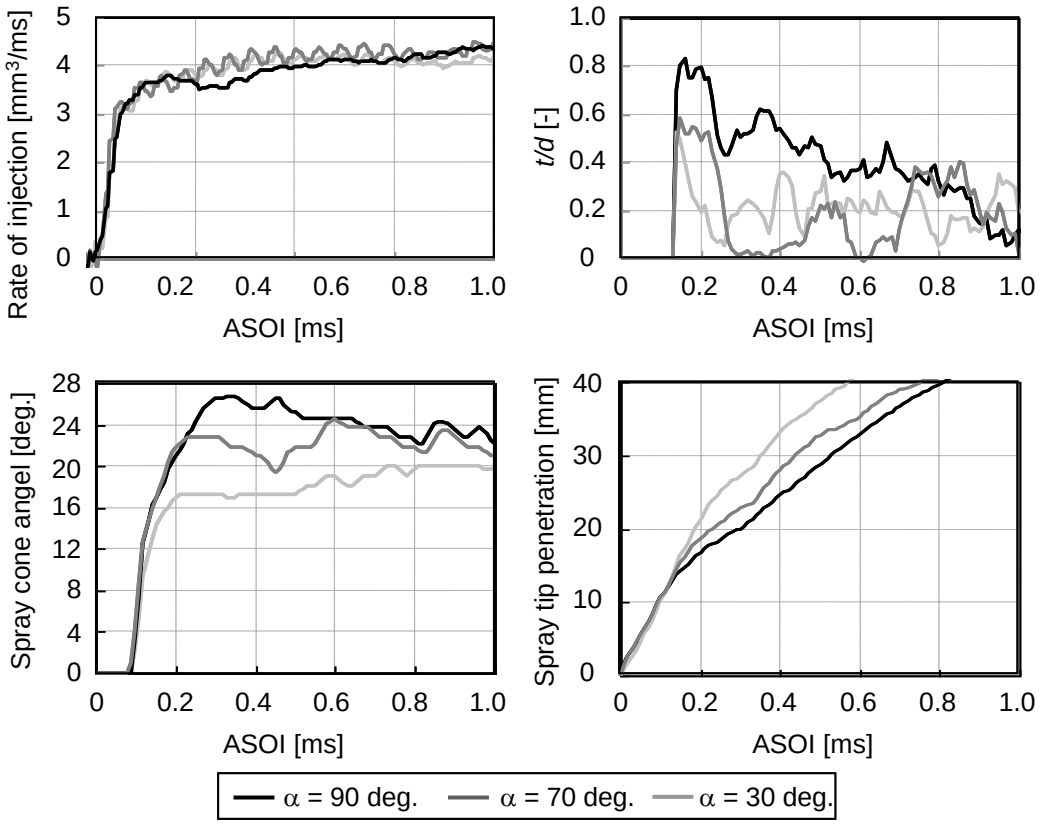

Fig. 11. Relation of string-type cavitation and spray characteristics

Conclusions

The relationship between the vortex flow, cavitation, and spray behavior of real-size diesel nozzle was analyzed by both experimental measurement and numerical simulation. In order to investigate the effect of the vortex flow by the shape of the needle tip, a flow was visualized by employing a transparent nozzle. The following conclusions were drawn:

1. The shape of the needle tip, which can control the vortex flow in the nozzle sac, was confirmed by the micro-PIV and CFD analysis of internal flow in the nozzle sac. In the nozzle with needle of small tip angle, the vortex flow was inhibited near the nozzle hole in the sac so that, the fuel near the sac inlet more smoothly flowed into the nozzle hole during the fuel injection. On the other hand, the large vortex flow in the nozzle sac was formed near the nozzle hole by the nozzle with the needle of large tip angle.
2. The weak vortex flow with the small angle of needle tip decreased the occurrence frequency of the cavitation in nozzle sac and the string-type cavitation thickness in nozzle hole. These results are suggested that the weak vortex flow unable to connect the string-type cavitation in the nozzle hole and another hole is not able to develop the string-type cavitation originating from swirling flow in the nozzle hole. Thus, the vortex in nozzle sac affects the string-type cavitation through the strength of the swirling flow in nozzle sac.
3. The small angle of the needle tip is caused for small spray cone angle, large spray tip penetration and stable rate of injection due to stable small string-type cavitation thickness. These results show that the spray characteristics are affected by the string-type cavitation: therefore, the vortex flow in nozzle sac affect the spray characteristics through the string-type cavitation behavior.

References

[1] Blessing M., Koning G., Kruger C., Michela U. and Schwarz V. (2003) Analysis of flow and cavitation phenomena in diesel injection nozzle and its effects on spray and mixture formation, SAE paper 2003-01-1358.

[2] Gavaises M. and Andriotis A. (2006) Cavitation Inside Multi-hole Injectors for Large Diesel Engines and Its Effect on the Near-nozzle Spray Structure, SAE Paper 2006-01-1114.

[3] Giancarlo C. and Fulvio P. (2013) Hole Cross Section Shape Influence on Diesel Nozzle Flow, SAE Technical Paper 2013-01-1609.

[4] Han J-S., Lu P-H., Xie X-B., Lai M-C. and Henein N. A. (2002) Investigation of diesel spray primary break-up and development for different nozzle geometries, SAE paper 2002-01-2775.

[5] Hayashi T., Suzuki M. and Ikemoto M. (2012) Analysis of Internal Flow and Spray Formation with Real size Diesel Nozzle, Proceeding of the 12th Triennial International Conference on Liquid Atomization and Spray Systems.

[6] Hayashi T., Suzuki M. and Ikemoto M. (2013) Effects of internal flow in a diesel nozzle on spray combustion, International Journal of Engine Research 2013 14: pp646-653.

[7] Kawamura K., Saito A., Katsumi N. and Ueda R. (1998) MEASUREMENT OF INJECTION RATE AT EACH HOLE OF VCO NOZZLE, Symposium (ILASS-Japan) on Atomization 7, pp271-276.

[8] Kim J-H., Nishida K., Shimizu M. and Hiroyasu H. (1998) Flow characteristics in a diesel injection nozzle under steady flow condition, Atomization, Vol. 7, No.18.

[9] Kurimoto N., Suzuki M., Yoshino M. and Nishijima Y. (2011) Response Surface Modeling of Diesel Spray Parameterized by Geometries Inside of Nozzle, SAE Technical Paper 2011-01-0390.

[10] Matsumoto M., Matsushima E. and Senda J. (2010) Clarification of Cavitation influence on spray atomization, the science and engineering review of Doshisha university, Vol.51, No.2.

[11] Sou A., Sugimura R. and Ohashi R. (2012) Cavitation Flow in Nozzle of Liquid Injector, Proceeding of the 12th Triennial International Conference on Liquid Atomization and Spray Systems.

[12] Roth H., Gavaises M. and Arcoumanis A., (2002) Cavitation initiation, Its development and link with flow turbulence in diesel injector nozzles, SAE paper 2002-01-0214.

Visualising injection events in a fully operational diesel injector with a multi-hole transparent tip.

M. Winterbourn[1], C.C.E. Soteriou[1], N. Mitroglou[2], M. Gavaises[2], C. Daveau[1]

[1]Delphi Diesel Systems Ltd, Courteney Road, Hoath Way, Gillingham, Kent, ME8 0RU, UK
E-mail: mark.winterbourn@delphi.com
Telephone: +44 (0)1634 874241

[2]School of Engineering and Mathematical Sciences, City University London, Northampton Square, EC1V 0HB, UK
E-mail: enquiries@city.ac.uk
Telephone: +44 (0)20 7040 5060

Abstract.

The fluid conditions between injections in the diesel nozzle sac have been the subject of some conjecture. The residual level of vapour/gas between injections can affect the initial phase of the injection event with regard to both the quantity and jet formation.
A study has been undertaken using a real size standard injector with a multi-hole transparent nozzle tip to investigate the characteristics before, during and after injection. These were visualised under realistic operating conditions for both single and multiple injection events.
The paper describes how the tip was designed, including the location of the metal/transparent boundary, fitting the transparent tip to the metal and the problems overcome in manufacturing and running the samples. Also included are results from a hydraulic test bench confirming the performance of the injector. Furthermore, the experimental procedure including clamping the tip to the injector, the lighting plan and high speed imaging from two directions simultaneously are detailed.
The results presented include images of the transient cavitation structures during injection and the evolution of the three phase mixture after injection. The trajectory of the needle valve is also shown.
Finally the paper discusses the insight gained from this study and the possible implications for future injector design and performance.

1. Introduction.

The diesel nozzle plays a crucial role in the quality of the combustion process. The conditions within the sac prior to injection, specifically the residual level of vapour/gas, can affect the initial phase of the injection both with regard to quantity and jet formation. These conditions have been the subject of some conjecture and study, usually using simulation.

In order to investigate and ascertain the transient characteristics before, during and after injection, a study has been undertaken using a real size standard injector with a multi-hole transparent nozzle. These were visualised under realistic operating conditions for both single and multiple injection events. Rather than attempting to put a window into a nozzle, the investigations were carried out using fully transparent nozzle tips [1]. This avoided known problems of visual access and lighting. The transparent tips were attached to a nozzle of a fully functioning injector.

The tips were manufactured in acrylic, due to the difficulties in machining the correct geometry in other materials, such as glass or crystal. There have been studies done using these more robust materials [2] but these have simplified geometry. Although the acrylic limited the maximum pressure that could be tested, it was felt that this was an acceptable compromise in order to achieve a nozzle geometry representative of a real component.

The injector used in the tests was a modified Delphi DFI1. Sample nozzles were manufactured and hydraulically tested by Delphi. The acrylic tips were manufactured and tested at City University, who had previous experience of manufacturing and testing real size transparent tips.

2. Experimental method.

2.1 Selecting the nozzle geometry.

Standard Light Duty nozzles have very small sacs, in order to reduce hydrocarbons. However, the small sac geometry would have made visualisation of the flows inside the sac more difficult. It was therefore decided to increase the size of the sac. The larger sac volume made visualisation easier but may have affected the delay between the needle opening and the spray emerging from the hole compared to a standard nozzle.

In order to check the design, some sample nozzles with the required geometry were manufactured and tested in injectors. ROI tests showed that performance was reasonable. Figure 1 is an example rate trace at 300bar for a logic pulse of 2ms.

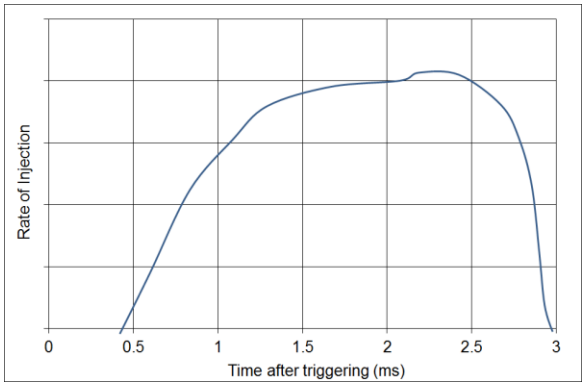

Fig. 1. Rate of injection at 300bar for 2ms logic pulse

2.2 Location of the nozzle/tip interface.

In order to visualise the flows, the whole of the tip would be transparent. This meant that the position of the interface between the metal nozzle and the acrylic tip had to be decided. There were three possibilities for this, see fig 2. The first possibility was above the needle valve seat line. This had the advantage of being able to visualise the whole seat region. However, it meant that the needle would impact on the transparent acrylic, which would not withstand the stress. The second possibility was below the seat, above the sac entry. This also allowed a large area to be visualised. The disadvantage was that aligning the seat line would be crucial, since a small difference would create a flow disturbance. The last option was to position the interface below the sac entry. This had the advantage that any minor misalignment would not disturb the flow, but the visualisation area would be very small. The advantages and disadvantages of each location were considered, along with ease of manufacture, and the “below the seat line” option was chosen.

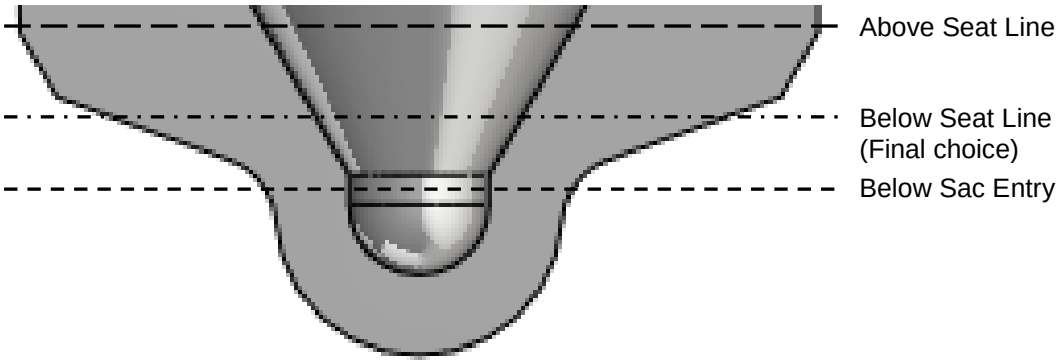

Fig. 2. The three possible locations for the nozzle/tip interface

2.3 Outer form of the tip.

Reproducing the external geometry of the metal nozzle was not required for the transparent tip. The curved outer surface would distort the internal view of the sac and holes and make loading the tip, to seal it against the nozzle, difficult. Therefore, the outer form of the tip in the sac area would have to be flat. However, we also wanted to visualise realistic sprays. The spray form is affected by the exit hole shape, so the curved surface of the nozzle had to be accurately replicated. These requirements suggested that a single geometry would not be adequate. The tip needed to combine flat and curved surfaces as appropriate. A “hybrid” design was developed which had a rectangular upper section for viewing the sac and holes. The middle section was curved to replicate the hole exit geometry. The lower section was cylindrical with a flat bottom to carry the load and for ease of manufacture, see fig 3.

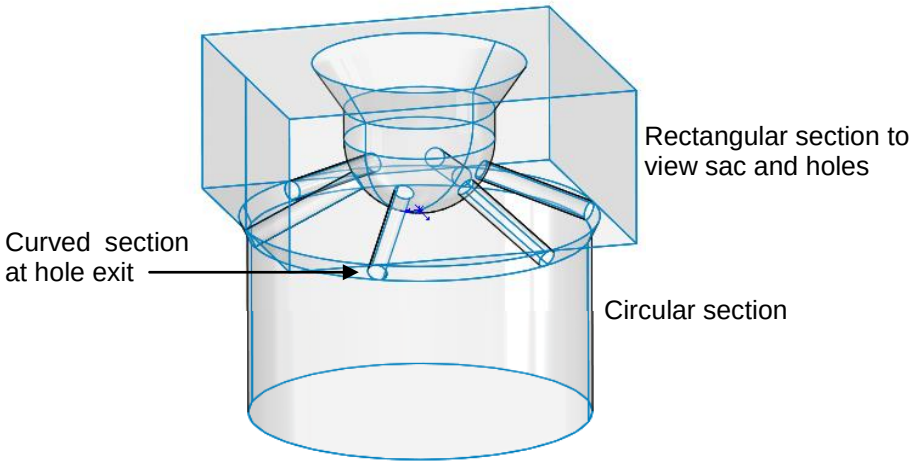

Fig. 3. The “hybrid” shape developed for the transparent tip

.

A problem was anticipated for this design, as shown in fig 4. The flow inside the end of the holes would be obscured by the curved section. This was judged to be an acceptable compromise in order to obtain representative sprays.

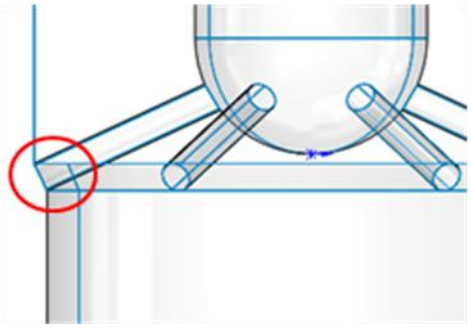

Fig. 4. The end portion of the hole would be obscured by the circular outer form of the tip

2.4 Aligning and attaching the tip.

Having chosen to attach the tip to the nozzle between the seat line and sac entry, it was crucial to get good alignment between the nozzle and the tip to avoid any flow disturbances. The sample nozzles with the experimental geometry were measured. Rather than attempting to measure the nozzle itself, dental impression paste was injected into the nozzle to get a positive mould of the internal geometry, see fig 5. This impression was measured to check the geometry was within tolerance and then used a reference for the transparent tips.

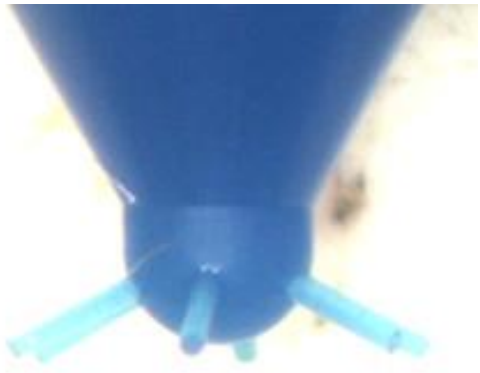

Fig. 5. Impression of the internal geometry of the sample experimental nozzle

In order to help with the alignment of the transparent tip, it was decided to leave a lip on the nozzle to positively locate it with reference to the nozzle set, see fig 6.

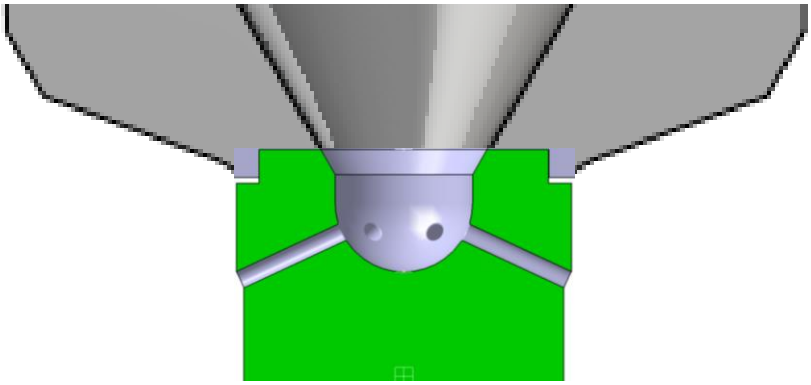

Fig. 6. Interface between the transparent tip and metal nozzle showing the lip

One of the first tips to be manufactured is shown in fig 7. Figure 7a shows the tip balanced on the fingertip to give an idea of scale. The close up view, fig 7b, clearly shows the hybrid external shape and the protrusion to fit into the the locating recess in the nozzle. The flat faces of this tip had not yet been polished to give good optical to the sac volume.

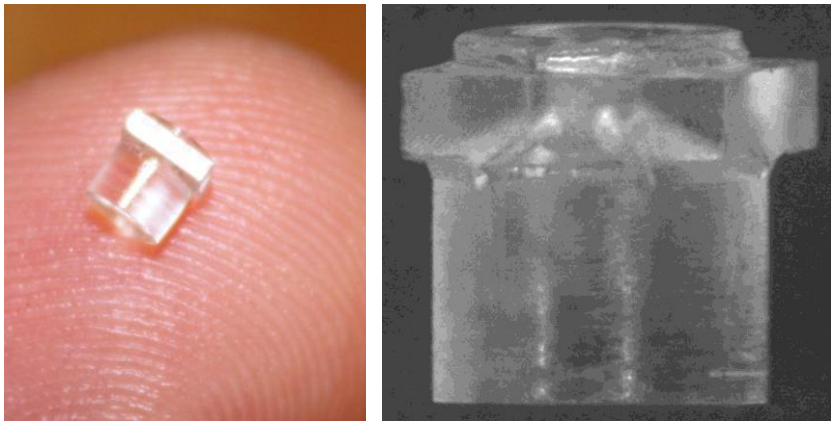

(a) (b)

Fig. 7. Pictures of one of the first transparent tips to be made, showing the external geometry

One of the sample nozzles was machined to remove the tip, fig 8. An apparatus was developed to enable us to attach the tips to the nozzle with an appropriate load to seal them and to take impressions.

Fig. 8. Sample nozzle with the tip machined off and recessed to allow attachment of transparent tip

An impression of one the first transparent tips to be manufactured is shown in fig 9a. This shows very poor alignment with the nozzle and poor sac geometry. It also shows that the holes were located in the wrong place in the sac, almost exiting from the bottom of the sac.

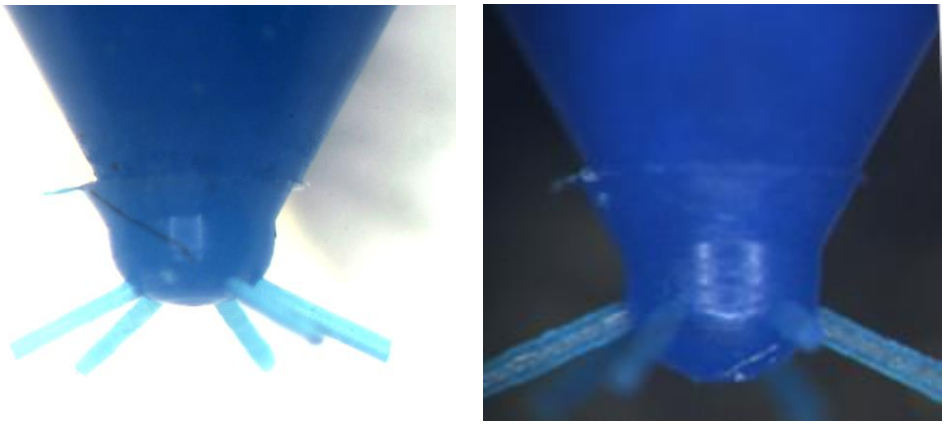

(a) (b)

Fig. 9. Impressions taken from transparent tips for (a) an early sample with bad alignment and poor sac shape and (b) better alignment and sac shape of an improved sample before honing

Various changes and improvements were then made to the manufacturing process in order to produce better tips. This included producing a special tool which machined the seat and sac geometry simultaneously. This had the benefit of maintaining very good consistency between tips. An impression of one of these tips is shown in fig 9b. The tip has much better alignment and a smoother interface between the tip and the nozzle. The sac geometry is also much closer to that required and the location of the holes is better. The impression was taken before the sample had been honed, so the holes in the picture have a rough appearance. Honing smoothed out many of the surface imperfections.

2.5 Hole shape.

The shape of the holes in the nozzle is very important. Nozzle holes in current diesel FIE are usually tapered with a larger diameter at the sac end, tapering to a smaller diameter at the nozzle exit. The hole entry has some degree of rounding which is achieved by a process called honing [11].

Initially, the transparent tips were going to be made with various levels of taper. However, it was found that this was not possible and only parallel holes were manufactured. The transparent tips were honed to give a similar amount of inlet rounding to the real nozzle.

Figure 10a shows the measurements taken from an impression of the real nozzle holes, clearly illustrating the taper. The measurements taken from impressions of a transparent tip prior to honing are shown in fig10b. While there is quite a lot of spread in the results and there is no taper, the general size is similar to the real holes.

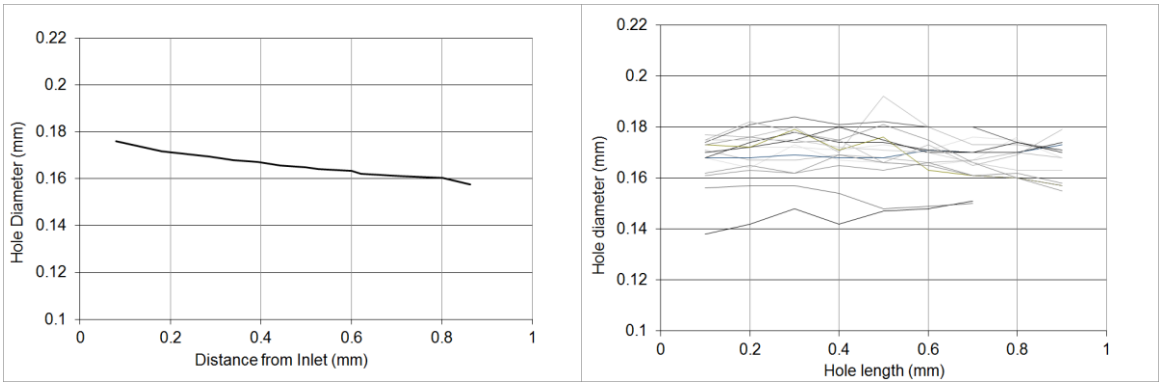

Fig. 10. (a) Average diameters taken from measurements of the hole profile of a real nozzle, (b) measurements of the hole profile from several transparent tips

The honing process produces rounding at the entry of the hole. Obviously, there is a big difference between honing a real metal nozzle and the transparent tip. The honing process had to be adapted, by trial and error, to give the same rounding on the transparent tips as the real nozzle. Figure 11a shows the rounding at the entry of the hole on an impression from a real nozzle, while fig 11b shows the equivalent from a transparent tip impression. These show that adapting the process was successful, with very similar levels of rounding on both parts.

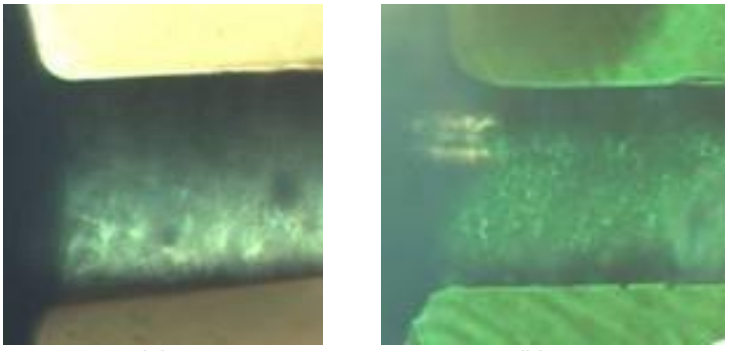

Fig. 11. Close up of the impressions from (a) a real nozzle and (b) a transparent tip showing the rounding at the hole entry

2.6 Sealing the tip.

During the tests the transparent tip would have to maintain contact with the nozzle and seal against leaks at the interface. The apparatus to achieve this is shown in fig 15. The injector and nozzle were clamped in place. The tip was then placed on the nozzle and held in place using an acrylic lever. The lever was made from acrylic so that the tip could be viewed from the bottom. The lever transmitted the force of an adjustable spring onto the tip. A large force was required to seal the interface between the transparent tip and the nozzle against the internal fluid pressure. However, too large a force could have resulted in distortion of the tip. A force of 240N was needed to seal the nozzle at 400bar.

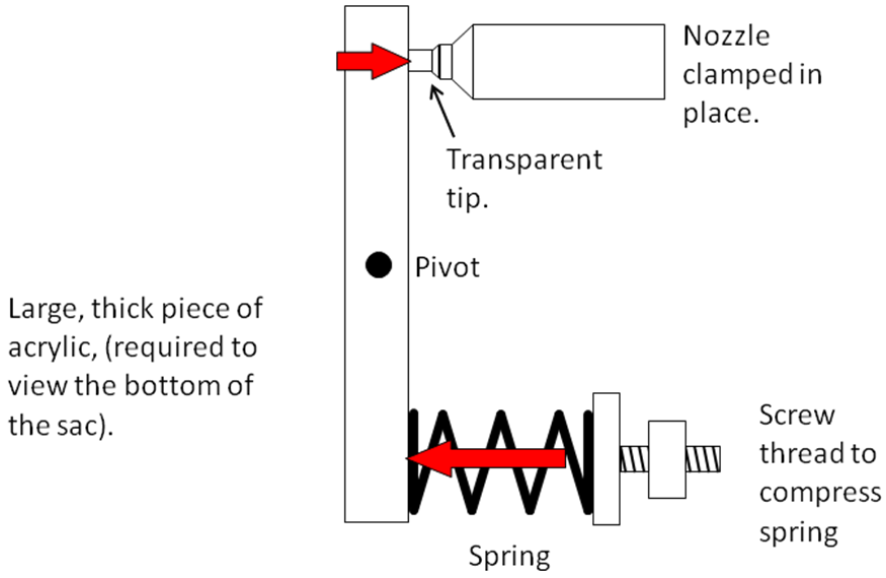

Fig. 15. Schematic of the apparatus to seal the transparent tip against the nozzle

2.7 Experimental setup.

The experimental setup is shown in fig 16 and fig 17. Figure 16 shows the clamped injector, (circled, left of picture, half way up) and the transparent tip held in place by the transparent lever. The 2 cameras and associated lights are also shown. The light was focused on to the tip using a variety of lenses, with glass filters to remove the heat before it was focused on the tip. The large funnel structure removed the atomized fuel and air from the area. Figure 17 is a close up view taken from fig 16. It shows the detail of the injector clamping and the transparent lever.

The two high speed cameras, which can be seen in the left half of fig 16, were synchronised to give views from the side and bottom simultaneously. The side view was lit from behind the tip and the bottom view was lit from the same side as the camera. Some visualisation was done which concentrated on the sprays. However, the developed sprays are not described in detail here. This is because their characteristics are strongly influenced by the hole shape, which on these samples is not typical of current diesel technology [11].

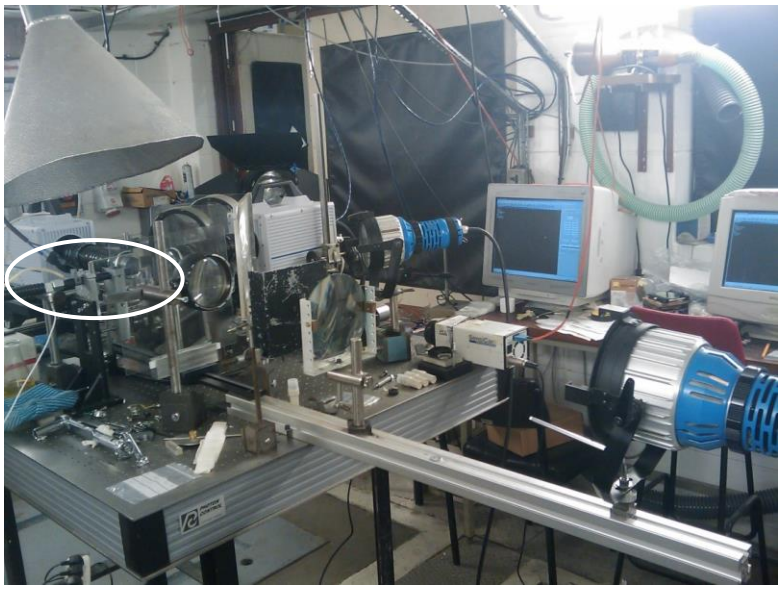

Fig. 16. Experimental setup at City University, with injector circled

Fig. 17. Close up of injector

2.8 Test parameters.

Originally the project had some ambitious goals. The maximum injection pressure was to be 500bar, with back pressure up to 20bar at room temperature. The maximum injection pressure was reduced to 400bar in the actual tests due to sealing problems. The back pressure was also reduced to atmospheric. This was due to the size of the sealing apparatus, which wouldn't fit in a test chamber.

Each injection slightly wears the tip. Previous tests have indicated that this wear results in a measurable change in geometry and visible opacity after approximately 100 injections. In these tests each tip was monitored and replaced when it showed any signs of wear. This was after 60-90 injections per tip. In all, 20 transparent tips were tested. For each tip the data were recorded as sets of 10 injections.

Results were recorded for single main injections and also for pilot/main injections. The logic pulse for the single injection was 2ms. The pilot/main injections had logic pulses of 0.5ms for the pilot and 1.5ms for the main, with a dwell of 1ms between them.

Frame rates for the high speed cameras were mostly 30,000fps, with some movies taken at 50,000 fps.

During the experiments, two transducers were used to monitor the system pressures, at the rail and injector-end HP pipe. The injector-end pipe pressure was recorded for every test to ensure that the injection pressure was consistent. The traces for one set of 10 injections are shown in fig 18. As can be seen, the pressure during injection is very consistent.

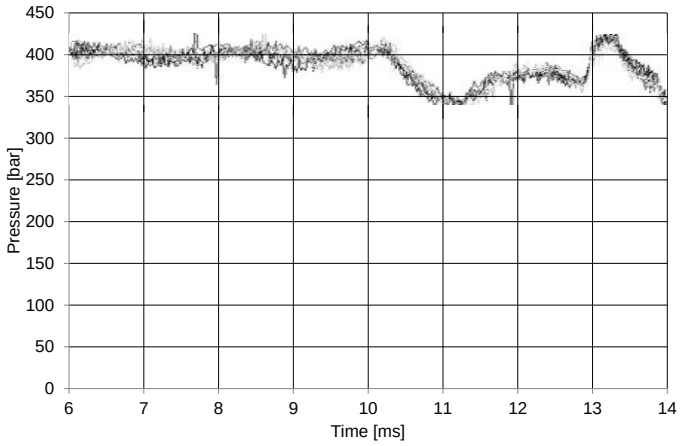

Fig. 18. Traces of injector-end HP pipe pressure for 10 consecutive injections

3. Results and discussion.

3.1 Needle lift.

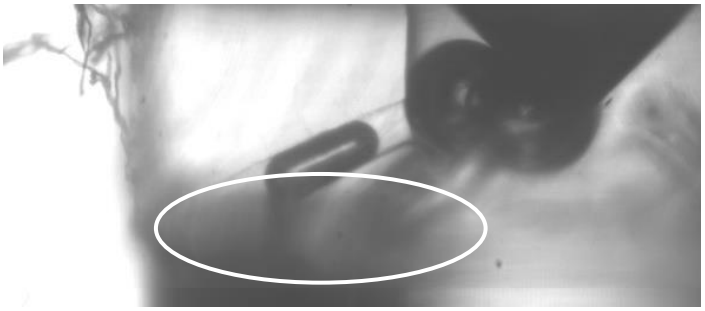

Fig. 19. Still taken from an injection movie prior to the start of injection

Figure 19 clearly shows the needle valve. It was possible to process the images so that outline of the needle was tracked throughout the injection, to give needle lift plots. The plots for 10 consecutive, single injection events at 300bar are shown in fig 20. In these results the lift has been normalised to the maximum lift recorded during the tests. The needle opening is quite slow due to the relatively low injection pressure. The bubbles that can be seen in the sac on fig 19 block the view of the needle position at the beginning and end of injection, causing more variability and uncertainty in these regions.

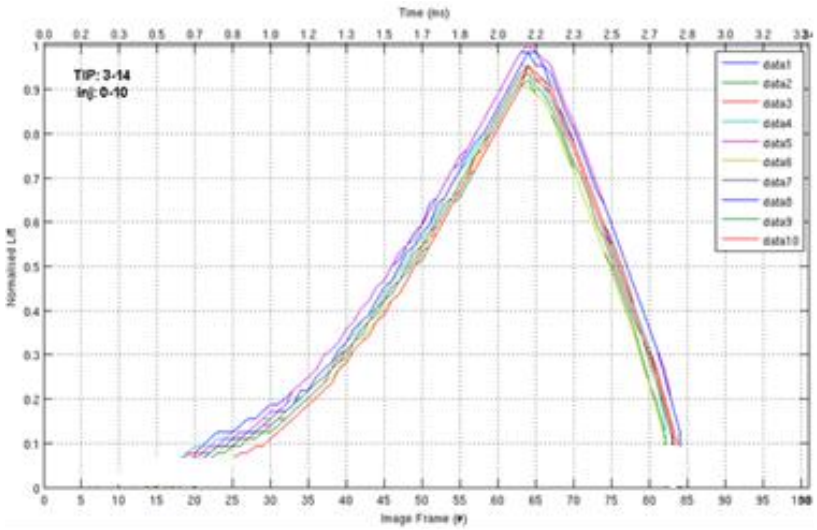

Fig. 20. Needle lift traces obtained by tracking the needle from 10 consecutive injections at 300bar, (details at the start and end of injection are not included as bubbles in the sac obscured the view)

The mean needle lift for 10 injections is shown in fig 21, plotted against time after triggering. Figure 21(a) shows the mean results for a single, main injection and 21(b) is a pilot/main injection sequence. It shows that the mean lift of pilot injection, (0.5ms) reaches about 10% of the maximum lift. Mean of main injection, (1.5ms) reaches about 70% of the maximum lift.

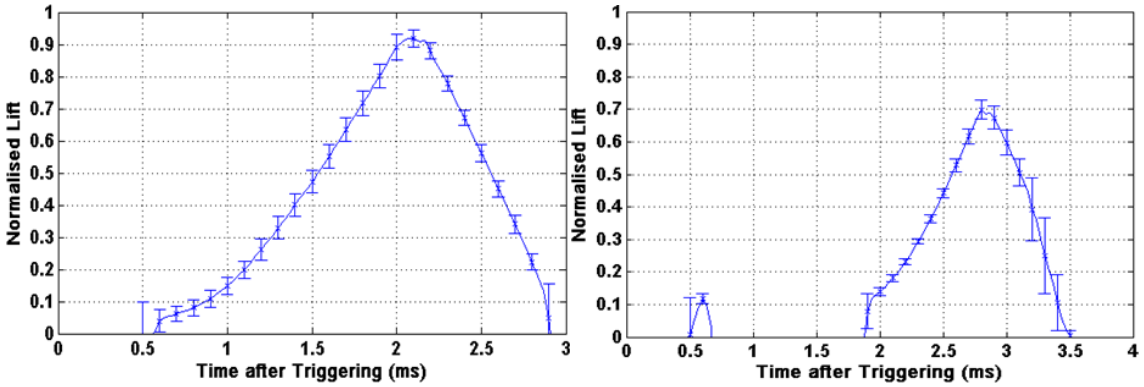

(a) (b)

Fig. 21. Mean traces for needle lift for both main, (a) and pilot/main, (b) injections

Figure 22 shows the lift results for 10 injections at 400bar. The needle opens faster and is able to spend some time at full lift due to the higher pressure. The bubbles in the sac made obtaining results for low lift particularly hard at this condition.

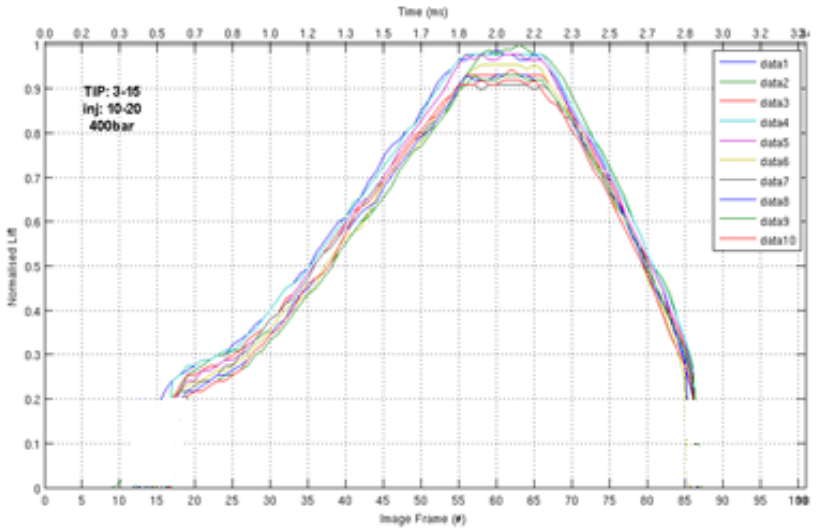

Fig. 22. Needle lift traces obtained by tracking the needle from 10 consecutive injections at 400bar, (details at the start and end of injection are not included as bubbles in the sac obscured the view)

3.1.1 Off-axis needle movement.

Significant off-axis, or lateral, needle movement has been seen in several nozzles in studies using x-ray phase contrast, [4], for example].

The transparent tip nozzle also allowed us to study the off-axis movement of the needle during the course of an injection, as well as any variation in the off-axis motion over 10 injections. There was no significant off-axis motion of the needle and the off-axis variation over a 10 injection series was no more than 3.5um. This shows that the path followed by the needle is extremely consistent.

3.2 300bar single injection – opening.

Figure 23 is a series of images showing the initial opening phase of a main injection at 300bar. Prior to the start of injection, all the movies showed liquid and large bubbles inside the sac and holes, fig 23(a). The fact that these were always on the same side of the injector is not significant, since the injector was operated horizontally and the bubbles always rose to the “top” of the sac. After the injection, all the movies showed a mixture of liquid and bubbles inside the sac and holes.

In a real injector, prior to the first injection in a cycle, it is unlikely that any liquid would be present since the high temperatures would burn off any two phase mixture left in the sac. However, it is likely that this mixture will persist between multiple injections. Therefore the initial conditions inside the sac before an injection will be different dependent where it is located in a multiple injection strategy.

In fig 23(b) the needle has started to move up and off its seat. As it moves, its displacement draws the bubbles up the sac and holes and towards the seat. There is no evidence of flow coming into the sac, because the volume of fuel displaced by the needle due to its movement is greater than the volume of flow coming through the seat restriction.

The volume of flow coming through the seat restriction has increased in fig 23(c), such that it is greater than the volume displaced by the needle. This flow distorts the top of the bubble in the sac. At the very top of the image there are some small bubbles just starting to enter the sac. This cavitation is what we would expect from previous CFD work, caused by very high velocity flow in the restriction between the needle and the nozzle body.

Figure 23(d) shows more small bubbles entering the sac from upstream. The bubble in the hole has moved down the hole towards the exit. Part of one of the bubbles from the sac has been pushed down the hole. The remaining large bubbles in the sac have started to break down into smaller bubbles.

In fig 23(e) liquid has started to emerge from the hole. More bubbles have been pushed out of the sac into the hole. They have moved further down the hole towards the exit. All of the large sac bubbles have broken down into much smaller bubbles.

In fig 23(f), the needle has lifted sufficiently such that large velocities are not generated in the seat restriction, so the small bubble cavitation is no longer entering the sac from upstream. The initial liquid injection from the hole has formed a mushroom head, followed by a weak flow of liquid and air from the hole. The bubbles in the hole have become stretched along the central axis. Some of the bubbles from the sac have entered the hole from the bottom of the entrance.

Figure 23(g) shows that the liquid spray has become stronger. The bubbles in the sac and holes consist only of small bubbles. The bubbles in the sac are rapidly vacating the sac through the holes.

In figs 23(h), (i) and (j) the spray becomes stronger and most of the bubbles have left the sac. Cavitation was formed at the bottom of the entrance to the hole.

In all these images the needle is still at a very low lift. The sequence then continues to higher lifts, with no bubbles remaining in the sac and geometric cavitation forming in the holes. Cavitation forming at the bottom of the entrance to the hole is normally seen at low lifts. However, in this nozzle the cavitation at the bottom of the hole was seen throughout the injection. This is connected to the shape of the holes on the transparent tips which, as previously mentioned, are not representative of a typical modern diesel nozzle. The flow patterns change very little as the injection progresses. Later in the injection, string cavitation formed within the sac. String cavitation is discussed in [3] [5] and [6].

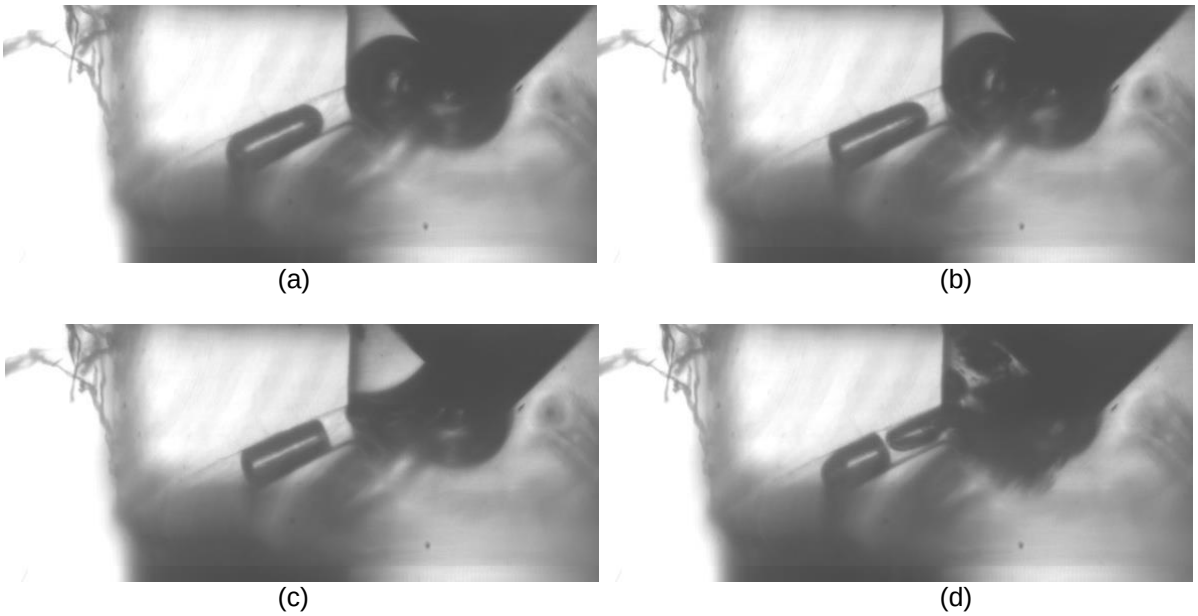

(a) (b)

(c) (d)

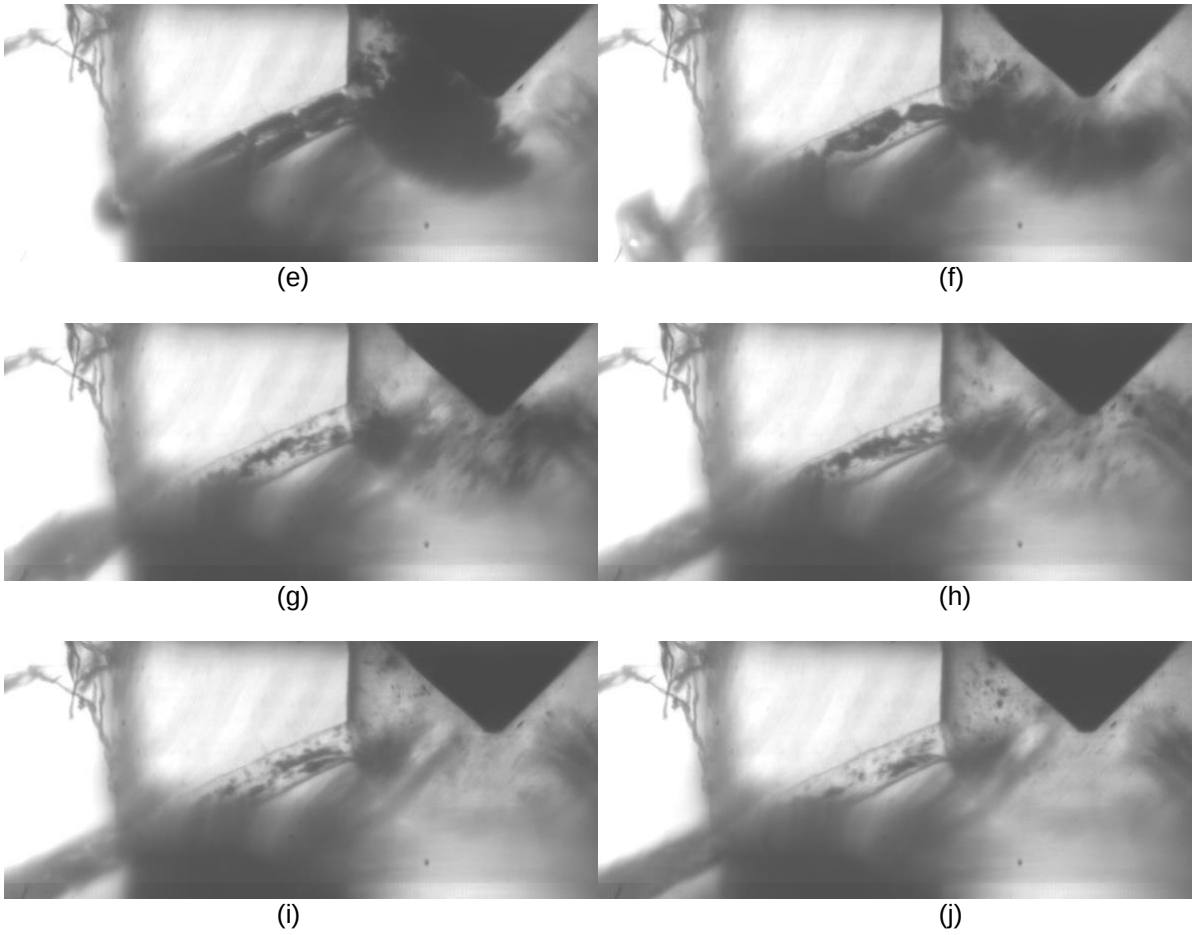

Fig. 23. Initial opening phase of a main injection at 300bar

3.2 300bar single injection – closing.

In fig 24(a) the needle has already closed most of the way to its seat. Just before it hits the seat, some small bubble cavitation can be seen entering the sac from upstream, for the reasons discussed above.

The needle has hit its seat in fig 24(b). The spray has continued out of the holes, which partially evacuates the sac and results in the sac starting to fill with bubbles. There is a central spiral, possibly hollow, along the axis of the hole, connected to the sac [7] [8] [9] [10]. Flow continues out of the hole after needle closure, as we have seen on CFD, but the spray is getting weak.

Figure 24(c) shows the spray has almost stopped and the sac has now filled with bubbles.

In fig 24(d) the spray has stopped. The hole has a large bubble in it and the sac has a large number of circulating bubbles. Given time, these coalesce into large bubbles. Other injections show very similar conditions in the sac at the end of injection, however there was a lot of variability in the conditions of the holes. Sometimes the holes were full of air, sometimes full of liquid and varying levels between

The two phase mixture was also seen in a study by Argonne National Labs, [12]. Several CFD studies of the transient injection event have been carried out internally, on different nozzle types, which have shown this two phase mixture at the end of injection.

(a) (b)

(c) (d)

Fig. 24. Closing phase of a main injection at 300bar

3.3 300bar pilot/main injection, between injections.

Prior to the pilot injection, the conditions in the sac shown in fig 25(a), were similar to those prior to a single main injection without pilot, fig 23(a), consisting of a few large bubbles. However, the conditions inside the sac prior to the second injection, fig 25(b), consisted of a lot of small bubbles, similar to those after a main injection, fig 24(d). The small bubbles had not had enough time to coalesce into large bubbles. It was clear that there was a difference in the sac conditions before a single main injection and an injection after a pilot. However, it was not possible to see any differences between the formation of the sprays for these two cases.

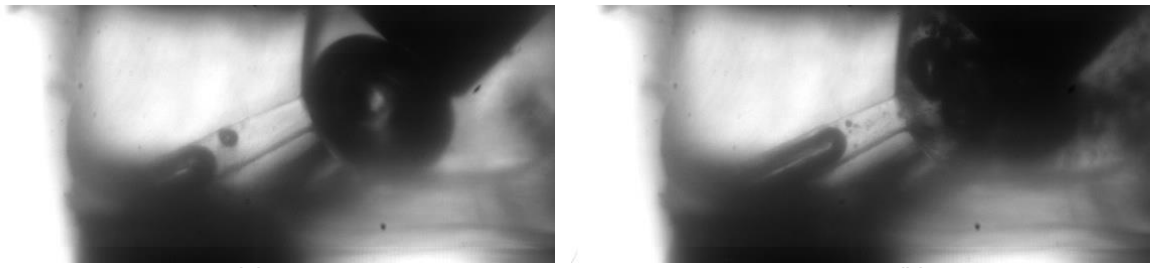

(a) (b)

Fig. 25. Conditions in the sac and holes prior to (a) a pilot injection and (b) injection after pilot

Further study of fig 25(b) showed that there appeared to be fewer bubbles in the sac than compared with fig 24(d). Many other injections were then studied and it was found that there were consistently fewer bubbles in the sac after a pilot than after a main. To illustrate this, 2 frames were processed with adjusted brightness and contrast to increase the appearance of the bubbles. Figure 26(a) is the same frame as fig 25 (b), which is 1ms after the pilot has finished. Fig 26(b) is 1ms after the main injection has finished. It is clearly shown that there are fewer bubbles in the sac after a pilot, fig 26(a), than after a main injection, fig 26(b).

As with a single main injection, there was a lot of variability in the conditions within the holes both prior to the pilot and prior to the main injection.

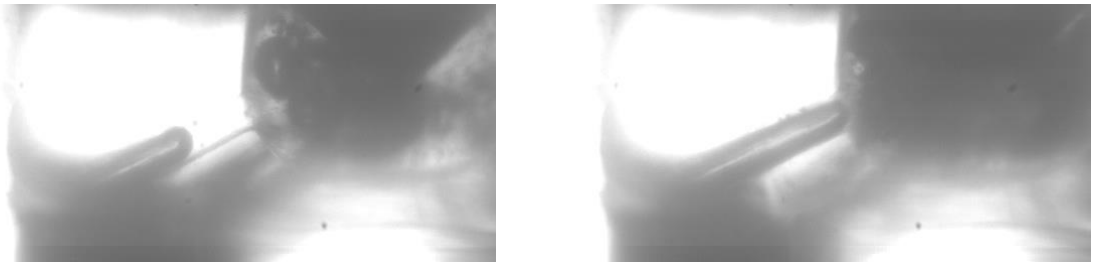

(a) (b)

Fig. 26. Conditions in the sac 1ms after the (a) pilot injection and (b) the main injection. Note that the brightness and contrast of both these images has been adjusted to highlight the bubbles.

3.4 Tests at 400bar.

Results were also taken at 400bar for both single injections and pilot/main injections. The results were very similar to the 300bar case, with no significant differences.

4. Main discussion points.

There are several factors in these results that are relevant to the performance and design of real injectors.

Before discussing those points, mention should be made of two features which are somewhat different from those with standard equipment running on an engine. Firstly, it is likely that between injection cycles on an engine, the two phase mixture in the holes and sac would evaporate. Therefore the details seen in the transparent sac at the start of an injection cycle are not directly relevant to the hot running conditions on an engine. Secondly, the geometry of the holes, (lack of realistic taper) means that at high needle lifts, the flow patterns within the holes are unrealistic.

The most important information to come out of this project relates to the details at the beginning and at the end of the injection events, as well as in between the pilot and the main injections. These details are relevant to the performance and design of real injectors.

When the needle first lifts, there is a delay between the needle leaving its seat and flow entering the sac. This in turn causes a further delay to the fuel leaving the holes. This effect is due to the volume displacement of the needle.

After a pilot, the sac is filled with a mixture of small bubbles and fuel. For a subsequent injection, this mixture may persist under normal engine conditions and influence the initial filling of the sac and holes. The difference between having a fully evacuated sac and a sac containing a two phase mixture may also influence the formation of the spray plumes.

The conditions in the sac after injection will have relevance to the combustion process, and in particular to the level of unburned hydrocarbons (UHC) in the emissions. One of the implications of the work described in this paper is that the two phase mixture in the sac will strongly depend on the injector dynamics at the end of injection. A fast needle closure with no bounce will maintain momentum in the fuel leaving the holes. This in turn will encourage more complete sac evacuation, where most or all of the fuel in the sac after needle closure exits the sac as part of the normal injection. This is likely to produce lower UHC emissions. With pilot injection, there is no high momentum of the flow with less needle displacement to encourage sac evacuation. Hence more fuel will remain in the sac, potentially to contribute to the level of UHC in the emissions.

The results shown in this paper give an indication of this, but they are at low injection pressure. At high pressure, it is likely that the phenomenon will be much more marked.

In normal engine running it is common to see higher levels of HC at light load and with multiple small injections. This fact supports the hypothesis above regarding the link between injector closing dynamics, sac evacuation and UHC emissions.

4. Conclusions.

1. When the nozzle opens, injection is delayed due to needle displacement out of the sac.
2. When the nozzle closes, the fuel continues to flow out of the sac and holes under its own momentum and is augmented by the needle displacement during closure.

   a. The sac is therefore partially evacuated, leaving a two-phase mixture.
   b. Between injection cycles on an engine, it is likely that any remaining fuel will evaporate, leaving only vapour/gas in the sac for the start of the next injection cycle.
   c. Between multiple injections on an engine, the two phase mixture may persist, giving different conditions in the sac at the start of the second and subsequent injections. This may influence performance.
3. A deduction from these results is that more complete sac evacuation at the end of injection is likely to reduce UHC emissions.
4. A further deduction is that an injector with fast needle closure, giving a positive end of injection is likely to increase sac evacuation at the end of injection, and thereby result in lower UHC emissions.

References.

[1] Blessing, M. et al., 2003. Analysis of Flow and Cavitation phenomena in Diesel Injection Nozzles and its Effects on Spray and Mixture Formation 2003-01-1358, s.l.: SAE Technical Paper Series.

[2] Butcher A J, Aleiferis P G, and Richardson D. Development of a real-size optical injector nozzle for studies of cavitation, spray formation and flash-boiling at conditions relevant to direct-injection spark-ignition engines. International Journal of Engine Research December 2013 14: 557-577, first published on October 1, 2013 doi:10.1177/1468087413497004

[3] Gavaises, M. et al., 2009. Characterization of String cavitation in Large-Scale Diesel Nozzles with Tapered Holes, s.l.: American Institute of Physics; Physics of Fluids, 21

[4] Kastengren A, Powell C F, Liu Z, Fezzaa K and Wang J. High-speed x-ray imaging of diesel injector needle motion. *Proceedings of the ASME Internal Combustion Engine Division Spring Technical Conference*, Paper ICES2009-76032 (2009).

[5] Mitroglou N and Gavaises M. Mapping of cavitating flow regimes in injectors for medium-/heavy-duty diesel engines. International Journal of Engine Research December 2013 14: 590-605, first published on October 24, 2013 doi:10.1177/1468087413500491

[6] Mitroglou N, McLorn M, Gavaises M, Soteriou C and Winterbourn M. (2014). Instantaneous and ensemble average cavitation structures in Diesel micro-channel flow orifices. Fuel, 116, pp. 736-742. doi: 10.1016/j.fuel.2013.08.060

[7] Soteriou C C E, Andrews R J & Smith M. Cavitation, Hydraulic Flip and Atomization in Direct Injection Diesel Sprays. C465/051/93 IMechE Conference - Experimental and Predictive Methods in Engine Research and Development, London, Nov 1993.

[8] Soteriou C, Andrews R & Smith M. Direct Injection Diesel Sprays and the Effect of Cavitation and Hydraulic Flip on Atomization. SAE 950080. SAE Congress 1995, Detroit.

[9] Soteriou C, Andrews R, Smith M, Torres N and Kunkulagunta R. Through the Diesel Nozzle Hole – a Journey of Discovery. ILASS Americas, Dearborn MI, May 2001.

[10] Soteriou C, Andrews R, Smith M, Torres N and Kunkulagunta R. Through the Diesel Nozzle Hole – a Journey of Discovery II. ILASS Europe, Zurich, September 2001.

[11] Soteriou C, Lambert M, Zuelch S and Passerel D. The Flow Characteristics of High Efficiency Diesel Nozzles with Enhanced Geometry Holes. Thiesel 2006.

[12] Swantek A B, Duke D, Tilocco F Z, Sovis N, Powell C F, Kastengren A L. End of injection, mass expulsion behaviors in single hole diesel fuel injectors. 26th Annual Conference on Liquid Atomization and Spray Systems, Portland, OR, May 2014.

Cavitation in Mini-Sac Nozzle and Injected Liquid Jet

Raditya Hendra Pratama[1], Akira Sou[1], Yoshitaka Wada[2], Hideaki Yokohata[2]

[1]Graduate School of Maritime Sciences. Kobe University. 5-1-1, Fukaeminami, Higashinada, Kobe 658-0022 Japan.

E-mail: sou@maritime.kobe-u.ac.jp
Telephone: +(81)-78-431-6294
Fax: +(81)-78-431-6294

[2]MAZDA Motor Corporation. Japan.

E-mail: wada.yos@mazda.co.jp
E-mail: yokohata.h@mazda.co.jp

Abstract. Improvement and control of fuel spray characteristics in a diesel engine is necessary to increase thermal efficiency and reduce exhaust gas emissions. It has been pointed out that cavitation occurs in a nozzle of a fuel injector and affects the injected spray characteristics. A large effort has been paid to understand a turbulent cavitating flow in a mini-sac nozzle, which has a complicated geometry and a variable needle lift. In this study, an experiment is carried out to visualize unsteady cavitation and to measure flow in a sac of simple two-dimensional scale-up mini-sac nozzles with an asymmetric transverse inflow flowing through a sac inlet corner, various needle lifts, various distance between the corner and the nozzle to understand the effects of the upstream geometry on cavitation and an injected liquid jet. Visualization by using a digital camera and a flash light is conducted to obtain images of cavitation and the jet with a high spatial resolution. High speed visualization is conducted to clarify the effects of the upstream flow on cavitation and the liquid jet deformation. Particle Image Velocimetry (PIV) analysis is carried out to investigate the flow pattern in the sac. The results show that (1) long distance L_{SN}/W from the upstream sac corner to the nozzle and high needle lift S/W reduce the lateral inflow velocity component, which decreases cavitation thickness and, therefore, liquid jet angle, and (2) a large inlet velocity fluctuation above the inlet edge of the nozzle caused by the sac inlet corner at short distance L_{SN}/W induces the wavy surface of the super cavitation film and hydraulic flip, and large fluctuations in cavitation thickness and length, and finally suppresses the large decrease in liquid jet angle at hydraulic flip.

Notation

L	*Nozzle length.*	V	*Mean velocity in nozzle.*
L_C	*Cavitation length.*	W	*Nozzle width.*
L_{SN}	*Distance between needle seat edge and nozzle.*	$W_C(x)$	*Cavitation width.*
S	*Needle lift (mini-sac nozzle).*	Z	*Needle lift (VCO nozzle).*
x	*Downward position from the inlet.*	θ	*Jet angle.*

1. Introduction

Optimization of fuel spray distribution and enhancement of fuel spray atomization in diesel engines enable us to increase the thermal efficiency and to reduce exhaust gas emissions. Since cavitation occurring in a nozzle of a fuel injector plays an important role in fuel atomization, a large effort has been paid to understand cavitation in a symmetric single hole nozzle [5, 9, 10]. Through the visualization of two-dimensional (2D) symmetric single nozzle, basic cavitation patterns and mechanism to induce its liquid jet deformation at super cavitation were clarified [5]. However, cavitation in multi-hole nozzle injectors, such as Valve-Covered-Orifice (VCO) nozzles and mini-sac nozzles, shows a complicated and asymmetric behaviour [1-4, 6-10]. Iida et al. [6] observed an asymmetric cavitation using 2D sac nozzle. By focusing on the effects of an asymmetric inflow on cavitation and the jet, the authors visualized cavitation in 2D nozzles with an asymmetric inflow and

various needle lifts to clarify the increases in cavitation thickness and liquid jet angle by the decrease in needle lift [11]. Figure 1(a) represents the geometry of a mini-sac nozzle. The differences between the VCO and mini-sac nozzles are the sac volume and the sac inlet corner upstream of the nozzle. In a multi-hole mini-sac nozzle, nozzle holes are located at various distance from the sac inlet corner. Although the corner and the distance between it and the nozzle may affect cavitation and the jet, its effects have not been understood yet.

In this study, cavitation in some 2D nozzles shown in Fig. 1 (b) with the upstream corner is visualized. We vary its distance from the corner to the nozzle and needle lift. Injection pressure is varied to observe the cavitation pattern under various mean velocities V in the nozzle. High speed images are taken to investigate the unsteady cavitation which affects liquid jet deformation. Particle Image Velocimetry (PIV) analysis is carried out to examine the flow pattern in the sac with various distances and needle lifts.

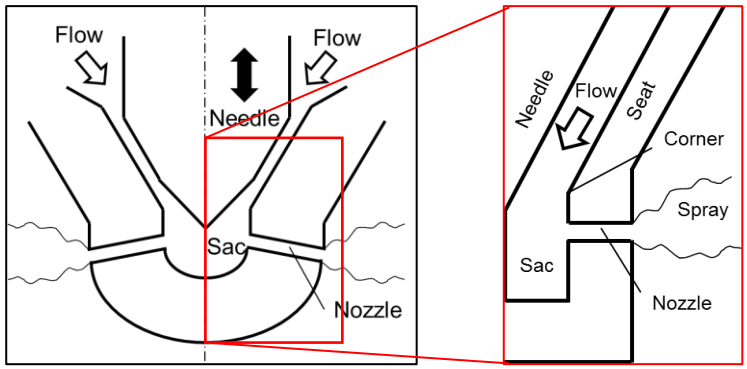

(a) Schematic of mini-sac nozzle (b) 2D Model nozzle

Fig. 1. Mini-sac nozzle and the present model nozzle

2. Experimental Setup

Figure 2 represents the schematic picture of experimental setup. Filtered tap water at 30 $\pm$ 0.5 ^{o}C in temperature is injected into ambient air through various mini-sac model nozzles. High spatial still images of cavitation and a liquid jet are captured using a digital cameras (Nikon D800) and a flash lamp (Nisshindenki Co., Micro Flash Stroboscope, MS-1000/LH-15M, 2-4 μs in duration). A high-speed image of cavitation is taken using Photron FASTCAM SA-X2 (87137 fps) and a metal-halide lamp (Kyowa Co. Ltd., MID-25FC).

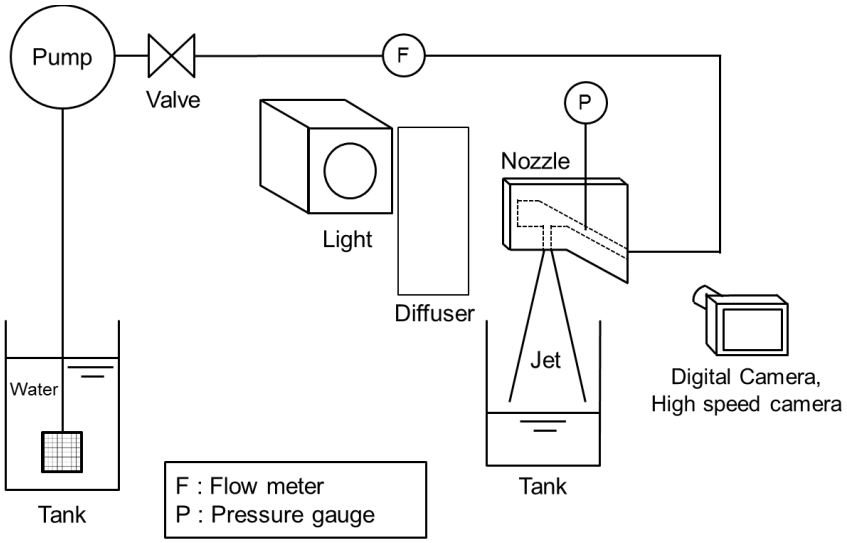

Fig. 2. Schematic of experimental apparatus

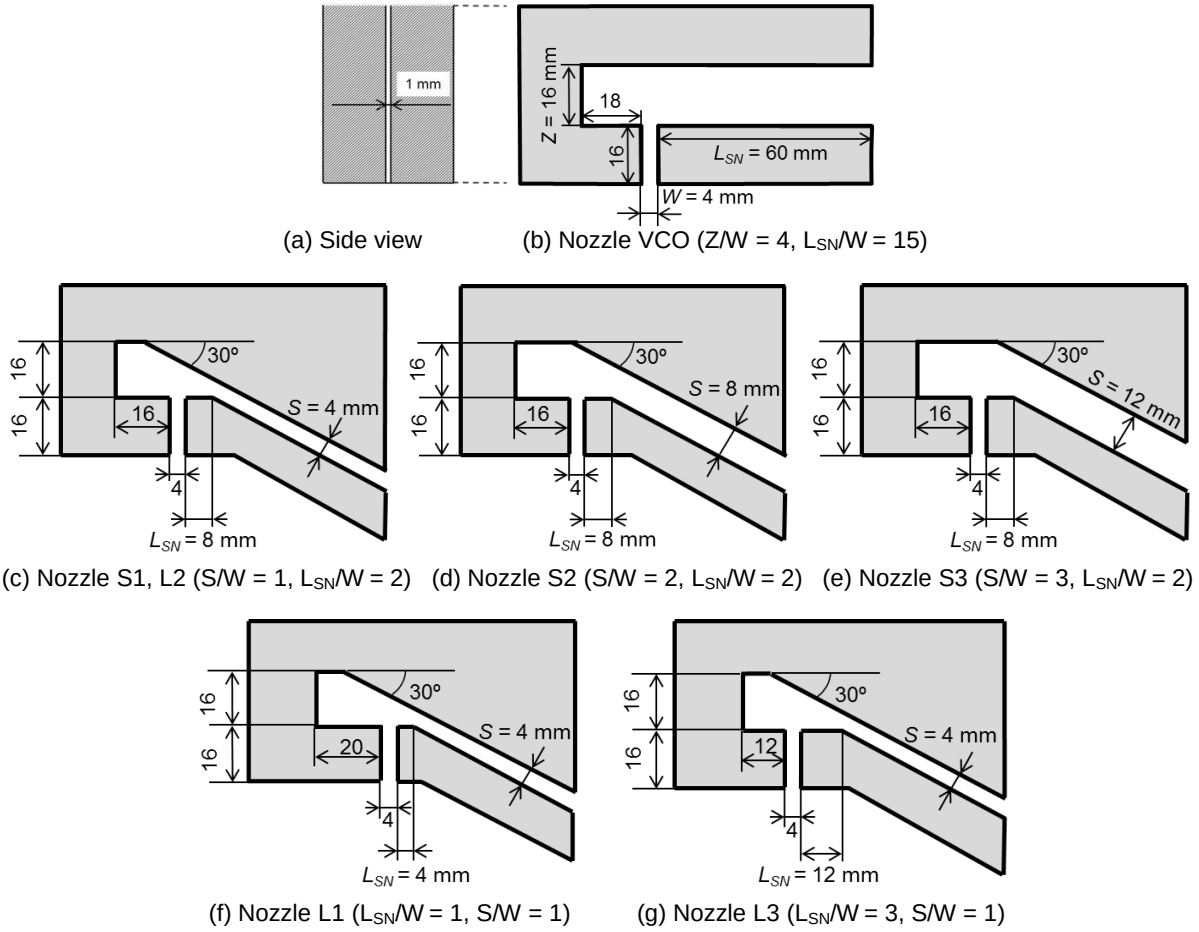

(a) Side view (b) Nozzle VCO (Z/W = 4, L_{SN}/W = 15)

(c) Nozzle S1, L2 (S/W = 1, L_{SN}/W = 2) (d) Nozzle S2 (S/W = 2, L_{SN}/W = 2) (e) Nozzle S3 (S/W = 3, L_{SN}/W = 2)

(f) Nozzle L1 (L_{SN}/W = 1, S/W = 1) (g) Nozzle L3 (L_{SN}/W = 3, S/W = 1)

Fig. 3. Mini-sac model nozzles

Table 1. Dimensions of the nozzles

Nozzle	L [mm]	W [mm]	Z [mm]	S [mm]	L_{SN} [mm]	Z/W	S/W	L_{SN}/W
VCO	16.0	4.00	16.0	-	60.0	4.0	-	15.0
S1, L2	16.0	4.00	-	4.0	8.0	-	1.0	2.0
S2	16.0	4.00	-	8.0	8.0	-	2.0	2.0
S3	16.0	4.00	-	12.0	8.0	-	3.0	2.0
L1	16.0	4.00	-	4.0	4.0	-	1.0	1.0
L3	16.0	4.00	-	4.0	12.0	-	1.0	3.0

We manufactured six simplified 2D nozzles shown in Fig. 3 in order to investigate the effects of the upstream corner at the end of the seat, the distance between the corner and the nozzle, and the needle lift. The nozzle consists of the stainless steel thin flat plates to form the side walls and front and back plates made of transparent acrylic plates. The width W, length L and thickness of the nozzles are 4.00 mm, 16.0 mm, and 1.0 mm, respectively. The inlet edges of the nozzles were made to be sharp whose radius of the curvature are less than 30 micrometers. The three nozzles shown in Figs. 3 (c), (d) and (e) have medium distance L_{SN} of 8.0 mm between the corner and the nozzle (L_{SN}/W = 2) and low needle lift (clearance S between the seat and the needle is 4.0 mm, S/W = 1), medium needle lift (S/W = 2) and high needle lift (S/W = 3), respectively. The other set of the nozzles shown in Figs. 3 (f), (c) and (g) have low needle lift (S/W = 1) with short distance (L_{SN}/W = 1), medium distance (L_{SN}/W = 2) and long distance (L_{SN}/W = 3), respectively. The nozzle shown in Fig. 3 (b) has no corner in the upstream (L_{SN}/W = 15), which represents VCO nozzle with 16.0 mm in needle lift Z as a reference

nozzle to examine the effects of the corner. Table 1 summarizes the principal dimensions of the nozzle used in the present experiment.

Tracer particles with 50 μm in mean diameter are introduced into the water for Particle Image Velocimetry (PIV) analysis to measure the flow field above the nozzle, whose height is 1.6 mm and the width is 8.0 mm, by taking its image with 150 x 750 pixels and 100000 fps, so that the spatial resolution is 11 μm/pixel, The interrogation window size is set to be 33 x 33 pixels, and the search window is 81 pixels in the PIV analysis through the sensitivity analysis on the both window sizes.

3. Results and Discussion

Figure 4 shows the cavitation in the nozzles with various needle lifts S and mean velocities V in the nozzle. Cavitation appears mainly along the right wall and its thickness is as thick as half of the nozzle width W due to the major inflow from the right. Cavitation inception occurs near the right inlet edge. It extends downstream with mean velocity V, and reaches almost to the exit, which is called super cavitation [2, 9]. Further increase in V results in the imperfect hydraulic flip (IHF) [8], at which cavitation reaches the exit. The length L_C of the cavitation along the right wall decreases and the small cavitation at the left inlet corner slightly increases with increasing needle lift ratio S/W due to the decrease in the lateral inflow velocity from the right.

Figure 5 shows the image of the cavitation together with the injected liquid jet near the nozzle. The liquid jet deforms asymmetrically due to the asymmetric inflow. The left interface of the jet is almost straight without spreading outward only with small waves. The right interface deforms largely especially at super cavitation with low needle lift ratio (S/W = 1) due to the thick cavitation along the right wall reaching near the exit, and does not deform largely at imperfect hydraulic flip [11]. The jet deforming structure is slanted due to the higher velocity at the left and the lower at the right [11].

Figure 6 shows the cavitation and the jet with various distance ratios L_{SN}/W and velocities V. Similar trends on cavitation and jet are observed. In the 2D VCO nozzle without a upstream corner ($L_{SN}/W = 15$), cavitation film near the inlet at super cavitation and hydraulic flip is smooth and steady along the outer edge of the separated boundary layer. Cavitation near the inlet at super cavitation is unsteady with wavy surface especially at the short distance ratio of $L_{SN}/W = 1$ due to the unsteady inflow induced by the corner. For shorter L_{SN} ($L_{SN}/W = 1$), a thicker and longer cavitation appears due to the higher lateral inflow, which enhances a larger jet deformation.

Length L_C of cavitation along the right wall normalized by the nozzle length L as well as its standard deviation are plotted against the mean velocities V in Figs. 7 and 8. As shown in Fig. 7, L_C/L and its fluctuation are larger at smaller lift ratio S/W due to a larger lateral inflow velocity with a stronger fluctuation. As shown in Fig. 8, L_C/L is larger at smaller distance ratio L_{SN}/W since the height of the sac over of the nozzle is higher to allow the inflow from the top rather than from the right. It should be noted that for the 2D VCO nozzle with $L_{SN}/W = 15$ the fluctuation in L_C/L is smaller than those of the mini-sac nozzles with an upstream corner.

Figures 9 and 10 show the jet angle θ and its standard deviation. Jet angle θ is measured at 16 mm downstream from the nozzle exit. The jet angle θ increases with mean velocity V unless hydraulic flip is formed [11]. For the nozzle with lower needle lift ratio S/W and shorter distance ratio L_{SN}/W, jet angle θ is larger due to the larger lateral upstream velocity and the larger fluctuation in the cavitation length. Note that the decrease in jet angle θ at hydraulic flip is drastic for the VCO nozzle without a corner due to the smooth and steady interface of the cavitation. At low lift S/W = 1, not only jet angle θ but also its fluctuation are drastically larger than those for the higher lift nozzles.

The thickness W_C of cavitation along the right wall at super cavitation is measured at various downward positions x from the inlet. Figure 11 shows the cavitation thickness ratio W_C/W and its standard deviation with various needle lift ratios S/W and distance ratios L_{SN}/W. The figures clearly show that the nozzles with smaller needle lift ratio S/W and shorter distance ratio L_{SN}/W result in a thicker cavitation due to the larger lateral inflow velocity at the right inlet edge, which clearly explains the reason of the longer cavitation length L_C/L and the larger jet angle θ. The fluctuation in cavitation thickness W_C/W at low lift S/W is larger than that at higher S/W, and that at shorter distance L_{SN}/W is slightly larger than that at larger L_{SN}/W. Note that the fluctuation in W_C/W for the VCO nozzle without a corner ($L_{SN}/W = 15$) is almost zero near the inlet ($x < 6$ mm).

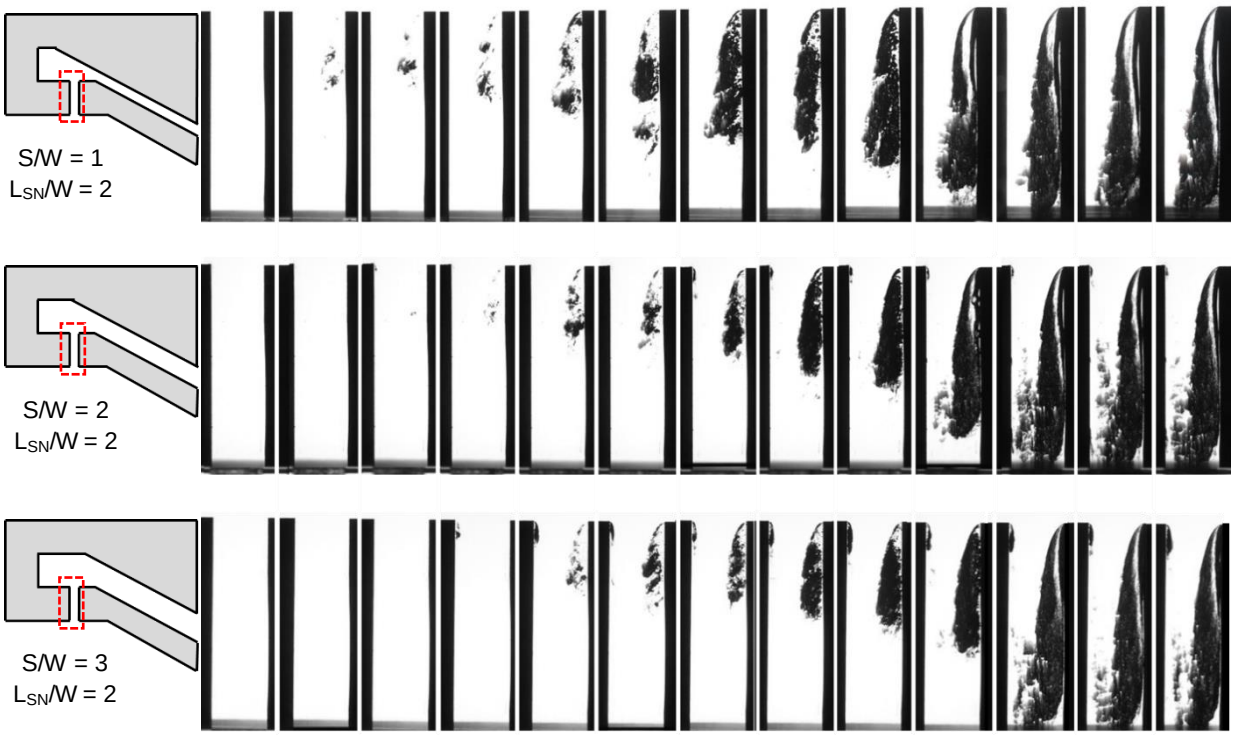

Fig. 4. Cavitation in mini-sac nozzle with various needle lift ratios S/W and mean velocities V

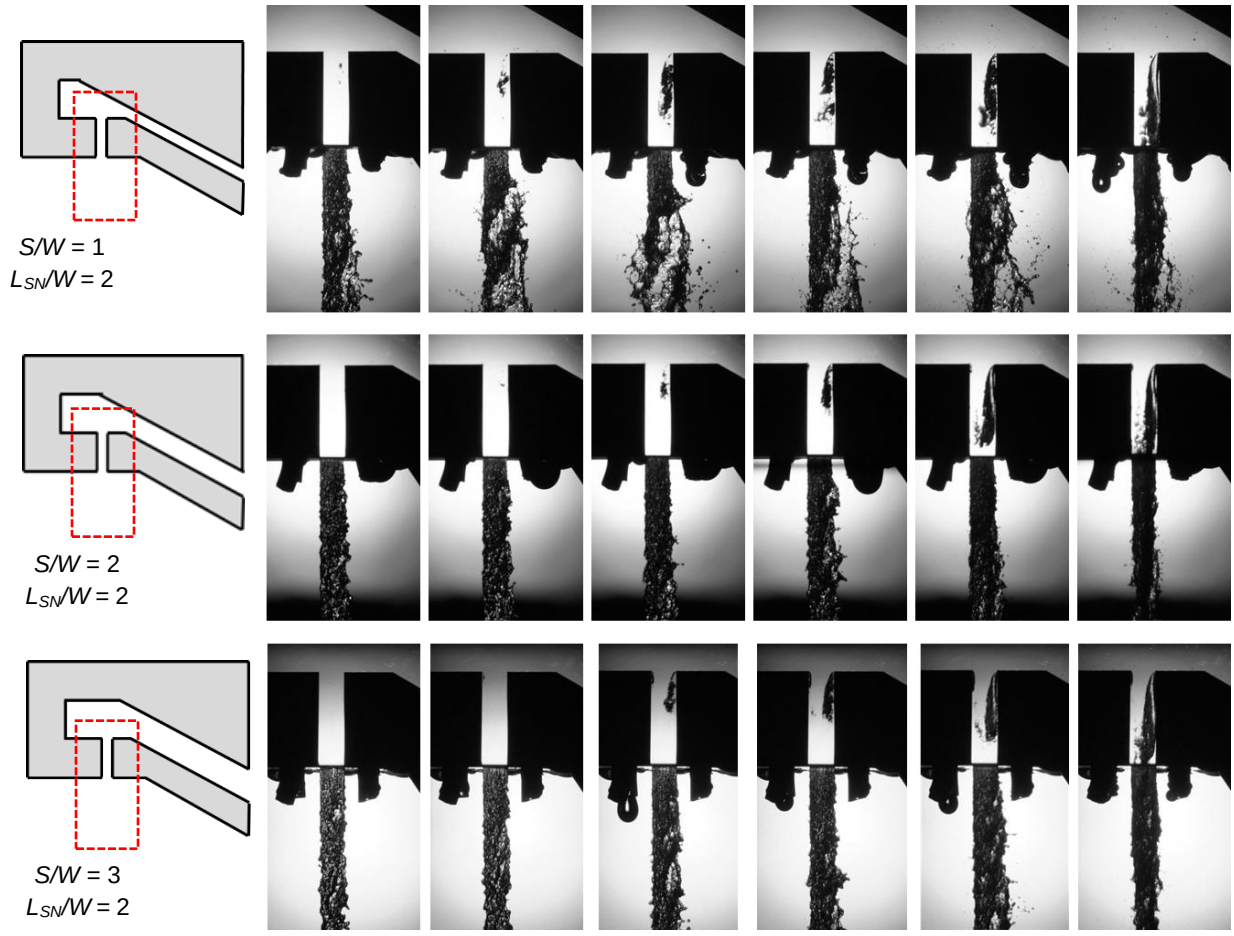

Fig. 5. Cavitation and jet in mini-sac nozzle with various needle lifts ratios S/W and mean velocities V

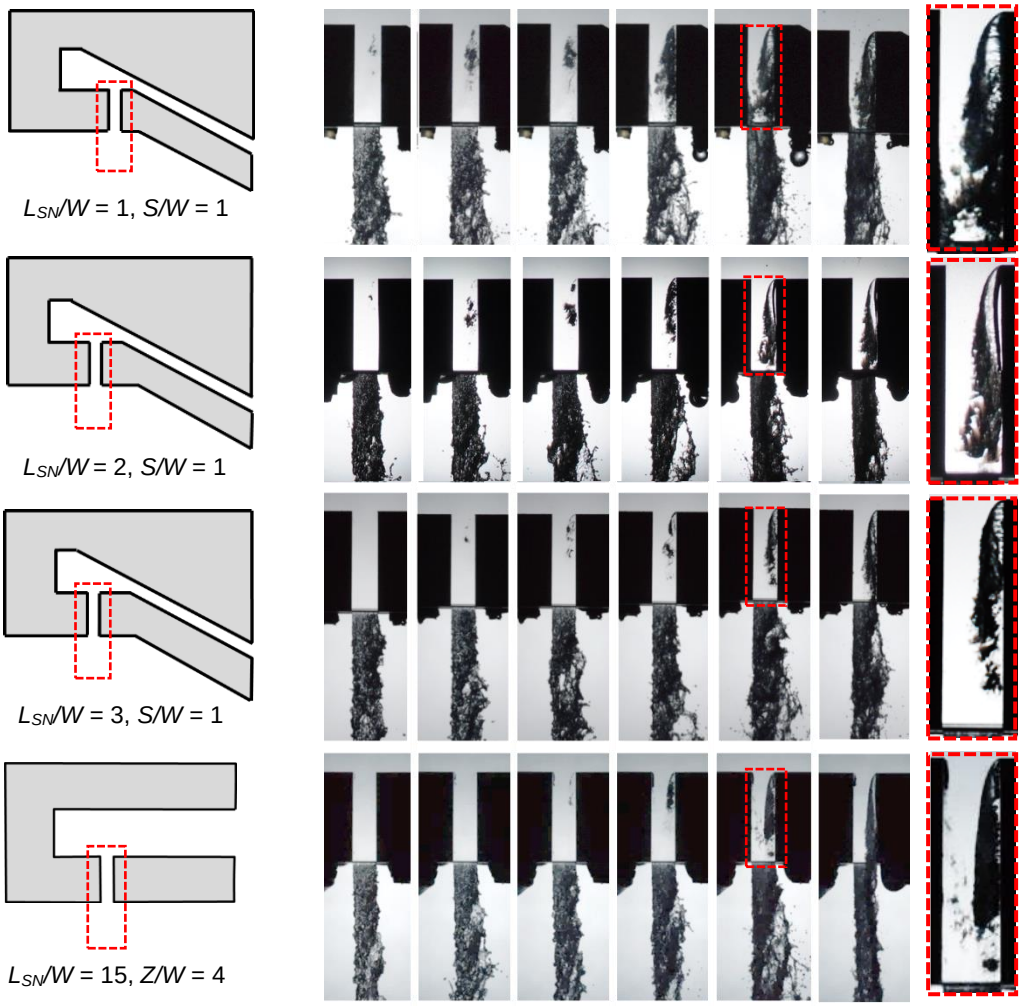

Fig.6. Cavitation and jet in mini-sac nozzle with various distance ratios L_{SN}/W and mean velocities V

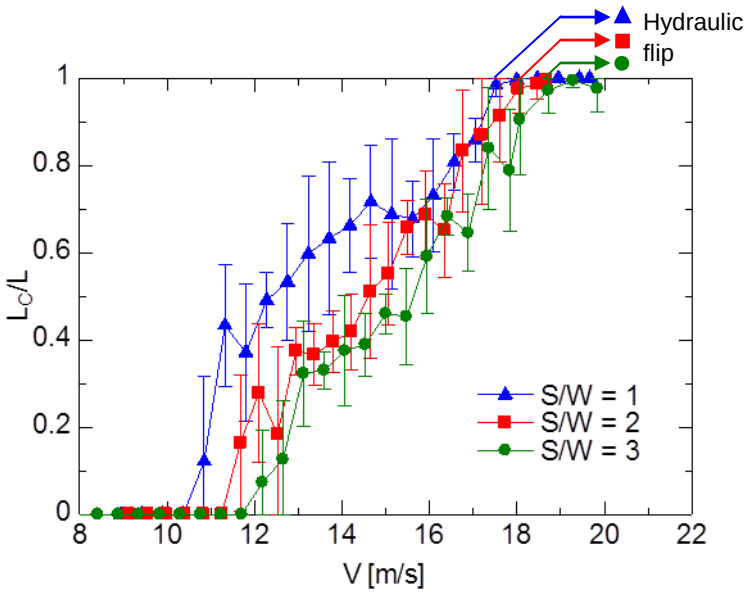

Fig. 7. Cavitation length ratio L_C/L versus mean velocity V with its standard deviation at various needle lift ratios S/W (L_{SN}/W = 2)

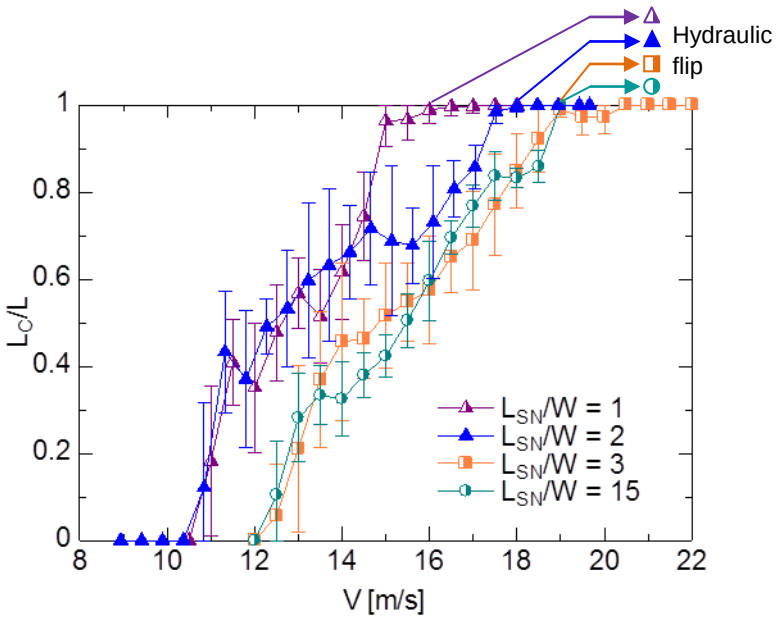

Fig. 8. Cavitation length ratio L_C/L versus mean velocity V with its standard deviation at various distance ratios L_{SN}/W (S/W = 1)

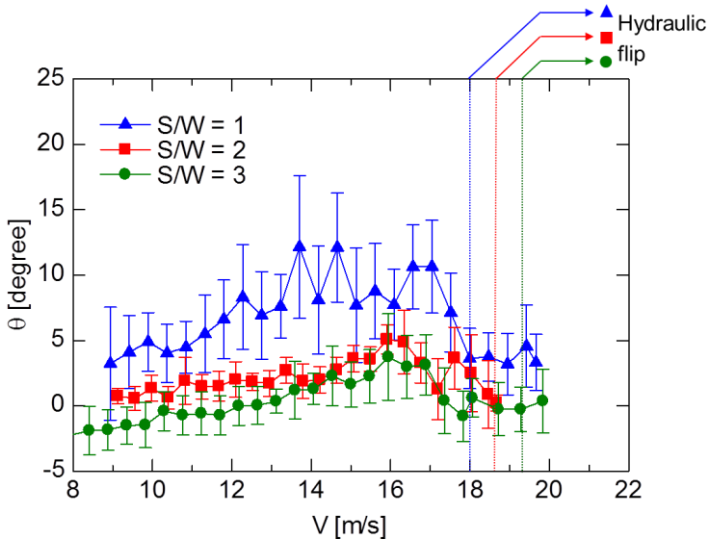

Fig. 9. Jet angle θ versus mean velocity V with its standard deviation at various S/W

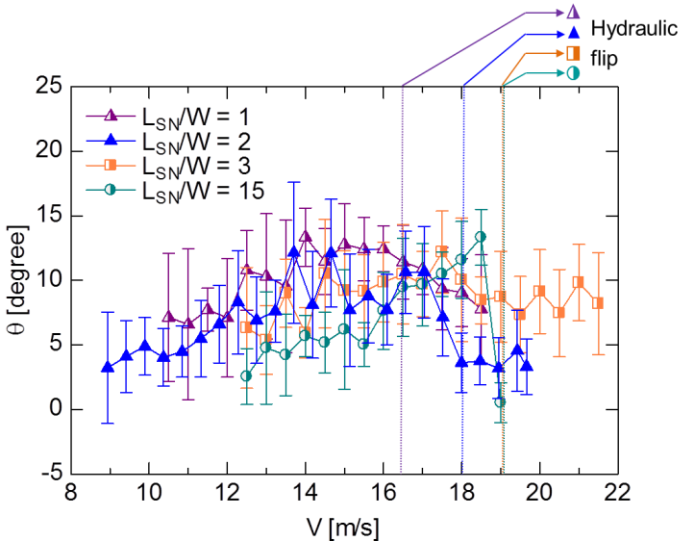

Fig. 10. Jet angle θ versus mean velocity V with its standard deviation at various L_{SN}/W

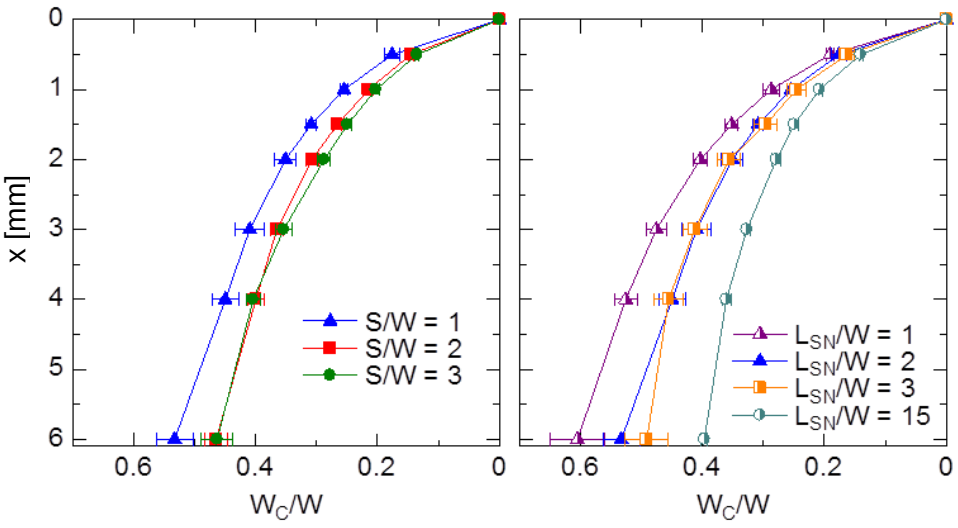

(a) Effect of S/W (b) Effect of L_{SN}/W

Fig. 11. Cavitation thickness ratio W_C/W with its standard deviation at super cavitation under various S/W and L_{SN} conditions

Figure 12 shows an example of a high speed image of super cavitation for low lift of S/W = 1, short distance of $L_{SN}/W = 2$ and V = 16.6 m/s. The image was captured with 87137 fps so that the images with 11.48 μs in time interval can be achieved to clearly observe transient behavior. In this paper images are presented every 20 pictures. Cavitation length gradually extends downstream with time and decreases with the shedding of a cavitation cloud or the collapse of cavitation. The fluctuation takes place every about 1 to 2 ms. It was reported in the previous paper [11], that cavitation near the inlet edge in the 2D VCO nozzles without an upstream corner consists of a large transparent film attached to the inlet and does not change in time. As shown in Fig. 12, in the mini-sac nozzles with an upstream corner cavitation near the inlet edge is not steady and the film may collapse.

Image analysis for the high speed image shown in Fig. 12 was conducted to measure the time history of void fraction in the region between 0.7 L and 0.8 L near the exit. The region was carefully select to represent the fluctuation in cavitation length. The original pictures for the period of 5.75 ms were converted to binary images by carefully determine the threshold and the void fraction in the region were calculated. Figure 13 shows calculated cavitation fraction for S/W = 1, $L_{SN}/W = 2$ and V = 16.6 m/s. The result shows the fluctuation pattern of the void fraction, that is, large cavitation clouds are shed with a long interval (about 1 to 2 ms) and a partial collapse of the tail of the cavitation occurs with a short interval (about 0.3 to 1 ms). The large cavitation shedding frequency agrees with that of the explosive liquid jet deformation, and that of the partial cavitation collapse with that of small-scale jet interface deformation.

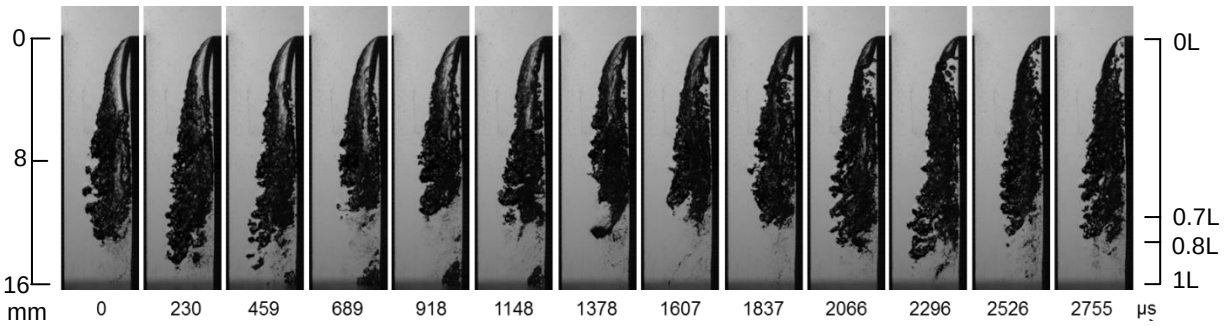

Fig. 12. High speed image of cavitation in the mini-sac nozzle (S/W = 1, $L_{SN}/W = 2$, V = 16.6 m/s)

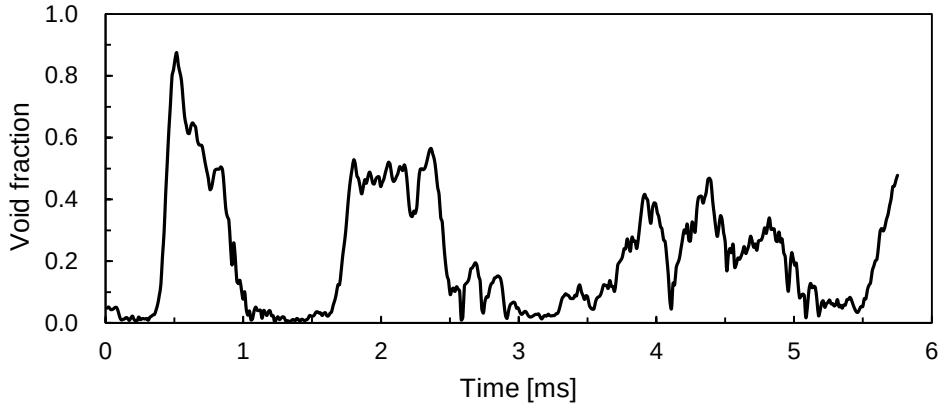

Fig. 13. Cavitation fraction in the area between 0.7L and 0.8L from the nozzle inlet (S/W = 1, $L_{SN}/W = 2$, V = 16.6 m/s)

In order to clarify the larger lateral inflow velocity near the inlet edge in the cases of shorter distance ratio L_{SN}/W, liquid velocity distribution above the right inlet edge for L_{SN}/W = 1 and 3 are obtained by PIV analysis and shown in Fig. 14 (a) and (b), respectively. The needle lift ratio S/W is 1 and the mean velocity V in the nozzle is 15.0 m/s (super cavitation) for the cases. Each velocity vector is the average value of more than 90 velocities excluding some error velocities obtained from 100 high speed images of 100000 fps. Time interval between a pair of the PIV images is 10 μs. The result clearly points out that the velocity above the right inlet edge at the shorter distance of L_{SN}/W = 1 has a larger magnitude and a larger lateral velocity component. It can also be seen from the velocity fields that the thickness of the boundary layer above the sac wall is thicker for the shorter distance of L_{SN}/W = 1. These results clearly confirm the reasons of the thick cavitation and the resulting large jet angle in the small L_{SN}/W = 1.

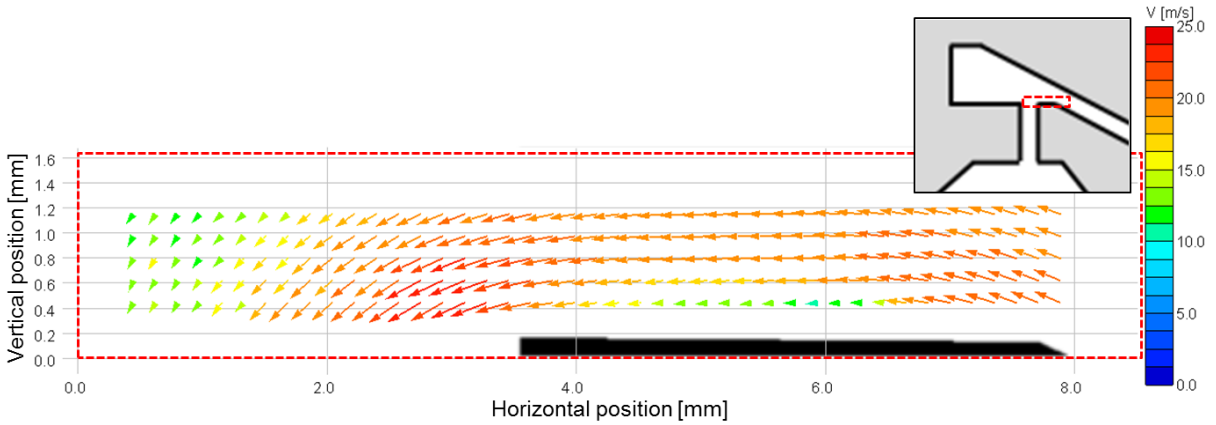

(a) L_{SN}/W = 1

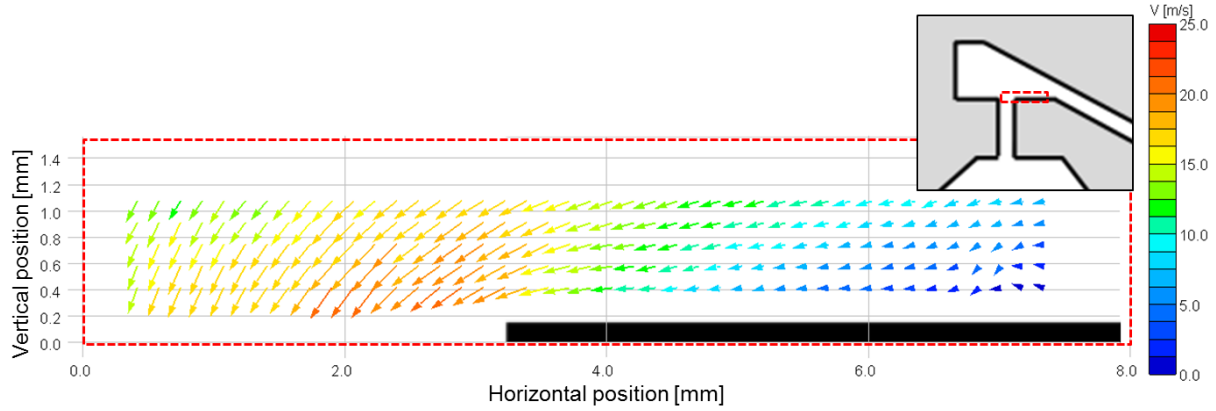

(b) L_{SN}/W = 3

Fig. 14. Velocity field in mini-sac (L_{SN}/W = 1 and 3, S/W = 1, V = 15.0 m/s)

Conclusions

In order to examine the effects of the corner upstream of the nozzle for mini-sac nozzle and the distance between the sac inlet corner and the nozzle, a visualization of a cavitation and the discharged liquid jet into the ambient air as well as PIV analysis were conducted using some 2D mini-sac model nozzles with various needle lift ratios S/W and various distance ratio L_{SN}/W. As a result, the following conclusions were obtained. (1) Long distance L_{SN}/W from the upstream sac corner to the nozzle and high needle lift S/W reduce the lateral inflow velocity component, which decreases cavitation thickness W_C/W and, therefore, liquid jet angle θ. (2) A large inlet velocity fluctuation above the inlet edge of the nozzle caused by the sac inlet corner at short L_{SN}/W induces the wavy surface of the super cavitation film and hydraulic flip, and large fluctuations in cavitation thickness and length, and finally suppresses the large decrease in liquid jet angle at hydraulic flip.

References

[1] Andriotis A, Gavaises M and Arcoumanis C (2008) Vortex Flow and Cavitation in Diesel Injector Nozzles. Journal of Fluid Mechanic: Vol. 610. pp 195-215.

[2] Chaves H, Ludwig Ch (2005) Characterization of Cavitation in Transparent Nozzles Depending on the Nozzle Geometry. Proceedings of ILASS 2005: pp 259-264.

[3] Chaves H, Miranda R and Knake R (2007) Particle Image Velocimetry Measurements of the Cavitating Flow in a Real Size Transparent VCO Nozzle. Proceedings of ICMF 2007: S4_Mon_C_6.

[4] Hayashi T, Suzuki M and Ikemoto M (2012) Visualization of Internal Flow and Spray Formation with Real Size Diesel Nozzle. Proceedings of ICLASS 2012.

[5] Hiroyasu H, Arai M and Shimizu M (1991) Break-up Length of a Liquid Jet and Internal Flow in a Nozzle. Proceedings of ICLASS 1991: pp 275-282.

[6] Iida H, Matsumura E, Tanaka K, Senda J, Fujimoto H and Maly RR (2000) Effect of Internal Flow in a Simulated Diesel Injection Nozzle on Spray Atomization. Proceedings of ICLASS 2000: pp 345-350.

[7] Miranda R, Chaves M, Martin U and Obermeier F (2003) Cavitation in a Transparent Real Size VCO Injection Nozzle. Proceedings of ICLASS 2003.

[8] Soteriou C, Andrews R, Torres N, Smith M and Kunkulagunta R (2001) Through the Diesel Nozzle Hole - A Journey of Discovery II. Proceedings of ILASS-Europe 2001.

[9] Sou A, Hosokawa S and Tomiyama A (2007) Effects of Cavitation in a Nozzle on Liquid Jet Atomization. International Journal of Heat and Mass Transfer: 50-17-18: pp 3575-3582.

[10] Sou A, Hosokawa S and Tomiyama A (2010) Cavitation in Nozzles of Plain Orifice Atomizers with Various Length-to-Diameter Ratios. Atomization and Sprays: 20-6: pp 513-524.

[11] Sou A, Raditya HP, Tomisaka T and Kibayashi S (2012) Cavitation Flow in Nozzle of Liquid Injector. Proceedings of ICLASS 2012.

Effect of Needle Lift on Atomization in Diesel Fuel Spray

K. Komada[1], H. Tajima[2], D. Tsuru[2], D. Sakaguchi[1] and H. Ueki[1]

[1]Graduate School of Engineering, Nagasaki University, 1-14 Bunkyo-machi Nagaski, Japan.

E-mail: komada@nagasaki-u.ac.jp
Telephone: +(81) 95 819 2526
Fax: +(81) 95 819 2534

[2]Kyushu University. Japan

E-mail: tasima@ence.kyushu-u.ac.jp
Telephone: +(81) 92 583 7592
Fax: +(81) 92 583 7593

Abstract. Temporal and spatial changes in the velocity and size of droplets of diesel fuel sprays were investigated near the nozzle orifice and was correlated with the needle valve lift of the injector nozzle. A laser 2-focus velocimeter (L2F) was used for measurements of velocity and size of droplets. The L2F has a micro-scale probe which consists of two foci. The focal diameter is about 3μm, and the distance between two foci is 17μm. The data sampling rate of the L2F system was markedly high as 15MHz. Fuel sprays were injected intermittently into the atmosphere by using a common rail injector. The orifice diameter of the injector was 0.112mm and the rail pressure was 40MPa. The periods of solenoid energizing were set at 0.5, 1.0 and 1.5ms. Measurement position was located in the plane 10mm downstream from the exit of the nozzle orifice. The measurement result showed that droplet velocities under longer energizing duration took maximum values, before the needle was fully opened. This suggests that the droplet velocity is limited by the nozzle orifice throttle. It was found that the droplet velocity is affected by the decrease in rail pressure due to the fuel injection and the increase in rail pressure due to the needle valve closing. The droplet size in the case of shorter energizing duration is relatively small. It is thought that small sized droplets come from the cavitation inside the nozzle due to the low needle valve lift. The small sized droplets under shorter energizing duration are observed over the spray section near the nozzle orifice.

1. Introduction

Multiple fuel injection is commonly used for controlling diesel combustion to cope with design requirements; higher thermal efficiency, lower exhaust emissions, and lower combustion noise. It is known that these requirements are in a trade-off relation. Research works on the combustion related to the multiple fuel injection have been conducted by many researchers. Ultraviolet visible optical diagnostics was applied in the combustion chamber of a diesel engine in order to study the multiple fuel injection (Mancaruso et al. 2008). The effects of two-stage fuel injection on the UHC and CO emissions was investigated by varying the dwell between the two injections as well as the fuel quantity in each injection (Li et al. 2010). The understanding of post injections for soot reduction in diesel engines was reviewed (O'Connor et al. 2013). Detailed information about fuel sprays is needed for further improvement of combustion, because the multiple injection utilizes sprays with different conditions. Cavitation developing upstream and inside the diesel micro-channel orifices of transparent multi-hole fuel injector nozzles was characterised using a high speed visualisation system (Mitroglou et al. 2014). A flow visualization experiment system with a transparent scaled-up multi-hole injector nozzle tip was setup for validating numerical simulation of cavitating flow in the nozzle (He et al. 2013). A study was conducted about the influence of the needle lift on the internal flow and cavitation in diesel injector nozzles by CFD (Salvador et al. 2013). It is understood that the cavitating fuel flow inside the nozzle and its variation with needle lift affect the spray behavior outside the nozzle. Optical techniques have been used for the non-intrusive measurements of the inner structure of diesel fuel sprays. Experimental studies on Diesel fuel sprays were carried out in a constant volume bomb to investigate the atomization and mixing process by applying the phase doppler anemometry (PDA) (Pribicevic et al. 2012). Droplet size distributions in sprays injected from a single-hole nozzle were measured by a laser

diffraction particle analysing system (Chen et al. 2013). The spatial distribution of fuel mass in the near-nozzle region was investigated by using X-ray for understanding the effect of the shape of nozzle hole inlet on the spray characteristics (Im et al. 2009). In spite of intensive research activities, there are a few knowledge about the microscopic structure inside diesel fuel sprays where the number density is high.

The velocity of droplet is obtained by a laser 2-focus velocimeter (L2F) based on the measurement of time-of-flight when a droplet flies between two foci. The L2F has a high optical signal-to-noise ratio, so an adverse effect of multiple scattering of droplets on the accuracy of spray measurement is small even in high number density sprays. The L2F methods were applied to measure droplets inside the breakup length (Caves et al. 2001) (Schugger et al. 2000). The authors showed that the velocity and the size of droplets can be simultaneously obtained by adding the measurement of time-of-scattering to the L2F (Ueki et al. 1994). The measurement of the velocity and size of droplets was successfully conducted by the developed L2F at 0.5 mm downstream from nozzle orifice (Ueki et al. 2004). The time variation of spray tip penetration near the nozzle orifice observed by macroscopic images was related to the size of droplets inside sprays measured by the L2F (Komada et al. 2013).

In the present study, temporal and spatial changes in the velocity and size of droplets near the nozzle orifice was investigated and was correlated with the needle valve lift of the injector nozzle.

2. Experimental setup

2.1 Fuel spray measurement system

The light probe of the L2F consists of highly focused two laser beams as shown in Fig.1. The diameter F of the focus is about 3μm, and the distance S between two foci is 17μm, and the length L is about 20μm in the direction of optical axis. It can be mentioned that the L2F used in the present study has a micro-scale probe. When a droplet flies through both upstream and downstream foci, time-of-flight t_1, time-of-scattering t_2 on the upstream focus and time-of-scattering t_3 on the downstream focus are measured. The velocity of a droplet is obtained by dividing the distance between two foci S with the measured time-of-flight t_1,

$$u = \frac{S}{t_1} \tag{1}$$

The relation used for the estimation of droplet size is that the ratio of the time-of-flight and the time-of-scattering corresponds to the ratio of the distance between two foci S and the droplet size d_p plus the focus size F. The time-of-scattering can be estimated by averaging two time-of-scattering. The droplet size d_p can be estimated by

$$d_p = u \cdot \frac{(t_2 + t_3)}{2} - F \tag{2}$$

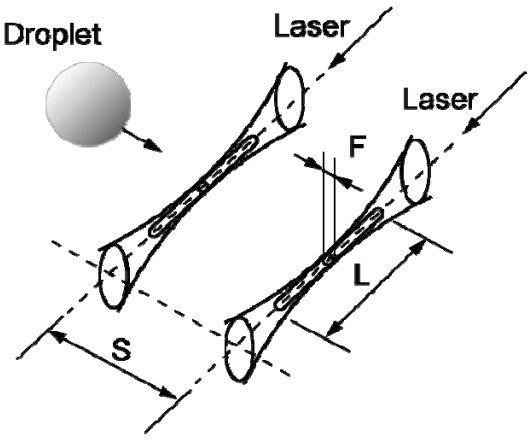

Fig. 1. Measurement probe of L2F

Figure 2 shows the fuel spray measurement system. A common rail injector was used to control the time, duration and pressure of injections. The clock signal with a frequency of 6MHz was used for recording the time when the L2F data was acquired. This is equivalent to 0.17μs time window for each data. The *z*–axis is the spray axis. Two foci of the L2F probe were set in such a way that the direction from the upstream focus to the downstream focus was adjusted to the spray axis. The light source is a semiconductor laser which has a maximum power of 100mW and a wave length of 835 nm. A non-spherical lens which has a focal length of 8 mm and a numerical aperture of 0.5 is adopted as the condenser lens. By the optical system with a length of 350mm including the light source, the backscattering light of a droplet at the focus is guided to a Si-APD (Silicon Avalanche Photo Diode), and it is converted into an electrical signal. The time-of-flight and time-of-scattering are measured by the digital counter which is mainly constituted of a FPGA (Field Programmable Gateway Array) with a clock frequency of 480MHz. The maximum data sampling rate of the L2F system is 15MHz.

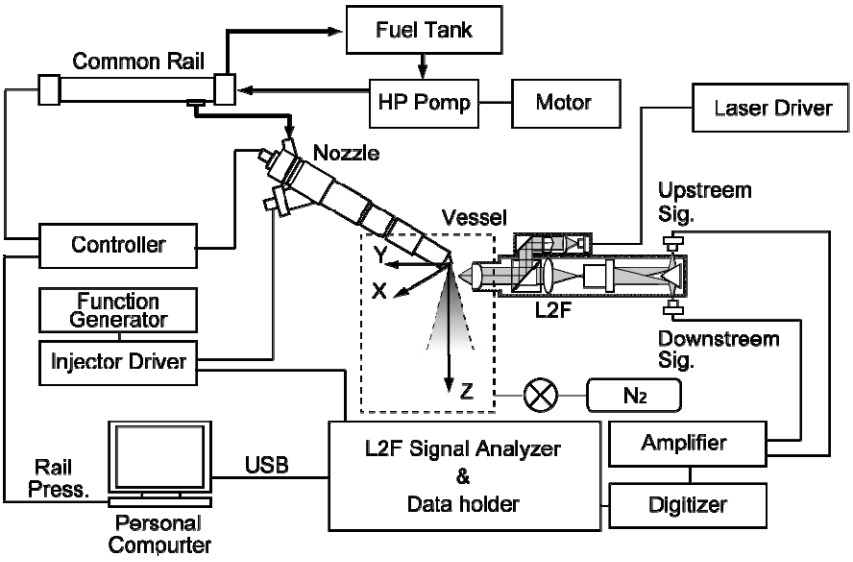

Fig. 2. Fuel spray measurement system

2.2 Experimental condition

Table 1 shows the experimental condition. The number of holes of the injector nozzle was 8, and the diameter of the nozzle orifice was 0.112mm. One of the 8 spray plumes was measured by the L2F while the remaining 7 spray plumes were shielded. The rail pressure was set at 40MPa. The injector energizing duration was varied from 0.5 to 1.5ms. The injection interval was 1000ms. Simultaneous measurements of velocity and size of spray droplets were conducted at each measurement position 10 mm downstream from the exit of the nozzle orifice. The ambient temperature was 296±6K.

Table 1 Experimental condition

Hole diameter (mm)	0.112
Number of holes	8
Injection interval (ms)	1000
Energizing duration (ms)	0.5, 1.0, and 1.5
Rail pressure (MPa)	40
Ambient pressure (MPa)	0.1
Ambient temperature (K)	296

Table 2 shows the injection condition. The injection quantities for three injection durations were respectively 0.5, 2.5, and 4.2 mg/injection. The injection rate was increased with the energizing duration. Figure 3 shows the time variation of the needle lift. Three needle lift curves have the same gradient in the valve opening stage. The needle was not fully opened under the energizing duration of 0.5 and 1.0ms, and the maximum needle lift under the energizing duration of 1.0ms was larger than that under the energizing duration of 0.5ms. The needle was fully opened in the middle of injection duration under the energizing duration of 1.5ms.

Table 2 Injection condition

Energizing duration (ms)	Injection duration (ms)	Injection quantity (mg)	Injection rate (mg/ms)
0.5	0.5	0.5	1.0
1.0	1.7	2.5	1.5
1.5	2.3	4.2	1.8

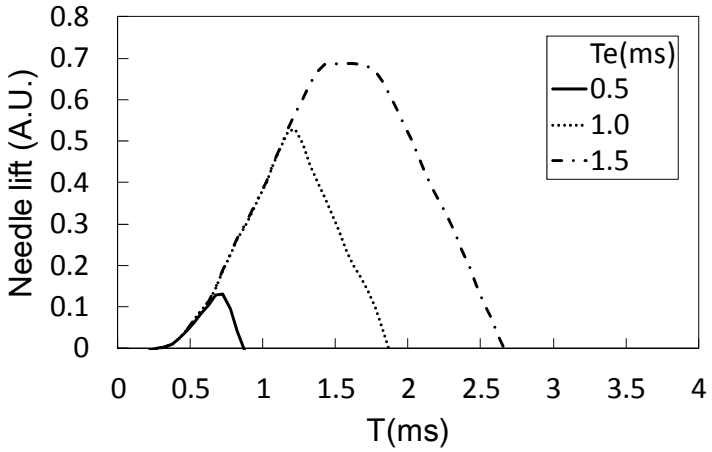

Fig. 3. Time variation of needle lift

The measurement was conducted during 10-150 injections. The number of droplets observed was 20,000 at each measurement position. The condenser lens was cleaned after it was misted by droplets of diesel fuel in several tens of injections. Table 3 shows the measurement position. The measurement positions were located at an even distance from each other. Figure 4 shows the spray image and measurement plane.

Table 3 Measurement positions

x	0, ±0.3, ±0.6, ±0.9, and ±1.2(mm)
z	10(mm)

z=0mm z=10mm

Fig. 4. Spray image and measurement plane; *T* = 0.8ms after energizing the injector

3. Result and discussion

3.1 Temporal change of velocity and size of droplets

The frequency of droplet observed changes with time and space. Figure 5 shows the number of droplets within a time window of 0.1ms at the spray center. The axis of ordinates is the time after the start of energizing the injector solenoid. The number of droplets increased with the degree of needle valve opening in the early stage of injection under all the three energizing durations. The number of droplets under T_e=1.0ms was nearly the same as the one under T_e =1.5ms until T=1.2ms, while the needle lift curves coincided with each other. Droplets were observed after the injection duration under all the three energizing durations, and the period when the droplets were observed increased with the energizing duration.

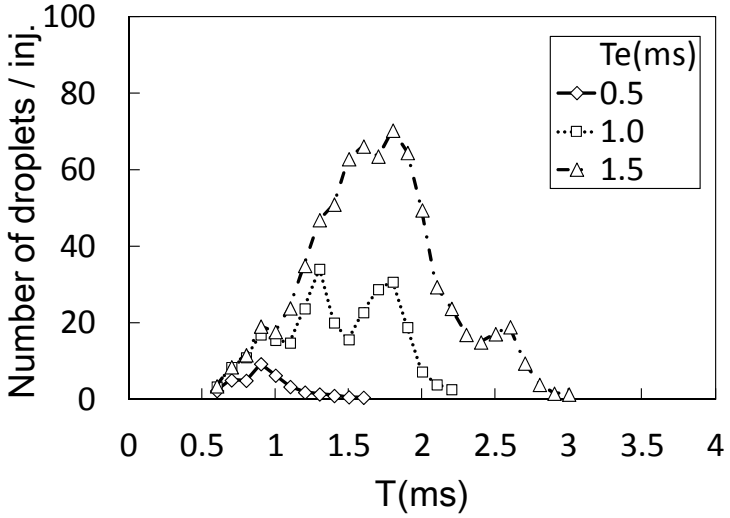

Fig. 5. Number of droplets observed at each injection; x=0mm

Figure 6(a) shows the time variation of the arithmetic mean velocity within each time window of 0.1ms at the spray center. The velocity under all the three energizing durations increased with time at the valve opening stage until T=0.7ms, while the three needle lift curves coincided with each other. The velocity under T_e =0.5ms decreased within the early stage of injection because the injection duration was short. The velocities under T_e =1.0ms and T_e =1.5ms took maximum values at T=0.9ms, before the needle was fully opened. It is understood that the velocity limitation was caused by the orifice throttle. The velocity under T_e =1.0ms was the same as the one under T_e =1.5ms until T=1.3ms, while the needle lift of both cases coincided with each other. Low velocity droplets were observed after the needle valve closed under all the three energizing durations. The velocities under T_e =1.0ms and T_e =1.5ms decreased near the middle of injection duration and increased after that. It is understood that the decrease in velocity is caused by the decrease in the rail pressure due to fuel injection. The increase in velocity began at the time when the needle valve started to close. It is understood that the increase in velocity is caused the increase in the rail pressure. The number of droplets under T_e =1.0ms increased at T=1.5ms when the increase in velocity was observed. Figure 6(b) shows the time variation of the arithmetic mean size within each time window of 0.1ms. The droplet size under T_e =0.5ms decreased during the injection duration. The droplet size under T_e =1.5ms increased in the former half of the period of needle valve opening, and was larger than the droplet size under T_e =0.5ms. The fuel flow inside the nozzle might affect the size of droplets outside the nozzle. The effect of needle lift on the instantaneous cavitation structure in Diesel orifices was investigated experimentally (Mitroglou et al. 2014). The result showed that the cavitation forming in the needle seat area was pronounced during the opening stages of the needle valve and that cavitation bubbles were created at the needle seat area during the latest stages of the valve closing phase. Based on the result of L2F measurements in the present study, it is understood that the droplet size in the case of shorter energizing duration was smaller because of the cavitation inside the nozzle due to the low

needle valve lift. And it is also understood that the droplet size in the case of longer energizing duration was larger because of the small cavitation inside the nozzle due to the high needle valve lift.

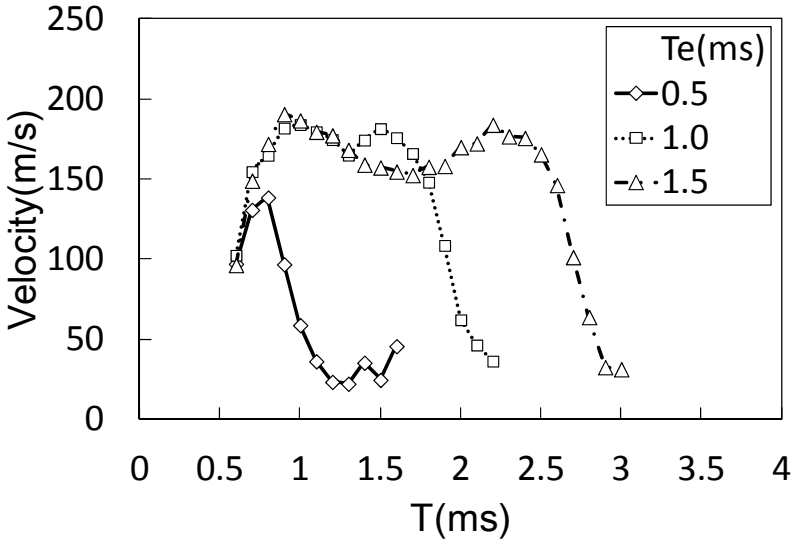

(a) Velocity

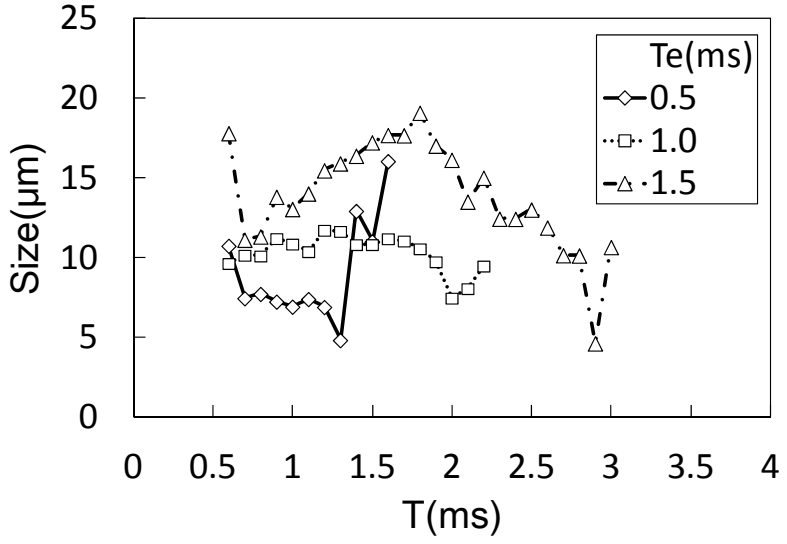

(b) Size

Fig. 6. Time variation of velocity and size of droplets; x=0mm

3.2 Distribution of velocity and size of droplets

Figure 7(a) shows the distribution of the number of droplets observed within a period of 0.1ms when T=1.2ms. The needle valve was closed before this time under T_e =0.5ms. The needle valve reached a peak under T_e =1.0ms and did not reach a peak under T_e =1.5ms at this time. A larger number of droplets were observed at the position between the center and periphery of the spray, that is, the number of droplets had an M shaped distribution. It is thought that the droplet breakup occurred at the position between the center and periphery of the spray, because the difference between the velocity of droplets and the velocity of surrounding air at this position may be higher than that at other positions. Figure 7(b) shows the distribution of the number of droplets observed within a period of 0.1ms when T=1.5ms. The needle valve was on a closing stage under T_e =1.0ms and reached a peak under T_e =1.5ms at this time. The number of droplets under T_e =1.5ms was larger than that at the spray center and was smaller than that at the spray periphery at T=1.2ms. Figure 7(c) shows the

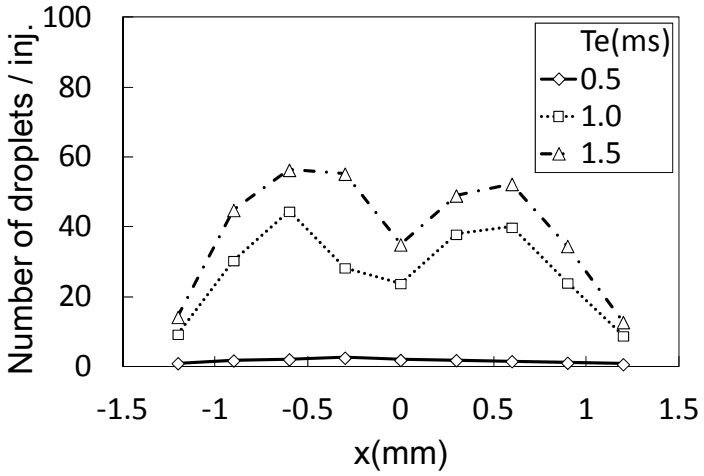

(a) T=1.2ms

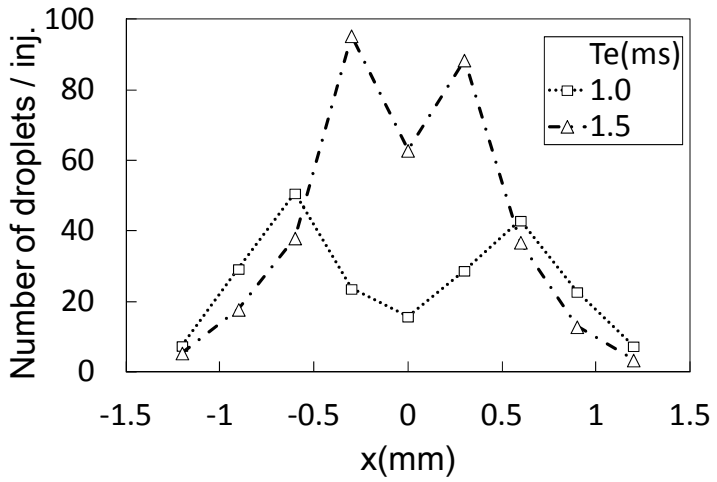

(b) T=1.5ms

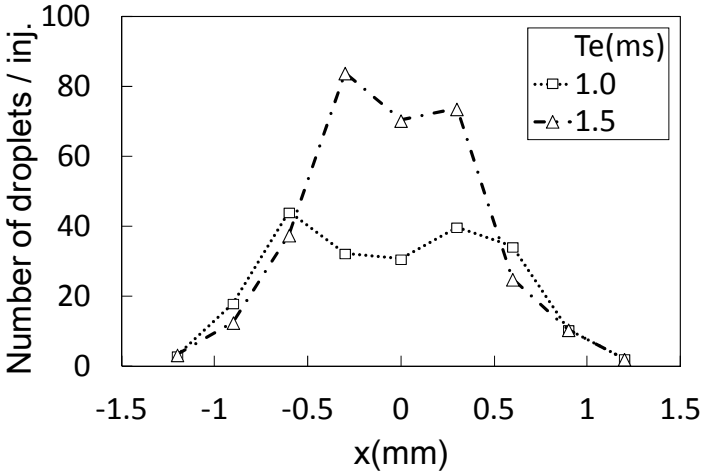

(c) T=1.8ms

Fig. 7. Spatial distribution of number of droplets observed at each injection

distribution of the number of droplets observed within a period of 0.1ms when T=1.8ms. The needle valve was closed before this time both under T_e =0.5ms and T_e =1.0ms. The needle valve began to close under T_e =1.5ms at this time. The distribution of the number of droplets was similar to that at T=1.5ms. As a result, the number of droplets near the spray center increased with the energizing duration. The number of droplets under T_e =1.5ms was larger than that under T_e =1.0ms. It is thought that the increase in the number of droplets was due to a high injection rate.

Figure 8(a) and (b) show the spatial distributions of the velocity and size of droplets at T=1.2ms within a time window of 0.1ms. The mean velocity of droplets under T_e =0.5ms was low about 30m/s. The velocity of droplets was highest near the spray center and was lower on the periphery of spray both under T_e =1.0ms and T_e =1.5ms. The size under longer injection duration was larger than that under shorter injection duration over the spray section. The size at the spray center was larger than that at the spray periphery both under T_e =1.0ms and T_e =1.5ms.

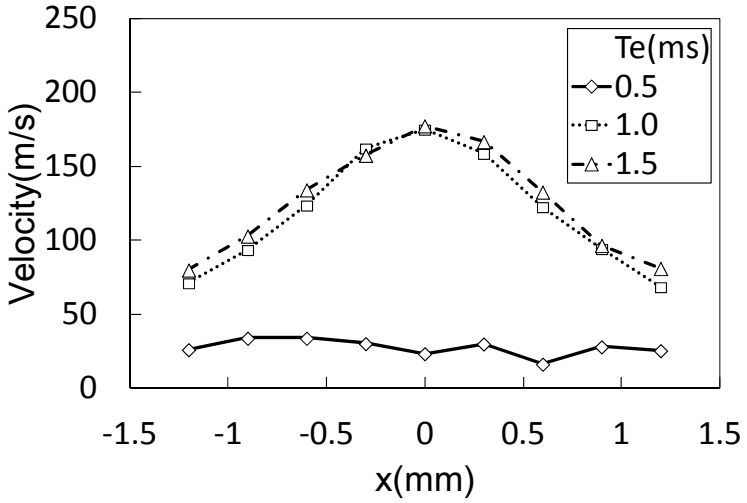

(a) Velocity

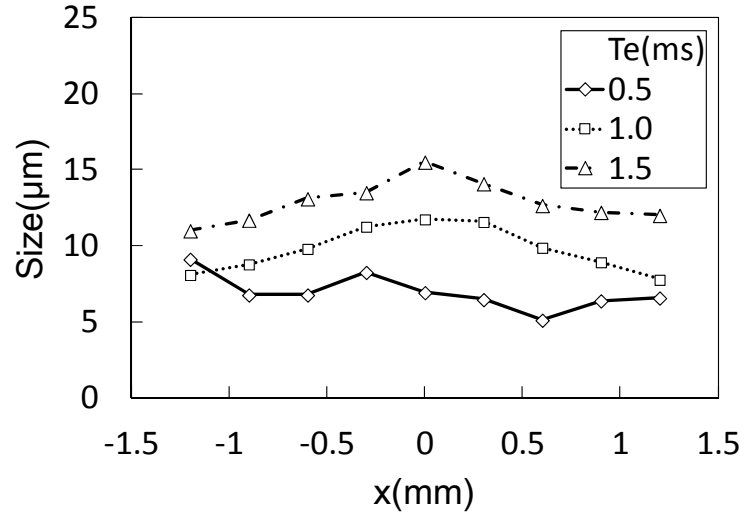

(b) Size

Fig. 8. Spatial distribution of velocity and size of droplets; T = 1.2ms

Figure 9(a) and (b) show the spatial distributions of the velocity and size of droplets at T=1.5ms within a time window of 0.1ms. Droplet velocity at the spray center was larger than that at the spray periphery both under T_e =1.0ms and T_e =1.5ms. It can be noted that the velocity under T_e =1.5ms was lower than that under T_e =1.0ms. The lower droplet velocity over the spray section may be caused by the decrease in the rail pressure due to longer fuel injection. The droplet size at the spray center was slightly larger than that at the spray periphery under T_e =1.0ms. The droplet size at the spray center was markedly larger than that at the spray periphery outside a radius of 0.5mm under T_e =1.5ms. Figure 10(a) and (b) show the spatial distributions of the velocity and size of droplets at T=1.8ms within a time window of 0.1ms. The velocity at the spray center was higher than that at the spray periphery both under T_e =1.0ms and T_e =1.5ms. The maximum velocity at the spray center under T_e =1.5ms was higher than that under T_e =1.0ms. The relation between two maximum velocities shown in this figure was inverted in order to Fig.9. The distribution of droplet size was similar to the one shown in Fig.9. It is understood that a lot of large droplets were concentrated near the spray center under the longer injection duration.

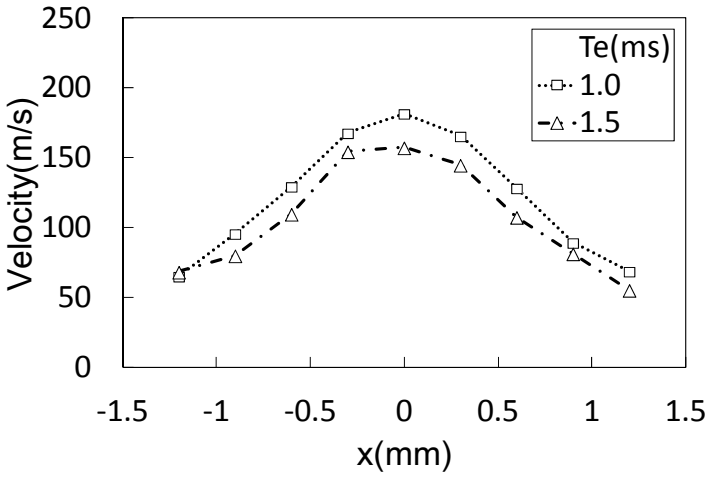

(a) Velocity

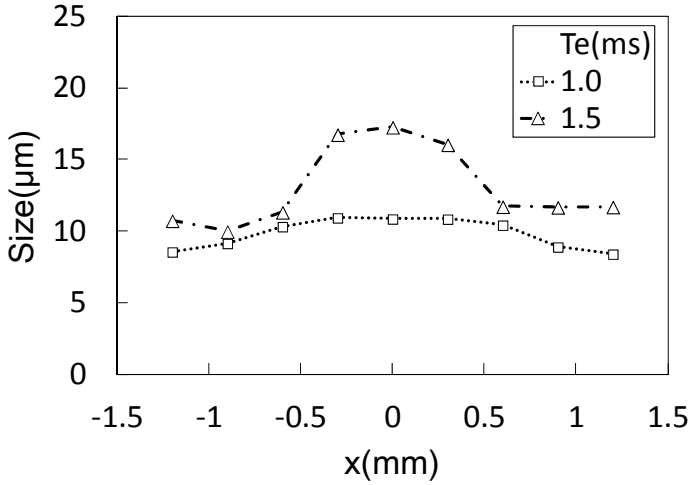

(b) Size

Fig. 9. Spatial distribution of velocity and size of droplets; T = 1.5ms

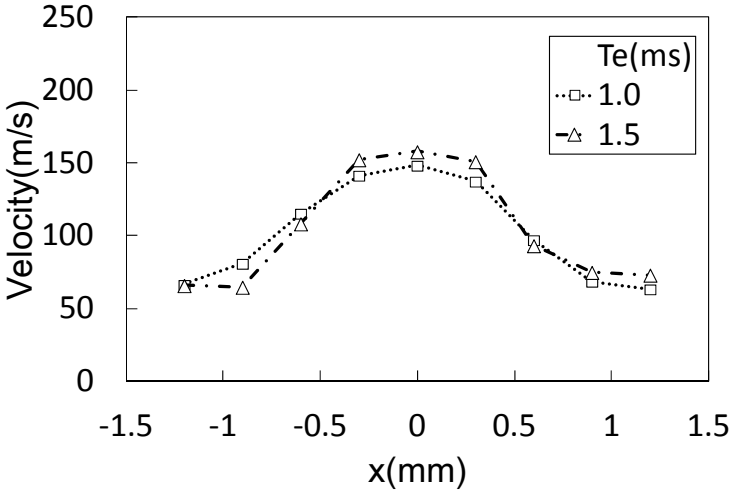

(a) Velocity

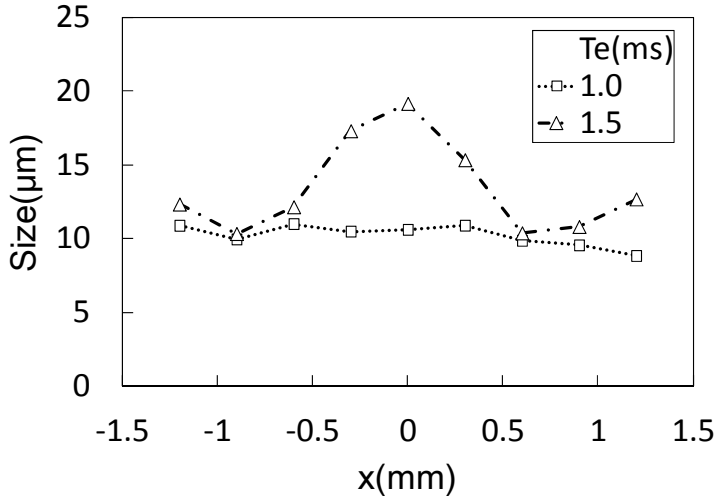

(b) Size

Fig. 10. Spatial distribution of velocity and size of droplets; *T* = 1.8ms

Conclusions

A laser 2-focus velocimeter (L2F) was applied for the measurement of diesel fuel sprays injected from a common rail injector at a rail pressure of 40 MPa. Measurement position were located in the plane 10mm from the nozzle exit. The velocity and size of droplets were measured under the injection period from 0.5ms to 1.5ms. Temporal and spatial changes in the velocity and size of droplets near the nozzle orifice was investigated and was correlated with the needle valve lift of the injector nozzle. Conclusions were as follows.

1. The velocities under longer energizing duration take maximum values, before the needle is fully opened. The droplet velocity is limited by the nozzle orifice throttle.

2. The velocity of droplets is affected by the decrease in rail pressure due to the fuel injection and the increase in rail pressure due to the needle valve closing. The velocity change caused by the rail pressure change appears over the spray section near the nozzle orifice.

3. The droplet size in the case of shorter energizing duration is relatively small. It is understood that small droplet come from the cavitation inside the nozzle due to the low needle valve lift. The size reduction is observed over the spray section near the nozzle orifice.

4. A lot of large droplets were concentrated near the spray center under longer injection duration.

References

Chaves.H, Kirmse.C, and Obermeier.F. (2001) Velocity Measurements of Dense Diesel Sprays in Pressurized Air, Proceedings of Spray 2001, TU Hamburg-Harburg, pp. II. 2-1-II. 2-8

Chen.P-C, Wang.W-C, Roberts.W.L, Fang.T. (2013) Spray and atomization of diesel fuel and its alternatives from a single-hole injector using a common rail fuel injection system, Fuel, 103, 850–861

He.Z, Zhong.W, Wang.Q, Jiang.Z, Fu.Y. (2013) An investigation of transient nature of the cavitating flow in injector nozzles, Applied Thermal Engineering, vol.54, pp.56-64

Im.K.-S, Cheong.S.-K, Powell.F Christopher, Liu Xin, and Wang Jin (2009) Effects of Internal Cavitation on Breakup of High-Pressure Diesel Sprays, Proceedings of ICLASS 2009, pp.1-6

Komada.K, Sakaguchi.D, Tajima.H, Ueki.H, Ishida.M. (2013) Relation between Tip Penetration and Droplet Size of Diesel Spray, SP-2345, Fuel Injection and Sprays, 2013, Paper 2013-01-1599, pp.139-147

Li.T, Suzuki.M, Ogawa.H. (2010) Effect of two-stage injection on unburned hydrocarbon and carbon monoxide emissions in smokeless low-temperature diesel combustion with ultra-high exhaust gas recirculation, International Journal of engine research, vol.11, no.5, pp.345-354

Mancaruso.E, Merola.S.S, B M Vaglieco.B.M. (2008) Study of the multi-injection combustion process in a transparent direct injection common rail diesel engine by means of optical techniques, International Journal of engine research, vol.9, no.6, pp.483-498

Mitroglou.N, McLorn.M, Gavaises.M, Soteriou.C, Winterbourne.M. (2014) Instantaneous and ensemble average cavitation structures in Diesel micro-channel flow orifices, Fuel, vol.116, pp.736–742

O'Connor. J, Musculus. M (2013) Post Injections for Soot Reduction in Diesel Engines: A Review of Current Understanding, SAE International Journal of Engines 6, Paper 2013-01-0917

Pribicevic.I, Sattelmayer.T. (2012) Investigation of the Diesel spray atomization process with use of Phase Doppler Anemometry at high injection pressures and at engine-like gas density, Proceedings of the 16th Symposium on Applications of Laser Techniques to Fluid Mechanics, pp.1-12

Salvador.F.J, Martínez-López.J, Caballer.M, De Alfonso.C. (2013) Study of the influence of the needle lift on the internal flow and cavitation phenomenon in diesel injector nozzles by CFD using RANS methods, Energy Conversion and Management, vol.66, pp.246–256

Schugger.C, Meingast.U and Renz.U. (2000) Time-Resolved Velocity Measurements in the Primary Breakup Zone of a High Pressure Diesel Injection Nozzle, Proceedings of ILASS-Europe 2000, Darmstadt, pp.1-5

Ueki.H, Ishida.M and Sakaguchi.D (1994) Simultaneous Measurement of Particle Size and Velocity by Laser 2-Focus Particle Analyzer, Proceedings of ICLASS94, pp.483-490

Ueki.H, Ishida.M, Sakaguchi.D and Naganuma.M (2004) Simultaneous Measurements of Velocity and Size of Diesel Fuel Droplet near Nozzle Orifice by Laser 2-Focus Velocimeter with Micro-Scale Probe Volume, Proceedings of Thiesel, pp.369-380

Cinema-Stereo Imaging of Fuel Dribble after the End of Injection in an Optical Heavy-Duty Diesel Engine

W.E. Eagle [1], M.P.B. Musculus[1]

[1]Sandia National Laboratories. USA

E-mail: sandia@national.gov
Telephone: +(1) 925.294.2795
Fax: +(1) 925.294.1004

Abstract. Unintended fuel delivery after the scheduled injection event can negatively affect engine performance. This "injector dribble" increases fuel consumption, emissions of unburned hydrocarbons, particulate matter, and the burden on exhaust after-treatment systems. The importance of injector dribble for modern engine multiple injection systems motivates a study of the mechanisms and dependencies that characterize its behavior. Here, we use high-speed digital cinematography to observe the spatial and temporal development of injector dribble after the scheduled fuel injection, throughout the expansion stroke. Parametric variations of injector nozzle size and nozzle body, fuel volatility, ambient temperature and pressure, fuel rail pressure, injection schedule including multiple injections, and combustion effects, provide a comprehensive characterization of injector dribble. From the imaging results, we confirm that injector dribble is a common phenomenon occurring across a wide range of operating conditions including various injector designs and nozzle geometries. While we do not provide an absolute quantification of the amount of fuel that is dribbled, the visual extent and temporal progression of dribble is strongly affected by many of the parametric variations. Three important features are noted across all conditions studied: 1) immediate dribble (liquid drops) occurring shortly after the end of injection with observed duration from 0.5 to 1.8ms, 2) 'late cycle' dribble occurring between 20 and 5 bar cylinder pressures, and 3) 'blow-down' dribble in which bulk in-cylinder flows strip liquid from the injector tip, especially after exhaust valve opening. A fourth feature, a hanging droplet persisting until the compression stroke, was observed in one set of full-cycle experiments with one injector, but was not explored for other injectors. We also discuss some physical mechanisms potentially responsible for dribble. One likely candidate is ambient-gas ingested after the end of injection, which may later play an important role in actuating the 'late-cycle' dribble.

1. Introduction

Achieving targets for both low pollutant emissions and high fuel-efficiency for internal combustion engines requires precise fuel mixing and well controlled combustion. In direct-injection diesel engines, fuel and air mixing that yields clean combustion occurs at the interface(s) created during the fuel spray event. However, from images of combustion in optically accessible direct-injection diesel engines, we know that some fuel leaves the injector outside of the scheduled high-pressure fuel-spray event. We broadly apply the term 'dribble' to describe any undesired delivery of fuel from the injector.

Dribbled fuel may leave the injector nozzle either as low-velocity droplets or as fuel vapor. Low-velocity droplets experience minimal fluid-dynamic enhancement to droplet break-up and vaporization, leading to slower mixing. If dribbled fuel ignites, combustion may occur in a less desirable diffusion-dominated regime. Fuel vapor that leaves the nozzle could produce a similar diffusion-flame structure when turbulent mixing is low, or it may go partially reacted or even unreacted into the exhaust stroke.

1.1 Prior art – Studies of transient injector behaviors including dribble

Preventing dribble was the principle objective of early fuel injector designs, since large quantities of unintended fuel would lead to unstable engine operation. Fuel-injection systems in diesel engines introduced many anti-dribble features in the late 1930-1940s, including pop-valves, anti-dribble valves and check valves (Williams and Smith 1945; Thomas 1939). These early efforts likely prevented *excessive* dribble, but did not eliminate it. At the time, diagnostics were not available to detect the small

amount of dribble that remained, but that level of dribble did not substantially affect engine performance relative to the requirements for that era. However, robust, reliable, and repeatable fuel delivery, ideally without dribble, is needed to achieve future emissions and fuel consumption targets (Dolenc 1990).

Dribble has been previously observed or inferred in various ways using optical engines. In conventional diesel combustion, for which ignition occurs before the end of fuel injection, dribble is difficult to observe directly because of interference from combustion luminosity and/or light scattering from soot particles. The presence of dribble can be inferred, however, from visible combustion luminosity due to soot production from fuel dribble near the injector tip after the end of the main injection (Espey and Dec 1993; Schwarz et al. 1999). In low-temperature combustion with positive ignition dwell, the start of combustion occurs after the end of injection, so that dribble can be observed more directly (Musculus, Miles, Pickett 2013).

Recent studies on injector behaviors demonstrate the potential impact of dribble on soot/particulate matter and unburned hydrocarbon emissions. Visible and UV flame luminosity measurements indicate that dribble causes high-sooting regions near the injector after the end of injection (Taschek et al. 2005). In the case of multiple-injection schemes, significant scatter exists in the effectiveness of close-coupled post-injection strategies to minimize soot emissions, yet the contribution of dribble to this scatter was not assessed (O'Connor and Musculus 2013). Injector nozzle sac-volume effects on fuel enrichment leading to unburned hydrocarbon (UHC) emission was confirmed via in-cylinder optical and tailpipe diagnostics of UHC emissions (Musculus and Lachaux 2007; Koci et al. 2009; Ekoto et al. 2009).

Figure 1 is a conceptual model that was proposed for single injection, low-temperature combustion, which includes dribble (Musculus, Miles, and Pickett 2013). According to the conceptual model, large, long-lived droplets dibbled after the end of injection create locally fuel-rich pockets within an overall fuel-lean region near the injector, the combination of which may contribute to soot and/or unburned

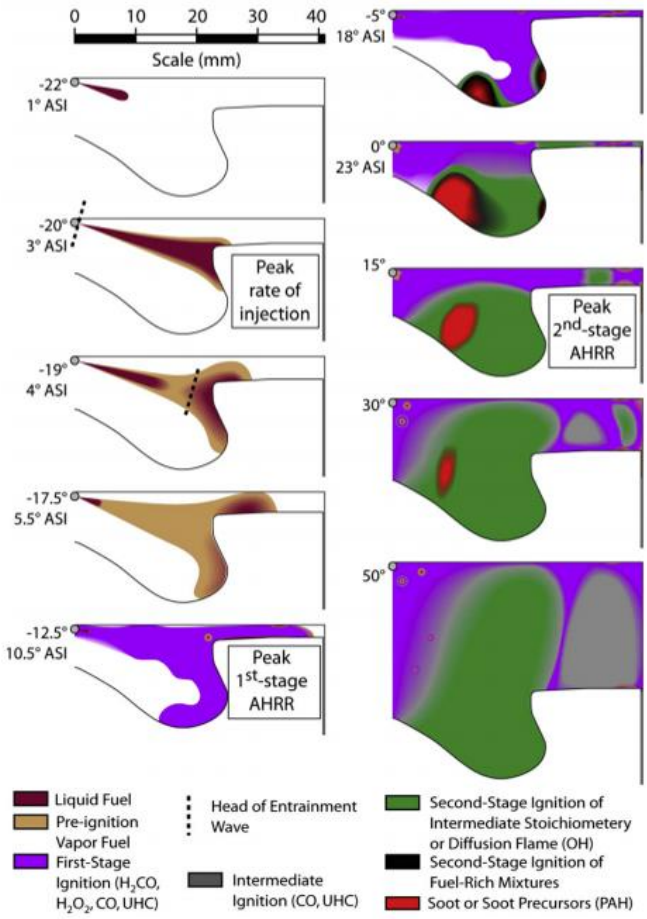

Fig. 1. A conceptual model of lean, low-temperature, light-duty early-injection diesel combustion. Dribbled fuel is indicated by the small disks near the injector after the end of injection, colored as liquid or vapor fuel, according to the figure legend. (M. P. B. Musculus, Miles, and Pickett 2013)

hydrocarbon emissions (Musculus, Miles, and Pickett 2013). Multi-injection strategies have shown promise in reducing engine-out unburned hydrocarbons (UHC) arising from incomplete combustion in the residual fuel-lean region near the injector, but these have demonstrated asymptotic behavior in the 'heavy' UHC, indicating the persistent presence of a source related to the injector sac volume, which may be linked to fuel dribble (Koci et al. 2009). Better understanding of the mechanisms and dependencies that characterize the dribble behavior are needed to inform design choices to minimize the impact of dribble on soot/PM and UHC emission.

1.2 Study aims

Despite evidence of dribble in the literature, to our knowledge, there is no comprehensive taxonomy for dribble events. The aim of this work is to provide such a catalog and classification by imaging dribble in an optical engine. Once identified, correlations between potential sources of dribble and the imaging results can be sought.

Here, we use stereo cinematography in a heavy-duty single-cylinder optical engine to provide simultaneous imaging data of dribble from below (piston window) and from the side (cylinder-wall window) for multiple high-pressure, solenoid-driven, common-rail injectors. To demonstrate different classes of dribble events, we present selected images from 25kHz imaging of light elastically scattered off liquid fuel acquired over 2880 crank angle degrees (CAD) from four consecutive cycles operated in a non-reacting environment. For other tests involving various parametric variations, we observe dribble over a more limited crank angle range, from 320 to 540 CAD[*], The varied parameters include: three types of injector bodies with various nozzle configurations, two fuel types, injection timing including post-injection, injection rail pressure, and both non-reacting and reacting cases.

In the results, we identify three different dribble behaviors. These dribble behaviors are not exclusive, in that multiple behaviors may be observed at different times associated with a single injection event. We also quantify the total injection duration, noting that for smaller orifice size the actual duration lengthens for a constant solenoid energizing duration. Following the end of the intended injection event, we quantify the duration of immediate dribble, marked by liquid droplets that are generally individually identifiable (not spray-like), leaving a few of the nozzle holes. A second dribble occurs between 30 to 60 crank angle degrees after the immediate dribble, when we see liquid fuel leaving from every nozzle orifice. At cylinder pressures near 5 bar, the late-cycle dribble event is further marked by condensation of diesel fuel vapor into a cloud of fine droplets near the injector tip. As the exhaust valve opens, blow down induces additional dribble from the nozzle. The final dribble behavior is the appearance of a liquid drop at the injector tip. The imaging diagnostic provides quantitative timing of these events, but as yet, we do not quantify of the amount of fuel dribbled. The results support the conclusion that dribble is a common phenomenon, observed universally across a range of operating conditions and available injector configurations tested here.

2. Experimental setup

2.1 Hardware specification

This study uses a Cummins N-series heavy-duty production engine modified for optical access using a Bowditch extended piston (Espey and Dec 1993). It has a bore of 140mm [5.5in] and a stroke of 152mm [6.0in] for a per-cylinder displacement of 2.34L [143 in^3]. Engine specifications are in Table 1.

The piston has a right-angle cylindrical bowl, with a fused-silica piston-crown window for imaging from below. To allow spray illumination and imaging access at TDC conditions, a portion of the piston bowl-rim spanning 100° of the bowl circumference is removed. The illustrated experimental setup appears as Fig. 2.

Five common-rail injectors are considered in total; three Cummins XPI heavy-duty injectors, one Bosch light-duty injector, #211199, being used in the ECN ("Engine Combustion Network"), and one Delphi DFI-1.5 light-duty injector. All injectors were solenoid-actuated mini-sac designs. Table 2 provides all nozzle geometries and injector builds considered. Table 2 also provides details of the five different mini-sac nozzles we tested among the XPI injectors. With each injector, we used two fuels: Diesel US-2007 certification fuel and neat n-heptane. Their reference properties are listed in Table 3.

[*] Top dead center is nominally 360 CAD

Table 1. Engine Specifications

Engine Variable	Specification
Engine base type	Cummins N-14, DI diesel
Number of cylinders	1
Cycle	4-stroke
Number of intake valves	2
Number of exhaust valves	1*
Exhaust valve opening	485° †
Intake valve opening	703° CAD†
Exhaust valve closing	27° CAD †
Intake valve closing	195° CAD †
Combustion chamber	Quiescent, direct injection
Swirl ratio	0.5 (approx.)
Bore	139.7 mm [5.5 in]
Stroke	152.4 mm [6.0 in]
Bowl width	97.8 mm [3.85 in]
Displacement	2.34 liters [142 in^3]
Connecting rod length	304.8 mm [12.0 in]
Piston pin offset	None
Geometric compression ratio	9.93:1‡

*In this optically accessible diesel engine, one of the two exhaust valves of the production cylinder head was replaced by a window and periscope (see Fig. 3).

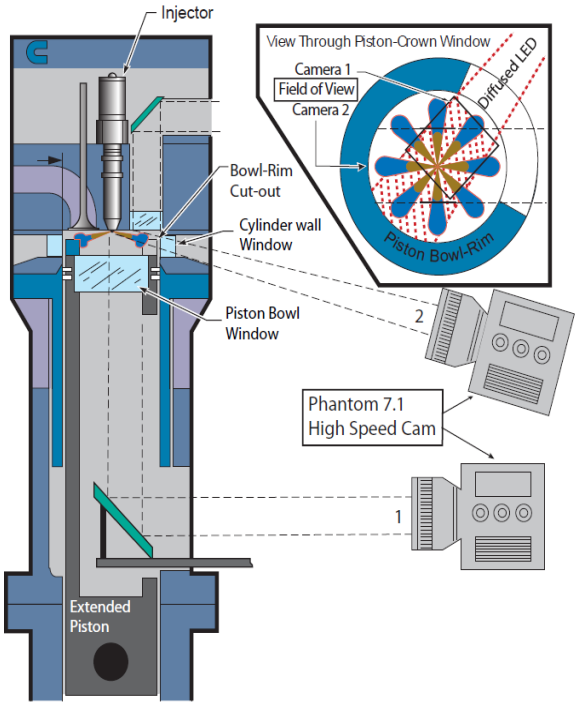

Fig. 2. Experimental setup of the single-cylinder engine, lighting configuration, and two-camera setup. Camera field of view and piston bowl cut-out is shown in the upper right.

†All valve timings correspond to the crank angle of the first detectable movement from fully closed.

‡ The compression ratio achieved is lower than previous experiments with this setup due to the large bowl-rim cut-out.

Table 2. Fuel Injector Specifications

Fuel injector build(# tested)	Cummins XPI (3)	Bosch 'ECN Spray B' (1)	Delphi DFI-1.5 (1)
Number of holes & arrangement	8, equally-spaced	3	8, equally spaced
Pull-in / Hold Current [amps]	21 / 12	18 / 12	16.5 / 7
Nozzle Tip [orifice diameter, spray incl. angle]	0.090mm, 152° 0.131mm, 152° 0.200mm, 152° 0.200mm, 160°	0.090mm, 145°	0.200mm, 156°
Start of injection (SOI) delay from start of solenoid energizing (SSE) at 1000bar rail pressure*	0.400ms [2.9CAD] 0.400ms [2.9CAD] 0.480ms [3.4 CAD] 0.360ms [2.6 CAD]	0.320ms [2.3 CAD]	0.320ms [2.3 CAD]
Extra duration of injection (EDOI) for a duration of solenoid energizing (DSE) of 1ms at 1000bar rail pressure	1.400ms 0.700ms 0.000ms 0.400ms	0.840ms [6.0 CAD]	0.160ms[1.2 CAD]

*SOI and EOI determined from optical imaging, ±0.04ms

Table 3. Reference Fuel Properties

	Diesel Certification Fuel (2007)	n-Heptane
Density	841.7 kg/m^3	687.3 kg/m^3
Viscosity (STP)	2.35 cs	0.6285 cs
Cetane Number	45.7	56

2.2 Engine and camera operation

Engine and camera operation conditions are listed in Table 4. Top dead center (TDC) conditions (16.6kg/m^3 and 936K) correspond to typical low-boost conventional diesel operation. These values are computed using a polytropic compression (exponent = 1.36) from the estimated in-cylinder conditions at the start of compression that are empirically corrected for heat transfer during induction (Sjöberg and Dec 2004; Bobba et al. 2010). Since the dribble phenomenon would be occluded by a combusting spray, the majority of the experiments are run without combustion by using pure nitrogen as the intake gas. Two injection procedures are followed for non-reacting cases: sequential injections (on:off, 4:6) and skip fired (1:9) injections. When the engine is fired (reacting, with 18% intake oxygen), 9 motored cycles separate each injector firing.

Two Phantom 7.1 high-speed cameras simultaneously captured images of scattered light off dribbled fuel droplets from two different perspectives. Imaging specifications are listed in Table 4. As illustrated in Fig. 2, one camera (piston camera) images from below and a second camera (cylinder-side camera) views the injection through the cut-out in the piston bowl-rim. The piston camera is equipped with a 5mm extender tube (Nikon) for close imaging using a 50mm glass Nikon f/2.0 lens and is mounted in a 45° rotated orientation. In this arrangement, the spray of interest appears in the 1:30o'clock position in Fig. 2 and in the 6o'clock position in the resulting images. The cylinder-side camera is equipped with a 5mm extender tube and a 85mm glass Nikon f/1.8 lens. The resolution of the images is 256x256 and from both cameras and the scale is nominally 0.135mm/pixel. The exposure time for both cameras is 25µs. Sequences of camera frames are triggered at a specific engine crankshaft angle, and then proceed at 25000 frames per second (25kfps, 40µs period) using a time-based clock independent of the engine shaft encoder. At a crankshaft speed of 1200 rotations per minute (RPM), this provides approximately 3.5 images per CAD. By the end of one cycle, the camera framing clock may drift relative to the crank angle position due to small engine speed variations. Therefore the camera clock is synchronized each cycle to the crankshaft.

A custom driver for a red light-emitting diode (1.5mm^2 Cree XPE-R5 bin 0801) developed at Sandia provides controllable light pulses at high intensity [Carlen, *personal communication*]. The total optical power delivered from this configuration is 0.74W continuous at 0.7A driver operating current†. A 25mm collimating lens (20mm focal-length aspheric condenser lens) is placed in the path of the LED, resulting in an arriving optical power during continuous operation of 0.21W. However, an increased output is

Table 4. Engine and camera operating conditions.

Engine Variable	Operating Condition	Cameras	Phantom 7.1
Engine Speed	1200 ±10 RPM*	Frame Rate	25kHz (40µs)
Engine Load Range	1-6 bar gIMEP†	Exposure Time	25 µs
Intake O_2	0%, 18.0% ± 0.2	LED delay/duration	7 µs / 15 µs
Intake Pressure	206 ± 10 kPa	Lens	Nikon 55mm, 85mm
Intake Temperature	156 ± 2°C	f/#	1.8, 2.0 (respectively)
Intake Mass Flow	41.4 ±0.5g/s	Fuel Rail Pressure	800, 1000, 1600 ±20 bar
TDC Motored Density	16.6 ± 0.4 kg/m^3	BDC Pressure	164 ± 10 kPa
TDC Motored Temperature	936 K	BDC Temperature	78 ±4°C

* A crank angle degree is assumed to be 139 microseconds for the purpose of conversion to the time domain.
†gIMEP = Gross Indicated Mean Effective Pressure, calculated using indicated work done during compression and expansion strokes only.

† compare LED optical power of 32W/cm^2 to a mercury arc lamp's 153mW/cm^2

possible by 'overdriving' the LED in bursts of short pulses at higher peak current. In this case, the LED driver is supplied at 5.1 volts and limited to a maximum current of 1.4 amps by a Tektronix PWS2323 power supply‡. The LED driver is triggered by an Agilent 33500B Waveform Generator in external trigger burst pulse mode. During burst pulse mode the delivered optical power is increased by a factor of 3 to 0.6W. The start of illumination in burst pulse mode occurs with a 7µs delay relative to an input trigger (the start of the camera exposure) and each pulse has a 15µs duration.

Table 5 lists the experimental protocol followed for each fuel and injector hardware combination. Up to 30 injections were recorded at each condition. Nominal injector energizing time (duration of solenoid energizing, DSE) is 1ms at 1000bar rail pressure. A Cummins universal solenoid driver powered by BK Precision 1623 DC power supply at 60V and an Electrostatics LS15 DC power supply at 15V, provides the solenoid with starting current (pull-in) for 740µs followed by hold current duration of the energizing time (current is injector dependent, see Table 2). At the end of each series of engine runs in a parametric variation, static firing images of the injector spray (without the engine running) are compared to static images from the beginning to ensure that no significant changes occurred in the injector during the testing that might affect results. In the case of fuel variation for instance, we noted that switching from n-heptane to diesel fuel and back required approximately 200 static injections to adequately flush the fuel from the injector/accumulator (however data for mixed fuels is neither archived nor presented here).

Table 5. Experimental Protocol

	SSE/DSE [CAD/ms] ‡	SSE/DSE2 [CAD/ms] ‡	P_{rail} [bar] ‡	Motored Speed [RPM] ‡	Cylinder Gas‡
Spray Start	-/1.0	-/-	1000	0	100% N2
TDC timing	347/1.0	*	*	1200	*
Early timing	327/1.0	*	*	*	*
Late timing	357/1.0	*	*	*	*
w/post	347/1.0	371/0.350†	*	*	*
High P TDC	*	-/-	1600††	*	*
Low P TDC	*	*	800	*	*
Fired TDC	*	*	1000	Skip Fired 10Hz	18% O_2
Fired TDC w/post	*	363/0.350	*	*	*
Spray End	-/1.0	-/-	*	0	100% N2

* values are unchanged from above; SSE (start of solenoid energizing) DSE (duration of solenoid energizing)
† Post Injection SSE timing varied, depending on extended injector needle lift during main injection, among 363, 367, and 371CAD
††1600 bar rail pressure could not be achieved with the Delphi due to limited pump capacity relative to the injector's static leak.
‡ for uncertainties in P_{rail}, RPM, and gas composition, see Table 4. DSE was repeatable to within 0.01ms.

3. Results

3.1 Image post-processing

The dynamic character of dribble revealed by the high-speed elastic-scatter movies is discussed in the following sections. Since movies cannot be included in print, static images are presented here. Unfortunately, dribble is less apparent by visual inspection in unproccesed static images than when viewing dynamic sequences of images in movies. The essential problem is that there are many features on the cylinder head with a scattering signal as strong as or stronger than the scattering signal from the dribbled fuel droplets. Small nicks on the firedeck are a particular problem, because they are of similar physical scale as the dribbled droplets. On visual inspection of a dynamic movie, the dribbled fuel is readily apparent because of its motion relative to the static features on the cylinder head. To help improve the visibility of the moving features of dribble in the static images presented here, the images are post-processed according to the two steps described below. Additionally, the dynamic high-speed

‡ The current through the junction will tend to increase as the temperature rises due to power dissipation; so current-regulated drivers are preferable to voltage-regulated drivers.

elastic scatter movies, in which the dribble is readily apparent both with and without post-processing, are made available on the Engine Combustion Network website (Eagle and Musculus 2014).

Post-processing to improve the visibility of the features of dribble in static images consists of two steps, shown in Fig. 3. First, using eight instantaneous images taken at the same CAD but from different engine cycles (example one such image is on the left in Fig. 3), the ensemble-averaged image is computed (center column in Fig. 3). This step helps to average out cycle-to-cycle variation in the dribble behavior. Although the dribble features identified herein are characteristic of every engine cycle, their extent, the timing of their appearance, and their spatial distribution changes from cycle to cycle. As a result, unraveling the effects of cycle-to-cycle variations from those of the controlled parametric variations described in the following sections is difficult when comparing any two instantaneous cycles. Instead, some statistical analysis is required. Here, for the purposes of presentation in written form, the statistical analysis consists of ensemble-averaging images at each crank angle from multiple cycles. Because of averaging, the visual appearance of some features of dribble, for instance the population individual droplets, can be "multiplied" if droplets exist in different locations in different images. For instance, if two images from different cycles each have 10 droplets in different non-overlapping locations, upon averaging, the images will show 20 droplet features. Nevertheless, this multiplication occurs for all images so that they are comparable relative to each other. For examples of dribble without averaging, see the dynamic movies available online (Eagle and Musculus 2014).

The second post-processing step is to calculate the absolute value of the difference between two averaged images separated by some dwell in time, in this case, five frames (about 1.5°CA at the engine speed of 1200 RPM and a camera frame rate of 25kfps). Comparing the center and right images in Fig. 3, this differencing step removes static features which appear consistently (e.g. nicks on the cylinder head, as well as other static features) which otherwise would appear similar to elastic scatter from liquid droplets. (We explored simple background subtraction for this purpose, but it was not as effective as the differencing scheme because illumination of static features changed throughout the cycle depending on the scattering environment on any particular cycle.) The differencing step does not completely eliminate strong reflections from static features on the cylinder head, but the moving dribble (e.g. in the 4 o'clock and 10o'clock positions in the piston-view image in Fig. 3) now stands out much better. In the images, the red dot identifies the injector tip, the horizontal black line identifies the vertical location of the firedeck near the injector in the side-view image (bottom of Fig. 3), and concentric circles of 0.446cm radial increments are provided for scale.

3.2 Dribble classification

In Fig. 4, selected images during the dribble event highlight different types of diesel-fuel dribble from the full-cycle dataset with the Delphi injector, both before (top) and after (bottom) image post-processing. As a reference, along with each pair of simultaneous images, we present the recorded average (non-combusting) cylinder pressure and the actual injection duration. The CADs of the imag-

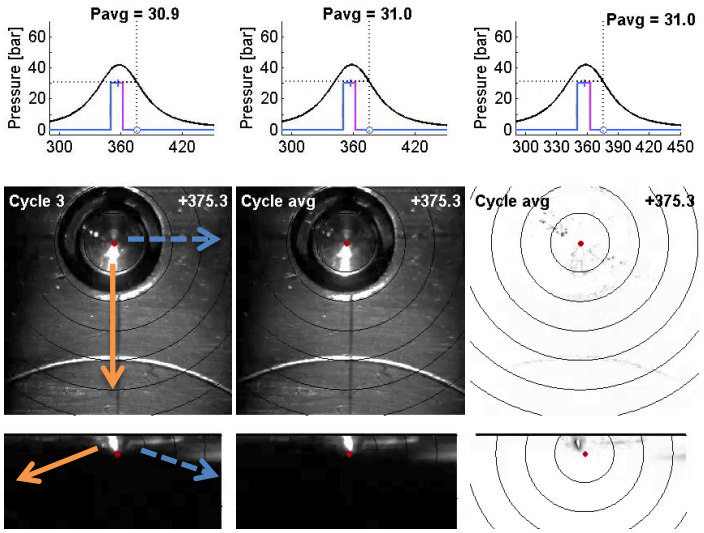

Fig. 3. Image processing of dribble: example unprocessed instantaneous elastic scatter image (left), ensemble-average of eight images at the same crank angle from multiple cycles (center), absolute value of differece of two averaged images separated by five frames (right). Arrows in the leftmost pane indicate the relative perspective of the images.

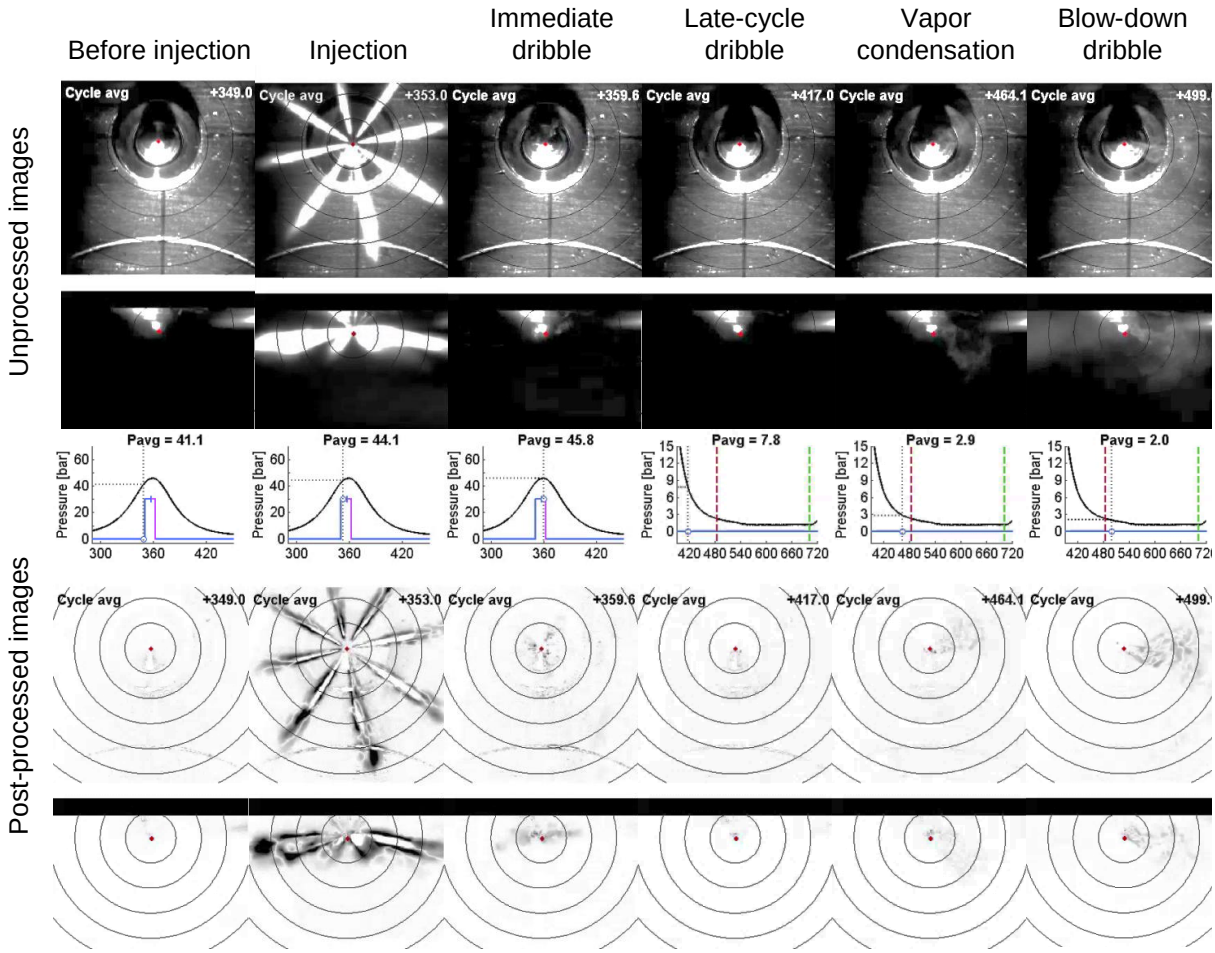

Fig. 4. Sequence of dribble phenomena in eight-cycle ensemble-averaged images before (top) and after (bottom) post-processing. Left to right: prior to injection (349.0CAD), during injection (353.0CAD), immediate dribble (359.6CAD), late dribble (373 CAD), late-cycle dribble (417.0CAD), fuel vapor condensation (464.1CAD), blow-down dribble after exhaust valve opening (499.0 CAD). In addition to imaging, each frame displays the cylinder pressure trace (black) and injector fire signal(blue). Dashed vertical lines indicate exhaust (485CAD, red) and intake (703CAD, green) valve openings. Delphi injector, non-combusting conditions

es are listed, and a small white circle and dotted lines indicate where in the pressure cycle the image is taken. A square pulse on the plot represents the time from actual start of injection (SOI) to the actual end of injection (EOI). Both SOI and EOI were determined from visual inspection of the elastic-scatter images. Depending on the injector, SOI occurs roughly 300-400 microseconds after the start of solenoid energizing (SSE). EOI also occurs some time after the end of solenoid energizing (ESE), with a dwell that depends on injector design, nozzle size, injection pressure, and injection duration (also see Table 2). The square wave showing the duration of injection (DOI) is color-coded to show ESE. Until ESE, the injection pulse is blue. A small hash on the pulse indicates ESE, after which the line color changes to red until EOI. This allows the reader to visually asses the start and duration of injection as determined from the imaging relative to the solenoid energizing time.

In the imaging data, we see several distinct events associated with dribble. Prior to injection, at 349.0CAD, no liquid fuel is apparent within the field of view, thus the post-processed image (bottom) shows the ‘background’ level of intensity deviation caused by small variations in reflections from static features on the surface. The next image to the right, at 353.0CAD, is from the middle of the injection event, which is visible from 349.6 to 357.6CAD. Following injection, the first ’immediate’ dribble (IDr) event occurs from 359.0 to 363.3CAD. In instantaneous images, numerous liquid-fuel drops exit from a few, but not all, of the nozzle orifices. Among 30 instantaneous realizations (not shown), there is no preferred dribble location; instead dribble emerges with no discernible pattern from between 1 and 4 of the orifices (see 359.6CAD image in Fig. 4). The eight-image averages presented here convey the general propensity of dribble.

The second ‘late-cycle’ dribble (LDr) event occurs later in the expansion stroke, from 389 to 424CAD, where, in the case of diesel fuel, we see liquid slowly emerging/collecting/bubbling from

each orifice of the injector simultaneously (e.g. 417.0CAD image). Even with the image processing, the late cycle dribble is difficult to discern in static images, but is much more apparent in dynamic movies, even unprocessed (Eagle and Musculus 2014). Later in the expansion stroke, from 435 to 490CAD, as the cylinder pressure decreases, fuel vapor condenses (VC) into a cloud of fine droplets near the injector (see 464.1CAD image). The appearance of this cloud indicates that vapor fuel is likely exiting the injector during the late-cycle dribble, and/or liquid dribble has vaporized to some degree. This vapor condenses as local mixtures become super-saturated when the cylinder pressure/temperature decreases.

During exhaust blow-down (BD) and into the exhaust stroke from 494 to 625CAD, bulk in-cylinder flows in the vicinity of the injector after exhaust valve opening strip more fuel from the injector nozzles/sac and draws droplets directly into the exhaust. Later, from 717 to 165CAD of the following cycle, a single attached liquid fuel drop remains hanging on the injector tip. This hanging drop disappears slowly over the course of the intake and compression, such that by the start of the next injection, no liquid fuel is visible on the injector tip. Even with post-processing, the hanging drop is not apparent in static images (none shown here), but the dynamic movies convey the evolution of the hanging droplet (Eagle and Musculus 2014). No other features of dribble are observed using the diagnostics employed here.

3.3 Parametric variations

This section describes how various parametric variations affect dribble. The parametric variations are: 1) orifice size, 2) fuel type, 3) timing of SOI, 4) fuel-rail pressure, 5) addition of a post injection (0.350ms DSE), 6) combustion reaction using air diluted with nitrogen to 18% oxygen, and 7) injector body type. For each parametric variation, we selected a combination of injector and fuel that illustrate the effects on dribble. Also, the durations of the scheduled injection event, the immediate and late-cycle dribble, and fuel vapor condensation are quantified in terms of CAD and cylinder pressure ranges over which they occur and indexed in tables in the Appendix. The data are acquired over a more limited crank-angle range compared to the data in Fig. 4 to record the immediate and late-cycle dribble, and may miss some or all of the vapor condensation, blow-down dribble, and hanging droplet features. The same image processing scheme shown in Fig. 3 and applied in Fig. 4 is also applied to the images from the parametric variations. Tables A1-A7 in the appendix parallel the figures presented in the parametric variations, and show the relevant specifications of hardware and operating conditions.

3.3.1 Orifice size

Before exploring parametric variations of engine operating conditions with a given fuel and injector, the characteristics of dribble are investigated across a range of orifice sizes. Given that dribble issues from the combined volume of the injector sac and orifices, it is reasonable to expect that orifice size might affect dribble. Shown in Fig. 5 are images under non-combusting conditions using diesel fuel with the Cummins XPI injector with three different orifice sizes of 200 micron (top row), 131 micron (middle row), and 90 micron (bottom row). The dribble features are present with all three orifice sizes, though the visible extent of dribble is difficult to differentiate among the three configurations. Larger orifices perhaps yield the greatest population of immediate dribble. However, it is the intermediate nozzle, not the smallest size that shows the least immediate dribble for this configuration.

3.3.2 Fuel type

To explore the influence a fuel type on dribble, operation with n-heptane is compared to diesel fuel in Fig. 6, using the Cummins XPI injector with eight 90-micron orifices. Immediately noticeable is the asymmetric nature of the n-heptane spray (bottom-left image), as well as its reduced liquid penetration. Needle motion induced by the reduced viscosity of n-heptane compared to diesel fuel, as well as the higher volatility of n-heptane, likely contribute to these differences. As shown in Fig. 6, the immediate dribble with n-heptane (bottom row) is similar to that with diesel fuel (top row), but the late-cycle dribble is visibly increased, and it appears much like a very late, secondary injection (see 433.0CAD image). The remarkable increase in late-cycle dribble may also be due to the higher volatility of n-heptane, or to dissolved gases, as discussed in section 4. Presumably due to the higher vapor pressure of n-heptane, very little vapor condensation is apparent, though the vapor dribble may be similar for the two fuels.

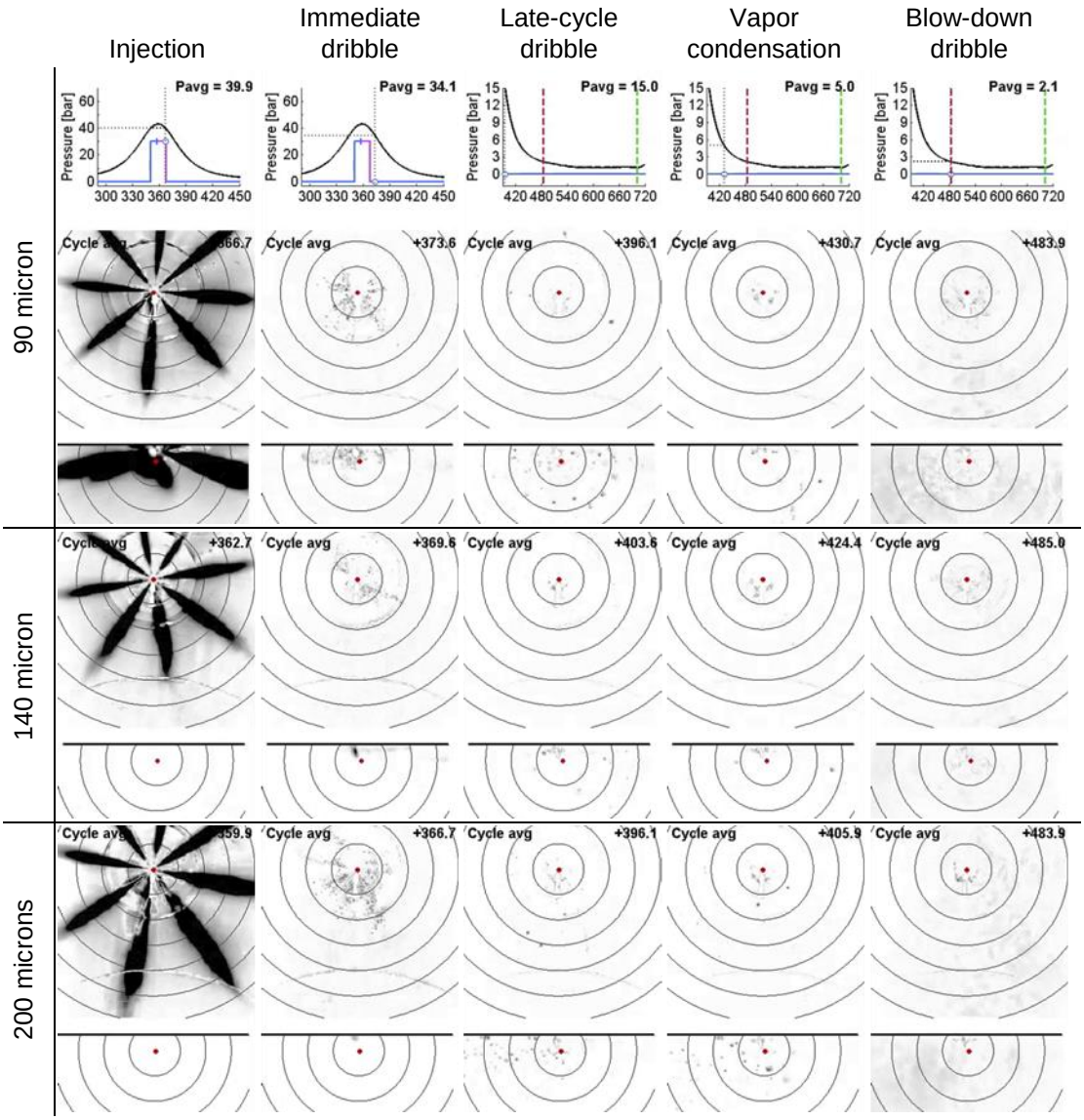

Fig. 5. Orifice size influence on selected features of dribble phenomena (5 panes left to right) in ensemble-averaged images with a single injection under non-combusting conditions: 90 micron (top row), 140 micron (middle row), and 200 micron (bottom row). Side view imaging during spray injection is not available for the 140 or 200 micron nozzles (also see Table A1 in the Appendix)

3.3.3 Start of injection

The effect of varying the timing of SOI on the dribble features is shown in Fig. 7. The injector is the Cummins XPI, with 140 micron orifices and using n-heptane fuel. While the dribble features described below are also present with diesel fuel, as described in the previous sub-section, they are much more apparent in static images with n-heptane, so the images presented here are for n-heptane. Average images for an early injection timing (SOI = 330 CAD), a standard injection timing (SOI = 350 CAD), and a late injection timing (SOI = 360) are presented in the top, middle, and bottom rows, respectively.

The signal distribution from the immediate dribble varies only slightly among the three injection timings. The timing of the immediate dribble is roughly the same relative to the end of injection, regardless of the SOI timing. Hence, the varying conditions at the end of injection, especially in-cylinder pressure, do not appear to visibly affect the timing of the immediate dribble.

By contrast, the second dribble event, late-cycle dribble, seems to occur at the same phase in the engine cycle, with only a slight effect of the injection timing. That is, the late-cycle dribble seems to be weakly connected to the injection event, if at all. Late-cycle dribble appears to be more strongly affected by the ambient in-cylinder conditions, most likely cylinder pressure. For early, standard, and late injections, the late-cycle dribble occurs in crank angle ranges of 387-441CAD, 399-448CAD, and 398-446 CAD, when the cylinder pressure ranges from 18.8-4.6 bar, 12-3.7bar, and 14.9-3.8 bar, respec-

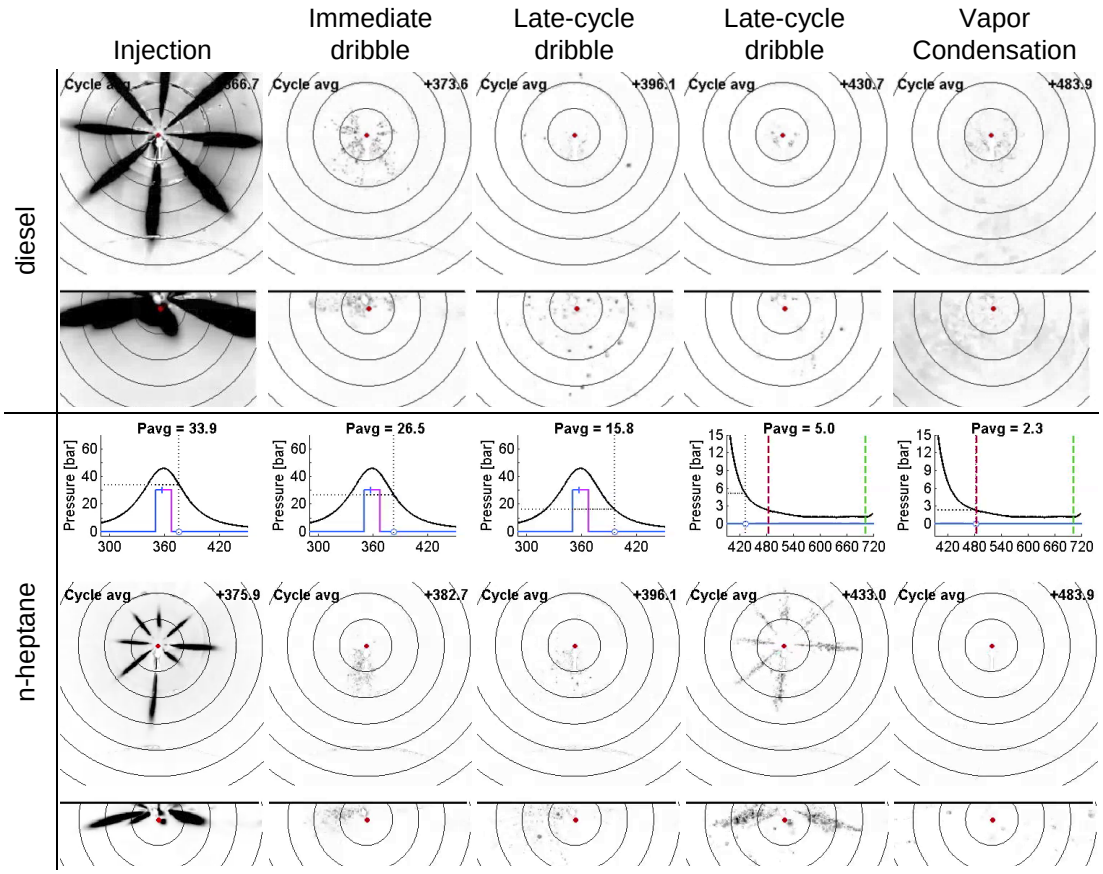

Fig. 6. Fuel influence on selected features of dribble phenomena (5 panes left to right) in ensemble-averaged images with a single injection under non-combusting conditions. Diesel fuel (top row) or n-heptane (bottom row). Cummins XPI 90 micron (also see Table A2 in the Appendix)

tively. Vapor condensation only occurs with diesel fuel (although n-heptane is shown in Fig.7, see e.g. Fig. 6) and consistently begins at cylinder pressures between 4 and 5 bar.

3.3.4 Fuel-rail pressure

Although many of the dribble features occur well after the end of injection, when the connection to the pressure in the fuel rail would presumably be weak, fuel rail pressure nevertheless has a visible effect on dribble. The images in Fig. 8 show characteristic features of dribble using diesel fuel under non-combusting conditions with the Cummins XPI injector at fuel rail pressures of 1600bar (top row), 1000bar(middle row), and 800bar (bottom row).

It appears that the population of droplets from the immediate dribble is slightly greater at 1600 and 1000bar than at 800bar rail pressure. Fuel-vapor condensation also appears somewhat greater at the highest rail pressure. Late-cycle dribble occurs around 5 bar cylinder pressure regardless of fuel rail pressure. At the lowest rail pressure of 800bar, there is also a trend of less late-cycle dribble and particularly less vapor condensation. However, when the fuel is changed, this trend with injection pressure reverses. Using n-heptane fuel, the quantity of late cycle dribble appears to reduce with increasing rail pressure and increase at the lower rail pressure (not shown here).

3.3.5 Post-injection

To explore how the features of dribble, in particular the immediate dribble, are affected by multiple injections, a post-injection is added to an unchanged main injection, imaged in Fig. 9. The injector is the Cummins XPI with eight 90-micron orifices, and n-heptane fuel is injected under non-combusting conditions in the top half of Fig. 9 (comparisons of combusting conditions are deferred until the next subsection). The top-left quadrant shows a single main injection at TDC, and the top-right quadrant shows the same main injection but with a post injection at 371CAD SSE. The post injection does not appear to strongly affect the immediate dribble from the main injection, other than to disrupt its full duration because of the reopening of the needle during the post injection (not shown). The post injection has its

own immediate dribble event, with a duration and droplet population similar to the immediate dribble of a main injection, which adds to the late-cycle dribble from the main injection (compare 396.1CAD im-

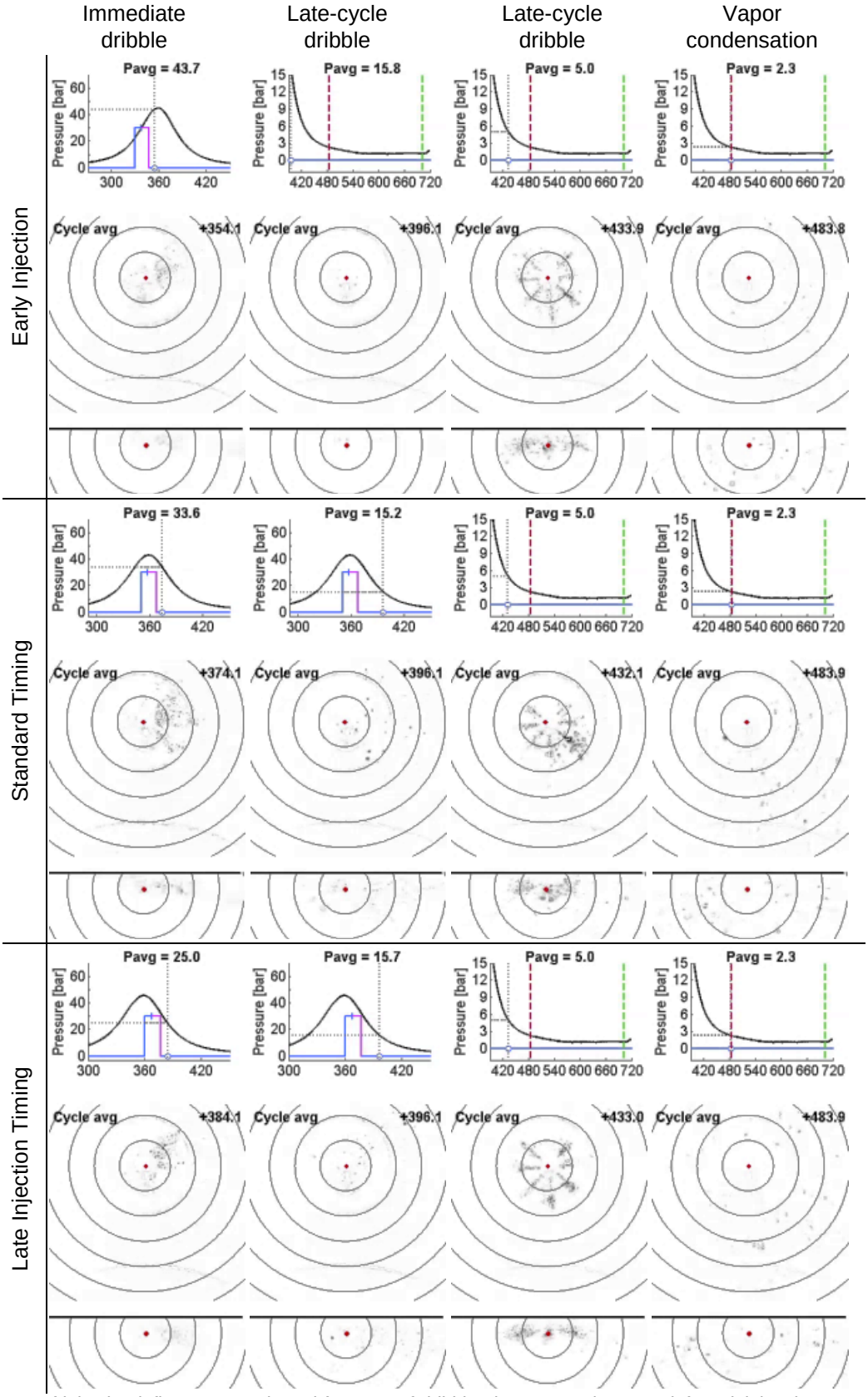

Fig. 7. Start of injection influence on selected features of dribble phenomena (4 panes left to right)early SOI=330 CAD (top row), baseline SOI=350 CAD (middle row), and late SOI=360 CAD (bottom row). XPI injector, 130 micron nozzle, n-heptane fuel (also see Table A3 in the Appendix).

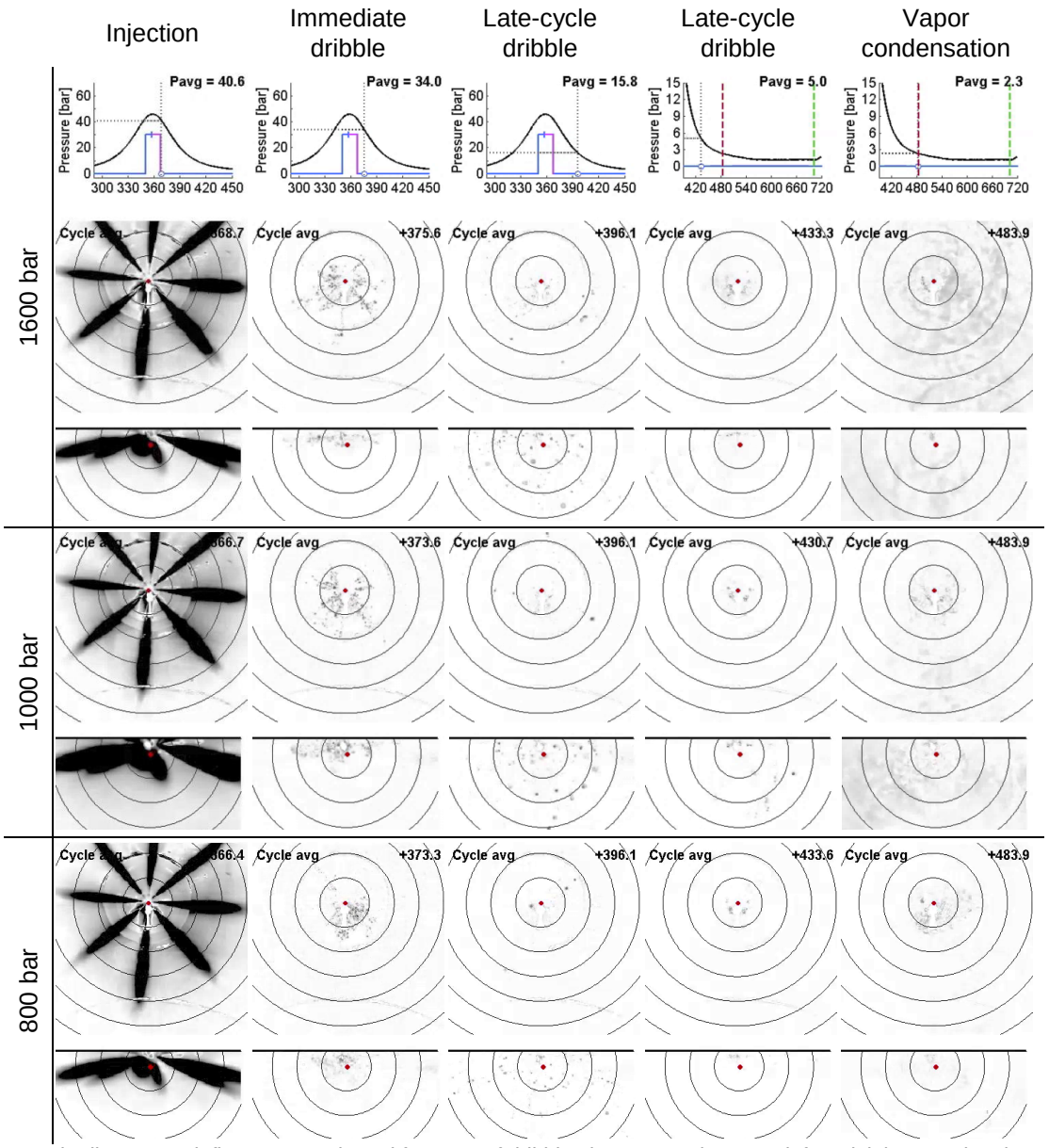

Fig. 8. Fuel rail pressure influence on selected features of dribble phenomena (5 panes left to right): 1600 bar (top row), 1000 bar (middle) and 800 bar (bottom). XPI injector, 0.090mm orifices, diesel fuel (also see Table A4 in Appendix).

ages in the top two quadrants in Fig. 9). The later part of the late-cycle dribble (433.3CAD) and vapor condensation (483.9CAD) events appear to be unaffected by the presence of a post-injection, occurring at nearly identical cylinder pressures of 5 and 2.5 bar, respectively.

3.3.6 Combustion reactions

With combustion, the later dribble features are obscured to varying degrees by light emission from combustion, but for the conditions investigated here, the immediate dribble and the overall impact of dribble on combustion is nevertheless evident. Images of key dribble features under non-combusting and combusting conditions, and for both single-injection and post-injection conditions, are presented in Fig. 9. For the single-injection condition (left side of figure), the individual droplets of late-cycle dribble present under non-combusting conditions (396.1 CAD, top-left quadrant) appear larger under combusting conditions because of the light emission from combustion (396.1 CAD, bottom-left quadrant). Also, emission from the combustion of earlier immediate dribble adds to the distribution of signal (396.1 CAD, bottom-left quadrant). Hence, under this particular combusting condition, the immediate dribble and potentially some of the late-cycle dribble is clearly reacting to some degree. Both late-cycle dribble emerging at lower cylinder pressure (433.3 and 447.3CAD on left side) and the vapor condensation (483.8CAD) are similar with and without combustion, and light-emission from combus-

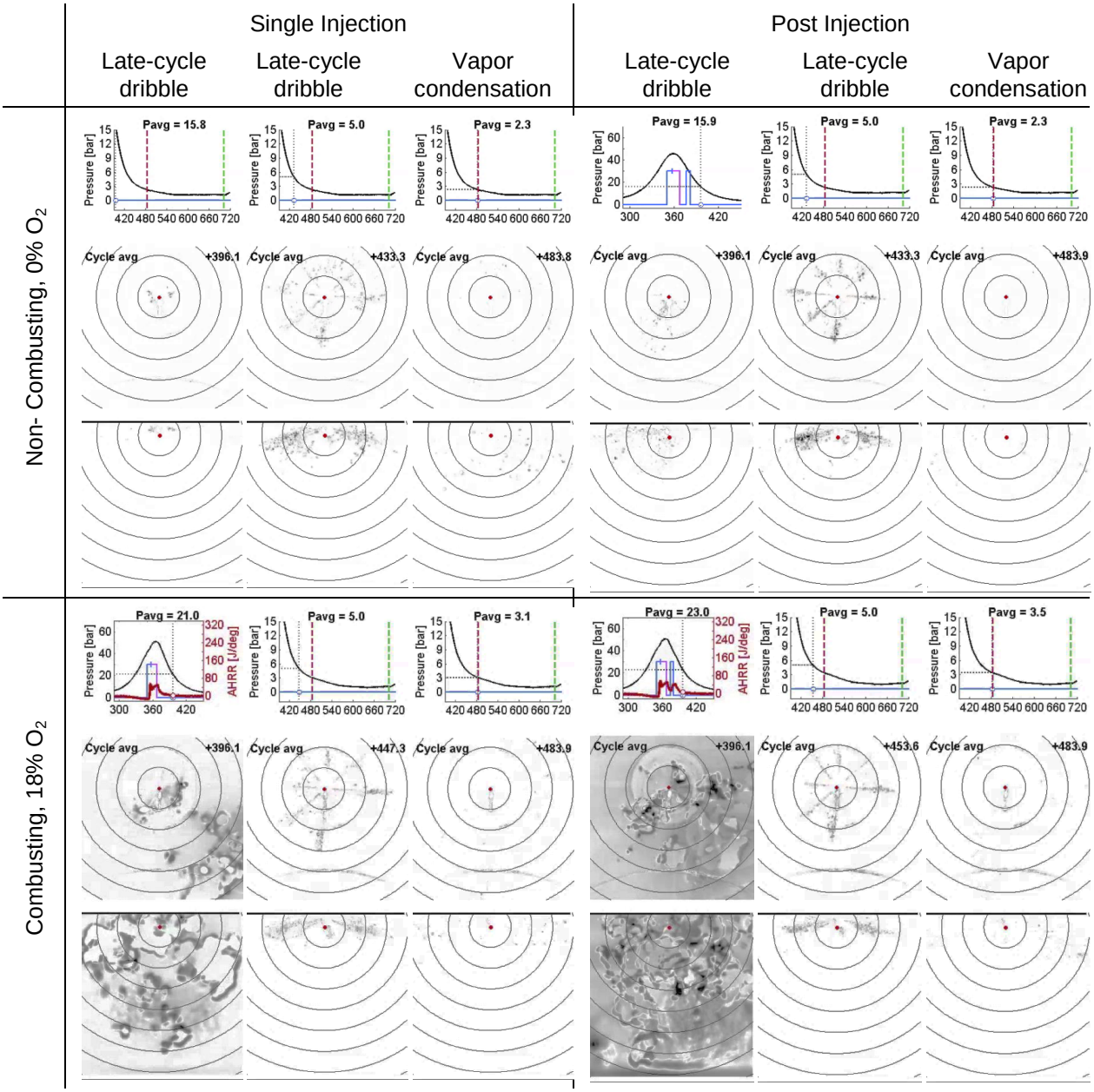

Fig. 9. Post injection and combustion influence on selected features of dribble phenomena (3 image panes left to right in each of four blocks): oxygen-free non-combusting (top half) and 18% intake oxygen combusting (bottom half) conditions with either a single injection (left side) of with a post-injection (right side). Cummins XPI 90micron orifices, n-heptane fuel (also see Table A5 in Appendix).

tion is not apparent for the very late-cycle dribble under this condition. With a post-injection (right half of Fig. 9), the same observations comparing combusting to non-combusting conditions apply in roughly the same way to each of the dribble events.

3.3.7 Injector design

In addition to operational variables, it is reasonable to expect that injector design may also affect dribble features. In Fig. 10, images from three different injectors are compared using diesel fuel. Since the Bosch Spray injector has relatively small holes, a similar small-hole tip was used in the Cummins XPI injector. Only one orifice size is available for the Delphi DFI-1.5 injector. The top row is from the Cummins XPI, the bottom left is from the Bosch spray B, and the bottom right is from the Delphi DFI-1.5. All three of the characteristic features of dribble previously identified in Fig. 4 exist for these injectors, though they are less apparent with diesel fuel (n-heptane data are not available with all three injectors) and smaller orifices and/or with fewer holes than in previous figures. (The reader is encouraged to view the dynamic movies (Eagle and Musculus 2014) for more clearly visible dribble among the three

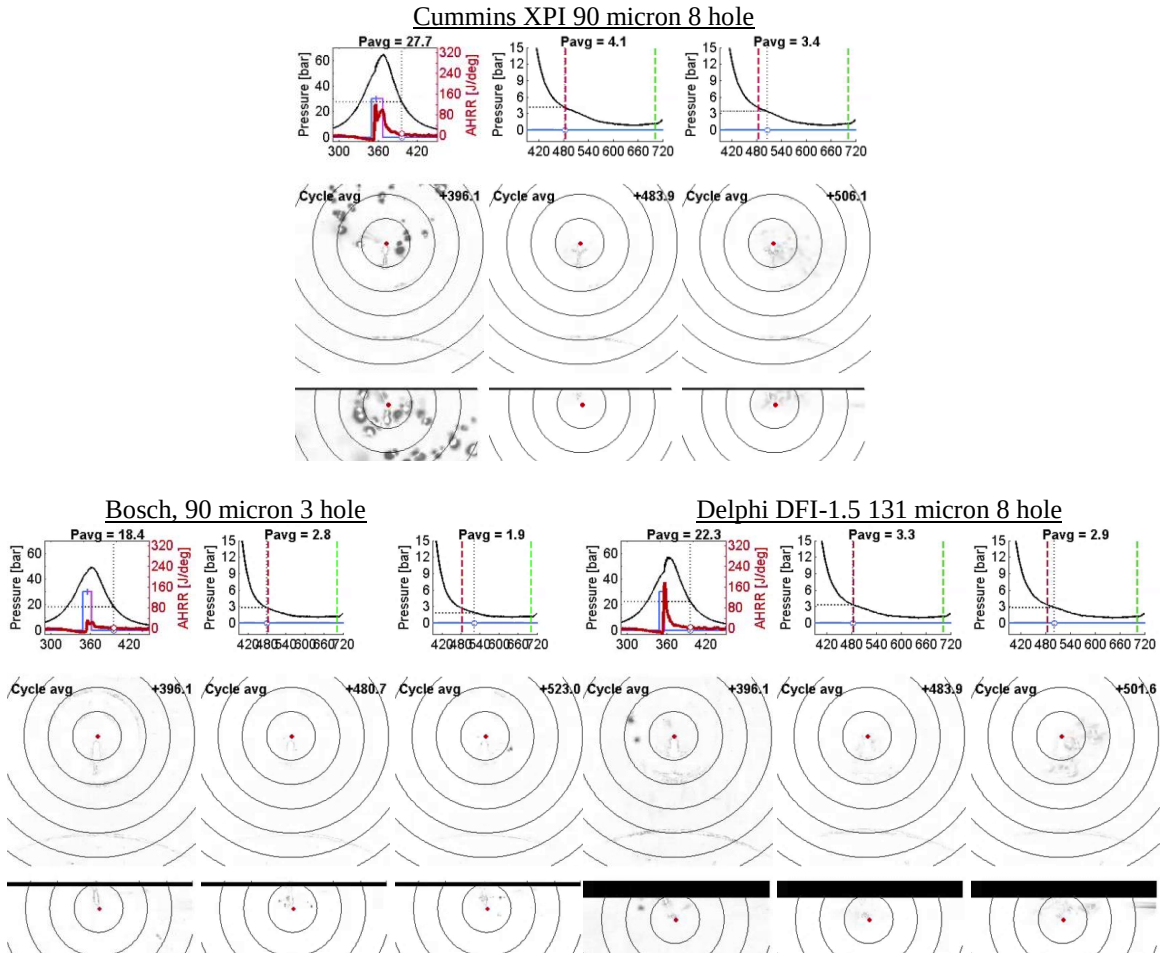

Fig. 10. Injector manufacturer influence on selected features of dribble phenomena (3 panes left to right in each block) with a single injection under combusting conditions with 18% intake oxygen. Cummins XPI 90-micron (top), the Bosch spray B 90-micron (bottom left), and the Delphi DFI-1.5 131-micron (bottom right) injectors, diesel fuel (also see Table A6 in the Appendix).

injectors). Vapor condensation is not visible before the exhaust valve opens at 485CAD, but during the exhaust blow-down it is visible in both the Cummins and Delphi injectors (506.1 and 501.6 CAD). Because it has only three holes, the Bosch Spray B injector delivers much less fuel during the scheduled injection than the other two injectors, and the vapor dribble concentration may also be lower, leading to less condensation, though some large liquid droplets appear during blow-down.

4. Potential physical processes contributing to dribble

The imaging data thus presented, we now discuss some of the physical processes that may play a role in dribble. The discussion is necessarily speculative because we have limited information about the injector dynamics and physical processes and flows internal to the nozzle after the end of injection. Several candidate physical processes may be responsible for dribble. Unfortunately none of the available measurements are capable of definitively differentiating among these potential processes. Nevertheless, the discussion below spans our expectations and the available information.

4.1 Injector dynamics

One of the first likely explanations for dribble is that the needle does not seal properly. In this case, fuel is delivered to the nozzle tip at low flow and hence dribbles out of the orifices after the end of injection. A related phenomenon would be needle bounce, which creates one or more undesired injections. The immediate dribble described here does not resemble needle bounce, however, because the fuel emerges slowly and steadily over a relatively long duration, and without a classic conical spray-like character. Needle bounce typically yields quick, higher velocity sprays resembling a very short injection. Hence, the immediate dribble does not appear to be caused by classic injector needle bounce. The late-cycle dribble with n-heptane in Fig. 6 does resemble needle bounce somewhat, in that the

fuel emerges in sprays from all of the orifices, albeit at low velocity and with a small spreading angle. The late dribble is so long after the end of injection, and uncorrelated to the time after the end of injection, that it is unlikely that it is caused by injector dynamics. (A more likely explanation is described below in sections 4.2 and 4.3). Nevertheless, some sort of internal leaking inside the injector cannot be ruled out with the data available. If internal leakage were *solely* responsible, however, then it must be common to all three of the injector manufacturers tested, since all three showed evidence of dribble.

4.2 Ingested ambient gas

Recent high speed X-ray measurements have shown that after the end of injection, bubbles of gas from the combustion chamber enter the sac (Swantek, Powell, et.al. 2014). As hot combustion-chamber gases are ingested into the injector, it is likely that their temperature decreases when surrounded by the relatively cool injector and fuel. Cool gases contract so that more gas can be ingested into the nozzle. After the gas is ingested, surface tension effects in the remaining liquid fuel could close the nozzle orifices, trapping ingested gas in the nozzle sac. The ingested bubbles may lead to dribble in two ways. First, the ingested gas may immediately displace liquid fuel within the sac and orifices. The liquid fuel that emerges from the injector either may be included in the tail of the main injection event, or it may be part of the immediate dribble, depending on the timing of the ambient gas ingestion relative to the end of injection. Second, as the cylinder pressure decreases during the expansion stroke, the ingested gas bubbles should expand, which would further displace fuel from the sac. The gradual late-cycle dribble observed with diesel fuel may be associated with this process. Also, depending on the surface tension effects, some of the ingested gas could either penetrate the fuel surface, expelling bubbles of gas at the nozzle. The influence of ingestion of hot cylinder gases coking of injector nozzles is a related and potentially important consideration depending on fuel and operating conditions, but this is not explored here.

4.3 Fuel compressibility effects

At rail pressures, compressibility can be significant, with fuel volume decreasing by as much as 7% for diesel fuel and 14% for n-heptane (CRC Handbook, 1984). After the end of injection, as the sac pressure decreases, expansion of fuel in the sac may contribute to some degree to the immediate dribble. However, during the throttling that occurs when the needle closes, the sac pressure should be reduced as the end of injection is approached, allowing the compressibility of the fuel to be relieved to a large degree as the end of injection is reached. Hence, immediately after flow past the needle ceases, it is unlikely that sufficient sac pressure remains to explain the immediate dribble. During the expansion stroke, the reduction of cylinder pressure would decompress fuel in the sac somewhat, but the fuel would only expand by between 0.3-0.6% as the cylinder pressure decreases from TDC pressures to exhaust pressure. Expansion of ingested gas bubbles, as described in the previous section, would likely be much greater, and would likely be a much greater contributor to late-cycle dribble if present.

4.4 Dissolved gases in the fuel

During the handling and pumping of the fuel to high common-rail pressures, it is possible that the fuel is imparted with dissolved gases, which could then be relieved when the fuel experiences a lower pressure after the end of injection (Battino, Rettich and Tominaga 1984). It is possible that as the pressure decreases, such gases could emerge from solution and propel the remaining liquid fuel out of the injector nozzles. The dynamics of the evolution of dissolved gases under direct injection conditions is not established, but nucleation and the timescales of the pressure reduction may be important for the rate at which dissolved gas is evolved. It is conceivable that lacking proper nucleation sites or sufficient time for bubbles to grow as the pressure is reduced, the dissolved gas mixtures could become super-saturated. An analogous example is carbonated beverages, which are typically super-saturated and can release dissolved gases very quickly if disturbed (e.g., dropped, shaken) or if suddenly provided with nucleation sites (adding material or pouring into another container). If a super-saturation condition is achieved, the evolution might occur catastrophically, which could result in a sudden expansion pushing fuel out of the nozzle. The considerable increase in late-cycle dribble for n-heptane relative to diesel fuel in Fig. 6, which correlates in the gas solubility for these two fuels, is compelling.

4.5 Differences in fuel flow among orifices

In multi-hole nozzles, differences in flow and/or geometry among the orifices will yield different mass and momentum flow rates through each of the orifices. As injection ends and flow through the orifices rapidly decreases, flow may cease in different orifices at different times. Consequently, the remaining momentum in the higher-flow orifices may draw flow back into the nozzle through other orifices that have ceased flowing. This reverse flow would draw in ambient gas, and the connection between orifices through the sac could allow much of the sac and orifice volume to be emptied of liquid fuel. The immediate dribble, which issues apparently randomly from different orifices on different cycles, may reflect such flow imbalances that vary from cycle to cycle, affecting from which orifice(s) the dribbled fuel emerges. Cycle-to-cycle variability of in-cylinder gas-phase flow structures may also affect and potentially actuate the dribble depending on the local flow velocities and differential pressure fields in the vicinity of the injector nozzle.

5. Limitations and uncertainties

This study is limited in its conclusions owing to the qualitative nature of the imaging data presented. The authors have made every effort to ensure the qualitative trends described in each image presented are broadly representative of images of the data collected, for instance by using ensemble-averaged images. However, more quantitative data is necessary to solidify the claims and assertions thus far inferred. Quantification must include an accurate estimate of volume of fuel delivered per injection, as well as the fuel density at the injection point, and ideally, some quantification of the fuel dribbled during each event. Accurate measurements of these volumes and densities (affected by pressure, fuel temperature, dissolved gasses, among others) are currently unavailable. One possibility is holographic image reconstruction of the dribble event to estimate the sizes of larger fuel drops or topology of condensed vapor clouds.

Although not presented here, consecutive fired injection (as opposed to 1:9 cycle skip-firing described in section 2.2) has been tested to assess the effect of skip firing on the results presented. While there didn't appear to be any differences in injection behavior when the injector was sequentially vs skip fired, it is possible that the low-load cases tested thus far yield nozzle tip temperatures in the optical engine that are lower than in a continuously-fired metal engine. The effects of varying nozzle temperature (and varying fuel temperature) are also not considered here.

Conclusions

We used elastic-scatter imaging of liquid fuel droplets emitted during and after the end of fuel injection in a direct-injection heavy-duty optical engine to characterize injector dribble behavior while performing parametric variations of hardware and operating conditions. Through image post-processing illustrated in Fig. 3, we could identify and better visualize the 'average' dribble behavior. These imaging data provide support for the following conclusions.

First and foremost, injector dribble appears to be universal, appearing for every injector model, nozzle configuration, operating condition, and fuel tested here. Various factors clearly affect the degree of dribble, but the characteristic phenomena are always identifiable in the imaging data. Three characteristic features of dribble can be roughly identified across all conditions:

1. Immediate dribble of liquid droplets, which begins within a few crank angle degrees after the end of the scheduled injection, and can last for ten or more crank angle degrees. Examples of immediate dribble include the second image in the parameter variations of Figs. 5, 6, 8.
2. Late-cycle dribble, which occurs during the expansion stroke but before the exhaust stroke. The late-cycle dribble appears to be connected to the cylinder pressure, beginning at roughly the same cylinder pressure (12-20bar) over the whole range of conditions tested. Evidence of fuel vapors escaping the sac in the non-reacting conditions is inferred by the vapor condensation occurring with diesel fuel starting between 4 and 5bar cylinder pressure. Examples of late-cycle dribble can be seen clearly in Figs. 4-6, as well as Figs. 7 (n-heptane) and 8 (diesel).
3. Blow-down dribble, which occurs between exhaust valve opening and into the exhaust stoke, induces the emergence of liquid droplets or vapors from the sac that are stripped away from the injector by bulk in-cylinder flows, especially related to blow-down and exhaust flows. Under the conditions explored here, this fuel emerges so late in the cycle that it doesn't react and is drawn directly into the exhaust stream. Illustrative examples of blow-down dribble are in Fig 4 (non-reacting conditions) and Fig 10 (reacting conditions)

A fourth feature, consisting of a hanging droplet appearing at end of the exhaust stroke and surviving until the early compression stroke of the following cycle, was observed in full-cycle imaging for one of the injectors, but was not explored for other injectors.

Most data presented here were under non-combusting conditions, but combustion does not appear to affect the presence of the characteristic dribble features. For the combustion conditions investigated here, immediate dribble can ignite near the injector tip and produce visible sooty droplet burning. Much of the late-cycle dribble does not visibly ignite, and in many cases can be seen being drawn directly into the exhaust after exhaust valve opening, including condensed vapor.

Though only two fuels were tested here, differences among the fuels were quite stark. Compared to diesel fuel, late-cycle dribble for n-heptane was much increased, appearing quite spray-like, though very late in the cycle. Also, trends in the visible dribble with rail pressure move opposite directions depending on fuel type.

As a discussion of work yet to be done, we noted that the data gathered thus far does not provide enough information to identify the causes of dribble, but we speculated on several physical mechanisms that may contribute to the dribble event. More work is necessary to demonstrate which factors may be used to control dribble towards first mitigating and finally eliminating the undesired dribble event.

Acknowledgements

The optical engine experiments were performed at the Combustion Research Facility, Sandia National Laboratories, Livermore, CA. Support for this research was provided by the U.S. Department of Energy, Office of Vehicle Technologies. Sandia is a multi-program laboratory operated by Sandia Corporation, a Lockheed Martin Company for the United State Department of Energy's National Nuclear Security Administration under contract DE-AC04-94AL85000. The authors gratefully acknowledge the contributions of Dave Cicone for his assistance in maintaining the research engine used in this study.

References

Battino, Rubin, Timothy R. Rettich, and Toshihiro Tominaga 1984. "The Solubility of Nitrogen and Air in Liquids" Journal of Physical Chemistry Reference Data, vol. 13(2) 563-600

Bobba, Mohan K, Clément Chartier, Bengt Johansson, Öivind Andersson, and Mark P B Musculus. 2010. "Planar Laser-Diagnostics of Soot and OH with Post-Injections in a Heavy-Duty LTC Diesel Engine." In *Thermo and Fluid Dynamic Processes in Direct Injection Engines*.

CRC Handbook of tables for Apllied Engineering Science 2nd Edition , p95 Boca Raton Press, 1984.

Dec, J. 1997. "A Conceptual Model of DI Diesel Combustion Based on Laser-Sheet Imaging." *SAE Technical Paper* (970873). doi:10.4271/970873.

Dolenc, A. 1990. "The Injection Equipment of Future High-Speed DI Diesel Engines with Respect to Power and Pollution Requirements." *Proceedings of the Institution of Mechanical Engineers, Part D: Journal of Automobile Engineering* 204: 49–58. doi:10.1243/PIME_PROC_1990_204_132_02. http://pid.sagepub.com/content/204/1/49.full.pdf+html.

Dreeben, Thomas, Larry Millen, Marvin Wells, and James Woolworth. 1992. "Effect of Sac Volume on Injector Performance." *SAE International* (920680) (February 1). doi:10.4271/920680. http://papers.sae.org/920680/.

Eagle, W Ethan, and Mark PB Musculus. 2014. "2014 Thiesel Dribble Movies," available from Engine Combustion Network at http://www.sandia.gov/ecn/pub-links/cdl/Thiesel2014.php.

Ekoto, Isaac W., Will F Colban, Paul C Miles, Sungwook Park, David E Foster, and Rolf D Reitz. 2009. "Sources of UHC Emissions from a Light-Duty Diesel Engine Operating in a Partially Premixed Combustion Regime." *SAE Int. J. Engines* 2 (1): 1265–1289.

"Engine Combustion Network." http://www.sandia.gov/ecn/.

Espey, Christoph, and John E Dec. 1993. "Diesel Engine Combustion Studies in a Newly Designed Optical-Access Engine Using High-Speed Visualization and 2-D Laser Imaging". SAE International . doi:10.4271/930971. http://dx.doi.org/10.4271/930971.

Koci, Chad P., Youngchul Ra, Roger Krieger, Mike Andrie, David E Foster, Robert M Siewert, Russell P Durrett, Isaac Ekoto, and Paul C Miles. 2009. "Detailed Unburned Hydrocarbon Investigations in a Highly-Dilute Diesel Low Temperature Combustion Regime." *SAE Int. J. Engines* 2 (1): 858–879.

Musculus, Mark P. B., and Thierry Lachaux. 2007. "End-of-Injection over-Mixing and Unburned Hydrocarbon Emissions in Low-Temperature-Combustion Diesel Engines." *SAE Technical* 2007: 776–790. doi:10.4271/2007-01-0907. http://subscriptions.sae.org/content/2007-01-0907/.

Musculus, Mark P. B. 2009. "Entrainment Waves in Decelerating Transient Turbulent Jets." *Journal of Fluid Mechanics* 638 (October 7): 117–140. doi:10.1017/S0022112009990826. http://www.journals.cambridge.org/abstract_S0022112009990826.

Musculus, Mark P.B., Paul C. Miles, and Lyle M. Pickett. 2013. *Conceptual Models for Partially Premixed Low-Temperature Diesel Combustion*. *Progress in Energy and Combustion Science*. Vol. 39. Elsevier Ltd. doi:10.1016/j.pecs.2012.09.001. http://linkinghub.elsevier.com/retrieve/pii/S0360128512000548.

O'Connor, Jacqueline, and Mark Musculus. 2013. "Post Injections for Soot Reduction in Diesel Engines: A Review of Current Understanding." *SAE Int. J. Engines* 6 (1): 400–421. doi:10.4271/2013-01-0917. http://www.sae.org/technical/papers/2013-01-0917.

Pickett, Lyle M., Julien Manin, Raul Payri, Michele Bardi, and Jaime Gimeno. 2013. "Transient Rate of Injection Effects on Spray Development." *SAE International* (September): 15–16. doi:10.4271/2013-24-0001. http://www.sae.org/technical/papers/2013-24-0001.

Schwarz, V, G König, P Dittrich, K Binder, and Daimlerchrysler Ag. 1999. "Analysis of Mixture Formation , Combustion and Pollutant Formation in HD Diesel Engines Using Modern Optical Diagnostics and Numerical Simulation." *SAE Technical Paper* 1999-01-36. doi:doi:10.4271/1999-01-3647.

Sjöberg, Magnus, and John E Dec. 2004. "An Investigation of the Relationship Between Measured Intake Temperature , BDC Temperature , and Combustion Phasing for Premixed and DI HCCI Engines." *SAE Technical Paper* 2004-01-19. doi:10.4271/2004-01-1900.

Swantek, A. B., Duke, D., Tilocco, F. Z., Sovis, N., & Powell, C. F. 2014 "End of Injection , Mass Expulsion Behaviors in Single Hole Diesel Fuel Injectors." In 26th ILASS Americas, Portland, OR

Taschek, M, P Koch, J Egermann, and A Leipertz. 2005. "Simultaneous Optical Diagnostics of HSDI Diesel Combustion Processes." *SAE Int. J. Engines* (724).

Thomas, Hugh K. 1939. *Automobile Engineering*. London: Sir I. PItman & Sons.

Williams, D S D, and J. Millar Smith. 1945. *The Oil Engine*. London: English University Press.

Appendix

Table A1. Parametric variation of orifice size, section 3.3.1, Fig. 5, Cummins XPI Injector, diesel fuel

Orifice Size [microns]	SOI/DOI [CAD / ms]‡	Immediate Dribble / Duration [CAD / ms]‡	Late Dribble start/ Cylinder Pressure [CAD / bar] ‡	Vapor cloud visible / Cylinder Pressure [CAD / bar] ‡
90	349.6 / 2.4	367.6 / 1.44	403 / 12	438 / 4.5
131	349.9 / 1.8	363.9 / 1.68	389 / 18	424 / 5.3
200	349.6 / 1.5	361.3 / 1.76	389 / 19	426 / 5.2

Table A2. Parametric variation of fuel type, section 3.3.2, Fig. 6
Cummins XPI Injector, 0.090mm nozzle

Fuel	SOI/DOI [CAD/ms] ‡	Immediate Dribble / Duration [CAD/ms] ‡	Late Dribble start / Cylinder Pressure [CAD] ‡	Vapor cloud visible / Cylinder Pressure [CAD] / [bar] ‡
diesel	349.6/2.4	367.6 / 1.44	403 / 12	438 / 4.5
n-heptane	349.9/1.8	368.1 / 1.08	394 / 17	N/A

Table A3. Parametric variation of start of injection, section 3.3.3, Fig. 7
Cummins XPI Injector, 0.090mm nozzle, diesel fuel

Timing	SOI/DOI [CAD/ms] ‡	Immediate Dribble / Duration [CAD/ms] ‡	Late Dribble start / Cylinder Pressure [CAD] ‡	Vapor cloud visible / Cylinder Pressure [CAD] ‡
Early	329.9 / 2.4	347.9 / 0.76	390 / 20	425 /5.5
Standard	349.9 / 2.4	367.6 / 1.68	403 / 12	438 / 4.5
Late	349.6 / 2.4	378.1 / 1.93	405 / 11	443 / 4.2

Table A4. Parametric variation of fuel-rail pressure, section 3.3.4, Fig. 8
Cummins XPI Injector, 0.09mm nozzle, n-heptane fuel

Fuel Rail Pressure [bar]	SOI/DOI [CAD/ms] ‡	Immediate Dribble / Duration [CAD/ms] ‡	Late Dribble start / Cylinder Pressure [CAD] ‡	Vapor cloud visible / Cylinder Pressure [CAD] ‡
1600	349.3 / 3.8	377.6 / 1.16	407 / 11	N/A
1000	349.6 / 2.5	368.1 / 1.08	394 / 17	N/A
800	349.9 / 2.4	367.6 / 0.56	394 / 19	N/A

Table A5. Parametric variation of post-injection and combustion, sections 3.3.5 and 3.3.6, Fig. 9
Cummins XPI Injector, 0.09mm nozzle, n-heptane fuel

Injection, Intake O_2 [% by vol.]	SOI/DOI [CAD/ms] ‡	Immediate Dribble / Duration [CAD / ms] ‡	Late Dribble start / Cylinder Pressure [CAD / bar] ‡	Vapor cloud visible / Cylinder Pressure [CAD / bar] ‡
Single, 0	349.6 / 2.42	367.6 / 1.44	403	N/A
With post, 0	349.9 / 1.83	381.3 / 1.68	398 / 15	N/A
Single, 18	349.6 /	Combusts	412 / 13	N/A
With post, 18	349.6 /	Combusts	421 / 10.2	N/A

Table A6. Parametric variation of injector design, section 3.3.7, Fig. 10, diesel fuel

Injector, orifice size [microns]	SOI/DOI [CAD / ms] ‡	Immediate Dribble /Duration [CAD / ms] ‡	Late Dribble start [CAD / bar] ‡	Vapor cloud visible / Cylinder Pressure [CAD / bar] ‡
Cummins XPI, 90	349.6 / 2.4	367.6 / 1.4	403 / 12	438 / 4.5
Bosch Spray B, 90	349.3 / 1.8	364.4 / 0.8	418 / 7.6	444.1 / 4.0
Delphi DFI-1.5, 131	349.6 / 1.3	361.3 / 1.8	413 / 8.8	441.9 / 4.7

The Modelling of Single and Multi-Component Droplet Evaporation

J.D. Camm[1], R. Stone[1], M.H. Davy[1] and D. Richardson[2]

[1]Department of Engineering Science, University of Oxford, Parks Road, Oxford, OX1 3PJ, UK

E-mail: joseph.camm@eng.ox.ac.uk
Telephone: +(44) 1865 283467

[2]Powertrain Research & Technology, Jaguar Land Rover, Whitley Engineering Centre, Abbey Road, Whitley, Coventry, CV3 4LF, UK

Abstract. An explicit model for the evaporation of a spherical single component fuel droplet is presented that takes account of temperature dependent fuel and vapour properties, evolving droplet internal temperature distribution and enhancement to heat and mass transfer due to droplet motion. This has been developed to model multi-component fuels, using non-ideal vapour-liquid equilibrium. Both well-mixed and unmixed droplet evaporation have been considered as limiting cases of the real behaviour of multi-component droplet evaporation. Single-component results for iso-octane are presented and compared with spray images to correlate droplet lifetime with overall spray lifetime. An empirical droplet size distribution is fitted to the experimental extent of the spray. Statistics from this distribution are compared with previously measured droplet sizes and droplet size correlations. Multi-component results are presented for binary ethanol/iso-octane mixtures and for a mixture of hydrocarbons representative of gasoline, with and without added oxygenates (methanol and ethanol). The effect of whether well-mixed droplet evaporation or unmixed droplet evaporation is assumed is investigated.

Notation

A	Droplet projected area
B_T	Heat transfer number
B_Y	Mass transfer number
C_D	Drag coefficient
c_p	Fuel isobaric specific heat capacity
d	Droplet diameter
D	Binary diffusion coefficient
F_D	Drag force
h	Specific enthalpy of fuel vapour
L	Latent heat of vaporization
L_{eff}	Effective latent heat of vaporization
Le	Lewis number
M	Molar mass
$\dot{m}$	Evaporation rate
Nu	Nusselt number
P	Total pressure
P_v	Fuel vapour pressure
r	Radial coordinate
Re	Reynolds number
Sc	Schmidt number
Sh	Sherwood number
T	Temperature
t	Time
U	Relative droplet velocity
X	Liquid mass fraction
x_i	Proportion of droplets with diameter d_i
Y	Vapour mass fraction
α	Thermal diffusivity
Δr	Finite difference grid separation
ΔP	Injection pressure
Δt	Timestep
ε	Currently vaporizing mass flux fraction
γ	Activity coefficient
λ	Thermal conductivity
ν	Kinematic viscosity
σ	Surface tension
μ	Dynamic viscosity
ρ	Density
	Subscripts:
A	Air
c	Critical condition
F	Fuel vapour
i	Referring to component i
L	Liquid fuel
R	Reference condition
s	Surface of droplet
ss	Steady state
0	Initial
∞	Conditions far from droplet

1. Introduction

The vaporization of liquid fuel in a Direct Injection Spark Ignition (DISI) engine is a complex process that should be completed in a relatively short time, before spark ignition occurs. The presence of inhomogeneous zones or liquid droplets in the combustion chamber will lead to locally rich combustion and the generation of excessive amounts of particulate matter in the exhaust. Regulations restricting both the mass and the number of particulates that a DISI engine vehicle may emit over a drive cycle will come into action in 2014/2015 (*Official Journal of the European Union*, 2012).

The fuel exiting the nozzle of a high pressure DISI injector is readily atomized into small droplets, for a range of fuel temperatures (e.g. Aleiferis and van Romunde, 2013). The droplets then proceed into the cylinder, losing mass by evaporation until eventually no liquid remains. There may be both secondary atomization of the initial droplets into smaller droplets and collisions between droplets causing droplet sizes and droplet trajectories to alter.

To improve understanding of how injection strategy and fuel composition affect the evaporation of droplets in fuel sprays in a DISI engine, a simplified model of one droplet has been created. This aims to show trends rather than give accurate numerical solutions for an entire spray.

Results for a single component fuel model will be presented for iso-octane (2,2,4-trimethylpentane) droplets. Comparisons will be made with images of iso-octane sprays in an optical access engine with a spray-guided DISI system, which have been post-processed to extract estimates of total spray surface area according to Mie scattering theory. Estimates for the initial droplet distribution from the injection system under cold and hot conditions will be calculated.

A multi-component fuel model is introduced with non-ideal vapour-liquid equilibrium modelled using the UNIFAC method. This model can be run with a constant liquid composition (unmixed evaporation or frozen composition) or with a distillation-like varying liquid composition (well-mixed evaporation). The well-mixed model is thought to be more appropriate for low temperatures when the time for internal mixing by the internal droplet vortex is shorter than the droplet lifetime. The unmixed assumption will be more accurate for higher air and fuel temperatures when droplet lifetime is shorter and the internal mixing time is comparable to the lifetime. Thus the well-mixed model may be more applicable to early direct injection or cold start, whereas unmixed evaporation may be an appropriate assumption for the higher temperatures encountered in the compression stroke. There will be intermediate temperatures where the effectiveness of the mixing of the different liquid species should be considered.

2. Droplet Evaporation Theory

2.1 Single droplet, single component evaporation

The lifetime of a single, stationary, spherical droplet composed of only one liquid species in a stagnant gas is calculable from a well-established theory, which the following section draws on (e.g. Faeth, 1977; Lefebvre, 1989; Sirignano, 2010). This classical theory assumes that the droplet remains at a uniform temperature throughout its lifetime – the wet bulb temperature – the temperature at which the heat transferred to the droplet from the surroundings is exactly equal to the heat required to evaporate the liquid at the surface at the current evaporation rate. Additional assumptions (Faeth, 1977) require that the droplet surface moves inwards slowly, pressure is uniform, surface tension is ignored, no air dissolves into the droplet, there is no radiation heating of the droplet, there is no combustion, mass diffusion is given by Fick's law and heat conduction is given by Fourier's law.

For droplets evaporating in the cylinder of a DISI engine, the initial temperature of the liquid fuel could be quite hot (perhaps 120°C) and the steady state wet bulb temperature will be lower than the cylinder air temperature, which is likely to be lower than the initial fuel temperature for early injection. Therefore, most droplets will first cool towards the wet bulb temperature. Figure 1 shows the cooling process by depicting the temperature in the droplet and in surrounding air for various times after injection.

From the assumptions mentioned above, the solutions of the equations of conservation of energy and mass give the steady state evaporation rate $\dot{m}_{ss}$ of the spherical stationary droplet as

$$\dot{m}_{ss} = 2\pi d\rho D \ln(1 + B_Y) = 2\pi d \frac{\lambda}{c_p} \ln(1 + B_T) \tag{1}$$

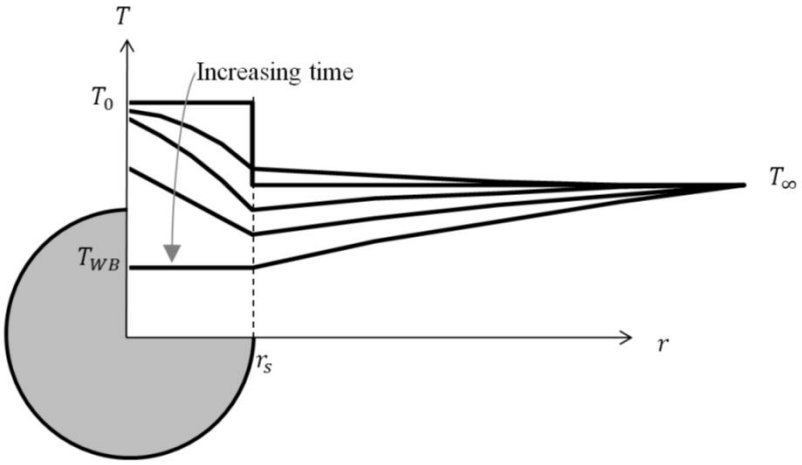

Fig. 1. Droplet and surroundings temperature histories. Initially, the droplet is at T_0 and the air is at T_∞. The droplet surface and then its interior begin to cool towards the wet bulb temperature T_{WB} and air close to the droplet tends to the droplet surface temperature

where d is the current droplet diameter, ρ is the fuel vapour/air mixture density, D is the mass diffusivity of the fuel species through air, λ is the thermal conductivity of the fuel vapour/air mixture and c_p is the specific heat capacity of the fuel species only. The mass and heat transfer numbers are B_Y and B_T respectively and are given by

$$B_Y = \frac{Y_{FS}-Y_{F\infty}}{1-Y_{FS}} \text{ and } B_T = \frac{h_\infty - h_s}{L_{eff}} \quad (2)$$

where Y_F is the fuel vapour mass fraction, h is the fuel vapour specific enthalpy, subscripts s and ∞ refer to the droplet surface and far from the droplet respectively and L_{eff} is an effective latent heat of vaporization for the fuel species given by

$$L_{eff} = L + \left(\pi\lambda_L d^2 \left.\frac{\mathrm{d}T}{\mathrm{d}r}\right|_{s,L}\right)/\dot{m} \quad (3)$$

For a uniform temperature model, the surface liquid temperature gradient $\left.\frac{\mathrm{d}T}{\mathrm{d}r}\right|_{s,L}$ is zero and $L_{eff} = L$.

The fuel vapour mass fraction at the surface can be found by calculating the equilibrium fuel mole fraction at the surface $\tilde{Y}_{FS}$, using the vapour pressure P_v and total pressure P, and converting it to a mass fraction using the fuel and air molar masses M_F and M_A:

$$\tilde{Y}_{FS} = P_v/P \quad (4)$$

$$Y_{FS} = \frac{M_F\tilde{Y}_{FS}}{M_F\tilde{Y}_{FS}+M_A(1-\tilde{Y}_{FS})} \quad (5)$$

The fuel vapour pressure will be a function of droplet surface temperature. Equation 1 for evaporation rate gives rise to the d^2 law of droplet evaporation, whereby

$$\frac{\mathrm{d}}{\mathrm{d}t}(d^2) = -K = -\frac{8\rho D\ln(1+B_Y)}{\rho_L} \quad (6)$$

for a given liquid fuel density ρ_L. Thus, the droplet lifetime is d_0^2/K. Equation 6 could be used to quantify the lifetime of a single droplet of initial size d_0 or an entire spray with an initial Sauter Mean Diameter (SMD) of d_0. However, in the case of a spray, the high relative velocities between droplet and air that are usually encountered cause increased evaporation due to convective enhancements. Additionally, the initially hot droplet will provide extra energy for evaporation of fuel at the surface, meaning there will be further enhancements to the evaporation rate until the temperature is uniform.

A useful model that incorporates these two complexities was shown by Abramzon and Sirignano (1989), who gave the two equations for evaporation rate as

$$\dot{m} = \pi d \rho D \mathrm{Sh}' \ln(1 + B_Y) \tag{7}$$

$$\dot{m} = \pi d \frac{\lambda}{c_p} \mathrm{Nu}' \ln(1 + B_T) \tag{8}$$

A modified Sherwood number Sh' can be defined for droplet evaporation as $\mathrm{Sh}' = \mathrm{Sh}\, B_Y / \ln(1 + B_Y)$, where $\mathrm{Sh} = k_Y d / D$ and k_Y is the mass transfer coefficient. In the absence of forced convection and Stefan convection, the Sherwood number for diffusion from a sphere will be equal to 2. With Stefan convection included, $\mathrm{Sh}' = 2$ for the stationary case and $\mathrm{Sh} \neq 2$. Abramzon and Sirignano (1989) also presented correction factors for the effect of the Stefan flow on the mass and thermal boundary layers. Their procedure, also adopted in the model here, was to calculate a convection-enhanced Sherwood number as

$$\mathrm{Sh}_0 = 2 + f(\mathrm{Re}, \mathrm{Sc}) \tag{9}$$

then obtaining the modified Sherwood number to be inserted into Eq. 7 by

$$\mathrm{Sh}' = 2 + \frac{(\mathrm{Sh}_0 - 2) B_Y}{(1 + B_Y)^{0.7} \ln(1 + B_Y)} \tag{10}$$

A similar procedure can be used to calculate the modified Nusselt number Nu' using B_T in place of B_Y and the Prandtl number in place of the Schmidt number. It has been recommended (Faeth, 1977; Sirignano, 2010) that Reynolds number Re is calculated using the free stream air density ρ_A and the air/fuel vapour mixture viscosity μ, and the Schmidt number Sc in the normal fashion:

$$\mathrm{Re} = \frac{\rho_A U d}{\mu} \text{ and } \mathrm{Sc} = \frac{\mu}{\rho D} \tag{11}$$

The velocity U must be the droplet velocity relative to the surrounding air. A range of functions f may be used; here the correlation of Clift et al. (1978) is recommended (Abramzon and Sirignano, 1989), for $\mathrm{Re} < 400$:

$$f = \begin{cases} (1 + \mathrm{Re}\,\mathrm{Sc})^{1/3} - 1, \text{when } \mathrm{Re} < 1 \\ (1 + \mathrm{Re}\,\mathrm{Sc})^{1/3} \mathrm{Re}^{0.077} - 1, \text{when } \mathrm{Re} > 1 \end{cases} \tag{12}$$

The drag force F_D on a small sphere at very low Reynolds number was given by Stokes (see Lefebvre, 1989) as

$$C_D \equiv \frac{F_D}{0.5 \rho_A U^2 A} = \frac{24}{\mathrm{Re}} \tag{13}$$

Here $A = \pi d^2 / 4$ and Re is as defined in Eq. 11. Experimental data can be better approximated for $\mathrm{Re} < 1000$ (Faeth, 1977; Lefebvre, 1989) if the drag coefficient is taken as

$$C_D = \frac{24}{\mathrm{Re}} + \frac{4}{\mathrm{Re}^{1/3}} \tag{14}$$

which is used throughout this work. It is assumed that the aerodynamic forces on the droplet do not significantly distort its shape from spherical.

So far, the physical properties of the air/fuel mixture have been treated as constant in this analysis, which simplifies the integration of the energy and species conservation equations. The approach by previous researchers (Faeth, 1977; Sirignano, 2010) has been to pick a reference temperature T_R and reference fuel mass fraction Y_{FR} that represents an average condition in the air/fuel vapour region, and then evaluate all properties at that reference condition and treat the properties as taking that value from $r = r_s$ to $r = \infty$. The average used here is the 1/3 rule of Sparrow and Gregg (1958), whereby

$$T_R = \frac{2}{3} T_s + \frac{1}{3} T_\infty \tag{15}$$

$$Y_{FR} = \frac{2}{3}Y_{Fs} + \frac{1}{3}Y_{F\infty} \quad (16)$$

Usually, ambient fuel vapour concentration is zero and Eq. 16 becomes $Y_{FR} = \frac{2}{3}Y_{Fs}$.

In order to model evaporation of droplets with varying initial temperatures, an extension to the simple model previously described is necessary. If the temperature of the fuel is close to the wet bulb temperature, a uniform droplet temperature equal to T_{WB} is quickly established throughout the droplet. However, if the liquid droplet is initially much hotter than the gas into which it is injected, or *vice versa*, the heating or cooling period can be a significant part of the droplet's lifetime. Given an initial liquid temperature T_0, the history of the temperature distribution within the droplet can be found by solving

$$\frac{\partial T}{\partial t} = \alpha\left(\frac{\partial^2 T}{\partial r^2} + \frac{2}{r}\frac{\partial T}{\partial r}\right) \quad (17)$$

which is the conductive heat equation in spherical coordinates, where α ($= \lambda_L/\rho_L c_{pL}$) is the thermal diffusivity of the liquid fuel, using the liquid fuel heat capacity c_{pL}, the liquid fuel thermal conductivity λ_L and the liquid fuel density ρ_L. Solution of this equation assumes that the fuel droplet is a sphere of stationary liquid, meaning there is no enhancement to heat transfer through the droplet by convection induced by internal droplet motion. In reality, aerodynamic effects will cause circulation of the liquid within the droplet and also a distortion of its shape (Sirignano, 2010). Thus, the two models described here can be considered to bracket the real behaviour of the droplet temperature distribution: one denoting infinitely quick heating or cooling, the other denoting conduction limited heating or cooling.

The heat equation has been discretized using the forward difference method with the boundary conditions

$$\left.\frac{\partial T}{\partial r}\right|_0 = 0 \quad (18)$$

$$\left.\frac{\partial T}{\partial r}\right|_{s,L} = \dot{m}(L_{eff} - L)/\pi\lambda_L\, d^2 \quad (19)$$

To use the liquid surface boundary condition in Eq. 19, the current evaporation rate must be calculated using Eq. 7 and B_Y. Then B_T is calculated using Eq. 8, and finally L_{eff} can be calculated from the expression for B_T in Eq. 2.

The droplet radius is discretized into N grid points between centre and surface, separated by Δr. For conditional stability, this requires the time step to be limited at each step to $\Delta t < (\Delta r)^2/2\alpha$, although further reduction can be required to ensure stability. The time step is calculated at each iteration. The temperatures calculated at the N grid points are passed on to the next iteration and may be corrected by interpolation for the fact that the grid points will have moved inwards by the next time step. For the work presented here the errors by ignoring this were minimal. Throughout this work, $N = 8$ has been used since there was only a negligible difference in droplet lifetime between simulations using $N = 8$ and simulations using $N = 16$.

This model requires that the gas phase physical properties are updated at each iteration since the surface temperature, and hence the reference temperature and reference fuel mass fraction, will vary as the droplet evaporates.

2.2 Multi-component fuel evaporation

The main differences between the single component model and the multi-component model are in the ways the fuel properties are calculated, and in the need for a multi-component vapour-liquid equilibrium (VLE) model. Liquid and gas mixture properties are calculated using non-ideal mixture rules to get accurate estimates. Equation 14 is used to calculate the evaporation rate of all fuel species, using the reference air/fuel mixture density ρ, a mole weighted average of the individual diffusion coefficients D and a mass transfer number B_Y based on the overall fuel mass fraction at the surface of the droplet. The surface mole fraction of fuel vapour could be calculated using Raoult's law, where for fuel species i, the relationship between the liquid mole fraction $\widetilde{X}_i$ and the vapour mole fraction $\widetilde{Y}_i$ is given by:

$$\widetilde{X}_i P_{vi} = \widetilde{Y}_i P \quad (20)$$

Raoult's law will give reasonable results for mixtures of pure hydrocarbons but when alcohols (e.g. methanol or ethanol) are present, an extension to the equation containing an activity coefficient γ_i should be used:

$$\gamma_i \widetilde{X}_i P_{vi} = \widetilde{Y}_i P \tag{21}$$

For high pressure situations, a fugacity coefficient is also included on the right-hand side of Eq. 21. However, for DISI engines, the pressures encountered by the droplets will be low enough that this may be considered unity. The activity coefficients can be estimated from pure component properties using, for example, a cubic equation of state or a model such as ASOG or UNIFAC. Alternatively, if there is data for the multi-component system a correlation such as NRTL or UNIQUAC may be used. In this work, UNIFAC has been adopted to calculate γ_i, due to the availability of parameters for the components that were to be modelled and past success in using the method to simulate distillation curves of model gasoline fuels (Leach et al., 2013).

2.2.1 Well-mixed multi-component droplet evaporation

When a droplet is in motion relative to the air surrounding it, as in the case of fuel droplets issuing from a fuel injector, shear stresses will act on the surface of the droplet. These will in turn cause the liquid in the droplet to circulate around in an internal vortex that is toroidal in shape (Sirignano, 2010). This internal vortex will take a short time to be established once there is relative motion between the droplet and air. This will provide mixing within the droplet that will enhance both mass and heat transfer. As applied to multi-component droplets, when a lighter component evaporates from the surface, perfect mixing within the droplet will allow this component to be instantaneously replenished to the surface to continue evaporation. This would allow distillation-like evaporation to happen, where the liquid fuel and vapour at the surface are always in equilibrium and Eq. 25 is applicable. This is likely to be the case for larger droplets where there is rapid mixing due to fast air motion but slow evaporation, should such a droplet exist.

When there is any kind of mixing, the overall composition of the droplet will begin to change. In order to track the change in liquid composition, it is necessary to know the composition of the small element of liquid that is currently vaporizing. By setting the vapour diffusion coefficients equal for each species, it can be shown (Sirignano, 2010) that the individual species' mass transfer numbers B_{Yi} are equal to the overall mass transfer number B_Y calculated from Eq. 7b using the overall surface fuel mass fraction, $Y_{Fs} = \sum Y_{is}$. Assuming zero ambient fuel vapour concentration,

$$B_Y = B_{Yi} = \frac{Y_{Fs}}{1-Y_{Fs}} = \frac{Y_{is}}{\varepsilon_i - Y_{is}} \tag{22}$$

where ε_i is the mass flux fraction of species i present in the liquid currently vaporizing. With knowledge of the current B_Y, each ε_i is given by $\varepsilon_i = Y_{is}(1 + B_Y)/B_Y$ and the change in mass of component i is $\varepsilon_i \dot{m} \Delta t$. Hence, the liquid composition $\widetilde{X}_i$ can be updated ready for the next iteration. It is also noted that the correct form of mixture latent heat of vaporization should be

$$L = \sum_i \varepsilon_i L_i \tag{23}$$

2.2.2 Frozen composition multi-component droplet evaporation

If the liquid inside the droplet can be considered stationary, for example if the droplet is stationary or if the evaporation is faster than the rate at which the internal vortex can circulate, then the evaporation may proceed with a frozen composition. This can occur since the liquid phase diffusion mass transport is very slow in comparison to both the forced convective transport when there is an internal vortex and to the evaporation rate of the droplet. By assuming a uniform liquid composition equal to the initial liquid composition of the fuel, over the lifetime of the droplet, it can be seen that the energy input to the droplet surface will only be able to vaporize what is currently present there. The vapour composition will vary slightly throughout the lifetime, even with the diffusion coefficients of each species set equal, since the vapour pressure and activity coefficient of each species will have a unique dependence upon temperature and the surface temperature will vary.

The frozen composition (zero liquid diffusivity) and the well-mixed composition (infinite liquid diffusivity) can be seen as limits to the real behaviour. To model accurately the internal composition, the spherical diffusion equation should be solved:

$$\frac{\partial Y_i}{\partial t} = D_i \left(\frac{\partial^2 Y_i}{\partial r^2} + \frac{2}{r} \frac{\partial Y_i}{\partial r} \right) \quad (24)$$

This must be solved for all but one of the species, the final species given by mass balance. For cases where an internal vortex is expected, a convective enhancement to D_i in Eq. 24 can be used (see Sirignano, 2010).

2.3 Activity coefficients with UNIFAC

The UNIFAC method is a semi-empirical group interaction method (Fredenslund et al., 1975) that requires only the knowledge of the properties and chemical structure of the pure components in any fluid mixture, plus the interface temperature and liquid composition. The form of the expression for γ_i is the same as the UNIQUAC experimental correlation with empirical constants based on chemical groups present in the liquid in place of parameters evaluated from experimental binary systems. These can be looked up in a table during the simulation and rapidly output into the main VLE relationship, Eq. 21. The UNIFAC method gives reasonable estimates of activity coefficients for species with intermediate mole fractions, but can be in error more significantly for species with very low concentrations (Poling et al., 2001).

3 Single Component Spray Images and Post Processing

Iso-octane was sprayed into a static, single cylinder optical engine, which was fitted with a full height optical liner. The cylinder pressure was atmospheric and two cylinder head temperatures were investigated, 20°C and 80°C. The cylinder head contained the six-plume direct injection multi-hole injector shown in Fig. 2 and in both cases sufficient time was allowed so as to be confident that the fuel injector had reached the temperature of the cylinder head coolant. The cylinder air temperature was also measured in each case; it was 20°C during the cold fuel test and 36°C during the hot fuel test due to proximity to the 80°C cylinder head. Eight injection events at each temperature were performed, with duration 1 ms and injection pressure 150 bar. Multiple injections were performed to ensure stable injector operation. Images were taken of the sprays at 5000 frames per second using a Photron high speed camera. Each spray was illuminated from the side using an overdriven array of green LEDs.

The tip of the injector is not visible in the images taken in this work, being obscured by the engine cylinder head. The vertical distance between the injector and the first visible spray in the images is 14 mm. Background images are recorded with the LEDs switched on before each injection. For each injection event, the background image is subtracted pixel by pixel from all subsequent images to give an image of the spray alone. This removes light reflected from the cylinder liner and removes the obscuring effect of any deposits built up on the liner. The subsequent presence of fuel spray inside the cylinder causes light to be dispersed around the cylinder differently from frame to frame, and some of the brighter parts of the spray may cause the camera to saturate.

Two images obtained during the cold fuel test are shown in Fig. 3, one from the near the start of injection and one of the subsequent cloud of droplets. There are some artefacts of the background light on the right hand side, which obscure the images here. These are present in all images so will have little effect on the estimates of the amount of spray present.

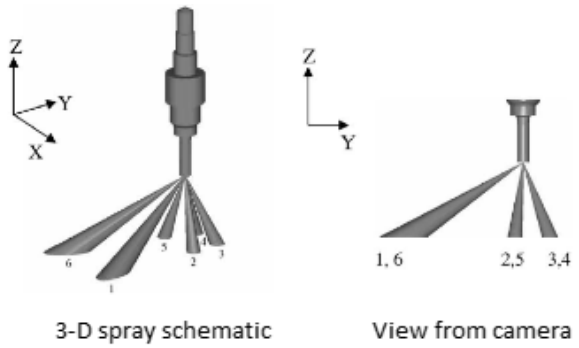

Fig. 2. Multi-hole fuel injector plume orientations (adapted from Serras-Pereira et al., 2010, where the same injector was used)

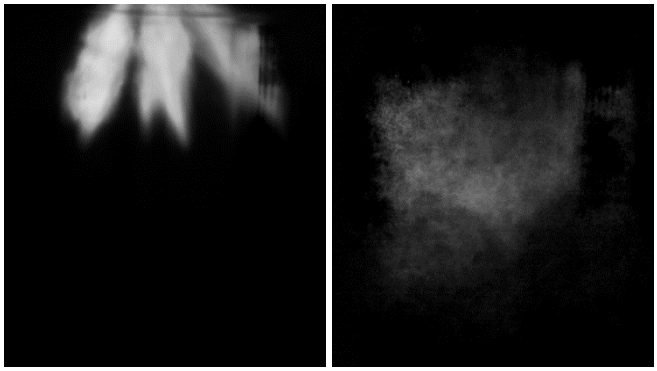

Fig. 3. Images obtained from the optical engine. Left: early spray image with background subtracted showing distortion to plumes 1 and 6 due to the intense background light in that region. Right: late spray image with background subtracted and pixel values multiplied by 5 for visualization

To estimate the amount of spray present in each image, a threshold is set to remove some of the background light that has managed to survive the background subtraction and the pixel values in the resulting image are summed to give a spray integral. The light incident on the droplets is scattered elastically off the surface (Mie Scattering) meaning the light intensity received at the camera is theoretically proportional to the local droplet surface area (Zhao, 2012). Hence, the spray integral gives an estimate of the total surface area of the droplets in the spray. Once the spray integral reaches a predetermined lower threshold, it is determined that the spray has completely evaporated. This evaporation threshold was tested and validated by visual inspection of the spray images but will be an approximation. Figure 4 shows the mean and standard deviation from the eight injection events at both hot and cold conditions. The estimated spray lifetime was 80.0 ms for the cold spray and 24.0 ms for the hot spray. It can be seen that the peak amount (total surface area) of fuel for the hot spray was lower and slightly earlier. This is supported by the observation that the maximum plume penetrations were lower for the hot fuel case, as expected, whereas the plume tip velocities in each case were similar.

4 Comparison to Droplet Simulations

The simple single droplet model described here can be applied as a simple engineering tool to estimate droplet sizes and initial velocities that may be present when a liquid fuel jet atomizes after injection. In the static sprays investigated here, the droplets will spend a large portion of their lifetime travelling at low speed relative to the air around them, so they will have a low enough Weber number to remain spherical. However, droplets will collide with each other and the walls, there will be a reduction in the heat transfer to each droplet as they are close enough to compete for energy from the surroundings and there will be an accumulation of fuel vapour between the droplets that will alter the mass transfer characteristics.

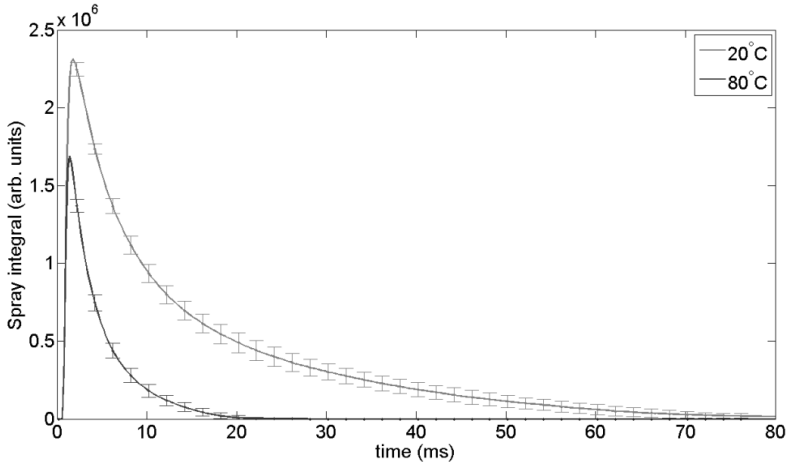

Fig 4. Spray integral for 20ºC and 80ºC iso-octane spray. The 80°C spray is the first to fully evaporate. The error bars denote one standard deviation either side of the mean, for eight injection events at each temperature, and are reasonably uniform in magnitude throughout the spray lifetime

Droplet size distributions for iso-octane and gasoline sprays have been presented in previous work using the same fuel injector as used here (Aleiferis and van Romunde, 2013). Droplet sizes were recorded 25 mm downstream of the injector using a Phase Doppler Analyzer (PDA) and Laser Diffraction (LD) The results indicated that a range of droplet sizes up to 30 μm for gasoline sprays are to be expected, with a range of velocities between 10 m/s and 120 m/s. The larger droplets (above 15 μm) were mostly associated with the spray tip region in that study.

Figure 5a shows simulation results for iso-octane droplets in this size range (4 μm – 30 μm), with an initial velocity of 90 m/s and gas and initial droplet temperatures the same as those from the 20°C iso-octane spray in terms of droplet diameter, d. Figure 5b shows results at the same initial velocity but corresponding to the conditions of the 80ºC iso-octane spray. It is possible to perform a least squares fit of a normalized linear combination of the d^2 histories to the experimental spray to estimate an initial droplet size distribution. This is appropriate since the total amount of light scattered from the spray is proportional to the sum of the surface areas of the droplets from which light was scattered. It was chosen to fit the droplet simulation results from the peak in the experimental spray integral (found at time t_{max}) as it is from this point forward that all the droplets are in the field of view of the camera. It was assumed that the droplets were all formed at the start of injection.

The fitting procedure proceeds by taking an initial guess of the proportion x_i of droplets of initial size d_i present in the initial spray, such that $\sum_i x_i = 1$. The sum $\sum_i x_i d_i(t)^2$ is calculated for each time step after the peak spray in the corresponding experiment, using the droplet diameter histories $d_i(t)$ shown in Fig. 5. This quantity and the experimental spray integral are both normalized to ensure at $t = t_{max}$ they are equal to one and the two quantities are compared. A standard solver can then be used to optimize the values x_i in a least squares sense.

For the two experimental cases observed here, comparisons between the fitted normalized droplet surface area and the experimental spray integral are made in Figs. 6a and 6b, for hot and cold sprays respectively. The calculated droplet distributions are shown in Figs. 7a and 7b. The calculated mean diameters ($\bar{d}$) and Sauter mean diameters (SMD or d_{32}) are given in Table 1. It is expected that the hotter spray will produce smaller droplets; however, the mean droplet size for the hot spray is slightly larger than for the cold spray. The SMDs are ranked in the expected order. It must be borne in mind that these results are generated from pixel sums of post-processed spray images under the assumption that scattered light is exactly proportional to the surface area present in the spray, so any distribution estimate is approximate.

Table 1. Fitted droplet distribution statistics for hot and cold iso-octane sprays

Parameter	Hot spray	Cold spray
$\bar{d}$	10.8 μm	10.0 μm
d_{32}	13.2 μm	14.6 μm

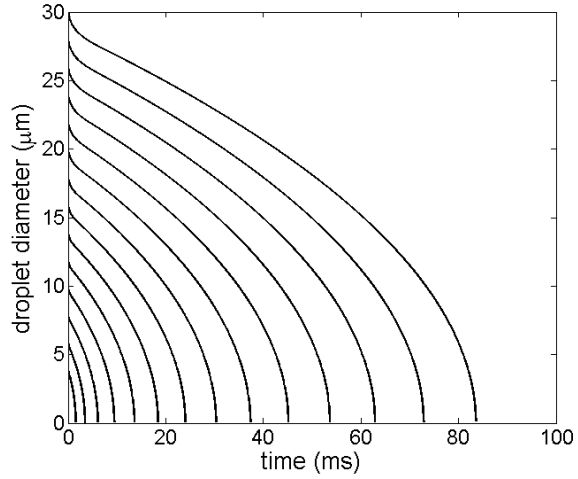

Fig. 5a.

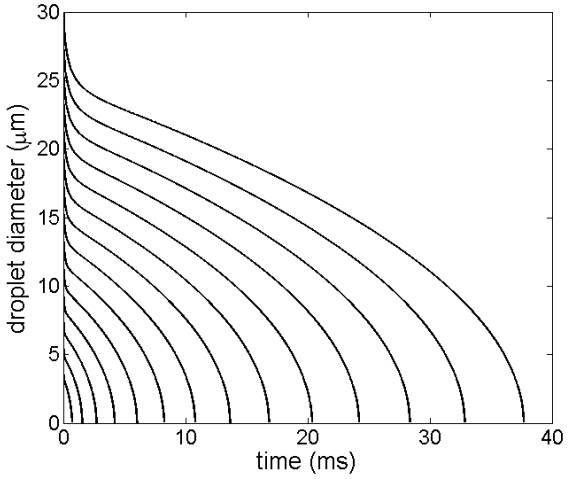

Fig. 5b.

Fig. 5. Droplet life histories of a family of 14 droplets with initial sizes from 4 μm to 30 μm and initial velocity of 90 m/s. Fig. 5a. shows droplets initially at 20ºC injected into an atmosphere of 20 ºC and Fig. 5b. shows droplets initially at 80ºC injected into an atmosphere of 36ºC. The initially hot droplets have a lifetime less than 50% of the corresponding cool droplets and additionally lose a more significant proportion of their mass early on, while their temperature is still much greater than the steady state wet bulb temperature

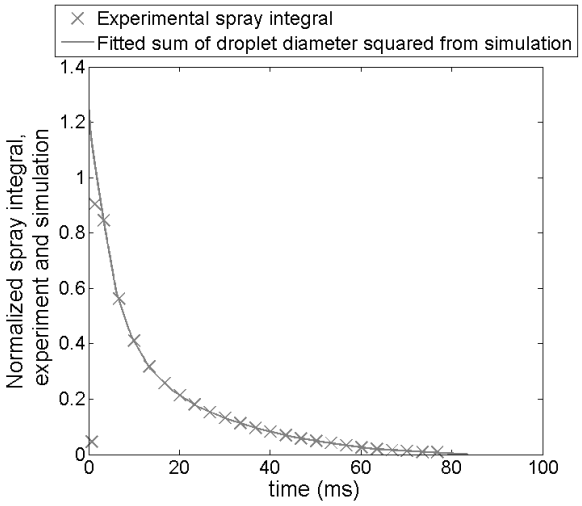

Fig. 6a

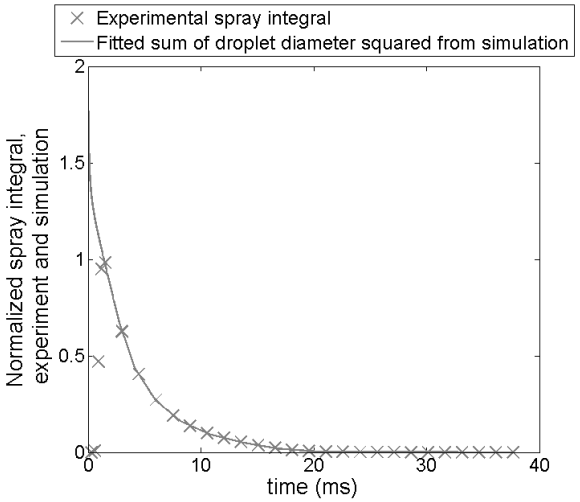

Fig. 6b

Fig. 6. Plots showing fit of weighted sum of the simulated droplets to experimental spray integral, for cold (20°C) spray (Fig. 6a) and hot (80°C) spray (Fig. 6b). The fitting was performed for the portion of the experimental data (X) after the early peak at a value of 1

The SMD of a spray can also be calculated from correlations, such as the Elkotb correlation (Elkotb, 1982) that was developed for diesel, kerosene and gasoline fuels and mixtures of these. The relationship Elkotb presented was

$$d_{32} = 3.08\nu_L^{0.385}(\sigma\rho_L)^{0.737}\rho_A^{0.06}\Delta P^{-0.54} \qquad (25)$$

where the liquid kinematic viscosity ν_L is in m²/s, surface tension σ is in N/m, liquid density ρ_L and cylinder air density ρ_A are in kg/m³ and injector pressure ΔP is in Pa, giving d_{32} in m. The liquid properties are primarily functions of the liquid temperature in the injector and are sourced from Poling et al. (2001) and Jasper (1972). The air density is calculated from the cylinder pressure and temperature using the ideal gas equation of state and the injector pressure here was 150 bar. The calculated SMD for the cold spray conditions was 11.7 µm and for the hot spray conditions it was 6.4 µm. The SMD of the distributions fitted here are slightly larger than these but in the right order of magnitude.

Aleiferis and van Romunde (2013) presented droplet size results for iso-octane injected at 150 bar into a 1 bar quiescent chamber, for fuel temperatures of 20°C and 90°C. For the cold fuel, the SMD was ~16 µm using the PDA and ~12 µm using LD, and for the hot fuel test the SMD was ~15 µm using PDA and ~10 µm using LD. These results are in better agreement with the spray image derived distributions presented in this work. The results presented here will predict droplet sizes averaged across all droplets formed: during nozzle opening, injector steady state and injector closing.

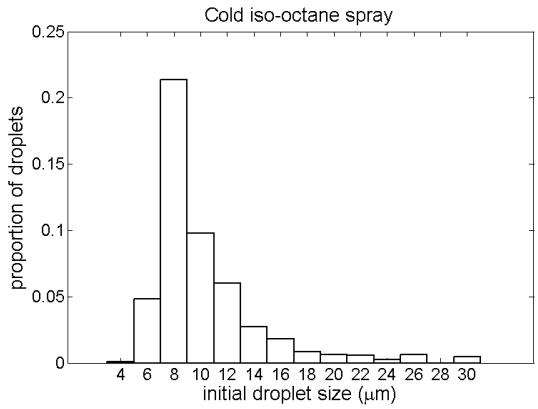

Fig. 7a

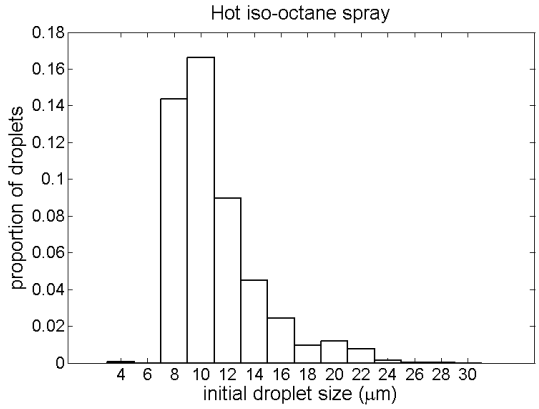

Fig. 7b

Fig. 7. Histograms showing the droplet distributions required to produce the best fit of the sum of the droplet simulations to the experimentally observed spray integral, for the cold (20°C) and hot (80°C) iso-octane sprays. The cold spray contains a greater amount of droplets over 24 µm but contains also more droplets at 6 µm and 8 µm

5. Multi-component results

In order to improve understanding of multi-component mixtures, both a bi-component mixture (iso-octane and ethanol, which has been investigated recently by Bader et al. (2013)) and a model gasoline with seven hydrocarbon components, with the addition of ethanol and methanol, have been investigated. Results from subcooled droplet simulations for the two fuels are reported here, with the two limiting cases of well-mixed, distillation-like evaporation and unmixed, frozen composition evaporation applied to the model.

5.1 Bi-component results

In Fig. 8, droplet diameter histories for the bi-component droplets are presented, for a stationary droplet of initial size 15 μm, for different pressures, initial droplet temperatures and ambient temperatures. In this work, E10 refers to 10% by mole ethanol (around 4% by volume) and E40 is 40% by mole ethanol (around 19% by volume). For the simulations at 293 K (Figs. 8a and 8b), there can be seen to be little difference in droplet lifetime between the two limiting cases. Compared to the 293 K test at 1 bar (Fig. 8a), both reducing the pressure (Fig. 8b) and increasing the temperatures (Fig. 8c) shorten the lifetime.

As the pressure is lowered or the temperature is raised, it is seen that the well-mixed model begins to show an increased evaporation rate relative to the unmixed model. This is because the well-mixed model for the compositions presented will allow the ethanol to evaporate first, since both the E10 and E40 mixtures are on the ethanol side of the ethanol/iso-octane azeotrope.

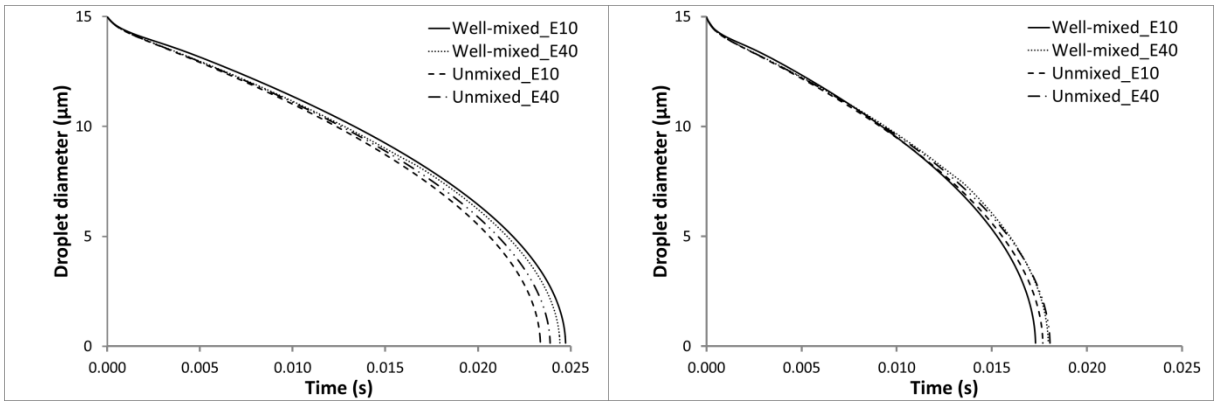

Fig. 8a **Fig. 8b**

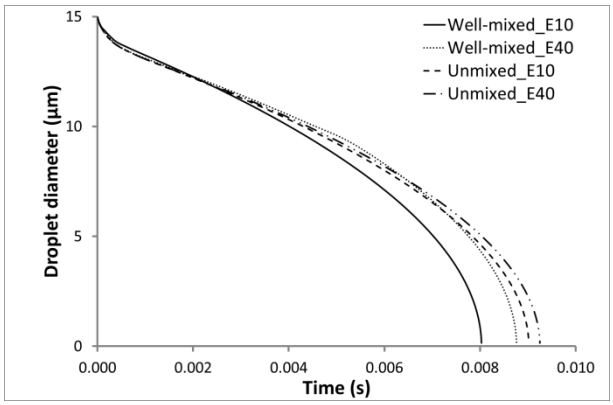

Fig. 8c

Fig. 8. Droplet diameter histories for two ethanol/iso-octane mixtures (10% and 40% ethanol by mole) with both well-mixed, distillation-like evaporation and unmixed, frozen composition evaporation. Fig. 8a presents droplets at an initial liquid temperature of 293 K and ambient temperature of 293 K, with a pressure of 1 bar. Fig. 8b is as Fig. 8a but with a pressure of 0.5 bar. Fig. 8c is as Fig. 8a but with both ambient and initial liquid temperatures at 333 K

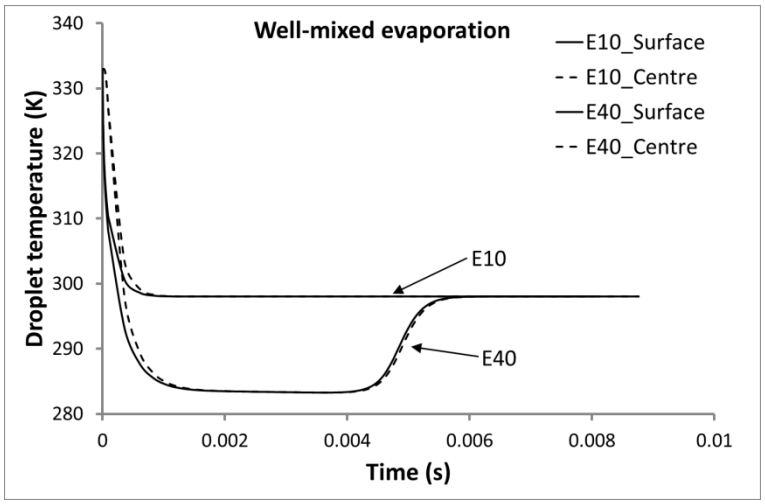

Fig. 9. Droplet surface and centre temperatures for the well-mixed evaporation case at 1 bar and 333 K initial and ambient temperatures (see Fig. 8c). In the E10 droplet, all of the ethanol has evaporated by the time the iso-octane steady state temperature is reached (less than 1 ms), and the droplet subsequently remains at this temperature. The E40 droplet continues to cool to the ethanol/iso-octane mixture steady state temperature and remains there until most of the ethanol has evaporated (around 4 ms) before its temperature rises

For droplets in an ambient temperature of 333 K, the steady state droplet temperature of pure iso-octane is around 298 K, whereas for both of the two mixtures presented (10% ethanol and 40% ethanol) it is close to 283 K. At this lower temperature, the total fuel mass fraction at the surface is lower, the mass transfer number B_T is lower and hence so is the evaporation rate $\dot{m}$. The droplet temperature histories for the case where ambient and initial liquid temperature is 333 K are shown in Figs. 9 and 10. The steady state temperature may be verified by calculating the temperature at which the following equation is satisfied:

$$1 + B_Y = (1 + B_T)^{\mathrm{Le}} \tag{26}$$

where $\mathrm{Le} = \lambda/\rho D c_p$ is the Lewis number, and B_T will use $L_{eff} = L$ since the droplet will be at uniform temperature.

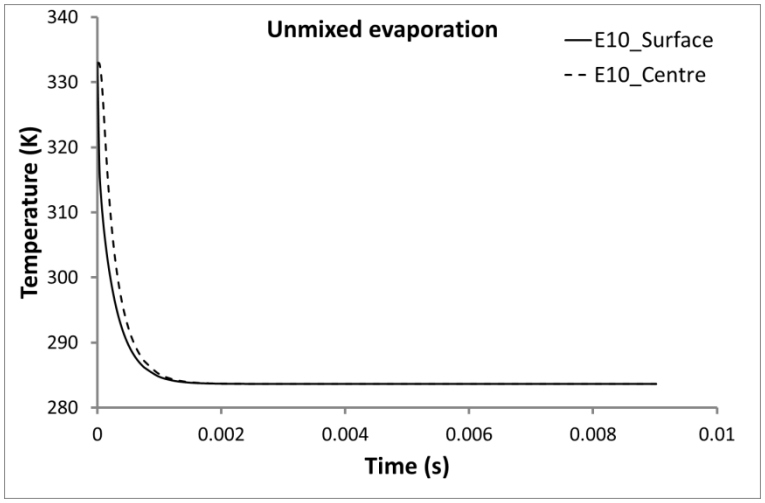

Fig. 10. Droplet surface and centre temperature history for the unmixed evaporation case of the E10 droplet at 1 bar and 333 K initial liquid and ambient temperatures (see Fig. 8c). Since the liquid composition is constant, once the droplet reaches a steady temperature, it stays there. For the E40 droplet, the temperature curve is similar since the behaviour of the ethanol/iso-octane mixture is highly non-ideal resulting in a nearly constant bubble point temperature across a wide range of intermediate compositions, as shown in, e.g., Wen and Hu (2007)

5.2 Multi-component results: hydrocarbon fuel

A seven component hydrocarbon fuel has been used to model gasoline for droplet evaporation. The composition is the same as one of the fuels tested in Leach et al. (2013), and is given in Table 2 in the Base fuel column. Since this is a mixture of hydrocarbons, it behaves close to ideally (the maximum activity coefficient encountered is 1.35). This base fuel has had 20% by volume ethanol and 15% by volume methanol added to it to model two oxygenate blends, E20 and M15. These proportions both give around 37% by mole alcohol in the fuel. The exact composition of these is in Table 2.

This fuel was initially designed to have good coevaporation of the medium components (octanes and toluene) and of the heavy components (decanes and trimethylbenzene). This fuel was simulated using both the well-mixed and unmixed limits for droplet evaporation. The droplet diameter history is presented in Fig. 11 for initial liquid temperatures of 293 K and 333 K at 1 bar. The ambient temperature was 333 K in both cases.

Table 2. Composition (% by volume) of the model hydrocarbon fuel and the E20 and M15 derivatives

Component	Base fuel	E20 fuel	M15 fuel
n-pentane	5.00	4.00	4.25
iso-octane	41.68	33.34	35.43
n-octane	13.89	11.11	11.81
toluene	29.93	23.94	25.44
2,2,3,3-tetramethylhexane	1.48	1.18	1.26
n-decane	4.69	3.75	3.99
1,3,5-trimethylbenzene	3.33	2.66	2.83
ethanol	0	20.00	0
methanol	0	0	15

The model fuel was also tested with an initial temperature 293 K with ambient pressure set to 0.5 bar. Looking at the plot of diameter squared against time for this case, shown in Fig. 12, there are two identifiable regions of near constant gradient for the well-mixed curve. The transition occurs at around 9 ms. This may be verified in Fig. 13 by observing the plot of the liquid mole fraction throughout the droplet lifetime for the well-mixed case, where the medium components leave the droplet between 9 ms and 11 ms and the heavy components are all present until near the end of the droplet lifetime.

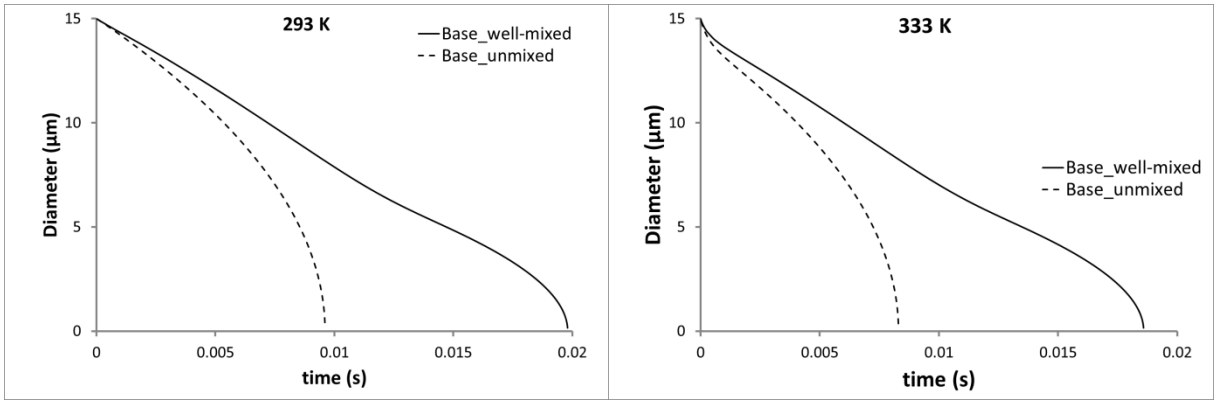

Fig. 11a **Fig. 11b**

Fig. 11. Well-mixed and unmixed multi-component base fuel droplet evaporation droplet histories. The unmixed evaporation lifetime is much shorter (in the case of Fig. 11b, it is less than 50% of the well-mixed case). The unmixed evaporation proceeds similarly to the d^2 law behaviour seen in the single component cases, apart from the initial cooling phase, whereas the well-mixed evaporation could be adequately described by a linear decrease in droplet diameter with time, for the two cases presented here

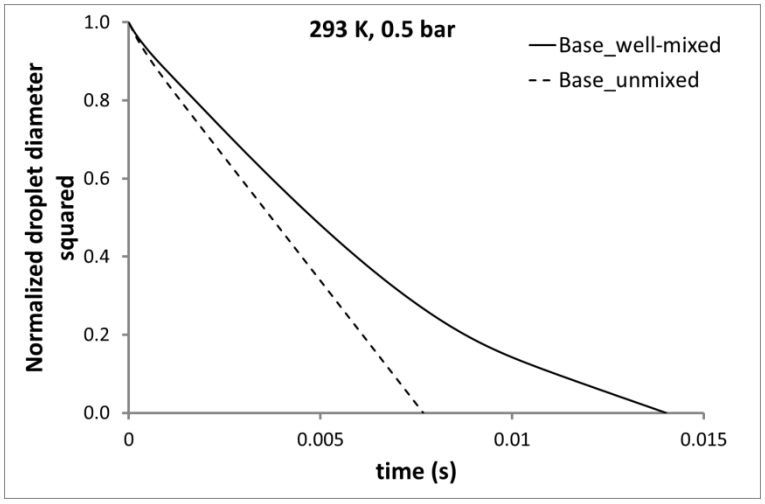

Fig. 12. Normalized droplet diameter squared for the base fuel, for initial liquid temperature of 293 K, ambient temperature of 333 K and ambient pressure of 0.5 bar. As expected, the reduction in pressure has reduced the droplet lifetimes in both mixing cases

5.3 Addition of oxygenates

By adding ethanol or methanol to the hydrocarbon blend previously introduced, the evaporation behaviour of the fuels can change markedly due to highly non-ideal behaviour of mixtures of alcohols with hydrocarbons, (for example Wen and Hu, 2007). In addition, both ethanol and methanol have relatively large values of vapour pressure P_v and enthalpy of vaporization L, so will cause both an increase in surface fuel mass fraction and a reduction in droplet temperature during evaporation. These effects will compete, so the addition of ethanol or methanol may increase or decrease droplet lifetime in different situations.

Figure 14 shows the droplet diameter history for the base fuel droplet, the E20 droplet and the M15 droplet with both well-mixed and unmixed results, at 293 K initial liquid temperature and ambient temperature and 0.5 bar pressure. For both limiting cases, the M15 droplet is the slowest to evaporate, whereas the E20 droplet is fastest under well-mixed conditions but slower than the base hydrocarbon fuel droplet for the unmixed case. The differences in lifetime between the well-mixed and unmixed cases are smaller for the oxygenate fuel blends than with the base hydrocarbon fuel.

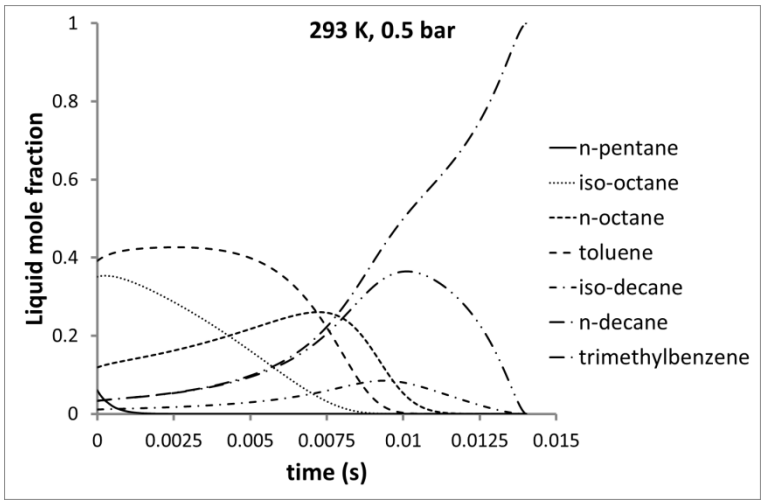

Fig. 13. Liquid mole fractions for the base fuel (hydrocarbons only) for the well-mixed droplet presented in Fig. 12. The n-pentane is lost most rapidly, then the medium components (octanes and toluene) finish evaporating around 9 – 11 ms, and the heavy components (decanes and trimethylbenzene) persist until droplet evaporation is completed

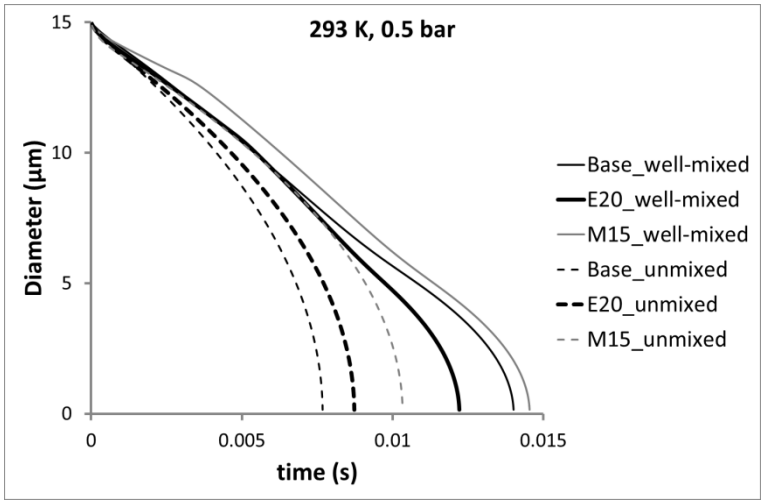

Fig. 14. Droplet diameter history for all three multi-component blends at 293 K initial liquid temperature and ambient temperature, and 0.5 bar ambient pressure. The thick black line represents the E20 droplets, the greyed line represents the M15 droplets

To understand the differences in lifetime caused by the addition of alcohols, under the two limiting mixing cases, the droplet temperature variation with time can be analysed. Figure 15 shows the surface temperature histories for the three fuels for both the unmixed and well-mixed cases. The alcohol droplets show significantly more initial cooling in both cases, and in the constant composition case the temperature does not recover. Comparing Fig. 14 with Fig. 15, it can be seen that the cooler the steady state temperature, the longer the droplet lifetime. Therefore, for the unmixed case in these low temperature conditions it seems the evaporation rate will be controlled by the steady state temperature, and hence the fuel mixture enthalpy of vaporization (as weighted by mass flux fraction in Eq. 23) will be important.

For the well-mixed droplets, the initial cooling is followed by an increase in droplet temperature of all three fuels as the remaining liquid in the droplet becomes less volatile. The lower volatility will lower the fuel vapour mass fraction at the surface $Y_{Fs} = \sum Y_{is}$, lowering B_Y and B_T and raising the surface temperature gradient as in Eq. 19. Once the alcohol has evaporated, the reduced enthalpy of vaporization L will also raise the surface temperature gradient. A large positive surface temperature gradient will cause droplet heating.

For the droplets studied here, the well-mixed limiting case seems to cause a slower overall evaporation despite the higher temperatures observed during the latter part of the droplets' lifetimes. This can be attributed to the lower volatility of the remaining liquid as lighter components evaporate. Therefore, the surface fuel vapour mass fraction will decrease even as the temperature increases.

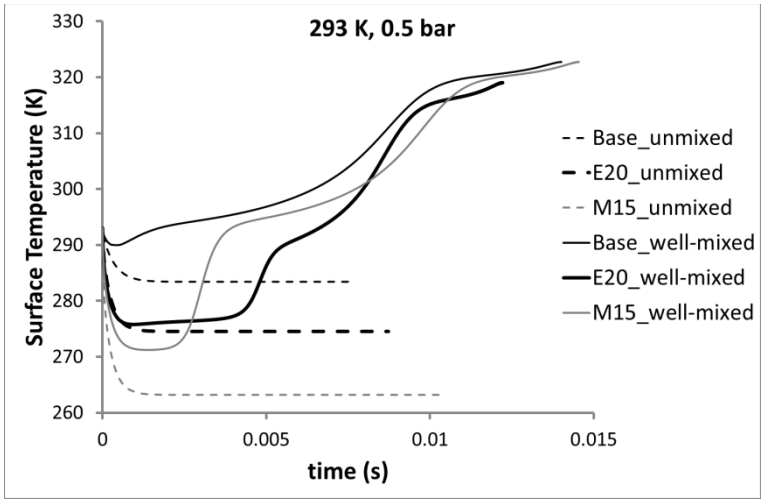

Fig. 15. Droplet surface temperatures for 293 K initial liquid temperature and ambient temperature, and 0.5 bar ambient pressure for both models

The differences in the lifetimes of the ethanol and methanol containing droplets is of interest in relation to the mixture preparation of oxygenate fuel blends in DISI engines. The E20 droplet is faster to evaporate than the M15 droplet in both limiting cases, which may be due to the lower initial degree of cooling exhibited by the E20 droplet or due to differences in the non-ideality of the VLE of ethanol and methanol with the hydrocarbon components. Further research is needed to establish how these types of blends will behave in the liquid diffusion-controlled regimes in between the limiting cases presented here and what the effects on droplet lifetime will be with different oxygenate contents in the fuel.

6 Conclusions

A droplet evaporation model has been presented for a single-component subcooled droplet and a series of droplet size histories has been generated for iso-octane fuel droplets injected into an atmospheric environment with initial droplet temperatures of 20°C and 80°C. These have been compared to Mie scattering spray images taken under the same conditions, using a static optical engine and high speed camera. The sum of the pixels belonging to the spray has been calculated for eight spray images, at each condition, to generate an experimental spray amount history. Since the amount of scattered light should be proportional to spray surface area, it has been compared with the droplet diameter squared histories of the simulated droplets. An empirical distribution of droplets has therefore been fitted to the experimental data throughout the spray lifetime, for initial droplet sizes between 4 µm and 30 µm. The resulting distributions are comparable in magnitude to those expected from the Elkotb droplet size correlation and to droplet size measurements taken using the same injector and fuel as the one in the present study.

The droplet model has been generalized to deal with multi-component mixtures and non-ideal vapour-liquid equilibrium using the UNIFAC method. The option of well-mixed, distillation-like evaporation or unmixed, frozen composition evaporation is possible with the model, although real droplet behaviour is likely to lie somewhere in between. Simulation results for two ethanol/iso-octane mixtures have been presented and the effect of the type of evaporation assumed explored. A seven component hydrocarbon fuel has been modelled, with the option of the addition of 20% by volume ethanol or 15% by volume methanol. The effects of adding the ethanol and methanol have been explored. With well-mixed evaporation assumed, the addition of ethanol reduced the evaporation time whereas the addition of methanol increased the evaporation time slightly. With the unmixed evaporation model, the addition of alcohol reduced the lifetime, which can be attributed to the reduced steady-state temperatures that will occur due to the higher enthalpy of vaporization of the alcohol components. Future experiments to capture spray images or measure spray droplet size distributions of these or similar fuel blends will be important to truly understand which evaporation model is more appropriate under these conditions.

Future work may include modelling the fuel components with different diffusion coefficients and modelling their evaporation rate individually. This will also require the examination of additional terms in the energy conservation equation relating to inter-diffusion. For further applicability to DISI engine conditions, superheated droplet vaporization or flash boiling will need to be incorporated in to the droplet evaporation model.

References

Abramzon B and Sirignano WA (1989) Droplet Vaporization Model for Spray Combustion Calculations. Int. J. Heat Mass Transfer: vol. 32: pp. 1605-1618.

Aleiferis PG and van Romunde ZR (2013) An Analysis of Spray Development with Iso-octane, N-pentane, Gasoline, Ethanol, and N-Butanol from a Multi-hole Injector under Hot Fuel Conditions. Fuel:, vol. 105: pp. 143-168.

Bader A, Keller P, Hasse C (2013) The influence of non-ideal vapour-liquid equilibrium on the evaporation of ethanol/iso-octane droplets. Int. J. Heat Mass Transfer: vol. 64: pp. 547-558.

Clift R, Grace JR and Weber ME (1978) Bubbles, Drops, and Particles. New York: Academic.

Elkotb MM (1982) Fuel Atomization for Fuel Modelling. Prog. Energy Combust. Sci.: vol. 8: pp. 61-91.

Faeth GM (1977) Current Status of Liquid and Droplet Combustion. Prog. Energy Combust. Sci.: vol. 3: pp. 191-224.

Fredenslund A, Jones RL and Prausnitz JM (1975) Group-Contribution Estimation of Activity Coefficients in Nonideal Liquid Mixtures. AIChE J.: vol.21: pp. 1086-1099.

Jasper JJ (1972) The Surface Tension of Pure Liquid Compounds. J. Phys. Chern. Ref. Data: vol. 1: pp. 841-1009.

Leach FCP, Stone R and Richardson D (2013) The Influence of Fuel Properties on Particulate Number Emissions from a Direct Injection Spark Ignition Engine. SAE paper 2013-01-1558.

Lefebvre AH (1989) Atomization and Sprays. New York: Hemisphere.

Official Journal of the European Union (2012). Commission Regulation (EU) No 459/2012, OJ L 142/16 of 29 May 2012.

Poling BE, Prausnitz JM and O'Connell JP (2001) The Properties of Gases and Liquids, Fifth Edition. New York: McGraw-Hill.

Serras-Pereira J, van Romunde Z, Aleiferis PG, Richardson D, Wallace S and Cracknell RF (2010) Cavitation, Primary Break-up and Flash Boiling of Gasoline, Iso-octane and N-pentane with a Real-size Optical Direct-injection Nozzle. Fuel: vol. 89: pp. 2592-2607.

Sirignano WA (2010) Fluid Dynamics and Transport of Droplets and Sprays, Second Edition. Cambridge: CUP.

Sparrow EM and Gregg JL (1958). Trans. ASME: vol. 80: pp. 879-886.

Wen C-C and Hu C-H (2007) Vapor–liquid equilibria for binary and ternary mixtures of ethanol, 2-butanone, and 2,2,4-trimethylpentane at 101.3 kPa. Fluid Phase Equilibria: vol. 258: pp. 131-139.

Zhao H (2012) Laser Diagnostics and Optical Measurement Techniques in Internal Combustion Engines. Warrendale: SAE International.

Studying combustion variability and knock in a downsized SI engine using Large-Eddy Simulation

C. Angelberger[1], A. Robert[1,2], O. Colin[1]

[1]IFP Energies Nouvelles. 1 et 4 Avenue de Bois Préau. 92852 Rueil Malmaison. France

[2] PSA Peugeot-Citroën, Vélizy, France

E-mail: christian.angelberger@ifpen.fr

Abstract. Highly boosted spark ignition (SI) engines are more and more attractive for car manufacturers in terms of efficiency and *CO*2 emissions. However, thermodynamic conditions encountered in these engines promote the occurrence of abnormal combustions like knock or super-knock, which are experimentally difficult to analyze due to the risks of engine damage. The Reynolds Averaged Navier-Stokes (RANS) method mainly used in industry for piston engines is not the most appropriate as knock does not always affect the mean cycle captured by RANS. Using an accurate LES compressible code and improved versions of ECFM-LES (Extended Coherent Flame Model) and TKI (Tabulated Kinetics of Ignition) models allowing a full uncoupling of flame propagation and auto-ignition reaction rates, this work demonstrates for the first time that LES is able to describe quantitatively knocking combustion in a realistic downsized SI engine configuration. A quantified knock analysis is conducted based on a specific post-processing of both numerical and experimental data. LES is able to predict the in-cylinder pressure variability, the knock occurrence frequency and the mean knock onset crank angle for several spark timings. A 3D analysis also demonstrates that knock occurs at random locations, mainly at the exhaust valves side. Knock intensity is found proportional to the fresh gases mass burned by auto-ignition at low knock intensities, while an exponential increase at the highest intensities suggests the influence of additional factors like the knock location in the cylinder or complex behavior of knocking combustion. The LES visualizations show that at the latest spark timings, only local auto-ignition spots are observed leading to low knock intensities. On the contrary, for the earliest spark timings, a deflagration to detonation transition occurs for these conditions, leading to extremely high knock intensities.

Complex physics modelling of diesel injector nozzle flow and spray supported by new experiments

J. Shi[1], N. Guerrassi[1], G. Dober[1], K. Karimi[1] and Y. Meslem[1]

[1]Delphi Automotive
Bascharage - Luxembourg

E-mail: junmei.shi@delphi.com; noureddine.guerrassi@delphi.com; gavin.dober@delphi.com; kourosch.karimi@delphi.com; yann.meslem@delphi.com

Telephone: +(352) 5018 5226
Fax: +(352) 5018 7800

Abstract. This work is dedicated to developing effective numerical models for investigating the effect of injection hole geometry on the internal nozzle flow and spray behaviour. Focus was given to the numerical accuracy for the injection rate prediction and the capability of the numerical approach to predict the effect of nozzle geometry and operating conditions on the spray geometry and dynamics. The numerical simulations were based on a coupled approach for nozzle flow and spray in combination with primary and secondary breakup models. The needle motion profiles were obtained from 1D hydro-mechanical simulation by using AMESim. In order to account for the complex physics involved in the nozzle flow and spray formation, special modelling efforts have been made. The full energy equation including viscous heating and mechanical work was applied to consider the thermal hydraulic effect linked to a strong local depressurisation inside the nozzle and viscous dissipation in the boundary layer flow. For good predictive accuracy, the fuel properties like density, viscosity, and speed of sound were modelled as a function of local pressure and temperature, which was implemented as user defined function (udf) routines within the Fluent 14.5 solver. In order to understand the impact of the nozzle hole geometry on the spray behaviour, the flow structure and the atomisation energy of the flow at the nozzle hole exit was analysed. For the spray simulation, the explicit coupling approach of AVL FIRE has been used to avoid empirical assumptions for the jet velocity and dispersion angle, which are usually needed in standard spray simulation approaches.

Transient injection rate was measured for pressures ranging from 100bar to 2000bar in the hydraulic test rig under controlled temperatures. It was found that two nozzles, one with normal lower taper and inlet honing and the other with a larger taper but without honing, both starting with the same flow efficiency under the standard nozzle calibration pressure of 100bar, the honed design produces 7% higher flow efficiency than the un-honed design. This is because the flow discharge coefficient of the honed nozzle increases with increasing pressure and the flow efficiency of un-honed design falls with pressure. The simulation taking into account of variable fuel property as functions of local pressure and temperature greed very well with the measured quantities for both injectors. The dynamics of the spray were also investigated using new experiments that allowed for the measurement of the spatial and temporal spray momentum evolution. Additionally, high speed video photography, using the Mie scattering technique was adopted to measure both the macro and micro structure of the liquid jet. Experimental tests were performed at ambient temperatures, with back pressures up to 60bar in a static spray chamber. These data were applied for the evaluation of the nozzle simulations and the coupled simulation approaches for linking the nozzle flow with the spray.

Combining both CFD and microscopic visualisation results, the differences in flow efficiency and spray features between the two nozzles can be explained.

Notation

d *Nozzle exit diameter.*
r *Spray radius.*

1. Introduction

The transport sector is responsible for approximately 22% of the world's global energy consumption. Urbanisation and population and economic growth in developing countries are expected to nearly double the demand of fossil fuels usage from this sector over the next two decades compared

to today's levels (ExxonMobil, 2012). Almost 2/3 of liquid fuel will be consumed by Diesel engines that represent the dominant and most efficient powertrain in both light duty and commercial transportation systems as well as in a number of electricity generators. Policy makers around the globe are continuing to tighten fuel consumption and emissions legislation for passenger cars. For example, Euro 6 demands a 55% reduction in NOx emissions over Euro 5 levels and simultaneously will see the introduction of new drive cycles and testing methodologies so that real driving emissions will be significantly lower for all regulated emissions components. As a result, research efforts are focused on developing more efficient combustion system that reduce pollutants through various engine operating strategies, fuelling strategies, and novel design concepts of the combustion system. The fuel injection system, e.g. injector function, nozzle design, and injection control, is a key component of modern diesel engine to achieve the fuel economy and emission targets.

Today, nozzle design optimisation or nozzle individual tailoring for engine application still relies on the experimental testing of a large number of prototypes. This is because the process and mechanism of spray formation under practical diesel injection conditions is still far from being understood. It is of great interest, both to Fuel Injection Equipment (FIE) suppliers and to their customers to have an effective simulation approach which is capable of predicting how the spray behaviour depends on the injector function and the nozzle design for full range of operating conditions on an engine. Such a predictive simulation requires two main tasks: a complete representation of the complex physics of internal nozzle flow including realistic fuel properties, cavitation, turbulence and vortex dynamics, viscous heating; and the development and evaluation of a coupled simulation model for nozzle flow and spray for prediction of the effect of nozzle design on the spray behaviour.

2. Literature Review

The nozzle geometry is known to influence the flow efficiency, the spray characteristics, and the engine performance. Developing a high efficiency nozzle is demanded by OEMs in order to improve fuel economy and to reach future emission regulations. This is because higher efficiency more effectively converts rail pressure energy into spray momentum and which leads to better atomization, better fuel-air mixing and higher gas turbulence in the engine for better combustion. It has been shown that an increase of inlet rounding, of the nozzle length over diameter ratio or of the level of the hole conicity typically increases the discharge coefficient (Dober, et al., 2012), (von Kuensberg Sarre, et al., 1999), (Ning & Reitz, 2008) and hence the injection velocity.

So far, the calibration of nozzle flow efficiency is usually carried out under the condition of 100bar vs. atmospheric. Under this condition, the effect of taper and honing level on the nozzle flow efficiency has been extensively investigated over the last half century both by measurements and by numerical simulations. It is known among the fuel injection community that the same flow efficiency can be reached for two very different nozzle designs, e.g. one using a low taper and high rounding and the other using larger taper and low honing or even no honing. It is reported in (Soteriou, et al., 2006) and (Dober, et al., 2012) that the flow discharge coefficient of high efficiency conical nozzles increases by several percent at high injection pressure than the value measured at the standard calibration condition. This brings advantages for the engine power and emissions at high load (Dober, et al., 2012). This also indicates that todays' nozzle flow efficiency calibration practice is not precise for realistic engine applications. The flow coefficient behaviour of the large taper un-honed nozzle design under high injection pressure is so far not sufficiently investigated. Understanding of this behaviour and the link between nozzle design and spray is one of the motivations of the present research.

There have been numerous investigations dedicated to understanding the impact of nozzle design on the nozzle flow, and to link the nozzle flow to the spray behaviour. Usually the nozzle flow dynamics are characterized by strong flow direction deflection, flow separation, cavitation, and acceleration / deceleration. When the flow turns sharply from the needle seat area, or the sac into the nozzle hole, this results in the formation of complex vortex structures in both the sac volume and at the entrance to the nozzle holes (Shi, et al., 2010). The motion of the vortices is highly transient. Cavitation can occur in the vortex cores, due to low local pressure or due to the strong pressure drop (Reid, et al., 2010) (Roth, et al., 2002) which then affects the spray structure (Blaisot, et al., 2012). In addition, it is reported that, the collapse of cavitation in the downstream region is a major source of vorticity production, resulting in the formation of hair-pin vortices (Dittakavi, et al., 2010). Also, cavitation bubble collapse increases the local turbulence of the flow (Sou, et al., 2012). The transient interaction of turbulence and cavitation in the nozzle flow also causes jet pulsation and has a strong impact on the spray formation process, morphology, jet stability, and spray penetration (Payri, et al., 2004), (Andriotis & Gavaises, 2009), (Blaisot, et al., 2012), (Zigan, et al., 2013). This phenomenon is known to be highly dependent on the injection hole geometry (Im, et al., 2013). The level of inlet rounding as

well as the hole conicity additionally impacts the level of turbulence and cavitation occurrence (Soriano Palao & Mouvanal, 2011) and through these phenomena the spray structure. However, the influence of these parameters on spray features such as the liquid breakup length, the dispersion angle or the SMD are difficult to understand based on a individual measurement techniques or purely by simulation. Progress can only be made by combination of different measurement techniques together with simulation. Due to the fact that the standard nozzle flow efficiency calibration is performed under a delta pressure of 100bar. Most of the CFD investigations on the flow efficiency neglect the thermodynamic effect of the flow and do not consider the fuel property variation in response to the local pressure and temperature variation in the nozzle, e.g. (Soriano Palao & Mouvanal, 2011). This simplification is acceptable for the 100bar vs. 1bar calibration condition and good agreement between simulation and measurement can be obtained as soon as the mesh resolution is sufficient and a 2nd order discretization scheme is applied. However, this simplification is not justified under realistic engine operation conditions. Standard EURO6 passenger car diesel engine applications use rail pressures of 2000bar or more, and are expected to reach 3000bar in a few years. The fuel in the injection nozzle experiences strong depressurization and significant temperature variation inside the injection hole due to the local pressure variation and the viscous heating effect. This further causes significant variation of local fuel properties. In fact, there have been continuous efforts in establishing correlation models for the fuel properties as functions of pressure and temperature, e.g. the liquid equation of state by (Bode, 1990), the viscosity equation of (Schmidt, 1999) and the polynomial function correlations as is described in (Kolev, 2002). Both types of fuel property correlations have been implemented in the 1D hydraulic simulation code AMESim (LMS Imagine, 2011) It is only recently, that a few investigations have considered this complex physics in their numerical models, see e.g. (Theodorakakos, 2012), who applied the diesel fuel property data from public literature (Kolev, 2002). Our fuel correlation evaluation indicates that the Bode and Schmidt equations have better accuracy for the Diesel ISO 4113 test fuel. These two correlations provide a good basis for the present work to model the complex physics of the thermal hydraulic phenomenon of the nozzle flow under strong depressurization.

Today, the state-of-the art engineering spray simulation still needs empirical assumptions for the initial ligament diameter, jet velocity and spray dispersion due to the lack of predictive breakup models. This type of simulation approach is not feasible to establish the link between the nozzle design, nozzle flow characteristic and spray behaviour. There is some efforts in developing a coupled simulation approach for the nozzle flow and spray, either by a unified simulation with implicit coupling or by two separated simulations one for nozzle flow and the other for the spray by using the nozzle simulation file to avoid the empirical assumptions for the spray simulation (AVL, 2013).The latter approach, also called explicit coupling is applied in the present study since this method is straightforward and robust.

3. Research Overview and Objectives

The work presented in this paper, highlights the numerical model development for the prediction of, hydraulic discharge coefficients and spray behaviour in order to interpret simultaneous experimental investigations. The work uses two different nozzle types, having the same customer specification, discharge coefficient and flow at 100bar, but a 7% difference in the flow efficiency at higher injection pressures. Both nozzles fit with the design engineer requirements but one type of design gives better performance at high pressures. Whilst one nozzle showed an increase of efficiency with an increase of pressure, the other nozzle showed a decrease in efficiency with an increase of pressure. The operating pressures and temperatures were between 100 & 2000 bar and 316 & 403 K respectively. Engine experiments confirmed that the Low taper honed nozzle (see **Figure 1**, called A) produces more power and less soot emissions at full load operating conditions or could make equal performance to the higher taper un-honed nozzle (called B) with significantly lower rail pressures.

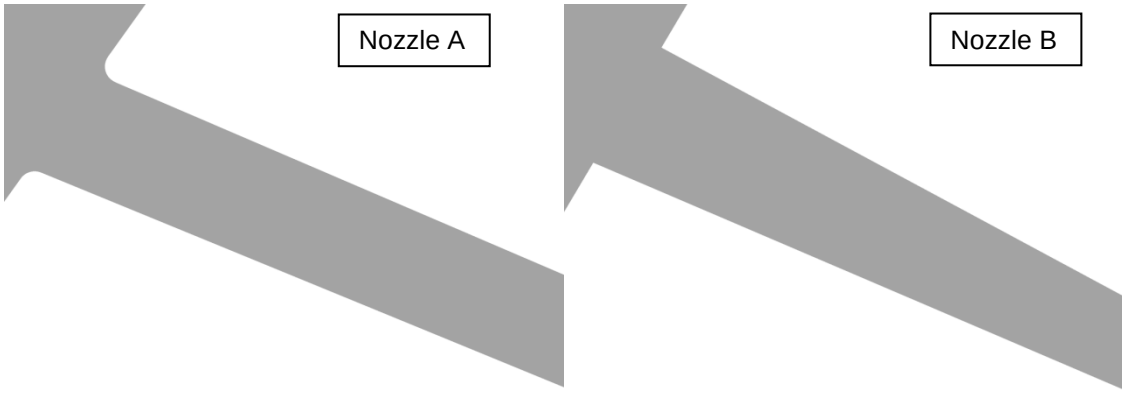

Figure 1: Nozzle A with low taper and normal honing; Nozzle B with higher taper and un-honed.

To further assess the impact of these nozzle geometries experimentally, the macroscopic spray characteristics were obtained applying Mie scattering technique. However, results showed only minor differences between the two nozzles, with a slightly larger penetration length at low as well as high injection pressures, and a smaller dispersion angle at the start of injection at low injection pressures for the honed injector. Resolved spray momentum measurements were also carried out at 8mm away from the nozzle exit. The results confirmed that the honed nozzle produces higher momentum and a more focused spray distribution.

The modelling was used to understand the causes of the observed phenomena, so as to help to build fundamental knowledge of the impact of nozzle geometry on flow and spray behaviour. For reasons of brevity, this paper focuses on two aspects of the modelling methodology: the fuel property model; and coupled nozzle flow and spray simulations. To understand the nozzle flow behaviour, a complex physics model was applied. The full energy equation including viscous heating and mechanical work was applied to consider the thermal hydraulic effect linked to the strong depressurisation inside the injection nozzle and viscous dissipation in the boundary layer flow. Fuel properties such as density, viscosity, and speed of sound were modelled as a function of local pressure and temperature, which were then implemented as user defined functions (udf) within the Fluent 14.5 solver. Numerical investigations assuming constant fuel properties were also carried out. It was found that the behaviour of the discharge coefficient can only be reproduced by the complex physics model.

In order to understand the impact of the nozzle hole geometry on the spray behaviour, the flow structure and the atomisation energy of the flow at the nozzle hole exit was analysed. For the spray simulation, the explicit coupling approach of AVL FIRE, which uses the nozzle simulation results at hole exit as the inlet condition for a Lagrangian spray simulation, which avoids the need to assume injection velocity and dispersion angle. Moving needle simulations corresponding to the spray measurement conditions were carried out using the needle lift profile obtained from 1D AMESim simulation. Through a comparison of nozzle flow and spray simulation results with the Mie characterisation results and the momentum measurements, the physical mechanisms responsible for linking the nozzle geometry to the hydraulic flow and spray observed from experimental investigation can be understood.

4. Modelling Approaches

Eulerian modelling of nozzle flow with cavitation

The CFD calculations were performed with the commercial CFD solver ANSYS-Fluent 14.5. To describe the two-phase flow, a homogeneous two-fluid mixture model was used. With this, the liquid and gaseous phases are considered as a homogeneous mixture sharing the velocity and pressure fields. The transient flow is described by an unsteady Reynolds-averaged Navier–Stokes (URANS) approach using the k-omega shear stress transport (SST) turbulence model. The cavitation was accounted for by a Rayleigh–Plesset equation based model. The continuity equation of the mixture and the transport equation for the vapour phase can be described below:

$$\frac{\partial \rho_m}{\partial t} + \frac{\partial \rho_m U_i}{\partial x_i} = 0 \qquad (1)$$

Where U_i represents the mass weighted velocity components, (with *i, j* = 1...3), α is the vapour volume fraction and ρ_v and ρ_l are the vapour and liquid density, respectively. From this the value of the liquid

volume fraction (1-α) can be calculated. The average mixture density ρ_m was also calculated from the mass fraction of liquid and vapour phase in their respective cells:

$$\rho_m = \alpha\rho_v + (1-\alpha)\rho_l \tag{2}$$

The transport equation for the vapour phase can be written below

$$\frac{\partial \rho_v \alpha}{\partial t} + \frac{\partial \rho_v \alpha U_i}{\partial x_i} = S_{lv} \tag{3}$$

Applying the Rayleigh-Plesset equation leads to the following calculation model for cavitation-induced mass transfer at phase change:

$$S_{lv} = \begin{cases} sign(p_b - p)F_1 \dfrac{3\alpha_0(1-\alpha)\rho_v}{R_b}\sqrt{\dfrac{2}{3}\dfrac{p_b - p}{\rho_l}} & if\ p < p_b \\ sign(p_b - p)F_2 \dfrac{3\alpha\rho_v}{R_b}\sqrt{\dfrac{2}{3}\dfrac{p - p_b}{\rho_l}} & if\ p > p_b \end{cases} \tag{4}$$

S_{lv} represents the source/sink term of the mass during phase change due to cavitation. If the ambient pressure p drops below the vapour pressure p_b, a part of the liquid mass is converted to the vapour phase (cavitation). If the ambient pressure is higher than the vapour pressure, vapour condensation occurs. The, $sign(p_b-p)$ indicates the direction of the mass transfer. α_0 represents the volume fraction of the cavitation nuclei in the fluid. R_b is the average bubble radius and F_1, F_2 are the evaporation and condensation coefficients introduced to account for different bubble expanding and shrinking velocities depending on the respective fluid and boundary conditions.

The Reynolds-averaged momentum equations of the whole mixture consisting of liquid and vapour phases can be described by

$$\frac{\partial \rho_m U_i}{\partial t} + \frac{\partial \rho_m U_i U_j}{\partial x_j} = -\frac{\partial p}{\partial x_i} + \frac{\partial \tau_{ij}}{\partial x_j} \tag{5}$$

with

$$\tau_{m,ij} = (\mu_m + \mu_{mt})\left(\frac{\partial U_i}{\partial x_j} + \frac{\partial U_j}{\partial x_i}\right) - \frac{2}{3}(\rho_m k + \mu_{mt}\frac{\partial U_k}{\partial x_k})\delta_{ij} \tag{6}$$

In equation (6) μ_m is the dynamic molecular viscosity of the mixture and μ_{mt} is the turbulent viscosity which is solved by the turbulence model.

The energy equation is given by:

$$\frac{\partial}{\partial t}\sum_{k=l,v}(\alpha_k\rho_k h_k) + \frac{\partial}{\partial x_j}\sum_{k=l,v}(\alpha_k\rho_k U_j h_k) = \frac{\partial p}{\partial t} + \frac{\partial}{\partial x_j}\sum_{k=l,v}(\alpha_k k_{k,eff}\frac{\partial T}{\partial x_j}) - \frac{\partial}{\partial x_j}(\tau_{m,ji}U_i) - p\frac{\partial U_j}{\partial x_j} \tag{7}$$

where the last two terms represent the viscous heating and expansion work in the flow.

Liquid property model

Special efforts were spent on modelling the realistic fuel properties under the strongly depressurising conditions within the injector nozzle flow. The fuel properties like liquid density, viscosity and the speed of sound are modelled with a udf of local pressure and temperature. For the density the modified Bode equation of state (Bode, 1990) (LMS Imagine, 2011) is applied, namely,

$$\rho(P,T) = \frac{\rho_b(1-\alpha T)}{1 - A.\ln\left(1 + \dfrac{\dfrac{p}{p_{ref}}}{b_0 + b_1.T + b_2.T^2 + b_3.T^3}\right)} \tag{8}$$

For the viscosity, the modified Schmidt correlation (LMS Imagine, 2011), (Schmidt, 1999) as shown below is applied:

$$\mu(P,T) = a_1 exp^{\frac{\rho_\mu}{a_5.(1+a_6T)-\rho_\mu}} \tag{9}$$

with

$$\rho_\mu = \frac{\rho_b.(1-\alpha T)}{1 - a_3.\ln\left(\frac{a_1 - a_4.T + \frac{p}{p_{ref}}}{a_1 - a_4.T}\right)} \tag{10}$$

The speed of sound of the liquid phase is derived from the density equation:

$$c^{-2} = \frac{1}{v^2}\left[\left(\frac{\partial v}{\partial p}\right)_T + \frac{T}{c_P}\left(\frac{\partial v}{\partial T}\right)_p\right)^2\Bigg] \tag{11}$$

$$\text{with } v = \frac{1}{\rho}, \qquad c_P = c_P\left(p_0, T\right) - T\int_{p_0}^{p}\left(\frac{\partial^2 v}{\partial T^2}\right)_p \mathrm{dp}$$

The coefficients of the above correlations were obtained by least-square data fitting to the measurement data from the NADIA project. The maximum error of the calculations compared with the experimental data over the pressure and temperature ranges were, 0.2% for the density, 2.1% for the dynamic viscosity and 3.1% for the liquid speed of sound.

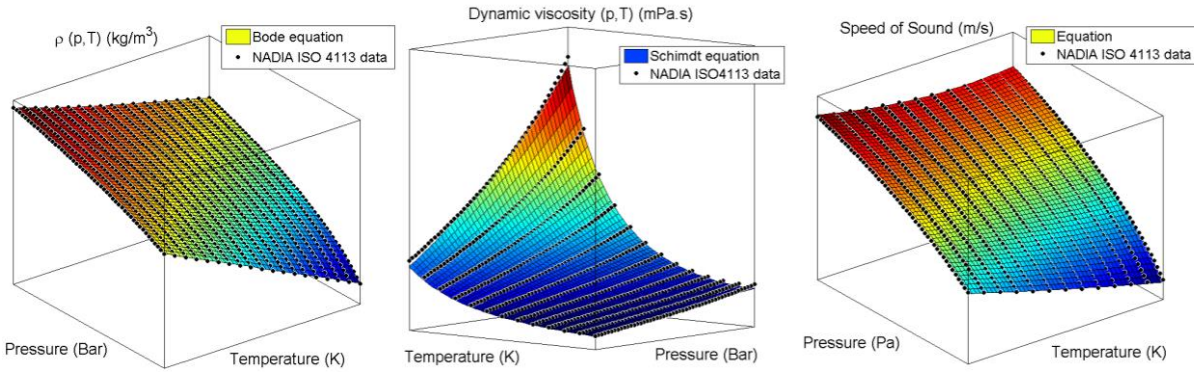

Figure 2: A comparison of measured (points) and simulated fuel properties (surface). Raw data is derived from the NADIA project.

The equations are solved by the SIMPLEC algorithm using the 1st order implicit scheme for temporal discretisation, a 2nd order upwind scheme for spatial discretisation of the pressure and the momentum equations, and the QUICK scheme for the remaining equations.

As demonstrated in **Figure 3**, strong temperature variations occur inside of the nozzle hole linked to the depressurisation process. This results in a significant variation of fuel density and viscosity within the flow field. Therefore, it is very important to consider the complex physics of thermal hydraulic when simulating fuel injection.

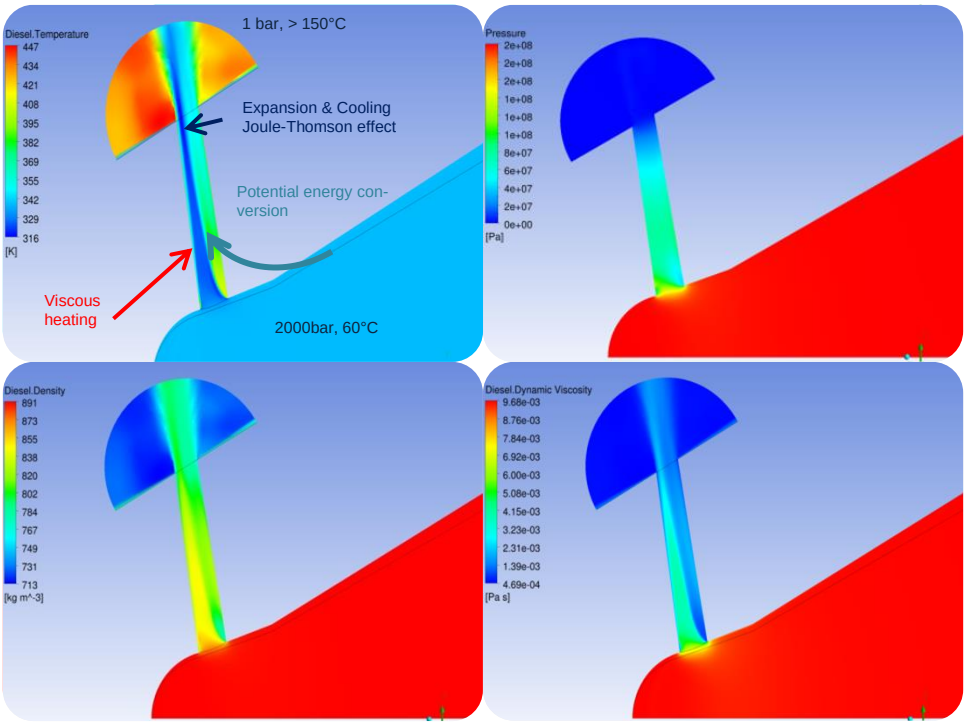

Figure 3: Flow through the nozzle is subjected to strong pressure gradients, leading to strong gradients in density, viscosity and temperature. CFD boundary conditions are taken from hydraulic injection measurement and 1D injector simulations.

In order to understand the link between nozzle flow and spray propagation, the turbulent energy T_{ke} and the kinetic energy of flow motion in the axial direction of injection hole and in the non-axial directions E_k at the nozzle exit were monitored during the simulation. These quantities are expected to have an impact on the atomisation quality and spray behaviour (Dumouschel, et al., 2005). The turbulent kinetic energy is defined as:

$$T_{ke} = \frac{1}{2}\left(u'^2 + v'^2 + w'^2\right) \tag{12}$$

where u', *v'* and *w'* are fluctuations of the velocity components. The non-axial kinetic energy E_k is an indication of the intensity of the non-axial motion, e.g. swirling vortex in the nozzle hole, which is mainly generated by the flow deflection and acceleration at the hole entry and is expected to have an effect on the atomisation efficiency. These quantities can be obtained from the radial and tangential velocity components along the nozzle hole axis.

$$E_k = \frac{1}{2}(u_r^2 + u_T^2) \tag{13}$$

These quantities were defined as local variables, and mass flow rate weighted averages were calculated over the nozzle orifice exit plane.

Explicit coupled simulation of nozzle flow and spray

In order to study the effect of nozzle geometry on the spray behaviour, the explicit coupling approach of AVL FIRE (AVL, 2013) was applied. This approach uses the nozzle file, i.e. the Eulerian nozzle flow solution data at the nozzle exit plane, as the boundary condition for the Lagrangian spray simulation. The Blob Injection Primary breakup model was applied to simulate the competing effect of turbulence breakup enhanced by cavitation and the aerodynamic breakup. Denoting the turbulence length and time scale by:

$$r_T = C_\mu{}^{0.75}\frac{k^{1.5}}{\varepsilon}, \quad \tau_T = C_\mu\frac{k}{\varepsilon} \tag{14}$$

The turbulence breakup rate is calculated by

$$\frac{dR}{dt} = \frac{r - C_3 r_T}{C_4 \tau_T} \tag{15}$$

The cavitation effect on turbulence production is obtained by tracking the bubble radius R and the rate of change dR/dt by solving the Rayleigh-Plesset equation. With these values the turbulence production due to cavitation can be calculated from the energy release from bubble collapse following the approach described in (Baumgarten & Merker, 2004).

The aerodynamic breakup rate is calculated using the WAVE Child breakup model following the surface wave development concept of (Liu & Reitz, 1993).

$$\frac{dr}{dt} = \frac{(r - r_{stable})}{\tau_a} \tag{16}$$

$$\tau_a = \frac{3.726.C_2.r}{\Lambda.\Omega} \tag{17}$$

$$r_{stable} = C_1.\Lambda \tag{18}$$

The inter-phase momentum transfer was accounted for by the drag force based on the Grace correlation and the turbulence dispersion (Gosman & Ioannides, 1983). The particle interaction for dense spray was considered by using the model of O'Rourke (O'Rourke, 1989). The Dukowicz vaporization model (Dukowicz, 1993) was applied for evaporation despite the fact that evaporation is not significant in the present spray investigation which is based on measurements at room temperature.

The workflow is as follows: first, the 1D AMESim simulation was applied to obtain the needle lift profile. Then moving-needle nozzle flow simulation was carried out using this needle lift profile and a nozzle file was generated. This file was used as the inlet boundary condition for the Lagrangian spray simulation. This coupled simulation approach avoids the empirical assumptions on initial jet velocity and spray cone angle and thus is feasible for investigating the link between nozzle geometry and spray.

5. Experimental Approaches

5.1 Hydraulic Test Benches

Historically, a hydraulic test bench is used to characterise diesel fuel injection equipment. Of primary importance to understand the injector function is to measure the Rate of Injection (ROI). A well-known technique to measure the ROI is a rate tube, where fuel is introduced at the end of a long tube and the pressure wave caused by the acceleration of the fluid is measured and used to estimate the ROI. The modern test equipment implementation of this is the IAV Injection Analyser (**Figure 4**). This equipment is a very powerful measurement tool and gives a great deal of information about an injector's hydraulic and mechanical performance.

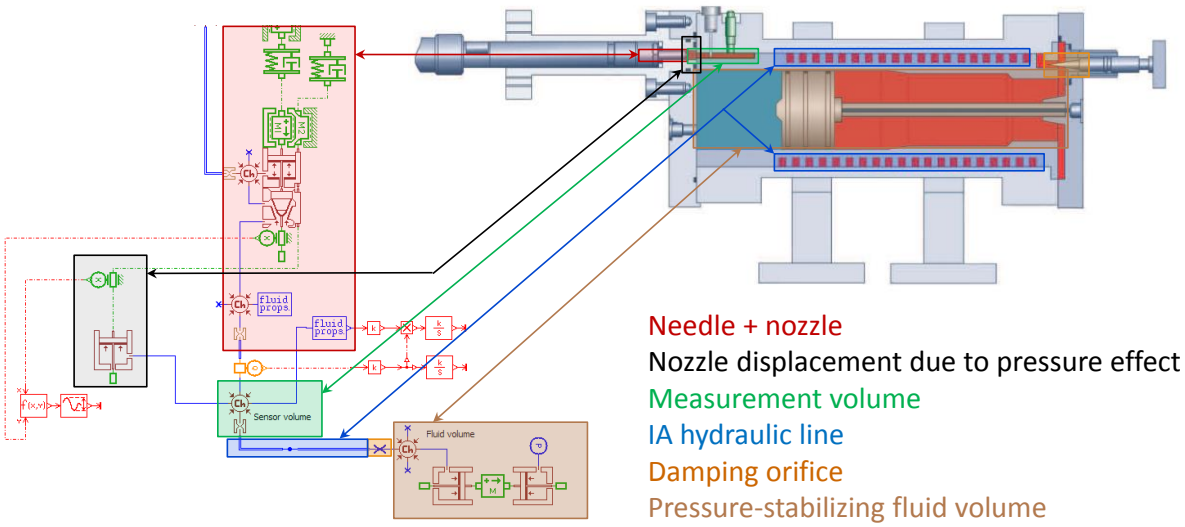

Figure 4: Injection Analyser Design (IAV GmbH, 2008) and its modelisation within AMESim

Key to obtaining the most information from the Injection Analyser is to reproduce the real ROI signal from the measured ROI. **Figure 5** illustrates that there are several features on the measured ROI which are not real injection features but related to non-ideal thermal effects within the rate tube or mechanical movement of the nozzle body. Consequently, measured ROI must be corrected before it is used according to specific algorithms to compensate for the known non-ideal effects. In addition, if processed properly then specific information such as the end of needle lift can be seen in pressure waves which affect the ROI. Such information is very important to validate the modelling of the nozzle needle lift in the absence of direct measurements of the nozzle needle position.

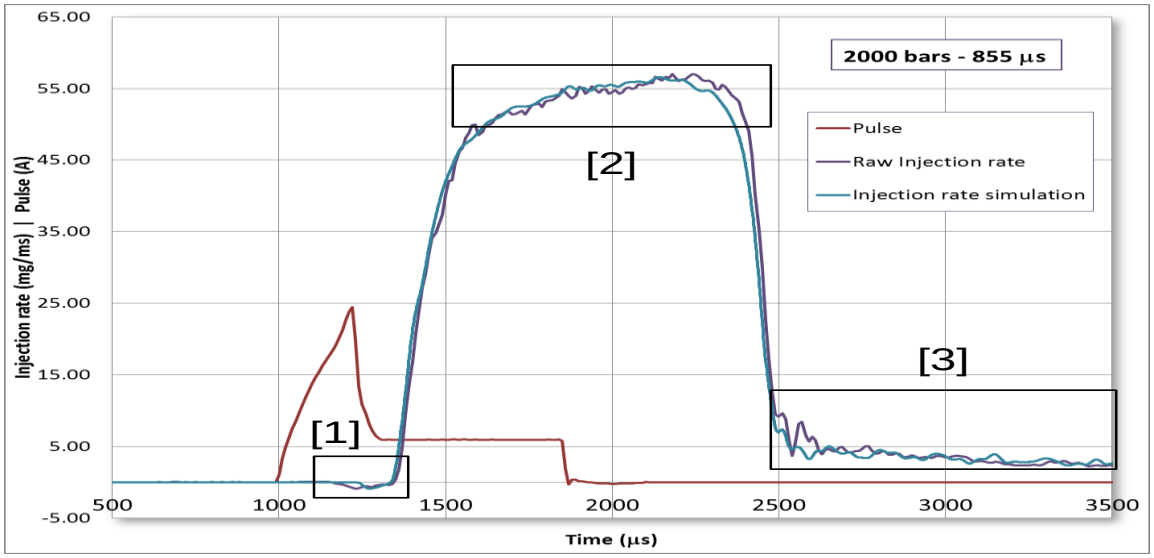

Figure 5: A comparison of the experimental rate of injection from the Injection Analyser and a simulated measurement signal using a 1D hydraulic-mechanical model in AMESim. Matching the key features of the injection rate is necessary over several areas of the injection rate diagram (ie. [1], [2], [3])..

A second hydraulic test bench was also used for the characterisation of the static nozzle flow. This rig applies fuel pressure to the nozzle and measures the flow rate. Temperature, rail pressure and downstream pressure are all controllable within the ranges to which the nozzle is normally subjected. This rig is primarily used for the measurement of the nozzle hole discharge efficiency (C_d) which is an important nozzle performance parameter often correlating with engine emissions.

5.2 Momentum Rig, Test Bench

Useful though the hydraulic characterisation is, it does not directly correlate with spray or droplet velocity and thus mixing energy. Further it has been known for some years that fuel sprays take different shapes including their penetration and dispersion angles, and that there is not one optimal spray shape for all combustion system designs.

The spray momentum and its shape can be measured by directing the fuel spray on to a force plate as shown in **Figure 6**. The plate is arranged to measure the force necessary to destroy all of the axial momentum in the fuel spray/jet (Greeves, et al., 2008), (Postrioti, et al., 2011). The plate or force sensor can be rotated about a vertical or horizontal axis passing through the spray hole origin. The sensor can also be translated closer to or further away from the spray hole origin. This enables the collection of information about the distribution of spray momentum across the spray and along the spray length. Delphi has several momentum rigs, which are similar in design. One such type (MR1) is dedicated to the simultaneous measurement of total spray force and flow of a nozzle operated with continuous flow over periods of up to 1minute. The other (MR2) is dedicated to the spatial and temporal mapping of the spray force through the jet and along its length for a real operating injector.

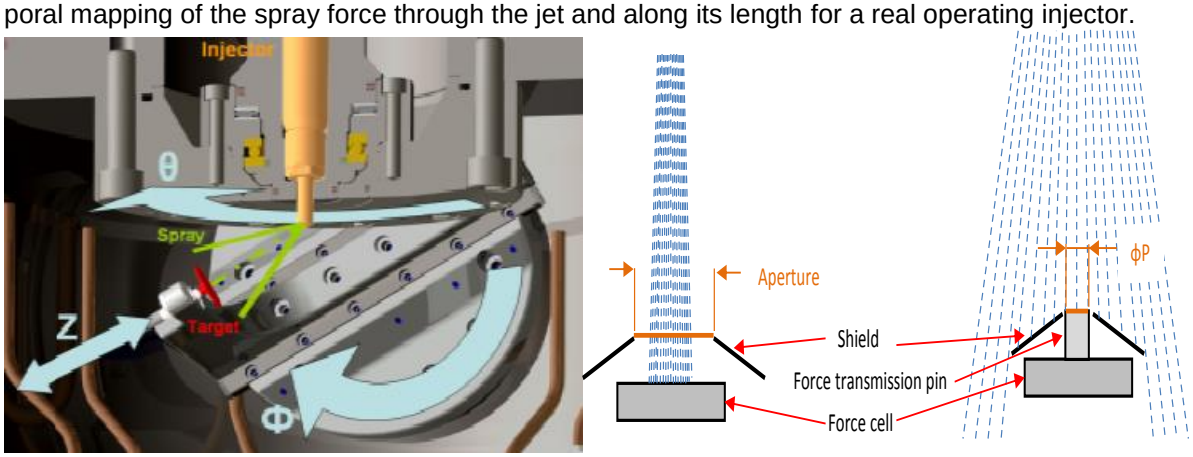

Figure 6: Momentum Rig Device (left), Sensors(right) can be configured to measure the entire spray force (MR1) or to map the spatial variation in spray force (MR2)

MR1 is important for direct measurement of the C_d and the C_v. From these values the C_a can also be calculated, see equations (19)→(22). This rig is mainly used at 100bar rail pressure and atmospheric backpressure with the objective of achieving very high accuracy in force and flow of better than 0.5%. It is noted that the exact target design is critical to achieving the desired measurement accuracy. The basic configuration is illustrated in **Figure 6**. Whilst it is possible to also use this rig for the investigation of the spray shape through investigation of how the load on the force cell changes as the spray is rotated outside of the measurement aperture (Dober, et al., 2012), it cannot investigate in detail the internal spray momentum distribution. Furthermore, the maximum rail pressure is limited to ~100bar, the back pressure to atmospheric pressure, and the time response of the system is very slow, relative to typical diesel injection events.

$$C_d = \dot{m} / \dot{m}_{th} = \dot{m} / (\rho_{fuel} . \mathrm{Area}_{hole} . U_{th}) \tag{19}$$

$$U_{th} = \sqrt{2(P_1 - P_2)/\rho_{fuel}} \tag{20}$$

$$\eta_n = \frac{\dot{\mathrm{Mom}}}{\dot{Mom}_{tham}} = \frac{F_p}{(\dot{m} . U_{th})} \tag{21}$$

$$C_d = C_a \times C_v = C_a . \eta_n \tag{22}$$

MR2 does not have these shortcomings, and hence, it allows for the investigation of the spatial and temporal evolution of spray momentum at realistic rail pressures and back-pressures. The backpressure on this rig can be increased up to 85 bar, and the rail pressure up to 3000 bar. The target sensor (**Figure 7**) has a 1mm sensing aperture. The test results presented in this paper are taken at atmospheric backpressure and with the sensor at a distance of 8mm from the spray hole exit, which represents the minimum distance which the sensor can approach the nozzle. The sensor position test pattern is indicated in **Figure 7**. Tests are made for a number of injection events to ensure a stable repeatable spray and then a windowing of the force signal (**Figure 7**) is applied to extract the average

fully developed spray force on the sensor. These test conditions and processing steps are intended to allow for a close correlation of the spray momentum distribution with the nozzle flow simulations at full needle lift.

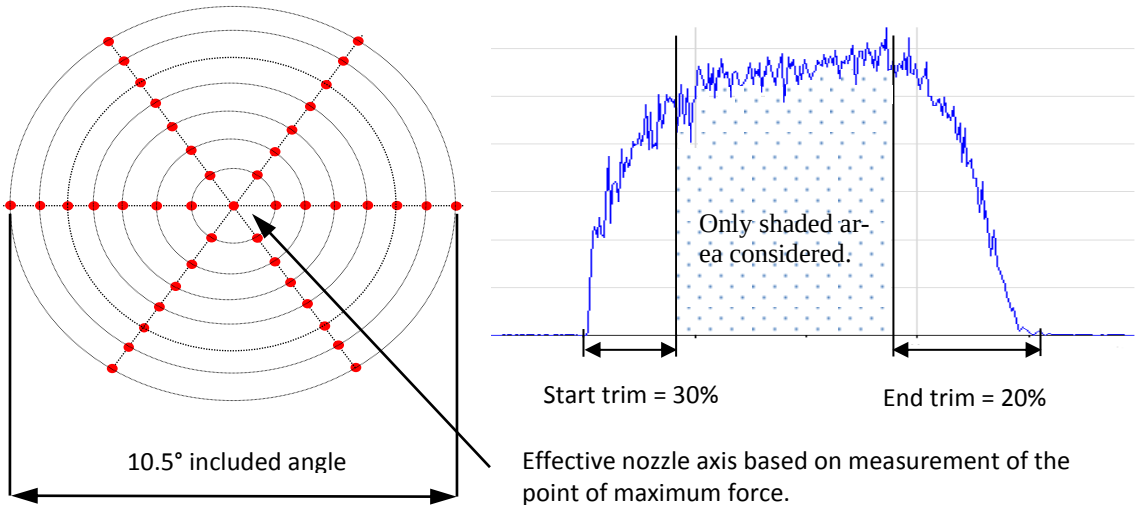

Figure 7: Sensor Position test pattern (left); Signal time windowing applied to extract the mean fully developed spray force (right)

5.3 Spray Visualisation

Further spray characterisation experiments were carried out using a high pressure, ambient temperature static rig, to visualise the evolution of the emerging Diesel fuel without evaporation. A nitrogen environment was used, in order to suppress combustion **Figure 8**.

The optical access to the static chamber was provided by three windows. Two side windows for illumination of the subject (30mm x 140mm), and the third window for visualisation of the emerging fuel spray (Ø140mm).

Prior to the start of experiments, the static chamber was brought to an ambient temperature, via a pump circulating water at 25°C around the water jacket of the static chamber. This insured a consistent operating temperature throughout the experiments.
For comparative reasons, the chamber pressure was kept to 60bar.

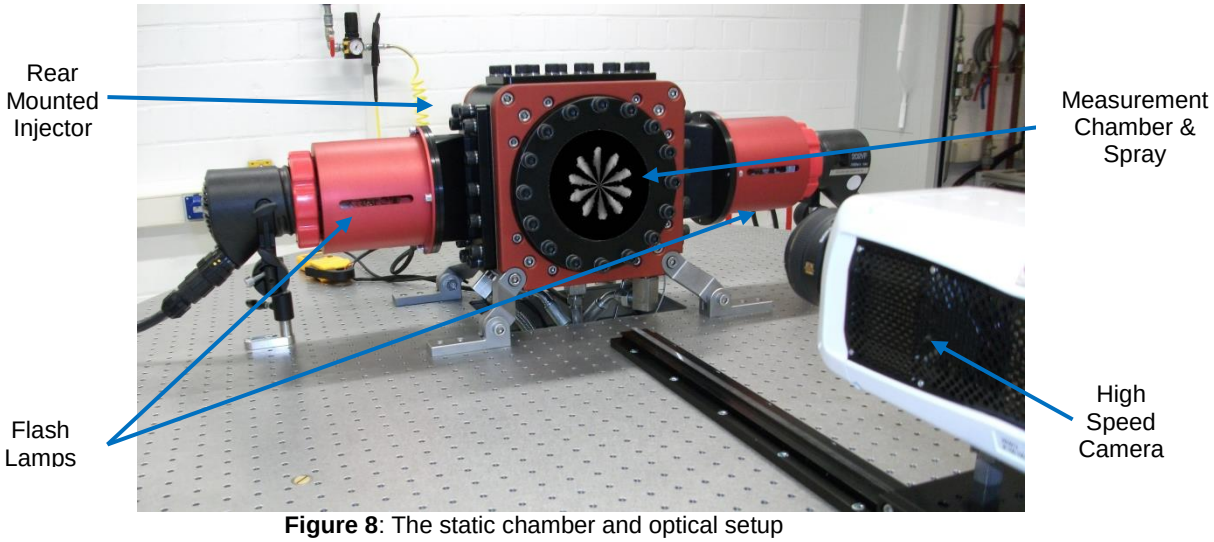

Figure 8: The static chamber and optical setup

To capture the evolution of the emerging spray from the nozzle, a Phantom V711 high speed video camera was used in this series of experiments. The camera featured a 12-bit monochromatic Complementary Metal-Oxide Semiconductor sensor (*CMOS*) and a maximum electronic shutter exposure of 0.3 μs.

With a maximum recording rate of 1.4 million frames per second and a maximum resolution of 1280 × 800, compromise between acquisition rate and resolution was obtained with a frame rate of 42341 per second, with a corresponding maximum resolution of 368 × 368 respectively. With frame exposure set to 0.3 μs for the Phantom camera, over-exposure protection ensured optimum image quality for every pixel, regardless of illumination levels within the recorded images. To ensure maximum intensity of the recorded images, the gamma correction factor was set to 1.0.

For the illumination of the subject, a Cordin high intensity Xenon light source, with two flash heads was used. With 5 intensity level adjustable from 364J to 1300J, compromise between *f* number and intensity was made to realise the maximum depth of field.

6. Results and Discussion

6.1 Diesel Fuel Injection Equipment

All test and simulation data uses Delphi Diesel Fuel Injection Equipment. Furthermore the focus has been on light duty common rail fuel injection equipment using the DFI1.20 injectors. The DFI1.20 injectors are Delphi's next generation servo-solenoid injectors. They are manufactured to an exact quality standard and have very low levels of shot to shot and part to part dispersion in performance. The injectors used in this series of experiments, have a low volume µsac design and an untruncated needle tip design.

The common rail and the delivery pipes were typically instrumented with Kistler pressure transducers for a high frequency and high fidelity measurement of inlet pressure to the injectors. The fuel delivery and the rail pressure were controlled either by an open Delphi ECU or flexible injector driver module.

The primary test injectors presented in this paper were identical apart from their nozzle hole shape. The difference in the hole shape is described in **Figure 1**. This makes the entry to the nozzle holes either sharp edged (un-honed) or rounded edged (honed). Otherwise the injectors had the same cone angle, same outlet diameter, and equivalent hydraulic flow under standard test conditions at 100bar v atmospheric pressure.

6.2 Nozzle flow hydraulic efficiency

The flow discharge coefficient, C_d also known as flow efficiency, is an important index of the fuel delivery characteristic of a nozzle design. This quantity is usually estimated based on fuel density evaluated at the downstream or cylinder pressure and the upstream or rail temperature. It is observed in the measurements that C_d increases with increasing pressure for the nozzle with inlet honing (Nozzle A), whilst the flow efficiency falls with pressure for the nozzle with higher taper but without inlet honing (nozzle B) (**Figure 9**). The phenomenon that C_d increases with increasing pressure has been commonly reported in the literature. The opposite trend observed for the un-honed nozzles has not been reported.

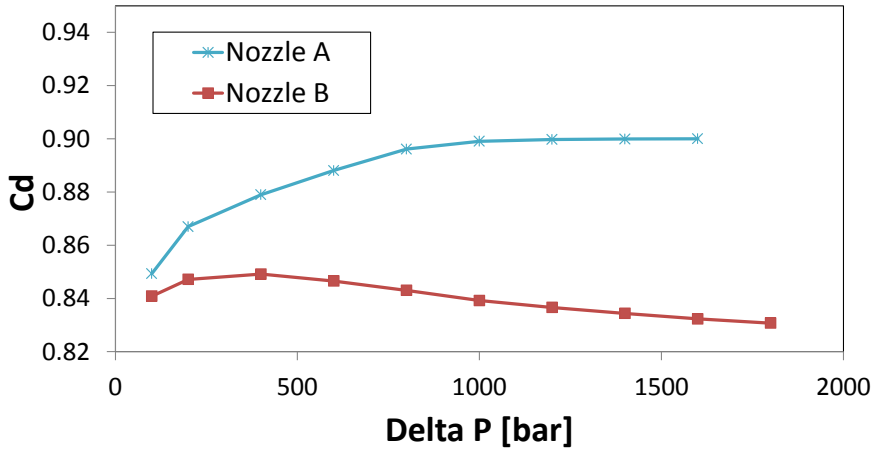

Figure 9: C_d taken from experimental measurement; the injector needles were removed; backpressure set to 5bar; nozzle A is honed, & nozzle B is un-honed.

In order to understand the flow efficiency behaviour observed in the measurement, extensive numerical experiments using various fuel properties and operating conditions were carried out for different nozzle designs. Both variable fuel properties as described in section 4 and constant fuel property values evaluated based on the pressure and the corresponding temperature measured at the nozzle inlet or outlet, or based on some artificial combinations were applied. Since the fuel property, especially the viscosity varies significantly for different test cases, very different C_d behaviour is predicted as shown in **Figure 10** for a honed nozzle design. If the fuel property evaluated at inlet pressure and inlet temperature is applied, decreasing C_d with increasing injection pressure is predicted even for this design. This behaviour has been reported before in the literature (Soteriou, et al., 2006), while the physical cause was not discussed. This is because the fuel viscosity increase caused by pressure increase is more important than the velocity increase and consequently the Reynolds number decreases with increasing injection pressure.

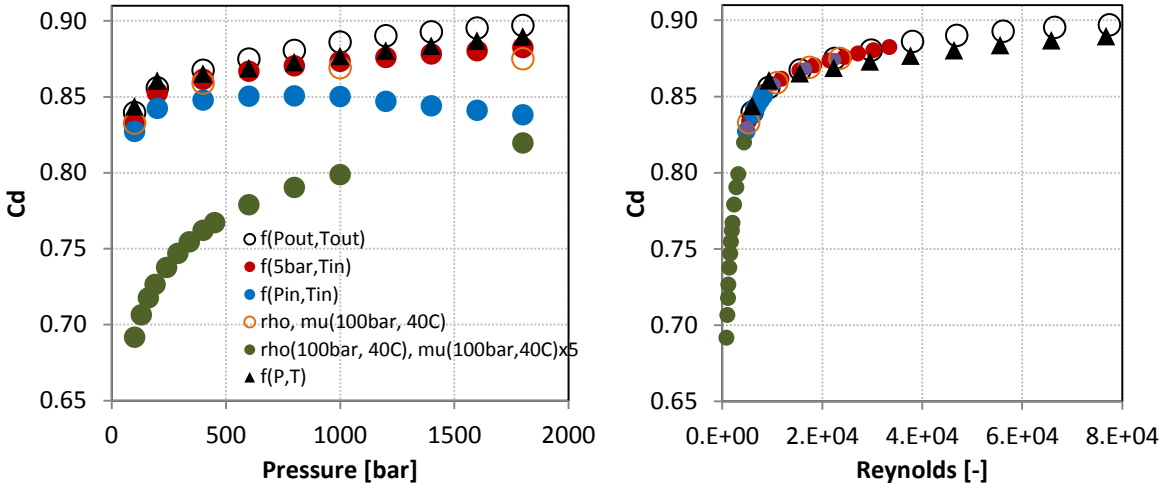

Figure 10: Fuel property impact on the simulated C_d vs. rail pressure on the left, and vs. Reynolds number on the right. In contrast to other results in this paper, these data were obtained with a 1st order upwind scheme.

Despite the different behaviour, all the data obtained by using constant fuel properties can be well correlated by the Reynolds number (**Figure 10**). The results obtained by using the variable fuel properties could not be represented by the same correlation. The authors investigated different designs with and without injection hole inlet honing, and a good correlation for C_d versus Reynolds number can be obtained in all cases where constant density and viscosity were applied for the entire computational domain. In addition, depending on the Reynolds number, the C_d curve indicated three different flow regimes (**Figure 11**), such as Laminar flow, low Reynolds number turbulent flow, and high Reynolds number turbulent flow. The authors believe that a good correlation can also be obtained for the variable fuel property results, if the representative pressures and temperatures can be determined for the C_d and the Reynolds number calculation in a similar way to what has been shown before in the literature (Shi, et al., 2004).

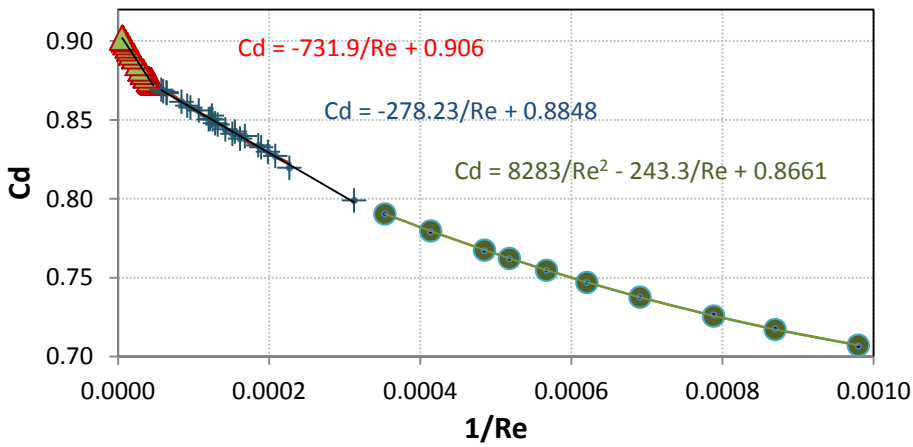

Figure 11: Relationship between Cd and 1/Reynolds number. A correlation of Cd at different flow Regimes.

The impact of variable fuel property model on Cd prediction is further demonstrated in **Figure 12**. In this figure it can be seen that it is possible to predict the performance of the honed injector with either variable or fixed fuel properties, whereas the un-honed simulation results are very sensitive to the fuel property assumptions. The trend that C_d decreases with increasing pressure as observed in the measurements could not be predicted if the local variable fuel property is not applied. As previously mentioned, the reason is likely to be that the Reynolds number at the nozzle hole exit is no longer representative of the main pressure losses for these types of nozzle hole shapes.

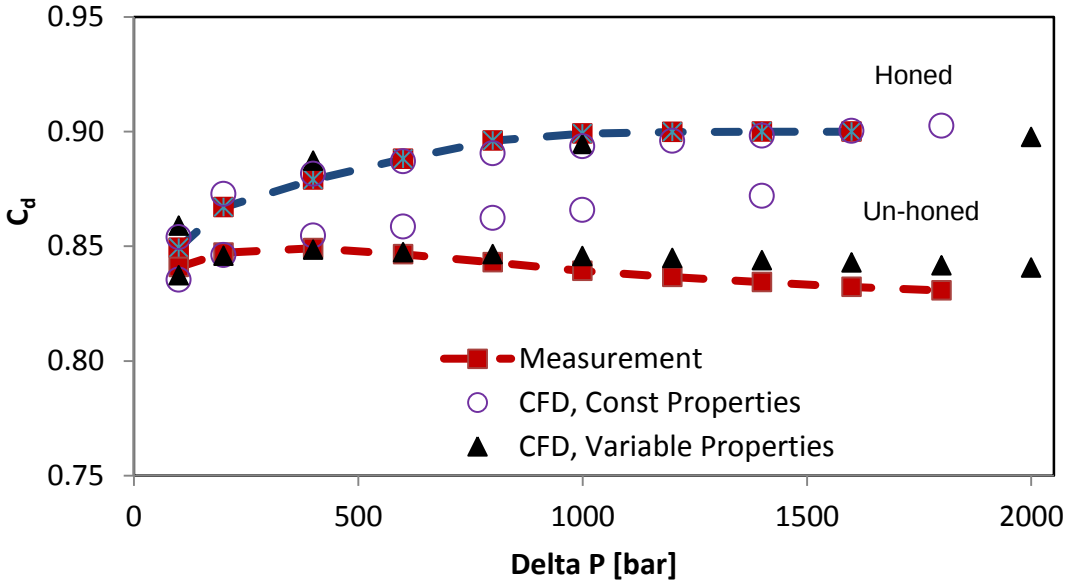

Figure 12: Results indicate the impact of delta pressure on the Cd. The honed injector has a very different C_d evolution as compared to the un-honed injector.

The different C_d behaviour for the honed and un-honed designs at increasing pressure has a practical significance. In common practice of nozzle calibration, C_d is measured at a condition of 100bar vs. atmospheric backpressure. Under these conditions, both the honed and un-honed designs have a similar C_d value, nevertheless, the un-honed design produces lower power on engine at high load than the honed design due to the flow efficiency decrease with increasing pressure.

The difference between the respective C_d behaviours of the honed and un-honed designs can be understood from the flow development along the injection hole length. The distribution of velocity projection along the injection hole axis, namely the axial velocity, over the cross-sections are shown in **Figure 13**. It is obvious from these images that there is significantly larger flow recirculation at the hole entry for the un-honed nozzle than for the honed nozzle. This indicates that the flow losses for the un-honed nozzle will be concentrated further towards the hole entry, where the fuel pressure is high and the density and viscosity are also high.

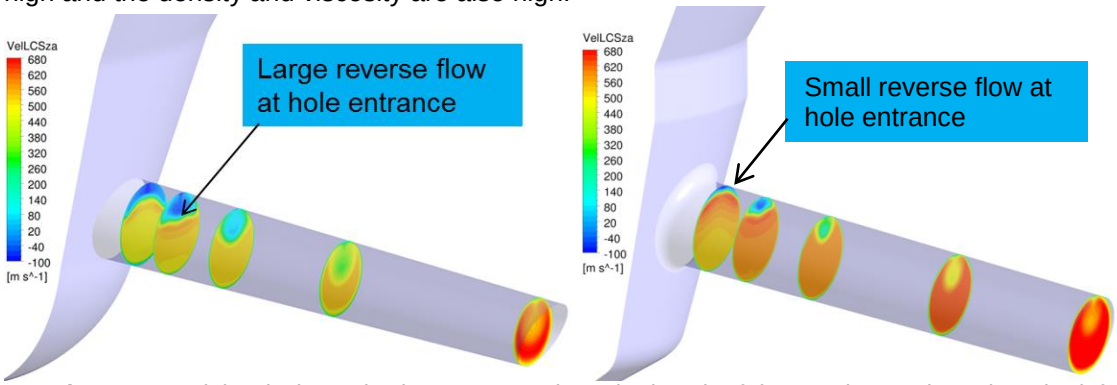

Figure 13: Axial Velocity projection contours along the length of the nozzle. Un-honed on the left, and Honed on the right.

Further analysis of the flow properties in particular the coefficient of area, C_a, (equation (19)) along the hole length **Figure 14** illustrates how the un-honed nozzle produces a larger separation zone at the hole entrance. It is noted that if the density is fixed for all pressures, the measured C_d trend for the un-honed nozzle cannot be reproduced by simulation. This indicates that the inertia loss rather than the viscous loss is responsible for the decrease of C_d observed. The higher the inlet densi-

ty, the more difficult it is for the flow to follow and to adapt to the sudden geometry change at the hole entrance.

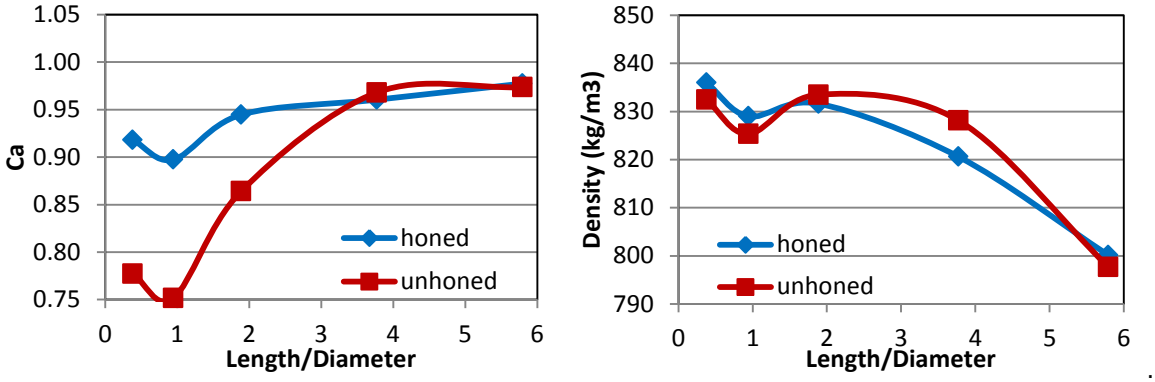

Figure 14: Variation of C_a and fuel density along the nozzle hole length for the nozzles in **Figure 13**. Rail pressure 1970bar; Backpressure 125bar; needle lift 300µm.

6.3 Spray Geometry and Momentum Investigation

The spray simulations were run under various rail pressures and backpressures to compare with the different experimental conditions of the two spray momentum rigs and the optical spray measurement chamber. In the test results presented in this paper, the optical rig was run at 60bar backpressure to mimic the real operating pressures on an engine, but both momentum rigs were run under atmospheric backpressure conditions. The purpose of the low pressure with the momentum rigs was to minimise the aerodynamic influence on the spray in order to better link measured spray momentum distribution to the nozzle orifice design and the nozzle flow.

MR1 produced the following (**Table 1**) of absolute characteristics of the nozzle flow in terms of the C_d, C_a and C_v at 100bar vs. atmospheric test conditions. The C_d values compare very well with the steady state flow rig results and simulation results. The C_a and C_v likewise also compare very well with the simulations run under the same pressure conditions. However, such conditions are not very representative of real engine operating conditions for diesel injectors, nevertheless, they allow for an initial validation of the performance of the flow models.

Table 1: Total spray force and total flow per hole at 100bar Rail Pressure and atmospheric backpressure. Force Sensor at 15mm, measurements over 1minute.

Nozzle Type	Test ref	C_d	C_a	C_v (Mom. Efficiency)
Un-honed (250um)	1222	81.5	94.2	86.5
Honed(250um)	1236	83.1	93.0	89.4
Un-honed (no needle)	1211	83.8	91.8	91.2
Honed (no needle)	1232	85.4	92.6	92.3

In contrast, MR2 gives a more realistic operating condition, closer to a real operating injector, but for comparison purposes, its data has been processed to only consider the spray force during the period of the injection corresponding to full needle lift. As 100bar rail pressure test condition is inappropriate for a real operating condition of an injector, different pressure conditions are applied. Two test cases are considered corresponding to a typical operating condition of an injector. These are a low pressure case of approximately 400bar and a high pressure case of approximately 1600bar rail pressure. For comparison purposes, it is useful to normalise the measured spray forces by dividing by the pressure. As the spray velocity is proportional to the square-root of the pressure and the force is proportional to the square of the velocity, the force should theoretically be linear with the pressure.

It can be seen immediately that the close correlation of the normalised spray force of MR1 and the CFD of the nozzle flow at the hole exit at low pressures. Both the simulation and the experimental measurements correspond to high needle lift conditions. Furthermore, the differences in normalized spray force between the honed and the un-honed injectors are very similar in measurement and simulation.

Next, the comparison of the spray simulation and the MR2 at low injection pressures, both the simulation and the experiment consider real operating conditions, with 1.5ms injection duration. The comparison is simplified by only considering the high needle lift portion of the spray. Consequently a

time averaged force is calculated by considering the region between 30% of the spray and 80% of the spray duration. The results for the momentum difference between the two designs are similar in measurement and in simulation, c.a. 8%, nevertheless, the predicted spray force is about 20% lower than in measurement for each case. The causes for the discrepancy can be due to the limited spatial resolution and calculation algorithm in the measurement and might also be caused by the spray models and are under investigation. Consequently it is proposed to focus mainly on the difference (predicted and measured) between the honed and the un-honed injectors. This of course has a high degree of correlation with very similar results. At low pressure, these differences are 7→9%. At high pressures, the momentum difference at the hole exit between honed and un-honed injectors increases from 5% to 17%. This increase is related to the C_d evolution. At high pressures a similar increase in the differences in the spray simulations and measurements is also recorded. These have increased from 7→9% to 11→13%. Such a close prediction of the effect of the geometry on the spray momentum is welcome.

Table 2: Comparison of simulation and measurements of nozzle flow and spray momentum. Low Nozzle ΔP uses 400bar Rail Pressure and High Nozzle Nozzle ΔP uses 1600bar Rail Pressure

			Honed	Unhoned	Honed/Unhoned-1	
	Nozzle ΔP	Distance from nozzle hole	Force / Δpressure		Force Difference	COMMENTS
	[bar]	[mm]	[N/100bar]	[N/100bar]	[%]	
Experiment - MR1	100	15	0.128	0.123	3.9%	Full Needle Lift
CFD Nozzle Hole Exit	Low	0	0.130	0.124	5.4%	Full Needle Lift
CFD Spray	Low	8	0.106	0.099	6.7%	Time Average (30-->80%)
Experiment - MR2	Low	8	0.117	0.107	8.8%	Time Average (30-->80%)
CFD Nozzle Hole Exit	High	0	0.149	0.127	17.3%	Full Needle Lift
CFD Spray	High	8	0.120	0.108	10.9%	Time Average (30-->80%)
Experiment - MR2	High	8	0.156	0.138	12.7%	Time Average (30-->80%)

In terms of the spray shape that is predicted, it is possible from a specific processing of the MR1 data to produce a profile of the spray force under full needle lift conditions. These are illustrated in **Figure 15**. It is obvious from these plots that the honed injector has a higher maximum force peak and a more concentrated spray profile. However the differences are small compared to the impact of needle lift or eccentricity on the spray shape.

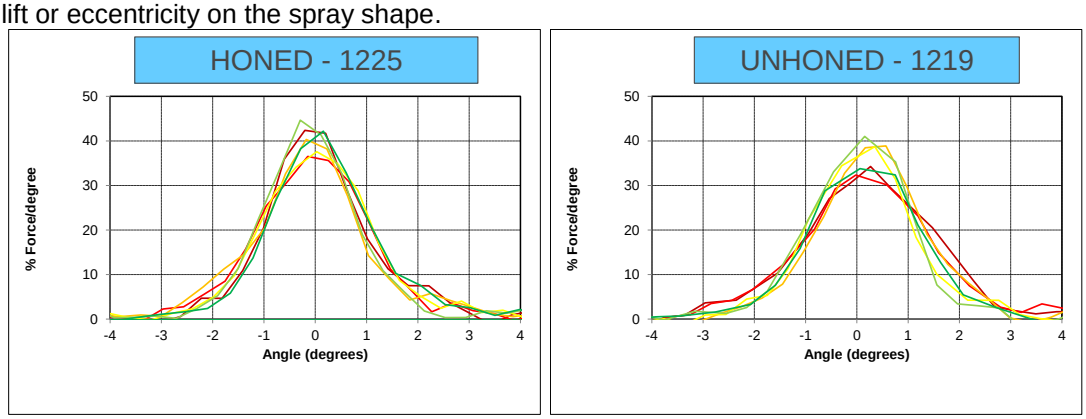

Figure 15: Spray profile measured at 100bar rail pressure and atmospheric backpressure, as the jet is moved off the target sensor. Each line represents a different nozzle hole from the same injector.

MR2 can also be used to measure a spray force profile through the spray but in 2 dimensions. **Figure 16** illustrates a comparison of the momentum rig spray force, the nozzle hole flow and the simulated spray force. Similar features in the flow are clear. Most important amongst these are the higher force peaks from the honed injector, at both low and high pressures and the narrower spread of the spray from the honed injector.

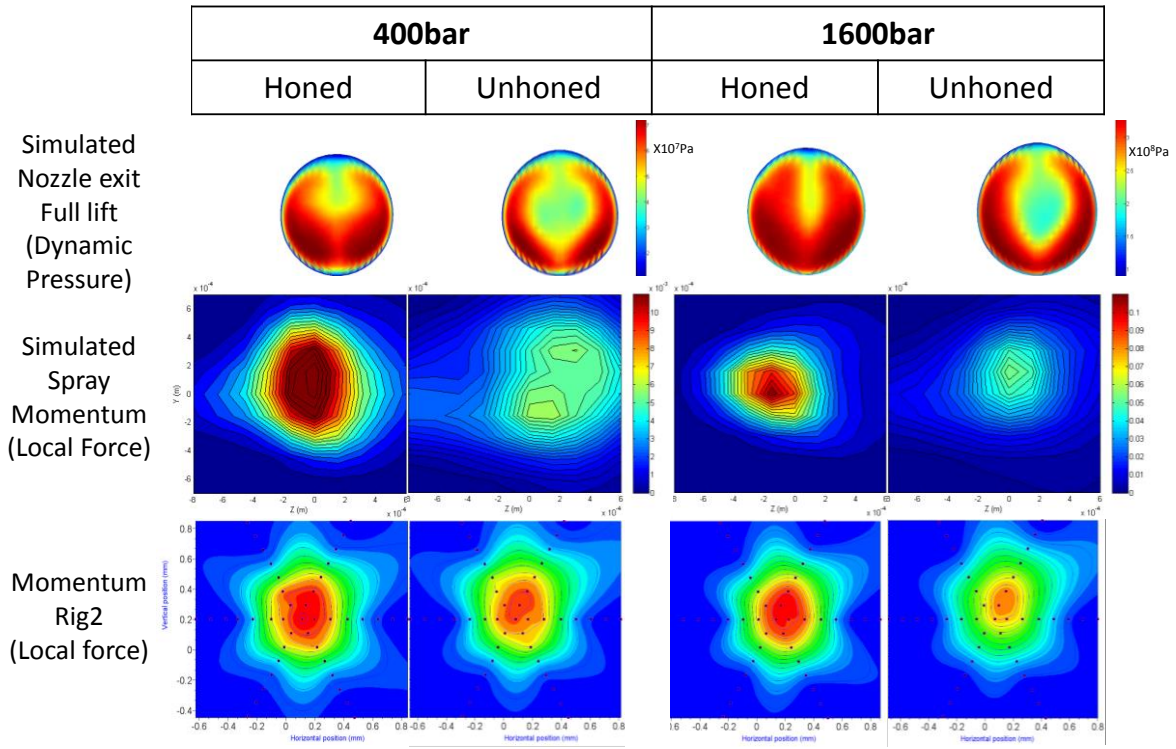

Figure 16: On the top, simulated nozzle dynamic force (density*velocity^2) at hole exit. In the middle, force distribution through the spray measured on MR2 at 8mm. on the bottom, simulated liquid spray momentum at 8mm. Note the different scales for low and high pressure. Narrower profile with higher peak is obvious for the honed injector.

The next step in the validation process, is to compare the simulated spray results under typical pressure conditions with spray visualisation data. In this case the backpressure in the spray chamber was raised to 60bar. Such an increase in backpressure has a very large impact on the spray penetration and the dispersion angle compared with an atmospheric backpressure condition. The comparison for the low pressure and high pressure case is presented in **Figure 17**.

As can be seen, a good prediction of the absolute spray penetration and of the difference between the honed and un-honed injectors is made. It is noted that the honed nozzle produces higher spray momentum and thus a slightly higher penetration under both high and low injection pressures. This difference follows from the C_d difference measured and simulated between the nozzles. The C_d difference is related to the C_v difference between the nozzles and should be related to the far field, fully developed spray penetration by a square root relationship as shown by (Naber & Siebers, 1996) and others. Whilst less well predicted in absolute terms, the dispersion angle trends are well reproduced. The main feature of interest here is at the start of injection, when operating at 400bar. Here the un-honed nozzle is also both measured and predicted to produce a larger spray dispersion angle. Whilst at high pressure and full lift conditions, there is very little difference between the injector's dispersion angles.

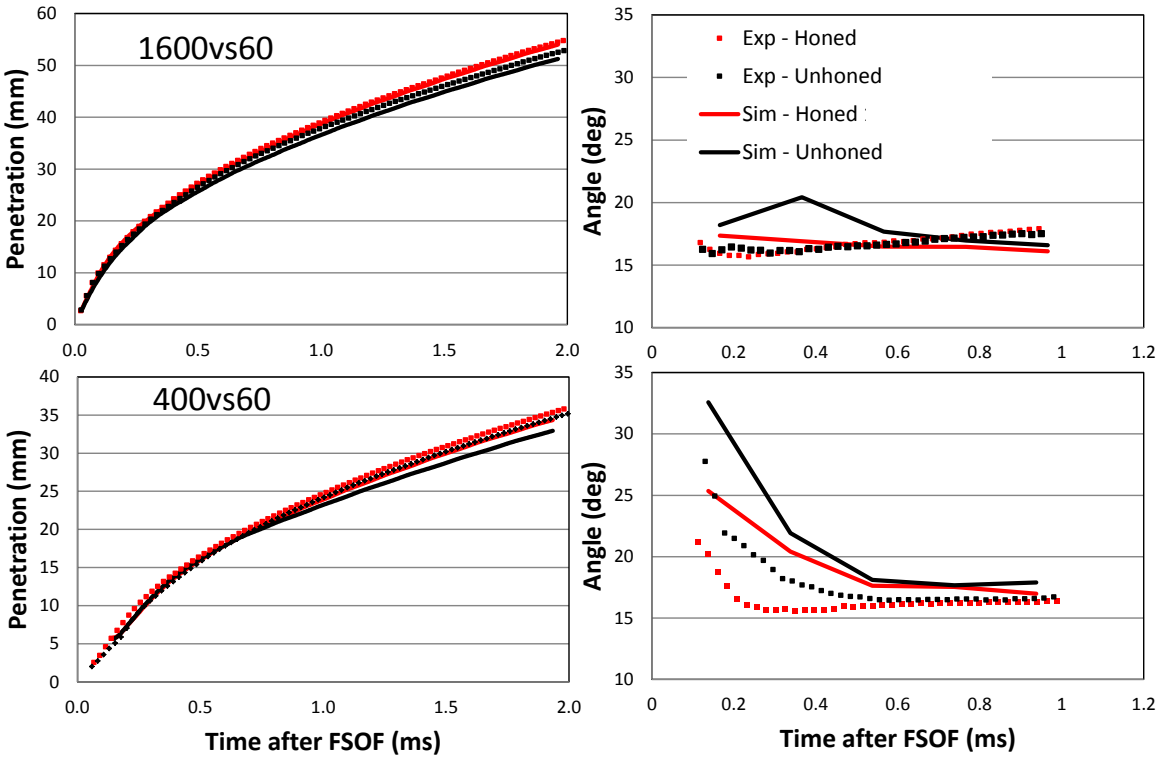

Figure 17: Comparison of liquid penetration measurements with modelled values.

In order to explain these phenomena, we can examine the atomisation energy, namely the non-axial kinetic energy and the turbulent energy at the nozzle hole exit from CFD. The turbulent kinetic energy at the 400bar case (Figure 18) and also the non-axial kinetic energy (not shown here) are much higher at low needle lifts. That might be the reason why the dispersion angle is larger at the start of injection. It can also be seen in Figure 18, that the un-honed nozzle has much higher turbulence at the start of injection, than the honed design also in line with its higher dispersion angle.

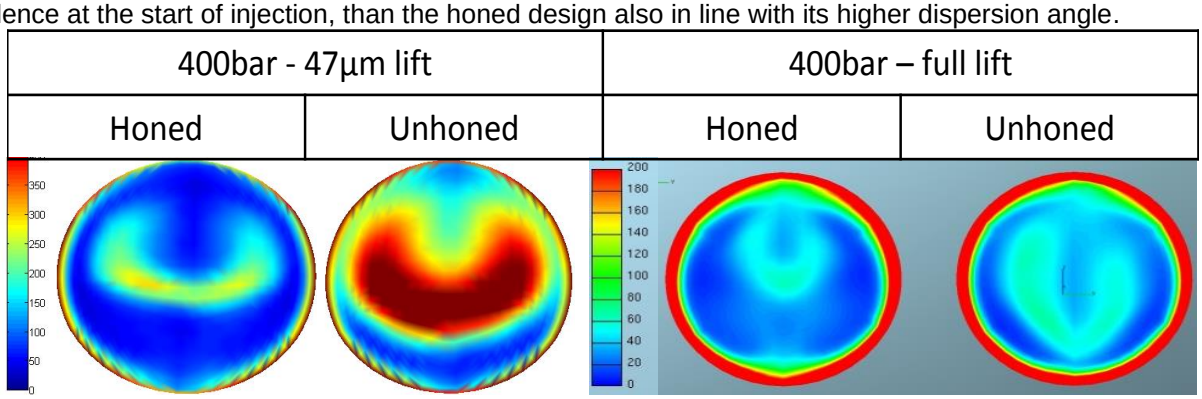

Figure 18: Turbulent Kinetic Energy at the nozzle hole exit. Rail Pressure 400bar; 47um lift, image on the left, and full lift on the right.

As mentioned, the spray investigation was performed in a high pressure static chamber with 60bar back pressure. Under these conditions, the aerodynamic effect is significant. For this reason, the fully developed spray geometry of both nozzle designs are not substantially different (**Figure 19**). Both for the developing and developed spray, the coupled simulation approach is able to capture these main spray features and the difference between both nozzle designs, both for near nozzle spray and for macroscopic spray geometry development.

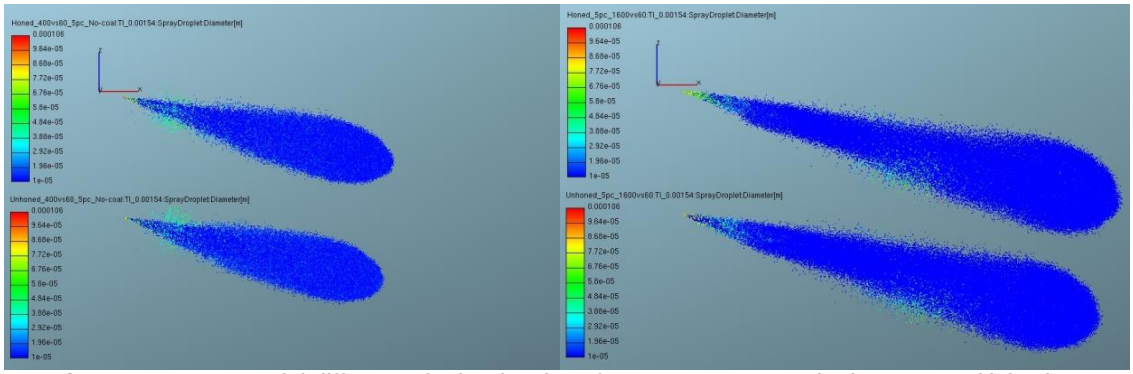

Figure 19: No essential difference in the developed spray geometry at the late stage of injection; 400bar vs. 60bar on the left; 1600bar vs. 60bar on the right

7. Conclusions

The work presented shows numerical and experimental investigations on the effect of injection hole geometry on flow and spray behaviour under various operating pressures and temperature conditions. Focus has been given to modelling the fuel property model and the complex thermal hydraulic linked to the strong depressurisation occurring inside the injection nozzle and to a coupled simulation approach for nozzle flow and spray simulation in order to link the nozzle design and nozzle flow to the spray behaviour. Various new measurement techniques including a high pressure nozzle flow rig, a high pressure spray momentum rig, and optical spray visualisation were applied to validate the spray performance and simulations, in order to reach a complete understanding of the flow phenomena. Based on the combination of the simulation and experimental data the following conclusion can be obtained:

- Based on the fuel property at back pressure and rail temperature, the discharge coefficient of the honed nozzle increases with increasing pressure, while the flow efficiency of the higher taper un-honed nozzle falls with increasing pressure. Starting with the same C_d at 100bar pressure, the low taper honed nozzle can have 7% higher flow delivery than the higher taper un-honed nozzle at 2000bar pressure, even if they have the same specification at 100bar (C_d, flow, exit hole). This is expected to have an impact on the spray behaviour and engine performance.

- The CFD simulation using the complex thermal hydraulic model, which takes into account the full energy equation including pressure work and viscous heating and fuel property dependence on the local pressure and temperature, is capable of capturing the honing effect on the flow efficiency.

- The trend that C_d falls with increasing pressure for the higher taper un-honed nozzle is mainly due to the throttling effect caused by inertia effect at the hole entry. With increasing pressure, the fuel density and viscosity increase, which happens more rapidly than the increase in the velocity, and leads to a lower effective Reynolds number. If the fuel property is not treated as a function of local pressure and temperature, the C_d behaviour cannot be captured by simulation for the un-honed nozzle.

- The low taper honed nozzle produces higher momentum and higher penetration corresponding to the percentage of the flow efficiency advantages against the un-honed design. In addition, the honed design produces a more compact spray momentum than the un-honed one.

- The developed spray geometry at high chamber pressure is similar for both designs, while the un-honed nozzle produces higher spray dispersion at the start of injection. The CFD results indicate that the un-honed nozzle produces much higher turbulent kinetic energy than the honed one. At high needle lifts the turbulent kinetic energy difference is much less significant.

- The explicit coupled simulation approach in combination with the Blob primary breakup model developed by AVL, is capable of capturing the inlet honing effect on the spray in terms of spray momentum distribution and in terms of spray geometry. This applies both

for fine differences in the developed spray penetration length and for the significant differences in the dispersion angle at the start of injection.

References

Andriotis, A. & Gavaises, M., 2009. Influence on Vortex Flow and Cavitation on Near-Nozzle Diesel Spray Dispersion Angle. *Atomization and Sprays,* Volume 19, pp. 247-261.

AVL, 2013. *AVL FIRE User Document, Lagrangian multiphase module,* Graz: AVL.

Baumgarten, C. & Merker, G., 2004. Fundamental Investigation on the influence of cavitation on Primary break-up of high Pressure liquid Jets. *Proc. of the DFG Research Program "Atomization and Spray Processes", Schriftenreihe Mechanische Verfahrenstechnik,* 3(1).

Blaisot, J. et al., 2012. *NADIA_bio : New advanced diagnosis dor Diesel injection analysis and bio fuels.* Rouen, SIA.

Bode, B., 1990. Verfahren zur Extrapolation wichtiger Stoffeigenschaften von Fluesigkeiten unter hohem Druck. *Tribo-logie und Schmierungstechnik,* Volume 37, pp. 197-202.

Dittakavi, N., Chunekar, A. & Frankel, S., 2010. Large Eddy Simulation of Turbulent-Cavitation Interactions in a Venturi Nozzle. *Journal of Fluid Engineering,* 132(12).

Dober, G., Karimi, K. & Guerrassi, N., 2012. *Mixture Preparation and Combustion Analysis, a Key Activity for Future Trends in Diesel Fuel Injection Equipment.* Rouen, SIA.

Dukowicz, J., 1993. *Quasi-steady droplet change in the presence of convection,* Los Almos: Los Almos National Scientific Laboratory.

Dumouschel, C., C. J. & Triballier, K., 2005. Experimental Analysis of a Liquid Atomization Process at Low Weber Number. *Experiments in Fluids,* 39(4), pp. 651-666.

ExxonMobil, 2012. *The Outlook for Energy: A View to 2040,* s.l.: ExxonMobil.

Giannadakis, E. et al., 2007. Evaluation of the predictive capability of diesel nozzle cavitation models. *SAE Technical Paper Series,* Volume SAE2007-01-0245.

Gosman, A. & Ioannides, E., 1983. Aspects of Computer Simulation of Liquid-Fueled Combustors. *Journal of Energy,* 7(6), pp. 482-490.

Greeves, G. et al., 2008. *Nozzle momentum efficiency definition, measurement and importance for diesel combustion.* Como Lake, ILASS.

IAV GmbH, 2008. *Injection Analyzer - Instrument for Simultaneously Measuring Injection Rate and Injected Fuel Quantity for Use in Diesel and Gasoline Direct-Injection Systems,* Gifforn: Ingenieurgesellschaft Auto Verkehr GmbH.

Im, K. et al., 2013. Unraveling the Geometry Dependence of In-Nozzle Cavitation in High-Pressure Injectors. *Nature Scientific Report,* Volume 3, p. 2067.

Kolev, N., 2002. *Multiphase flow dynamics.* Berlin Heidelberg: Springer Verlag.

Liu, A. & Reitz, R., 1993. Modeling the Effects of Drop Drag and Break-up on Fuel Sprays. *SAE Technical Paper Series,* Volume SAE930072.

LMS Imagine, 2011. *HYD Robert Bosch fuel property, Tech. Bulletin No. 118,* s.l.: LMS Imagine.Lab AMESim.

Naber, J. & Siebers, D., 1996. Effects of Gas Density and Vaporization on Penetration and Dispersion of Diesel Sprays. *Transactions of the SAE,* Volume SAE960034.

Ning, W. & Reitz, R., 2008. A Numerical investigation of nozzle geometry and injection condition effects on Diesel fuel Injector flow physics. *SAE CRC Technical Paper Series,* Volume SAE2008-01-936.

O'Rourke, P., 1989. Statistical Properties and Numerical Implementation of a Model for Droplet Dispersion in Turbulent Gas. *Journal of Computational Physics,* 83(2), pp. 345-360.

Payri, F., Bermudez, V., Payri, R. & Salvador, F., 2004. The influence of cavitation on the internal flow and the spray characteristics in diesel injection nozzles. *Fuel,* 83(4), pp. 419-431.

Postrioti, L., Battistoni, M., Ungaro, C. & Mariani, A., 2011. Analysis of Diesel Spray Momentum Flux Spatial. *SAE Technical Paper Series,* Volume SAE2011-01-0682.

Reid, B., Hargrave, G., Garner, C. & Wigley, G., 2010. An investigation of string cavitation in a true-scale fuel injector flow geometry at high pressure. *Physics of Fluids,* 22(3).

Roth, H., Gavaises, M. & Arcoumanis, C., 2002. Cavitation Initiation, Its Development and Link with Flow Turbulence in Diesel Injector Nozzles. *SAE CRC Technical Paper Series,* Volume SAE2002-01-0214.

Schmidt, J., 1999. *Einfluss der Thermodynamik auf das Betriebsspiel von Diesel-Einspritzpumpenelemneten, PhD thesis ,* Stuttgart: Universitaet Stuttgart.

Shi, J. & Arafin, M., 2010. *CFD investigation of fuel property effect on cavitating flow in generic nozzle geometries.* Brno, ILASS.

Shi, J. et al., 2004. Heating effect on steady and unsteady horizontal laminar flow of air past a circular cylinder. *Physics of Fluids,* Volume 16, p. 4331 – 4345.
Shi, J. et al., 2010. *URANS and SAS analysis of flow dynamics inside a DISI injection nozzle.* Borno, ILASS-Europe.
Soriano Palao, O. & Mouvanal, S., 2011. Numerical Study of the Effect of Conicity and Inlet Rounding of Diesel Injector Nozzles and its Influence on Spray Characteristics. *SAE Technical Paper Series,* Volume SAE2011-28-0120.
Soteriou, C., Lambert, M., Zuelch, S. & Passerel, D., 2006. *The flow characteristics of high efficiency Diesel nozzles with enhanced geometry holes.* Valencia, Thiesel Int. Conf. on Thermo- and Fluid Dynamic Processes in Diesel Engines.
Sou, A., Pratama, R., Tomisaka, T. & Kibayashi, Y., 2012. *Cavitation Flow in Nozzle of Liquid Injector.* Heidelberg, ILASS.
Theodorakakos, A., 2012. *Simulation of heating effects caused by extreme fuel pressurization in cavitating flows through Diesel fuel injectors.* Singapore, CAV2012.
von Kuensberg Sarre, C., Kong, S. & Reitz, R., 1999. Modeling the Effects of Injector Nozzle Geometry on Diesel Spray. *SAE CRC Technical Paper Series,* Volume SAE1999-01-0912.
Zigan, L. et al., 2013. Fuel property and fuel temperature effects on internal nozzle flow, atomization and cyclic spray fluctuations of a direct injection spark ignition-injector. *International Journal of Engine Research,* 12(4), pp. 543-556.

CFD modelling of combustion in Heavy-Duty Diesel Engines

G. D'Errico[1], T. Lucchini[1], A. Onorati[1], G. Hardy[2]

[1]Department of Energy. Politecnico di Milano. Via Lambruschini 4, 20156 Milano, Italy.
[2]FPT Motorenforschung AG. Schlossgasse 2, Postfach 80, 9320 Arbon, Switzerland.

E-mail: gianluca.derrico@polimi.it
Telephone: +(39)0223998613
Fax: +(39)0223998050

Abstract. The design and optimization stages of combustion systems for modern Heavy Duty Diesel engines must be supported by reliable CFD tools for the definition of the chamber geometry and injection strategy. To be fully predictive in terms of in-cylinder thermodynamics and flame structure, the employed combustion models must account for complex chemistry and turbulence-kinetics interactions. Within this context, the authors have implemented into an open-source code a model based on the multiple Representative Interactive Flamelets approach (*mRIF*) and applied it to Diesel combustion simulations. New numerical techniques were integrated in the proposed *mRIF* model in order to speed up the CPU time in integrating chemistry and the β-pdf of the chemical species to compute composition in the CFD domain. A parallel validation was performed both with constant-volume and Heavy-Duty Diesel Engine experiments, selecting similar operating conditions. In such way, both flame structure and heat release rate predictions are analyzed and the model capabilities with respect to its set-up and mesh structure are assessed.

1. Introduction

Development of heavy duty Diesel engines is strongly affected by more and more demanding requirements for a contemporary reduction of both fuel consumption and pollutant emissions. To fulfill such objectives, a combination and integration of different technologies is necessary: efficient combustion systems, engine downsizing, new after-treatment devices and heat recovery [7, 8, 11, 19]. In particular, fuel-air mixing and combustion processes must be investigated and optimized in detail since they both affect the quality of exhaust gases and energy conversion efficiency. Within this context, promising solutions appear to be the use of very high injection pressures (up to 3000 bar), further increase of full-load bmep, extension of engine operating range with advanced combustion modes and dual fuel combustion. However, Diesel combustion is a very complex process involving many interacting physical phenomena including evolution of multi-phase flows, hydrocarbon auto-ignition and diffusion flame propagation in a inhomogeneous, turbulent high-pressure flow [4]. To this end, both advanced numerical and experimental tools are necessary for a detailed study of the combustion process. For what concerns numerical approaches, nowadays research is focused on the development of models based on complex chemistry and including turbulence-kinetics interactions for a proper prediction of auto-ignition, flame structure evolution, soot and NO_x emissions formation.

Most of the models which are used for combustion simulations with detailed chemistry are based on flame structure assumptions (equivalent stretched diffusion flame, partially-stirred reactor, homogeneous reactor, ...) and compute chemical composition or reaction rate in each computational cell accordingly [9, 24]. Among the available approaches, both Representative Interactive Flamelets (RIF) and zero-dimensional Conditional Moment Closure (CMC) operate a coordinate transformation that makes possible to solve the diffusion-reaction problem in the mixture fraction space, that is considered to be the predominant variable in non-premixed combustion problems [2, 27]. The effects of local flow are incorporated in the scalar dissipation rate variable and chemical composition is estimated by assuming a presumed statistical distribution of each chemical species that depends on mixture fraction and its variance. Since most of the development efforts for Heavy Duty Diesel Engine Combustion are focused to full-load conditions (where a large amount of fuel is injected at very high pressures), both heat transfer and flame-wall interaction processes need also to be properly taken into account.

This work presents a methodology for combustion and pollutant emissions prediction in Heavy-Duty Diesel engines, based on the application of a Multiple Representative Interactive flamelet model (*mRIF*) which was successfully applied in past works [5, 6] for simulations at constant-volume conditions. The *mRIF* model approximates the flame structure as a set of multiple unsteady laminar diffusion flames (*flamelets*) and their evolution is computed in the mixture fraction space [2] where species and energy equations are solved. The effects of mixing are incorporated in the scalar dissipation rate, which is calculated as a conditional average of its distribution in the CFD domain. The use of multiple flamelets ensures a better prediction of both flame structure and auto-ignition, since spatial variations of the scalar dissipation rate are properly taken into account [2, 12]. The *mRIF* model allows realistic simulations of Diesel with detailed chemistry, but incorporating large mechanisms in it (more than 50 species) drastically increases the computational time. In particular, the need to integrate the PDF for any chemical species in all the cells of the CFD domain introduces significant computational overheads. To this end, in this work two new techniques were developed to reduce the CPU time when the *mRIF* model is applied to IC engine combustion simulations. The first one is represented by the so-called *virtual species* approach, where a limited set of chemical species is used in the CFD domain to represent the entire set of the flamelet species. In this way, the PDF is integrated for a very limited number of chemical species but it is possible to adopt very large mechanisms. To further reduce the computational time, the PDF integration in the mixture fraction space is performed for clusters of cells having similar values of mixture fraction and variance. Finally, the TDAC algorithm was integrated into the *mRIF* model, ensuring a significant reduction of CPU time when detailed chemistry is used, since it combines on-line techniques for reduction of chemical mechanism and reaction rates tabulation [3]. In this way, the ODE solver operates only on a limited number of computational cells for each time-step, with a reduced set of species and reactions.

The proposed approaches for combustion modeling were implemented in the Lib-ICE code, where the *mRIF* model was recently developed and validated [5, 6]. Lib-ICE is based on the OpenFOAM technology (`www.openfoam.org`) and includes a set of well validated spray sub-models to properly describe fuel atomization, secondary breakup and evaporation [15, 17]. Validation was performed into different steps. First, a set of operating conditions which are critical in terms of fuel consumption and emissions for a heavy duty diesel engine were identified. Then, the methodology was assessed at constant-volume conditions, simulating reacting and non-reacting cases with ambient temperature and pressure which are similar to those found at start of injection time in the studied engine. Computed data of ignition delay and flame lift-off were compared with experimental ones and the flame structure was analyzed to understand the capabilities of the model to properly describe propagation and stabilization of a turbulent diffusion flame. Finally, engine simulations were carried out for the three selected operating points. Validation at engine conditions was performed by comparing computed and experimental data of in-cylinder pressure, and heat-release rate.

2. Computational models

2.1. Multiple representative interactive flamelets (MRIF)

This model is based on the laminar flamelet concept, assuming that the smallest turbulent time and length scales are much larger than the chemical ones and there exists a locally undisturbed sheet where reactions occur [2]. This sheet can be treated as an ensemble of stretched counter-flow diffusion flames, called *flamelets*. The advantage of such treatment is that all reacting scalars only depend on the mixture fraction variable, Z, which is related to the local fuel-to-air ratio for non-premixed combustion. Hence, local chemical composition can be estimated from the Z field in the CFD domain, assuming that its sub-grid distribution can be represented by a β-pdf. To this end, transport equations for both Z and its variance $\widetilde{Z''^2}$ need to be solved:

$$\frac{\partial \rho \tilde{Z}}{\partial t} + \nabla \left(\rho \mathbf{U} Z \right) - \nabla \cdot \left(\frac{\mu_t}{Sc_Z} \nabla \tilde{Z} \right) = \dot{S} \tag{1}$$

$$\frac{\partial \rho \widetilde{Z''^2}}{\partial t} + \nabla \left(\rho \mathbf{U} \widetilde{Z''^2} \right) - \nabla \cdot \left(\frac{\mu_t}{Sc_{\widetilde{Z''^2}}} \nabla \widetilde{Z''^2} \right) = 2 \frac{\mu_t}{Sc_{\widetilde{Z''^2}}} \left| \nabla Z \right|^2 - \rho \chi$$

The sink term appearing in Eq. 2 is the average scalar dissipation rate, which is function of the turbulent time scale and mixture fraction variance:

$$\chi = C_\chi \frac{\varepsilon}{k} \widetilde{Z''^2} \tag{2}$$

where the constant C_χ was set to 2 in this work. In order to properly account for local flow and turbulence effects on the flame structure and predict flame stabilization, a multiple number of flamelets was used. Each one is representative of a certain portion of the injected fuel mass, and chemical composition in each cell is computed from mixture fraction and flamelet marker distribution as follows:

$$Y_i(\vec{x}) = \sum_{j=1}^{N_f} M_j \int_0^1 Y_{j,i}(Z)\, P\left(Z, \widetilde{Z''^2}\right) dZ \tag{3}$$

For each flamelet marker, the following transport equation is solved:

$$\frac{\partial \rho \tilde{M}_j}{\partial t} + \nabla\left(\rho \mathbf{U} \tilde{M}_j\right) - \nabla \cdot \left(\frac{\mu_t}{Sc_Z} \nabla \tilde{M}_j\right) = \dot{S}_{M_j} \tag{4}$$

where the source term $\dot{S}_{M_j}$ corresponds to $\dot{S}$ only for a specified interval of the injection duration, while it is zero elsewhere. Flamelet markers must also satisfy the following relation:

$$Z = \sum_{j=1}^{N_f} M_j \tag{5}$$

The local flame structure is defined by the flamelet equations that are solved assuming unity Lewis number [2] in the mixture fraction space:

$$\rho \frac{\partial Y_i}{\partial t} = \rho \frac{\chi_z}{2} \frac{\partial^2 Y_i}{\partial Z^2} + \dot{\omega}_i \tag{6}$$

$$\rho \frac{\partial h_s}{\partial t} = \rho \frac{\chi_z}{2} \frac{\partial^2 h_s}{\partial Z^2} + \dot{q}_s \tag{7}$$

where Y_i is the mass fraction of the species i, ρ is the density, Z the mixture fraction, $\dot{\omega}_i$ is the chemical source term of species i, h_s the sensible enthalpy and $\dot{q}_s$ the heat released by the chemical reactions. Eqns. 6 - 7 are solved on a 1-D mesh with the finite volume method, by employing an ODE stiff solver to properly compute $\dot{\omega}_i$. Effects of mixing related to turbulence and flow-field are grouped into the scalar dissipation rate term χ_z expressed as:

$$\chi_z = \widehat{\chi_{st,j}} \frac{f(Z)}{f(Z_{st})} \tag{8}$$

$f(Z)$ has an erfc-profile [21], while scalar dissipation rate at stoichiometric mixture fraction conditions $\widehat{\chi_{st,i}}$ for each flamelet is computed as an average of the local values in each computational cell:

$$\widehat{\chi_{st,j}} = \frac{\int_V M_j \chi_{st,l}^{3/2} \rho \tilde{P}(Z_{st})\, dV'}{\int_V M_j \chi_{st,l}^{1/2} \rho \tilde{P}(Z_{st})\, dV'} \tag{9}$$

where P is a β-function, whose parameters depend on mixture fraction and its variance. In each cell $\chi_{st,l}$ is computed following the Hellstrom formulation [2]:

$$\chi_{st,l} = \frac{\chi}{\int_0^1 \frac{f(Z)}{f(Z_{st})} \tilde{P}(Z)\, dZ} \tag{10}$$

Fig. 1 summarizes the operation of the *mRIF* combustion model, illustrating the mutual interactions between the CFD and flamelets domains. At each time-step, average stoichiometric scalar dissipation rate values are passed to each flamelet, that solves Eqn. 6-7 accordingly. The chemical composition in the CFD domain is computed from the mixture fraction, its variance and the flamelet marker distribution. Temperature is updated from new chemical composition and total enthalpy, whose variation is only due to flow and spray evaporation. For further information, the reader is referred to [12].

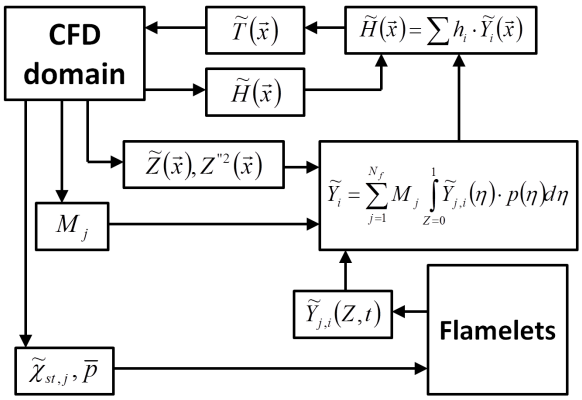

Figure 1: Operation of *mRIF* model: interaction between flamelets and CFD domain

2.2. Reduction of computational time

One of the advantages of the *mRIF* model compared to other ones based on detailed chemistry is represented by the fact that the reaction-diffusion problem is solved in the mixture fraction space, which is approximated as a one-dimensional grid with a limited number of points (100-200). This drastically reduces the CPU time required for chemistry integration and makes possible to use large mechanisms (more than 100 species) with a better prediction of both combustion and pollutant emissions. However, mechanisms with many species introduce very high computational overheads since:

1. When increasing the number of flamelets, the time spent in chemistry integration for all of them becomes very high and, again, limits the maximum number of species that can be used;

2. Integration of the PDF of the chemical species to compute composition in the computational domain, according to Eq. 3, requires a significant amount of time. Being N_c the number of cells in the CFD mesh, N_z the number of points in the mixture fraction domain, N_f the total number of flamelets and N_s the chemical species in the mechanism, the number of operations needed is approximately $N_c \times N_z \times N_f \times N_s$ which is of the order of 10^{10} in case of $N_c = 3 \cdot 10^4$, $N_z = 200$, $N_f = 50$ and $N_s = 100$.

To reduce the CPU time required by the *mRIF* combustion model and make it suitable for practical calculations efforts were focused towards the development of efficient solutions both for integration of the β-pdf and to handle detailed chemistry in the flamelet domain. For what concerns point 1, the TDAC algorithm was employed to drastically reduce the CPU time required by the ODE stiff solver to compute reaction rates for each chemical species. To address point 2, two new approaches were developed named *virtual species* and *cell clustering*, respectively.

2.2.1. Tabulation of dynamic adaptive chemistry (TDAC)

When detailed chemistry is incorporated in combustion models, it is necessary to consider that chemical time-scales are much smaller (2-4 orders of magnitude) than the CFD time-step which is generally used $(10^{-7} - 10^{-5})$. For this reason, ODE stiff solvers need to be employed to properly compute the chemical species reaction rates that are used in the chemical species transport equations, as shown in Eqns. 6. However, operation of ODE solvers significantly increase the computational time since it involves sub-cycling and computations of large jacobians. Hence, the sizes of mechanisms employed in practical simulations are generally limited to 50 species and 100 reactions [14, 20] with a consequent lack in terms of accuracy mainly when advanced combustion modes, high EGR conditions and soot formation processes need to be computed. To make the use of more detailed mechanisms possible (up to 150 species for Diesel combustion) in a reasonable amount of time, the TDAC algorithm [3] was employed in this work that combines the ISAT and DAC techniques [13, 25].

The ISAT algorithm intends to reuse computationally demanding results, e.g. the integration of large and stiff ODE systems, by storing those results and all the necessary data to retrieve them. During

computation, given a query point, ψ^q, it computes a linear approximation of the mapping:

$$\mathbf{R}(\psi^q) \approx \mathbf{R}^l(\psi^q) = \mathbf{R}(\psi^0) + \delta\mathbf{R}^l \ , \tag{11}$$

where $\delta\mathbf{R}^l = \mathbf{A}(\psi^0)(\psi^q - \psi^0)$ and $\mathbf{A}$ is the mapping gradient matrix defined by

$$A_{ij}(\psi^0) = \frac{\partial R_i(\psi^0)}{\partial \psi_j} \ . \tag{12}$$

The linear approximation defined by equation (11) is valid in the region of accuracy (ROA) where the following condition is respected:

$$|\mathbf{R}(\psi^q) - \mathbf{R}^l(\psi^q)| = |\delta\mathbf{R} - \delta\mathbf{R}^l| \leq \varepsilon_{\mathrm{ISAT}} \ , \tag{13}$$

where $\varepsilon_{\mathrm{ISAT}}$ is a user-specified tolerance and $\delta\mathbf{R} = \mathbf{R}(\psi^q) - \mathbf{R}(\psi^0)$. During the calculation, the table is built up according to the received queries. It consists of a binary tree with leafs and nodes. The leafs store ψ, $\mathbf{R}(\psi)$, $\mathbf{A}(\psi)$ and the ROA description. The nodes contain the rules that allow to scan the binary tree to retrieve the appropriate point [25].

The DAC method computes reduced mechanisms that are valid for the local thermo-chemical conditions. In this work, DAC has been extended to full CFD meshes with wall heat transfer. The reduction algorithm is executed before every call to the stiff solver according to the directed relation graph (DRG) method, which identifies the relevant species and reactions according to the thermodynamic conditions in each cell [13].

The coupling of ISAT and DAC performed in this work is schematically illustrated in Figure 2. When ISAT receives a query ψ^q that needs to integrate the ODE set, it provides ψ^q to the DAC algorithm which then finds the reduced mechanism for the local thermo-chemical conditions and provides the reduced set of active species ψ_a^q to the ODE solver. This solver computes the reaction mapping for the reduced set R(ψ_a^q) that is used by ISAT to build the reaction mapping R(ψ^q) in the full composition space. Using simplification methods at distinct levels combines their effects and allows a significant reduction of the computational cost. The use of TDAC ensures speed-up factors ranging from 10 to 1000 depending on the mechanism size and simulated combustion mode [3].

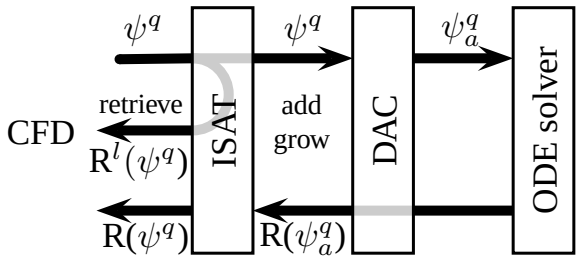

Figure 2: TDAC: combination of ISAT and DAC

2.2.2. The virtual species approach

To properly employ detailed chemistry for the *mRIF* combustion model but, at the same time, avoid accounting in the geometry domain for all the species included in the chemical mechanism, the *virtual species* approach was developed in this work. A reduced set of chemical species $Y_{v,i}(\mathbf{x})$ is considered in the CFD mesh and composition of $Y_{v,i}(Z)$ in the mixture fraction space is computed to consistently preserve both mass and thermodynamic properties of the entire set of chemical species used in each flamelet. In this way, the β-pdf is integrated only for $Y_{v,i}$ in a limited amount of CPU time. In particular, seven chemical species were used in this work (N_2, O_2, $fuel$, CO_2, CO, H_2O, H_2) and their composition in the mixture fraction space $Y_{v,i}(Z)$ is computed for any flamelet j as follows:

- For very rich mixtures ($\phi > 4$), where six virtual species are considered (N_2, $fuel$, CO_2, CO, H_2O, H_2):

$$\sigma_H\left(Z\right)_j = \sum_{i=1}^{N_s} N_{H,i} \cdot x_i\left(Z\right)_j = \sum_{k=1}^{N_v} N_{H,k} \cdot x_{v,i}\left(Z\right)_j \tag{14}$$

$$\sigma_C\left(Z\right)_j = \sum_{i=1}^{N_s} N_{C,i} \cdot x_i\left(Z\right)_j = \sum_{k=1}^{N_v} N_{C,k} \cdot x_{v,i}\left(Z\right)_j \tag{15}$$

$$\sigma_O\left(Z\right)_j = \sum_{i=1}^{N_s} N_{O,i} \cdot x_i\left(Z\right)_j = \sum_{k=1}^{N_v} N_{C,k} \cdot x_{v,i}\left(Z\right)_j \tag{16}$$

$$\sigma_N\left(Z\right)_j = \sum_{i=1}^{N_s} N_{N,i} \cdot x_i\left(Z\right)_j = \sum_{k=1}^{N_v} N_{N,k} \cdot x_{v,i}\left(Z\right)_j \tag{17}$$

$$h\left(Z\right)_j = \sum_{i=1}^{N_s} Y_i\left(Z\right)_j h_i\left(T\big(Z\big)_j\right) = \sum_{k=1}^{N_v} Y_{i,v}\big(Z\big) h_i\big(T\left(Z\right)\big) \tag{18}$$

- In case of lean, stoichiometric or rich mixtures ($\phi \leq 4$), seven virtual species are taken into account (O_2 is added to the set) and an additional equation is solved to preserve also the mass specific heat:

$$c_p\left(Z\right)_j = \sum_{i=1}^{N_s} Y_i\left(Z\right)_j c_{p,i}\big(T\left(Z\right)_j\big) = \sum_{k=1}^{N_v} Y_{i,v}\left(Z\right)_j c_{p,k}\big(T\left(Z\right)_j\big) \tag{19}$$

In Eqns. 14-19, σ is the total number of elements (C, H, O and N) in each flamelet for a mixture fraction value Z; N_s is the total number of species in the flamelet domain; N_v is the total number of virtual species (six or seven); N is the total number of elements (C, H, O and N) in each chemical species; x refers to mole fractions; Y refers to mass fractions; h is the mass specific enthalpy (sensible + formation); c_p is the mass specific heat.

2.2.3. Cell clustering for β-pdf integration

The *virtual species* approach reduces the number of chemical species for which integration of the β-pdf is necessary. However, such step still remains time-consuming when many flamelets (> 20) and fine meshes (30000 - 100000 cells) are used as it happens in engine simulations. Furthermore, due to the axy-symmetrical nature of the Diesel spray, it is expected that many cells will have very similar values of both mixture fraction and variance. For this reason, using the same chemical composition computed from the flamelet domain for groups of cells with similar Z and $\widetilde{Z''^2}$ is expected to save a large amount of time without compromising the accuracy of the computed results. Such approach was followed in this work: cells are grouped into Z-$\widetilde{Z''^2}$ zones according to user-specified parameters, then the β-pdf integration is performed for each zone and computed chemical composition is mapped back from zones to the corresponding CFD cells. At each time-step, cells are clustered into zones according to:

- Minimum and maximum values of mixture fraction and variance in the CFD domain;
- Discretization parameters for the creation of the Z-Z''^2 space, specified by the user.

A schematic of the cell clustering algorithm developed for the β-PDF integration is illustrated in Fig. 3.

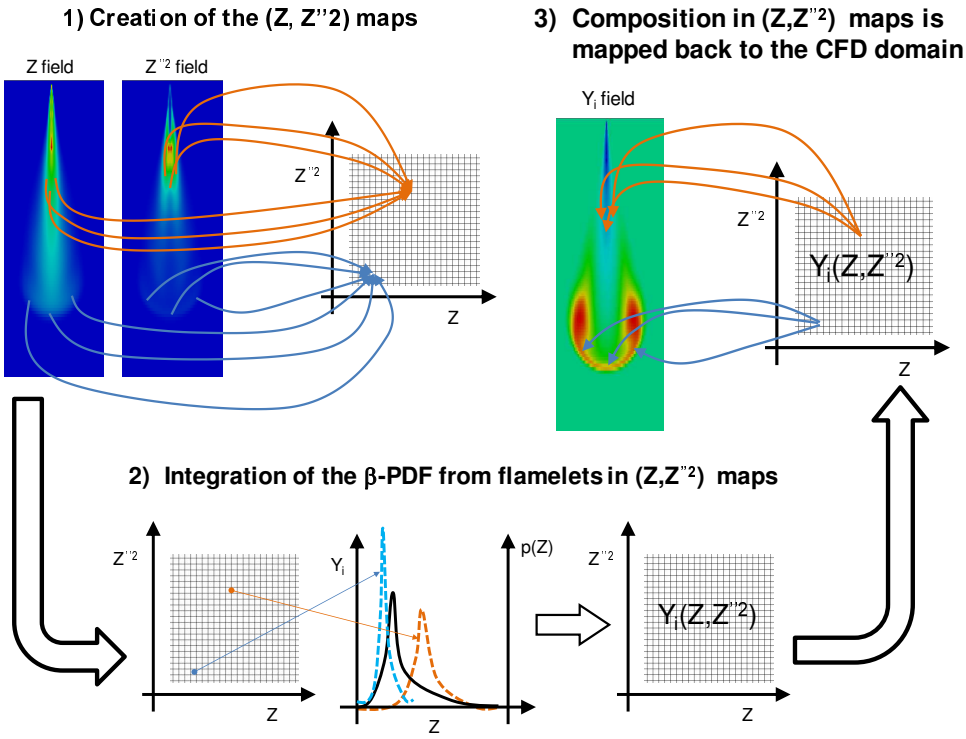

Figure 3: Cell clustering algorithm developed for the β-PDF integration. Step 1: Creation of the Z-Z''^2 according to user specified parameters; Step 2: Integration of the β-PDF from flamelets in the Z-Z''^2 maps; Step 3: Composition in Z-Z''^2 maps mapped back to the CFD domain.

3. Experimental validation

3.1. Heavy Duty engine data

Experiments carried out for a heavy-duty, Euro 6 Diesel engine were used to validate the proposed approach for combustion modeling. The main engine data are summarized in Table 1. The Common-Rail injection system operates at a maximum pressure of 1600 bar and delivers fuel to the six cylinders through 8-hole nozzle injectors.

Table 1: Main data of the simulated engine

Cylinders	6
Bore	128 mm
Stroke	144 mm
Compression ratio	16.5
Swirl ratio	1.4
Injection system	Common-Rail
Maximum injection pressure	1600 bar
Hole number	8
Nozzle hole diameter	0.2 mm
Air management	VGT turbocharger + wastegate

Validation of the proposed CFD methodology was performed using three operating points displayed in Fig. 4 with each one of them being of relevance for operation, design and optimization of heavy-duty diesel engines. In particular, operating point 1 represents full-torque conditions, where a large amount of fuel is injected and interaction between flame and wall is expected to influence significantly the combustion process. Fuel consumption is minimum in operating point 2, while in the middle-load

condition (operating point 3) soot emissions need to be controlled. For both such operating points a double injection strategy (pilot + main) was used. Further details about the simulated conditions are provided in Tab. 2. Finally, Tab. 3 summarizes the in-cylinder estimated thermodynamic conditions which are found at SOI time for the three selected operating points.

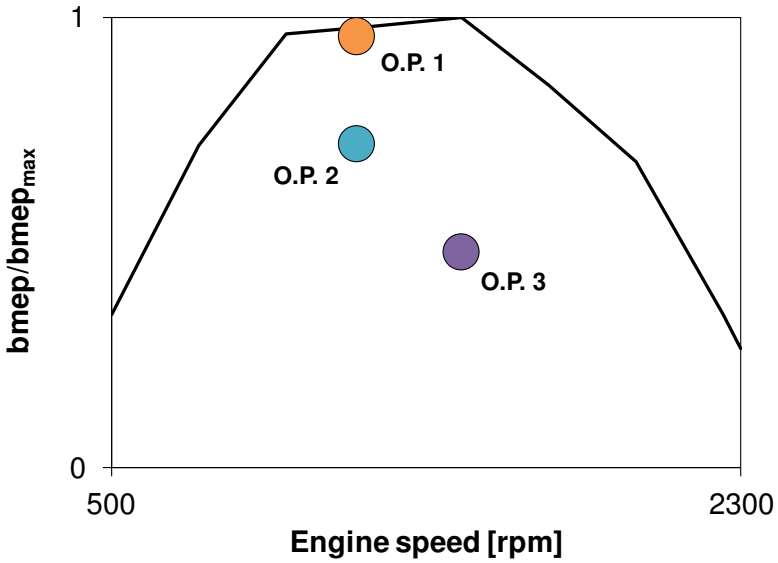

Figure 4: Simulated engine operating points.

Table 2: Details of the simulated operating points

Operating point	Speed [rpm]	Load [%]	λ [-]	EGR [%]	Injection strategy	Injection pressure [bar]
1	1200	100	1.5	0	Only main	750
2	1200	75	1.8	0	Pilot + main	750
3	1500	50	2.1	0	Pilot + main	1100

Table 3: Details of the simulated operating points

Operating point	Pressure [bar]	Temperature [K]	density [kg/m^3]
1	103	943	38
2	99	943	37
3	82	952	30

3.2. Validation at constant-volume conditions

For a proper prediction of the combustion process at different engine loads and accounting for injection pressure variations, reliable numerical tools are necessary to estimate how such engine parameters affect liquid spray evolution, air/fuel mixing process, ignition delay and flame propagation. To this end, a preliminary validation was carried out at constant-volume conditions, simulating n-dodecane spray combustion in the so-called *Spray-A* experiment carried out in the Sandia Combustion Vessel, whose data are publicly available within the context of the Engine Combustion Network database [18, 22]. Fuel is delivered through a single-hole, 90 μm nozzle at pressures ranging between 500 and 1500 bar. Calculations were carried out in a 2D, axy-symmetric mesh with grading: it has a minimum mesh size of 0.1 mm and a successive growth ratio of 1.01. The grid represent a 1/72 portion of the combustion chamber, with a 108 mm height and 54 mm width; it has 216 cells in the axial direction and 108 in the radial one. Oxidation process of n-dodecane is described by means of a skeletal detailed reaction mechanism with 106 species and 420 reactions [26]. Its size can be considered acceptable for CFD computations of diesel spray combustion both at constant-volume and in engine geometries. operating

points were considered for what concerns constant volume conditions, and they are summarized in Tab. 4. Initially, non-reacting conditions (operating point SA1) were considered to properly assess and validate the spray model. Then, effect of injection pressure on combustion process was evaluated (points SA2, SA3, SA4), following variation of engine speed for the considered engine. Purpose of points SA5 and SA6 is to verify if the adopted kinetic mechanism is able to reproduce ignition delays at ambient oxygen conditions and densities similar to those found in the studied diesel engine. Despite some important differences between engine and Sandia vessel experiments exist mainly in terms of injector sizes, there are also important similarities for what concerns injection pressure and ambient conditions. Hence, validation of the proposed model for the spray-A experiment represent a first important step towards its application to combustion simulations in heavy-duty engines.

Table 4: Details of the simulated operating points

Operating point	Temperature [K]	Density [kg/m^3]	Inj. press. [bar]	O_2 [% by vol.]	Injection duration ms
SA1	900	22.8	150	0	4
SA2	900	22.8	150	15	4
SA3	900	22.8	100	15	4
SA4	900	22.8	50	15	4
SA5	900	22.8	150	21	4

Non reacting conditions were first simulated, to properly assess the spray sub-models. Here, the KHRT model by Reitz et al. [23] was used to predict both primary and secondary atomization. The standard $k-\varepsilon$ model was used for turbulence with the C_1 constant modified to 1.55 as it is commonly done to predict penetration and diffusion of jets. Validation of the spray model is illustrated in Figs. 5(a)-(b) for the non-reacting condition ($T = 900$ K, $\rho = 22.8$ kg/m^3). Fig. 5(a) compares computed and experimental data of liquid and vapor penetration for different instants after start of injection (ASOI). In Fig. 5(b), computed distribution of mixture fraction is compared with post-processed and averaged experimental data that were obtained by means of the Raleigh-scattering technique [10]. The model properly reproduces the experimental trends in terms of liquid and vapor penetration. Furthermore, distribution of mixture fraction is rather well predicted in the entire domain and this is a very important pre-requisite for the validation of any combustion model.

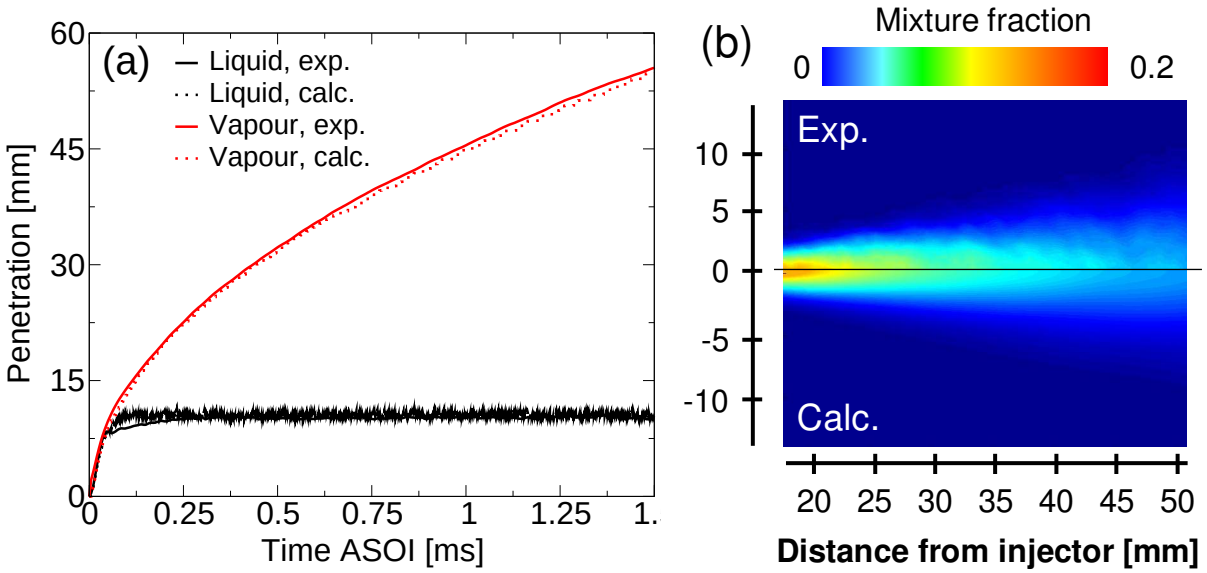

Figure 5: (a): Spray model assessment and validation: comparison between computed and experimental data of fuel liquid and vapor penetrations; (b): Comparison between computed and experimental distributions on a symmetry plane at 4 ms after start of injection. Ambient conditions: $\rho = 22.8 kg/m^3; T = 900K$

Once the spray model was properly assessed, combustion simulations were carried out for the remainder of the operating points listed in Tab. 3. For what concerns the *mRIF* setup, every 0.1 ms from the start of injection a new flamelet was introduced and initialized with the solution taken from the previous one both in terms of temperature and chemical species distribution in the mixture fraction domain. Figs. 6(a)-(b) reports a comparison between computed and experimental ignition delays: numerically ignition delay was defined as the time from the start of injection to the time where the maximum rate of maximum temperature rise happens, while the lift-off length (LOL) was defined as the distance from the injector to the axial position of 2% of its steady-state OH mass fraction. These definitions were both suggested from the Engine Combustion Network. In Fig. 6(a) it is possible to see that the proposed combustion model follows rather well the experimental trend in terms of ignition delay time. In particular, with respect to the baseline case (SA2), a reduction of injection pressure slightly increase the ignition delay time (SA3 and SA4). For what concerns case SA5, the increase of oxygen concentration (21% compared to 15% by volume) is responsible for the reduction of ignition delay. No experimental data were available for SA6 conditions, with the highest density, however the ignition delay reduction compared to the baseline condition seems to be reasonable and mainly related to the highest chemical species reaction rates due to the higher ambient density. Despite ignition delay data are estimated rather well, there is a slight overestimation for any case of approximately 0.15 ms which can be mainly ascribed to the kinetic mechanism used.

A proper prediction of the flame stabilization process seems to be very important for a proper estimation of soot formation and heat release, as discussed in [10]. In past works [5, 6] authors illustrated that, for the *mRIF* model, the mechanism governing flame-lift off is represented by the auto-ignition of a diffusion flame. In particular, flamelets evolving in the CFD domain initially experience very high scalar dissipation rate values above the extinction limit χ_{ig} and no chemical reaction occurs. As soon as the scalar dissipation rate goes below χ_{ig} chemical reactions start to occur and ignition for each flamelet is mainly affected by mixture fraction distribution, ambient conditions and fuel chemistry. However, estimation of the scalar dissipation rate requires a very accurate description of the fuel-air mixing process with a very fine mesh near the nozzle. Use of coarse grids or not properly accounting for the axy-symmetry of the spray will lead to underestimation of the scalar dissipation rate and, consequently, to non-correct prediction of the lift-off length. Here lift-off lengths are rather well-predicted for all the analyzed conditions. In particular, effect of injection pressure seems to be properly reproduced by the *mRIF* model.

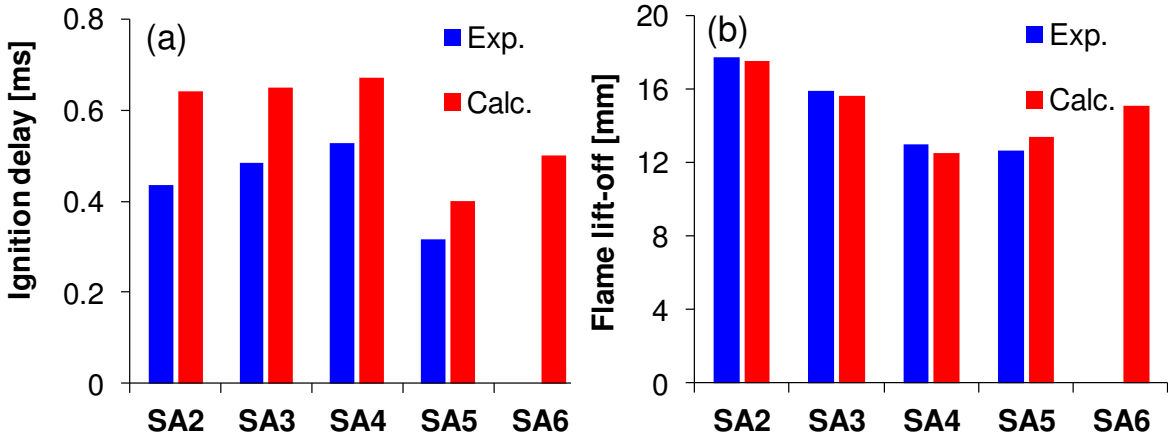

Figure 6: (a): Comparison between computed and experimental data of ignition delay for the selected reacting operating conditions; (b):Comparison between computed and experimental data of lift-off length for the selected reacting operating conditions.

Reduction of injection pressure seems to have two opposite effects: increase of ignition delay and, at the same time, reduction of flame lift-off length. Ignition delay time is mainly affected by the evolution of the scalar dissipation rate for the first flamelets. In particular, Figs. 7(a)-(b) displays, at 0.2 and 0.6 ms after SOI the distribution of the scalar dissipation rate for the three different injection pressures considered. On the same figure, the stoichiometric mixture fraction iso-contour is also shown with white line. Few instants after start of injection (0.2 ms ASOI), Fig. 7(a), it is possible to see that reduced vapor penetration is responsible for higher scalar dissipation rate values in the stoichiometric region for the low

injection pressure case. Later during injection (0.6 ms ASOI), distribution of scalar dissipation rate in the computational domain changes and, in particular, for the highest injection pressure it is possible to see that there is a large region where scalar dissipation rate remains higher. For this reason, ignition of the first flamelets will be faster for the cases with high injection pressure, but next ones will find higher scalar dissipation rate values and they will require more time to be ignited. Since auto-ignition of a diffusion flame is the stabilization mechanism for the *mRIF* model, higher injection pressures will lead to increased lift-off lengths.

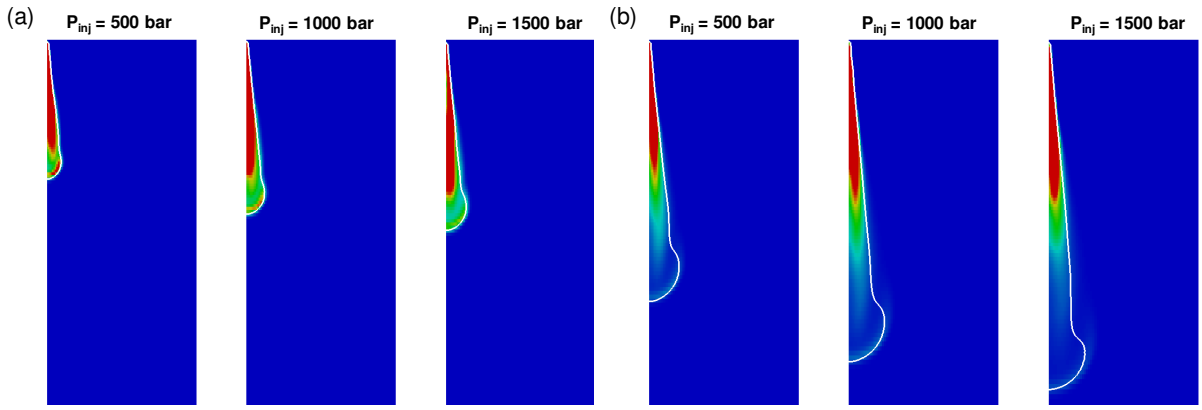

Figure 7: (a): Distribution of the scalar dissipation rate at 0.2 ms ASOI for the cases SA2, SA3 and SA4; (b): Distribution of the scalar dissipation rate at 0.6 ms ASOI for the cases SA2, SA3 and SA4. Scalar dissipation rate range: 0 (blue) - 200 (red).

3.3. Engine simulations

Once the proposed approach was assessed and properly validated at constant-volume conditions, simulations of the combustion process were carried out in the heavy duty engine for the three selected operating points listed in Tab. 2. A 1/8 sector of the combustion chamber was simulated, and details of the computational mesh are displayed in Fig. 8. Additional compensation volumes were included either in the head and in the crevices parts to properly fit the experimental compression ratio. To keep the mesh resolution as much constant as possible in the radial direction, two prismatic layers of cells were inserted to increase the number of cells when moving far from the nozzle. To improve prediction of heat transfer, a boundary layer with three cells (0.1 mm thickness) was placed on piston, liner and cylinder head boundaries. Simulations were carried out with the same spray setup used for constant-volume calculations, and the temperature wall-functions from Angelberger [1] were used to model heat transfer. Mesh motion was performed using the dynamic mesh layering technique [16], keeping the cells in the spray region fixed and moving the ones in the piston bowl.

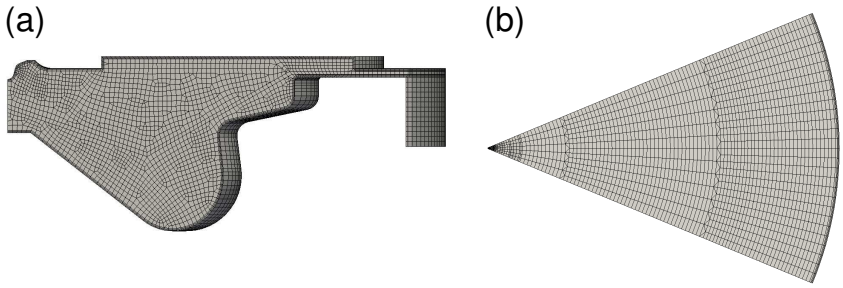

Figure 8: Computational mesh used for combustion simulations of the heavy-duty engine. (a): side view; (b): top view.

Simulations start ad IVC, initial in-cylinder thermo-dynamic conditions were derived from measured data of air flow rate, in-cylinder pressure and air-fuel ratio. Velocity was initialized accounting for instantaneous piston velocity u_p (linearly varying from zero at the head to u_p in the bowl) and swirl ratio, with

a wheel flow velocity profile assumed along the cylinder radius. The number of flamelets used depends on the amount of injected fuel mass, for this reason operating point 1 employs 30 flamelets, while for the other two conditions 20 flamelets are adopted for the main injection event and one for the pilot. Such setup does not differ too much from the one used for simulations at constant-volume conditions. Again, new flamelets belonging to the same injection event are initialized with the species and temperature profiles of the previous one. Fig. 9(a) compares computed and experimental data of in-cylinder pressure profiles for the three different operating conditions. For what concerns the full-load case, it is possible to see that experimental pressure profile is rather well reproduced by the model. However, peak cylinder pressure is slightly overestimated, and this is mainly affected by the heat release rate (HRR) profile, which is shown in Fig. 9(b). After ignition, in fact, the *mRIF* model predicts a higher combustion speed and this aspect seems to be mainly affected by the mesh resolution used, which is too coarse close to the nozzle. Hence, the predicted scalar dissipation rate remains always well below the extinction limit with a consequent overestimation of the HRR, since flame propagation will also take place close to the nozzle. Heat release rate reaches a maximum around TDC, then it remains constant for approximately 10 CAD. During such period, a diffusion flame structure is fully established, and combustion is both influenced by spray dynamics and flame-wall interaction.

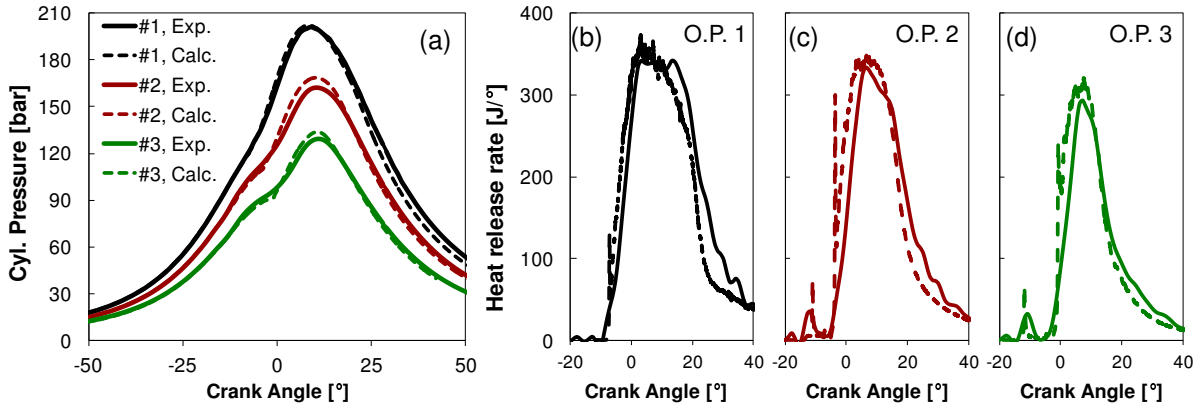

Figure 9: Validation of the *mRIF* model for Heavy Duty Engine simulations: (a) Comparison between computed and experimental pressure traces for operating points 1, 2 and 3; Comparison between computed and experimental heat release rate profiles for operating points 1 (b), 2 (c), 3 (d).

To clarify how flame wall-interaction affects the combustion process, flame structure was post-processed in terms of temperature field, scalar dissipation rate distribution and its evolution versus time for several flamelets. First of all, it is possible to see that numerically flame and wall starts interacting around 2 CAD BTDC, as it can be seen in Fig. 10(a). This involves the first flamelet and Fig. 10(d) illustrates that, such phenomenon keeps its stoichiometric scalar dissipation rate higher than the next ones. Looking at evolution of the scalar dissipation rate during injection, Figs. 10(a)-(b), it is possible to see that χ is very high (> 100) in the core of the jet where the mixture is rich, then χ decreases along the jet axis. However, interaction between flame and wall has the beneficial effect of increasing the scalar dissipation rate, allowing to better oxidize the rich combustion products which were generated in the core of the jet. Flame-wall interaction seems to mainly influence combustion for the first flamelets where the piston is very close to TDC. For the remainder of the flamelets, flame-wall interaction does not seem to play a big role because both in-cylinder charge motion and turbulence decay to not affect the scalar dissipation rate which is continuously decreasing. When looking at heat release rate profile, it is possible to see that simulations predicts a earlier decay of combustion speed around 15 CAD, while experimental HRR remains constant for 5 CAD more. Such discrepancy seems, again, to be mainly related to the mesh structure which is not completely spray-oriented. For this reason, numerical diffusion will enlarge the spray region and reduce the jet velocity at the tip with a negative effect of the predicted scalar dissipation rate at the walls. For what concerns the other two operating points, at 75% and 50% load, agreement is acceptable even if there is a slight overestimation of the maximum cylinder pressure due to the overestimated heat release rate after auto-ignition. For both the cases, flame-wall interaction does not seem to play a big role mainly due to the reduced amount which is injected compared to the full-load case.

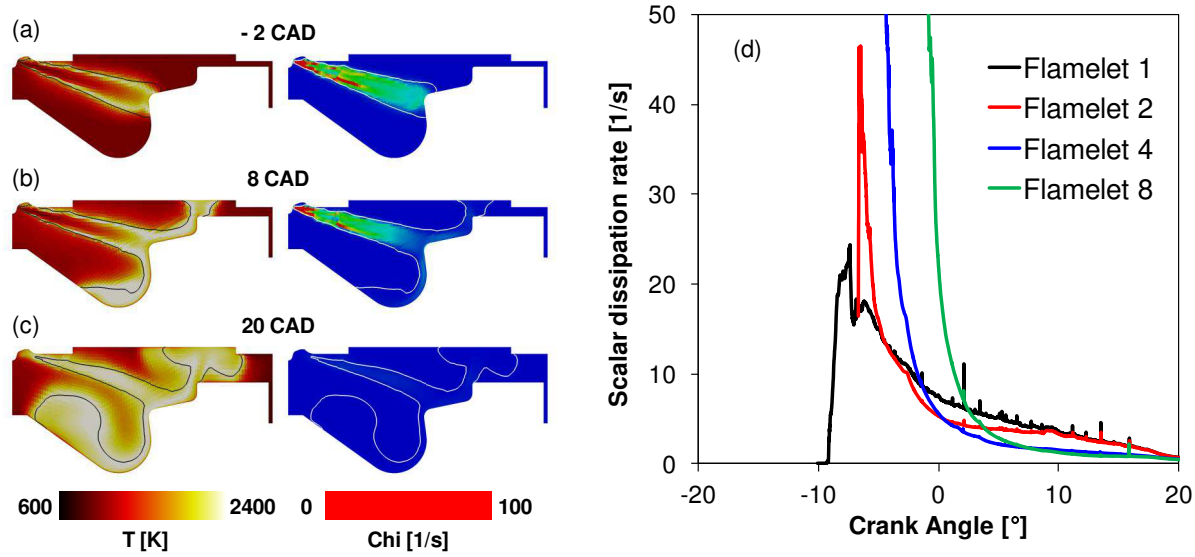

Figure 10: Flame structure analysis of the combustion process for the Heavy Duty Diesel engine: (a) Temperature and scalar dissipation rate distributions at -2, 8 and 20 CAD TDC; (b) evolution of the stoichiometric scalar dissipation rates for flamelets 1, 2, 4 and 8.

4. Conclusions

This work was focused on the development of a CFD methodology for the prediction of the combustion process in Heavy Duty diesel engines. To this end, the *mRIF* (multiple Representative Interactive Flamelets) was implemented into the Lib-ICE code and applied to both constant-volume and engine simulations. Several techniques were then integrated in order to speed up the CPU time in integrating chemistry and the β-pdf of the chemical species to compute composition in the CFD domain. Satisfactory results were achieved, since the model is able to properly reproduce experimental trends of both ignition delay and flame lift-off for the different conditions, including variation of injection pressure which is quite important for operation of Diesel engines. However, it is necessary to correctly predict the distribution of the scalar dissipation rate, mainly close to the nozzle region, in order to predict the stabilization of the flame. In order to do this, a very fine and spray-oriented mesh seems to be absolutely necessary to describe the mixture fraction and its variance field. Once the proposed approach was validated at constant-volume conditions, engine simulations were carried out in a Heavy Duty engine for three different operating points of interest: full, 75% and 50% load. Despite results can be considered satisfactory, results are affected by mesh resolution and structure which produces an underestimation of the scalar dissipation rate and, consequently, influences heat release rate close to the nozzle and flame wall-interaction process. For this reason, most of the future efforts will be dedicated at improving engine grid generation process to be able to better reproduce both liquid and vapor jet dynamics.

References

[1] ANGELBERGER, C., POINSOT, T., AND DELHAY, B. Improving Near-Wall Combustion and Wall Heat Transfer Modeling in SI Engine Computations. *SAE Paper 972881* (1997).

[2] BARTHS, H., HASSE, C., AND PETERS, N. Computational fluid dynamics modelling of non-premixed combustion in direct injection diesel engines. *International Journal of Engine Research 1 (3)* (2000), pp. 249–267.

[3] CONTINO, F., JEANMART, H., LUCCHINI, T., AND DERRICO, G. Coupling of in situ adaptive tabulation and dynamic adaptive chemistry: An effective method for solving combustion in engine simulations . *Proceedings of the Combustion Institute Vol. 33(2)* (2011), pp. 3057–3064.

[4] DEC, J. E. A Conceptual Model of DI Diesel Combustion Based on Laser-Sheet Imaging. *SAE Paper 970873* (1997).

[5] D'ERRICO, G., LUCCHINI, T., CONTINO, F., JANGI, M., AND BAI, X.-S. Comparison of well-mixed and multiple representative interactive flamelet approaches for diesel spray combustion modelling. *Combustion Theory and Modelling 18*, 1 (2014), 65–88.

[6] D'ERRICO, G., LUCCHINI, T., STAGNI, A., FRASSOLDATI, A., FARAVELLI, T., AND RANZI, E. Reduced Kinetic Mechanisms for Diesel Spray Combustion Simulations. *SAE Paper 2013-24-0014* (2013).

[7] DIWAKAR, R., AND SINGH, S. NOx and Soot Reduction in Diesel Engine PCCI Combustion: A Computational Investigation. *International Journal of Engine Research 9(3)* (2008), pp. 195–214.

[8] FERRARESE, A., DIAS, M., BRUNO, R. A., REJOWSKI, E., AND PRACA, M. PCU Solutions to Heavy Duty Diesel Engines after Proconve P7. *SAE Paper 2012-36-0358* (2012).

[9] GOLOVICHEV, V., NORDIN, N., JARNICKI, R., AND CHOMIAK, J. 3-D Diesel Spray Simulations Using a New Detailed Chemistry Turbulent Combustion Model. *SAE Paper 2000-01-1891* (2000).

[10] IDICHERIA, C. A., AND PICKETT, L. M. Quantitative Mixing Measurements in a Vaporizing Diesel Spray by Raileigh Imaging. *SAE Paper 2007-01-0647* (2007).

[11] KNECHT, W. Strategies for Future Heavy Duty Diesel Engines for Commercial Vehicles. *International Journal of Vehicle Design 14* (2006), pp.67–82.

[12] LEHTINIEMI, H., ZHANG, Y., RAWAT, R., AND MAUSS, F. Efficient 3-D CFD Combustion Modeling with Transient Flamelet Models. *SAE Paper 2008-01-0957* (2008).

[13] LIANG, L., STEVENS, J. G., RAMAN, S., AND FARRELL, J. T. The use of dynamic adaptive chemistry in combustion simulation of gasoline surrogate fuels. *Combustion and Flame 156*, 7 (2009), 1493 – 1502.

[14] LIU, S., HEWSON, J. C., CHEN, J. H., AND PITSCH, H. Effects of strain rate on high-pressure nonpremixed n-heptane autoignition in counterflow. *Combustion and Flame Vol. 137* (2004), pp. 320–339.

[15] LUCCHINI, T., D'ERRICO, G., AND ETTORRE, D. Numerical investigation of the spraymeshturbulence interactions for high-pressure, evaporating sprays at engine conditions. *International Journal of Heat and Fluid Flow 32*, 1 (2011), 285 – 297.

[16] LUCCHINI, T., D'ERRICO, G., JASAK, H., AND TUKOVIC, Z. Automatic Mesh Motion with Topological Changes for Engine Simulation. *SAE Paper 2007-01-0170* (2007).

[17] LUCCHINI, T., D'ERRICO, G., ONORATI, A., BONANDRINI, G., VENTUROLI, L., AND GIOIA, R. D. Development of a CFD Approach to Model Fuel-Air Mixing in Gasoline Direct-Injection Engines. *SAE Paper 2012-01-0146* (2012).

[18] MEIJER, M., SOMERS, B., JOHNSON, J., NABER, J., LEE, S.-Y., MALBEC, L. M., BRUNEAUX, G., PICKETT, L. M., BARDI, M., PAYRI, R., AND BAZYN, T. Engine combustion network (ecn): Characterization and comparison of boundary conditions for different combustion vessels. *Atomization and Sprays 22*, 9 (2012), 777–806.

[19] MONTENEGRO, G., TORRE, A. D., ONORATI, A., BROGGI, D., SCHLAGER, G., AND BENATZKY, C. CFD Simulation of a Sliding Vane Expander Operating Inside a Small Scale ORC for Low Temperature Waste Heat Recovery. *SAE Paper 2014-01-0645* (2014).

[20] PATEL, A., KONG, S. C., AND REITZ, R. D. Development and Validation of a Reduced Reaction Mechanism for HCCI Engine Simulations. *SAE Paper 2004-01-0558* (2004).

[21] PETERS, N. Laminar diffusion flamelet models in non-premixed turbulent combustion. *Progress in Energy and Combustion Science 10* (1984), 319–339.

[22] PICKETT, L. M., GENZALE, C. L., BRUNEAUX, G., L.-M. MALBEC, L.-M., HERMANT, L., CHRISTIANSEN, C., AND SCHRAMM, J. Comparison of diesel spray combustion in different high-temperature, high-pressure facilities. *SAE International Journal of Engines 3*, 2 (2010), 156–181.

[23] REITZ, R. D. Modeling Atomization Processes In High Pressure Vaporizing Sprays. *Atomization and Spray Technology Vol. 3* (1987), pp. 309–337.

[24] SENECAL, P. K., POMRANING, E., AND RICHARDS, K. J. Multidimensional Modelling of Direct-Injection Diesel Spray Liquid Length and Flame Lift-off Length using CFD and Parallel Detailed Chemistry. *SAE Paper 2003-01-1043* (2003).

[25] SINGER, M., AND POPE, S. Exploiting ISAT to solve the equations of reacting flow. *Combustion Theory and Modelling Vol. 8* (2004), pp. 361–383.

[26] SOM, S., LONGMAN, D., LUO, Z., PLOMER, M., AND LU, T. Three Dimensional simulations of diesel sprays using n-dodecane as a surrogate. In *Eastern States Section of the Combustion Institute Fall Technical Meeting* (2011).

[27] WRIGHT, Y. M., BOULOUCHOS, K., PAOLA, G. D., AND MASTORAKOS, E. Multi-dimensional Conditional Moment Closure Modelling Applied to a Heavy-duty Common-rail Diesel Engine. *SAE Paper 2009-01-0717* (2009).

3D numerical analysis of diesel combustion under cold ambient conditions

Yoshihiro Imaoka, Toru Nishizawa, Shuichi Iio, Manabu Hasegawa, Atsushi Teraji, Keiji Kawamoto

Powertrain Engineering Division 1, Nissan Motor Co., Ltd., 560-2, Okatsukoku, Atsugi-shi Kanagawa 243-0192, Japan

E-mail: y-imaoka@mail.nissan.co.jp
Telephone: +(81) 50 3789 6011
Fax: +(81) 46 282 8833

Abstract. A lower compression ratio has been demanded for diesel engines in recent years to improve fuel consumption, exhaust emissions and maximum power recently. However, low compression ratio may have combustion instability issues under cold temperature condition, especially just after engine started.

As the first step in this study, cold temperature combustion was investigated on the basis of an in-cylinder pressure analysis, it was found that higher heat release around top dead center, which was mainly attributed to pilot injection, was a key factor in reducing engine speed fluctuation.

3D CFD simulations were conducted to obtain a better understanding of combustion under a cold condition, particularly mixture formation near the glow plug. Specifically for this purpose, Timescale interaction (TI) combustion model was developed for simulating combustion phenomena. This model was based on a reasonable combustion mode, taking into account the characteristic time scale of chemical reactions and turbulence eddy break-up. In addition, the parameters of the ignition model and computational grids near the glow plug were improved for application to cold start conditions.

The results revealed that controlling the fuel mass and temperature surrounding the glow plug appropriately by multiple pilot injections contributed to improving combustion stability under cold start conditions. The results showed that ignition and combustion started near the glow plug in a low temperature condition as a result of a temperature increase caused by chemical reactions. Both the temperature and fuel mass near the glow plug have to be high enough to improve heat release at top dead center.

1. Introduction

Diesel engines are a promising technology for protecting the global environment thanks to their relatively high thermal efficiency that results in lower carbon dioxide (CO_2) emissions. In recent years, the compression ratio of passenger vehicle diesel engines has been reduced to improve fuel consumption, output power and emissions [1-5]. However, a low compression ratio may induce unstable combustion at low temperatures. Reported measures for preventing instability include optimization of the combustion chamber design, reduction of cooling losses, raising of the in-cylinder gas temperature by exhaust gas recirculation and improvement of the air-fuel mixture distribution by modifying the fuel injection strategy [6, 7]. Recent studies have shown that multiple injections are effective for improving the in-cylinder mixture distribution because of the relatively short fuel tip penetration. It was also reported that the glow plug is a key component for combustion stability under low temperature condition and ignition was started around the glow plug [8, 9]. However, there are no reports about the effectiveness of a multiple injection strategy focusing on improvement of the air-fuel mixture and temperature distribution near the glow plug. The purpose of this study was to clarify the relationship between the air-fuel mixture distribution and various multiple injection patterns based on both experiments and 3D CFD simulations, with special attention paid to the region near the glow plug under low temperature conditions.

2. Test apparatus and method

Table 1 shows the test engine specifications used in this study. The test engine was a 4-cylinder direct injection diesel engine with a compression ratio of 15.0:1. In order to investigate the relationship between a multiple injection strategy and combustion stability improvement at low temperatures, combustion analyses were conducted using a special glow plug that was combined with an in-cylinder pressure sensor. The relationship between the surface temperature of the glow plug and the applied voltage was confirmed prior to the engine tests. The relationship obtained was applied to control the glow plug surface temperature to the target value by means of voltage control. The actual surface temperature of the glow plug was also monitored by a thermocouple embedded under the tip of the glow plug heater. The glow plug was located at the top of the combustion chamber as seen in Figure 1. Before experimental tests were conducted, the engine was soaked at a -15 °C ambient temperature until the coolant and engine oil temperatures were reduced to a level equal to the ambient temperature. The engine was motored at a constant speed on a dynamometer and fuel was injected in designated injection patterns.

Table 2 shows the properties of the test fuel. This study was specifically targeted at improving combustion stability under low temperature conditions. Therefore, the Cetane number was set at a relatively low level of 46 to create a severe condition.

Table 1 Test engine specifications

Engine Type	4 Cylinder Di Diesel
Displacement	2,488 cm^3
Bore	89.0 mm
Stroke	100.0 mm
Compression Ratio	15.0:1
Fuel Injection Equipment	Common Rail System
Nozzle Hole Diameter	0.158 mm
Number of Nozzle Holes	8
Swirl Ratio	3
Type of Glow Plug	Rapid Ceramic
Turbocharger	Variable Geometry Turbo

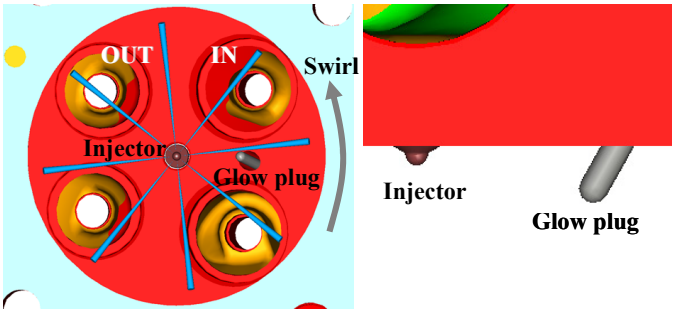

Fig. 1 Layout of glow plug in cylinder head

Table 2 Properties of test fuel

Type of Fuel		Diesel
Cetane Number		46
Density		0.8321 g/cm^3
Viscosity		1.729 mm^2/s
Sulfur Content		10 ppm
Distillation	IBP	173 °C
	50%	240 °C
	FBP	301 °C

3. 3D CFD simulations

A modified time-scale interaction (TI) combustion model was used in this study to investigate in-cylinder combustion in detail under low temperature conditions [10]. The TI combustion model was designed to be adaptable to various operating conditions of diesel engines. It consisted of two kinds of combustion models: the Universal Coherent Flamelet Model (UCFM) [11], which has been developed to predict mainly pre-mixed combustion, and the Characteristic Time-scale Combustion (CTC) model [12], which has been mainly used to simulate diffusion combustion. The two models were selected and applied by factoring the characteristic time scales of the chemical reactions and turbulent mixing into the scope of application of each model. In order to simulate a low temperature engine starting condition, the accuracy of the ignition model was further improved, a specific high temperature wall was introduced to imitate the glow plug, and the computational grids surrounding the glow plug were modified.

3.1 Time-scale interaction combustion model

As outlined in Figure 2, in the initial stage of diesel combustion, the air-fuel mixture that forms during the ignition delay begins to burn, thus consuming the oxygen in the fuel jet. After most of the oxygen in the fuel jet is consumed, the fuel is subsequently consumed by diffusion combustion in the region where the fuel jet surface mixes with the surrounding air. Dec [13] made this process clear on the basis of visualization experiments using laser-sheet imaging. Because the interior of the fuel jet is fuel-rich, the laminar burning velocity is extremely slow and the flame cannot sustain combustion. Consequently, the characteristic time scale of the chemical reactions is greater than that of macroscopic turbulent mixing, resulting in the local formation of a well-stirred combustion field. The fuel-rich mixture, which is generated by air entrainment in the upstream region of the fuel jet, then goes into the fuel-rich combustion region [14]. This process presumably explains the reasons for the occurrence of fuel-rich combustion that is rate-controlled by the chemical reactions including auto ignition.

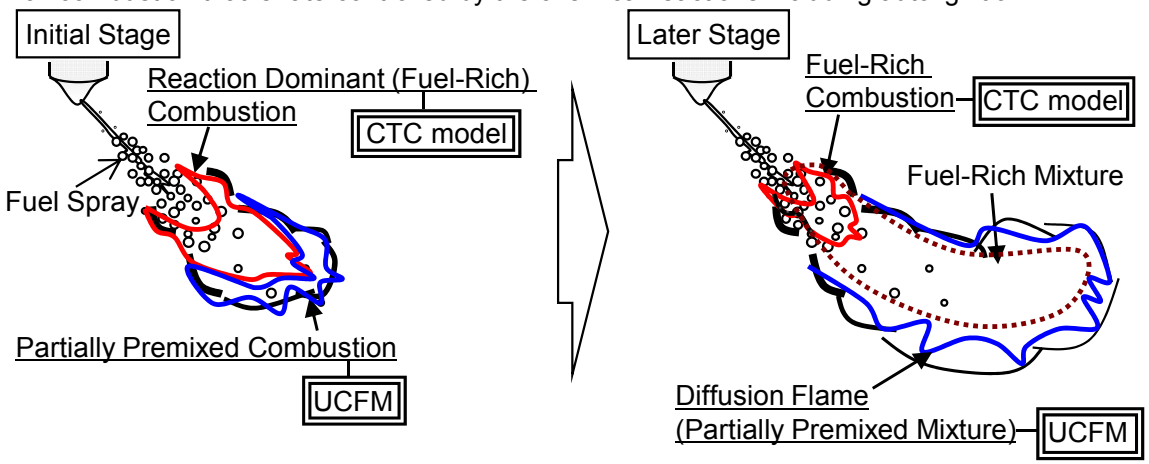

Fig. 2 Concept of TI combustion model

Therefore, the modified TI combustion model applies the UCFM to combustion in the region where the characteristic time scale of the chemical reactions is smaller than that of turbulence mixing and turbulence is the rate-controlling parameter. The CTC model is applied to combustion in the reaction rate-controlled region where the characteristic time scale of the chemical reactions is dominant owing to the influence of a fuel-rich or -lean mixture, among other factors. The CTC model determines the fuel consumption rate on the basis of the characteristic time scales of the chemical reactions and turbulence. The application range of the CTC model was defined on the basis of a non-dimensional Damköhler number Da, consisting of these two characteristic time scales. This approach enables the two combustion models to be applied to the regions matching the actual combustion fields. Da is expressed as a ratio of the integral characteristic time scale of turbulent flow τ_t to the characteristic time scale of the chemical reactions τ_{kin} (i.e., $Da = \tau_t/\tau_{kin}$). When Da is less than a certain value, it is assumed that the progress of combustion contributes more to the characteristic time scale of the chemical reactions than to that of turbulent flow. Accordingly, the scope of application of the CTC model is defined as

$$Da \leq a \tag{1}$$

where a = 1.0 when the characteristic time scales of turbulence mixing and the chemical reactions are equal.

3.2 Combustion model in the turbulence rate-controlled region

The results of Dec's visualization experiments [13] showed that the initial partially premixed mixture at an equivalence ratio from 0.78 to 2.02 forms the diffusion flame that is the main combustion mode in diesel engines. Because the combustion reaction zone in this region is extremely thin, the diffusion combustion region in a diesel engine can be considered as an agglomeration of laminar flamelets using a flame front model [15-17] Accordingly, the UCFM [11] developed by the authors as a high-accuracy premixed combustion model was applied to combustion in the region where turbulence is the rate-controlling parameter.

In the UCFM, the flame area is expressed macroscopically in terms of the flame area density Σ, and flamelets are expressed by solving the transport equation of Σ. The transport equation of Σ is written as

$$\frac{\partial \Sigma}{\partial t} + \frac{\partial u_i \Sigma}{\partial x_i} = \frac{\partial}{\partial x_i}\left(\frac{\nu_t}{\sigma_c}\frac{\partial \Sigma}{\partial x_i}\right) + S - D \qquad (2)$$

where ν_t is the coefficient of turbulent viscosity, σc is the turbulent Schmidt number, S is the source term and D is the extinction term. A model of the source term S was newly created for the UCFM, and the model proposed by Bouldier et al. [18] was adopted for the extinction term D.

The source term S in Eq. (2) was modeled as shown below using the flame area growth S_T attributed to turbulent combustion and the growth S_L attributed to laminar combustion.

$$S = S_T + S_L \qquad (3)$$

The turbulent combustion source term S_T is expressed in the UCFM as

$$S_T = \alpha_0 \sqrt{Ret}\,\frac{\varepsilon}{k}\Gamma\Sigma \qquad (4)$$

where α_0 is a model constant, k, ε and Ret indicate the turbulent energy, the turbulence dissipation rate and the turbulent Reynolds number, respectively, and Γ denotes the intermittent turbulence net flame stretch (ITNFS) model [19], which expresses the stretching and quenching of the flame front by turbulence.

The source term S_L attributed to laminar combustion is expressed as shown in the following equation using the ratio of the combustion gas temperature T_b to the unburned gas temperature T_u and its product with the laminar burning velocity U_L, as well as the attenuation function expressed as the Karlovitz number and taking into account the Kilmov-Williams criterion [20].

$$S_L = \beta_0 \exp(-\beta_1 Ka)\frac{T_b}{T_u}U_L\Sigma^2 \qquad (5)$$

where β_0 and β_1 are model constants.

In the UCFM, the fuel consumption rate ω_{Fchem} is derived as

$$\omega_{Fchem} = \min\left(Y_{TF}, Y_{TO2}/\zeta_{st}\right)\rho_u U_L \Sigma \qquad (6)$$

using the unburned mixture density ρ_u, the hypothetical fuel mass fraction Y_{TF} and the hypothetical oxygen mass fraction Y_{T02}, both of which will be explained later, the laminar burning velocity U_L and the flame area density Σ. Here, the notation ζ_{st} is the ratio of the oxygen mass fraction to the fuel mass fraction relative to a stoichiometric mixture ratio. It was hypothesized that the laminar burning velocity U_L of high carbon number fuels is approximately the same. The U_L of iso-octane, whose flame speed is almost equivalent to that of the chemicals contained in diesel fuel, was used in the calculations.

3.3 Combustion model in the reaction rate-controlled region

In the region of reaction rate-controlled combustion, it is assumed that there are various fields where the characteristic time scale of the chemical reactions is greater than that of turbulent mixing, including a high-turbulence field and fuel-rich or -lean fields. For diesel combustion in particular, a fuel-rich field is mainly hypothesized, making it necessary to consider the mixing time of the un-reacted fuel and oxygen when determining the chemical reaction time. In addition, because the characteristic time scale of the chemical reactions increases due to the low oxygen concentration, it is necessary to consider both characteristic time scales simultaneously. Therefore, it was decided to use the CTC model [12], which takes both characteristic time scales into account locally, as the combustion model in the reaction rate-controlled region. The mixing of the un-reacted fuel and oxygen is expressed using the characteristic time scale of turbulence τ_t. Using the characteristic time scale of the chemical reactions τ_{kin}, the rate of reduction of the mass fraction of each species, dY_i/dt, can be expressed as shown in the following equation.

$$\frac{dY_i}{dt} = \frac{Y_i - Y_i^*}{\tau_{kin} + f\tau_t} \quad (7)$$

where Y_i* is the momentary equilibrium concentration of each species. The characteristic time scale of the chemical reactions τ_{kin} and that of turbulence τ_t are expressed as an Arrhenius type function and as a vortex dissipation type function, respectively, as indicated in the following equations.

$$\tau_{kin} = A^{-1}[Fuel]^{0.75}[O_2]^{-1.5}\exp(E_A/RT) \quad (8)$$

$$\tau_t = cm_2\frac{k}{\varepsilon} \quad (9)$$

Values of A = 7.68 × 10^9, E_A = 77.3 kJ/mol and cm_2 = 0.142, as determined by Kong et al., [12] were used as the respective model constants. The notation f is a function having a value between 0 and 1, which is determined by the progress of combustion. It is expressed as shown below using the oxygen concentration Y_{02} and the hypothetical oxygen concentration Y_{T02}, which will be explained later.

$$f = \frac{1 - e^{-r}}{0.632} \quad (10)$$

$$r = 1 - \frac{Y_{O_2}}{Y_{TO_2}} \quad (11)$$

Based on the foregoing discussion, the fuel consumption rate in the TI combustion model is derived with Eq. (6) in the turbulence rate-controlled region and with Eq. (7) in the reaction rate-controlled region.

3.4 Mass fraction equations

The combustion gas temperature T_b and the unburned gas temperature T_u are needed to find the laminar burning velocity and the fuel consumption rate in each combustion mode. To calculate these temperatures, the mass fraction of each species in the burned region is found, in addition to solving the transport equations for the mass fraction of each species in the unburned region as well as their mass conservation equations and enthalpy conservation equations. The unburned region is defined as a hypothetical space in the TI combustion model so that the burned and unburned regions can be considered with one cell. The mass conservation equation for the fuel and the transport equation for the hypothetical unburned fuel are shown below.

$$\frac{\partial\rho Y_F}{\partial t} + \frac{\partial\rho u_i Y_F}{\partial x_i} = \frac{\partial}{\partial x_i}\left(\frac{\rho\nu_t}{\sigma_c}\frac{\partial Y_F}{\partial x_i}\right) + \omega_{Fchem} + \omega_{Fevap} \quad (12)$$

$$\frac{\partial\rho Y_{TF}}{\partial t} + \frac{\partial\rho u_i Y_{TF}}{\partial x_i} = \frac{\partial}{\partial x_i}\left(\frac{\rho\nu_t}{\sigma_c}\frac{\partial Y_{TF}}{\partial x_i}\right) + \omega_{Fevap} \quad (13)$$

where Y_F is the fuel mass fraction, Y_{TF} is the hypothetical unburned fuel mass fraction, U_L is the laminar burning velocity, ω_{Fchem} is the fuel consumption rate, and ω_{Fevap} is the increase in the fuel quantity due to evaporation. Y_{TF} is a variable that varies only due to fuel transport and is not changed by combustion. Hence, $Y_{TF} = Y_F$ in the unburned state and $Y_{TF} > Y_F$ in the burned region.

The unburned combustion gas temperature T_u is derived by calculating it with the following enthalpy equation.

$$\frac{\partial\rho h_u}{\partial t} + \frac{\partial\rho u_i h_u}{\partial x_i} = \frac{\partial}{\partial x_i}\left(\frac{\rho\nu_t}{\sigma_c}\frac{\partial h_u}{\partial x_i}\right) + \frac{\rho}{\rho_u}\frac{\partial}{\partial x_i}q_{ui} + \frac{\rho}{\rho_u}\left(\frac{\partial p}{\partial t} + u_i\frac{\partial}{\partial x_i}p\right) + \rho\varepsilon \quad (14)$$

where p indicates the pressure and q_{ui} is a heat diffusion vector.

3.5 Optimization of constants of the shell model

In order to predict ignition phenomena in a low temperature starting condition precisely, the constants of the shell model [21] were optimized using a genetic algorithm. The items optimized were the experimental results for Ciezki's [22] shock tube ignition delay time using an n-heptane and air mixture, and for further compensation, Tsurushima's [23] prediction results obtained with a chemical

reaction model were applied. Optimization was carried out over a wide range of conditions. an ambient pressure ranging from 1 to 8 MPa, an equivalence ratio ranging from 0.5 to 2 and an EGR ratio ranging from 0 to 50 %, considering the adaptation of various operating conditions. The modeFRONTIER, a general-purpose optimization tool, was used. To minimize the objective function $\Delta\tau$ in Eq. (15), the parameters of the shell model (Af1,Af2, Af3, Af4, Ap1, Ap2, Ap3, Aq, Ab, At, Ef1, Ef2, Ef3, Ef4, Ep1, Ep2, Ep3, Eq, Eb, Et) were optimized.

$$\Delta\tau = \sum\left(\tau_t - \tau_{shell}\right) \qquad (15)$$

where τ_t is the ignition delay measured by Ciezki or calculated by means of Tsurushima's model and, τ_{shell} is the calculated ignition delay using the shell model. The optimized parameters are showns in Table 3

Table 3 Optimized parameters of shell model

Parameter		Parameter	
Ap1	7.94330E+11	At	1.70000E+13
Ep1	7.50000E+02	Et	8.25000E+03
Ap2	5.19000E+12	Af1	2.62350E-04
Ep2	1.38750E+04	Ef1	-4.20520E+03
Ap3	4.84800E+13	Af2	4.81800E+02
Ep3	5.76000E+03	Ef2	-9.04290E+03
Aq	3.10000E+12	Af3	1.80000E+01
Eq	3.82220E+04	Ef3	1.47800E+04
Ab	8.20000E+17	Af4	3.16450E+05
Eb	5.04000E+04	Ef4	3.21250E+04

Figures 3 and 4 illustrate examples of the calculated ignition delay before and after optimization. The calculated results before optimization deviated from the measured value, but after optimization the predicted values were in good agreement with measured data, including the cold temperature conditions.

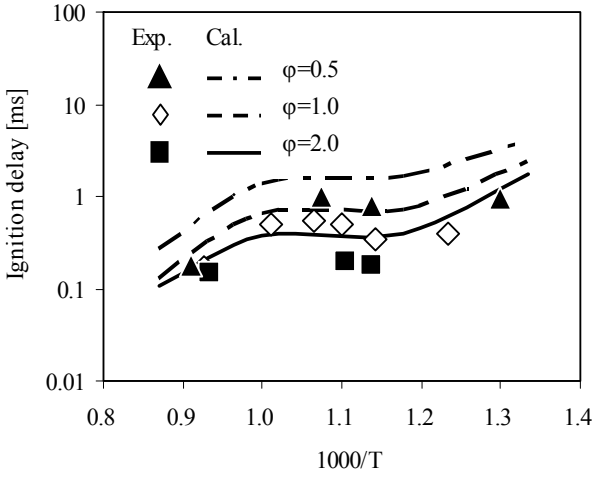

Fig. 3 Comparison of measured and calculated ignition delay by using original shell parameters at an initial pressure of 4 MPa and equivalence ratios of 0.5, 1.0 and 2.0

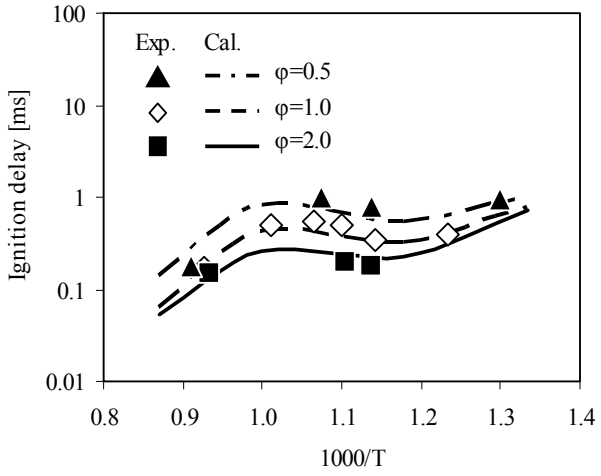

Fig. 4 Comparison of measured and calculated ignition delay by using optimized shell parameters at an initial pressure of 4 MPa and equivalence ratios of 0.5, 1.0 and 2.0

4. Calculation method

4.1 Outline of model

Calculations were performed in this study with STAR-CD, a general-purpose CFD analysis code, in order to validate the modified TI combustion model. The Renormalization Group (RNG) k-ε model [24], was used as the turbulence model. In the discretization procedure, the implicit scheme was used as the time propagation method, the Monotone Advection and Reconstruction Scheme (MARS) was used to discretize the convection term, and the Pressure-Implicit with Splitting of Operators (PISO) algorithm was used as the solution for velocity and pressure.

The physical models used in this study are listed in Table 4. The Kelvin-Helmholz / Rayleigh-Taylor (KH-RT) hybrid model [25] was used as the spray model. This model combines the KH model of liquid jet breakup with the RT model of the breakup of liquid drops beyond the breakup length. Fuel viscosity that affects the breakup is adjusted by the temperature. A shell model [21] was used for judging the low-temperature reaction mechanism below 1100 K and auto ignition.

Table 4 Configuration of simulation model

Combustion	TI Combustion Model
Turbulence	RNG k-ε Model [24]
Drop Breakup	KH-RT Model [25]
Ignition	Shell Model [21]
Burnt Gas Dissociation	Post Chemistry Model

4.2 Glow plug adaptation

In this study, a rectangular high temperature wall was added to the model to imitate the glow plug. Figure 5 shows the computational grid surrounding the glow plug. According to Oomori's measured results [26], in order to predict the temperature fraction, including the thickness of the thermal boundary layer, the grid size should be 0.5 mm or less. Considering this requirement, the computational grid sizes were restricted from 0.13 to 0.3 mm in this study.

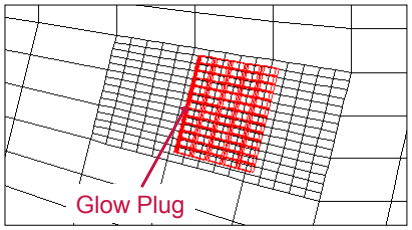

Fig. 5 Computational grid near the glow plug

Figure 6 presents examples of the temperature fraction near the glow plug simulated in this study. As seen in the figure, the temperature fraction including the thermal boundary layer near the wall was obtained with a computational grid subdivision from 0.13 to 0.3 mm.

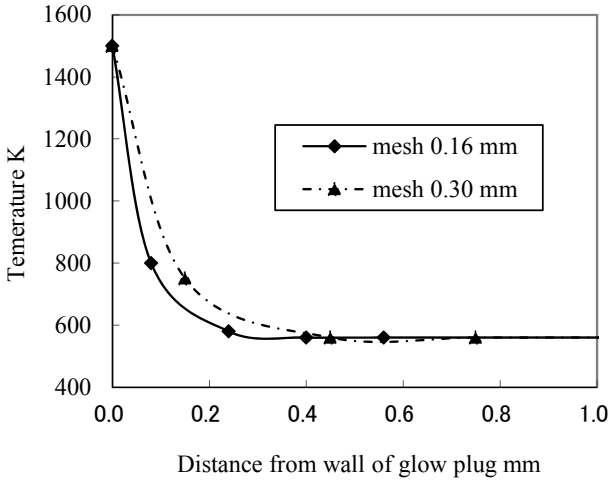

Fig. 6 Temperature fraction near the glow plug at -30 deg. ATDC

5. Validation of calculation results

5.1 Experimental diesel engine

Numerical calculations were performed using this model and compared with experimental results. In order to simulate precisely the air-fuel mixture formed by the spray, the injector and glow plug positions were determined so as to be the same as in an actual engine. The sector shape, depicted in Figure 7, for one injector nozzle hole was configured such that the calculation cells did not move in the direction of fuel injection. Table 5 shows the operational conditions used in the experiment and simulation, and the fuel injection conditions are given in Table 6. In this comparison, four fuel injections were applied and the parameters were the injection timing, quantity of fuel injected in each injection and the fuel pressure. The four experimental conditions that differed the most were simulated for verification.

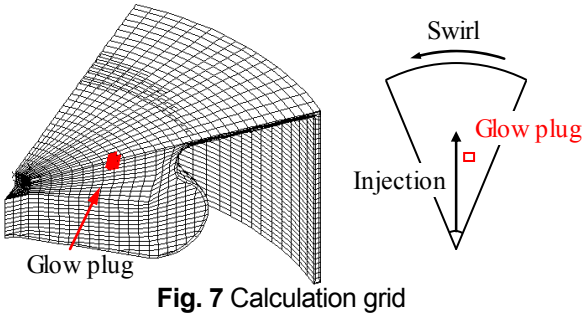

Fig. 7 Calculation grid

Table 5 Experimental conditions

Engine Speed	1100 rpm
Fuel Injection Amount	25 mm^3/st.cyl
Ambient Temperature	258 K
Fuel Cetane Number	46

Table 6 Injection conditions

No.	Injection pattern	$P_{inj.}$ MPa
1	-30deg. ATDC TDC	70
2	-30deg. ATDC TDC	50
3	-30deg. ATDC TDC	50
4	-30deg. ATDC TDC	70

5.2 Validation of heat release rate patterns

Predicting performance accurately requires good agreement of the rate of heat release in the simulation. Therefore, comparisons were made of the heat release rate patterns between the experimental and simulation results. Figure 8 shows comparisons of the heat release rate as a function of the crank angle until top dead center. Experimental results were averaged for 200 consecutive cycles right after injection was started, while the simulation results only reflect the initial boundary condition, so a direct quantitative comparison would be difficult. However, the predicted results tended to agree with the experimental results with respect to the order of the ignition timing and the heat release rate at top dead center. Figure 9 shows a comparison of the mass burnt (MB) 0% timing relative to the crank angle between the experimental and simulation results. The heat release rate becomes negative just after fuel injection due to vaporization heat, and after ignition, it gradually increases because of the chemical reactions and becomes positive. In this study, MB0% was defined as the time when the integral of the heat release rate crosses 0. As seen in the figure, the simulated results for MB0% show a linear relationship with the experimental data. It was concluded that the TI combustion model can predict the timing for the onset of heat release with reasonable accuracy.

These results lead to the conclusion that the TI combustion model can reproduce the heat release regions in an engine cylinder with reasonable accuracy including under cold temperature conditions.

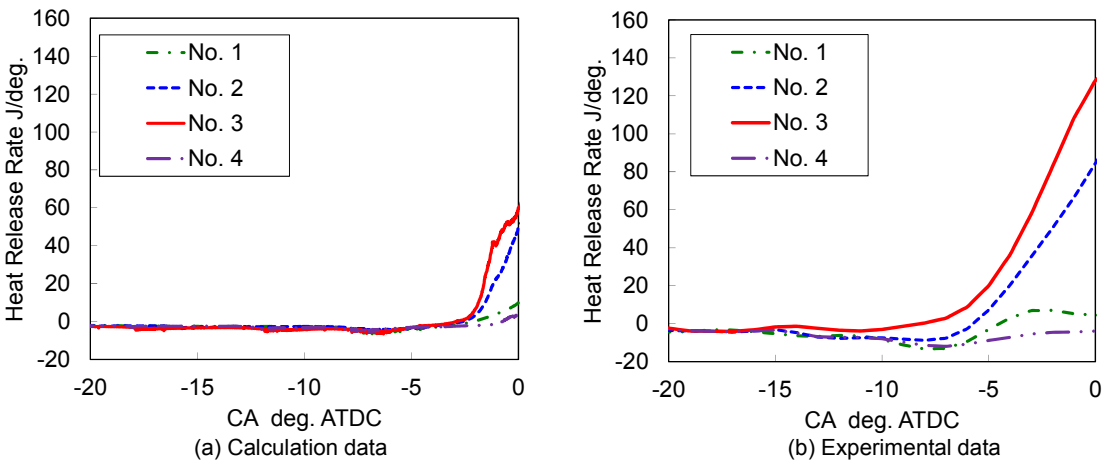

Fig. 8 Comparisons of heat release rate under different injection patterns

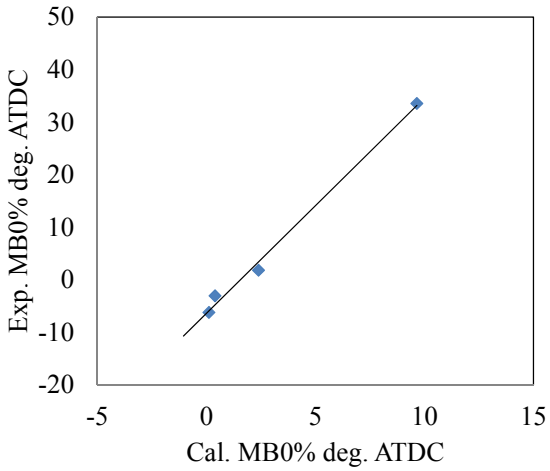

Fig. 9 Comparisons of mass burnt 0% timings under different injection patterns

The calculated results were analyzed at the time of firing to identify the combustion state in one cylinder of the test engine. Figure 10 shows the temperature distribution and the mass fraction of radicals R calculated with the shell model. How the reaction of the fuel is guided to the high temperature zone surrounding the glow plug is important in promoting ignition under low temperature start conditions. Radical generation and ignition of the air-fuel mixture in each injection from near the glow plug were promoted to start ignition at top dead center.

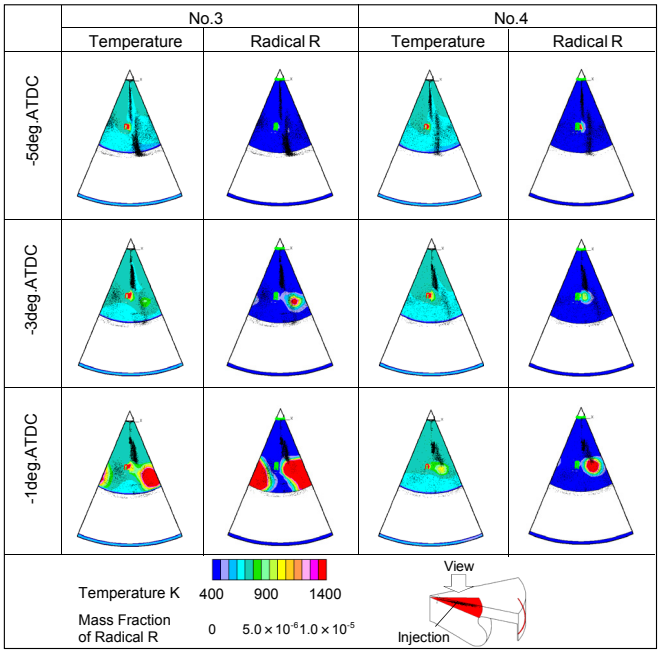

Fig. 10 Comparisons of temperature and mass fraction of radicals under different injection patterns

5.3 Calculation of full-scale cylinder

A full cylinder calculation was carried out to understand combustion more clearly after ignition under the cold start condition. Figure 11 shows the computational grid of the full-scale cylinder with the glow plug. Grids near the glow plug were between 0.05mm and 0.3mm in size. Figures 12 and 13 show the heat release rate and temperature distribution in the high temperature zone for two of the combustion patterns examined. In this calculation, ignition in each condition starts near the glow plug, the same as in the calculation with the sector model. The air-fuel mixture of the swirl downstream starts the sequential ignition pro-

cess, and the high temperature zone expands under injection pattern No. 3 (Figure 12). The heat release rates in this condition increase in response to the expansion of the high temperature zone. Under the condition with injection pattern No. 4 (Figure 13), the ignition timing near the glow plug occurs 15deg.CA later than in injection pattern No. 3. As a result of the longer ignition delay, the heat release rates are lower during the cycle. According to these simulation results with a full-scale cylinder, ignition and combustion under the low temperature condition start near the glow plug, the same as in the calculation with the sector model, and the strength of the heat release rates is determined by how much earlier ignition occurs around the glow plug.

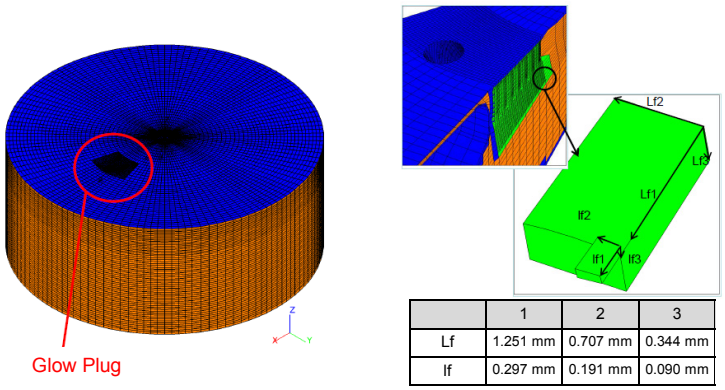

	1	2	3
Lf	1.251 mm	0.707 mm	0.344 mm
lf	0.297 mm	0.191 mm	0.090 mm

Fig. 11 Computational grid of full-scale cylinder

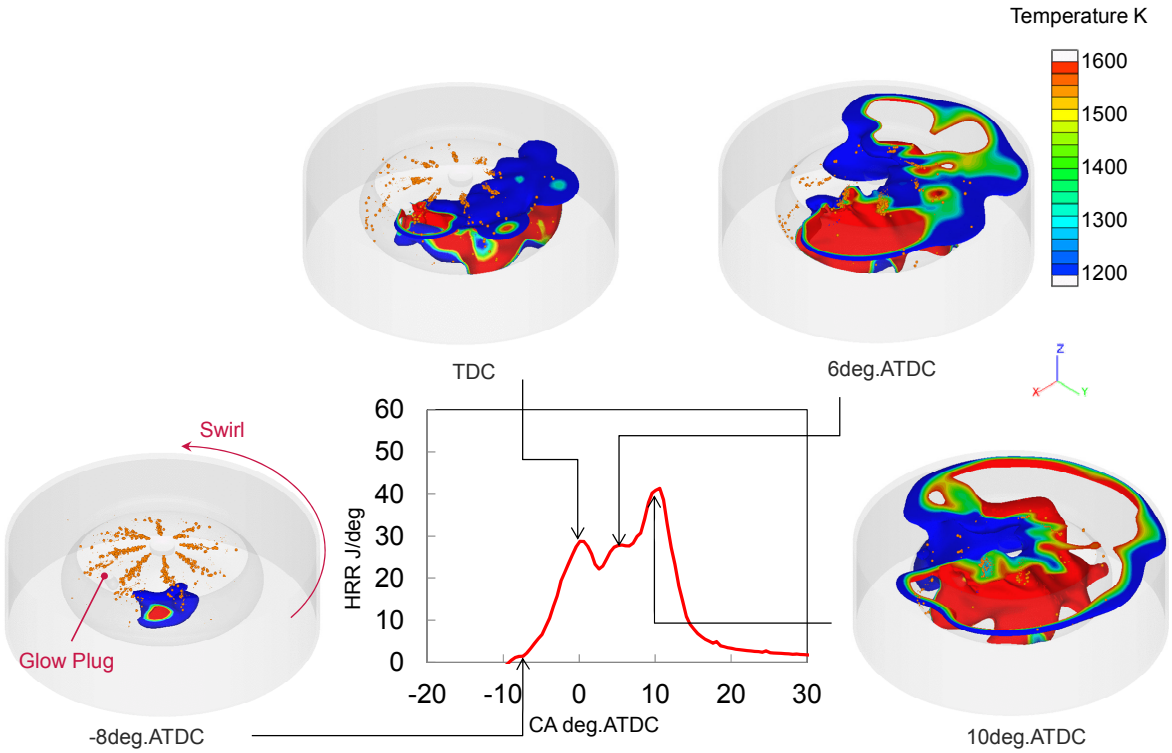

Fig. 12 Calculation results for injection pattern No.3

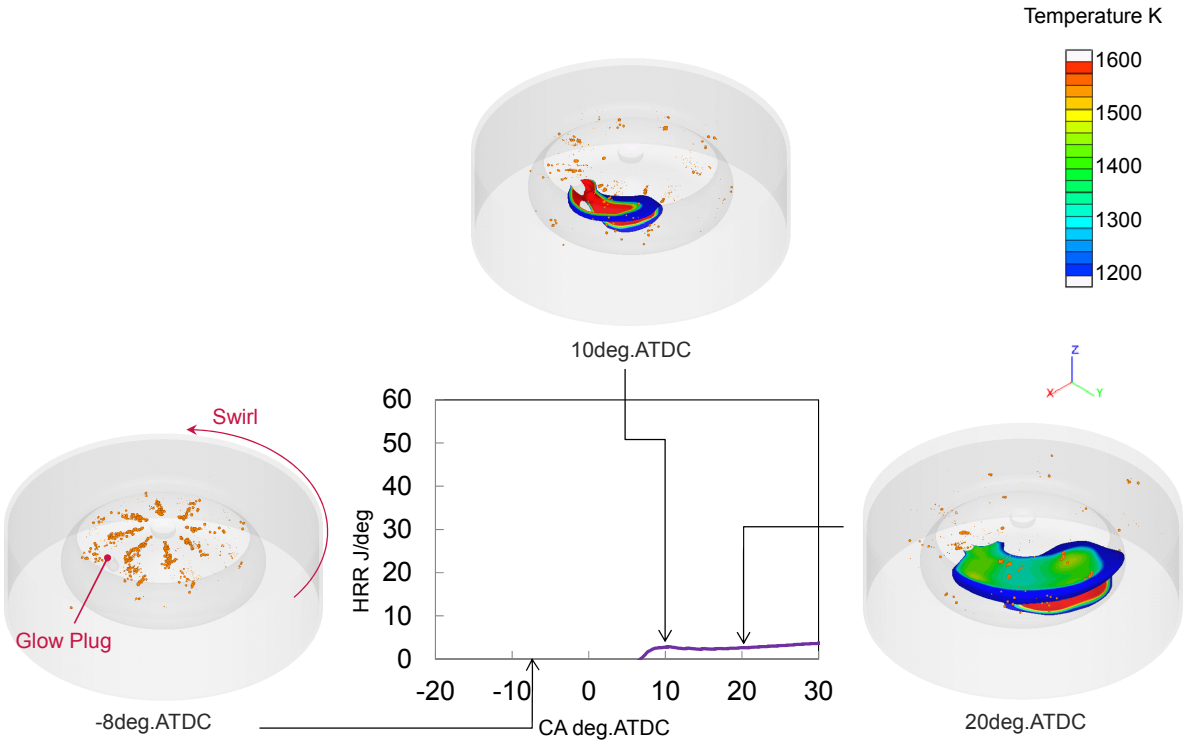

Fig. 13 Calculation results for injection pattern No.4

6. Study of injection patterns

6.1 Comparison of multiple injection patterns

The optimized model with the sector shape was applied to the study of the multiple injection patterns. Table 7 shows the operating conditions used in the calculations. The case with two pilot injections is denoted as A and was the baseline injection pattern in this study. In case B, the first pilot injection was split into two injections, followed by a third pilot injection, and in case C, the first and third pilot injection quantities were reversed from those in case B.

Table 7 List of multiple pilot injection patterns

Case	Injection Pattern
A	Pilot Inj. 1 Pilot Inj. 2 Main Inj. -30° -20° -10° TDC
B	Pilot Inj. 1 Pilot Inj. 2 Pilot Inj. 3 Main Inj. -30° -20° -10° TDC
C	Pilot Inj. 1 Pilot Inj. 2 Pilot Inj. 3 Main Inj. -30° -20° -10° TDC

6.2 Calculation results

Figure 14 shows the start of the heat release rates calculated with the sector model. The heat release rate at TDC with injection pattern C is the highest of the three tested injection patterns. Injection pattern A has the lowest heat release rate at TDC among these three cases.

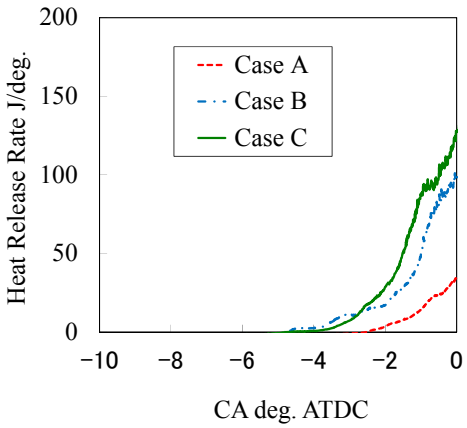

Fig. 14 Comparison of start of heat release rates calculated by with the sector model

6.3 Experimental results

Experiments were conducted to compare the injection patterns under a low ambient temperature condition for the purpose of confirming the calculation results. Figure 15 shows a comparison of the cycle-by-cycle heat release rates between injection patterns A and C. With injection pattern C, the heat release rate increased and the onset of heat release advanced. Figure 16 shows a comparison of the indicated mean effective pressure (IMEP) and the standard deviation of IMEP for 200 consecutive cycles between injection patterns A and C. As clearly seen in this figure, with injection pattern C, IMEP was improved markedly and also the standard deviation decreased, indicating that combustion was stabilized by the modified multiple pilot injection pattern.

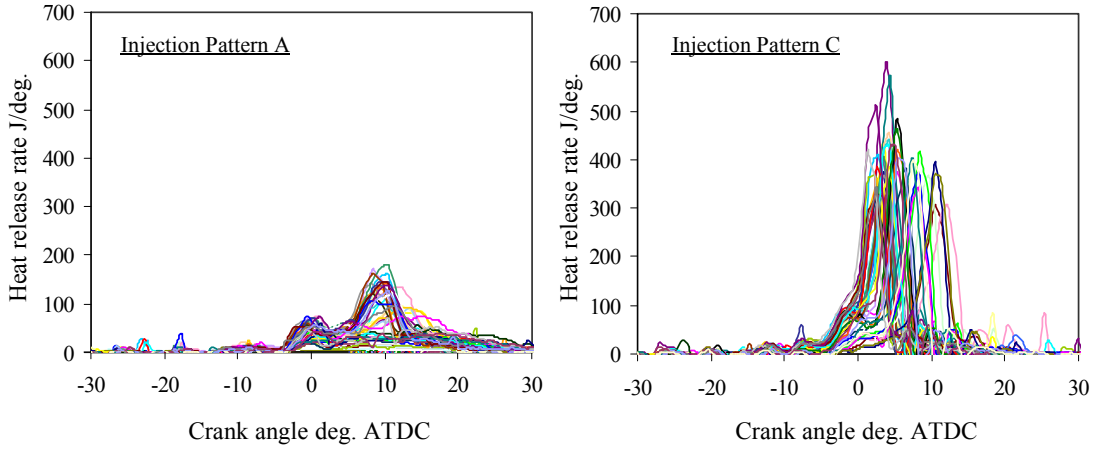

Fig. 15 Comparison of cycle-by-cycle heat release rates between injection pattern A and C

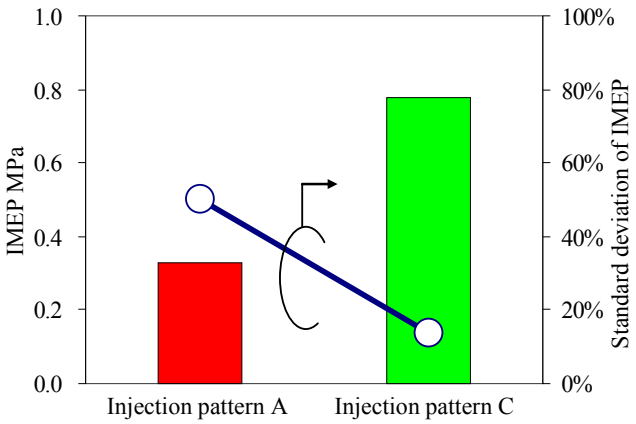

Fig. 16 Comparison of IMEP and standard deviation of IMEP between injection pattern A and C

6.4 Consideration of the mechanism

Because the calculation results were mainly focused on the glow plug, whole cells around one layer from the glow plug surface were averaged in terms of temperature and fuel mass. Figure 17 presents the calculation results for the average temperature and fuel mass as a function of the crank angle. Case C that had the largest fuel quantity in the first pilot injection showed the highest fuel mass around the glow plug near -25deg.ATDC. In the interval from -26 to -15deg.ATDC, the fuel mass around the glow plug was higher in case C that had three pilot injections than in case A. In particular, the temperature drop just after the start of the first pilot injection was mitigated because of the lower vaporization heat of the injected fuel. The temperature showed a similar trend by -15deg.ATDC but increased in the later part in Case C presumably because of the heat released by chemical reactions.

Because the calculated results indicated that multiple injections tend to improve the fuel mass and temperature distribution around the glow plug, experiments were conducted under the same operating conditions. Figure 18 shows the relationship between the average fuel mass and average temperature around the glow plug and in the interval from the start of the first pilot injection until the start of the main injection. As seen in this figure, the fuel mass and temperature were improved in the order of Case A, B and C, implying that combustion might be improved in this same order. The results were then correlated with the experimental IMEP data obtained with an actual engine. Figure 19 shows the relationship between the average temperature and average fuel mass predicted by simulation and the experimental IMEP results. As indicated in these figures, as the temperature or fuel mass increases, IMEP increases. Both the average temperature and fuel mass show a relatively linear relationship with IMEP.

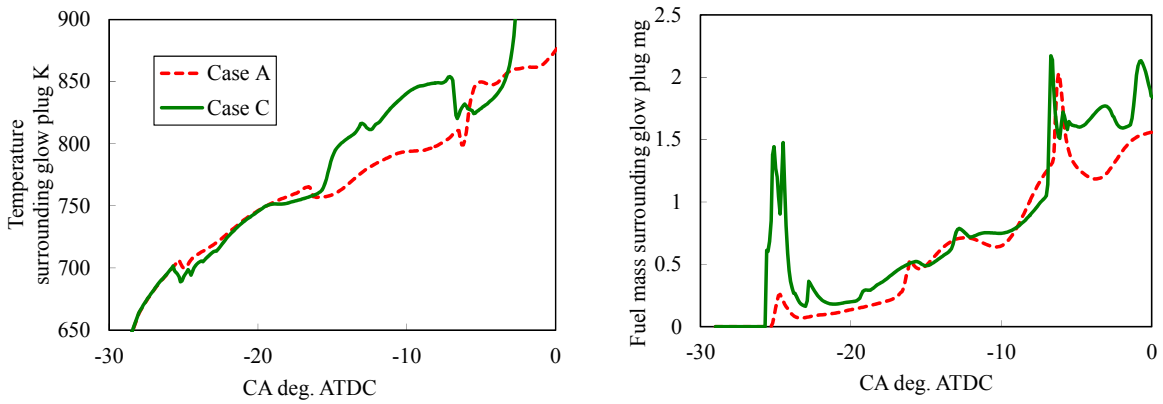

Fig. 17 Comparison of IMEP and standard deviation of IMEP between injection patterns A and C

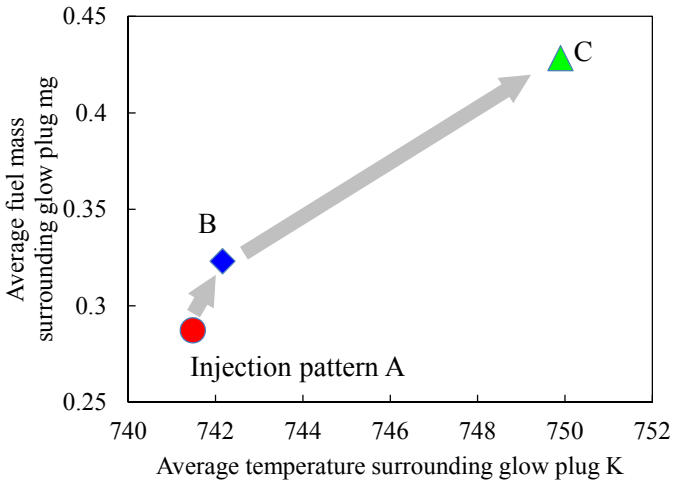

Fig. 18 Relationship between average temperature and fuel mass surrounding glow plug

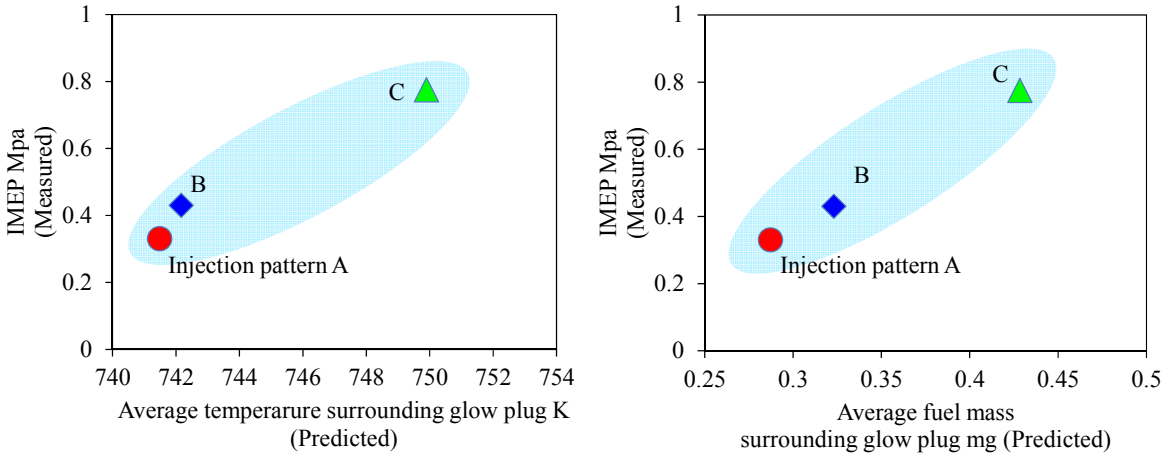

Fig. 19 Relationship between predicted temperature, and fuel mass and measured IMEP

Conclusions

Experiments and 3D CFD simulations were performed in this study to investigate the relationship between the air-fuel mixture distribution and multiple injection patterns. The 3D CFD simulation model was modified to predict combustion in low temperature conditions. The following conclusions can be drawn from the results obtained.

1. By optimizing the constants of the shell model using a genetic algorithm, the simulated ignition delay below 900K agreed well with the experimental results.
2. Simulated results for MB0% showed a linear relationship with the experimental data.
3. The simulation results revealed that ignition and combustion in low temperature conditions started near the glow plug due to the temperature increase caused by chemical reactions.
4. Combustion stability in the test engine was improved by applying an injection pattern suggested by the simulation results obtained in a parameter study.
5. IMEP and combustion stability can be improved by increasing the fuel mass and temperature surrounding the glow plug.

References

1. Kimura, S., Aoki, O., Kitahara, Y., Aiyoshizawa, E., "Ultra-Clean Combustion Technology Combining a Low-Temperature and Premixed Combustion Concept for Meeting Future Emission Standards," SAE Technical Paper 2001-01-0200, 2001

2. Kawamoto, K., Araki, T., Shinzawa, M., Kimura, S., Shifuya, M, "Combination of Combustion Concept and Fuel Property for Ultra-Clean DI Diesel," SAE Technical Paper 2004-01-1868, 2004
3. Ikeda, M., Mizoguchi, K., Kajiura, S., Yokoyama, J., Kawamoto, K., Kurozumi, N., "Outline and Clean Diesel Technologies of a New 2.5L Diesel Engine Complying with Euro5 Regulations," Preprints of JSAE Lecture Series, No. 152-10, 2010
4. Inagaki, K., Mizuta, J., Fuyuto, T., Hashizume, T., Ito, H., "Low emissions and high-efficiency diesel combustion using highly dispersed sprays with restricted in-cylinder swirl and squish flows (First Report), " Preprints of JSAE Lecture Series, No.88-10, 2010
5. Hashizume, T., Kawae, T., Kuzuyama, T., Kono, M., Inagaki, K., Tomoda, T., "Low emissions and high-efficiency diesel combustion using highly dispersed sprays with restricted in-cylinder swirl and squish flows (Second Report), " Preprints of JSAE Lecture Series, No.88-10, 2010
6. Koyama, T., Fujiwara, K., Nagae, M., Ito, H., Ohki, H., Tomoda, T., "Study of the Technology for Low Compression Ratio in Passenger Car Diesel Engines, " JSAE Paper No.20114505, 2011
7. Hatabu, A., Niwa, Y., Maruo, K., Deguchi, H., Terazawa, Y., "New Generation Clean Diesel Engine for Passenger Car, " Preprints of JSAE Lecture Series, No.75-12, 2012
8. Chartier, C., Aronsson, U., Andersson, O., Egnell, R., "Effect of Injection Strategy on Cold Start Performance in an Optical Light-Duty DI Diesel Engine, " SAE Paper 2009-24-0045, 2009
9. Walter, B., Perrin, H., Dumas, J.P., Laget, O., "Cold Operation with Optical and Numerical Investigations on a Low Compression Ratio Diesel Engine, " SAE Paper 2009-01-2714, 2009
10. Teraji, A., Imaoka, Y., Tsuda, T., Noda, T., Kubo M., and Kimura, S. "Development of a Time-scale Interaction Combustion Model and Its Application to Gasoline and Diesel Engines, " Proceedings of the Combustion Institute, Volume 32, Issue 2, pp. 2751-2758, 2009
11. Teraji, A., Tsuda, T., Noda, T., Kubo, M., Itoh, T., "Development of a Novel Flame Propagation Model (UCFM: Universal Coherent Flamelet Model) for SI Engines and its Application to Knocking Prediction," SAE Paper 2005-01-0199, 2005
12. Kong, S.C., Han, Z.W., Reitz, R.D., "The Development and Application of a Diesel Ignition and Combustion Model for Multidimensional Engine Simulation, " SAE Paper 950278, 1995
13. Dec, J.E., "A Conceptual Model of DI Diesel Combustion Based on Laser-Sheet Imaging," SAE Paper 970873 , 1997
14. Fujimoto, H., "Location of First Visible Flame of Diesel Spray, " JSME annual meeting 2006, Vol. 8, pp. 421-426, 2006
15. Eickhoff, H., Lenze, B., Leuckel, W., 20th Symp. (Int.) on Combustion, pp. 311-318, 1984
16. Peters, N. and Williams, F.A., AIAA 20th Aerospace Sciences Meeting, pp. 82-111, 1980
17. Peters, N., Laminar Diffusion Flamelet Models in Non-Premixed Combustion, Prog Energy Combust Sci, Vol. 10, pp. 319-339, 1984
18. Bouldier, P., Henriot, S., Poinsot, T., Baritaud, T., "A Model for Turbulent Flame Ignition and Propagation in Spark Ignition Engines, 24th ,Symp. (Int.) on Combustion, " The Combustion Institute, pp. 503-510, 1992
19. Meneveau, C., Poinsot, T., "Stretching and Quenching of Flamelets in Premixed Turbulent Combustion, " Combustion and Flame 86, pp. 311-322, 1991
20. Williams, F.A. "A review of some theoretical considerations of turbulent flame structure, " AGARD Conference Proceedings, No. 164, pp. II 1-1 to II 1-25, 1975
21. Halstead, M.P., Kirsch, L.J., Prothero, A., Quinn, C.P., "A mathematical model for hydrocarbon autoignition at high pressure, " Combustion and Flame, 1975
22. Ciezki, H.K., Adomet, G., "Shock-Tube Investigation of Self-Ignition of n-heptane-Air Mixture Under Engine Relevant Conditions, " Combustion and Flame, pp.421-433, 1993.
23. Tsurushima, T., "A new skeletal PRF kinetic model for HCCI combustion", Proceedings of the Combustion Institute, " Vol. 32, pp.2835-2841
24. Han, Z.Y. and Reitz, R.D. "Turbulence Modeling of Internal Combustion Model for Multidimensional Engine Simulations, " SAE Paper 950278, SAE Transactions, 104(3), 502－518, 1995
25. Beale, J.C. and Reitz, R.D., "Modeling Atomization Spray Atomization with the Kelvin-Helmholtz/Rayleigh-Taylor Hybrid Model, " Atomization and Sprays, Vol. 9, pp. 623-650, 1999
26. Ohmori, T., Kobori, S., "Measurements of Temperature Distribution in Thermal Boundary Layer at Combustion Chamber of Internal Combustion Engine", The 15th anniversary of the foundation of the Kanto branch of JSME, pp.269-270, 2009

Comparing accuracy and efficiency between a multi-zone model and artificial neural networks in dynamic simulations of PCCI diesel engine combustion for engine control

B. Jochim[1], R. Zweigel[2], M. Korkmaz[1], D. Abel[2] and H. Pitsch[1]

[1]Institute for Combustion Technology, RWTH Aachen University, Templergraben 64, D-52056 Aachen, Germany.

E-mail: bjochim@itv.rwth-aachen.de
Telephone: +(49) 241 80 97592
Fax: +(49) 241 80 92923

[2]Institute for Automatic Control, RWTH Aachen University, Templergraben 64, D-52056 Aachen, Germany.

Abstract. Low-temperature combustion concepts have received interest due to their potential of simultaneous reduction in nitric oxides, soot and unburned hydrocarbons. However, the successful implementation into internal combustion engines is hindered by very early combustion phasing resulting in high noise and lower engine efficiency. To overcome this, model-based control of the engine is required. That emphasizes the need for developing efficient but accurate models, which is particularly difficult due to the nonlinearity of the physical and chemical processes encountered in PCCI diesel engine combustion.
In this work, a recently developed efficient and accurate multi-zone model validated by experimental data obtained at stationary conditions, is utilized for transient simulation of PCCI diesel engine combustion. For this purpose, the multi-zone model describing the high-pressure combustion cycle from intake valve closure to exhaust valve opening is combined with a gas exchange model to account for the whole engine cycle. In this way, the model can be applied for transient simulations to assess its capability of capturing cycle-to-cycle variations. The results of the multi-zone model are compared to experimental data and to results obtained by an artificial neural network (ANN) implemented in the current combustion controller.
The control variables include indicated mean effective pressure (IMEP), combustion phasing (CA_{50}) and engine-out emissions of nitrogen oxides and unburned hydrocarbons. While the multi-zone model is not real-time capable, its accuracy is found to be very good. It captures the engine behaviour at dynamic operating conditions and reproduces the experimental data with satisfying accuracy. Even though the artificial neural net is faster, the multi-zone combustion model does not require exhaustive experimental data for training or calibration and allows for more detailed analysis. Thus, the multi-zone model proves to be an adequate simulation tool for description and analysis of cycle-to-cycle dynamics in the PCCI diesel engine.

Notation

A	*Area*
c_p	*Specific heat capacity at constant pressure*
D_z	*Diffusion coefficient, assumed identical for all considered chemical species*
h	*Enthalpy*
Δh_v	*Latent heat of vaporization*
h_{wall}	*Wall heat transfer coefficient*
m	*Mass*
$\dot{m}_{ik}$	*Mass exchange rate between zones i and k*
p	*Pressure*
$\dot{\rho}^s$	*Source term due to fuel vaporization*
$\dot{Q}_{wall}$	*Wall heat transfer*
t	*Time*
V	*Volume*

W *Molar mass*
x_α *spatial coordinate with α=x,y,z denoting the three Cartesian dimensions*
χ *Scalar dissipation rate*
Y_j *Mass fraction of species j*
Z *Mixture fraction*

1. Introduction

There is a strong demand to explore new combustion concepts capable of meeting the stringent future emission standards, such as Tier 2 Bin5 on the North American market or EURO VI on the European market. Due to its potential to simultaneously achieve high efficiency and low pollutant engine-out emissions, many engine researchers have investigated low-temperature combustion (LTC) processes. Applied to a diesel engine, it is frequently called Premixed Charge Compression Ignition (PCCI) or Premixed Compression Ignition (PCI) and has emerged as an interesting alternative to conventional diesel combustion in the part-load operating range [11, 16, 27]. It involves relatively early injection timings, high external EGR rates and cooled intake air, leading to a low-temperature combustion process with low nitrogen oxide (NO_x) and particulate emissions. A general review of LTC processes can be found in [7, 30]. However, in contrast to conventional diesel combustion, early direct-injection LTC combustion might lead to combustion phasing located before top dead centre (TDC), which often increases noise and reduces engine efficiency. Sophisticated model-based closed-loop control of the combustion process is one means to overcome this difficulty. Against this background, the paper deals with the validation of a reduced, stand-alone multi-zone combustion model for application in model-based control of the PCCI combustion process.

The most important characteristics for the operation of an internal combustion engine are the engine's load and its combustion efficiency. The former is directly dependent on the indicated mean effective pressure (IMEP). The latter can be characterized by the combustion phasing, which is defined by the crank angle, at which 50 % of the injected fuel mass is burned (CA_{50}). In an automotive application, the engine's load is set by the driver. With respect to CA_{50}, a set point can be determined, which is dependent on the operating condition and gives the best combustion efficiency. These two variables are the main focus of the controller to be developed. For influencing the process, the start of injection (SOI), the external exhaust gas recirculation (EGR) and the fuel mass injected (FMI) are suitable actors.

In the recent past, several efforts have been reported in the literature that aim at controlling engine combustion [4, 13, 14, 25]. The standard procedure for creating a controller includes the modelling part as the first step [1, 5, 24, 26]. Often these models differ in several aspects from models widely used for gathering a deeper understanding of combustion details, such as three-dimensional computational fluid dynamics (CFD) models [2, 6, 22, 23]. From the viewpoint of automatic control, the dynamics describing the dependency of the system's outputs (IMEP, CA50) on the actors (SOI, external EGR rate, and total fuel mass injected) are of highest priority. Nevertheless, model accuracy for stationary operating conditions is also important. Another requirement is an acceptable calculation speed, as it is usually applied in dynamic closed-loop simulations. Therefore, a novel multi-zone combustion model for the use in closed-loop control is developed. The stand-alone multi-zone model covers the nonlinear dependencies within the high-pressure part of the engine cycle and is extended by a physically inspired description of the gas exchange part of the engine cycle. For the use in closed-loop simulations, the system's dynamics have to be covered. For this reason, the combustion model is further extended by a dynamic air-path model. This novel procedure integrates the detailed knowledge from combustion simulation tools into closed-loop control and establishes a broad field of possibilities for testing completely new controlled process variables.

This paper is arranged as follows: Chapter 2 deals with the combustion modelling approach employed in the present investigation. The theory and assumptions underlying the multi-zone model and the derivation of the inter-zonal mixing model are reviewed. Chapter 3 contains the experimental and numerical setup. In the following Chapter 4, stationary validation of the multi-zone model is carried out and the integrated model composed of the stand-alone multi-zone model extended by a gas exchange model and the air-path model is validated against transient experimental data and compared to results obtained with an artificial neural network as combustion model. Finally, the conclusions and major findings from the paper are summarized.

2. Multi-zone combustion model

2.1 Multi-zone model

The multi-zone model employed in this work is based on a chemistry solver that uses multiple zero-dimensional reactors. The equations governing species mass fractions, temperature, and pressure change in the multi-zone chemistry code are given below:

$$\frac{\mathrm{d}Y_{ij}}{\mathrm{d}t} = \frac{1}{m_i}\sum_{k=1}^{n_z}\dot{m}_{ik}(Y_{kj} - Y_{ij}) + \frac{\dot{\omega}_{ij}}{\rho_i} + \frac{\dot{\rho}_{ij}^{s}}{\rho_i}, \tag{1}$$

$$\begin{aligned}\frac{\mathrm{d}T_i}{\mathrm{d}t} = {} & \frac{1}{m_i\bar{c}_{pi}}\sum_{k=1}^{n_z}\dot{m}_{ik}(\bar{h}_k - \bar{h}_i) \\ & - \frac{1}{m_i\bar{c}_{pi}}\sum_{j=1}^{n_{sp}}h_{ij}\sum_{k=1}^{n_z}\dot{m}_{ik}\left(Y_{kj} - Y_{ij}\right) \\ & - \frac{1}{\rho_i\bar{c}_{pi}}\sum_{j=1}^{n_{sp}}h_{ij}\dot{\omega}_{ij} + \frac{1}{\rho_i\bar{c}_{pi}}\frac{dp}{dt} \\ & + \frac{1}{\rho_i\bar{c}_{pi}}\sum_{j=1}^{n_{sp}}\dot{\rho}_{ij}^{s}\cdot\Delta h_{vj} \\ & - \frac{1}{m_i\bar{c}_{pi}}\dot{Q}_{\mathrm{wall},i}\,,\end{aligned} \tag{2}$$

$$\begin{aligned}\frac{\mathrm{d}p}{\mathrm{d}t} = {} & -\frac{p}{V}\frac{\mathrm{d}V}{\mathrm{d}t} + \frac{p}{V}\sum_{i=1}^{n_z}V_i\left(\frac{1}{m_i}\frac{\mathrm{d}m_i}{\mathrm{d}t} + \frac{1}{T_i}\frac{\mathrm{d}T_i}{\mathrm{d}t}\right. \\ & \left. + \bar{W}_i\sum_{j=1}^{n_{sp}}\frac{1}{W_j}\frac{\mathrm{d}Y_{ij}}{\mathrm{d}t}\right).\end{aligned} \tag{3}$$

In Eq. (1), Y_{ij} denotes the mass fraction of species j in zone i, and $\dot{\omega}_{ij}$ is the corresponding chemical source term. $\dot{\rho}_{ij}^{s}$ accounts for the source term due to fuel vaporization. It is zero for all species except for the fuel ($\dot{\rho}_{ij}^{s} = 0, j \neq \text{fuel}$). The first term on the right-hand side of Eq. (1) describes the mass exchange between the zones, where $\dot{m}_{ik}$ is the rate at which mass is transported between zones i and k. Here, n_z stands for the total number of zones. Similarly, in Eq. (2) the first and second term on the right-hand side represent the enthalpy exchange between zones due to enthalpy stratification between zones and due to species stratification between zones, respectively. Δh_{vj} denotes the latent heat of vaporization of species j and $\dot{Q}_{\mathrm{wall},i}$ is the wall heat transfer of zone i. In Eqs. (2) and (3), n_{sp} accounts for the number of species employed in the underlying chemical mechanism. The equation of state is used to derive Eq. (3), which solves for the pressure across the zones. Through this equation, all zones are thermodynamically coupled with each other.

Wall heat transfer is described as

$$\dot{Q}_{\mathrm{wall},i} = \sum_{l=1}^{n_{\mathrm{wall}}}A_{\mathrm{wall},l,i}\cdot h_{\mathrm{wall},l,i}(T_i - T_{\mathrm{wall},l})\,, \tag{4}$$

where n_{wall} denotes the total number of walls in the engine, $A_{\mathrm{wall},l,i}$ the area of wall l belonging to zone i, $h_{\mathrm{wall},l,i}$ the heat transfer coefficient of zone i to wall l, T_i the temperature of zone i, and $T_{\mathrm{wall},l}$ the temperature of wall l.

2.2 Mixing model

Mixing in the multi-zone model is accounted for by allowing the different zones to exchange mass and energy with each other, in addition to the interaction through the pressure. They exchange their scalar quantities, i.e. species composition and enthalpy, based on the rate at which they exchange their mass.

In previous works, Felsch et al. [10] have developed a multi-zone mixing model that was further applied by Jochim et al. [17]. In these publications, the mass exchange rate between adjacent zones $\dot{m}_{ik}$ was calculated according to:

$$\dot{m}_{ik} = r_{MB} \cdot A \cdot \frac{m_i + m_k}{(m_i \bar{c}_{pi} + m_k \bar{c}_{pk})} \cdot h_{wall}\,. \tag{5}$$

In Eq. (5), $\bar{c}_{pi}$ is the average heat capacity at constant pressure of zone i and the area A is computed from the volumes of the two neighboring zones. r_{MB} is a parameter that is adjusted to yield the desired level of mixing. However, in addition to the required tuning depending on the operating conditions, it is difficult to develop adequate models for the mixing parameter r_{MB} as it lacks physical meaning.

For these reasons, a physics-based approach for the description of the mixing was developed and implemented into the existing multi-zone model. In analogy to flamelet based combustion models that have been shown to be highly accurate simulation tools for diesel engine simulations [19, 20] it is constructed such that in the limit of an infinite number of zones the unsteady flamelet equations as in the representative interactive flamelet (RIF) model [3] are satisfied.

Similarly to the conservation equation of the mass fractions in the multi-zone model (Eq. (1)), the mass fractions in RIF are governed by:

$$\frac{\partial Y_j}{\partial t} = \frac{\chi}{2}\frac{\partial^2 Y_j}{\partial Z^2} + \frac{\dot{\omega}_j}{\rho}\,. \tag{6}$$

Here, Z is the mixture fraction and χ denotes the scalar dissipation rate, which is defined as

$$\chi = 2D_Z \left(\frac{\partial Z}{\partial x_\alpha}\right)^2, \tag{7}$$

where D_Z is the diffusion coefficient in mixture fraction space that is assumed identical for all considered chemical species. x_α denotes the spatial coordinate with $\alpha = x, y, z$ representing the directions in a three dimensional Cartesian coordinate system.

The mixing terms of the multi-zone model have to satisfy the respective terms in the RIF equations accounting for differential diffusion in mixture fraction space. The procedure is illustrated deriving the mass exchange rate $\dot{m}_{ik}$of the multi-zone model that determines the mass exchanged between zones i and k. The first terms on the right-hand side of Eq. (1) and Eq. (6) have to be equal:

$$\frac{1}{m_i}\sum_{k=1}^{n_z} \dot{m}_{ik}(Y_{kj} - Y_{ij}) \overset{\text{def}}{=} \frac{\chi}{2}\frac{\partial^2 Y_{ij}}{\partial Z^2}\,. \tag{8}$$

By considering a zone i exchanging mass with zones h and l, discretizing the right-hand side and reordering, one obtains:

$$\begin{aligned} &\frac{1}{m_i}\left[\dot{m}_{ih}\left(Y_{hj} - Y_{ij}\right) + \dot{m}_{il}\left(Y_{lj} - Y_{ij}\right)\right] \\ &\cong \frac{\chi_i}{2}\frac{Y_{hj}(Z_i - Z_l) + Y_{lj}(Z_h - Z_i) - Y_{ij}(Z_h - Z_l)}{\frac{1}{2}(Z_h - Z_l)(Z_h - Z_i)(Z_i - Z_l)} \\ &\cong \chi_i\left(\frac{Y_{hj} - Y_{ij}}{(Z_h - Z_l)(Z_h - Z_i)} + \frac{Y_{lj} - Y_{ij}}{(Z_h - Z_l)(Z_i - Z_l)}\right). \end{aligned} \tag{9}$$

From this equation, the mass exchange rates $\dot{m}_{ih}$ and $\dot{m}_{il}$ determining the mass fluxes between zone i and zones h and l, respectively, can be directly obtained to:

$$\dot{m}_{ih} = \frac{m_i \chi_i}{(Z_h - Z_l)(Z_h - Z_i)}, \quad \dot{m}_{il} = \frac{m_i \chi_i}{(Z_h - Z_l)(Z_i - Z_l)} \tag{10}$$

With these two terms, mixing between zone i and its two adjacent zones can be described. The mixing between the zones depends on the mass m_i of zone i, the resolution in mixture fraction space and the scalar dissipation rate χ_i.

2.3 Chemistry model

A major aspect in modeling engine combustion is the treatment of the chemistry. The advantage of using a zero-dimensional multi-zone model is that complex chemical mechanisms can be used. For the PCCI combustion simulations in this work, combustion chemistry in the multi-zone model is described by a detailed chemical kinetic mechanism that comprises 59 elementary reactions among 38 chemical species. This mechanism describes low-temperature auto-ignition and combustion of n-heptane, which serves as a surrogate fuel for diesel in these simulations. Furthermore, it accounts for thermal NO formation. The chemical mechanism for n-heptane was constructed by Peters et al. [21]. The NO-submechanism, which is part of the full mechanism, is the extended Zeldovich mechanism [12].

3 Experimental and numerical setup

3.1 Experimental setup

3.1.1 Engine

At the Institute for Combustion Technology at RWTH Aachen University, experiments were carried out with a 1.9l GM Fiat diesel engine. This engine is equipped with a second-generation Bosch Common-Rail injection system. The mounting of the engine on the test bench is shown in Fig. 1 and all relevant engine data are provided in Tab. 1.

A more detailed description regarding the engine, the test cell equipment, and the injection rate measurements can be found in Vanegas et al. [28].

3.1.2 Operating Conditions

The engine was operated at part-load conditions with single injection at a speed of 2000 rpm, an external EGR rate within almost 0 % up to 50 %, the fuel mass injected (FMI) varying between 8.5 and 17.5 mm^3 and the start of energizing (SOE) ranging from 10 to 50 deg crank angle (CA) before top dead center (bTDC). The external EGR rate was cooled before mixing with the fresh air in the intake section.

Table 1. GM Fiat engine specifications

Engine type	Four-cylinder research engine
Displacement volume	1900 cm^3
Bore	82.0 mm
Stroke	90.4 mm
Connecting rod length	145.0 mm
Compression ratio	17.5:1
Injection system	7-hole solenoid injector
Included spray angle	120.0 deg
Hole diameter	0.141 mm
Swirl number	2.5
Fuel	diesel

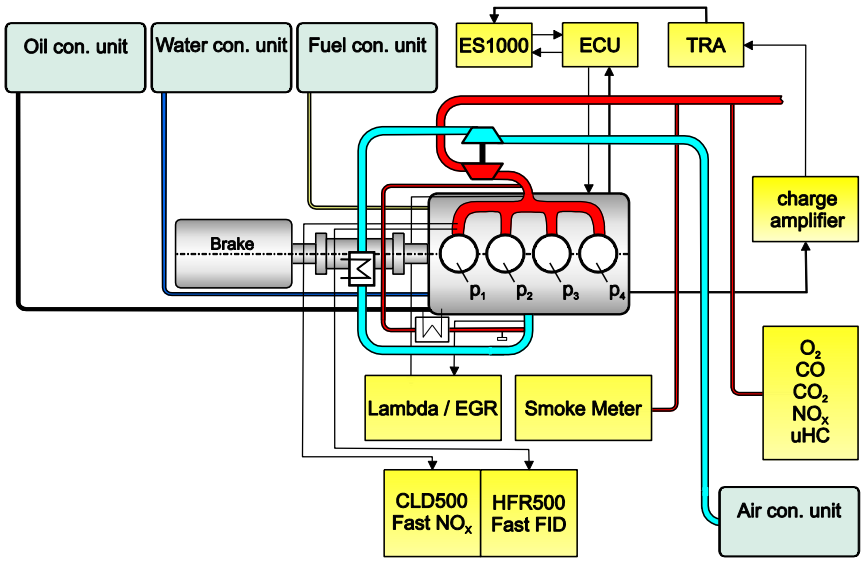

Fig. 1. Engine test bench

105 different operating points within this range were measured at stationary conditions. The rail pressure was was 750 bar for all different engine operating conditions. The engine operating conditions are summarized in Table 2.

Additionally, engine measurements at transient operating conditions were performed at a speed of 2000 rpm. The operation parameters SOE, FMI and EGR were changed independently and together within 10 and 45 deg CA bTDC, 12.5 and 17.5 mm^3 per cycle and 15 and 45 %, respectively. The overall data set comprises around 15000 cycles.

3.2 Numerical Setup

3.2.1 3D CFD RIF

Computations with the computational fluid dynamics (CFD) code AC-FluX interactively coupled with the representative interactive flamelet (RIF) model to account for combustion processes, were performed for selected engine operating conditions presented in section 4.1. All computations started from intake valve closure (IVC) at -165.6 deg CA aTDC and ended at exhaust valve opening (EVO) at 149.1 deg CA aTDC. In the first part of the CFD simulation, AC-FluX was run alone. For every operating condition, RIF was initialized at start of injection. The starting solution at IVC was initialized with pressure and temperature taken from the experiments. The internal EGR rate was assumed to be 5 %. The velocity field was initialized with a swirl number of 2.5.

Two different computational meshes were used throughout the simulations to provide an optimal computational mesh for any piston position. One grid was used for the compression phase and one for the combustion and expansion phase. This procedure allowed for rearranging the cells shortly before the beginning of the combustion event. In the computational mesh for the combustion and expansion phases, in comparison to the one for the compression phase, the mesh resolution in the bowl region was refined. For both meshes, a cell layer removal technique was applied in the cylinder region throughout the simulations. This was done in order to account for the compression and expansion of the grid cells along the cylinder axis due to the piston movement. The remap between both grids took place 5 deg CA before the injection event. There is no sensitivity on the results when advancing or retarding the remap of the solution.

Table 2. Engine operating conditions

Engine speed	2000 rpm
Rail pressure	750 bar
Fuel mass injected (FMI)	8.5, 11, 12, 13.5, 16 and 17.5 mm^3/cycle
External EGR rate	Between 0 % and 50 %
Start of energizing (SOE)	10, 20, 30, 40 or 50 deg CA bTDC

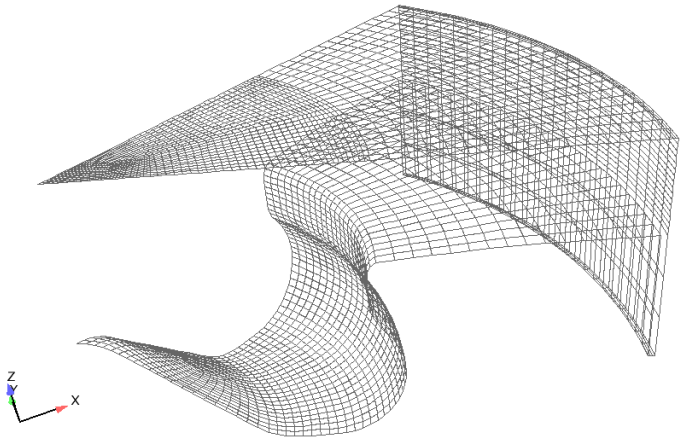

Fig. 2. Computational grid at -25.0 deg CA aTDC. Cyclic boundaries are removed for illustration purposes

An outline of the computational mesh for the combustion phase is given in Fig. 2. A sector grid representing 1/7th of the combustion chamber is used for the simulations, thereby taking advantage of the axial symmetry with respect to the placement of the nozzle holes. In Fig. 2, the cyclic boundaries are removed for the sake of a clear insight into the bowl. The mesh size was 52704 cells at top dead center (TDC). The wall temperatures were set based on experimental experience and held constant during the simulations. The spray model parameters were adjusted once and held unchanged for all additional simulations. The parameters used in this work are within the recommended parameter range proposed by Weber et al. [29].

3.2.2 0D Multi-Zone Model

For all engine operating conditions presented in section 4.1, computations were also performed with the reduced, stand-alone multi-zone model. For reasons of consistency, the initial conditions, start and end of simulation were held identical to the simulations carried out with the CFD-RIF approach. The multi-zone model was run with 10 zones.

The scalar dissipation rate χ is crucial for precise multi-zone model simulations as it determines the mixing between zones. For validation purposes, the scalar dissipation rate data was directly taken from CFD-RIF simulations for a selected number of simulations including variations of EGR, FMI and EGR. The influence of these operation parameters on the scalar dissipation rate is depicted in Fig. 3. Here, the scalar dissipation rate is shown as calculated in CFD-RIF. It is clearly visible that the injection timing has the strongest impact, as it influences the position and the magnitude of the maximum value. Moreover, the change of the maximum value is more distinct for changes in SOE as compared to changes in the injected fuel mass and external EGR.

To be able to simulate a larger number of cases, an appropriate model for the scalar dissipation rate is required to avoid an unfeasible number of CFD simulations. In order to do this, 120 generic CFD-RIF simulations were performed that included variations in start of injection from 10 to 50 deg CA bTDC, EGR from 10 to 50 % and FMI from 10 to 20 mm^3 per cycle. Additionally, the influence of inlet temperature and pressure was investigated.

Based on the achieved scalar dissipation rate data, an algebraic expression for the scalar dissipation rate of the following form was devised:

$$\chi = a\left(e^{-b\cdot CA^*} - e^{-c\cdot CA^*}\right). \tag{11}$$

Here, CA^* represents an offset crank angle position and a, b and c are parameters to be optimized using nonlinear optimization. Each parameter depends on the set variables SOE, FMI and EGR in the following form:

$$\begin{aligned} a = {} & a_1 + a_2 SOE + a_3 FMI + a_4 EGR \\ & + a_5 SOE\ FMI + a_6 SOE\ EGR \\ & + a_7 FMI\ EGR + a_8 SOE^2 \\ & + a_9 FMI^2 + a_{10} EGR^2 \\ & b = b_1, c = c_1. \end{aligned} \tag{12}$$

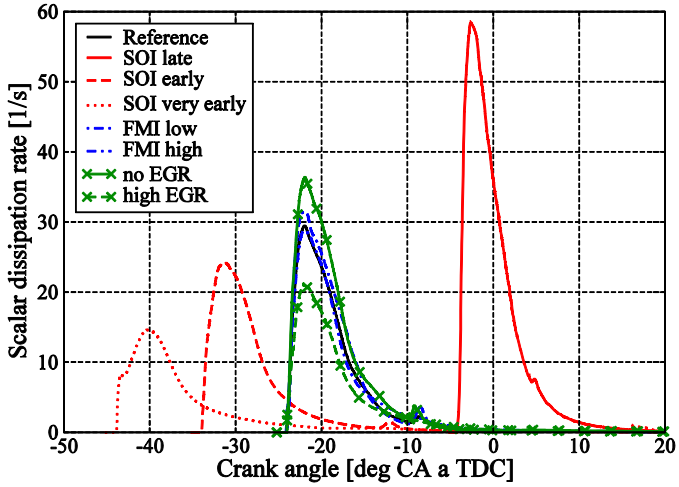

Fig. 3. Scalar dissipation rate as calculated in CFD-RIF for variations of start of energizing (SOE), fuel mass injected (FMI) and external exhaust gas recirculation (EGR)

The model complexity and the achieved model quality can be used as criterion for the number of free parameters. Functions with multiple free parameters were investigated. In the present work, an approach with 14 parameters was selected as the best trade-off between model complexity (number of parameters) and prediction capability (low model error).

The validity of the algebraic approach was tested by constructing different sets of models. For two cases, Fig. 4 depicts the optimized algebraic function. One uses 87 operating points for training the model and 19 for validation, the second one 19 for training and 87 for validation. For both cases almost equal results are found and compared to data of the scalar dissipation rate as computed in CFD-RIF simulations. An absolute error average of $0.82\ s^{-1}$ of the algebraic function compared with the simulation data is achieved. More detailed explanations referring to the development of this modeling approach may be found in [31].

3.2.3 Integrated model

A cascaded control structure is used for the PCCI diesel engine with an underlying, fast air path controller (10 ms) and an overlying, cycle-based combustion controller (60 ms at a speed of 2000 rpm). Its structure can be seen in Fig. 5 and is based on the work presented in [8]. Here, the task of the air path controller is to adjust a demanded EGR of the overlying combustion controller. This is achieved by manipulating the position of the EGR valve and the variable geometry turbine using a model-based predictive control (MPC) strategy. A physics-based model with additional, data-driven parts forms the non-linear, dynamic air path model used within the MPC. The combustion controller, on the other hand, controls combustion characteristic variables such as IMEP, CA_{50} and minimizes engine emissions. It uses a model based optimal controller with an internal neural network model of the combustion.

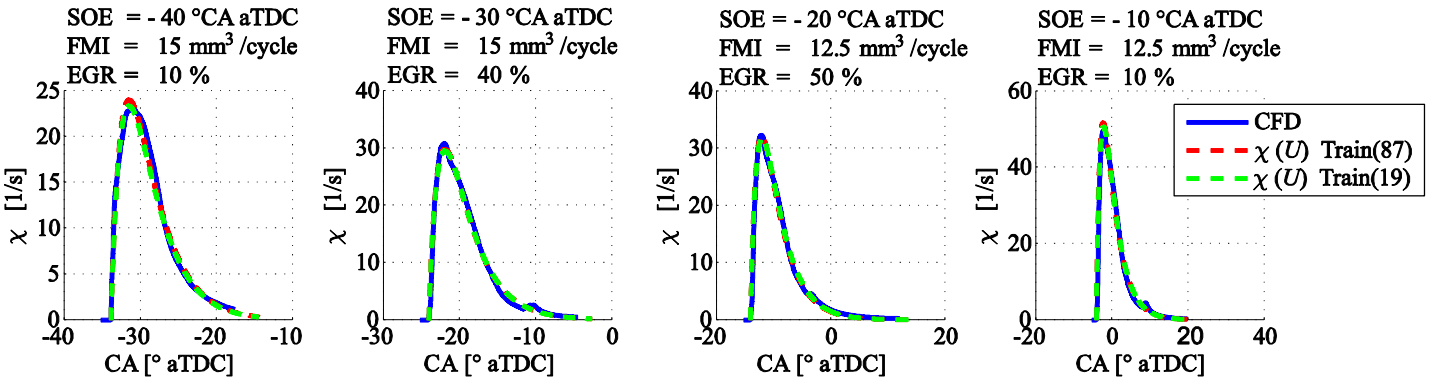

Fig. 4. Estimation capability of both models with 14 parameters

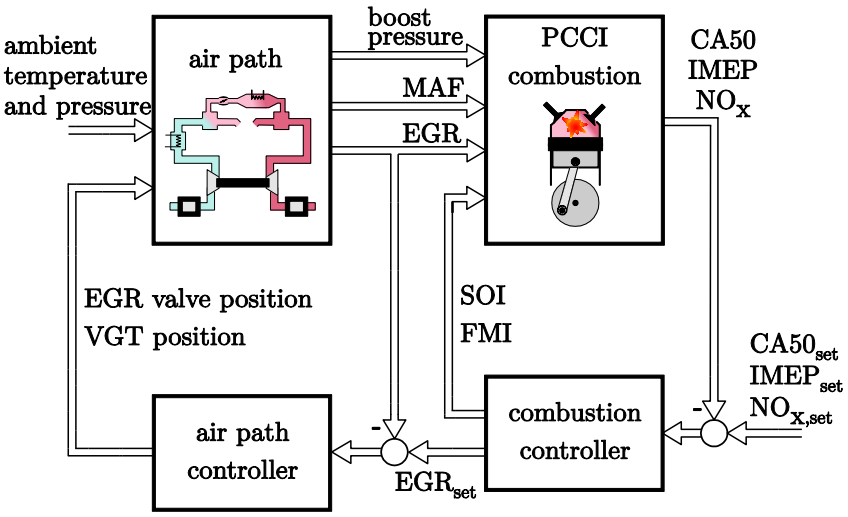

Fig. 5. Cascaded control structure of the diesel engine [8]

Until now, the model of the combustion controller is based on an artificial neural network, which requires substantial experimental data for parameterization and optimization. Therefore, an efficient and accurate combustion model has been developed here that incorporates the physical and chemical mechanisms for a precise description of the PCCI combustion. The aim of this paper is the validation of the multi-zone combustion model for application in a realistic virtual test bed environment.

The multi-zone combustion model describing the high pressure cycle of the engine is complemented by a mean value gas exchange model. It is physically inspired by pumping losses and introduced in [15]. For a more detailed outline of the model including its adjustment and validation, the reader is referred to [10]. Additionally, the engine air path is dynamically modelled. Thereby, the complete system dynamics are reproduced by the plant models of the air path and the combustion. Details about the air path model may be found in [9].

4 Results and discussion

In this section, the results obtained with the CFD-RIF code, the multi-zone model and the integrated model are presented and discussed by comparison to experimental data. First, results at stationary operating conditions are shown. Then, the capability of the multi-zone model to correctly calculate dynamic engine operation is investigated.

4.1 Stationary operating conditions

Of the 105 measured operating points, 14 were selected to validate the multi-zone approach. The selected operating points were chosen to represent SOE, FMI and EGR. In Fig. 6, results with both models as well as experimental data are depicted for varying start of energizing (SOE). The SOE varies between 10 and 50 deg CA bTDC with an increment of 10 deg CA. The injected fuel mass was held constant at 13.5 mm^3 per cycle while the external EGR was nearly constant at 25 %.

The experimentally observed trends for indicated mean effective pressure (IMEP), combustion phasing (CA_{50}), engine-out emissions of nitrogen oxide (NO_x) and unburned hydrocarbons (HC) are well captured with both models. However, some deviations can be observed with the multi-zone model. At the earliest injection timing, the IMEP is slightly overpredicted, NO_x emissions are too high and less HC emissions are obtained. At SOE 40, both NOx and HC emissions are again underestimated. This might indicate some insensitivity of the reduced combustion model with respect to early injection timings, but the overall agreement is still very well. Similar findings were obtained for variations in EGR and FMI that were reported in [18].

For further validation of the reduced multi-zone combustion model, simulations were carried out for all 105 operating conditions. For the calculation of the scalar dissipation rate, two different approaches were applied. The presented modeling approach shown in Eq. (10) (MZM mod) is compared to results with scalar dissipation rate data obtained by linear interpolation between the cases computed with CFD. The data used for the interpolation are identical with those employed for the optimization of the algebraic model.

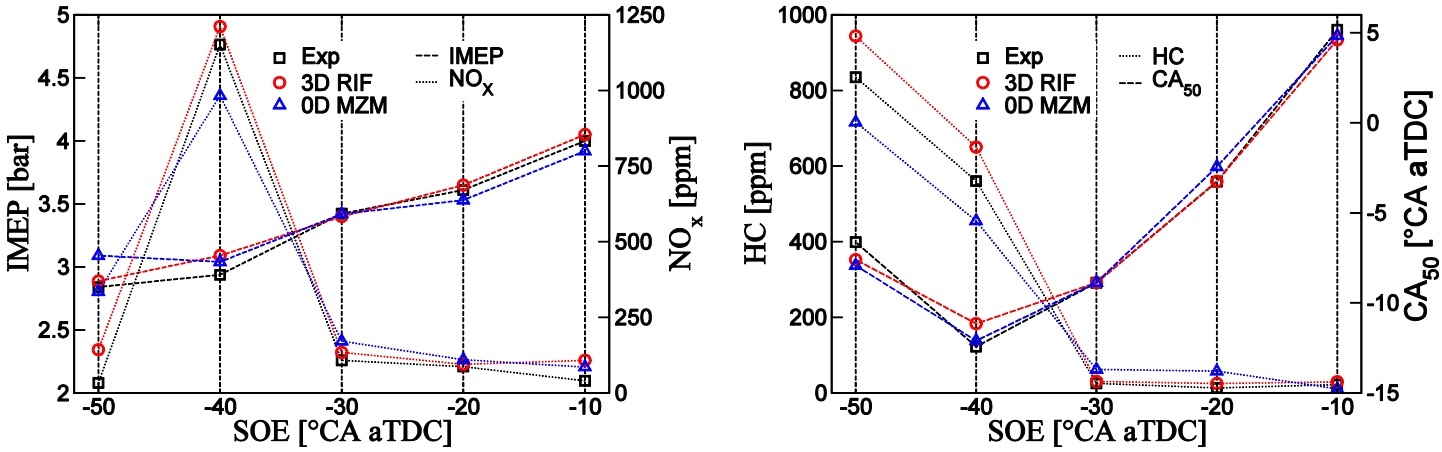

Fig. 6. Indicated mean effective pressure (IMEP) and nitrogen oxide emissions (NO_x) (left) as well as combustion phasing (CA_{50}) and unburned hydrocarbon emissions (HC) (right) for a variation in start of energizing (SOE) calculated with CFD-RIF and multi-zone model compared to experimental results

Exemplarily, results for IMEP and HC emissions for all 105 cases are shown in Fig. 7. For the IMEP, it is clearly visible that the multi-zone model captures the experimental trend with both approaches for computing the scalar dissipation rate very well. However, a few operating conditions exist, where noticeable differences occur. With respect to the HC emissions, more distinct differences are observed. For example, at injection timings of 50 and 40 deg CA bDC, the HC emissions are mostly underestimated.

To further assess the quality of the simulation results, the cumulative probability for obtained differences between models and experiment are evaluated. Fig. 8 shows the cumulative error probabilities for IMEP and CA_{50}. The errors for emissions of NO_x and HC are shown in Fig. 9. The data are calculated such that for each operating point, the difference between each model and experimental data is computed. Then, the cumulative probability for each difference is readily obtained.

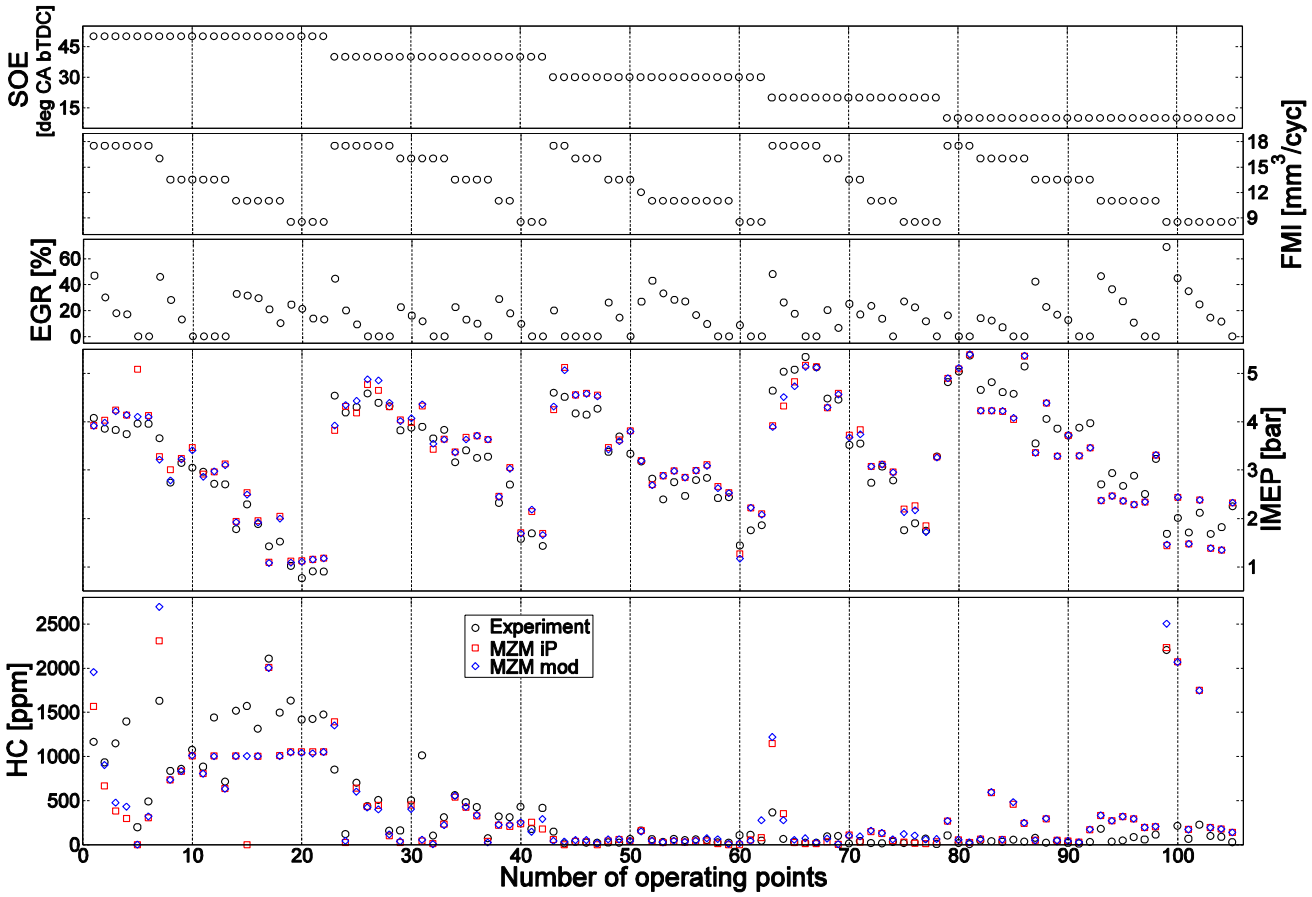

Fig. 7. Indicated mean effective pressure (IMEP) and unburned hydrocarbon emissions (HC) dependent on set variables start of energizing (SOE), fuel mass injected (FMI) and exhaust gas recirculation (EGR)

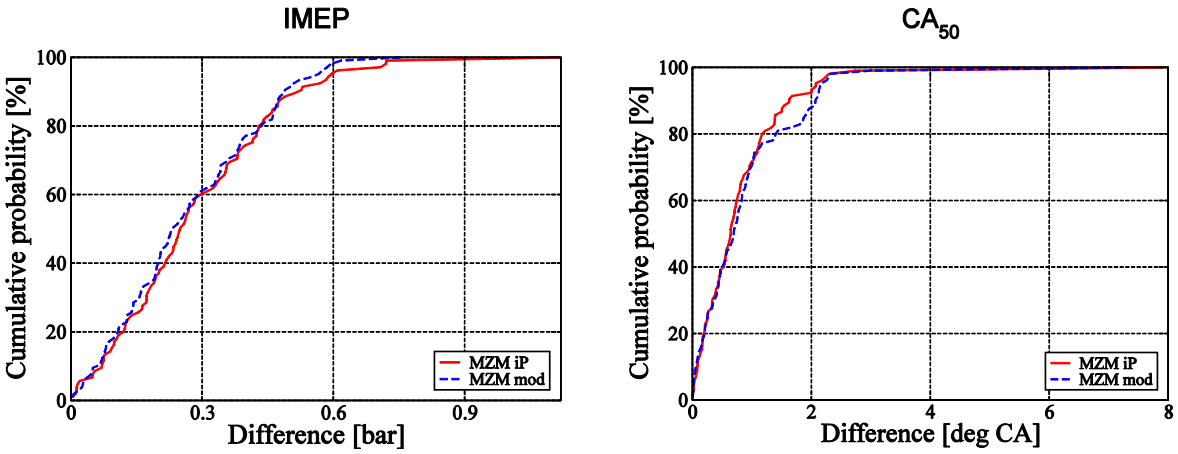

Fig. 8. Cumulative probability of differences between multi-zone model with algebraic model (MZM mod) and linear interpolation (MZM iP) and experimental data for indicated mean effective pressure (IMEP) and combustion phasing (CA_{50})

For the IMEP and the combustion phasing, sufficient results can be achieved. For more than 90 % of the simulations, the computed results for the indicated mean effective pressure differ from the experiments by less than 0.6 bar. Similarly, for the CA_{50} more than 60 % of the computed data deviate less than 1 deg CA from the experiments. For the combustion phasing, it is interesting to note that the results depend on the approach chosen for the computation of the scalar dissipation rate. While the approach based on interpolation achieves differences less than 2 deg CA for more than 90 % of the simulations, the modeling approach fares less successful.

Regarding the engine-out emissions of nitrogen oxide and unburned hydrocarbons, the deviations are more distinct. While this is partially attributed to a noticeable number of operating points with very high emission levels, further improvements will be subject to future work. For NO_x, 47 % of the simulations differ less than 100 ppm from the experiments and above 80 % less than 300 ppm. For HC emissions, comparable differences are observed, with 55 % of all simulations resulting in less than 100 ppm deviation and more than 80 % yielding less than 300 ppm deviation. Neither for NO_x nor for HC significant differences are observed due to the determination of the scalar dissipation rate.

Overall, due to the high measured emission levels up to 2500 ppm for NO_x and HC, the multi-zone model fares relatively well even for emission predictions and combined with very good agreement for IMEP and CA_{50}, it proves to be a reliable tool for PCCI diesel engine simulations at stationary operating conditions. Additionally, it can be concluded that the algebraic approach provides suitable scalar dissipation rate data as by application of this model, only slightly less convincing results are obtained for the combustion phasing compared to the interpolation method. Regarding IMEP and nitrogen oxide emissions, the algebraic approach even fares slightly more successful.

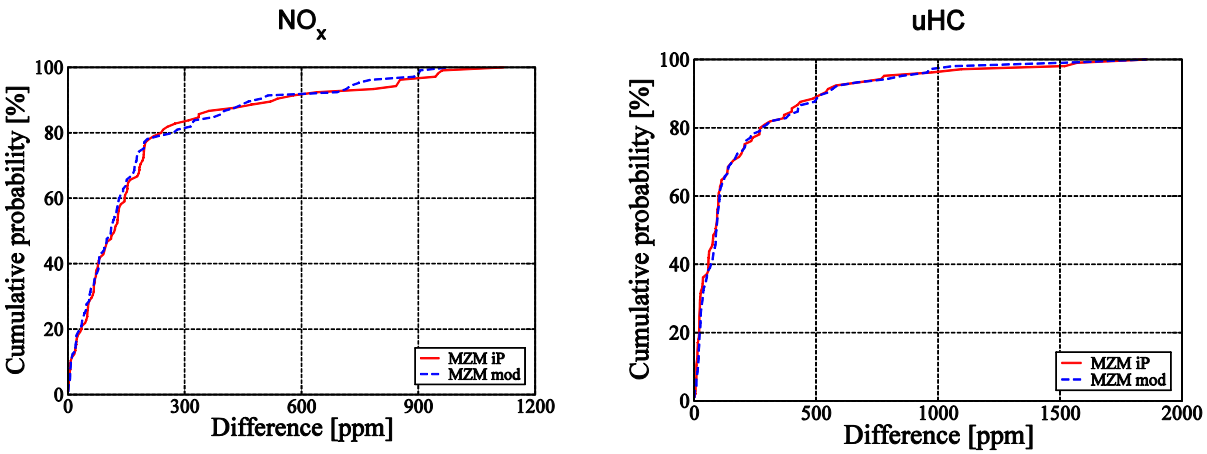

Fig. 9. Cumulative probability of differences between multi-zone model with algebraic model (MZM mod) and linear interpolation (MZM iP) and experimental data for emissions of nitrogen oxide (NO_X) and unburned hydrocarbons (HC)

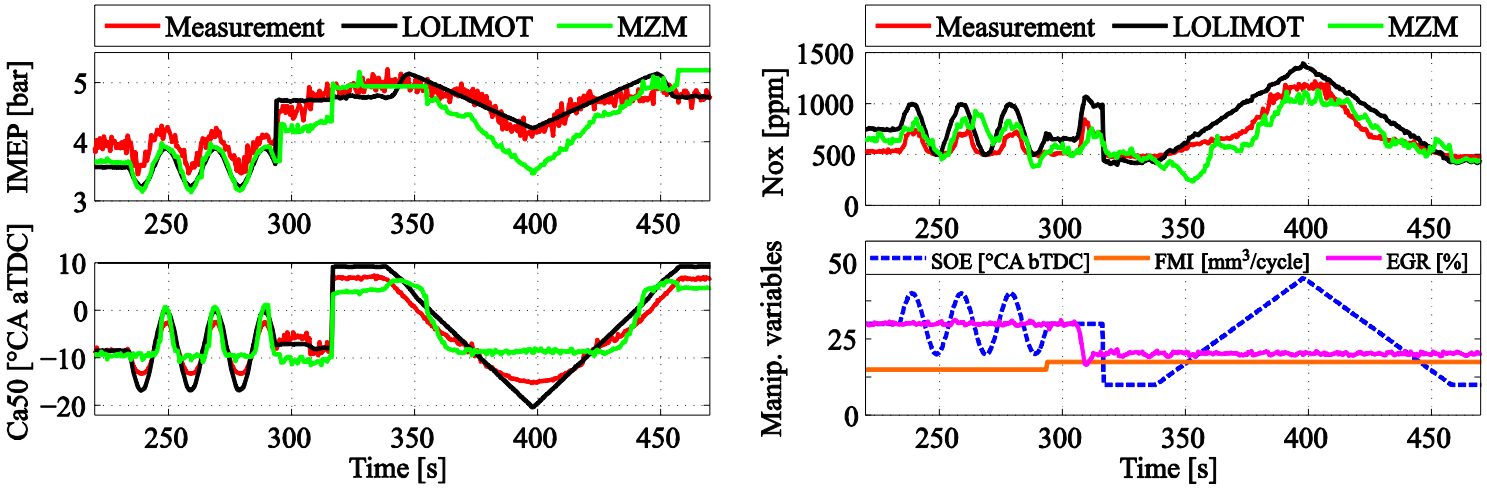

Fig. 10. Comparison of the LOLIMOT model and the multi-zone combustion model against measured engine data

4.2 Transient operating conditions

For application in diesel engine control, the multi-zone combustion model needs to be capable of representing transient engine operation with reasonable accuracy. While finally to be tested in controlled operation, in this paper its capability is tested by implementing the multi-zone model into the integrated model that also includes the mean-value gas exchange model and the air path model of the engine. In Fig. 10, a part of a simulation is shown that starts at 200 s and ends at 500 s. These 5000 engine cycles include one step change in EGR as well as FMI and multiple variations in SOE. On the lower right, changes of these operating parameters are depicted over time. The other three plots compare the results of indicated mean effective pressure, combustion phasing and nitrogen oxide emissions as obtained from engine measurements, artificial neural network and multi-zone model. The latter one uses the algebraic expression to compute scalar dissipation rate data. For the artificial neural network, a local linear model tree (LOLIMOT) with Gaussian activation function is chosen. LOLIMOT nets with 12 neurons were identified using 168 engine measurement points for model training and 36 points for model validation [31].

It can be seen that the prediction of both models is overall quite good. However, for the indicated mean effective pressure, the multi-zone model underestimates the experimental data around 400 s as opposed to the LOLIMOT model. Similar findings are obtained for the combustion phasing as the multi-zone model predicts retarded combustion phasing at around 400 s and for the sinusoidal changes in SOE between 200 and 300 s. At these timings, some differences are also observed for the LOLIMOT model that predicts too early combustion phasing. With respect to nitrogen oxide emissions, both models achieve reasonable results. Slightly better prediction capability can be attributed to the multi-zone combustion model that captures the trends at the sinusoidal changes in SOE between 200 and 300 s more precisely than the LOLIMOT model.

Conclusions

This paper proposes a new approach for the integration of detailed physical combustion knowledge into closed-loop simulations. Closed-loop simulations are a necessary and common tool in the development process of controllers. A reduced, stand-alone multi-zone approach was presented for modeling compression ignition combustion. It was first validated against experimental and CFD data for SOE, EGR and FMI variations with the scalar dissipation rate data directly taken from CFD simulations. Then, an algebraic approach to determine the scalar dissipation rate was presented that allowed for the simulation of 105 operating points to further validate the prediction capability of the reduced multi-zone model. Sufficient agreement between simulation and experiments was observed. Moreover, it could be shown that the algebraic approach to determine scalar dissipation rate data is suitable.

The stand-alone multi-zone model is capable of describing the PCCI combustion characteristics for the high-pressure part of the engine cycle. The controller to be developed shall actuate SOI, external EGR rate, and total fuel mass injected to control the IMEP of the whole engine cycle, the CA50 as well as engine-out emissions like nitrogen oxide and unburned hydrocarbons. For this pur-

pose, the multi-zone model was extended by a mean value gas exchange model that accounts for gas exchange losses. To capture engine dynamics, the combustion model is extended by an air-path model. The air-path model runs at 10 ms and provides inlet temperature, inlet pressure and actual EGR rate based on the set variables. This integrated model was validated against transient experimental engine data and the results were compared to those obtained with an artificial neural network. While some differences were observed, the overall agreement is found to be satisfactory. Therefore, it can be concluded that the multi-zone combustion model is capable of describing PCCI diesel engine combustion efficient and accurate at stationary and transient operating conditions. Thus, it allows for application in model-based engine control.

References

1 Albrecht A, Grondin O, Le Berr F and Le Solliec G (2007) Towards a Stronger Simulation Support for Engine Control Design: a Methodological Point of View. Oil & Gas Science and Technology - Rev. IFP: vol. 62: pp 437–456.

2 Barths H, Hasse C and Peters N (2000) Computational fluid dynamics modelling of non-premixed combustion in direct injection diesel engines. International Journal of Engine Research: vol 1: pp 249–267.

3 Barths H, Pitsch H, Peters N (1999) 3D Simulation of DI Diesel Combustion and Pollutant Formation Using a Two-Component Reference Fuel. Oil & Gas Science and Technology - Rev. IFP: vol. 54: pp 233–244.

4 Bengtsson J, Strandh P, Johansson R, Tunestål P and Johansson B (2006) Hybrid control of homogeneous charge compression ignition (HCCI) engine dynamics. International Journal of Control: vol 79: pp 422–448.

5 Bengtsson J, Strandh P, Johansson R, Tunestål P and Johansson B (2007) Hybrid modelling of homogeneous charge compression ignition (HCCI) engine dynamics - a survey. International Journal of Control: vol 80: pp 1814–1847.

6 Colin O and Benkenida A (2004) The 3-Zones Extended Coherent Flame Model (ECFM3Z) for Computing Premixed/Diffusion Combustion. Oil & Gas Science and Technology - Rev. IFP: vol. 59: pp 593–609.

7 Dec JE (2009) Advanced compression-ignition engines – Understanding the in-cylinder processes. Proc. Combust. Inst.: vol 32: pp 2727–2742.

8 Drews P (2011) Identifikation und modellbasierte Regelung des Dieselmotors mit Niedertemperatur-Verbrennung, RWTH Aachen University, PHD thesis.

9 Drews P, Hoffmann K, Beck R, Gasper R, Vanegas A, Felsch C, Peters N and Abel D (2009) Fast Model Predictive Control for the Air Path of a Turbocharged Diesel Engine. European Control Conference, Budapest, Hungary.

10 Felsch C, Hoffmann K, Vanegas A, Drews P, Barths H, Abel D and Peters N (2009) Combustion model reduction for Diesel engine control design. International Journal of Engine Research: vol. 10: pp 359-387.

11 Harada A, Shimazaki N, Sasaki S, Miyamoto T, Akagawa H and Tsujimura K (1998) The Effects of Mixture Formation on Premixed Lean Diesel Combustion. SAE Paper 980533.

12 Heywood JB (1988) Internal Engine Combustion Fundamentals. McGraw-Hill, New York.

13 Hillion M, Buhlbuck H, Chauvin J and Petit N (2009) Combustion Control of Diesel Engines Using Injection Timing. SAE Paper 2009-01-0367.

14 Hillion M, Chauvin J, Grondin O and Petit N (2008) Active Combustion Control of Diesel HCCI Engine: Combustion Timing. SAE Paper 2008-01-0984.

15 Hoffmann K, Drews P, Abel D, Felsch C, Vanegas A and Peters N (2009) A Cycle-Based Multi-Zone Simulation Approach Including Cycle-to-Cycle Dynamics for the Development of a Controller for PCCI Combustion. SAE Paper 2009-01-0671.

16 Iwabuchi Y, Kawai K, Shoji T and Takeda Y (1999) Trial of New Concept Diesel Combustion System - Premixed Compression Ignited Combustion. SAE Paper 1999-01-0185.

17 Jochim B, Felsch C, Drews P, Vanegas A, Hoffmann K, Abel D, Peters N and Pitsch H (2011) A multi-zone combustion model with detailed chemistry including cycle-to-cycle dynamics for diesel engine control design. Proc. Inst. Mech. Eng., Part D: vol. 225, pp 1235-1252.

18 Jochim B, Vanegas A, Pitsch H (2013) Development of an efficient and accurate multi-zone model for model-based PCCI Diesel engine control, VDI-Berichte: vol. 2161: 377–386.

19 Peters N (1984) Laminar Diffusion Flamelet Models in Non-Premixed Turbulent Combustion, Prog. Energy Combust. Sci.: vol. 10: pp 319–339.

20 Peters N (1986) Laminar Flamelet Concepts in Turbulent Combustion, Proc. Combust. Inst.: vol. 21: pp 1231–1250.
21 Peters N, Paczko G, Seiser R and Seshadri K (2002) Temperature cross-over and non-thermal runaway at two-stage ignition of n-heptane. Combust. Flame: vol. 28: pp 38–59.
22 Pope SB (1985) PDF methods for turbulent reactive flows. Prog. Energy Combust. Sci: vol. 11: pp 119–192.
23 Reitz R and Rutland CJ (1995) Development and testing of diesel engine CFD models. Prog. Energy Combust. Sci.: vol. 21: pp 173–196.
24 Shaver GM, Gerdes JC, Roelle MJ, Caton PA and Edwards CF (2005) Dynamic Modeling of Residual-Affected Homogeneous Charge Compression Ignition Engines with Variable Valve Actuation. Journal of Dynamic Systems, Measurement, and Control: vol 127: pp 374–381.
25 Shaver GM, Roelle MJ, Caton PA, Kaahaaina NB, Ravi N, Hathout J-P, Ahmed J, Kojić A, Park S, Edwards CF and Gerdes, JC (2005) A physics-based approach to the control of homogeneous charge compression ignition engines with variable valve actuation. International Journal of Engine Research: vol 6: pp 361–375.
26 Shaver GM, Roelle MJ and Gerdes JC (2006) Modeling cycle-to-cycle dynamics and mode transition in HCCI engines with variable valve actuation. Control Engineering Practice: vol. 14: pp 213–222.
27 Takeda Y and Keiichi, N (1996) Emission Characteristics of Premixed Lean Diesel Combustion with Extremely Early Staged Fuel Injection. SAE Paper 961163.
28 Vanegas A, Won H, Felsch C, Gauding M and Peters N (2008) Experimental Investigation of the Effect of Multiple Injections on Pollutant Formation in a Common-Rail DI Diesel Engine. SAE Paper 2008-01-1191.
29 Weber J, Spiekermann P and Peters N (2005) Model Calibration for Spray Penetration and Mixture Formation in a High-Pressure Fuel Spray Using a Micro-Genetic Algorithm and Optical Data. SAE Paper 2005-01-2099.
30 Yao M, Zheng Z and Liu H (2009) Progress and recent trends in homogeneous charge compression ignition (HCCI) engines. Prog. Energy Combust. Sci.: vol 35: pp 398–437.
31 Zweigel R, Albin T, Heßeler, F-J, Jochim B, Pitsch H, Abel D (2013) Greybox modeling of the diesel combustion by use of the scalar dissipation rate. Proceedings of the European Control Conference: pp 3961-3966.

Effects of in-cylinder non-uniformities on mixture preparation in a light-duty Diesel engine operating a light-load Partially Premixed Combustion strategy

F. Perini[1], K. Zha[2], D. Sahoo[2], S. Busch[2], P. C. Miles[2], R. D. Reitz[1]

[1]Engine Research Center, University of Wisconsin-Madison. Madison, WI, USA.

E-mail: perini@wisc.edu, reitz@engr.wisc.edu
Telephone: +(1) 608-263-2735

[2]Combustion Research Facility, Sandia National Laboratories. Livermore, CA, USA.

E-mail: kzha@sandia.gov, sbusch@sandia.gov, pcmiles@sandia.gov
Telephone: +(1) 925-294-1512

Abstract. The emissions, performance, and control of advanced combustion strategies such as Partially Premixed Combustion (PPC) is strongly affected by local fuel-air mixture preparation. In this work, we combine computational and experimental approaches to study the effects of combustion chamber geometric details and intake-induced non-uniformities in the temperature and velocity fields on the operation of a single cylinder, light-duty diesel engine operating in a slightly boosted, light-load partially-premixed compression ignition (PPCI) mode. A comprehensive computational model of the single-cylinder research engine was developed considering the complete intake and exhaust ducts and the plenums' geometries, as well as adjustable throttling devices used to obtain different swirl ratios. The in-cylinder flow predictions were validated against PIV measurements at different swirl ratio configurations, confirming the reliability of the RANS turbulence modeling approach in capturing ensemble-averaged flow field properties. A batch of multidimensional simulations was then set up to model corresponding mixture preparation experiments, faturing a non-reactive charge and a single, early injection pulse, under different swirl ratio and injection pressure conditions. Finally, the effects of geometric details on velocity field non-uniformity were studied, showing that, even if it is not possible to simulate differences arising from deposits or injector nozzle-by-nozzle non-uniformities, detailed multidimensional modeling can noticeably improve the predictability of local mixture quantities that affect ignition and pollutant formation.

1. Introduction

The success of advanced, fuel-efficient and environmentally sustainable combustion strategies such as reactivity-controlled compression ignition (RCCI), homogeneous-charge compression ignition (HCCI), partially-premixed compression ignition (PPCI), and gasoline direct-injection compression ignition (GDICI) will be determined by the possibility to control combustion development locally, in-cylinder. Much of the understanding developed by the study of these combustion modes has been made possible by advances in computer modeling, which in the last decade has allowed the incorporation of detailed chemistry calculations in engine CFD simulations [22]. The availability of detailed chemistry enabled accurate predictions of local ignition and in-cylinder pollutant emission sources, in simulations that already provided reasonably accurate estimates of the effect of phenomena such as wall boundary layers and of spray-turbulence interactions on mixture ignition and extinction.

However, comprehensive combustion calculations in realistic engine geometries need extensive computational resources, and predicted spray development typically shows significant mesh dependency. Thus, in the engine design phase, a sector mesh approach is still usually employed, where only one axisymmetric slice of the combustion chamber is modeled, assuming that both geometric and flow symmetries occur.

In this work, we implement and employ advanced, mesh-independent spray models in the Engine Research Center unstructured KIVA (KIVA-ERC) CFD solver for internal combustion engine

calculations, to study the effects of in-cylinder geometric and flow non-uniformities on mixture preparation in the Sandia National Laboratories (SNL) light-duty optical Diesel engine facility. Particle Image Velocimetry (PIV) of the flow field during intake and Planar Laser Induced Fluorescence (PLIF) of fuel tracer measurements were used to assess and compare the accuracy of the computational models in predicting local flow and compositional non-uniformities when using either a sector mesh or the full engine geometry representation.

2. Experimental Setup

All of the experiments were run in the Sandia National Laboratories optical Diesel engine facility. The experimental setup features a single cylinder engine, modified from a production GM 1.9L light-duty engine [6,8,18,20,23-24]. A schematic of the experimental configuration is reported in Figure 1. The engine features optical access through fused silica windows located at the top of the cylinder liner, as well as a fused silica piston which retains the full geometric details of the production piston. The only differences consist of a wider and deeper crevice region, which was designed to allow imaging within the piston bowl, and which slightly reduces the engine's effective compression ratio. The engine is equipped with a second-generation, 7-hole Bosch common-rail CRI2.2 fuel injector. The swirl ratio of the in-cylinder flow can be arbitrarily adjusted through throttle plates which are fitted in each of the intake ports, allowing for effective swirl ratios ranging from about Rs = 1.5 up to about Rs = 5.5. A summary of the engine's main geometric parameters and the operating conditions used for this study are reported in Table 1.

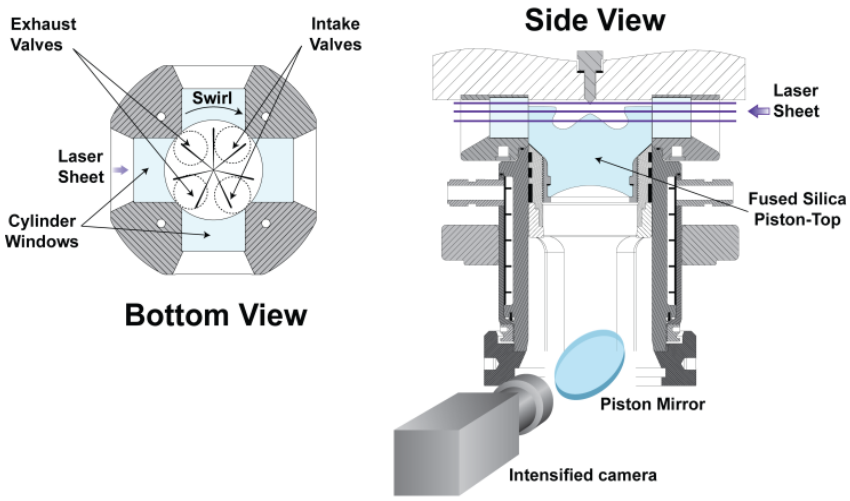

Fig. 1. Optical engine setup, including the three laser sheet locations and camera viewing direction.

Mixture preparation data for a non-reacting operating condition were obtained by planar laser-induced fluorescence (PLIF) [24,20]. Toluene was added as a fuel tracer to a PRF25 binary fuel mixture made of 25% iso-octane and 75% n-heptane. In order to realize non-reacting conditions, the engine was fed with a pure nitrogen charge. The nitrogen mass flow and intake temperature were calibrated in order to match the same near-TDC density and temperature of the corresponding operating condition with a reacting charge [24]. Ensemble averaged PLIF images of in-cylinder equivalence ratios were taken at four different swirl ratios: Rs = 1.5, 2.2, 3.5, 4.5, and at three horizontal planes within the combustion chamber: one (P1) located halfway within the squish region; one (P2) located at the bowl rim height, and a third one (P3) located deep within the piston bowl, at the height where it has its maximum radial extension. The plane positions varied due to changing piston position at every measurement timing, typically every 2.5 crank angle degrees from the start-of-injection and until TDC.

PIV measurements of flow patterns during the intake and compression strokes [28,29] were taken using borosilicate glass particles with 2 μm diameter, every 15 crank angle degrees during the intake and compression strokes. Measurements were taken at three horizontal planes located at fixed distances from the fire-deck, namely dz = 10.0, 13.5 and 17.0 mm.

Table 1. Engine and Experimental Setup details

Engine specifications	
Bore x stroke [mm]	82.0 x 90.4
Unit displacement [cm^3]	477.2
Compression ratio	16.4 : 1
Squish height at TDC [mm]	0.88
Bosch CRI2.2 Injector parameters	
Number of holes	7
Included angle [deg]	149
Nozzle diameter [mm]	0.14
Fuel properties for mixture preparation studies	
Composition [mole fractions]	75% nC_7H_{16}
	25% iC_8H_{18}
Fluorescent tracer [mass fr.]	0.5% C_7H_8
Equivalent Cetane Number [-]	47
Operating conditions	
Intake charge composition	100% N_2
Intake pressure [bar]	1.5
Intake temperature [K]	300.0
Engine speed [rpm]	1500
Injected fuel mass [g]	0.0088
Start of injection [deg aTDC]	-23.3
Rail pressure [bar]	860
Swirl ratio [-]	1.5, 2.2, 3.5, 4.5

3. Computational Setup

Two computational models, employing either a sector mesh featuring one seventh of the combustion chamber, as adopted in previous studies [7,14,17], or a full engine geometry, including the intake and exhaust ports and pressure-damping vessels as used in the experiments [16], were built. Both models were run using a new, unstructured implementation of the KIVA-ERC code, similar to the finite volume KIVA-4 code [25].

3.1 Spray model implementation

The code was extensively bug-fixed and many computational efficiency improvements were introduced to handle large grids and large numbers of species efficiently.

The ERC-developed spray models were implemented, with a focus on computational efficiency and on the possibility to handle unstructured grids. The spray models included the hybrid Kelvin-Helmholtz/Rayleigh-Taylor breakup model, with Levich's breakup distance concept [3]; the unsteady gas-jet theory model for velocity field estimation in the under-resolved near-nozzle region [1]; a grid-independent collision model featuring deterministic collision parameter estimation and extended collision outcomes [12]; and a computationally improved version of the discrete multi-component vaporization model by Torres *et al*. [26]. A similar spray model setup has been shown to provide almost grid-independent prediction of spray drop sizes and jet penetration histories [27].

This model setup was improved by the introduction of dynamic parcel storage allocation to reduce the number of spray model parameters. In the new configuration, the 'blob' injection model [25], which models the initial liquid jet core as a train of 'blobs', with diameter equal to the effective orifice diameter, injects the exact number of blobs such that each computational parcel only includes one blob. Note that, after breakup occurs, a computational parcel typically tracks the behavior of an equivalent cloud of spray drops, which size distribution is modeled in terms of an equivalent Sauter Mean Radius (SMR). Then during runtime, as parcels undergo breakup, collisions, and vaporization,

and thus increase in number, the parcel storage size is updated based on the current requirements. The standard KIVA approach requires the user to specify a desired (and typically not large) number of parcels, which each contains more than one blob, introducing a further source of under-resolution in the spray.

Finally, the fuel drop drag model was improved by introducing a more accurate and fully analytical formulation of a sphere's drag coefficient [11], suitable for Reynolds numbers up to $Re = 2 \cdot 10^6$, which features all surface boundary layer regimes. The model was also extended with a Mach number effect estimation through a multiplier which is computed efficiently as a function of the Mach and Reynolds numbers [2] using Bezier interpolation. In the simulations, the RNG k-epsilon turbulence model [10] was used, while thermo-chemistry properties were evaluated using the SpeedCHEM chemistry solver [15] and the ERC reaction mechanism for Primary Reference Fuels (PRF) [21].

3.2 Engine model

Both the sector and full engine computational grids have been validated in previous studies: the sector mesh [7,14] for partially-premixed compression ignition (PPCI) and pilot injection mixture preparation [17], and the full mesh [16] for PIV flow measurement experiments [19], respectively. Both grids feature an average cell resolution of 0.7 mm in the combustion chamber near TDC, which leads to a total of 92850 and of 682091 cells at BDC, respectively.

A representation of the cross-sectional discretization for both grids is reported in Figure 2. The simplified geometry allowed the sector discretization to be extremely smooth, and the cell layers to be axisymmetrically rotated, while in the full geometry a body-fitted approach was employed. Also, Figure 2 shows how the effective squish height at TDC used in the sector mesh can deviate significantly from the actual, local squish height due to the non-even piston squish surface, which includes valve cut-outs, and due to the presence of a non-negligible volume fraction within the valve recesses. All of these factors deteriorate the sector model's accuracy in capturing the amount of flow being directed towards the interior of the combustion chamber from the squish region, as the piston approaches TDC.

The full mesh retains all piston and head geometric details, including valve cut-outs on the piston surface, valve recesses on the head, as well as the correct crevice size for the optical piston, which is slightly thicker and significantly deeper than the corresponding metal production piston [6]. Wide usage was made of O-grid structures: these are blocking structures useful to correctly discretize near-wall regions in circular shapes, where the kernel of the circular structure is occupied by a square block, and four other blocks are connected to each of its edges, filling the space up to the circular shape, and being inter-connected at 45-degree diagonals. O-grid structures were used to match all round and cylindrical shapes in the domain, including liner, valves, seats, ports, and piston bowl, to avoid badly skewed cells at all the relevant wall surfaces and thus achieve optimal wall boundary modelling. Specific attention was devoted to modelling the squish region, enclosed between the cylinder head and a virtual surface representing the piston crown when at TDC. In this region, a total of 10 cell layers was used, to achieve the same resolution as in the sector mesh, and to guarantee appropriate resolution of the flow structures during valve movement. The same layer thickness was used for the valves and valve seats, where eight more layers were used.

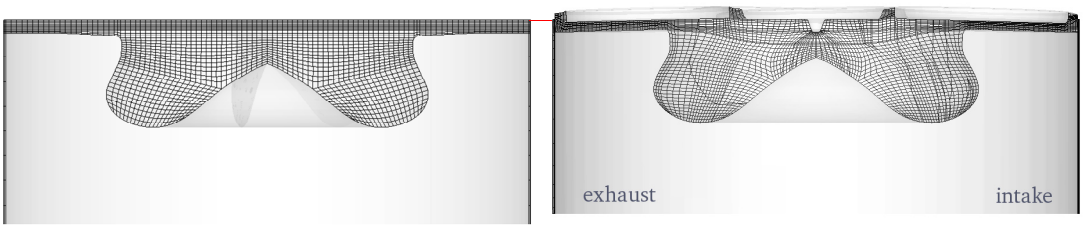

Fig. 2. Comparison between sector (left) and full engine mesh (right) at TDC

The same O-grid approach used for the valves was also applied to the injector protrusion region, which could thus be introduced in the engine model (shaped according to the injector drawings and a measured protrusion value of 1.85 mm). In this way, the near-nozzle region could be modelled using a homogeneous and axisymmetric discretization, meant to reduce, if not completely avoid, mesh dependency effects on predicted jet-to-jet differences in the spray simulation.

Also, the computational domain for the full engine mesh, which already included both intake and exhaust ports, was improved by incorporating the pressure damping vessels at the outlets, as reported in Figure 3. Thanks to the availability of time-resolved intake and in-cylinder pressure measurements, all flow and mixture preparation studies were initialized at exhaust valve opening (EVO), so that the simulation of the complete exhaust and intake strokes allowed proper flow and turbulence development.

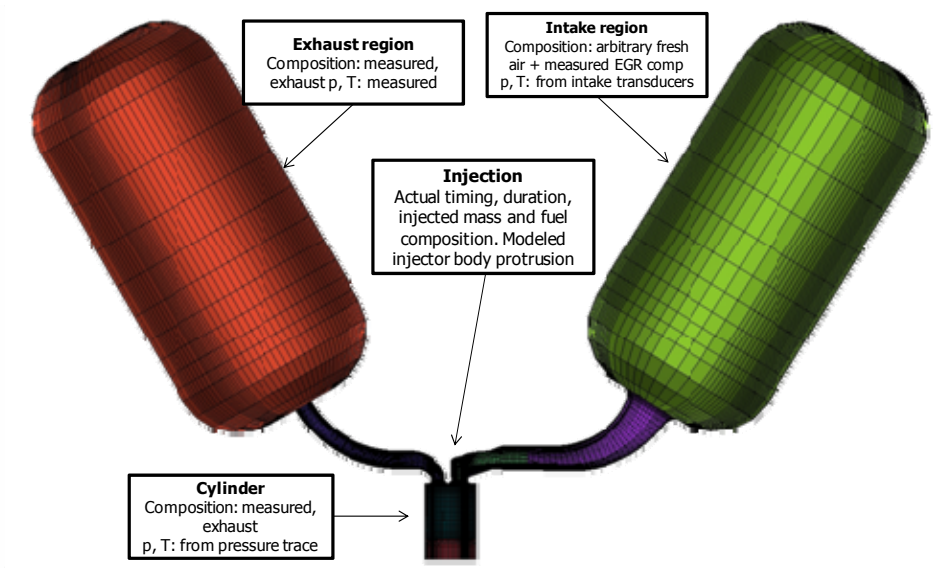

Fig. 3. Overview of the full engine geometry simulation setup

3.3 Swirl generation modeling

The optical engine in this study features a swirl control device (Figure 4) placed immediately upstream of the in-head portions of the intake ports, and downstream of the intake runners [13]. This device contains two ducts having the same cross-sectional shape as the intake ducts, where two throttle plates, which have a vertical rotation axis, are placed. Both plates can be fixed at arbitrary rotations by means of a series of pins, that allow for complete port throttling control.

A structured plate meshing strategy was adopted to accomplish the plate modelling in the intake ducts, as reported in Figure 4. A simplified representation of the plates was introduced in the ports, by deactivating one layer of cells in either the streamwise or the crosswise direction, and rotating them up to the requested orientation angle. In this way, it was possible to maintain a block-structured, hexahedral mesh discretization that allows for accurate wall boundary treatment, at the price of a slight simplification in the plate shape.

In a detailed swirl modelling study [16] it was seen that this plate model is able to capture in-cylinder swirl trends well for a wide variety of plate orientations. Minor deviations from what was seen in the experiments occurred at plate angles between 50 and 70 degrees and led to underpredicted swirl by not more than about 20%. These are the conditions where the throttle model features maximum cell distortion.

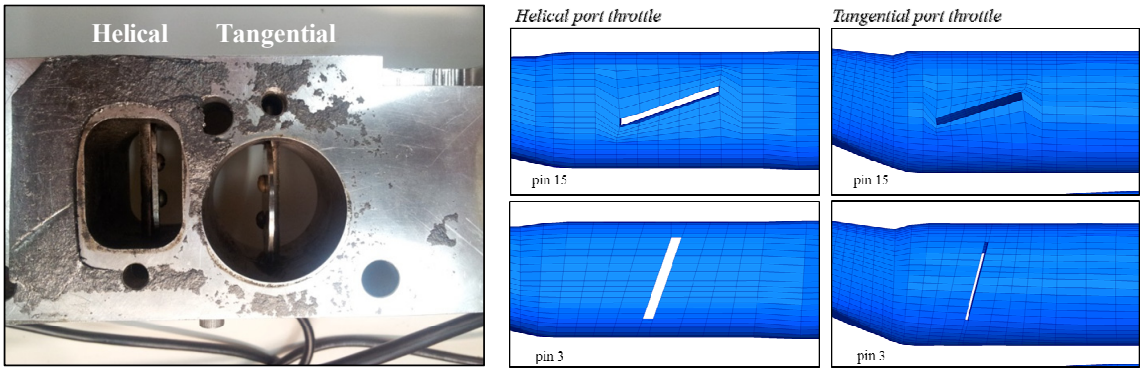

Fig. 4. Details of the swirl plates, and corresponding port mesh distortion strategy.

The in-cylinder flow structures at IVC for the four swirl ratios used in this study are reported in Figure 5. As the figure shows, the different swirl values obtained using different throttling strategies also lead to noticeably different in-cylinder flow structures.

The baseline configuration features Rs = 2.2, and both throttle plates are completely open. Here, the in-cylinder flow configuration is determined by port design, as significant swirling velocities are seen to enter the combustion chamber with a characteristic eddy length of the order of the intake valve diameter. At the same time, most of the large, cylinder-bore-scale momentum enters the combustion chamber from the tangential port, but with locally smaller velocity magnitudes at the crank angle shown.

Both configurations with higher swirl ratios were achieved by only throttling the helical port. This corresponded to having almost only one active intake port, thus changing engine breathing, but at the same time removing the smaller-scale intake swirl velocity components that partially oppose the large-scale flow entering from the tangential port. Both of these strategies are seen in Figure 5 to lead to significantly more solid-body-like vortex structures in-cylinder, and also significantly larger velocities within the bowl region, which may be relevant for increasing the efficiency of mixing in that region later in the cycle [9].

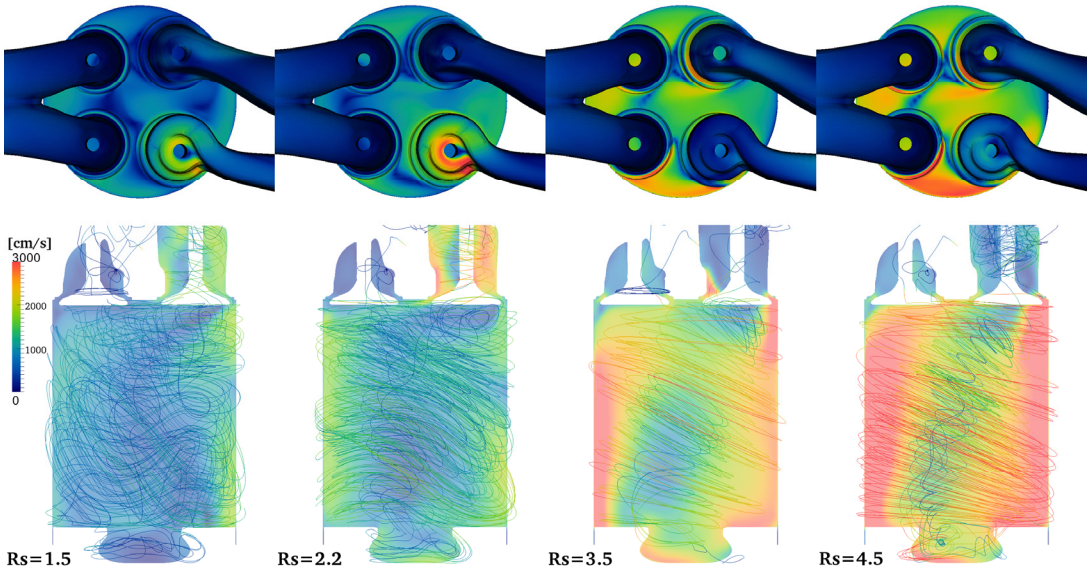

Fig. 5. Differences in predicted velocity field structures at BDC during the intake stroke. Velocity magnitudes (top) in the ports and near cylinder head; (bottom) at vertical planes intersecting the intake valves, also showing velocity streamlines.

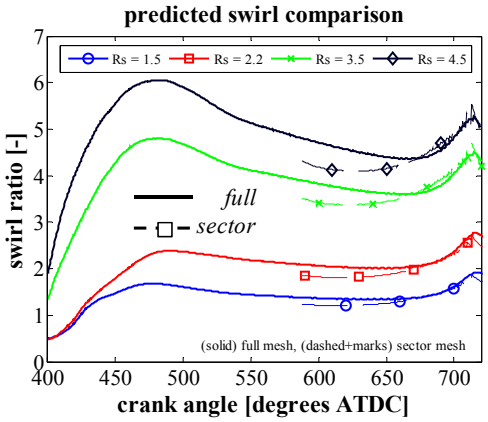

Fig. 6. Comparison between predicted in-cylinder swirl ratios with full (solid) and sector (dashed, marks) meshes

On the contrary, the lowest IVC swirl ratio was obtained by throttling both intake ports. The helical port was partially throttled by 20 degrees, and the tangential port throttled by 60 degrees [13]. The limited throttling of the helical port led to the significant swirl velocity components generating eddies at the intake valve scale. However, lack of significant large-scale flow entering from the tangential port led to a final vortex structure which is not very coherent and which still contains significant vertical velocity components.

In order to transfer the flow information into the sector mesh simulations, it was necessary to calibrate the IVC swirl profile with an 'effective' swirl ratio value. This was due to the fact that the axisymmetric mesh representation quickly destroys flow non-uniformities. Furthermore, azimuthal momentum conservation is enforced. Thus, the swirl ratio predicted with a sector mesh at the end of the compression stroke was observed to be significantly higher than the swirl ratio predicted with the full engine geometry, even when the same value was initialized at IVC. In order to have comparable results in terms of flow properties when injection occurs, the IVC swirl ratio value was calibrated at each swirl condition in order to match the near-TDC swirl ratios predicted by the full geometry calculation. This led to initializing the sector simulations at IVC with swirl ratios Rs = 1.236, 1.856, 3.502, 4.303, respectively.

4. Results

4.1 Flow study

The full geometry engine model was able to capture intake swirl ratios and near-TDC averaged tangential velocity profiles well, when compared to flow bench and PIV measurements [16]. However, the previous experiments had been used to provide suitable initialization data for sector mesh simulations, and did not provide sufficient insight into the development of the complex in-cylinder flow structures, and on the effects they have on fuel-air mixing.

Thus, current PIV experimental efforts [28,29] on the light-duty optical engine are focused on understanding the role of non-uniform, port- and piston-induced flow structures on fuel-air mixing and combustion development in the engine. Preliminary experimental data from the baseline Rs = 2.2 swirl configuration were used to assess the validity of the model, and to study the structure of the intake flow. It should be noted that in these experiments, the same swirl ratio as the baseline case [4] was achieved with a slightly different throttling strategy, that featured partial throttling of the helical port. The same configuration was used for the corresponding simulations.

Figures 7 to 9 summarize comparisons between predicted and measured velocities at three horizontal planes placed in the upper part of the combustion chamber, at distances dz = 10.0, 13.5, 17.0 mm from the fire-deck. The measurements were taken for a range of crank angles during the induction

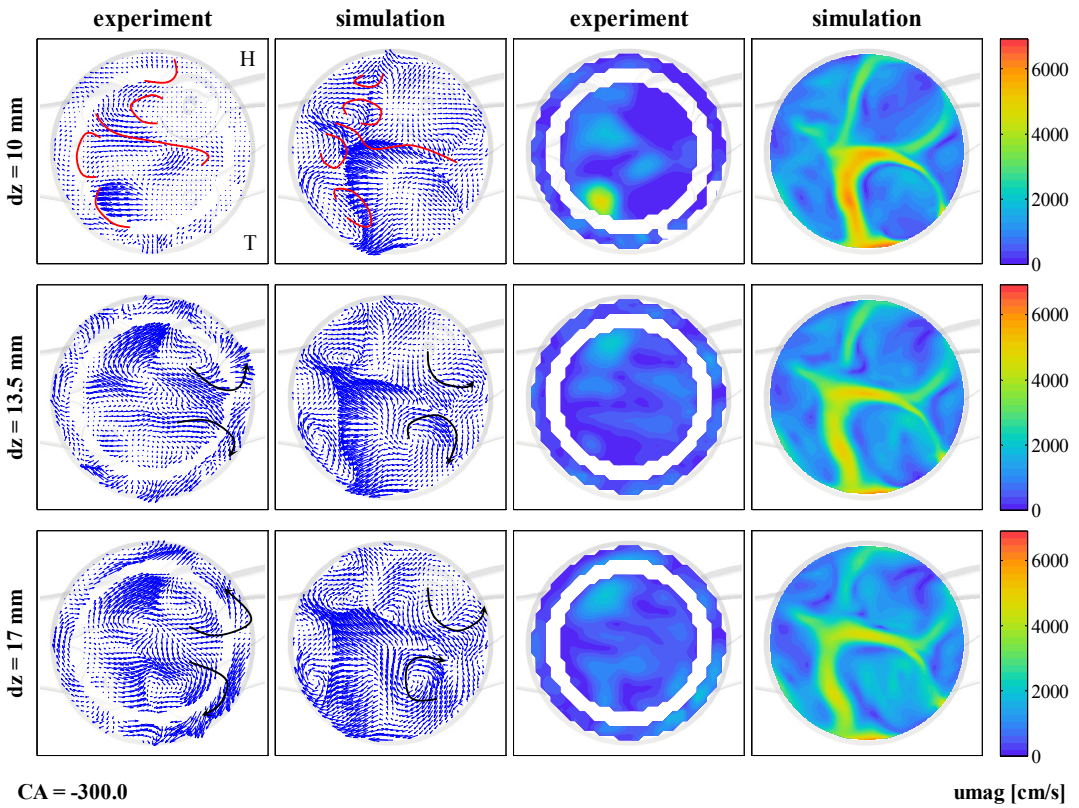

Fig. 7. Comparison between predicted and measured velocity vectors (left) and magnitudes (right, in cm/s) at the three PIV measurement planes, CA = 300 degrees bTDC.

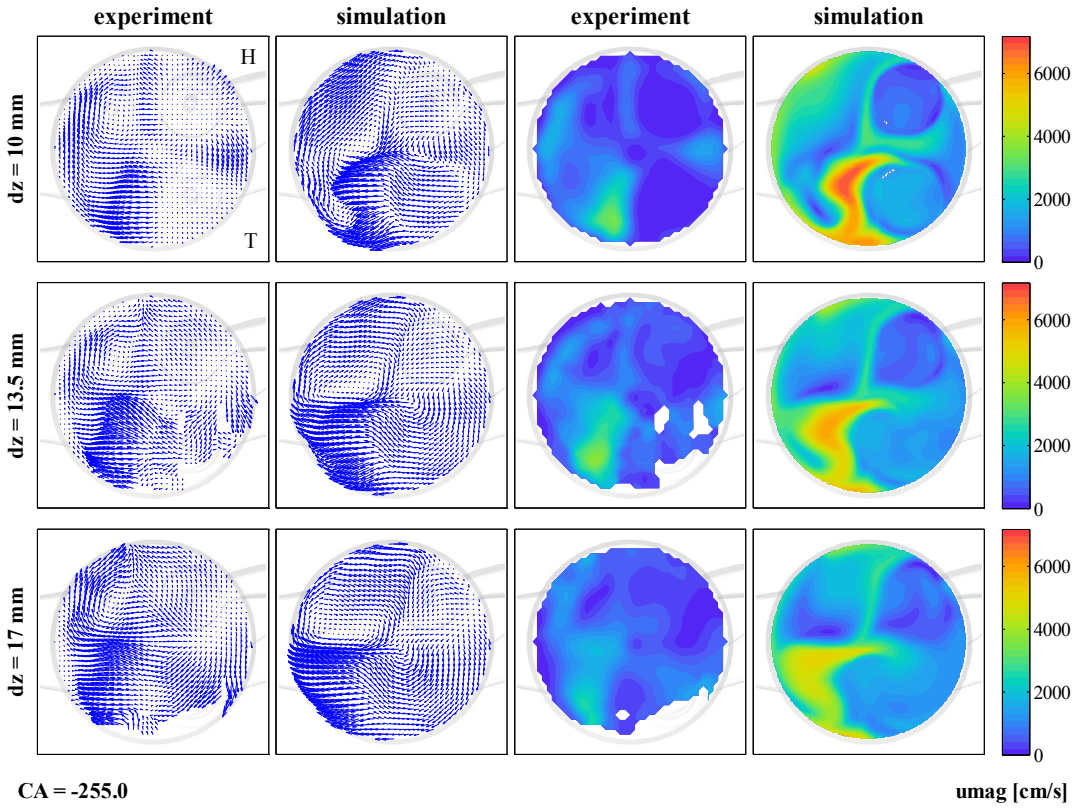

Fig. 8. Comparison between predicted and measured velocity vectors (left) and magnitudes (right, in cm/s) at the three PIV measurement planes near maximum valve lift, CA = 255 degrees bTDC

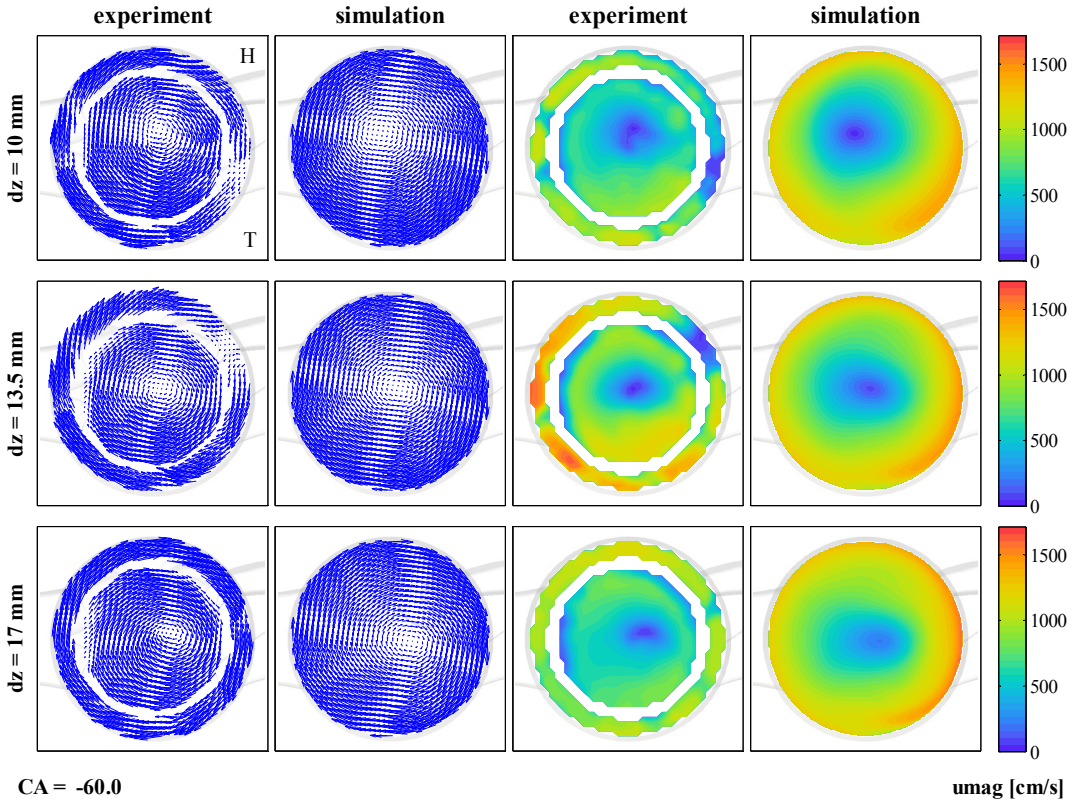

Fig. 9. Comparison between predicted and measured velocity vectors (left) and magnitudes (right, in cm/s) at the three PIV measurement planes after IVC, CA = 60 degrees bTDC

stroke, where the position of the optical piston, the intake valves and the laser sheet did not cause either loss of information or extreme signal noise. For the sake of brevity, we only show a few significant crank angles: CA = -300, -255, -60 degrees aTDC, which represent typical flow conditions after intake valve opening (IVO), near maximum intake valve lift, and after intake valve closure (IVC).

In the early intake flow of Figure 7, the simulation shows a 'momentum wall', displaced almost axially between the intake and the exhaust ports, due to the intake flow from either valve, which pushes towards the exhaust side, causing formation of four distinct vortex structures in the region below the exhaust valves (highlighted in red in the Figure). The same recirculation structures can be seen in the experiment too, even if more weakly defined, as stronger momentum from the tangential port is unbalancing the flow more towards the upper half of the plane. Interestingly, both the experiment and the simulation show that, as the horizontal section is moved downwards, it is possible to notice the formation of two counter-rotating vortices (highlighted in black in Figure 7) behind the wall formed by the intake flow, below the intake valves. These structures are formed by momentum transfer from the region with higher pressure, near the 'momentum wall', and the near-wall region behind the valves, following a mechanism which is evidently not much different than what happens around aircraft wings.

When approaching maximum valve lift, as in Figure 8, the intake flow is more developed and it is possible to recognize clearer similarities between the experimental measurements and the simulation, both in flow structure and in velocity magnitudes. First, the formation of stronger velocity components at the outlet of the tangential intake valve (lower-right corner) fosters the generation of a cylinder-bore-scale large eddy, which has already traveled for almost half of the circumferential extent of the cylinder bore, as witnessed by the large tangential velocity components present near the liner in the second, upper-left quadrant of the plane. Both measurement and simulation also show how the flow entering through the helical port, which has a well-defined eddy size of the order of the valve diameter, is also getting deviated into the main-stream large-scale eddy within these planes. This leads to the formation of a stagnation region below the upper left exhaust port.

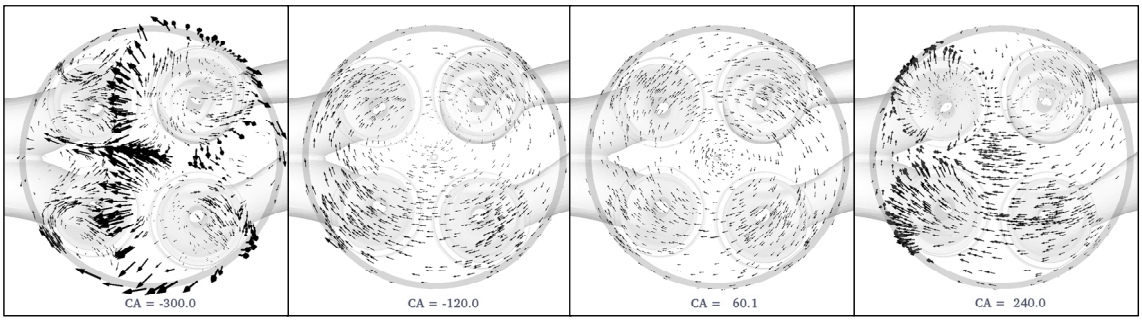

Fig. 10. Distinct flow regimes during the cycle. Crank angles (left to right): -300, -120, +60, +240 aTDC

After IVC, as shown in Figure 9, no intake flow is occurring, and the velocity field structure within the combustion chamber gradually rearranges itself into a unique, large-scale vortex, whose swirl center is not axial with the cylinder but has a precessive movement and a vertical tilt, which ultimately reflects the flow non-uniformity.

Four different regimes were seen as the major flow structure types occurring during the engine cycle. These regimes are summarized in Figure 10. The first one represents flow during intake. Intake velocities enter the combustion chamber with strong vertical components, and the momentum ratio between the tangential and the helical port is mostly determined by the throttling strategy. Whatever the ratio, both ports contribute to the formation of a definite 'momentum wall' which initially splits the combustion chamber in half – the part below the exhaust valves is pushed towards the liner, and thus recirculation regions form. The part below the intake valves sees the formation of two eddies having the size of the valves, set into motion by the pressure difference introduced by the intake flow.

The second flow regime in the engine starts to form close to IVC, when a cylinder-bore-scale vortex forms and gradually absorbs all of the residual non-vortex structures. As a result, the vortex center tilts within the combustion chamber, and exhibits a precessing movement.

The third flow regime is established after TDC, during the expansion stroke. In this case where no spray events occur, most of the momentum non-uniformities have dissipated, and the flow now shows an axisymmetrical vortex structure.

Finally, when the exhaust valves open, and flow starts entering the exhaust ports, residual swirling velocity components are small. Thus, an almost uniflow scavenging is established, with the main motion direction from the intake to the exhaust valve region.

4.2 Mixture preparation study

The code was used to study mixture preparation in the presence of a single-pulse injection, typical of a Partially Premixed Combustion (PPC) strategy, at all four swirl ratios. The operating condition represented a 1500 revs/min, slightly boosted, low-load case, with 3 bar indicated mean effective pressure (IMEP), and an EGR ratio of 55%. The injection profile for the 8.8 mg fuel was measured experimentally [5] for the same PRF fuel blend used in the engine experiments. The mixture preparation experiments were run using a non-reacting, pure nitrogen gas composition, and showed that most of residual engine-out unburned hydrocarbon (UHC) and carbon monoxide (CO) emissions which occur in the combusting cases are due to overly-lean mixtures forming, especially in the squish region and in the central, upper part of the combustion chamber, and not undergoing complete oxidation. Figures 11 to 16 compare the sector simulation results with the mixture preparation experiments [20,24].

In the squish plane (P1), as reported in Figures 11-13, the simulations reveal two distinct phenomena affecting the vapor jet development. In the central part of the cylinder, the jet is twisted by the swirling velocities into a hook-like structure, which is more significant the stronger the swirl ratio. This structure evolves throughout the cycle. Early after the end of injection (Figure 11) it still appears to be

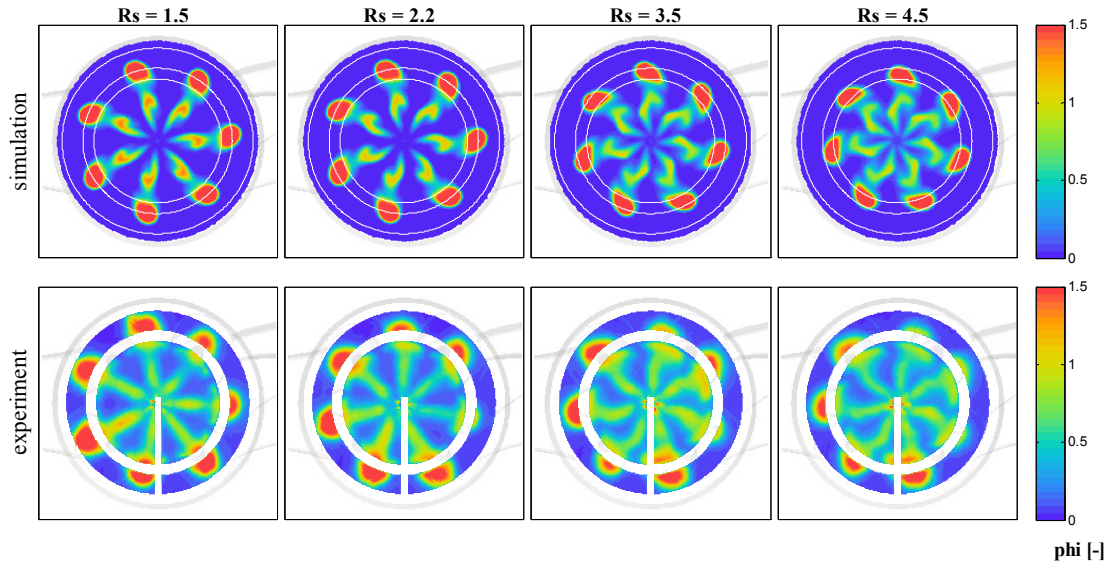

Fig. 11. Squish plane (P1) PRF25 mixture preparation comparison. Swirl ratios: 1.5, 2.2, 3.5, 4.5; CA = -15.0.

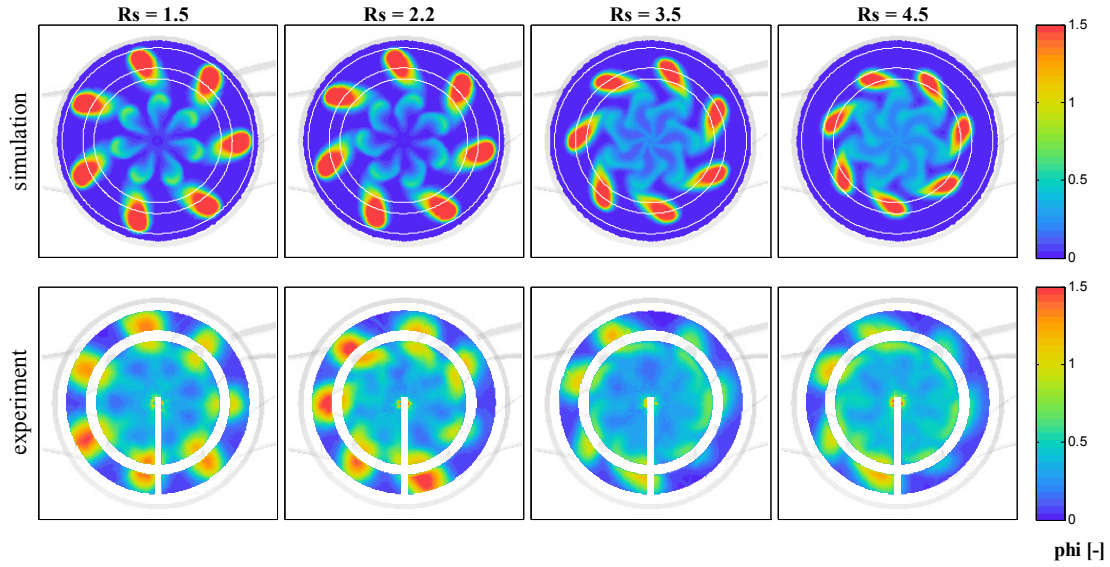

Fig. 12. Squish plane (P1) PRF25 mixture preparation comparison. Swirl ratios: 1.5, 2.2, 3.5, 4.5; CA = -10.0.

definite, and quite self-contained. Later, after the end of injection (Figure 13), immediately before high temperature heat release takes place, the jets are completely mixed to an almost homogeneous, lean ($\phi < 0.5$) equivalence ratio. The simulations show a slight under-prediction of the mixing phenomenon in the lowest swirl cases, where turbulent diffusion is a more significant part of the mixing process, suggesting the sector approach's inability to capture the in-cylinder turbulence levels.

Jet penetration into the squish region is also crucial to pollutant formation. In Figure 11 the model shows an over-dependency of jet tip penetration on swirl ratio compared to that seen in the experiments. The penetration is well captured at Rs = 1.5 and 2.2, while it is quite underestimated at the highest swirl ratios. However, both the simulations and the experiments indicate a clear reduction in penetration with higher flow swirl.

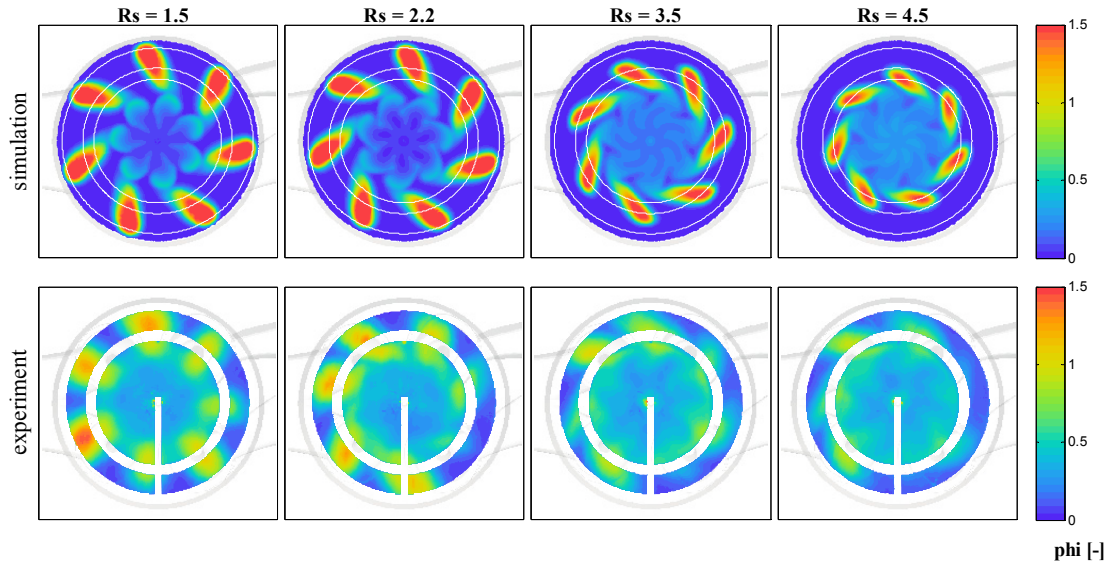

Fig. 13. Squish plane (P1) PRF25 mixture preparation comparison. Swirl ratios: 1.5, 2.2, 3.5, 4.5; CA = -5.0.

Mixture preparation at the bowl rim (plane P2) is linked to penetration into plane P1, especially as far as targeting of the fuel jet against the rim is concerned. The simulation shows significant impingement against the rim already at -15 degrees aTDC (Figure 14). This phenomenon is not seen in the experimental images due to the limited extent of the measurement that cannot reach the bowl rim wall due to interference from bowl rim reflections. Here most of the jet-to-jet differences are seen, not only in the peak equivalence ratio, but also in its shape and thickness. It should be also noted that the experimental image also retains some details, including the nozzle exits, which are part of the background and are not intersected by this plane.

Closer to the high temperature heat release phase, in Figure 15, the simulations still show quite well defined jet structures, which are much more blurred in the experimental images. This is again consistent with the underprediction of turbulent diffusion by the model; however, good agreement in terms of the average in-plane equivalence ratios is seen.

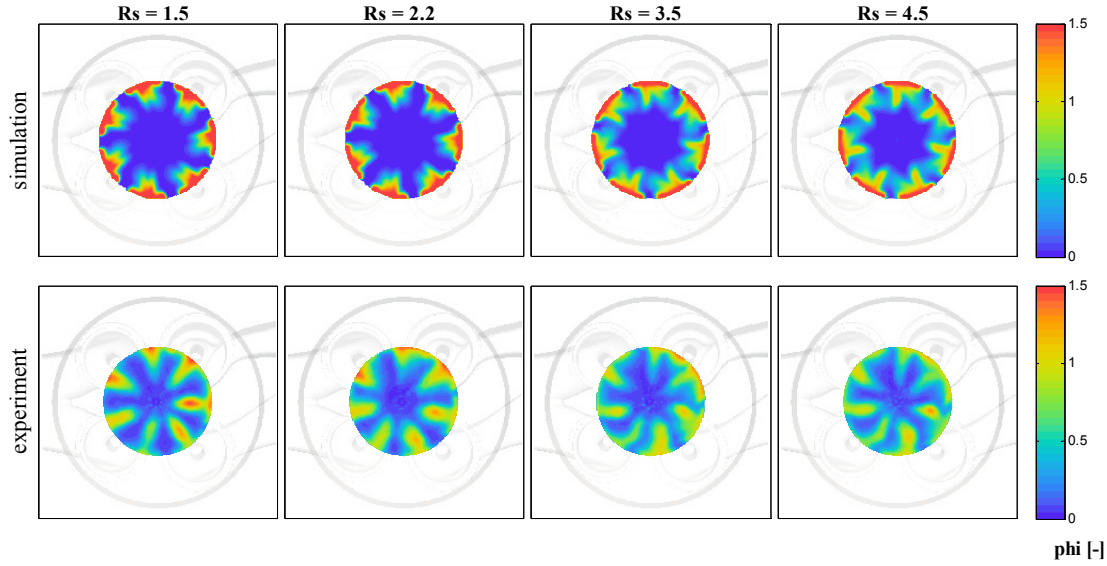

Fig. 14. Bowl rim plane (P2) PRF25 mixture preparation comparison. Swirl ratios: 1.5, 2.2, 3.5, 4.5; CA = -15.0.

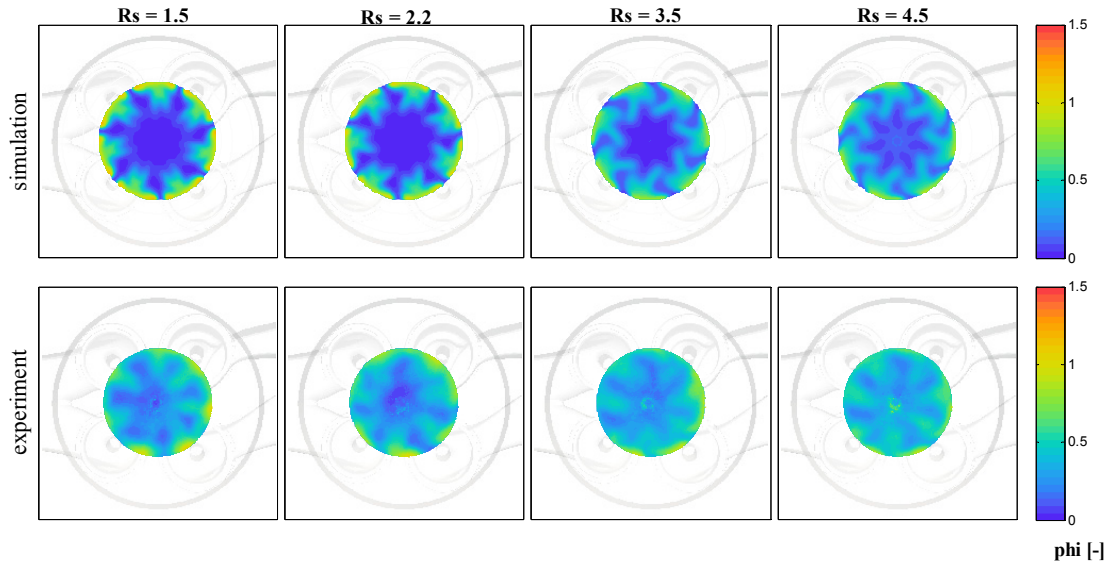

Fig. 15. Bowl rim plane (P2) PRF25 mixture preparation comparison. Swirl ratios: 1.5, 2.2, 3.5, 4.5; CA = -10.0.

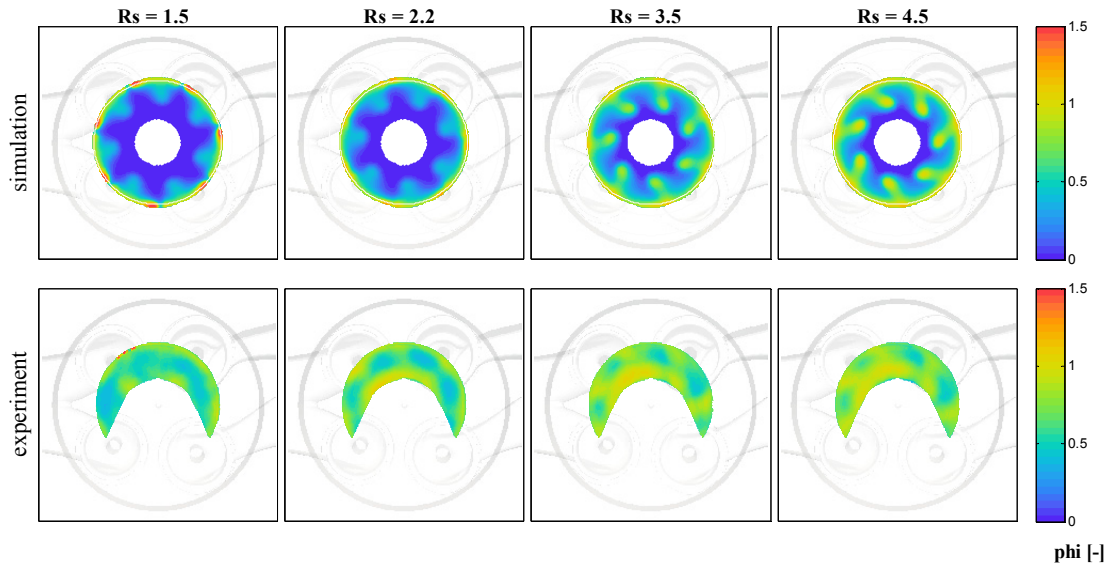

Fig. 16. Bowl plane (P3) PRF25 mixture preparation comparison. Swirl ratios: 1.5, 2.2, 3.5, 4.5; CA = -5.0.

Finally, penetration deep into the bowl, crossing plane P3 (Figure 16), and re-appearing towards the center of the combustion chamber after having travelled along floor of the bowl, is both an indicator of how well jet penetration is captured, and of how well the mixing has been predicted. Simulations at all swirl ratios were able to capture the jet tip penetration re-entering plane P3, but at a larger radius than seen in the experiments, i.e., farther from the cylinder center. This suggests that the angular momentum in the head of the jet is greater in the simulation than is seen experimentally. It is this angular momentum, causing the jet to spin out toward the bowl periphery, that inhibits the jet from following the bowl contour. At the same time, mixing appears to have been again slightly underestimated. In the experiments the jet structures can still be identified, but the average equivalence ratios were quite well captured.

Summary and Conclusions

A computational model of the Sandia National Laboratories light-duty optical access engine was built using an unstructured version of the KIVA code for which a comprehensive set of spray models has been implemented. Two grids, one representing one seventh axisymmetric sector of the combustion chamber, and a full engine grid including the intake and exhaust ports, vessels, and the swirl generation plates in the optical engine, were used to test the model performance at predicting flow and mixture preparation.

The following conclusions were derived from this study:

- Sector mesh models are quite effective in providing a reasonable estimate of the in-cylinder spray structure and mixture preparation. However, they cannot explain the effects that local geometric features have on the fuel-air mixing process. They also cannot properly resolve the turbulence flow field, which, even with well resolved meshes, results in a lack of mixing due to underpredicted turbulent diffusion.

- The present full geometry flow structure study suggests that the engine's port design, usually tailored for conventional diesel combustion strategies, may be relevant for the optimization of engines running lean and low-temperature combustion strategies, where an excess of mixing can lead to the formation of lean mixture pockets that can misfire, causing high unburned hydrocarbon and carbon monoxide emissions.

- The present spray simulations demonstrated the overall reliability of spray models with axisymmetric, equally spaced grids, but still need further validation with arbitrary grids, including non-polar displaced, skewed or unstructured cells.

The study suggests that proper engine design for advanced combustion strategies still requires research in improving the understanding and suitably modeling both spray and turbulence properties. However, flow details seen with the RANS simulation framework appear to be suitable for engineering design applications.

Acknowledgements

This work was performed at the University of Wisconsin-Madison Engine Research Center and at the Combustion Research Facility of Sandia National Laboratories in Livermore, California. Support for this research was provided by the U.S. Department of Energy, Office of Vehicle Technologies. Sandia is a multi-program laboratory operated by Sandia Corporation, a Lockheed Martin Company, for the United States Department of Energy's National Nuclear Security Administration under contract DE-AC04-94AL85000.

The authors would also like to acknowledge ANSYS inc. for granting ICEM CFD licenses for mesh generation to the Engine Research Center.

References

1. Abani N, Munnannur A, Reitz RD, "Reduction of Numerical Parameter Dependencies in Diesel Spray Models", Journal of Engineering for Gas Turbunes and Power 130, 032809, 2008.
2. Bailey AB, Hiatt J, "Sphere Drag Coefficients for a Broad Range of Mach and Reynolds Numbers", AIAA Journal 10(11), 1436-1440, 1972.
3. Beale JC, Reitz RD, "Modeling Spray Atomization with the Kelvin-Helmholtz/Rayleigh-Taylor hybrid model", Atomization and Sprays 9, 623-650, 1999.
4. Bergin M, Reitz RD, "Effect of Flowfield Non-Uniformities on Emissions Predictions in HSDI Engines", SAE technical paper 2011-01-0821, 2011.
5. Busch S (2014) personal communication.
6. Colban WF, Kim D, Miles PC, Oh S, Opat R, Krieger R, Foster D, Durrett R, Gonzalez MA, "A Detailed Comparison of Emissions and Combustion Performance Between Optical and Metal Single-Cylinder Diesel Engines at Low Temperature Combustion Conditions", SAE technical paper 2008-01-1066, 2008.

7. Dempsey A, Wang B, Reitz RD, Petersen B, Sahoo D, Miles PC, “Comparison of Quantitative Equivalence Ratio Measurements with CFD Predictions for a Light-Duty Low Temperature Combustion Diesel Engine”, SAE Int. J. Engines 5(2):2012, doi:10.4271/2012-01-0143.
8. Ekoto IW, Colban WF, Miles PC, Park SW, Foster DE, Reitz RD, Aronsson U, Andersson, O, “UHC and Co emissions Sources from a Light-Duty Diesel Engine Undergoing Dilution-Controlled Low-Temperature Combustion”, SAE technical paper 2009-24-0043, 2009, doi:10.4271/2009-24-0043.
9. Ge H-W, Reitz RD, Willelms W, “Modeling the effects of In-Cylinder Flows on HSDI Diesel Engine Performance and Emissions”, SAE Int. J. Fuels Lubr. 1, 293-311, 2008. Doi:10.4271/2008-01-0649.
10. Han Z, Reitz RD, “Turbulence Modeling of Internal Combustion Engines Using RNG k-epsilon Models”, Combustion Science and Technology 106, 267-295, 1995.
11. Morrison FA, “Data Correlation for Drag Coefficient for Sphere”, Department of Chemical Engineering, Michigan Technological University, 2013.
12. Munnannur A, Reitz RD, “Comprehensive collision model for multidimensional engine spray computations”, Atomization and Sprays 19(7), 597-619, 2009.
13. Opat RM, “Investigation of mixing and temperature effects on UHC/CO emissions for highly dilute low temperature combustion in a light-duty Diesel engine, M.Sc. Thesis, University of Wisconsin-Madison, 2006.
14. Perini F, Dempsey A, Sahoo D, Miles PC, Reitz RD, “A computational investigation of the effects of swirl ratio and injection pressure on wall heat transfer in a light-duty diesel engine”, SAE technical paper 2013-01-1105, 2013.
15. Perini F, Galligani E, Reitz RD, “An analytical Jacobian approach to sparse reaction kinetics for computationally efficient combustion modelling with large reaction mechanisms”, Energy and Fuels 26(8), 4804-4822, 2012.
16. Perini F, Miles PC, Reitz RD, “A comprehensive modeling study of in-cylinder fluid flows in a high-swirl, light-duty optical diesel engine”, Computers and Fluids, submitted, 2013.
17. Perini F, Sahoo D, Miles PC, Reitz RD, “Modeling the ignitability of a pilot injection for a Diesel Primary Reference Fuel: impact of injection pressure, ambient temperature and injected mass”, SAE technical paper 2014-01-1258, 2014.
18. Petersen BR, Ekoto IW, Miles PC, “An Investigation into the Effects of Fuel Properties and Engine Load on UHC and CO Emissions from a Light-Duty Optical Diesel Engine Operating in a Parttially Premixerd Combustion Regime”, SAE Int. J. Engines 3 (2010), 38-55. Doi:10.4271/2010-01-1470
19. Petersen BR, Miles PC, “PIV Measurements in the Swirl-Plane of a Motored Light-Duty Diesel Engine”, SAE Int. J. Engines 4(1), 1623-1641, 2011.
20. Petersen BR, Sahoo D, Miles PC, “Review of Equivalence Ratio Measurements in a Light-Duty Diesel Engine Operating in a Lioght-Load Partially Premixed Regime”, THIESEL 2012 Conference on Thermo- and Fluid Dymanic Processes in Direct Injection Engines.
21. Ra Y, Reitz RD, “A reduced chemical kinetic model for IC engine combustion simulations with primary reference fuels”, Combustion and Flame 155(4), 713-738, 2008.
22. Reitz RD, “Directions in Internal combustion engine research”, Combustion and Flame 160(1), 1-8, 2013.
23. Sahoo D, Miles PC, Trost J, Leipertz A, “The Impact of Fuel Mass, Injection Pressure, Ambient Temperature, and Swirl Ratio on the Mixture Preparation of a Pilot Injection”, SAE Int. J. Engines 6(3):2013, doi:10.4271/2013-24-0061.
24. Sahoo D, Petersen B, Miles PC, “Measurement of Equivalence Ratio in a Light-Duty Low Temperature Combustion Diesel Engine by Planar Laser Induced Fluorescence of a Fuel Tracer”, SAE Int. J. Engines 4(2):2011,2312-2325, doi:10.4271/2011-24-0064.
25. Torres DJ, Trujillo MF, “KIVA-4: An unstructured ALE code for compressible gas flow with sprays”, Journal of Computational Physics 219(2), 943-975, 2006.
26. Torres DJ, O’Rourke PJ, Amsden AA, “A discrete multicomponent fuel model”, Atomization and Sprays 13(2-3), 1-42, 2003.
27. Wang Y, Ge H-W, Reitz RD, “Validation of Mesh- and Timestep-Independent Spray Models for Multi-Dimensional Engine CFD Simulation”, SAE Int. J. Fuels Lubr. 3(1), 277-302, 2010.
28. Zha K (2014) personal communication.
29. Zha K, Busch S, Miles PC, “Progress Towards In-Cylinder PIV Measurements throughout the Full Intake and Compression Strokes”, Sandia National Laboratories technical report SAND 2014-3118P, 2014.

The Future of the Combustion Engine Beyond 2020

T. Koch

Karlsruhe Institute of Technology. Institut für Kolbenmaschinen. Rintheimer Querallee.
76131 Karlsruhe. Germany.

E-mail: tomas.a.koch@kit.edu

Abstract. Current studies on the personal mobility and freight transport on surface estimate in the whole world a distinct increase until 2050. The challenging task will be to meet the rising need for mobility and decrease meanwhile the environmental impact of traffic.

In the last two decades legislation on vehicle emissions have been introduced in the most important markets. The active emission limits, e.g. Euro 6 or SULEV, have been significantly reduced in relation to previous emission limits. Nevertheless many cities in the world suffer from high particles and NO_x concentrations in the air. The discrepancy maybe explained by driving under real operating conditions with higher emission levels. Additionally the observed extension of the average lifetime of vehicles might influence the contribution of engines with old emission standards.

Estimations on paths to future mobility are presented and have to be based on an energy balance. Introducing an Energy balance of Germany with detailed investigations enables a perspective for regenerative based energy future. The results indicate that energy for traffic was one of three almost equally high energy demands (households, industry) in 2011. Studies on future energy demands suppose a reduction in these two areas, whereas the energy demand on traffic will be the highest energy demand in 2050. Therefore solutions to uncouple the energy demand and the carbon dioxide emissions have to be addressed. A very promising path, the use of renewable energies for electricity in city vehicles and production of fluid fuels can be a possible solution.

Investigations of Closely Coupled Pilot and Main Injections as a Means to Reduce Combustion Noise

Stephen Busch[1], Kan Zha[1], Paul C. Miles[1]

[1]Sandia National Laboratories, Engine Combustion Department; PO Box 969, MS 9053; Livermore, CA 94551-0969

E-mail: sbusch@sandia.gov
Telephone: +1-925-294-2216
Fax: +1-925-294-1004

Abstract:

Various pilot-main injection strategies are investigated in a single cylinder optical Diesel engine. With a pilot injection that is advanced from the main injection by 300 µs or more, a 9 dB reduction in combustion noise is achieved. It is observed that as the dwell between a single pilot and the main injection is decreased towards zero, combustion noise passes through a minimum and a further reduction of 3 dB is possible. This additional decrease in combustion noise is not associated with increases in smoke or NO_x emissions. The injection schedules employed in the engine are analyzed with a hydraulic injection analyzer to provide rate shapes for each of the dwells tested. Two distinct injection events are observed even at the shortest dwell tested, and various rate shaping effects are observed with the main injection event as the dwell is adjusted. High-speed elastic scattering imaging of liquid fuel is performed in the engine to examine initial spray penetration rates; these are compared to the measured rates of injection. The penetration rate results provide evidence that rate shaping of the initial phase of the main injection is occurring in the engine and that this rate shaping is consistent with the injection rate data. Although changes in the main injection rate are believed to occur in the engine, experimental evidence suggests that these changes are not responsible for the observed trend in combustion noise as dwell changes. The combination of thermodynamic data and rate of injection data support the theory that the main injection interacts with the pilot mixture field and influences its combustion, thus playing a role in decreasing combustion noise. The relative phasing of the pilot and main heat release may play a significant role in reducing combustion noise; further studies will focus on combustion phasing effects.

Nomenclature

AHRR	Apparent heat release rate
ASSE	After the start of solenoid energizing
ATDC	After top dead center
CAD	Crank angle degrees
COV	Coefficient of variation
δt	Energizing dwell
ET	Energizing time
FIR	Finite impulse response
FSN	Filter smoke number
HDA	German acronym: Hydraulischer Druckanstieg (hydraulic pressure increase)
ID	Ignition delay
$IMEP_g$	Gross indicated mean effective pressure
m_{pilot}	Pilot injection quantity
SOC	Start of combustion
SOI_{pilot}	Start of pilot injection
SSE	Start of solenoid energizing
TDC	Top dead center
UHC	Unburned hydrocarbons

1. Introduction / Motivation

To improve customer acceptance and reduce noise pollution, it is desirable to make automotive Diesel engines quieter. Pilot injections have long been used in direct injection Diesel engines as a means to

reduce combustion noise (Russell *et al.*, 1993; Dürnholz *et al.*, 1994). The mechanism by which noise is reduced is as follows: the heat released by the pilot fuel increases temperatures and radical concentrations within the cylinder and therefore decreases the ignition delay of the fuel injected during the main injection. Combustion of the main injection is therefore predominantly mixing-controlled and characterized by lower rates of heat release than for premixed combustion. The relatively small amount of pilot fuel, combined with the interruption in the rate of injection, results in a smaller amount of premixed combustion than for a single injection. In this way, combustion noise is suppressed through the use of a pilot. Advances in fuel injection hardware, such as common rail systems and fast response injectors, have made multiple injection strategies robust and effective. Piezo injectors are well known for their precision and short reaction times, but state-of-the-art solenoid injectors can reliably deliver up to eight injections per cycle with very short separation times between injection events (Fiat, 2009). Split armature modules enable closely spaced injections and even zero hydraulic dwell (delay) between injection events and thus injection rate shaping (Bosch, 2011; Fiat, 2009).

Dürnholz *et al.* investigated the effects of a pilot injection on combustion noise, fuel economy, and emissions with various pump-line-nozzle injector configurations in a passenger car Diesel engine (1994). Their injection system made it possible to vary the quantity, timing, and rate of the pilot injection. For an engine speed of 2000 rpm and a “medium” load, combustion noise depended strongly on the pilot quantity; minimal combustion noise levels were achieved with a pilot quantity of between 2 and 3 mm^3/str. The noise minimum corresponds to a minimum in ignition delay for the main injection, and to approximately 8% of the fuel being burned before the start of the main injection. Measured combustion noise was always lower with a pilot than without, but the noise increased for hydraulic dwells (injection interrupt durations) shorter than approximately 12 °CA (1000 µs at 2000 rpm).

Badami *et al.* performed investigations using a common rail system with solenoid injectors in a passenger car Diesel engine (2001). They examined three different operating points with pilot-main injection strategies and varied pilot injection quantity and energizing dwell at each point. At a fixed load, pilot injection quantity affected not only the combustion noise at a given energizing dwell, but also the trend in combustion noise with changing dwell. Moreover, trends in combustion noise for different operating points were quite different for a given pilot injection quantity. At moderate engine loads (bmep/n: 5 bar/1500 rpm and 8 bar/2000 rpm), combustion noise sometimes changed dramatically for energizing dwells shorter than 500 µs. At the highest load tested (8 bar/2000 rpm) and for the larger pilot injection quantities tested, combustion noise was observed to decrease dramatically at the shortest energizing dwells (near 86 µs). Badami *et al.* show that by varying only the dwell for a given pilot injection quantity, combustion noise can vary by as much as 3 dB; this is equivalent to a factor of 2 in acoustic power.

Ricaud and Lavoisier optimized multiple injection settings in a single-cylinder, small-bore engine with a piezoelectric injector for several multiple injection strategies (2002). Dwell and quantity were varied for each injection event, as well as the start of the main injection, the rail pressure, and the EGR rate. For a pilot-main injection strategy, combustion noise varied significantly as dwell and pilot injection quantity were changed. Furthermore, the pilot fuel quantity resulting in the lowest combustion noise level depended on the dwell. The noise-optimal pilot injection quantity was smallest for intermediate dwells. For noise-optimized operation, peak heat release rates are the same for the pilot and the main combustion events. This observation was made for several operating points, and it was suggested that the noise-optimized settings are a balance between excessive pilot heat release and excessive main combustion heat release.

Properly applied multiple injection strategies can be beneficial for combustion noise, fuel consumption, and pollutant emissions, and are therefore a powerful tool. However, with so many calibration parameters, including injection and dwell durations for each injection event; rail pressure; and injection train phasing; developing engine calibrations over the entire operating map is a complicated and time consuming process. A particular injection train may yield minimal combustion noise for a given operating point, but it may not be obvious why these parameters are optimal or why different parameters are necessary for a different operating point. Without a detailed understanding of the mechanisms by which noise can be decreased with multiple injections and closely coupled pilot injections, it will be difficult to reduce the amount of effort necessary to develop and optimize such calibrations. The goal of this work is to provide insight into the interactions between the pilot and main injections within the injector and within the cylinder, and increased understanding of how combustion noise is impacted by these interactions.

In this study, a pilot-main injection strategy is investigated at moderate load in an optical small-bore Diesel engine. The pre-production injector used is a fast-acting, pressure-balanced, solenoid-actuated injector, which enables very closely coupled injection events. Engine testing is performed for a dwell sweep at a moderate load, and trends in exhaust emissions, heat release rates, and

combustion noise are measured. The injection schedules used in the engine testing are measured with a hydraulic injection analyzer to provide rate shapes for each of the dwells tested. High speed elastic scattering images are taken in the engine to provide information about the liquid fuel as it is injected into the cylinder. The comparison between the rate shape data and liquid penetration data provide information about the changes in the rise rate of the main injection as dwell changes. The combination of rate shape and thermodynamic data provides evidence of the interaction between the main injection and the pilot mixture field.

2. Experimental Setup

2.1. Engine and Fuel Injector

The single-cylinder optical Diesel engine used in this study is based on a modified 1.9 L GM four valve head. The main geometric specifications are provided in Table 1. The engine features a Bowditch-style piston, which is fitted with a titanium piston top for the cylinder-pressure based and emissions measurements; and with a fused-silica piston top for the optical investigations described below. The geometrically identical piston tops feature a reentrant bowl and valve cut-outs.

Table 1: Engine geometry and fuel properties

Engine Geometry		
Valves	[-]	4
Bore	[mm]	82
Stroke	[mm]	90.4
Displacement Vol.	[L]	0.477
Geometric CR	[-]	16.69

Fuel
42 vol% n-$C_{16}H_{34}$; 58 vol% iso-$C_{16}H_{34}$

Optical access through the sides of the combustion chamber is provided by fused silica windows (50 mm wide by 25 mm tall) located at the top of the cylinder liner. These windows are positioned to allow unobstructed optical access into the clearance volume, even when the piston is located at TDC. The engine is equipped with a Kistler 6125b pressure transducer mounted in the location of the production engine glow plug, and the in-cylinder pressure is acquired every 0.25° crank angle (CA).

The injector used in this study is a pre-production solenoid injector, which is equipped with a pressure-balanced nozzle control valve to enable very closely spaced injection events. The mini sac nozzle has equally spaced holes with exit diameters of 139 µm and conicity of 1.5; the included angle of the holes is 149°. Flexible control of solenoid energizing durations (referred to as ET) and energizing dwells is provided by a Genotec injector controller. For this study, dwell refers to the time between the end of the pilot energizing signal and the beginning of the main energizing signal (see Fig. 1). The dwell is varied between 80 and 1200 µs.

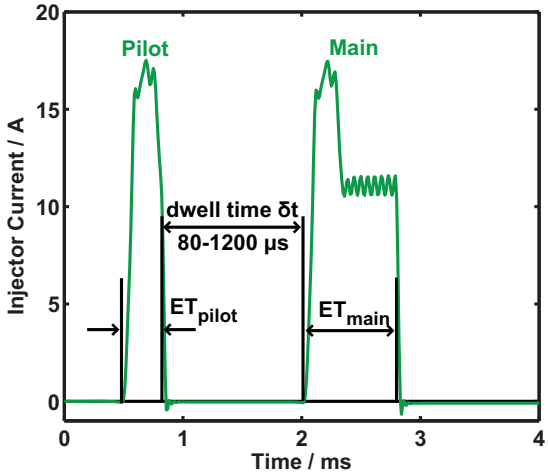

Fig. 1: injector solenoid energizing and dwell definition

2.2. HDA

The Moehwald HDA (HDA is a German acronym for hydraulic pressure increase: Hydraulischer Druckanstieg) is a commercially available injection rate and mass measurement device that utilizes the change in hydraulic pressure that results from injecting fluid into a closed, fluid-filled chamber. It is essentially an evolution of Zeuch's original measurement device (1961). The underlying measurement principle relies on both the measured pressure in a constant-volume chamber and the speed of sound of the fluid within the chamber. With the assumption of a reversible, adiabatic (isentropic) injection into the chamber, the injection mass flow rate can be expressed as follows:

$$\frac{dm}{dt} = \frac{V\frac{dP}{dt}}{\frac{dP}{d\rho}} = \frac{V}{c^2}\frac{dP}{dt}, \qquad (1)$$

where:

m is the mass of fluid in the chamber,
V is the volume of the chamber,
t is time,
P is the chamber pressure, and
ρ is the fluid density
c is the speed of sound in the fluid

Integration of equation (1) between two points in time (and thus two discrete pressures) yields a cumulative mass:

$$m_{1-2} = \int_{\tau_1}^{\tau_2} \frac{dm}{dt} dt = V \int_{P_1}^{P_2} \frac{1}{c(P(t))^2} \frac{dP}{dt} dP \qquad (2)$$

So, for a given chamber volume, the mass flow rate and cumulative mass can be determined if the time-dependent pressure and pressure-dependent speed of sound are known. Whereas Zeuch assumed a constant value for the compressibility of his fuel (1961), in the HDA the speed of sound is measured directly. Hence, uncertainties in fluid properties such as density and bulk modulus do not adversely affect the accuracy of the results.

A schematic diagram of the HDA setup is shown in Fig. 2. A PC is used to communicate with the injector driver and the HDA control module. Fuel is supplied by a small feed pump to a high pressure, three-piston pump, after which it flows into a production common rail. Rail pressure is controlled via modulation of the metering valve in the CP1. A PC is used to communicate with the injector driver and the HDA control module. The configuration of the fuel injection hardware is essentially unchanged from the setup used for engine testing.

The HDA's cylindrical chamber has a volume of 128 ml, and its walls are temperature controlled via an external heated recirculator that pumps heat transfer fluid through the chamber walls. A piezoresistive pressure sensor is mounted in the cylinder wall halfway between the top and the bottom of the chamber. The pressure signal is passed through an analog anti-aliasing filter with a cutoff frequency of 25 kHz before being digitized with 16-bit resolution at a rate of 100 kHz. Additional digital processing of the pressure signal accounts for the temperature dependence of the pressure sensor

sensitivity, as well as nonlinearities in the sensor output. Finally, the pressure signal is digitally filtered using a raised-cosine, finite-impulse-response (FIR) filter with a cutoff frequency of 10 kHz. In addition to the injection rate, the solenoid current is measured using a Pearson Model 411 Current Monitor placed around the injector cable and digitized at 100 kHz.

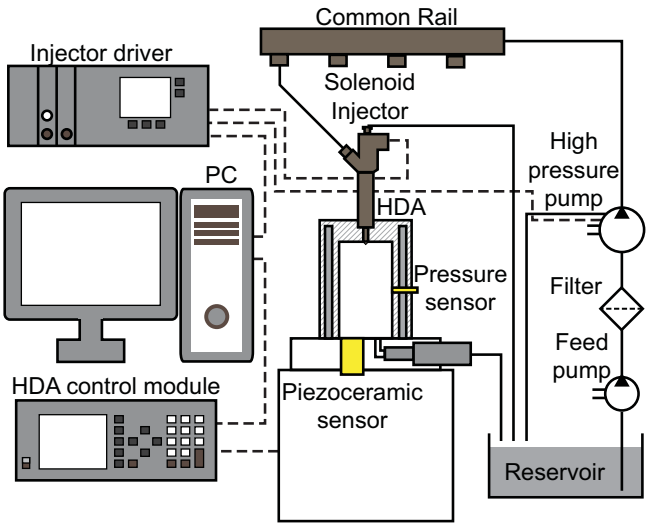

Fig. 2: Setup of the HDA and auxiliary components

To measure the speed of sound, an electronic pulse is sent to a piezoceramic sensor, which creates a pressure wave that travels through the fluid in the chamber, is reflected at the top of the chamber, and detected by the same sensor upon its return. A clock speed of 75 MHz yields a timing resolution of 13.33 ns, and quantization noise is reported to be on the order of 0.1 m/s (Moehwald, 2008). Neglecting any uncertainty in the chamber height, the total uncertainty in the speed of sound is estimated to be 0.25 m/s, which is typically less than 0.025% of the measured value.

The analysis of multiple cycles yields statistical information about a particular set of operating conditions. This includes the mean and the standard deviation of the injected mass, among other quantities. For the current work, no systematic difference was observed between the mean values and standard deviations when the statistics were taken over either 50 or 100 cycles. For this reason, each data point presented in this paper represents the ensemble average of 50 injections. Hydraulic starts of injection are identified by the positive-sloped zero crossings observed at the beginning of each injection event.

2.3. Engine Operating Conditions and Procedure

Initial testing was performed with the metal piston to characterize the operation of the engine as dwell is varied. For these tests, the engine was operated with a constant engine speed, $IMEP_g$, injection pressure, and pilot injection quantity (see Table 2). The engine was operated in skip-fire mode; fuel was injected in every fifth cycle. The main injection duration was adjusted to maintain the engine load ($IMEP_g$), and the injection train was block-shifted to achieve a near-constant 50% mass fraction burned angle of 13 °CA ATDC. The intake mass flow rate was held constant throughout the testing and resulted in a motored TDC density of approximately 21.8 kg/m^3. EGR was simulated by replacing intake air with a mixture of nitrogen and CO_2 and matching the total mass in the cylinder to the mass that would be present with real EGR. The residual fraction that would be expected in a continuously fired metal engine was also simulated in this manner. Exhaust emissions (NO_x, smoke number, CO, and UHC) were measured during skip-fired operation and corrected to represent emissions levels obtained in continuously-fired operation. For each operating point, the engine was motored for approximately 90 seconds to allow the intake and exhaust pressures to stabilize. An emissions measurement was taken just before the engine was skip-fired, and a second emissions measurement was taken after approximately 60 seconds of skip-fired operation and averaged over 20 seconds of operation.

After the initial engine testing, the injector was tested in the HDA. Rates of injection were measured for the injection schedules developed during the engine testing, among others. The HDA

chamber pressure was set to be consistent with the cylinder pressure at the time of injection. Fuel and chamber temperatures were held constant at 90°C, although measured rates of injection are not sensitive to fuel temperature at temperatures above 60°C. The injector was then reinstalled in the engine and the fused silica piston top was installed. Intake air mass flow was replaced with pure nitrogen to prevent combustion and the associated window fouling. Four of the injection trains developed in fired operation were used for the optical measurements.

For each fired operating point, combustion noise is calculated from 50 cycles' worth of raw cylinder pressure data according to the routine provided in (Shahlari *et al.*, 2013), which is similar or identical to the routines used by commercial devices to compute combustion noise. The average of these 50 values is reported here for each case. Apparent heat release rate (AHRR) is computed with an iterative, two-zone model, in which temperature and composition dependent gas properties are taken into account. Heat transfer and crevice flow effects are partially compensated by subtracting the AHRR of a motored pressure trace from the AHRR of the fired trace. A cosine-symmetric low pass FIR filter is used to smooth the fired cylinder pressure traces before the AHRR is calculated. Its pass band edge is located at 5 kHz. This preserves the frequency content of the cylinder pressure traces in the frequency bands most relevant to combustion noise. The AHRR traces shown in this work are ensemble averaged over 50 fired cycles.

Table 2: Engine operating parameters

Engine speed	[rpm]	1500
Swirl ratio (Ricardo)	[-]	2.2
$IMEP_g$	[bar]	9.0 ± 0.1
Injection pressure	[bar]	800
m_{Pilot}	[mg/str]	1.5
Dwell time δt for initial testing (δt…step size…δt)	[µs]	0 (no pilot) 80…*20*…200 300…*100*…500 600…*200*…1200
Dwell time δt for optical measurements	[µs]	0, 90, 140, 300
Intake temperature	[K]	347.15
TDC temperature	[K]	925
TDC density	[kg/m^3]	21.8
EGR	[%]	10.3 (includes 3.3% residual fraction)
MFB50	[CAD ATDC]	13 ± 0.5

2.4. Optical setup

An elastic scattering imaging technique was developed to provide temporally and spatially resolved information about the fuel injection process for several dwells. Imaging was performed with a Photron SA-X2 monochromatic CMOS camera at a rate of 120 kfps. For a constant engine speed of 1500 rpm, this equates to a crank angle resolution of 0.075 CAD. Images were captured through the fused silica piston with a 105 mm focal length f/3.5 Nikkor lens. The cylinder head and valves were airbrushed with a thin coat of matte black heat resistant paint to minimize reflections. A high repetition rate, high intensity, short-pulse LED illumination system was employed to provide sufficient image intensities at these high frame rates. A red LED with a 3x3 mm^2 chip proved to be robust and sufficiently bright with pulse widths of 1.5 µs and peak forward currents exceeding 45 A. The LED pulses were timed so that each camera frame is exposed for the entire LED pulse duration. A system of three plano-convex lenses was developed to increase the amount of light that was passed into the cylinder. The setup in the test bench including the "focusing optics" is depicted in Fig. 3, along with an example of a raw image.

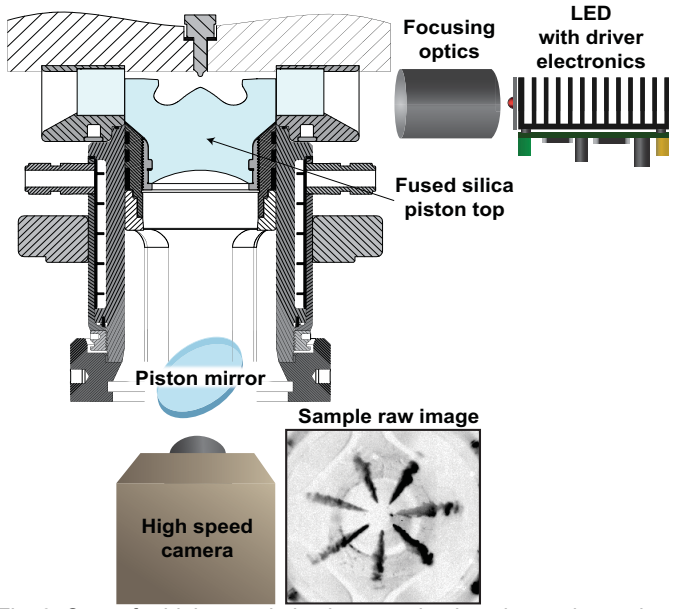

Fig. 3: Setup for high speed elastic scattering imaging and sample raw image (inverted grayscale color map, 0-512 counts, gamma = 0.7)

The LED and its lens system were positioned outside of the liner window on the intake side of the engine. The incoming light is scattered by the strong density gradients at the fuel jets, and the angle of incidence relative to the jet axis is different for each jet. This non-axisymmetric illumination complicates the image analysis, but each jet is treated independently in the image processing. Errors associated with non-uniform illumination are negligible in comparison to the changes observed with changing dwell. The trigger to start acquiring images is the signal used to trigger the injector driver to start injecting, i.e. it occurs at the start of solenoid energizing (SSE). In each injected cycle, 300 images are taken to capture the entire pilot and main injection events. Images are taken for 45 consecutive (skip-fired) cycles for each dwell tested.

The raw images are distortion corrected with an automated routine based on ray tracing, background subtracted, and thresholded before starts of injection, liquid lengths, and penetration rates are computed from them. These procedures are described in the Appendix, where an example of a processed image is also shown.

3. Results

As described above, initial investigations are performed with the metal piston top and with fired operation. Dwell is varied from 80 μs to 1200 μs, and a single injection serves as a reference. The resulting trend in combustion noise is shown in Fig. 4 for two runs, but experiments have also been performed with a second, nominally identical injector, and the results are closely repeatable. Standard deviations for a given dwell are typically less than 0.4 dBA. Although the highest standard deviations typically occur for dwells of less than 200 μs, they are often comparable to the standard deviation for a single injection. The single injection case is shown in this work as a dwell of zero.

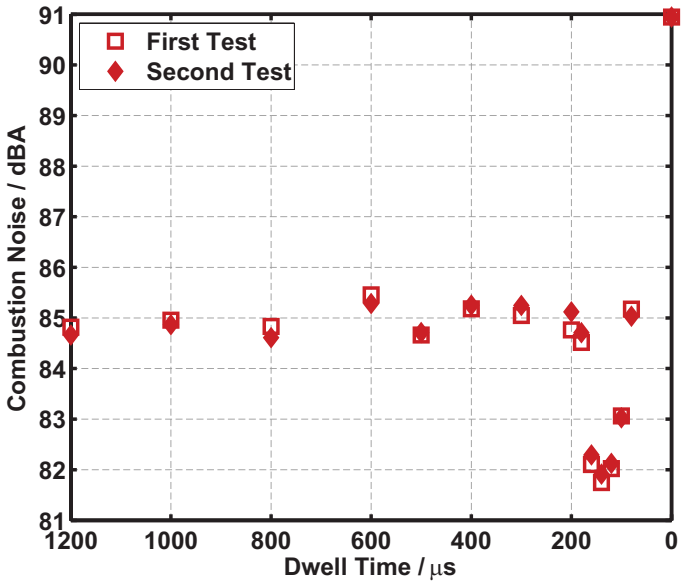

Fig. 4: Combustion noise vs. dwell for the pilot-main injection strategy

The use of a pilot injection significantly decreases noise levels below the level obtained with a single injection: for dwells longer than 200 μs this reduction is approximately 6 dB. However, a further decrease in combustion noise is observed as the dwell decreases below 200 μs, and the minimum occurs at a dwell of 140 μs. The minimum noise levels are approximately 3 dBA below the levels obtained with longer dwells; 3 dB corresponds to a factor of two in terms of acoustic power. Understanding the causes of this noise minimum is the goal of this research project. For dwells shorter than 140 μs, combustion noise levels again increase, and for a dwell of 80 μs, combustion noise levels are close to the 85 dBA level that is measured for longer dwells. For all dwells tested, the COV of $IMEP_g$ remains below 2.5%, but the COV values are typically slightly higher at dwells near 140 μs than for other dwells. Normalized indicated specific exhaust emissions and filter smoke numbers for these tests are shown in Fig. 5; they have been normalized by the levels measured for the single injection case.

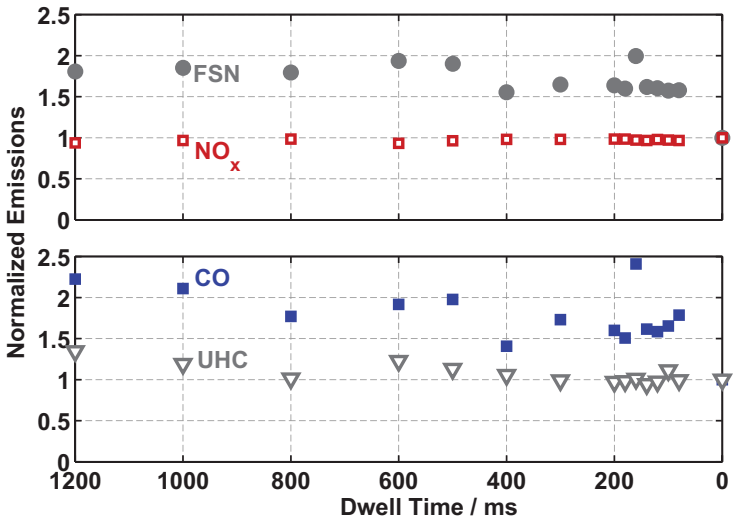

Fig. 5: Normalized exhaust emissions: FSN, NO_x, CO, and UHC vs. dwell

For this operating point, NO_x emissions are highest with a single injection, but only slightly lower with a pilot injection. They do not change significantly as dwell changes. FSN levels are higher with a pilot injection than without. Local maxima in FSN occur at dwells of 600 μs and 160 μs. The behavior in FSN at dwells less than 200 μs is not always repeatable: local maxima appear at different dwells

and their magnitudes vary from test to test, but local maxima in FSN values are never observed for a dwell of 140 μs. Higher FSN levels are typically associated with higher CO levels, which suggests that the rich mixtures responsible for the formation of soot may also be responsible for the formation of excess CO. Unburned hydrocarbon (UHC) levels are generally low; they correspond to approximately 0.1% of the injected fuel mass. For shorter dwells, UHC levels are most similar to those obtained with a single injection. Note that the noise minimum seen in Fig. 4 at a dwell of 140 μs occurs without penalties in pollutant emissions (when compared to other dwells). This trend has been observed in repeated emissions tests.

Each injection schedule developed during the fired tests has been measured outside of the engine with the HDA. Because the injector solenoid current is measured both in fired engine operation and with the HDA, the measured injection rates can be synchronized with the measurements taken in the engine (engine speed is assumed to remain constant throughout the portion of the cycle during which the injection occurs). Rates of injection are shown together with calculated apparent heat release rate (AHRR) data for several dwells and for the single injection case in Fig. 6. At this point, it is assumed that the rates of injection measured with the HDA represent those obtained with fired engine operation.

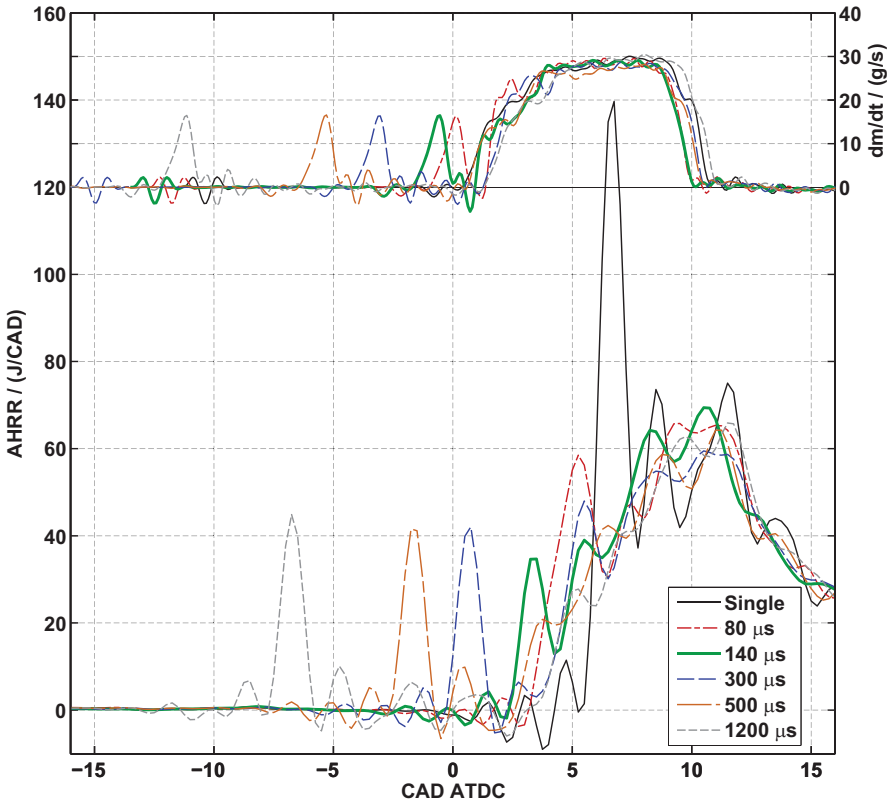

Fig. 6: Rates of injection (top) and AHRR data (bottom) for several dwells and the single injection case

As the dwell changes, the phasing of the injection train is adjusted to maintain combustion phasing (as indicated by MFB50). The timing of the main injection changes much less than the timing of the pilot injection as the dwell is changed. For a dwell of 1200 μs, the heat release associated with the pilot injection occurs before the start of the main injection. The same is largely true for a dwell of 500 μs, as well. However, for a dwell of 300 μs, the main fuel injection begins as the pilot heat release is finishing. For dwells shorter than this, the main injection overlaps with the pilot heat release. Peak apparent heat release rates for the pilot mixture are typically slightly higher than 40 J/ CAD for dwells of 300 μs and longer. However, as the dwell decreases below 300 μs, the peak apparent pilot heat release rate decreases and reaches a minimum at a dwell near 140 μs. After this, it becomes difficult to distinguish the heat release attributed to the pilot injection from that attributed to the main injection, even though two distinct injection events are observed even for a dwell of 80 μs. The AHRR curve for a dwell of 80 μs indicates that the initial heat release peak is larger than the pilot heat release peaks observed for longer dwells. For this operating point, the pilot injection decreases peak heat release

rates below the single injection levels by a factor of more than two. The differences in AHRR traces are most pronounced during the early stages of combustion; after approximately 10 CAD ATDC, it is difficult to distinguish between the various AHRR curves.

In a separate test, the start of the main injection as detected by the HDA was held constant for a variety of dwells; the trend in combustion noise was essentially unchanged.

Based on the type of data shown in Fig. 6, an ignition delay (ID) can be defined based on the detected start of pilot injection and the calculated start of apparent heat release. The start of the pilot injection is defined as the last zero crossing of the rate of injection curve before the pilot injection is clearly detected. The start of combustion is defined as the last zero crossing before the first significant peak in the AHRR signal. For longer dwells, this is attributed to the combustion of the pilot injection, but for very short dwells, it is unclear if the heat release is due only to the pilot or if combustion of the main injection begins at the same time. In this case and in the case of a single injection, the start of combustion simply refers to the start of measurable heat release. The start of pilot injection and start of combustion are illustrated in Fig. 7 for a dwell of 300 µs. SOI_{pilot}, SOC, and ID are shown in Fig. 8 for all dwells tested.

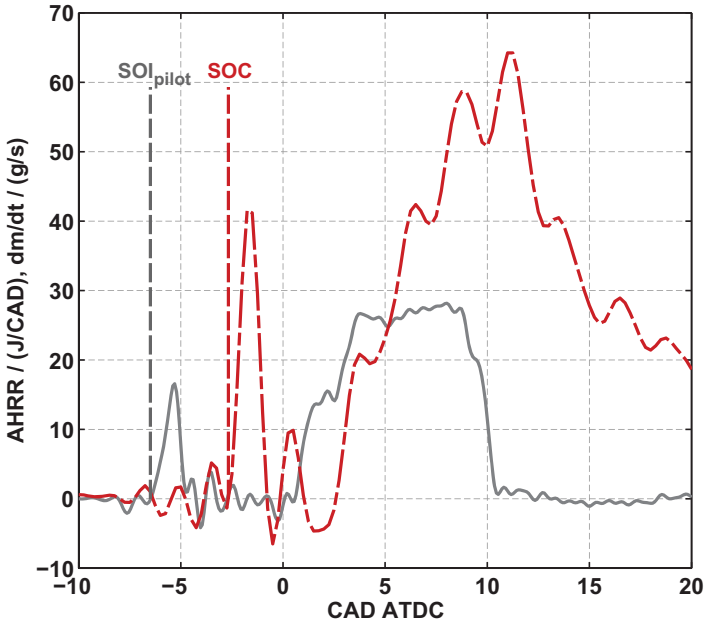

Fig. 7: Definition of start of injection for the pilot injection (SOI_{pilot}) and the start of combustion (SOC)

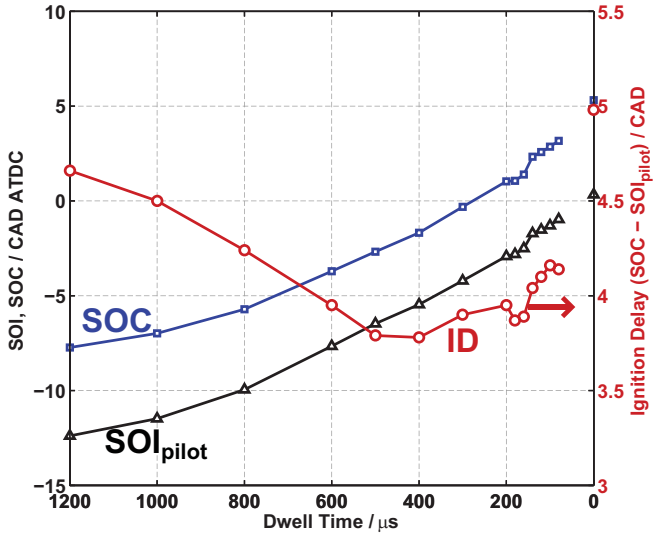

Fig. 8: Start of pilot injection (SOI_{pilot}), start of combustion (SOC), and ignition delay (ID) vs. dwell (single injection shown at zero dwell)

The ignition delay obtained with a single injection is longer than the ignition delay obtained with a pilot injection regardless of dwell. The pilot injection timing is dictated by the dwell, the pilot injection energizing time, and the desired CA50. As mentioned above, the timing of the main injection does not change significantly for these tests, so the trend in SOI_{pilot} is logical. As dwell increases above 400 µs, the pilot fuel is injected into an increasingly cooler environment, so the ignition delay becomes longer. For dwells shorter than 400 µs, the ignition delay begins to increase until a dwell of 200 µs. It then decreases slightly for a dwell of 180 µs, but increases dramatically as dwell decreases further.

The injection rate data shown in Fig. 6 suggest that the shape of the main injection rise rate changes with changing dwells. Of particular interest are the rate shapes for dwells of 300 µs and shorter, as the combustion noise changes significantly over this range of dwells. A separate test was performed with the HDA for a variety of dwells and constant main injection energizing times (as opposed to a variable main injection energizing time to maintain the desired load). The resulting injection rate traces are plotted against time after the start of solenoid energizing (ASSE) of the pilot injection in Fig. 9.

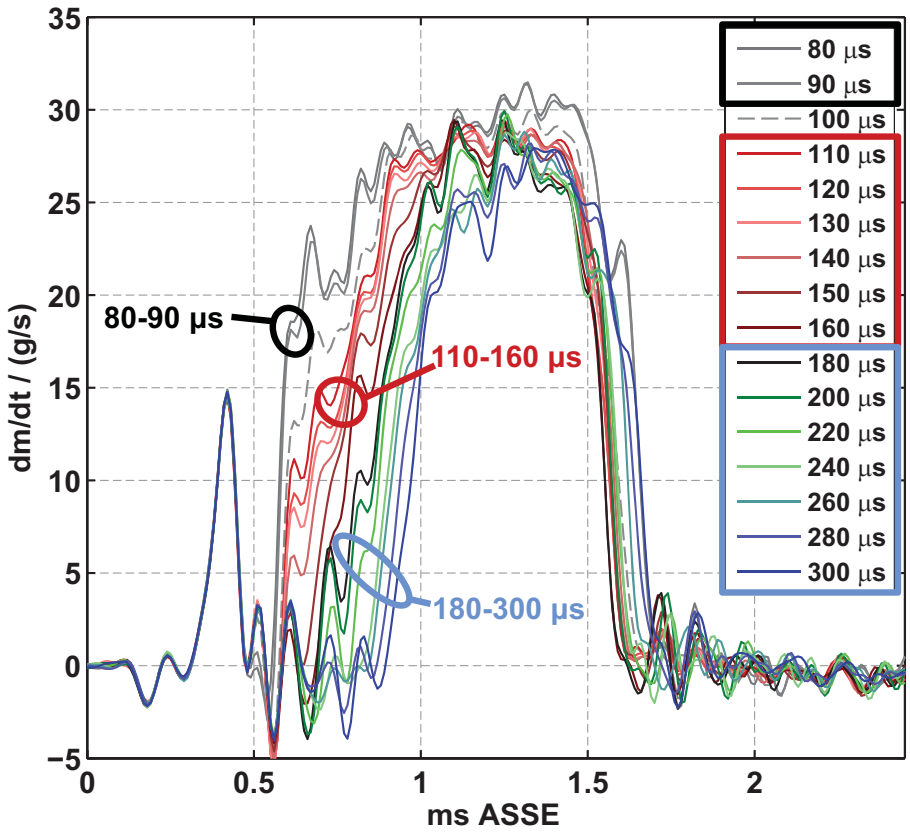

Fig. 9: Injection rates for constant main injection energizing time parameterized by dwell

As expected, the rate shape of the pilot injection is unaffected by changes in dwell. However, as dwell increases from 80 µs, the main injection rise rate transitions through three distinct regimes: a very rapid rise rate at the shortest dwells; a rise rate similar to a single injection for intermediate dwells; and a rise rate that is delayed but with a slightly enhanced rise rate compared to the single injection for longer dwells. The transitions between these regimes occur abruptly; a change in dwell of 20 µs can have a significant impact on the main injection rise rate shape. Dwells of 80 and 90 µs result in main injection rate shapes that are nearly identical.

Because the injection trains shown in Fig. 9 are phased according to the start of solenoid energizing for the pilot injection, they do not convey how the injection train timing would need to be changed to maintain combustion phasing in the engine. Rates of injection as they occur in the engine are presented in Fig. 6, but the main injection rise rate behavior is difficult to see. The main injection

rate traces are shown more clearly in Fig. 10, along with the injection rate of the single injection and the solenoid energizing currents for each operating point.

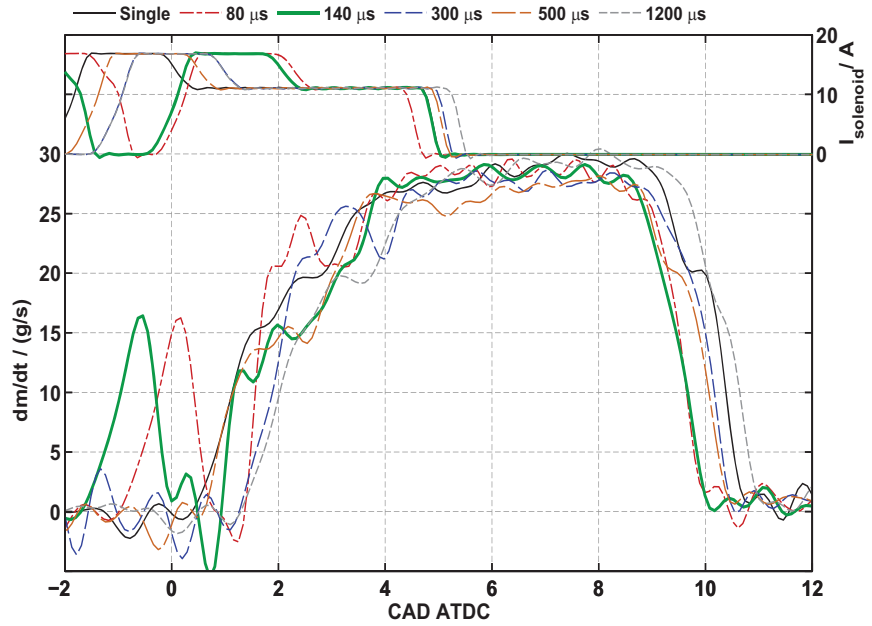

Fig. 10: Injection rates (bottom) and solenoid energizing currents (top) for various dwells and for a single injection

As indicated in Fig. 9, the main injection rise rate for a dwell of 80 µs is the steepest of all dwells tested. Compared to the single injection, the rise rate for a dwell of 140 µs is slightly more intense for the initial stage of the injection, but less intense during the latter part of the initial increase. The main injection rise rate for a dwell of 500 µs, however, is very similar to the rise rate for a dwell of 140 µs. The rise rate for a dwell of 1200 µs starts later than for other dwells and is comparable to the single injection rise rate. The trends described here do not correspond to the combustion noise trends shown in Fig. 4.

Because the three regimes identified in the main injection rate shape (shown in Fig. 9) occur at dwells that seem relevant for the trend in combustion noise (see Fig. 4), optical measurement techniques were applied in the engine to search for evidence of main injection rate shaping. The following operating points were chosen to be investigated with the high-speed elastic scattering measurements:

- Dwell of 90 µs
- Dwell of 140 µs
- Dwell of 300 µs
- Single injection

The simplest information to extract from the imaging data are the optically detected starts of injection. These are compared to the starts of injection as measured by the HDA and shown relative to the start of solenoid energizing (SSE) for the pilot and main injections (denoted with subscripts “p” and “m”, respectively) in Table 3. For every dwell tested, the start of the main injection could clearly be identified in the imaging, thus confirming that even for very short dwells, the pilot and main are separate injection events (cf. Fig. 10). Data for the single injection are omitted, as they are essentially the same as for the pilot injection.

Table 3: Starts of injection as measured by the HDA and detected in imaging data

Dwell (µs)	$SOI_{p,HDA}$ (µs $ASSE_p$)	$SOI_{p,images}$ (µs $ASSE_p$)	$SOI_{m,HDA}$ (µs $ASSE_m$)	$SOI_{m,images}$ (µs $ASSE_m$)
300	311	342	289	320
140	310	342	139	155
90	308	342	170	185

The delay between the start of solenoid energizing and the detected starts of injection are nearly constant for the pilot injection. The start of injection as detected by the HDA occurs sooner than the optically detected start of injection; the time difference between these two events is nearly constant and on the order of 30 μs. For the main injection, the delay between SSE and SOI is smaller than for the pilot for dwells shorter than 300 μs; this trend is observed both with the HDA and with the optical data. For a dwell of 140 μs, this delay is shorter than for the other dwells tested. However, the injection train is block-shifted to achieve the desired combustion phasing for each dwell so this delay is insignificant. The difference in delay times between HDA data and imaging data is smaller for dwells less than 300 μs.

Liquid penetration lengths are computed from the imaging data as described in the appendix for each of 45 cycles. The temporal development of the liquid length measured at one jet is shown in Fig. 11 for each cycle, as is the ensemble-averaged liquid length. Aside from an anomaly at the beginning of the pilot injection that is related to limitations of the background subtraction routine, the liquid penetration behaves nearly linearly for the rise rate of both injection events. This rise rate behavior is highly repeatable for both injections for all cases tested.

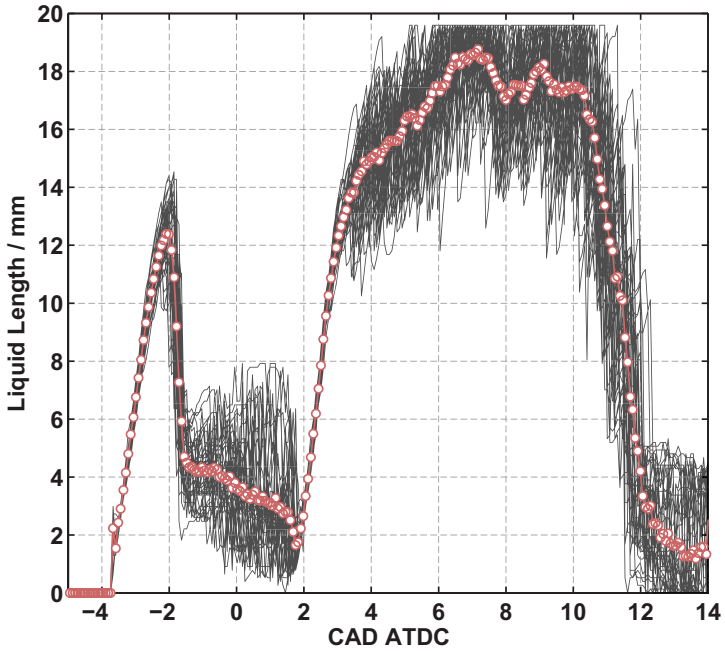

Fig. 11: Liquid lengths for individual cycles (black) and ensemble averaged (line with circle markers) for a dwell of 300 μs

The initial linear liquid penetration is consistent with the short-time behavior of a diesel jet as described in (Naber and Siebers, 1996) and measured by others, for example Hiroyasu and Arai (1990) and Reitz and Bracco (1979). The initial liquid penetration rate of the pilot injection is comparable to the data shown in (Payri *et al.*, 2008) for a similar ambient density, rail pressure, and nozzle hole size. For some cycles, the penetration of liquid fuel extends past the edge of the image. This is evidenced in Fig. 11 by clipping of the individual cycles. As a result, the ensemble-averaged liquid length is not accurate for crank angles between approximately 5 and 11 CAD ATDC. The computed liquid lengths after the initial pilot injection penetration and before the start of the main injection fluctuate from cycle to cycle. This is due to liquid fuel that either dribbles from the injector or to remaining liquid fuel near the injector. The liquid jet penetration behavior is not the same for every jet; some are characterized by shorter pilot injection liquid lengths and wider pilot injection spreading angles. These differences typically become smaller for the main injection. One such jet is chosen for comparison between the various dwells, but the general trends observed in liquid penetration are similar for other jets, particularly during the main injection rise rate. The ensemble-averaged liquid lengths are compared in Fig. 12 for each dwell tested and for the single injection.

The liquid length behavior for the pilot injection does not appear to change as dwell is varied. The end of the pilot injection is characterized by a contraction in liquid length, and for the dwell of 300 μs, the measured liquid lengths become noisy and erratic during the hydraulic dwell. This behavior is

attributed to the background subtraction routine, as no liquid fuel is observed in this region of the image at this time. As the main injection starts, the liquid length again increases, and the rates of these increases appear to be different for each dwell. After the rise rate phase, the liquid length behaves similarly for all of the dwells.

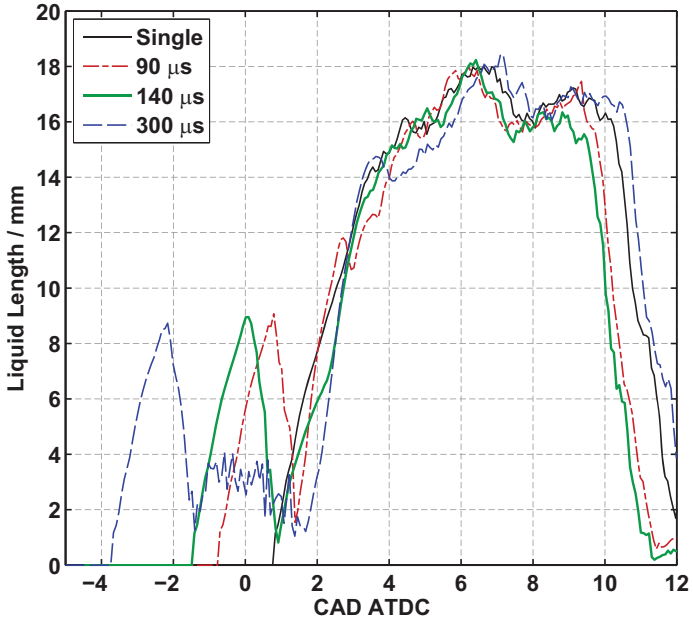

Fig. 12: Liquid length comparison for a single jet with dwell as a parameter

In order to characterize the differences in the liquid length behavior during the first phase of the main injection, the time derivative of the liquid length curves is calculated and averaged over all seven jets. The resulting penetration rate curves are shown in Fig. 13. Note that the injection rate shape is shown for a dwell of 80 μs, whereas the penetration rate is shown for a dwell of 90 μs; the injection rate shapes shown in Fig. 9 suggest that the differences in rate shapes between these two dwells are minimal. Only positive penetration rate values are shown in Fig. 13.

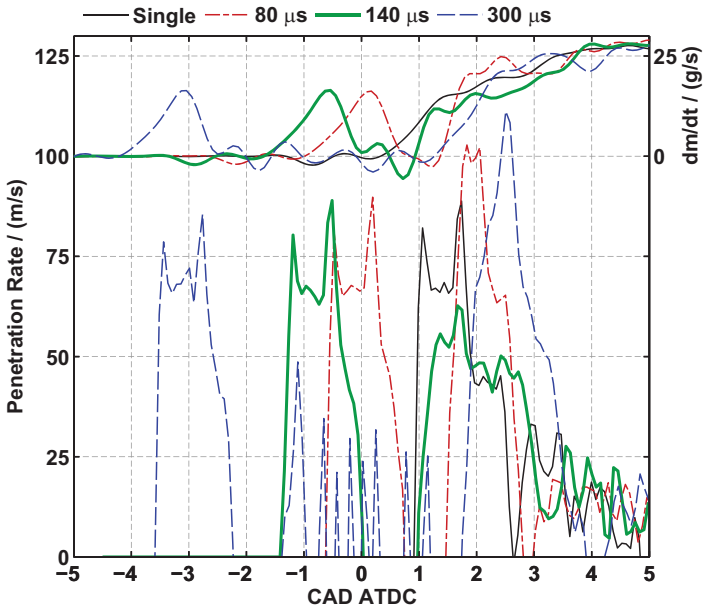

Fig. 13: Optically-measured liquid penetration rate and rate of injection as measured by the HDA with dwell as a parameter

The shape of the optically-measured jet penetration rate curves for the pilot injection events are very similar to one another and to that of the single injection. The phasing of the pilot injection penetration rates relative to their corresponding injection rate profiles (measured with the HDA) is consistent for each dwell. As indicated by the rate of injection data (HDA), the single injection begins at a crank angle before any main injections, followed by the main injection for a dwell of 140 μs. This behavior is also observed in the (optical) penetration rate data. However, optical data indicates that the main injection for a dwell of 90 μs begins at an earlier crank angle than for a dwell of 300 μs. This does not agree with the trend shown in the HDA data. The peak main injection penetration rates (optical) for a dwell of 140 μs are lower than for any other case; this behavior is consistent with the lower rates of injection (HDA) for this dwell. The phasing and amplitudes of the maxima in the penetration rates agree qualitatively with the corresponding trends in the injection rate data.

4. Discussion

The comparison between rates of injection as measured by the HDA and the optically-determined jet penetration rates provides strong evidence that injection rate shaping of the first phase of the main injection is occurring, and that this rate shaping changes as dwell changes. The qualitative agreement between these two data sets lends credibility to the rates of injection measured outside the engine with the HDA.

When taken alone, the data shown in Fig. 13 provide evidence that the rate shaping of the main injection may play a significant role in the combustion noise trend shown in Fig. 4. However, if all of the main injection rate shapes measured by the HDA are representative of the true injection rate behavior during fired engine operation, then significant evidence exists to refute this claim. For example, Fig. 10 shows that the main injections for dwells of 80 μs and 1200 μs begin at nearly the same crank angle. The rates of injection increase much faster and reach higher levels for the dwell of 80 μs, and indeed the AHRR data for these two dwells (shown in Fig. 6) are significantly different from one another. However, the combustion noise for a dwell of 80 μs is only 0.4 dB louder than for a dwell of 1200 μs, which equates to a factor in acoustic power of approximately 1.1. Furthermore, the injection rate shapes for dwells of 140 μs and 500 μs are very similar. Differences in the AHRR behavior of these two dwells exist, but they are certainly less significant than for the comparison between 80 μs and 1200 μs. In the 140-500 μs dwell comparison, the difference in combustion noise is approximately 3 dB, which is a factor of two in acoustic power and much more significant that the noise difference between the cases of 80 μs and 1200 μs. These results are not consistent with the notion that main injection rate shaping can significantly affect combustion noise. We do not have evidence to suggest that the rates of injection measured by the HDA are inaccurate. Rather, the optical measurements promote confidence in the accuracy of the HDA results. It is hypothesized that in this case, the combustion noise trend is caused primarily by other factors.

One such factor may be the result of the interaction between the pilot mixture field and the main injection. The lower peak rates of pilot heat release for a dwell of 140 μs, combined with the temporal overlap between the pilot heat release and the main injection (see Fig. 6), support the theory that the main injection can influence the pilot mixture combustion process. The abrupt increase in ignition delay for dwells shorter than 180 μs shown in Fig. 8 provides further evidence that the main injection can interfere with the ignition process of the pilot mixture. The resulting decrease in peak pilot mixture heat release rates may play a role in creating the combustion noise minimum observed for a dwell of 140 μs.

As dwell is changed through a large range of values, it is conceivable that the way in which the main injection mixture field is ignited or inflamed also changes. Computational modeling presented in (Hasse and Peters, 2005) indicates that a premixed, near-stoichiometric, strained flame propagates through the pilot mixture field and towards the main injection mixture field. The associated transfer of heat and mass between the two mixture fields is ultimately responsible for the ignition of the main injection mixture field. Large mixture fraction gradients in the pilot mixture field increase the propagation speed of the premixed flame, thus shortening the inflammation delay for the main injection mixture field. The timing of the main injection relative to the pilot injection was not discussed in this work, but it would most certainly change the way in which these two mixture fields interact.

Another factor that may contribute to the observed trend in combustion noise is the effect of the changing relative phasing between the pilot and main injection heat release. Initial results indicate that this phasing change could be a significant, if not dominant factor; it must therefore be the subject of future studies.

5. Summary

A sweep of pilot-main energizing dwell was performed in a small-bore, light-duty Diesel engine at a moderate engine load. Dwell varied between 1200 μs and 80 μs as engine load and combustion phasing (MFB50) were held constant; a minimum in combustion noise was recorded for a dwell of 140 μs without a penalty in pollutant emissions. The injection schedules used during the engine testing were evaluated offline using the fuel injection equipment together with an injection rate measuring device. Optical scattering measurements at 120 kfps were made in the engine with motored (non-combusting) operation to examine the injection behavior at several dwells and processed using an automated image distortion correction routine based on ray tracing to determine liquid length and liquid penetration rates.

Both the rate of injection results and the calculated jet penetration rates suggest that rate shaping of the first phase of the main injection is occurring in the engine (see Fig. 10 and Fig. 13), and the trends in these data agree qualitatively. However, the lack of clear correlation of both heat release data and measured rates of injection with combustion noise does not support the idea that main injection rate shaping is responsible for the significantly lower combustion noise levels measured at dwells near 140 μs. These data suggest that the main injection and the (possibly combusting) pilot mixture field do interact, and the resulting impact on the heat release associated with the pilot injection may play a role in creating the observed minimum in combustion noise. Additionally, the relative phasing of the pilot and main heat release is believed to play a significant role in determining combustion noise for close-coupled pilot injections. In this work, we've shown that with an optimized pilot-main injection strategy, combustion noise can be reduced by 3 dB compared to non-optimized pilot-main strategies with no emissions penalty.

Acknowledgements

The authors thank Ethan Eagle and Jeremie Dernotte for their insightful comments on this work. Support for this work was provided by the United States Department of Energy (Office of Vehicle Technologies) and by General Motors Corporation (agreement FI083070326). This work was performed at the Combustion Research Facility of Sandia National Laboratories in Livermore, California. Sandia is a multiprogram laboratory operated by Sandia Corporation, a Lockheed Martin Company, for the United States Department of Energy's National Nuclear Security Administration under contract DE-AC04- 94AL85000.

References

Badami, M., Millo, F., and D'Amato, D., "Experimental Investigation on Soot and NOx Formation in a DI Common Rail Diesel Engine with Pilot Injection," SAE Technical Paper 2001-01-0657, 2001, doi:10.4271/2001-01-0657.

Diesel Systems: Common Rail Systems CRS2 with 1,600 to 2,000 bar and solenoid injectors. Robert Bosch GmbH, Diesel Systems, 2011. Available online March 2014.

Dürnholz, M., Endres, H., Frisse, P., "Preinjection A Measure to Optimize the Emission Behavior of DI-Diesel Engine," SAE Technical Paper 940674, 1994, doi:10.4271/940674.

The new 1.3 Multijet II 95 HP (Euro5) engine is making its first appearance on the Fiat 500 and 500C. Fiat Group Automobile Press, 25 Nov. 2009. <www.fiatgroupautomobilespress.com/cartelle/zoom/4594>, Available March 2014.

Hasse, C., Peters, N., "Modelling of ignition mechanisms and pollutant formation in direct-injection Diesel engines with multiple injections," International Journal of Engine Research, Vol. 6, No 3, pp. 231-246, June 1, 2005.

Hiroyasu, H. and Arai, M., "Structures of Fuel Sprays in Diesel Engines," SAE Technical Paper 900475, 1990, doi:10.4271/900475.

McFarlane, N.J.B., Schofield, C.P., "Segmentation and tracking of piglets in images," Machine Vision and Applications, Vol. 8, Issue 3, pp. 187-193, 1995.

Moehwald HDA instruction manual: "Injection analysis using the method of hydraulic increase of pressure." Moehwald GmbH, Sept. 24, 2008.

Naber, J. and Siebers, D., "Effects of Gas Density and Vaporization on Penetration and Dispersion of Diesel Sprays," SAE Technical Paper 960034, 1996, doi:10.4271/960034.

Payri, R., Salvador, F.J., Gimeno, J., de la Morena, J., “Macroscopic Behavior of Diesel Sprays in the Near-Nozzle Field,” SAE Int. J. Engines, Vol. 1, Issue 1, 2008; SAE technical paper 2008-01-0929.

Reitz, R. and Bracco, F., "On the Dependence of Spray Angle and Other Spray Parameters on Nozzle Design and Operating Conditions," SAE Technical Paper 790494, 1979, doi:10.4271/790494.

Ricaud, J.C. and Lavoisier, F., “Optimizing the multiple injection settings on an HSDI diesel engine,” Proceedings of the Conference on Thermo- and Fluid-Dynamic Processes in Diesel Engines, pp. 251-275, Valencia, 2002.

Russell, M., Young, C., and Nicol, S.W., "Modulation of Injection Rate to Improve Direct Injection Diesel Engine Noise," SAE Technical Paper 900349, 1990, doi:10.4271/900349.

Shahlari, A., Hocking, C., Kurtz, E., and Ghandhi, J., "Comparison of Compression Ignition Engine Noise Metrics in Low-Temperature Combustion Regimes," SAE Int. J. Engines 6(1):541-552, 2013, doi:10.4271/2013-01-1659.

Smith, W.J., Modern Optical Engineering, 4th ed., McGraw-Hill, New York: 2008.

Zeuch, W., „Neue Verfahren zur Messung des Einspritzgesetzes und der Einspritz-Regelmäßigkeit von Diesel-Einspritzpumpen.“ MTZ Vol. 22, Issue 9, 1961.

Appendix: Image Distortion Correction and Processing

Because imaging is performed through the piston, the raw images are distorted. The distortion pattern depends on both the crank angle and the location of the object plane relative to the piston. While automatic distortion correction routines exist in commercial image capture software packages, they often require human intervention if the distortion becomes too extreme. For this work, a new approach to automated image distortion correction has been developed based on ray tracing. This approach takes advantage of the axisymmetry of the piston (except for the valve cut-outs, which do not affect images of the fuel injection), so the problem of distortion correction is reduced to two dimensions (a radial dimension and a dimension parallel to the cylinder axis). The simulation of rays and their interaction with the piston is simulated with the methodology described below.

A ray is defined by its starting point and direction of propagation. The intersection of the ray's path and a surface is computed and the interaction of the ray with the surface simulated. Depending on the nature of the surface, the ray may be reflected, refracted, or absorbed. It is then transformed into a new ray (defined by its origin at the intersection and its new direction). Refraction is computed according to Snell's law (Smith, 2008).The ray is traced in this manner until it leaves the system. Cubic splined surfaces with continuous first derivatives define the two-dimensional piston perimeter (shown in Fig. 14).

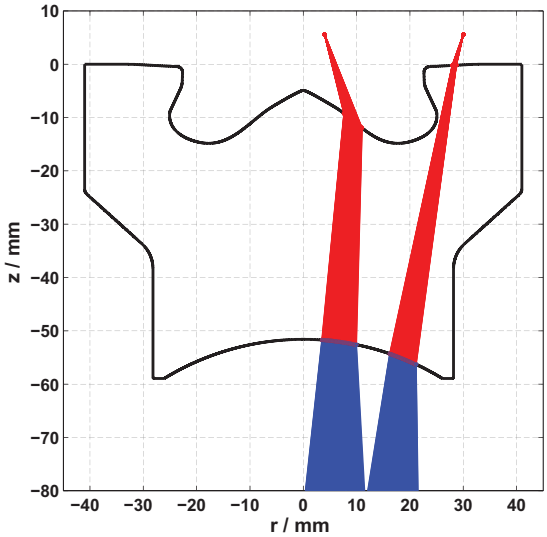

Fig. 14: Ray bundles originating from two points in 2-D space above the piston and their paths through the piston towards the mirror

A fan of rays with their origins at a given point in space above the piston is defined, and each is traced until it leaves the system. The rays that determine the form of the distorted image are those that reach the piston mirror and camera. In the case of this simulation, these rays are assumed to be the ones that pass through a long (~250 mm) absorptive vertical tube (diameter 49.8 mm) located below the piston so that they reach the elliptical piston mirror (depicted in Fig. 3). The ray bundles shown in Fig. 14 represent the rays that leave from these two original points and reach the piston mirror. Rays leaving these points at any other angle will not reach the mirror. In other words, only rays that would reach the piston mirror are allowed to leave the system. It is observed that the rays leaving the piston and reaching the turning mirror are divergent (shown by the bundles of rays leaving the bottom of the piston in Fig. 14). Therefore, one or several virtual images are formed at the back-projected intersections of these rays with one another. In this way, a point in real space is mapped to a cloud of intersection points that are the virtual image of the original point. The virtual images of objects above the piston (calibration targets, liquid fuel, etc.) are what the camera "sees".

For crank angles near TDC and ray fan origins in or near the piston bowl, the virtual images that form are often confined to very small spaces, such that they can be represented by a single point with reasonable precision (typically better than 100 μm in the radial direction). For this work, a mapping between the real world and the virtual image is defined in this manner. A series of ray fans located at various points along a line inside the cylinder can be traced and represent the radial mapping function of a surface in real space. Once this mapping function is known, an image is distortion-corrected as follows:

1. The center of the cylinder is determined from the raw (distorted) image; this is performed manually, as the location of the center does not change from experiment to experiment.
2. The distance between the center point and each pixel (i.e. radius) in the raw image is computed.
3. The radii determined in step 2 are scaled by an empirically determined scaling factor (the ratio of distance in virtual image space to pixels in the captured images) to determine their magnitude (in mm).
4. The virtual image radii are used as inputs to the radial mapping function to yield undistorted radii.
5. The undistorted radii are scaled by a constant (8 pixels/mm) to determine the spatial scaling of the final image.
6. The pixels of the original image are moved into their new positions as defined by the undistorted radii (the angular position of each pixel remains unchanged).
7. A two-dimensional, bi-linear interpolation scheme is used to “fill in the blanks”, that is the locations where no information is available after the initial pixel displacement procedure described in step 6.

It is observed that the distortion of a horizontal plane changes dramatically as the plane is moved parallel to the cylinder axis towards the piston pip. This is a problem when imaging the injection jets, as they are not oriented in a horizontal plane. Ray tracing is therefore performed for ray fans located along the theoretical jet axis (inclined by 15.5 ° to the cylinder head). An example of such a ray tracing simulation is shown in Fig. 15 for a limited number of ray bundles. The black dots indicate the locations of the virtual images of each point along the jet axis. Mapping functions generated in this manner are created for crank angles between 12 CAD BTDC and 30 CAD ATDC in increments of 2 CAD. They are combined in three-dimensional space (crank angle, virtual image radius, undistorted radius) and a surface is fitted to them. This surface is used to determine the mapping function (via bilinear interpolation) for any arbitrary crank angle within this range. In this way, any image can be automatically distortion corrected if the crank angle at which it was taken is known.

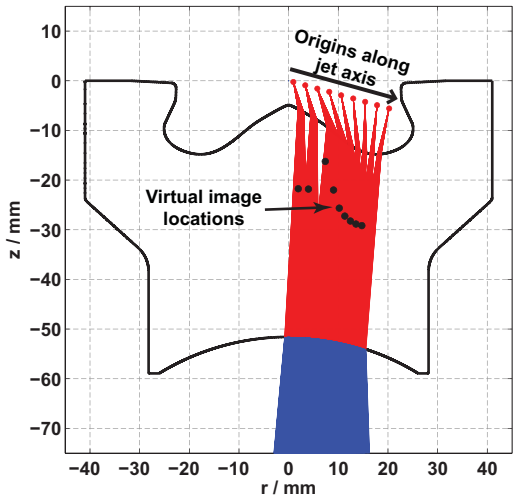

Fig. 15: Example of ray tracing with ray bundle origins located along the injection jet axis and black dots to show the locations of virtual images

For this work, the distortion corrected images are scaled to a resolution of 8 pixels per mm along the jet axis. Testing of this procedure with calibration targets oriented along the jet axis indicate that it introduces an uncertainty in liquid length measurements of something on the order of 2 pixels, or 0.25 mm along the jet axis. However, any errors in liquid length measurements will be largely consistent between different cases, as the distortion correction is the same for a given crank angle. This facilitates comparison between images taken for various dwells.

Once the images in a sequence have been distortion corrected, steps are taken to isolate the injection jets from the background. For this work, the approximate median method described in (McFarlane and Schofield, 1995) is used to model the background. This method relies on a sequence

of images, which in this case are the sequences of 300 distortion corrected images for every injected cycle. The background model is initialized as the first image (taken at SSE, at which point the injection has not yet started). For each subsequent image in the sequence, the background model is updated and a background subtracted image is created, then thresholded. This method effectively removes features attributed to the background, such as the valves and the injector tip. Finally, each jet's image data is isolated and processed individually. Liquid lengths are calculated according to the methods given by Naber and Siebers with some subtle differences (1996). Liquid lengths are initially computed from the images and are measured from the empirically determined center of the chamber (not the apparent origin of the jet, which cannot be adequately distinguished from the injector's axis with the resolution provided by this system). The distance between the injector axis and the nozzle exits is subtracted from this distance. This length represents the projection of the true liquid length, which exists along the jet axis, onto a horizontal plane. The liquid lengths reported in this work are calculated by dividing this length by the cosine of 15.5 °. A threshold value of 3% of the maximum intensity for the jet in question proved to be robust for all cases. Liquid lengths are calculated for each jet in each frame in every image sequence. An example of a distortion corrected, background-subtracted image is shown in Fig. 16. The locations where the projected liquid length is computed are shown with small "+" symbols, and a large "+" is positioned at the center of the image.

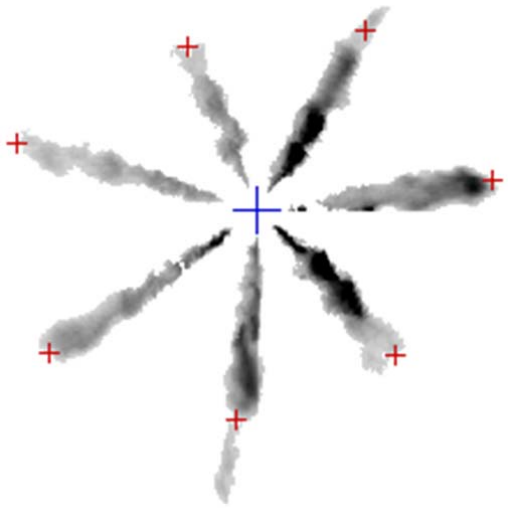

Fig. 16: Distortion corrected, background-subtracted image; displayed with an inverted grayscale color map, 0-512 counts, gamma = 0.7

The visually detected starts of injection events are defined by the frame for a given operating point at which bright spots at the injector nozzle holes are visible in every cycle. For the preceding frame, these bright spots are visible only for some cycles, so there is some scatter in the visually detected start of an injection event. This scatter never involves more than two frames, so the combined temporal uncertainty and scatter in the visually detected start of injection are on the order of 15 μs.

An optimized combustion system dedicated to a 1.5l down-speeded Diesel engine.

P.Gastaldi[1] and L.Mermaz-Rollet[1]

[1]Renault Powertrain Division – 1 allée Cornuel – F-91510 Lardy, France

E-mail: patrick.gastaldi@renault.com
Telephone: +(33) 176 87 05 14
Fax: +(33) 176 87 05 29

Abstract. During the last decades, the necessity to significantly reduce both the local pollution, particularly in large urban areas, and the global earth warming, led car manufacturers to optimize the Diesel engines; as the successful down-sizing strategy is limited for small displacement powertrains, mainly because of a difficult combustion optimization with small bores, some other solutions had to be investigated. Among them, down-speeding seems to be quite promising. Following this idea, a 1.5 liter two valve large production engine has been adapted with a Roots compressor in order to enhance low end torque and thereby to allow long gear ratios. At the same time, the combustion system has been strongly improved by the use of new small hole nozzles and high injection pressures.

Notation

BMEP Brake mean Effective Pressure
IMEP Indicated Mean Effective Pressure (high pressure cycle only in this document)
ISFC Indicated Specific Fuel consumption
VNT Variable Nozzle Turbine

1. Introduction

The worldwide concern linked to both the earth global warming and the local pollution in urban areas has led public authorities and automotive manufacturers to set up new rules for the upcoming regulations. Concerning CO_2 in Europe, the target is to achieve average emissions of 95 g/km for passenger cars in 2020 as the starting point was 140 g/km in 2007. The trend is the same in other large countries but also for light duty vehicles as shown in Fig.1. As the effort has been focused on soot particles between Euro4 and Euro5, the target is now to divide NOx by a factor larger than 2 between Euro5 and the final Euro6 limit –see Fig.2. This evolution is accompanied by a significant effort to measure fuel consumption and emissions on cycles which would be closer to the actual use of the customers. The proposed WLTP cycle therefor presents engine operating points with higher speeds and loads (Fig.3).

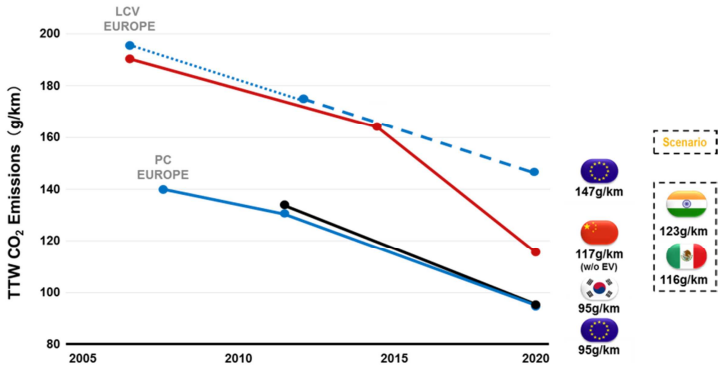

Figure 1: evolution of CO_2 regulations

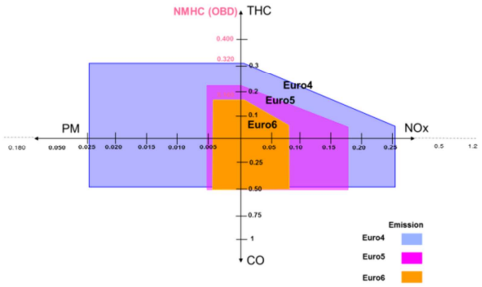

Figure 2: evolution of pollutant limits in Europe

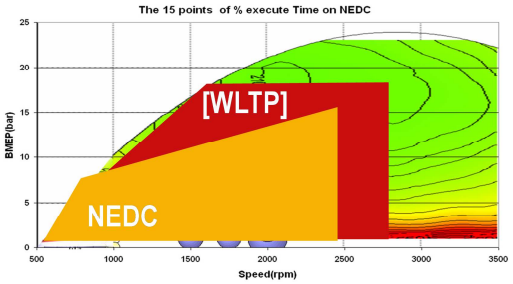

Figure 3: new driving cycle procedure

To achieve this difficult task, while integrating the necessity to keep the overall cost of the engine associated to the after-treatment system as low as possible, the down-sizing solution has up to now been successful for numerous applications; limitations nevertheless exist in terms of NOx limits and combustion optimization for tomorrow, particularly due to high loads, and especially for small displacement engines. In this case, down-speeding could provide a significantly interesting alternative.

2. Down-speeding a small displacement engine.

2.1 Potentialities and challenges

The down-speeding concept for Diesel emerged from the basic relation between high load and high efficiency; Figure 4 is presenting an example of the fuel consumption map for a small displacement engine. For a given power requirement on the shaft, increasing the load while reducing the engine speed allows to improve the global efficiency by a simultaneous reduction of the friction losses and a rise of the indicated efficiency. This advantage is nevertheless balanced by an emission increase at constant power, a higher torque requirement at low revolutions as presented in Fig. 5 and a higher stress on the crankshaft and on the bearings. The present paper analyses in detail the measures applied to the combustion system and quickly presents a potential solution for the air charging.

A parallel advantage of the down-speeding, due to the extra torque at low engine rev, is provided by the possibility to increase the length of the gearbox ratios and therefore to obtain a better fuel consumption at constant vehicle speed.

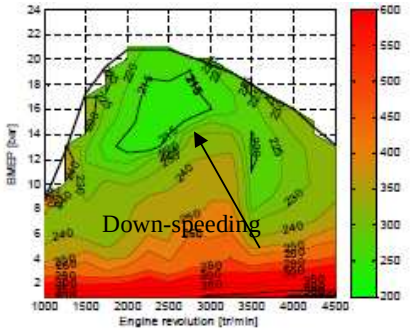

Figure 4: typical BSFC map of a small Diesel engine

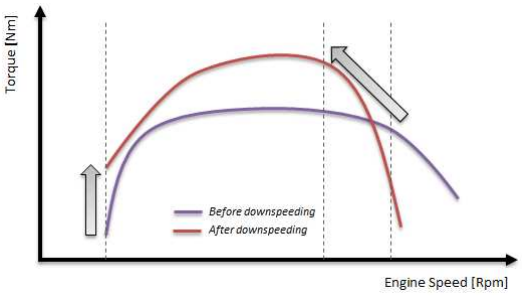

Figure5: new torque requirement for down-speeding

2.2 Application to a small displacement engine.

A large production two valve four cylinder engine, whose characteristics are summarized in Table 1, has been chosen as a basis for this evaluation. It was equipped with a very up to date EGR system, integrating both high pressure and low pressure routes. The specific power of around 56 kW/l,

still compatible with the two valve arrangement (Gastaldi and alii, 2006), has to be maintained as the torque might be increased by up to 35% at very low engine speed as illustrated in Fig.6.

Table 1: main characteristics of the basic engine

Engine Main Properties	
Bore	76 mm
Stroke	80.5 mm
Compression Ratio	15.5
Swept Volume	1.46L
Number of cylinders	4
Exhaust Gas Recirculation	High + Low pressure loop

Figure 6: full load requirement

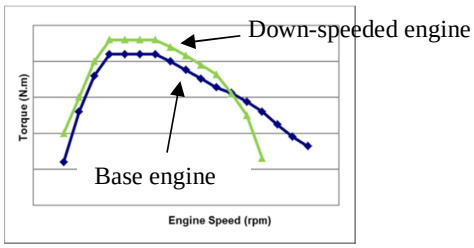

2.3 Improvement of the combustion system.

The standard piston has been chosen for the presented investigation, with a bowl centered versus the cylinder liner. The core of the work consisted in optimizing the injection and especially the nozzle definition, in terms of number and diameter of the holes, and the rail pressure. Table 2 thereafter describes the different variants of the prototype piezo driven Continental system used during the tests. The choice of a very high injection pressure associated to small holes was driven by both the quite high specific performances of the engine and the necessity to keep soot emissions as low as possible or, with other words, to secure the capability of using high EGR levels to reduce NOx at high loads.

Table 2

Main injection system characteristics					
Supplier		Continental			
Injection system		piezo			
Maximum Rail Pressure		up to 2000 bars			
Injector inclination versus cylinder axis		15.5°			
Nozzles	Hydraulic flow *(cm3/30s/100 bars)*	reference			ref – 20%
	Number of holes	7 holes	8 holes	9 holes	8 holes
	Hole diameter	**108 µm**	**98 µm**	**94 µm**	**94 µm**
	Sheet angle	reference			

2.4 Improvement of the air system.

The low speed torque requirement added to high specific power needs justified the use of a double staged compound; during this investigation, a mechanical roots type compressor associated to a variable nozzle turbocharger (VNT) has been evaluated. The air system was adapted with a dedicated air-to-air intercooler (Fig.7). The roots compressor was directly driven by the engine crankshaft. It had no internal compression but 4 helical lobes with a 160° pattern. Several drive ratios provided by a gear box were available and it could be declutched when needed.

For a small Diesel engine, using a mechanical roots type compressor gives the advantage of a more compact engine exhaust face. Nevertheless, the key point is concerning the balance between the positive low pressure IMEP and the negative friction losses; this compromise has a great influence on the final fuel consumption. A pertinent evaluation of the efficiency of the Roots compressor was not possible during these tests because the prototypes were not really representative of production products in terms of size and technical achievement. It is the reason why all the ISFC data are only concerning the high pressure loop of the thermodynamic cycle.

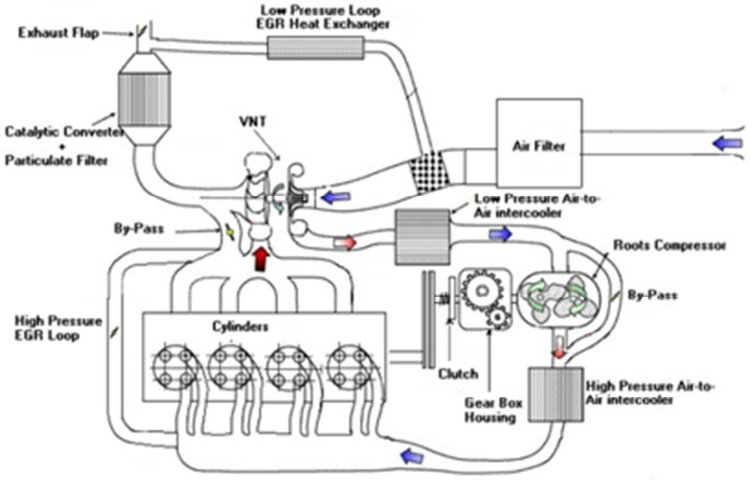

Figure 7: schematic view of the air system

3. Tests results

3.1 Full load performances.

3.1.1. Effect of the injection pressure

The aim of the test was to evaluate the impact of the rail pressure with the standard 7 hole injector. The maximum cylinder peak pressure and the exhaust gas temperature before the turbine were limited as on the stock engine but the rated speed to achieve the maximum power density of 56 kW/l was decreased down to 3500 rpm.

Figure 8 presents the evolution of the heat release for different rail pressures between 1600 and 2000 bars at a constant relative equivalence ratio of 0.8 and a constant swirl level. At 2000 bars, the combustion is significantly quicker and presents a more intense diffusion controlled phase due to both a higher mass flow rate during the injection and a better fuel atomization and evaporation. This rather early end of combustion is synonym of a reduced gas temperature before the turbine.

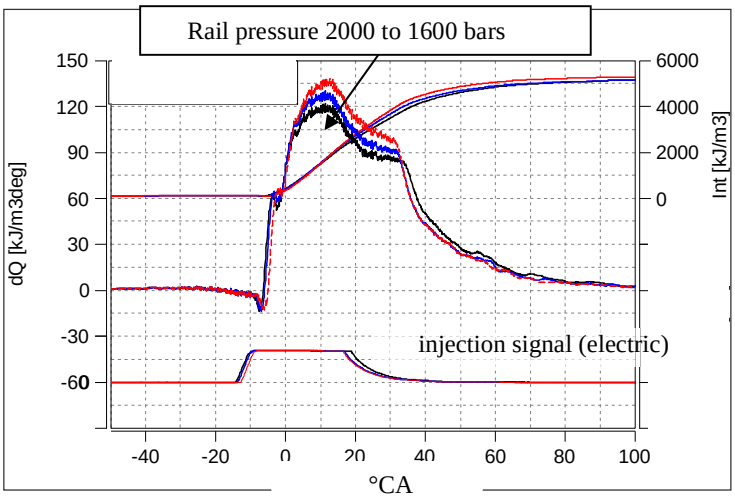

Figure 8: heat release rate at 3500 rpm, constant equivalence ratio 0.80, effect of the rail pressure

This advantage could be used either to increase the equivalence ratio and thereby the power at constant ISFC or to operate leaner, thereby with a better efficiency, if the power remains constant as shown in Fig.9. Up to 5 g/kWh could thereby be saved.

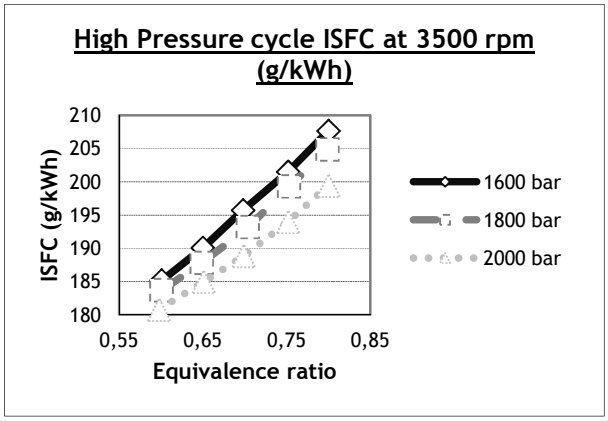

Figure 9 : ISFC at 3500 rpm for different rail pressures

3.1.2. Effect of the number of holes

As described in Table 2, the increase of the number of holes was matched with the reduction of the orifice diameter in order to keep the same hydraulic flow as for the reference. The swirl level was constant for all the configurations and set at the minimum value achievable on the cylinder head due to the 2 valves architecture. The injection timing has been adapted in order to obtain the same heat release; the rail pressure was constant and equal to 2000 bars. As presented in Fig.10, the 8 and 9 hole nozzles provide the same significant advantage of around 0.4 FSN compared to the 7 holes reference in term of smoke level for the richest mixture. With this combustion chamber configuration, a further decrease of the swirl, reducing spray overlap, would probably have been necessary to take benefit of the 9 holes variant.

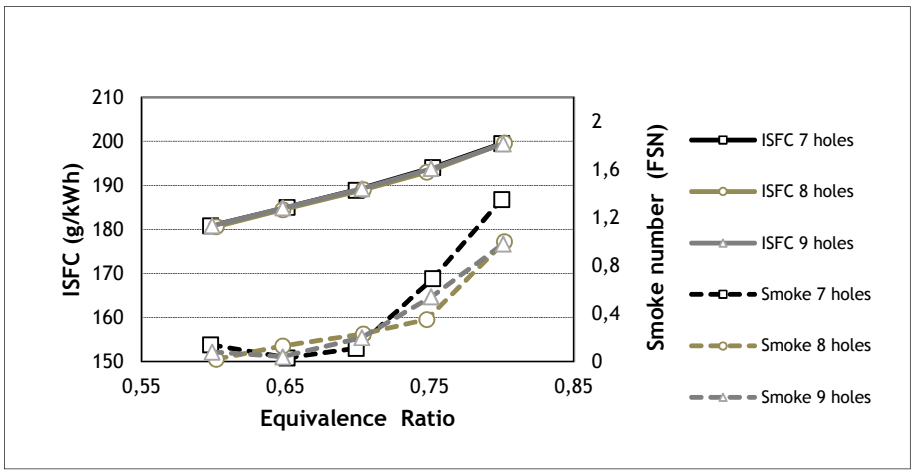

Figure 10*:* impact of the number of holes – Rail pressure 2000 bars – constant heat release

The reduction of the holes diameter, while improving fuel atomization, generates a more intense diffusion controlled combustion as shown in Fig.11. This result is completely coherent with the analysis achieved in the past and particularly within the DICO consortium (Bruneaux and alii, 2012).

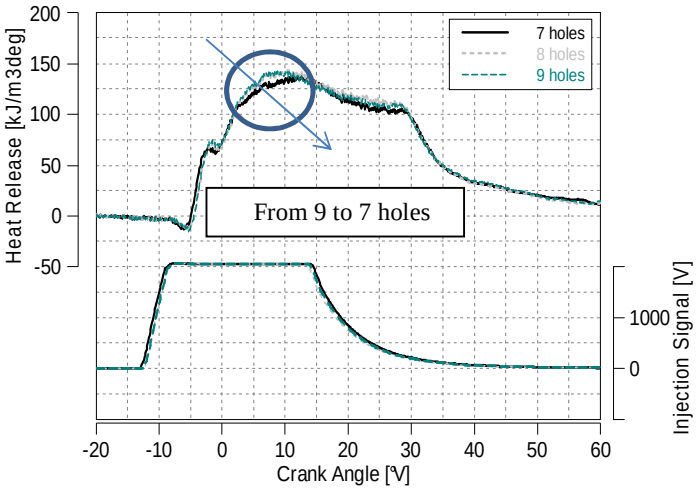

Figure 11: heat release rate at 3500 rpm - equivalence ratio 0.8 - rail pressure 2000 bars

3.1.3. Effect of the hydraulic flow

The choice of the hydraulic flow is a key point concerning the trade-off between full load performances and part load emissions; during this evaluation, the 8 hole nozzle has been chosen with two different flows, the first one keeping the same value as the reference configuration and a second one with a 20% flow reduction. The rail pressure was kept constant at 2000 bars. Figure 12 shows the results obtained at 3500 rpm

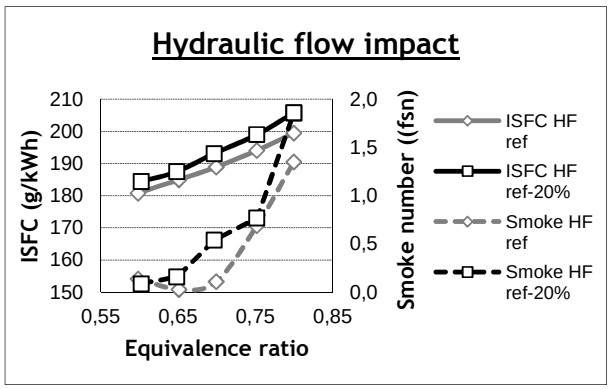

Figure 12: effect of the hydraulic flow – 3500 rpm – rail pressure 2000 bars –

At constant equivalence ratio, a reduced hydraulic flow provided a slight disadvantage in fuel consumption and smoke as illustrated by Fig.12. But the association of a reduced hydraulic flow and a high rail pressure led to a significant advantage in peak power at 3500 rpm in comparison with the reference configuration, keeping the maximum cylinder pressure and the turbine inlet temperature constant, as shown in Fig.13.

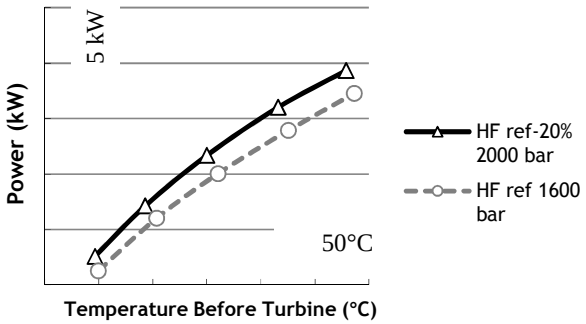

Figure 13: equivalence ratio sweep at 3500 rpm, constant peak pressure

3.1.4. Effect of the air flow

The torque at low speed is a critical parameter for down-speeding, especially for small displacement engines whose atmospheric BMEP is naturally reduced. To obtain better performances in this range of operating points, a Roots type compressor has been added to a conventional Variable Nozzle Turbine; different gear ratios have been tested to optimize the air flow. As noticed earlier, the state of development of the used prototypes didn't allow to take the induced mechanical losses into account but this point would obviously need to be investigated later on in the project.

Figure 14 shows the impact of the air system on the maximum torque obtained between 1000 and 2000 rpm. The benefit of the Roots compressor below 1500 rpm is clearly visible with an advantage between 50 and 75 Nm compared to the solution with the original turbocharger. The torque target necessary to use sufficiently long gear ratios and thereby significantly reducing the fuel consumption has been outperformed.

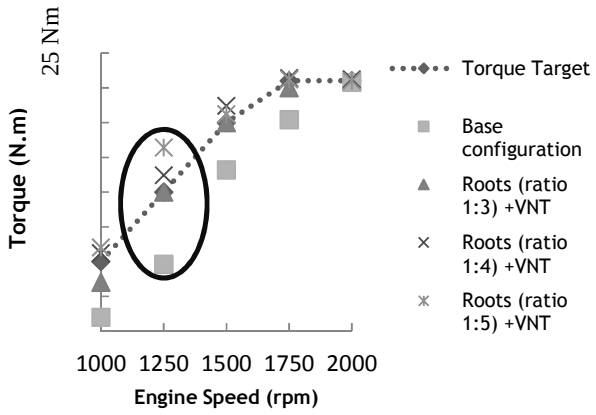

Figure 14: air flow impact at low engine speed – same smoke level

3.2. Part load performances

3.2.1. Effect of the number of holes

The compromise between NOx and soot levels is of first order of importance even with the use of advanced after-treatment systems. The size of the different components, from the oxidation catalyst

to the Nox trap or the SCR, is obviously influencing the overall cost of the powertrain and the packaging possibilities on different platforms, especially for small vehicles.

On the other side, the regeneration frequency of the catalytic soot filter, or the presence of soot in oil, is influencing the customer fuel consumption and the oil drain intervals.

Figure 15 is showing how the number of nozzle holes is impacting the soot/NOx relation at 1750 rpm and 7 bars IMEP, with the same fuel consumption and noise levels. A 0.5 FSN reduction of the soot has been achieved by the 8 holes variant for the lowest NOx levels.

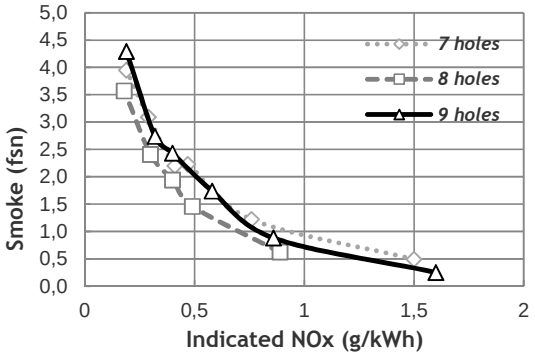

Figure 15: soot/NOx trade-off – 1750 rpm – 7 bars IMEP – same ISFC and noise

For other operating points, representative of the NEDC cycle, the conclusion is not so clear between the 8 and the 9 holes versions, with some advantages for the 9 holes variant as demonstrated in Fig.16. Nevertheless, the best compromise between full load and part load has been obtained with the 8 holes configuration.

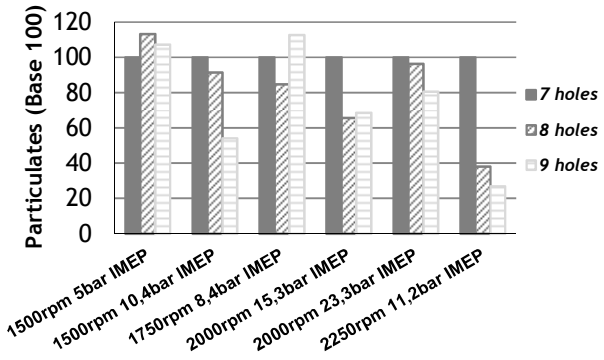

Figure 16: particle emissions on different operating points – constant NOx, noise and ISFC.

3.2.2. Effect of the hydraulic flow

A 20% reduction of the hydraulic flow, applied to the 8 hole nozzle, allowed to significantly reduce the smoke emissions at constant NOx, ISFC and noise levels as shown by Fig.17 and 18.

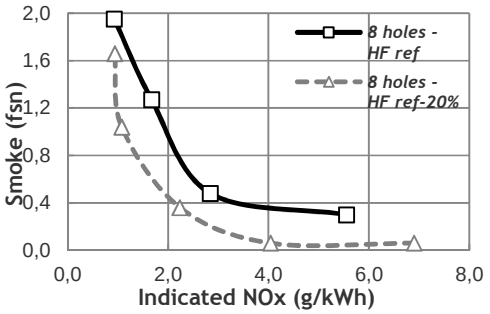

Figure 17: soot/NOx trade-off at 1500 rpm – 9 bars IMEP

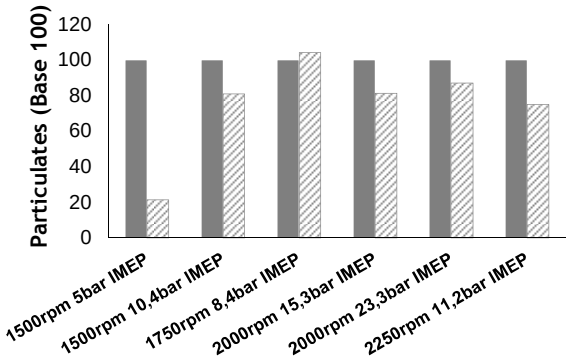

Figure 18: soot emissions at constant NOx, ISFC and noise

4. Conclusion.

The use of a Roots compressor associated to a conventional VNT allows to significantly improve the low end torque of a small displacement Diesel engine and thereby to adopt a down-speeding strategy to significantly reduce fuel consumption.

At the same time, small holes nozzles with a reduced hydraulic flow and an increased rail pressure, can secure the achievement of a high power density of 56 kW/l with a two valves per cylinder arrangement, as well as low emissions in terms of soot and NOx. This result is clearly due to the fuel atomization improvement.

Nevertheless, some more investigation still have to be led in order to optimize the behavior of the Roots compressor in terms of friction and to secure the absence of coking (Argueyrolles and alii, 2007) with small nozzle holes, especially for worldwide applications with different fuel qualities.

References

Argueyrolles B, Dehoux S, Gastaldi P, Grosjean L, Lévy F, Michel A, Passerel D: Influence of injector nozzle design and cavitation on coking phenomenon, Proceedings of JSAE 2007

Bruneaux G, Defransure F, Garsi C, Gastaldi P, Griffaton B, Kashdan J, Le Ru JP, Lombard B, Malbec LM, Nicolas B, Topenot E DICO**:** a new step towards emission free diffusive combustion, Proceedings of Thiesel 2012

Gastaldi P, Dehoux S, Lahjaily H: Development of Diesel combustion chambers for automotive engines : potential of the 2 valve design, Proceedings of SIA Lyon 2006

Application of JP-8 to Premixed Charge Ignition (PCI) Combustion in a Single-Cylinder Diesel Engine

Y. Park[1] , C. Bae[1] , C. Mounaïm-Rousselle[2] and F. Foucher[2]

[1]Korea Advanced Insititue of Science and Technology(KAIST), Department of Mechanical Engineering, KAIST, 373-1, Guseong-Dong, Yuseong-Gu, Daejeon 305-701, Korea.

E-mail: csbae@kaist.ac.kr
Telephone: +(82) 42 350 3044
Fax: +(82) 42 350 5044

[2]University of Orléans, PRISME, 8 Rue Léonard de Vinci, 45072 Orléans cedex 2

E-mail: christine.rousselle@univ-orleans.fr, fabrice.foucher@univ-orleans.fr
Telephone: +(00) 33 2 38494362
Fax: +(00) 33 2 38 41 73 83

Abstract. An aviation fuel, jet propellant-8 (JP-8) has been used as the single fuel for military vehicles to simplify the logistic supply. The emission regulations on military vehicles are forcing the engines fuelled with JP-8 to become cleaner. In this study, JP-8 was applied to premixed charge ignition (PCI) combustion, which is beneficial for low nitrogen oxides (NOx) and particulate matter (PM) emissions, in a single-cylinder diesel engine under two operating conditions. The JP-8 performance was also compared with diesel fuel. The main injection timings of two fuels were varied from 24 to 30 crank angle degree before top dead center (CAD bTDC) to prepare a premixed in-cylinder charge. Without exhaust gas recirculation (EGR), it was found that the ignition delay with JP-8 was 2~3 CAD longer than that with diesel fuel due to its lower cetane number although JP-8 has a better evaporation characteristics. This retarded combustion phase with JP-8 led to a higher indicated mean effective pressure (IMEP) compared with diesel fuel. The peak of heat release rate was lower with JP-8 because of locally leaner air-fuel mixture resulted from the prolonged ignition delay and the superior evaporation characteristics. This resulted in lower NOx and Smoke emissions with JP-8. With EGR, JP-8 also showed an improved trade-off relationship between NOx and Smoke emissions compared with diesel fuel due to its better evaporation characteristics which made the air-fuel mixture more homogeneous and leaner and lower aromatic contents. However, the 'EGR sensitivity', which is defined as the level of CA 50 retardation and increase of ignition delay according to the EGR rate, was lower for JP-8 compared to diesel fuel. In other words, the combustion phase with JP-8 was less affected by the EGR.

1. Introduction

After the Second World War, the NATO nations had established a policy that unifies all petroleum fuels used in the military field to the single fuel, named as single fuel concept (SFC). [US army 1991, Papagiannakis et al. 2006] The purpose of SFC is that simplify the logistics supply chain for petroleum fuels in the military field. As a result of SFC, jet propellant 8 (JP-8) was chosen for the single fuel. JP-8 is a commercial kerosene-type jet fuel including three additives; corrosion inhibitor, lubricity improver and anti-freeze additive. After the establishment of SFC, many researches that apply JP-8 to conventional diesel engines have been conducted widely. [Lestz et al. 1992, Kouremenos et al. 1997, Lacey et al. 1992] Most of the researches were carried out under conventional compression ignition (CI) combustion regime. From the previous researches, it was found that using of JP-8 without the modification of diesel engines did not show any critical problems in the engine operation [Lestz et al. 1992, Kouremenos et al. 1997]. However, deteriorations in fuel consumption and maximum torque were turned up due to the lower density of JP-8 than diesel fuel [Fernandes et al. 2007]. In terms of emission characteristics, it was reported that JP-8 emitted lower smoke compared with diesel fuel [Fernandes et al. 2007, Yu et al. 2012]. Recently, OEMs which produce military engines are consider-

ing the emission regulations when they design and produce military engines [Lutz et al. 2011]. The emissions from military vehicles are also receiving attention in the military field [Lee et al. 2012, Mosburger et al. 2008]. Thus, nowadays, cleaner combustion with JP-8 has been required.

Premixed Charge Ignition (PCI) combustion is a kind of advanced combustion strategies which can reduce nitrogen oxides (NOx) and particulate matter (PM) simultaneously [Lewander et al. 2008, Lee et al. 2006]. PCI combustion is realized by moderately early fuel injection timing (20 ~ 40 crank angle degree before top dead center, CAD bTDC) and mild exhaust gas recirculation (EGR) rate, which lead to the prolonged mixing time and the lowered combustion temperature [Lewander et al. 2008, Lee et al. 2006]. The air and fuel are well mixed before the start of combustion, and then the combustion progresses with the low combustion temperature. Therefore, the formation of NOx and PM is suppressed due to the reduction of rich or stoichiometric region in the air-fuel mixture.

In the current work, the authors tried to apply JP-8 to PCI combustion in a single-cylinder diesel engine, and compare with diesel in regard of emission characteristics and power output.

2. Experimental setup and conditions

2.1 Experimental setup

The engine experiment was run on a 0.5 L single-cylinder direct-injection compression-ignition diesel engine. The detailed specifications of the engine and the fuel injection equipment are listed in Table 1. Figure 1 shows the schematic diagram of experimental setup. The engine was operated by an alternating current (AC) dynamometer at constant speed. The in-cylinder pressure was measured using a piezo-electric pressure tranducer (Kistler, 6056A type), which substituted the glow plug, at every 0.2 CAD and the heat release rate was derived using the measured in-cylinder pressure of 100 cycles. The gaseous emissions including NOx, hydrocarbon (HC), carbon monoxide (CO) and carbon dioxide (CO_2) were measured by an exhaust gas analyzer (HORIBA, MEXA-1500d). Smoke emission was measured by a smoke meter (AVL, 415S). The engine coolant and lubrication oil were circulated through the engine by separate pumps. The fuel injection pressure was controlled by a pressure control valve driver (Zenobalti Co., ZB-1200). The injection timing was controlled by a programmable injector driver (Zenobalti Co., IDU-5000B). The properties of JP-8 and diesel fuel are listed in Table 2. JP-8 has lower cetane number, liquid density, kinetic viscosity and aromatic contents. JP-8 also has lower distillation temperature, as shown in Fig. 2, which means superior evaporation characteristics.

Table 1 Specification of engine and fuel injection system

Engine specification	
Engine type	Single-cylinder, common rail diesel engine
Displacement vol. [cc]	498
Bore x stroke [mm]	84 x 90
Compression ratio	16
Number of valve	4
Fuel injection equipment	
Injector type	Piezo-actuated injector
Number of hole	8
Diameter of hole [mm]	0.13
Included angle [°]	150

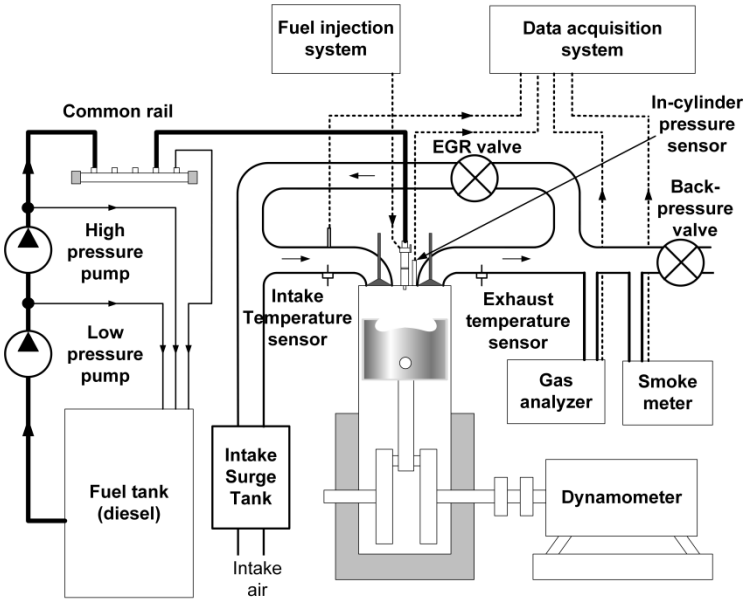

Fig. 1 Schematic diagram of experimental setup

Table 2 Properties of JP-8 and diesel fuel

	ASTM method	JP-8	Diesel fuel
Cetane number	ASTM D976	45	52.8
Liquid density [kg/l]	ASTM D4052	0.79	0.82
Low heating value [MJ/kg]	ASTM D3338	43.4	42.5
Kinetic viscosity [cSt]@ 313K	ASTM D445	1.2	2.6
Sulfur content [wt ppm]	ASTM D4294	100	3.93
Aromatic content [% vol.]	ASTM D1319	18	30

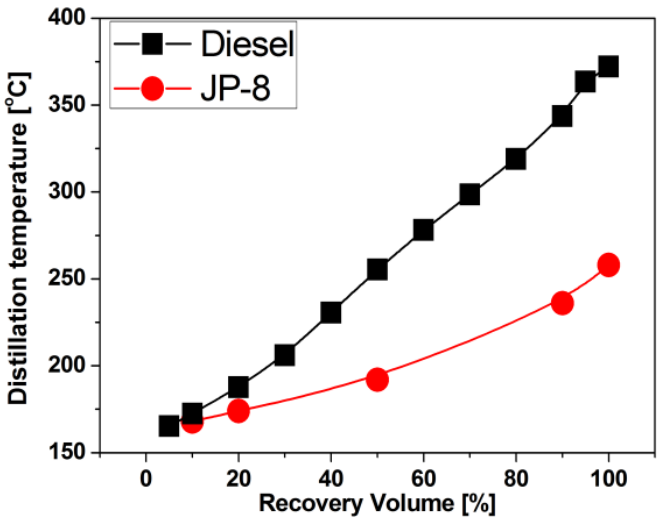

Fig. 2 Distillation temperature curves for JP-8 and diesel fuel

2.2 Experimental conditions

The engine experimental conditions are listed in Table 3. The experiments were conducted under two load conditions, specified as condition A and B. The injection quantity for diesel fuel were 8 and 16 mg/stroke, while for JP-8 were 7.7 and 15.6 mg/stroke in order to inject the same input energy considering the difference in low heating value. The injection pressure of 50 MPa was adopted for condition A and B. The injection timings for condition A were swept from 24 to 28 CAD bTDC. For condition B, the injection timings were swept from 26 ~ 30 CAD bTDC. The EGR rate defined as CO_2 concentration ratio in intake manifold to that in exhaust was varied from 0 ~ 30 % by manipulating the EGR valve for condition B. The ambient and fuel temperature were kept constant at 300 K and 303 K, respectively. The combustion duration was defined as the crank angle between CA 10(the crank angle where the mass fraction burned reached 10 %) and CA 90 (the crank angle where the mass fraction burned reached 90 %). The ignition delay was defined as crank angle between the start of injection signal and CA 10. The CA 50 which is the crank angle where the mass fraction burned reached 50 % was chosen for the representative of the combustion phase [Ickes et al. 2009].

Table 3 Engine experimental conditions

	Condition A	Condition B
Engine speed [rpm]	1200	
Injection quantity [mg/st]	8 (7.7 for JP-8)	16 (15.6 for JP-8)
Injection pressure [MPa]	50	
Injection timing [CAD bTDC]	24 ~ 28	26 ~ 30
EGR rate [%]	-	0 ~ 30
Ambient temperature [K]	300	
Fuel temperature [K]	303	

3. Results and discussions

3.1 Combustion characteristics without EGR

The combustion characteristics including in-cylinder pressure, heat release rate and combustion phase of JP-8 and diesel fuel were compared without EGR at first for investigating the effects of fuel properties themselves. Figure 3a shows the in-cylinder pressure, heat release rate and combustion phase of condition A with the injection timing of 26 CAD bTDC. It was found that JP-8 showed lower maximum in-cylinder pressure and peak of heat release rate compared with diesel fuel. JP-8 also showed longer ignition delay and combustion duration although JP-8 had superior evaporation characteristics which could promote the mixing process of air and fuel. These results were attributed to the lower cetane number of JP-8 [Kidoguchi et al. 2000, Lee et al. 2011]. The ignition delay of JP-8 was prolonged due to its lower cetane number, which resulted in locally leaner air-fuel mixture formation compared with diesel fuel so the leaner mixture with JP-8 combusted with lower maximum in-cylinder pressure, peak of heat release rate and slower combustion rate [Kim et al. 2013]. The low temperature reaction (cool flame) which resulted from the enough mixing time due to the advanced injection timing also appeared for two fuels [Ickes et al. 2009, Yao M et al. 2009]. Figure 3b compares the combustion characteristics of JP-8 and diesel fuel under condition B, and showed a similar trend to condition A. It can be confirmed that the peak of heat release rate with JP-8 were lower than that with diesel fuel although the engine load increased. It is also because JP-8 has superior evaporation rate and longer ignition delay due to lower cetane number as mentioned above, which led to locally leaner air-fuel mixture formation, finally smoother and slower combustion rate.

Figure 4 depicts the ignition delay and CA 50 quantitatively for both fuels according to the injection timings under operating conditions A and B. The results showed that JP-8 showed longer ignition delay and more retarded CA 50 for conditions A and B, which was attributed to lower cetane number of JP-8. In particular, the CA 50 was hardly changed with respect to the injection timing variation while the ignition delay was varied in bigger magnitude. This might be because PCI combustion process is dominated by the chemical kinetics due to the enough air-fuel mixing time while conven-

tional combustion is dominated by the physical process as well as the chemical kinetics. From these observations, it is clearly confirmed that the lower cetane number of JP-8 is more dominant to the start of combustion and the combustion phase than its better evaporation characteristics.

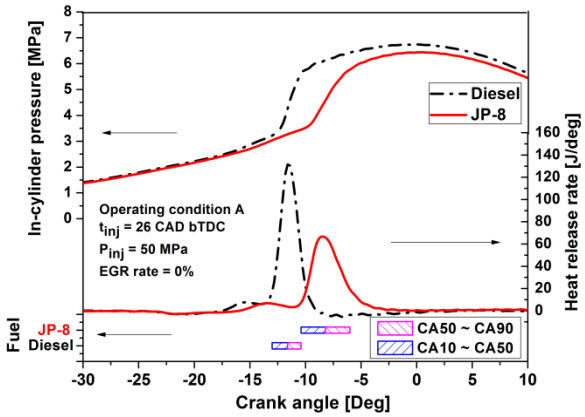

(a)

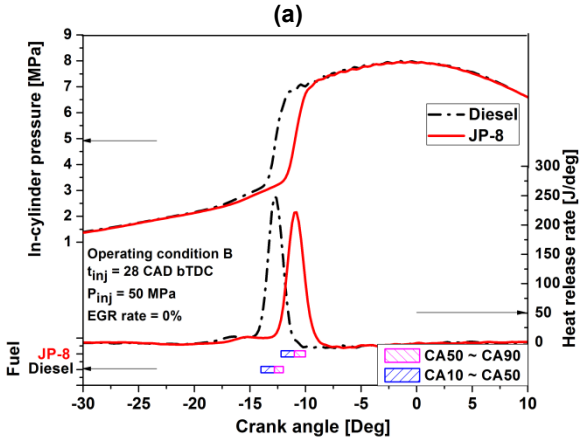

(b)

Fig. 3 In-cylinder pressure, heat release rate and combustion duration for JP-8 and diesel fuel of (a) operating condition A and (b) operating condition B (injection pressure = 50 MPa, EGR rate = 0 %, injection timing = for (a) 26 CAD bTDC and for (b) 28 CAD bTDC)

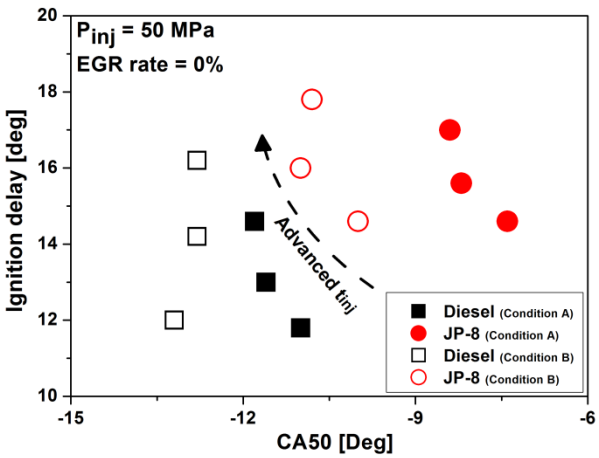

Fig. 4 CA 50 and ignition delay variations of JP-8 and diesel fuel (injection pressure = 50 MPa, EGR rate = 0 %)

3.2 IMEP and Emissions Characteristics without EGR

The characteristics of indicated mean effective pressure (IMEP), NOx and smoke emissions for conditions A and B are shown in Figs. 5a and 5b, respectively. The IMEP with JP-8 was slightly higher than that with diesel fuel for both operating conditions. It was attributed to that JP-8 had somewhat retarded combustion phase compared with diesel fuel, as shown in Fig. 4. More retarded combustion phase with JP-8 produced more positive work during the expansion stroke, which led to the higher IMEP.

In terms of NOx emissions, JP-8 emitted lower NOx for both operating conditions. This result is opposite to previous study which was carried out under conventional combustion regime which has near-TDC injection timing [Lee et al. 2011, Lee et al. 2012]. The longer ignition delay and better evaporation characteristics with JP-8 made the combustion smoother, which led to the reduction of NOx.

In regard of smoke emission, for condition A, overall smoke emission levels were quite low (below 0.1 FSN) for both fuels because the injected fuel quantity was too low. Smoke emission for condition B showed that lower smoke with JP-8 was emitted compared to diesel fuel. There might be several reasons for the lower smoke emission with JP-8. First, the fuel-rich region with JP-8 was less produced by the faster evaporation rate which could promote the air-fuel mixing process so that less smoke was emitted with JP-8 [Lee et al. 2011, Yu et al. 2012, Pandey AK et al. 2010]. Second, the difference in aromatic contents portion between JP-8 and diesel fuel can affect smoke emission. JP-8 used in this study has lower aromatic contents as shown in Table 2. It is widely known that fuels containing high aromatic contents are more difficult to be cracked to small species [Kee et al. 2005]. Thus, the fuels with high aromatic contents which are cracked incompletely produce more polycyclic hydrocarbons, known as the precursor of smoke, thereby emitting more smoke and particulates emissions [Kidoguchi et al. 2000, Heywood 1988].

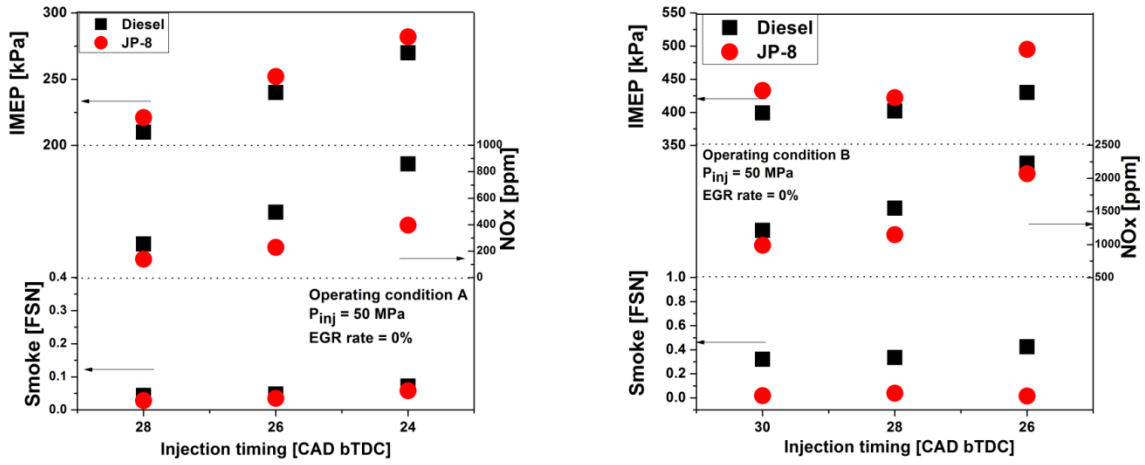

Fig. 5 IMEP, NOx and Smoke emissions characteristics for JP-8 and diesel fuel of (a) operating condition A and (b) operating condition B (injection pressure = 50 MPa, EGR rate = 0 %)

3.3 Effects of EGR on JP-8 and diesel fuel

EGR was introduced to operating condition B for additional NOx reduction and combustion phasing control. The EGR rate was changed from 0 % to around 30 %, which emitted NOx level below 50 ppm for both fuels.

Figure 6 shows the variations of CA 50 and ignition delay according to the EGR rate change with the injection timing of 28 CAD bTDC. The CA 50 and ignition delay were retarded and prolonged monotonically as the EGR rate increased. This trend came from the typical effects of EGR, which slower the reaction rate [Ladommatos et al. 1996]. JP-8 showed more prolonged ignition delay and retarded CA 50 at the maximum rate of EGR due to its lower cetane number.

The trade-off relationship between NOx and smoke with EGR is presented in Fig. 7. It is well known that EGR is very effective to reduce NOx by lowering the combustion temperature while increasing smoke due to the lack of oxygen [Maiboom et al. 2008]. From Fig. 7, it is clearly found that

the trade-off relationship could be improved with JP-8. It is mainly attributed to longer mixing time, better evaporation characteristics and lower aromatic contents of JP-8, which led to better local equivalence ratio distribution.

Figure 8a shows HC and CO emission with EGR rate of 0 % and 28.5 %. HC and CO emission increased dramatically as the EGR rate increased. The combustion temperature was lowered by the effects of EGR, which resulted in the increase of incomplete combustion product such as HC and CO [Chen et al. 2014]. EGR also made the air-fuel mixing period longer, consequentially the increase of fuel-lean mixture, which cannot take part in the combustion. In terms of fuel type, it can be seen that HC emission with JP-8 was higher than that with diesel fuel regardless of the EGR rate. The main reason for this result is that more locally fuel-lean mixture with JP-8 was formed due to higher volatility and longer ignition delay of JP-8, as mentioned in the previous part. On the other hand, CO emission with JP-8 was lower than that with diesel fuel. The formation of CO is originated in partial fuel oxidation [Ickes et al. 2009]. As demonstrated in Fig. 8, higher HC emission with JP-8 reflected that JP-8 had less chance to partial oxidation of HC, thus, higher CO with JP-8 was obtained [Ickes et al. 2009]. The CA 50 and IMEP with EGR rate of 0 % and 28.5 % are depicted in Fig. 8b.

As mentioned in the previous part, the higher IMEP was attained with JP-8 when EGR was not introduced due to more retarded CA 50. As the EGR rate was increased, the IMEP for both fuels increased evidently, which resulted from that the EGR forced the over-advanced combustion phase to move toward TDC, allowing more expansion work production. However, the IMEP increase level with JP-8 was not equivalent to that with diesel fuel when the EGR rate reached 28.5 %. To investigate the cause for the difference in IMEP increase level for each fuel in detail, 'EGR sensitivity' was defined as the level of CA 50 retardation and increase of ignition delay according to the EGR rate, and was shown in Fig. 9. The x-axis means the relative retardation of CA 50 compared with no EGR case, and the y-axis stands for the increase of ignition delay, in the same manner. The results showed that the EGR sensitivity with diesel fuel was bigger than that with JP-8 when the EGR rate increased to 28.5 %. It means that the combustion phase with JP-8 was getting less sensitive to EGR while the EGR rate increasing. Therefore, the IMEP with JP-8 was not increased equivalently to diesel fuel as the EGR rate reached 28.5 % even though the absolute CA 50 with JP-8 was more retarded than that with diesel fuel, as can be seen in Fig. 6. This phenomenon may come from different fuel properties between JP-8 and diesel fuel. However, the operating conditions including engine load, speed, injection pressure, injection timing should be diversified to make more general conclusions for the effects of EGR on combustion phase according to fuel type.

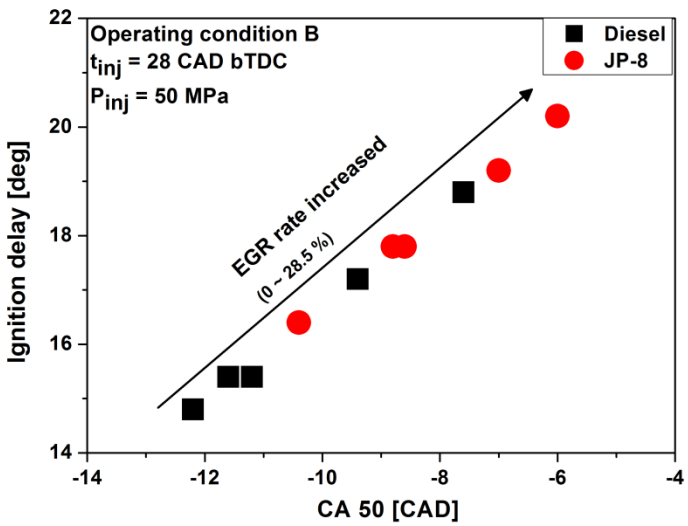

Fig. 6 CA 50 and ignition delay variations of JP-8 and diesel fuel (operating condition B, injection pressure = 50 MPa, injection timing = 28 CAD bTDC)

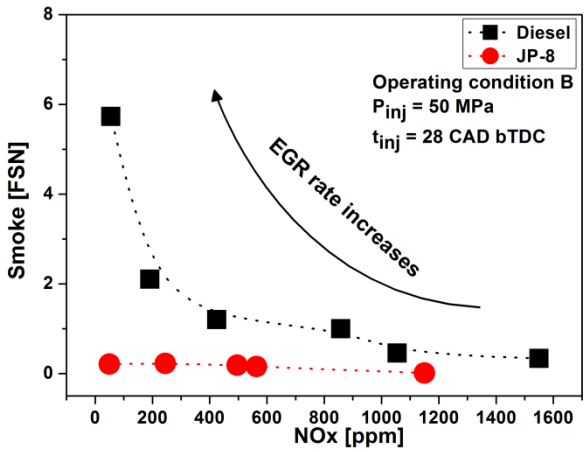

Fig. 7 The trade-off relationship between NOx and Smoke with EGR

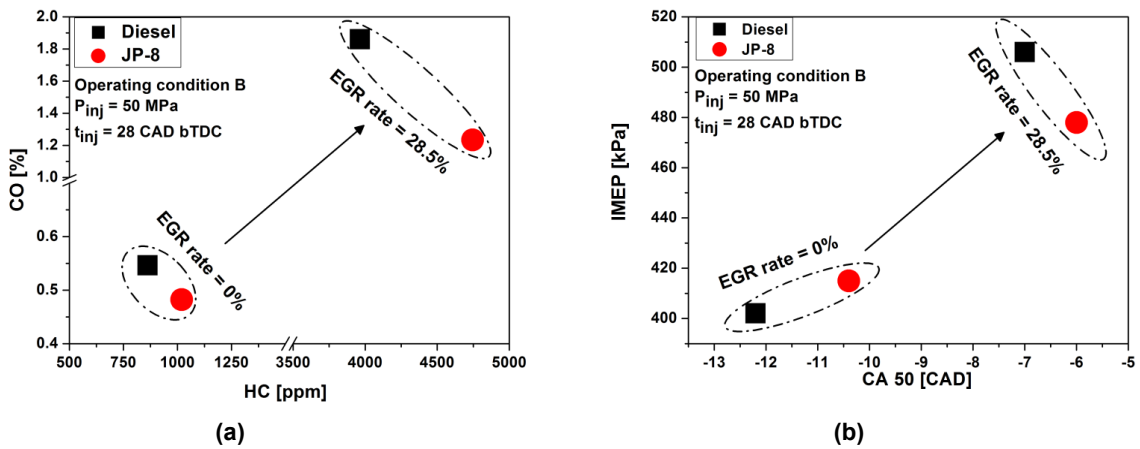

Fig. 8 Effects of EGR on (a) HC/CO emissions and (b) CA 50/IMEP (operating condition B, injection pressure = 50 MPa, injection timing = 28 CAD bTDC)

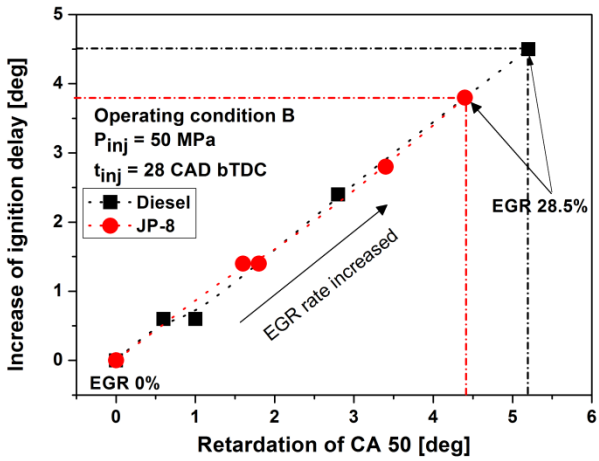

Fig. 9 Sensitivity to EGR for JP-8 and diesel (operating condition B, injection pressure = 50 MPa, injection timing = 28 CAD bTDC)

4. Conclusions

In the present work, an aviation fuel, JP-8 was applied to premixed charge ignition (PCI) combustion in a single-cylinder diesel engine, and was compared with diesel fuel. Experiments were performed under two operating conditions. The combustion and emissions characteristics with and without exhaust gas recirculation (EGR) were analyzed. The major findings from this study are summarized as follows:

(1) PCI combustion with JP-8 showed longer ignition than that with diesel fuel because of lower cetane number of JP-8 even though JP-8 has superior evaporation characteristics which is helpful for mixing process of the air and the fuel.

(2) PCI combustion with JP-8 showed lower peak of heat release rate and longer combustion duration because locally leaner mixture was formed due to longer ignition delay resulted from lower cetane number and superior evaporation rate of JP-8 compared to diesel fuel.

(3) Higher IMEP with JP-8 was attained in PCI combustion due to more retarded combustion phase compared with diesel fuel.

(4) Lower NOx and smoke were emitted with JP-8. It was attributed to locally leaner mixture and lower aromatic contents. The trade-off relationship between NOx and smoke could be also improved with JP-8 when the EGR was applied. However, HC emission with JP-8 was higher than that with diesel fuel due to fuel-lean mixture formation with JP-8.

(5) JP-8 showed lower level of IMEP increase compared with diesel fuel. This was because the combustion phase with JP-8 was less sensitivity to the EGR rate. This phenomenon may come from different fuel properties between JP-8 and diesel fuel.

5. Acknowledgement

This work is supported by the ‘Industrial Strategic Technology Development Program (10039673) funded by the Ministry of Knowledge Economy (MKE, Korea).

This work is also financially supported by the **‘Erasmus Mundus ‘BEAM program’**.

6. References

Belvoir R-D & E Centre (1991) JP-8 single fuel forward report. US army.

Chen Z, Wu Z, Liu J, Lee C (2014) Combustion and emissions characteristics of high n-butanol/diesel ratio blend in a heavy-duty diesel engine and EGR impact. Energy Conversion and Management vol. 78: pp.787-795.

Fernandes G, Fuschetto J, Filipi Z, Assanis D, Mckee H (2007) Impact of military jp-8 fuel on heavy-duty diesel engine performance and emissions. J Automot Eng vol. 221(D8): pp.957–970.

Heywood JB (1988) Internal combustion engine fundamentals. International editions. McGraw-Hill.

Ickes AM, Bohac SV, Assanis DN (2009) Effect of fuel cetane number on a premixed diesel combustion mode. International Journal of Engine Research vol. 10: pp.251-263.

Kee S, Mohammadi A, Kidoguchi Y, Miwa K (2005) Effects of aromatic hydrocarbons on fuel decomposition and oxidation process in diesel combustion. SAE paper 2005-01-2086.

Kidoguchi Y, Yang C, Miwa K (2000) Effects of Fuel Properties on Combustion and Emission Characteristics of a Direct-Injection Diesel Engine. SAE paper 2000-01-1851.

Kim K, Kim D, Jung J, Bae C (2013) Spray and combustion characteristics of gasoline and diesel in a direct injection compression ignition engine. Fuel vol. 109: pp.616-626.

Kouremenos DA, Rakopoulos CD, Hountalas DT (1997) Experimental investigation of the performance and exhaust emissions of a swirl chamber diesel engine using jp-8 aviation fuel. Int J Energy Res vol. 21(12): pp.1173–1185.

Lacey PI, Lestz SJ (1992) Effect of low-lubricity fuels on diesel injection pumps – part I: field performance. SAE Paper 920823.

Ladommatos N, Abdelhalim S, Zhao H, Hu Z (1996) The Dilution, Chemical, and Thermal Effects of Exhaust Gas Recirculation on Diesel Engine Emissions - Part 1: Effect of Reducing Inlet Charge Oxygen. SAE paper 961165.

Lee J, Bae C (2011) Application of JP-8 in a heavy duty diesel engine. Fuel vol. 90: pp.1762-1770.

Lee J, Oh H, Bae C (2012) Combustion process of JP-8 and fossil Diesel fuel in a heavy duty diesel engine using two-color thermometry. Fuel vol. 102: pp.264-273.

Lee S, Reitz RD (2006) Spray Targeting to Minimize Soot and CO Formation in Premixed Charge Compression Ignition (PCCI) Combustion with a HSDI Diesel Engine. SAE paper 2006-01-0918.

Lestz SJ, LePera ME (1992) Technology demonstration of US army ground material operating on aviation kerosene fuel. SAE Paper 920193. SAE Trans J Fuels Lubr vol.112(4): pp.204–225.

Lewander M, Ekholm K, Johansson B, Tunestål P, Milovanovic N, Keeler N, Harcombe T, Bergstrand P (2008) Investigation of the Combustion Characteristics with Focus on Partially Premixed Combustion in a Heavy Duty Engine. SAE paper 2008-01-1658.

Lutz T, Modiyani R (2011) Brake Thermal Effciency Improvements of a Commercially Based Diesel Engine Modified for Operation on JP 8 Fuel. SAE paper 2011-01-0120.

Maiboom A, Tauzia X, Hetet JF (2008) Experimental study of various effects of exhaust gas recirculation (EGR) on combustion and emissions of an automotive direct injection diesel engine. Energy vol. 33: pp.22-34.

Mosburger M, Fuschetto J, Assanis D, Filipi Z, McKee H (2008) Impact of High Sulfur Military JP-8 Fuel on Heavy Duty Diesel Engine EGR cooler Condensate. SAE paper 2008-01-1081.

Pandey AK, Nandgaonkar MR (2010) Performance, Emission and Pump Wear Analysis of JP-8 Fuel for Military Use on a 558 kW, CIDI Diesel Engine. SAE paper 2010-01-1518.

Papagiannakis RG, Kotsiopoulos PN, Hountalas DT, Yfantis E (2000) Single fuel research program comparative results of the use of jp-8 aviation fuel versus diesel fuel on a direct injection and indirect injection diesel engine. SAE Paper 2006-01-1673.

Yao M, Zheng Z, Liu H (2009) Progress and recent trends in homogeneous charge compression ignition (HCCI) engines. Progress in Energy and Combustion Science vol. 35: pp.398-437.

Yu X, Zha K, Florea R, Jansons M (2012) Comparison of In-Cylinder Soot Evolution in an Optically Accessible Engine Fueled with JP-8 and ULSD. SAE paper 2012-01-1315. SAE Trans J Fuels Lubr Vol. 5: pp.875-891.

Combustion system design of the new PSA Peugeot Citroën PureTech 1.2 l e-THP engine

P. Souhaité[1], S. Mokhtari[1] and A. Tellier[1]

[1]PSA Peugeot Citroën, La Garenne-Colombes, France

E-mail: smail.mokhtari@mpsa.com
Telephone: +(33) 01-56-47-27-29
Fax: +(33) 01-56-47-87-69

Abstract. PSA Peugeot Citroën teams have been involved for a long time to address the two major environmental challenges linked to transport, climate change and air quality. They introduced several original technologies for both gasoline and Diesel engines in order to reduce fuel consumption (thus CO_2 emissions) and pollutants emissions such as nitrogen oxides (NOx), Carbon monoxide (CO) or particulate matter (PM and PN).

The objective of this paper is to focus on a key brick to reach the 95 g of CO_2 per km required by the European Commission by 2020: The new 3-cylinder PSA PEUGEOT-CITROEN PureTech 1.2 e-THP. This new PSA Peugeot Citroën 3-cylinder 1.2L turbocharged direct injection gasoline engine was developed to achieve a challenging fuel economy target while keeping a high level of performances.

To reach that goal, PureTech 1.2 e-THP engine offers high specific performance, to get all benefits of the downsizing by gear set optimisation, with a robust combustion system using a central direct injection and dual cam phasers. The ISFC was optimised by using Atkinson cycle at low load and by finding the best trade-off between valve overlap and exhaust opening at mid-load. The high performances of the engine (230 N.m @ 1750 rpm and 96 kW @5500 rpm) lead to a real challenge for the design of the combustion system in order to manage risks regarding abnormal combustion, knock and oil dilution. One of the key components of the combustion system is the injector which has been designed to ensure optimal Air/Fuel mixture in all conditions. This was achieved through the use of a 200 bar multi-injection system. Thanks to CFD, in-cylinder spray/mixture formation, injector position and design were optimised and the best designs were extensively tested on engine bench in order to define the best trade-off between: emissions, gasoline/oil dilution, combustion stability with high EGR rate, full load combustion and abnormal combustion, and spark plug fouling.
To ensure performance and reliability at full load with a 10.5:1 compression ratio, the water jacket, injection settings and valve overlap have been optimised. A specific work has been also done on the ignition system to perform the A/F mixture ignition at maximum BMEP. As a result, in comparison with the 1.6L NA replaced engine, a fuel economy of 17% is achieved on NEDC cycle with respect to Euro6.1 emissions regulation.

1. General gasoline challenges

The global context of mobility and environmental performance that each car manufacturer has to consider regarding its powertrain development, either thermal or hybrid, is shaped around three major challenges:

- The infrastructure and mobility challenge with the increase of urbanisation
- The environmental challenge through a demanding regulation, declining resources, and more and more eco-responsible customers

- The technical and industrial challenge to meet our clients' expectations in terms of quality, engine lifetime, safety and quality/price ratio.

In the light of this, the reduction of CO2 emissions, to limit global warming, and the reduction of vehicle pollutants, to improve the quality of the air, are the spearhead to offer vehicles that are each time more environment friendly. On all markets, the CO2 regulation induces technical improvements year after year to reach more and more severe targets.

Thanks to continuous improvements in technology over the past years, the PSA Peugeot - Citroën Group has gained a solid know-how in the field of low-CO2 emission vehicles. For the last few years, the Group was the car-maker with largest market share in Europe on the segment of vehicles below 120 g. And our current ranges already include mainstream Gasoline cars emitting less than 100g of CO2.

Enhanced technologies are mandatory to reduce fuel consumption and to meet the standards enacted by the European Union in the field of greenhouse gas emissions, while maintaining the driving quality. To address these challenges, the PSA Peugeot Citroën Group develops its thermal motorisations offer based on a balanced strategy in between gasoline and diesel.

The new PureTech family of three-cylinder gasoline engines is a key brick to reach those targets. This PureTech family is composed of:

- 1.0l and 1.2l naturally aspirated PFI engines, covering the power range from 50 kW to 60 kW launched mid-2012.
- 1.2l Turbocharged Direct Injection engines, covering the power range from 80 kW to 96 kW.

The most demanding targets have been set for PureTech engines:

- to keep the leadership in terms of CO2,
- to contribute to car weight decrease,
- to optimize cost and the Time to Market,
- to achieve new steps in Quality level,
- to develop world-wide engine,
- to meet the Group ambition of moving upmarket thanks to the « fun to drive » of the turbo derivatives,
- no compromise on NVH requirements of European market and also Chinese market, which is particularly demanding

In this paper, we will describe the main features of the combustion system of the PureTech 1.2l e.-THP Turbocharged Direct Injection engine.

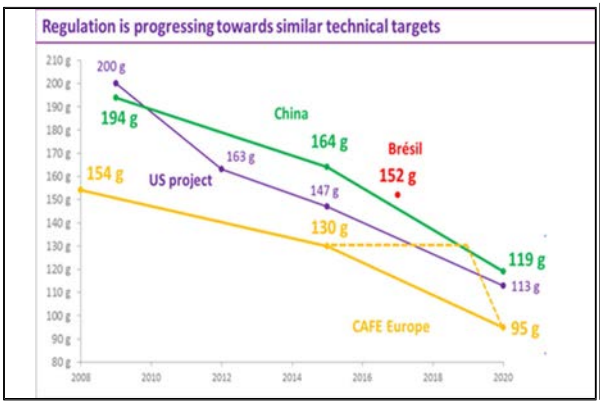

Fig. 1. Forecasted CO2 markets regulation

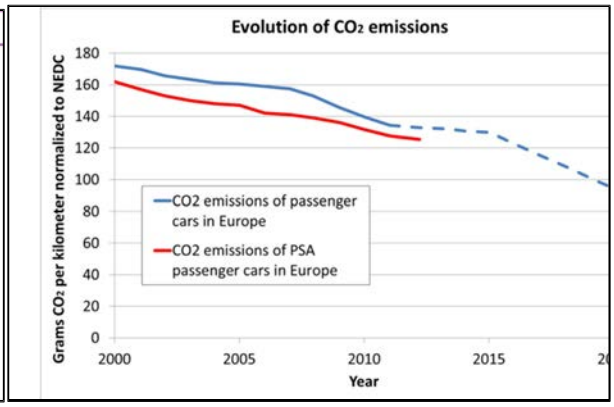

Fig. 2. CO2 emissions of passenger cars in Europe

Fig. 3. 1.2 l e-HTP

2. Main features of PureTech 1.2l e-THP

To reach a challenging fuel economy target while keeping a good level of drivability, Puretech 1.2l e-THP engine offers high specific performances, 192 N.m/l and 80 kW/l, to get all benefits of the down-sizing and down-speeding by gear set optimisation with a robust combustion system, with a compression ratio of 10.5:1, using a central direct injector and dual cam phasers.

Figure 4 shows the full load curve of the Pure Tech 1.2l e-THP engine: low end torque of 230 N.m at 1750 rpm and maximum power of 96 kW at 5500 rpm. The compression ratio for countries with poor fuel quality has been adjusted to 9.6:1 to ensure reliability at full load. That allows to get a maximum torque up to 3500 rpm.

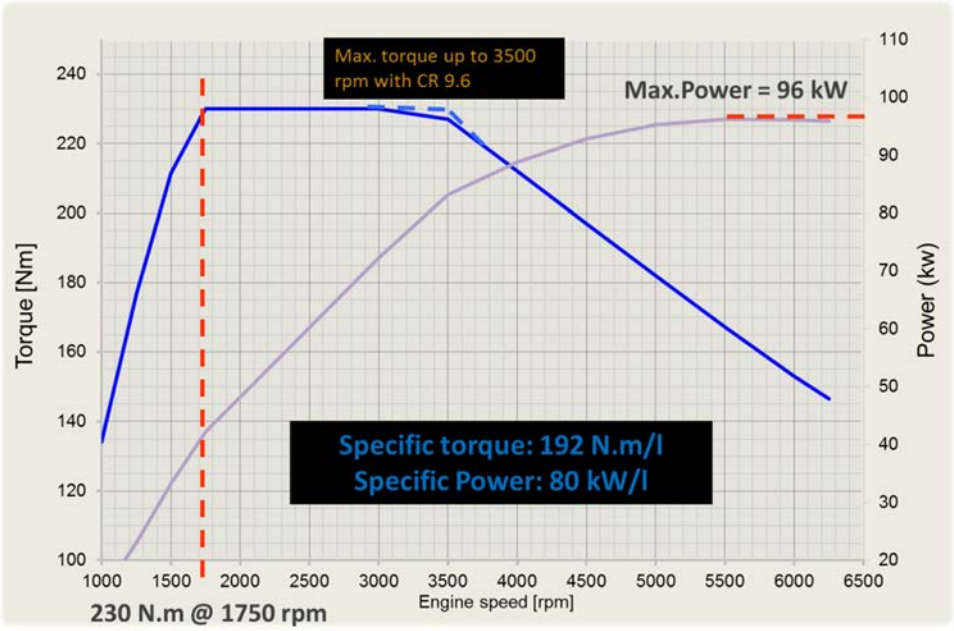

Fig. 4. Full load curve of the 1.2 l e-THP

Table 1. Main features of the 1.2 l e-HTP

Mains features		**1,2 L e-THP 110 HP**	**1,2 L e-THP 130 HP**
Type		***3 cylinders***	
Emissions regulation		***Euro 6.1***	
Consumption on 308 (NEDC)	*g C02/km*	***102***	***107***
Max power	*Kw/HP*	***81kw/110 HP @ 5500 tr/min***	***96 kw/ 130HP @ 5500 tr/min***
Max torque	*Nm*	***205 @ 1500 tr/min***	***230 @ 1750 tr/min***
Fuel system		*Direct Injection, 200 bars, central mounted injectors, 5 holes laser drilling injectors, multiple injection mode: up to 3 injections per cycle*	
Turbocharged system		*Single scroll turbocharger: max. boost-pressure ,1.4 bar and max. speed 270 000 tr/mn*	
Electrical management		*Smart monitoring of the electrical production and consumers, battery load optimisation and stop start system.*	
Displacement	*Cm3*	***1199.1***	
Compression ratio		***10.5 : 01***	
Bore/stroke	*mmXmm*	***75 X 90.5*** *With 7.5 mm crankshaft offset*	
Cylinder-block		*Aluminum vacuum die casting with additional heat treatment. aluminum coating liners inserts during the die casting.*	
Crankshaft / con-rod		*Steel crankshaft T42 and M42, con rod with high iron material characteristic 38MnSiV4*	
Balancer shaft		*Mono anti-rotating shaft , driving unit base on gear mounted on the crankshaft and decoupled counter-gear on the balancer - shaft. Associated with High inertia TVD Pulley*	
Oil pump		*Sensored regulation oil pump*	
Cylinder head		*Sand cast process. Hardened by air soak treatment. Aluminum Alloy: AS7 CU 0.5 Mg 0.3 / Heat treatment: T7. Integrated exhaust manifold*	
Timing System		*2 composite camshaft, wet belt driving unit*	
"Box size" (L x W x H)	*mm*	*637 X 595.5 X 687*	
Weigth PSA procedure W/o	*kg*	*8O.5 kg*	
Fuel	*RON*	*91-98*	

Mains features of the Pure Tech 1.2l e-THP are listed in the Table 1 all focusing on performance and fuel economy targets:

- A cylinder unit volume of 399.7 cm3 improves the indicated efficiency
- Bore/Stoke ratio of 0.83 maximises indicated efficiency and minimised friction losses
- For minimizing friction losses, con-rod length, piston pin offset and crankshaft/liner offset were also optimised.

3. Combustion system and air loop design

3.1 Global description

Key features of the combustion and air loop system are illustrated Figure 5

- Conventional single stage turbocharger with Air Charge Air Cooler (described section Turbocharger)
- Direct injection system with centrally located injectors, up to 200 bar injection pressure and multi-injections capability
- Intake and exhaust Variable Valve Timing for fuel consumption and performance optimisation
- Relatively high compression ratio (10.5) considering the high specific torque
- Low bore/stroke ratio (0.83)
- High tumble air motion generated by intake pipes shape, enhanced through combustion chamber and piston head shape optimisation
- High energy ignition system
- Efficient cylinder head cooling for abnormal combustion limitation
- Water cooled integrated exhaust manifold. This system helps maintaining the inlet turbine temperature under 980°C (peak) without important mixture enrichment.

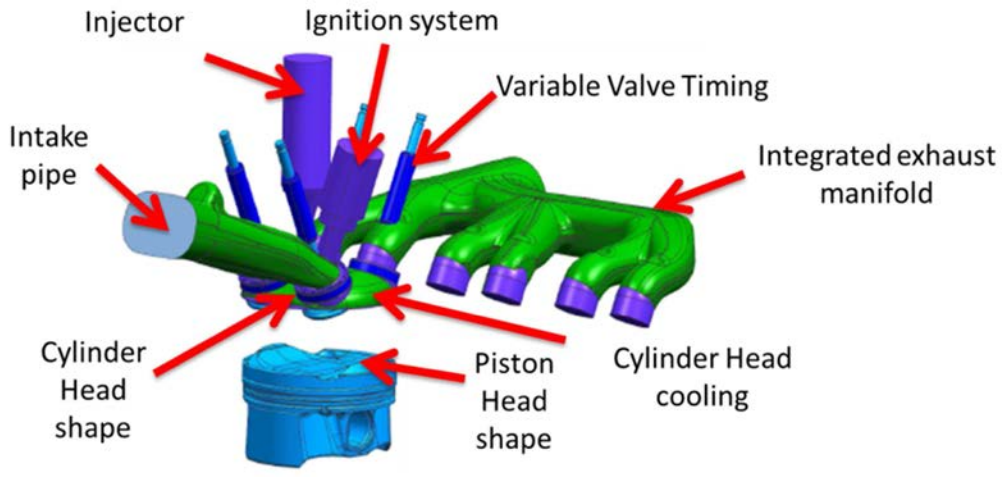

Fig. 5. Combustion system overview

3.2 Method used for system optimisation

Intensive CFD investigations were performed to rank the different possible configurations regarding mixture preparation (including spray/wall impingement), air charge motion, combustion process, robustness to knock and auto-ignition.

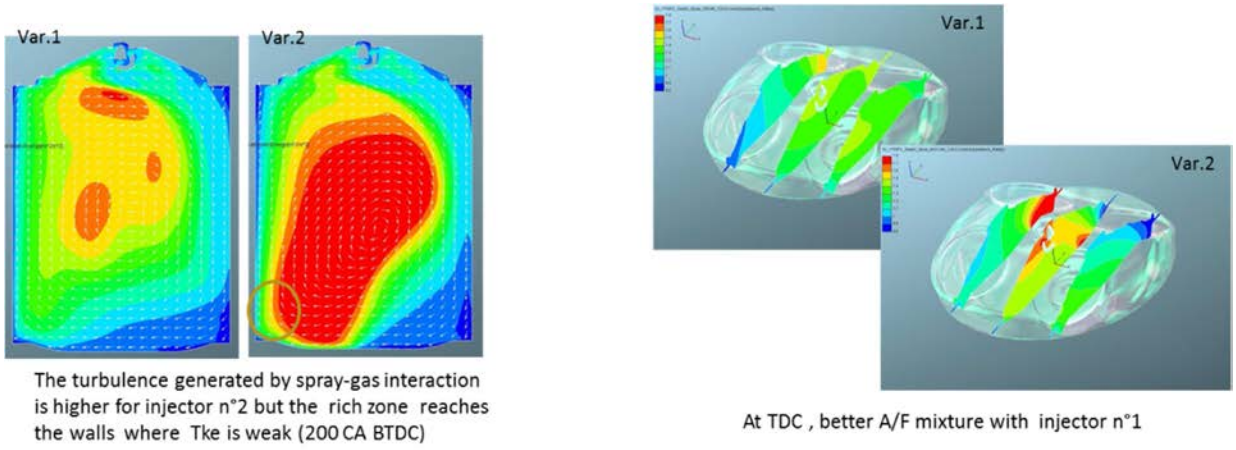

Fig. 6. Mixture preparation – Typical CFD output

Parameters considered were intake pipes' geometry, injector characteristics (number of holes, targeting, droplet size…), combustion chamber shape (piston head, pent roof…). As an example, Figure 6 shows typical CFD outputs used to compare injectors.

The selected configurations were then tested on engine bench for fine optimisation and convergence toward the best trade-off between full load behavior (performance, resistance to abnormal combustion), fuel consumption, emissions, gasoline-into-oil dilution, combustion stability, resistance to injector coking and spark plug fouling.

3.3 Combustion chamber and intake ducts

The engine displacement has been fixed to 1.2 litre. This has been identified as the right scaling considering the 96 kW performance target and the customer demand for C class vehicles attributes.The combustion chamber uses a relatively low bore/stroke ratio (0.83). This is favorable for combustion efficiency but leads to constraints for valves / injector / spark plug packaging and cooling efficiency. A suitable arrangement has been defined, characterized by:

- Injector and spark plug aligned on crankshaft axis (asymmetric combustion chamber)
- Valve inner seat diameter of 25.15 mm on the inlet side, 22.3 mm on the outlet side
- M12 spark plug
- Optimized cooling in the exhaust valve area (water jacket, water bridge between valves, sodium cooled valves, optimized valve seats material as illustrated Figure 7).

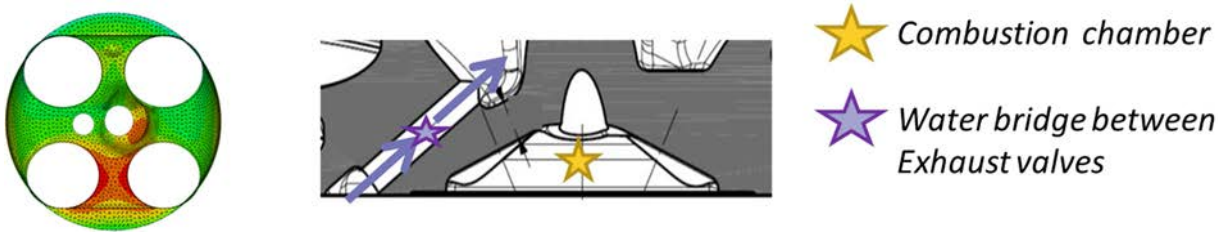

Fig. 7. Cylinder head wall temperature before applying cooling measures and water bridge illustration

Intake ducts were optimized to rise the tumble ratio up to 1.55 with small penalty on the flow coefficient. The piston head shape allows enhancing the tumble during intake and maintaining it during the compression stroke. The resulting highly turbulent flow field results in:

- Improved mixture preparation
- Faster combustion and hence reduced knock sensitivity at high load
- Acceptance of a high level of residual gas (up to 35%) thus reducing fuel consumption at part load

The compression ratio is set to 10.5 (for markets using RON 95 fuels). This value realizes the best compromise between the following objectives and constraints:

- Fuel consumption emissions minimisation
- Full load performance and knock limitation
- Architecture constraints (maximum cylinder pressure and heat flux, exhaust and catalyst temperature)
- Acyclism and driveability
- Robustness against abnormal combustion (pre-ignition, heavy knock)

This high value (considering the high low end torque) has been obtained thanks to cooling and air flow optimisation (described above), triple injection strategies and combustion chamber scavenging (see next sections).

3.4 Injector and spray

The above described optimisation process converged toward a 5 holes injector. Figure 8 shows some of its characteristics.

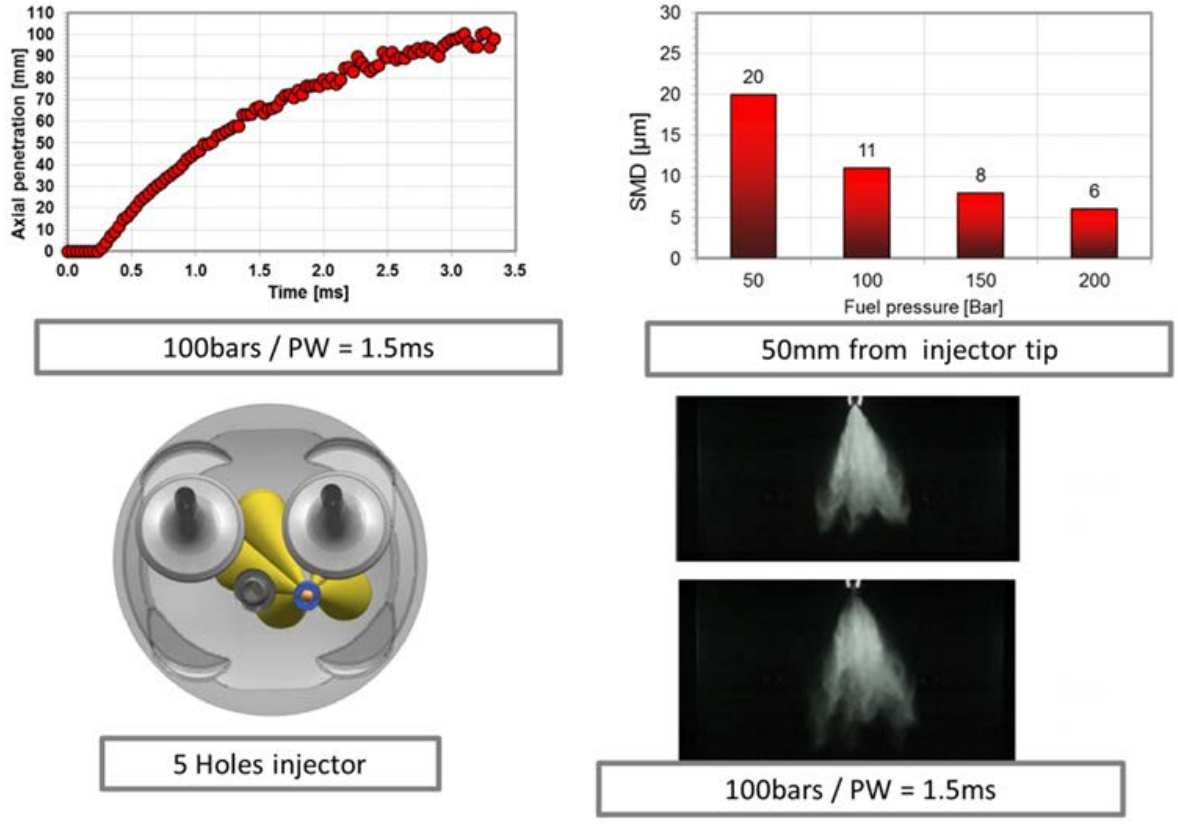

Fig. 8. Injector characteristics

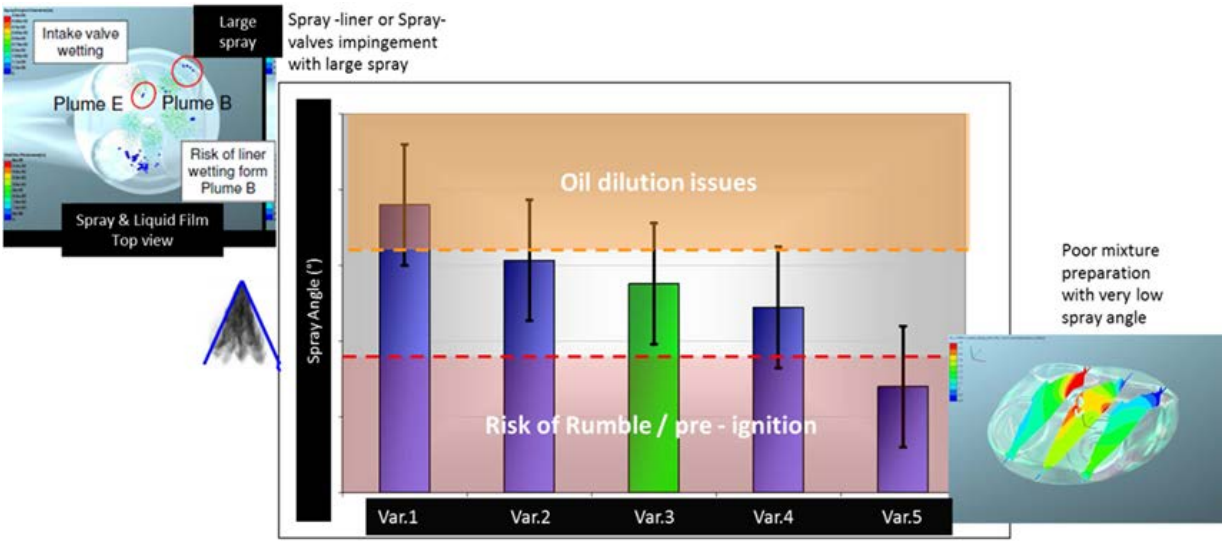

Fig. 9. Spray angle optimization

Figure 9 illustrates how the spray angle has been optimized to achieve a good compromise between oil dilution issues with large spray angle and worsened mixture preparation with low angle leading to bad combustion process and increased abnormal combustion risks ("rumble" / pre-ignition).

Injector protrusion has been optimized to avoid coking, and minimize particulate emission drift as illustrated Figure 10.

Figure 11 shows the injection strategy:

- Base strategy: 200 bar injection pressure, single injection phased to optimise particulate emissions
- Reduced injection pressure (100 bars) at low load to avoid too much dispersion of injected quantities (goal: maintain injection duration above minimum injection duration)
- Triple injection at low engine speed (up to 3000 RPM) and high load to avoid knock and pre-ignition: main injection during induction, second injection (~25% of total injected mass) near BDC, third (~10% of total injected quantity) around 90° before TDC (depending on spark advance).

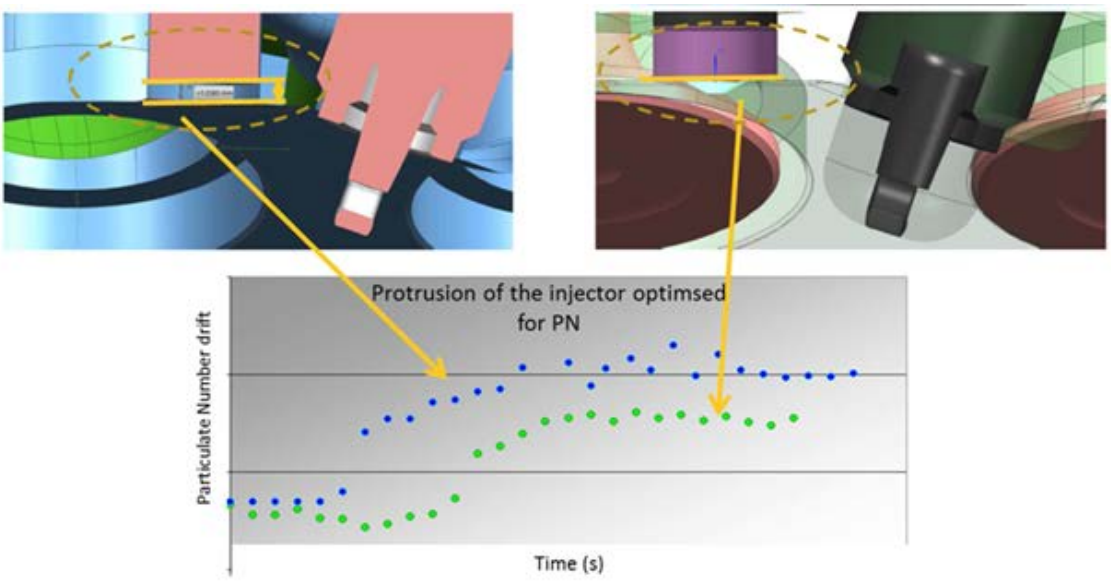

Fig. 10. Protusion injector optimization

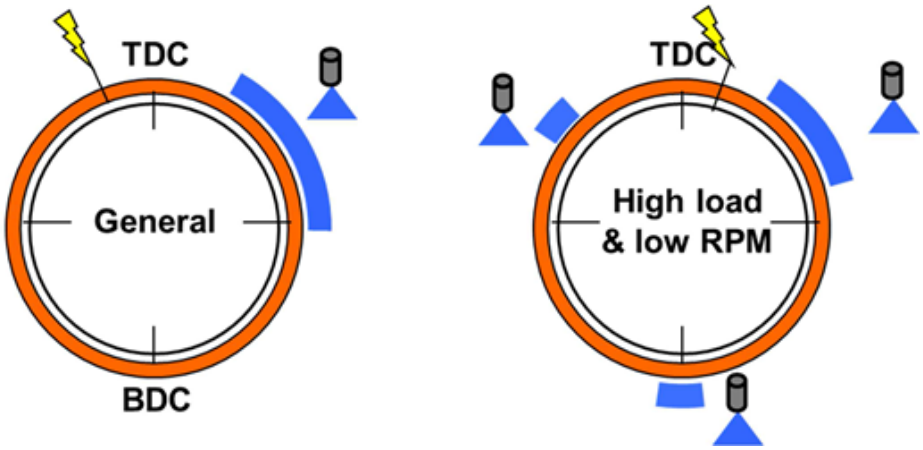

Fig. 11. Injection strategy

3.5 Ignition system

The particularly high specific torque and high EGR rate requires special attention on the ignition system to achieve robust ignition and minimize spark plug electrodes wear:

- The coil delivers a secondary current up to 130 mA to perform the ignition of the mixture at maximum load.
- The primary current is adjusted depending on the engine operating point to obtain the best compromise between combustion quality and electrodes wear.

Figure 12 shows the influence of the electrodes gap on the ignition of air/fuel mixture.

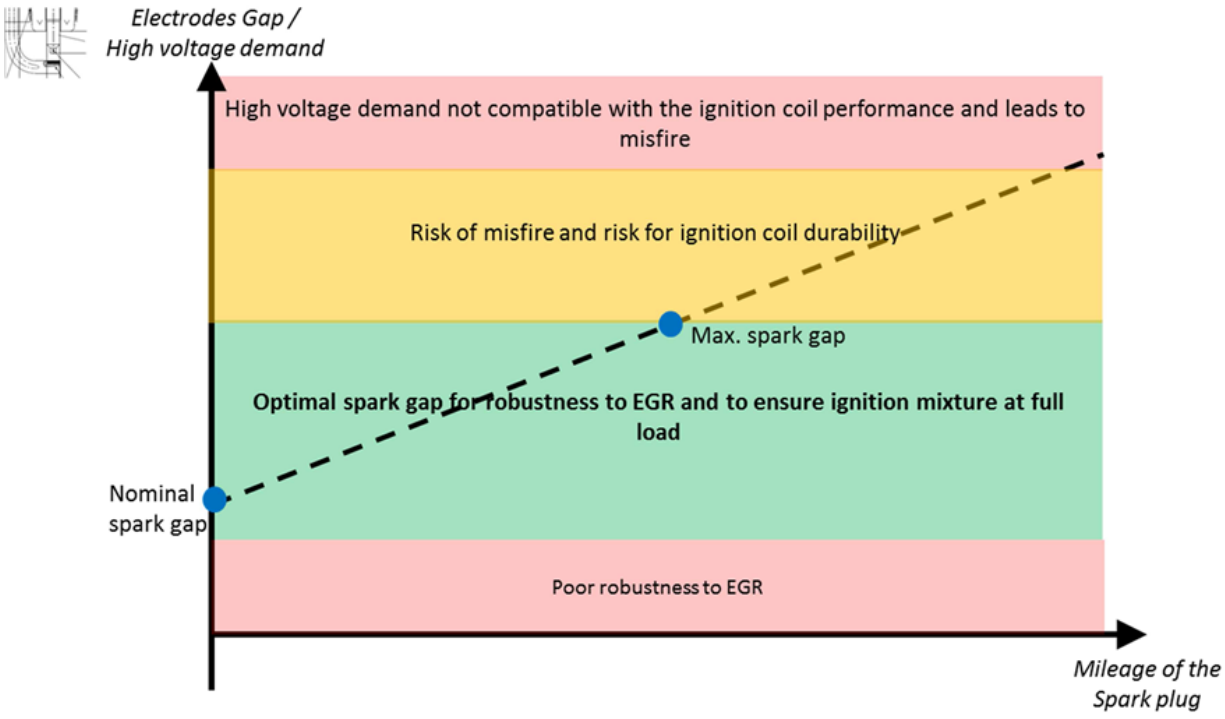

Fig. 12. Impact of the electrodes gap on the mixture ignition

3.6 Dual variable valve timing

The two camphasers are used to:

- Improve fuel consumption by reducing pumping and thermal losses at part load through suitable combination of "late Atkinson" settings (delayed intake and exhaust valve closing – See illustration Figure 13) and valve overlap optimisation.
- Improve engine performance at full load, including combustion chamber scavenging at low engine speed (possible thanks to direct injection).

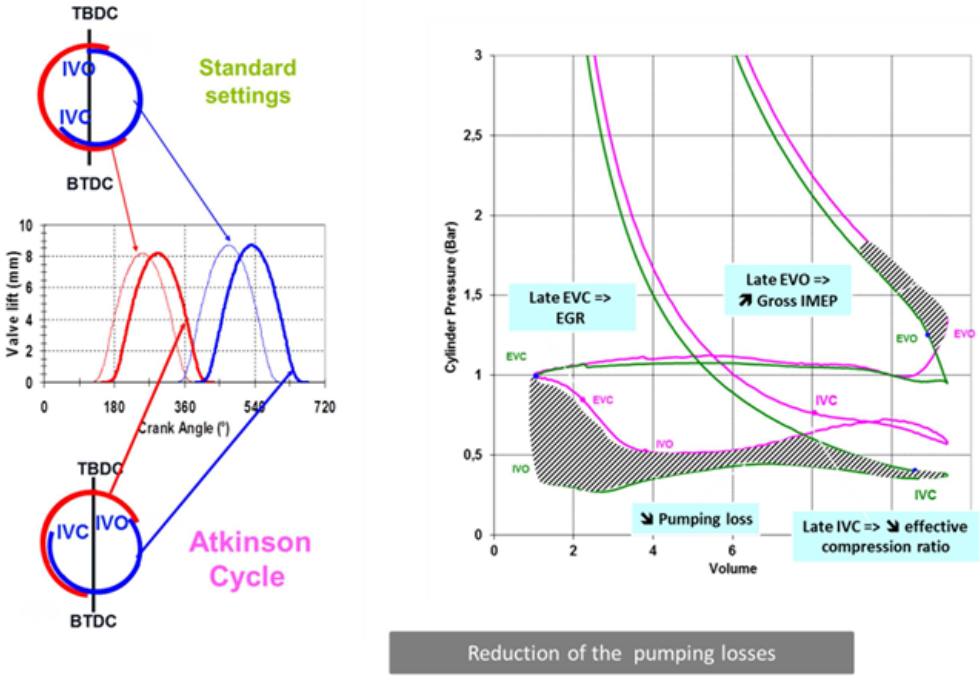

Fig. 13. Atkinson cycle

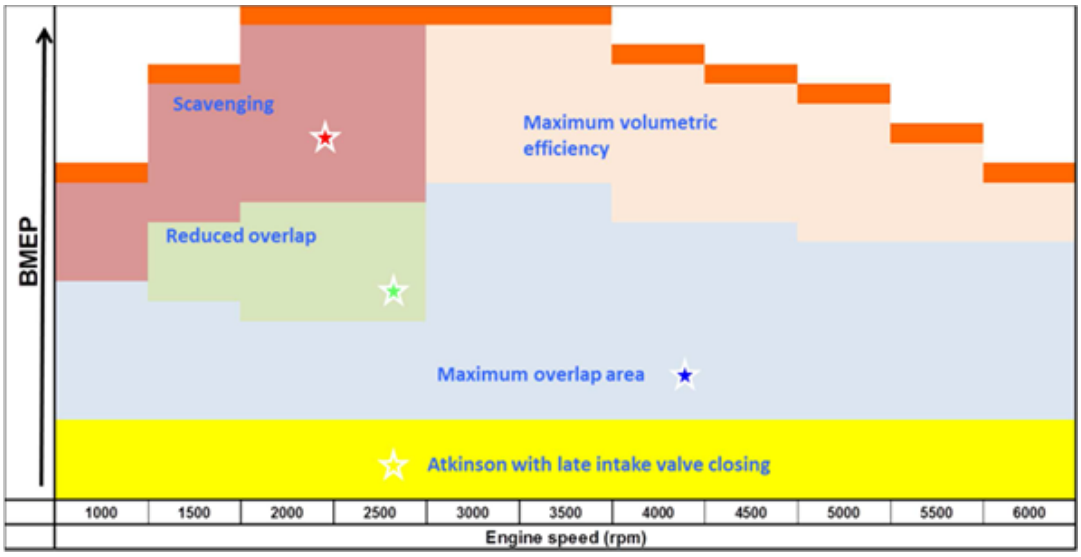

Fig. 14. Valve settings strategies

Figure 14 and Figure 15 illustrate how the different valve setting strategies are used depending on engine and load:

- At low load: late Atkinson settings and EGR control through exhaust valve closure for fuel consumption optimisation
- At mid load: high valve overlap to obtain high EGR rate for fuel consumption and particulates emission reduction
- At low engine speed and mid / high load (where inlet pressure is higher than exhaust pressure): reduction of the valve overlap to minimize fuel consumption under emission and catalyst temperature constraints
- At full load: optimized settings for performance, including scavenging control at low engine speed.

Besides, special valve settings are used during transients to minimize torque response.

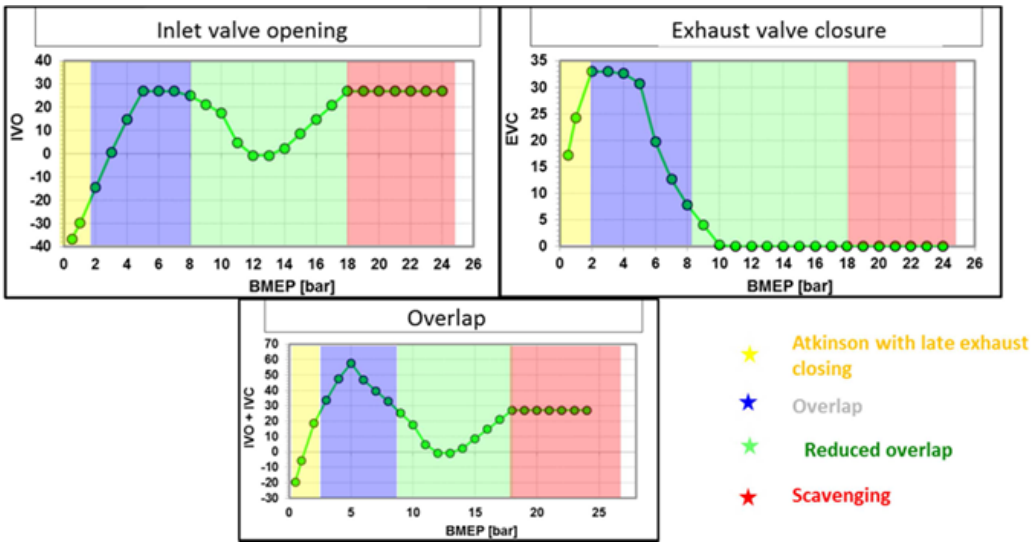

Fig. 15. Typical low engine speed valve settings (indicative)

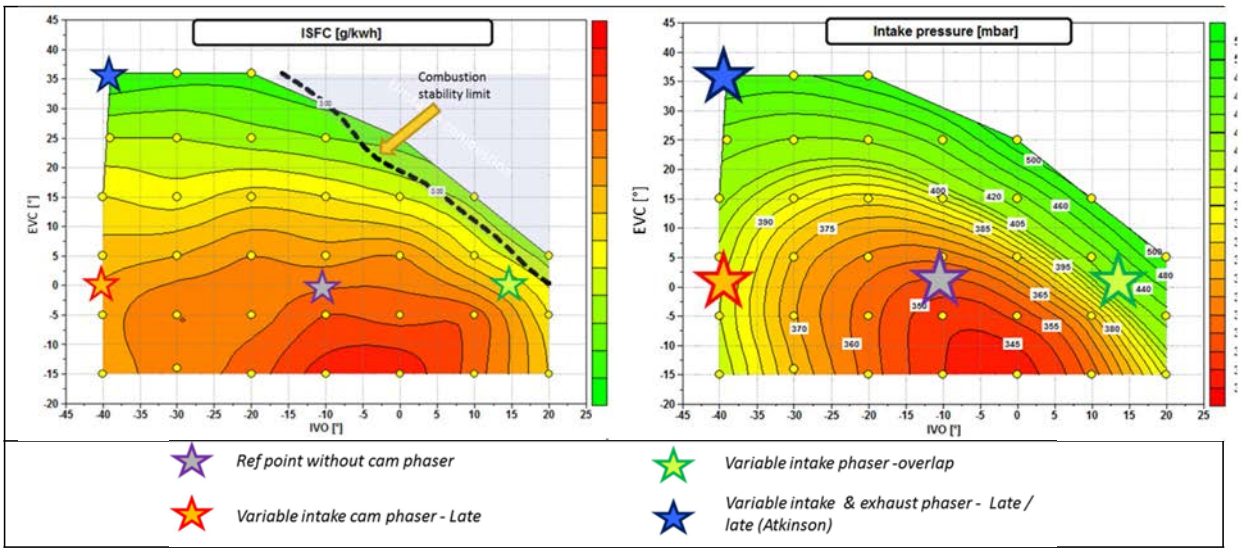

Fig. 16. Optimal settings at 2000/2 (ISFC MAP and Intake pressure MAP)

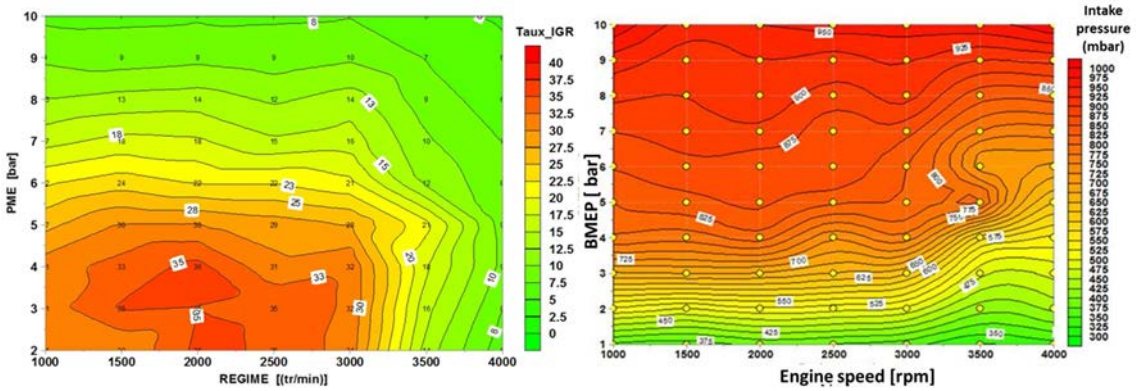

Fig. 17. EGR rate and inlet pressure maps

Figure 16 shows the fuel consumption for different EVC and IVO values at 2000 rpm and 2 bar BMEP. For this operating point the minimum ISFC is reached with Atkinson settings by reducing pumping and thermal losses. These valve setting strategies coupled with tumble enhancement allowed up to 35% Exhaust Gas recirculation at part load and "dethrottled" operation on a large operating range as shown on Figure 17.

3.7 Turbocharger

The exhaust manifold integrated to the cylinder-head allows to compact the exhaust side of the engine. Besides, the volume between the exhaust valves and the turbine wheel is reduced: this configuration optimises the use of the pressure pulsation in order to increase the low end torque.

The turbine housing material is a stainless steel 1.4826 in order to ensure the robustness for a max exhaust gas temperature of 980°C. The semi-floating radial bearing system with axial bearing integrated was optimized to obtain the best compromise between robustness and reduction of the friction losses. The aerodynamic characteristics are optimized in order to guarantee the robustness of the max power operating point without negative impact on the transient behaviour.
The main characteristics of the turbocharger are listed in table 2.

From 1750 rpm to 6000 rpm engine speed, the relative boost pressure is in a range from 1 to 1.4 bar which positions this 3-cylinder engine as a reference compared to our competitors.

The turbocharger is equipped with an Arm&Valve monoblock. This monoblock design presents the particularity of a sphere / cone sealing contact interface between valve and seat which is a first worldwide. This technology allows to eliminate the metallic noise usually generated by the shock between the arm and the valve, while keeping the sealing quality and so the low end torque and transient behaviour. The global dimensioning of the wastegate kinematic and the material choices were reworked and adapted to resist to the high instantaneous exhaust gas pressure specific to this high performance 3-cylinder engine.

Table 2. 1.2 l e-THP turbocharger main characteristics

	Compressor side	Turbine side
Wheel diameter	41 mm	37 mm
AR	0.50	0.29
TRIM	51	76
Max speed	270 000 rpm	270 000 rpm

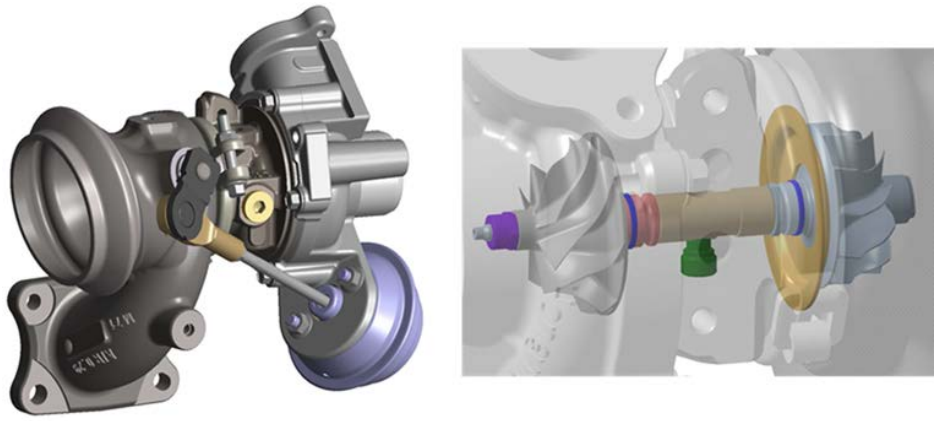

Fig. 18. 1.2 l e-THP turbocharger

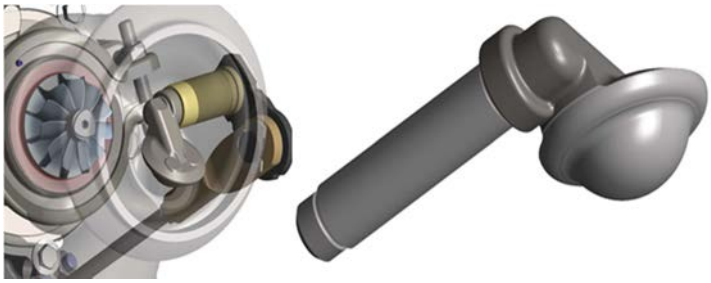

Fig. 19. Monoblock arm & valve design

Fig. 20. Clearance compensation

An additional spherical shape integrated to the valve head was adapted in order to obtain a better progressivity of the discharge. This allows improving the engine load controllability. The second effect is a 20% reduction of the aerolic force transferred to the wastegate kinematic.

The external part of the wastegate kinematic was the object of acoustic improvement. Usually on gasoline engine, the kinematic noises are limited by the strategy which consists to close the valve, even on certain atmospheric functioning points, to put the different clearances under constraint and avoid the metallic shock. This type of strategy generates a CO2 drawback impact due to increase of pumping losses and so it is not adapted to the small gasoline engine. To avoid this type of strategy, we integrated a spring which compensates the clearance during the engine life.

3.8 Lambda map

Thanks to the integrated exhaust manifold and the inlet turbine temperature allowed up to 980°C (peak), a wide operating range at lambda one is possible: this limits the fuel consumption penalty due to the exhaust thermal protection.

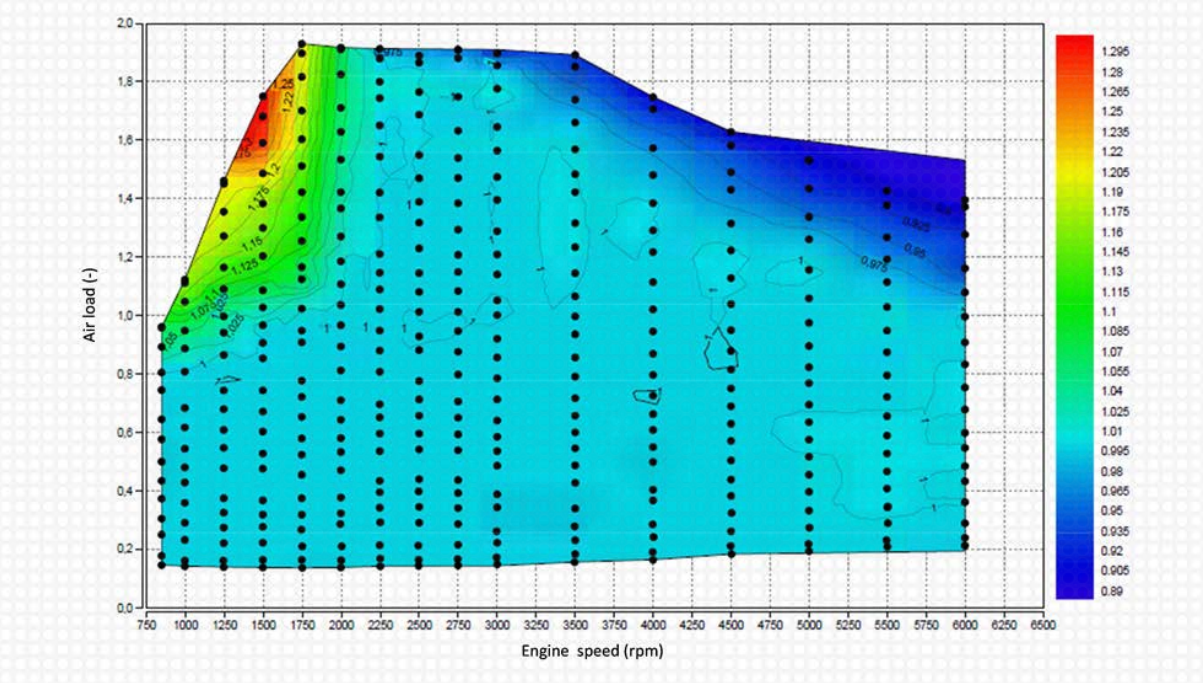

Fig. 21. Lambda map

4. 1.2 l e-THP 130 HP engine attributes

4.1 Full load performance

Figure 22 shows the specific torque curve compared to three "best in class" competitors. Remarkable features are:

- A high maximum torque of 230 Nm (192 Nm/l) at 1750 RPM and even 200 Nm (167 Nm/l) reached at 1500 RPM
- 96 kW maximum power (80 kW/l), with 90 kW (75 kW/l) already at 4000 RPM

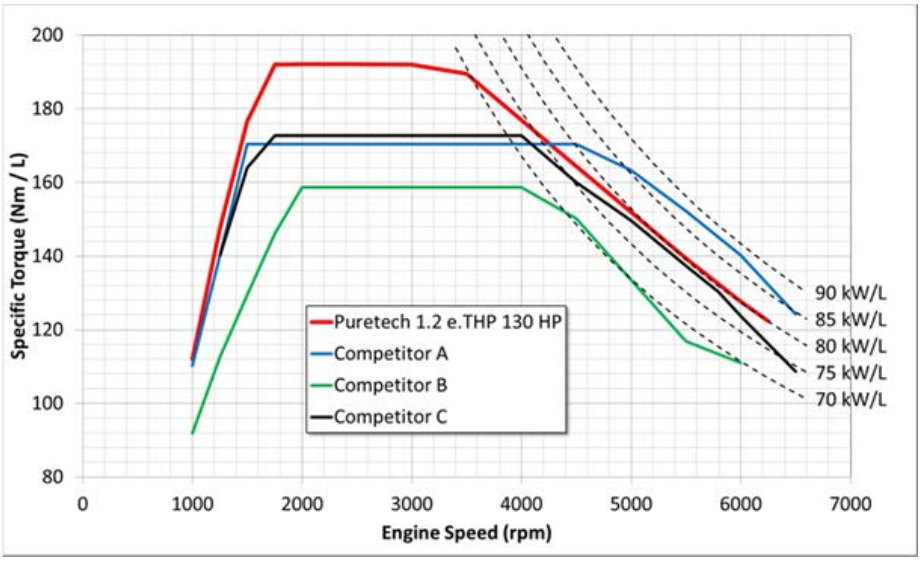

Fig. 22. Specific torque compared to competitors

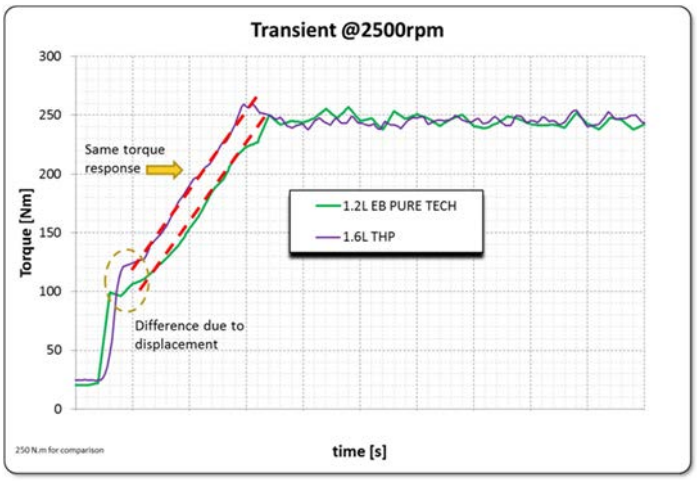

Fig. 23. Transient response compared to a 1.6 l boosted engine

Fig. 24. New Peugeot 308 acceleration and elasticity compared to replaced vehicle and competitors

Despite the high boosting rate, the transient torque response is comparable to a 1.6 l TGDI engine with the same maximum torque, as shown on Figure 23.

As shown Figure 24, Peugeot 308 vehicle acceleration and (mainly) elasticity are significantly improved compared to former version with 1.6 NA, comparable or better than equivalent "best in class" current vehicles of the same category.

4.2 CO_2 emissions and fuel consumption

Figure 25 shows the BSFC map obtained, on which have been plotted engine running conditions (RPM x BMEP) under different driving patterns: NEDC cycle, future "WLTC" cycle, typical highway use. The key characteristics are:

- A minimum BSFC value of 237 g/kwh, comparable to state of the art NA engines with the same unit displacement.
- A large area where the BSFC is under 240 g/kwh, allowing near to optimal fuel consumption in most of driving conditions without requiring too high gear ratios.

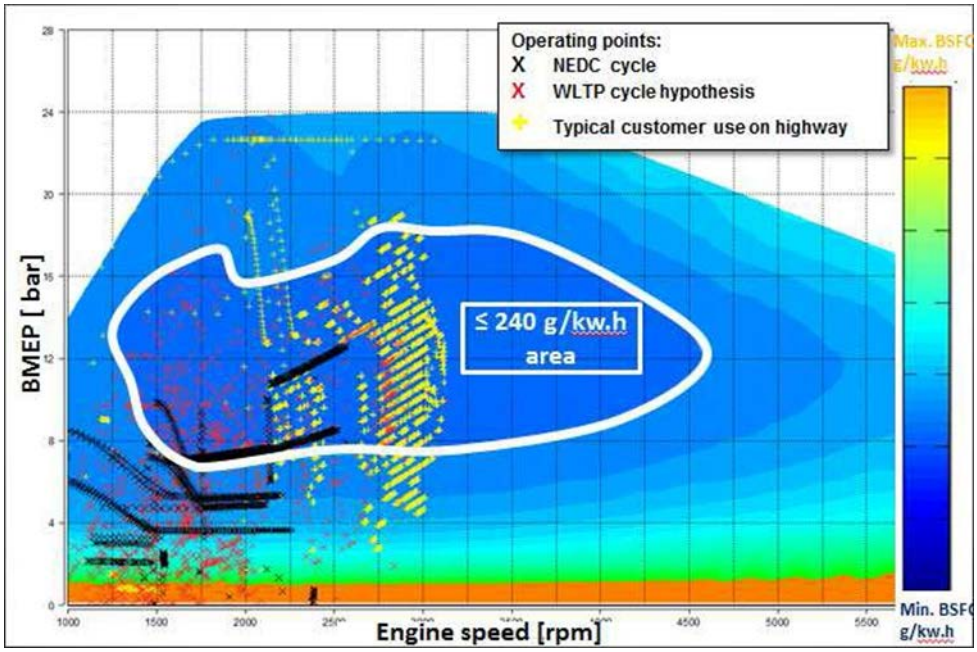

Fig. 25. BSFC map

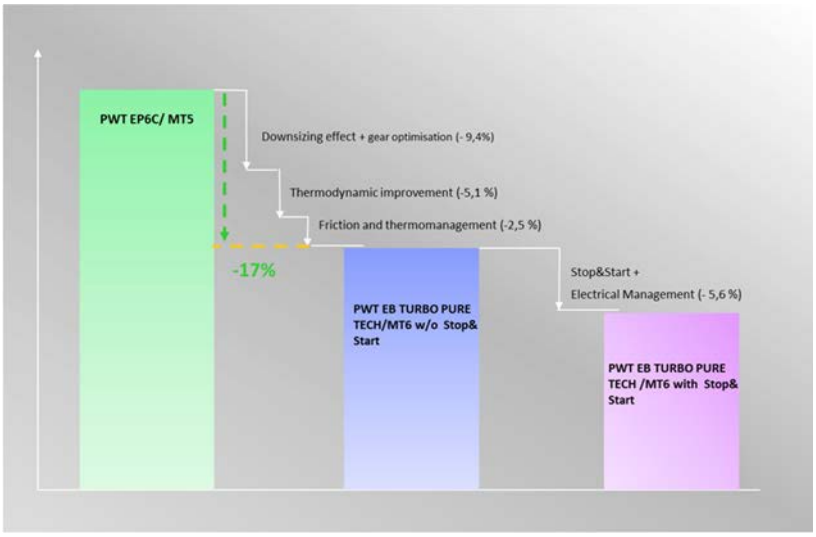

Fig. 26. CO2 improvement compared to replaced powertrain

Together with the downsizing and down-speeding effects allowed by the high specific performance and Stop Start functionality, BSFC map contributes to 21% improvement of CO2 emissions compared to former 1.6 NA powertrain, as shown in Figure 26.

Conclusions

The new PSA Peugeot Citroën PureTech 1.2 e-THP engine, by means of significant technological breakthroughs, provides outstanding performance and fun to drive coupled to drastically reduced CO2 emission whilst preserving a high level of components and industrial commonality with the Naturally Aspirated versions.

Its maximum power of 96 kW, peak torque of 230 Nm, high torque at low rpm and fuel economy improvement of 21% vs. the 1.6 NA Valvetronic replaced engine, make it a perfect balance between fuel economy and fun to drive.

A remarkable property of this engine, among others, is its wide low BFSC operating range, ensuring robust fuel saving for a wide range of driving profiles.

Acknowledgments

The authors acknowledge the contribution of our colleagues and/or team members at PSA Peugeot Citroën.

References

Gouzonnat F., Merckx P., Cazenave R., Le Coq s., Demesse F. (2013). New challenges encountered when designing highly downsized gasolines engines (through new PSA Peugeot Citroën powertrain examples). SIA France Strasbourg 2013- December 5th.

Marez P., Mokhtari S. Tellier A. (2013). New PSA PEUGEOT CITROEN EB Turbo PureTech 1.2 l gasoline engine. RWTH AACHEN – December 9th, 2013

Dognin C., Mokhtari S., Pagot A., Vangraefschepe F., Zaccardi J.M. (2009). Optimal design for a highly downsized gasoline engine. SAE Technical Paper 2009-01-1794

Improvements in Thermal Efficiency of Premixed Diesel Combustion with Optimization of Combustion Related Parameters and Fuel Properties

H. Ogawa[1], Q. Xiong[1], T. Obe[1], Y. Sakane[1], and G. Shibata[1]

[1]Hokkaidi University N13, W8, Kitaku, Sapporo, Japan.

E-mail: h-ogawa@eng.hokudai.ac.jp
Telephone: + (81) 11 706 6434
Fax: + (81) 11 706 6383

Abstract. The influence of combustion related parameters and fuel volatility on the premixed diesel combustion was experimentally investigated in a modern DI diesel engine and the evaporation process of the fuel spray in the combustion chamber was analyzed with CFD simulation. With optimizing the fuel injection timing and the intake oxygen content, ultralow NOx and smokeless premixed diesel combustion with high thermal efficiency and acceptable levels of CO and THC emissions is possible with both diesel fuel and normal heptane. The optimum fuel injection timing for the indicated thermal efficiency is when the fuel spray does not enter the squish area, maintaining the 50% heat release crank angle at around TDC. The indicated thermal efficiencies reach the maximum at around 12% intake oxygen concentration. The indicated thermal efficiency in the premixed diesel combustion with normal heptane is slightly higher than with diesel fuel and very similar to the conventional diesel combustion in a wide IMEP range below 0.8 MPa. The indicated thermal efficiency decreases with advancing injection timings mainly due to the deterioration in the combustion efficiency when the fuel is injected to the outside of the piston cavity. The degree of decrease in the indicated thermal efficiency with advancing injection timings is more significant with diesel fuel than with normal heptane due to the wall wetting.

Notation

CA50	*50% heat release crank angle [ºCA ATDC]*
C_{in}/C_{ex}	*Carbon quantity ratio between the input to and the exhaust from the engine*
$dp/d\theta_{max}$	*The maximum rate of heat release [MPa/ºCA]*
O_{2in}	*Intake oxygen concentration [%]*
ROHR	*The rate of heat release [J/ºCA]*
ϕ_{ex}	*Exhaust loss [%]*
ϕ_{other}	*Other losses ($\eta_u - \eta_i - \phi_{ex}$) [%]*
$\phi_{Woschni}$	*Cooling loss during the combustion period calculated with Woschni's equation [%]*
η_{glh}	*The degree of constant volume heat release [%]*
η_i	*Indicated thermal efficiency [%]*
η_u	*Combustion efficiency [%]*
θ_{inj}	*Fuel injection timing [ºCA BTDC]*
θ_{premix}	*Premixing period [ºCA]*

1. Introduction

The low temperature premixed diesel combustion with a large quantity of exhaust gas recirculation (EGR) is an effective approach to simultaneously establish low nitrogen oxide (NO_X) and particulate matter (PM) emissions as well as high thermal efficiency due to lower cooling loss with short combustion periods, and it has attracted much attention [1-13]. For premixed diesel combustion with direct injection, the ignition has to occur after the end of the fuel injection with a long ignition delay to remove over-rich mixture before the ignition. However, with direct injection of a low-volatility fuel including diesel fuel under the low in-cylinder gas temperature during the longer ignition delay, wall wetting and oil dilution with liquid fuel spray impinging on the combustion chamber walls are not easily avoided and

may result in deterioration in the thermal efficiency [8, 11]. To solve these problems and improve the spray evaporation process, the utilization of high volatility fuels without high distillation temperature components may be effective and have the potential to increase the thermal efficiency of the premixed diesel combustion.

In the present research, the influence of fuel volatility on the thermal efficiency of premixed diesel combustion was investigated in a DI diesel engine with supercharging, common rail fuel injection, and low pressure loop EGR. An ordinary diesel fuel (JIS No.1) and normal heptane were tested to elucidate the influence of fuel volatilities on the thermal efficiencies in premixed diesel combustion. The evaporation process in the fuel spray during the ignition delay and the quantity of liquid fuel impinging on the combustion chamber wall were analyzed with the CFD code FIRE. The injection timing and the intake oxygen content were optimized to establish high thermal efficiencies and low exhaust gas emissions in the premixed diesel combustion with ordinary diesel fuel, comparable to those with normal heptane. Finally, the optimized premixed diesel combustion with ordinary diesel fuel and normal heptane was compared with the modern conventional diesel combustion with pilot injection and a low EGR rate.

2. Experimental apparatus and procedure

The experiments were conducted on a single-cylinder, supercharged, four-stroke cycle, direct injection diesel engine with common-rail fuel injection and low pressure loop cooled EGR. The specifications of the test engine are shown in Table 1 and the operating conditions are in Table 2. The boost pressure was set at 175 kPa (absolute) with a supercharger driven by an electric motor, and an electric heater and an intercooler were installed after the supercharger to maintain the intake gas temperature constant at 40°C. The cooled EGR was realized with the exhaust gas passed through a diesel particulate filter (DPF) and an EGR cooler. The recirculated exhaust gas was mixed with the intake air before the supercharger with the low pressure loop. The exhaust gas pressure was maintained with a throttle valve at 175 kPa (absolute), the same as the boost pressure. The engine speed was everywhere set at 2000 rpm and the fuel injection pressure at 160 MPa.

As shown in Table 2 (panel with 3.1 in top line), the influence of fuel injection timing on the characteristics of premixed diesel combustion with ordinary diesel fuel and normal heptane was firstly examined at an intake oxygen concentration of 11% and an IMEP of 0.8 MPa, changing fuel injection timing from 10°CA BTDC to 40°CA BTDC. The results are described in 3.1 below.

Secondly, the influence of intake oxygen concentration on the characteristics of premixed diesel combustion with ordinary diesel fuel and normal heptane was examined at an IMEP of 0.8 MPa. Here, the 50% heat release crank angle, CA50 was maintained at the optimum timing (4°CA ATDC) for the indicated thermal efficiency, with changing the fuel injection timing. This is detailed in the 3.2 panel of Table 2, and the results are described in 3.2.

Thirdly, the premixed diesel combustion with diesel fuel and normal heptane was compared with the ordinary diesel combustion with a pilot injection for various IMEP conditions. Here, the intake oxygen concentration for the premixed diesel combustion was set at 11%, and injection timing was flexibly varied under consideration of the thermal efficiency and the maximum rate of pressure rise. For the conventional diesel combustion, the intake oxygen concentration was set at 16%, the pilot injection timing was at 11°CA BTDC, and the main injection timing was at TDC. This is detailed in the 3.3 panel of Table 2, and the results are described in 3.3.

Figure 1 shows the position of the piston and fuel sprays at the different fuel injection timings for the premixed diesel combustion. With the injection timing of 40°CA BTDC, fuel spray does not enter the combustion chamber and directly impinges on the cylinder liner wall. With the injection timing of 25°CA BTDC the fuel spray impinges the edge of the piston cavity, and a part of the fuel enters the squish area and reaches the cylinder liner wall. With 10°CA BTDC, almost all of the fuel spray enters the combustion chamber and very little fuel spray enters the squish area.

Table 1. Engine specifications

Number of cylinders	1
Bore × stroke	85 × 96.9 mm
Displacement	550 cm^3
Compression ratio	16.3
Fuel injection system	Common rail system
Nozzle hole	0.125 × 7 − 156º

Table 2. Experimental conditions

Engine speed		2000 rpm
Fuel injection pressure		160 MPa
Boost pressure (abs.)		175 kPa
Intake gas temperature		40ºC
Coolant temperature		80ºC
Lubricant oil temperature		80ºC
3.1 Influence of fuel Injection timing		
Mode	Premixed diesel	
IMEP	0.8 MPa	
Intake oxygen	11.0%	
Injection timing	Variable (10-40ºCA BTDC)	
CA50	Varied	
3.2 Influence of intake oxygen concentration		
Mode	Premixed diesel	
IMEP	0.8 MPa	
Intake oxygen	Variable	
Injection timing	Varied for CA50	
CA50	4ºCA BTDC	
3.3 Comparison at various IMEP		
Mode	Premixed diesel	Conventional diesel
IMEP	Variable	Variable
Intake oxygen	Variable	16.0%
Injection timing	15ºCA BTDC	Pilot: 11ºCA BTDC Main: TDC
CA50	Near TDC	Varied

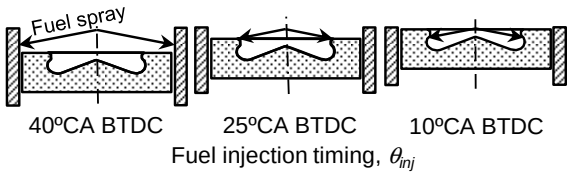

Fig. 1. Position of the piston and fuel spray at different fuel injection timings

Table 3 shows the properties of the tested fuels. The influence of fuel volatility on the thermal efficiency of the premixed diesel combustion was investigated with ordinary diesel fuel (JIS special No.1) and normal heptane, which have similar ignitabilities. Lubricity improver (R655) was added to the normal heptane in a volume fraction of 300 ppm.

Table 3. Properties of the tested fuels

	Diesel fuel	n-Heptane
Density [g/cm^3]	0.834	0.685
10% Distillation temperature [ºC]	217	100*
50% Distillation temperature [ºC]	281	
90% Distillation temperature [ºC]	342	
Carbon [wt%]	86.2	83.9
Hydrogen [wt%]	13.8	16.1
Stoichiometric ratio	14.7	15.2
LHV [MJ/kg]	42.9	44.5
Cetane number	54.2	–

* Boiling point

3. Results and discussion

3.1 Influence of fuel Injection timing on premixed diesel combustion with ordinary diesel fuel and normal heptane

The influence of fuel injection timing on the characteristics of premixed diesel combustion with ordinary diesel fuel and normal heptane was examined at an intake oxygen concentration of 11% maintained with cooled EGR and an IMEP of 0.8 MPa, changing fuel injection timings from 10°CA

BTDC to 40°CA BTDC. Figure 2 shows the 50% heat release crank angle (CA50) and the premixing period, θ_{premix}, defined as the crank angle from the end of fuel injection to the ignition for the various fuel injection timings. For all injection timings and both fuels, the premixing periods, θ_{premix}, are sufficiently long to establish the premixed diesel combustion and increase with advancing injection timings. When the injection timing is set at 20ºCA BTDC or later, the CA50 is around the top dead center and advances with advancing injection timings. When the injection timing is advanced from 25ºCA BTDC, the CA50 is almost unchanged at 4ºCA BTDC, slightly earlier than the optimum timing for the thermal efficiency. There is little difference between diesel fuel and normal heptane in the premixing period and CA50 as the ignitabilities are similar.

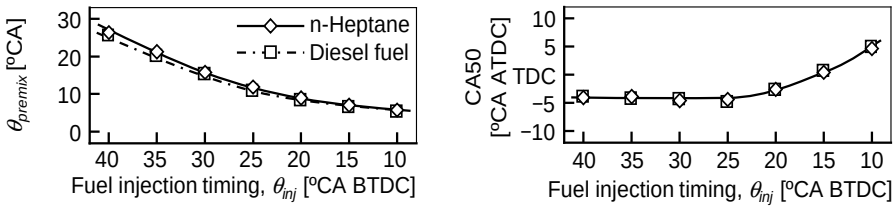

Fig. 2. The 50% heat release crank angle, CA50 and the premixing period, θ_{premix} for the various fuel injection timings (IMEP: 0.8 MPa, O_{2in} = 11%)

Figure 3 shows the indicated thermal efficiency, η_i, the degree of constant volume heat release, η_{glh}, the combustion efficiency calculated from the THC and CO concentrations in the exhaust gas, η_u, and the exhaust loss from the temperature and quantity of exhaust gas, ϕ_{ex}, for various fuel injection timings, at the same operating conditions as in Fig. 2. When the injection timing is set at 20ºCA BTDC or later, the indicated thermal efficiencies with diesel fuel are slightly lower than with normal heptane, but exceed 47%. With normal heptane the indicated thermal efficiencies reach around 49% with the injection timings at 15 or 20ºCA BTDC. When the injection timing is advanced from 25ºCA BTDC, the indicated thermal efficiency decreases remarkably with advancing injection timings for both fuels mainly due to deterioration in the combustion efficiency calculated from the exhaust gas compositions. The deterioration in the indicated thermal efficiency with diesel fuel is more significant in spite of the larger combustion efficiency from the exhaust gas compositions and the smaller exhaust loss than with normal heptane. It is impossible to identify the difference in the indicated thermal efficiency between diesel fuel and normal heptane from this figure.

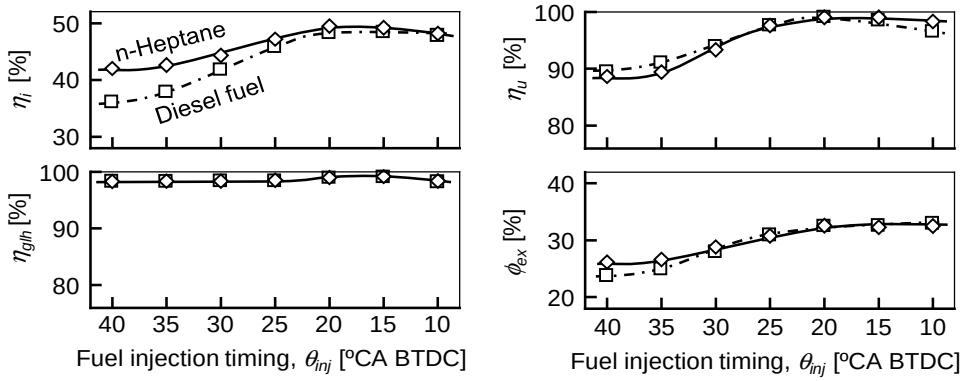

Fig. 3. The indicated thermal efficiency, η_i, the degree of constant volume heat release, η_{glh}, the combustion efficiency calculated from the exhaust gas compositions, η_u, and the exhaust loss, ϕ_{ex}, for the various fuel injection timings (IMEP: 0.8 MPa, O_{2in} = 11%)

Figure 4 shows the other losses, ϕ_{other}, the cooling loss during the combustion period calculated with Woschni's equation, $\phi_{Woschni}$, and the carbon quantity ratio between the input to and the exhaust from the engine, C_{ex}/C_{in} for the various fuel injection timings, at the same operating conditions as in Figs. 2 and 3. Here, the other losses, ϕ_{other} are calculated with the following equation based on the energy balance.

$$\phi_{other} = \eta_u - \eta_i - \phi_{ex}$$

η_u: The combustion efficiency calculated from the carbon monoxide (CO) and total hydrocarbon (THC) concentrations in the exhaust gas

η_i: The indicated thermal efficiency calculated with the fuel consumption per cycle and the in-cylinder pressure

ϕ_{ex}: The exhaust loss calculated from the temperature and quantity of exhaust gas

The other losses, ϕ_{other} include the cooling loss as a main component and also the unburned fuel which does not reach the gas analyzer.

As shown in Fig. 4, when the fuel injection timing is later than 20ºCA BTDC, the other losses increase slightly with advancing fuel injection timings mainly due to the increase in the cooling loss for both fuels, which is also shown in the cooling loss with Woschni's equation, $\phi_{Woschni}$. When the fuel injection timing is advanced from 20ºCA BTDC, the other losses increase more significantly than the later injection case even when $\phi_{Woschni}$ decreases. Especially, the other losses with diesel fuel are more significant than with normal heptane. The increase in the other losses with advanced fuel injection timings may be due to the increase in the unburned fuel which does not reach the gas analyzer. This mechanism is also strongly suggested from the result that the carbon quantity ratio between the input to and the exhaust from the engine, C_{ex}/C_{in} with diesel fuel decreases remarkably when advancing the fuel injection timing while C_{ex}/C_{in} with normal heptane remains unchanged. The unburned fuel, which does not reach the gas analyzer, may be fuel which enters the crankcase and the liquid phase hydrocarbon emissions which are not sampled in the gas analyzer.

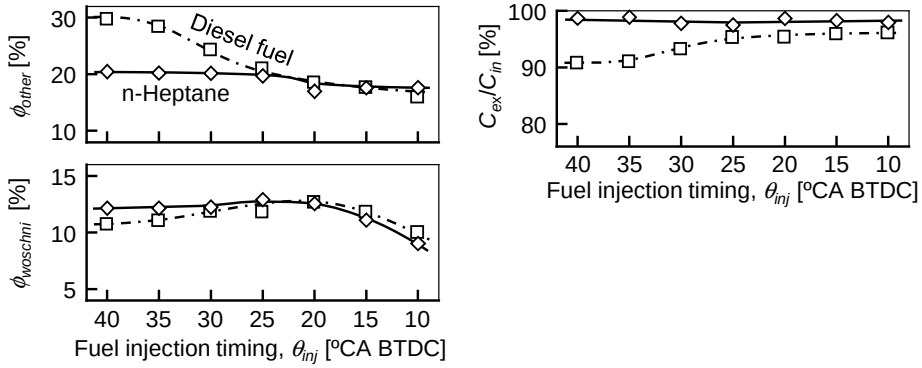

Fig. 4. The other losses, ϕ_{other}, the cooling loss with Woschni's equation, $\phi_{Woschni}$, and the carbon quantity ratio between the input and the exhaust from the engine, C_{ex}/C_{in} for the various fuel injection timings (IMEP: 0.8 MPa, O_{2in} = 11%)

Figure 5 shows the exhaust gas emissions for various fuel injection timings, at the same operating conditions as in Figs. 2, 3, and 4. There is little difference between diesel fuel and normal heptane in the trends of CO, THC, and NOx emissions. When the fuel injection timing is 25ºCA BTDC or later, the CO and THC emissions are at acceptable levels. When the fuel injection timing is earlier than 25ºCA BTDC, the CO and THC emissions increase significantly with advancing fuel injection timings. The NOx emissions from both fuels are very low, between 0.01 and 0.02 g/(kW·h) and no smoke is emitted at any of the injection timings here.

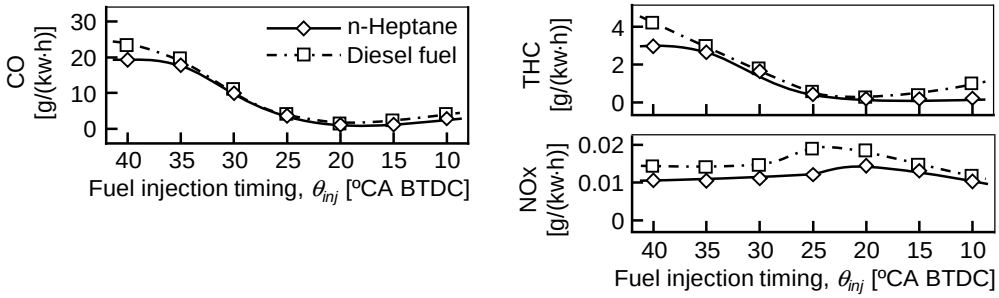

Fig. 5. The exhaust gas emissions for the various fuel injection timings (IMEP: 0.8 MPa, O_{2in} = 11%)

Figure 6 shows the in-cylinder pressure and the rate of heat release (ROHR) of diesel fuel and normal heptane for four fuel injection timings. Very similar ROHR diagrams are obtained with diesel fuel and normal heptane at the same injection timings. Regardless of the injection timings and the fuels, the shape of the rate of heat release diagram features the characteristics of typical premixed diesel combustion: an ignition delay substantially longer than the injection period, the presence of a low temperature heat release, and a single high temperature heat release.

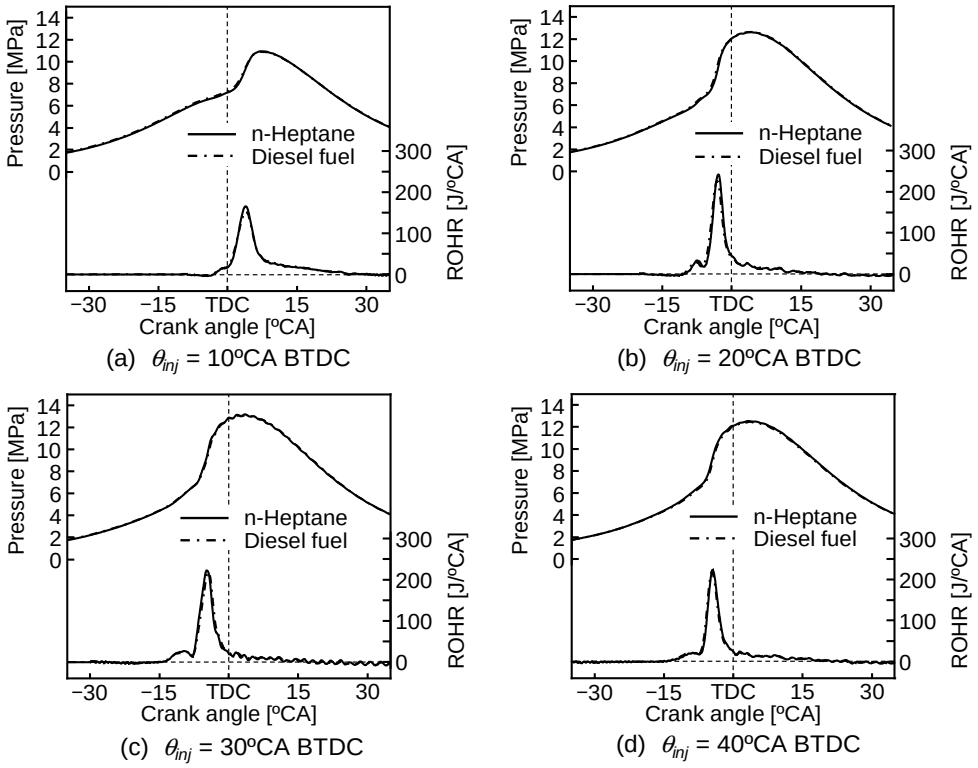

Fig. 6. The in-cylinder pressure and the rate of heat release (ROHR) of diesel fuel and normal heptane for four fuel injection timings (IMEP: 0.8 MPa, O_{2in} = 11%)

Table 4. Sub-models and the initial conditions for the CFD simulation

Spray	Discrete droplet model
Breakup	WAVE
Turbulence	k-ε model
Initial pressure	0.17 MPa (160ºCA BTDC)
Initial temperature	340 K (160ºCA BTDC)

To elucidate the influence of fuel injection timing on premixed diesel combustion with diesel and normal heptane, the evaporation process in the fuel spray during the ignition delay and the quantity of liquid fuel impinging on the combustion chamber wall were analyzed with the CFD code FIRE. Here, the specifications and the combustion chamber shape of the engine are the same as the engine in the experiments, and the operating conditions in Fig. 6 were analyzed. Table 4 shows the sub-models and the initial conditions for the CFD simulation.

Figure 7 shows the results of CFD simulation for the distributions of the liquid phase fuel spray (left) and the equivalence ratio of the gas phase (right) in the cross section of the combustion chamber including the center axis of the fuel spray for four fuel injection timings. For all injection timings the spray of the diesel fuel impinges on the piston or cylinder liner just after around 2ºCA after the start of injection while the spray tip penetration of normal heptane becomes slower just before the walls and a rich mixture is formed around the spray tip, showing active evaporation. In contrast, leaner mixture is formed around the spray tip of the diesel fuel, showing less evaporation.

At the 40ºCA BTDC injection timing (Fig. 7 (a)), liquid fuel spray impinges directly on the cylinder liner with the diesel fuel while almost all liquid fuel spray is evaporated before impingement with normal heptane. The impingement of liquid diesel fuel on the cylinder liner may result in the increases in the fuel entering into the crank case and in the other losses, ϕ_{other} in Fig. 4. Almost all evaporated fuel stays in the squish area for both fuels, causing the increase in the CO and THC emissions in Fig. 5 and the lowering in the combustion efficiency, η_u in Fig. 3.

At the 30ºCA BTDC injection timing (Fig. 7 (b)), almost all fuel spray and evaporated gas jet reach the top of the piston for both fuels. With the diesel fuel, some part of the fuel spray and evaporated gas jet reach the cylinder liner, and this may be a cause of the increase in fuel entering into the crank case, but the quantity of the impinging fuel is much smaller than at the 40ºCA BTDC injection timing. With normal heptane little fuel spray and evaporated gas jet reach the cylinder liner and the rich mixture stays in the squish area.

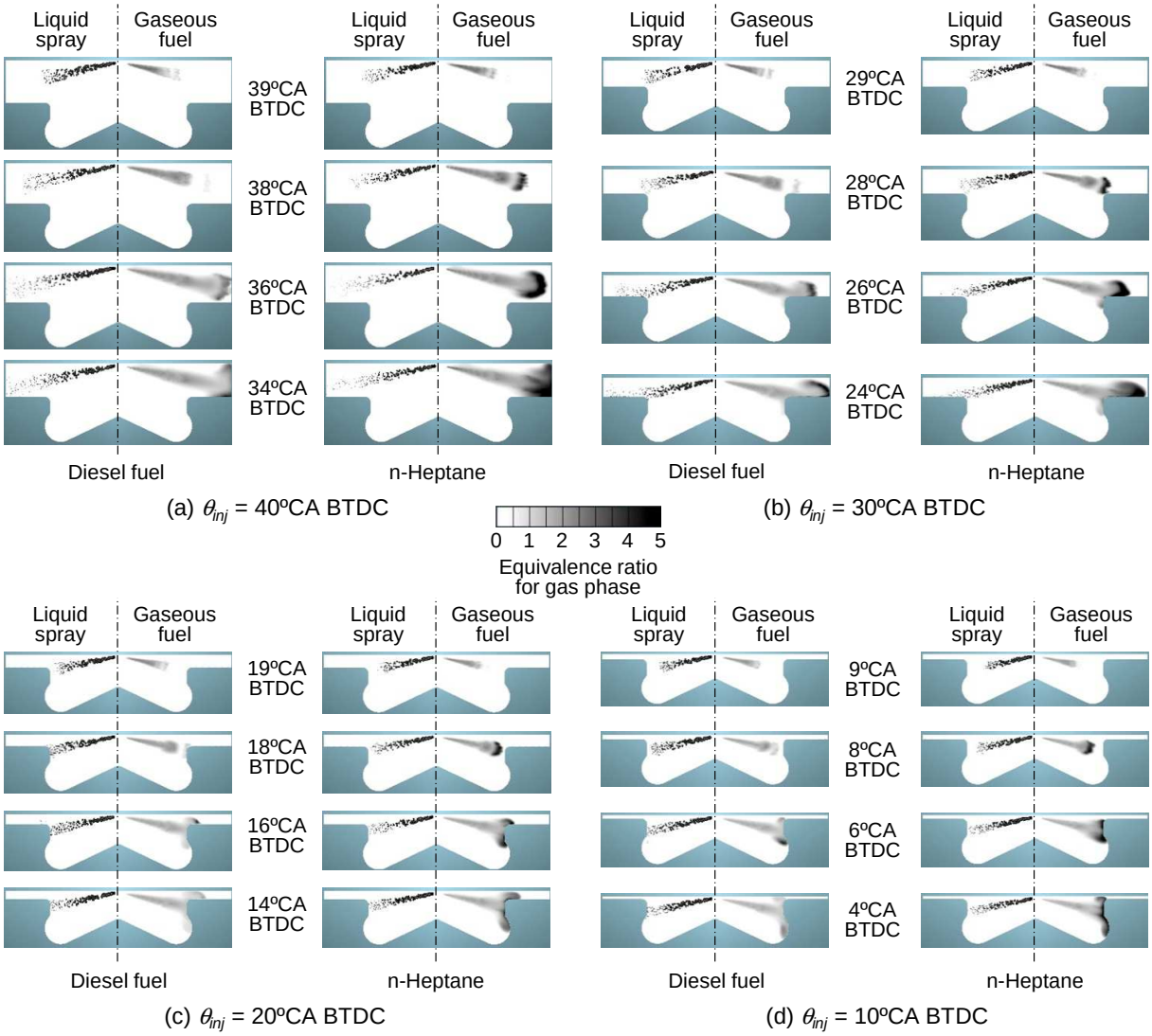

Fig. 7. The distributions of the liquid phase fuel spray (left) and the equivalence ratio of the gas phase (right) in a cross section of the combustion chamber (IMEP: 0.8 MPa, O_{2in} = 11%)

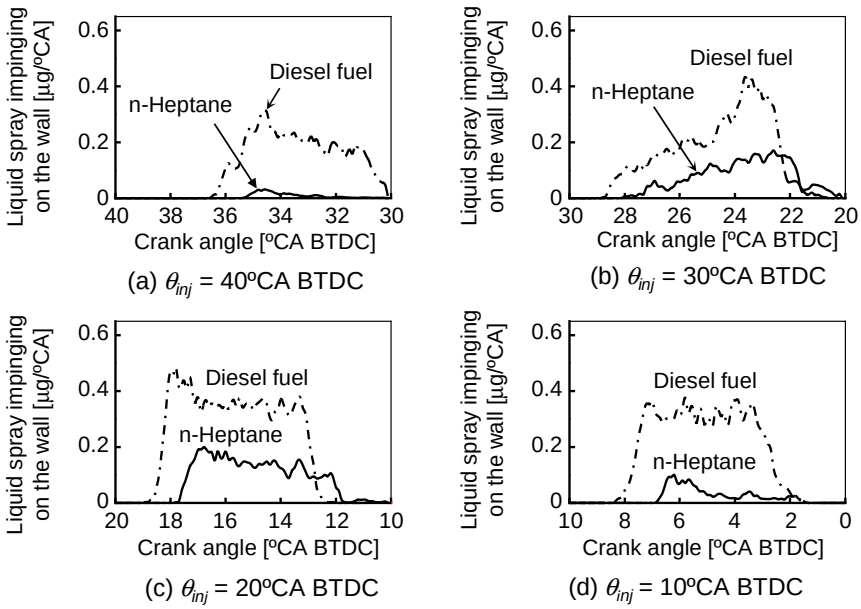

Fig. 8. The quantity of liquid spray impinged on the walls at the four injection timings (IMEP: 0.8 MPa, O_{2in} = 11%)

At the 20 ºCA BTDC injection timing (Fig. 7 (c)), liquid fuel spray and evaporated fuel jet reach the upper part of the rim of the piston cavity, and some part of mixture enters the squish area near the piston cavity. However, the fuel spray and the mixture do not reach the deep part of squish area and the cylinder liner for both fuels. At the 10ºCA BTDC injection timing (Fig. 7 (d)), liquid fuel spray and evaporated fuel jet also reach the lower part of the rim of piston cavity and evaporated fuel jet spreads on the piston cavity wall for both fuels, but very little mixture enters the squish area. These characteristics of the injection timings (10º and 20ºCA BTDC) result in smaller unburned losses for both diesel fuel and normal heptane.

Figure 8 shows the quantities of liquid fuel spray impinged on the piston and the cylinder liner at the four injection timings shown in Fig. 7. With diesel fuel a lot of liquid phase spray impinges on the wall while much less liquid spray impinges with normal heptane for all four injection timings here.

3.2 Influence of intake oxygen concentration on premixed diesel combustion with ordinary diesel fuel and normal heptane

The influence of intake oxygen concentration on the characteristics of premixed diesel combustion with ordinary diesel fuel and normal heptane was examined at an IMEP of 0.8 MPa. Figure 9 shows the fuel injection timing, θ_{inj}, and the premixing period, θ_{premix} for various intake oxygen concentrations changed with the EGR rate when the 50% heat release crank angle is maintained at the optimum combustion phase for the indicated thermal efficiency, 4ºCA ATDC, changing the fuel injection timing. With decreasing intake oxygen contents, the fuel injection timing has to be advanced due to increases in the ignition delay, but all injection timings for both fuels are later than 20ºCA ATDC when little spray and mixture enter the squish area. The premixing periods have positive values everywhere so that the ignition occurs after the end of the fuel injection. However, when the intake oxygen concentrations are larger than 15%, the premixing periods are less than 3ºCA and the premixing is not sufficient to establish premixed diesel combustion, which will be shown in the rate of heat release diagrams in Fig. 13.

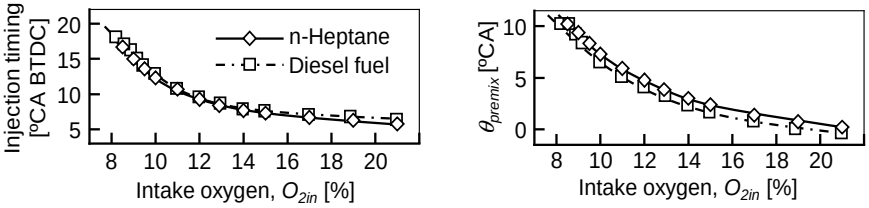

Fig. 9. The fuel injection timing, θ_{inj}, and the premixing period, θ_{premix} for the various intake oxygen concentrations, O_{2in} (IMEP: 0.8 MPa, CA50: 4ºCA ATDC)

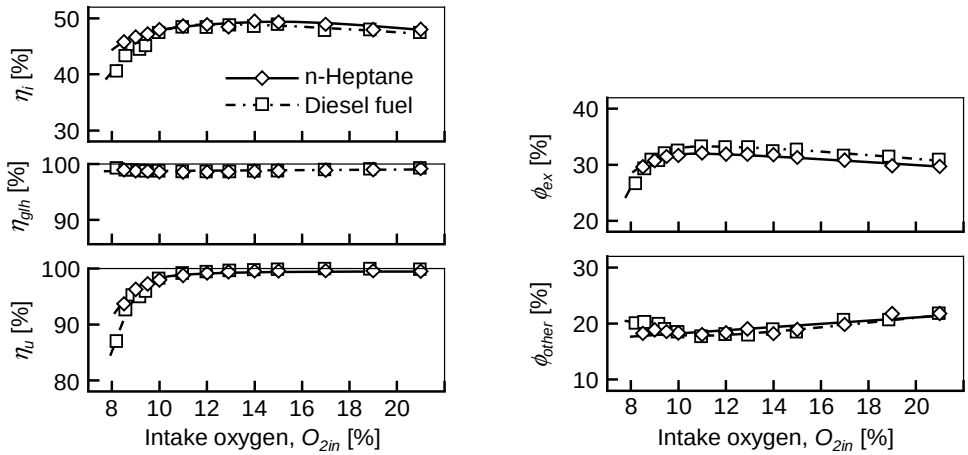

Fig. 10. The indicated thermal efficiency, η_i, the degree of constant volume heat release, η_{glh}, the combustion efficiency calculated from the exhaust gas compositions, η_u, the exhaust loss, ϕ_{ex}, and other losses, ϕ_{other}, for the various intake oxygen concentrations, O_{2in} (IMEP: 0.8 MPa, CA50: 4ºCA ATDC) (IMEP: 0.8 MPa, CA50: 4ºCA ATDC)

Figure 10 shows the indicated thermal efficiency, η_i, the degree of constant volume heat release, η_{glh}, the combustion efficiency calculated from the THC and CO concentrations in the exhaust gas, η_u, the exhaust loss, ϕ_{ex}, and other losses, ϕ_{other} for various intake oxygen contents, at the same operating

conditions as in Fig. 9. There is little difference between diesel fuel and normal heptane except for the low intake oxygen concentrations as the fuel injection timings are later than 20ºCA ATDC in these cases. With decreasing intake oxygen concentrations from 21%, the indicated thermal efficiencies increase slightly and reach the maximum at around 12% intake oxygen concentration for both fuels. This is due to the decreases in the other losses with the decreasing cooling losses. The exhaust losses increase slightly with decreasing intake oxygen concentrations due to the decreases in the ratio of specific heat with increasing carbon dioxide and water in the in-cylinder gas. When the intake oxygen concentrations are reduced below 10% the indicated thermal efficiencies decrease significantly mainly due to the decreases in the combustion efficiency calculated from the THC and CO concentrations in the exhaust gas.

Figure 11 shows the exhaust gas emissions for various intake oxygen concentrations, at the same operating conditions as in Figs. 9 and 10. There is little difference between diesel fuel and normal heptane in the trends of the exhaust gas emissions in these results. Smokeless and very low NOx combustion with acceptable levels of CO and THC emissions is possible with both fuels when the intake oxygen concentrations are set between 11% and 15%.

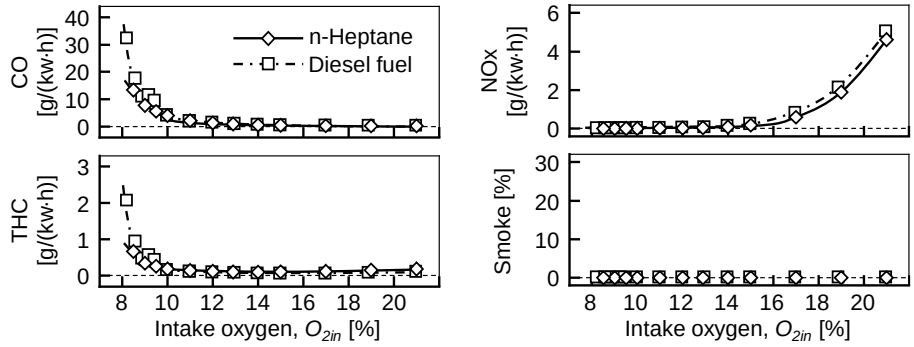

Fig. 11. The exhaust gas emissions for the various intake oxygen concentrations, O_{2in} (IMEP: 0.8 MPa, CA50: 4ºCA ATDC)

Figure 12 shows the maximum rate of pressure rise and the engine noise for various intake oxygen concentrations, at the same operating conditions as in Figs. 9, 10, and 11. The maximum rate of pressure rise and the engine noise with diesel fuel are slightly lower than with normal heptane for a wide range of intake oxygen concentrations, and decrease with reducing intake oxygen concentrations for both fuels below 12% intake oxygen concentration where the indicated thermal efficiencies are also highest (left top panel of Fig. 10). However, the maximum rate of pressure rise is relatively high when the intake oxygen concentration is above 10%, and this may be a problem which must be overcome.

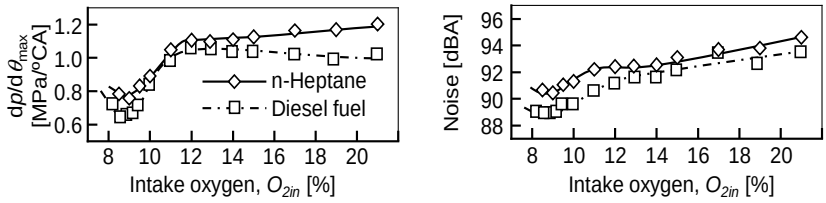

Fig. 12. The maximum rate of pressure rise and the engine noise for the various intake oxygen concentrations, O_{2in} (IMEP: 0.8 MPa, CA50: 4ºCA ATDC)

Figure 13 shows the in-cylinder pressure and the rate of heat release (ROHR) of diesel fuel and normal heptane for four intake oxygen concentrations. Very similar ROHR diagrams are obtained with diesel fuel and normal heptane at the same intake oxygen concentrations. With 21% intake oxygen concentration (Fig. 13 (a)), the shape of the rate of heat release diagram features the characteristics of ordinary two stage diesel combustion with the first premixed and the second diffusive combustion. With 15% intake oxygen concentration (Fig. 13 (b), the premixing is promoted, but diffusive combustion is still observed. With 11% intake oxygen concentration (Fig. 13 (c)), the shape of the rate of heat release diagram features the characteristics of premixed diesel combustion: the presence of a low temperature heat release, and a single high temperature heat release with little diffusive combustion. With 9% intake oxygen concentration (Fig. 13 (d)), the combustion is similar to the 11% intake oxygen concentration, but the rate of heat release is milder.

From the results in this section, clean and smooth premixed diesel combustion with high thermal efficiency is possible with ordinary diesel fuel when the intake oxygen concentration is set around 11% and the CA50 is optimized with the fuel injection timing.

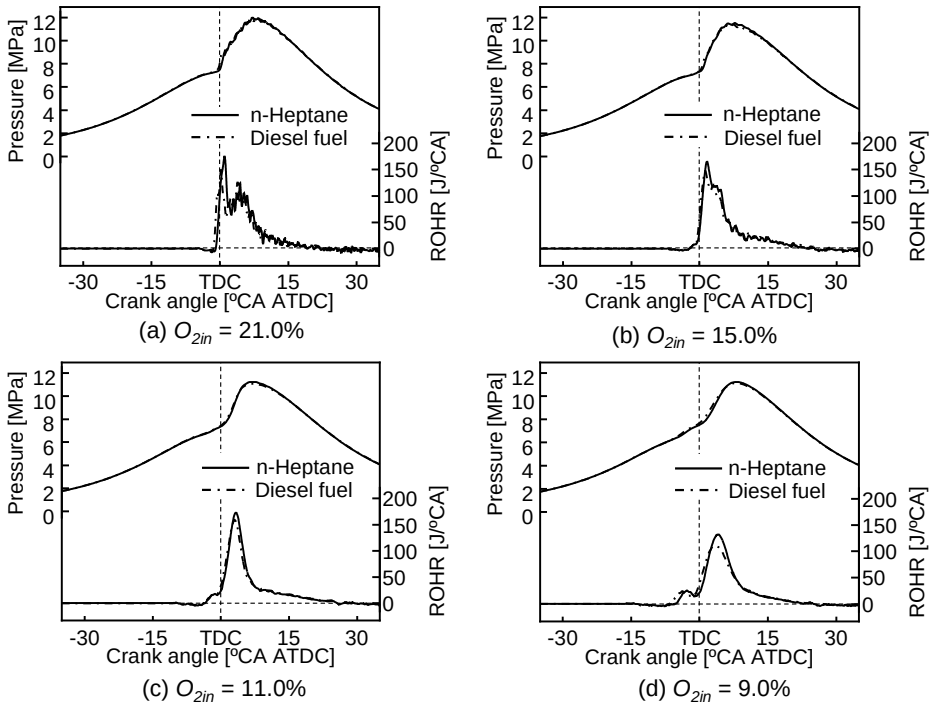

Fig. 13. The in-cylinder pressure and the rate of heat release (ROHR) of diesel fuel and normal heptane for four intake oxygen concentrations, O_{2in} (IMEP: 0.8 MPa, CA50: 4ºCA ATDC)

3.3 Comparison between the optimized premixed diesel combustion and conventional diesel combustion for various IMEP conditions

The results of premixed diesel combustion with ordinary diesel fuel and normal heptane at the optimized intake oxygen concentrations and CA50 was compared with the conventional diesel combustion with the experimental conditions shown in Table 2 (bottom panel), for various IMEP conditions.

Figure 14 shows the indicated thermal efficiency, η_i, the degree of constant volume heat release, η_{glh}, the combustion efficiency calculated from the THC and CO concentrations in the exhaust gas, η_u, the exhaust loss, ϕ_{ex}, and the other losses, ϕ_{other} for various IMEP conditions. With diesel fuel, the indicated thermal efficiency with the premixed diesel combustion is slightly lower than with the conventional diesel combustion in a wide IMEP range mainly due to the decreases in the combustion efficiency, η_i and the increases in the other losses, ϕ_{other}. The exhaust loss with the premixed diesel combustion is smaller than with the conventional diesel combustion due to the larger degree of constant volume heat release, showing a high potential of the premixed diesel combustion. With normal heptane, the indicated thermal efficiency with the premixed diesel combustion is higher than with diesel fuel due to decreases in the other losses, ϕ_{other}, and are very similar to the conventional diesel combustion with diesel fuel over a wide IMEP range.

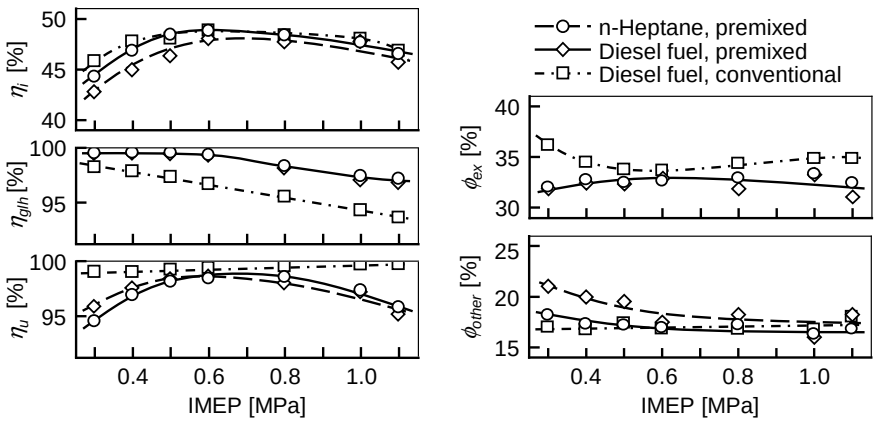

Fig. 14. The thermal efficiency related parameters for the various IMEP conditions with premixed diesel combustion with diesel fuel and normal heptane, and with conventional diesel combustion

Figure 15 shows the exhaust gas emissions and the engine noise for various IMEP conditions, at the same operating conditions as in Fig. 14. The NOx emissions are at extremely low levels in the premixed combustion with both fuels over a wide IMEP range. In the middle IMEP range between 0.5 and 0.8 MPa, very low NOx and smokeless operation with acceptable levels of CO and THC emissions is possible with premixed diesel combustion for both diesel fuel and normal heptane. However, in the high IMEP range above 0.8 MPa, the CO, THC, NOx, smoke, and engine noise increase with increases in IMEP, showing that the premixed diesel combustion is not suitable for high IMEP operation. In the low IMEP range below 0.5 MPa, the CO and THC emissions increase with decreases in IMEP with the premixed combustion for both diesel fuel and normal heptane, and further optimization will be necessary to suppress the emissions.

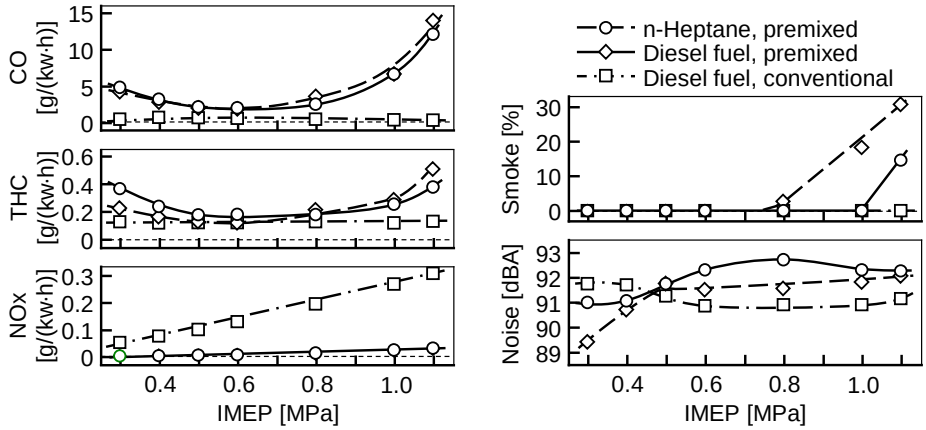

Fig. 15. The exhaust gas emissions and the engine noise for the various IMEP conditions with premixed diesel combustion with diesel fuel and normal heptane, and with conventional diesel combustion

4. Summary

In this research, the influence of combustion related parameters and fuel volatility on the premixed diesel combustion was experimentally investigated in a modern DI diesel engine and the evaporation process of fuel spray in the combustion chamber was analyzed with CFD simulation. The results may be summarized as follows:

1. The indicated thermal efficiency decreases with advancing injection timings when the fuel is injected to the outside of the piston cavity and the degree of decrease in the indicated thermal efficiency is more significant with diesel fuel than with normal heptane. The decreases in the indicated thermal efficiency with advancing injection timings are mainly due to a deterioration in the combustion efficiency calculated from the exhaust gas compositions. The difference of the indicated thermal efficiencies between diesel fuel and normal heptane at early injection timings is due to the different behaviors of the other losses including the cooling loss and the unburned fuel which does not reach the gas analyzer. The amounts of unburned fuel which does not reach the gas analyzer are larger with diesel fuel than with normal heptane while there is little difference in the cooling losses.
2. The increase in the unburned fuel which does not reach the gas analyzer may be due to the adhesion of high distillation temperature components on the walls of the combustion chamber, resulting in a larger quantity of unburned fuel entering the crank case and the liquid phase hydrocarbon emissions which are not sampled to the gas analyzer.
3. The CFD simulation showed that a not inconsiderable quantity of liquid phase spray impinges on the wall with diesel fuel while much less liquid spray impinges with normal heptane.
4. With decreases in the intake oxygen concentration from 21% and maintaining the 50% heat release crank angle at 4ºCA ATDC by changing the injection timing, the indicated thermal efficiencies increase slightly and reach the maximum at around 12% intake oxygen concentration for both diesel fuel and normal heptane. When the intake oxygen concentrations are reduced below 10% the indicated thermal efficiencies decrease significantly mainly due to the decreases in the combustion efficiency calculated from the THC and CO concentrations in the exhaust gas. The ignition delay and the premixing period (the crank angle between the end of fuel injection and ignition) increased gradually with decreases in the intake oxygen concentration, and the ordinary diesel combustion with diffusive combustion changes to premixed combustion without diffusive combustion taking place. Smokeless and very low NOx combustion with acceptable levels of CO and THC emissions

is possible with diesel fuel and normal heptane when the intake oxygen concentrations are set between 11% and 15%.

5. With diesel fuel, the indicated thermal efficiency with the premixed diesel combustion is slightly lower than with the conventional diesel combustion over a wide IMEP range mainly due to the decreases in the combustion efficiency and the increases in the other losses. However, with normal heptane, the indicated thermal efficiency with the premixed diesel combustion is higher than with diesel fuel due to decreases in the other losses and similar to the conventional diesel combustion with diesel fuel in a wide IMEP range. The exhaust loss with the premixed diesel combustion is smaller than with the ordinary diesel combustion due to the larger degree of constant volume heat release, showing the excellent potential of the premixed diesel combustion to establish a high thermal efficiency.

Acknowledgement

The authors express their appreciation to Infineum Japan Ltd. for their donation of the lubricity improver (R655).

References

1. Akihama K, Takatori Y and Inagaki K et al. (2001) Mechanism of the smokeless rich diesel combustion by reducing temperature. SAE Technical Paper 2001-01-0655.
2. Hasegawa R and Yanagihara H (2003) HCCI combustion in DI diesel engine. SAE Technical Paper 2003-01-0745.
3. Ickes A M, Bohac S V and Assanis N D et al. (2009) Effect of fuel cetane number on a premixed diesel combustion mode, Int. J. Engine Res.10(4):251–263.
4. Li T, Okabe Y. and Izumi H and Ogawa H (2006) Dependence of ultra-high EGR and low temperature diesel combustion on fuel properties. SAE Technical Paper 2006-01-3387.
5. Li T, Izumi H and Shudo T and Ogawa H (2007) Characterization of low temperature diesel combustion with various dilution gases. SAE Technical Paper 2007-01-0126.
6. Li T, Suzuki M and Ogawa H (2008) Effects of in-cylinder temperature and fuel air mixing quality on smokeless low temperature diesel combustion. Proc. COMODIA, 135–142.
7. Li T, Suzuki M and (2009) Characteristics of smokeless low temperature diesel combustion in various fuel–air mixing and expansion of operating load range. SAE Technical Paper 2009-01-1449.
8. Li T, Moriwaki R. and Ogawa H (2012) Dependence of premixed low-temperature diesel combustion on fuel ignitability and volatility. Int. J. Engine Res.13 (1):14-27.
9. Ogawa H, Li T and Miyamoto N, (2007) Characteristics of low temperature and low oxygen diesel combustion with ultra-high EGR. Int. J. Engine Res. 8(4):365–378.
10. Sakai A, Takeyama H, Ogawa H and Miyamoto N (2005) Improvements in PCCI Combustion and Emissions with Lower Distillation Temperature Fuels. Int. J. Engine Res. 6(5):433-442.
11. Takeda T, Nakagome K and Niimura K (1996) Emission characteristics of premixed lean diesel combustion with extremely early staged fuel injection. SAE Technical Paper 961163
12. Xiong Q, Inaba K, Ogawa H and Shibata G (2013) Influence of Fuel Properties on Operational Range and Thermal Efficiency of Premixed Diesel Combustion. SAE Int. J. Fuels Lubr., 6:1005-1013, 2013-32-9054.
13. Xiong Q, Inaba K, Obe T, Ogawa H and Shibata G (2013) Improvements in Thermal Efficiency of Premixed Diesel Combustion with Low Distillation Temperature Fuels. SAE Paper, 2013-01-2624.

Analysis of combustion concepts in a newly designed 2-stroke HSDI compression ignition engine

J. Benajes[1], R. Novella[1], D. De Lima[1] and P. Tribotté[2]

[1]CMT – Motores Térmicos. Universitat Politècnica de València. Camino de Vera s/n, E-46022 Valencia, Spain.

E-mail: rinoro@mot.upv.es
Telephone: +(34) 963 877 650
Fax: +(34) 963 877 659

[2]Renault SAS. 1 Avenue du Golf, E-78288 Guyancourt, France.

E-mail: pascal.tribotte@renault.com
Telephone: +(33) (0)1 76 85 49 12
Fax: +(33) (0)1 76 85 77 16

Abstract. Conventional CI engines still provide higher thermal efficiency compared to their main competitor, the gasoline SI engines. However, the mixing-controlled combustion stage of the conventional diesel combustion (CDC) concept intrinsically generates both nitrogen oxides (NO_X) and particulate matter emissions, so these pollutants should be managed by optimizing as much as possible the combustion process. Additionally, a relatively new approach, known as Partially Premixed Combustion (PPC), has been designed to operate CI engines in a range bounded by fully premixed combustion and fully mixing-controlled combustion concepts, attaining extremely low pollutant emissions while keeping control over the combustion timing with the injection event.
The already confirmed high flexibility of the innovative 2-stroke poppet valves HSDI CI engine under development in terms of air management settings to control the cylinder conditions and affect final combustion environment encouraged the authors to perform a detailed optimization of the CDC concept in an attempt to find the real limits of this engine configuration. Additionally, its compatibility with the PPC concept using a high octane fuel (gasoline RON95) with a triple injection strategy for reducing pollutant emissions at medium-to-low load conditions has been evaluated considering also the impact on engine efficiency.
Results at low speed and medium load confirm how the engine configuration provides potential for attaining state-of-the-art emission levels operating with the CDC concept, and how emissions and efficiency can be optimized by adjusting the air management settings without facing any additional trade-off aside from that usual between NO_X and soot. The feasibility of combining this engine configuration with the PPC concept using gasoline as fuel for controlling pollutant emissions has been also corroborated and, with a fine tuned triple injection strategy, engine efficiency even improves compared to that obtained operating with a well optimized CDC concept.

Notation

ACT^{-1} **80%MBF**	*Gas mixing capacity at 80% of the mass burnt fraction.*
ΔP	*Pressure drop between the intake and the exhaust.*
ϕ	*In-cylinder equivalence ratio.*
IGR	*Internal Gas Recirculation.*
$ISFC_{corr}$	*Corrected indicated specific fuel consumption.*
P_{int}	*Absolute mean intake pressure.*
Q_{del}	*Delivered flow rate (fresh air flow + EGR).*
$Q_{tot\ trapped}$	*Total trapped flow rate (trapped fresh air + trapped EGR + IGR).*
SoE	*Start of energizing current of the injector.*
T_{ad} **max**	*Maximum adiabatic flame temperature.*
T_{ad} **80%MBF**	*Adiabatic flame temperature at 80% of the mass burnt fraction.*
VVT(int, exh)	*Variable Valve Timing positions (intake, exhaust).*
YO_2 **IVC**	*Oxygen concentration at the intake valve closing.*
YO_2 **EVO**	*Oxygen concentration at the exhaust valve opening.*

1. Introduction

Over the last years, engine research efforts are being focused on improving engine efficiency in order to decrease CO_2 emissions and fuel consumption, while fulfilling the increasingly stringent pollutant emissions regulations. In this framework, there is a real need to develop smaller Internal Combustion Engines (ICE) with higher power density. With this motivation, an innovative 2-stroke HSDI compression ignition (CI) engine with four poppet valves in the cylinder head is being investigated for a heavily downsized passenger car application, where high power-to-mass ratio is mandatory. The idea behind this new engine concept is to depart from a conventional HSDI diesel 4-stroke engine (1460 cm^3, 4 cylinders) and implement a 2-stroke operation cycle to downsize the engine displacement by a factor of two, obtaining a 2-stroke engine (730 cm^3, 2 cylinders) with equivalent NVH and similar torque response than the base 4-stroke 4 cylinder engine [36].

Conventional CI engines are well known for their higher thermal efficiency compared to gasoline SI engines, but the characteristic mixing-controlled combustion stage of the Conventional Diesel Combustion (CDC) concept still represents an important pollutant source of nitrogen oxides (NO_X) [11, 12, 19] and particulate matter emissions [13, 37]. Thus, a very detailed optimization of the CDC concept by adjusting the air management and injection settings is nowadays mandatory to control these emissions keeping the competitive engine efficiency.

Aside from the efforts to optimize the CDC concept, a relatively new approach known as Partially Premixed Combustion (PPC) concept has been designed to operate CI engines in between fully premixed combustion and fully diffusive combustion concepts, where low emissions can still be attained while retaining control over the combustion timing with the injection event. The injection process is advanced towards the compression stroke to be detached from the combustion event, enabling partial mixing of the mixture to avoid over-rich regions where soot is formed, whereas NO_X emissions are reduced by lowering combustion temperatures by the introduction of large amounts of EGR [25].

Research work performed by Kalghatgi and co-workers in both large [17, 18] and small [15] single-cylinder engines demonstrated how injecting a fuel with higher resistance to auto-ignition such as a gasoline close to (but before) TDC was suitable for extending mixing times before the onset of combustion. As a result, low engine-out soot and NO_X emissions were obtained in a wider range of engine loads compared to PPC of diesel-like fuels. The authors identified that the mixture stratification on equivalence ratio is mandatory for allowing proper control over the combustion phasing with the injection timing, as for assuring the ignitability of the cylinder charge.

Further research in heavy-duty and light-duty 4-stroke diesel engines operating with PPC concept using gasoline-like fuels and ethanol performed respectively by Wisconsin-Madison University [14], Lund University [10, 16, 21-23, 34] and more recently by Delphi Corporation [31-33], confirmed the possibility to implement the PPC concept with very high efficiency, very low NO_X emissions and low soot levels in a wide load operating range. However, the octane number is closely linked to the load range since the fuel ignition properties should be optimized to the given operating condition [15].

Focusing on the 2-stroke HSDI CI engine configuration under development, the potential of the early-injection Homogeneous Charge Compression Ignition (HCCI) concept using diesel fuel for reducing simultaneously NO_X and soot emissions at low load conditions was experimentally proven [5]. However, the high reactivity of diesel fuel added to the high residual gas fraction (IGR) characteristic of the scavenge loop architecture, made it impossible to attain a properly-phased combustion even operating at low loads with optimized engine settings and hardware, so this combustion concept was discarded [6]. Nevertheless, the high flexibility in terms of air management settings to control the cylinder conditions and affect final combustion environment, also observed operating with CDC concept [7], encouraged the authors to explore the potential of the PPC concept for pollutant control using a high octane fuel (RON95 gasoline) with a single injection strategy at medium-to-low load conditions. The compatibility of this concept with the 2-stroke configuration in terms of assuring precise control of the onset of combustion and stable PPC operation at low loads was demonstrated [8].

Recent research work extended the PPC operation to 5 bar and 3 bar of IMEP, when using a single injection strategy with RON95 gasoline. Low NO_X emissions (below 0.4 g/kWh) and zero soot emissions were obtained at these medium/low load conditions, while 98% of combustion efficiency and good combustion stability (covariance of the IMEP under 3%) was retained. However, at higher load (10 bar of IMEP) a transition between premixed and mixing-controlled combustion was observed depending on the particular in-cylinder conditions, and the conventional trade-off between NO_X and soot emissions was recovered [9].

Thus, present investigation evaluates the strengths and limitations of the 2-stroke poppet valves CI engine under development operating with the CDC concept using diesel fuel and also with the PPC concept using RON95 gasoline. This study was carried out at medium-to-high load (10.4 bar of IMEP) and medium speed (1500 rpm) operating conditions and it includes a detailed analysis of air management and combustion processes together with the exhaust emissions and engine efficiency levels. A design of experiments methodology was used to define the optimum air management conditions operating in CDC, and the available statistical models were used to predefine proper cylinder conditions to assure stable and safe PPC operation. With the aid of CFD calculations, a triple injection strategy was finally selected for improving results operating with PPC, and parametric studies of the injection timing were experimentally carried out to evaluate the performance of the PPC concept.

2. Experimental setup

2.1 Engine architecture and hardware

Experimental activities were performed in the single-cylinder research version of an innovative Renault engine concept consisting of a 2-cylinder 2-stroke HSDI CI engine with scavenge loop, which is currently under development. Table 1 contains the main engine characteristics.

Table 1. Main engine specifications

Engine type	2-stroke compression ignition
Displacement	365 cm^3 (single-cylinder version)
Bore × Stroke	76 mm × 80.5 mm
Connecting Rod Length	133.75 mm
Compression ratio	17.6:1 (effective CR from 13:1 to 8.8:1)
Number of Valves	4 (2 intake & 2 exhaust)
Type of scavenge	Poppet valves with scavenge loop
Valvetrain	Double overhead camshaft with VVT
Nominal intake valve timing (set at VVT=0)	IVO=161.9 cad aTDC IVC=251.6 cad aTDC
Nominal exhaust valve timing (set at VVT=0)	EVO=122.6 cad aTDC EVC=226.9 cad aTDC

The cylinder head, shown in Fig. 1, has four poppet valves with double-overhead camshafts and a staggered roof geometry, specifically designed for baffling the flow of air between the intake and exhaust valves, allowing proper scavenging of the burnt gases while keeping short-circuit losses as low as possible during 2-stroke operation. A hydraulic cam-driven Variable Valve Timing system allows delaying intake and exhaust valve timings with a cam phasing authority of +30 degrees from base timing. Then, the effective compression ratio, effective expansion ratio and overlap period between intake and exhaust, can be modified by adjusting the valve timing angles as desired, providing great flexibility to substantially modify air management characteristics. In this research, the key valve timing angles (EVO/EVC/IVO/IVC) were defined at 0.3 mm of valve lift. The definition of the engine architecture, boost system requirements, combustion chamber geometry and scavenging characteristics of this newly designed engine were reported by the authors in previous publications [30, 36].

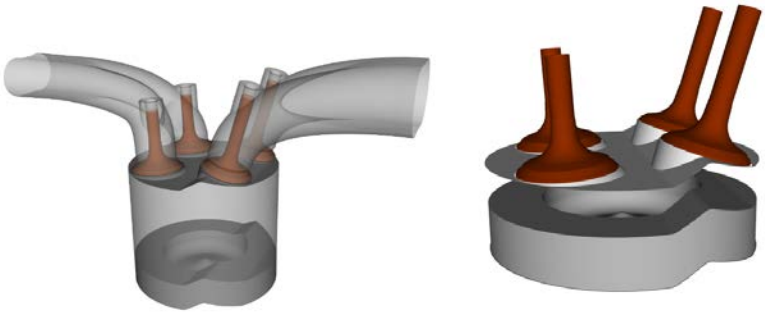

Fig. 1. Sketch of the cylinder head designed for the 2-stroke engine architecture (Patent Renault FR2931880)

A conventional piston bowl geometry optimized for diesel combustion was selected for the studies presented in this research, providing a geometric compression ratio of 17.6. Additionally, an optimized 8 hole injection nozzle with 90µm of hole diameter and 155º included spray angle, was used during the tests performed in CDC; while a different nozzle with same flow rate (# holes and diameter) but slightly lower included angle (148º) was selected for testing the PPC concept. The injection system is a Delphi common rail prototype designed for injecting diesel fuel up to a maximum rail pressure of 1800 bar. Since the injector configuration was fully optimized for CDC concept, a future detailed optimization of the injector operating with the PPC concept is expected to provide a better nozzle configuration in terms of number of holes, holes diameter and/or spray included angle.

Mass flow rate and spray momentum flux were measured in a dedicated test rig [28, 29] for the selected injection hardware at analogous test conditions using diesel and gasoline. The injection characteristics are required to be used as inputs of the detailed CFD calculations and also for the combustion analysis from the experimental information.

The injection system main characteristics, as well as the most important fuel properties are detailed in Table 1 for the tests performed with CDC and PPC concepts.

Table 2. Injection system characteristics and most relevant fuel properties

	CDC tests (diesel fuel)	**PPC tests (gasoline fuel)**
Injection System	Delphi DFI1.5 Common rail HSDI system	
Injector nozzle	155º AN, 8 holes, 90 µm	148º AN, 8 holes, 90 µm
Maximum allowed Injection Pressure	1800 bar	1100 bar
Test fuel	Regular fuel pump Diesel	Unleaded gasoline with lubricity additive
Cetane Number	46.6	-
Research Octane Number	-	94.6
H/C ratio	2.06 mol/mol	1.76 mol/mol
O/C ratio	0 mol/mol	0 mol/mol
Oxygen content	<0.5 % (m/m)	<0.17 % (m/m)
Stoichiometric air/fuel ratio (by mass)	14.802	14.37
LHV	42.124 MJ/kg	42.82 MJ/kg
Density (15ºC)	843.3 kg/m^3	758.1 kg/m^3
Kinematic viscosity (40ºC)	2.46 cSt	0.44 cSt

2.2 Test cell characteristics

The research single-cylinder engine is assembled into a fully instrumented test cell, equipped with independent water and oil cooling circuits, an external compressor unit for providing compressed air (oil and water-free) and simulate the required boosted conditions, and an additional low pressure EGR system to provide arbitrary levels of cooled EGR even at very high intake pressures. In the 2-stroke configuration with scavenge loop a positive pressure drop between the intake and exhaust ports, denoted as ΔP, is mandatory over the complete range of engine speeds to allow the proper scavenging of the burnt gases and minimize the rate of internal gas recirculation (burnt gases which are not expelled out of the cylinder after the exhaust event). Therefore, the exhaust backpressure is adjusted by a throttle valve after the exhaust settling chamber, allowing precise control of the ΔP across the engine.

Data of O_2, CO, CO_2, HC, NO_X, N_2O and EGR rate is measured with a state-of-the-art HORIBA gas analyzer. Smoke emissions, in filter smoke number (FSN) units, are measured by an AVL 415 Smokemeter. Additionally, a tracer gas method (using methane as a tracer gas) was implemented to experimentally measure the trapping efficiency (or trapping ratio) in each engine test, which is defined as the mass of delivered charge that has been trapped in the cylinder before combustion divided by the mass of delivered charge supplied to the cylinder (fresh air plus EGR). The internal gas recirculation (IGR) ratio is then defined as the fraction of residual gases retained from the previous combustion cycle in the total trapped mass in the cylinder. The IGR ratio and total trapped mass are estimated in each engine test by simplified thermodynamic calculations.

Instantaneous high frequency signals such as cylinder pressure (Pcyl), pressures at the intake and exhaust ports, rail pressure and energizing current of the injector, among others, are sampled with a resolution of 0.2 cad. Cylinder pressure is measured using a piezoelectric sensor, while a different piezorresistive pressure sensor is placed at the cylinder liner close to the BDC to reference the piezoelectric sensor signal. The most important global combustion parameters like indicated mean effective pressure (IMEP), maximum cylinder pressure (P_{max}), pressure gradient (dP/da), combustion noise, combustion phasing angles and heat release rate (RoHR); as well as the initial thermodynamic conditions and wall temperatures required for performing the setup of the CFD model, are calculated from the cylinder pressure signal by means of in-house combustion analysis software ("CALMEC") [20, 26].

2.3 CFD Model setup

The computational model was built in the CONVERGE CFD platform. Full coupled open and closed cycle computations using the full intake/exhaust and cylinder geometries were carried out since the combustion chamber is non-symmetric. The computational domain at the intake valve closing (IVC) angle is shown in the left plot from Fig. 1. The CFD code uses a structured Cartesian grid with base cell size of 3 mm. Three additional grid refinements linked to flow velocity and temperature were performed by means of an adaptive mesh refinement (AMR) as well as a fixed three level refinement within the spray region.

The injection rate profile was generated from the experimental database available after the injector characterization (mass flow rate and spray momentum flux) performed in dedicated test rigs. The diesel-like injection of gasoline is simulated by the standard Droplet Discrete Model. Gasoline fuel physical properties are defined using iso-octane as surrogate. Spray atomization and break-up are simulated by means of the KH-RT model. Turbulent flow is modeled by means of the RNG k-ε model with wall-functions in order to account for wall heat transfer. Concerning combustion modeling, a direct integration of detailed chemistry approach was used by means of the CONVERGE code and the SAGE solver. Finally, the chemical mechanism of a PRF blend of n-heptane (5%) and iso-octane (95%) has been used in as fuel surrogate after calibrating their respective mass fractions to reproduce the ignition characteristic of the RON95 gasoline.

The setup and validation of the CFD model was performed at the reference case operating with the PPC concept and the three injection strategy. The quality of the model was evaluated by comparing its combustion and emissions results with those obtained experimentally in the engine. Fig. 2 compares the CFD and experimental cylinder pressure and RoHR profiles, including also the data related to exhaust emissions. The CFD model performance is considered as suitable for being used along the evaluation of the potential of the PPC concept.

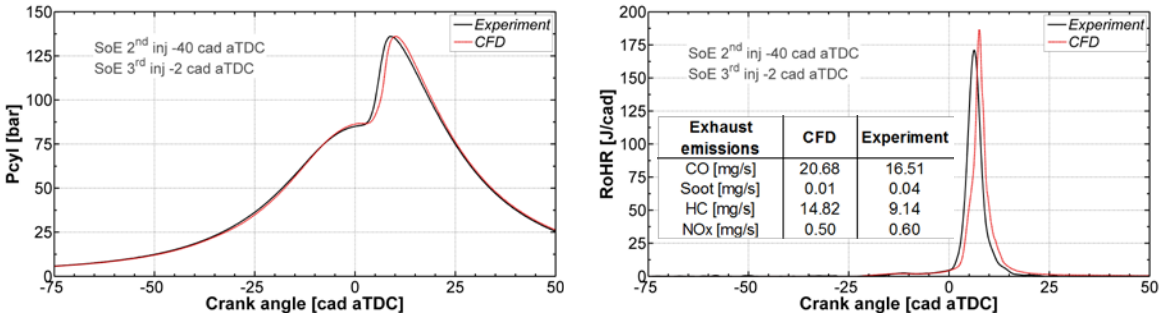

Fig. 2. CFD model validation at the reference point operating with gasoline PPC concept

3. Methodology

The engine operating condition selected for this investigation corresponds with a medium speed (1500 rpm) and medium-to-high load (10.4 bar of IMEP) operating point, and the most relevant experimental conditions as well as the expected targets in terms of exhaust emissions and noise are described in Table 3. The pollutant emissions and noise limits imposed along this initial evaluation of the engine concept corresponds to the Euro 5 levels measured on the equivalent 4-stroke engine in terms of unitary displacement and geometry.

Table 3. Experimental test conditions and emissions and noise limits

Engine speed	1500 rpm
IMEP	10.4 bar
Intake air temperature	35ºC
Coolant and oil temperature	90ºC
NO_X limit (without/with NO_X after-treatment)	2.15 mg/s / 10.75 mg/s
HC limit	0.65 mg/s
CO limit	18.65 mg/s
Smoke limit (with DPF)	4.6 FSN
Noise limit	88.3 dB

In order to evaluate the performance of this innovative 2-stroke HSDI CI engine with poppet valves configuration in a strictly controlled test environment, it was necessary to define a fast and efficient experimental methodology, which was based on isolating the optimization of the air management parameters from that of the injection parameters. Based on this objective, for the analysis and optimization in CDC, a dedicated Design of Experiments (DoE) technique (Central Composite Design) was selected for easily identifying cause/effect relations of air management parameters on the cylinder conditions, and consequently on combustion process and exhaust emissions. This methodology based on a design of experiments optimization was applied in CDC in two stages. In a first stage, focusing on finding the most suitable cylinder conditions to fulfill the emission limits, especially in terms of NO_X and soot, while keeping low fuel consumption. In a second stage, focusing on further improving engine efficiency (lowest possible fuel consumption) assuming the use of a NO_X after-treatment device (SCR or NO_X trap), and therefore, relaxing the NO_X emissions limits. The main air management settings selected as factors for the air management DoE are the EGR rate, intake pressure, pressure difference between intake and exhaust (ΔP) and valve overlap duration or intake/exhaust valve timing. The tests were performed keeping a constant injection pressure of 1000 bar and with 2 injection events, one small pilot injection of 2.2 mg/st placed at -19 cad aTDC, and a main injection, for which the injected quantity and timing (SoE 2^{nd}) are adjusted to maintain a constant value of IMEP of 10.4 bar and a CA50 phased at 6.8 cad aTDC. The ranges of variation for the air management settings included as factors in the DoE, as well as the main injection settings are included in Table 4.

Table 4. Main engine settings and their ranges of variation for the DoE optimization performed in conventional diesel combustion conditions. a) DoE fulfilling NO_X limit, b) DoE assuming relaxed NO_X limit.

EGR [%]	P_{int} [bar]	ΔP [bar]	Overlap [cad]	VVT(int,exh) [cad]	P_{rail} [bar]	SoE 1^{st} [cad]	SoE 2^{nd} [cad]*	Fuel ratio [%]
a) DoE performed to fulfill NO_X emissions limit								
Min: 15 Max: 25	**Min: 2.4 Max: 2.6**	**Min: 0.5 Max: 0.7**	**Min: 70 Max: 80**	Min: (13, 18) Max: (13, 28)	1000	-21	-7*	10/90
b) DoE performed assuming relaxed NO_X limit								
Min: 0 Max: 20	**Min: 2.4 Max: 2.6**	**Min: 0.45 Max: 0.85**	73.4	**Min: (0,10) Max: (20,30)**	1000	-21	-7*	10/90

For evaluating the potential of the PPC concept with triple injection strategy using gasoline fuel, preliminary air management settings were selected using the mathematical models of the responses obtained with the DoE, in order to find the condition with the highest air trapped mass which allowed introducing the required high EGR rates needed to achieve proper PPC operation with low NO_X and soot emissions, good combustion stability and high efficiency, while simultaneously avoiding operating close to knocking-like combustion conditions. Regarding the three injection strategy selected for PPC operation, first, the range of injection timing was pre-defined with the CFD model by performing parametric studies of the injection timing for each of the three injections; and afterwards, the main trends observed in the calculations were validated with parametric variations of the injection event directly in the engine. The most relevant engine settings chosen for each study is detailed in Table 5.

Table 5. Main engine settings selected for the parametric optimization of the injection timing performed in gasoline PPC conditions. a) SoE swept of 2nd injection, b) SoE swept of 3rd injection

EGR [%]	P_{int} [bar]	ΔP [bar]	Overlap [cad]	VVT(int,exh) [cad]	P_{rail} [bar]	SoE 1st [cad]	SoE 2nd [cad]	SoE 3rd [cad]	Fuel ratio [%]
a) SoE swept of 2nd injection									
43.5	2.75	0.71	78.4	(5,20)	850	**Ref: -60**	**Min: -42 Max: -34**	**Ref: -2**	20/64/16
b) SoE swept of 3rd injection									
43.5	2.75	0.71	78.4	(5,20)	850	**Ref: -60**	**Ref: -40**	**Min: -8 Max: +2**	20/64/16

Finally, the optimum point in CDC fulfilling NO_X and soot targets, the optimum point in CDC with relaxed NO_X limit and the optimum point found in gasoline PPC operation; were selected to be compared in detail. Then, the benefits and limitations of CDC and gasoline PPC concepts will be described to evaluate the compatibility of these concepts with the proposed 2-stroke engine architecture.

4. Results & Discussion

4.1 Analysis of the Conventional Diesel Combustion (CDC) concept

This analysis will be focused on the first DoE performed in CDC, denoted as "a)" in Table 4, designed to fulfil the emissions targets. The DoE methodology allows using statistical models of the responses not only for providing guidelines for optimization, but also for understanding the physical phenomena and existing relations between air management and combustion conditions which then will determine exhaust emissions and engine efficiency. The proposed methodology for optimizing air management conditions in the 2-stroke engine under study has been described in detail in a previous investigation performed at a different engine operating condition corresponding to a low load (5.5 bar of IMEP) and medium speed (1500 rpm) point [7].

Table 6 shows the most important statistic quality indicators to check the fit of the quadratic mathematical model for most important measured or calculated responses. The regression coefficient is very close to 1 ("perfect fit") in most of the responses directly measured on the engine, while it slightly decreases (still being acceptable) for the post-processed parameters. Concerning fuel consumption, it was more difficult to assure a perfect fit since the measured range of variation was quite small, around 5%, with some small dispersion of less than 1% on the measured central points of the DoE, but the fit quality was considered as acceptable for further analysis.

Fig. 3 shows the relation between trapping ratio and delivered charge mass (fresh air plus EGR) with the two most influential inputs (ΔP and overlap) and also with two key air management parameters (the total mass trapped in the cylinder ($Q_{tot\ trapped}$) and the in-cylinder effective equivalence ratio (ϕ_{eff})). According to this figure, increasing ΔP results in higher Q_{del} levels at the expenses of decreasing trapping ratio by the unavoidably increment of in short-circuit losses due to the cylinder flow path generated by the masking surface. Keeping suitable trapping ratio levels demands to decrease valve overlap, since it directly controls the short-circuited mass flowing from the intake to the exhaust. Intake pressure has slight effects on trapping ratio, but much lower than those of ΔP and valve overlap, while the EGR rate has a very small effect on trapping ratio as expected.

Concerning the IGR ratio, previous studies showed how decreasing trapping efficiency improved the scavenging of burnt gases out of the cylinder, until reaching a practical lower limit, from which decreasing IGR furthermore was not possible [36]. In the present research, the ranges for the air management parameters were pre-selected in advance to assure the lowest percentage of IGR ratio. Within these ranges, the IGR ratio remained approximately constant for all the measured points at levels of around 26 to 27%.

Table 6. Statistical analysis of measured & estimated responses

Measured & estimated responses	R^2 [-]	RMSE	PRESS RMSE
Trapping ratio [%]	0.993	0.0033	0.0041
Delivered air flow (fresh air + EGR) [kg/h]	0.997	0.166	0.2
Effective In-cylinder equivalence ratio [-]	0.948	0.0066	0.0077
Oxygen concentration at IVC [%]	0.976	0.00064	0.00066
NO_X emissions [mg/s]	0.990	0.097	0.114
Soot emissions [FSN]	0.964	0.133	0.173
Indicated specific fuel consumption [g/kWh]	0.966	0.394	0.562
Corrected indicated specific fuel consumption [g/kWh]	0.947	0.898	1.131

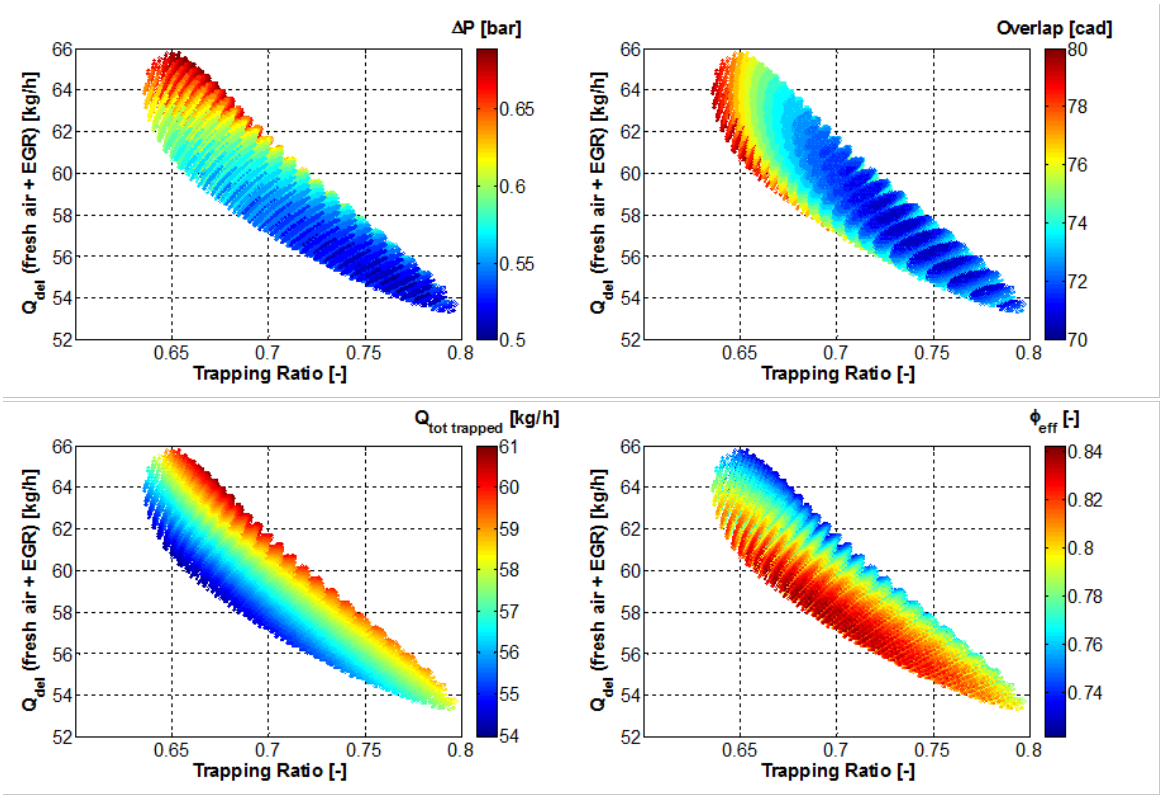

Fig. 3. Air management characteristics. a) Δp, b) Overlap, c) total mass trapped and d) effective in-cylinder equivalence ratio as function of delivered flow and trapping ratio

The best combination between trapping ratio and Q_{del} providing the highest $Q_{tot\ trapped}$ is attained with trapping ratio ranging between 66%-68% and Q_{del} around 63-65 kg/h, which corresponds to relatively high ΔP and medium to low values of valve overlap as observed in Fig. 3.c. Accordingly, Fig. 3.d confirms how the zone with the highest $Q_{tot\ trapped}$, and therefore higher fresh air mass trapped, corresponds to the zone with the lowest values for ϕ_{eff} calculated from the fuel stoichiometric air/fuel ratio, the injected fuel quantity and the usable air available in the trapped charge.

Regarding the combustion process, on the 2-stroke poppet valves architecture it is highly sensitive to the cylinder conditions and then to the air management settings. Thus, the maximum cylinder pressure ranges from 105 bar to 115 bar, and it is phased around 8.4 to 9.6 cad aTDC. This maximum cylinder pressure is determined by $Q_{tot\ trapped}$ and by the cylinder absolute pressure at the IVC, which is controlled by the scavenging process and basically by the valve overlap. The maximum pressure gradient ranges from 3.9 to 4.7 bar/cad, the combustion noise ranges from 86 to 88 dB (below the limit in all cases) and combustion stability traced by the coefficient of variation of IMEP (Cov IMEP) remains below 1.2% in all cases, which are conventional levels operating with the CDC concept.

From previous discussion, it is evident how the understanding of the relations between the cylinder conditions and the main combustion-related parameters, which are directly linked with the final level of NO_X and soot emissions, is critical in this 2-stroke engine configuration. The maximum adia-

batic flame temperature (T_{ad} max) is a suitable tracer on the formation of nitrogen oxides since the thermal mechanisms involved in NO_X formation are chemically controlled and then determined by combustion temperature and oxygen availability at the flame periphery [12, 19]. Furthermore, the late diffusive stage of combustion, between EoI and EoC, is critical for defining the final soot emissions level since the soot oxidation process is substantially slowed down due to the fast decrease of cylinder gas temperature and density. It is known how the soot formed inside the flame is oxidized outside the flame around the stoichiometric zone, by the attack of OH-radicals which are thought to be the major mechanism responsible for soot oxidation in near stoichiometric conditions as in the case of diffusion flames [11].

Increasing local temperatures at the late stages of combustion and assuring the presence of oxygen is mandatory to increase the rate of formation of OH-radicals and enhance the soot oxidation chemical process [3, 35]. Different authors have used the adiabatic flame temperature at final stages of combustion to describe the late soot oxidation process [2, 4, 27], therefore, the adiabatic temperature calculated at the time where 80% of the fuel has been burnt (T_{ad} 80%MBF) was considered representative of the late soot oxidation temperature.

Fig. 4 illustrates the intrinsic relations between the key cylinder conditions, the combustion parameters and the NOx and Smoke emission levels. Fig. 4.a clearly shows how decreasing YO_2 IVC by increasing EGR rate or by decreasing ΔP and overlap will decrease T_{ad} max, and consequently NO_X formation, due to the dilution effect of the inert exhaust gas inside the combustion chamber. However, as a counterpart, the reduction in fresh air trapped mass will increase ϕ_{eff}. Additionally, the reduction of T_{ad} max by decreasing YO_2 IVC directly leads to an equivalent reduction in T_{ad} 80%MBF, so soot oxidation is worsened as reflected by the increment in smoke emissions observed in Fig. 4.b.

It is worth to remark that soot oxidation is also controlled by other parameters besides the temperature at the final stages of combustion. Previous investigations have shown how the spray mixing capacity is proportional to the square root of the product between density and oxygen concentration, if the injection velocity and fuel properties are kept constant [1, 3]. Thus, the mixing capacity calculated at 80% of the MBF (ACT^{-1} 80%MBF), which is crucial for the late soot oxidation process, has been used to trace the spray mixing conditions during the late diffusive combustion stage.

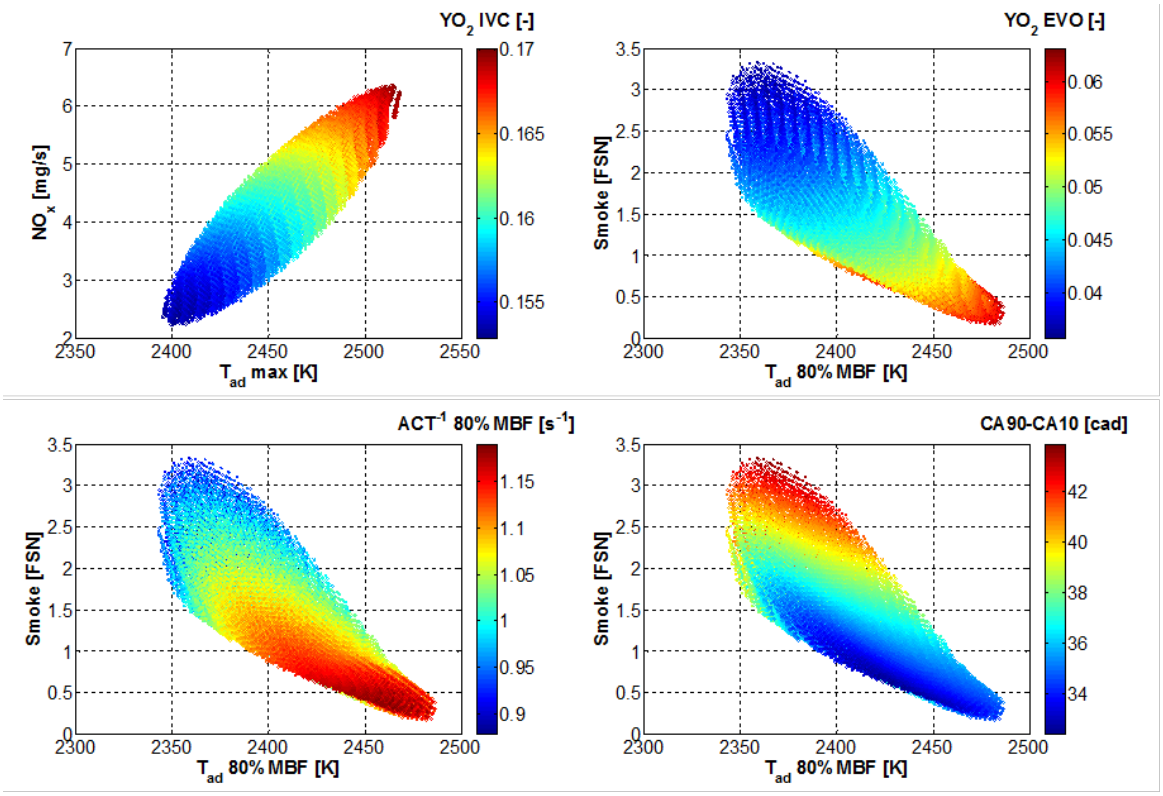

Fig. 4. Combustion characteristics. a) NO_X as function of T_{ad} max and YO_2 IVC, b) smoke as function of T_{ad} 80%MBF and YO_2 EVO, c) smoke as function of T_{ad} 80%MBF and ACT^{-1} 80%MBF, d) smoke as function of T_{ad} 80%MBF and CA90-CA10

Fig. 4.c shows how both YO_2 EVO and ACT^{-1} 80%MBF are the key parameters controlling soot oxidation, as reflected in lower smoke emissions in the points with higher fresh air mass trapped (higher YO_2 then lower ϕ_{eff}) and improved mixing conditions. It is worth to recall that the mixing capacity will account for the effects of both YO_2 and gas density, therefore the mixing rate will increase with higher total trapped mass, and also when combustion ends earlier in the cycle (represented with the combustion duration CA90-CA10), so the final stage of combustion occurs at enhanced cylinder conditions, as confirmed by Fig. 4.d.

Finally, the smoke-NO_X trade-off will be used for defining the range of variation of the most important emissions along the points of the DoE, and for linking the final emissions levels to the engine fuel consumption. As previously observed in Fig. 4, NO_X emissions ranges from 6.5 mg/s to 2.2 mg/s along the points of the DoE and smoke level ranges from 0.15 FSN to 3.18 FSN; while the optimization targets established were 2.15 mg/s and 4.6 FNS respectively. CO emissions sharply increases (up to 22 mg/s) above the required target (18.65 mg/s) when NO_X emissions decreases, following the same trend as soot emissions; while HC emissions are slightly above the target (0.65 mg/s) in most of the points, as shown respectively in Fig. 5.a and Fig. 5.b.

In terms of engine performance, Fig. 5.c illustrates how the indicated fuel consumption is closely related with the emissions levels and therefore with the combustion performance. The points with medium-to-high T_{ad} max and enhanced mixing process have low smoke emissions, medium-to-high NO_X levels and low ISFC, mainly because combustion takes place in a favorable environment for the fuel-energy conversion processes, where the fresh air trapped mass and YO_2 IVC are high and consequently ϕ_{eff} is low. Keeping these cylinder and combustion conditions, it is possible to find the best compromise between NO_X, soot and ISFC; which in Fig. 5.c would correspond to the points with 0.75 FSN of smoke, 3.8 mg/s of NO_X and 190 g/kWh of ISFC. However, Fig. 4.a shows how reducing furthermore YO_2 IVC to decrease T_{ad} max below 2400 K is mandatory to push NO_X emissions below the 2.2 mg/s limit, but both smoke emissions and ISFC increase up to 3 FSN and 200 g/kWh respectively.

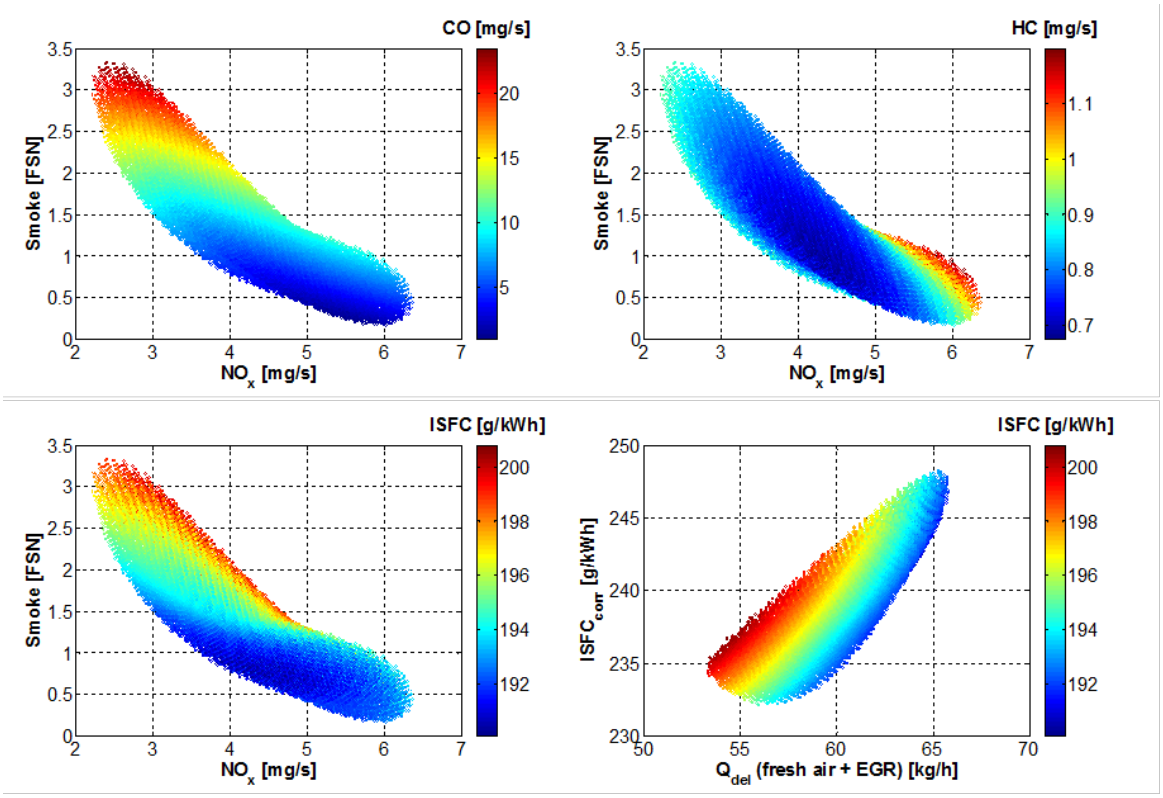

Fig. 5. Exhaust emissions and performance. Smoke as function of NO_X and a) CO emissions, b) HC emissions and c) ISFC and d) $ISFC_{corr}$ as function of delivered flow and ISFC

Since the two cylinder engine concept presents a double stage supercharging system, with a mechanical volumetric charger set downstream to a WG turbocharger [30, 36], the ISFC has been corrected ($ISFC_{corr}$) in order to account for the compression work demanded by the air charging devices to achieve the required intake conditions. This correction is useful for estimating qualitatively the increase in BSFC expected at the two cylinder engine with fully assembled air charging system, and to avoid conditions which are not feasible in the two cylinder engine due to very high pressure ratios or extremely high air flow rates.

Fig. 5.d illustrates how increasing Q_{del}, mostly by decreasing trapping ratio, causes a sharp increment in $ISFC_{corr}$ despite the almost constant ISFC level. In this case, the additional Q_{del} increases the power demanded by the air management devices, but it is not really used to improve the combustion process and then since most of the flow is directly bypassed. As a result $ISFC_{corr}$ increases because the negligible benefits in ISFC do not compensate the increase in power demanded by the air charging devices, especially by the mechanical supercharger. Therefore, decreasing $ISFC_{corr}$ demands a good combination of initially medium-to-low ISFC with also medium-to-low Q_{del} to avoid too high power demands of the air management devices. Consequently, the global efficiency of this 2-stroke engine configuration is extremely sensitive to the performance of the turbocharger and supercharger devices, and this should be carefully considered in further stages of development.

This described methodology has been used to analyze the two DoE performed operating with the CDC concept. The first DoE (already discussed) was designed to fulfill the NO_X limit, while the second DoE was designed relaxing the NO_X limit (assuming a SCR or deNO_X after-treatment device) and with slightly different ranges and restrictions for the air management inputs defined with the aim of decreasing fuel consumption as much as possible.

The mathematical models of the responses generated by both DoE were also used to select optimum points in terms of air management settings, which comply with the required restrictions in terms of exhaust emissions and fuel consumption. These optimum points were experimentally tested in the engine and results will be discussed in detail in the section 4.3.

4.2 Analysis of Partially Premixed Combustion (PPC) using gasoline fuel

The air management settings selected with the aid of the mathematical models generated by the DoE performed in CDC, previously shown in Table 5, correspond to considerably higher EGR rate (43.5%), higher intake pressure and ΔP (2.75 and 0.71 bar) and higher overlap (78.4 cad) compared to CDC. With these settings, the air management parameters correspond to 67% of trapping ratio, 67 kg/h of Q_{del}, 35% of IGR ratio, 0.83 of ϕ_{eff} and 12% of YO_2 IVC, and they were almost constant due to their weak relation with the injection settings.

For the reference point (base case) the three injection pattern included a very small 1st injection at SoE_1 -60 cad aTDC, a main 2nd injection where most of the fuel is injected at SoE_2 -40 cad aTDC, and a small 3rd injection close to TDC at SoE_3 -2 cad aTDC.

Regarding the 1st injection, CFD results confirmed how injecting here only the 10% of the total fuel quantity, the liquid fuel impingement onto the cylinder walls is avoided even using a 148º spray included angle injector and relatively high injection pressure of 850 bar. However, results also showed negligible effect of SoE_1 over the combustion onset and RoHR profiles, as well as on exhaust emissions, so 1st injection timing was finally not experimentally swept.

The effect of SoE_2 over the cylinder pressure and RoHR is shown in Fig. 6 for CFD simulations (upper plots) and experimental results (lower plots). In the case of CFD simulations, SoE_2 was swept from -34 to -52 cad aTDC, while in the case of experimental results the swept stops at SoE_2 was -42 cad aTDC due to poor combustion stability and misfiring for earlier injection timings. Both CFD and experimental results reveal how the 2nd injection controls both the combustion onset and phasing. Early SoE_2 increases ignition delay and then the mixing time available for leaning the local equivalence ratios before the start of combustion. As a result, combustion onset & phasing shift towards the expansion stroke as confirmed by CA10 and CA50, and combustion is smoother and misfire trending as shows the RoHR profile. Late SoE_2 closer to TDC decreases ignition delay and mixing time before the start of combustion, so the local equivalence ratio stratification increases enhancing the reactivity of the mixture. Then, combustion onset & phasing advance towards the TDC as also confirmed by CA10 and CA50, while combustion is faster, shorter and knock-like trending according to the RoHR profile.

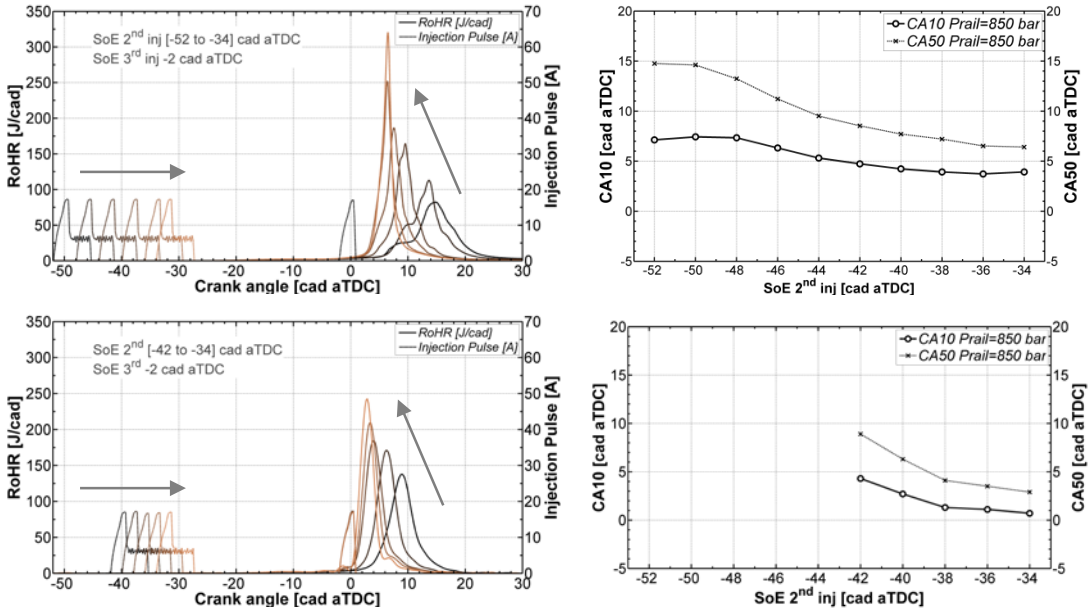

Fig. 6. Effect of SoE_2 over a) RoHR and injection pulse and b) CA10 and CA50 for CFD (upper plots) and experimental (lower plots) results

Focusing on combustion-related parameters, Fig. 7 shows how for latest SoE_2 -34 cad aTDC the maximum cylinder pressure is close 150 bar with a very high pressure gradient equal to 22 bar/cad, and noise level over 100 dB, which is caused by the close to knocking fast and short combustion phased near to TDC. For SoE_2 -42 cad aTDC the combustion is smoother, longer and shifted towards the expansion stroke, so the maximum cylinder pressure decreases to 123 bar, pressure gradient to 10 bar/cad and noise to 93 dB.

Retarding combustion phasing to the expansion stroke by advancing SoE_2 brings a consequent increase in the cycle-to-cycle dispersion which cannot be predicted by the CFD simulations, and even when not affecting Cov IMEP (which remained between 1% and 1.5%), becomes noticeable when observing the covariance of the maximum cylinder pressure in Fig. 7.d. For SoE_2 earlier than -42 cad aTDC, once the cycle-to-cycle dispersion started to increase and misfire cycles appeared, combustion process could not be sustained properly.

Local conditions were extracted from the CFD simulations in order to further understand the high sensitivity of the combustion process to SoE_2. This analysis was performed at SoE_3 to avoid undesired interferences from the 3rd injection, so the local equivalence ratios distribution generated only by the 1st and 2nd injections will be investigated in detail.

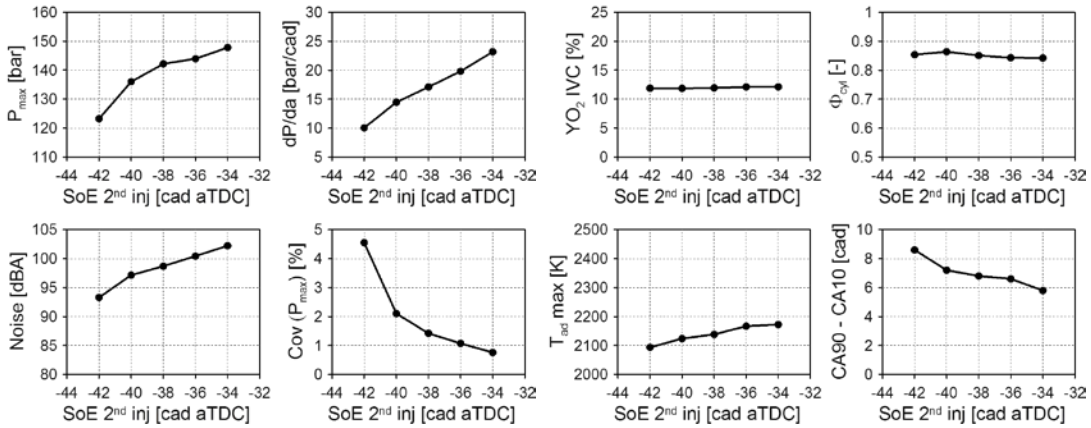

Fig. 7. Effect of SoE_2 over in-cylinder conditions and combustion characteristics for experimental results

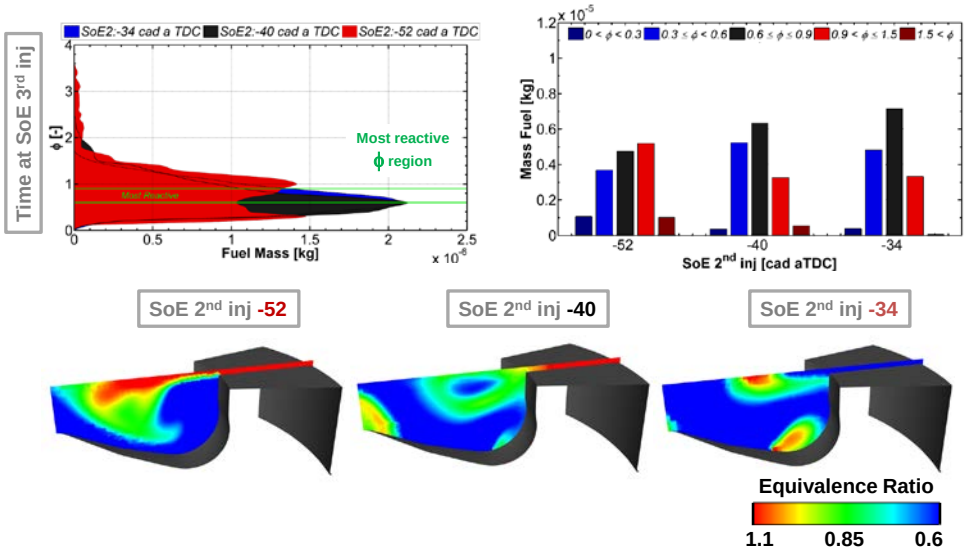

Fig. 8. Local conditions evaluated at the time just before injecting the 3rd injection. a) Equivalence ratio distribution as function of fuel mass, b) histogram of fuel mass and c) spatial equivalence ratio distribution for SoE_2 equal to -52, -40 and -34 cad aTDC

Fig. 8 shows a detailed description of the fuel mass at different local equivalence ratios (Fig. 8.a) and a summary in form of histogram (Fig. 8.b), together with the spatial distribution of the local equivalence ratios in a plane cutting the combustion chamber (Fig. 8.c). This analysis includes three different SoE_2 cases: SoE_2 -40 cad a TDC (reference), SoE_2 -34 cad aTDC (latest) and SoE_2 -52 cad aTDC (earliest). Comparing the latest SoE_2 with the reference case, both Fig. 8.a and Fig. 8.b confirm how higher fuel mass is under the most reactive equivalence ratios due to reduced mixing time and ignition delay. The higher reactivity of the mixture at the start of combustion explains why retarding SoE_2 the combustion rate increases enhancing the knocking trend, as reflected also by the higher maximum pressure gradient.

As a counterpart, advancing SoE_2 is expected to gradually shift the local equivalence ratio distribution towards leaner and then less reactive conditions due to the extended mixing times as a result of the longer ignition delays. However, according to Fig. 8.a and Fig. 8.b, for the earliest SoE_2 the fuel mass under rich equivalence ratios increases compared to the reference case, while the fuel mass under the most reactive equivalence ratio zone decreases. For the earliest SoE_2 some rich zones (ϕ over 1) are observed in the squish region in Fig. 8.c, meaning that the spray is getting split by the bowl lip, directing part of the fuel inside the bowl but also pushing fuel into the squish region where mixing conditions are worsened by the lack of air and lower wall temperature [24]. The fuel trapped in the squish region takes more time to properly mix with air so it remains in rich equivalence ratios by the moment when the 3rd injection starts, and the remaining fuel inside the bowl reaches lean equivalence ratios faster. Therefore, less fuel mass is observed at the most reactive equivalence ratios; as it was previously observed in Fig. 8.a. These CFD results explain why it is not possible to test experimentally the points with SoE_2 earlier than -42 cad aTDC due to physical limitations in the current injection hardware given by the use of a conventional wide angle nozzle optimized for diesel combustion. Nevertheless, this opens a possibility for extending the range of operation of the PPC concept in terms of 2nd injection timing by performing a dedicated optimization of the engine hardware in order to extend the window between knock and misfire extreme conditions.

Fig. 9 shows the exhaust emissions experimentally obtained sweeping SoE_2. NO_X emissions are substantially decreased (below 1 mg/s) compared with CDC in all points due to the strong reduction in combustion temperature (traced by T_{ad} max), while soot emissions are also lower than the levels observed in CDC when fulfilling the NO_X limit. It is evident how operating with the gasoline PPC concept allows avoiding the NO_X-soot trade-off by decreasing simultaneously both emissions. NO_X emissions decrease for early SoE_2 as the straight effect of the retarded and softened combustion process with lower combustion temperatures. Additionally, smoke also decreases due to the extended ignition delay and thus the mixing time available for the 3rd injection, which is the one acting as the main source of soot emissions by increasing local equivalence ratios at the onset of the combustion process. However, on the other side CO and HC emissions increase.

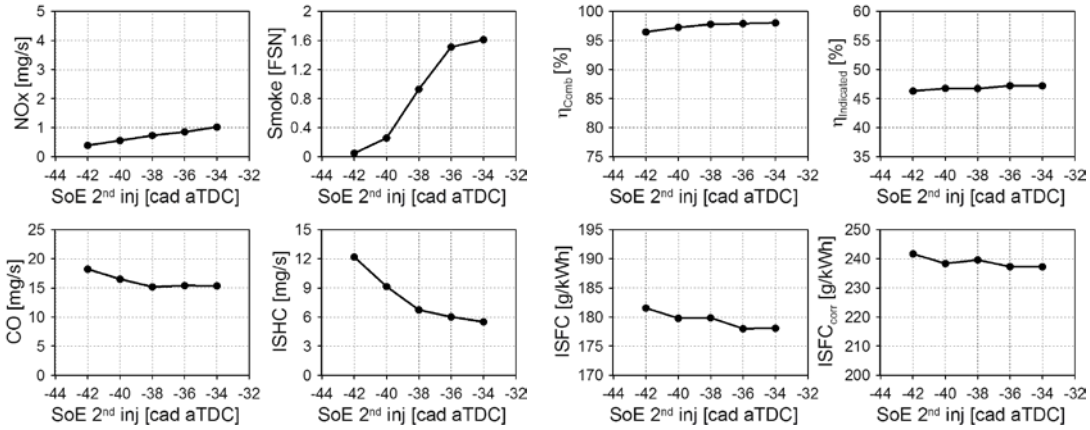

Fig. 9. Effect of SoE_2 over exhaust emissions and engine performance

Combustion efficiency is relatively lower operating in PPC than in CDC and follows the increase in CO and HC emissions, but it remains over 96%-97%, which is in the range or in some cases higher than other results reported in the literature [32]. Finally, indicated efficiency ranges between 46.5% and 47.5% corresponding to ISFC ranging between 181 to 178 g/kWh, so ISFC decreases by 5% compared to the optimum point in CDC with relaxed NO_X limit and 10% compared to the optimum point fulfilling NO_X limit. Despite the clear benefits in ISFC, $ISFC_{corr}$ ranges between 237 and 241 g/kWh and is kept at similar levels than those obtained in CDC with low NO_X limit, due to the increase in mechanical power demanded by the air management devices to achieve the highly demanding equivalence ratio and external EGR rate combinations required to operate in PPC.

The effect of SoE_3 on the cylinder pressure and RoHR profiles is shown in Fig. 10 for CFD simulations (upper plots) and experimental results (lower plots). In CFD simulations, the SoE_3 was swept from -12 to 8 cad aTDC, while in the experiments it was swept from -8 to 2 cad aTDC, being limited by the onset of knocking combustion on earlier SoE_3 and the very high soot emissions on later SoE_3. Both CFD and experimental results evidence negligible effects of SoE_3 on the start of combustion, so the onset of combustion is mainly controlled by the 2nd injection. On the contrary, the influence of SoE_3 on the development of the combustion process is important as observed in the RoHR profiles. Advancing SoE_3 increases the ignition delay and the available mixing time, allowing partial mixing of the fuel injected during this 3rd injection, so the reactivity of the global mixture at the onset of combustion increases and combustion trends to knocking conditions as indicates the fast and short RoHR profile observed in Fig. 10. On the contrary, retarding SoE_3 shortens the ignition delay and the available mixing time and, as a result, the combustion of the fuel injected in this 3rd injection shifts from a highly premixed process to a mixing-controlled process with the critical impact on emissions explained later.

The experimental results shown in Fig. 11 corroborates how the maximum cylinder pressure, the pressure gradient and combustion noise are substantially increase advancing SoE_3 up to levels close to 150 bar and over 20 bar/cad and 100 dB for the earliest SoE_3. However, the effect of retarding SoE_3 from -2 cad aTDC (reference case) on maximum pressure, pressure gradient and noise is moderate despite the longer combustion duration. Finally, $Cov(P_{max})$ levels assure suitable combustion stability independently from SoE_3 and, as in the case of the onset of combustion, the cycle-to-cycle dispersion is mostly controlled by the 2nd injection.

Local conditions were extracted from the CFD simulations in order to further understand the high sensitivity of the combustion process to SoE_3. This analysis was performed at CA10 as it is a suitable tracer of the onset of combustion, so the local equivalence ratios distribution generated by the three injections will be investigated in detail. Fig. 12 shows a detailed description of the fuel mass at different local equivalence ratios (Fig. 12.a) and a summary in form of histogram (Fig. 12.b), together with the spatial distribution of the local equivalence ratios in a plane cutting the combustion chamber (Fig. 12.c). This analysis includes three different SoE_3 cases: SoE_3 -2 cad a TDC (reference), SoE_3 -12 cad aTDC (earliest) and SoE_3 8 cad aTDC (latest). For the earliest SoE_3 the fuel mass within the most reactive equivalence ratios zone is substantially increased, explaining the higher reactivity of the charge and the faster and sharper RoHR profile trending to knock. For the reference SoE_3, the 3rd injection is being mixed so there is a clear stratification on local equivalence ratios from rich to lean values. For the latest SoE_3, the 3rd injection has not been injected yet, as seen in the RoHR shown in Fig. 10 and therefore, the local equivalence ratio distribution corresponds to the mixing conditions of only the 1st and 2nd injections.

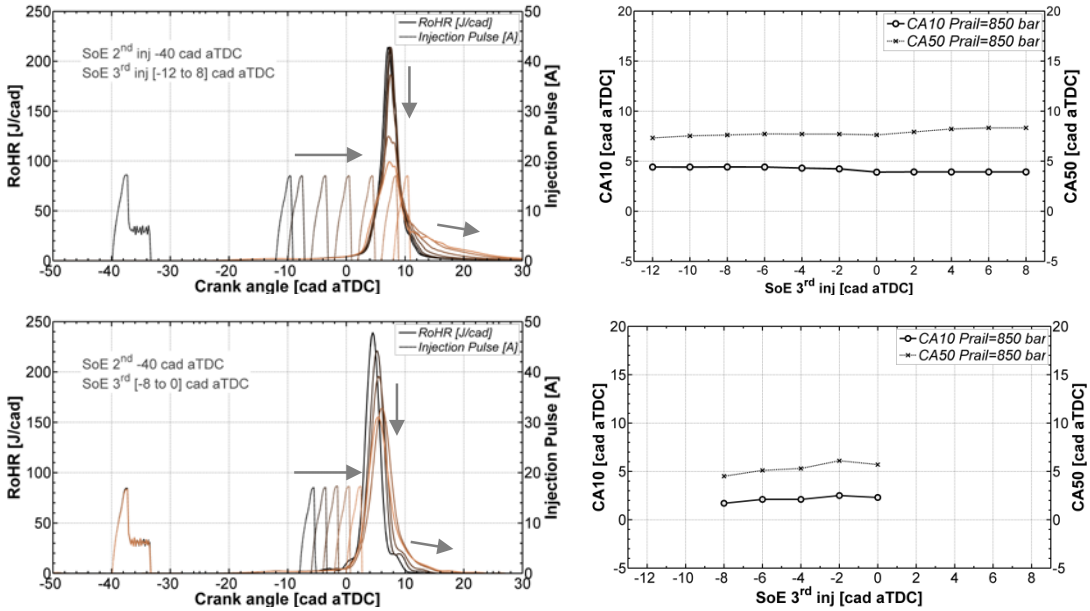

Fig. 10. Effect of SoE_3 over a) RoHR and injection pulse and b) CA10 and CA50 for CFD (upper plots) and experimental (lower plots) results

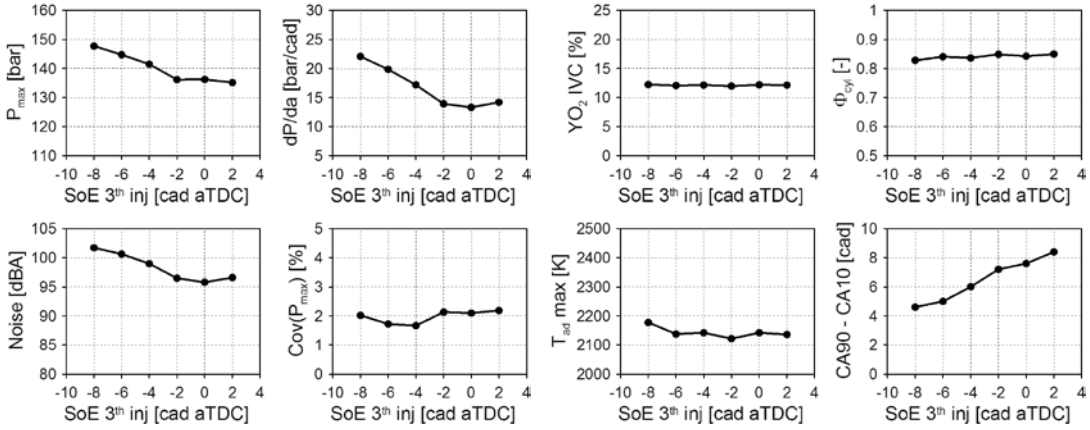

Fig. 11. Effect of SoE_3 over in-cylinder conditions and combustion characteristics for experimental results

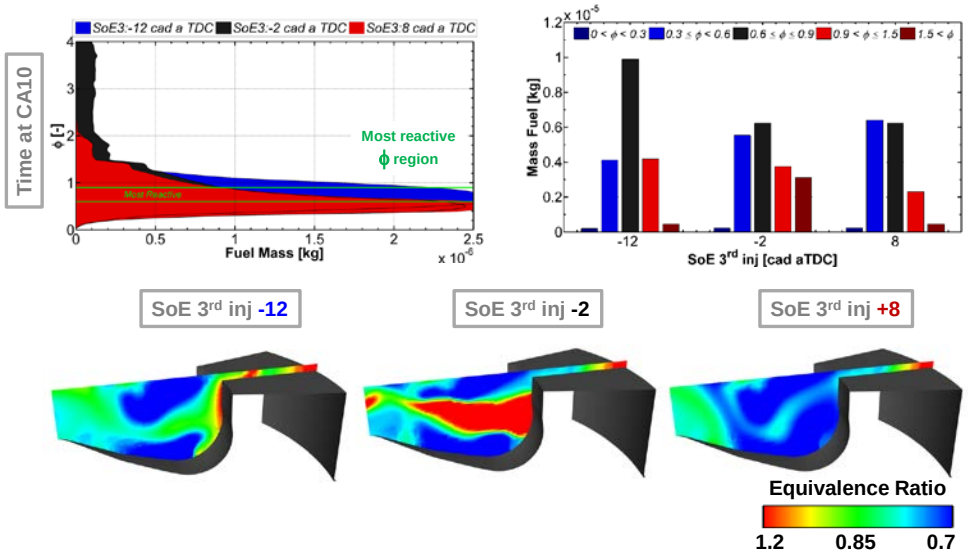

Fig. 12. Local conditions at CA10. a) Equivalence ratio distribution as function of fuel mass, b) histogram of fuel mass and c) spatial equivalence ratio distribution for SoE_3 equal to -12, -2 and 8 cad aTDC

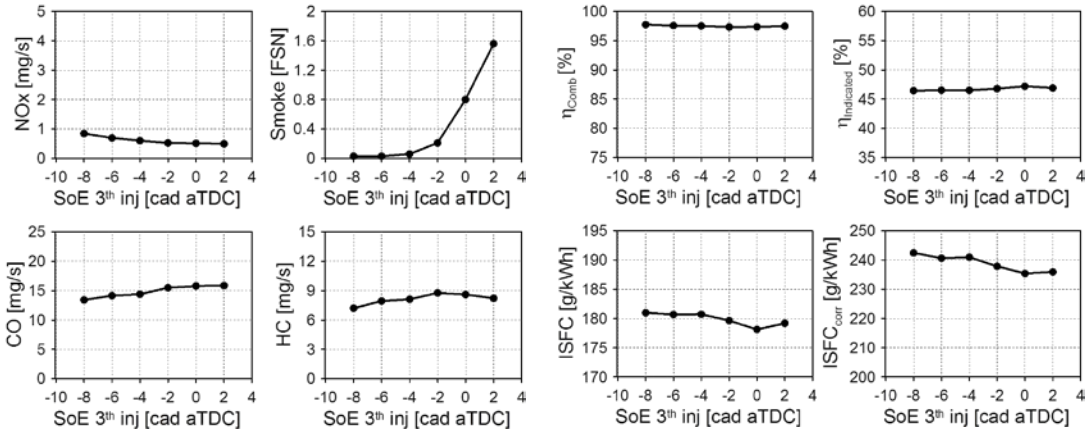

Fig. 13. Effect of SoE_3 over exhaust emissions and engine performance

In terms of exhaust emissions, Fig. 13 confirms how retarding SoE_3 decreases NO_X emissions due to the slight reduction in combustion temperature caused by the smother and longer combustion process. However, soot emissions increase due to extended mixing-controlled stage, recovering the NO_X-soot trade-off characteristic of the CDC concept. This is corroborated by the trend followed by CO emissions since they also slightly increase retarding SoE_3 as a result of worse CO oxidation into CO_2 due to the shifting of the already extended mixing-controlled combustion stage towards the expansion stroke. HC emissions remained almost constant because they are mostly influenced by the 1st and the 2nd injections. Fig. 13 shows how combustion efficiency is always higher than 97% and it is basically independent from SoE*3*, while indicated efficiency is at levels around 47% and it is neither substantially affected. Finally, ISFC slightly increases advancing SoE_3 due to the fast and short combustion close to knocking conditions, going from 178 g/kWh to 181 g/kWh and as consequence $ISFC_{corr}$ also increase from 236 g/kWh to 242 g/kWh.

4.3 Comparative analysis of CDC and gasoline PPC concepts.

The optimum point in CDC fulfilling low NO_X limit, the optimum point in CDC with relaxed NO_X limit, and the optimum point operating with gasoline PPC were selected to be compared in terms exhaust emissions and engine efficiency. Table 7 summarizes the main engine settings, air management characteristics, exhaust emissions and fuel consumption levels experimentally measured.

In the optimum fulfilling low NO_X limit the engine operates with a trapping ratio of 71.4%, Q_{del} of 59.68 kg/h, ϕ_{eff} of 0.83 and YO_2 IVC of 15.19%. The selected in-cylinder conditions allows reaching the required emissions limits, with NO_X emissions of 2.13 mg/s, smoke of 2.99 FSN and CO and HC of 13.02 mg/s and 0.36 mg/s respectively. Finally, at this point an indicated efficiency of 43.47% was obtained, which corresponds with an ISFC of 196.6 g/kWh, and $ISFC_{corr}$ of 238.75 g/kWh if the compression work demanded by the SC/TC devices is considered. Increasing NO_X limit assuming a NO_X aftertreatment device, the air management settings can be re-adjusted to favor fuel consumption at the expense of increasing NO_X emissions. The new optimum point defined presents lower EGR, slightly lower intake pressure and ΔP and slightly lower overlap. These new air management settings allowed increasing trapping ratio to 80.7%, decreasing Q_{del} to 50.7 kg/h, decreasing ϕ_{eff} to 0.71 and increase YO_2 IVC to 17.02%. These conditions give higher NO_X (6.41 mg/s), lower smoke and CO emissions (0.53 FSN and 5.09 mg/s) and slightly higher HC emissions (0.5 mg/s). However, operating with lower ϕ_{eff} and improved combustion conditions allowed increasing indicated efficiency to 45.75%, which correspond with an ISFC of 186.5 g/kWh; while $ISFC_{corr}$ is also decreased to 216.14 due to the reduction in Q_{del} by the new air management settings.

Finally, operating the engine with the PPC concept using RON95 gasoline demands increasing intake pressure, overlap and ΔP to increase Q_{del} and fresh air mass trapped, allowing increasing EGR to 43.5%. In these particular conditions trapping ratio decreases to 68% with IGR of 35%. This combination of fresh air trapped, EGR and IGR allow decreasing YO_2 IVC to 12% while keeping ϕ_{eff} at 0.85. Operating with gasoline PPC was possible decreasing simultaneously NO_X and soot emissions down to 0.5 mg/s and 0.21 FSN, while increasing indicated efficiency to 47%, which is the highest value observed so far in the engine at this load condition. Combustion efficiency keeps at relatively high levels (97.4%) and proper combustion stability is assured with a CoV IMEP of 1.6%. CO emissions in-

creases compared to CDC (15.5 mg/s), but they are kept within the established limit, and HC emissions are considerably higher (8.77 mg/s) compared to CDC probably due to poor injector nozzle matching. Combustion noise noticeably increases when operating in PPC due to the fast and short combustion process generated. Therefore, despite the clear interest of combining the 2-stroke configuration under development with the gasoline PPC concept it is evident how performing a detailed optimization of engine hardware and injection settings to widen the range of operation in terms of SoE_2 and SoE_3 is mandatory for further improving these results.

Table 7. Optimum points operating with CDC after performing the DoE air management optimization.

Optimum points measured in CDC and gasoline PPC concept	a) CDC low NO_X limit	b) CDC with relaxed NO_X	Gasoline PPC concept
EGR [%]	26	12	43.5
P_{int} [bar]	2.576	2.5	2.75
ΔP [bar]	0.55	0.45	0.71
Overlap [cad]	76	73.4	78.4
VVT(int,exh) [cad]	(+13,+24)	(+10, +20)	(+5, +20)
Trapping ratio [%]	71.4	80.7	67.9
IGR ratio [%]	26	30	35
Delivered air flow (fresh air + EGR) [kg/h]	59.68	50.7	66.0
Effective In-cylinder equivalence ratio [-]	0.83	0.71	0.85
Oxygen concentration at IVC [%]	15.19	17.02	11.98
Oxygen concentration at EVO [%]	3.90	6.23	4.01
NO_X emissions [mg/s]	2.13	6.41	0.5
Smoke emissions [FSN]	2.99	0.53	0.21
CO emissions [mg/s]	13.02	5.09	15.49
HC emissions [mg/s]	0.36	0.5	8.77
Noise [dB]	86.39	88.0	96.5
Indicated efficiency [%]	43.47	45.75	46.8
ISFC [g/kWh]	196.6	186.5	179.4
$ISFC_{corr}$ [g/kWh]	238.75	216.14	237.5

Conclusions

A detailed investigation evaluating two combustion concepts, the CDC concept using diesel fuel and the PPC concept using RON95 gasoline, was carried out in the 2-stroke poppet valves HSDI CI engine configuration under development. The most relevant conclusions after the analysis of the results are included below:

Operating with the CDC concept

- For understanding the physical processes linked to 2-stroke engines, it is recommended switching from a particular engine settings to the in-cylinder gas thermodynamic conditions, which later controls the combustion process development, final emissions level and efficiency.
- The optimum combination of trapping ratio and $Q_{tot\ trapped}$ is obtained with the highest values of ΔP but with the lowest values of valves overlap.
- Low NO_X emissions levels are attainable by reducing YO2 IVC to decrease T_{ad} max along the combustion process, either by introducing EGR or by affecting air management conditions.
- Reducing T_{ad} max by decreasing YO2 IVC leads to a consequent decrease of the temperatures along the late diffusive combustion stage (T_{ad} 80%MBF), worsening soot oxidation process resulting in higher soot emissions. Nevertheless, increasing the total trapped mass to increase in-cylinder density and enhance the mixing process helps to improve soot oxidation.
- After the optimization process, it was possible to reach the NO_X emissions limit (2.13 mg/s) keeping smoke level also below the target (2.99 FSN) and an engine efficiency of 43.47%. When relaxing the NO_X limit, assuming the use of a NO_X after-treatment device, it is possible to increase indicated efficiency to 45.75% with 0.53 FSN of smoke and 6.41 mg/s of NO_X.

Operating with the PPC concept

- CFD calculations and experimental results confirmed how the 2nd injection controls both the onset of the combustion as its phasing, whereas the 3rd injection has negligible effect over the start of combustion but controls combustion rate and duration.
- Advancing SoE_2 retards the combustion phasing and softens the combustion process decreasing maximum cylinder pressure, pressure rise rate and noise. The earliest SoE_2 is limited by the appearance of misfire cycles, which are linked to the interaction between the spray and the piston bowl, so the earliest SoE_2 is constrained by the need of avoiding directing the spray towards the squish region. The latest SoE_2 is limited by the onset of knocking combustion, which is promoted by the reduced mixing time thus higher reactivity at the start of combustion.
- The injection timing of the 3rd injection, SoE_3, mainly controls soot emissions but also determines combustion rate and duration. Advancing SoE_3 increases the available mixing time of the 3rd injection, so the excessively high equivalence ratios where soot is formed can be avoided. However, it also results in a higher fraction of the fuel in the most reactive equivalence ratios zone, which increases the trend towards knocking conditions with very fast and short combustion process.
- By properly phasing SoE_2 and SoE_3 it is possible to decrease simultaneously NO_X and soot (0.5 mg/s and 0.2 FSN respectively), while combustion efficiency is kept in 97.4% and indicated efficiency increases to 46.8%.

The final comparison between the general results provided by both combustion concepts confirms the benefits of the PPC concept in terms of NO_X and soot emissions control even improving by 5% to 10% the indicated efficiency. However, a detailed optimization of engine hardware to optimize its compatibility with this combustion concept is expected to allow even further improvements.

Acknowledgments

This research has been partially sponsored by the European Union in framework of the POWERFUL project, seventh framework program FP7/2007-2013, theme 7, sustainable surface transport, grant agreement No. SCP8-GA-2009-234032. The authors gratefully appreciate this support.

The authors want to express their gratitude to CONVERGENT SCIENCE Inc. and IGNITE3D Engineering GmbH for their kind support for performing the CFD calculations using CONVERGE software.

References

[1] Arrègle J, López JJ, García JM and Fenollosa C (2003) Development of a zero-dimensional Diesel combustion model. Part 1: Analysis of the quasi-steady diffusion combustion phase. Appl Therm Eng: vol 23: pp 1301-1317.

[2] Benajes J, Novella R, Arthozoul S and Kolodziej C (2010) Particle Size Distribution Measurements from Early to Late Injection Timing Low Temperature Combustion in a Heavy Duty Diesel Engine. SAE Technical Paper 2010-01-1121.

[3] Benajes J, Novella R, García A and Arthozoul S (2011) The role of in-cylinder gas density and oxygen concentration on late spray mixing and soot oxidation processes. Energy: vol 36: pp 1599-1611.

[4] Benajes J, García-Oliver JM, Novella R and Kolodziej C (2012) Increased particle emissions from early fuel injection timing Diesel low temperature combustion. Fuel: vol 94: pp 184-190.

[5] Benajes J, Novella R, De Lima D, Dugue V and Quechon N (2012) The potential of highly premixed combustion for pollutant control in an automotive two-stroke HSDI diesel engine. SAE Technical Paper 2012-01-1104.

[6] Benajes J, Novella R, De Lima D, Quechon N and Obernesser P (2012) Implementation of the early injection highly premixed combustion concept in a two-stroke HSDI engine. SIA Diesel Powertrain Congress 2012, France, June 5-6.

[7] Benajes J, Novella R, De Lima D, Tribotte P, Quechon N, Obernesser P, et al. (2013) Analysis of the combustion process, pollutant emissions and efficiency of an innovative 2-stroke HSDI engine designed for automotive applications. Appl Therm Eng: vol 58: pp 181-193.

[8] Benajes J, Molina S, Novella R and De Lima D (2014) Implementation of the Partially Premixed Combustion concept in a 2-stroke HSDI diesel engine fueled with gasoline. Appl Energy: vol 122: pp 94-111.

[9] Benajes J, Novella R, Martín J and De Lima D (2014) Analysis of the Load Effect on the Partially Premixed Combustion Concept in a 2-Stroke HSDI Diesel Engine Fueled with Conventional Gasoline. SAE Technical Paper 2014-01-1291.

[10] Borgqvist P, Tunestal P and Johansson B (2012) Gasoline Partially Premixed Combustion in a Light Duty Engine at Low Load and Idle Operating Conditions. SAE Technical Paper 2012-01-0687.
[11] Dec JE (1997) A Conceptual Model of DI Diesel Combustion Based on Laser-Sheet Imaging. SAE Technical Paper 970873.
[12] Dec JE and Canaan RE (1998) PLIF Imaging of NO Formation in a DI Diesel Engine. SAE Technical Paper 980147.
[13] Flynn PF, Durrett RP, Hunter GL, Zur Loye AO, Akinyemi OC, Dec JE, et al. (1999) Diesel combustion: An integrated view combining laser diagnostics, chemical kinetics, and empirical validation. SAE Technical Paper 1999-01-0509.
[14] Hanson R, Splitter D and Reitz R (2009) Operating a Heavy-Duty Direct-Injection Compression-Ignition Engine with Gasoline for Low Emissions. SAE Technical Paper 2009-01-1442.
[15] Hildingsson L, Kalghatgi G, Tait N, Johansson B and Harrison A (2009) Fuel Octane Effects in the Partially Premixed Combustion Regime in Compression Ignition Engines. SAE Technical Paper 2009-01-2648.
[16] Kaiadi M, Johansson B, Lundgren M and Gaynor JA (2013) Sensitivity Analysis Study on Ethanol Partially Premixed Combustion. SAE Int J Engines: vol 6: pp.
[17] Kalghatgi G, Risberg P and Ångström H (2007) Partially Pre-Mixed Auto-Ignition of Gasoline to Attain Low Smoke and Low NOx at High Load in a Compression Ignition Engine and Comparison with a Diesel Fuel. SAE Technical Paper 2007-01-0006.
[18] Kalghatgi GT, Risberg P and Ångström H (2006) Advantages of Fuels with High Resistance to Auto-ignition in Late-injection, Low-temperature, Compression Ignition Combustion. SAE Technical Paper 2006-01-3385.
[19] Kitamura Y, Mohammadi A, Ishiyama T and Shioji M (2005) Fundamental Investigation of NOx Formation in Diesel Combustion Under Supercharged and EGR Conditions. SAE Technical Paper 2005-01-0364.
[20] Lapuerta M, Armas O and Hernández J (1999) Diagnostic of D.I. Diesel Combustion from In-Cylinder Pressure Signal by Estimation of Mean Thermodynamic Properties of the Gas. Appl Therm Eng: vol 19: pp 513-529.
[21] Lewander M, Johansson B and Tunestål P (2011) Investigation and Comparison of Multi Cylinder Partially Premixed Combustion Characteristics for Diesel and Gasoline Fuels. SAE Technical Paper 2011-01-1811.
[22] Manente V, Johansson B, Tunestal P and Cannella W (2010) Effects of Different Type of Gasoline Fuels on Heavy Duty Partially Premixed Combustion. SAE Int J Engines: vol 2: pp 71-88.
[23] Manente V, Tunestal P and Johansson B (2010) Effects of Ethanol and Different Type of Gasoline Fuels on Partially Premixed Combustion from Low to High Load. SAE Technical Paper 2010-01-0871.
[24] Musculus MPB, Miles PC and Pickett LM (2013) Conceptual models for partially premixed low-temperature diesel combustion. Prog Energy Combust Sci: vol 39: pp 246-283.
[25] Okude K, Mori K, Shiino S and Moriya T (2004) Premixed Compression Ignition (PCI) Combustion for Simultaneous Reduction of NOx and soot in Diesel Engine. SAE Technical Paper 2004-01-1907.
[26] Payri F, Molina S, Martín J and Armas O (2006) Influence of measurement errors and estimated parameters on combustion diagnosis. Appl Therm Eng: vol 26: pp 226-236.
[27] Payri F, Benajes J, Novella R and Kolodziej C (2011) Effect of Intake Oxygen Concentration on Particle Size Distribution Measurements from Diesel Low Temperature Combustion. SAE Technical Paper 2011-01-1355.
[28] Payri R, García JM, Salvador F and Gimeno J (2005) Using spray momentum flux measurements to understand the influence of diesel nozzle geometry on spray characteristics. Fuel: vol 84: pp 551-561.
[29] Payri R, Salvador FJ, Gimeno J and Bracho G (2008) A new methodology for correcting the signal cumulative phenomenon on injection rate measurements. Exp Tech: vol 32: pp 46-49.
[30] Pohorelsky L, Brynych P, Macek J, Vallaude P-Y, Ricaud J-C, Obernesser P, et al. (2012) Air System Conception for a Downsized Two-Stroke Diesel Engine. SAE Technical Paper 2012-01-0831.
[31] Sellnau M, Sinnamon J, Hoyer K and Husted H (2011) Gasoline Direct Injection Compression Ignition (GDCI) - Diesel-like Efficiency with Low CO2 Emissions. SAE Technical Paper 2011-01-1386.
[32] Sellnau MC, Sinnamon J, Hoyer K and Husted H (2012) Full-Time Gasoline Direct-Injection Compression Ignition (GDCI) for High Efficiency and Low NOx and PM. SAE Int J Engines: vol 5: pp.
[33] Sellnau MC, Sinnamon J, Hoyer K, Kim J, Cavotta M and Husted H (2013) Part-Load Operation of Gasoline Direct-Injection Compression Ignition (GDCI) Engine. SAE Technical Paper 2013-01-0272.
[34] Solaka H, Aronsson U, Tuner M and Johansson B (2012) Investigation of Partially Premixed Combustion Characteristics in Low Load Range with Regards to Fuel Octane Number in a Light-Duty Diesel Engine. SAE Technical Paper 2012-01-0684.
[35] Tree DR and Svensson KI (2007) Soot processes in compression ignition engines. Prog Energy Combust Sci: vol 33: pp 272-309.
[36] Tribotte P, Ravet F, Dugue V, Obernesser P, Quechon N, Benajes J, et al. (2012) Two Strokes Diesel Engine - Promising Solution to Reduce CO2 Emissions. Procedia - Social and Behavioral Sciences: vol 48: pp 2295-2314.
[37] Xu Y and Lee C-fF (2004) Investigation of Soot Formation in Diesel Combustion Using Forward Illumination Light Extinction (FILE) Technique. SAE Technical Paper 2004-01-1411.

The Effect of Jet Spacing on the Combustion Characteristics of Diesel Sprays

T. Bazyn[1] and C. Koci[1]

[1]Caterpillar Inc. USA

E-mail: bazyn_tim@caterpillar.com
Telephone: +(1) 309 578 5666
Fax: +(1) 309 578 9900

Abstract. Mixing-controlled, compression-ignition combustion in a typical Diesel engine emanates from a fuel injector with multiple orifices from a central location equally spaced around the tip at an included angle. The combustion of these orifices can be characterized by the liftoff length, the distance from the start of the spray to the start of combustion, which has been shown to be important to soot formation. However, little is known about how the neighboring jets affect the combustion and spray characteristics from these sprays. Measurements of the plume interaction effects from multiple-orifice diesel sprays were performed using an optically accessible high temperature pressure vessel (HTPV). This vessel is capable of continuous temperatures up to 1000 K and pressures up to 15 MPa. The combusting fuel jets were analyzed by examining the filtered light emission from the combustion region with high speed cameras, with spectral filters looking at the OH chemiluminescence, CH chemiluminescence, and soot luminosity. Mie scattering from the liquid droplets was also measured. In this study, fuel injector tips with different numbers of identically-sized orifices were tested to identify the effects of plume spacing on mixing-controlled, compression-ignition combustion. As the number of orifices increased and the plume spacing correspondingly decreased, the liftoff length was shown to decrease. In general, this decrease showed a threshold below which the jets burn individually and above which the jet spacing affects the liftoff behavior. In the regime where liftoff is not affected by the neighboring jets, the liftoff length is established at a quasi-steady value similar to that of a single jet. Below the threshold jet spacing, the liftoff length is briefly established near the single-jet liftoff length, and then retracts towards the nozzle transiently. This liftoff retraction is accompanied by an increase in soot formation and a shift in the combustion behavior. Gaining understanding of the effect of jet spacing on combustion and emissions formation has important implications in combustion system design, particularly in the area of low-soot combustion strategies.

1. Introduction

Multi-orifice injectors are utilized in almost every production reciprocating engine combustion system. The number of orifices can be low (3-5) or at times quite high (10-15). Mechanical design and combustion rate considerations influence the choice of the number of orifices, size of the orifices, and spacing of the orifices. Often times as the engine bore increases, the orifice number requirement increases to enable utilization of the cylinder's air. This orifice number optimization is also governed by the emissions and performance trade-off curves for the combustion system. A balance of the mechanical design criteria (e.g. nozzle sac structural stresses and cavitation probability) and performance criteria is often achieved through the development process. In order to fully assess the combustion performance regarding fuel air mixing, heat release rate, and emissions formation, a high level of fundamental multi-orifice understanding is desired. This understanding is key to enabling analysis and simulation throughout the combustion system development. Understanding how the multi-orifice fuel jets mix and burn, through concepts like liftoff length, is a prime example of the knowledge needed.

Focusing on the combustion characteristics of fuel air mixing, existing mixing research has predominantly been concentrated on using single-orifice nozzles for ease of experimental setup and analysis. The use of the single-orifice nozzles has been shown to be successful to isolate the main affects and key phenomenon influencing combustion and mixing (Picket and Siebers 2004, 2005, 2006). Research studies focusing on the use of multi-orifice injectors have been widely conducted, but in a lesser focused spectrum than single-orifice injectors. Examples of these studies are (Inagaki et al. 2011) and (Kono et al. 2012) where highly dispersed sprays, through the use of high orifice number nozzles, were used to assess cooling loss reduction, emissions and efficiency optimization.

Another context for the present study on the effect of jet spacing on combustion is the application of sootless combustion to Diesel engine applications. This concept extends from the work at

Sandia National Labs where diesel fuel jets burning with conventional diffusion flame structure were shown to exhibit little or no smoke formation when mixing is enhanced prior to the location where combustion begins, which is termed the liftoff length (Pickett and Siebers 2004, 2005, 2006). This is accomplished by manipulating the liftoff and mixing parameters (such as increasing injection pressure, decreasing injector orifice diameter, and lowering ambient temperature) so that enough air is entrained into the jet to cause combustion to occur only in regions that the average equivalence ratio is less than 2, where soot formation is avoided. A general characteristic of this type of combustion is that the liftoff length of the fuel jet occurs substantially downstream from the liquid penetration length, and the term "lifted flame" has been used to describe this type of enhanced air-entrainment combustion. One way that has been proposed to achieve sootless combustion in practical engine applications is to decrease the individual orifice size and then increase the number of orifices on the injector tip. However, in tests performed by (Bergstrand and Denbratt 2003) as well as unpublished results at the author's institution, this methodology was found to not produce sootless combustion as expected, instead showing significant increases in soot emissions.

As mentioned above, experiments with relatively large number of orifices have shown significant increases in soot emissions in experiments. This marked difference in combustion behavior could reasonably be expected to be due to one or more of the following explanations:

- The proximity of neighboring spray jets could be causing a fundamental difference in spray behavior influencing the air entrainment and general flow field surrounding each individual jet, with less air entrainment prior to the combustion location leading to increased soot formation in the jet.
- The proximity of the neighboring combusting jets could be causing a change in the combustion characteristics of each individual jet, such as heat and/or mass transfer from the neighboring jets or alteration of the surrounding flow field leading to a significant shrinking of the liftoff length, leading to significantly enhanced soot formation in the jet.
- The proximity of the neighboring flames as they interact with the wall of the piston bowl could lead to a recirculation of the combustion products into the spray jets, which would lead to shorter liftoff lengths and less oxygen in the jet.

These mechanisms demonstrate that the plume interaction phenomenon could be due to fundamental spray behavior of the individual plumes, combustion behavior of the individual plumes, or macroscopic in-cylinder flow field alteration. The first two possible causes mentioned could be observed in the spray behavior and combusting jet behavior of these multi-orifice injectors, respectively. The third possible cause would only be observed in engine-like geometries. In fact, (Polonowski et al. 2012) studied the effect of re-entrained gases on the liftoff length behavior of diesel sprays, and found definite instances where this behavior is observed. However, this re-entrainment led to less significant soot increases than was observed in the aforementioned multi-orifice experiments, and this re-entrainment phenomenon was also observed in injectors with a relatively standard number of orifices. Additionally, research measuring the wall jet mixing in the recirculation region of neighboring fuel jets, (Chartier et al. 2012), illustrated that closer angularly spaced fuel jets do not necessarily produce richer recirculation regions. This was found to be linked to the amount of time the wall jets, which were found to have reduced air entrainment compared to free jets, were allowed to develop before interacting in the recirculation regions. Thus, the third explanation above is not likely the only cause of the large increase of soot results from large number of orifices. Therefore, this work will examine the spray and combustion behavior of multi-orifice injectors with the intention of looking for explanation for significant soot increases from closely spaced jets, in addition to the general understanding of jet spacing that is applicable to all applications of diesel-like combustion.

The main efforts in the present work were to focus on how the phenomenon studied under single-orifice conditions changed when moved to multi-orifice conditions, and a specific emphasis on how the multi-orifice jet angular spacing comes into significance. A series of experiments will be discussed that were designed to evaluate multiple sets of production-based injectors with the same nozzle orifice sizes and included spray angles, but varying angular jet space (i.e. number of orifices per nozzle). The experiments utilized non-vaporizing spray visualization and combusting jet imaging under high temperature and density conditions. The results will be displayed in the context of sootless combustion by utilizing conditions that produce little to no soot formation for isolated jets.

2. Experimental Methodology

2.1 Multi-Orifice Injector Tips

The ability to manufacture and quantitatively measure the geometry of multi-orifice injector tips was crucial to the meaningfulness and analysis of the present scope of work. Multi-orifice tips were manufactured and then analysed through x-ray tomography and standard nozzle steady flow tests. Verification of the geometry of the different orifice-number tips was completed to ensure the orifice size, orientation, and alignment was consistent with the desired design intent. An example of typical results is illustrated in Fig. 1 for a 9-orifice nozzle.

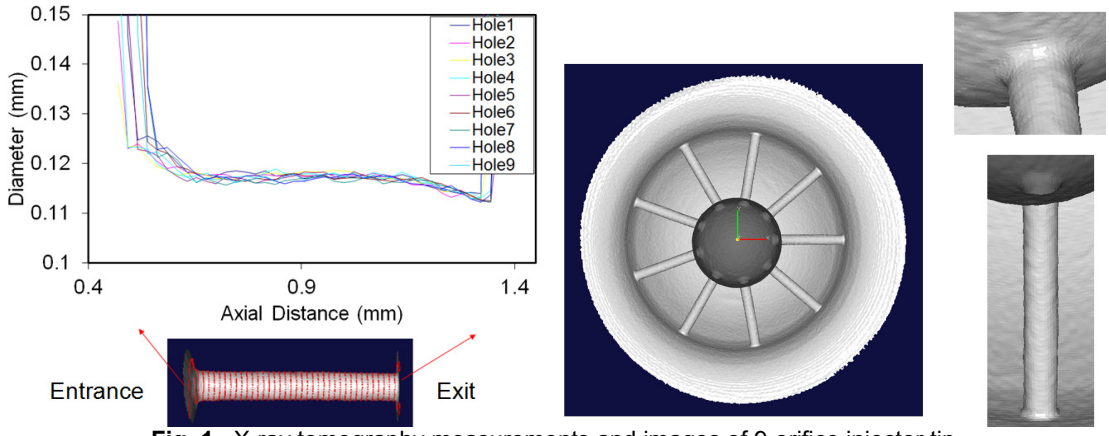

Fig. 1. X-ray tomography measurements and images of 9-orifice injector tip

2.2 Non-vaporizing and Combusting Spray Imaging

Non-vaporizing spray visualization experiments were conducted at the Unheated Pressure Vessel facility at Caterpillar's spray visualization laboratory. The Unheated Pressure Vessel is of a typical constant volume chamber type, with the ability to replicate top dead-center engine densities through pressurization of nitrogen at atmospheric temperatures. High-speed imaging is acquired through the use of three optical windows across from and perpendicular to the injector access.

Combusting experiments were conducted at the High Temperature Pressure Vessel facility at Caterpillar's spray visualization laboratory. This facility is shown schematically in Fig. 2. The system is a continuous flow chamber, where high temperature gas is heated as it flows through the chamber. The inlet gases are currently capable of being mixtures of air and nitrogen, so 0 to 21% oxygen with the balance nitrogen can be achieved. This enables testing of evaporating sprays or combusting sprays. The gases enter the vessel on the bottom, flow upwards through two 15 kW electric heating elements, and then into the test section. The combustion is visible through three optical windows across from and perpendicular to the injector axis. After the spray, the gases exit through the five separate tube-in-tube heat exchangers, where they are cooled to an intermediate temperature before heading to two larger heat exchangers for cooling to ambient temperature. The maximum gas pressure of the vessel is 15 MPa, while the maximum temperature capability of the heating system is 1000 K. Thus, top dead-center conditions can be maintained in the vessel, and the combustion can occur under conditions similar to those in the cylinder of a heavy duty diesel engine. The walls of the vessel are shielded from the high temperature environment by an inner liner with its own windows, and this liner is heated and insulated. Thus, the outer pressure-bearing walls and windows are not exposed to the high temperature gases.

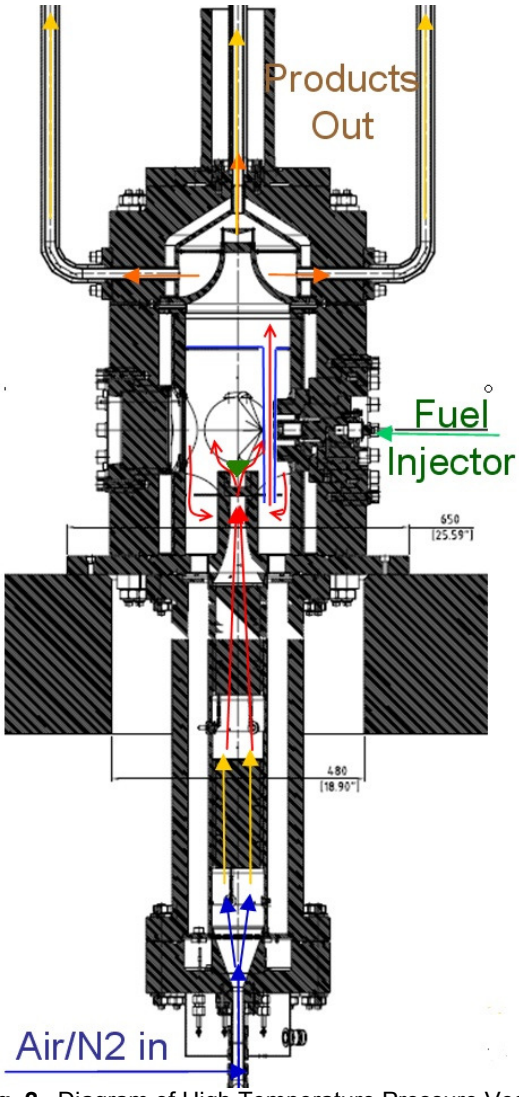

Fig. 2. Diagram of High Temperature Pressure Vessel

2.3 Combustion Diagnostics

Three simultaneous optical diagnostics were recorded for each combustion experiment, with a general optical setup schematic shown in Fig. 3. The first is a high speed movie recorded with the Photron Ultima APX camera of the combustion event natural luminosity with no spectral filtering operated at 15000 frames per second. The second is a high speed movie recorded with the Phantom V12 high speed camera viewed through a 430 nm interference filter with a 10 nm bandpass. This filter was coupled with a 105 mm f/2.8 Nikkor lens. This filter is centered around the light emission from the A-X transition of CH. This excited state CH* is most likely excited from chemical reactions. The captured light could include a significant amount of light from soot luminosity as well for highly sooting conditions. These images can be interpreted as an indicator of the location of significant concentrations of CH* and/or hot soot, and thus show the location of the high temperature heat release, but skewed towards the fuel rich areas where CH* is likely to be present. However, when significant hot soot is present, the soot luminosity likely dominates the chemiluminescence signal. The third diagnostic is a time-integrated image of the combustion luminosity filtered by an interference filter centered at 307 nm (10 nm bandpass) and a UG-11 Schott glass filter. This combination captures the light around the A-X transition of OH at 308 nm. The flame was imaged through a 105 mm f/4.5 UV Nikkor lens. Chemiluminescence imaging of OH* has been a common marker for liftoff length in the literature, and will be used in this study as well. These images can be interpreted as the location of the high temperature heat release, but skewed towards the lean regions where OH concentrations would be higher. The images were processed to measure the liftoff length using the method of (Pauls et al. 2007).

Throughout the course of the present work, an upgrade to the High Temperature Pressure Vessel optical facility was completed which allowed for more optimal image positioning relative the camera positions and the addition of liquid spray visualization, through Mie scattering measurements of the liquid droplets. The reader should note that the inclusion of the spray visualization and the different image positioning occurs after the first set of experiments in Fig. 6. The upgraded combustion diagnostics and imaging can be seen starting in Fig. 8, and the upgrade is the purposeful reason for the change in the presentation of the images from the different experiments before and after the upgrade.

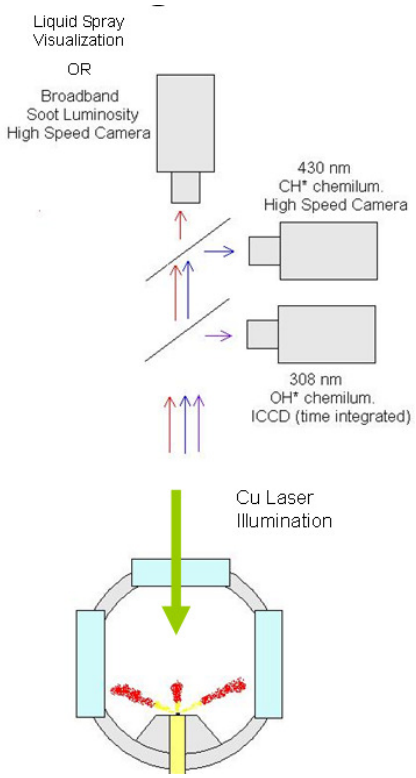

Fig. 3. Diagram of optical diagnostics

The temperature field in the vessel has been quantified (Bazyn and Martin 2011). Outside of the boundary layer a few millimeters from the wall, the temperatures are within 15 K of the center temperature (typically within 5 K), with the lowest temperatures near the water-cooled injector tip. This provides reasonable confidence in the uniformity and repeatability of the test section conditions. However, the temperature measurements did indicate a significantly cooler wall temperature, and measurements with different diameter thermocouples demonstrated that a correction for the radiation losses from the thermocouple is required. Thus, the data in this report have been corrected for the radiation losses from the thermocouple.

2.4 Experimental Conditions

A common rail type fuel injector was used for all of the present study. The injector had Piezo type actuation with a nominal orifice size of 112 microns. The general injector characteristics and range of orifice numbers can be seen in Table 1. The characteristic of the injection rate profile is extremely square (i.e. top hat), with opening/closing ramp times on the order of tens of microseconds as measured by a force transducer momentum rate setup. Laboratory fuel supply pressure was generated with a pneumatic pump and sufficiently large accumulator (~1L) to maintain consistent injector inlet pressure as the total nozzle flow increases as the orifice-number increases. The present injector and laboratory setup allowed for 100, 200, and 300 MPa injector inlet pressures to be utilized consistently throughout all the different orifice-number nozzles.

All cold spray imaging experiments were completed at a density of 25 kg/m^3, while combustion imaging in the High Temperature Pressure Vessel was completed at two different pressures, 60 and 100 bar. Temperature sweeps at each pressure were performed from 750 to 950 K which resulted in a density range of 22-28 kg/m^3 and 37-47 kg/m^3 for 60 and 100 bar respectively.

Table 1. Table of Fuel Injector Characteristics

Characteristic	Value
Injector Type	Common Rail
Actuator	Piezo
Orifice Size	112 microns
Number of Orifices	6,7,8,9,10,14,18
Orifice Steady Flow per Orifice	0.14 kg/min @ 41 MPa
General Rate Shape Profile	Square, Top Hat

3. Results and Discussion

The results presented in this work include a series of tests to isolate the effects of the potential jet interaction mechanisms. Cold spray tests will be presented first to identify any appreciable difference in the macroscopic spray behavior, such as spray dispersion, shape, and penetration, resulting from additional plumes. Heated constant pressure combustion measurements will be subsequently presented, with the intent to look for plume interaction observed in the liftoff length and soot formation differences in the near-nozzle combustion region.

The first set of tests included cold spray testing of the 6, 10, 14, and 18-orifice nozzles. These tips all had an orifice diameter of 112 μm and an included spray angle of 130 degrees. The following set of images in Fig. 4 shows the spray development for the 10, 14, and 18-orifice injector tips at 200 MPa injection pressure at a chamber density of 25 kg/m^3. These images have been scaled so that they appear the same size (the width and height for the bottom set of images is 93 mm).

From these images, it is clear that the plumes are getting quite close together as the number of plumes is increased to 18. However, there does not appear to be a significant change in the amount of penetration observed or the shape of the individual sprays. This can be seen in Fig. 5, which is the quantification of the penetration for these three sets of images. The first phenomenon to note is that the 14 and 18-orifice tips demonstrate a marked difference in penetration for every other jet around the spray. It should be noted that only the jets with similar interior nozzle geometry are shown in this figure. The explanation for this difference stems from the drilling pattern and interior nozzle geometry, and will be explained in an appendix at the end of the paper. A similar difference in the spray behavior in two row tips with a similar orifice pattern (two rows of orifices with a single included angle) has also been observed in another study (Payri et al. 2004). The 6-orifice nozzle was also measured and had a similar spray behavior to the 10-orifice nozzle, but is not shown for visual simplification.

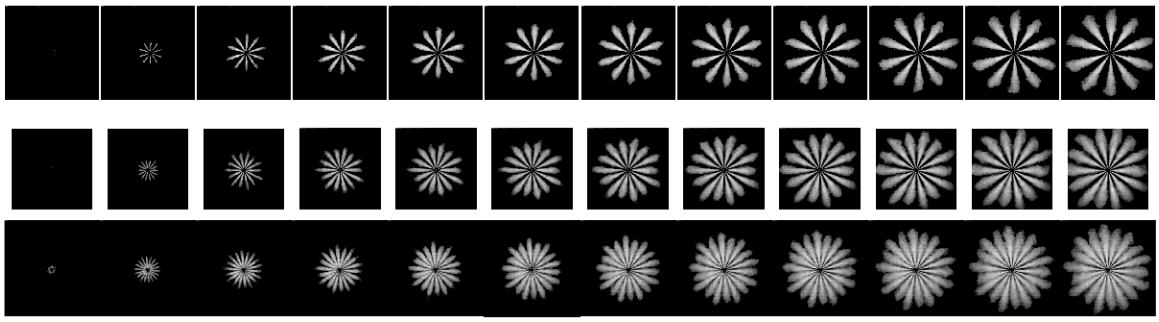

Fig. 4. Images of room-temperature spray visualization from 10, 14, and 18-orifice nozzles at 25 kg/m^3 chamber density and 200 MPa injection pressure

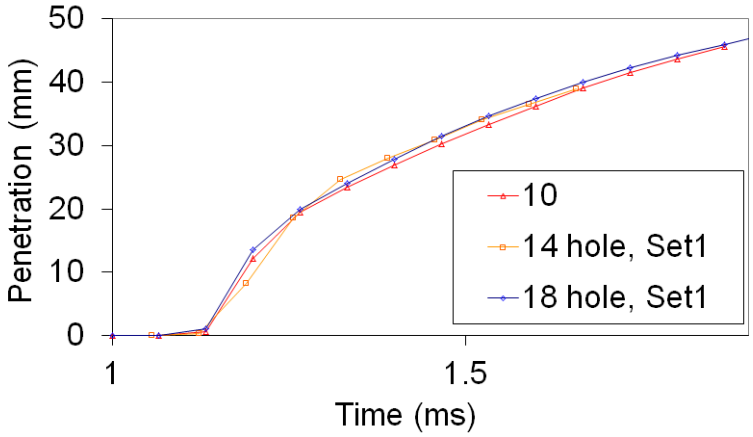

Fig. 5. Penetration of spray jets vs. time for the 10, 14, and 18-orifice nozzles at 25 kg/m3 chamber density and 200 MPa injection pressure

The similarity in spray penetration indicates that the sprays do indeed behave in a similar macroscopic fashion to an isolated jet. Other studies on the effect of plume spacing, such as (Malbec and Bruneaux 2010, Pawlowski et al. 2009, Pawlowski et al. 2006, Rhim and Farrell 2001, 2002) measured the sprays and velocity fields surrounding jets with reduced jet spacing and found relatively small differences in total air entrainment and the spray behavior. The cold spray results thus do not indicate a dramatic change in spray structure, even for an 18-orifice nozzle, that would cause a major change in the combustion behavior of the jet.

The next results observe the combusting spray behavior of the multi-orifice tips. As mentioned in the introduction, two sets of experiments were conducted, and the first set examined major differences in jet spacing using 6, 10, and 14-orifice tips, while the second set examined a more narrow range of jet spacing by using 8, 9, and 10-orifice tips to look at the onset of plume interaction. A representative sample of images throughout the development of the combustion event is shown in Fig. 6. The top row of each set of images shows the broadband light emission, which is largely an indication of soot luminosity as mentioned in the introduction, while the next row is a filtered image for CH* chemiluminescence. The last column of images shows a time-averaged image over the entire combustion event, with the bottom row showing OH* chemiluminescence (which was only acquired on a time-averaged basis). The black line appearing in the images is a thermocouple that was used for temperature measurements of the combustion chamber in the first set of tests only. Small lines have been added to the images at the location where the image processing routine has detected the liftoff length for each particular image.

The 6-orifice injector images show conditions that can be described as sootless combustion. A lack of soot formation is seen in the dark upper images, with small pockets of soot luminosity only occasionally observed. The CH* chemiluminescence images show that the liftoff length reaches a quasi-steady value at a relatively long liftoff length. This long liftoff length allows adequate pre-mixing of the fuel and air before combustion, avoiding the overly rich combustion regions where soot is formed. This behavior agrees with observation of single-orifice nozzles in this lab as well as in the literature.

However, as the number of orifices increases from 6 to 10, a different behavior is observed. Initially, the behavior is very similar, with the liftoff being established at a relatively long distance from the nozzle and combustion occurring without soot formation. However, the combustion zone begins to retract back to the nozzle, leading to insufficient pre-mixing necessary to allow sootless combustion. By the end of the long injection event, all of the jets now have a measurably shorter liftoff length and are thus forming significant amounts of soot.

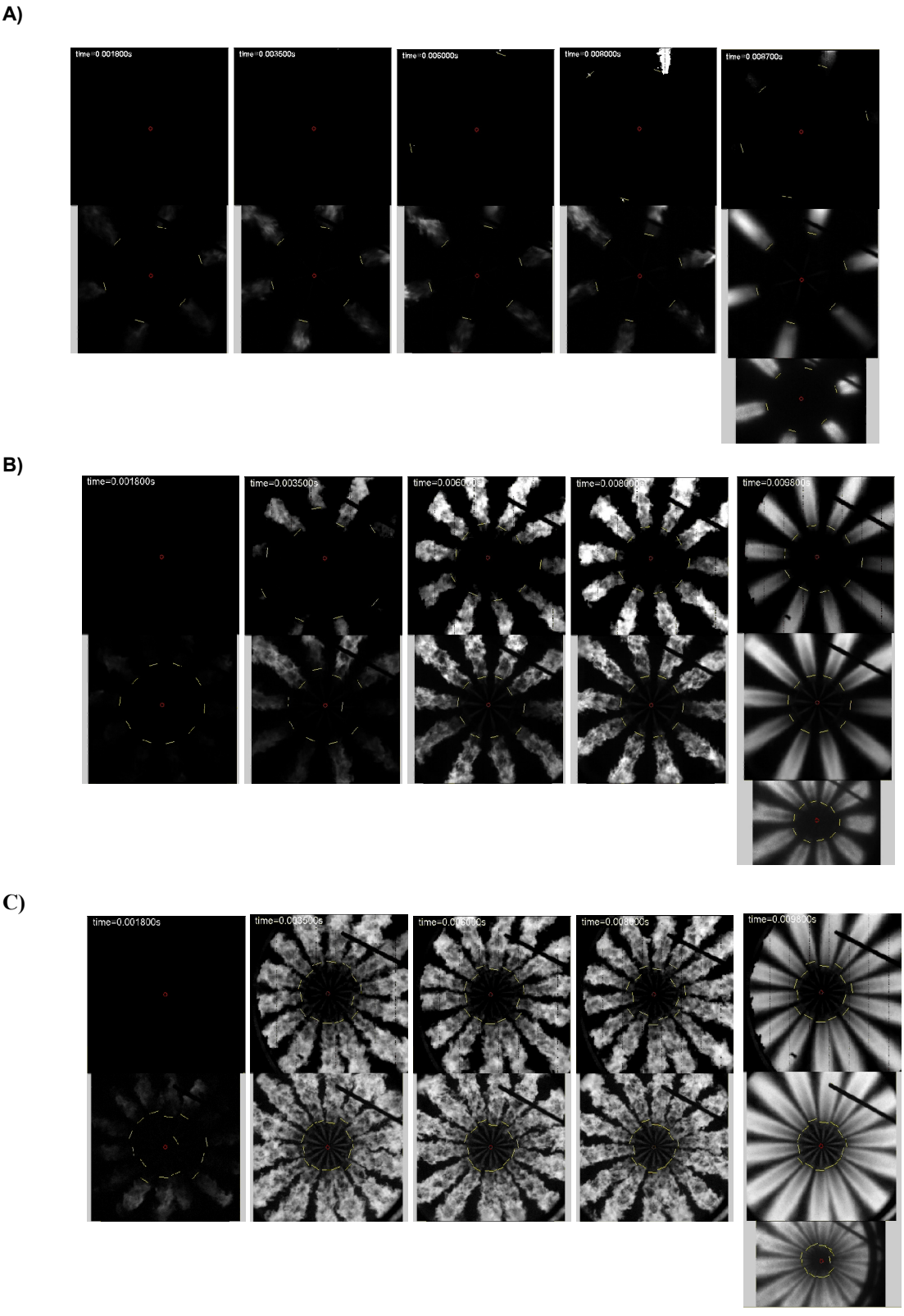

Fig. 6. Time sequence of images showing the natural luminosity (top) and CH* chemiluminescence (bottom) for the 6, 10, and 14-orifice injector in image sets A, B, and C, respectively at 805 K, 60 bar, and 300 MPa injection pressure. The last image on the right most column represents a time-average over the entire injection event and shows natural luminosity (top), CH* chemiluminescence (middle) and OH* chemiluminescence (bottom). The image-processed liftoff lengths are shown as yellow lines on the images

As the orifice spacing decreases further for a 14-orifice nozzle, another type of behavior can be observed. Here, the first set of images shows the liftoff length being established at a distance shorter than that observed for 6-orifice or single-orifice injectors. Then, the liftoff length retracts very quickly to a relatively short length and remains at this length for the rest of the combustion event. There appears to be a quasi-steady liftoff length for this nozzle, but it is significantly shorter than that observed for the 6-orifice and single-orifice injectors. The jets form soot almost immediately after the start of combustion and continues throughout the event. The lifted flame combustion mode with adequate pre-mixing to avoid soot formation is not present.

The trends outlined above can be further enforced with the plots shown in Fig. 7. This set of plots shows the liftoff as calculated from image processing of each of the images (broadband, 430 nm, and 308 nm). The dotted lines show the results of the time-integrated images, while the solid lines show the transient behavior.

The 6-orifice case has no plotted data for the broadband light emission because very little signal was obtained in this non-sooting condition, and thus no measurements could be made. The 10-orifice case has no broadband liftoff distance data at first, but the broadband liftoff data appears a few milliseconds into the plot once the jets have become sooting. These data demonstrate the significant variation in the transient behavior of the liftoff length. The 6-orifice case quickly realizes a steady liftoff length. The 10-orifice case retracts relatively slowly over much of this long injection event, while the 14-orifice case has a relatively short transient period and then reaches a relatively short steady state liftoff length.

There are a few possible reasons for this transient liftoff retraction and the overall shorter liftoff lengths observed with closely-spaced orifices. One potential source of the retraction behavior could be the flow interaction between the closely spaced jets. Hot combustion products or radical species from the neighboring jets could be entrained or turbulently mixed into the jet causing ignition to occur further upstream. In addition, the neighboring fuel jet could also cause a decrease in the strain rate at the external edge of the jet. Previous researchers (Venugopal and Abraham 2007) have reviewed theories for liftoff length stabilization and argued that the local strain rate (scalar dissipation) is one of the key parameters in determining the liftoff length. Whereas free jets will be surrounded by a relatively quiescent environment, parts of these jets will be neighbored by another jet flowing in the same direction. This co-flow could lead to a significant decrease in the local strain rate, allowing the local areas of combustible mixture to avoid being quenched and thus form a stable flame. Another potential cause could be radiative feedback from the neighboring jet. Radiative heat transfer from the jet could lead to increased local temperatures, which in turn could also cause a liftoff length retraction. The retraction is likely not caused by overall temperature increase inside the chamber, as the volume of the chamber is very large and very little pressure increase is observed.

It should be noted that a large set of temperature, pressure, and injection pressure conditions were run for each nozzle, and the global parameters for those tests will be presented along with the global parameter results for the 8, 9, and 10-orifice injectors near the end of this section.

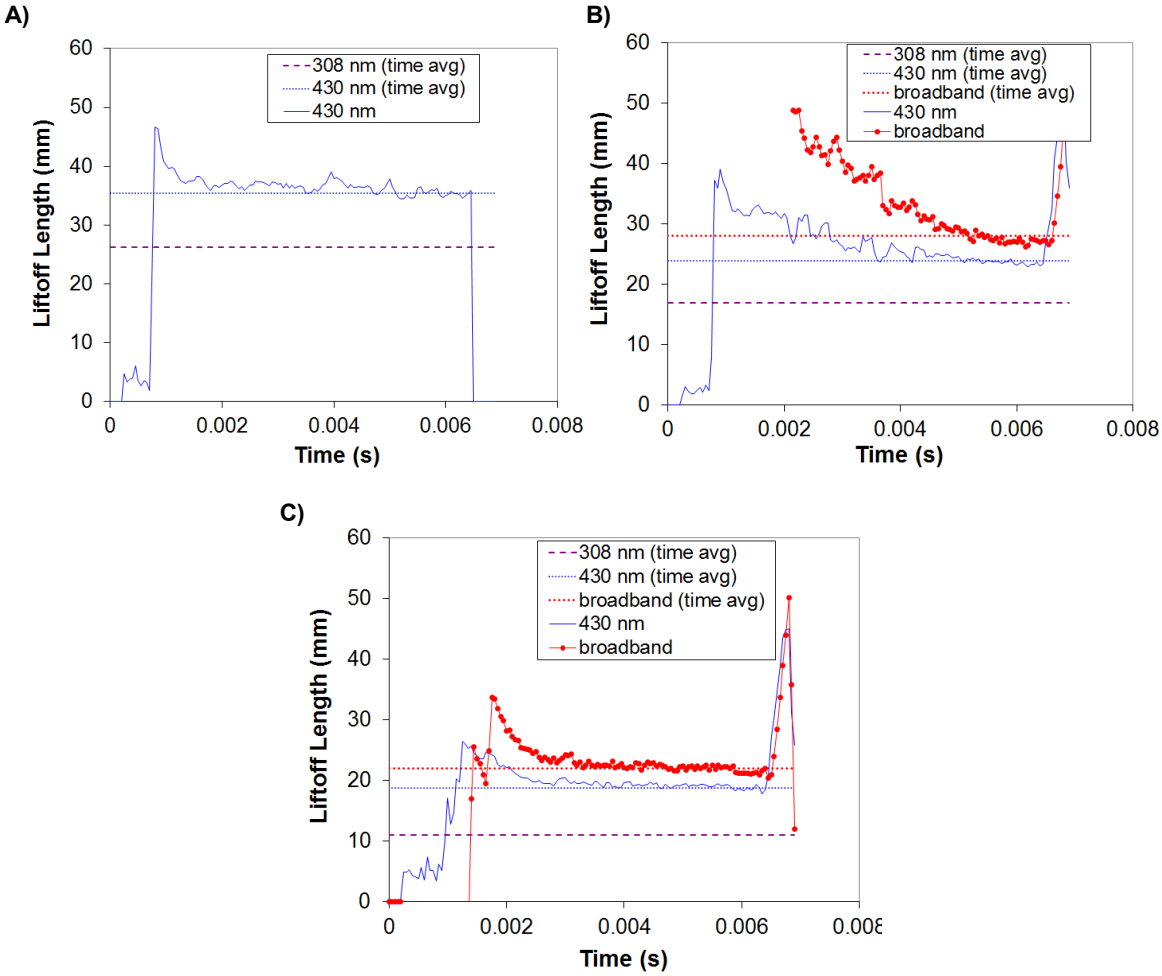

Fig. 7. Plots of the liftoff length versus time at 805 K and 60 bar with 300 MPa injection pressure for the A) 6-orifice injector, B) 10-orifice injector, and C) 14-orifice injector

Because of the significant difference observed in the combustion behavior of 6, 10, and 14-orifice nozzles, the next set of experiments used 8, 9, and 10-orifice nozzles. This range of nozzles was selected to get better resolution of the orifice spacing when jets transition from behaving similar to a free jet and start to become influenced by a neighboring jet, as seen in the 10-orifice injector in the previous section. The results from the second set of tests is shown in Fig. 8 using the aforementioned refined/upgraded imaging setup at 780 K ambient temperature, 100 bar ambient pressure, and 300 MPa injection pressure. In this figure, the time series of images is displayed downwards, while the different diagnostics are displayed left to right. Four different times are shown in each figure. At each time, 3 images are shown corresponding to simultaneous 430 nm (CH* chemiluminescence) and broadband light emission (soot luminosity) along with non-simultaneous (same conditions but different experiment) spray visualization. In the same row as the last time, a time averaged image of the 308 nm light emission is shown as well. The lines on the images show the instantaneous liftoff length (or liquid length in the case of spray visualization) calculated from that image. The liftoff length calculated from the time-averaged OH images will be used in the following figures as the single characteristic liftoff length for each condition.

For each of the nozzles, the first image set occurs after the liquid spray has emerged from the nozzle but ignition has not yet occurred. All of the nozzles exhibit very similar liquid lengths. The second set of images is captured at a time when combustion is occurring and the chemiluminescence from the flame is visible. For all nozzles, the liftoff at this early time is relatively similar as shown in the plots of the time development in Fig. 9 (similar to Fig. 7). However, shortly after ignition, the 10-orifice nozzle again exhibits a retraction in the liftoff length, as shown in the images for the third and fourth times of Fig. 8C. The liftoff length slowly moves back towards the nozzle. Eventually, this causes some of the jets to become significantly sooting, while the 8 and 9-orifice nozzles appear to remain mostly non-sooting. Again, this transient retraction is a significantly different behavior than is observed in single-orifice nozzles, and is an important finding of this work. The 9-orifice nozzle does not show a significant time dependent retraction, but does display a slightly shorter liftoff length. Thus, the

onset of the neighboring jet causing a significant impact on the combusting spray behavior appears to occur right around jet spacing of the 9-orifice tip.

A)

CH Chemilum Broadband (soot) Spray Vis. OH Chemilum. (time avg.)

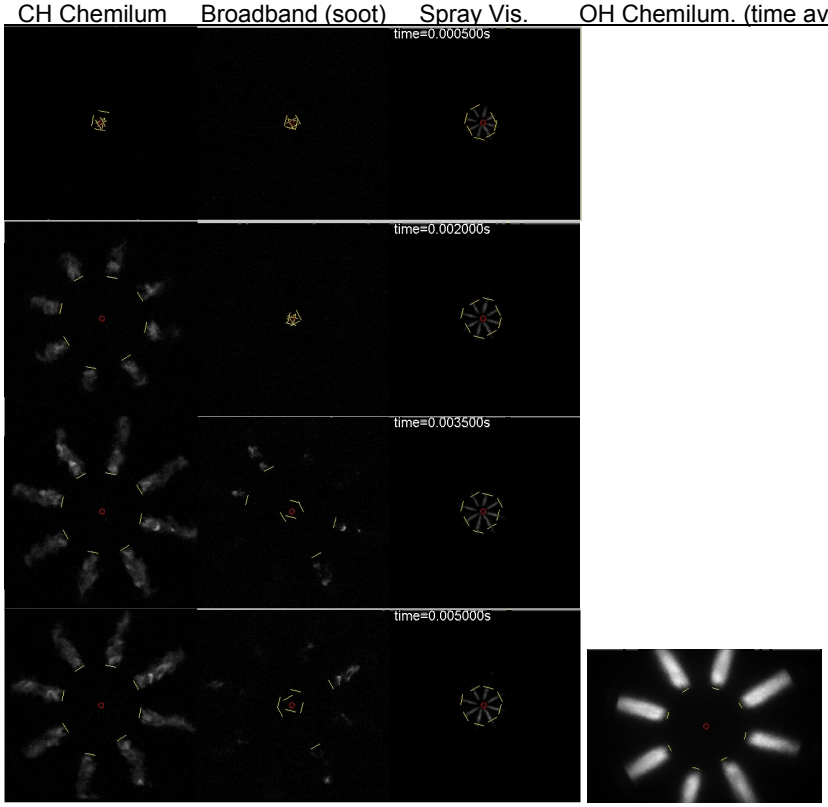

B)

CH Chemilum Broadband (soot) Spray Vis. OH Chemilum. (time avg.)

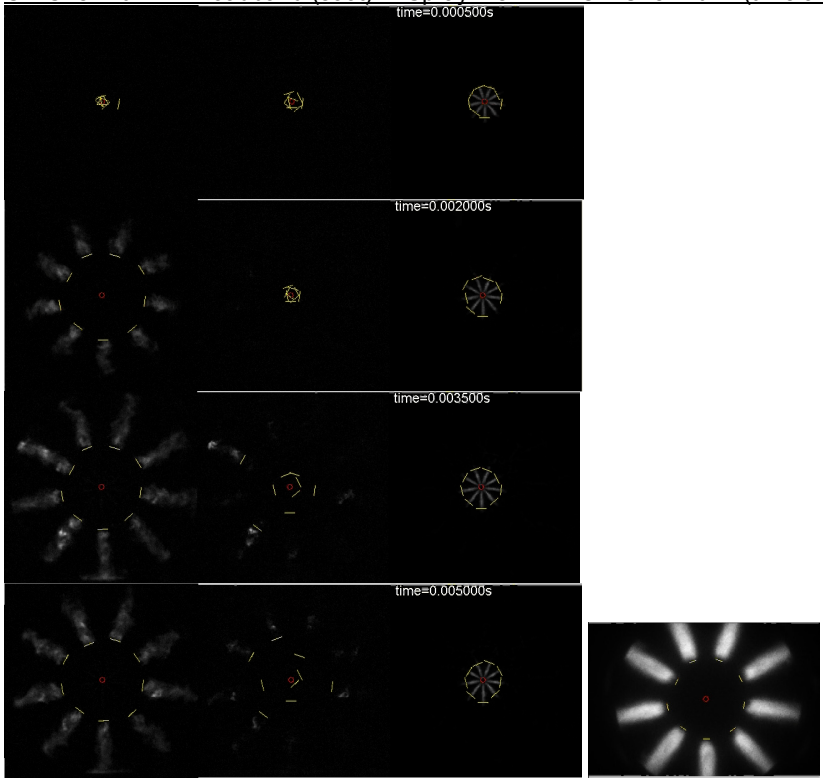

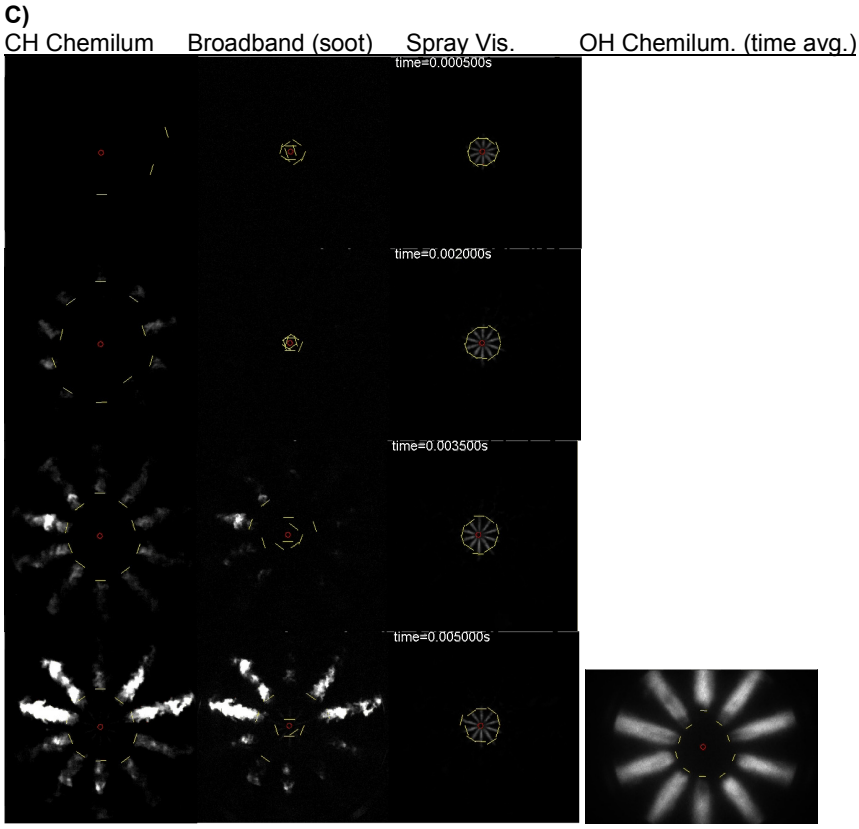

Fig. 8. Sequence of images showing the combustion development for the 8, 9, and 10 orifice injector tips (in image sets A, B, and C, respectively) at 780 K, 100 bar, and 300 MPa injection pressure

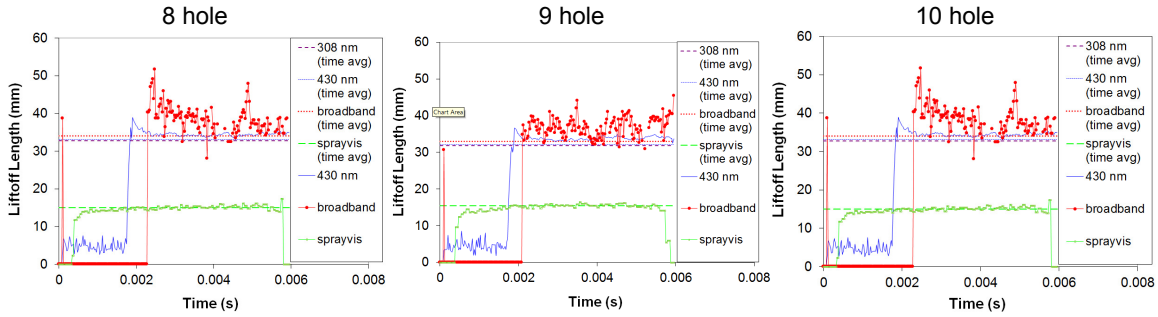

Fig. 9. Liquid, OH chemiluminescence liftoff, and CH chemiluminescence liftoff length measurements versus time for the set of images sampled in Fig. 8

While the previous look at a single condition highlighted the fact that less plume spacing causes a transient liftoff length retraction and shorter liftoff lengths, those results also hold in general over a wider range of experimental conditions. The compiled liftoff length data from 6 to 14 orifices for temperature sweeps, while maintaining the chamber pressure at 100 bar, for three different injection pressures is shown in Fig. 10. The top plots show the liftoff length, while the bottom plots show the equivalence ratio at the liftoff length calculated according to the cross-section averaged mixing model used by (Picket and Siebers 2004) and shown in Eq. 1.

$$\varphi = \frac{2*(A/F)_{st}}{\sqrt{1+16(x/x^{+})^{2}}-1}\text{, where } x^{+} = \sqrt{\frac{\rho_f}{\rho_a}}\frac{\sqrt{C_a}d}{a\cdot\tan(\theta/2)} \qquad (1)$$

While the conditions do not uniformly produce a change from the sootless to sooting regime as the number of orifices is increased, the changes in liftoff length versus number of orifices is fairly re-

peatable. It is generally true that the liftoff length does not change significantly between 6 and 8 orifices. The 9-orifice injector often shows a slightly shorter liftoff length than the 8-orifice injector. Then, as orifice number is increased to 10, a significant change in liftoff length occurs. A further increase to 14 orifices produces a very short liftoff length.

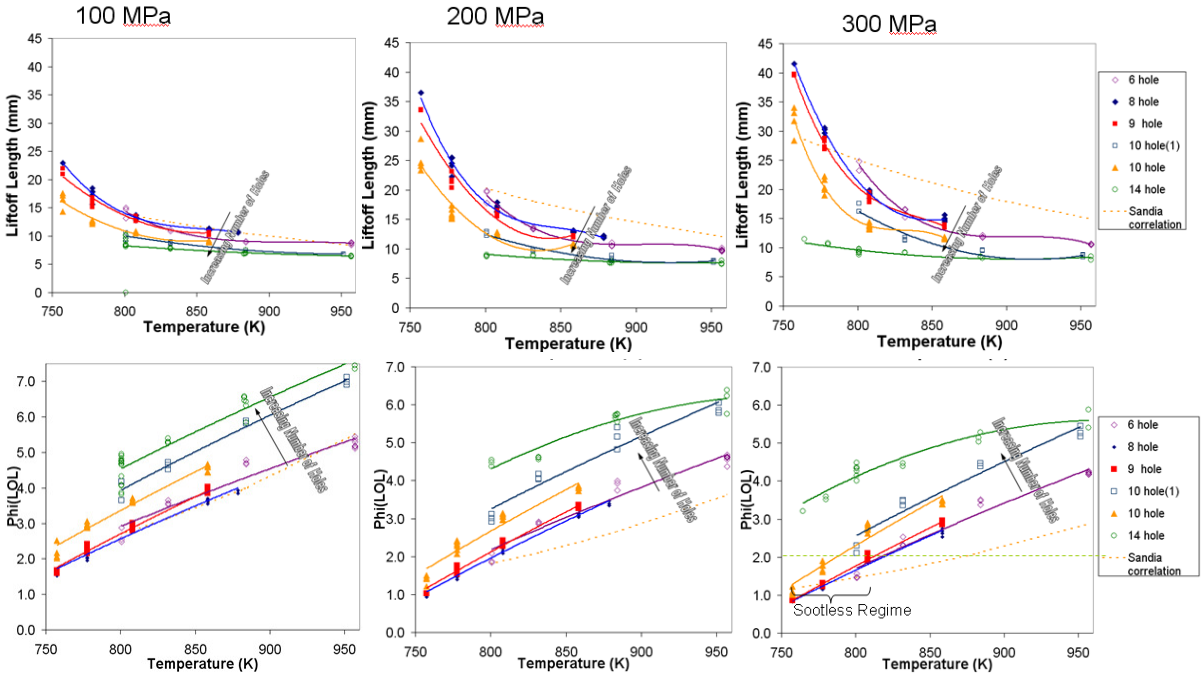

Fig. 10. Compiled results for liftoff length and equivalence ratio at the liftoff length from 6-14 orifice nozzles at 100 bar ambient pressure at 100, 200, and 300 MPa

This data provides important guidance to the plume spacing limit for diesel fuel injection, with particular relevance to conditions aimed at achieving sootless combustion. Clearly, around 9 orifices (a plume spacing of 36 degrees), there is a threshold plume spacing in terms of liftoff length behavior. Above this value, the liftoff is shortened, and below this value, the jets burn relatively unperturbed by the neighboring jets. Thus, the practical limit for plume spacing without significantly decreasing size of the regime where conditions produce sootless combustion is around 36 degrees. It is also instructive to note that the cold spray tests showed no significant change in the bulk spray behavior as the jet spacing decreased. Thus, the observed difference in liftoff behavior is a combustion effect as opposed to a spray effect. Likely causes for this behavior include a change in the fluid dynamics in the region between the jets. Current theories of liftoff often suggest that the fluid strain extinguishes ignition prior to the liftoff length. The neighboring jets could be impacting the fluid strain in the region between the jets, allowing combustion to occur in that region. Another likely cause could be heat transfer from the neighboring jet, which heats the mixture and accelerates the reactions.

The aforementioned jet spacing limits may also be important in general diesel combustion applications. However, the importance in maintaining liftoff length in general mixing-controlled diesel engine combustion is less obvious because soot emissions are a complicated mix of controlling soot formation and enhancing soot oxidation, and one study showed little correlation between the liftoff length and engine-out soot emissions (Lequien et al. 2013). However, Sandia (Pickett and Siebers 2006) demonstrated a strong correlation in the soot formation in the jet and the liftoff length, and the soot formation levels will certainly lead to differences in engine out-soot when oxidation conditions are equal. While the complicated landscape of Diesel engine combustion system design does not lend itself to creating experiments with equal oxidation and differing levels of soot formation, it would be unreasonable to discount the repeatable and observable effect of liftoff length retraction and corresponding increase in soot formation with jet spacing less than 36 degrees

The data which did not appear to be perturbed by a neighboring jet, i.e. the 6 and 8-orifice injectors, has been compared to the correlation developed at Sandia National Labs (Pickett and Siebers 2005) (Eq. 2). This comparison is shown in Fig. 11 (solid lines). Clearly, the agreement is poor, especially in the temperature dependence as temperature is reduced. In addition, the injection pressure dependence also seems off, showing a smaller dependence in our application. This is potentially not

surprising, and this data, which was aimed at sootless combustion, was taken in a lower temperature and higher injection pressure regime as compared to the data recorded at Sandia, which was more aimed at conventional Diesel operation. To match our observed sensitivity, a different correlation has been developed, as shown in Eq. 3 and the dotted lines in Fig. 11. A significant difference is the form of the temperature dependence, which in our correlation is of the form $(T-T_o)^n$. This form fits better to the notion that below an ignition temperature, the liftoff length is infinitely long. Thus, it is more likely to fit the data at lower temperatures than a simple power law fit. The value of 730 K for T_o is a fit to our data, but also provides a reasonable value for the ignition temperature as observed in our experiments. It is important to note that this correlation is proposed to fit our data, and the Sandia correlation represents a fit to data that was recorded in a different range of experimental conditions (e.g. higher temperatures) and with significantly different nozzle geometry.

$$LOL = C\rho^{0.85}T^{-3.74}d^{0.34}P_{inj}{}^{0.5}Z_{st}{}^{-1} \quad (2)$$

$$LOL = C(T-730)^{-0.74}(\Delta P)^{0.38}d^{0.2}\rho_g^{-0.85}Z_{st}^{-1} \quad (3)$$

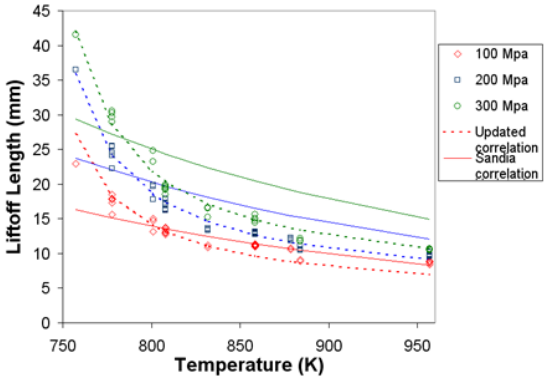

Fig. 11. Comparison of the Sandia Correlation and proposed alternative scaling to the experimental data for the 6 and 8-orifice injectors

Conclusions

The spray plume interaction effects in mixing controlled diesel combustion were investigated through the use of a range of multi-orifice nozzles and an optically accessible High Temperature Pressure Vessel (HTPV). The HTPV allowed spray experiments to be conducted at conditions emulating that of top dead center in a heavy-duty diesel engine. Spray interaction effects were analyzed under a lifted flame regime, which helped to evaluate sensitive liftoff length trends at conditions where transitions in the trends occur.

Cold spray visualizations were utilized to confirm plume spacing effects on the general flow field and spray patterns, while the experiments in the HTPV were used to confirm and interrogate plume interaction effects in combusting environments. Optical diagnostic imaging of natural soot luminosity, CH chemiluminescence, OH chemiluminescence, and liquid fuel droplet Mie scattering provided the fundamental data to assess mixing and liftoff length trends. The following conclusions can be formulated from the current data and discussions surrounding the effect of plume spacing in multi-orifice nozzles.

- For a range of 6-18 orifice nozzles, no significant difference in the macroscopic behavior of spray plumes was observed in the non-reacting, cold spray environment. As the orifice spacing was reduced, the individual plumes continued to behave as that of a single plume, indicating any plume spacing induced flow field differences had a minor influence on the general spray behavior. Additionally, different vertical orifice placement in the nozzle sac wall, due to physical space constraints of nozzles with high numbers of orifices, did show that the spray penetration could be affected. This was attributed to different orifice flow and cavitation behavior as outlined in the appendix, not due to plume to plume interaction effects.
- As the orifice count was increased from 6 to 14, under a lifted flame regime, a significant shortening of the liftoff length was found as indicated by a retraction of the OH chemiluminescence and the appearance of large regions of natural soot luminosity within the plume. The

plume spacing was found to be a significant factor in the ability for the combustion to retain a sootless combustion state, as indicated by liftoff length, liquid length, and soot luminosity.

- The transition period from conditions where combusting plumes retained a single plume liftoff behavior, to the onset of conditions where the plumes began to be affected by the neighboring plumes, was found to be near an orifice count of 9 (inter-jet angle of 36˚). 9-orifice nozzles produced steady liftoff lengths slightly reduced from <8-orifce nozzles, while 10-orifice nozzles produced time dependent liftoff length behaviors that retracted significantly as the injection proceeded. 14-orifice nozzles produced the shortest liftoff length trends with a relatively fast initial time dependent behavior.
- The above described multi-orifice liftoff length behavior was found to be consistent over fuel injection pressures from 100-300 MPa and from ambient temperatures from 750-950 K. The inclusion of a $(T-T_o)^n$ dependency in the published liftoff length correlations was required to fit the present data sets.

References

Bazyn T and Martin G (2011) Spray Combustion Measurements in a Flow-Through High Temperature, High Pressure Chamber. Proceedings of ILASS Americas 23rd Annual Conference on Liquid Atomization and Spray Systems, Ventura, CA.

Bergstrand P and Denbratt I (2003) The Effects of Multirow Nozzles on Diesel Combustion. SAE Technical Paper 2003-01-0701, doi:10.4271/2003-01-0701.

Blessing M, König G, Krüger C, Michels U, and Schwartz V (2003) Analysis of Flow and Cavitation Phenomena in Diesel Injection Nozzles and Its Effects on Spray and Mixture Formation," SAE Technical Paper 2003-01-1358, doi:10.4271/2003-01-1358.

Chartier C, Sjoholm J, Kristensson E, Andersson , et al., (2012) Air-Entrainment in Wall-Jets Using SLIPI in a Heavy-Duty Diesel Engine. SAE Int. J. Engines 5(4):1684-1692, doi:10.4271/2012-01-1718.

Inagaki K, Mizuta J, Fuyuto, T, Hashizume T, et al., (2011) Low Emissions and High-Efficiency Diesel Combustion Using Highly Dispersed Spray with Restricted In-Cylinder Swirl and Squish Flows. SAE Int. J. Engines 4(1): pp 2065-2079, doi:10.4271/2011-01-1393.

Kono M, Basaki M, Ito M, Hashizume T, et al., (2012) Cooling Loss Reduction of Highly Dispersed Spray Combustion with Restricted In-Cylinder Swirl and Squish Flow in Diesel Engine. SAE Int. J. Engines 5(2): pp 504-515, doi:10.4271/2012-01-0689.

Lequien G, Andersson Ö, Tunestal P, and Lewander M (2013) A Correlation Analysis of the Roles of Soot Formation and Oxidation in a Heavy-Duty Diesel Engine. SAE Technical Paper 2013-01-2535, doi:10.4271/2013-01-2535.

Malbec L and Bruneaux G (2010) Study of Air Entrainment of Multi-hole Diesel Injection by Particle Image Velocimetry - Effect of Neighboring Jets Interaction and Transient Behavior After End of Injection. SAE Int. J. Engines 3(1):pp 107-123, doi:10.4271/2010-01-0342.

Payri F, Benajes J, Gonzales C, and Donde R (2004) The Effects of Injector Hole Convergence on Diesel Combustion and Emissions. Int. J. Vehicle Design 36(4): pp 385-402, doi:10.1504/IJVD.2004.005809.

Pauls C, Grünefeld G, Vogel S, and Peters N (2007) Combined Simulations and OH-Chemiluminescence Measurements of the Combustion Process using Different Fuels under Diesel-Engine like Conditions. SAE Technical Paper 2007-01-0020, doi:10.4271/2007-01-0020.

Pawlowski A, Kneer R, Lippert A, and Parrish S (2009) Investigation of the Interaction of Sprays from Clustered Orifices under Ambient Conditions Relevant for Diesel Engines. SAE Int. J. Engines 1(1): pp 514-527, doi:10.4271/2008-01-0928.

Pawlowski A, Kneer R, Vogel S, Peters N, Pinson J, and Lippert A (2006) Investigation of the Flow Field Between Diesel Sprays to Characterize Spray-Spray Interaction. Paper No. ICLASS06-138, ICLASS-2006, 10th International Conference on Liquid Atomization and Spray Systems, Aug. 27 - Sep. 1, 2006, Kyoto, Japan.

Pickett L and Siebers D (2004) Soot in Diesel Fuel Jets: Effects of Ambient Temperature, Ambient Density, and Injection Pressure. Combustion and Flame 138: pp 114-135, doi:10.1016/j.combustflame.2004.04.006.

Pickett L and Siebers D (2005) Orifice Diameter Effects on Diesel Fuel Jet Flame Structure. Journal of Engineering for Gas Turbines and Power 127: pp 187-196, doi:10.1115/1.1760525.

Pickett L and Siebers D (2006) Soot Formation in Diesel Fuel Jets Near the Lift-Off Length. Int. J. Engine Res. 7: pp 103-130, doi:10.1243/146808705X57793.

Polonowski C, Mueller C, Gehrke C, Bazyn T, et al. (2012) An Experimental Investigation of Low-Soot and Soot-Free Combustion Strategies in a Heavy-Duty, Single-Cylinder, Direct-Injection, Optical Diesel Engine. SAE Int. J. Fuels Lubr. 5(1): pp 51-77 doi:10.4271/2011-01-1812.

Rhim D and Farrell P (2001) Effect of Gas Density and the Number of Injector Holes on the Air Flow Surrounding Non-Evaporating Transient Diesel Sprays. SAE Technical Paper 2001-01-0532, doi:10.4271/2001-01-0532.

Rhim D and Farrell P (2002) Air Flow Characteristics Surrounding Evaporating Transient Diesel Sprays. SAE Technical Paper 2002-01-0499, doi:10.4271/2002-01-0499.

Venugopal R and Abraham J (2007) A Review of Fundamental Studies Relevant to Flame Lift-off in Diesel Jets. SAE Technical Paper 2007-01-0134, doi:10.4271/2007-01-0134.

4. APPENDIX

In Fig. 5, the spray penetration for orifices with similar nozzle geometry was shown to be similar despite differences in plume spacing. However, the images clearly showed that all of the jets in both the 14 and 18-orifice nozzles did not penetrate equally. If the stated conclusion that spray behavior is similar despite orifice spacing is to be believable, then the difference between the orifices within those two nozzles must be explained. This appendix explains that the alternating orifices for these two nozzles are drilled on two axially separated rows with the same included angle, and this difference in internal nozzle geometry leads to a marked difference in penetration for these two rows.

Figure A1 shows a spray image that has been separated into segments for each jet, with each jet numbered for reference and the penetration and cone angles for the jet shown on the picture. It is clear that there was a difference in the spray behavior between every other orifice. As can be seen in the image, the orifices with an even number (designated by the starting position of the '#' for each label) tended to almost uniformly penetrate less than the orifices with the odd number. In addition, those orifices also show wider cone angles. Figure A2 shows the penetration data for the odd numbered orifices designated as Set 1, while the even numbered orifices are grouped together as Set 2. It is clear that the 10-orifice injector results agree well with Set 1 for both the 14 and 18-orifice injectors, while the Set 2 results also agree well with each other for the 14-orifice tips. The data represent an average over all plumes in the set over six shots, and thus this trend is repeatable, with each set of plumes exhibiting consistent behavior.

Because of the large number of orifices and the need to space them out around the tip to avoid stress problems on the sac interior, the 14 and 18-orifice nozzles have the orifices drilled on two rows. The orifices have the same included angle, but are at different heights in the sac. Thus, it appears likely that the geometry involved in the location and shape of these two rows leads to a substantially different spray plume geometry. Figure A3 shows the geometry of the spray orifices, with the lower row shown on the left side of the image and the upper row shown on the right half of the image. It is important to note that these two rows were evenly spaced such that every orifice on the upper row was directly between two orifices on the lower row. This phenomenon is somewhat surprising and unexpected, but potentially indicates flow field in the sac among the two rows of orifices or possibly manufacturing differences in the geometry of each of the two rows (which was not seen in x-ray tomography data). A reference in the literature (Payri et al. 2004) also showed similar differences in two row tips with a similar orifice pattern (two rows of orifices with a single included angle).

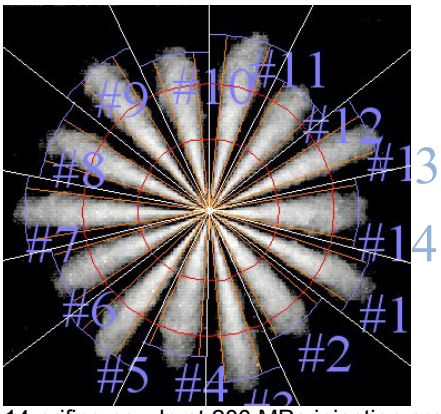

Fig. A1. Image of spray pattern for 14-orifice nozzle at 200 MPa injection pressure and chamber density of 25 kg/m^3

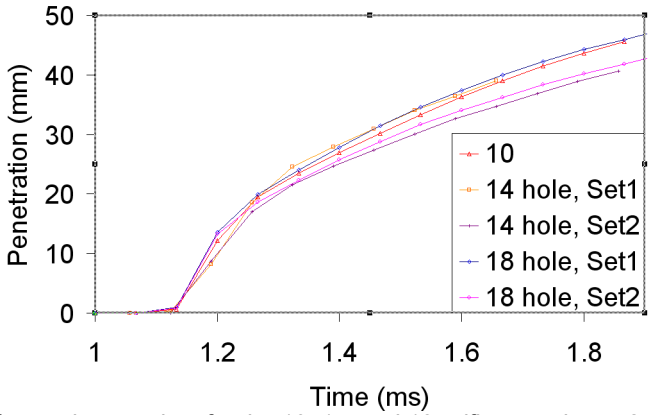

Fig. A2. Penetration of spray jets vs. time for the 10, 14, and 18-orifice nozzles at 25 kg/m3 chamber density and 200 MPa injection pressure, including both the upper row of orifices (Set1) and lower row of orifices (Set2)

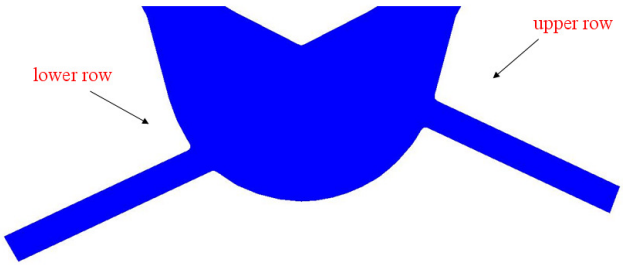

Fig. A3. Geometry of the flow region for the two-row nozzle

It is very difficult to measure differences in the flow pattern on the interior of these tips. However, computation fluid dynamics (CFD) can be used to examine the fuel flow within the nozzle to look for differences between the two orifices that lead to the difference in the observed spray pattern. Therefore xFD, Caterpillar's in-house three dimensional CFD code, was used to do a calculation of the flow in the nozzle. This code includes calculations to include possible cavitation of the fuel. The cavitation code has been validated against measurements of cavitation formation in optically accessible nozzles.

The geometry for the simulation was generated using the as-designed geometry for the part and adding an 18 micron radius (observed in x-ray measurements) on the inlet to simulate the effect of the hydrogrinding process. The boundary conditions of the simulation were set so that the area above the injector needle is exposed to approximately 200 MPa fuel, and the outlet of the orifices are exposed to the chamber pressure of 2.07 MPa. The exit velocity, mass flow rate, and fraction of the orifice exit area not effectively blocked by fuel vapor are shown in Figs. A4-6, respectively. The velocity plot shows that there is relatively little difference in velocity between the two rows. However, Fig. A5 shows a significant difference in mass flow rate (~3%). This difference in mass flow rate can be at-

tributed to differences in the cavitation behavior of these two nozzles, as shown in Fig. A6. This plot shows the effective blockage caused by cavitated fuel vapor at the exit of the nozzle, with the higher value indicating less blockage due to fuel vapor and cavitation. The two nozzles have similar exit velocities because they see the same upstream pressure, but the increased vapor present in the lower row leads to a lower mass fuel rate through those orifices.

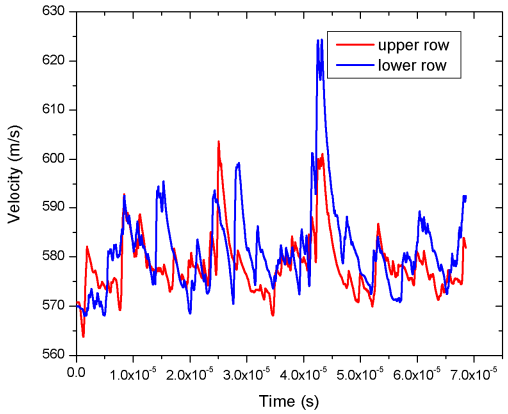

Fig. A4. Velocity at the exit of the nozzle from CFD calculations of the 14-orifice injector nozzle

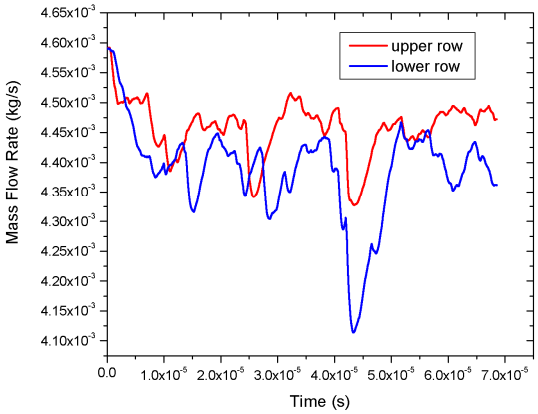

Fig. A5. Mass flow rate at the exit of the nozzle from CFD calculations of the 14-orifice injector nozzle

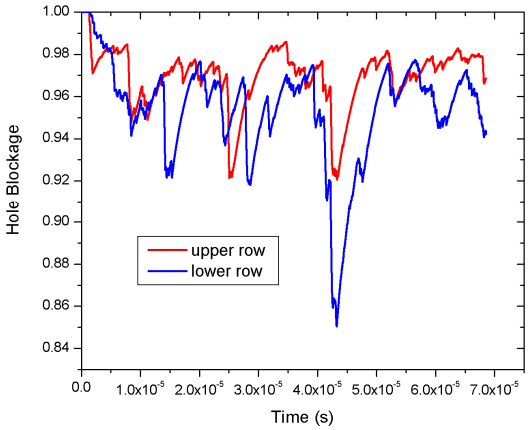

Fig. A6. The fraction of the orifice blocked by vapor at the exit of the nozzle from CFD calculations of the 14-orifice injector nozzle

Figure A7 shows the instantaneous pressure field in the nozzle. The low pressure regions near the entrance to the orifices are an indication of cavitation. The lower orifice clearly shows a lower

pressure as the fuel turns the corner to enter the orifice. The sharper corner turn is a result of the lower position of the orifice, and thus the importance of this entrance angle between the sac and orifice is illustrated. Additionally, these simulations suggest there are potential benefits of changing this angle through a differently-shaped sac.

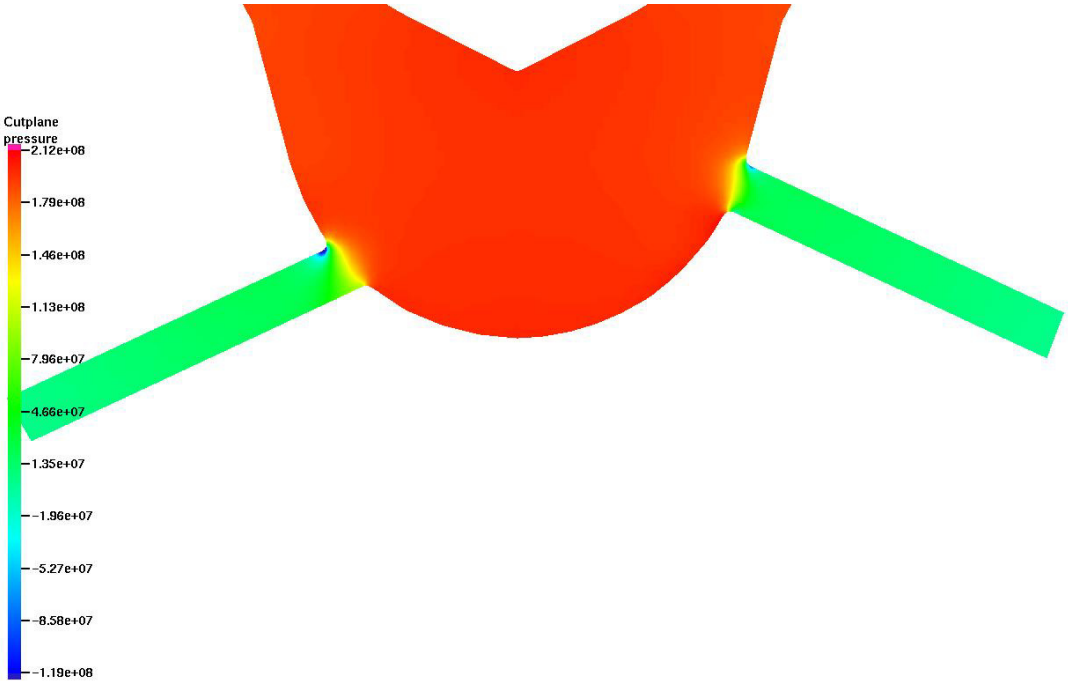

Fig. A7. Instantaneous look at the pressure field in the nozzle, showing a low pressure region in the lower orifice where cavitation occurs

These results agree qualitatively with the spray results presented earlier in that the increased cavitation observed in the lower orifice would lead to less penetration for that row of orifices. Cavitation will lead to less penetration through two primary mechanisms. First, a lower fuel rate through the orifice will lead directly to lower penetration because the jet has less mass. Second, the cavitation leads to an increase in the spreading cone angle of the jet, which has been observed in our lab and by various published studies (Blessing et al. 2003). This causes an increase in air entrainment and momentum transfer, thus causing less penetration by the jet. This study has illustrated the importance of the entrance angle into the orifice and has explained the spray pattern observed for the two-row injector tips. Because the 6, 8, 9, and 10-orifice tips used in this study all have similar interior nozzle geometry to the upper set of orifices, it is reasonable to compare these results with the upper row of spray jets for the 14 and 18-orifice tips as was done in the body of this paper.

Overview of Argonne Gasoline Compression Ignition Research: Progress and Approaches to Expand the Operating Regime

S. Ciatti

Argonne National Laboratory. 9700 South Cass Avenue, Bldg. 362. Argonne, IL 60439-4815. USA.

E-mail: sciatti@anl.gov

Abstract. Energy and environmental concerns have prompted the pursuit of advanced technologies for use in transportation. Low Temperature Combustion (LTC) engines are one viable pathway to improve conventional engine efficiency and reduce their pollutant formation. However, many LTC strategies create challenges in retaining the operating speed/load range of conventional engines. This presentation will highlight the effort at Argonne National Laboratory to expand and optimize the operating range for one exciting LTC strategy – Gasoline Compression Ignition (GCI). Leveraging high performance computing simulations and x-ray fuel injection characterization, Argonne researchers have achieved GCI operating range from idle to 20 bar BMEP load through the use of modified injector nozzles, and multiple injections, using 87 AKI gasoline running in a GM 1.9L turbodiesel engine. The methodology to achieve this wide load range will be covered, as well as future efforts to improve fuel efficiency.

Understanding soot optical properties through dual-wavelength diffused back-illumination imaging

J. Manin, S.A. Skeen and L.M. Pickett

Combustion Research Facility. Sandia National laboratories. 7011 East Ave, Livermore, CA.

E-mail: jmanin@sandia.gov

Abstract. Two-dimensional high-speed dual-wavelength diffused back-illumination imaging was applied to measure soot volume fraction produced by n-dodecane sprays injected in a constant-volume, high-pressure, high-temperature vessel. The fuel was injected with a common-rail diesel injector equipped with a single 90-µm diameter orifice belonging to the family of injectors used in the Engine Combustion Network (ECN). The experiments performed in this work used two wavelengths, which, when combined with the Rayleigh-Debye-Gans theory, can provide information about the optical and morphological properties of soot. Soot concentrations at engine-relevant conditions (high ambient pressure) have been obtained thanks to the diagnostic and have been seen to compare well with previous experiments from our group using laser extinction or laser-induced incandescence. Analysis of the extinction signals measured at two wavelengths indicated that the optical parameters and the choice of refractive index were not significantly affected by soot morphological parameters but rather by optical properties of soot. Especially, it has been observed that soot optical parameters were changing depending on the location in the flame and that using an invariant optical refractive index for soot throughout the entire flame was inappropriate for quantification of soot concentrations in two dimensions.

1. Introduction

Although direct-injection (DI) diesel engines have the capacity for significantly higher efficiencies than spark -ignited gasoline engines, they can be plagued by particulate matter (PM) emissions (mainly soot) formed in the fuel-rich regions of the combusting fuel jets. More stringent PM emissions standards for diesel engines have led to the use of additional exhaust after-treatment such as diesel particulate filters, which increase the cost of diesel engine production while negatively impacting fuel economy. A more economical approach to reducing soot emissions from DI diesel engines lies in the development of combustion strategies to reduce or eliminate soot in -cylinder. The successful development of such strategies, by experimental or computational means, can benefit from time-resolved, quantified measurements of soot volume fraction (f_v) as a function of the available operational parameters.

The Laser extinction method (LEM) and laser-induced incandescence (LII) represent the most commonly used in-situ optical diagnostics used to measure f_v in flames. In some cases, laser scattering measurements have been coupled to LEM measurements to obtain additional information about primary particles and aggregates [14]. While single-color LEM measurements alone can only provide information about f_v, soot particle cool-down with LII in conjunction with an accurate physical model can yield information about f_v and primary particle size. In both cases, knowledge of the particles' optical properties (i.e., refractive index) is required. The uncertainty in the refractive index of soot is well-documented and is generally accepted to be large [22]. The vast majority of LEM and LII measurements have been made at atmospheric pressure and under steady, laminar flame conditions.

Prior studies by our group have used 2-D planar LII in conjunction with path-averaged LEM to obtain quantitative f_v measurements during the quasi-steady period of spray combustion at pressures and temperatures relevant to diesel engines [13]. A weakness of 2-D planar LII comes from conditions when soot concentrations are high, producing an optically thick flame causing significant laser attenuation. The soot may not be heated up to the same temperature throughout the entire flame, which leads to reduced incandescence signals. Also, the LII signal from particles can be significantly reduced because of the presence of other soot particles in the path between the laser sheet and the detector, called signal trapping [12]. These two phenomena are not necessarily important under atmos-

pheric flames, but they quickly become predominant when the ambient pressure is increased, as in diesel engines.

The introduction of the dual-wavelength diffused back-illumination imaging diagnostic from our group [8] demonstrated the capability to measure soot in high pressure flames, in which the elevated soot concentration limits the reliability of the LII measurements. Also, the built-in calibration offered by the extinction-based technique, thanks to the initial intensity, makes implementation and calibration of this diagnostic easier than LII, for instance. The development of ultra-fast high-power LEDs combined with the progress in high-speed imaging made it possible to measure soot extinction in two dimensions as a function of time, thus providing transient and simultaneous information about soot formation and oxidation. We also used 3-D tomographic reconstruction of the soot field by assuming flame axisymmetry to provide a three-dimensional map of soot volume fraction. Manin et al. [8] demonstrated that shorter visible wavelengths have advantages when measuring soot concentration, because of the higher optical extinction cross-section and lower soot luminosity, making the signal-to-noise ratio of the measurements higher. They used the Rayleigh-Debye-Gans (RDG) theory to calculate the necessary optical parameters (dimensionless extinction coefficient of soot at both wavelengths) from morphological parameters obtained via soot sampling in similar pressure flames. They found that the differences in extinction between the two wavelengths across the soot field were better explained by change in refractive index of soot rather than by modifications of soot morphology (number of particles per aggregate). The results of the dual-wavelength experiments indicated that the refractive index of soot was wavelength-dependent, especially in the soot formation region in which the results implicated higher molecular absorption than the commonly used values. The implication of their results is expected to be significant when attempting to quantify soot volume fraction as noted by Dalzell and Sarofim [3] who found that relatively small changes in refractive index (both real and imaginary parts) have large impacts on extracted soot volume fraction.

In this work, we measured the 2-D temporal evolution of f_v in high-pressure spray flames using the high-speed dual-wavelength diffused back-illumination extinction technique. We also utilized RDG calculations to help us understand the behavior of the optical response of soot when changing parameters such as soot morphology or refractive index. Cross-comparisons between the optics theory and the dual-wavelength experiments confirmed that the morphological parameters of soot have little to do with the wavelength effects recorded throughout the flame, as reported by Manin et al. [8]. The results from the dual-wavelength imaging have been used to obtain the experimental dispersion exponent (also called Angstrom exponent), which is a measure of the difference in optical extinction with respect to wavelength. This metric accounts for wavelength dependencies upon soot optical properties, making it convenient for comparison to previously published results (e.g., [10, 17]).

2. Experimental apparatus

2.1 Constant volume vessel and injection system

An optically accessible high-pressure and high-temperature combustion vessel has been used for these experiments [18]. This vessel is a pre-burn type combustion chamber, which means that a combustible mixture of gases is ignited to reach the desired thermodynamic conditions at the time of injection. Prior to and during operation, the temperature of the entire vessel is maintained at 188^{o}C by electric heaters. Spark plugs ignite the combustible gas mixture to rapidly elevate pressure and temperature within the vessel. After ignition and combustion, the pressure and temperature decrease during a short cool-down period until the target conditions are reached and the spray is injected. At the time scales of the event (a few milliseconds), the conditions inside the chamber are considered constant and fine-wire thermocouple measurements in the chamber demonstrated the relatively uniform temperature distribution across the testing section.

This chamber is capable of simulating charge gas conditions over a wide range of operating pressures and temperatures (up to 35 MPa and 1400 K), including that of diesel engines at top-dead-center. The combustion chamber can be operated with different oxygen partial pressures to simulate the addition of exhaust gas into the intake port of an engine (EGR). Different ambient conditions have been performed for this test campaign: ambient temperatures from 700 to 1200 K, ambient densities

from 7.6 to 22.8 kg/m^3 and oxygen concentrations from 13 to 21 % (by volume). However, only a few operating points have been selected, for the interest and conciseness of this document. The reader is referred to Refs. [20, 9] for a more complete overview of the influence of various experimental parameters on measured soot volume fraction in diesel-like flames using this same diagnostic technique. These parameters include various fuels; ambient temperatures and pressures; and oxygen concentrations. The nearly cubical chamber is approximately 1-liter in volume and each side can be equipped with a window for optical access. Two spark plugs are mounted on one side of the cube to ignite the premixed gases. The fuel injector is mounted on another side of the chamber, leaving four sides for optical access to the event. Figure 1 provides visual information about the lay-out of the vessel and its optical accesses, as well as the optical diagnostics that are detailed later.

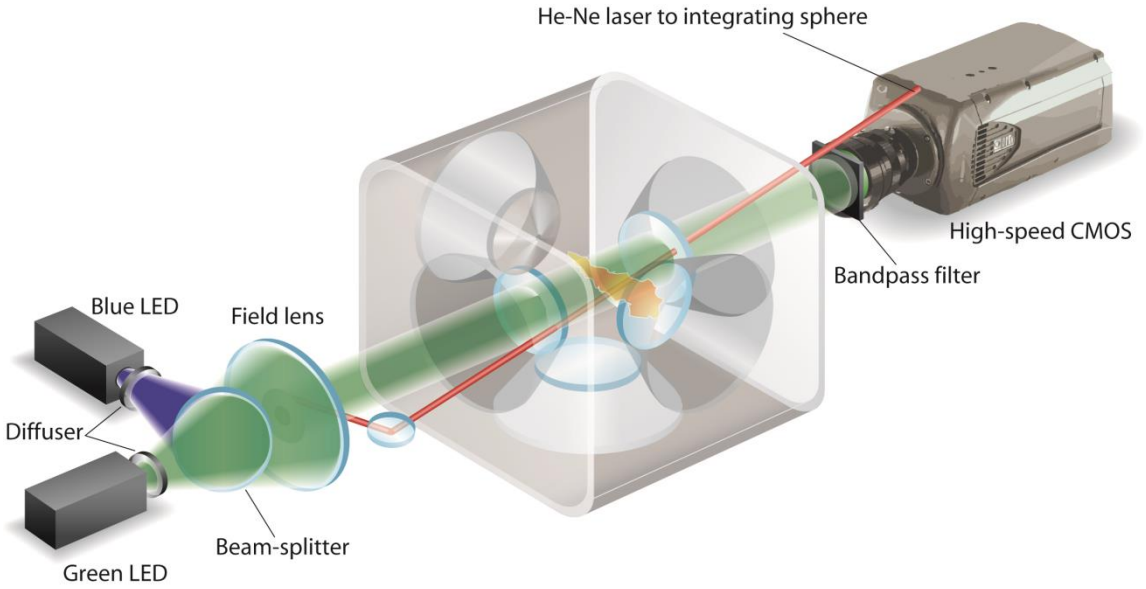

Fig. 1. Optically accessible combustion vessel in the center. The dual-wavelength diffused back-illumination optical arrangement with LED lighting (left) and high-speed imaging system (right)

A commercially available common-rail, solenoid-actuated injector equipped with a single-hole nozzle of 0.090 mm diameter has been used in this study. The axially drilled orifice has a converging conical shape (KS 1.5) and hydro-grinding has been performed to optimize flow and minimize cavitation. This injector (serial # 210370) is part of the ECN family of injectors (www.sandia.gov/ecn). The nozzle tip of the fuel injector is held at a constant temperature of 363 K during operation. The rest of the injection system is composed of a common-rail, high-pressure lines, and an air-driven fuel pump. Even though injection pressure has been varied to study the influence of this parameter on soot formation, all the results shown hereafter only correspond to an injection pressure of 150 MPa. High-grade n-dodecane has been used as a fuel to meet the standards of the ECN working group.

2.2 Dual-wavelength diffused back-illumination extinction imaging

The two-color, diffused, back-illumination diagnostic setup implemented in this work consists of a dual wavelength illumination source and a high-speed camera on opposing sides of the spray in a line-of-sight arrangement. High-output, ultra-fast, blue (406 nm, 17 nm FWHM) and green (519 nm, 34 nm FWHM) LED drivers have been developed in-house to make this experiment possible. Although the illumination spectra for both LEDs are somewhat broad, the wavelength dependence should be easily noticeable in the RDG calculations as the wavelength difference is substantial (more than 100 nm). Both LEDs are capable of short, high-power (in excess of 40 W peak power) pulses of light at repetition rates up to several megahertz. An LED pulse duration of 2 µs was chosen as a compromise between illumination intensity and speed sufficient to "freeze" the soot fields within high velocity sections of the fuel jet. Each LED passed through a 50° circular pattern engineered diffuser with the intent of creating Lambertian intensity profiles. A dichroic beam-splitter with a transition centered on 485 nm efficiently combined the two illumination sources into one virtually identical beam of light. A 150-mm diameter, 150-mm focal length Fresnel lens focused the light onto the testing section (i.e., the spray)

to create a relatively large (more than 60 mm in diameter), uniformly illuminated background. This arrangement aims at efficiently illuminating the sprays in environments subject to large density gradients (causing beam steering) with minimal light intensity losses (more than 90 % transmission).

On the side of the vessel opposite the illumination source, the high-speed camera (operating at 82.000 frames per second (kfps) for these tests) was equipped with a 50 mm f/1.2 Nikkor lens and a 500 D close-up lens to maximize the collection angle by allowing the camera to be placed closer to the spray. The exposure time was set to 1.3 µs in order to acquire the highest intensity period of the LED illumination. To effectively image the dual-wavelength extinction signals, a special combination of filters was placed in front of the camera objective. The filter transmits from 375 nm to 475 nm and from 500 nm to 565 nm (both measured at FWHM), resulting in a dual-bandpass filter transmitting the majority of the spectra from both the blue and the green LEDs. A neutral density filter of OD 2.1 was added to reject most of the broadband luminosity from the flame.

The concentration of soot is related to the amount of light that has been absorbed or scattered by the soot cloud. The two-dimensional extinction measurements were converted to optical thickness, *KL*, using the Beer-Lambert law:

$$\frac{I}{I_0} = \exp(-KL). \tag{1}$$

I and I_0 are the transmitted and incident intensities, respectively; *K* is the dimensional extinction coefficient and *L* the path length through the soot cloud. The soot concentration, or soot volume fraction, f_v, can be obtain from the *KL* extinction measurements as shown in Eq. 2:

$$f_v = \frac{K.\lambda}{k_e}, \tag{2}$$

where λ is the wavelength of the incident light and k_e the non-dimensional extinction coefficient. Note that both extinction coefficients (*K* and k_e) are wavelength-dependent. The dimensionless extinction coefficient can be obtained from the following relationship:

$$k_e = (1 + \alpha_{sa}) \cdot 6\pi \cdot E(m). \tag{3}$$

This relationship has been used in this study with the Rayleigh-Debye-Gans (RDG) theory, following the methodology described by Manin et al. [8], to compute the scattering-to-absorption ratio α_{sa}, which corresponds to the ratio of the scattering and absorption cross-sections. As introduced earlier and noted by many, the dimensionless extinction coefficient depends on the wavelength of the incident light. The refractive index function *E(m)* in Eq. 3 represents the imaginary part of $(m^2-1)/(m^2+2)$, in which *m* is the complex refractive index of the soot particles. This means that k_e depends upon the scattering-to-absorption ratio and the refractive index of soot.

3. Results and discussions

Images from the dual-wavelength soot diagnostic are presented first in this section, which lead to time and ensemble average extinction maps for both wavelengths. Similar measurements were used previously by Manin et al. [8] to compute the *KL* ratio used to analyze soot morphological and optical properties in conjunction with RDG calculations. Note that most of the data presented in this work has been obtained with an improved optical setup, aiming at rejecting natural luminosity even further. Comparable results and comments can still be found in Ref. [8], but the analysis carried out in the present work goes beyond what was done previously. This is the purpose of the second part of the results section which focuses on optical characteristics of soot, comparing extinction measurements acquired at two wavelengths to RDG calculations.

3.1 Soot optical extinction and soot volume fraction

A time-sequence of KL extinction images taken from the soot onset to the beginning of the period over which the flame and soot field are considered steady is shown in Fig. 2. In these images, the fuel injector is located on the left and the flame is propagating from left to right. The *KL* values in this figure correspond to extinction of the blue (406 nm) LED at an ambient temperature of 1000 K, an ambient density of 22.8 kg/m^3 and an O_2 mole fraction of 15 %. Under these conditions, soot is first detected at an axial location approximately 35 mm from the injector orifice less than 1 millisecond after the start of injection (ASOI), indicated at the top left corner of each time step. Though *KL* time-sequences are not shown here for the other ambient conditions studied, the axial distance from the injector orifice to the location where soot is first observed and the time to soot ASOI decrease with increasing temperature, density, and oxygen concentration.

The images in Fig. 2 show that a large amount of soot forms in the head of the jet as it propagates into the ambient. The soot cloud associated with the head also begins separating from the upstream soot cloud in the region between 50 and 60 mm at about 2 ms ASOI. At 2.75 ms ASOI, the head has completely separated from the upstream soot cloud. This occurs presumably due to rapid entrainment of the ambient oxidizer behind the jet head leading to a brief transient period of enhanced mixing and soot oxidation.

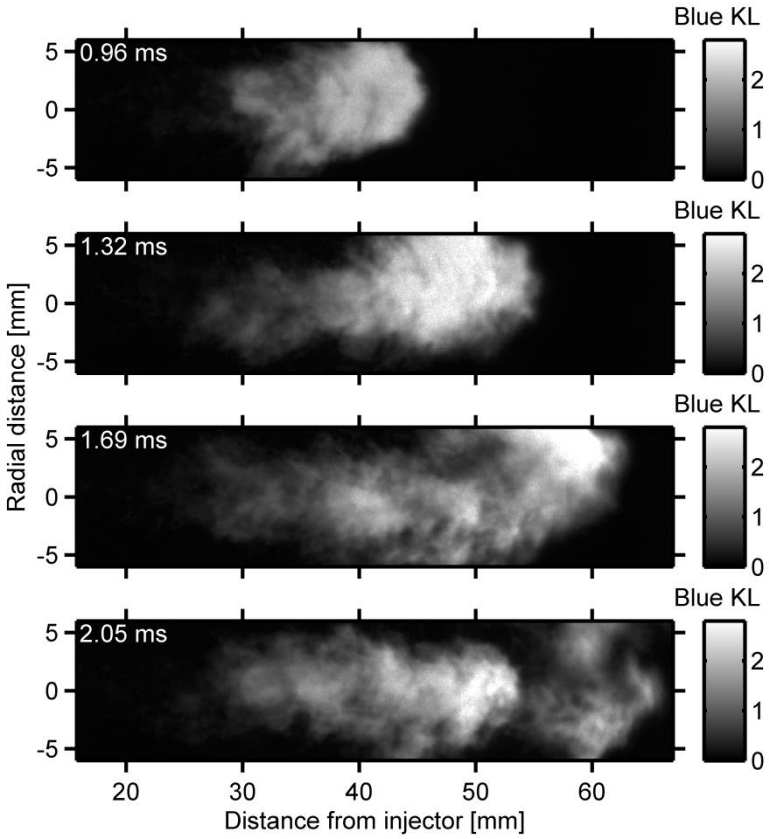

Fig. 2. Time-sequenced images of soot optical extinction (KL) as measured by the blue illuminations. Time after start of injection at upper left. (Ambient temperature is 1000 K, density is 22.8 kg/m^3 and oxygen mole fraction is 15 %)

The quasi-steady time period of the spray flame begins after the head of the jet passes through the camera's field of view and ends at injector closing. We determined *K* for use in Eq. 2 via tomographic inversion of time- and ensemble-averaged *KL* images from multiple identical injection events. Time-averaging was performed over the quasi-steady period of the flame (approximately 4 ms, representing more than 100 images per injection and per wavelength). Ensemble averaging included a minimum of 5 injections for each specific experimental condition. The averaged *KL* images result in a relatively smooth (i.e., free from stochastic variations) and nearly axisymmetric *KL* field as shown in Fig. 3. The scales on both maps are made different to enhance the dynamic range of the display. It can thus be noted that the extinction measured with the blue illumination is greater than that measured with the green. This difference comes from the larger extinction cross-sections in the blue,

mainly due to the larger molecular absorption of soot at shorter wavelengths. As argued by Manin et al. [8], the higher extinction levels measured by the blue extinction signal effectively increases signal-to-noise ratio as the noise sources (e.g., flame, beam steering) are expected to be similar for both wavelengths (note: the flame emission leaking through the dual-bandpass filter is recorded on both the blue and green images). On the other hand, the shorter illumination wavelength of the blue LED might suffer from absorption from soot precursors (polycyclic aromatic hydrocarbons or PAHs), expected in upstream regions. Imaging spectroscopy from our group did not show any evidence of extinction for wavelengths around 400 nm in the soot precursor region; but more analysis is needed in that regard to clearly discard potential effects of PAHs absorption.

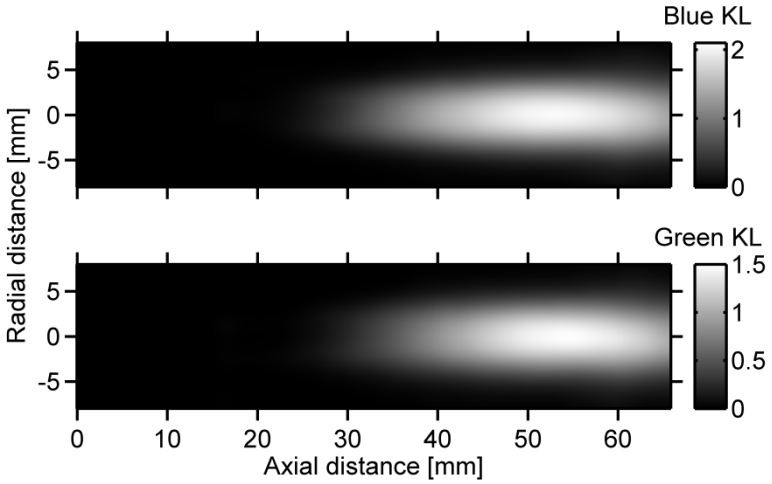

Fig. 3. Time- and ensemble-averaged map of soot optical extinction (KL) during the quasi-steady period as measured by the blue and green LED illuminations (1000 K, 22.8 kg/m^3 and 15 % O_2)

As mentioned in the introduction, the soot volume fraction has been obtained through tomographic reconstruction using an inverse Radon transformation to extract maps of the dimensional extinction coefficient K similarly to the method described in Ref. [8]. Some assumptions are required to extract soot volume fraction from extinction measurements, and these assumptions have been observed to have large impacts on soot quantities [3]. As detailed earlier based on the calculations from Manin et al. [8], the soot morphological properties, as well as their optical characteristics determine the value of soot concentration, depending on the choices made when converting from KL to f_v. The morphological properties of soot (such as primary particle diameter and number of particles per aggregate) have been obtained through soot sampling in similar flames [5, 8]. The optical properties of soot will be discussed in the following pages; however, initial parameters are required at this point to apply Eq. 2 and obtain f_v. The parameters used by Manin et al. [8] have been applied in this work as well and are given in Table 1.

Table. 1. Baseline morphological and optical parameters of soot and characteristics of the optical system

Parameters	**Values**
Fractal prefactor k_f	8.36
Fractal dimension D_f	1.77
Refractive index m	1.75-1.03i
Extinction coefficient k_e	7.76 (blue), 7.46 (green)
Scattering-to-absorption α_{sa}	0.10 (blue), 0.06 (green)
Aggregate size N_p	150
Particle diameter d_p [nm]	16
Collection angle [mrad]	162
Wavelength λ [nm]	406 (blue), 519 (green)

The values for k_f, D_f, N_p and d_p have been assigned based on the results of TEM soot sampling under similar conditions [5]. The morphological properties used in this study present reasonable agreement with other works reporting on soot sampled in diesel-like flames [7, 1]. The dimensionless

extinction coefficients k_e and the scattering-to-absorption ratio α_{sa} reported in Table 1 correspond to RDG calculations assuming a constant refractive index for both wavelengths. As detailed in the introduction, the experiments and calculations from Manin et al. [8] demonstrated that using identical optical properties for soot at both wavelengths everywhere across the entire soot field was incorrect. This aspect is going to be developed in the next section. Note that using the arithmetic mean to obtain an averaged primary particle size from the distribution might not be appropriate, but this is beyond the scope of this manuscript and the results presented later may mitigate the influence of morphological properties on optical properties for extinction-based soot quantification. Once the initial parameters (Table 1) are fixed, the wavelength dependence of soot extinction is used to investigate the impact of optical properties (refractive index) and morphology (aggregate size and particle diameter) on the measurements as discussed in the results section.

The three-dimensional soot volume fraction obtained by applying Eq. 2 with the blue and green extinction signals is shown in Fig. 4, in false color to highlight the gradients. Unlike Fig. 3 which was a path averaged map of optical extinction, the 2-D maps in Fig. 4 represent the soot volume fraction taken on a plane intersecting the jet or flame axis, obtained via tomographic (inverse Radon) reconstruction.

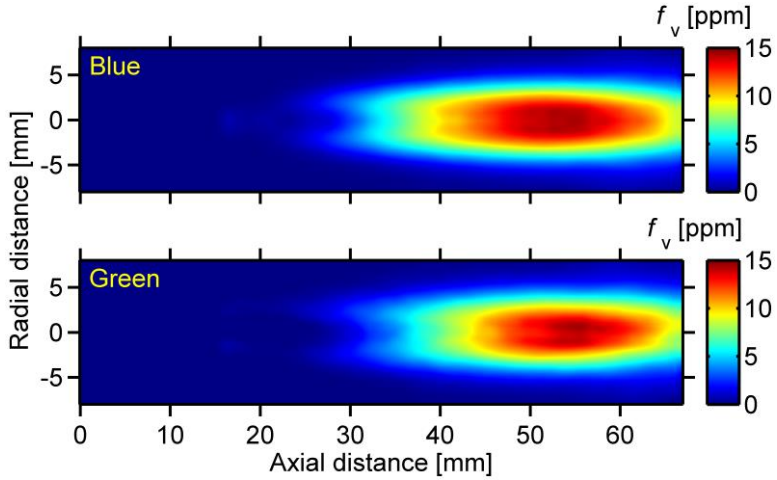

Fig. 4. Soot volume fraction on a plane corresponding to the axis of the flame as measured by the blue and green two-dimensional extinction signals and after tomographic reconstruction (1000 K, 22.8 kg/m^3 and 15 % O_2)

The soot volume fraction maps shown in Fig. 4 can be compared to LII experiments with the laser sheet crossing the flame on the jet axis. As observed in previous LII experiments for instance [13], we can notice the soot wings upstream (around 30 mm) as well as lower soot concentration in the middle of the jet until the maximum soot concentration measured around the flame axis between 50 and 55 mm downstream of the injector outlet. The wings and lower soot concentration in the central channel of the flame at upstream locations indicate that most of the soot is to be found on the periphery of the flame, rather than in the center. In their study, Manin et al. [8] observed some slight differences between the soot volume fraction measured with the blue illumination and that measured with the green LED, especially noticeable in upstream regions up to 40 mm downstream, as can be observed in Fig. 4. They attributed the mismatch to soot maturity and differences in optical characteristics, demonstrating the influence of soot optical properties (namely the refractive index), as mentioned earlier in this manuscript.

3.2 Optical properties of soot and dispersion exponent

As detailed in the introduction, recent work from Manin et al. [8] used the dual-wavelength soot extinction measurements coupled with Rayleigh-Debye-Gans calculations for fractal aggregates to investigate the impact of morphological and optical properties of soot and explain the non-uniformly distributed soot concentration (f_v) across the soot field. The study found that based on optics theory (RDG), the differences in extinction between the two wavelengths seemed to be better explained by variations in refractive index rather than by morphology-induced change in optical properties. The results of the dual-wavelength experiments indicated that optical properties of soot (refractive index)

were wavelength-dependent, especially in the soot formation region in which the results pointed toward higher molecular absorption than the commonly used values. The wavelength dependence of the refractive index of soot has generally been quantified by the dispersion exponent mentioned above. The dispersion exponent α, not to be mistaken for the scattering-to-absorption ratio α_{sa} , characterizes the impact of the illumination wavelength on the non-dimensional optical extinction coefficient (*K*) as defined by the following equivalence [3]:

$$\propto \equiv -\frac{\partial\, ln(K)}{\partial\, ln(\lambda)}. \qquad (4)$$

The logarithmic relationship between the extinction coefficient and the wavelength of the illumination ensued from soot extinction measurements by Rossler and Behrens [15], who found the logarithmic representation of their data to provide a nearly linear fit. For α to be equal to the right side of Eq. 4, the y-intercept of the curve fit must be found. For simplicity, this offset is not going to be considered in the present study, and as such, values of a may not be representative or comparable to other measurements. A wide spread in dispersion exponent can be found in the literature, and the real impact of soot characteristics on α is not yet fully understood. Siddall and McGrath [17] investigated the dispersion exponent of soot from several sources and found that using a constant α was satisfactory over the visible wavelength range. But their experiments were performed holding a disc in a small laminar diffusion flame, which may have perturbed the flame, in addition to providing information at a single location in the flame. At the same time, studies after Millikan's work [10], for instance, have demonstrated that the hydrogen-to-carbon ratio (H/C) of soot can significantly influence the optical properties of soot, including α [3, 17, 16]. These observations have been supported through extinction and scattering measurements of soot by D'Alessio et al. [2] in which H/C ranged from 0 to 0.5, corresponding to measured α variations from approximately 0.6 to 1.8, in the same order. All the aforementioned studies confirmed that higher α values are expected in regions where soot is nascent (high H/C), while lower α values, closer or below unity, are applicable for regions with more mature soot particles (low H/C).

Nevertheless, due to the lack of solid information about soot optical properties under specific flame conditions applied in engines (i.e., changing oxygen concentrations, fuels and ambient pressures), researchers have utilized correlations to estimate α as a function of wavelength for their experiments. However, such relationships do not account for changes in morphology, optical properties, or even maturity of the soot particles. Skeen et al. [19] computed the dispersion exponent using the correlation from Siddall and McGrath [17], with the constants proposed by Musculus [11] and found that α varied from 1.46 to 1.31 over the wavelength range of their spectroscopic data (366 to 700 nm, respectively). The dual-wavelength two-dimensional extinction measurements performed in this work may help understand the maturity of soot across the soot field based on the extinction maps measured at two wavelengths and correlate maturity with optical characteristics.

Figure 5 shows a map of the dispersion exponent as measured by the blue and green extinction signals and applying Eq. 5, which is a reformulation of Eq. 4, obtained after substitution of the soot volume fraction f_v with the thanks to the other wavelength term:

$$\alpha = -\frac{ln\left(\frac{K_b}{K_g}\right)}{ln\left(\frac{\lambda_b}{\lambda_g}\right)}. \qquad (5)$$

Here, the subscript *b* and *g* refer to the blue and green illumination wavelengths, respectively. Note that only the regions above an extinction level of *KL* = 0.1 (roughly equivalent to 1 ppm) for both wavelengths have been selected to compute α from the extinction signals. The pixel-by-pixel-based ratio to obtain such a map would highlight uncertainties coming from potential extinction signal misalignment from the two illumination sources. It must be noted that the map shown in Fig. 5 has been computed from the two-dimensional *KL* extinction, which are 1-D path-averaged measurements. As such, it can be argued that because the signals are the result of the contribution from the different lay-

ers of the soot field, as shown on the soot volume fraction plane mapped in Fig. 4, the dispersion coefficient displayed here corresponds to path-averaged quantities and may require further considerations for a thorough analysis.

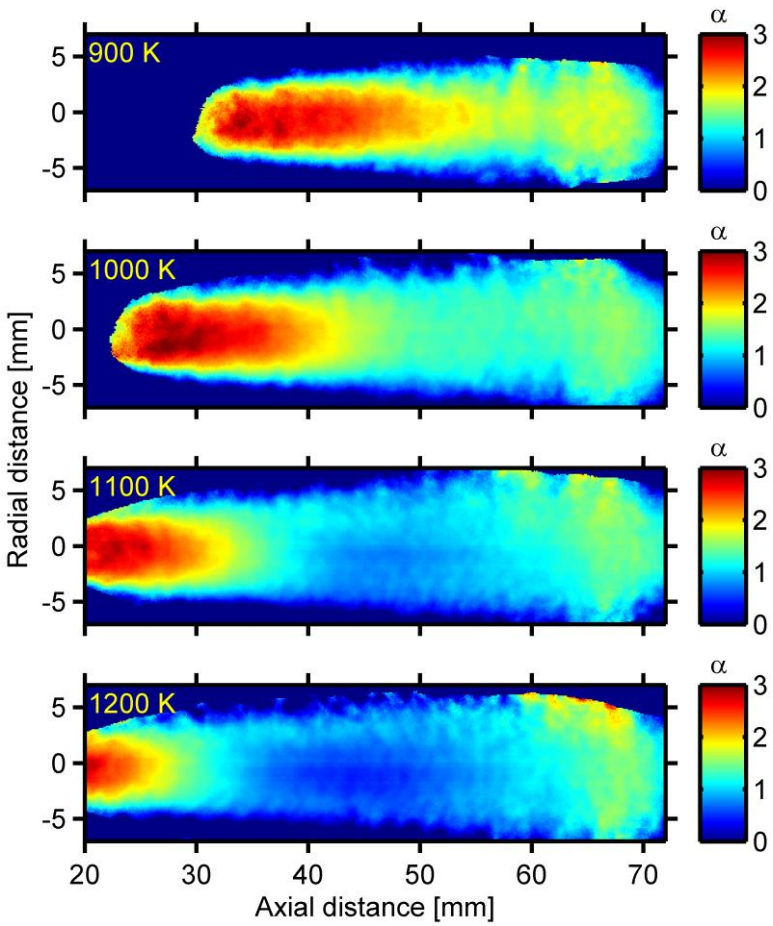

Fig. 5. Maps of the dispersion exponent obtained after applying Eq. 5 with the 2-D extinction signals measured with the dual-wavelength diffused back-illumination imaging system at different ambient temperatures (22.8 kg/m^3, 15 % O_2)

The map displayed in Fig. 5 shows higher values of the dispersion exponent in the upstream region for all ambient temperatures, while the values decrease with progression downstream in the flame. The area closer to the injector, where α values are higher (up to almost 3), corresponds to the region where soot is formed. Higher values of the dispersion exponent are anticipated in this region because the nascent soot expected there is known to exhibit higher H/C, which has been related to higher α values in previous studies [17, 2]. It is interesting to notice that the dispersion exponent values in this region are similar for the wide range of ambient temperatures tested in this campaign. After the soot formation region, the dispersion exponent decreases. This decrease in α can easily be associated with maturation of soot, as reported by D'Alessio [2] for instance. It is unclear at this point why differences in α are measured in this region between the different ambient temperatures: α around 1.5 have been measured at 900 K, while values around 0.5 were measured at 1200 K). It can be speculated that the optical properties as well as the structure of soot may induce such differences because of the temperature of the surrounding gases, impacting adiabatic flame temperature. Other reasons such as flame correction or camera negative image lag may explain these results; further investigation is needed in that regard. The region further downstream, near the tip of the soot field, where oxidation takes place, displays rising values of the dispersion exponent (1.5 to almost 2). Soot in this region being oxidized, changes in optical properties must be expected, as commented by Manin et al. [8]. It must be noted that because of the mathematical expression of the dispersion exponent (partial derivative of natural logarithmic quantities), the uncertainty surrounding α may be important. Error analysis will be addressed in future works, but it can be noted that the α quantities reported in the present investigation present relatively good agreement with previously published data.

The RDG approximation can be used in a similar fashion to the way Manin et al. [8] investigated the morphological and optical properties of soot using the calculation to provide a better understanding of these properties together with the application of the dual-wavelength diffused back-illumination imaging technique. The parameters listed in Table 1 have been used to vary the dispersion exponent (via variation of the dimensionless extinction coefficient) as with respect to the real and imaginary parts of the refractive index, the aggregate size, and the primary particle diameter. It must be mentioned that the Rayleigh-Debye-Gans theory for fractal aggregates (RDG-FA) only is an approximation of the light when scattered by small particles with non-spherical shapes such as soot aggregates (considered as fractal shape-like shapes). More information about the formulation of the RDG-FA theory as applied in this study can be found in Ref. [6]. Nevertheless, and despite the fact that disagreements among the community concerning modeling of soot optical extinction and scattering are still large, recent studies have demonstrated the validity of the RDG approximation [4, 23] under similar conditions.

As evident in Eq. 4, the dispersion exponent depends upon the complex refractive index of soot through the dimensionless extinction coefficient (Eq. 3), as well as the scattering-to-absorption ratio α_{sa}, which is affected by the soot morphological properties: primary particle size and number of particles per aggregate, as well as by the refractive index of soot. Figure 6 shows the results of RDG-FA calculations performed to obtain the dispersion exponent by varying the primary particle diameter and the number of primary particles per aggregate, while keeping the refractive index constant at *1.75-1.03i*. Note that all the calculations presented in this document assumed the parameters compiled in Table 1, except when the parameter is varied.

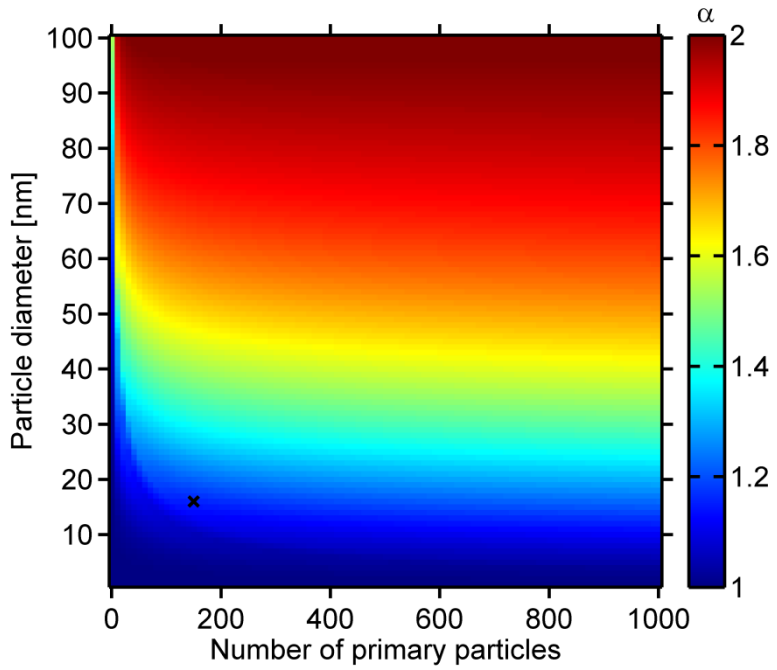

Fig. 6. Evolution of the dispersion exponent α as a function of the number of primary particles per aggregate and the primary particle diameter. The black cross corresponds to the morphological parameters listed in Table 1

The spread in the results of the calculations of α along the vertical direction means that the primary particle diameter has a significant impact on the difference between the dimensionless extinction coefficients at both wavelengths. This is believed to be caused by a progressive change in the light scattering regime of the soot particles' optical response: from Rayleigh to Mie. Such behavior is expected based on the optics theory (Mie) because the amount of scattered light increases exponentially with primary particle diameter, while the increase is linear with the number of particles per aggregate. This explains why increasing the number of particles per aggregate seems not to play a major role in the dispersion exponent, as demonstrated by the nearly constant α moving along the horizontal direction (e.g., from left to right). As an example, tripling the number of particles per aggregate from the initial number (from 150 to 450) results in a 20-25 % increase in α, a far smaller increase than the variations observed in Fig. 5. Note that the RDG-FA calculations may also induce errors in this case

because of the way the effective extinction cross-section of the soot particles aggregate is approximated. Further effort is needed to confirm the validity of the RDG-FA over the range of parameters varied in this study to complement the work of Zhao and Ma [23].

The implication of the results presented in Fig. 6 on soot is expected to be limited because the primary particle diameter has been seen to be relatively constant across the flame, while the number of primary particles per aggregate varies widely [5]. Similar behavior has already been observed through calculations using the RDG-FA theory and a similar methodology by Manin et al. [8] for the *KL* ratio. Based on the results from Fig. 6 and the different parameters impacting the extinction coefficient of soot (see Eq. 3), we anticipate similar conclusions concerning k_e when soot particle morphological parameters are varied. The limited variations plotted in Fig. 6 for the dispersion exponent does not mean that morphological properties have little impact on soot optical characterization. Changes in morphological properties across the flame are simply unlikely to result in excessive errors when measuring soot via light extinction. Nevertheless, accurate knowledge of morphological properties is necessary to correctly estimate k_e, used to compute soot volume fraction (see Eq. 2).

As described earlier regarding Eq. 3, k_e is affected by the refractive index of soot. To investigate the impact of refractive index on α, both the real and imaginary parts of the complex refractive index have been varied, covering wider ranges than those typically found in the literature. Figure 6 shows the results of α as a function of refractive index. The mapping lays out the real component of the complex refractive index of soot on the horizontal axis, while the vertical axis corresponds to the imaginary part. As for Fig. 6, the parameters of Table 1 were used for the calculations.

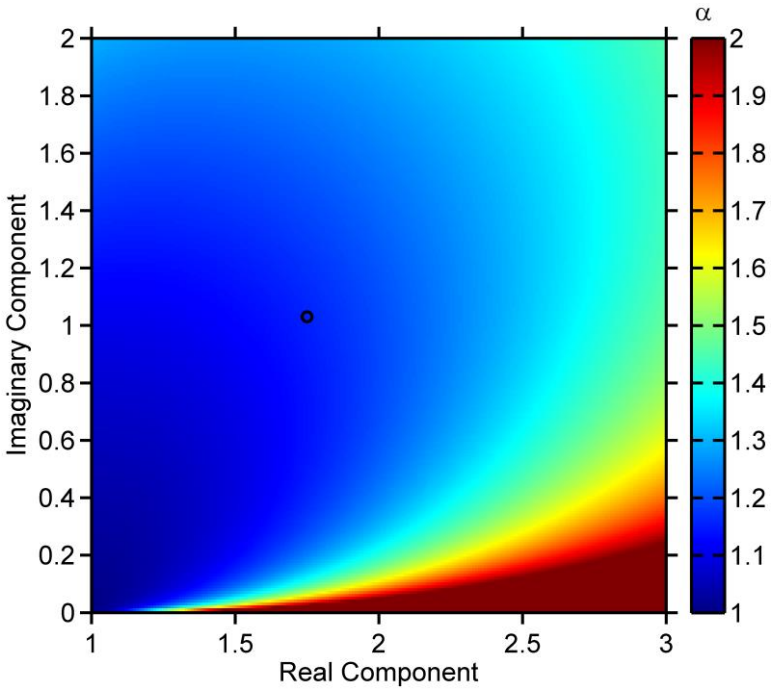

Fig. 7. Map of the dispersion exponent α as a function of the real and imaginary parts of the complex refractive index of soot. The black circle corresponds to the refractive index listed in Table 1

Over the range of complex refractive index considered in Fig. 7, the variations in α are limited, even more so when we take into account the range typically found for soot optical refractive index available in the literature. Typical refractive index values used for soot extinction-based measurements would limit the space on Fig. 7 from around 1.5 to 2.0 on the horizontal axis (real part), and 0.5 to 1.0 on the vertical axis (imaginary part). Such space limits α values to a range of approximately 1.1 to 1.2.

Comparing the dispersion exponent mapped in Fig. 5 to the value listed in Table 1 or the limited change achieved by varying morphological and optical parameters (Figs. 6 and 7) highlights the need for a different explanation concerning the variations in soot optical properties across the flame. The dispersion exponent as calculated from the RDG-FA approximation using the morphological and

optical parameters of Table 1 varied across typical refractive index values (Fig. 7) is unlikely to be appropriate in the soot formation region, where the measured dispersion coefficient shows values ranging from approximately 2 to almost 3 (Fig. 5). These results confirm the conclusions from Manin et al. [8] that the refractive index of soot must be modified depending on illumination wavelength and position in the flame.

Additional calculations have been performed with a constant refractive index of soot for the blue illumination, but with a variable refractive index for the green illumination wavelength. As anticipated after the work from Manin et al. [8], such an approach should yield different results than the map displayed in Fig. 7. Figure 8 shows the dispersion exponent as a function of the relative difference between the complex refractive index of the two illuminations by taking the ratio of the refractive index used for the blue (constant) over that used for the green (varied). Note that because the real part of the refractive index of soot cannot have values below unity, the ratio for the real component is taken as:

$$\text{Relative difference (Real)} = \frac{n_1 - 1}{n_2 - 1}, \tag{6}$$

with n_1 and n_2 corresponding to the real part of the refractive index soot for the blue and green illuminations, respectively. The relative difference for the imaginary part is simply computed by doing the ratio of the imaginary parts κ_1 and κ_2:

$$\text{Relative difference (Imaginary)} = \frac{\kappa_1}{\kappa_2}. \tag{7}$$

The black circle indicates no change in refractive index between blue and green illuminations. It also represents the baseline α, based on the RDG calculations. As noted earlier, using an invariant refractive index to measure and quantify soot from extinction across the flame is incorrect (especially in the soot formation region), regardless of the value, as shown by the limited α variation mapped in Fig. 7. The refractive index of soot for the blue extinction signal taken as the baseline constant is the value listed in Table 1: *1.75-1.03i*.

The dispersion exponent map shown in Fig. 8 demonstrates that slight changes in refractive index between the two wavelengths yields huge variations in optical response. It is important to remember that because the dispersion exponent is directly related to the dimensionless extinction coefficient (Eq. 4), both these parameters are linked, as are the variations mapped in Fig. 8. An inappropriately selected refractive index of soot would affect soot volume fraction quantification widely, as already mentioned earlier in the paper and reported by Dalzell and Sarofim [<dalzell1969>] 45 years ago. For instance, assuming the refractive index listed in Table 1 for the blue wavelength, while using the commonly used refractive index value of *1.57-0.56i* [21] for the green extinction measurements would induce a difference in the dimensionless extinction coefficient of approximately 50 %; in other words, the soot volume fraction quantities would now be reduced by half.

The two-dimensional dispersion exponent maps of the soot field shown in Fig. 5, together with the results of the calculations plotted in Fig. 8 confirms the conclusions from Manin et al. [8] regarding the relationship between refractive index of soot and location in the flame: the refractive index must be varied when probing the soot formation region. Based on the results of Fig. 5, in the soot formation region (upstream of 40 mm), where soot aggregates with high H/C are expected, the dispersion exponent increases and thus, the refractive index of soot should be moved toward the top left corner or along the orange arc on Fig. 8. Because of the relatively high imaginary component of the refractive index used in this work compared to other studies available in the literature, a decrease in the real component may be more appropriate (moving to the left in Fig. 8). Real component values of the refractive index in the range of 1.4 to 1.5 would match α from the experiments in the soot formation region seen in Fig. 5. Note that changing the constant refractive index of soot when measured with the blue extinction to the *1.57-0.56i* cited before changes the contours of Fig. 8 by relocating the black circle closer to the bottom of the arc. This case would now call more for a slight decrease in the real component of the refractive index and a larger increase in the imaginary component, closer to the value listed in Table 1.

A similar trend can be hypothesized for the refractive index of soot probed in the oxidation region. The growth in α in this region being smaller, an increase in the imaginary part of the complex refractive index of soot can also be theorized. In any case, the refractive index should be located along the green-colored arc plotted in Fig. 8. Concerning the central region of the flame, where soot is expected to be mature, the possibilities for modification of the refractive index are numerous, and depend upon ambient temperature as discussed after Fig. 5. At lower ambient temperature, α decreases after formation down to a leveling off value, until the flame tip, meaning that soot maturation and oxidation regions are merged as optical properties of soot (α) are concerned. At higher temperature though, it has been seen that α decreases in the soot maturation region and then increases again in the oxidation region. Values in the central region of the flame at the highest ambient temperature tested (1200 K) have been observed to be slightly above 0.5. From Fig. 8, the most likely path toward lower α would be a reduction in the imaginary term of the refractive index, i.e., lower molecular absorption.

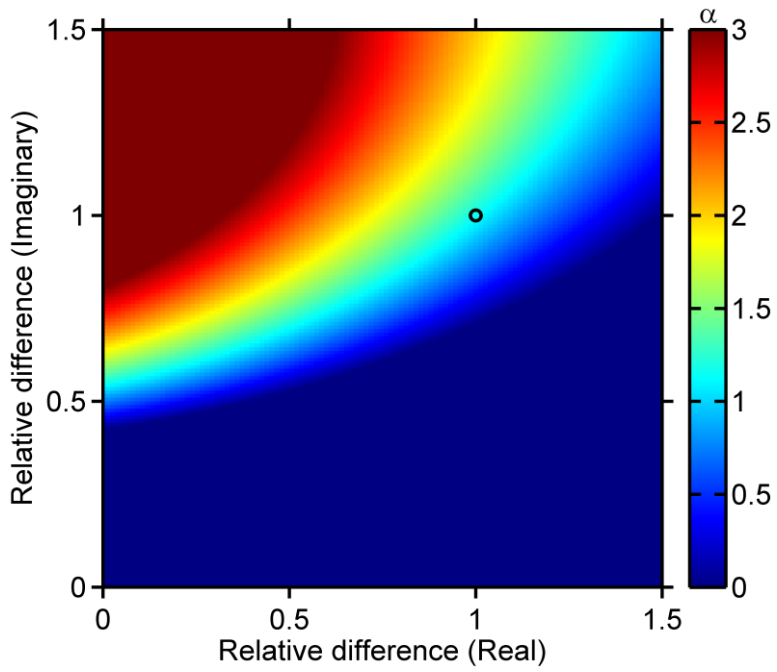

Fig. 8. Evolution of the dispersion exponent α as a function of the relative difference for the real and imaginary parts of the complex refractive index of soot between the blue and green illumination wavelengths. The black circle corresponds to the initial refractive index (baseline): *1.75-1.03i*

As detailed above, the approach of using 1-D path averaged extinction measurements may only be valid in the formation and oxidation regions, where soot structure and maturity are expected to be more uniform. Future experiments will concentrate on transient soot formation and oxidation processes by generating enough statistics to obtain valid time-resolved 3-D soot volume fraction data via tomographic reconstruction of the dual-wavelength diffused back-illumination images. The tomographic reconstruction of K can potentially be used to extract information about α or k_e in three dimensions to provide guidance regarding soot maturity and optical parameters as a function of space and time in diesel-like diffusion flames.

Conclusions

In this work, we measured soot volume fraction using a recently developed high-speed, 2-D, dual-wavelength extinction technique. The extinction setup uses high intensity, ultra-fast LEDs in conjunction with engineered diffusers and a field lens to produce pulsed, highly efficient diffused back-illumination. The diffused incident light greatly reduces the effects of beam steering, such that over the quasi-steady period of injection, the observed extinction due to beam steering is near zero. The use of two wavelengths and the comparison between the measurements of the dispersion exponent and calculations using the Rayleigh-Debye-Gans approximation for fractal aggregates have shown that mor-

phological properties of soot do not play a major role on the discrepancies of optical extinction measured throughout the flame. However, the results do not diminish the importance of accurate knowledge about soot morphological properties when attempting to measure soot quantitatively via extinction-based measurements. Rather, the differences in extinction between the two wavelengths seem to be better explained by variations in refractive index in certain regions such as soot formation or oxidation, as supported by the higher dispersion exponent measured in these regions. The analysis aimed at lower values of the real component of the refractive index of soot and higher imaginary term in the soot formation and oxidation regions, compared to the baseline refractive index. The central part of the flame had to be ignored in this study because of the more complex and multi-layered soot structure but future works will focus on the core region of flame as well. These results are only preliminary and additional measurements are needed to understand optical properties of soot; this will lead to better quantitative soot volume fraction measurements in two or three dimensions.

References

[1] T. Aizawa, H. Nishigai, K. Kondo, T. Yamaguchi, J.-G. Nerva, C. Genzale, S. Kook, and L. Pickett. Transmission electron microscopy of soot particles directly sampled in diesel spray flame-a comparison between us# 2 and biodiesel soot. *SAE International Journal of Fuels and Lubricants*, 5(2):665–673, 2012.

[2] A. D'alessio, F. Beretta, and C. Venitozzi. Optical investigations on soot forming methane-oxygen flames. *Combustion Science and Technology*, 5(1):263–272, 1972.

[3] W. H. Dalzell and A. F. Sarofim. Optical constants of soot and their application to heat-flux calculations. *J. Heat Transfer*, 91(1):100–104, 1969.

[4] A. C. Garcia-Lopez, A. D. Snider, and L. H. Garcia-Rubio. Rayleigh-Debye-Gans as a model for continuous monitoring of biological particles: Part I, assessment of theoretical limits and approximations. *Optics express*, 14(19):8849–8865, 2006.

[5] S. Kook and L. M. Pickett. Soot volume fraction and morphology of conventional, fischer-tropsch, coal-derived, and surrogate fuel at diesel conditions. *SAE International Journal of Fuels and Lubricants*, 5(2):647–664, 2012.

[6] U. O. Koylu and G. M. Faeth. Optical properties of overfire soot in buoyant turbulent diffusion flames at long residence times. *Journal of heat transfer*, 116(1):152–159, 1994.

[7] U. O. Koylu, C. S. McEnally, D. E. Rosner, and L. D. Pfefferle. Simultaneous measurements of soot volume fraction and particle size/microstructure in flames using a thermophoretic sampling technique. *Combustion and Flame*, 110(4):494–507, 1997.

[8] J. Manin, L. M. Pickett, and S. A. Skeen. Two-color diffused back-illumination imaging as a diagnostic for time-resolved soot measurements in reacting sprays. *SAE Paper 2013-01-2548 - SAE Int. J. Engines*, 6:1908–1921, 2013.

[9] J. Manin, S. Skeen, L. Pickett, E. Kurtz, and J. Anderson. Effects of oxygenated fuels on combustion and soot formation/oxidation processes. *SAE Paper 2014-01-2657*, 2014.

[10] R. C. Millikan. Optical properties of soot. *J. Opt. Soc. Am.*, 51(6):698–699, 1961.

[11] M. P. B. Musculus. Measurements of the influence of soot radiation on in-cylinder temperatures and exhaust NOx in a heavy-duty DI diesel engine. *SAE Paper 2005-01-0925*, 2005.

[12] L. M. Pickett, J. A. Caton, M. P. B. Musculus, and A. E. Lutz. Evaluation of the equivalence ratio-temperature region of diesel soot precursor formation using a two-stage lagrangian model. *International Journal of Engine Research*, 7(5):349–370, 2006.

[13] L. M. Pickett and D. L. Siebers. Soot in diesel fuel jets: effects of ambient temperature, ambient density, and injection pressure. *Combustion and Flame*, 138(1-2):114–135, 2004.

[14] R. Puri, T. F. Richardson, R. J. Santoro, and R. A. Dobbins. Aerosol dynamic processes of soot aggregates in a laminar ethene diffusion flame. *Combustion and flame*, 92(3):320–333, 1993.

[15] F. Rossler and H. Behrens. Bestimmung des absorptionskoeffizienten von russteilchen verschiedener flammen. *Optik*, 6:145–151, 1950.

[16] C. R. Shaddix, A. B. Palotas, C. M. Megaridis, M. Y. Choi, and N. Y. C. Yang. Soot graphitic order in laminar diffusion flames and a large-scale jp-8 pool fire. *International Journal of Heat and Mass Transfer*, 48(17):3604–3614, 2005.

[17] R. G. Siddall and I. A. McGrath. The emissivity of luminous flames. *Symposium (International) on Combustion*, 9(1):102–110, 1963.

[18] D. L. Siebers. Liquid-phase fuel penetration in diesel sprays. *SAE Transactions*, 107:1205–1227, 1998.

[19] S. Skeen, J. Manin, L. Pickett, K. Dalen, and A. Ivarsson. Quantitative spatially resolved measurements of total radiation in high-pressure spray flames. *SAE Paper 2014-01-1252*, 2014.

[20] S. A. Skeen, J. Manin, K. Dalen, and L. M. Pickett. Extinction-based imaging of soot processes over a range of diesel operating conditions. *8th U. S. National Combustion Meeting*, 2013.

[21] K. C. Smyth and C. R. Shaddix. The elusive history of m = 1.57–0.56 i for the refractive index of soot. *Combustion and flame*, 107(3):314–320, 1996.

[22] C. M. Sorensen. Light scattering by fractal aggregates: A review. *Aerosol Science & Technology*, 35(2):648–687, 2001.

[23] Y. Zhao and L. Ma. Applicable range of the Rayleigh-Debye-Gans theory for calculating the scattering matrix of soot aggregates. *Applied optics*, 48(3):591–597, 2009.

Experimental and numerical kinetic characterisation of n-heptane oxidation

M.H. Hakka[1]*, R.F. Cracknell[1], A. Pekalski[1], P.-A. Glaude[2], F. Battin-Leclerc[2]

[1]Shell Global Solutions, Concord business Park, Threapwood Road, Manchester M22 0RR, United Kingdom

[2] Laboratoire Réactions et Génie des Procédés, CNRS, Université de Lorraine, 1 rue Grandville, BP 20451, 54001 Nancy Cedex, France.

E-mail: Hichem.Hakka@Shell.com
Telephone: +(44) 161 499 4891

Abstract. Oxidation of normal heptane, a potential diesel surrogate fuel, has been investigated in a jet-stirred reactor under rich mixture conditions, from low to high temperature (550-1100 K), and at atmospheric pressure. A detailed kinetic mechanism has been developed using computer-aided generation (EXGAS), including a C_0-C_6 reaction base. The mechanism has allowed a good prediction of the experimental results obtained. Data from the literature measured in a jet-stirred reactor at 10 atm have also been correctly modeled. A considerable prediction improvement is obtained compared to the existing kinetic mechanisms. The model provides a better characterisation of the chemistry in the rich portion of a diesel spray.

1. Introduction

n-Heptane is one of the two primary reference fuels used for the rating of the octane index of gasolines. It is also a component of commercial gasoline, and a potential surrogate for the n-alkanes present in diesel and jet fuels [1]. Therefore, the oxidation of n-heptane has been the subject of many kinetic studies [2] [3].

However, very few detailed experimental and computed studies of the oxidation of n-heptane with product analysis cover the fuel rich mixture conditions relevant to the combustion of the automotive diesel engines. As shown by the work of Kosaka et al. [4], the auto-ignition of diesel fuel starts, usually, in the rich mixture pocket after fuel injection. Furthermore, in the rich premixed reaction zone, partial oxidation of the fuel yields hydrocarbon fragments that become the building blocks of soot particulates inside the engine [5].

Chakir et al. [6] studied the oxidation of n-heptane using a jet-stirred reactor (JSR) in the temperature range of 950-1200 K at atmospheric pressure for equivalence ratios (from 0.2 to 2), and inlet fuel mole fractions of 0.0015 and 0.002.

JSR experimental investigations of n-heptane oxidation were also conducted by Dagaut et al. [7] at temperatures from 550 to 1150 K, at 1013.25 kPa (10 atm), equivalence ratios from 0.3 to 1.5, and an initial n-heptane mole fraction of 0.001. Several products were quantified as a function of temperature, such as carbon oxides, C_1-C_2 species and alkenes. The authors detected 2-methyl-5-ethyl-tetrahydrofuran (cis and trans) and 2-methyl-tetrahydrofuran.

Simon et al. [8] have studied the oxidation of n-heptane in a jet-stirred reactor for an equivalence ratio of 5.5, an inlet fuel mole fraction of 0.0909, a constant temperature of 923 K and residence times from 0.1 to 0.9 s at sub-atmospheric pressure of 29.33 kPa (220 Torr). They quantified carbon oxides, olefins, water, acetaldehyde, and propanal. However, the profiles of reactants were not reported. Hence, the carbon balance could not be verified. Note that due to the very low pressure in this work, the data were not used for validation in the current study.

As part of a continuing effort to get better understanding of hydrocarbon oxidation chemistry in a wide range of conditions, we have experimentally and numerically investigated the kinetics of n-heptane from low to high temperature (550-1100K) in a JSR for a fuel rich mixture, $\varphi = 3$. The results will help to better understand the rich reaction zone formed by different low-temperature combustion (LTC) and conventional diesel strategies.

2. Experimental method

The experimental study of the oxidation of n-heptane has been performed with an apparatus which has already been used for the studies of the thermal decomposition and the oxidation of organic compounds [9][10], and more recently for the study of the stoichiometric oxidation of n-heptane [3].

The oxidation of n-heptane was carried out in a JSR with an internal volume of 86.5 cm^3. The reactor, made of fused silica, is operated at a constant temperature and pressure. Experiments were performed at a temperature range of 550 to 1100K, a constant pressure of 800 Torr (1.06 bar), an equivalence ratio of 3, with fuel mole fraction of 0.005, at a residence time of 2 s. n-Heptane was provided by VWR International (purity ≥ 99%), and helium and oxygen by Messer (purity of 99.999% for He and 99.995% for O_2).

The heating of the reactor was achieved by means of electrically insulated resistors directly coiled around the vessel. Temperature was measured by using a thermocouple located inside the reactor in a glass finger. In order to obtain a spatially homogenous temperature inside the reactor, reactants were preheated at a temperature close to the reaction temperature. Residence time in the preheating section was approximately 1% of the total residence time. Despite the exothermicity of the reaction, the temperature gradient in the vessel was lower than 5 K.

The liquid reactant flow was regulated by a Coriolis liquid flow controller, mixed to the carrier gas, helium, and then evaporated by passing through a single pass heat exchanger. Carrier gas and oxygen flow rates were controlled by gas mass flow controllers. The fuel/oxygen/helium mixtures were premixed prior the introduction into the reactor. The accuracy of the liquid and gas flow rates was around 0.5%.

The outlet products were analyzed online by gas chromatography thanks to a heated transfer line (at around 473 K) between the reactor outlet and the chromatograph sampling valve which was also heated. This temperature was high enough to avoid condensation.

Three gas chromatographs were used for the quantification of the different species. The first gas chromatograph, equipped with a Carbosphere packed column, a thermal conductivity detector (TCD) was used for the quantification of O_2, CO, and CO_2. Whilst hydrogen and water were detected in GC-MS, they were not quantified. The second GC was fitted with a PlotQ capillary column, a methanizer, and a flame ionization detector (FID) and was used for the quantification of molecules from methane to reaction products containing up to 5 carbon atoms and of small oxygenated compounds. Note that the methanizer allowed the quantification of formaldehyde by FID. The third GC was fitted with a HP-5 capillary column and a FID, and was used for the quantification of hydrocarbons and oxygenated species with more than five heavy atoms (i.e. carbon and oxygen atoms). The identification and the calibration of light species (e.g. carbon oxides, C_1-C_4 hydrocarbons) were performed by injecting gaseous samples. The identification of species which were not available was performed using a fourth gas chromatograph coupled with a mass spectrometer (GC-MS) operating under the same conditions as the gas chromatograph used for the quantification, enabling the direct comparison of both chromatograms. The mass spectra of all detected reaction products were included in the spectra database “NIST 08”.

The calibration was performed by injecting known amounts of the pure substances when available, otherwise the method of the effective carbon number was used (species having the same number of carbon atoms and the same functional groups were assumed to have the same response in the FID). The detection threshold was about 1 ppm for the heaviest species (FID) and about 100 ppm for carbon oxides and oxygen (TCD). Based on the repeatability of the experiments, uncertainty estimates on obtained mole fractions were about ± 10% (measured reading).

2. Experimental results

The experimental results were obtained at an equivalence ratio of 3, a n-heptane mole fraction of 0.005, at a residence time of 2 s. Numerous oxidation products were quantified. They are classified as follow:

- carbon oxides,
- olefins and poly-unsaturated hydrocarbons: methane, ethane, ethylene, acetylene, propene, propane, allene, propyne, 1-butene, 1-pentene, 1-hexene, heptanes isomers, 1,3-butadiene,
- aromatic hydrocarbons: benzene (traces, below 5 ppm),

- oxygenated species: formaldehyde, acetaldehyde, acrolein, propanal, 2-ethyl 5-methyl tetrahydrofuran (cis and trans), and 2-propyl tetrahydrofuran

The results displayed in Fig. 1 and 2 show that below 600K, a low temperature oxidation of n-heptane takes place with the formation of CO, CO_2, and oxygenated species. A large fraction of hydrocarbon (about 40% of the initial fuel) is converted. This corresponds to the so-called cool-flame region. From 600 to 800K, the negative temperature coefficient (NTC) zone starts leading to a decrease of the reactivity. Above 800K, the high temperature oxidation of n-heptane occurs with the rapid production of CO, CO_2, and saturated and unsaturated hydrocarbons until the complete consumption of the fuel.

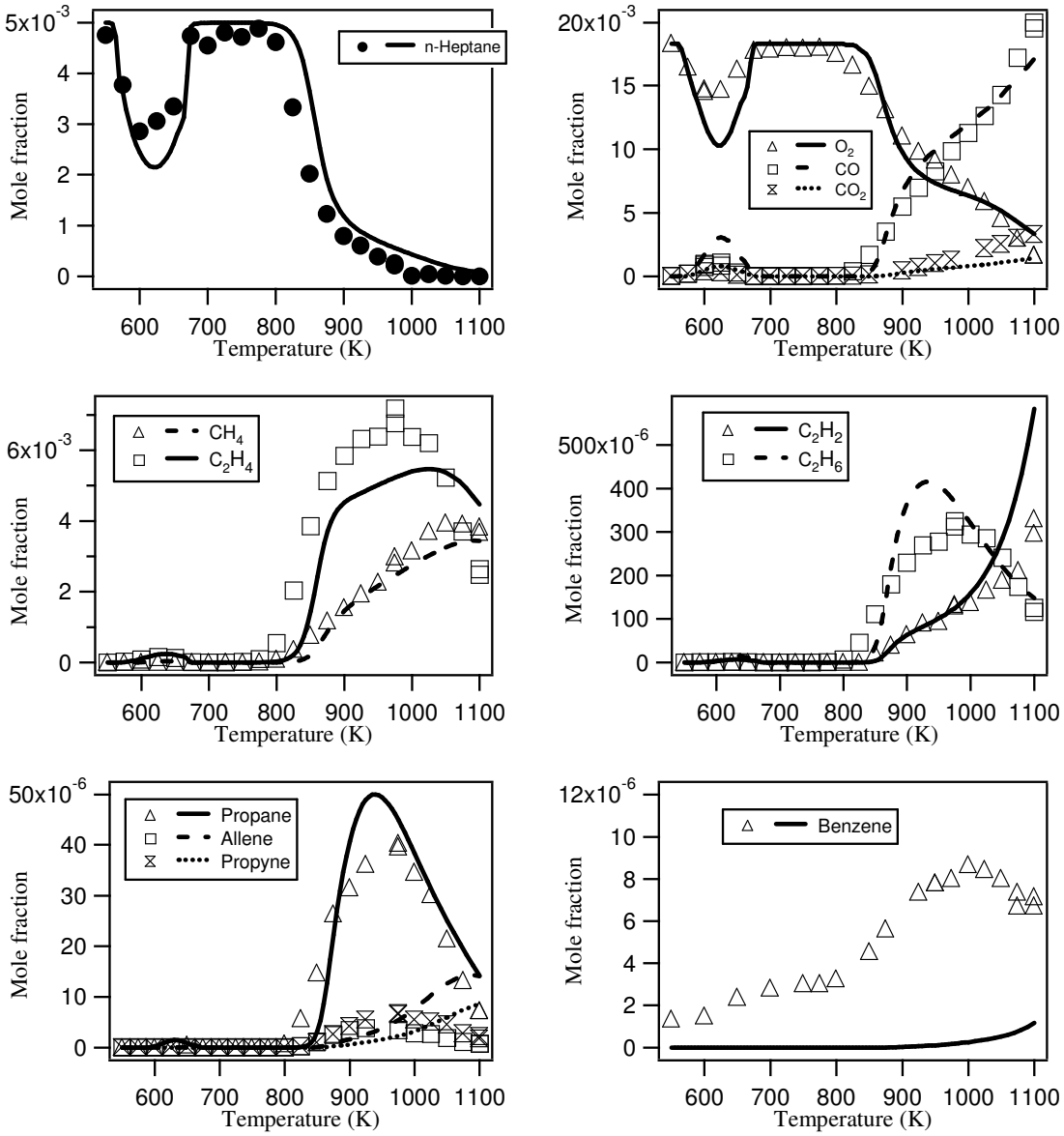

Fig. 1. Jet-stirred reactor results - experiments and simulations: Reactants, carbon oxides, C_1-C_3 species, benzene (at φ=3, $X_{n\text{-heptane}}$= 0.005, τ=2s conditions) mole fraction evolution with temperature

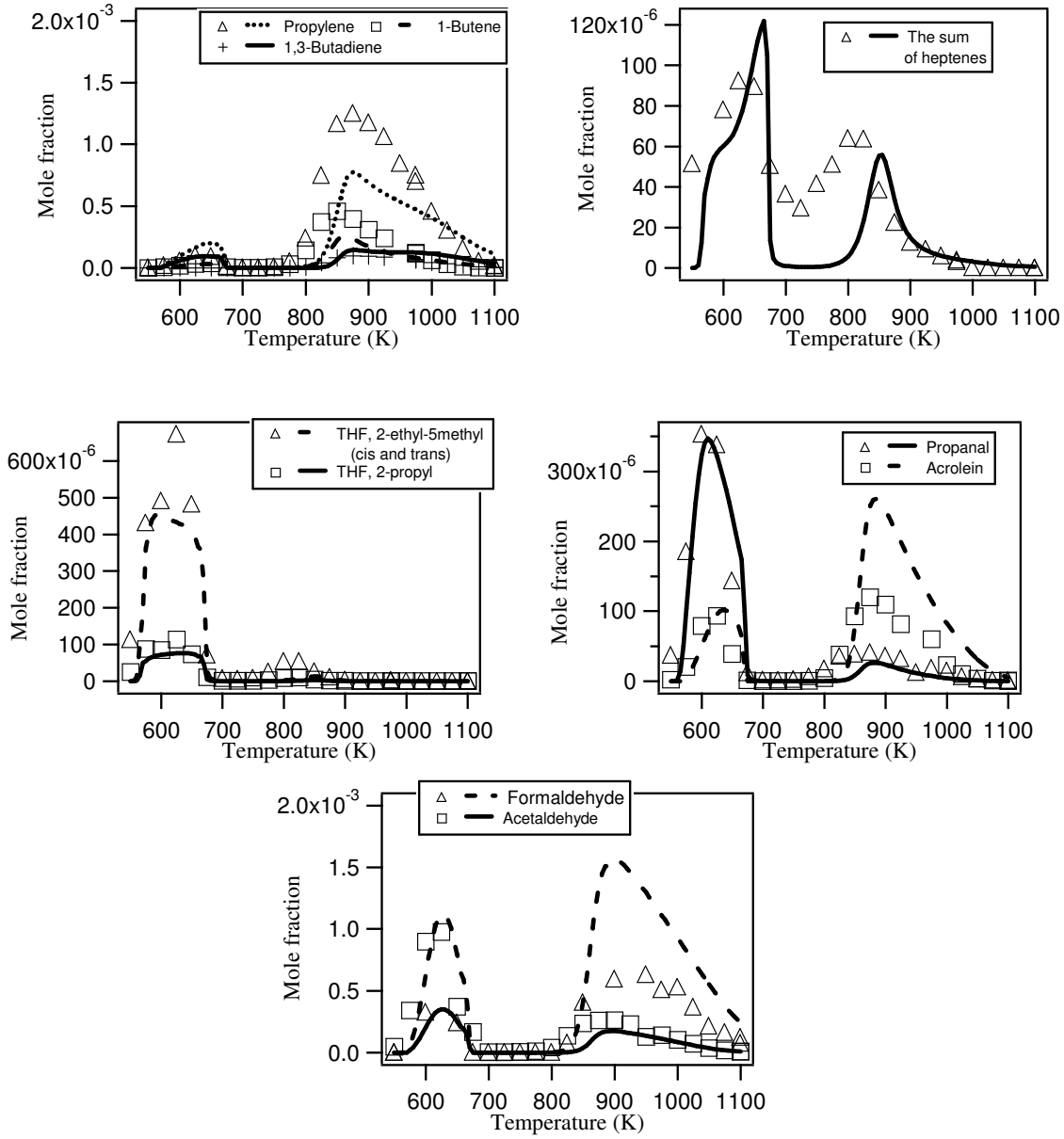

Fig. 2. Jet-stirred reactor results - experiments and simulations: Olefines, 1,3-butadiene, oxygenated species (at φ=3, $X_{n\text{-heptane}}$= 0.005, τ=2s conditions) mole fraction evolution with temperature.

It is worth noting that due to the high dilution in both experimental conditions, no aromatic compounds were observed except benzene with very low concentrations.

3. Modelling

The current model of the oxidation of n-heptane was generated with software EXGAS. The reaction generation rules used in the software and its structure have already been comprehensively described in [11][12], therefore, only the main features are given here. Models generated with EXGAS are made of three parts: a comprehensive primary mechanism, where the only molecular reactants are the initial organic compounds and oxygen; a comprehensive C_0–C_2 reaction base, including the reactions involving radicals or molecules containing less than three carbon atoms; and a lumped secondary mechanism, containing the reactions consuming the molecular products of the primary mechanism with three or more carbon atoms. The molecules formed in the primary mechanism and consumed in the secondary mechanism, with the same molecular formula and the same functional groups, are lumped into one unique species, without distinguishing between the different isomers. This

avoids an explosion of the number of molecules in the models. Globalized reactions in the secondary mechanism were considered, which promote the formation of radicals having more than two carbon atoms, the reactions of which are already included in the primary mechanism [11].

To better represent the chemistry at the rich conditions, we incorporated automatically to the mechanism the C_3-C_6 reaction base for unsaturated hydrocarbons [13]. This sub-mechanism includes the reactions of C_3-C_6 unsaturated hydrocarbons as well as the formation pathways of benzene and toluene.

To enhance the prediction of the n-heptane model, the recent rate constant for the decomposition of H_2O_2 proposed by Troe [14] was used. In addition, activation energies for all the oxidations of alkyl radicals by O_2 yielding the conjugated olefin and HO_2 radical were reduced from 5 to 4 kcal/mol. Eventually, the pre-exponential factor for all peroxide decompositions was set to $4x10^{15}$ as proposed in [15].

It is worth noting that isomers of heptenes and cyclic ethers were not lumped to provide more information.

4. Validation studies

Simulations have been performed using CHEMKIN-PRO package [16]. Computed profiles have been compared to the experimental results obtained in a jet-stirred reactor presented in this work, as well as to the ones obtained at higher pressure [7].

4.1 Atmospheric pressure JSR results (current results)

The comparison of the predicted and the obtained experimental concentration profiles at equivalence ratio of 3, fuel inlet mole fraction of 0.005, and a residence time of 2 s, is illustrated in Fig. 1 and 2. These figures show that the developed model can reproduce well the position of the NTC zone, its amplitude (in order of magnitude), and the mole fraction profiles of carbon monoxide, methane, acetylene, ethylene, ethane, and propane. The formation of carbon dioxide, and propylene is underestimated. The agreement deteriorates for allene and propyne, which mole fractions are however below 10 ppm.

In general, concentrations of unsaturated species are reproduced satisfactorily by the model except the formation of 1,3-butadiene and 1-pentene at low temperature where the agreement is not good. This can be explained by some loss of information in the model due to the lumping strategy and the global rules of consumption of species. As far as heptene isomers are concerned, the three isomers were identified and quantified and a satisfactory agreement is obtained on the sum of their concentrations. The benzene concentrations are underestimated by the model, showing that this model lacks of reaction channel able to produce this aromatic ring at low temperature.

For oxygenated species displayed, the concentration of acetaldehyde is underestimated by a factor of 2.5 at low temperature and satisfactorily reproduced at high temperature, whereas the formation of acrolein is well predicted at low temperature and overestimated above 850K. The concentration profile of propanal is very well reproduced by the model on the whole range of temperatures. In addition to aldehydes, we compared the C_7 tetrahydrofuran isomers profiles to the computed ones, the results show that the model predicts very well these oxygenated species.

Although not presented in the note, the model was also validated using the experimental results obtained at equivalence ratio of 1, n-heptane mole fraction of 0.005, and a residence time of 2 s [3]. The model predicts well the concentration profiles of most species under this condition.

4.2 High pressure JSR results [7]

In addition, the present kinetic mechanism was used to reproduce the jet-stirred reactor experimental data obtained by Dagaut et al. [7]. The experiments were performed with a rich mixture of n-heptane/O_2/N_2 at equivalence ratio of 1.5, 0.1% (mol.) of initial fuel concentration, at high pressure of 10 atm, and a residence time of 1 s.

Figure 3 illustrates the comparison between predicted results and experimental ones. In general, a good fit is obtained for fuel consumption and formed species from low- to high-temperature

domain. Hence, the model can be used to characterise the rich oxidation of n-heptane at high pressure.

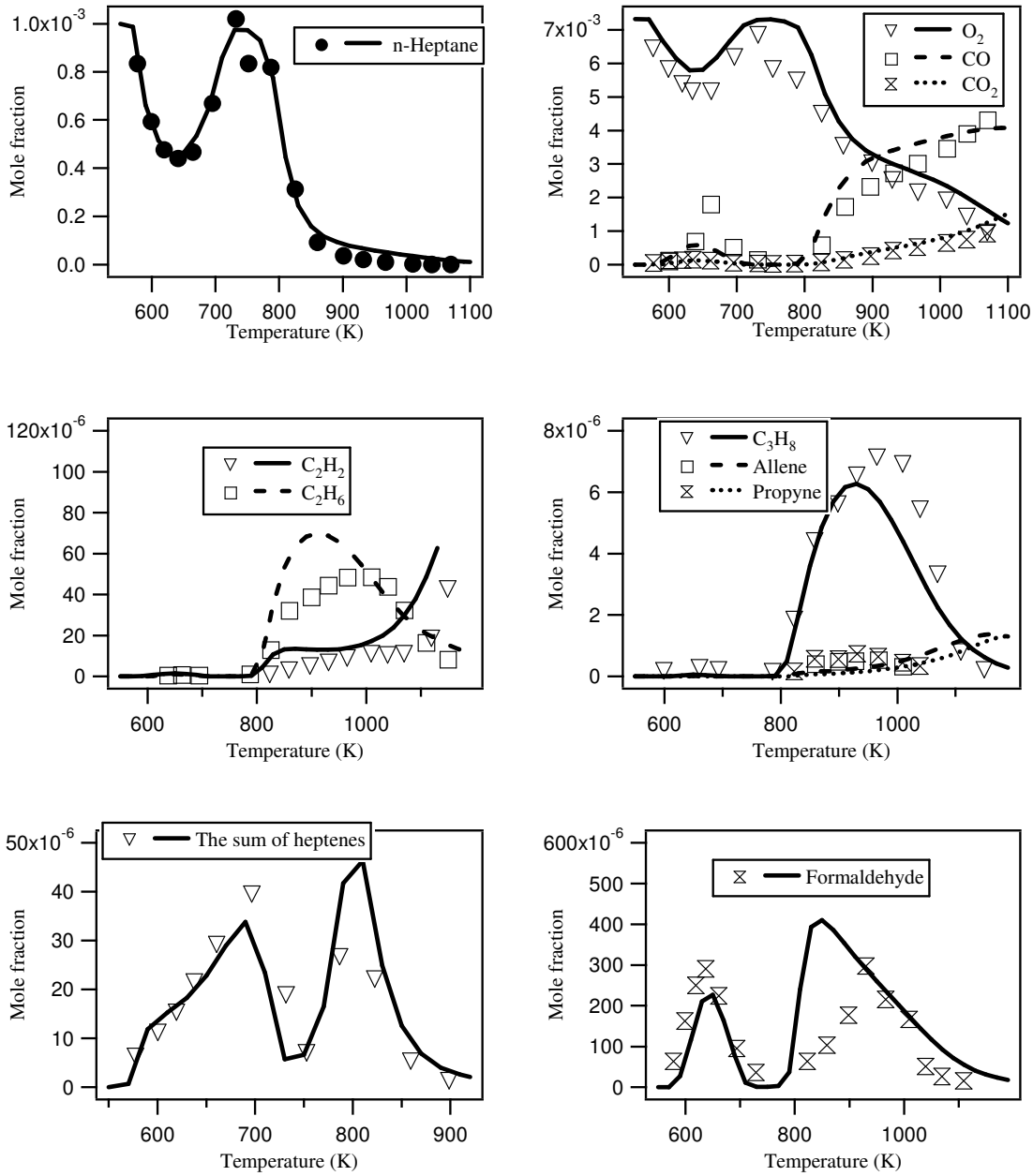

Fig. 3. High-pressure jet-stirred reactor results - experiments [7] and simulations at φ=1.5, $X_{n\text{-heptane}}$= 0.001, τ=1s conditions.

5. Discussion

A detailed analysis was performed to investigate the reactions influencing the reactivity of n-heptane at rich mixture. Figure 4 presents the sensitivity analysis were performed at 600K, 850K, and 950K for the current studied condition. It was also interesting to do the same for the stoichiometric condition studied by Herbinet et al. [3] under the same condition of the current study. A positive value indicates an inhibiting effect and a negative value indicates a promoting one.

As expected, at both low and high temperatures (625 K and 950 K), H-atom abstraction by ·OH radicals at primary and secondary n-heptane sites are the most effective reactions in promoting n-heptane conversion regardless of the equivalence ratio. At the end of the NTC region, the reaction ·OH + ·OH + M = H_2O_2 + M is the most important.

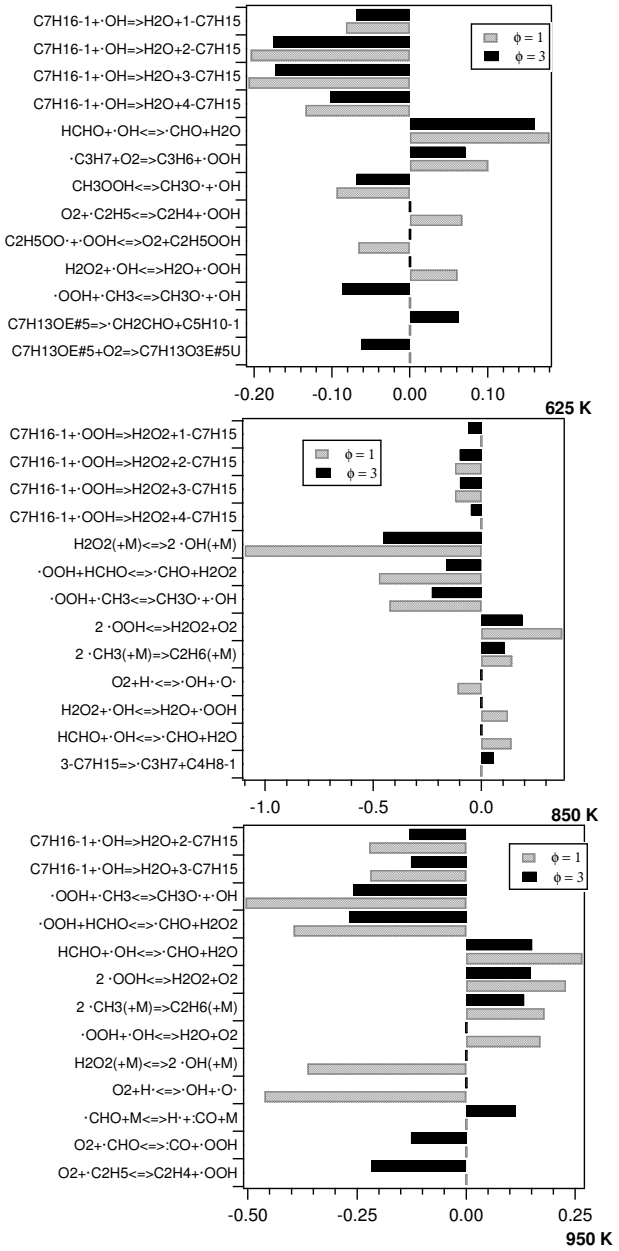

Fig. 4. Sensitivity analysis for n-heptane oxidation in a jet-stirred reactor at current conditions (φ=3, n-heptane mole fration of 0.005, τ=2s) and at condition reported in [3] (φ=1, n-heptane mole fration of 0.005, τ=2s).

More specifically at φ = 3 and 625 K, the reaction of methyl with HO_2· radical promotes the overall reactivity of n-heptane. The sensitivity analysis revealed that the radical obtained by H-abstractions from C_7 tetrahydrofuran isomers are important. Their addition to O_2 accelerates the oxidation of n-heptane whereas the opposite effect is noticed when the unimolecular decomposition of these cyclic ethers occurs. Note that we observed C_7 oxolanes mole fractions twice higher under rich condition compared to those measured at stoichiometry.

As temperature increases (850 K), in addition to reactions important at both equivalence ratios, the decomposition of the 3-heptyl radical obtained by H-abstraction from n-heptane appears inhib-

iting the reactivity under only rich mixture condition. On the other hand, O_2 + H• = •OH + •O• reaction shows a promoting effect for only stoichiometric condition.

At 950 K, the rich mixture reactivity is accelerated by the addition of •CHO and ethyl radical to O_2 forming •OOH and respectively CO and C_2H_4. These reactions, specific to φ=3 condition, provide a •OOH source for the reactions with the largest promoting effect •OOH + •CH3 = CH3O• + •OH and •OOH + HCHO = •CHO +H_2O_2. Furthermore, despite the formation of H• radical by the reaction of •CHO + M = H• + :CO + M at equivalence ratio 3, this reaction slow-down the overall reactivity of n-heptane, since it competes with the reaction of •CHO radical with O_2 .

Conclusions

New detailed experimental data were obtained for the ultra-rich oxidation of n-heptane in a JSR. The investigated conditions allowed to observe a pronounced NTC behavior occurring at φ = 3. These data were used in conjunction with ones taken from the literature measured at φ=1.5, in a high pressure JSR, to develop a new detailed kinetic mechanism.

The agreement between computed and experimental JSR results was in general very good at rich and ultra-rich fuel mixtures at atmospheric and high pressure conditions. Further refinement is still needed, especially to better predict the benzene mole fraction.

The model reproduced well literature results obtained at stoichiometry under the same current investigated conditions (this is not presented in the note).

The study revealed that under ultra-rich mixture (φ=3), the concentrations of aldehydes and C_7 tetrahydrofuran isomers are twice higher than at stoichiometricity. Hence, these two molecules can be used to mark the start of the ultra-rich low-temperature oxidation reactions in a transient spray under compression ignition conditions.

Acknowledgements

The work has been financed under the European Commission Marie Curie Transfer of Knowledge Scheme (FP7) pursuant to Contract LOWCAFF-251492 and was performed within a framework of a research and technological development program with the title LOW CARBON FUTURE FUELS.

References

Battin-Leclerc F (2008) Detailed chemical kinetic models for the low-temperature combustion of hydrocarbons with application to gasoline and diesel fuel surrogates. Progress in Energy and Combustion Science vol 34: pp 440-498.

Biet J, Hakka MH, Warth V, Glaude PA, Battin-Leclerc F (2008) Experimental and modeling study of the Low-Temperature oxidation of large alkanes. Energy and Fuels vol 22 pp 2258-2269.

Buda F, Bounaceur R, Warth V, Glaude PA, Fournet R, Battin-Leclerc F (2005) Progress toward a unified detailed kinetic model for the autoignition of alkanes from C_4 to C_{10} between 600 and 1200 K. Combustion and Flame vol 142 pp 170-186.

Chakir A, Bellimama M, Boettner JC, Cathonnet M (1992) Kinetic study of n-heptane oxidation. Int. J. Chem. Kinet. vol 24 pp 385-410.

CHEMKIN-PRO 15112, Reaction Design: San Diego, (2011).

Dagaut P, Reuillon M, Cathonnet M (1994) High pressure oxidation of liquid fuels from low to high temperature. 1. n-Heptane and iso-Octane. Combustion Science and Technology vol 95 pp 233-260.

Farrell JT, Cernansky NP, Dryer FL, Friend DG, Hergart CA, Law CK, McDavid RM (2007) Experimental database and kinetic models for surrogate diesel fuels. SAE 2007-01-0201.

Hakka MH, Bennadji H, Biet J, Yahyaoui M, Sirjean B, Warth V, Coniglio L, Herbinet O, Glaude PA, Billaud F, Battin-Leclerc F (2010) Oxidation of methyl and ethyl butanoates. In. J. Chem. Kinet. vol 42 pp 226-252.

Hakka MH, Glaude PA, Herbinet O, Battin-Leclerc F (2009) Experimental study of the oxidation of large surrogates for diesel and biodiesel fuels. Combustion and Flame vol 156 pp 2129-2144.

Herbinet O, Husson H, Serinyel Z, Cord M, Warth V, Fournet R, Glaude PA, Sirjean B, Battin-Leclerc F, Wang Z, Xie M, Cheng Z, Qi F (2012) Experimental and modeling investigation of the low-temperature oxidation of n-heptane. Combustion Flame vol 159 pp 3455-3471.

Husson B, Ferrari M, Herbinet O, Ahmed SS, Glaude PA, Battin-Leclerc F (2013) New experimental evidence and modeling study of the ethylbenzene oxidation. Proc. Combust. Inst. Vol 34 pp 325-333.

Kosaka H, Aizawa T, Kamimoto T (2005) Two-dimensional imaging of ignition and soot formation processes in a diesel flame. Int. J. Engine Research vol 6 pp 21-42.

Marinov NM, Pitz WJ, Westbrook CK, Vincitore AM, Castaldi MJ, Senkan SM, Melius CF (1998) Aromatic and polycyclic aromatic hydrocarbon formation in a laminar premixed n-butane flame. Combustion Flame vol 114 pp 192-213.

Mehl M, Pitz WJ, Westbrook CK, Curran HJ (2011) Kinetic modeling of gasoline surrogate components and mixtures under engine conditions. Proc. Combust. Inst. 33 193-200.

Sahetchian KA, Rigny R, Tardieu de Maleissye J, Batt L, Anwar Khan M, Mathews S (1992) The pyrolysis of organic hydroperoxides (ROOH). Proc Combust Inst vol 24 pp 637-43.

Simon Y, Scacchi G, Baronnet F (1996) Études des réactions d'oxydation du *n*-heptane et de l'isooctane. Canadian Journal of Chemistry vol 74 pp 1391-1402.

Troe J (2011) The thermal dissociation/recombination reaction of hydrogen peroxide $H_2O_2(+M)\Leftrightarrow 2OH(+M)H2O2(+M)\Leftrightarrow 2OH(+M)$ III.: Analysis and representation of the temperature and pressure dependence over wide ranges. Combustion and Flame vol 158 pp 594–601.

Investigation of the Combustion in both Metal and Optical Diesel Engines Using a High-Glycerol-Ethers/Diesel Blends

C. Beatrice, G. Di Blasio, M.Lazzaro, E. Mancaruso, R. Marialto, L. Sequino, and B.M. Vaglieco

Istituto Motori. Consiglio Nazionale delle Ricerche. Via Marconi, 4, 80125 Napoli, Italy.

E-mail: e.mancaruso@im.cnr.it
Telephone: +(39) 081 7177187
Fax: +(39) 0812396097

Abstract. In this paper, a glycerol ethers mixture (GEM) obtained from etherification of glycerol with tert-butyl alcohol and isobutylene has been used in blend (10% and 20% v/v) within a commercial diesel fuel to feed a single cylinder research engine derived from a Euro5 compliant four cylinder engine. The engine has been run in three significant operating points in the NEDC (New European Driving Cycle) emission homologation area. The results have shown the possibility to burn the diesel/GEM blends without significant impact on combustion characteristics and efficiencies while, due to the oxygen content of the GEM, important benefits are obtained in terms of NO_x-PM trade-offs at the exhaust. Moreover, tests have been performed on a diesel engine with optical access through the piston bowl. The injection and combustion processes of the pilot have been investigated by means of the simultaneous use of digital imaging in the visible and infrared ranges in order to have more information on the vapour distribution, the fuel motion before the ignition and the location of hot gas.

Notation

ATDC	*After Top Dead Centre*
BMEP	*Brake Mean Effective Pressure*
BTDC	*Before Top Dead Centre*
CA	*Crank Angle*
CI	*Compression Ignition*
CN	*Cetane Number*
CO	*Carbon Monoxide*
CO_2	*Carbon Dioxide*
CR	*Common Rail*
DI	*Direct Injection*
ECU	*Engine Control Unit*
EGR	*Exhaust Gas Recirculation*
FSN	*Filter Smoke Number*
GEM	*Glycerol ethers mixture*
GHG	*Greenhouse Gases*
HC	*Hydrocarbon*
HR	*Heat Release*
ICE	*Internal Combustion Engine*
IMEP	*Indicated mean effective pressure*
ISFC	*Indicated specific fuel consumption*
LHV	*Lower Heating Value*
MBF50	*Mass Burned Fraction 50%*
NEDC	*New European Driving Cycle*
NO_x	*Nitric Oxides*
O_2	*Oxygen at the exhaust*
PM	*Particulate Matter*
PRR	*Pressure Rise Rate*
ROHR	*Rate Of Heat Release*
SC	*Single Cylinder*
SOI	*Start of Injection*
UHC	*Unburned Hydrocarbon*

1. Introduction

In recent years, the interest in new sustainable energy resources is increasing worldwide, especially in the transportation sector where the market is mainly governed by petroleum derivative fuels. The interest originates from the future emission regulations, which will significantly limit the emissions of internal combustion engines (ICE),

along with the global warming issues related to the greenhouse gases (GHG) and the need to reduce the dependency of the fossil fuels since the fuel demand has significantly increased worldwide. For these reasons, the European Union (EU) has imposed directives and legislations aiming at replacing 10% of transport fossil fuels with biofuels by 2020 [1] looking forward to large-scale production of second generation biofuels [2].

Biofuels can play an important role in addressing both the GHG emissions of transport and the dependency on mineral oil, although most of the reductions in emissions will be delivered by improved efficiency and electrification. Different global energy scenario studies indicate that in this century biomass may contribute much more: up to 40-60% of total energy demand by 2050 of which transportations represent about the 30% [3, 4]. For this reason, the research for new biofuels has been becoming one of the major topics investigated by the scientific community. The production of biodiesel is mainly supported in the EU while in the US similar targets are in place [4]. Biodiesel is produced from triglycerides derived mainly from vegetable oils or animal fats. Recently, new biofuel production methods have been investigated such as oil produced from algae and oleaginous yeasts indicating new sources which, contrary to energy crops, do not conflict with the cultivation of land for food [5]. As a result of the increasing biofuel production, also the production of glycerol, which is the main by-product of the transesterification process, will grow proportionally.

Thus, the question arises from a cost-effective and efficient use of such a glycerol surplus. The combustion of glycerol ‘‘as it is’’ would represent a desirable solution. Unfortunately, because of its detrimental physical and chemical properties (e.g., high viscosity, low lower heating value (LHV), low autoignition quality) raw glycerol is hardly usable in conventional energy production plants, such as fuel burners or ICEs [6, 7]. However, a proper design of the burner and refractory combustion chamber could allow to effectively burning crude glycerol, although a high particulate matter concentration is detected at the exhaust [8]. Alternative routes for glycerol recovery are represented by its energetic upgrading into high value products, such as synthesis of gases and oxygenate additives for gasoline, biodiesel and diesel fuels [9, 10]. An industrially relevant route for the conversion of glycerol into oxygenated chemicals involves the etherification with isobutylene (IB) or tert-butyl alcohol (TBA) to tert-butyl ethers [10, 11]. These oxygenated compounds, when blended with diesel or biodiesel fuels, improve engine performance leading to a reduction in particulate matter, hydrocarbons, carbon monoxide and unregulated aldehydes emission [12]. Specifically, higher ethers of glycerol possess suitable combustion properties, which improve the low temperature properties of diesel fuel (pour point and cold filter plugging point) and reduce the viscosity of biodiesel fuel. However, since mono-tert-butyl ethers of glycerol (1-MBG; 2-MBG) have a low solubility in diesel fuel, the etherification of glycerol, taking place with a consecutive reaction path, should be mainly addressed towards the formation of a mixture of di-tert-butyl ethers (1,3-DBG; 1,2-DBG) and/or tri-tert-butyl ether (TBG) [13-17].

However, in order to assess their applicability within the compression ignition (CI) ICE of diesel-glycerol ethers mixtures (GEM) many aspects must be considered such as effects on lubricity, corrosiveness, elastomer deterioration, stability in the whole fuel line, impact on the injector nozzle etc. Of course, the characterization of all of these is a long-term work and requires a proper fuel availability. In this framework, since GEM was produced in a lab-scale plant, its availability was very limited. Therefore, the study of fuel-engine interaction was limited to a detailed characterization of the impact of the alternative fuel on the combustion process as well as on the engine efficiency and pollutant emissions.

To this aim, two diesel-glycerol ethers mixtures (GEM) at different volume ratio, 10% and 20% in volume named GEM10 and GEM20, respectively, were tested, in both metal and optical engines. In metal engine this research study aims to give an overview of the fuel-engine interaction and it was limited to a detailed characterization of the impact of the alternative fuel on the combustion process as well as on the engine efficiency and pollutant emissions. Moreover, optical diagnostics are good tools to investigate in-cylinder combustion phenomena and to provide useful correlations between macroscopic parameters such as in cylinder pressure and rate of heat release (ROHR) and the microscopic ones such as in-cylinder flame temperature and soot concentration. Visible and infrared (IR) imaging provide useful information about the injection and processes in terms of temporal evolution and spatial distribution. Performing the same injection strategies on both metal and transparent engines at 2000 rpm the same behaviour of the ROHR was realized and, thus, the information detected in the optically accessible engine has been useful to better understand the in-cylinder combustion process and the pollutants formation.

2. EXPERIMENTAL SET UP AND METHODS

Experimental activity was performed on both metal and optical engines to analyze the effect of two diesel-glycerol ethers mixtures (GEM) at different volume ratio, 10% and 20% in volume named GEM10 and GEM20, respectively, on combustion and pollutant formation.

2.1 Metal Engine

The experimental activities were carried out on a prototype single cylinder (SC) research CI engine, which has a modern combustion system design derived from a Euro5 compliant four cylinders engine; it represents the state of the art of the automotive technology. The cylinder head is derived from production series, but it has been modified to work in SC mode. The auxiliary systems (for boost, cooling, lubrication, etc.) are not directly coupled to the engine in order to allow for a maximum flexibility of their parameters without influencing the load conditions.

A fully programmable electronic control unit (ECU) allows the operator to modify the fuelling strategy, swirl ratio, EGR level, boost and backpressure values offering flexibility pertaining to the operating conditions. The fuel consumption is measured by means of AVL 733mass flow meters. The scheme of the engines layout is laid out in Fig. 1, while in Table 1 the engine properties are described.

Table 1. Engines characteristics

	Metal engine	**Optical engine**
Displacement volume [cc]	475	522
Stroke [mm]	90	92
Bore [mm]	82	85
Compression ratio	16.5:1	
Number of Valves	4	
Diesel Injection System	Common rail, 7 holes injector 440cm^3/30s	

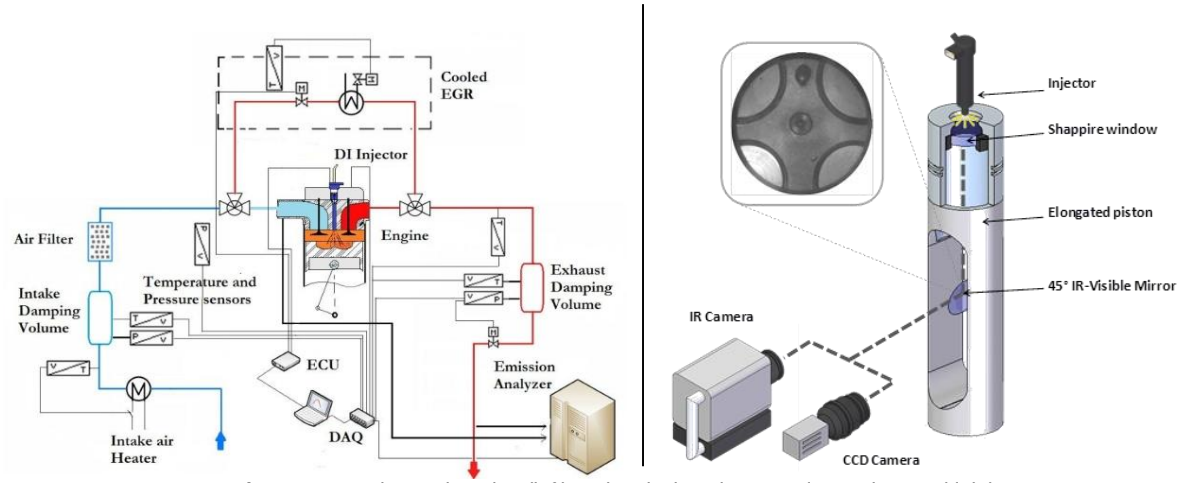

Fig. 1. Research metal engine (left) and optical engine experimental setup (right)

The pressure traces were recorded by a Kistler piezoelectric pressure transducer fitted inside the combustion chamber. The net rate of heat release (ROHR) was calculated in real-time by the AVL IndiMicro indicating system. The filter smoke number (FSN) was measured by an AVL 415S smoke-meter and cross checked with the AVL Microsoot Sensor, when the values of smoke were at the limit of the sensitivity of the smoke meter. The gaseous emissions were recorded with an ABB, Emerson and Ecophysics devices for UHC, CO-CO_2-O_2 and NO_x respectively.

2.2 Optical Engine and Experimental Set-up

The optical single-cylinder (SC) engine used for combustion diagnostics was equipped with the combustion system architecture and injection system of the metal SC engine. The engine elongated piston and the experimental apparatuses are shown in Fig. 1. The engine specifications are reported in Table 1. The optical engine utilized a conventionally extended piston with a piston crown window of 46 mm diameter which provided full view of the combustion bowl by locating an appropriate 45° fixed visible-IR mirror inside the extended piston. The window was made of sapphire. Moreover, the combustion bowl volume and the bowl wall shape were the same as the production engine one. To match the in-cylinder conditions of the metal engine tests, an external air compressor was used to supply pressurized intake air that was well filtered, dehumidified, and preheated.

Like for the metal one, the optical engine was equipped with Common Rail injection system managed by a fully opened ECU. The solenoid driven injector mounted in the transparent engine had the same characteristics of that of the metal engine (Table 1).

To analyze the injection signals, a Hall-effect sensor was applied to the line of the solenoid. As for the metal engine, to measure the cylinder pressure in motored and fired condition, an AVL piezoelectric pressure transducer was set in the glow plug seat of the engine head. For each operating condition investigated, via AVL Indimodule indicating system, the cylinder pressure and the qualitative signal of the drive injector current were digitized and recorded at 0.2° crank angle (CA) increments and ensemble-averaged over 150 consecutive combustion cycles. Moreover, the cyclic variation was measured and it resulted less than 1% with respect to the maximum pressure and less than 3% with respect to the indicated mean effective pressure (IMEP). The heat release rate was calculated from the ensemble-averaged pressure data using the first law of thermodynamics and the perfect gas model [18].

The filter smoke number (FSN) was measured by an AVL 415S smoke-meter. Gaseous emissions were measured with conventional systems by means of probes placed in the exhaust pipe. In particular, NO_x and O_2 concentrations were measured by means of electrochemical sensors, while UHC, CO, and CO_2 concentrations were detected by means of no-dispersive infrared detectors (AVL DIGAS 4000).

2D imaging measurements in both visible and infrared wavelength range were carried out in order to investigate the spray and combustion evolution in the bowl of GEM fuels. Visible imaging analysis was performed by a charge coupled device (CCD) camera through the 45° mirror. The camera used was the PixelFly VGA COLOR; it has 640 x 480 pixels (pixel dimensions of 9.9 x 9.9 μm^2) and a high sensitivity over a wide visible range. It was used in order to take images during the injection and combustion processes. A visible objective, Nikkor 55 mm f/3.5, was used. Due to speed limitation of CCD camera, only one image was recorded in a given cycle. The resolution of camera was 0.1 mm per pixel. The spray was enlightened by means of two halogen continuous lamps via the 45° mirror. During both the pilot and main events several images from separate cycles were recorded up to the end of visible injection. Five repetitions were performed in order to carry out statistical analysis of the spray tip penetration and dispersion angle. No lamps were used to record the combustion phase. The synchronization of the CCD camera with the engine was obtained by a delay unit connected with the signal coming from the engine shaft encoder. The synchronization system could be adjusted to obtain single images at a desired crank angle. In particular, the images were recorded with an exposure time of 41 μs that corresponded at 0.5°CA of the shaft encoder at 2000 rpm. Visible imaging of the combustion event has allowed performing two-color pyrometry in order to evaluate the in-cylinder soot.

IR imaging was performed using the FLIR Phoenix fast camera (320×256 pixels) able to detect light in the range 1.5-5 μm. The IR camera had a sensor made of Indium Antimonide (InSb) and it was equipped with a 25 mm, f/2.3 objective. The resolution of camera was 1.1 mm per pixel. Images from IR camera were detected with an exposure time of 10 μs. Moreover, in order to prevent the saturation of the detected images, a neutral density filter, with 10% attenuation was used. The detection frequency of the IR camera was 3003 Hz that corresponds to an angular step of 4°CA at 2000 rpm. The IR camera was cycle resolved but it could not be triggered at desired crank angle. Finally, a filter at 3.9μm was installed in front of the IR camera. This wavelength has been chosen because of its strong sensitivity to sub-pixel "hot-areas"; it is used for fire detection from satellite monitoring [19]. Moreover, at this wavelength, the filter is able to detect the liquid phase of the injected fuel.

3. TESTING METHODOLOGY AND FUEL CHARACTERISTICS

The test procedure was chosen in order to provide additional experimental information when using GEM in blend with commercial diesel evaluating its impact/potential as fuel component. The operating points chosen for this research study are listed in Table 2. They were performed, using the Euro5 engine parameter calibration (injection, boost, swirl, EGR, etc.) derived from the real four-cylinder engine, at fixed engine speed (2000 rpm) and varying the loads. The performed test points were widely used to evaluate the engine performance during the NEDC, even if they work in stationary operating conditions. However, a more extended engine campaign from the engine performance point of view has been performed previously [21]

Table 2. Test points

Test point	RPM	IMEP [bar]	BMEP* [bar]	EGR [%]
2000x2	2000	4	2	39
2000x5	2000	7	5	33
2000x10	2000	12	10	21

BMEP of the real four-cylinder engine*

The point at 2 bar of Brake Mean Effective Pressure (BMEP) is representative of the low load operating conditions; the load point at 5 bar of BMEP, is identified as a critical operating point for soot and NO_x emission control; at medium load (10 bar of BMEP), the performance differences in terms of thermal efficiency, noise and impact on engine functionality are more noticeable. Previous studies [6, 7, 21] were mainly devoted at evaluating the engine-fuel interaction in conventional engine operating conditions (e.g. pilot plus main injection, etc.). In the present work, the investigation on the optical engine was aimed at deepening on the injection and combustion process mainly at low load conditions (2000x2) where problems related to the complete fuel oxidation occurred and, at 2000x5, to analyse the phenomena related to the significant reduction in soot emissions.

The GEM impact on engine combustion characteristics was evaluated by testing the following fuels:

(a) reference EN590 European commercial diesel;
(b) blend of 10% v/v of GEM in diesel (GEM10);
(c) blend of 20% v/v of GEM in diesel (GEM20).

The main physical and chemical characteristics of the pure GEM and the blends are reported in Table 3.

Table 3. Fuels physical and chemical properties

Feature/Method	Units	Commercial Diesel EN590	GEM10	GEM20
Density @ 15 °C (EN ISO 12185)	[kg/m^3]	829	833	838
Cetane Number (EN ISO 5165)	[-]	51.8	49.3	46.5
Low Heating Value (ASTM D3338)	[MJ/kg]	42.4	41.3	40.3
Flash Point (ASTM D93/IP 34/ EN ISO 2719)	°C	72	65	52
Kinematic Viscosity 40°C (ASTM D445)	[mm^2/s]	2.7	3.421	3.295
Cloud Point (ASTM D2500)	°C	-2.2	-2	-2
Cold Filter Plugging Point (EN 116)	°C	-19	-18	-18
Lubricity 60°C (ISO 12156-1)	µm	382	245	235
Distillation (ASTM D86)	IBP [°C]	159	152	146
	10%vol. [°C]	194	195	196
	50%vol. [°C]	268	261	255
	90%vol. [°C]	333	320	308
	95%vol. [°C]	350	335	321
	FBP [°C]	361	345	330
Carbon (ASTM D5991)	[mol%]	~85.5	~83.1	~79.9
Hydrogen (ASTM D5991)	[mol%]	~13.5	~12.7	~11.9
Oxygen (ASTM D5991)	[mol%]	~1.4	~4.2	~8.2
$(A/F)_{st}$	[-]	14.5	13.7	12.2

The choice of the GEM10 was driven by avoiding significant alterations of the fuel blend characteristics during the experiments ensuring engine reliability. Moreover, since biodiesel-derived raw glycerol is about 10 wt.% of the primary oil, GEM10 could represent a possible blending target, in the hypothesis that all the raw glycerol is converted into GEM. The GEM20 was prepared with the objective to evaluate the impact on the engine combustion characteristics of blends with higher GEM ratios. This is useful to carry out trends on combustion and emission characteristics as a function of the GEM fraction in the blend. Finally, no phase separation occurred at room temperature after 4 weeks neither at 10 nor at 20% v/v of GEM in diesel.

4. RESULTS AND DISCUSSIONS

In this section an analysis of the tests results will be presented. Firstly, the impact of the blends on the combustion characteristics and emissions is regarded either on the metal engine or on the optical engine. The optical engine calibration parameters were settled in order to reproduce similar combustion rate (ROHR) conditions. Secondly, a trade off emission analysis performing the EGR sweep will be presented for all the tested points.

4.1 Combustion analysis in metal engine

In this paragraph, a comparison of the emissions, in-cylinder pressure evolution (p) and the rate of heat release rate (ROHR) for the three blends (Diesel, GEM 10 and GEM 20) is reported. In the performed test points, the engine was operated with a conventional pilot plus main injection strategy. The start of injection (SOI) and the injection duration were varied to achieve the reference diesel combustion barycentre and the reference diesel IMEP values, respectively; while the other injection parameters (dwell time, pressure, etc.) were kept constant.

The combustion and emission analysis at 2000x5 are here omitted for brevity since the results are intermediate between those described in the points 2000x2 and 2000x10.

Fig. 2 shows the comparison among the tested fuels at 2000x2 and 39% of EGR. The injection phasing was settled to maintain constant the MBF50% and equal to the calibration value. The traces comparison (p and ROHR) evidence a drift in the combustion peaks due to the differences in the pilot HR. In the case of using GEM there is practically no pilot combustion as shown in Fig. 2 (top right). The differences increase moving from diesel to GEM10 and GEM20. This result is linked to the reduction of cetane number (CN) and to the lower boiling curve of GEM-diesel blend. For this reason, to keep constant the combustion barycentre (MBF50%), the injection phasing (see injection pattern) was significantly advanced, shifting the combustion towards more premixed conditions. Fig. 3 shows the negative impact on efficiencies and pollutant emissions of the GEM's poorer pilot combustion.

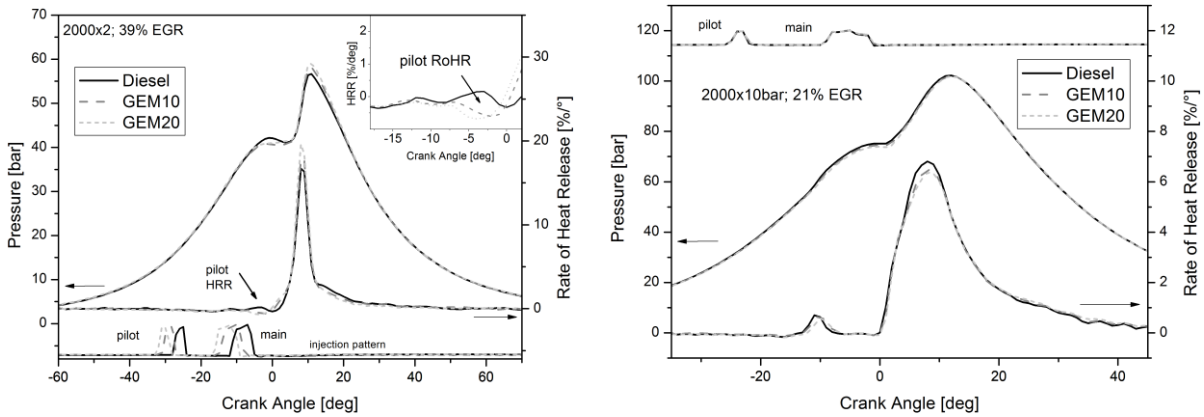

Fig. 2. Pressure, ROHR and injection energizing pattern at 2000x2bar (left) and 2000x10bar (right) for the diesel and the two blends

Fig. 2 (right) reports also the comparison between the tested fuels at 2000x10 and 21% of EGR. In this case, the comparison shows a negligible cylinder peak pressure differences indicating a negligible GEM effect on the combustion phasing. Analysing previous authors results [6, 7], involving the use of a single fuel injection strategy, GEM 10 shows a delay in terms of start of combustion (SOC) compared to diesel also at higher loads. Indeed, in this point, both the use of the conventional pilot plus main injection strategy and the comparable pilot HR, reduce the ignition delay drift and the combustion noise flattening globally the combustion differences (despite the slightly delayed pilot HR for GEM20). Intermediate results between the two described points were evidenced at 2000x5.

Within the chosen blending ratio and at medium–high load conditions, the addition of GEM to neat diesel does not impact significantly on the combustion characteristics, such as autoignition, combustion duration, phasing, etc..

In Fig. 3 the trends in terms of efficiencies and emissions are represented increasing the load as reported. This analysis assesses the engine and emission performance using the reference Euro 5 engine calibration parameters. Regarding the trends of the fuel conversion efficiency (η_{fuel}), except the 2000x2 operating point, no significant variations with respect to diesel fuel were observed for both GEM 10 and GEM 20. At 2000x2, the slightly lower η_{fuel} of GEM blends are attributable to the lower combustion efficiency (see ROHR trace for pilot combustion in Fig. 2), linked to the fuel over-mixing at low load conditions that brings to over-lean regions in the combustion chamber [22, 23]. This result is also confirmed from the emission data displayed in Fig. 3 (top-right). Increasing the load, the efficiency drift is annulled and an improvement of efficiency was measured at 2000x10. Indeed, the higher combustion temperatures and the improved pilot and main HR increases the combustion and the thermal efficiencies respectively.

As evidenced in other literature data [12, 24], the main effects of the oxy-fuels are on the soot emission suppression. GEM 20 shows clearly the best soot reduction potential. In fact, the intramolecular oxygen plays a fundamental role in terms of PM reduction mainly in high sooting operating points, as 2000x5 and 2000x10. Penalties in the unburned gaseous emissions, like HC and CO, were particularly evidenced at 2000x2. In this case, the pilot combustion inefficiency and the fuel overmixing play the main role in the pollutant emissions [24].

Generally, oxygenated fuels tend to increase NO_x emission. At lower loads EGR is the main controller on the emitted NO_x. However, at 2000x10 an increase of about 10% was observed for GEM blends, although it was not evident a clear trend of NO_x emission increment versus GEM fraction in the blend (e.g. GEM 10 versus GEM 20). The NO_x emission increase is due to the rising of the combustion temperature explainable by the following factors: firstly, the intra-molecular oxygen in GEM tends to improve the combustion process in locally rich zones of the combustion chamber increasing as a consequence the flame temperature; secondly, the oxygen reduces the PM production and thus the associated radiation heat losses; finally, the strong impact of EGR on NO_x formation is mitigated by the lower EGR rate for higher loads points as in the presented point. In fact, in this point, the EGR rate is about 21%, masking only partially the GEM impact on NO_x formation.

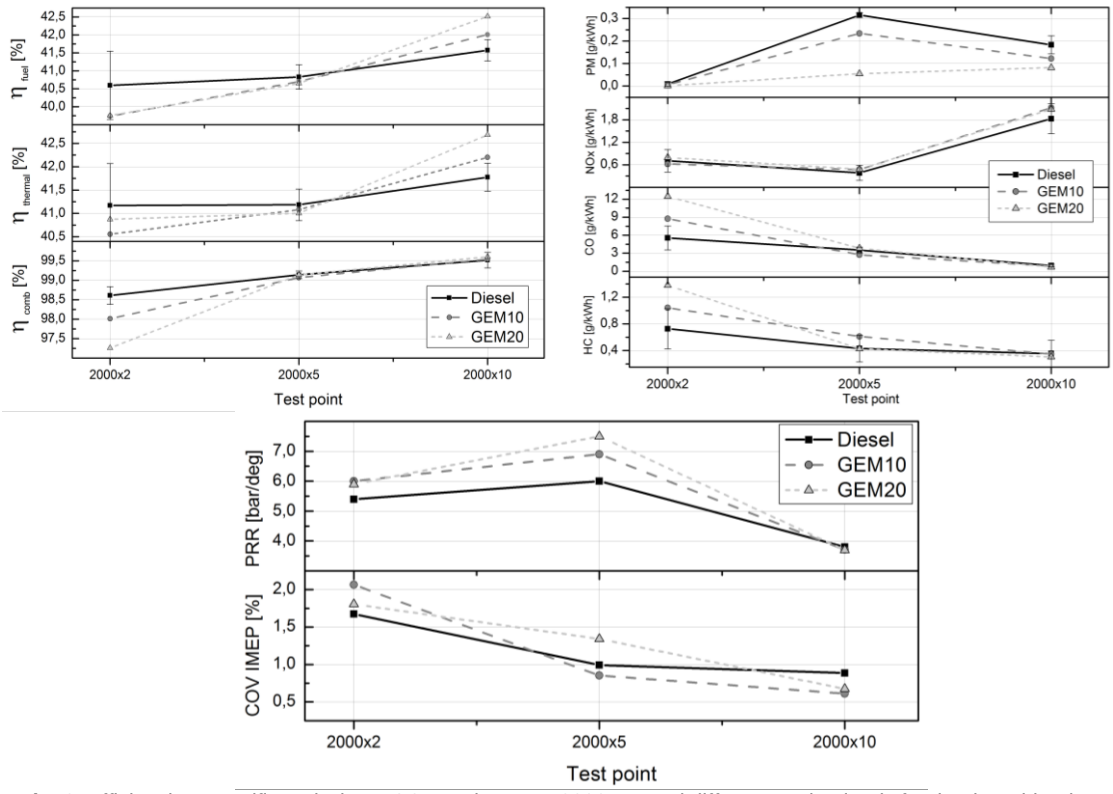

Fig. 3. Efficiencies, specific emissions, COV and PRR at 2000rpm and different engine loads for the three blends.

Fig. 3 (bottom) shows the trends of maximum PRR and COV IMEP for the different engine operating points. Even though both GEM 10 and GEM 20 show a slight PRR rise, the increment remains in acceptable ranges. In this case, the use of a pilot plus main injection strategy mitigates excessive combustion noise when low cetane number fuels, such as GEM, are burned. In the same way, the cycle-to-cycle stability for the GEM blends, represented by the COV IMEP, does not show significant drift from the diesel only.

It is also noteworthy that the oxygen fuel content reduces the LHV and increases the indicated specific fuel consumption (ISFC). The η_{fuel}, calculated as [18]:

$$\eta_{\mathrm{fuel}} = \frac{1}{\mathrm{ISFC} \cdot \mathrm{LHV_{blend}}} = \eta_{\mathrm{comb}} \cdot \eta_{\mathrm{thermal}}$$

tends to increase slightly for the GEM fuels. This result means that the ISFC increment depends only on the reduced LHV of both GEM10 and GEM20 blends, but within the tested blending ratios, the oxygenated fuels show improved thermal efficiencies thanks to its lower combustion duration and improved combustion process efficiencies.

4.2 Combustion and emission analysis in optical engine

An investigation of the combustion behaviour has been performed by means of optical diagnostic in a transparent single cylinder engine with a similar architecture of the metal engine. The engine has been run in two operating points at 2000 rpm - 2 bar of BMEP and at 2000 rpm - 5 bar of BMEP since negligible differences were noted at 2000x10 between diesel and GEM. Moreover, in order to better detect the difference in combustion behaviour only the mixture at GEM percentage (GEM20) was used in the optical engine and compared to diesel fuel. The injection strategy investigated was the same for diesel and GEM20, respectively.

The history of the in-cylinder pressure, ROHR and drive injector current have been reported in Fig. 4 for both the tested fuels and the operating conditions. Fig. 4 shows that GEM20 is able to reproduce the same pressure profile of the diesel fuel at 2000x2. For both the fuels, no combustion of the pilot injection has been noted. At 2000x5, the curves of in-cylinder pressure overlap at the start of combustion but the GEM20 reached higher and retarded peak pressure. From the ROHR curve, it can be noted that the pilot ignition is less intense for the GEM20 than the diesel fuel. As just noted analysing the in-cylinder pressure data of the metal engine this is due to the CN, boiling curve, LHV, of the GEM20. For this reason, the fuel injected with both pilot and main events burns together producing a higher peak of ROHR curve and higher maximum of the pressure signal.

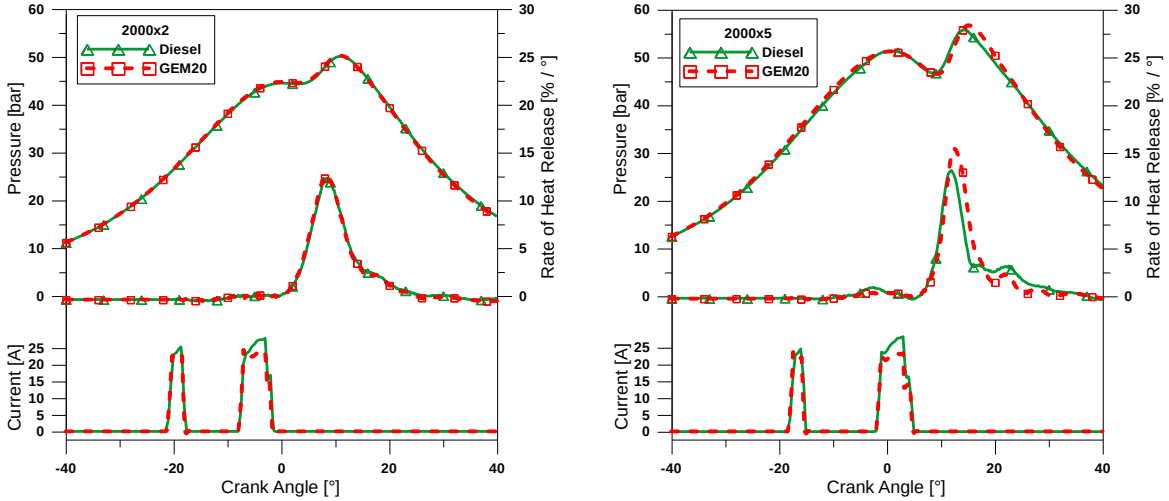

Fig. 4. Pressure, ROHR and drive injector current, for both the tested fuels at 2000x2 (left) and at 2000x5 (right)

In order to understand the effect of pilot injection and mixing on the premixed combustion both pilot and main injections were detected in the bowl. In Fig. 5, images of both injections for diesel and GEM20, respectively, have been reported. Only the point 2000x5 has been showed as an example; it is the condition with higher injected fuel quantity.

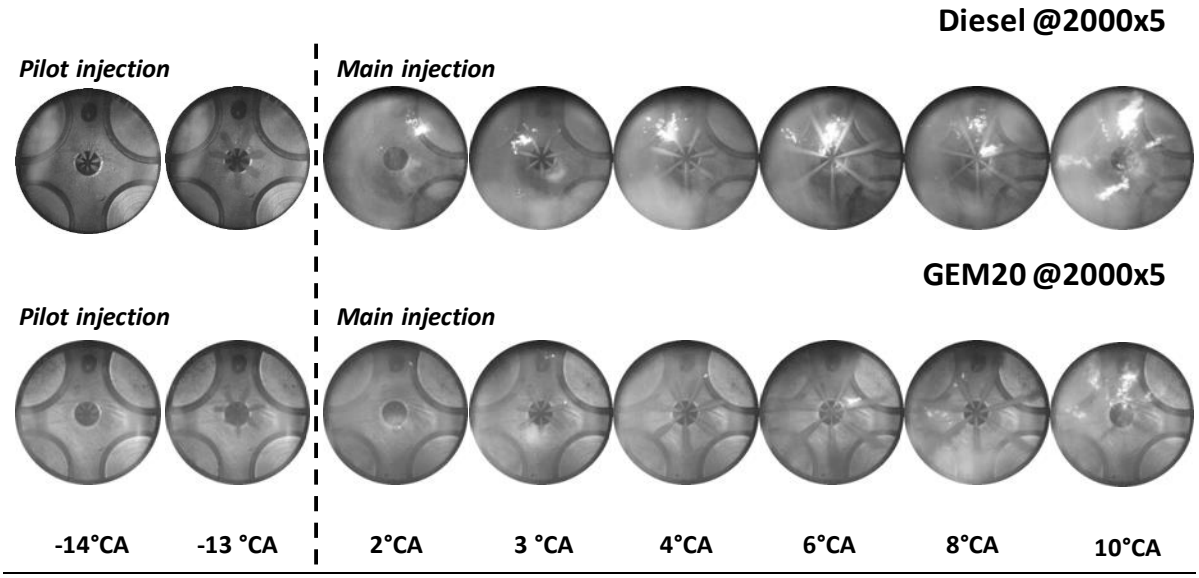

Fig. 5 Images of pilot and main injection for diesel and GEM20 at 2000x5

Even if the start of injection for pilot was at 17.5°CA before the top dead center (BTDC) the jet was noted in the bowl three crank angle (CA) degree later. This delay was due to mechanical and electric of the injector. Pilot injection for both fuels lasts 2.5°CA and the jets immediately disappear in the bowl due to strong evaporation of the fuel. Images of the main injections show clearly the seven jets penetrating and spreading in the bowl volume available from the nozzle tip toward to the chamber wall. The main injection starts at 2° CA and can be considered finished at 10°CA. For the diesel fuel, high luminous flames are noted. These flames are due to the combustion of the pilot fuel that has mixed with the air and has reached the auto-ignition conditions. On the contrary, only weak luminous spots can be detected when GEM20 is injected.

In Fig. 6, the average axial penetration curves and jet cone angle curves for diesel and GEM20 have been reported. The first row refers to the condition 2000x2, the second one reports data of the condition 2000x5. Curves of pilot injection of two fuels overlap indicating that there is no significant effect of fuels characteristics for short injection duration. Different observations can be made for the main injection; in this case, the energizing time is longer and the injector opens completely. In both load conditions tested, GEM20 penetrates less in the early injection phase whilst at later penetration it advances diesel, this change in the penetration behaviour has been detected at 3°CA after the start of injection. The behaviour in the early stage has been noted also for other biofuels [19] and it is due to the higher viscosity of GEM20 than diesel. Viscous forces generate leakages and slow down the fuel flow through the nozzle. Moreover, the higher density and viscosity of GEM20 is supposed to produce larger mean diameter of fuel droplets. Since the inertia of the big droplets is high, their penetration in the combustion chamber

will be higher as well [9]. This could explain the GEM20 behaviour observed in the second stage of the penetration curve. Finally, in the late injection, the GEM20 spray tip evaporates and starts to recede. This phenomenon is more evident in the condition at 2000x5 because of the longer duration of the injection event. In particular, at higher load, GEM penetration recedes in advance with respect to diesel fuel in the late injection phase. The measurements of the spray cone angle show that the GEM20 is characterized by narrower cone angles during the whole injection process. This is consistent with higher penetration of GEM20.

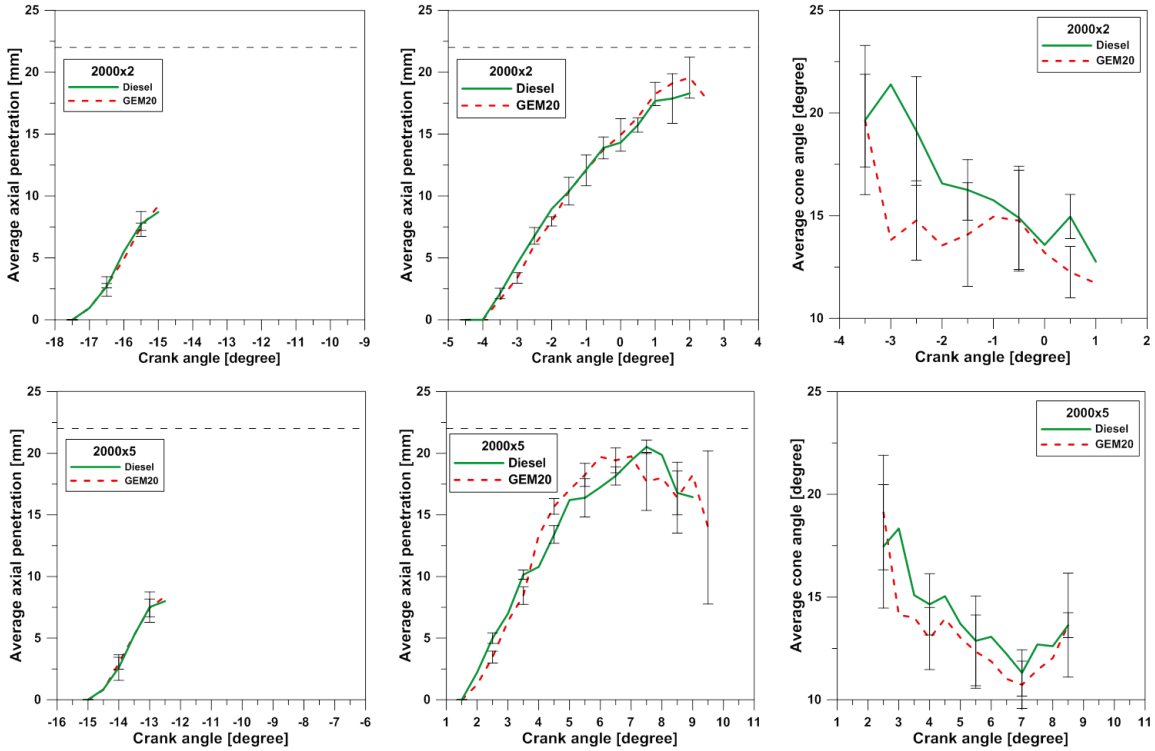

Fig. 6. Average axial penetration of pilot and main and jet cone angle of main for diesel and GEM20 at 2000x2 (up) and 2000x5 (down)

To investigate the reactions that take place in the combustion chamber before the detection of the first flames, the optical analysis has been extended from the visible spectrum to the IR range in the wavelength range 1,5-5 µm. At the operating point 2000x5, a selection of images detected in the visible, in IR and in IR with a filter at 3.9 µm for diesel and GEM20 has been reported in Fig. 7 and Fig. 8, respectively. The images at 3.9 µm have been used to identify the liquid phase of the injections and the source of the flames. For this reason, it can be assumed that if the jets are not detectable in the images at 3.9 µm but they are observable in the full IR spectrum, then they are the jets evaporating and mixing in the bowl. Moreover, if a luminosity peak is detected at 3.9 µm, then the combustion reactions are starting. In Fig. 7, for diesel at 2000x5 it can be noted that at the end of pilot injection no liquid fuel is visible in the combustion chamber but reacting vapour from -12°CA to 0°CA, as it results from images in the full IR spectrum and with a filter at 3.9 µm. In particular, at -4°CA the image at 3.9 µm reports some spots in the centre of the chamber that emit high intensity radiations, this identify the start of combustion of the pilot injection. This process is not detectable in the visible range but it is evident in the full IR spectrum images. This is consistent with the detection of pilot SOC from the ROHR analysis. Reactions of the pilot injection continue also during the main injection, at 4°CA. Here, there is the start of luminous combustion with presence of flames in the visible images. In Fig. 8, the same analysis has been performed using GEM20 fuel. Some differences have been noted; in particular, the pilot injection spreads in the volume available but no combustion reactions are visible at -4°CA as it was for diesel. Moreover, the first combustion reaction with GEM20 occurs at 12°CA, i.e. the start of main combustion. Images of the operating point 2000x2 have not been reported to shorten the text. In this condition, both the tested fuels have shown almost the same behaviour. After the pilot injection, the vapor spreads in the combustion chamber and no reactions are detectable in the IR range until the appearance of visible flames.

The imaging analysis performed in the visible and infrared range has produced results that agree with the macroscopic observations made on pressure signal and ROHR. The pilot combustion was absent for both fuels at 2000x2, while, at 2000x5, only the pilot injection of diesel burned. For the GEM20, the misfire of the pilot injection and the subsequent combustion of main and pilot not ignited fuel produced higher peak of the ROHR as noted in Fig. 4.

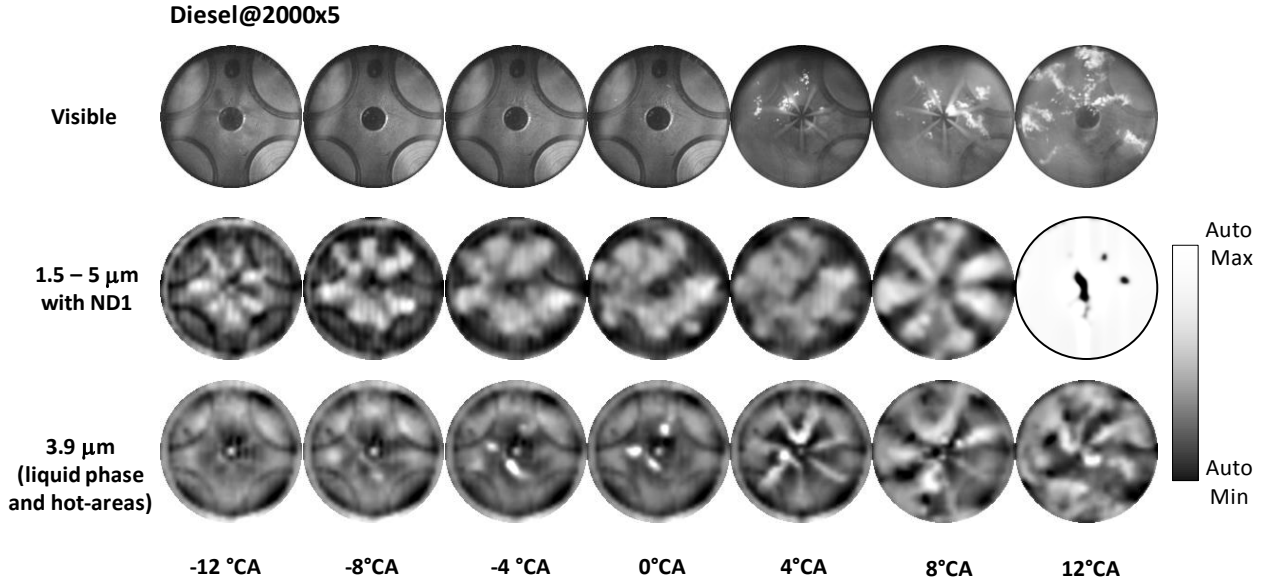

Fig. 7. Images of injection phase in the visible range (up), in the full infrared range (middle) and at 3.9 μm (down), for diesel fuel @2000x5

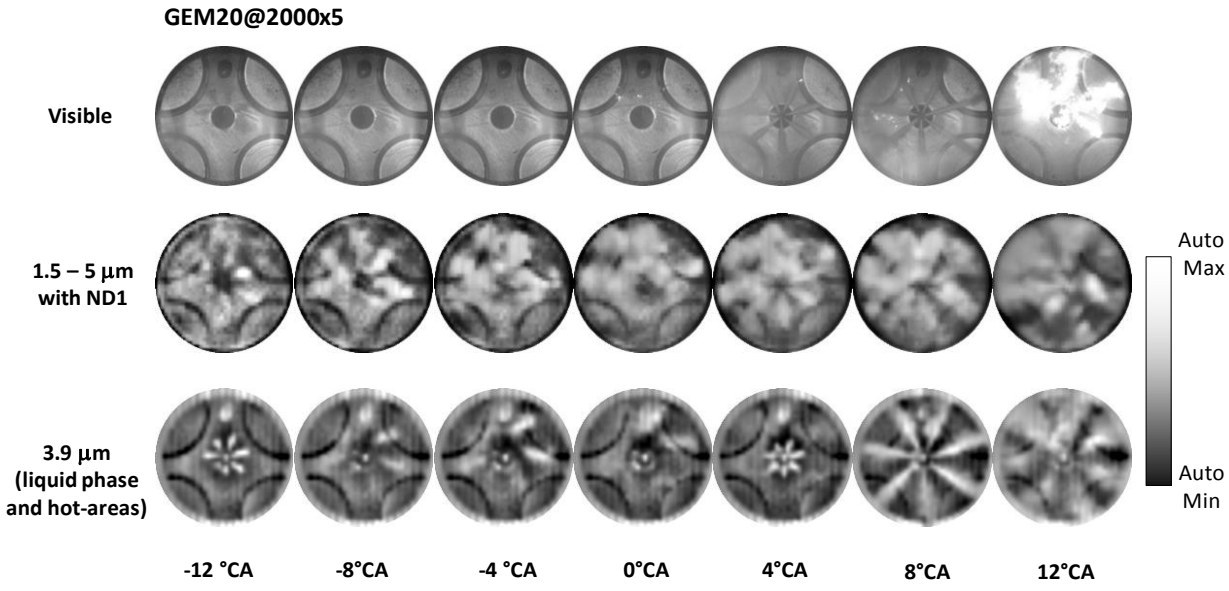

Fig. 8. Images of injection phase in the visible range (up), in the full infrared range (middle) and at 3.9 μm (down), for GEM20 fuel @2000x5

In addition, two-colour pyrometry has been performed by visible images that allowed the evaluation of the in-cylinder soot during the combustion. Fig. 9 and Fig. 10 report the curves of integral soot versus crank angle and, as an example, the visible flame images and the processed ones representative of in-cylinder soot concentration. At 2000x2, the two curves start almost at the same crank angle at around 4°CA. The soot formation slope is slightly lower for GEM20 and both the fuels reach the maximum value at about 14°CA. Nevertheless, the lowest integral value can be observed for GEM20. Similar observations can be made at the point 2000x5 as shown in Fig. 10. The start of soot formation occurs before for GEM20 (6°CA) because the fuel of the pilot and main injection burns all at once while the soot formation for diesel starts at 10°CA. The ascending slope of the curves is different; in particular GEM20 has the lowest velocity of soot formation. The peak value of integral soot is at 18°CA for both tested fuels, and then diesel fuel has the fastest oxidation. The longer duration of soot oxidation observed for GEM20 is due to its higher oxygen content that helps reduce the soot which was formed during the main combustion.

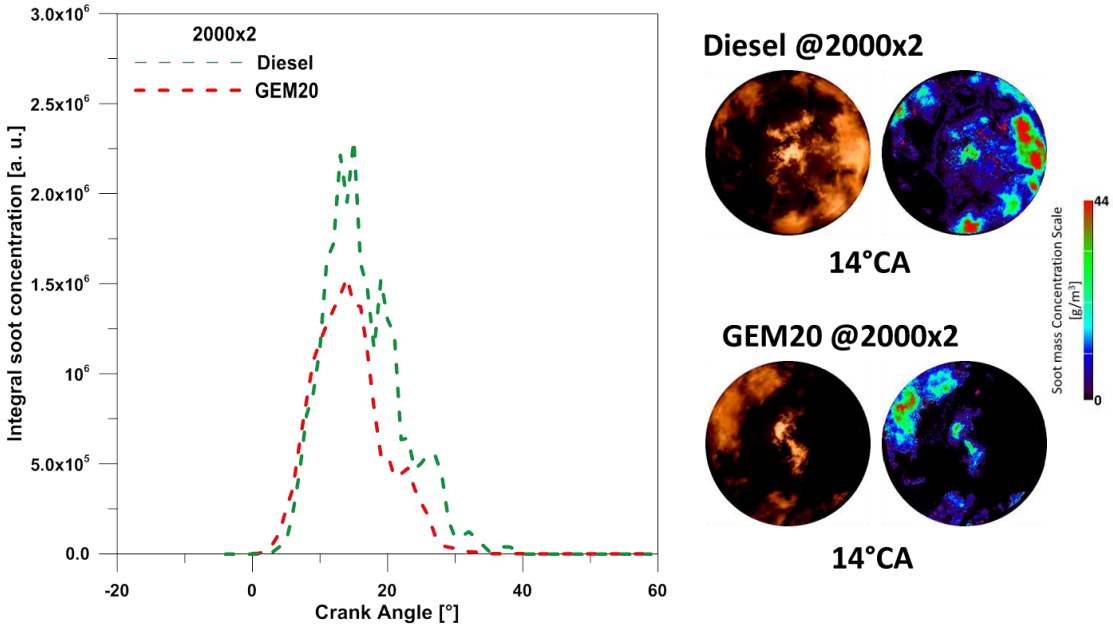

Fig. 9. Integral soot along crank angle of in-cylinder soot and visible images and processed soot spatial distirbution images, for diesel and GEM20 at 2000x2

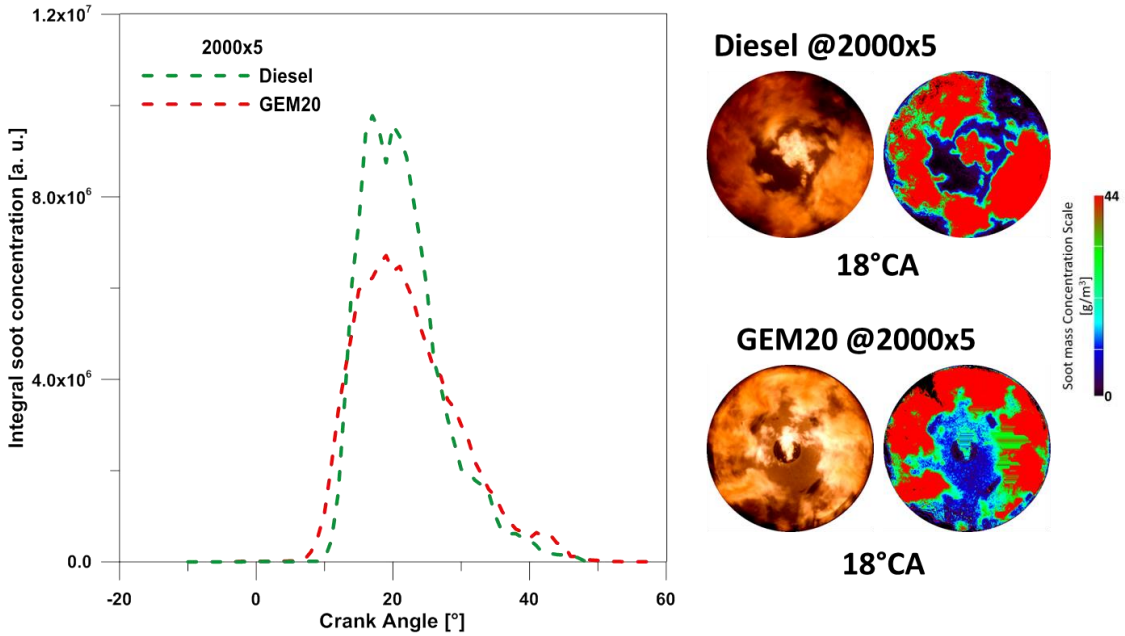

Fig. 10. Integral soot along crank angle of in-cylinder soot and visible images and processed soot spatial distirbution images, for diesel and GEM20 at 2000x5.

Exhaust emissions of the optical engine run with diesel and GEM20 have been reported in Fig. 11. Emission measurements in the operating conditions at 2000x2 and 2000x5 have put in evidence the benefits of using GEM20 blends in CI engine. At 2000x2, even if GEM20 has a less efficient combustion producing higher concentrations of CO and HC with respect to diesel fuel, it allows reducing the NO_x and PM emissions. At 2000x5, due to higher injected fuel quantities and, then, higher temperature, the GEM20 shows CO and HC production comparable to diesel fuel. Due to the higher peak of the ROHR, GEM20 produces more NO_x in this operating point. However, also in this case, the PM emission is strongly reduced due to the enhanced in-cylinder oxidation process and the fuel oxygen content.

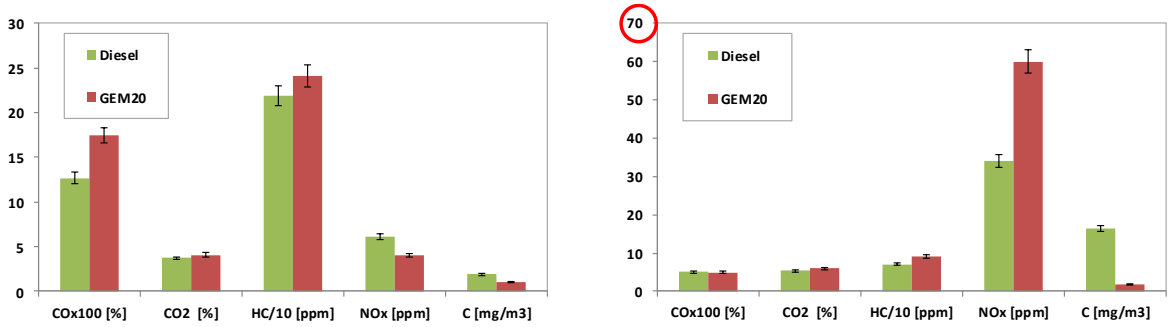

Fig. 11. Optical engine exhaust emission using diesel and GEM20, at 2000x2 (left) and at 2000x5 (right)

4.3 Trade offs by EGR sweep in metal engine

In this section are presented the results of the EGR sweep in terms of NOx-PM trade-off by varying the EGR rate for the metal engine. The trade-off analysis is chosen in order to evaluate the potential of the GEM blends, to improve the typical diesel NOx-PM trade-off. This analysis is particularly important for operating conditions, where NOx and PM emissions become critical for emission regulations. Fig. 12 shows the evolution of the trade-offs by varying the EGR rate, at 2000x2, 2000x5 and 2000x10, for the three blends. At lower loads (e.g. 2000x2) due to the very low values of PM at the exhaust, it makes sense to plot the trend of NOx-CO since the CO become more critical. Generally, in the diesel engine calibration, the interception of the trace with the diagram bisector is chosen as the best compromise in terms of particulate and NOx emissions.

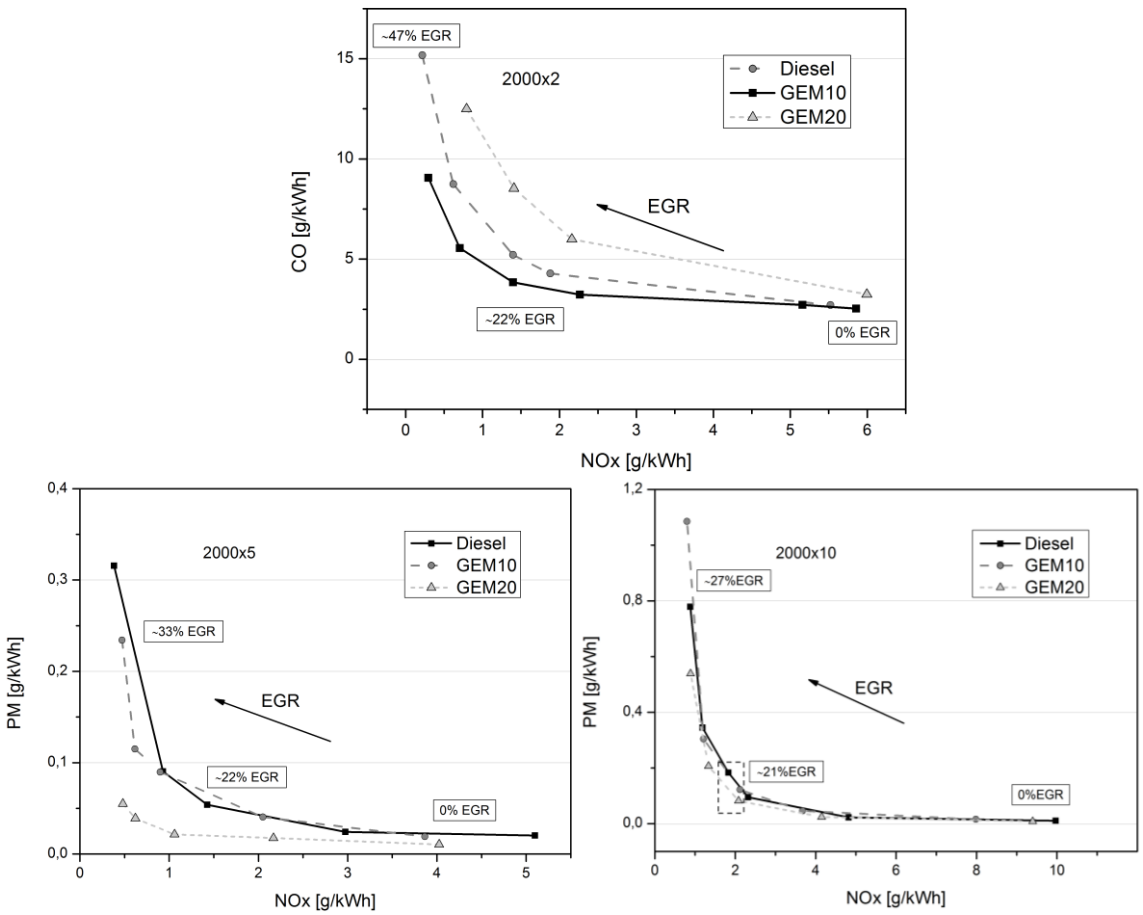

Fig. 12. Specific trade-offs by EGR sweep in the points 2000x2, 2000x5 and 2000x10 for metal engine

At low load conditions (2000x2), the trade off NOx-CO highlights an increase of CO as the GEM in diesel increase. As described in the previous section, this is mainly due to the general lower combustion efficiency of the fuel of the pilot injection. The trade-offs, in the other points, show the beneficial effects of GEM as PM suppressor in diesel combustion and GEM20 shows the best results in terms of particulate reduction at same level of NOx. At

2000x5, GEM 20 presents clearly the lowest trace, indicating the lowest PM production at same NOx exhaust emission level. The PM improvements are particularly evident at the highest EGR rate. Such result is typical for oxygenated fuels [0, 22, 23]. The major benefits are notable at 2000x5 because at this point the engine is more critical in terms of PM emission control and is one of the operating points with the highest weight factors in the NEDC emission estimation procedure. In this point, the best compromise between PM-NOx-combustion noise is generally founded adopting a calibration with late premixed combustion phasing [25]. In this condition, a slight advancing of the combustion phasing due to the variation of the fuel quality or a drift in the engine control produces a sharp increase of soot production [26]. Therefore, the PM emission index improvement in this test point appears significantly favourable for the engine performance on NEDC procedure when GEM is blended to the diesel fuel.

Due to the lower EGR rates and higher injection pressure and combustion temperatures, at medium-high loads (e.g. 2000x10) the benefits on particulate matter of the GEM addition are less evident.

Conclusions

A detailed engine test investigation using GEM in blends with diesel fuel was carried-out. The tests were planned performing the engine at real operating conditions. It was outlined that:

- the use of GEM blends have shown any significant impact on the in-cylinder combustion process, compared to diesel only use, even employing the reference Euro5 engine parameter calibration;
- infrared imaging has shown that there are no reactions for the pilot injection of GEM at lower load operating conditions (i.e., 2 bar of IMEP). Indeed the lower CN of the GEM seems critical for unburned emissions and combustion efficiency; an injection parameter optimization (i.e., pilot injection quantity and timing) should be adopted;
- GEM20 has the same penetration of diesel fuel during the pilot injection. For longer periods, the GEM20 penetrate faster even if this difference is no longer significant in the late injection. GEM20 jets are characterized by narrower angles during the whole injection process.
- GEM addition is effective for PM emissions suppression, without substantial penalties on the other regulated pollutant emissions (NOx, HC and CO); optical in-cylinder soot diagnostic denotes lower soot formation for GEM20;

The results discussed in the present paper show a good potential of the GEM as supplementary biofuel in order to increase the biodiesel production chain efficiency and improve the quality of the future sustainable fuels for compression ignition engines.

Acknowledgments

We thank the Italian Ministry of Agriculture, Food and Forestry for partially funding of this work through ‘‘TERVEG’’ Project (National funding call ‘‘bando bioenergetico DM 246/2007, GU No. 94 del 27/11/2007).
We thank also Mr. Alessio Schiavone, Mr. Carlo Rossi and Mr. Roberto Maniscalco for their technical assistance in the engine testing.

References

7 Beatrice, C., Di Blasio, G., Lazzaro, M., Cannilla, C., Bonura, G., Frusteri, F., Asdrubali, F., Baldinelli, G., Presciutti, A., Fantozzi, F., G., Bidini, F., Bartocci, P., “Technologies for energetic exploitation of biodiesel chain derived glycerol: Oxy-fuels production by catalytic conversion”. Appl. Energy, (2013), Pages 63-71, ISSN 0306-2619, doi: 10.1016/j.apenergy.2012.08.006.

8 Bohon, M.D., Metzger, B.A., Linak, W.P., King, C.J, Roberts, W.L., “Glycerol combustion and emissions”. Proc. Combust. Inst., 2011; 33: 2717–24.

15 Deutsch, J., Martin, A., Lieske, H.,“Investigations on heterogeneously catalysed condensations of glycerol to cyclic acetals”. J. Catal. 2007; 245: 428–35.

21 Di Blasio, G., Beatrice, C., Dijkstra, R., and Boot, M., “Low Cetane Number Renewable Oxy-fuels for Premixed Combustion Concept Application: Experimental Investigation on a Light Duty Diesel Engine”. SAE Technical Paper 2012-01-1310, 2012, doi:10.4271/2012-01-1310.

20 Di Blasio, G., Bonura, G., Frusteri, F., Beatrice, C. et al., "Experimental Characterization of Diesel Combustion Using Glycerol Derived Ethers Mixtures," SAE Int. J. Fuels Lubr. 6(3):2013, doi:10.4271/2013-24-0104.

22 Dijkstra, R., Di Blasio, G., Boot, M., Beatrice, C., et al., “Assessment of the Effect of Low Cetane Number Fuels on a Light Duty CI Engine: Preliminary Experimental Characterization in PCCI Operating Condition”. SAE Technical Paper 2011-24-0053, 2011, doi: 10.4271/2011-24-0053.

1 Directive 2009/28/EC of the European Parliament and of the Council of 23 April 2009 on the promotion of the use of energy from renewable sources and amending and subsequently repealing Directives 2001/77/EC and 2003/30/EC (Text with EEA relevance).

14 Frusteri, F., Arena, F., Bonura, G., Cannilla, C., Spadaro, L., Di Blasi, O., “Catalytic etherification of glycerol by tert-butyl alcohol to produce oxygenated additives for diesel fuel”. Appl. Catal. 2009; A 367: 77–83.

6 Frusteri, F., Cannilla, C., Bonura G., Spadaro, L., Mezzapica, A., Beatrice, C., Di Blasio, G., Guido, C., “Glycerol Ethers Production and Engine Performance with Diesel/Ethers Blend”. Top. Catal. (2013), ISSN 0306-2619, doi: 10.1007/s11244-013-9983-7.

16 Frusteri, F., Frusteri, L., Cannilla, C., Bonura, G., “Catalytic etherification of glycerol to produce biofuels over novel spherical silica supported Hyflon® catalysts”. Biores. Technol. 2012; 118: 350–358.

12 González D., M., Piel, W., Asmus, T., Clark, W. et al., “Oxygenates screening for Advanced Petroleum-Based Diesel Fuels: Part 2. The Effect of Oxygenate Blending Compounds on Exhaust Emissions”. SAE Technical Paper 2001-01-3632, 2001, doi:10.4271/2001-01-3632.

11 Guido, C., Beatrice, C., Di Iorio, S., Napolitano, P. “Assessment of Closed-Loop Combustion Control Capability for Biodiesel Blending Detection and Combustion Impact Mitigation for an Euro5 Automotive Diesel Engine”. SAE Technical Paper 2011-01-1193, 2011, doi:10.4271/2011-01-1193.

3 Hamelinck, C.N., Faaij, A.P.C., “Outlook for advanced biofuels”. Energy Policy 34, 17 (2006): 3268-3283.

18 Heywood, J.B., “Internal Combustion Engine Fundamentals”. McGraw-Hill, 1988.

4 Hoogwijk, M., Faaij, A.P.C., Eickhout, B., de Vries, B., Turkenburg,W.C., 2003c. Potential of biomass energy under four land-usescenarios, Part A: the geographical and technical potential. Manuscript. United States Environmental Protection Agency, Office of Transportation and Air Quality, EPA-420-F-10-056, Nov. 2010.

17 Karinen, R.S, Krause, A.O.I., “New biocomponents from glycerol”. Appl. Catal. 2006; A 306: 128–33.

26 Kimura, S., Aoki, O., Ogawa, H., Muranaka, S. et al., "New Combustion Concept for Ultra-Clean and High-Efficiency Small DI Diesel Engines," SAE Technical Paper 1999-01-3681, 1999, doi:10.4271/1999-01-3681.

23 Litzinger, T., Stoner, M., Hess, H, Boehman, A., “Effects of oxygenated blending compounds on emissions from a turbo-charged direct injection diesel engine”. Int. J. Engine Res 2000; 1:1.

24 Mancaruso, E., Sequino, L., and Vaglieco, B. M., “First and second generation biodiesels spray characterization in a diesel engine”. Fuel, 90(9):2870–2883, 2011.

13 Melero, J.A., Vicente, G., Morales, G., Paniagua, M., Moeno, J.M., Roldán R., “Acid catalyzed etherification of bio-glycerol and isobutylene over sulfonic mesostructured silicas”. Appl. Catal. 2008; A 346: 44–51.

25 Napolitano, P., Guido, C., Beatrice, C., and Di Blasio, G., "Study of the Effect of the Engine Parameters Calibration to Optimize the Use of Bio-Ethanol/RME/Diesel Blend in a Euro5 Light Duty Diesel Engine," *SAE Int. J. Fuels Lubr.* 6(1):263-275, 2013, doi:10.4271/2013-01-1695.

9 Rahmat, N., Abdullah, A.Z., Mohamed, A.R., “Recent progress on innovative and potential technologies for glycerol transformation into fuel additives: a critical review”. Renew. Sustain. Energy Rev. 2010; 14: 987–1000.

19 RAMMB: Regional and Mesoscale Meteorology Branch. http://rammb.cira.colostate.edu/training/tutorials/goes_39um/

2 Sims, R., Taylor, M., Saddler, J., Mabee, W., “From 1st to 2nd Generation Biofuel Technologies: An overview of Current Industry and RD&D Activities”, International Energy Agency. OECD/IEA, http://www.iea.org/papers/2008/2nd_Biofuel_Gen.pdf, Nov. 2008.

10 Valliyappan, T., Bakhshi, N.N., Dalai, A.K., “Pyrolysis of glycerol for the production of hydrogen or syngas”. Bioresour. Technol., 2008; 99: 4476–83.

5 Vlysidis, A., Binns, M., Webb, C., Theodoropoulos, C., “A techno-economic analysis of biodiesel biorefineries: Assessment of integrated designs for the co-production of fuels and chemicals”. Energy 36 (2011) , doi.org/10.1016/j.bbr.2011.03.031.

Methodology for Analysis and Simulation of Dual Fuel Combustion in Large Engines

M. Krenn[1], G. Pirker[2], A. Wimmer[1,2], S. Djuranec[3], M.C. Meier[3], U. Waldenmaier[3] and J. Zhu[3]

[1]IVT – Institute for Internal Combustion Engines and Thermodynamics
Graz University of Technology, Inffeldgasse 19, 8010 Graz, Austria

E-mail: krenn@ivt.tugraz.at
Telephone: +(43) 316 873 30132
Fax: +(43) 316 873 30102

[2]Forschungsgesellschaft für Verbrennungskraftmaschinen und Thermodynamik mbH
Inffeldgasse 19, 8010 Graz, Austria

E-mail: pirker@ivt.tugraz.at
Telephone: +(43) 316 873 30130
Fax: +(43) 316 873 30102

[3]MAN Diesel & Turbo SE
Stadtbachstrasse 1, 86153 Augsburg, Germany

E-mail: markus-christian.meier@man.eu
Telephone: +(49) 821 322 1022

Abstract. Due to the increasing availability of natural gas and the inherently low emissions of gas engines together with the stringent emission legislation, the importance of natural gas as engine fuel will significantly grow in the near future.
Due to great improvements in efficiency and power output in recent years, large gas engines have registered significant growth in the area of stationary power generation. In addition, low emission gas engines are also regarded as a preferable solution to reaching stringent future emission limits for marine applications. In this respect, dual fuel operation is of particular interest for reasons of safety because of the reliability of the basic Diesel concept and for reasons of economics because of the possibility of using the boil-off on LNG tankers.
Dual fuel technology is also being intensively discussed for many other applications, e.g. locomotive propulsion. Therefore, dual fuel engines are very promising for future applications.
In order to reduce the development time of new dual fuel engines, it is important to use reliable simulation tools for the optimization of the working cycle. At present, the nature of dual fuel combustion has not yet been well described by models.
Therefore, this paper deals with the development of a simulation model to predict the combined burn rate of diesel fuel and natural gas. As a starting point, suitable burn rate models for both diesel fuel as well as gas have to be designed. The great challenge is to understand the influence of gas concentration on the ignition delay of diesel fuel and the impact of each fuel on the combustion process of the other fuel.
A special analysis tool has to be developed before a database for model validation can be created. Aside from the burn rate, an additional criterion for the validity of analysis and simulation can be found in the NO concentration. Consequently, a NO model based on a two zone thermodynamic description is required.
The analysis and simulation tools will be developed using measurement data from a single cylinder research engine. In order to ensure the transferability to other engines, the models will also be validated on a different sized multi-cylinder engine.

Notation

r	$Reaction\ rate$
k	$Reaction\ speed\ constant$
c	$Concentration$
n	$Reaction\ order$
T	$Temperature$
τ	$Time$
t	$Time$
Q	$Heat$
m	$Mass$
h	$Specific\ enthalpy$
H	$Enthalpy$
u	$Specific\ inner\ energy$
p	$Pressure$
R	$Gas\ constant$
LCV	$Lower\ caloric\ value$
R	$Gas\ constant$

Indexes

ID	$Ignition\ delay$
a	$Activation$
O	$Oxygen$
H	$Homogeneous\ charge$
D	$Diesel\ fuel$
U	$Unburned$
B	$Burned$
V	$Vapor$
P	$Package$
F	$Fuel$
ENT	$Entrainment\ model$

1. Introduction

According to a prognosis made by the International Energy Agency (IEA) about the development of global power generation as divided into shares of the individual areas (World Energy Outlook 2012) (Warnecke et al. 2013), the share of natural gas will increase significantly in the next 20 years and quantitatively double. The main impetus for this development comes from the large natural gas resources in conventional and unconventional deposits (shale gas, tight gas and CBM) which should last over 250 years, the development of the price of natural gas (especially in the U.S.), the discussion about how to stop using nuclear energy in various countries (e.g. Germany and Japan) and the fact that due to the lower amount of carbon in comparison with other fossil fuels, natural gas is seen as a technology that can be used to bridge the gap between carbon-based and “carbon-free” energy supply and mobility.

Due to great increases in efficiency and power output in recent years, large gas engines have registered significant growth in the area of stationary power generation. In addition, low emission gas engines are favored as a solution to the problem of how to meet the very stringent emission requirements for marine applications. In addition to pure SI operation, dual fuel (DF) technology (from gas operation with diesel pilot injection to pure diesel operation) is a promising approach. In the meanwhile, DF technology is being intensively discussed for many other applications such as locomotives and marine applications.

DF engines combine the advantages of two fundamentally different engine processes. These engines can be fired either with liquid fuels such as marine diesel oil or heavy fuel oil, consequently using a diesel cycle, or they can be fired with a wide range of gaseous fuels such as natural gas or boil off gas, using an Otto cycle principle. This flexibility results in environmental advantages in terms of emission savings and fuel savings; on the other hand, there is the possibility to choose the most suitable fuel for the ship owner and operator. While heavy fuel oil or marine diesel can be chosen outside the emission controlled areas (ECAs), the engine can be operated with natural gas inside the ECAs to fulfill the requirements of the IMO Tier III (see fig. 1).

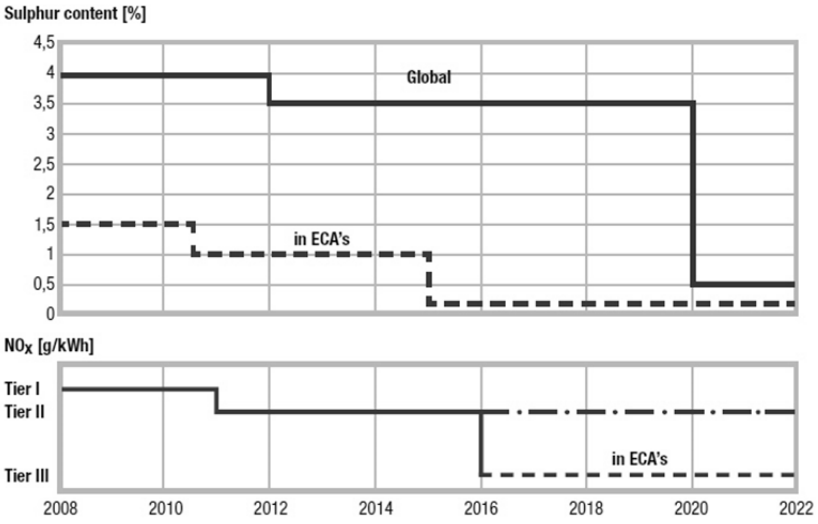

Fig. 1. Implementation schedule for IMO emission limits (Menage et.al. 2013)

The dynamic behavior of the gas engine is inferior to that of a conventional diesel engine because the load acceptance of the gas engine is greatly limited by the knock limit. Dual fuel engines can exploit the advantages of the diesel mode for transient operation. However, here too new strategies for more favorable transient behavior must be developed in parallel to the desired improvements in efficiency and emissions. One great challenge is the considerably higher number of degrees of freedom resulting from operation with two fuels.

The following paper is concerned with one specific type of dual fuel engine in which a homogeneous lean mixture of natural gas and air is introduced into the cylinder, after which a relatively small amount of diesel fuel is injected that ignites the cylinder charge after inflammation. Optimization of this engine concept turned out to be difficult due to the large number of degrees of freedom. As a result, engine cycle simulation is often the means for optimizing the engine. This procedure has turned out to be efficient in terms of time and cost as compared to pure test bed development. In the optimization process, however, combustion must be reproduced as accurately as possible.

The paper describes the development of a 0D simulation model capable of describing dual fuel combustion. To guarantee the applicability of this tool to a variety of engine layouts, universal laws of physics are used when possible to set up the model.

2. Test engines

Both investigated engines 35/44DF and 51/60DF have been designed by MAN Diesel & Turbo SE for all kinds of application such as diesel-mechanic, diesel-electric and constant speed generator application. Two different kinds of cylinder arrangement are available, inline and vee configuration. This results in a power range of 6.4MW to 18MW covered complementary by 35/44DF and 51/60DF as can be seen Figure 2 (right). Figure 2 (left) presents the main technical data of the 35/44DF.

Specification	Dimension	50 Hz	60 Hz
Bore / Stroke	mm	350 / 440	
Swept volume	liter/Cyl.	42.3	
Cylinder config.	-	6 - 10 / 12 - 20	
Speed	min^{-1}	750	720
Output	kW_m/Cyl.	530	510
BMEP	bar	20	
Power range	kW_m	3,060 - 10,600	

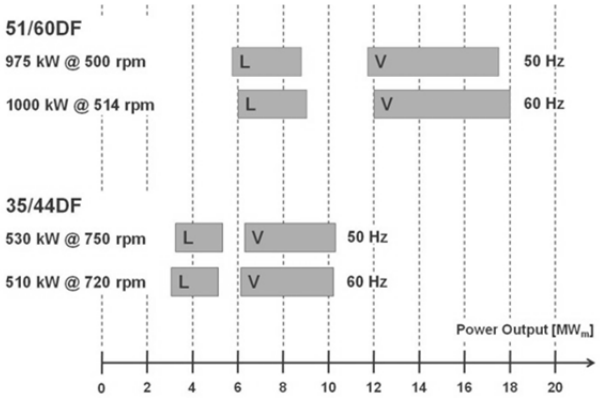

Fig. 2. Main technical data of 35/44DF (left); Dual Fuel Engine Portfolio of MAN Diesel & Turbo SE [2] (right)

2.1 Working principle of multi-fuel engines 35/44DF and 51/60DF

Both the 35/44DF and the 51/60DF have the same working principle, the 35/44DF will be explained in detail below.

The 35/44DF can be operated with multiple fuels, which requires two different fuel systems. First, the engine is equipped with a common rail system capable of a wide range of fuel types such as marine gas oil (MGO), marine diesel oil (MDO) as well as heavy fuel oil (HFO). Figure 3 (left) shows the combustion system used in the liquid mode. The fuel is pressurized by a mechanical pump that is directly driven by the engine's camshaft. Double-walled high pressure pipes connected to each other supply the accumulators with the compressed fuel. From these accumulators, the fuel flows through high pressure pipes to the main injectors, which placed in the center of the cylinder head to guarantee optimal liquid fuel combustion parameters. The common rail principle can be seen in Figure 4 (left). The injection system is under the direct electronic control of MAN Diesel & Turbo's engine management system SaCoSo*ne* (Safety and Control System on Engine).

Like the 51/60DF, the 35/44DF has a second independent fuel system for burning gaseous fuels with a wide range of methane numbers. The gas mode has been developed to run a lean mixture of gas that is ignited with a pilot diesel injection system (Figure 3 right). To this end, the system is equipped with multi-port gas admission so that each engine cylinder can be driven in its optimum range. The ignition system for gas mode is also a common rail system that injects approximately 1% of the engine's power output as diesel pilot fuel (Figure 4 left).

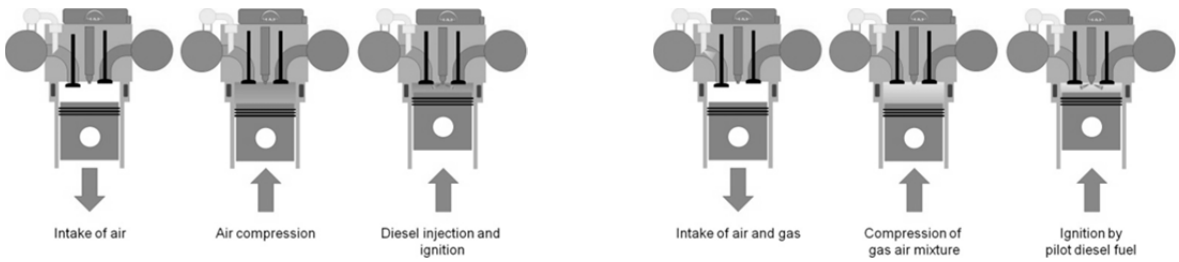

Fig. 3. Liquid fuel mode operation (left) and gas mode operation (right) (Menage et.al. 2013)

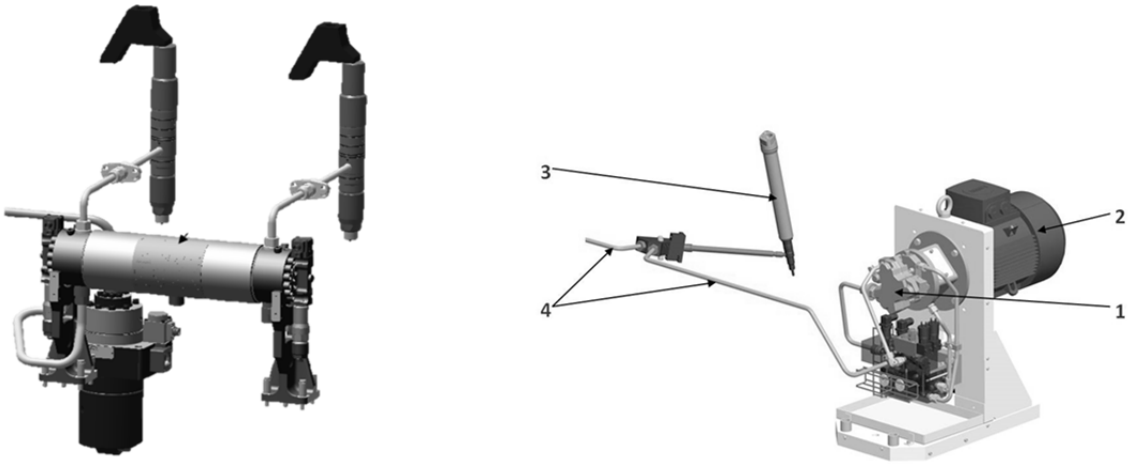

Fig. 4. Common rail system 35/44DF (left) and pilot injection system of 35/44DF (right) (Menage et.al. 2013)

The lean gas mixture is ignited with an electronically driven and controlled common rail system (see Fig. 4 right). The fuel is pressurized by a high pressure pump (1) that is electrically driven (2). The pilot injector (3) is supplied with compressed fuel via high pressure pipes (4) that connect all cylinders and act as an accumulator (see CR main injection system). The electronic control allows time- and mass-oriented regulation of the pilot injection and optimal gas ignition.

Because two different thermodynamically working principles are employed, the optimal configuration for gas admission, gas ignition and diesel combustion has been determined from intensive CFD calculations followed by tests on single-cylinder research engines.

The gas supply system is developed as a double walled casted gas manifold leading the gaseous fuel directly to each cylinder in compliance with marine classification societies and safety requirements for marine applications. As mentioned before, the cylinders are supplied via an electronically controlled multi-port injection system (Fig. 5 left) also controlled by SaCoSo*ne*.

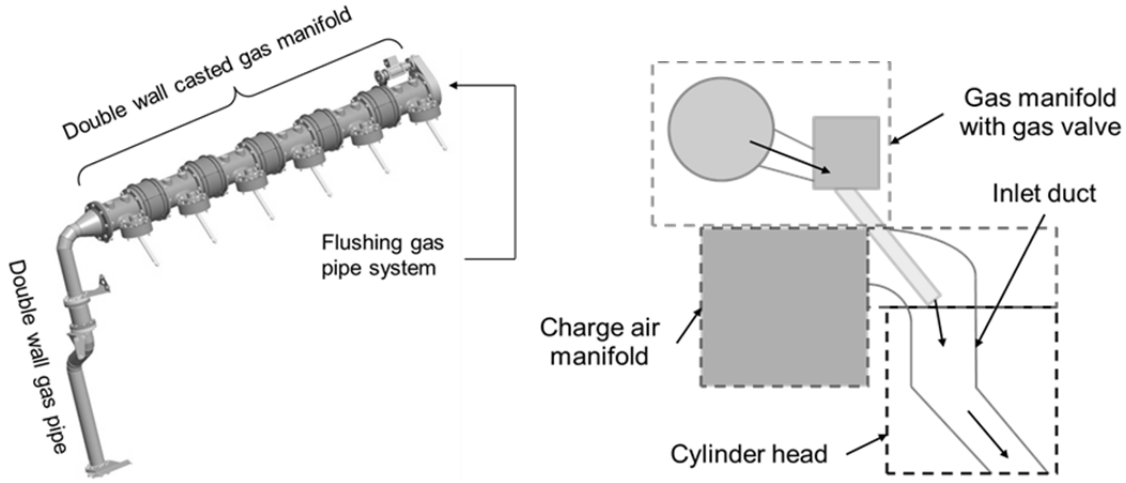

Fig. 5. On engine gas pipe system of 35/44DF (left) and gas flow illustration from gas pipe manifold to inlet air duct (right) (Menage et.al. 2013)

After passing the gas valves placed on each cylinder, the gas flows through the gas pipe manifold to the inlet air duct and finally reaches the combustion chamber. The complete gas system has been optimized with CFD calculations and was tested on a single-cylinder engine as well as on a multi-cylinder engine to guarantee optimal engine performance and fuel efficiency (Fig. 5 right).

3 Model description

A suitable method for analysis must first be developed before a simulation model describing dual fuel combustion can be created. The method for analysis must be able to describe combustion in which the mixture of two fuels constantly changes. The challenge with the calculation of a dual fuel engine combustion process is that both fuels that are used do not combust at the same time but rather in two specific phases. In the first phase, a specific diesel fuel is ignited, and the background gas mixture burns along with it. This phase of combustion must be considered to be inhomogeneous, which means that the combustion excess air ratio does not correspond to the overall excess air ratio. A considerable share of the NOx emissions is formed in this first phase of combustion. It is mainly the homogeneous background mixture that combusts during the second phase of combustion. Most of diesel fuel used to ignite the mixture has already been converted. This phase of combustion is considered to be homogeneous.

To describe this complex combustion process, a simple model for usage in pressure cycle analysis was developed that does not require any data from diesel injection. In contrast to commercially available software tools that only allow the excess air ratio to be described as either homogeneous or stoichiometric-lean, the new model uses an advanced and more realistic approach to describe the excess air ratio of the burning diesel fuel. The following illustration compares the results from pressure curve analysis using this method to the results from commercially available software. It presents the temperature of the unburned and burned zones during combustion in a dual fuel engine with a diesel share of 1% of the total added energy using different approaches.

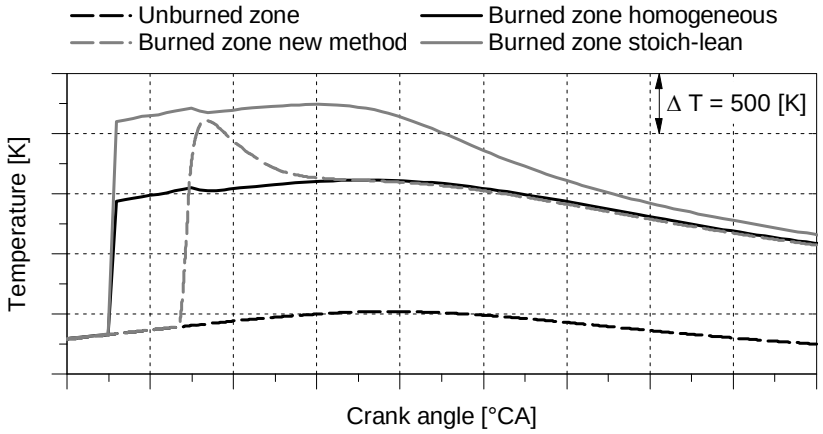

Fig. 6. Temperatures in the combustion chamber, two zone analysis using different approaches

It can be seen that the setting of a combustion excess air ratio to homogeneous mixed combustion or stoichiometric-lean combustion doesn't fit to the dual fuel combustion, yet the total fuel is always considered to be homogeneously blended, which is definitely not the case with a dual fuel engine. The result is a deviating temperature curve of the burned zone, the precise knowledge of which is particularly important for emission calculation. The influence of the calculation method on the rate of heat release, however, can be disregarded.

The simulation of dual fuel combustion must now describe the two combustion phases in detail. A slightly modified package model (Stiesch 2003) is used to model the diesel spray, which is responsible for ignition and the first phase of combustion. Because this phase is longer than that of a standard diesel engine, ignition delay is of great importance. In addition, the entrainment model (Tabaczynski et al. 1977) is used for the second phase of combustion, in which the majority of fuel (the background mixture) is converted. Both combustion models are connected to each other and used simultaneously.

3.1 Modeling ignition delay

Since the compression ratio of the dual fuel engine is lower than that of a diesel engine to avoid knocking combustion, the final compression temperature is lower. This lower temperature is one of the reasons for ignition delay being longer than with the pure diesel engine. The presence of an additional fuel also has an important impact on ignition delay. (Schlatter et. al. 2012) The correct precalculation of ignition delay and thus the start of combustion is essential to rate of heat release simulation. Both combustion duration and the maximum conversion rate greatly depend on the start of combustion. Small deviations when calculating ignition delay have an even higher effect on the subsequent simulation of combustion and thus on the efficiency, emission levels and knock behavior of the engine under investigation.

The Arrhenius equation is used to calculate ignition delay and yields a reaction rate r dependent on temperature T, an activation energy or activation temperature Ta and the concentrations c_i of the species influencing the reaction with the reaction orders n_i.

$$r = k \prod_i c_i^{n_i} \; e^{-\frac{Ta}{T}} \tag{1}$$

The reaction velocity constant k, the activation temperature and the reaction orders should be determined empirically. Ignition delay τ_{ID} can now be set as the inverse value of the reaction rate.

$$\tau_{ID} = \frac{1}{r} \tag{2}$$

The constants in Eq. (1) were determined using the chemical reaction kinetics software Cantera (Goodwin 2003). A homogeneous reactor with a constant volume was set up in Cantera. Pressure, temperature and composition were set as the initial conditions; diesel fuel was replaced by n-heptane and natural gas by methane. Finally, the period of time was calculated up to a rapid increase in the OH concentration. This period of time represents the ignition delay time. Version 2 of the n-Heptane Detailed Mechanism from Lawrence Livermore National Laboratory was used as the reaction mechanism (Curran et al. 2002).

Before the constants of the Arrhenius approach were calculated using nonlinear regression, the validity of this simplification was checked. For example, the influence of temperature on ignition delay time was discussed, cf. Figure 7. To illustrate this better, the logarithm of ignition delay timing is taken; the reaction velocity constants and concentrations were kept constant and thus can be illustrated by a replacement reaction velocity constant k':

$$\ln(\tau_{ID}) = \frac{T_a}{T} + \ln(k') \tag{3}$$

If the logarithm of ignition delay time plotted against the inverse value of the temperature yielded a line, the approach would be capable of reproducing ignition delay time correctly.

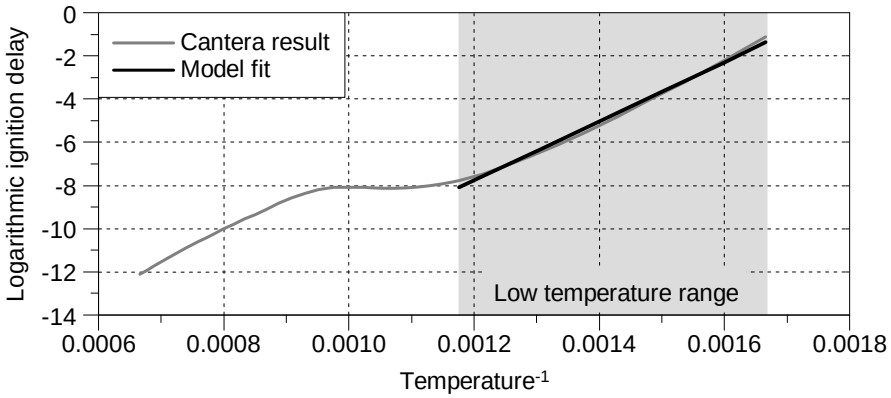

Fig. 7. Result of ignition delay calculation, Cantera, temperature varied, concentrations of the individual species kept constant.

As the graph above shows, the Arrhenius approach does not suffice to correctly describe ignition delay over the entire temperature range. The gas temperature range of the engine under investigation up to ignition, however, is clearly smaller. As a result, it suffices to consider the lower temperature range indicated above. This range can definitely be approximated linearly; a nonlinear regression was performed to determine the constants using LEC ParOS (Pirker 2009).

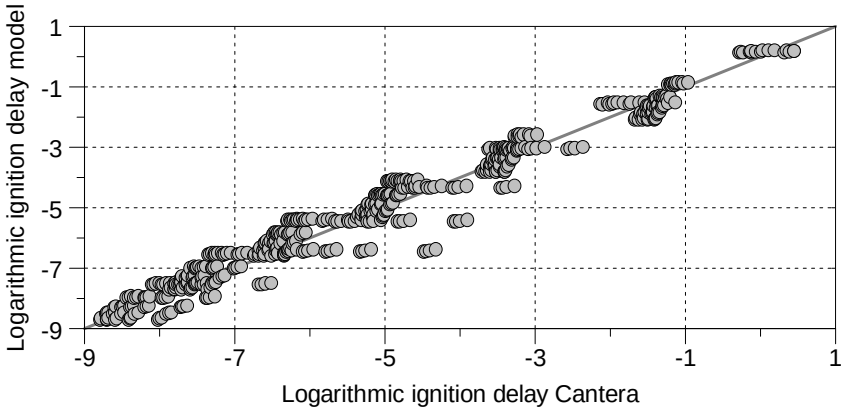

Fig. 8. Logarithmic ignition delay, comparison: simulation with Cantera vs. simplified model, low temperature range

The ignition delay equation determined in this way is as follows:

$$\tau_{ID} = 2.5 * 10^{-11}\, c_o^{0.65} c_{H,F}^{0.12}\, c_D^{-0.77}\, e^{\frac{13500}{T}} \qquad (4)$$

c_O represents the concentration of oxygen, $c_{H,F}$ the concentration of the homogeneously mixed fuel (natural gas) and c_D the concentration of the diesel fuel. Since the ignition delay determined in this way is only valid for a homogeneous volume, ignition delay in the combustion chamber must be modeled so that the diesel spray under investigation is formed from a variety of homogeneous volumes. For this reason, a package model was used to model the diesel spray.

3.2 Package model

The package model was originally developed to simulate diesel combustion. The diesel spray was divided into a large number of discrete ring-shaped packages (Hiroyasu et al. 1983). Although the fuel distribution throughout the entire combustion chamber is very inhomogeneous due to diesel injection, each individual package in the diesel spray can be regarded locally as homogeneous and also modeled as such. This means that from a local perspective, each package is composed of a homogeneous mixture of diesel fuel in a liquid and gaseous state and of the added background mixture consisting of natural gas and air.

The combustion chamber is described thermodynamically using a two zone model with one unburned gas zone and one burned zone (Merker et al. 2012). The packages are not defined as independent zones or systems in the combustion chamber but are modeled as subzones of the unburned gas zone. Thus the package model is only used to calculate the vaporization, ignition and combustion of the diesel fuel. The ignition delay model developed in section 3.1 can now be used in each package to determine the time to autoignition of the vaporized diesel fuel in the package. A combustion model for diesel fuel based on an Arrhenius approach has also been derived from the ignition delay model; it is used to model the oxidation of the ignited diesel fuel in the package.

3.2.1 How the package model works

The following illustration shows how the package model works. The parameters are added up from all the packages.

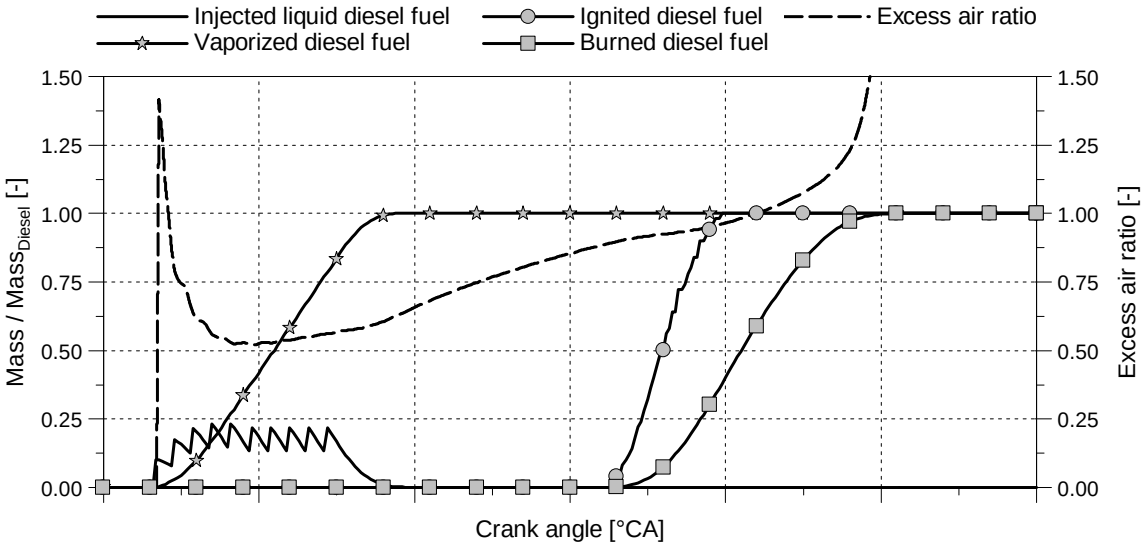

Fig. 9. Selected diesel fuel states and excess air ratio averaged over all packages (diesel fuel and natural gas). The diesel masses are normalized by the added diesel mass.

As soon as the diesel fuel is injected into the combustion chamber, it is divided into homogeneous packages. After a short time, the diesel fuel in the packages starts to vaporize. While the diesel fuel is vaporizing, the background mixture is also added to the package. This addition yields the excess air ratio curve in the package shown above. As soon as vaporization in the package has started, the ignition delay integral is also included in the calculation. When ignition occurs, all of the diesel fuel in the package is ignited and burned as described in the following approach.

3.2.2 Ignition delay in the package model

Knowledge of the temperature in the package is required to calculate the ignition delay time; as a result, the temperature of each package is calculated separately. Since parts of the package model are derived from the free spray theory, not all parameters are available in a differential form. Hence the first law of thermodynamics must be applied to the package in integral form. Droplet vaporization is represented as heat transfer out of the package and mass flow into the package. Since vaporization and combustion occur in the package at the same time, it was defined that packages should only be filled with a fresh charge. This means that combustion is illustrated as the removal of mass from the package.

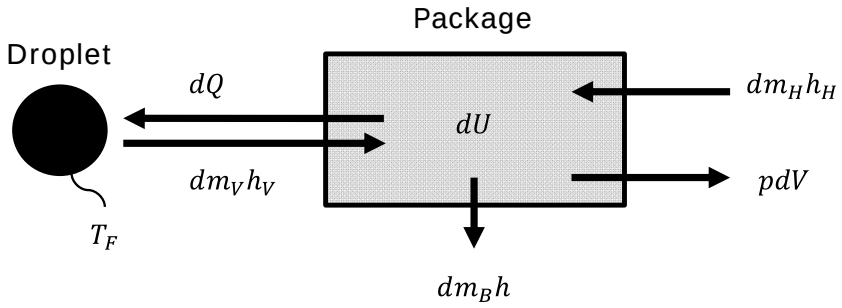

Fig. 10. Thermodynamic modeling of the package and the droplet in differential form

The mass of the gaseous part of the package is composed of vaporized diesel fuel m_V and homogeneous fresh charge added to the package m_H. The burned mass m_B must also be subtracted:

$$m = m_V + m_H - m_B \tag{5}$$

The vaporized diesel fuel mass that is added is a result of the vaporization of droplets in the package; the homogeneous fresh charge that is added can be obtained from the conservation of momentum equation.

The internal energy and temperature of the gaseous part of the package can thus be estimated using the following equation. In this approximation, pressure is kept constant, which makes the following integral formula possible:

$$u(T) = \frac{H_H + H_V - Q_V - H_B - m\,R\,T}{m} \tag{6}$$

When possible, differential equations are used to determine the individual terms:

$$H_V = \int h_V(T_F)\, dm_V \tag{7}$$

$$Q_V = \int dQ_V \tag{8}$$

$$H_B = \int h_P(T)\, dm_B \tag{9}$$

This is not possible with the homogeneously mixed mass; the actual temperature of the fresh gas zone in the combustion chamber T_U is used:

$$H_H = \mathrm{m_H}\, h_H(T_U) \tag{10}$$

Since the specific internal energy of the gaseous part of the package can also be calculated as a physical property, the temperature of this part of the package can be determined using Newton's method. The result is presented in the following figure.

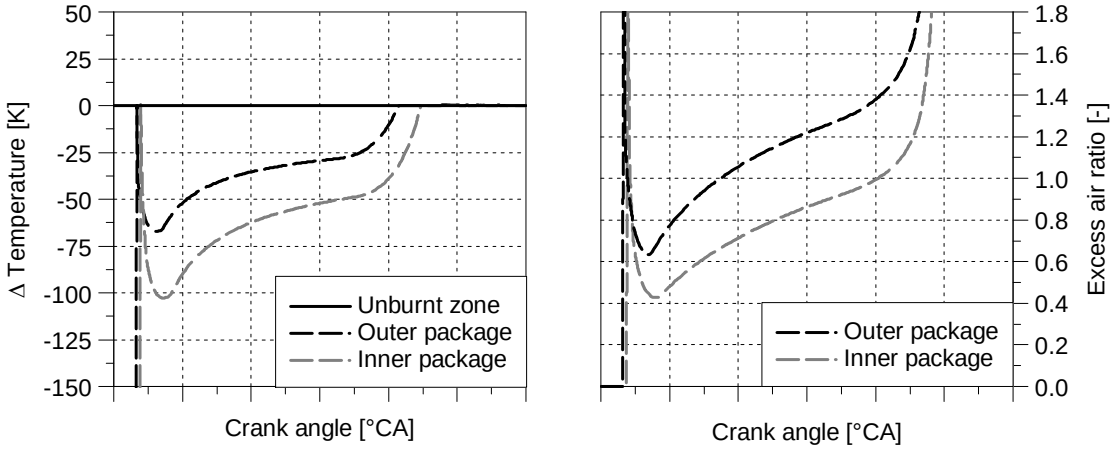

Fig. 11. Left-hand graph: Gas temperature of the innermost and outermost package of the first axial row; Right-hand graph: Excess air ratio of the innermost and outermost package of the first axial row.

To determine ignition delay, the concentrations of the species must still be determined by calculating the volume of the gaseous part of the package V_P, which can be done using the ideal gas law. The concentrations required in Eq. (4) can now be calculated.

Since both temperature and concentrations change during ignition delay, the actual ignition delay must be determined by integrating the reaction rate starting at the time of injection t_{INJ} using the following definition:

$$\int_{t_{INJ}}^{t} \frac{1}{\tau_{ID}}\, dt = 1 \tag{11}$$

3.2.3 Combustion

Combustion in the package starts as soon as the value of the ignition delay integral passes a certain threshold. The Arrhenius approach (Chmela et al. 2006) is used to describe premixed combustion in the package. Since the mathematical description of combustion is similar to that of ignition delay, the definition of the reaction rate determined above can be used to model combustion. The mass conversion rate of diesel fuel can be described as follows:

$$\frac{dm_D}{dt} = c_D\, V_P\, r \tag{12}$$

$$r = \frac{1}{\tau_{ID}} = 4 * 10^{10}\, c_O^{-0.65} c_{H,F}^{-0.12}\, c_D^{0.77} e^{-\frac{13500}{T}} \tag{13}$$

Assuming that only fresh gas is present in the package, the temperature is low and the simplified equations can be used once again. Assuming that the package is homogeneously mixed, the conversion rate of natural gas can be determined from the concentration ratio of natural gas $c_{H,F}$ to diesel fuel c_D:

$$\frac{dm_{H,F,P}}{dt} = \frac{c_{H,F}}{c_D}\frac{dm_D}{dt} \tag{14}$$

To obtain the total conversion rate of all packages, the instantaneous conversion rate of each package must be added up. The final equation for formulating the rate of heat release will be discussed below along with the conversion rate of the homogeneous background mixture.

3.3 Homogeneous background mixture

In a dual fuel engine, the main purpose of the diesel spray is to ensure that the homogeneous natural gas-air mixture ignites. An entrainment model is used to model the subsequent combustion of the natural gas. The diesel spray is modeled in a similar manner as a jet (Walther, et al. 2011); the penetration lengths of the packages obtained from the integral of the package velocities serve as the initial lengths for the jets. The surface of the jets defined in this way provides the baseline for the flame front surface of the entrainment model. The turbulent flame velocity is used to increase the surface of the jet. The rate of heat release calculation using the entrainment model starts at the point in time when the first package autoignites. The number of burning packages is also taken into account when modeling the flame surface in the entrainment model.

The turbulent flame velocity is calculated according to Zimont et al. (1997); the turbulence model used is that of Bargende (1991). The injection of diesel fuel is taken into account by the turbulence model (Walther et al. 2011). The laminar flame speed was estimated using the chemical reaction kinetics software Cantera. Since the fuel in the background mixture mostly contains methane, the GRI-Mech 3.0 reaction mechanism was used (Smith et al. 2000).

3.4 Superposition of the models

The conversion rate of the background mixture from the entrainment model and the conversion rate of the fuel in the packages from the package model (cf. section 3.2) are added together to obtain the total conversion rate:

$$\frac{dm_{H,F}}{dt} = \frac{dm_{H,F,ENT}}{dt} + \sum_P \frac{dm_{H,F,P}}{dt} \tag{15}$$

The final equation for the rate of heat release can now be formulated as follows:

$$\frac{dQ}{dt} = LCV_{H,F}\frac{dm_{H,F}}{dt} + LCV_D \sum_P \frac{dm_D}{dt} \tag{16}$$

4. Verification

The model is verified using measurement data from the two dual fuel engines described in section 2. A comparison is made between the simulated and analyzed rates of heat release as well as between simulated NOx formation and the measured values. NOx formation was calculated as in Pattas and Häfner (1973) while the composition and temperature of the burned zone were calculated using the ignition delay and rate of heat release models described above. The measurement data of the 35/44DF were from a single-cylinder research engine; the measurement data of the 51/60DF were from a multi-cylinder engine.

4.1 Single-cylinder research engine

A number of variations were investigated on the single-cylinder research engine. Results from one variation in injection timing are provided here as an example:

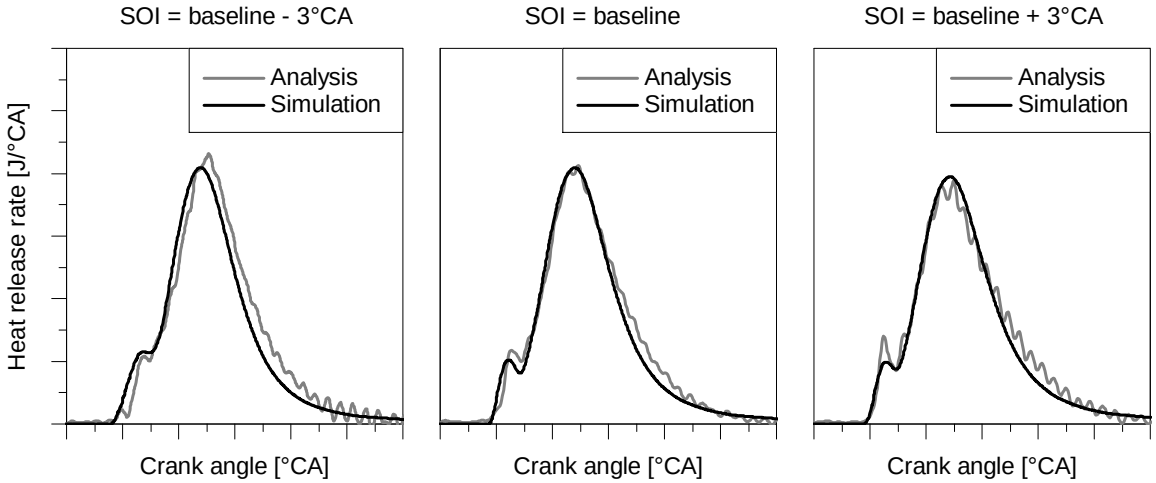

Fig. 12. Results from ignition delay and rate of heat release simulation: variation in injection timing, single-cylinder research engine

As is clearly visible in the figure above, ignition delay and thus the start of combustion can be reproduced very well. The quality of the combustion model is good enough to allow optimization of the engine using simulation. The following figure presents the results from the NOx model, where the injection timing and combustion excess air ratio of the background mixture were varied.

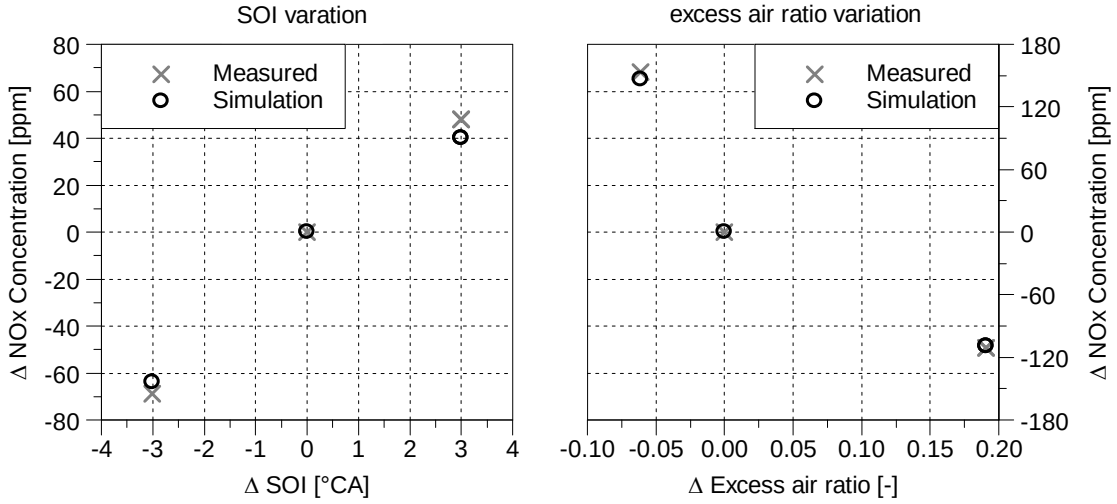

Fig. 13. Results from the NOx model, variation in injection timing (left) and in combustion excess air ratio of the background mixture (right) at constant load

As clearly visible in the figure above, the trends with the NOx model could be reproduced very well. The deviations can be regarded as satisfactory.

4.2 Multi-cylinder engine

A variation in load was investigated on the multi-cylinder engine. The calibration of the multi-cylinder engine requires a change in the share of diesel in the total added fuel as well as in the start of injection depending on load.

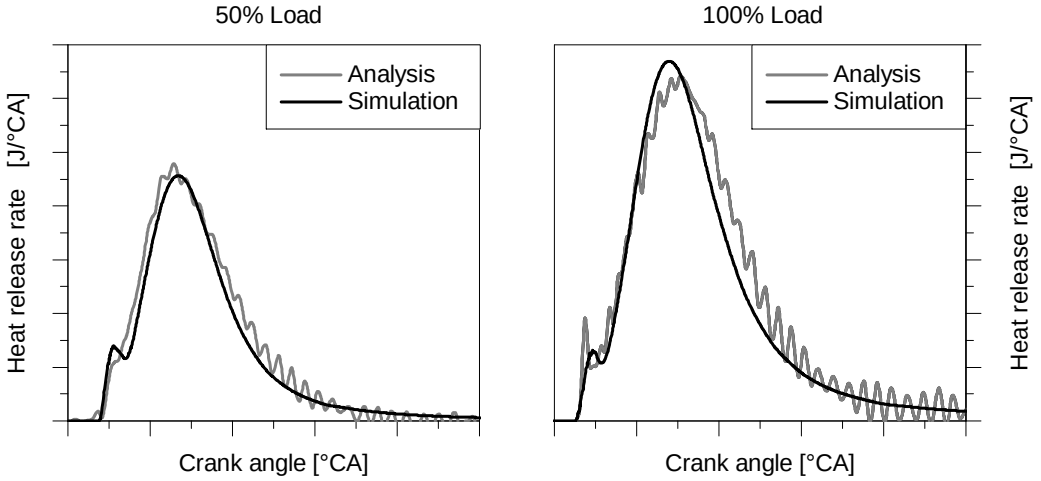

Fig. 14. Results from ignition delay and rate of heat release simulation, multi-cylinder engine

As the figure above makes clear, the rate of heat release can be modeled well with simulation. It must be emphasized that the data refers to the multi-cylinder engine where crank angle-dependent data is available from just one cylinder; air and fuel mass values are obtained by averaging the values from all the cylinders.

Conclusion

This paper describes a zero dimensional approach for predicting rate of heat release and NOx emissions in a dual fuel engine. A special analysis tool had to be developed before a database for model validation could be created.

The modeling of combustion is based on a two-stage approach combining the first phase of combustion, which is dominated by diesel fuel combustion, with the second phase of combustion, which involves homogeneous combustion of a background mixture consisting of natural gas and air. To describe the first phase, a package model is applied; the second phase is modelled using an entrainment model. Of particular importance is the description of ignition delay, which is considerably longer than that of a diesel engine. Verification of the model on two different engines showed that prediction of the rate of heat release in particular is good. The prediction of NOx emissions is good, although due to the great influence of the diesel combustion in the first phase, small errors in the combustion rate result in larger deviations in prediction of NOx emissions. Therefore, the completely accurate calculation of NOx emissions remains an essential part of development.

The analysis and simulation tools developed were validated using measurement data from a single-cylinder research engine as well as from a different sized multi-cylinder engine in order to ensure the transferability to other engines.

References

Bargende M (1991) Ein Gleichungsansatz zur Berechnung der instationären Wandwärmeverluste im Hochdruckteil von Ottomotoren. Disseration Technische Hochschule Darmstadt

Chmela F, Dimitrov D, Pirker G, Wimmer A (2006) Konsistente Methodik zur Vorausberechnung der Verbrennung in Kolbenkraftmaschinen. Motortechnische Zeitschrift 06/2006

Curran HJ, Gaffuri P, Pitz WJ, Westbrook CK (2002) A Comprehensive Modeling Study of iso-Octane Oxidation. In Combustion and Flame 129, pp: 253-280

Goodwin DG (2003) An open-source, extensible software suite for CVD process simulation. In Proceedings of CVD XVI and EuroCVD Fourteen, M Allendorf, F Maury, and F Teyssandier (Eds.), Electrochemical Society, 155-162

Hiroyasu H, Kadota T, Masataka A (1983) Development and Use of a Spray Combustion Modeling to Predict Diesel Engine Efficiency and Pollutant Emissions. Bulletin of the JSME, No. 214

Menage A, Gruand A, Berg P, Golloch R (2013) The New Dual Fuel Engine 35/44DF from MAN Diesel & Turbo SE. CIMAC World Congress, Shanghai, China

Merker GP, Schwarz C, Teichmann R (Eds.) (2012) Combustion Engines Development. Springer. Heidelberg

Pattas K, Häfner G (1973) Stickoxidbildung bei der ottomotorischen Verbrennung, Motortechnische Zeitschrift, Nr. 12

Pirker G, Chmela F, Wimmer A (2009) Automated Parameter Determination for IC Engine Simulation Models. SAE paper 2009-01-0674

Schlatter S, Schneider B, Wright Y, Boulouchos K (2012) Experimental Study of Ignition and Combustion Characteristics of a Diesel Pilot Spray in a Lean Premixed Methane/Air Charge using a Rapid Compression Expansion Machine. SAE paper 2012-01-0825

Smith GP, Golden DM, Frenklach M, Moriarty NW, Eiteneer B, Goldenberg M, Bowman CT, Hanson RK, Song S, Gardiner WC, Lissianski VV, Qin Z (2000) http://www.me.berkeley.edu/gri_mech/

Stiesch G (2003) Modeling Engine Spray and Combustion Processes. Springer, Berlin

Tabaczynski R, Ferguson C, Radhakrishnan K (1977) A Turbulent Entrainment Model for Spark-Ignition Engine Combustion. SAE paper 770647

Walther HP, Schlatter S, Wachtmeister G, Boulouchos K (2011) Erstellung eines phänomenologischen Modells zur Vorausberechnung des Brennverlaufs von Gasmotoren mit Piloteinspritzung. Abschlussbericht Forschungsvereinigung Verbrennungsmotoren e. V., Bad Neuenahr

Warnecke W, Karanikas J, Levell B, Mesters C, Schreckenberg J, Adolf J (2013) Gas – Eine Brückentechnologie für zukünftige Mobilität?, in 34. Internationales Wiener Motorensymposium, 25. - 26. April 2013.

Zimont V, Polifke W, Bettelini M, Weisenstein W (1997) An efficient computational model for premixed turbulent combustion at high Reynolds numbers based on turbulent flame speed closure. In ASME J. Eng. Gas Turbines Power 120, pp: 526-532

Virtual Fuel Approach: a new simulative methodology to analyse effects of fuel properties on mixture formation in compression ignition combustion

B. Graziano[1*], J. Mora Perez[1], F. Kremer[1], Prof. S. Pischinger[1], M. A. Reddemann[2], Prof. R. Kneer[2], K. A. Heufer[3], H. Rohs[3]

[1]VKA – Institute for Combustion Engines. RWTH Aachen University. Forckenbeckstraße 4, D-52074 Aachen, Germany

E-mail: graziano@vka.rwth-aachen.de
Telephone: +(49) (0) 241 80 48000
Fax: +(49) (0) 241 80 92630
* Corresponding author

[2]WSA – Institute of Heat and Mass Transfer. RWTH Aachen University. Augustinerbach 6, D-52056 Aachen, Germany

E-mail: info@wsa.rwth-aachen.de
Telephone: +(49) 241 80 95400
Fax: +(49) 241 80 92143

[3]FEV GmbH. Neuenhofstraße 181,D-52078 Aachen, Germany

E-mail: marketing@fev.com
Telephone: +(49) 241 5689-0
Fax: +(49) 241 5689-119

Abstract. Nowadays restrictions on pollutant emissions from internal combustion engines (ICEs) require a holistic investigation on possible optimization pathways of the combustion process. The Tailor-made Fuel from Biomass (TMFB) Cluster at RWTH Aachen University aims to design optimal production processes for biofuels as well as ideal surrogate fuels for ICE applications. This paper focuses on the effect of fuels' thermo-physical properties on the mixture formation process at part load engine operating points, where the spray behavior and the air entrainment process play a fundamental role on combustion quality and pollutant formation. A sensitivity analysis on liquid density, dynamic viscosity, surface tension and vapor pressure is herein presented to introduce a new simulative approach which allows a direct decoupling of fuel thermo-physical properties that affect in-cylinder mixture formation, while accounting for the complex set of thermodynamic boundaries present in diffusive turbulent combustions. The monitoring parameter proposed in this study is the air utilization. It is shown how this parameter allows studying the quality of the mixture formation process, linking the local equivalence ratios with soot formation and oxidation as well. The results of the sensitivity analysis suggest the following ranking in terms of mixture formation quality for a given engine operating load: di-n-ethers > n-alkanes > 1-alcohols. Furthermore, it is found that fuels with a carbon chain length of C8 atoms belonging to the ethers family allow an overall improvement of the mixture formation process.

1. Introduction

It is well-known that the mixture formation process plays a crucial role in combustion control and soot formation in direct injection (DI) Diesel engines. In small bore Diesel engines the spray interactions with the combustion chamber walls are dominated by the spray pattern and affect the combustion quality and the pollutant emissions at part load and cold start operating conditions. Phenomena like fuel injection, mixing with the surrounding air and evaporation determine the local in-cylinder equivalence air/fuel ratios (λ). Several studies have shown that the soot formation is affected by the thermodynamic boundaries of the air/fuel mixture prior to the first ignition kernel (i.e. within the lift-off

length) inside the partially premixed reaction zone of a laminar diffusion flame (Pickett et al., 2006; Siebers and Higgins, 2001; Jakob et al., 2013). Thus, understanding the impact of the mixture formation process on the local equivalence ratios allows gaining insights into the soot formation process. Studies on fundamental spray investigation have shown that the mixture formation process underlines a great dependence on fuel's thermo-physical properties, affecting both the air entrainment process and the spray penetration into hot compressed air. It was shown that the spray penetration length strongly depends on the fuel and air density (Siebers, 1999) and that the boiling behavior of the fuel controls the evaporation rate of the fuel (Higgins et al, 1999). Recently it was also demonstrated that the spray cone angle correlates with the liquid density and dynamic viscosity (Reddemann et al.; 2012), confirming the importance of the fuel properties on mixture formation.

In the TMFB Cluster of the RWTH Aachen University, fundamental investigations at high pressure vessels as well as engine testing focus on the impact of the fuels' molecular structure on the mixture formation process, in order to trace a link between the fuel properties and engine out emissions. Within TMFB, the fuel molecular structure is seen as further degree of freedom in the development of novel biofuels. Since there are unlimited possible molecular structure to screen, new techniques to find possible biofuel candidates need to be developed. Thus, the goal of this research is to join the insights of experimental investigations and translate them into a combustion performance indicator, e.g. the characteristic mixture formation number, to insert inside the design process of novel biofuels. The new idea brought into this study is a methodology, named Virtual Fuel Approach (VFA), aiming to include the complex set of engine-like combustion boundaries into the analysis of the mixture formation process in DI Diesel engines. Herein the preliminary sensitivity analysis on fuel thermo-physical properties is presented. In the next sections of the article the VFA is presented, followed by the validation of the simulative approach, the discussion of the simulations results and the conclusions.

2. Material and Methods

2.1 Virtual Fuel Approach

The VFA aims at finding the characteristic mixture formation number, on the base of a Computer Aided Engineering (CAE) methodology which uses the principle of superposition of effects to study the mixture formation process from an "in-cylinder" point of view. The main idea is to analyse in cold evaporative conditions the effect of fuels' thermo-physical properties on air/fuel mixing and evaporation, in order to isolate the effects of local air/fuel equivalence ratios on the soot emissions. The VFA allows a preliminary sensitivity analysis of different fuels in order to answer the following question: which fuel will guarantee a better mixture formation in a DI Diesel engine? The monitoring parameter proposed to underline the impact of the molecular structure on the mixture formation is the in-cylinder air utilization. The right-hand side of Figure 1 shows an explicative example of this characteristic number, which represents the volumetric fraction of air inside the combustion chamber, sorted per λ ranges. It includes the local λ ranges which are involved in the pollutant formation during the combustion process. In particular herein the air utilization is used to monitor the soot formation and oxidation potential of the fuel.

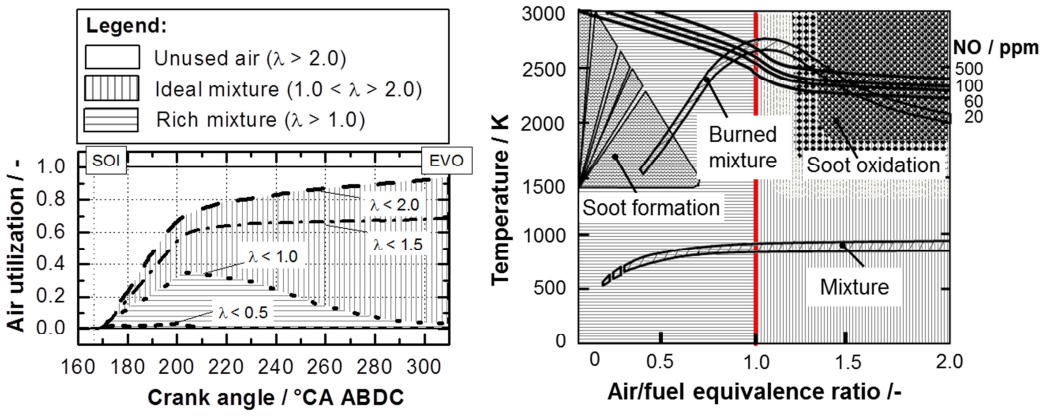

Fig. 1 Explicative figure of in-cylinder air utilization and its correlation with soot emissions (Pischinger, 2013)

As the right-hand side plot of Fig-1 explains, the λ values involved in the soot formation process are below the unity (area with horizontal pattern), while the ones responsible for the soot oxidation are greater than unity and lesser than two (area with vertical pattern).Thus, by evaluating these areas from the Starting of injection (SOI) till the Exhaust Valve Opening (EVO) time, it is possible to quantify the share of mixture involved respectively in the soot formation and oxidation process. The air utilization is sensitive to the air entrainment into the liquid fuel jet and to the evaporation process; thus, it represents an optimal candidate to monitor the dependence of the local λ distributions on the fuel properties. Previous studies have demonstrated that the air utilization correlates well with the in-cylinder soot formation (Adomeit et al, 2008; Rajamani et al. 2012) and that it can be used to optimize the mixture formation process prior to ignition, through the improvement of spray/bowl interactions (Cracknell et al., 2014).

Computational Fluid Dynamics (CFD) represents an effective tool to analyze in detail, the quality of the mixture formation process from an "in-cylinder" point of view accounting at the same time of the complex set of boundaries represented by the Diesel combustion process. Thus, KIVA 3V Release 2 with the Engine Research Center (ERC) model extensions was chosen to realize the VFA. The CFD code includes a modified RNG k-ε turbulence model, a Kelvin-Helmholtz (KH) and Rayleigh-Taylor (RT) spray model, a Shell auto ignition model, a laminar/turbulent Characteristic Timescale Combustion (CTC) model, a crevice flow model and a spray/wall impingement model. The code has a Hiroyasu single-step soot model and a uses a Zeldovich formulation for the NO_X emissions (Reitz et al. 1995, 1998). This KIVA code also includes the FEV Soot model which is based on the Nagle and Strickland-Constable (NSC) oxidation model (Adomeit et al. 2006, 2008). Further modifications were implemented to allow a direct decoupling of the thermo physical properties under examination, namely liquid density, dynamic viscosity, surface tension, vapor pressure and enthalpy of vaporization. Moreover, specific modifications were implemented to study in details the development of the spray inside the combustion chamber, such as increased output frequency for the droplet analysis and implementation of nine fixed radial sections where the spray momentum, liquid mass, relative velocities, Reynolds number, Weber number and Ohnesorge number were evaluated and averaged over the injection duration when the needle is fully open. The VFA approach uses a CFD model validated for Diesel fuel as the base to perform individual variation of the fuel's thermo-physical properties, while keeping all the others constant. In this way, it is possible to study only the effect of each property, on the mixture formation process.

Figure 2 gives an outlook of the investigation domain analyzed, it consists of n- alkanes, 1-alcohols and di-n-ethers in a range of chain length going from C8 to C16. These fuel families are characterized by the same Carbon/Hydrogen ratio for a given chain length and also by the same Oxygen/Carbon ratio, when looking to the oxygenated fuels. In this way, it is possible to analyze the impact of the functional family group on the mixture formation process. The minimum range of carbon content has been defined on the base of previous TMFB researches where it was found that Di-n-butyl Ether and 1-Octanol are proposed as surrogate fuels for DI Diesel combustion (Graziano et al., 2013; Jakob et al, 2013, Heuser et al., 2014). The choice to use as maximum range 16 carbon atoms is due to the relation between ignition properties and chain length: the longer the chain length, the higher is the ignitability, thus the cetane number (C16 of n-alkanes has the maximum cetane number of 100). This trend is valid among n-alkanes and 1-alcohols, but the di-n-ethers show instead a reversed trend: the shorter the molecule the higher is the cetane number. Although, in this part of the work the ignitability of the fuel is not accounted for, in future work it will be object of study in the VFA, thus the domain of investigation needs to be the same for both cold and hot mixture formation analysis. In the top-left plot of Fig. 2 the investigation domain of the liquid density at 20 °C is presented for n-alkanes, 1-alcohols and di-n-ethers. It can be observed for both n-alkanes and di-n-ethers families, that the trend is the same: the density increases with the molecular chain length. The 1-alcohols show instead a different trend, due to the local polarity caused by the hydroxyl group which is counteracted by the chain length increase due to the fact that the hydroxyl group is protected by steric hindrance of adjacent groups. A different approach was used to perform the sensitivity analysis of the dynamic viscosity, vapor pressure and surface tensions, since the boiling behavior of the fuels is accounted for in the CFD code. A thermodynamic model was used to predict the properties where there was lack of data in literature. The starting dataset consisted of: Di-n-Butyl Ether (8C), Di-n-Hexyl Ether (12C), Di-n-Octyl Ether (16C) for the di-n-ethers; 1-Octanol (8C), 1-Dodecanol (12C), 1-Hexadecanol (16C) for the 1-alcohols and n-octane (8C), n-decane (10C), n-dodecane (12C), n-tetradecane (14C), n-hexadecane (16C) for the n-alkanes (Daubert and Danner, 1993; Poling et. al, 2011). Afterwards, thermodynamic models were used to derive characteristic trends with the variation of the molecule's carbon content, through linear regression analysis. The range of temperatures analyzed goes from the melting temperature (T_M) to the critical temperature (T_C).

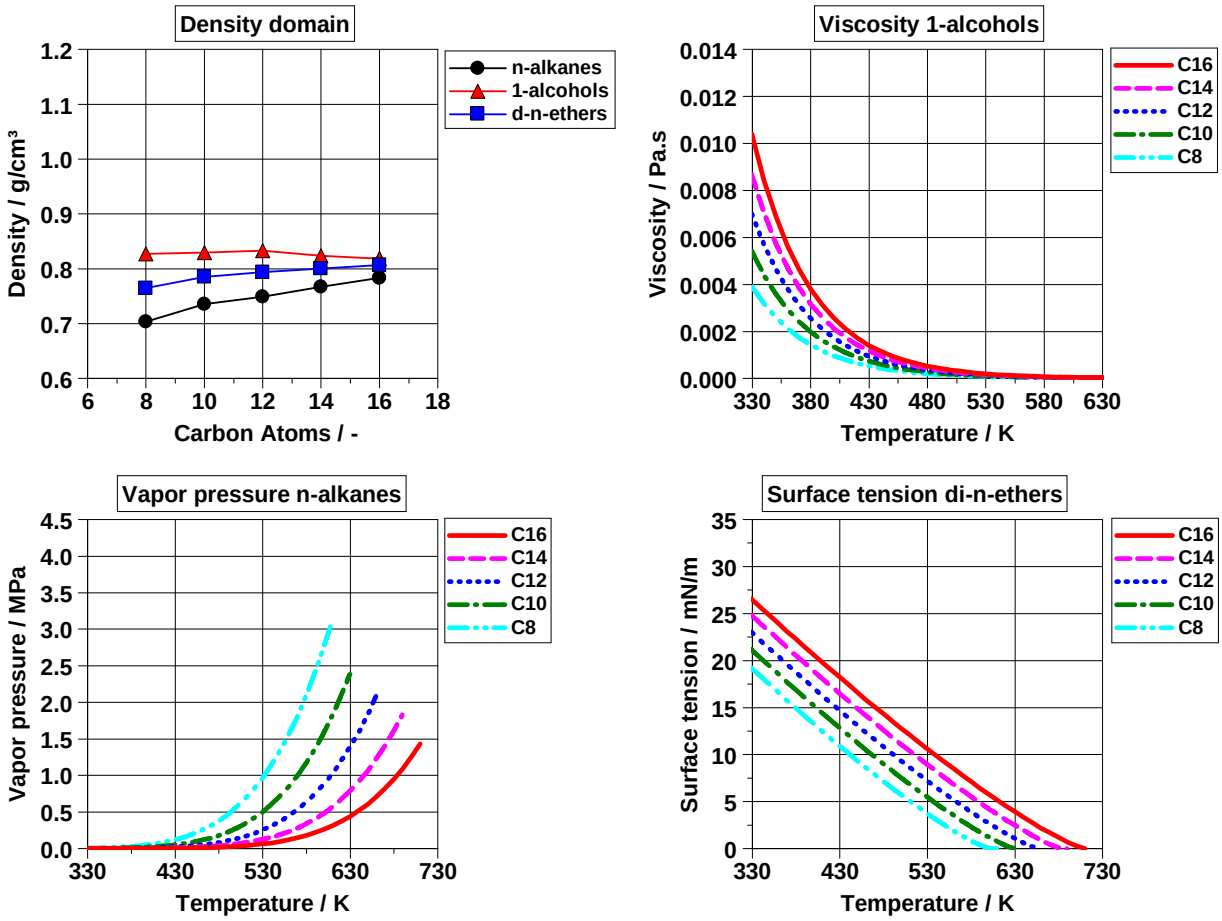

Fig. 2: Observation domain of liquid density at 20 °C, viscosity, vapor pressure and surface tension

For all the fuel families similar trends were observed for viscosity, vapor pressure and surface tensions with the variation of temperature. Thus, for the sake of brevity only one family is plotted in Fig. 2; i.e. 1-alcohols for dynamic viscosity, alkanes for vapor pressure and di-n-ethers for surface tension. In the left-top graph of Fig. 2 the dynamic viscosity for the 1-alcohols is plotted versus the temperature, sorted by carbon content. The range of temperature represented goes from the injection temperature of 330 K up to T_C. By looking at the viscosity curves at a fixed temperature, fuels with shorter chain length show smaller viscosities. For the dynamic viscosity the thermodynamic model used to derive the VFA curves, given in Table 2, is the Andrade equation (1934):

$$\mu = e^{A+BT} \tag{1}$$

where:

- μ is the dynamic viscosity;
- T is the temperature;
- A and B are constants which requires at least two sets of viscosity/temperature data to be determined as Eqs. 1.1-1.2 show.

$$A = \ln(\mu_1) - \frac{B}{T_1} \tag{1.1}$$

$$B = \ln\left({}^{\mu_2}/_{\mu_1}\right) / \left(\frac{1}{T_2} - \frac{1}{T_1}\right). \tag{1.2}$$

In the bottom-right plot in Fig. 2 the vapor pressure VFA curves are given for n-alkanes. The trend of the vapor pressure behavior with increasing chain length, for a given temperature, is the following: fuels with shorter chain length are more prone to vaporize. The Clausius – Clapeyron thermodynamic law was fulfilled to drive the sensitivity analysis on the vapor pressure and the heat of vaporization, since these two thermo-physical properties depend on each other and vary with temperature, as Eq. 2 states:

$$d(lnP_v)/d\left(\frac{1}{T}\right) = -\Delta H_v/R \cdot \Delta Z_v \tag{2}$$

where:

- P_v is the vapor pressure;
- $\Delta H_v$is the enthalpy difference between saturated vapor and liquid;
- ΔZ_v is the compressibility factor difference between saturated vapor and liquid;
- R is the universal gas constant.

To integrate Eq. 2 an assumption was made regarding the dependence of the term $\Delta H_v / \Delta Z_v$ on temperature. Both enthalpy and compressibility factors are functions of the temperature and both decrease with rising temperature, providing a compensating effect (Poling et. al, 2011). Therefore, in this study this group constant was evaluated at the T_{NB} and, as for the liquid viscosity variations, the term $\Delta H_v / \Delta Z_v$ at T_{NB} were studied via regression analysis to define its dependence on the molecule's carbon atoms for each fuel family. The same approach was applied to derive the pressure at T_{NB} ($P\big|_{T_{NB}}$) and T_{NB} dependence as well (Table 1).

The last property analyzed was the surface tension. In the bottom-left plot in Fig. 2, the trends with the variation of the carbon content and temperature are shown for the di-n-ethers family. The overall trend observed among the three families is the following: shorter chain length molecules have smaller surface tensions at a given temperature. The thermodynamic correlation used for the VFA is the Brock and Bird (1955) listed in Eq. 4, where the surface tension correlates with temperature. The reason is in the KIVA coding, which does not account for the density variation with temperature. A more detailed model should be included in this study, such as the Sudgen-Macleod (1924) correlation, where the surface tension correlates with the liquid and vapor density trough the Parachor temperature independent parameter but it goes beyond the scope of work. The law fulfilled to perform the sensitivity analysis of the surface tension is given in Eqs. 3-4.

$$\sigma / \left({P_C}^{2/3} \cdot {T_C}^{1/3} \right) = (0.132 \cdot \alpha_C - 0.279) \cdot (1 - T_r)^{11/9} \quad (3)$$

$$\alpha_C = 0.9076 \cdot \left[1 + \frac{\left(T_{br} \cdot ln\left({P_C}/{1.01325} \right) \right)}{1 - T_{br}} \right] \quad (4)$$

where:

- σ is the surface tension;
- P_c is the pressure at critical point;
- α_C is the Riedel (1954) according the Miller (1963) formulation;
- T_r is the reduce temperature at critical point, i.e. T/T_C;
- T_{br} is the reduced temperature at boiling point.

The right-bottom side plot in Fig. 2 shows the virtual curves for the sensitivity analysis of the surface tension. In this case a regression analysis was used to establish the dependency of P_C on the carbon atom content and three different VFA curves were defined for the fuel families under study as Table 1 lists. Here the details of the VFA curves for viscosity, vapor pressure and surface tension variations are shown and sorted per different fuel family. The functions obtained with the regression analysis are used to vary the VFA parameters on the base of the carbon content of the molecule's chain length. Thus, the ´x´ stands always for the number of carbon atoms available in the molecular structure of the fuel.

The sensitivity analysis of the thermo-physical properties was carried out on part load engine operating conditions, keeping both the injected fuel mass and the rail pressure constant at a given load point. Although this strategy is not followed on real engine applications, where different fuels are screened while keeping the injected energy constant at a given load point, to derive conclusions on the local λ distributions the injected mass must not change. The constant rail pressure was guaranteed for each simulation by adjusting the duration of injection, while keeping the same injection rate shaping. Thus, the change in spray penetration due to the needle opening time not affects the spray behavior while performing the sensitivity analysis.

Table 1: VFA parameters for dynamic viscosity, vapor pressure and surface tension

Property	VFA parameter	n-alkanes	1-alcohols	di-n-ethers
Dynamic Viscosity	**A**	y = -0.088x - 3.504R² = 0.97 R² = 0.98	y = -0.088x - 3.504 R² = 0.99	y = 0.013x - 4.8 R² = 0.99
	B	y = 96.716x + 303.65 R² = 0.99	y = 127.59x + 1666.2 R² = 0.99	y = 65x + 810 R² = 0.97
	$\mathbf{T_M}$	$y = -1.1451x^2$ + 36.256x - 6.6495 R² = 0.99	$y = -0.7869x^2$ + 26.808x + 92.833 R² = 0.99	$y = 0.1193x^2$ + 4.7864x + 154.37 R² = 0.99
	$\mathbf{T_C}$	$y = -0.9292x^2$ + 42.215x + 287.75 R² = 0.99	$y = -0.3794x^2$ + 24.507x + 475.49 R² = 0.97	y = -0.0933x2 + 15.851x + 479.64 R² = 0.99
Vapor pressure	**ΔHv /ΔZv**	y = 512.43x + 4302.7 R² = 0.98	y = 386.75x + 7865 R² = 0.98	y = 461.25x + 5788.3 R² = 0.97
	$\mathbf{P\big\vert_{T_{NB}}}$	y = 34155x + 753784 R² = 0.98	y = 36831x + 703327 R² = 0.99	y = 45742x + 528684 R² = 0.98
	$\mathbf{T_{NB}}$	y = 22.635x + 214.59 R² = 0.99	y = 19.675x + 298.5 R² = 0.99	y = 18.019x + 275.11 R² = 0.99
Surface tension	$\mathbf{P_C}$	y = -1.55x + 38 R² = 0.9722	y = -1.6975x + 40.3 R² = 0.99	y = -1.5625x + 39.717 R² = 0.95

2.2 CFD code validation

The CFD code was validated with regards to the spray and the combustion behavior, since the mixture formation is strongly affected by the spray pattern and spray/bowl interactions at part load engine operating conditions. Moreover, the degree of spray impingement on the combustion chamber walls at these engine loads plays also a key role in the mixture preparation and evaporation process, influencing the engine out emissions as well (Heywood, 2008). Thus, to enhance the confidence level in the spray model at engine part loads, high pressure vessel measurements for standard Diesel in cold evaporative conditions were used to validate the spray model in KIVA. Afterwards, the validated spray model was used to perform a combustion model validation for two part load points measured at the single cylinder Diesel research engine for standard Diesel fuel. The details of the experimental setup and of the optical techniques adopted to perform such measurements are described in details by Reddemann et al. (Reddemann et al., 2012). It is important to mention that the high pressure vessel is equipped with the same nozzle layout present in the single cylinder Diesel research engine, which is an 8 holes piezo-injector from BOSCH (the nozzle geometrical parameters are given in Table 2). Figure 3 depicts the engine load point analyzed in this work with the respective boundaries. In future work all four points represented with the black dots on the engine map of Fig. 3 will be used to complete the sensitivity analysis. Load point (LP) 1 is a part load point within the New European Driving Cycle (NEDC) and the LP 2 is a high part load point. The details of the single cylinder DI Diesel research engine test bench setup as well as the engine calibration for EURO6 norms are described in the work of Heuser et al. (Heuser et al. 2014). Table 2 lists the main engine characteristics and the geometrical nozzle parameters of the injector installed both at the test bench and the high pressure vessel. Two different computational domains were implemented in KIVA to validate the spray and the combustion process. The details of the CFD grids used for high pressure vessel and combustion simulations are given in Table 3.

Figure 4 shows the results of the spray model validation and list the thermodynamic boundaries investigated in the high pressure vessel as well. The different operating points (OPs) are representative of engine-like part and high-part loads boundary conditions chosen for this study. The breakup model of KIVA was validated with the aim to find an overall optimal compromise between the three different operating points, guaranteeing a validated spray behavior at different part loads in order to avoid the repetition of this simulation step for each engine point. The validation was executed taking

Load Point	LP 1	LP 2
Combustion center / °CA ATDC	9.2	10.8
Rail pressure / bar	1400	1800
Boost pressure / bar	2.29	2.60
Air density at TDC/ g/m^3	34	39
EGR rate / %	47	40
Injected mass /mg	20	29
Main injection begin / °CA ATDC	-3	-4.5
Injection duration / ° CA	10	13
Euro6 NO_X level g/kWh	0.4	0.6

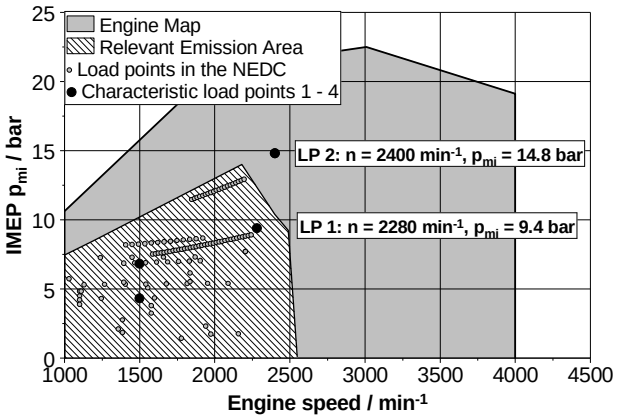

Fig. 3: Single cylinder research engine operating points used to validate the CFD code

Table 2: Single cylinder research engine setup

Displacement / cm³	390
Stroke / mm	88.3
Bore / mm	75
Compression ratio	15
Valves/cylinders	4
Fuel injection system	BOSCH Piezo Common Rail, 3rd generation
Max. injection pressure / bar	2000
Injector holes	8
Hole diameter / µm	109
Hole r/d	0.125
Hole L/D	9.4
Nozzle cone angle / °	153

Table 3: Details of the computation domain for spray and combustion validation

Grid application	Spray validation	Combustion validation
Grid type	45° sector / fixed	45° sector / moving
Grid size / n° cells	128576	46872
Characteristic angular cell size / °	1.25	1.45
Characteristic cell size−bowl radial / mm	1	0.9
Characteristic cell size−bowl vertical/ mm	1	0.9
Characteristic cell size−squish radial / mm	1	0.9
Max. Characteristic cell size−squish vertical / mm	1.4	4.4
Characteristic cell size−dead volume radial / mm	1.2	1.2
Characteristic cell size−dead volume vertical / mm	1.2	1.2

into consideration the liquid penetration length (LPL) and the spray cone angle. The CFD code shows good agreement overall with the experimental data. The penetration of the droplet in KIVA was evaluated considering 99 % of the liquid fuel mass and the cone angle was calculated at 50 % of LPL reproducing the measurement technique performed on the experimental setup (Reddemann et al., 2012). At OP 1 the simulated LPL crosses the experimental data at about 500 µs to increase up to a maximum of 41 mm, overestimating the experimental value by 3 mm at 1000 µs. This behavior is consistent with the observed underestimation of 4 degrees of the spray cone angle (bottom left plot in Fig. 3). At OP 2 the LPL validation shows the best agreement with experimental data since the maximum deviation from the experimental value is observed at 1000 µs and is only 2 mm and the cone angle matches the measured value. The validation of the spray for the OP 3 shows less agreement as demonstrated for the lower loads. The explanation is in the compromise chosen between the KH-RT hybrid breakup model parameters over the three load points. As a matter of fact, to achieve agreement for the boundaries of OP 1 and OP 2, with an air density of 20 and 25 kg/m^3 respectively, the model parameters were calibrated to avoid an overestimation of the LPL at 1000 µs greater than 5 mm but these settings are not optimal for the OP 3, where the ambient density is doubled. Thus an underestimation of 14 % is observed for the LPL at OP 3.

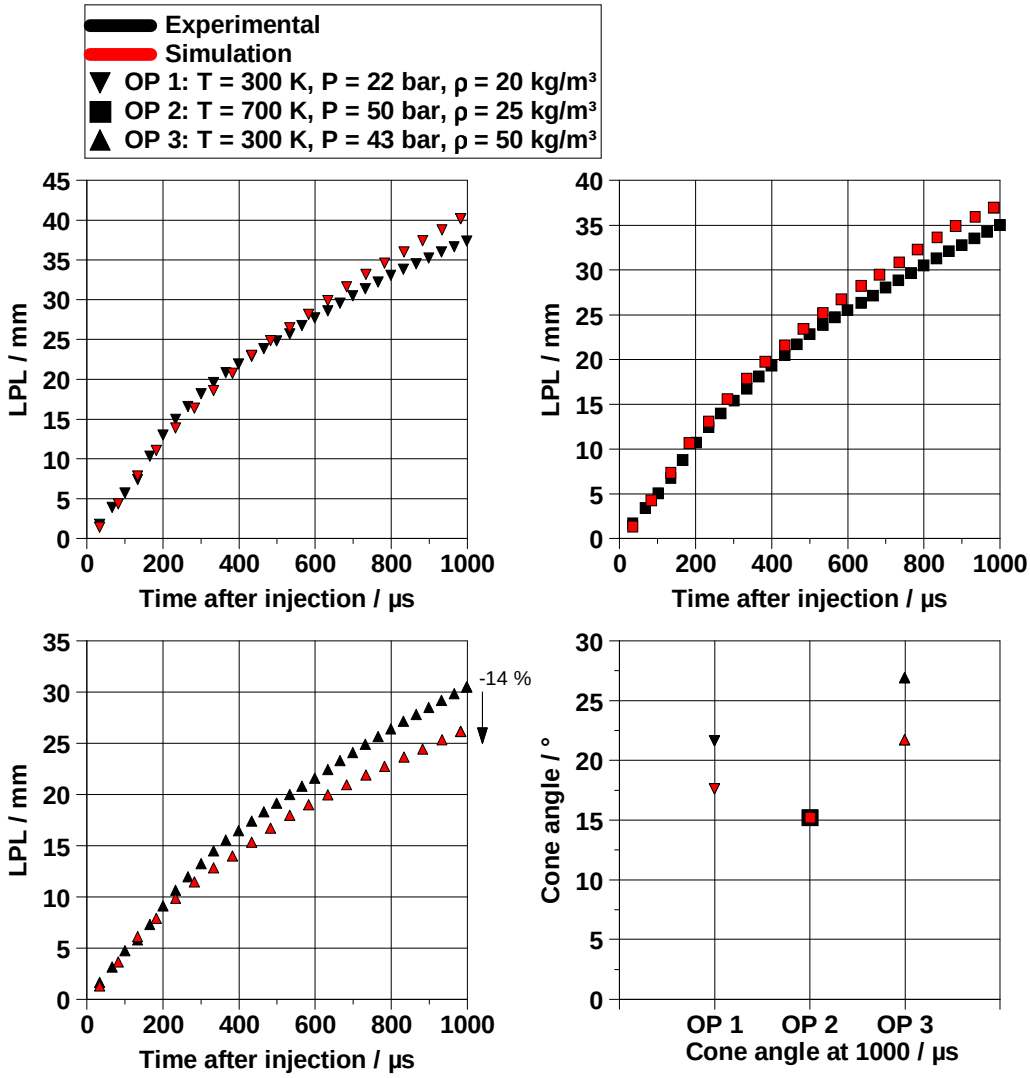

Fig. 4: Spray model validation at 700 bar of injection pressure and 1000 µs of injector duration

Figure 5 and Figure 6 show the results of the validation of the code respectively for LP 1 and LP 2. In each set of plots the in-cylinder temperature, pressure, Heat Release Rate (HRR) and air utilization are represented over crank angle degrees after bottom dead center (CA ABDC). This further validation step was performed in order to consider the right spray/bowl interactions and spray patterns present in the single cylinder research engine, accounting also for the movement of the piston and the swirl motion. KIVA has shown a good agreement overall with the experimental data for both the load points under study (red curves). In Fig. 5-6 the results of the calibrated and validated CFD code without ignition and combustion are represented in blue color. Looking at the differences in the air utilization trends with and without the combustion it is possible to observe the impact of the combustion boundaries on the mixture formation process. The overall effect is the enhancement of the evaporation process, resulting in larger areas for each λ range of interest.

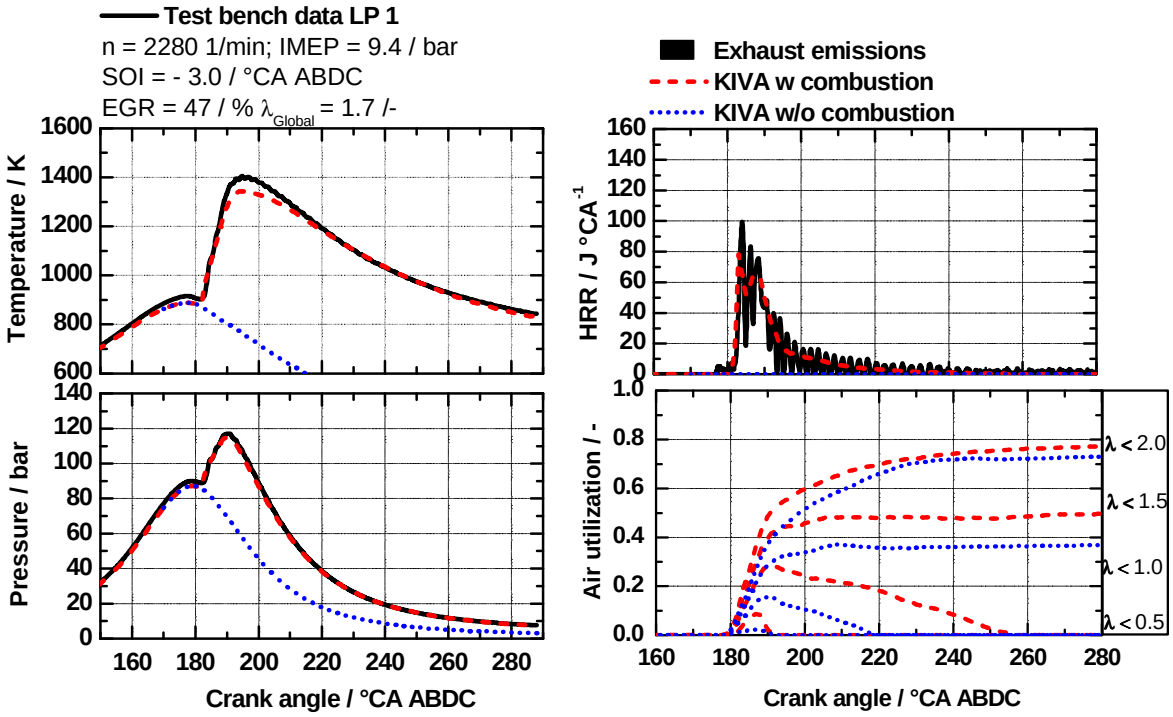

Fig. 5: Validation of the combustion process for the engine load point 2280 1/min at 9.4 bar IMEP

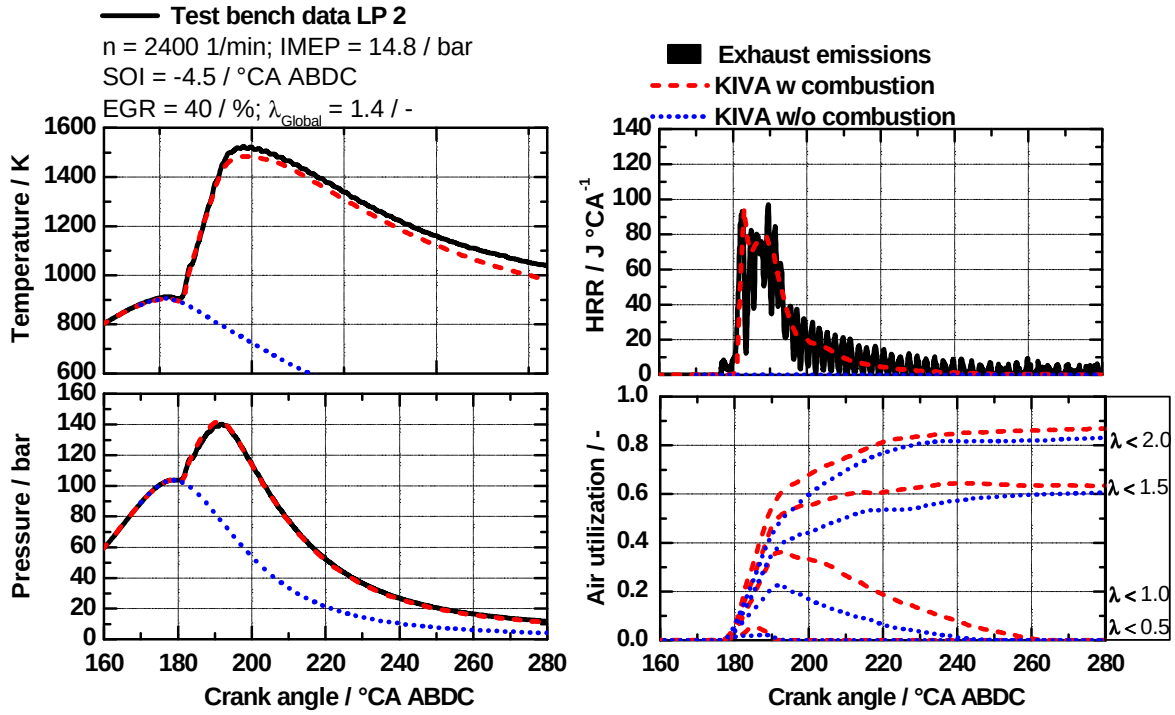

Fig. 6: Validation of the combustion process for the engine load point 2400 1/min at 14.8 bar IMEP

3. Results

In this section, the results of the sensitivity analysis are presented. Figure 7 gives an outlook of the sensitivity analysis performed for the dynamic viscosity (μ), where on the left-hand side column the trends of the air utilization for the LP 1 are presented. Each variation of the viscosity is represented

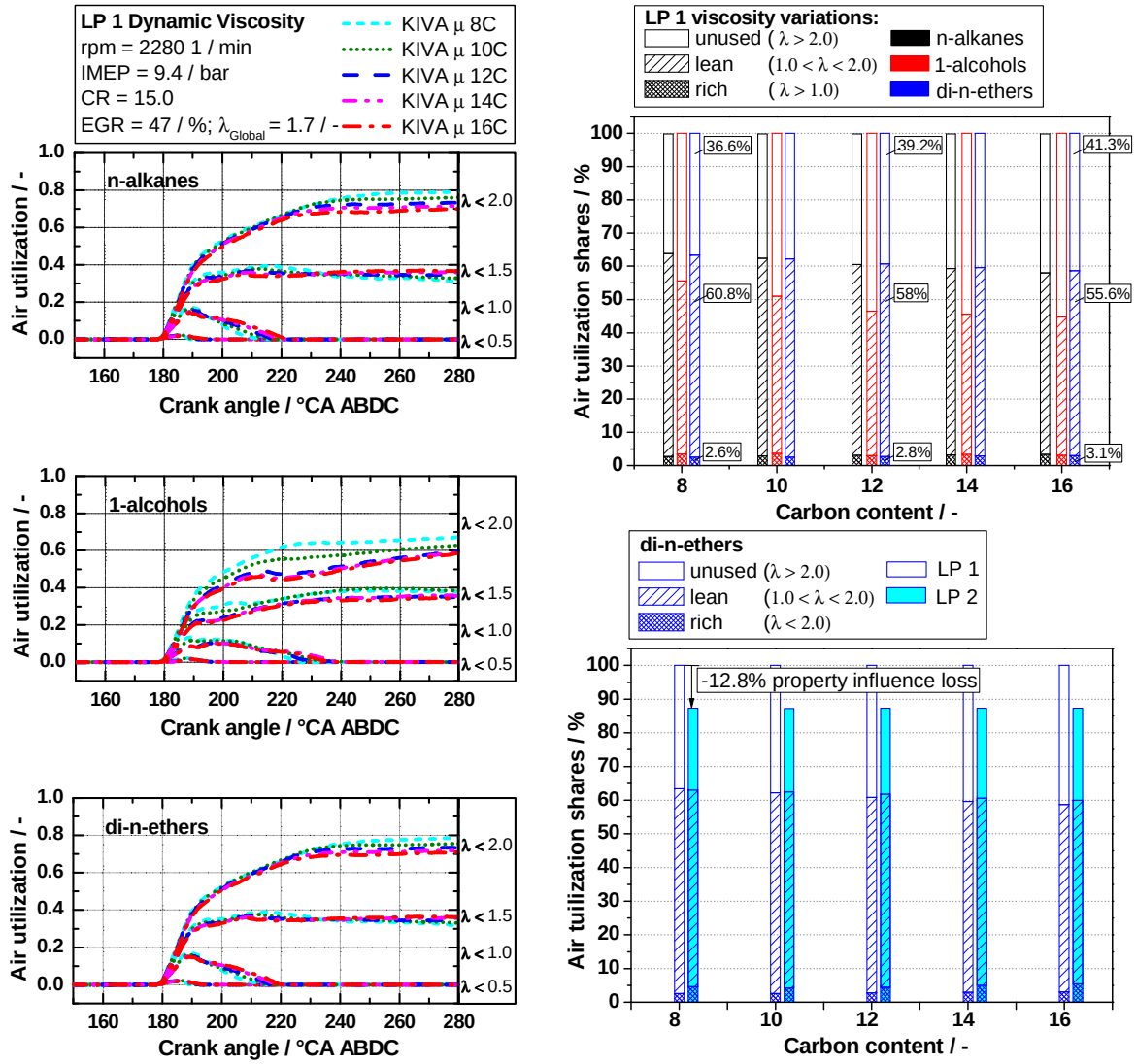

Fig. 7: Overview on the sensitivity analysis of dynamic viscosity on air utilization

with a different color for each of the fuel families studied. On the base of the correlation between the air utilization and the soot emission explained in the previous section of the article, the subscript areas of the λ curves of interest are analyzed. The overall trend of the air utilization is shown in the top-right picture of Fig. 7. Here the different fuel families are sorted by color (n-alkanes in black, 1-alcohols in read and di-n-ethers in blue) and the lean and rich share of mixture in the piston bowl are depicted with different pattern style with the variation of the molecule's carbon content. Overall the air utilization shows the same trend for all fuels: molecules with shorter chain length have better mixture formation as the lean areas ($1.0 < \lambda < 2.0$) are higher and the rich ($\lambda < 1$) and unused ($\lambda > 2$) are smaller. Thus, less viscous fuels are beneficial with regards to the mixture formation as they guarantee less soot formation and more soot oxidation potential. When looking to the family specific trend by fixing the carbon content, the n-alkanes and di-n-ethers show similar performances in terms of air utilization, while the 1-alcohols are clearly penalized by their higher viscosity. The values of the different air utilization shares are reported for the di-n-ethers in order to quantify the effect of the property variation on the mixture formation. When 4C are added into the molecule's chain, the unused area increases by 3 %; the lean share decreases approximately by 3 % and the rich by about 0.2 %. Whit an increase of C8 the unused share increase by 5 %, the lean shares decreases by 5 % and the rich increases by 0.5 %. On the bottom-right side of Fig. 7 the viscosity variations for di-n-ethers are shown for both LP 1 and LP 2. As listed in Fig. 3, at LP 2 the in-cylinder density at TDC is higher and the injected mass as well, therefore to analyze the effect of the fuel property at net increase of engine load a penalty factor accounting for the relative load increment is introduced. The total volume used for the mixture formation process is reduced by the relative increment in air density, which is why the maximum air utilization share does not achieve the 100 % for the LP 2. Comparing the two different engine points in this way, it is possible to evaluate a reduction of the influence of viscosity of about the 13 % when the engine

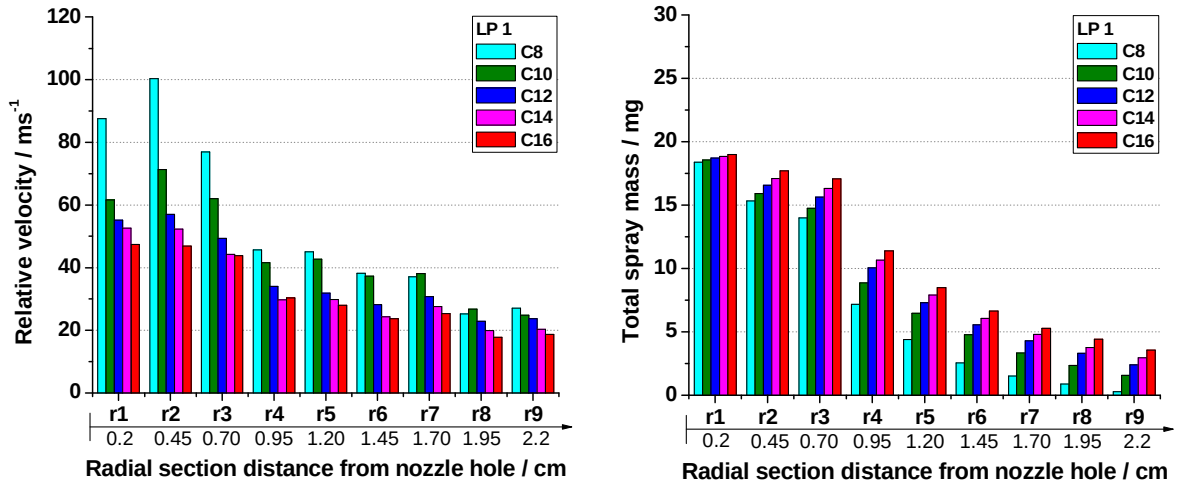

Fig. 8: Analysis of the influence of dynamic viscosity on the spray behavior at LP 1 for di-n-ethers

load increases. This trend was observed for all the properties analyzed; thus, from now ongoing only the LP 1 will be used to demonstrate the impact of the properties on the mixture formation. Figure 8 gives an abstract of the study performed on the spray development. The left hand side plot represents the relative velocity between the liquid and gaseous phase for di-n-ethers, averaged over the injection duration ad full needle opening. The shorter molecule, namely di-n- butyl ether, flows through the nozzle applying less shear forces, resulting in higher injection velocities. According to the Bernoulli's formulation of the flow through the nozzle, fuels with higher nozzle outlet velocities result in shorter duration of injection, at constant rail pressure. It was observed a 0.15 °CA increase in the injection duration for each two carbon atoms added in the molecule. The effect of viscosity on the nozzle flow behavior affects the discharge coefficient as well, which is reduced if the property increases. This change in the nozzle behavior is directly observable by looking at the first radial section where the higher relative velocity is shown by the C8 variation (cyan color). The impact of the nozzle behavior on the spray velocity decreases when moving away from the nozzle hole. As the spray penetrates further in the combustion chamber, the relative velocities decrease and the effect of the viscosity is less remarkable. This trend in the relative velocities implies that less viscous fuels allow a better air/fuel mixing and consequently a higher evaporation rate. Less viscous fuels have overall higher relative velocities and by varying the viscosity, keeping the density constant, also higher Reynolds number. Thus, the viscous shear within the spray is less and the mixture formation process is enhanced. The confirmation of the viscosity effect on the mixture formation is demonstrated in the left-hand side plot of Fig. 8, where the evaluation of the total spray liquid mass is performed among the different radial sections. The assumption made here is that the liquid mass passing through the ninth section, placed 2.2 cm away from the nozzle hole, will result in impinged mass on the piston walls, as the bowl radius for this engine is of 2.4 cm. It can be observed that the impinged mass is nearly zero for the less viscous fuel. This trend analyzed for ethers was observed for n-alkanes and 1-alcohols as well.

Figure 9 shows the results of the sensitivity analysis on the vapor pressure. In the left-hand side plot an overview on the air utilization is given for the fuel families under study. Overall the air utilization has the same trend for the different fuels: shorter molecule's chain (more volatile fuels) allows less share of unused air, while rich shares are minimum and lean maximum. The n-alkanes, due to their high volatility, show better mixture formation performances, followed by di-n-ethers and 1-alcohols. An increase of C4 in the n-alkane molecule determines an increase of 2 % of unused areas; a reduction of 2 % of lean shares of mixture and an increase of 0.2 % of the rich one. For the maximum increase of C8, the unused shares are increased by 5 %, the lean reduced by 6 % and the rich increased by 0.5 %. On the left-hand side of the Fig. 9 the evaluation of the impinged mass is presented for n-alkanes at LP 1. Higher volatile fuels (cyan color) allows to avoid impingement at LP 1 as the spray liquid mass is zero in the ninth section. This is due to the pronounced evaporation behavior of n-octane (C8). From the first section where the total fuel passing is about the total injected mass for all the different variations, moving further from nozzle hole the evaporation rate can be traced and n-octane has a nearly to zero total spray mass already at section six.

Figure 10 presents the results of the sensitivity analysis of the surface tension at LP 1. The right-hand side plot shows the overall air utilization trends for the fuels analyzed. It can be observed that di-n-ethers have the best air utilization shares distribution when looking at the plot for a fixed carbon content, followed by n-alkanes and 1-alcohols.

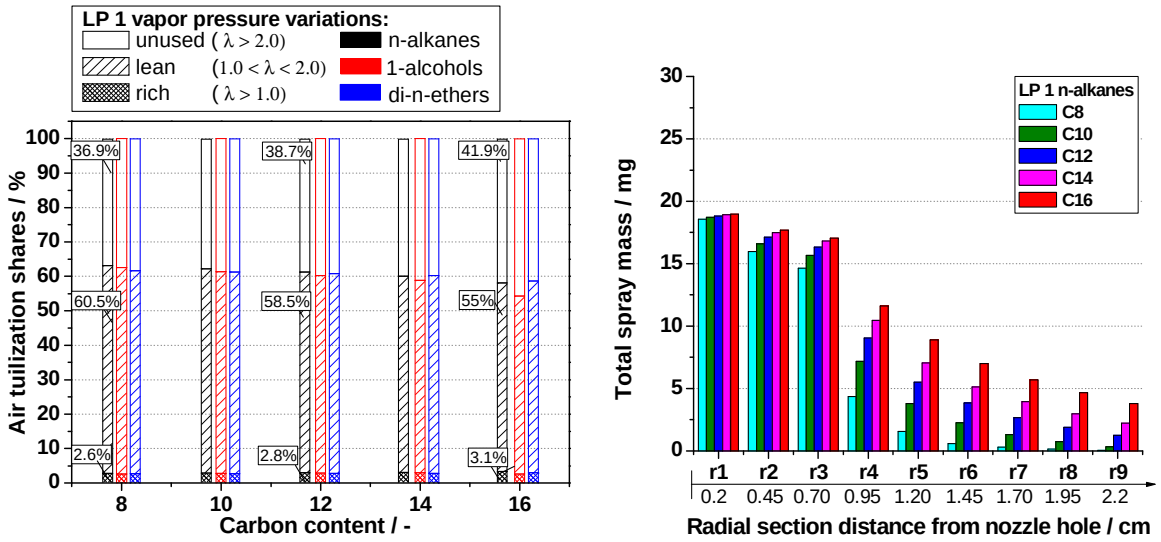

Fig. 9: Overview on the sensitivity analysis of vapor pressure on air utilization at LP 1

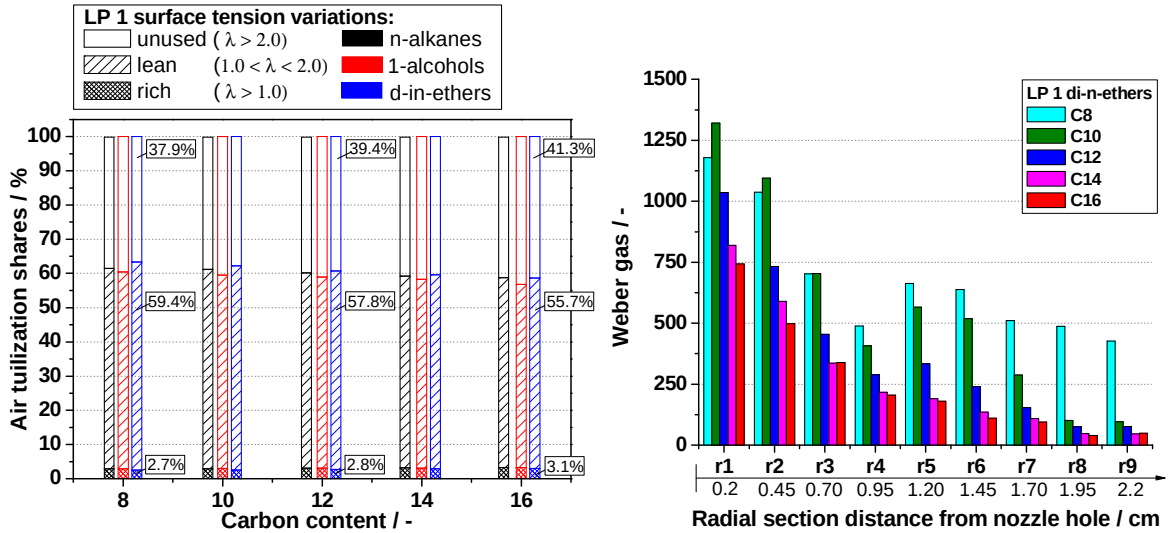

Fig. 10: Overview on the sensitivity analysis of surface tension on air utilization at LP 1

In particular, with an increase of the chain length by C4 the unused shares of mixture increase by 1 %, the lean decrease by about 2 % and the rich share increases by about 0.1 %. If the increase in the chain length is doubled the influence on the unused area is +3 %, on lean it is -4 % and on the rich zones it is +0.4 %. Overall, the trend observed for the surface tension sensitivity analysis is the following: fuels with less surface tension mix better with surrounding air and vaporize better showing a more pronounced breakup process. As a demonstration of this last statement the Weber number for the gaseous phase is presented over the different radial sections for di-n-ethers at LP 1. It is clear that fuels with shorter chain lengths improve the air/fuel mixing and result in better mixture formation. Although in the first two radial sections the C10 (di-n-octil ether) shows a better mixing, when the spray is moving further into the combustion chamber the C8 (di-n- butyl ether) performs better in terms of air/fuel mixing. In Table 4 the summary of the sensitivity analysis is given for an increment of C4 in the molecular structure at LP 1. It can be observed that within the molecules' investigation domain, the liquid density plays little role on the air utilization. In terms of influence on the air utilization a general overall trend can be stated with regards to the influence of each single property: viscosity plays the major role followed by vapor pressure, surface tension and density. In Table 5 the results of the summary of the sensitivity analysis is given for an increment of C8 in the molecular structure at LP 1. In this case, the ranking in terms of property influence on the air utilization is not confirmed.

Table 4: Sensitivity analysis summary for an increment of 4 carbon atoms in the molecular structure at LPLP 11

	n-alkanes			1-alcohols			di-n-ethers		
	rich	**lean**	**unused**	**rich**	**lean**	**unused**	**rich**	**lean**	**unused**
Viscosity	+0.2%	-2%	+2%	+2%	-8%	+5%	+0.2%	-3%	+3%
Vapor pressure	+0.2%	-2%	+2%	+0.2%	-3%	+2%	+0.1%	-2%	+2%
Surface tensions	+0.1%	-1%	+1%	+0.2%	-2%	+1%	+0.1%	-2%	+1%
Density	+0.08	-0.07	+1%	+0.2%	-0.5%	+0.2%	+0.1%	-0.8%	+0.9%

Table 5: Sensitivity analysis summary for an increment of 8 carbon atoms in the molecular structure at LP 1

	n-alkanes			1-alcohols			di-n-ethers		
	rich	**lean**	**unused**	**rich**	**lean**	**unused**	**rich**	**lean**	**unused**
Viscosity	+0.9%	-4%	+4%	+3%	-9%	+6%	+0.5%	-5%	+5%
Vapor pressure	+0.5%	-6%	+5%	+0.2%	-3%	+2%	+0.1%	-2%	+2%
Surface tensions	+0.3%	-3%	+3%	+0.5%	-4%	+4%	+0.4%	4%	+3%
Density	0.0	-2	+2%	0	-0.8%	+0.8%	+0.1%	-2%	+2%

4. Conclusions

In this work, two part load operating points were analyzed with regard to the mixture formation process through a sensitivity analysis performed on fuel thermo-physical properties. The sensitivity analysis was carried out following a superposition of effect principle, where each variation interval corresponded to an increment of 2 carbon atoms in the molecule's chain length. The family analyzed are n-alkanes, 1-alcohols and di-n-ethers. The VFA sensitivity analysis has shown that:

- The fuel thermo-physical properties have an impact on the air utilization and therefore on the local in-cylinder λ distribution.
- The role played by the fuel properties decreases as the engine operating load increases, because the aerodynamic drag plays a major role on the mixing process, dominating the breakup process.
- When the chain length is increased by C4 the property ranking underlined by the VFA sensitivity analysis is the following: dynamic viscosity > vapor pressure > surface tension > density.
- When the chain length is increased up to C8 the above mentioned ranking is not confirmed.
- Molecules with shorter chain length (C8) are beneficial with regards to the mixture formation since they allow smaller shares of rich mixture and unused air, showing at the same time larger lean mixture areas inside the combustion chamber.
- Among the three different fuel families the following ranking in terms of mixture formation can be stated: di-n-ethers > n-alkanes > 1-alcohols.

This work has also introduced the VFA as methodology to screen possible novel biofuels molecules in order to improve the mixture formation process inside DI Diesel engines. Investigation on oxygenated ring structures such as those of furans are object of future work in order to extend this approach to all the domain of investigation screened within the TMFB Cluster. Furthermore, the VFA will be extended to lower part load engine operating conditions to gather a complete understanding of the overall dependence on fuel thermo-physical properties of the mixture formation process.

Acknowledgment

This work was performed as part of the Cluster of Excellence ''Tailor-Made Fuels from Biomass'', which is funded by the Excellence Initiative by the German Federal and State Governments to promote Science and Research at German Universities.

References

Adomeit P. Rohs H., Körfer T., Busch H. (2006) Spray interaction and mixture formation in diesel engines with grouped hole nozzles. THIESEL Conference on Thermo-and Fluid Dynamic Processes in Diesel Engines.

Adomeit P., Busch H., Lamping M., Körfer T., Rohs H., Wix K., Sono H., Shibata M. (2008) Tailored combustion system layout by interlinking of CAE and experiment. THIESEL Conference on Thermo- and Fluid Dynamic Processes in Diesel Engines.

Cracknell R. F., Ariztegui J., Dubois T., Hamje H., Pellegrini L., Rickeard D., Rose K. D., Deppenkemper K., Graziano B., Heufer K. A., Rohs H (2014) Modelling a Gasoline Compression Ignition (GCI) Engine Concept. SAE paper 2014-01-1305.

Daubert T. E., Danner R. P. (1993). Physical And Thermodynamic Properties Of Pure Chemicals, Taylor & Francis; 3rd edition.

Graziano B., Jakob M., Kremer F., Pischinger S., Lee C., Fernandes R. X (2013) Investigation on the Ignition Sensitivity of 2-MTHF, Heptane and Di-n-butylether. European Combustion Meeting, Lund.

Heywood J. B. (1988). Internal Combustion Engines Fundamentals, McGraw Hill.

Heuser B., Kremer F. Pischinger S. (2014) Optimization of Diesel Combustion and Emissions with Tailor-Made Fuels from Biomass. SAE paper 2013-24-0059.

Heuser, B., Laible, T., Jakob, M., Kremer, F. et al. (2014). C8-Oxygenates for Clean Diesel Combustion. SAE paper 2014-01-1253.

Higgins B. S., Mueller C. J., Siebers D. L.(1999) Measurements of fuel effects on liquid-phase penetration in DI sprays. SAE paper 199-01-0519.

Jakob M., Klein D., Graziano B., Kremer F., Pischinger S (2013) Simultaneous shadowgraphic and chemiluminescent visualization to determine the mixture formation quality and ignition stability of diesel engine related surrogate fuels. 14. Tagung "DER ARBEITSPROZESS DES VERBRENNUNGSMOTORS", pp 11-127.

Kong, S., Han, Z., Reitz, R (1995) The development and application of a Diesel ignition and combustion Model for multidimensional engine simulation," SAE paper 950278.

Patterson M. A., Reitz R. D (1995). Modeling the effects of fuel spray characteristics on Diesel engine combustion and emission. SAE paper 980131.

Pickett, L. M.; Siebers, D. L. (2006) Soot formation in diesel fuel jets near the lift-off length. Int. J Engine Research, Volume 7, pp 103-130.

Pischinger S. (2013). Internal Combustion Engines, 6th edition of VKA lecture notes, RWTH Aachen University.

Poling B. E., Prausnitz J. M., O´Connel J. P. (2001) The properties of Gas and liquids. McGRAW-HILL,5th edition.

Reddemann M. A., Mathieu F., Cordes D. Kneer R (2012) Parametric study of fuel impact on spray behaviour using high speed visualization ICLASS 12th triennial International Conference on Liquid Atomization and Spray Systems.

Siebers D. L. (1999) Scaling liquid-phase fuel penetration in Diesel sprays based on Mixing-limited vaporization. SAE paper 1999-01-0528.

Siebers D., Higgins B. (2001) Flame lift-off on Direct-injection diesel sprays under quiescent conditions. SAE paper 2001-01-0530.

A History of Optically Accessible Engines and Their Impact on our Understanding of Engine Combustion Processes

P.C. Miles

Sandia National Laboratories. MS 9053-PO Box 969. CA 94551 Livermore. USA

E-mail: pcmiles@sandia.gov

Abstract. From the very start of the development of the internal combustion engine, engineers have attempted to visualize the in-cylinder mixing and combustion processes in an effort to increase their insight into the operation of the engine and to optimize their designs. Indeed, in 1872 Nicolaus Otto himself employed an optical model engine to investigate the mixing of fresh charge with the combustion residuals, using a hand-cranked model engine. From that time to the present, optical engines have proven to be invaluable tools for engine research, and have contributed greatly to our understanding not just of fuel-air mixing, but also of critical processes such as engine knock and pollutant formation.

More recently, with the advent of computer simulation as an engine design and optimization tool, optical studies have taken on an additional role: provision of quantitative data regarding the flow and scalar (temperature, composition, etc.) fields in engines over as wide a spatial extent and over as broad a crank-angle range as possible. These quantitative studies serve two inter-related purposes: first, to provide the data necessary to devise computationally tractable models of the in-cylinder processes governing combustion and emissions; and second, to validate and develop confidence in the accuracy of these tools.

In this lecture the development of optical engines is reviewed, spanning early efforts in simplified engines to the more recent development of high-pressure, high-speed engines that retain the geometric complexities of modern production engines. Limitations of these engines with respect to the reproduction of realistic metal test engine characteristics and performance are identified, as well as methods that have been used to overcome these limitations. Lastly, the role of the work performed in these engines on clarifying the fundamental physical and chemical processes governing the combustion process, and on laying the foundation for predictive engine simulation, is identified and discussed.

Fuel Accounting for the First Cranking Cycle of a GDI Engine

J.F. Rodríguez, W.K. Cheng

Sloan Automotive Laboratory, Massachusetts Institute of Technology, Cambridge, MA, USA

E-mail: jfrb@mit.edu
Telephone: +(1) 617 452 4771

Abstract. The fuel pathway for the first cranking cycle in a GDI engine is characterized quantitatively. The engine is fired for a single cycle in one cylinder at a specified cranking speed and coolant temperature of 20^{o} C. The fuel carbon is accounted for from measurements of the exhaust carbon (CO2, CO, and HC). The remaining carbon is assumed to go into the oil and crank case. The parameters studied are the amount of injected fuel, the injection timing, the intake pressure, the injection pressure and the cranking speed. Substantial fuel enrichment is needed to produce stable combustion in the first cycle, with significant residual fuel that goes into preparing the mixture of the second cycle and into the oil and crank case. The first cycle HC emissions as a fraction of the fuel are not sensitive to the fuel enrichment, the manifold absolute pressure, and the injection pressure.

Notation

EPA	Environmental Protection Agency
F/A	Fuel to air mass ratio
FEF	Fuel enrichment factor
FTP	Federal test procedure
GDI	Gasoline direct injection
HC	Hydrocarbon
m_C	Mass of carbon
m_f	Fuel mass injected
MAP	Manifold absolute pressure
MW	Molecular weight
NDIR	Non-dispersive infrared
NEDC	New European driving cycle
NIMEP	Net indicated mean effective pressure
P_{cyl}	Cylinder pressure
SI	Spark Ignition
SOI	Start of injection
t	time
V_{cyl}	Cylinder volume
λ	Air equivalence ratio
γ	Specific heat ratio
η_{vol}	Volumetric efficiency
ρint	Intake density

1. Introduction

Lowering fuel consumption and CO_2 emissions have become the leading agenda for engine development around the world. This eminence is a result of the stringent fuel economy standards aiming for CO2 emissions to around 100gCO_2/km (normalized to NEDC) by 2025 (Façanha 2012). Turbocharged gasoline direct injection (GDI) is a promising technology for spark ignition (SI) engines towards this goal. Compared to the naturally aspirating engines of the same performance, the turbocharged GDI engines have a CO2 reduction potential of up to 27% according to EPA estimates (EPA

& NHTSA 2012). The market penetration of GDI engines in the USA is up to 30% of the gasoline engine sales in 2012 (He 2013); a prognosticated market share of up to 97% by 2025 has been reported (EPA & NHTSA 2012).

The GDI technology has both advantages and drawbacks. Benefits include better knock resistance through charge cooling of the fuel spray, higher volumetric efficiency via cooling the intake air, and potential of pumping loss reduction via stratified lean part load operation. Directly injecting fuel into the combustion chamber, however, results in significant emission challenges for unburned hydrocarbons and particulates because of the substantial presence of liquid films on the combustion chamber walls.

The challenges are particularly severe during the cold-start and warm-up phases of the engine operation. Because of the inactivity of the catalyst during a significant part of the cold-start, up to 80% of the allowed HC emissions in the FTP stem from the first minute of operation (Hallgren 2005). The contribution from the cranking process is particularly important because cranking has two distinctive characteristics which are more severe than the rest of the certification cycle: coldest cylinder wall temperatures and lowest engine speed.

Direct injection onto the cold cylinder walls results in formation of fuel films with low evaporation. As a result, the amount of fuel that needs to be injected for the combustion events is significantly higher than what is required to prepare a stoichiometric charge with full evaporation. The large residual fuel that escapes the main combustion event becomes a source of HC emissions. Furthermore, the cold walls reduce post flame oxidation of the unburned HC.

The low engine cranking speed results in reduced charge motion, which in turn, causes poor air-fuel mixing. To avoid flame extinction due to lean pockets in the non-uniform mixture, it is necessary to even further increase the amount of injected fuel, with the associated negative impact on the HC emissions.

We have embarked on a systematic study of the emissions in the cold cranking process of a GDI engine. This paper reports on the fuel pathway and HC emissions in the first cycle of the cranking process. (The associated particulate emission will be reported in a later paper.) A carbon accounting analysis is used to deconstruct the amounts of fuel participating in combustion, being exhausted as HC emissions, staying in the combustion chamber for the second combustion event, and being absorbed in the oil or lost through blow-by.

2. Experimental Methodology

2.1 Engine and Engine Control

The engine used for this study is a GM Ecotec LNF engine; specification is given in Table 1. The engine features a centrally mounted spark plug and 4 valves per cylinder with variable valve timing for both intake and exhaust valves. The injection system consists of 4 side-mounted multi-hole injectors from Bosch driven by driver from Siemens.

The fuel, intake air and coolant temperature are fully conditioned. For the fueling system, a hydro-pneumatic accumulator pressurized by nitrogen was used, allowing pressures ranging from 30 to 110 bar to be set independent of the engine operation.

The engine control is achieved by an in-house developed controller, allowing a full customization of the engine parameters such as injection and spark timing, injection duration, split injection ratio and intake/exhaust cam phasing.

Table 1. Engine geometry and features

Basic geometry	
Engine type	In-line 4 cylinder
Displacement [cc]	1998
Bore [mm]	86
Stroke [mm]	86
Connecting rod [mm]	145.5
Compression ratio	9.2:1
Valve timing during cranking	
IVO	11 ˚CA ATDC
IVC	61 ˚CA ABDC
Max. intake valve lift	10.3 mm @ 126 ˚CA ATDC
EVO	52 ˚CA BBDC
EVC	10 ˚CA BTDC

Max. exhaust valve lift	10.3 mm @ 125 ˚CA BTDC
Fuel	
Tier II EEE certification fuel carbon mass fraction 86.5%	

2.2 Experiment Description

The engine crank-start is a highly transient process, with engine speed variations of up to 200rpm per combustion event. This process depends heavily on the first combustion event of each cylinder, and thus, as a first step to fully understand the cold cranking emissions, it is necessary to understand that first firing cycle of the engine.

To recreate the conditions during cold cranking, the engine coolant, engine oil, fuel and intake air temperatures were kept at 20°C. Even though the engine is equipped with variable cam timing, both camshafts were kept at their parked position (Table 1), since the low oil pressure at cranking speed does not allow the operation of the system. The parked position of the camshafts corresponds to a negative valve overlap of 20°CA, resulting in a reduced volumetric efficiency and effective compression ratio.

The experiment started with the engine being motored at the desired cranking speed (280 rpm except for the engine speed sweep experiments), until the temperature and exhaust HC concentration reached steady state to ensure the purging of residual hydrocarbons stored in the engine and lubricant, and to measure the background HC concentration. The throttle plate position was kept at a fixed position. Except for the MAP sweep experiments, the position corresponded to that at fast idle (2 bar NIMEP at 1200 rpm). The resulting MAP at cranking was at 0.9 bar, which was slightly lower than the typical value (1 bar) for the actual first cranking cycle because the engine had been motored for some time. (It will be shown in the MAP sweep experiments that this difference has no material impact on the results.) After this purge, a single injection and ignition event took place in cylinder #4: a metered amount of fuel was injected followed by combustion. Then, the engine continued to be motored at cranking speed and the exhaust stream measured, until the steady state was achieved again (Fig. 1). Throughout the complete experiment, the exhaust composition was measured and recorded during this time interval with 1^{o} crank angle resolution. This procedure was repeated 5 times for each experimental condition and the results reported are the averaged values.

The exhaust composition was measured with fast-response analyzers, sampling directly from the exhaust runner of the fired cylinder (cylinder #4). The hydrocarbon concentration was measured using a fast FID unit (Cambustion model FID400), with a response time $t_{10\text{-}90}$ of 10ms, and a sampling position 6cm from the exhaust valve. The CO and CO_2 concentration was measured with a fast NDIR unit (Cambustion model NDIR500), with a response time $t_{10\text{-}90}$ of 20ms, and a sampling position 8cm from the exhaust valve. The λ value was not directly measured, since the response time of conventional λ sensors is too slow (~150 ms). The λ values reported were calculated from carbon balance using the CO and CO_2 measurements (Silvis 1997).

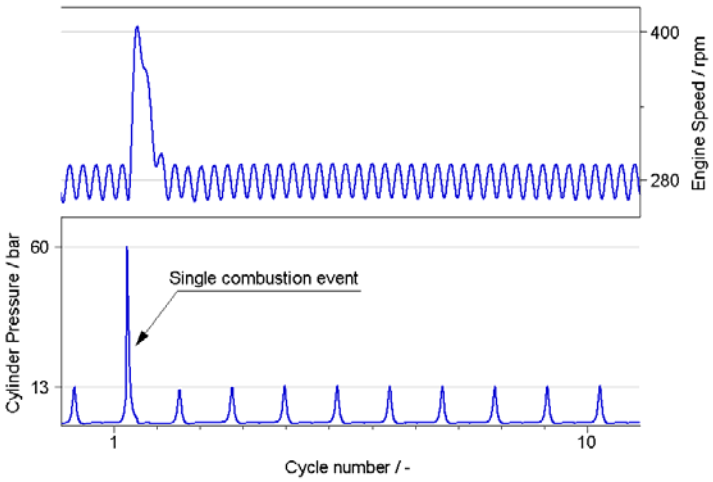

Fig. 1. Engine speed and cylinder pressure of the single cycle firing experiment.

2.3 Fuel Accounting

To understand the fuel pathway in the first cycle, a fuel carbon accounting analysis is performed to quantify the fuel carbon participating in combustion, the amount being exhausted as unburned hydrocarbons, and the amount that cannot be accounted for; the latter represents the fuel that goes into engine oil dilution and blow-by losses. The analysis is done by translating the fuel and exhaust mass flows to equivalent carbon mass flows, and then performing a control volume analysis around the cylinder (Eq. 1).

$$\dot{m}_{C,in} = \dot{m}_{C,out} + \dot{m}_{C,Eng} \tag{1}$$

The "in" flow corresponds exclusively to the fuel carbon injected, while the "out" flow encompasses the carbon mass flow due to the CO2, CO and HC content in the exhaust. The "engine" component of the carbon accounting represents the carbon mass that cannot be accounted for solely by the intake and exhaust flows; this amount corresponds to the fuel that goes into oil dilution and blow-by losses.

To relate the concentration measurements to mass flows, the exhaust mass flow has to be correctly synchronized with the fast analyzer signals. The exhaust mass flow was calculated using as inputs the cylinder pressure and the piston position. The model assumes the gas is ideal, and that the charge within the cylinder expands isentropically to expel the exhausted gas. Then the exhaust gas flow rate is obtained from continuity.

$$\dot{m}_{exh} = -\left(\frac{1}{\gamma \cdot P_{cyl}} \cdot \frac{dP_{cyl}}{dt} + \frac{1}{V_{cyl}} \cdot \frac{dV_{cyl}}{dt}\right) \cdot m_{cyl} \tag{2}$$

To align the exhaust flow with the fast analyzer measurements, the transit time of the exhaust gas from the exhaust valve to the sampling point needs to be considered. The transit time is determined from the cumulative exhaust gas volume between the sampling point and the exhaust valve. The carbon mass flow due to each constituent y can then be calculated by multiplying the measured wet molar concentration of the component by the exhaust molar flow using MW_{exh} (=28.9 g/mol) and the molecular weight of carbon (MW_C):

$$\dot{m}_{C,y} = \hat{x}_y \cdot \frac{\dot{m}_{exh}}{MW_{exh}} \cdot MW_C \tag{3}$$

For the motored cycles after the single cycle firing, the cylinder pressure is lower than the exhaust pressure when the exhaust valve opens, and the exhaust flow is initially backwards until the pressure equilibrates and the displacement flow commences (Fig. 2). Care was taken not to double count the emission for the reverse flow in the motored cycles.

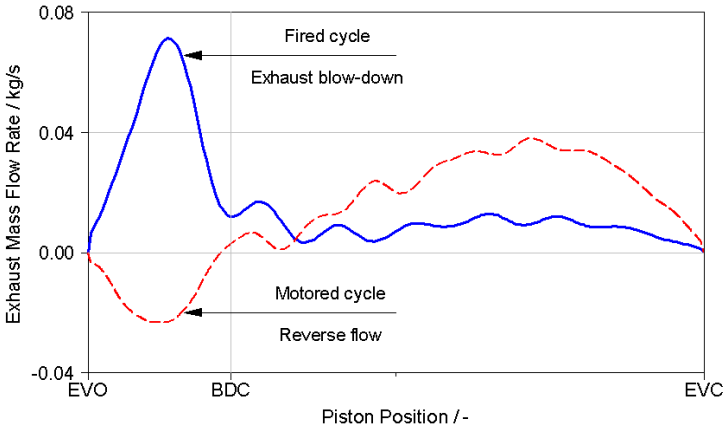

Fig. 2. Exhaust flow of the fired cycle and a motored cycle

2.4 Fuel Enrichment Factor

Since not all of the injected fuel goes into the charge mixture, a large amount of fuel has to be injected to achieve stable combustion in the first cycle. To quantify the amount of additional fuel required, a fuel enrichment factor (FEF) is defined:

$$FEF = \frac{m_{f,cyl}}{V_{cyl} \cdot \eta_{vol} \cdot \rho_{int} \cdot (F/A)_{stoich}} \quad (4)$$

Thus the fuel mass injected ($m_{f,cyl}$) is equal to FEF times the amount required to prepared a stoichiometric mixture with the inducted air. The volumetric efficiency is referenced to the intake manifold conditions; at cranking speed, and under motoring conditions, the value was measured to be 80%. This results in a fuel mass of 29.4mg for a FEF=1, at an intake temperature and pressure of 293K and 900mbar respectively.

2.5 Experimental Matrix

The scope of this paper focuses on six different engine parameters using a one-variable-at-a-time approach. The variables studied are: First cycle fuel enrichment factor (FEF, as defined in section 2.4), injection timing (single injection was used), spark timing, first cycle intake manifold pressure, fuel pressure, and engine cranking speed (Table 2). For the sweep of each parameter, the remaining parameters were held fixed at the nominal values.

Table 2. Experimental scope.

For the sweep of each parameter, the remaining parameters were kept at the nominal values

Variable	Sweep range	Nominal value
FEF [-]	1.7 to 3.5 with 0.2 increments	2.5
Injection timing [˚CA ATDC]	30 to 315 with 15 ˚CA increments	90
Spark timing [˚CA ATDC]	-45 to 20 with 5 ˚CA increments	-10
MAP [bar]	650 to 1000 with 50 mbar increments	0.9
Fuel pressure [mbar]	30 to 110 with 20 bar increments	50
Cranking speed [RPM]	280, 700, 1200	280

3. Results and Discussion

The primary goal of the experiment is to deconstruct the pathways for the single cycle injected fuel and to examine how the engine parameters affect the pathways. As such, the individual carbon mass flows due to each component (CO_2, CO, and HC) are integrated for each cycle, and the cycle-resolved results are summarized in three sets of numbers:

- The first set is the HC emissions respectively of the first, second and sum of the third-and-beyond cycles. The 1st (firing) cycle HC emissions give information of the emission performance; the 2nd (motoring) cycle HC emissions indicate the amount of the in-cylinder retained fuel from the first cycle that would contribute to the combustible mixture of the second cycle. The remaining HC are for total carbon balance so that the amount that goes into the engine oil and crankcase could be computed.
- The second set is the integrated CO2 and CO over the complete set of recorded cycles (approximately 50). These carbons represent the burned fuel, and are used to compute the overall combustible mixture λ value.
- The third set is the difference between the fuel carbon from the injected fuel and the cumulative carbon from the CO2, CO and HC measurements over the complete set of recorded cycles. This difference, labelled as the unaccounted for fuel carbons, represents the fuel that goes into the engine oil and crankcase.

3.1 FEF sweep

The outputs of the single-cycle-fired engine as a function of the FEF are shown in Fig. 3. The NIMEP increases with FEF (Fig. 3a), since more fuel goes into the charge mixture. This observation is confirmed by the decrease in λ values with FEF (Fig. 3b). The progression, however, is not linear – the increment of the fuel going into the combustible charge is large at low FEF, but the increment diminishes with increase in FEF.

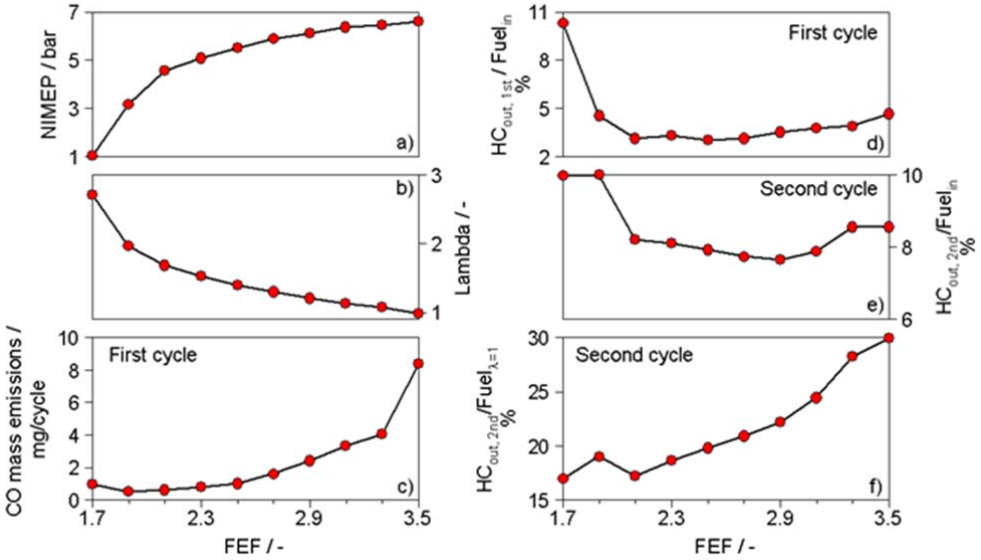

Fig. 3. Outputs of the single-cycle-fired engine as function of FEF

Since the λ value is calculated from carbon balance using the exhaust carbon values (Silvis 1997), it may be interpreted as the overall λ value of the burned mixture. For FEF increasing from 1.7 to 3.5, λ decreases from 2.8 to 1. Thus for the whole range of FEF, the burned mixture is overall lean. However, there is substantial CO emission (Fig. 3c), which is especially high (8 mg which corresponds to ~4% wet CO) at overall λ = 1. The high value suggests that indicates that the mixture was not homogeneous and rich burning pockets were present during combustion.

Turning attention to HC emissions, Fig. 3d shows the relative HC emissions with respect to the fuel injected. With the exception of the point at FEF=1.7 which resulted in a partial burn, the fraction of the fuel injected coming out of the engine as unburned HC remains roughly constant with increasing FEF at values between 3-4%, with a slight increase for higher FEF. This first cycle HC emissions will contribute directly to the tailpipe emissions, since the catalyst has not reached light-off temperature.

Fig. 3e shows the relative HC emissions for the second cycle, which is a motored cycle. This value is representative of the fuel fraction that would be available for second cycle combustion, and thus, it can be used to correct the second injection event, to avoid over enrichment. The relative HC emissions for the second cycle stay roughly constant at around 8% for FEF>1.9. To understand the impact that the residual HC could have on the second combustion event, the HC emissions are also plotted relative to the fuel necessary to achieve stoichiometric combustion. Fig. 3f shows that more than 20% of the fuel necessary to achieve stoichiometric combustion for the second combustion event is already in the cylinder in the form of residual HC for FEF>2.3.

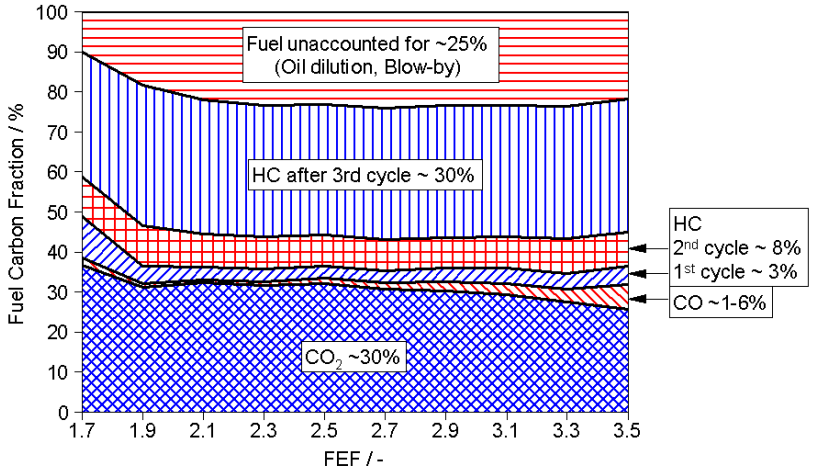

Fig. 4. Fuel carbon pathway as a function of FEF.

The fuel carbon pathway as a function of FEF is shown in Fig. 4. For FEF=1.7, the higher total CO_2 fraction is a result of the ongoing combustion after EVC, caused by the partial burn. Leaving the case with FEF=1.7 aside, the total combined CO_2 and CO fraction accounts to approximately 32%. This suggests that even at higher FEF, the fraction of the fuel participating in combustion stays constant. The HC emissions coming out of the engine on and after the third cycle, account to approximately 30%, the main source being desorption from the oil layer. Approximately 25% of the fuel cannot be accounted for. This fuel ends up in the oil or crankcase.

3.2 Injection timing sweep

Injection timing has a strong influence on mixture formation. Under warm operation conditions, early injection timings result in more homogeneous mixtures, while late injection timings result in higher heterogeneity and charge turbulence prior to ignition (Knop & Essayem 2013). At cold engine temperatures, the injection timing also determines the amount of liquid and location of the fuel impinging on the walls of the combustion chamber, resulting in liquid fuel films.

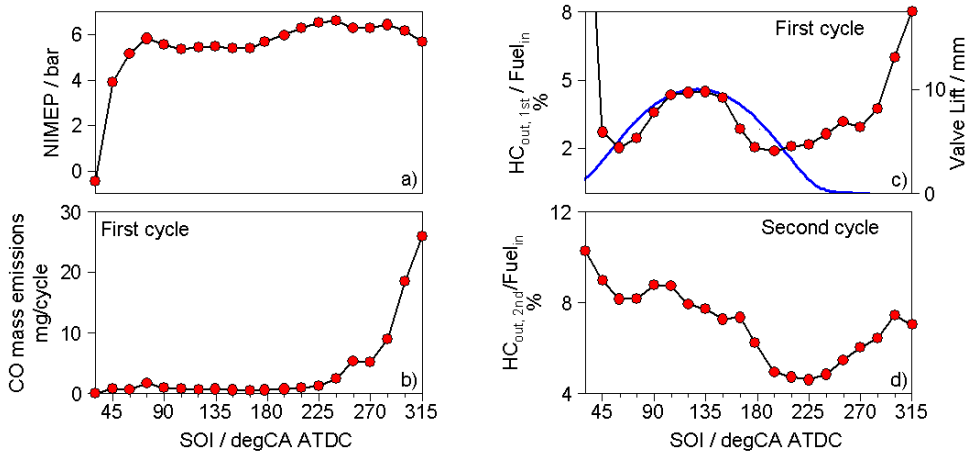

Fig. 5. Outputs of the single-cycle-fired engine as function of FEF

Figure 5 shows the outputs of the single-cycle-fired engine for injection timings ranging from SOI=30 to 315˚CA after TDC-intake. The NIMEP increases from 0 bar at SOI=30˚CA (misfire) to 6 bar at SOI=75˚CA (Fig. 5-a). This range corresponds to heavy piston impingement and bouncing of the injected fuel onto the cylinder head; the effect is diminishing as the injection timing is retarded to SOI=75˚CA (Ketterer & Cheng 2014). Beyond this range, the NIMEP stays relatively constant for injec-

tions during the intake stroke. For compression stroke injections, the higher in-cylinder pressure reduces the injection spray penetration, allowing for a better mixture formation and increased fraction of fuel evaporated. Consequently, an increase in NIMEP for SOI up to 225˚CA is seen. Up to this injection timing (SOI=225˚CA), the homogeneity of the mixture stays relatively constant, as can be seen by the constant low values of the emitted CO. The NIMEP trend then becomes flat, while the mixture becomes increasingly heterogeneous, up to an injection timing SOI=285˚CA where the fuel spray impinges again on the piston crown. The result is a very heterogeneous and rich mixture around the spark plug, characterized by high CO emissions (Fig. 5b) and slightly lower NIMEP.

For the HC emissions of the first cycle, four zones can be identified (Fig. 5c). The first zone, ranging from 0 to 30˚CA for the SOI, misfire occurs due to heavy piston impingement. The second zone, going from SOI=45 to 180˚CA, is characterized by interaction between the injection spray and the intake valve. The maximum HC emissions (4.5% of injected fuel) occur between a SOI of 120˚CA and 135˚CA corresponding with the maximum lift of the intake valve. To the left and right of that maximum, HC emissions follow the intake valve lift, achieving a minimum of 1.9% of injected fuel when the intake valve lift is lower than 4mm. The third zone corresponds to SOI=180 to 240˚CA, that is in the initial part of the compression stroke. In this zone there is not only a better utilization of the fuel, but also a flat region at low values of HC emissions. Finally, the fourth zone corresponds to late injection timings into the compression stroke, where the interaction between piston and injection spray gains importance, resulting in high HC emissions. Contrary to the first zone, the squish charge movement, together with higher cylinder pressure and temperature, contributes to fuel evaporation of the fuel film on the piston crown, resulting in a rich mixture around the spark plug.

The fuel available for the second cycle combustion varies significantly with the SOI of the first cycle (Fig. 5d), achieving a minimum value in the same range as does the first cycle HC emissions, that is, SOI during the early compression stroke.

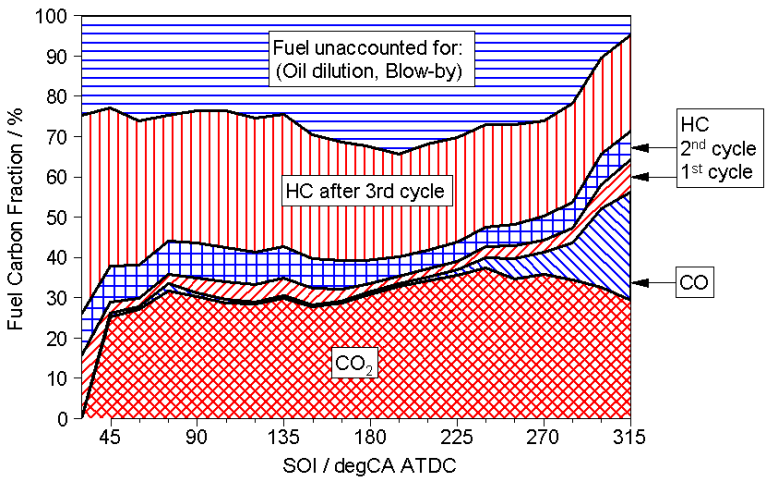

Fig. 6. Fuel pathway as a function of SOI.

Figure 6 shows the individual contributions of CO_2, CO and HC to the fuel carbon accounting. The combined total CO_2 and CO emissions show a monotonous increase with late injection timings. Although the combustion efficiency decreases with later injection, more fuel is taking part in combustion, suggesting that a lower FEF could be used to achieve an ignitable fuel-air mixture. The lower HC emissions after the third cycle, and the lower fraction of the unaccounted fuel for late injection, suggest that the diffusion of fuel in the oil is reduced, since the injection spray interacts less with the cylinder liner.

3.3 Ignition timing sweep

The use of retarded spark timing has been established as a common practice in the industry to reduce both catalyst light-off time and engine-out HC emissions (Hallgren & Heywood 2003, Eng 2005). In contrast, the influence of ignition timing on the first combustion cycle characteristics has only been examined in a few studies, for a reduced set on spark timings before TDC (Wiemer et al. 2007, Fan & Li 2012).

The first cycle NIMEP as a function of spark timing is shown in Fig. 7a. For both extremes of the spark timing spectrum there is a reduction in work output, with a higher impact on the side of late ignition. The maximum NIMEP is achieved in a plateau region from ignition =-25 to -5˚CA ATDC. Due to the low, but rapidly changing, engine speed, the usual notion of proper combustion phasing for MBT (CA50~7˚CA ATDC and Pmax~15˚CA ATDC) does not apply (Cheng & Zhao 2006). The NIMEP plateau region is a result of the competing effects between heat transfer to the cold cylinder walls and the location of the maximum cylinder pressure.

As shown in Fig. 7b, the CO production of the first combustion cycle has a high sensitivity to spark timing. Given that the amount of fuel, SOI, fuel pressure and engine speed were kept constant, mixture formation was similar. The production of CO is a result of locally rich mixture being burned. Retarding the spark has two effects. First, there is more time for mixing so there is less fuel rich pocket for CO production. Second, the charge temperature in the expansion stroke is higher so that post-flame oxidation of CO is promoted. Both effects reduce the CO emission.

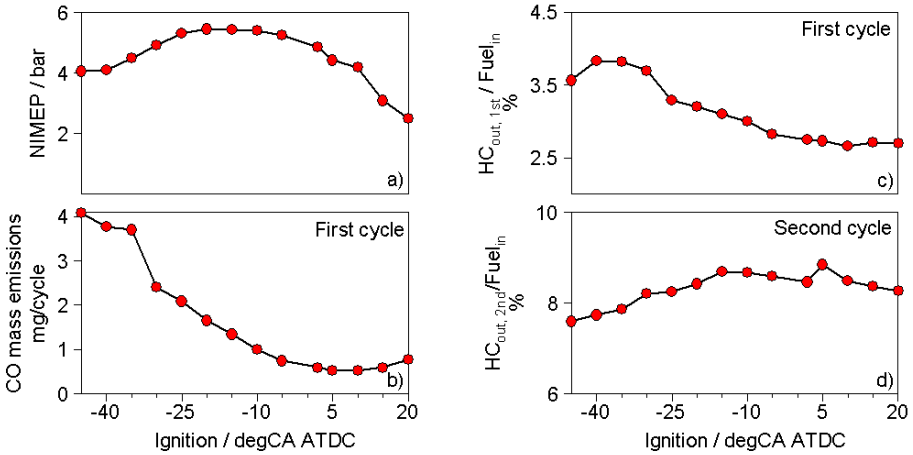

Fig. 7. Outputs of the single-cycle-fired engine as function of spark timing

The first cycle HC emissions are also favored by later ignition timing, with a lower sensitivity compared to the CO production (Fig. 7c). The higher burned gas temperatures resulting from spark retard, favor the post-flame oxidation of unburned HC in the bulk gas (Cowart 2005). The net effect is a decrease of HC as a fraction of the fuel from ~3.7 to 2.8%. The fuel available for the second cycle combustion (Fig. 7d) increases slightly with retarded spark timing. The lower HC emissions after the third cycle and the lower fraction of the unaccounted fuel for advanced spark timings (Fig. 8) are a direct consequence from the increased fraction of fuel taking part in combustion during the first cycle.

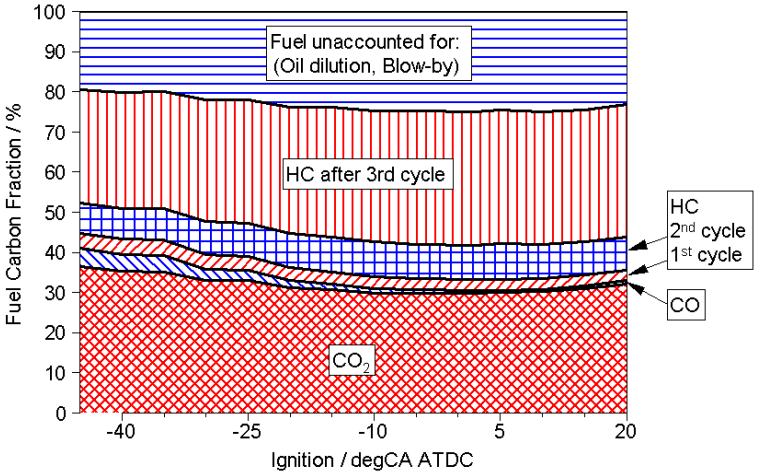

Fig. 8 Fuel pathway as a function of spark timing

3.4 Manifold Absolute Pressure sweep

Lower MAP can be beneficial for mixture preparation since less vaporized fuel is needed to form a combustible mixture (Lang et al. 2004). During cranking, MAP is a function of engine speeds and throttle position. In the experiment, the engine speed was kept constant and the throttle position was varied, achieving a minimum MAP value of 650mbar at a cranking speed of 280rpm for a fully closed throttle.

Since the engine was calibrated using a speed-density approach, the injected amount of fuel, and the cycle work output, are functions of MAP (Figs. 9a and 9c). To assess the fuel evaporation behavior at different MAP values, the gross indicated fuel conversion efficiency $\eta_{i,g}$ may be used. Since in the MAP sweep, the combustion phasing, and hence the conversion efficiency of the burned fuel, are approximately the same, $\eta_{i,g}$ becomes a ratio of the mass of fuel burned to the injected fuel, and is a measure of the fuel utilization efficiency. For increasing MAP values from 650 to 1000mbar, $\eta_{i,g}$ decreases slightly from 9.5% to 8.8%. Thus the fuel utilization decreases with more injected fuel.

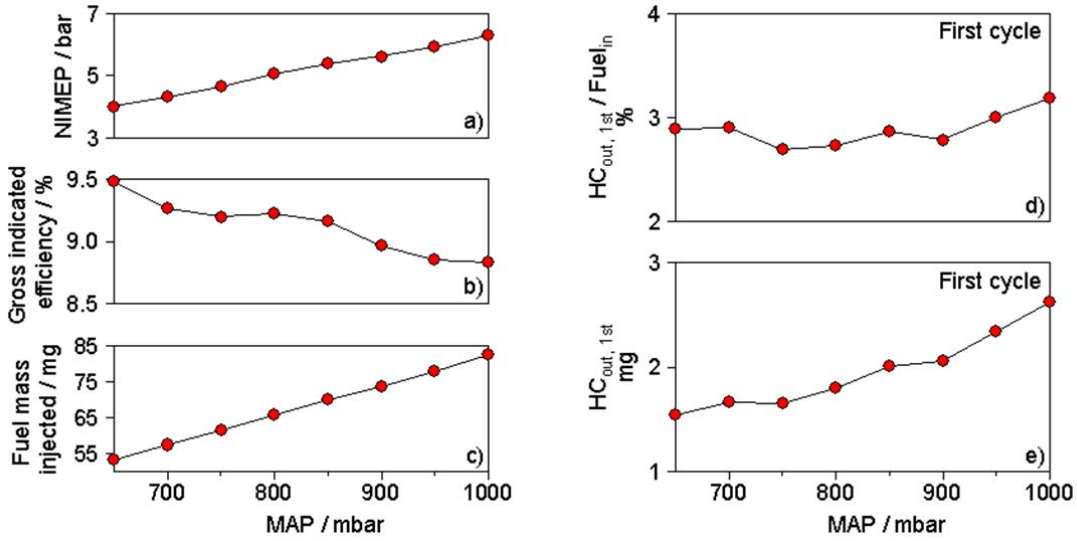

Fig. 9. Outputs of the single-cycle-fired engine as function of MAP

The relative first cycle engine-out HC emissions only increases modestly with MAP (Fig. 9d). In absolute terms, however, lower MAP allows a reduction in the injected fuel amount without overleaning of the mixture, and resulting in lower absolute HC emissions for the first cycle (Fig. 9e).

The distribution of the fuel carbon as a function of MAP is shown in Fig. 10. As MAP increases, while the relative HC emissions stay relatively constant for first and second cycle, the amount for third cycle on increases. This observation may be explained by the increase of the oil layer temperature because more fuel is burned with the increased MAP so that there is more desorption in the subsequent motoring cycle. The corresponding decrease of the oil dilution and blow-by amount lends support to this explanation.

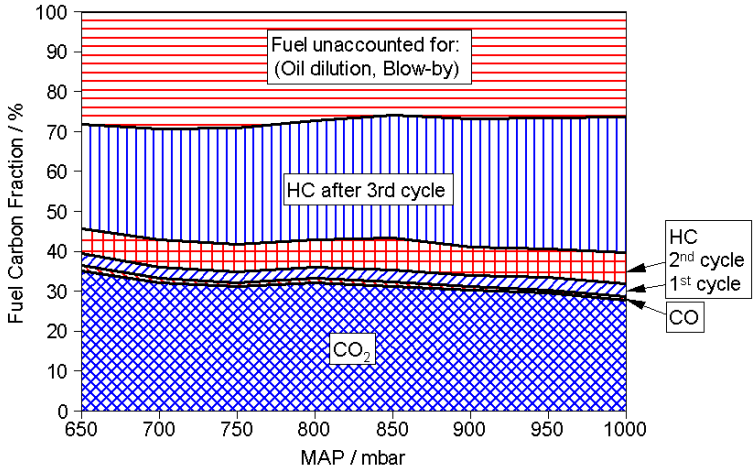

Fig. 10. Fuel pathway as a function of MAP

3.5 Fuel pressure sweep

Injection pressure influences the mixture formation of GDI engines through different mechanisms. First, a higher fuel pressure renders smaller fuel droplet diameter. The smaller droplets have better evaporation. They also have a lower inertia and exchange momentum readily with the charge; thus spray penetration and wall impingement are reduced. Second, higher fuel pressures result in higher nozzle velocities, and therefore higher momentum and penetration of the injection spray. The balance between these conflicting effects has been studied in the fuel pressure range from 5 to 40 bar (Landenfeld et al. 2004, Eiglmeier et al. 2007, Kudo et al. 2011). In this range, droplet size decreases sharply with increasing injection pressure from 100 µm at 5bar to roughly 30 µm at 40 bar and the advantages in reduction of droplet size are more significant than the disadvantages of increased spray penetration, resulting in better mixture formation and lower emissions. In this study, the fuel pressure range of 30 to 110 bar is examined. The lower value is what modern fuel pump could supply for the first injection cycle (Landenfeld et al. 2004); however, only modest reductions in fuel droplet size are achievable in this pressure range (e.g. from ~35 to 18 µm, as reported in Landenfeld et al. 2004). The fuel pulse width was adjusted to account for the different injection pressure.

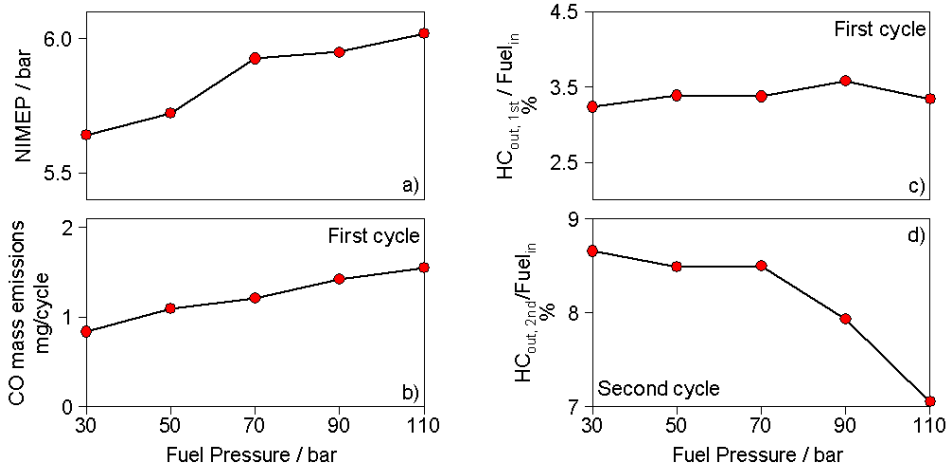

Fig. 11. Outputs of the single-cycle-fired engine as function of fuel injection pressure

The NIMEP increases with injection pressure (Fig. 11a). This observation suggests that mixture formation is favored by higher injection pressures. The CO emission also increases (Fig. 11b), in-

dicating that there may be more fuel rich regions. The HC emission as a fraction of the fuel, however, is not sensitive to the fuel pressure (Fig. 11c).

The second cycle HC emissions (Fig. 11d), as well as the HC emissions after the third cycle (Fig. 12), indicate that despite the higher fuel pressure and the corresponding potential increase in spray penetration, the fuel remaining in the combustion chamber after the first combustion event decreases with higher fuel pressures. The overall effect is that for injection pressure increasing from 30 to 110 bar, the fraction of fuel burned (as indicated by the fuel carbon used) only increases modestly, from 33 to 37%; the first cycle HC emissions as fraction of fuel remains approximately constant.

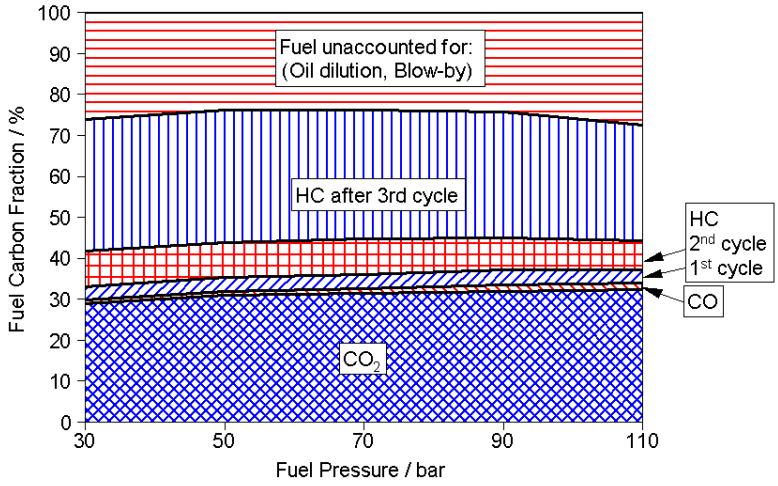

Fig. 12. Fuel pathway as a function of fuel pressure

3.6 Engine speed sweep

With the proliferation of start-stop systems and hybrid powertrains, the engine cranking speed is not limited anymore to the low speed of conventional starters. Hence a further dimension for engine start optimization could be explored. Three different engine speeds were assessed. These speeds correspond to conventional cranking speed (280rpm), idle (700rpm), and fast idle (1200rpm). The results are shown in Figures 13 and 14.

Since the mass burn per crank angle changes with engine speed due to the effect of crank angle speed and turbulence (Heywood 1988), combustion phasing is a function of engine speed. To decouple the effect of engine speed from that of combustion phasing on mixture preparation, the spark timing was modified for each engine speed to achieve a comparable CA50 (Fig. 13b).

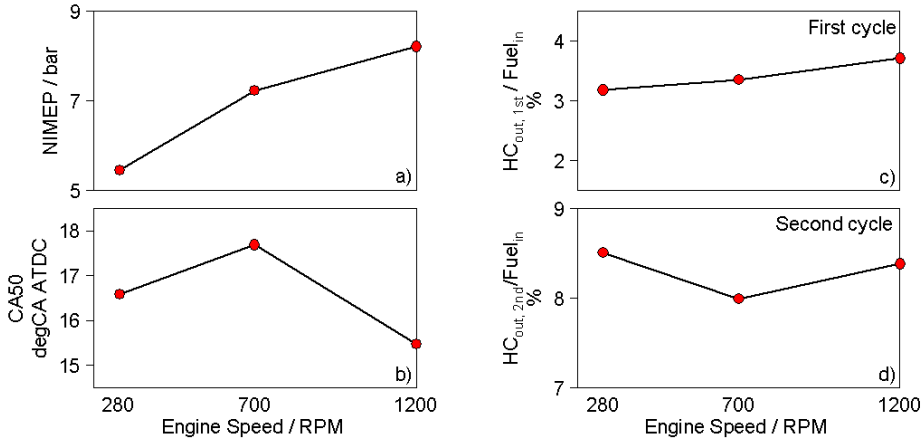

Fig. 13. Outputs of the single-cycle-fired engine as function of cranking speed

With the cranking speed increase from 280 to 1200 rpm, the NIMEP increases by 49% (from 5.5 to 8.2 bar); see Fig. 13a. The relative HC emissions, however, only increases modestly, from 3.2 to 3.8%; see Fig. 13c. The HC retained for the 2nd cycle remains approximately the same. However, it should be noted that if a certain value of NIMEP is targeted for the first cycle, the amount of fuel can be reduced for higher engine speeds, resulting in lower absolute HC emissions.

The fuel utilization, as measured by the fraction of fuel carbon conversion to CO and CO_2, improves by 20% (from 0.35 to 0.42); see Fig. 14. This increase is a result of the improved mixture formation from the higher turbulence, which more than compensates for the shorter preparation time at the higher speed. This improvement partially explains the amount of NIMEP increase. The remaining improvement is due to the reduction in heat loss with increase of engine speed.

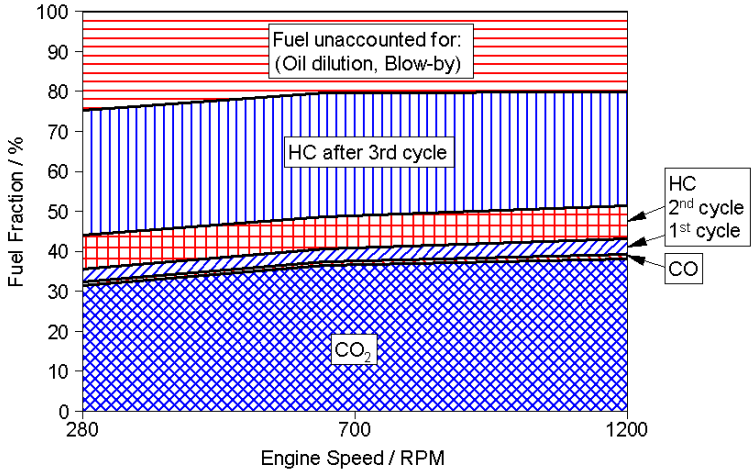

Fig. 14. Fuel pathway as a function of cranking speed

4. Conclusions

The first combustion cycle of a gasoline direct injection engine at cranking speed is characterized under cold start condition (air and coolant temperatures both at 20° C). Using a fuel carbon accounting analysis, this study quantifies the amount of fuel participating in combustion, the amount of HC emissions from the first combustion cycle, the residual fuel that goes into the mixture of the second combustion cycle, and the residual fuel that goes into the lubrication oil and crankcase.

A one-parameter-at-a-time approach is used to isolate the effects of the different parameters on the first cycle combustion and emissions behaviors. The parameters being studied are: fuel enrichment, injection timing, ignition timing, manifold absolute pressure (MAP), fuel injection pressure, and engine speed. The key findings are:

- When the injected fuel is increased from 1.7 to 3.5 times the amount required for forming a stoichiometric mixture with the ingested air, the overall λ decreases from 2.8 to 1. There is significant CO emission, indicating that the charge is non-uniform with fuel rich regions. The first cycle relative HC emissions (to the injected fuel), however, are not sensitive to the enrichment if there is no partial burn or misfire. The residual fuel contributes to 10 to 30% of the amount required to constitute a stoichiometric mixture for the second cycle.
- The injection timing determines the type and degree of interaction between the injection spray and the elements of the combustion chamber. For this particular engine configuration, injection during the early compression stroke results in lower relative HC emissions, due to reduced interaction with the intake valve and piston crown.
- Retarded spark timing provides a hotter charge in the expansion stroke and benefits post-flame oxidation. The results are reduced CO and HC emissions at the cost of lower work output.
- At lower MAP, less air is ingested, thus less fuel is needed to prepare a mixture of a given stoichiometric ratio. The fuel utilization (ratio of the burned fuel carbon to the injected fuel carbon) improves with reduced fuel. The relative HC emissions are not sensitive to MAP.

Because of the reduced fuel required at the lower MAP, the absolute HC emissions are reduced.

- Fuel utilization increases with injection pressure. The relative HC emissions, however, are not sensitive to injection pressure.
- Higher engine speed promotes turbulence. The improvement in turbulent mass transfer more than compensates for the reduction in mixture preparation time; hence fuel utilization improves with engine speed. The relative HC emissions increase modestly with higher engine speeds. At the same combustion phasing, NIMEP increases with engine speed because of the better fuel utilization and of the heat loss reduction. For a targeted NIMEP value, therefore, less fuel is needed at the higher engine speed, resulting in reduction of the absolute HC emissions.

Acknowledgements

The authors would like to acknowledge the support of this research by Borg-Warner, Chrysler, Ford Motor Company, and General Motors Company through a Consortium on Engine and Fuels Research.

References

Cheng, W. K., & Zhao, F. (2006). Transient Engine Startup and Shutdown Processes. In Technologies for Near-Zero-Emission Gasoline-Powered Vehicles (Vols. 1-Book, 1-Section, p. 1). SAE International.

Cowart, J. S. (2005). Post-Combustion In-Cylinder Vaporization During Cranking and Startup in a Port-Fuel–Injected Spark Ignition Engine. Journal of Engineering for Gas Turbines and Power, 128(2), 397–402.

Eiglmeier, C., Pfalzgraf, B., Helbig, J., Adam, S., Grigo, M., Dornhöfer, R., & Eiser, A. (2007). Der neue R4 – 2,0l TFSI SULEV/PZEV-Motor von Audi (Vol. 16. Aachener Kolloquium Fahrzeug- und Motorentechnik, p. 67).

Eng, J. A. (2005). The Effect of Spark Retard on Engine-out Hydrocarbon Emissions (SAE Technical Paper No. 2005-01-3867). Warrendale, PA: SAE International.

EPA & NHTSA. (2012). Final Rulemaking for 2017-2025 Light-Duty Vehicle Greenhouse Gas Emission Standards and Corporate Average Fuel Economy Standards (No. EPA-420-R-12-901).

Façanha, C., Blumber, K., & Miller, J. (2012). Global transportation energy and climate roadmap. International Council on Clean Transportation.

Fan, Q., & Li, L. (2012). Transient Characteristics of Cold Start Emissions from a Two-Stage Direct Injection Gasoline Engines Employing the Total Stoichiometric Ratio and Local Rich Mixture Start-up Strategy (SAE Technical Paper No. 2012-01-1068). Warrendale, PA: SAE International.

Hallgren, B. E. (2005). Impact of retarded spark timing on engine combustion, hydrocarbon emissions, and fast catalyst light-off (Thesis). Massachusetts Institute of Technology.

Hallgren, B. E., & Heywood, J. B. (2003). Effects of Substantial Spark Retard on SI Engine Combustion and Hydrocarbon Emissions (No. 2003-01-3237). Warrendale, PA: SAE International. Retrieved from http://digitallibrary.sae.org.libproxy.mit.edu/content/2003-01-3237

He, H., & Bandivadekar, A. (2013). Passenger car fuel-efficiency standards in China and the US: Stringency and technology, 2020–2025. International Council on Clean Transportation.

Heywood, J. B. (1988). Internal combustion engine fundamentals. New York: McGraw-Hill.

Ketterer, J. E., & Cheng, W. K. (2014). Gasoline Direct Injection Spark Ignition Engine Particulate Emission at Cold-Fast-Idle (SAE Technical Paper No. 2014-01-1368). Warrendale, PA: SAE International.

Knop, V., & Essayem, E. (2013). Comparison of PFI and DI Operation in a Downsized Gasoline Engine (SAE Technical Paper No. 2013-01-1103). Warrendale, PA: SAE International.

Kudo, H., Hirose, I., Kihara, T., Yamakawa, M., & Hitomi, M. (2011). MAZDA SKYACTIV-G 2.0L Gasoline Engine (Vol. 20th Aachener Kolloquium Fahrzeug- und Motorentechnik, p. 111).

Landenfeld, T., Kufferath, A., & Gerhardt, J. (2004). Gasoline Direct Injection - SULEV Emission Concept (SAE Technical Paper No. 2004-01-0041). Warrendale, PA: SAE International.

Lang, K. R., Cheng, W. K., Borland, M., Thomas, C., & Zhao, F. (2004). Effect of Intake Cam Phasing on First Cycle Fuel Delivery and HC Emissions in an SI Engine (SAE Technical Paper No. 2004-01-1852). Warrendale, PA: SAE International.

Silvis, W. M. (1997). An Algorithm for Calculating the Air/Fuel Ratio from Exhaust Emissions (SAE Technical Paper No. 970514). Warrendale, PA: SAE International.

Wiemer, S., Kubach, H., & Spicher, U. (2007). Investigations on the Start-Up Process of a DISI Engine (SAE Technical Paper No. 2007-01-4012). Warrendale, PA: SAE International.

Improved SCR Simulation and Control by Kinetic Modelling of the SCR Catalyst

M. Schönen[1], Y. Rosefort[1], I. C. Özyalcin[1] and V. Koll[2]

[1]FEV GmbH, D-52078 Aachen, Germany.

E-mail: schoenen@fev.com
Telephone: +(49) 241 5689 9852
Fax: +(49) 241 5689 507

[2]Institute for Combustion Engines
RWTH Aachen University, Germany

E-mail: koll_v@vka.rwth-aachen.de
Telephone: +(49) 241 5689 9824
Fax: +(49) 241 5689 507

Abstract. This paper presents a detailed view of the modelling of a kinetics-based approach for enhanced control of selective catalytic reduction (SCR) systems. The model uses the adsorption, desorption and oxidation of NH_3 on the catalyst surface as well as NO and NO_2-based SCR reactions for the simulation of the current NO_X reduction performance. It is demonstrated that the calibration process is very efficient due to the low number of parameters required for the kinetics-based model approach. Furthermore, data of engine bench measurements in transient cycles were obtained and compared against the simulation results of the kinetics-based real time model.

1. Introduction

The reduction of nitrogen oxides (NO_X) with selective catalytic reduction (SCR) has been established as a high performance technique in today's engine aftertreatment systems. However, there is still a lot of potential to increase controllability of urea dosing, especially for high efficiency SCR systems and improve the application process of this complex aftertreatment component. The need for further increase of control accuracy on NO_X reduction is additionally driven by upcoming legislative CO_2 limits, which would necessitate higher SCR conversion rates due to increased engine-out NO_X emissions.

Therefore, FEV has developed an enhanced SCR model, using physical and kinetic approaches. This model uses the adsorption, desorption and oxidation of NH_3 on the catalyst surface, as well as NO and NO_2 based SCR reactions for the simulation of the instantaneous NO_X reduction performance.

The SCR models are based on the well-known Arrhenius law. Furthermore, the limitations of the reaction, for example, by the diffusion processes are implemented as well. The modelling of NH_3 adsorption and desorption is performed by using the Langmuir adsorption isotherm.

One of the main development targets was to reduce the offline calibration effort with the help of this model-assisted approach. Due to the fact that the enhanced SCR model is kinetically based, it contains only a low number of calibration parameters. As a consequence only a very limited number of operating conditions have to be measured during the catalyst characterization on the test bench. Both, the calibration of NH_3 storage and SCR efficiency can be derived from SCR characterization at either the catalyst or engine bench.

For offline calibration purposes, the enhanced SCR model is integrated into FEV's exhaust aftertreatment toolbox FEV PROCal EAS.

2. Fundamentals

2.1 Reaction Kinetics

When investigating thermochemical processes, it is only possible to determine the final state based on the initial state. The specific reaction rate can be determined with reaction kinetics. The most important factor is the reaction rate. To define the reaction rate the mole densities have to be considered. In Eq. (1) the reactants A and B are used to form the products C and D.

$$A + B \overset{k}{\leftrightarrow} C + D \tag{1}$$

The rate of change of the mole density of A over time is proportional to the rate of change of the mole density of B over time as described in the Equation (2). /2/

$$r = -\left(\frac{dC_A}{dt}\right) = -\left(\frac{dC_B}{dt}\right) = kC_AC_B \tag{2}$$

The factor k is the velocity coefficient of the forward reaction and mainly dependent on the temperature. It describes the frequency of relative collisions of the reacting molecules and is for homogeneous reactions a function of the temperature. Besides the reaction rate, the activation energy E_a, which needs to be delivered by the reactants A and B, is another important factor. E_a is the minimum kinetic energy that is needed for the reaction. With empirical experiments, Arrhenius set up the Eq. (3) describing the relationship between activation energy, velocity coefficient, and temperature. Here A is a pre-exponential factor which characterises the number of collisions per unit time.

$$k(T) = Ae^{\left(-\frac{E_a}{RT}\right)} \tag{3}$$

The pre-exponential factor A is also dependent on the temperature but can be neglected for heterogeneous catalytic reactions.

In the Arrhenius diagram as shown in Fig. 2.1, the logarithm of k is plotted over 1/T, which brings a good approximation between the calculated and measured data.

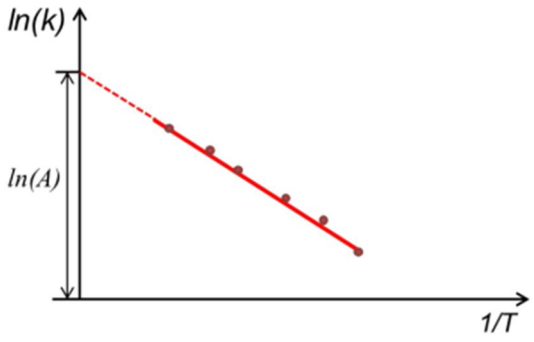

Fig. 2.1 Arrhenius diagram

The Arrhenius approach applies to the temperature range, where the reaction kinetics are the limiting factor. At high temperatures, the diffusion is slower than the kinetic reaction, which leads to a constant reaction rate in this temperature range. This is shown in Fig. 2.2.

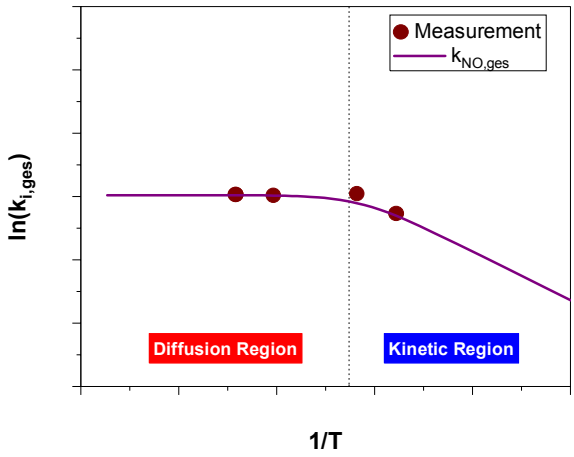

Fig. 2.2 Arrhenius diagram for diffusion and kinetic region

2.2 Reaction Mechanisms

Heterogeneous catalytic reactions can be described by the following three processes:

- Adsorption of the reactants on the surface
- Reaction on the surface
- Desorption of the products from the surface

Mostly adsorption and desorption are a lot faster than the catalytic reactions, which leads to a balance of adsorption and desorption.
For the adsorption a distinction must be made between two different types:

- Physisorption
- Chemisorption

Physisorption is highly reversible and does not change the adsorbed molecule which is held by van-der-Waals forces. In chemisorption, a chemical reaction takes place between the adsorbent and the molecule being adsorbed. Usually this reaction requires high temperatures and it is highly irreversible [4].
To describe the reaction rate, the adsorption depending on the gas pressure must be considered. The surface coverage θ, shown in Eq. (4), is dependent on the partial pressure of the free gas and its distribution as a function of the pressure at constant temperature is called adsorption isotherm.

$$\theta = \frac{number\ of\ taken\ adsorption\ spots}{number\ of\ available\ adsorption\ spots} \qquad (4)$$

A commonly used adsorption isotherm is the Langmuir-isotherm. Langmuir- isotherm approach it is assumed that the adsorption takes place on a mono layer and has no impact on the adsorption at nearby adsorption sites [1].
The conditions needed to describe the adsorption isotherm according to Langmuir are listed below [3]:

- Homogenous surface: the surface has a defined number of equal sites where the adsorption can take place
- No interaction between the adsorbed molecules
- The adsorption energy is independent from the surface coverage θ
- Mono layer of molecules: every site can only be taken once
- Dynamic balance: adsorption velocity and desorption velocity are equal

Eqs. (5) and (6) describe the rate of change over time for the adsorption and desorption.

$$r_{ads} = \frac{d\theta}{dt} = k_{ads} p_A N(1-\theta) \qquad (5)$$

$$r_{des} = \frac{d\theta}{dt} = -k_{des} N\theta \qquad (6)$$

The coefficients k_{ads} and k_{des} describe the velocity of adsorption and desorption and number of free places on the surface is expressed by the parameter N. At equilibrium ($r_{ads} = r_{des}$) the surface coverage does not change any more and the Langmuir isotherm can be defined as in Eq. (8).

$$\theta = \frac{Kp}{1 + Kp} \tag{7}$$

Where,

$$K = \frac{k_{ads}}{k_{des}} \tag{8}$$

The Langmuir isotherm is a good approximation for the calculation of catalyst storage capacity. There are different assumptions for the way kinetic reactions take place on the surface. One is the Eley-Rideal mechanism assuming that only the NH_3 molecules are adsorbed on the catalyst surface and then can react with NO_x. As a result, the reaction rate is also dependent on the surface coverage as shown in Eq. (9)

$$r_i = k_i \theta_{NH_3} p_{NO_x} = k_i \frac{K_{SCR} p_{NH_3} p_{NO_x}}{(1 + K_{SCR} p_{NH_3})} \tag{9}$$

where,

r_i: reaction rate of the reaction i [mole/m²s]
k_i: velocity coefficient of the reaction i [(m/mole)$^{n-1}$/s]
θ_{NH_3}: surface coverage of NH_3
p_{NO_x}: partial pressure of NO_x
K_{SCR}: equilibrium constant for adsorption and desorption of NH_3
p_{NH_3}: partial pressure of NH_3

With the three approaches, namely, Arrhenius, Langmuir and Eley-Ridal, the following SCR reactions were modelled with the following reaction rates listed in Table 2.1

Table 2.1. List of modeled reaction

Description	Reaction	Reaction Rate
NH_3 adsorption	$NH_3 + S \rightarrow NH_{3,s}$	$\dot{r}_{ads} = k_{ads} C_{NH_3} (1 - \theta_{NH_3})$
NH_3 desorption	$NH_{3,s} \rightarrow NH_3 + S$	$\dot{r}_{des} = k_{des} \theta_{NH_3}$
NO reaction	$4\ NH_{3,s} + 4\ NO + O_2 \rightarrow 4\ N_2 + 6\ H_2O$	$\dot{r}_{NO} = k_{NO} \theta_{NH_3} C_{NO}$
Fast reaction	$2\ NH_{3,s} + NO + NO_2 \rightarrow 2\ N_2 + 3\ H_2O$	$\dot{r}_{fast} = k_{fast} \theta_{NH_3} C_{NO} C_{NO_2}$
NO_2 reaction	$8\ NH_{3,s} + 6\ NO_2 \rightarrow 7\ N_2 + 12\ H_2O$	$\dot{r}_{NO_2} = k_{NO_2} \theta_{NH_3} C_{NO_2}$
NH_3 oxidation	$4\ NH_{3,s} + 3\ O_2 \rightarrow 2\ N_2 + 6\ H_2O$	$\dot{r}_{oxi} = k_{oxi} \theta_{NH_3} C_{O_2}$

For adsorption and desorption S is the component on the surface where the molecule can be adsorbed.

3. Model Setup

The kinetics-based model was developed in MATLAB/Simulink environment using state flow functions. The SCR brick is discretized into 10 catalyst slices of variable length using identical function of modelling. This enables a higher accuracy of simulation, especially during transient operation. Moreover, the multi-slice approach allows simulation of zone coated catalysts. Each catalyst slice includes a temperature model and NO_X conversion model. As shown in Fig. 3.1, the models are interdependent with respect to the parameters, heat flow q_{cat} and the catalyst temperature T_{cat}. The temperature model considers temperature losses to the environment by means of a heat flow and insulation function, as well as heat from exothermic chemical reactions inside the catalyst.

The principle functions of the NO_X conversion model implemented on each SCR slice is displayed in Fig. 3.2. The output parameters of each slice are used as input values for the slice located

downstream. Consequently, the 1st slice is fed with engine-out emissions and urea flow from the dosing system, while the result of the last slice indicates the tail pipe emissions in terms of NO_X and NH_3 slip. The conversion model functions are based on the adjusted equations explained in section 2.

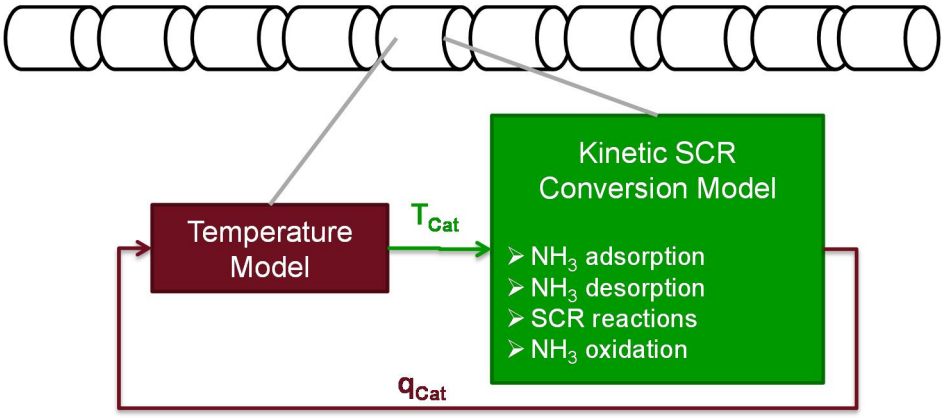

Fig. 3.1 Principle of the discrete multi-slice model

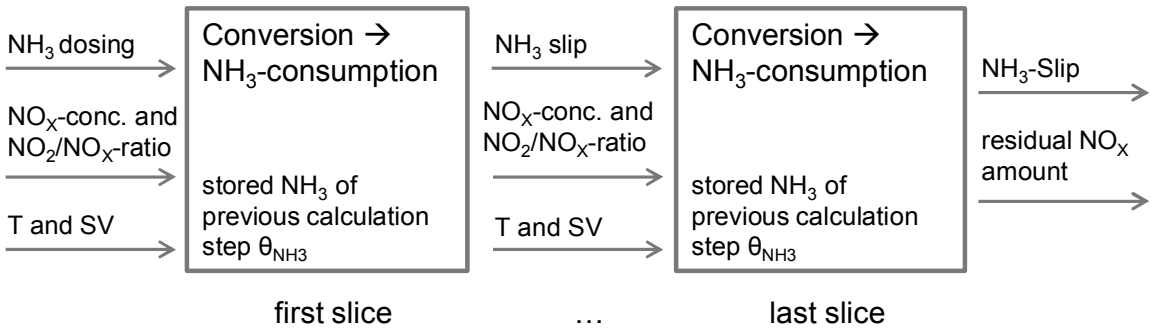

Fig. 3.2 Concept of the NO_X conversion slice model

For the model set up, the Langmuir isotherm was transformed to determine the NH_3 slip by assuming ideal gas conditions and by replacing the partial pressure with the NH_3 concentration. This is shown in Eq. (10), where the NH3 storage density ρ_{NH3} is defined with the maximum NH_3 storage density $\rho_{NH3,max}$, the equilibrium constant K_{adsdes} and the NH_3 concentration downstream catalyst

$$\rho_{NH_3} = \frac{K_{adsdes} C_{NH_3,Slip}}{1 + K_{adsdes} C_{NH_3,Slip}} \rho_{NH_3,max} \qquad (10)$$

The experiments showed that the maximum NH_3 storage density is not only dependent on the temperature but that it also slightly increases with higher NH_3 slip. This phenomenon is probably caused by NH_3 molecules taking sites also on other NH3 molecules or on other ceramic layers in the catalyst at very high partial pressures. This phenomenon was considered as described in Eq. (11).
An exponent for the NH_3 slip concentration can be considered but was neglected for the purpose of simplification which only caused small inaccuracies.

$$\rho_{NH_3,extra} = \Delta_{NH3} C_{NH_3,Slip} \qquad (11)$$

With this correction, Eq.(12) results, which was used for the simulation.

$$\rho_{NH_3} = \frac{K_{adsdes} C_{NH_3,Slip}}{1 + K_{adsdes} C_{NH_3,Slip}} \rho_{NH_3,max} + \Delta_{NH3} C_{NH_3,Slip} \qquad (12)$$

4. Results

The kinetic SCR model requires a total of 15 parameters and a characteristic curve. A summary of the parameters used in the model is given in Table 4.1. Three parameters and a characteristic curve are used for the NH_3 adsorption and desorption. To determine the behavior of a single chemical reaction, three parameters are sufficient. Therefore, three SCR reactions and the NH_3 oxidation require the remaining 12 parameters.

Table 4.1. Kinetic parameters varied during optimization of model calibration

Reaction	Parameter	Description
NH_3 adsorption and desorption	$E_{ads,des}$	Activation energy for adsorption and desorption
	$A_{ads,des}$	Pre-exponential factor for equilibrium constant $K_{ads,des}$
	rho_max	Characteristic curve for maximum storage capacity
	Δ_{NH3}	Correction factor for storage capacity
NH_3 oxidation	$\ln(A_{Oxi,kin})$	Y-axis intercept of kinetic Arrhenius diagram
	$E_{A,Oxi}/R$	Slope of kinetic Arrhenius diagram
	$\ln(A_{Oxi,dif})$	Logarithm of factor for diffusion region
NO reaction	$\ln(A_{NO,kin})$	Y-axis intercept of kinetic Arrhenius diagram
	$E_{A,NO}/R$	Slope of kinetic Arrhenius diagram
	$\ln(A_{NO,dif})$	Logarithm of factor for diffusion region
Fast reaction	$\ln(A_{fast,kin})$	Y-axis intercept of kinetic Arrhenius diagram
	$E_{A,fast}/R$	Slope of kinetic Arrhenius diagram
	$\ln(A_{fast,dif})$	Logarithm of factor for diffusion region
NO_2 reaction	$\ln(A_{NO2,kin})$	Y-axis intercept of kinetic Arrhenius diagram
	$E_{A,NO2}/R$	Slope of kinetic Arrhenius diagram
	$\ln(A_{NO2,dif})$	Logarithm of factor for diffusion region

4.2 NH_3 Adsorption and Desorption

For the validation of the modeling approach, and determination of kinetic parameters, storage curves from synthetic gas test bench are used. In order to obtain sufficient information about the storage capacity and storage behavior as a function of the temperature, at least 3 storage curves need to be measured. The adsorption and desorption parameter can be calibrated by the use of a NH_3 storage curve as shown in Fig. 4.1. The model prediction is sufficient for the adsorption and desorption model.

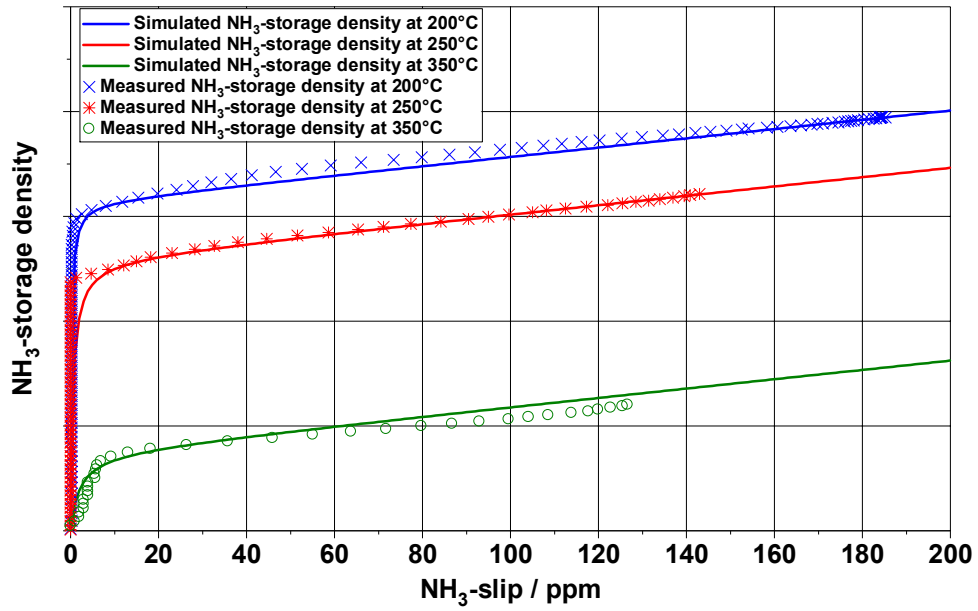

Fig. 4.1 Comparison of measured values with the calculation based on adopted Langmuir adsorption curve

With this measurement, the maximum storage capacity at a slip of 10 ppm can also be obtained as shown in Fig. 4.2.

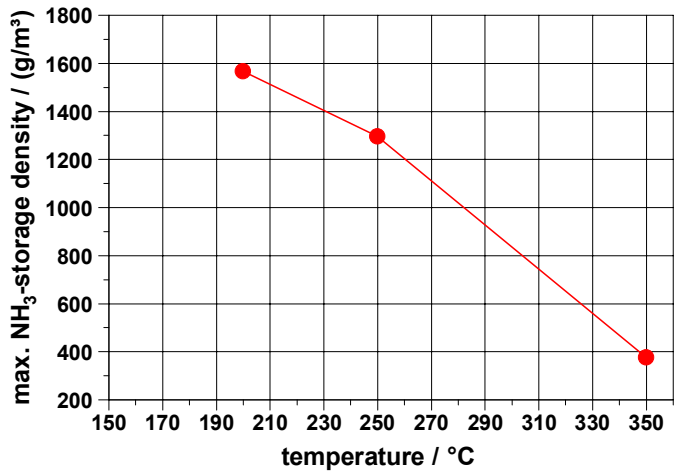

Fig. 4.2 Dependence of the maximum NH_3 storage capacity at 10 ppm NH_3 slip from temperature

With the measurement of the conversion efficiency at different NO_2/NO_X ratios, as well as temperatures, the other parameters for the NO reaction, the fast reaction, the NO_2 reaction as well as the NH_3 oxidation can be calibrated. The overall result of an NRTC (Non-Road Transient Cycle) test can be seen in the Fig. 4.3.

The overall accuracy of the model is quite good with regard to the NO_x accuracy as well as the NH_3 slip predication. Beside the good NO_X prediction especially the prediction of the NH_3 emissions is quite promising. This part of the simulation is very important for the integration of this model as an ECU function to describe NH_3 storage. With a good model, the NH_3 storage determination will be very exact and therefore low NO_X conversion efficiency as well as NH_3 breakthrough can be inhibited [5]. This is especially important for future emission concepts with increased engine-out emissions or future legislative NO_X limitations which require very low tailpipe emissions.

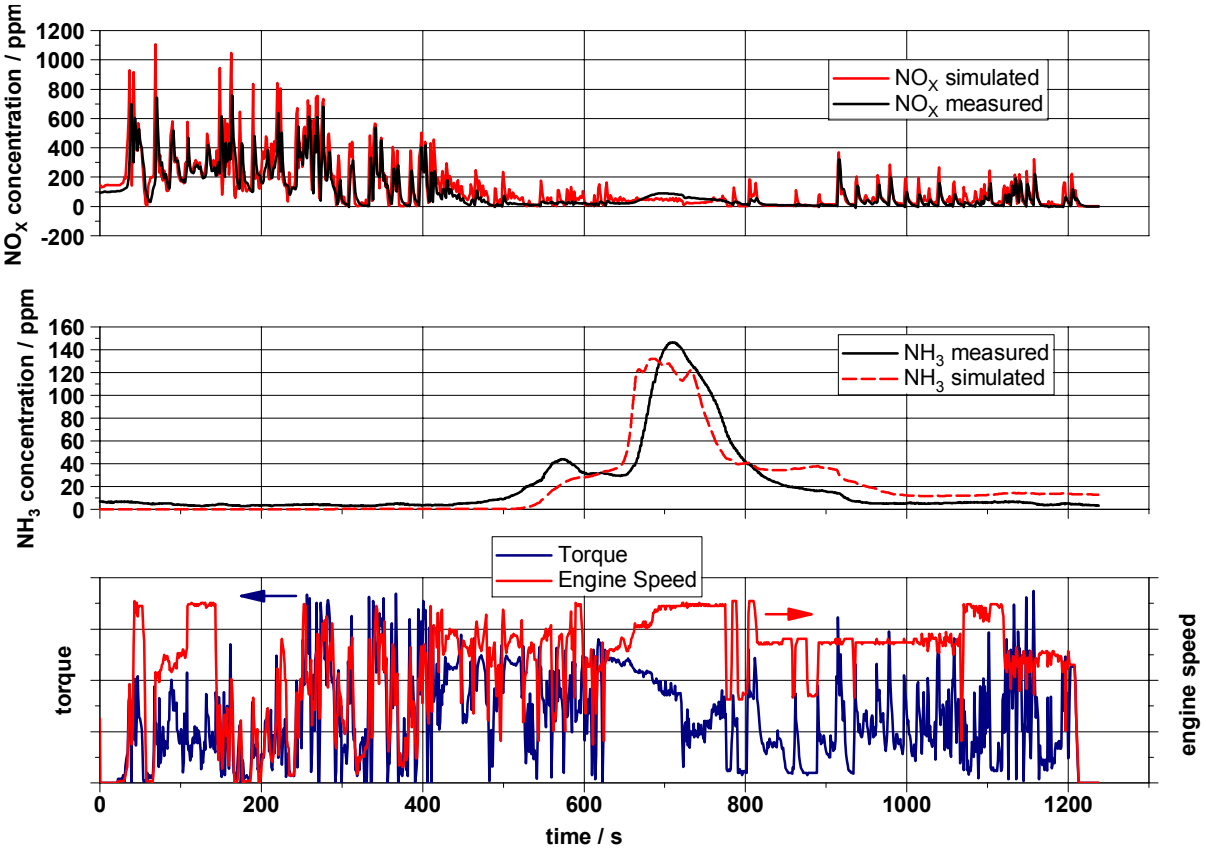

Fig. 4.3 Comparison of NH_3 and NO_X concentrations downstream of the SCR catalyst for the NRTC cycle

The accuracy of the NO_X emission can be analyzed more in detail by consideration of the cumulated emissions as shown in Fig. 4.4. The simulation results at the end of the cycle differ by about 5g from the measured values. Thus, the error in the tailpipe emissions is about 12%. In terms of NO_X conversion, the error is only about 4.5%.

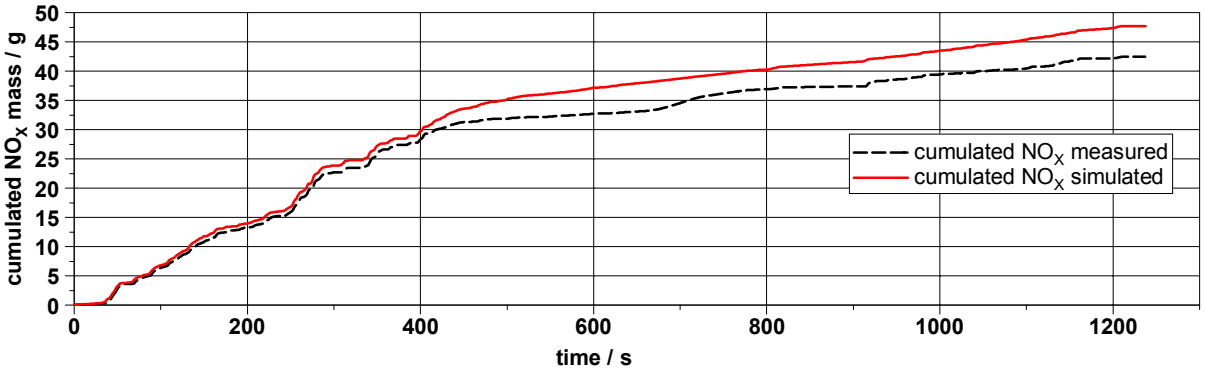

Fig. 4.4 Comparison of cumulative tailpipe NO_X emissions for the NRTC cycle

Summary and Outlook

In the developed kinetic SCR model, the SCR reactions are based on the Arrhenius equation and rate-limiting diffusion, while NH_3 adsorption and desorption are modeled with a modified Langmuir isotherm. For the NO and fast NO_2 reactions, the Eley-Ridal mechanism is assumed. The results show good correlation even in transient engine operation. The number of calibration parameters is very low compared to map-based approaches. The kinetic model offers fast characterization of SCR systems that could be used for simulation as well as for calibration purposes. The advantages of the model are

high accuracy and the small number of calibration parameters, which can be determined either at an engine test bench or at a synthetic gas gas bench.

To improve the model, functions for poisoning and ageing should be developed also on a kinetics basis. In addition, undesired reactions like N_2O formation should be considered, too.

Since efficient algorithms have been used during the implementation phase of the kinetic SCR model, the model provides full real-time capability for software integration into engine and aftertreatment control units software. In combination with a closed loop NH_3 storage or NH_3 slip control, this model could be used in the engine control to reach high efficiencies with low calibration effort. Consequently, current map-based SCR model approaches can be substituted in order to gain higher control accuracy of the SCR system during real engine operation.

References

Atkins PW (2002) Physikalische Chemie. 3. korrigierte Auflage [1]

Baerns M (1999) Chemische Reaktionstechnik. 3. durchgesehene Auflage [2]

Hagelüken C (2005) Autoabgaskatalysatoren. 2. aktualisierte und erweiterte Auflage [3]

Hagen J (1996) Technische Katalyse. VCH Mannheim [4]

Severin C, Wiartalla A, Körfer T and Holderbaum B (2008) Fuel penalty minimization of future exhaust aftertreatment systems due to tailored layout and intelligent control. 17. Aachen Colloquium Automobile and Engine Technology [5]

Impact of engine combustion on the reactivity of diesel soot from commercial vehicle engines

S. Lindner[1], A. Massner[1], U. Gaertner[1] and T. Koch[2]

[1]Daimler AG. Mercedesstr. 137, D-70327 Stuttgart, Germany.

E-mail: sven.s.lindner@daimler.com
Telephone: +(49) 711 17 20707

[2]IFKM – Institute of Reciprocating Machines. Karlsruhe Institute of Technology.
Rintheimer Querallee 2, D-76131 Karlsruhe, Germany.

E-mail: info@ifkm.kit.edu
Telephone: +(49) 721 608 42431
Fax: +(49) 721 608 48519

Abstract. The regeneration behaviour of diesel particulate filters is significantly influenced by the reactivity of the stored soot. However, there is still a lack of analyses which describe the effects that various engine operating parameters have on soot reactivity. A medium duty single-cylinder engine with common rail injection system was used to analyse the correlations between engine speed, load, combustion air fuel ratio and soot reactivity. Diesel particulate samples were directly collected from the exhaust stream. The temperature programmed oxidation (TPO) was used to reveal the reactivity to oxygen of the soot samples. Regeneration experiments were additionally carried out on a medium duty engine test bench to analyse the influence of soot reactivity on the regeneration efficiency in particulate filters.

The results give new insights into the relation between the diesel engine combustion process and soot reactivity.

1. Introduction

In the light of new legislative requirements and due to the environmental impact of pollutant emissions it has become necessary to introduce exhaust aftertreatment systems with particulate filters for diesel commercial vehicles to reduce particulate emissions. Firstly, the use of particulate filters has a detrimental effect on the fuel consumption of the engine due to the collected soot in the filter creating a higher backpressure. This soot has to be burned off in regular intervals at high temperatures of about 600 °C. Secondly, it is necessary to ensure a safe combustion of the soot without damaging the ceramic particulate filter in real driving conditions. The reactivity and composition of the filtered soot represents an important factor on the regeneration behaviour.

The in-cylinder soot formation is influenced by various parameters such as the engine speed, the fuel injection timing or the fuel mixture and its dispersion [8]. During the combustion process, depending on the operating point, the formed carbon black may be exposed to high temperatures and pressures up to 200 bars. As shown in Fig. 1, more than 95% of the soot is already oxidized in the cylinder [8].

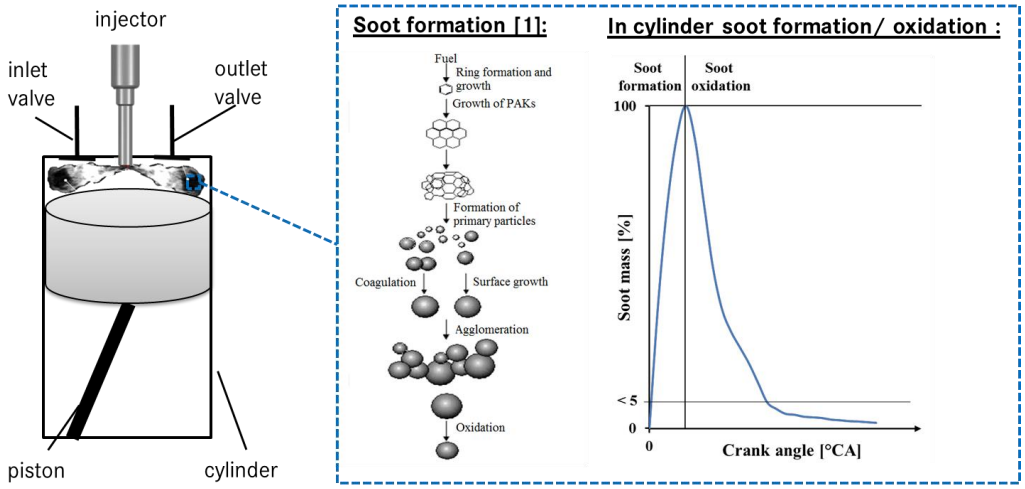

Fig. 1. Scheme of in-cylinder soot formation and oxidation

It is still under investigation how these processes influence the structure, composition and thus the reactivity of the final soot particles. Several studies have already addressed the influence of certain operating parameters. The study by Kuen Yehliu et al. [9] using a commercial vehicle diesel engine shows that more reactive soot is formed at increasing speed. However, it should be noted that the time of pre- and main injection and the air ratio in the different operating modes were not kept constant. In addition, the influence of the main injection timing was investigated. The results have shown that the later fuel is injected, the more reactive soot is formed. This is explained by a change in soot formation and subsequent oxidation. One reason could be that the soot formed is exposed to higher temperatures and builds graphitic structures, leading to a reduced reactivity. In the context of the FVV research project No. 954 “Reactive soot” [2] investigations were performed on a diesel engine which indicated, that in lean operation, reactive soot is generated under the condition of a retardation of the main injection as well as an early adjustment of the pre injection. In rich operation, a retardation of the main and post injection showed positive effects on soot reactivity. Zhu et al. [10] and Lee et al. [3] observed enhanced graphitising of soot particles with increasing load due to higher temperatures in the cylinder. However, it is not clear whether the variation of load, the air ratio and other operating parameters were kept constant.

To gain new insight of the relationship between the diesel engine combustion process and soot reactivity, variations of engine speed, load and the air fuel combustion ratio were carried out independently from other parameters on a medium duty single-cylinder engine. Soot samples were collected by using partial flow dilution systems. The reactivity of these samples was tested by method of temperature programmed oxidation (TPO).

2. Experimental

2.1 Soot sampling on a medium duty single-cylinder and heavy duty engine test bench

A 1,28 litre medium-duty single-cylinder engine with common rail system was used to analyse the correlations between engine combustion and soot reactivity. The common rail system allows independent variations of the injection pressure, timing and duration. In addition, it was possible to adjust the exhaust gas recirculation rate independently. The engine possessed a cylinder pressure indication in order to record the thermodynamic processes during combustion. Diesel fuel with 7% biodiesel in accordance with EN590 was used. The engine lube oil was free of those additives that accelerate soot combustion. Variations of the load, engine speed and combustion air fuel ratio were carried out in various operating points that are listed in Table 1. It shows the adjusted parameters and the operating parameters, which were kept constant for each variation. The engine speed was varied by increasing the injected fuel quantity and supplied air mass, the air ratio and rail pressure were kept constant. The engine load was also varied by increasing air and fuel mass at a constant ratio. The air ratio was changed by varying the air mass flow at a constant fuel amount.

Table 1. Operating points of the engine speed, load and air/fuel ratio variation

Adjusted Parameters	Engine Speed	Load	EGR	Start of Injection	Air/fuel ratio	Rail-pressure
[-]	[min^{-1}]	[Nm]	[%]	[°CA before TDC]	[-]	[bar]
Engine speed: 1800, 2000, 2200 min^{-1}	-	105	30,5	11,6	1,61	1860
Load: 55, 112, 167 Nm	1400	-	25	9,7	1,61	1380
Air/fuel ratio: 1,61; 1,40, 1,30; 1,20; 1,13	1400	112	27	9,7	-	1410

Furthermore, regeneration experiments on a 7,2 litre 6 cylinder medium duty engine were carried out to analyse the impact of soot reactivity on particulate filter regenerations. Particulate filters were loaded with soot from two different stationary points, Table 2, that differ in their reactivity. The first stationary point, SLP, is unchanged from series application while the second one, SLP accelerated, has got a higher egr rate and a lower combustion air fuel ratio. Soot samples were additionally taken for TPO-analysis during loading of the particulate filters. The engine peak power is at 223,7 kW. Same fuel according to EN 590 and oil without additives which accelerate soot combustion were used. The particulate filters were loaded in two different stationary points, Table 2.

Table 2. Stationary points for soot loading on the medium duty engine test bench

Stationary point	Engine speed/ Torque	Description
SLP	2200rpm/ 200Nm	Series application
SLP (accelerated)	2200rpm/ 200Nm	Higher egr, lower air/fuel ratio

The particulates were collected with a partial flow dilution system directly from the exhaust gas. The exhaust pipes were heated and insulated up to the filter holder at 180 °C. The soot samples were collected on metal fibre filters (basic material of Bekaert: Bekipor®, Fecralloy®, Material 1.4767, die-cut to 46,5mm und thermally treated at IWC TU Munich). During partial flow sampling the soot oxidation was frozen by cooling down to temperatures of about 50 °C so the unchanged carbon black of the raw emission could be collected.

2.2 Regeneration tests with a particulate filter

Regeneration experiments were carried out with two particulate filters, which were loaded with soot generated during the two stationary operating points mentioned in Table 2 with a target soot load of 4 g/l. After loading and weighing, the particulate filters were regenerated at a temperature of 550 °C for 20 minutes. Afterwards the regenerated particulate filters were reweighed and the regeneration efficiency was calculated as follows (1).

$$\frac{M_{Soot,before} - M_{Soot,after}}{M_{Soot,before}} \qquad (1)$$

2.3 Temperature programmed oxidation (TPO)

Based on the results of [6] temperature programmed oxidation (TPO) has been shown to be suitable for the determination of soot reactivity. Fig. 2 shows the procedure for the analysis of soot samples based on a schematic flow chart.

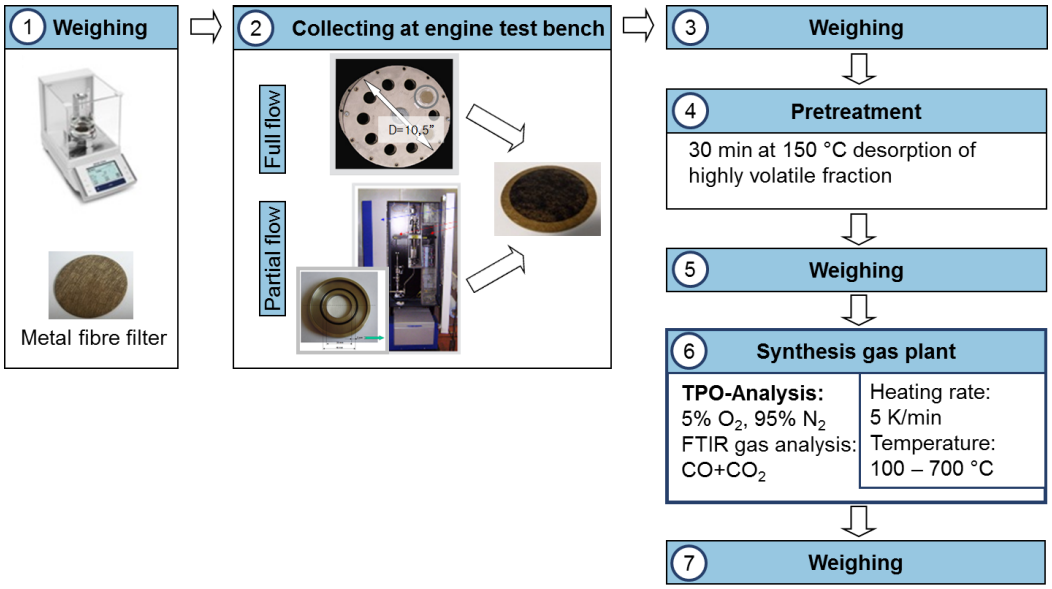

Fig. 2. Flow diagram of the TPO analysis [4]

After the determination of the initial weight of the metal fibre filters, the filters were loaded with soot, the target load being 3 to 6 mg. The mass is determined by differential weighing. The sample is heated up to 150 °C for 30 minutes in order to desorb the highly volatile components, and is then re-weighed. In the following temperature programmed oxidation, the sample is heated in a specific synthesis exhaust gas rig at the rate of 5 K/min between 100 and 700 °C and flowed through by a gas flow of 3 l/min consisting of 5% O_2 in N_2. Therefore the sample is inserted in a heated filter holder. A high resolution FTIR spectrometer is used for determination of the gaseous products of combustion CO and CO_2 [4]. The sample is taken down after cooling in a flow of compressed air to 100 °C. Subsequently the ash content is determined by weighing the sample again.

3. Results and discussions

3.1 Influence of engine speed

In order to investigate the impact of engine speed, soot samples generated at 1800, 2000 and 2200 min^{-1} were analyzed by temperature programmed oxidation. The TPO results are shown in Fig. 3. They demonstrate the normalized CO and CO_2 emissions during oxidation against temperature for the three different soot samples.

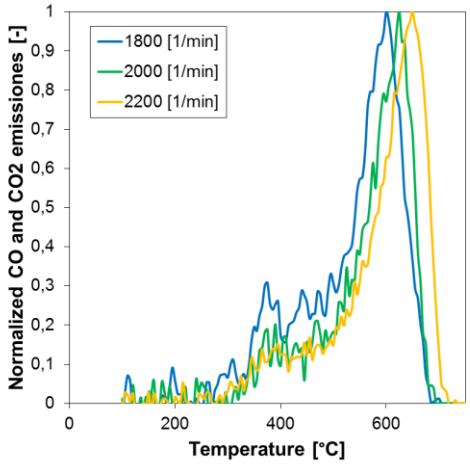

Fig. 3. TPO results of engine speed variation

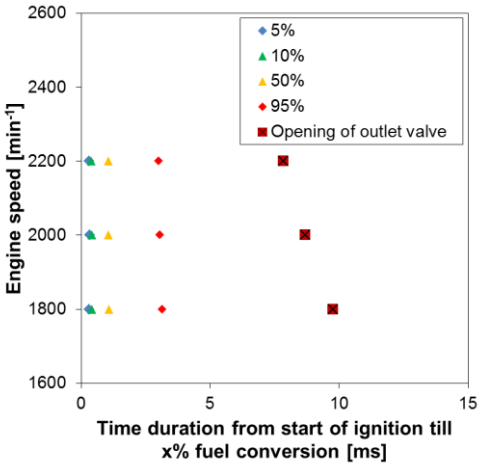

Fig. 4. Fuel conversion for different engine speeds

The oxidation curves show that soot sampled at the lowest engine speed of 1800 min^{-1} is oxidized at the lowest temperatures compared to the two soot samples generated at 2000 and 2200 min^{-1}. This is also shown by the temperature at the global maximum of the CO- and CO_2-emissions, which is a characteristic for the reactivity of a soot sample [4], [6]. While the soot collected at a speed of 1800 min^{-1} has got a temperature at global maximum of 600 °C, the one collected at 2000 min^{-1} has got 625 °C and at 2200 min^{-1} it is shifted one more 25 °C to 650 °C. The results also show that the combustion products in the temperature range of 300 to 450 °C increase with lower engine speeds. They indicate a higher amount of highly reactive surface groups that decompose in this temperature range. This contradicts the results of Yehliu [9], where the air ratio and the start of injection were not kept constant. Their results have shown a rising reactivity at higher engine speeds.

Fig. 4 shows the time durations between the start of ignition and fuel conversion of 5, 10, 50 and 95% and the opening of the exhaust valve for the three different engine speeds. This data was calculated by using the in-cylinder pressure curves. The results show that time that elapses between start of ignition and the fuel conversion up to 95% is nearly 3 ms for all three engine speeds. However, the time between 95% fuel conversion and the opening of the outlet valve becomes longer for lower engine speeds. While there are 4,8 ms at 2200 min^{-1} this duration increases by 16% for 2000 min^{-1} and by 36% for 1800 min^{-1}. In this part of the engine combustion process the soot formation is nearly completed and in-cylinder soot oxidation is predominant and the soot mass in the cylinder decreases as shown in Fig. 1. The present study indicates that in-cylinder soot oxidation does not only reduce the soot mass, it also affects its reactivity.

3.2 Influence of combustion air ratio

Different combustion air fuel ratios were adjusted by varying the supplied air flow and soot samples were collected in each stationary point. Fig. 5 shows the normalized oxidation curves against temperature during TPO analysis of these soot samples.

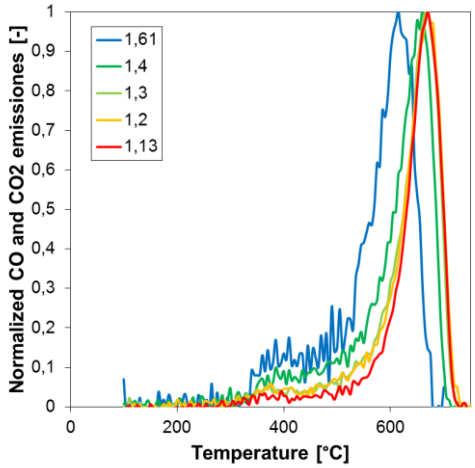

Fig. 5. TPO results of air/fuel ratio variation

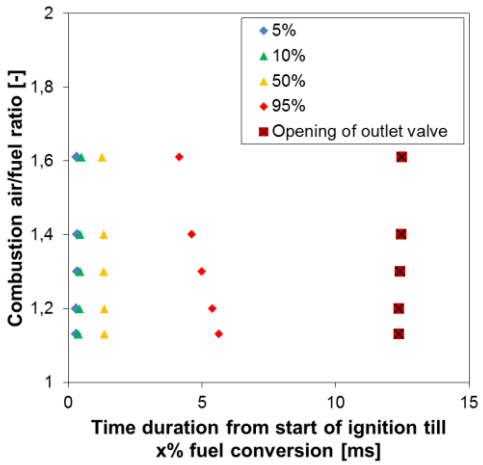

Fig. 6. Fuel conversion for different air/fuel ratios

The results show an increasing reactivity for soot formed at high combustion air ratios. The graph reveals that the higher the air fuel ratios the lower the temperature of the CO and CO_2 peak. The soot collected at the air fuel ratio of 1,61 shows the highest oxidation rates. The temperature at the global maximum is located at 615 °C. The increased reactivity of the carbon black is also noticeable in the temperature range of 300 to 450 °C due to significantly higher CO and CO_2 emissions. While the CO and CO_2 emissions of the soot at a global combustion air fuel ratio of 1,61 are at about 0,2, the ones from the soot generated at a ratio of 1,13 are lower than 0,05. The results indicate that not only the reactivity of the soot rises with increasing combustion air fuel ratio. Also the amount of highly reactive surface groups increases.

By varying the air fuel ratio, the soot formation and oxidation processes in the cylinder (Table 1) are affected, which in turn has got an impact on soot reactivity. According to [5] an increase in combustion air fuel ratio results in a reduced formation of soot. Fig. 6 shows the time durations between the start of ignition and fuel conversions of 5, 10, 50 and 95% for the different combustion air fuel ratios. The measurements show that the combustion is slowed down with decreasing air fuel ratios which can be noticed by means of the time between start of ignition and 95% fuel conversion. It can be de-

termined that there is more time for oxidation of the formed soot at higher combustion air ratios. Furthermore, the oxidation of the soot formed also accelerates due to higher oxygen concentrations in the combustion chamber.

As in the case of the engine speed variation, in-cylinder soot oxidation is proposed to be an important key factor for the reactivity of the emitted soot.

3.3 Influence of load

Different loads were adjusted by varying the supplied fuel and air flow at a constant air-fuel ratio. Soot samples were collected at a constant speed of 1400 min^{-1} and three different loads (25, 50 und 75 %). Fig. 7 shows the CO and CO_2 emissions of the collected soot samples plotted against temperature.

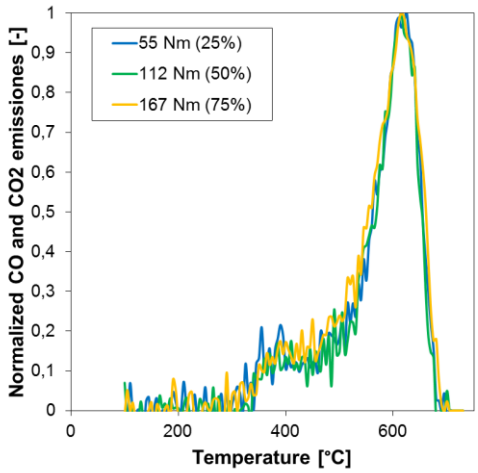

Fig. 7. TPO results of load variation

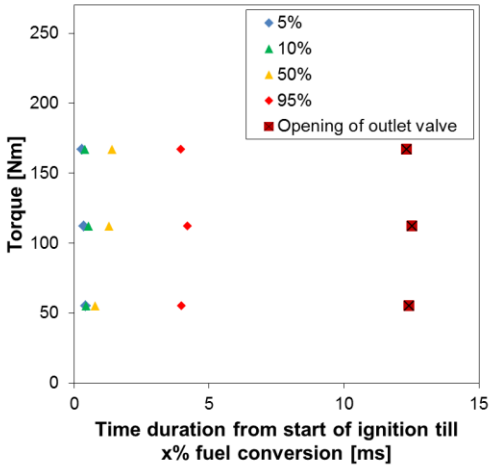

Fig. 8. Fuel conversion for different loads

The soot samples collected at 55, 112 and 167 Nm, which represent an engine load of 25, 50 and 75%, all show nearly identical oxidation rates. Not only the temperatures at the global maximum of oxidation products are at 615 °C for all three soot types, also the amount of highly reactive surface groups is comparable. The results show, that the load, so the amount of fuel-air mixture in the cylinder, has no impact on soot reactivity. Although the different stationary points show maximum pressures of 90 (at 25% load) to 200 bar (at 75% load) during combustion no effect on the reactivity is detected.

The calculated time durations from start of ignition up to 95% conversion in Fig. 8 show nearly identical values due to similar conversion curves for the three loads. This leads to a similar period of time for in-cylinder oxidation of the soot formed. The measurements indicate one more time that in-cylinder soot oxidation is one main influencing factor on soot reactivity.

4. Impact of soot reactivity on the regeneration behavior of particulate filters

In order to get an impression how the reactivity of soot influences particulate filter regenerations, two particulate filters were loaded with soot from two different stationary points (Table 2) and regenerated at 550 °C. Simultaneously, soot was collected on metal fiber filters and analyzed in the temperature programmed oxidation.

3.1 TPO analysis of the soot loading points

The results of the temperature programmed oxidation of the two soot loading points are shown in Fig. 9.

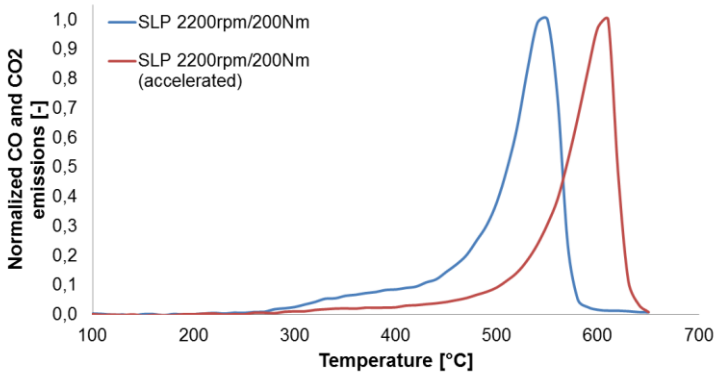

Fig. 9. TPO analysis of soot from SLP and SLP accelerated

Soot that was generated by the soot loading point SLP, according to series engine application (EPA 04 legislation) considerably begins to be oxidized at a temperature of about 450 °C. The temperature at the global maximum of CO and CO_2 emissions is already at 550 °C. Soot being collected from the accelerated soot loading point with a higher egr rate and a lower combustion air fuel ratio shows a much less reactive behavior. It begins to get oxidized at about 520 °C and shows a temperature at global maximum of emissions at 610 °C.

The following chapter shows the impact of these differences in soot reactivity on a particulate filter regeneration.

4.2 Particulate filter regeneration tests

The regenerations of the two loaded particulate filters were both carried out at a constant temperature of 550 °C for 20 minutes. The filters were reweighed after regeneration and the efficiency was calculated. Fig. 10 shows the calculated regeneration efficiency for both tests.

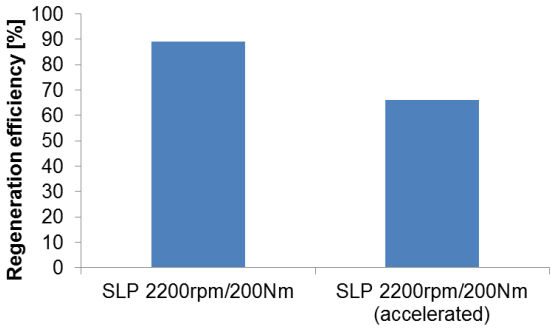

Fig. 10. Regeneration efficiency of SLP and SLP accelerated

Regeneration efficiency of the filter loaded with the higher reactive soot generated by the soot loading point SLP was quantified at 89 %. The more unreactive soot offered a 25 % lower regeneration efficiency at about 66 %.

These findings suggest that different soot reactivities found in temperature programmed oxidation with metal fibre filters correlate with the regeneration behavior on the test bench. In addition, the findings suggest that future engine design and calibration should take into account soot reactivity as a design parameter to optimize fuel consumption, regeneration safety and long term durability of the aftertreatment system.

5. Conclusion

The dependencies of engine speed, load and the combustion air fuel ratio on soot reactivity have been established on a medium duty single-cylinder test bench. The reactivity of the soot samples was analyzed by temperature programmed oxidation. The results have shown that the reactivity is significantly influenced by the global combustion air fuel ratio and engine speed. At high speeds less reactive soot is generated, since less time for in-cylinder soot oxidation is available. By lowering the combustion air fuel ratio, the fuel conversion is shifted to later crank angles, whereby there is less time and less oxygen available to oxidize the soot formed in the cylinder. An independent variation of the load has shown no effect on soot reactivity. This result was supported by the fact, that there was a constant period of time for soot oxidation in all variations. All results indicate that soot reactivity is significantly influenced by in-cylinder oxidation of the formed soot. The higher the time duration for in-cylinder soot oxidation the higher is the reactivity of the emitted soot. These initial results suggest that the structure and composition of the soot is mainly influenced by the late combustion phase. Further experiments should be performed in order to investigate this connection.

The regeneration tests in particulate filters have shown detrimental effects of soot re-activity on the efficiency of filter regenerations. The results confirm the need to operate particulate filter regenerations depending on the reactivity of the stored soot. This would lead to less fuel consumption during the regeneration and lower thermo mechanical stress of the diesel particulate filter. At the same time, catalyst aging is reduced.

Acknowledgements

The authors gratefully acknowledge the support of this work by Dr. Olaf Roehl of Daimler AG and Henrike Bladt and o. Univ.-Prof. Reinhard Niessner from the Institute of Hydrochemistry and Chemical Balneology, Department of Analytical Chemistry, of the Technical University of Munich.

References

[1] Bockhorn H (1994) Soot Formation during Combustion. Springer Verlag, Berlin.

[2] Fiebig M. (2010) Schönen M.; Grütering U.; Pischinger S. (2010) Einflüsse motorischer Betriebsparameter auf die Reaktivität von Dieselruss. MTZ 07-08/2010, pp 524-531.

[3] Lee K.; Cole R.; Sekar R.; Choi M.; Kang J.; Bae C.; Shin H. (2002) Morphological investigation of the microstructure, dimensions, and fractal geometry of diesel particulates. Proceedings of the Combustion Institute, vol 29, pp 647-653.

[4] Maßner A. (2011) Die Reaktivität von Dieselruß und die Auswirkungen auf den Betrieb von Abgasnachbehandlungssystemen. AVL Symposium Ludwigsburg.

[5] Oger B. (2012) Soot characterization in diesel engines using laser-induced incandescence. Brighton, University, Dissertation.

[6] Schmid J. (2012) Charakterisierung der Reaktivität und Struktur von Dieselruß mittels Temperatur-Programmierter-Oxidation und Raman-Mikroskopie.

[7] Schubiger R.; Boulouchos K.; Eberle M. (2002) Rußbildung und Oxidation bei der dieselmotorischen Verbrennung. MTZ 5/2002, pp 342-353.

[8] Wagner U.; Eckert P.; Spicher U. (2008) Possibilities of simultaneous in-cylinder reduction of soot and NOx emissions for diesel engines with direct injection. International Journal of Rotating Machinery.

[9] Yehliu K.; Armas O.; Vander Wal R.; Boehman A. (2013) Impact of engine operating modes and combustion phasing on the reactivity of diesel soot. Combustion and Flame, vol 160, pp 682-691.

[10] Zhu J.; Lee K.; Yozgatligil A.; Choi M. (2005) Effects of engine operating conditions on morphology, microstructure, and fractal geometry of light-duty diesel engine particulates. Proceedings of the Combustion Institute, vol 30, pp 2781-2789.

Individual optimization of effective compression and expansion ratios for thermal efficiency improvement using a single-cylinder diesel engine equipped with VVA system

A. Fukunaga[1], H. Osada[1], T. Okamoto[1], K. Shimada[1] and N. Uchida[1]

[1]New A.C.E Institute Co., Ltd. 2530 Karima, Tsukuba-shi, Ibaraki Pref. 305-0822, Japan.

E-mail: fukunaga@nace.jp osada@nace.jp t.okamoto@nace.jp shimada@nace.jp n_uchida@nace.jp
Telephone: +(81) 29 856 1801
Fax: +(81) 29 855 1800

Abstract. New technical path has been demanded to reduce both heat loss and mechanical loss with maintaining low exhaust emission characteristics for the improvement in thermal efficiency of current diesel engines. Heat loss reduction from the piston cavity wall by temporal and spatial spray flame control, partial insulation of the cavity, and etc. is one of the most promising measures for the improvement in thermal efficiency, however, it was experimentally found that most energy from heat loss reduction was not directly transformed into increase in brake work output, but rather into higher exhaust heat loss. For achieving further improvement in thermal efficiency without increasing exhaust heat loss, optimal expansion ratio has to be re-examined by taking variation of combustion and emission characteristics with compression ratio into account. From the point of view, individual optimization of effective compression and expansion ratios, like Miller cycle, was considered. The purpose of this study is to clarify the possibility of individual compression and expansion ratio control to improve the thermal efficiency using a supercharged single-cylinder heavy duty diesel engine with variable valve timings. In general, Otto cycle is more effective than limited-pressure cycle based on conventional diesel combustion, however the Otto-like cycle with diesel fuel, i.e. PCI combustion has a limitation in operating condition (the PCI combustion cannot be properly controlled at high load conditions.) So, a Miller-like limited-pressure cycle was employed as an idealized cycle. By an initial analysis of the idealized cycle, it was discovered that the effective expansion to compression ratio for achieving optimum thermal efficiency was expressed only with specific heat ratio, pressure ratio, and cut-off ratio. The latter two parameters are closely correlated with heat release rate diagram of conventional diesel combustion. Furthermore, optimal expansion ratio should be always higher than compression ratio. Tests were carried out at various combinations of effective compression ratio and expansion ratio by means of VVA system to confirm the effect of increasing effective compression ratio concurrent with effective expansion ratio which was relatively higher than compression ratio. In conclusion, it is confirmed that improvement in the gross-indicated thermal efficiency was certainly achieved by the increase in both effective compression ratio and expansion to compression ratio. These results proved the analysis of idealized cycle. The brake thermal efficiency was also improved using piston cavities having higher geometrical compression ratios than the baseline value of geometrical compression ratio (18.0:1), whereas, mechanical and pumping losses were much increased and suppressed further improvement in brake thermal efficiency. Nevertheless, combined with the measures to reduce heat loss from the wall (by means of high EGR rate), higher expansion ratio confirmed the potential to improve brake thermal efficiency by changing excess exhaust heat loss into the brake work.

Notation

Cv	*Specific heat at constant volume*	*kJ/kgK*
G	*Working gas mass*	*kg*
Ne	*Engine speed*	*rpm*
Pi	*Pressure at point i in ideal cycle*	*MPa*
Pb	*Intake boost pressure*	*kPa*
Pinj	*Fuel injection pressure*	*MPa*
Pmax	*Maximum in-cylinder pressure*	*MPa*
q	*Fuel quantity per stroke*	*mm3/st*
q1	*Total input energy for ideal cycle*	*KJ*

Ti	*Temperature at point i in ideal cycle*	*K*
Vi	*Volume at point i in ideal cycle*	*m3*
x	*Ratio of energy input during constant volume phase*	
α	$\varepsilon_{ex}/\varepsilon_c$	
α_{opt}	*Optimum α to maximize thermal efficiency*	
γ	*Specific heat ratio*	
ε	*Geometric compression ratio (of the piston)*	
ε_c	*Effective compression ratio*	
ε_{ex}	*Effective expansion ratio*	
η_{th}	*Theoretical thermal efficiency*	
λ	*Excess air ratio*	
ξ	*Cut-off ratio*	
ψ	*Pressure ratio*	

1. Introduction

In recent years, there have been notable political and social demands for lower fuel consumption powertrains in many of the world's major markets. Compared to spark ignited engines, diesel engines have a higher thermal efficiency in spite of more stringent exhaust emissions regulations in recent years. On the other hand, recent improvement in fuel consumption of diesel engines has not been significant, using only conventional measures. The SuperTruck program [3] represents a new approach for improving thermal efficiency by reducing energy losses and maximizing brake work, including novel technologies like waste heat recovery system. The LE55 engine [6] is another unique concept, which is the combination of faster combustion with higher peak cylinder pressure tolerance and exhaust energy recovery by a turbo-compound system. A previous paper by the present authors [4] described another approach for the improvement in brake thermal efficiency, which is wall heat loss reduction by a higher EGR rate combined with a multiple injection strategy. The data showed that both lower flame temperature due to higher EGR rate, and in-cylinder flame distribution control due to an optimized multiple injection strategy, were effective to reduce wall heat loss, thereby resulting in the brake thermal efficiency improvement. However, it was also confirmed that most energy from heat loss reduction was not transformed into brake work output, but rather into higher exhaust heat losses, as shown in Fig. 1.

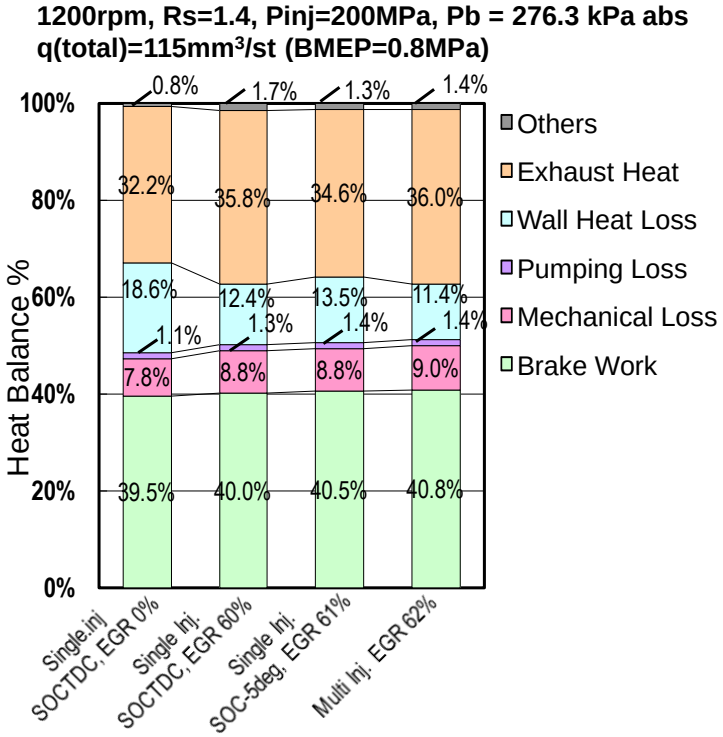

Fig. 1. The effect of EGR and injection strategy on heat balance diagrams (Data based on results from Ref. [4])

To transform excess exhaust heat loss into mechanical work, this study focused upon the higher expansion ratio. From the thermodynamic view point, an increase in compression ratio is also desirable to improve the theoretical thermal efficiency. On the other hand, higher boost pressures, higher BMEP, and higher EGR rates have already increased maximum cylinder pressures beyond the strength limit of current engines. To overcome this dilemma, a Miller-like limited-pressure (Sabathe) cycle could be effective. This study reveals the potential to maximize brake work of the current diesel engine by means of individual optimization of the compression and expansion ratios.

The equation of theoretical thermal efficiency for an ideal cycle having different compression and expansion ratios was firstly derived, and was then studied to find the optimum values for each ratio. Then, by utilizing three different pistons having different geometric compression ratios, namely 18.0 (baseline), 22.0 and 26.0, the potential of higher effective expansion ratio on the thermal efficiency under constant effective compression ratio was experimentally confirmed, with a single-cylinder heavy-duty diesel engine equipped with a variable valve actuation (VVA) system. Other issues were also discovered while applying a Miller-like limited-pressure cycle to the existing engine, and these will be discussed in this report as well.

2. Thermal efficiency of an idealized cycle

The theoretical cycle efficiency for a Miller-like limited-pressure cycle was derived. Figure 2 shows a pressure-volume diagram of the ideal cycle. The effective expansion ratio ε_{ex} is defined with the volume at top dead center (TDC) V_2 and the volume at end of expansion V_5, as shown in Equation 1. The effective compression ratio ε_c is defined by the volume at start of compression V_1 and the volume V_2 at TDC, as shown in Equation 2. Assuming both processes, from 1→2 and from 4→5 are isentropic, the theoretical thermal efficiency of this ideal cycle is derived as Equation 5 [5], which includes the parameters of a limited-pressure cycle, i.e. pressure ratio ψ (Equation 3) and cut-off ratio ξ (Equation 4)

$$\varepsilon_{ex} = \frac{V_5}{V_2} \tag{1}$$

$$\varepsilon_c = \frac{V_1}{V_2} \tag{2}$$

$$\psi = \frac{P_3}{P_2} \tag{3}$$

$$\xi = \frac{V_4}{V_3} \tag{4}$$

$$\eta_{th} = 1 - \frac{1}{{\varepsilon_c}^{\gamma-1}} \cdot \frac{\alpha(\alpha^{-\gamma}\psi\xi^{\gamma} - 1) + \gamma(\alpha - 1)}{(\psi - 1) + \gamma\psi(\xi - 1)} \tag{5}$$

where: $\alpha = \frac{\varepsilon_{ex}}{\varepsilon_c} = \frac{V_5}{V_1}$ is the ratio between the effective expansion ratio and the effective compression ratio.

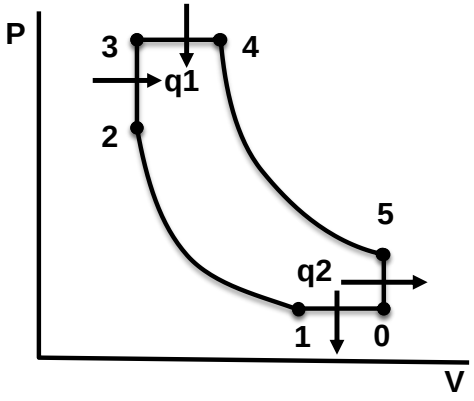

Fig. 2. Pressure-Volume diagram of ideal Miller-like limited-pressure cycle

To maximize the thermal efficiency of the ideal cycle, it would be necessary to extend the expansion stroke until P_5 reaches P_0, referred to as "complete expansion." At a completely expanded condition, the optimum effective expansion to effective compression ratio $\alpha := \alpha_{opt}$ is given by Equation 6.

$$\alpha_{opt} = \psi^{\frac{1}{\gamma}} \cdot \xi \geq 1 \qquad (6)$$

Equation 6 suggests that the optimum (maximum thermal efficiency) relationship between compression ratio and expansion ratio varies at each engine operating point. In other words, it varies with intake gas composition, temperature, and rate of heat release (ROHR.) Furthermore, it is noted that the effective expansion ratio should be always be higher than the effective compression ratio.

Quantitative analysis was next carried out using Equation 5 with realistic parameters. The left figure of Fig. 3 shows the effect of expansion to compression ratio α on the theoretical thermal efficiency, at various effective compression ratios, using a specific heat ratio γ = 1.35, pressure ratio ψ = 1.20, and cut-off ratio ξ = 1.10. As shown in the figure, the thermal efficiency increases with an increase in effective compression ratio, with an optimum expansion to compression ratio α_{opt} = 1.26. Reflecting Equation 6, the optimum remains at α= 1.26 regardless of the effective compression ratio. Another point of interest is the deterioration in thermal efficiency for $\alpha < 1$. Compared to the trend for $\alpha \geq 1$, the thermal efficiency drops sharply, especially at lower effective compression ratios.

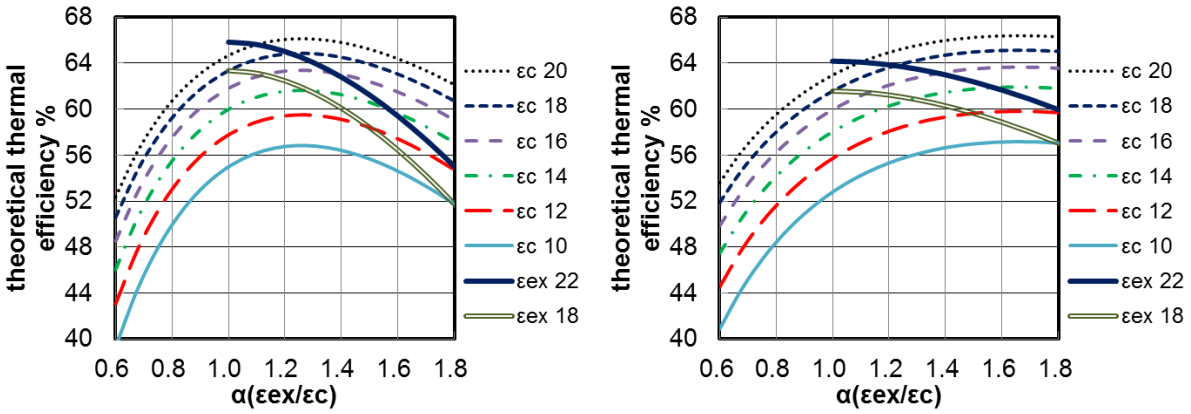

	Pressure Ratio ψ	Cut-off Ratio ξ	Specific Heat Ratio γ	α_{opt}
Left	1.20	1.10	1.35	1.26
Right	1.20	1.45	1.35	1.66

Fig. 3. Effect of α on theoretical thermal efficiency

A similar comparison is shown in the right figure of Fig. 3, for which the cut-off ratio ξ is 1.45 instead of 1.10. Other parameters were held the same. At higher ξ, which occurs when a diesel engine's load and/or speed increases, the optimum expansion to compression ratio α_{opt} shifts to a higher value. It is a given that the constant pressure combustion process will not be maintained when the combustion period of a typical diesel engine is extended. In conventional diesel combustion, however, the initial heat release spike (a form of constant volume combustion) will generally remain the same or decrease in intensity with increased engine load and/or speed. As a result, when combustion is complete the P-V diagram will consequently trace an expansion line equivalent to an ideal cycle line, but with a higher cut-off ratio ξ. The optimum expansion to compression ratio α_{opt} is proportional to ξ, as described in Equation 6, whereas it is less sensitive to variation in pressure ratio ψ due to the exponent, $1/\gamma$. For the practical approach to increase the expansion to compression ratio α by retarding IVC (at constant effective expansion ratio ε_{ex}), the thermal efficiency will decrease as α is increased, as shown by the two solid lines in Fig. 3. In addition, the reduction in trapped air in the cylinder is a major issue resulted in the deterioration of exhaust emissions.

3. Engine experiments

3.1 Experimental apparatus

To confirm the effect of extended expansion ratio on the thermal efficiency experimentally, a single cylinder direct-injection diesel engine was used in this study. Detailed specifications of the engine and fuel are shown in Table 1. This engine idealizes a turbocharged and after-cooled heavy-duty diesel engine. By using an externally driven supercharging device, high boost pressures are available (up to 500 kPa abs). The engine is also equipped with an electronically controlled high pressure common rail fuel injection system with a 300MPa of maximum injection pressure capability, a hydraulically driven camless VVA system, and a forged steel (Monotherm®) piston having both maximum in-cylinder pressure (Pmax) tolerance of 30 MPa and lower heat conductivity than aluminum pistons. The experimental system is shown schematically in Fig. 4. As shown, intake boost pressure, exhaust back pressure, and EGR rate can all be controlled independently. The intake manifold pressure and exhaust manifold pressure were made equal throughout the tests so that the external work done by the supercharging system is ignored [1], and the effect of actual turbocharger and EGR cooler efficiency with boost pressure and EGR rate are also excluded. Namely, the experiments were done under idealized supercharging conditions to investigate only the effect of combustion control on thermal efficiency.

Table 1. Engine and fuel specifications

Engine type	DI single cylinder OHV 4 valve
Displacement volume	2004 cc
Bore x Stroke	ϕ135 x 140 mm
Valve Actuation	Camless VVA (Sturman DHVVA)
Exhaust Valve Open (EVO)	0-81° BBDC @ 0.5 mm lift (ε =18.0) 0-84° BBDC @ 0.5 mm lift (ε =22.0) 0-82° BBDC @ 0.5 mm lift (ε =26.0)
Exhaust Valve Close (EVC)	1° ATDC @ 0.5 mm lift
Inlet Valve Open (IVO)	3° ATDC @ 0.5 mm lift
Inlet Valve Close (IVC)	0-85° ABDC @ 0.5 mm lift (ε =18.0) 0-96° ABDC @ 0.5 mm lift (ε =22.0) 0-86° ABDC @ 0.5 mm lift (ε =26.0)
Swirl ratio	1.4
Injector	Common rail system (Max. Pinj = 300 MPa)
Nozzle	Minisac ϕ0.181x9-150º
Piston type	Forged steel (Monotherm®)
Combustion Chamber Shape	Shallow Toroidal
Geometric Compression Ratio ε	18.0 (Baseline), 22.0, 26.0
Supercharging	External Supercharger
Fuel	Diesel fuel JIS #2 (typical specifications currently sold and consumed in Japan) • Cetane number: 57 • Sulfur: 5 ppm (mass based)

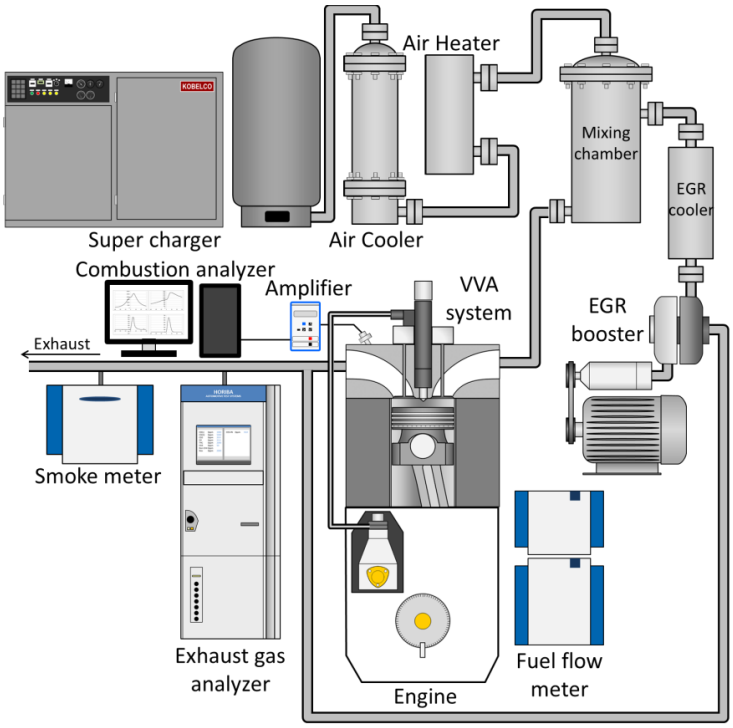

Fig. 4. Schematic of engine experimental system

3.2 Test conditions

To distinguish the effect of increased expansion ratio from variations in other combustion parameters and wall heat loss in the given limited-pressure cycle, these experiments were carried out at constant excess air ratio and fuel injection quantity. The boost pressure was then varied with IVC timing to maintain the targeted excess air ratio, since the actual cylinder volume is reduced under low effective compression ratios resulting from retarded IVC timings. Start of fuel injection was adjusted to set the start-of-combustion (SOC) at TDC. Table 2 summarizes the test conditions.

Table 2. Test conditions

Engine speed	1200 rpm
Fuel injection quantity	120 mm^3/st
Excess air ratio λ	2, 4
Approximate BMEP	0.8 MPa (40% load)
Fuel injection pressure	200 MPa
EGR ratio	0~53%
Intake O_2 concentration	20.9%~15.0 vol. %
Intake gas temperature	Controlled at 50 deg. Celsius
Boost pressure	Controlled to maintain excess air ratio
Start of combustion	TDC

4. Results and discussions

4.1 Effect of Increased ε_{ex} at Constant ε_c (ε = 18.0)

The effect of increased expansion ratio ε_{ex} on thermal efficiency (at constant effective compression ratio ε_c) was investigated with a piston having a geometric compression ratio ε = 18.0. The maximum effective expansion ratio ε_{ex} is always limited by the geometric compression ratio, so that the effective compression ratio ε_c always had to be reduced by delayed IVC in order to generate higher expansion

ratios. Figure 5 compares the effect of expansion to compression ratio α on gross-indicated thermal efficiency, gravity center (CG) of ROHR, and ratio of integrated apparent heat release to total fuel energy for various effective compression ratios. Tests were carried out at a constant 1200 rpm engine speed and 120 mm^3/st. fuel injection quantity, equivalent about 0.8MPa BMEP. ROHR CG is not equal to MFB50 (mass fraction burned 50%), but rather the geometric center of the ROHR diagram, which is closely correlated with the heat release rate pattern (spikes, decay, etc.) and degree of constant volume combustion at a constant SOC. As shown in Fig. 5, gross-indicated thermal efficiency was improved with an increase in expansion to compression ratio α at each ε_c. This result clearly supports the theoretical prediction described in Fig. 3. Furthermore, the observed gross-indicated thermal efficiency was higher with higher ε_c at constant effective expansion ratio ε_{ex}, which is also described in Fig. 3. Since the ROHR CG and ratio of integrated heat release to total fuel energy were nearly constant for each ε_c, except for the ROHR CG at ε_c=10 (where premixed combustion was dominant due to a longer ignition delay), the improvement in gross-indicated thermal efficiency could neither result from the reduction in heat loss nor the increase in the degree of constant volume combustion.

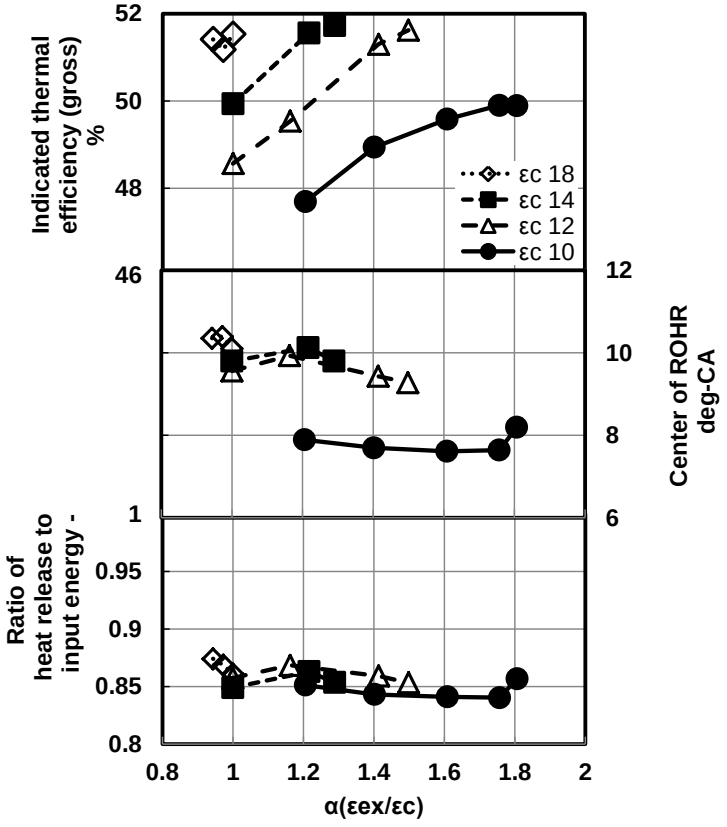

Fig. 5. Effect of α on gross-indicated thermal efficiency at constant ε_c (Ne =1200rpm, q =120mm^3/st, λ = 2, ε = 18.0)

Only for the case of ε_c=10, there was a slightly saturated trend on the gross indicated thermal efficiency with an increase in α. The theoretical meaning for the increased premixed combustion is the indicated thermal efficiency improvement with less deviation between the optimum expansion to compression ratio α_{opt} and the real expansion to compression ratio α by the increased pressure ratio ψ and decreased cut-off ratio ξ (as shown in Equation 6). In other words, the control of ROHR has a potential to improve the thermal efficiency by reducing the deviation between α and α_{opt}. The effect of changing pressure ratio ψ and cut-off ratio ξ were next investigated. Going back to the ideal cycle analysis, the combustion parameters are also described by [2]:

$$\psi = 1 + \frac{x \cdot q_1}{G \cdot C_v \cdot T_1 \cdot {\varepsilon_c}^{\gamma-1}} \tag{7}$$

$$\xi = 1 + \frac{1}{\gamma} \cdot \frac{(1-x) \cdot q_1}{G \cdot C_v \cdot T_1 \cdot {\varepsilon_c}^{\gamma-1} \cdot \psi} \tag{8}$$

As can be seen from Equations 7 and 8, an increase in the excess air ratio (equivalent to an increase in air mass G), reduces both pressure ratio and cut-off ratio by reducing the calorific value per unit working gas. In addition, the specific heat ratio γ will be increased by further dilution. Figure 6 shows the pressure-volume diagram at an excess air ratio of (a): 2 and (b): 4 for various α values. When α was at 1.8, the pressure-volume traces near BDC satisfied the state of complete expansion. These results show that the optimum expansion to compression ratio α_{opt} was reduced by a change in excess air ratio from 2 to 4.

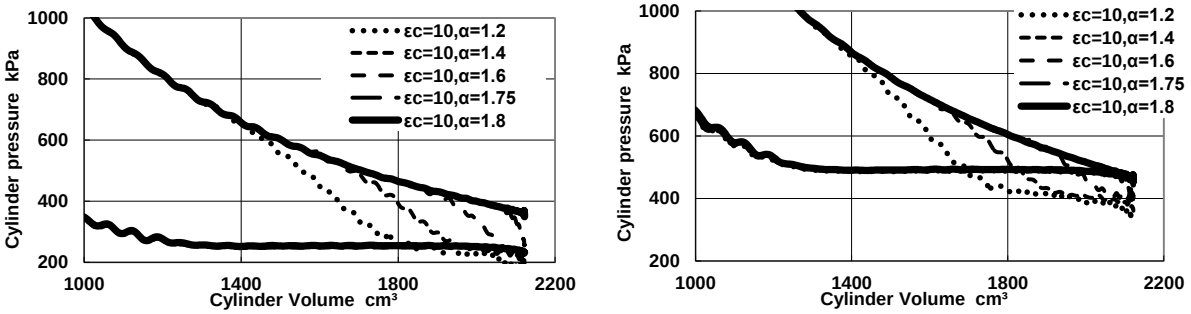

(a) $\lambda = 2$ (b) $\lambda = 4$

Fig. 6. Comparison of P-V diagram for various α at constant ε_c =10
(N_e =1200rpm, q =120mm^3/st, ε =18.0)

Figure 7 shows gross-indicated thermal efficiency, ROHR CG, and ratio of integrated apparent heat release to total fuel energy for various effective compression ratios under the same operating conditions as Fig. 5, except for the difference in excess air ratio. By comparing gross-indicated thermal efficiency between Fig. 7 and 5, an about 2% increase can be observed at higher excess air ratios. Furthermore, at a constant effective compression ratio ε_c=10, the thermal efficiency appears to reach a maximum at around α = 1.8, where the pressure-volume diagram fulfilled the complete expansion condition in Fig. 6 (b). This result also suggests that the thermal efficiency at a fixed ε_c = 10 would deteriorate for α above 1.8. Lean diluted (with high levels of working gas) combustion should be one of the effective and practical measures to improve the indicated thermal efficiency by reducing α_{opt}.

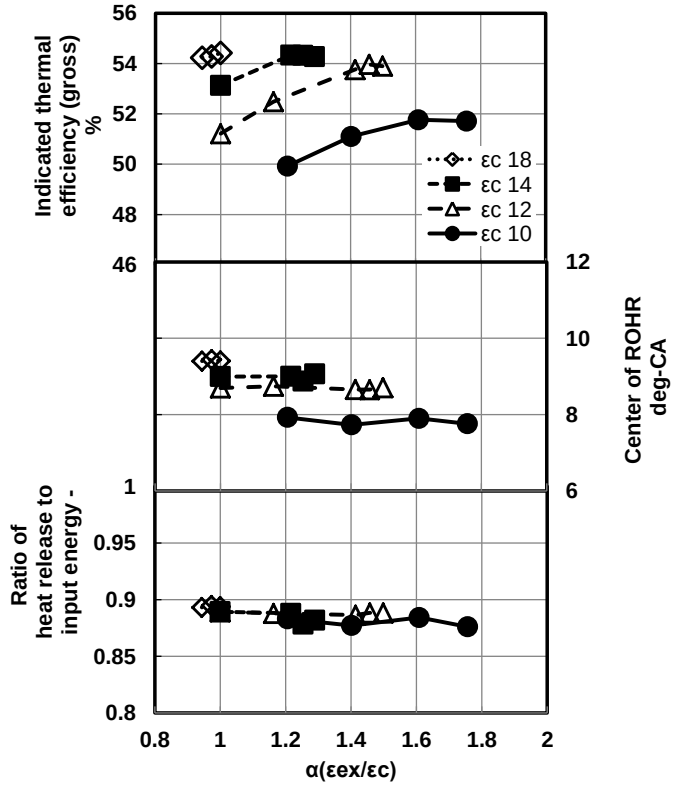

Fig. 7. Effect of α on gross-indicated thermal efficiency at constant ε_c
(Ne =1200rpm, q =120mm^3/st, λ = 4, ε = 18.0)

4.2 Effect of increased geometric compression ratio ε

To achieve both higher expansion to compression ratio α and higher effective compression ratio ε_c (compared to baseline) for better thermal efficiency, piston cavities with higher geometric compression ratio, ε = 22.0 and 26.0, were then experimented and compared with the result with the baseline piston. Another purpose of this test was to confirm the practical limit for the increased effective compression ratio under the condition of various expansion to compression ratio α.

Figure 8 compares the effect of expansion to compression ratio α on gross-indicated thermal efficiency, ROHR CG, and ratio of integrated apparent heat release to total fuel energy for various effective compression ratios, at 1200 rpm engine speed and 120 mm^3/st fuel quantity with geometric compression ratio ε = 22.0. These results show the same general trends as Fig. 5; namely, the gross-indicated thermal efficiency was improved at higher α for each ε_c, at constant combustion characteristics. On the other hand, the gross-indicated thermal efficiency with a geometric compression ratio of 22.0 did not show the distinct deterioration trend with decreased ε_c, nor the trend of improvement with increased ε_c. As shown in Fig. 3, the trend of higher thermal efficiency with increased ε_c and α is gradually saturated near the optimum expansion to compression ratio. There are still thermal efficiency advantages for higher ε_c (at the same α), however, there is less absolute difference between various effective compression ratios for the ε = 22.0 piston. This also helps explain why the gross-indicated thermal efficiency did not deteriorate with decreased ε_c.

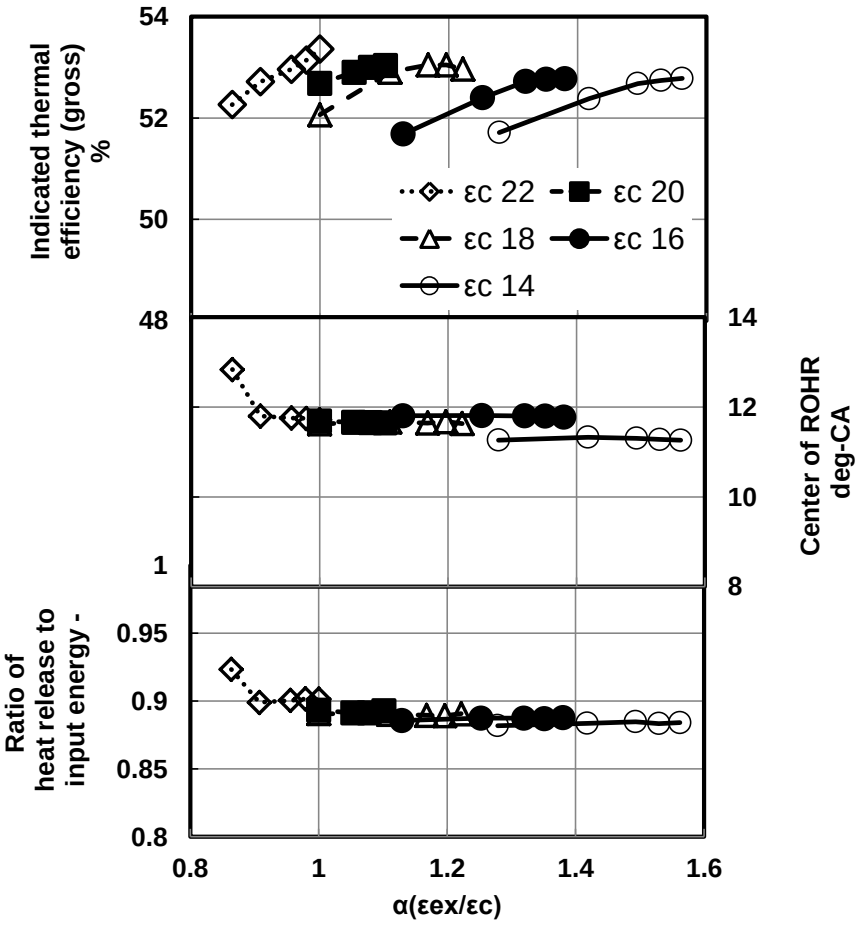

Fig. 8. Effect of α on gross-indicated thermal efficiency at constant ε_c (N_e = 1200rpm, q = 120mm^3/st, λ = 4, ε = 22.0)

Figure 9 combines the previous gross-indicated thermal efficiency results, and compares pumping loss, brake thermal efficiency, and friction loss for geometric compression ratios of 18.0, 22.0 and 26.0 at constant effective compression ratio ε_c=18. While the gross-indicated thermal efficiency still shows a significant overall-improvement with increase in α up to 59%, the brake thermal efficiency was obviously influenced by the increase in pumping and friction losses, resulting in suppression of improvements or rather in deterioration. But, even though the increase in brake thermal efficiency was less than that of the theoretical or gross-indicated thermal efficiency, the effect of increasing α with higher geometric compression ratio on the indicated thermal efficiency was experimentally confirmed.

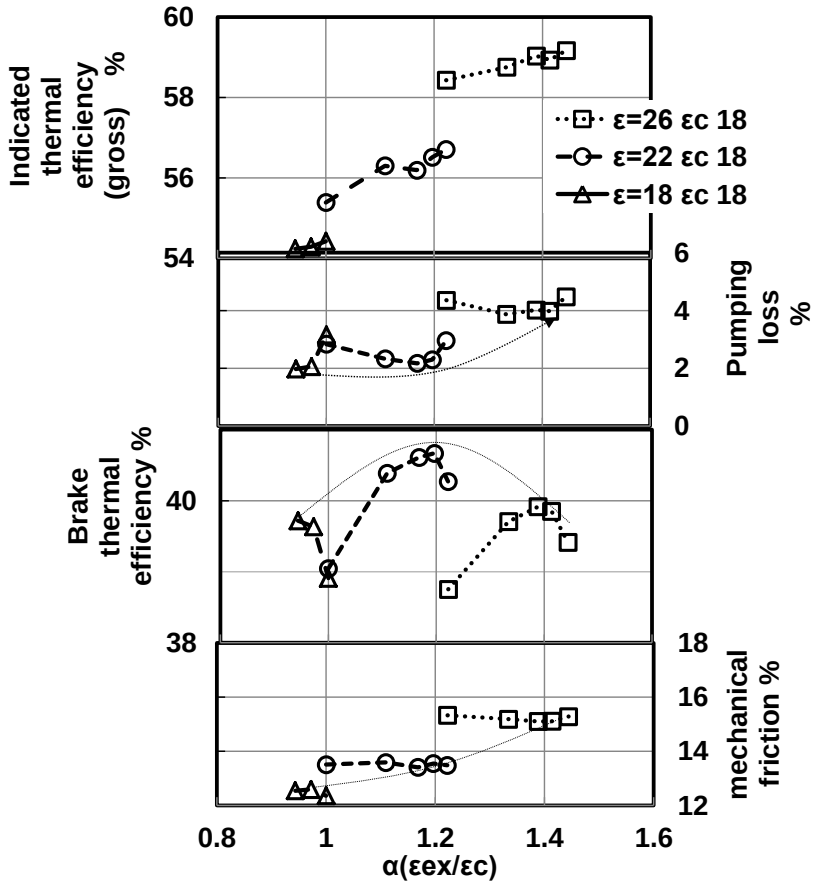

Fig. 9. Effect of α on gross-indicated thermal efficiency at constant ε_c =18 with various ε (N_e = 1200rpm, q = 120mm^3/st, λ = 4)

4.3 Combined effect of high EGR rate and increased expansion ratio ε_{ex}

As shown in the previous research results summarized as Fig. 1, both increased EGR rate and multiple injection strategy have a potential to reduce heat loss from the cylinder wall, while the most part of energy from wall heat loss was not changed into mechanical work, but into an increase in exhaust heat loss. Similar experimental results of this study are also found in Fig. 10, in comparison of first and fourth bar graphs from left or third and fifth bar graphs from left. Each pair had the same expansion to compression ratio α, whereas only oxygen content of intake air was different by increased EGR rate aiming the reduction of heat loss from the wall. Furthermore, Figure 10 also shows the much energy conversion from exhaust heat loss into mechanical work with an increase in effective expansion ratio ε_{ex}.

Since most current diesel engines have to be equipped with both turbocharger and aftertreatment catalyst, of which efficiencies are very sensitive to the quantity of exhaust energy, exhaust heat loss (upstream of turbocharger) can't be reduced from the current level to maintain engine performance and exhaust emissions. From this point of view, comparison between the first and fifth bar graph of the heat balance in Fig. 10 indicates the possibility to increase mechanical work by the heat loss reduction from the wall, without any change in exhaust heat loss (any drawbacks to the efficiencies of turbocharger and/or exhaust aftertreatment system.)

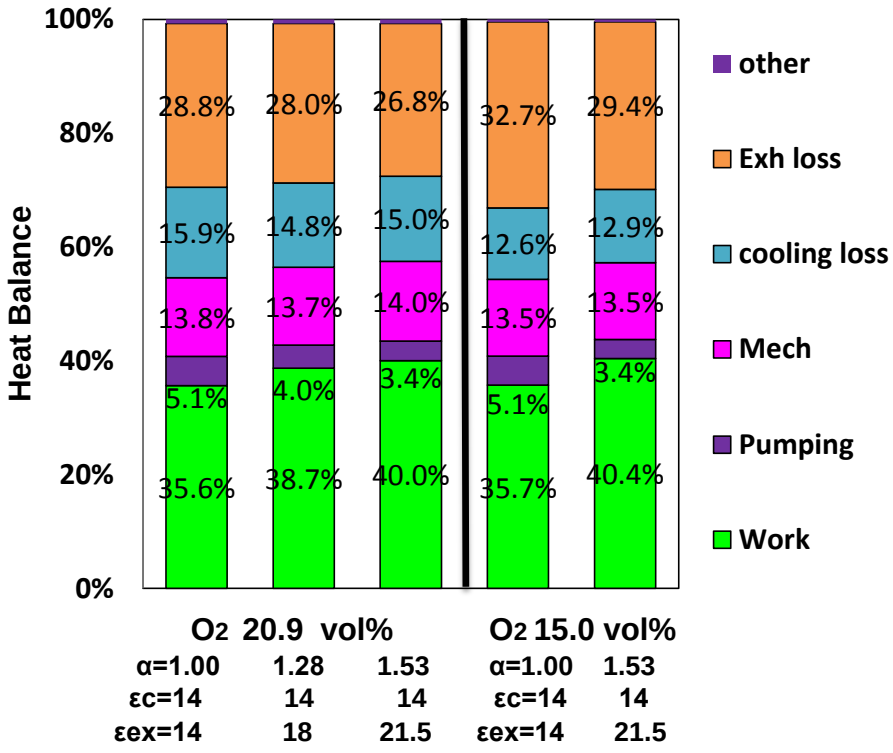

Fig. 10. Comparison of heat balance between different oxygen contents and different expansion ratio ε_{ex} at constant compression ratio ε_c =14 (N_e = 1200rpm, q = 120mm^3/st, *Pb* = 272kPa gage, ε = 22.0)

Conclusions

In this study, the possibility of individual compression and expansion ratio control for the improvement in the thermal efficiency was firstly theoretically examined, and then experimentally confirmed by means of a supercharged single-cylinder heavy duty diesel engine equipped with variable valve timing system.

- From the analysis of the theoretical thermal efficiency of the ideal Miller-like limited-pressure cycle, it was revealed that an increase in effective compression ratio ε_c and expansion to compression ratio α are essential for further improvement in the thermal efficiency, and optimum α is determined only the specific heat ratio γ, pressure ratio ψ, and cut-off ratio ξ.
- It was experimentally confirmed that the indicated thermal efficiency was improved by the increasing expansion ratio. Furthermore, the optimum α was possible to reduce by increased excess air ratio. Also, it was confirmed that the improvement in the indicated thermal efficiency was peaked out around complete expansion condition.
- Through the experiments with the geometric compression ratio up to ε = 26.0, the improvement in the gross-indicated thermal efficiency with an increase of both effective compression ratio ε_c and expansion to compression ratio α was still significant and was not saturated.
- For further improvement in the brake thermal efficiency, heat loss, mechanical loss and pumping loss should be simultaneously minimized, while keeping high indicated thermal efficiency.
- By combining the measures to reduce heat loss from the wall (e.g. increase in EGR rate) with appropriate pair of compression and expansion ratio, it is possible to increase mechanical work without any change in exhaust heat loss.

References

1. Aoyagi et al. (2005) Diesel Combustion and Emission using High Boost and High Injection Pressure in a Single Cylinder Engine. JSAE International Journal Series B 48 (4), pp 648-655
2. Challen, B. and Baranescu, R. (1999) Diesel Engine Reference Book Second Edition. Co-published SAE International and Butterworth-Heinemann, R-183, pp 5-26 (these equations were transformed from the original expression)
3. Energy Efficiency and Renewable Energy Vehicle Technologies Office (2013) FY 2012 Progress Report for Advanced Combustion Engine Research and Development. DOE-ACE-2012AR, IV-1-17,
   http://www1.eere.energy.gov/vehiclesandfuels/pdfs/program/2012_adv_combustion_engine.pdf
4. Osada, H. et al. (2013) Reexamination of Multiple Fuel Injections from the Thermal Efficiency Improvement Viewpoint in a Heavy-Duty Diesel Engine. SAE paper 2013-01-0909
5. Suzuki, T. and Watanabe, H. (1992) A Study on Miller System Applied C.I. Engine. Proceedings of JSAE Annual Congress (Autumn) No. 924-1(924009), pp 33-36 (written in Japanese)
6. Winsor, R. E. (1994) Detroit Diesel's LE55 Engine Concept. SAE Proceedings of the Annual Automotive Technology Development Contractor's Coordination Meeting, P-278, pp 375-381

Acoustic Characterization of Automotive Turbocompressors

A. J. Torregrosa[1], A. Broatch[1], R. Navarro[1] and J. García-Tíscar[1]

[1]CMT – Motores Térmicos. Universitat Politècnica de València. Camino de Vera s/n, E-46022 Valencia, Spain.

E-mail: abroatch@mot.upv.es
Telephone: +(34) 963 877 650
Fax: +(34) 963 877 659

Abstract. The performance of different experimental techniques proposed in the literature for acoustic characterization was assessed through the study of the noise generated by the compressor of an automotive turbocharger under different working conditions in an engine test cell. The most critical restrictions of in-duct intensimetry methods regarding frequency limitations are presented and experimentally demonstrated. The results provided by those methods were correlated against a reference intensity probe. A beamforming method based on three-sensor phased arrays appears to be the most reliable approach in the plane wave range, presenting higher accuracy than the more common two-microphone method and simple pressure level measurements. Also, preliminary results from a novel radiated noise quantification technique based on acoustic particle velocity are presented and discussed. The results indicate that further research on this topic is required.

1. Introduction

Turbomachinery-generated noise is nowadays one of the main concerns of automotive engineering, either aerial or terrestrial, as industry and society at large are today well aware of the many problems originated by acoustic pollution.

Once exclusive to jet aircraft and high performance engines, the use of turbomachinery is now widespread in internal combustion engines as a result of the current trend to downsize engines [17], since otherwise it would not be possible to maintain the same power output while reducing the displacement. In order to achieve this, the compressor must provide higher pressure ratios over a wide range of air mass flow, consequently operating in zones close to its surge limit [13] and farther from its maximum efficiency peak. At the same time it must provide the required mass flow without overspeeding.

As a result of this demanding requirements, even if the control system may assure the overall safety of the system, the noise generated by the turbocharger is becoming a noticeable issue that also needs to be controlled [14], either actively or passively. In fact, engine noise not only has negative effects on the environment in terms of acoustic pollution, but can also cause discomfort to vehicle passengers, as the engine noise quality is affected [3,19].

For this reason, the acoustical characterization of the compressor across critical or demanding operation zones or even across its entire operation map becomes increasingly necessary, and several studies on compressor noise characterization, analysis and mitigation can be found in the recent literature [11,22,23].

In this paper, various procedures that enable the synthesis of this acoustic information in the form of sound maps that cover a selected zone of the compressor map for relevant frequency ranges are assessed. Such representations provide a simple and clear visualization of noise phenomena for the possible operation points of the turbocharger in that zone.

An important consideration is that robust methodologies are needed to perform this acoustic characterization in the environment of production engine test cells, which are usually neither anechoic nor designed for acoustic measurements.

2. Experimental characterization

In order to obtain a noise map that characterizes noise generation by the compressor it is necessary to know the sound spectrum at several operating points and then extract the level of the different frequency bands of interest.

Reviewing the available literature on noise characterization of rotating machines, two different approaches are found. One of them is based on measuring radiated noise by means of exterior microphones inside an anechoic environment as done, for instance, by Čudina [7]. In engine conditions, however, it is difficult to separate the radiation of the compressor from the engine noise.

The other approach focuses on in-duct noise [24], using fast pressure sensors mounted flush inside the duct, in order to better identify the different internal flow phenomena involved in the generation of compressor noise. As this last approach can be more reliably applied to a non-anechoic engine test, this investigation is focused on it.

2.1. In-duct noise measurements

Some authors [12] rely on a single sensor to estimate the in-duct signal spectrum, whereas others use more sophisticated approaches introducing more sensors [24]. While the one-sensor method allows the calculation of sound pressure level (SPL), a scalar magnitude which only gives information of the sum of all waves at a particular point, sound wave decomposition enables the computation of the sound intensity level (SIL), a vector magnitude which offers information on the sound coming from a particular direction.

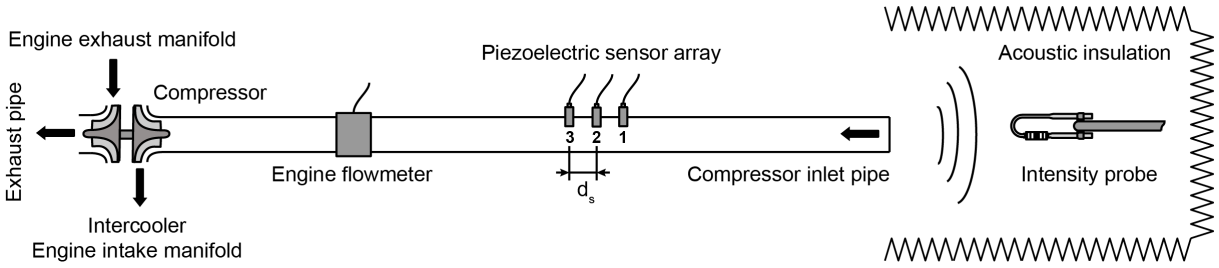

Fig. 1. Experimental setup for the acoustic measurements

The basis of decomposition methods is to consider that the pressure signal p measured at a given point of a duct is the linear superposition of a pressure wave traveling forward in the flow direction, p^+, and another pressure wave traveling backwards, p^-.

According to Morfey [18], the total intensity can be regarded as the sum of the upstream and downstream pressure spectra ($\hat{p}^+$ and $\hat{p}^-$) corrected with the mean Mach number (M_0) and characteristic acoustic impedance ($\rho_0 a_0$):

$$I = I^+ - I^- = \frac{1}{\rho_0 a_0}\left(|\hat{p}^+|^2(1+M_0^2) - |\hat{p}^-|^2(1-M_0^2)\right) \qquad (1)$$

In order to use this expression, it is thus necessary to select a measurement system that allows for wave decomposition. One of the standards is the *two-microphone method* used for example by Holland and Davies [15] and Tiikoja et al. [24], which uses the correlated spectra measured by two consecutive wall-flush mounted microphones to estimate the reflection coefficient and thus resolve both waves.

However, the two-microphone method is not free of drawbacks. The most important are the negative influence of interfering signals, which is not considered with only two microphones [5], viscothermal wave attenuation effects [1] and incoherence of the forward and backward signals, the last two being common in waves propagating in flows [9,15].

Some of these problems can be addressed using another method denominated *beamforming*, based in phased sensor arrays, which has been successfully used for the study of acoustic and pressure fields in ducts with flow [2,8,25].

The beamforming method can be applied to arrays of two or more microphones, weighting the signal of each one to “steer” the sensitivity of the array in the direction of interest (in this case, up-

stream and downstream of the pipe). A Linearly Constrained Minimum Covariance algorithm was applied in this case to find such weights (see [20] for details).

The experimental setup includes thus an array of piezoelectric pressure sensors flush-mounted in an extension of the compressor inlet pipe, so that the beamforming method, the two-microphone method, and the sound pressure level (SPL) of a single sensor could be tested.

A commercial intensity probe (B&K Type 4197) consisting of two phase-matched ½" microphones was also installed at the inlet mouth as a reference, surrounded by acoustic insulation mats in order to avoid reflections from the walls or other components. Fig. 1 shows this experimental setup.

Before applying the selected methods to the whole chart of the compressor, it is necessary to evaluate the restrictions that they impose in the frequency domain. While the SPL is only limited by the frequency response of the particular sensor, the decomposition algorithms of both the two-microphone method and the beamforming method present some common additional restrictions.

The first one is that both methods are formulated considering plane wave propagation, and are thus theoretically restricted to the frequency range below the onset of higher order modes. According to Eriksson [10], the cut-off frequencies for the first asymmetric and first radial modes can be approximated by

$$f_{asym} = 1.84\frac{a_0}{\pi D}\sqrt{1-M_0^2} \quad ; \quad f_{radial} = 3.83\frac{a_0}{\pi D}\sqrt{1-M_0^2} \qquad (2)$$

being D the pipe diameter. Also, around 10 diameters of straight pipe should be included at both sides of the array, and the nodes of the standing waves corresponding to 1/3 and 1/5 of the pipe length must be avoided.

Another restriction is related to the spatial resolution of the consecutive sensors [21], which imposes a cut-off frequency similar in concept to a Nyquist limit for spatial (rather than temporal) sampling, based on the separation (d_s) of the sensors. Above this frequency limit, erroneous spatial aliasing effects will be introduced. A simple approximation for this criterion is:

$$f_{alias} = \frac{a_0}{2d_s} \qquad (3)$$

In the low frequency range, it is necessary to consider that at sufficiently large wavelengths, the signal differences between consecutive sensors decrease below their sensitivity limit, invalidating the results. With the separator used between the microphones of the intensity probe this limit is at 250 Hz.

Fig. 2 shows the in-duct sound spectra computed with the three proposed methods: SPL with one sensor, two-microphone approach, and beamforming with three probes. The spectra measured at the orifice by the reference probe is superimposed in black. In this region, the beamforming method appears to follow the reference more closely.

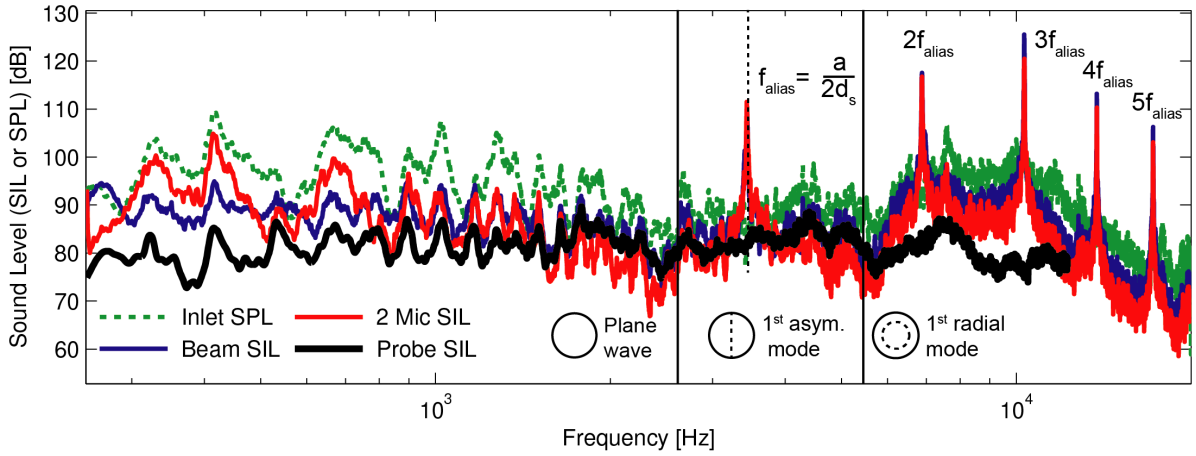

Fig. 2. Inlet in-duct sound spectra estimated by the three considered methods (SPL, beamforming and two-microphone) and orifice sound intensity spectrum as measured by the B&K intensity probe

It is also shown how spurious aliasing peaks occur at the frequency predicted by Eq. (3) when more than one sensor is used and how the onset of the 1st radial mode predicted by Eq. (2) marks a clear difference between the in-duct sound field and the sound field radiated by the inlet orifice.

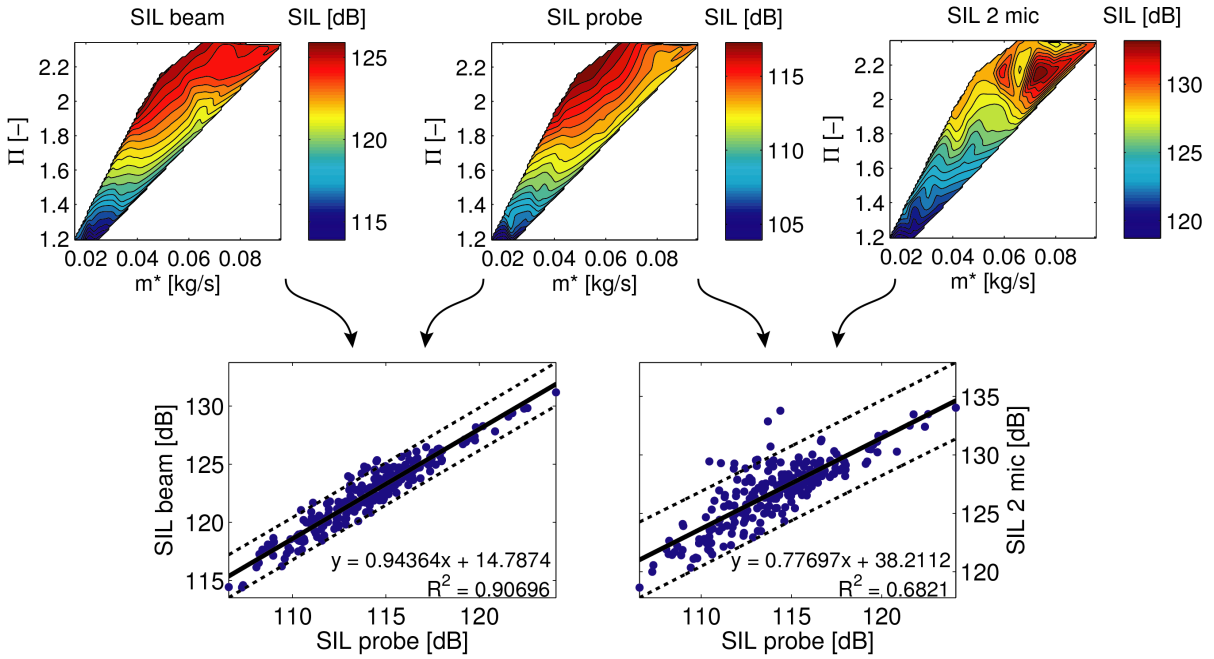

Fig. 3. In duct SIL maps of the compressor noise estimated by the beamforming method (top left), two-microphone method (top right) and SIL map of orifice noise as measured by the probe (top center), including correlations between the three measurements (bottom)

The results of applying Eq. (1) to compute SIL in the plane wave region of the spectra at different operating conditions of the compressor are shown in Fig. 3. Absolute levels at each working point were interpolated in order to get a continuous map. The beamforming and the two-microphone methods were used for in-duct SIL estimation and the intensity probe for measuring the reference orifice SIL. Correlations of these measurements are also provided, showing that in the plane wave range the beamforming method appears to perform up to 30% better in terms of R^2.

Fig. 4 shows a comparison between the SPL computed by selecting only one sensor of the array and the reference SIL of the probe. The correlation of these two measurements is better in terms of R^2 than the two-microphone method but still worse than the beamforming method.

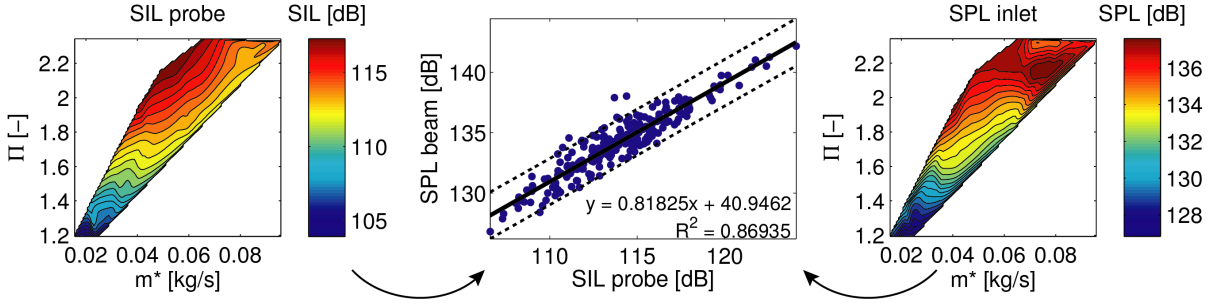

Fig. 4. Comparison of compressor sound maps (plane wave region) obtained through interpolation of SPL at the inlet 1st sensor and SIL at the probe, including a correlation between both

However, it should be noted that simple sound pressure level measurements can be influenced by the complex geometry of actual production pipes, which are remarkably more complex than the straight pipe used in this study. Also, it can be seen in Fig. 4 that, while at low pressure the sound maps are quite similar, SPL of one probe predicts a high sound level at high pressure ratio and high mass flow conditions, which is not the case for the intensity probe.

These high sound level points at high pressure ratio can be clearly seen as points lying outside the 95% observation confidence bounds of the correlation in Fig. 4. A similar problem can be seen in the correlation of the two-microphone method in Fig. 3, in which some outliers appear to distort the map at some operation zones. The beamforming method, however, appears to be more robust.

2.2. Radiated noise measurement

Besides in-duct measurements, another acoustic characterization approach consists in the measurement of noise radiated by the turbocharger and its pipes, in most cases using free field microphones at a given distance from the setup.

This method has the advantage of allowing measurements with the real geometry, without any modification in the pipes to mount the in-duct measurement sensors. However, for accurate measurements it is desirable that the test cell be anechoic in order to prevent disturbances in measurements caused by reflections in the engine cell walls and resonances created by the cavities of the engine or its ducts that appear as other noise sources.

As testing the whole engine setup requires a large and expensive anechoic chamber, the setup is sometimes reduced to just the turbocharger group, which is powered by an external compressor or electric motor, losing in this way the possibility of performing on-engine tests.

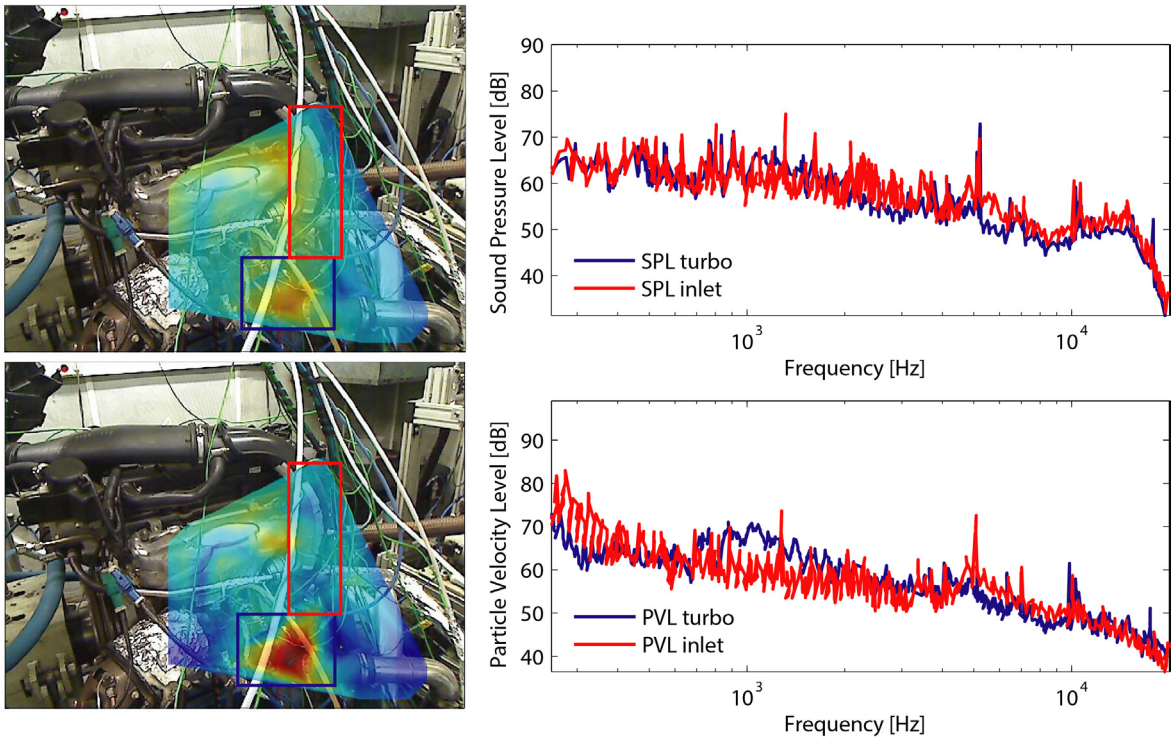

Fig. 5. Near field noise holograms (800-2000 Hz) obtained through SPL (top) and PVL (bottom), including detail of the spectra of two regions of interest: turbocharger group (blue) and compressor inlet (red)

However, a novel procedure based on measuring acoustic particle velocity level (PVL) may solve these issues [16] and enable on-engine testing in non-anechoic environments. This method makes use of two microscopic filaments acting as hot-wire flowmeters. Measuring the small voltage drop between the two, it is possible to derivate the acoustic particle velocity in the plane of the sensor.

Such a method, in this case a commercial solution providing acoustic holography-like maps of radiated noise level [6], has been tested on the (non-anechoic) engine test cell. The measuring probe of this device houses the two filaments on a MEMS chip and a traditional microphone, allowing the comparison of the performance of acoustic particle velocity measurements against traditional free-field sound pressure level (SPL) measurements.

Fig. 5 shows this comparison. SPL (top) and PVL (bottom) maps of the measured engine environment are provided by tracking the probe along the near field of the surfaces of interest. The frequencies considered in these maps have been restricted to the 800-2000 Hz range, where it is common that a broadband emission known as “whoosh noise” is produced by the turbocharger [11]. For two particular regions (turbocharger group and inlet duct, marked on the maps) the full pressure (top) and particle velocity (bottom) spectra are also provided.

The particle velocity technique clearly distinguishes the turbocharger as the source of an 800 – 2000 Hz broadband noise at this particular operating condition, identified as whoosh noise. The pressure method also appears to identify the turbocharger as the source, but the contrast with the surrounding areas is much less pronounced. This can be clearly seen in the SPL spectra, in which the level of this frequency band is similar in both zones (turbocharger and inlet in this case). In the case of the PVL spectra the turbocharger contribution is visibly higher.

However, the pressure method appears to be more sensitive to reflections in the near field and was thus unable to provide a clear identification. It should be noted that if characterization through in-duct techniques of this particular whoosh noise is intended, special attention should be placed on the outlet pipe, as this phenomenon is often found exclusively downstream of the turbocharger [4].

3. Conclusions

Characterization of the acoustic performance of a given compressor under engine conditions must start with the definition of test means. If an anechoic chamber capable of housing the entire engine is available, then free field microphones can be used to estimate the acoustic radiation, but even in this case it would be difficult to isolate the contribution of the compressor.

In order to quantify the compressor noise emission, an intensity probe can be located at the inlet orifice. However, intensity probes are quite expensive, and sufficient acoustic insulation is necessary to prevent reflections. Also, characteristics of the internal field that are not externally propagated will be lost.

In-duct noise measurements offer a cost-effective way to characterize the sound field generated by the compressor, if the ducts can be modified so as to include straight measurement sections. Single-sensor SPL may be used to investigate the upper frequency bands, but generally sound intensity is a better and more meaningful metric of the acoustic power output of the source.

Calculation of in-duct sound intensity can be achieved by using an additional consecutive sensor and decomposing the waves through the two-microphone method. However, the addition of a third sensor and the decomposition through the beamforming method appears to be more reliable along the full plane wave range, and especially in the lower frequencies (250 – 1000 Hz).

However, the restrictions of these intensity-based methods must be carefully considered, specially the influence of higher order modes and the aliasing frequency limit introduced by the spatial sampling imposed by the sensor spacing.

Regarding the external radiated noise, the particle velocity method has been able to provide more contrast than the pressure method and to correctly identify the turbocharger as the source of noise radiation at that particular “whoosh noise” band, in accordance with previous experience.

The particle velocity method could therefore be useful to reconstruct noise maps similar to those obtained using in-duct measurements, isolating the signal from the acoustic near field of the area of interest at different working conditions, without the need of modifying the original duct geometry or ensuring anechoic conditions. More research is being carried out on this topic.

4. Acknowledgements

This work has been partially supported by the Spanish Ministerio de Economía y Competitividad through grant Nº TRA2012-36954.

References

[1] Åbom M, Bodén H. Error analysis of two-microphone measurements in ducts with flow. J Acoust Soc Am 1988; 83:2429–38.

[2] Benajes J, Torregrosa AJ, Galindo J, Andrés I. Estimation of the volume velocity fluctuation at the tailpipe end of an IC engine exhaust system. Meas Sci Technol 2001; 12:1692.

[3] Brizon C, Medeiros EB. Combining subjective and objective assessments to improve acoustic comfort evaluation of motor cars. Appl Acoust 2012; 73:913–20. DOI: 10.1016/j.apacoust.2012.03.013

[4] Broatch A, Galindo J, Navarro R, García-Tíscar J. Methodology for experimental validation of a CFD model for predicting noise generation in centrifugal compressors. Int J Heat Fluid Flow 2014; DOI: 10.1016/j.ijheatfluidflow.2014.06.006

[5] Chung JY, Blaser DA. Transfer function method of measuring in-duct acoustic properties. I. Theory. J Acoust Soc Am 1980; 68:907.

[6] Comesaña D, Steltenpool S, Carrillo Pousa G, de Bree H-E, Holland KR. Scan and Paint: Theory and Practice of a Sound Field Visualization Method. ISRN Mech Eng 2013; 2013:1–11. DOI: 10.1155/2013/241958

[7] Čudina M. Noise generation by rotating stall and surge in vane-axial fans. Noise Control Eng J 2000; 48:77–84. DOI: 10.3397/1.2827969

[8] Desantes JM, Torregrosa AJ, Broatch A. Experiments on flow noise generation in simple exhaust geometries. Acta Acust united with Acust 2001; 87:46–55.

[9] Dokumaci E. A note on transmission of sound in a wide pipe with mean flow and viscothermal attenuation. J Sound Vib 1997; 208:653–5. DOI: 10.2460/javma.242.1.27

[10] Eriksson LJ. Higher order mode effects in circular ducts and expansion chambers. J Acoust Soc Am 1980; 68:545. DOI: 10.1121/1.384768

[11] Evans D, Ward A. Minimizing Turbocharger Whoosh Noise for Diesel Powertrains. SAE Tech Pap 2005; DOI: 10.4271/2005-01-2485

[12] Figurella N, Dehner R, Selamet A, Tallio K, Miazgowicz K, Wade R. Noise at the mid to high flow range of a turbocharger compressor. In: INTER-NOISE and NOISE-CON Congress and Conference Proceedings. 2012:8127–38.

[13] Galindo J, Serrano JR, Climent H, Tiseira A. Experiments and modelling of surge in small centrifugal compressor for automotive engines. Exp Therm Fluid Sci 2008; 32:818–26. DOI: 10.1016/j.expthermflusci.2007.10.001

[14] González A, Ferrer M, De Diego M, Piñero G, Garcia-Bonito JJ. Sound quality of low-frequency and car engine noises after active noise control. J Sound Vib 2003; 265:663–79.

[15] Holland KR, Davies POAL. The measurement of sound power flux in flow ducts. J Sound Vib 2000; 230:915–32. DOI: 10.1006/jsvi.1999.2656

[16] Jacobsen F, de Bree H-E. A comparison of two different sound intensity measurement principles. J Acoust Soc Am 2005; 118:1510. DOI: 10.1121/1.1984860

[17] Knecht W. Diesel engine development in view of reduced emission standards. Energy 2008; 33:264–71. DOI: 10.1016/j.energy.2007.10.003

[18] Morfey CL. Sound transmission and generation in ducts with flow. J Sound Vib 1971; 14:37–55.

[19] Nor MJM, Fouladi MH, Nahvi H, Ariffin AK. Index for vehicle acoustical comfort inside a passenger car. Appl Acoust 2008; 69:343–53.

[20] Piñero G, Vergara L, Desantes JM, Broatch A, Pinero G, Vergara L, et al. Estimation of velocity fluctuation in internal combustion engine exhaust systems through beamforming techniques. Meas Sci Technol 2000; 11:1585–95.

[21] Seybert AF. Two-sensor methods for the measurement of sound intensity and acoustic properties in ducts. J Acoust Soc Am 1988; 83:2233–9.

[22] Soh KY, Euo KK, Bae DH, Kang KT. Noise reduction in turbocharger system of diesel engines. In: INTER-NOISE and NOISE-CON Congress and Conference Proceedings. 2003:155–62.

[23] Teng C, Homco S. Investigation of Compressor Whoosh Noise in Automotive Turbochargers. SAE Int J Passeng Cars-Mechanical Syst 2009; 2:1345–51.

[24] Tiikoja H, Rämmal H, Abom M, Boden H. Investigations of Automotive Turbocharger Acoustics. SAE Int J Engines 2011; 4:2531–42. DOI: 10.4271/2011-24-0221

[25] Torregrosa A, Broatch A, Climent H, Andrés I. A note on the Strouhal number dependence of the relative importance of internal and external flow noise sources in IC engine exhaust systems. J Sound Vib 2005; 282:1255–63. DOI: 10.1016/j.jsv.2004.05.017

A Numerical Study of Trailing Edge Geometry for Low Inertia Automotive Mixed Flow Turbines

T. Leonard[1], S. W. Spence[1], J. Early[1] and D. Filisinger[2]

[1]Queen's University Belfast, Belfast, UK

E-mail: tleonard06@qub.ac.uk
Telephone: +(44) 028 9097 4569
Fax: +(44) 028 9097 1729

[2]IHI Charging Systems International GmbH, Heidelberg, Germany

Abstract. Mixed flow turbines can offer improvements over typical radial turbines used in automotive turbochargers, with respect to transient performance and low velocity ratio efficiency. Turbine rotor mass dominates the rotating inertia of the turbocharger's rotating assembly, and any reductions of mass in the outer radii of the wheel, including the rotor back-disk, can significantly reduce this inertia and improve the acceleration of the assembly. Off-design, low velocity ratio conditions are typified by highly tangential flow at the rotor inlet and a non-zero inlet blade angle is desirable for such operating conditions. This is achievable in a Mixed Flow Turbine without increasing bending stresses within the rotor blade, which is beneficial in high speed and high inlet temperature turbine designs.

This study considers the meridional geometry of Mixed Flow Turbines using a multi-disciplinary study to assess both the structural and aerodynamic performance of each rotor, incorporating both CFD and FEA. Variations of rotor trailing edge were investigated at different operating conditions representing both on- and off-design operation within the constraints of existing hardware geometries. In all cases, the performance is benchmarked against an existing state-of-the-art radial turbocharger turbine with consideration of rotor inertia and its benefit for engine transient performance. The results indicate the influence of these parameters and this report details their benefits with respect to turbocharging a downsized, automotive engine.

Notation

Λ	*Blade cone angle.*
I	*Moment of inertia.*
r	*Radius.*
ω	*Rotating velocity.*
τ	*Torque.*
M	*Meridional Length.*

Subscripts

t	*Turbine.*
tt	*Total-to-Total*
ts	*Total-to-Static*
b	*Bearing.*
c	*Compressor.*
h	*Hub.*
s	*Shroud.*
0	*Total/Stage Inlet.*
1	*Turbine Inlet.*
2	*Turbine Outlet.*

Acronyms

BMEP	*Brake Mean Effective Pressure.*
BSFC	*Brake Specific Fuel Consumption.*
CFD	*Computational Fluid Dynamics.*
CoG	*Centre of Gravity.*
FEA	*Finite Element Analysis.*
LE	*Leading Edge.*
MFT	*Mixed Flow Turbine.*
PR	*Pressure Ratio.*
RFT	*Radial Flow Turbine.*
RMS	*Root Mean Square.*
TE	*Trailing Edge.*

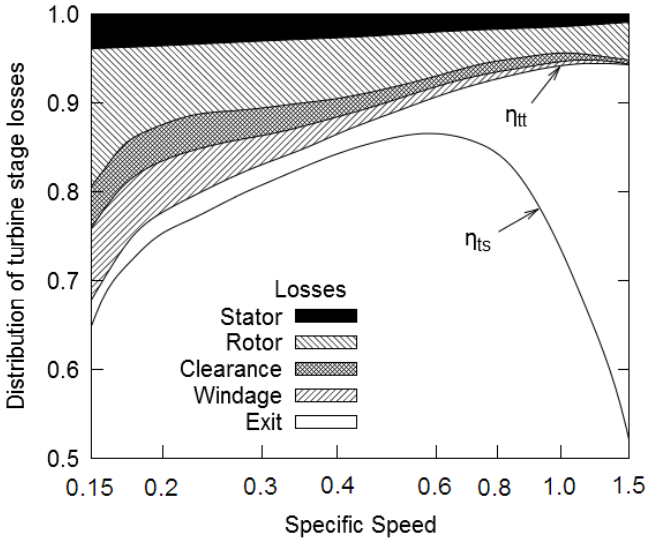

Fig. 1. Distribution of turbine losses for varying specific speed (Watson and Janota 1982)

1. Introduction

Turbocharging an internal combustion engine is an effective means of increasing an engine's BMEP. One benefit of this is an increase in the specific power output of an engine, which can be used to reduce installation size and mass for a given power requirement. An engine of reduced size and mass can be supported by a chassis and suspension of reduced mass and adequately decelerated by a lighter unsprung mass. Therefore, reducing engine size has a resulting effect of an overall greater reduction in vehicle mass and potential savings in fuel consumption. A downsized engine will also operate closer to its point of best fuel efficiency on its map of Brake Specific Fuel Consumption (BSFC) for typical urban driving cycles, which account for a large majority of driving conditions. Turbocharging a downsized engine presents issues, however, with respect to turbocharger response time and range: A downsized engine is reliant on inlet boost across all engine speeds to produce power comparable to larger displacement, naturally aspirated engine.

Engine volumetric flow rate is, simply, proportional to engine speed (Flaxington and Swain 1999) and at low engine speeds there is little flow from which the turbocharger turbine can extract work. If engine load is increased, then the turbine stage pressure ratio will also increase without an immediate increase in turbocharger speed. These conditions are described by a low value of turbine velocity ratio, also called blade speed ratio, as given by Eq. 1. Such conditions are typified by highly swirling flow at the inlet of the turbine and excessively positive values of incidence, which leads to increased rotor losses, as shown in Fig. 1 (Watson and Janota 1982), where a low value of velocity ratio corresponds to a low value of specific speed. Therefore, a non-zero inlet blade angle is beneficial in increasing efficiency at such conditions by giving less positive incidence at the inlet of the turbine (Lüddecke et al. 2012). Improved efficiency at such operating conditions can also benefit turbocharger response, providing more energy for accelerating the rotating assembly.

$$Velocity\,ratio = \frac{U}{c_{is}} = \frac{r\omega}{\sqrt{2C_pT_0\left[1-\left(\frac{1}{PR}\right)^{\frac{\gamma-1}{\gamma}}\right]}} \qquad (1)$$

The acceleration of a turbocharger rotating assembly, $d\omega/dt$, is a function of the moment of inertia of the rotating assembly, I, and the torque generated by the turbine, τ_t, less the torque absorbed by the bearings, τ_b, and the torque used by the compressor, τ_c, as shown by Eq. 2 (Chen et al. 2012). The torque absorbed by the compressor is a function of given operating conditions and the aerodynamic performance of the compressor and the use of technologies such as roller bearings can reduce τ_b. In the scope of turbine design, the moment of inertia, I, may be reduced while the torque produced by the turbine for a given operating conditions may be increased through improving turbine efficiency, to the benefit of turbocharger acceleration.

$$I\frac{d\omega}{dt} = \tau = \tau_t - \tau_b - \tau_c \quad (2)$$

The moment of inertia, I, is generally given by Eq. 3 and is a function of a mass, m, and the square of the radius of that mass, r, from the rotating axis. This indicates that any material removed from the outer radii of a rotor will yield the greatest reduction in moment of inertia. Equation 3 also indicates that adding material at lower radii of the rotor will not contribute as significantly to the inertia of the rotor.

$$I = mr^2 \quad (3)$$

A turbocharger turbine is typically made of dense, nickel alloy as it is exposed to high engine exhaust gas temperatures, and therefore contributes the large majority of the inertia of the complete rotating assembly. Alternate materials are available (Baines 2002), but there is generally an associated cost with this. As the transient response of a turbocharger is heavily dependent on the inertia of the turbine, it is often proposed that its efficiency may be compromised to reduce inertia, and this will benefit turbocharger response and, hence, engine transient performance. It has been demonstrated, using engine simulations, that a turbocharger with a turbine optimised for reduced inertia may attain improved inlet boost pressure after one second, in the event of an engine load step, when compared with a baseline turbine rotor and peak-efficiency-optimised turbine rotor (Iosifidis et al. 2013), as shown in Fig. 2. This inertia-efficiency compromise is ultimately validated through engine simulations and testing. Some suggested inertia-efficiency correlations have been published, suggesting that a 20% reduction in inertia may compensate for a 4-5% efficiency reduction at low velocity ratios and a 40% reduction in inertia could compensate for a 7-8% reduction in efficiency at low velocity ratios (Roclawski et al. 2013).

1.1 Mixed flow turbines

Mixed Flow Turbines (MFT) differ from a Radial Flow Turbines (RFT) as the leading edge (LE) is not at a constant radius; rather it is inclined at some angle, as shown in Fig. 3. Depending on the design of the turbine, and its associated hardware, the flow may pass normal to this leading edge. However, there are also situations where this is not the case and it is important to differentiate between these two angles. As a result, the convention shown in Fig. 3 has been adopted for this report, where the angle of the LE of the blade is called the blade cone angle, Λ, and the angle of the flow is called the flow cone angle, λ. The combination of the flow cone angle, λ, and the camber angle, or lean angle, of the blade's inlet can result in a non-zero inlet blade angle, while still maintaining a radial fibre blade structure (Leonard et al. 2013).

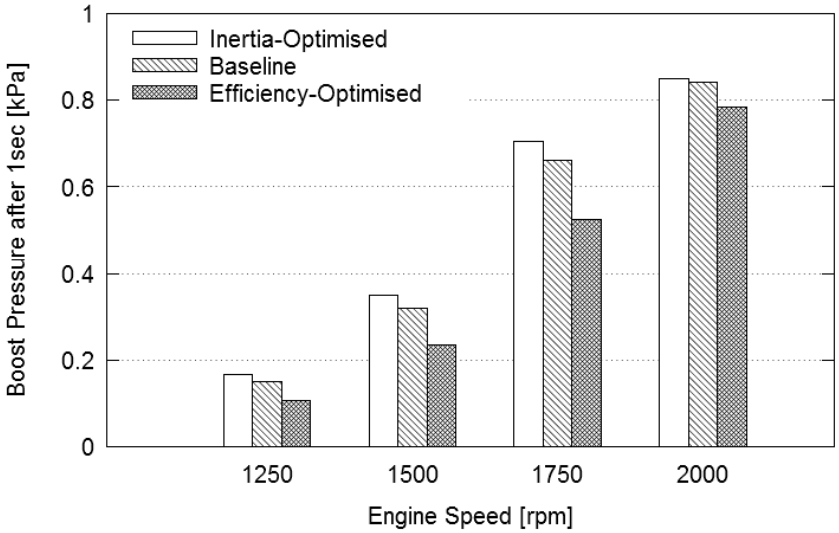

Fig. 2. Comparison of low inertia and higher efficiency turbine rotors (Iosifidis et al. 2013)

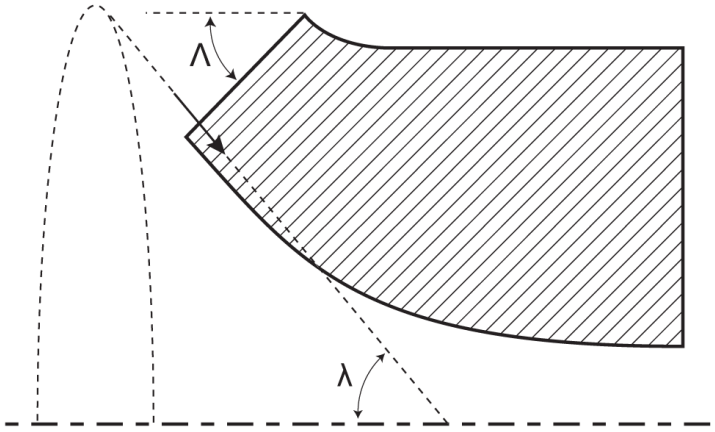

Fig. 3. Definition of flow cone angle, λ, and blade cone angle Λ

An MFT of similar frame size to an RFT can have reduced inertia. This is a result of the removal of material from the blades and rotor backdisk at the outer radii, r, which contributes significantly to the moment of inertia of a turbine wheel, as described by Eq. 3.

2 Rotor geometries

The MFT rotors studied were derived from an existing, state-of-the-art RFT, designated RT. The hub and shroud meridional contours were maintained from the RT turbine, and a blade cone angle, Λ, of 30° was applied to the LE while maintaining the radius of the shroud tip at a constant value. An inlet blade angle, β_1, of 30° was then applied, while maintaining the radial fibre of the blade. This geometry formed the basis of the MFT rotors and designated MT. The application of a blade cone angle, while maintaining the same shroud tip radius, resulted in a reduced meridional length at the hub of the rotor. Previous studies involving mixed flow turbines (Palfreyman et al. 2002) indicated that a shorter axial chord can result in a drop in aerodynamic efficiency as a result of increased exit velocities and blade wake losses. The findings of this work indicated that an 19% reduction in axial chord gave a reduction of 3-4 pts of efficiency. Therefore, two further rotors were therefore designed with an extended trailing edge to achieve the same hub meridional length as the RT rotor, one with an extension at both the hub and shroud, designated MT+hs, and one with the extension applied at the hub only, designated MT+h. The meridional projection of these geometries is shown in Fig. 4. Table 1 shows the geometry of these rotors, normalised to the baseline RT. The throat area for each rotor is also given in Table 1. The RT, MT and MT+hs rotor have the similar exducer geometry and exit blade angles and, as such, the throat area is similar for these rotors. The throat area of the MT+h rotor is larger than that of the rotors as a result of the reduced blade material at the shroud tip of the rotor exducer.

Table 1. Geometric properties of rotors

Rotor	Meridional Length, Shroud, M_s	Meridional Length, Hub, M_h	Throat Area
RT	1.00	1.00	1.00
MT	1.00	0.85	1.00
MT+hs	1.34	1.00	1.00
MT+h	1.00	1.00	1.06

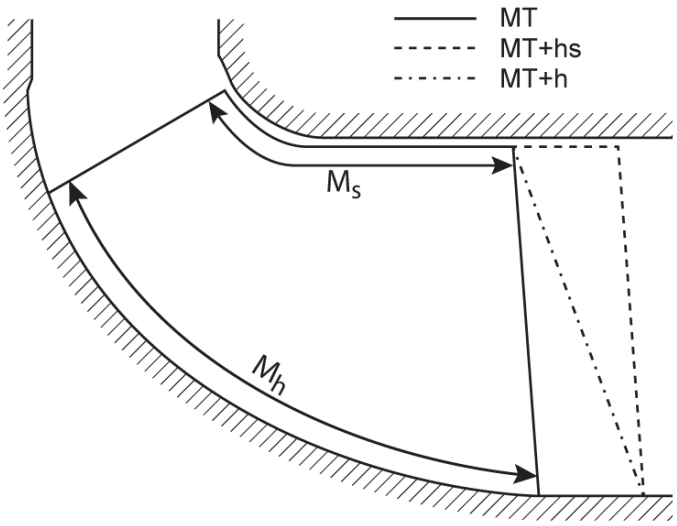

Fig. 4. Meridional projection of the variations of LE geometry

All of the rotors designed had radially fibred blades. As such, the shroud blade contour, and other intermediate contours of the blade, was a radial projection of the hub blade contour. Similar to the LE of a radially fibred MFT, (Abidat et al. 1992), the blade angle along the trailing edge from hub to shroud was a function of the hub blade profile in the exducer region of the blade, as illustrated in Fig. 6. As the trailing edge of the MT+h rotor is not at a constant axial position, the distribution of the exit blade angle, β_2, varied from that of the other rotors and was controlled in this way. Figure 7 shows the distribution of exit blade angle, β_2, along the TE for MT+h and other rotors. To achieve a valid comparison between these two LE angle distributions, the exducer region of the MT+h blade was modified so that the blade angle at the RMS exducer blade height matched that of the other rotors. This resulted in an exit blade angle that was more positive between the hub and the RMS radius and an exit blade angle that was more negative from the RMS radius to the shroud.

Each rotor was simulated for two geometries: A and B. Geometry A could correspond to a volute with a large A/r ratio and geometry B could correspond to a volute with a smaller A/r ratio. Typical absolute flow angles for these geometries, upstream of the rotor LE, are 60° and 72° respectively.

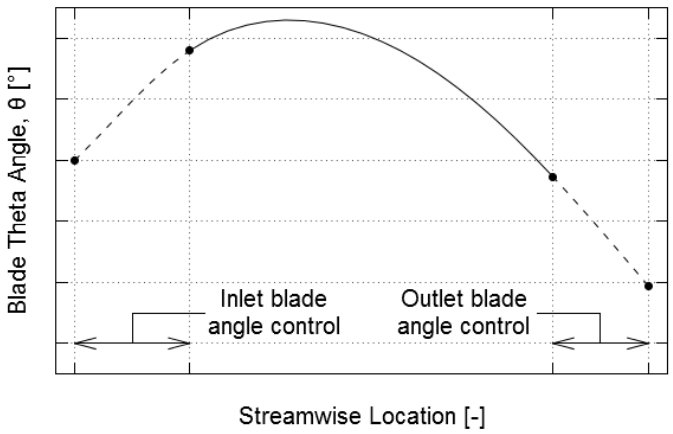

Fig. 6. Regions of hub definitions controlling LE and TE angle distribution

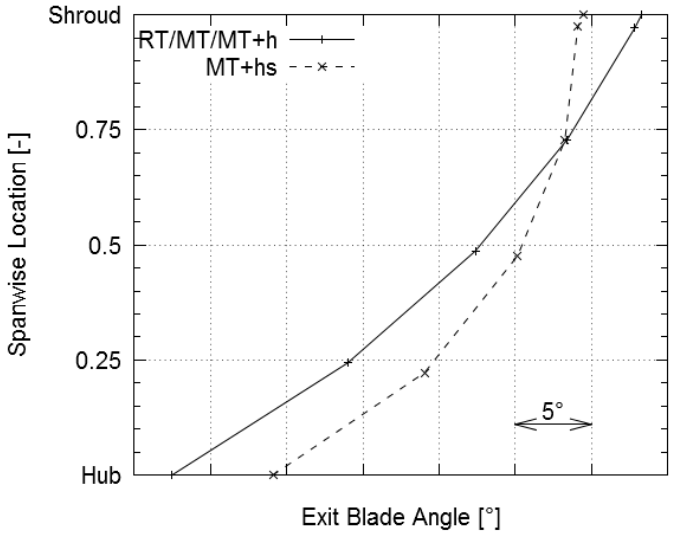

Fig. 7. Comparison of exit blade angle distribution of rotor variations

3 Numerical Model

The numerical model was designed to represent the topology of the Queen's University Belfast experimental turbine test rig. The design of this test rig replaces the function of a typical turbocharger turbine volute with a set of swirl generating vanes. These vanes create an equivalent rotor inflow angle to a volute without creating non-axisymmetric flow features exhibited by volutes, such as the disturbance generated in the region of the *tongue*. As a result of this substitution, a single passage model can be used with fewer assumptions, significantly reducing the computational costs of the numerical calculations.

The CFD analysis was performed using the ANSYS CFX package. A steady state approach was adopted using the Shear Stress Transport (SST) turbulence model, which has yielded good performance correlations with the QUB experimental turbine test rig for previous studies (Walkingshaw et al. 2010). Each domain consisted of structured, hexahedral elements with particular effort placed on controlling grid angles and element volume change ratios. The grid sizes were set based upon a grid independence study with approximately 700k elements in the turbine rotor domain. y+ was maintained below 3 for the majority of wall boundaries, with values not exceeding 11 where this was not achieved, to ensure that boundary layers were resolved by a minimum of 1 element. Convergence was considered adequate when Root Mean Square (RMS) residuals below $1x10^{-4}$ were achieved, with values below $1x10^{-5}$ set as a desirable target, and when values of interest such as efficiency and mass flow had achieved steady state values.

For each geometry, A and B, two constant speed lines were simulated with varying pressure ratio (PR); Speed 1 represents a higher rotating speed than Speed 2. Velocity ratio, U/c_{is}, was calculated using the RMS inlet blade height. It is acknowledged that this results in a lower U/c_{is} being calculated for a given set of operating conditions compared to the baseline RT, and this gives a shift of speed lines plotted in this way. For engine and compressor matching, shaft speed is a constraint; however for an aerodynamic study of turbine geometry, the use of average blade speeds can be considered a more valid consideration.

The FEA study was performed using the ANSYS Mechanical package. All rotors were modelled with constant radius fillets.

4 Mechanical results

The inertia and mass properties of the four rotors are shown in Table 2, with values normalised to the MT rotor. Adding material at the trailing edge of the rotor naturally increases the inertia of the rotor. When the trailing edge was extended uniformly, from hub to shroud, for the MT+hs rotor, the inertia of the rotor increased 10.1% relative to the MT rotor. When the trailing edge was extended in a variable manner, for the MT+h, with more material towards the hub, the inertia of the rotor increased 2.6% relative to the MFT rotor. This is verified by Eq. 3, with material added at lower radii not contributing significantly to the inertia of the rotor. Relative to the MT rotor, the RT rotor had an increase in inertia of 28.9%. Therefore, the inertia reduction of each MFT rotor may be compromised with efficiency as demonstrated in the literature. The published figures indicate that these inertia reductions could correlate to approximately 6% efficiency for the MT and MT+h rotors and 2% for the MT+hs rotor.

Table 2. Inertia and mass properties of rotors

Rotor	Inertia	Mass
MT	1.000	1.000
MT+hs	1.101	1.133
MT+h	1.026	1.071
RT	1.289	1.122

The results of the FEA stress analysis are shown in Table 3. The peak stress in the rotor backdisk did not vary significantly for the variants of the MT rotors, as the LE geometry was constant across each variant. The stress in the RFT rotor was significantly greater in this region as the backdisk had a greater radius compared with all of the MT rotors. Stresses in the exducer region varied for each rotor. The MT rotor had increased stress in this region relative to the RT rotor. This could be attributed to the removal of material from the back disk of the rotor which provides additional support to the blade. The MT+hs rotor had some reduction of stress in this region, though not greatly. The MT+h rotor had reduced stresses relative to all other rotor variants; particularly the stress at the base of the trailing edge was greatly reduced compared to the other designs. This reduction in stress could be exploited to reduce blade thickness to further reduce the inertia of the wheel and reduce the blade blockage in the throat region of the exducer.

Table 3. Stress results of rotors

Rotor	Stress, Backdisk	Stress, Exducer Fillet	Blade Stiffness
MT	-	-	-
MT+hs	~	~	↓↓
MT+h	~	↓↓	↑
RT	↑↑	↓	↓

The effects of the modifications on blade stiffness are also indicated in Table 3. Comparing the RT and MT rotors, the latter gave a stiffer blade. Although the removal of the backdisk material removes some support to the LE of the blade, the increased blade curvature, as a result of the reduced hub length and increased inlet blade angle, stiffens the blade. The addition of material along the entire TE results in a less stiff blade for the MT+hs, as a result of both the increased blade length and reduced rate of curvature. Adding material only in the hub region, as in the MT+h, resulted in an increase in blade stiffness relative to all other rotors. The additional material added, mainly towards the hub of the trailing edge, therefore provided support to the blade without increasing the length of the shroud of the blade which would reduce its stiffness, as is the case for the MT+hs rotor.

5 Aerodynamic results

5.1 Geometry A

The efficiency results for geometry A are shown in Fig. 8 and Fig. 9 for speed 1 and speed 2 respectively. For speed 1, the benefits of the 30° inlet blade angle of the MFT rotors are evident. At lower velocity ratios, all 3 MFT rotors show improved efficiency relative to the RT rotor. When considering points of equal pressure ratio, such as those indicated on Fig. 8, this efficiency improvement is still evident; a 2.0 pt efficiency increase is predicted for the MT rotor over the RT rotor, and the MT+h and MT+hs rotors show a 0.8 pt and 1.6 pt increase compared to the MT rotor, respectively. With increasing velocity ratio, the efficiency of the MT and MT+h rotors become similar while the MT+hs rotor shows an improvement across the complete speedline. At the highest velocity ratio, the efficiency of the MT+h rotor reduces by a greater amount than the other rotors.

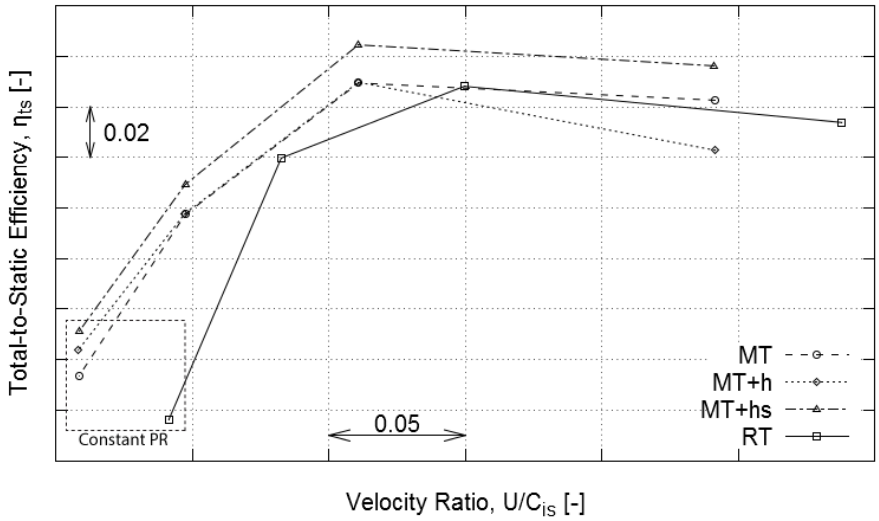

Fig. 8. Total-to-static efficiency vs velocity ratio for geometry A, speed 1

For speed 2, Fig. 9, a similar trend is observed; the MT+hs rotor shows an improved efficiency relative to the other MFT rotors, which show improved efficiency compared to the RT rotor at lower velocity ratios. Similar to speed 1, the efficiencies of the MFT rotors are comparable at a low velocity ratio and diverge as this increases. This trend can be explained by the distribution of losses shown in Fig. 1. At lower velocity ratios, exit losses only contribute a small portion of the overall losses; the rotor losses contribute the greatest losses. These rotor losses are largely a result of excessive positive incidence and, as the LE was kept constant for the 3 MFT rotors, little difference in efficiency is seen at the lower velocity ratios. However, for velocity ratios near peak efficiency and greater, exit losses become the dominant loss in the stage and the effects of the TE modifications become more apparent. At the maximum velocity ratio operating condition of speed 2, the MT and MT+h rotors have 4% and 6% greater mass flow averaged velocity at the turbine outlet and 3% and 11% reduced absolute flow angle relative to the MT+hs. According to Euler's turbomachinery equation, this results in less work extraction and, hence, a reduced efficiency for a given operating condition. This increased exit loss can be also be attributed to the increased blade loadings at the TE of these rotors, shown in Fig 10, which results in greater blade wake losses. Considering the pressure along the suction surface of the blades, at the RMS spanwise location, the pressure is lowest for the MT rotor, followed by the MT+h rotor, and the highest suction side pressure is predicted for the MT+hs rotor. This correlates with the reduction in the rate of curvature of each blade, Both the MT+h and MT+hs blade have a reduced rate of curvature relative to the MT rotor, but the MT+hs has a longer blade length at this point which leads to a further reduction in blade loading.

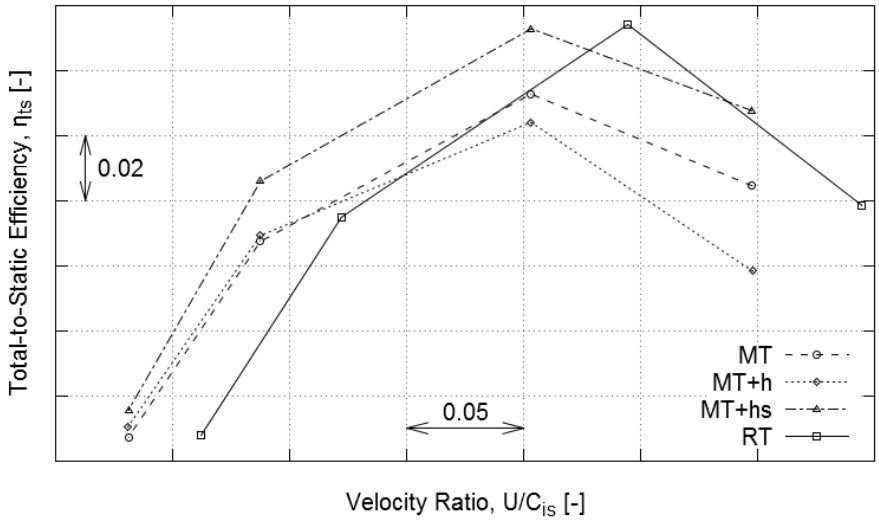

Fig. 9. Total-to-static efficiency vs velocity ratio for geometry A, speed 2

The mass flow for varying pressure ratio is shown in Fig. 11 for the rotors simulated. The mass flow of the RT, MT and MT+hs rotors are similar, as would be expected given their similar throat areas. The MT+h rotor shows an increased mass flow rate as would be expected, given its increased throat area.

The improvement in efficiency of the MT+hs is evident at both speeds simulated for geometry A. However, this improvement must be considered with respect to the mechanical performance of the rotor. The inertia of the rotor was increased relative to the other MFT rotors but was still less than the radial turbine and some improvement in transient performance may still be possible in this respect. However, the mass of the rotor, and hence materials costs, increased significantly. The stress in the blade fillets was largely similar to the MT rotor but the stiffness of the blade was significantly reduced, which may be a concern for low cycle fatigue.

The loss in efficiency of the MT+h rotor can also be considered in this way. As material was added at low radii, the inertia did not increase significantly, and a larger compromise in efficiency is possible at low velocity ratios. As the efficiency of the rotor was not significantly reduced at low velocity ratios, the transient performance of a turbocharger may be improved through this design. A reduction in stress was also achieved for this design and blade stiffness was greatly improved. The predicted increase in mass flow rate could also be exploited to further reduce the inertia of the rotor, either through scaling or through reducing the exducer diameter.

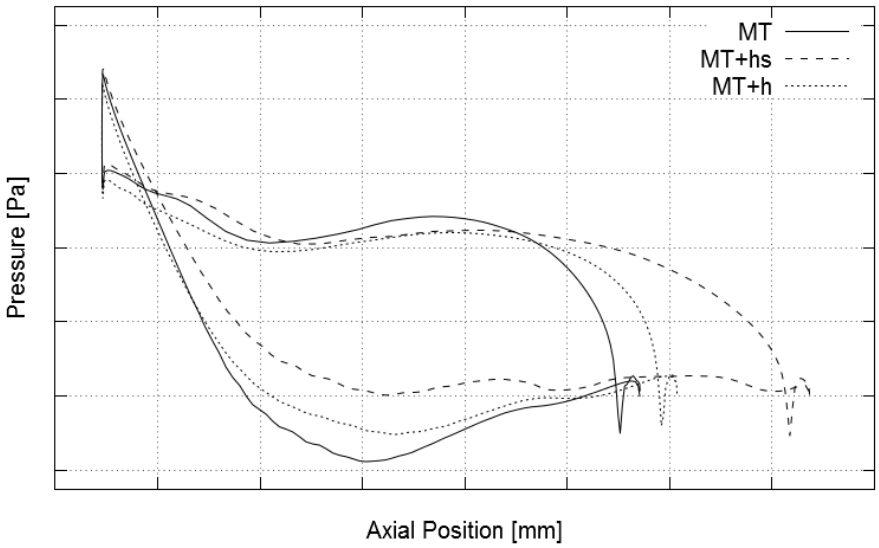

Fig. 10. Blade loading at the RMS spanwise location the for a high velocity ratio for geometry A, speed 2

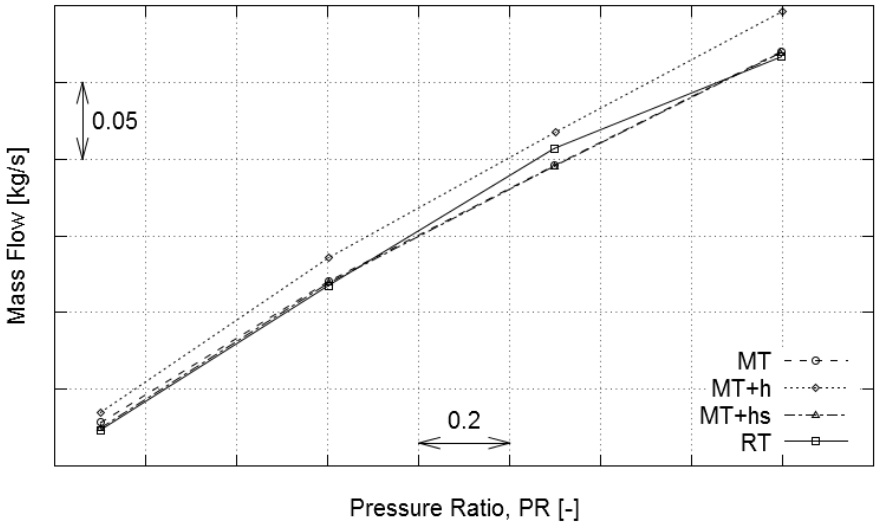

Fig. 11. Mass flow rate vs pressure ratio for geometry A, speed 2

5.2 Geometry B

The results for geometry B are shown in Fig 12. and Fig 13 for speed 1 and speed 2 respectively. For speed 1, at the lower velocity ratio, there was no diffrence in predicted efficiency for the MT rotors, but together they all showed an increased efficiency relative to the RT rotor. With increasing velocity ratio, the efficiency of the MFT rotors diverged, and the MT rotor showed the best efficiency followed by the MT+hs rotor, followed by the MT+h rotor. Particularly at the highest velocity ratio, the MT+h rotor showed a 1.5 pt reduction in efficiency relative to the other MFT rotors and fell below the efficiency of the RT rotor.

The results of the simulations for speed 2 with geometry B show a similar trend to speed 1. At the lower velocity ratios, the efficiency of the rotors were similar, but their efficiency diverged with increasing velocity ratio, with the MT+h rotor showing a relatively large efficiency reduction at the highest velocity ratio. Similar to geometry A, these values must also be considered with respect to the trade-off between inertia and efficiency, and at the low velocity ratios, turbocharger transient response may be improved.

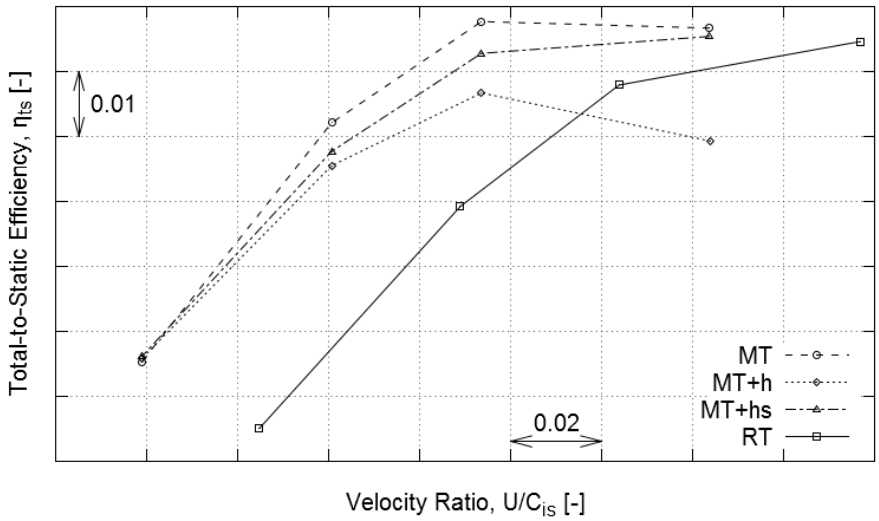

Fig. 12. Total-to-static efficiency vs velocity ratio for geometry B, speed 1

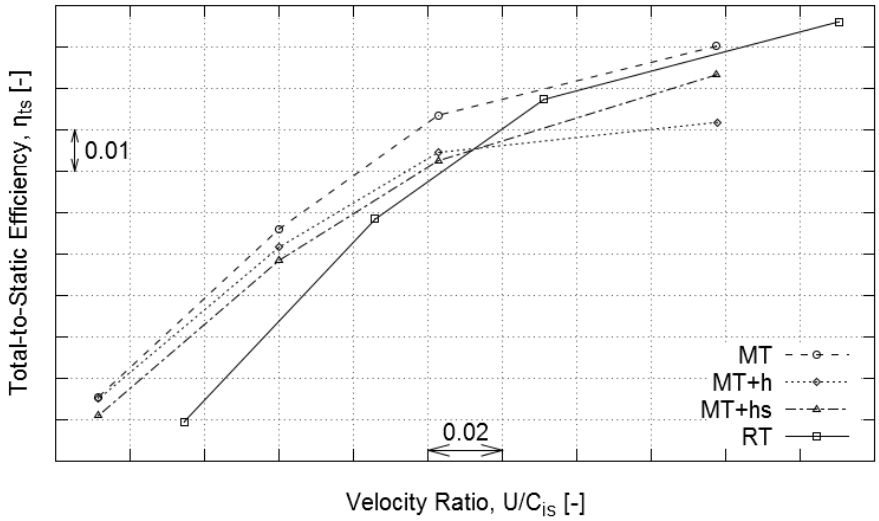

Fig. 13. Total-to-static efficiency vs velocity ratio for geometry B, speed 2

6.0 Conclusions

The base mixed flow turbine rotor, MT, exhibited improved low velocity ratio efficiency when compared to the radial turbine, as a result of its non-zero inlet blade angle. It also had a greatly reduced inertia, with material removed from the outer radii of the blade, and this could further improve the transient performance of the turbocharger, which will benefit the transient performance of a downsized automotive engine.

The mixed flow rotor with material added along the entire trailing edge, MT+hs, showed improved aerodynamic performance at some operating conditions, relative to the other MFTs simulated. The increased meridional length of the blade improved flow turning, reducing exit losses, and reduced blade loading at the exducer, resulting in reduced blade wake losses. The rotor's inertia increased relative to the base mixed flow turbine, MT, but this was still below the inertia of the radial turbine considered. Therefore, turbocharger response may still be improved relative to the radial turbine. The increase of meridional length also resulted in a reduction of blade stiffness.

The MT+h rotor, with material added only to the hub region of the blade, had the lowest predicted efficiency of the mixed flow turbines simulated. However, the inertia additions for this modification were minimal compared to the base mixed flow turbine, and a compromise of rotor inertia and efficiency may still be possible, resulting in an improved transient performance. The mass flow rate was also increased as a result of the increased throat area permitted by the blade design and this could be exploited to reduce the inertia of the rotor further. The MT+h rotor also exhibited the lowest stresses and greatest blade stiffness. This improved mechanical performance could be exploited to reduce blade mass and further reduce the inertia of the rotor. Based on the mechanical advantages of this trailing edge treatment, it may be possible to incorporate such features into an existing turbine wheel design.

In general, it was predicted that the efficiency of the turbine rotors was mostly insensitive to trailing edge variations for low velocity ratios. Where such low velocity ratio efficiency is goal, it may be possible to select a trailing edge design that improves the mechanical properties of the rotor, without incurring a large efficiency penalty.

Acknowledgements

The author would like to thank ANSYS Inc. for providing the packages used for both the aerodynamic and mechanical study of these rotors. The author would also like to thank IHI Charging Systems International GmbH for their continued support of the research undertaken at Queen's University Belfast.

References

Abidat M, Chen H, Baines N C and Firth M R (1992) Design of a highly loaded mixed flow turbine. Proceedings of IMechE A02291: vol 206: pp 95-107.

Baines N C (2002) Radial and mixed flow turbine options for high-boost turbocharger.7th International Conference on Turbocharger and Turbocharging.

Chen H, Cai T and Li P (2012) The transient response of turbocharger turbines. 10th International Conference on Turbochargers and Turbocharging. C1340/019

Flaxington D and Swain E (1999) Turbocharger aerodynamic design. Proceedings of IMechE C01398: vol 213, Part C: pp 397-408.

Iosifidis G, Walkingshaw J, Dreher B, Filsinger D, Ikeya N and Ehrhard J (2013) Tailor-made mixed flow turbocharger turbines for best steady-state and transient engine performance. 1st International Conference on Engine Processes, Berlin, TUBS GmbH

Leonard T, Spence S, Early, J and Filsinger D (2013) A numerical study of automotive turbocharger mixed flow turbine inlet geometry for off-design performance. 6th International Conference on Pumps and Fans. ICPFVI-021.

Lüddecke B, Filsinger D and Ehrhard J (2012) On Mixed Flow Turbines for Automotive Turbocharger Applications. International Journal of Rotating Machinery, Volume 2012, Art.-ID 589720. Doi:10.1155/2012/589720

Palfreyman D, Martinez-Botas R F and Karamanis K (2002) Computational and experimental investigation of the aerodynamics of turbocharger mixed-flow turbines.7th International Conference on Turbocharger and Turbocharging. C602/017/2002.

Roclawski H, Böhle M and Gagau M (2012) Multidisciplinary design optimization of a mixed flow turbine wheel. ASME Turbo Expo 2012, Copenhagen. GT2012-68233.

Walkingshaw J, Spence S, Ehrhard J and Thornhill D (2010) A numerical study of the flow fields in a highly off-design variable geometry turbine. ASME Turbo Expo 2010, Glasgow, UK. GT2010-22669.

Watson N and Janota M A (1982) Turbocharging the internal combustion engine. Page 167. The MacMillan Press Ltd. ISBN 0-333-24290-4.

Development of a turbocharger compressor with variable geometry for heavy duty engines

M. Wöhr[1], E. Chebli[1], M. Müller[1] , H. Zellbeck[2], J. Leweux[1] and A. Gorbach[1]

[1]Daimler AG, 70546 Stuttgart, Germany

E-mail: michael.woehr@daimler.com
Telephone: +(49) 711 17 51822
Fax: +(49) 711 3052132818

[2]TU Dresden, Institut für Automobiltechnik, 01062 Dresden

Abstract. This paper describes the first development phase of a centrifugal compressor with variable geometry which is designed to match the needs of future heavy duty engines. Requirements of truck engines are analyzed and their impact on the properties of the compressor map is evaluated in order to identify the most suitable kind of variable geometry. Our approach utilizes the transformation of engine data into pressure ratio and mass flow coordinates that can be displayed and interpreted using compressor maps. 1D and 3D-CFD fluid flow calculations are used to identify loss mechanisms and constraints of fixed geometry compressors. Linking engine goals and aerodynamic objectives yields specific recommendations on the implementation of the variable geometry compressor.

Notation

M	*Torque*
Ma	*Mach number*
N	*rotational speed*
μ	*load cycle specific fuel consumption*
Π_{tt}	*Total-to-total pressure ratio*
η	*Isentropic compressor efficiency*
C_p	*Specific heat capacity*
w_s	*Specific work input*
T	*Temperature*
T_t	*Total temperature*
κ	*Adiabatic exponent*
c_θ	*Tangential velocity*
c_m	*Meridional velocity*
β_2	*Backsweep angle*
u	*Impeller speed*

1. Introduction

While turbocharger turbines with variable geometry have been successfully investigated and developed for years, variable geometry compressors boosting internal combustion engines have never left the phase of early concept studies. This circumstance is mainly caused by the fact that requirements and constraints of the engine and its charging system were not considered as a whole at the first stages of the design process. This leads to concepts that fulfill the goals of engine development only partly or even fail to stay within certain constraints. At Daimler Trucks with its captive turbocharger development department, the research of engine and turbocharger thermodynamics and compressor aerodynamics go hand in hand and thus allow for a development approach of a variable compressor geometry where the concept can be matched exactly to the needs and requirements of future heavy duty engines.

The following course of actions was chosen to find the most suitable variability concepts:

1. Engine Performance Analysis
   - Identification of the goals and restrictions of future truck engines
2. Compressor Characteristics Analysis
   - Analysis of the impact of engine needs on the compressor map and behavior
3. Aerodynamic Loss Analysis
   - Aerodynamic investigation of the root causes that lead to the underperformance of fixed geometry compressors regarding the identified engine goals.
4. Conclusion
   - Formulation of the aerodynamic requirements for a variable system, estimation of the effects on compressor map and engine benefits

Previous work focusses mainly on the evaluation of variable compressor geometries rather than preliminary considerations. This section provides a brief overview of variable geometry compressor concepts and the engine goals to be achieved. In order to improve engine dynamics by manipulating the specific work of the compressor, variable radial and axial guide vanes can be used (Müller et al 2005; Lang et al 2006). Doing so the rotational speed of the turbocharger during part load operation can be raised decreasing the amount of energy needed to accelerate the rotor and thus yielding a faster transient response. Variable axial guide vanes are also used to extend the surge margin to lower flow rates (Fraser et al 2007; Uchida et al 2006; Wallace et al 1975). This is done by inducing a pre-swirl and thus influencing the incidence of the flow at the impeller blade leading edge. This enables the compressor to deliver boost pressure at very low mass flow rates. Hence the engine torque curve can be moved to lower engine speeds. The downside of adjustable geometric features in the inflow of the compressor is the inherent total pressure loss due to wall friction and possible flow separations contrary to the lossless upstream flow of fixed geometry compressors. Reducing losses after the impeller, variable geometry compressors with vaned diffusers are capable of increasing efficiency and improving the surge margin at the same time (Schenkel et al 2004; Oatway and Harp 1973; Berenyi and Raffa 1979). These concepts are characterized by stringent demands regarding the design and control of the adjustable system due to the high number of moveable parts and very narrow compressor maps of the static geometries.

The main contribution of this work is the identification of the most suitable type of variable geometry compressor by analyzing the engine goals and requirements and evaluating the consequences for the compressor characteristics and the underlying aerodynamics.

2. Analysis of Engine Performance and Compressor Characteristics

2.1 Overview of engine goals

Objectives of engine development that can be achieved with the aid of a variable geometry compressor are listed in Table 1. They can be divided into three degrading levels of importance. The first level is crucial and the third one means that there is only low necessity to improve this aspect but a variability should not worsen the current status. Although this paper focuses on heavy duty engines (>10l engine displacement) the investigation of engine goals has been done for medium duty engines as well in order to gain insight into common targets that might yield the desire for the same type of variable compressor geometries. The following sections give a further explanation of the engine target headlines and the relevance towards compressor properties and behavior.

Table 1. Overview of engine development objectives

Engine type / objective	Heavy Duty	Medium Duty
Decrease of fuel consumption	+++	+++
Increase of Low-End Torque	+++	+++
Improvement of Engine Brake	++	++
Support for Thermal Management	++	++
Decrease of Altitude Power Reduction	+	+++
Noise Reduction	+	+
Improvement of Dynamics	+	++
Improvement of Durability	+	+

2.2 Decrease of fuel consumption

Decreasing fuel consumption means reducing operating costs of the customer and at the same time helping to meat exhaust emissions regulations that gain both importance and demand.
The identify the most significant operating points regarding fuel consumption the amount of fuel injection per unit time is multiplied with the time distribution of a load cycle and divided by the total amount of consumed fuel. This yields a density function which equals 100% integrated along $\frac{M}{M_{max}}$ and $\frac{T}{T_{max}}$.

$$\mu = \frac{z(M,T)\cdot v_t(M,T)}{\iint z(M,T)\cdot v_t(M,T)\delta M \delta T} \qquad (1)$$

These values are shown in Figure 2 for two disparate duty cycles: Round track Stuttgart-Hamburg-Stuttgart (S-HH-S) with 40t tonnage and a typical distribution transport route with a tonnage of 25t. The engine in both cases is a 6 cylinder, 12.8l engine displacement satisfying the EuroVI exhaust emission regulations. The contour map shows the density function of fuel consumption for each operating point.

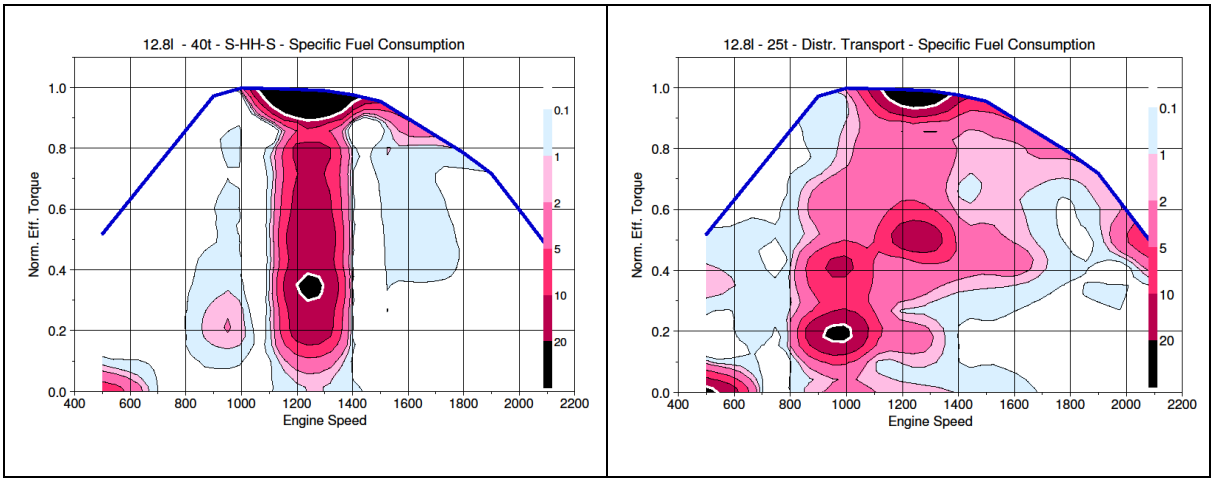

Fig. 1. Fuel consumption density for 40t S-HH-S roundtrack and 25t distribution transport route

While the truck running S-HH-S operates and consumes fuel in a very narrow speed band with a distinct fuel consumption peak at maximum torque, the distribution transport truck map looks very different with a wide spread speed area and many scattered consumption maxima.

Figure 1 shows for which operating points the engine efficiency has to be raised in order to decrease overall fuel consumption for a specific load cycle. With regards to the turbocharger, there are two ways to reduce fuel consumption by minimizing pumping work: Less backpressure at the turbine for the same amount of boost pressure or more boost pressure coming from the compressor using the same shaft power and thus the same turbine backpressure. Either way it is the compressor efficiency, which is directly linked to engine fuel consumption. Tests (Wöhr et al 2014) show that a 4% raise in compressor efficiency decreases fuel consumption by 1% at full load. Transferring the engine data of the load cycles to the corresponding compressor maps shows the regions where a reduction of compressor losses is most beneficial. Although the two diagrams in Figure 1 vary widely the outcome for the centrifugal compressor as can be seen in Figure 2 is very similar. It is not only the compressor peak efficiency that needs to be raised in order to save fuel for both duty cycles but rather the efficiency level close to the full load curve between the surge margin and the parabola of maximum efficiency. Under the premise of keeping the compressor size constant the adjustable geometric features of a variable compressor have to minimize the losses in the left half of the compressor map for all speeds.

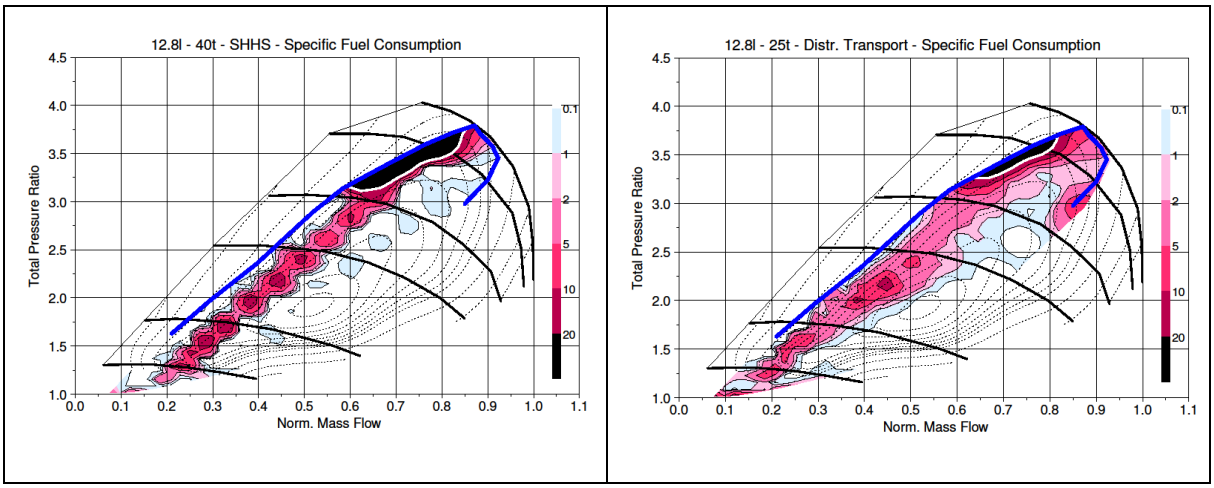

Fig. 2. Fuel consumption distribution rate in compressor map

2.3 Low-End Torque and Altitude Power Reduction

For reasons of downspeeding and driveability the torque at small engines speeds needs to be increased and the operating point of maximum torque has to move to lower engine speeds. This would mean for the full load curve in the compressor map to move to the left but soot- and surge limit stand in the way of this endeavor. Soot as a result of a combustion air deficit arises from the severely dropping compressor efficiency at small mass flow rates throughout all compressor speeds. To allow for higher torque at low engine speeds, losses that occur in the complete left half of the compressor map have to be minimized. Furthermore the surge limit has to move to the left which means the point of total flow reversal of a speedline needs to emerge at lower mass flow rates and/or higher pressure ratios.

High Altitude power reduction occurs when the air density and/or ambient temperature call for higher compressor rotational speeds and higher compressor outlet temperatures than allowed by material specifications. In this case the engine has to derate fuel injection in order to keep the speeds and temperatures at a level where durability is not affected. To avoid derating, shaft speed and outlet temperatures at a given operating point have to be lowered. Figure 3 indicates that the temperature critical region is located in the upper left corner of the compressor map. This is where efficiency has to be raised in order to avoid a temperature related derating. At high speeds more pressure build up is needed in order to accomplish the same pressure ratio at lower speeds and thus prevent critical rotational speeds at all mass flows.

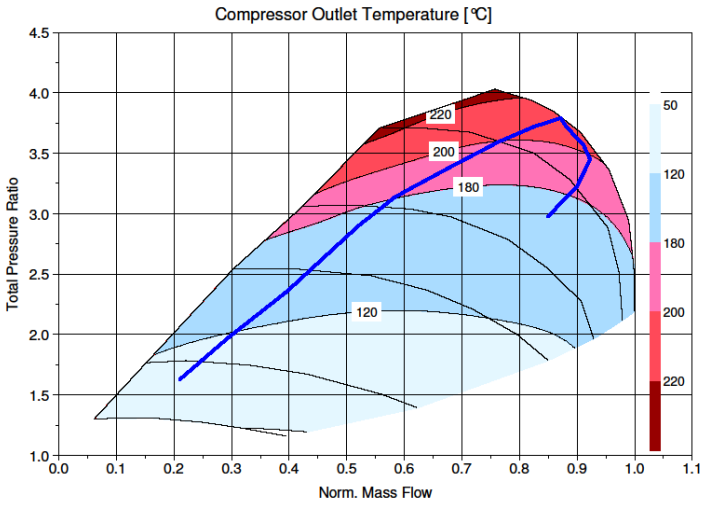

Fig. 3. Compressor outlet temperature map

2.3 Engine brake, Dynamics, Noise

The engine brake system has to be capable of dissipating more energy than stated by the engine power rating. While in braking mode the compressor operates at high mass flow rates and low pressure ratios. Its maximum speed limits the braking power output. It is reached not only because of the low boost pressure but also for the proximity to the choke margin. Compressor efficiency at high mass flow rates deteriorates very fast; pressure losses therefore are very high. Consequently two options are available for more braking power. An increase in pressure ratio or choke mass flow, both allow for higher masses at low pressure to be compressed and therefore enable more power supplied by the engine brake.

The turbocharger lag which is the most significant reason for deficient engine dynamics is caused by insufficient air supply to the engine at a load step. Besides increasing power delivery to the rotor at low engine load and speed by decreasing the turbine size or utilizing a variable turbine geometry, there are three alternatives that involve the centrifugal compressor:

1.) Decrease rotor inertia
    a. The rotor can accelerate faster when the inertia is smaller. However the compressor mass is very small compared to the turbine and so the leverage is negligible.
2.) Decrease difference of rotor speeds for load jump operating points
    a. Fewer revolutions needed for the same pressure ratio at the end of a load jump means less speed difference and thus less energy that has to go into the rotating system to speed up the inertia. An increase in specific work or efficiency is needed to keep the speed band as narrow as possible.
3.) Raise compressor efficiency
    a. A more efficient compressor at the operating points where the load step takes place implies directly a benefit to boost pressure and therefore air-supply.

Engine part load operating points correspond mainly to the center of the centrifugal compressor map and thus to the region of maximum efficiency. Along the way to the full load, the compressor passes through the left half of the compressor map until the full load curve is reached. Hence, analogous to the compressor conclusions arising from the engine efficiency target, the isentropic efficiency has to be raised at low mass flow rates for all speeds.

Turbocharger noise emissions can either arise from imbalance issues, commonly named as first order noise, from supersonic shocks at the impeller blade tips at very high rotational speeds or from flow incidence effects. Possible solutions are: Decrease of rotor speed by increasing the compressor specific work input at high speeds or decrease of the angle of incidence and flow turbulence at the impeller inlet.

2.4 Thermal Management, Costs, Durability

Engine exhaust gas after-treatment systems require high temperatures for catalysis or to burn soot residues in the diesel particulate filter. Piston outlet temperatures however meet those requirements only at high load and low engine speeds. If an engine is operated mainly at part load (e.g. city busses) the engine has to switch to specific regeneration modes for short time periods. The timing and procedure of these cycles is called thermal management. These can be backed by the charging system and a variable compressor respectively by preserving the compressor map width but deteriorating its efficiency. This way the temperature at position 2 after the compressor rises. This enables a higher piston outlet temperature.

Costs can emerge from the expenses of a single turbocharger or the need of a charging system with two or more turbo machines. Variable geometries can hardly reach the price of a fixed geometry but may help to avoid multiple charging systems depending on the requirements of the engine. Multi staged charging systems as used when the manifold intake pressure is higher than can be delivered by a single turbo can be replaced by a variable system that allows for higher pressure. Sequential turbo systems are commonly used when the engine needs a wider operating map than a single compressor has to offer. In this case a variable geometry needs to either move the surge margin to the smaller or the choke line to higher mass flows.

High and alternating rotational speeds of the turbocharger are main drivers for fatigue failures. Reducing speed and thus reducing the magnitude of speed differences at different operating points means the compressor has to raise its pressure ratio at all speed lines or utilize a variable system where the compressor can deliver all pressure ratios at a single speed by adjusting the specific work input.

2.5 Summary

In the previous subsections all engine goals are linked to desired compressor characteristics. These are mainly:

- Higher Efficiency at low flow rates Eta_lowMF
- Higher maximum efficiency Eta_max
- Higher pressure ratio PR
- Surge margin at lower flow rates Surge
- Choke margin at higher flow rates Choke

Matching engine and compressor goals in a matrix offers the opportunity to cluster both engine and compressor targets:

Table 2 Overview of compressor goals

Engine type / goal	Eta_lowMF	Eta_Max	Surge	PR	Choke
Decrease of fuel consumption	+++	+			
Increase of Low-End Torque	+++		+++		
Improvement of Dynamics	+++		++	+++	
Improvement of Durability		+++		+++	
Decrease of Altitude Power Loss		+++		+++	+++
Noise Reduction		+++		+++	+++
Improvement of Engine Brake				+++	+++

Not mentioned in the table above is the support for thermal management which can only be established by deteriorating compressor efficiency.
One can see that there are engine goals which conclude the same or similar compressor goals, e.g. durability and noise, both have the need for lower rotational speeds or efficiency and low end torque which have the need for higher compressor efficiency at low flow rates. Accomplishing one compressor goal means that multiple engine objectives may profit.

3. Aerodynamics

The following section identifies the aerodynamic shortcomings and constraints of a fixed geometry compressor with regards to the compressor goals as named in Table 2. This leads to the formulation of fluid dynamic requirements that need to be considered implementing a variable geometry compressor in order to achieve the engine objectives as stated in section 1.

3.1 Pressure Ratio and Efficiency

As derived in (Japikse 1996) the pressure ratio at a given rotational speed ω is a result (simplified by ignoring disk friction, cavity leakage and recirculation work) of the specific work w_s and compressor efficiency:

$$\Pi_{tt} = \left(1 + \frac{\eta}{C_p T_{1t}}(w_s)\right)^{\frac{\kappa}{\kappa-1}} \quad (2)$$

$$w_s = \omega(r_2 c_{\theta 2} - r_1 c_{\theta 1}) \quad (3)$$

Assuming constant compressor efficiency, there are only four ways to raise the total-to-total pressure ratio:

- Reduce Inlet diameter (only if there is swirl $c_{\theta 1}$)
- Decrease positive swirl or induce negative swirl at the inlet
- Increase outlet diameter
- Increase outlet tangential velocity

With respect to the development of a variable geometry compressor, especially the first two terms can be used for manipulating the specific work input. The latter two will be hard to implement without severe efficiency loss.

Besides raising the specific work another possibility to increase pressure ratio at constant speed is to raise compressor efficiency. Unfortunately this cannot be analyzed by simple equations but needs to be investigated with the help of 1D calculation tools and 3D-CFD. Utilizing one dimensional fluid equations as derived and validated in (Hamann et al 2014) the flow states at the interfaces between impeller, diffuser and volute can be evaluated and analyzed. This way the loss distribution for the whole compressor map can be made visible. One can see in Figure 4 that diffuser and volute do not only account for the majority of losses at every operating point at high speeds but the losses after the impeller even increase compared to the impeller at low mass flow rates. This shows that adjustable geometric features in the flow after the impeller have the most potential to increase overall efficiency and especially to reduce losses at low mass flow rates.

Main reason for the entropy production in the diffuser, especially at high speeds is the high Mach number of the fluid exiting the impeller. Mach numbers even increases at decreasing mass flow rates because the impeller blades are strongly backswept. At a given rotor speed, backsweep angle and impeller outlet temperature, the absolute outlet Mach number Ma_2 can be calculated with:

$$Ma_2 = \frac{\sqrt{2{c_{m2}}^2 + (u_2 - \tan(\beta_2)c_{m2})^2}}{\sqrt{\kappa R T_2}} \qquad (4)$$

This function has a minimum at:

$$c_m = \frac{\tan(\beta_2)u_2}{\tan(\beta_2)^2 + 2} \qquad (5)$$

and corresponds to meridional velocity at the point of maximum efficiency of the centrifugal compressor. According to (Krämer 2010) total pressure losses are proportional to squared velocity. Therefore major parts of the decreasing efficiency to the left and right of efficiency peak originate from increasing impeller outlet Mach number. Analyzing 3D-CFD-Simulations shows further reasons for losses at low mass flows. Values displayed in Figure 4b depict the dissipation power generation as derived in (Herwig and Kock 2007) and thus spots in the fluid regime that account for a decrease in efficiency. The high loss region right after impeller exit can be attributed to highly non uniform flow (Jet/Wake, described in (Eckardt 1975)) combined with high Mach numbers. Throughout the whole diffuser the fluid particles move on a logarithmic spiral (Japikse 1996): The smaller the mass flow, the higher the flow angle and thus the longer the flow path in the diffuser. The boundary layer thickens. Combined with the diffusion in the volute because the flow states are apart from the optimal design conditions the heavily weakened boundary layer may separate. This results in the loss region at the volute inlet.

A majority of loss mechanisms in the left half of the compressor map base on the high flow angle due to the high tangential velocity in the diffuser. Reducing tangential velocity means reduced Mach numbers, reduced flow path, thinner boundary layers and better flow conditions at volute inlet. Losses at high mass flows are mainly correlated to high Mach numbers due to high meridional velocity and the proximity of the choke margin which is analyzed in the next section.

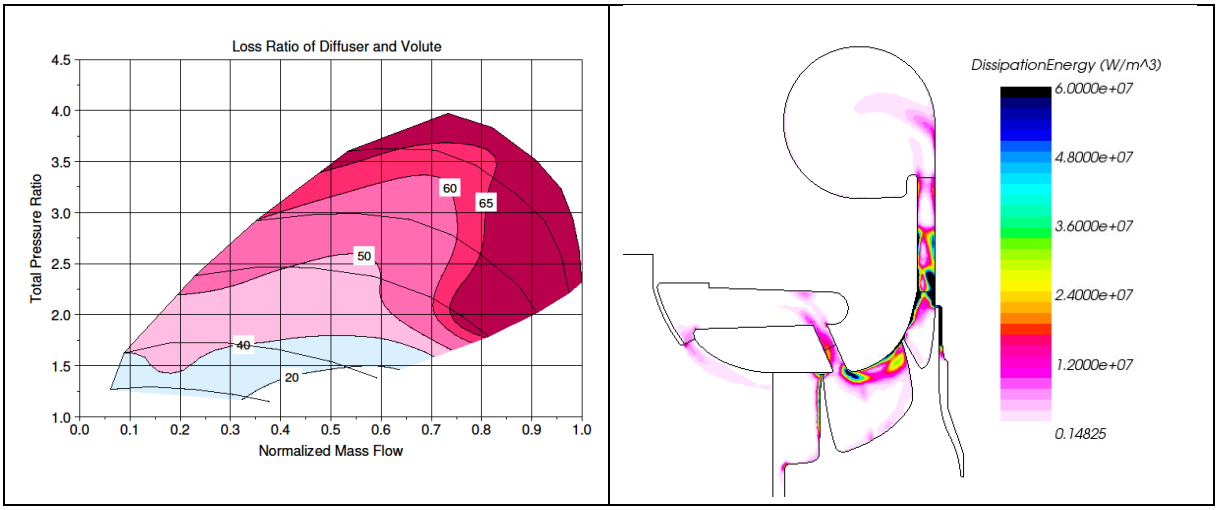

Fig. 4. a) 1D Loss Ratios (Hamann 2012) **b)** 3D-CFD loss analysis

3.2 Choke and Surge

Figure 5 shows the supersonic areas in the fluid regime at choke operating point. The surface where the fluid enters this supersonic area determines the narrowest cross section. In contrast to the classical convergent-divergent nozzle problem, this area of Mach1 transition is not straight but very curved. Supersonic speed is first reached at about 80% hub-to shroud after the ported shroud suction slot

from where it spreads to both sides until further downstream the whole passage is covered with supersonic fluid. Before reaching the strong shock in the diffuser that is accountable for heavy losses some fluid particles decelerate in the channel before they reach Mach1 again at the impeller exit.

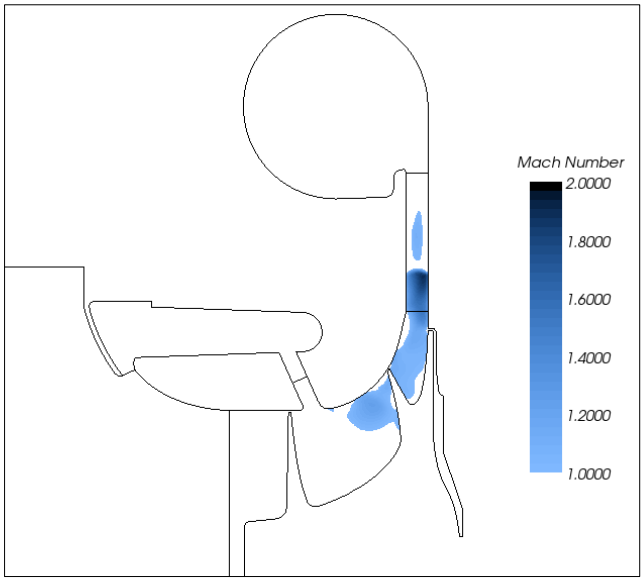

Fig. 5 Supersonic Flow Distribution at Choke

Besides raising charge air temperature before entering the compressor the only other way of increasing choke mass flow is to widen the narrowest cross section. If done locally at one point in the compressor, this will move the critical area further downstream with only little positive effect. Hence the whole channel cross section beginning after the suction slot of the ported shroud until the end of the pinch has to be widened in order to reach a distinct raise in choke mass flow.

The aerodynamic reasons for surge cannot be named in a similar simple fashion. Surge characteristics depend on the system in which the compressor is used and is a highly transient phenomenon. Flow separations in combination with a positive gradient of the speed line in the compressor map lead to complete flow reversal. To avoid surge a negative gradient of the speed line has to be maintained by reducing the losses that occur in the left half of the compressor map or raising the specific work.

3.3 Summary

In summary four aerodynamic goals are identified in order to reach the identified compressor requirements. These are:

- Tang. Vel. Diffuser – Decrease the tangential velocity in the diffuser
- Impeller Flow Area – Increase the Impeller Flow Area
- Neg. Preswirl – Decrease positive preswirl or induce negative swirl at impeller inlet
- Inlet Diameter – Decrease Inlet diameter, only effective if there is a preswirl

These aerodynamic goals can now be linked to the compressor requirements that can be met.

Table 3 Overview of aerodynamic goals

	Tang. Vel. Diffuser	Impeller Flow Area	Neg. preswirl	Inlet diameter
Eta_Max	x			
Eta_lowMF	xxx			
Surge	xxx		x	x
PR			xxx	xxx
Choke		xxx		

The aerodynamic objectives point to geometric measures that have to be implemented to reach the compressor and hence engine targets. The conclusions of these forethoughts lead to the following concepts:

- Decrease the tangential velocity in the diffuser with the help of **Variable Diffuser Vanes** for more efficiency at low mass flow rates and a better surge margin. Less fuel consumption and better low end torque characteristics will be the engine benefits.
- Raise the specific work output with the help of less or negative preswirl for turbocharger downspeeding and thus better engine dynamics, durability and less noise. **Variable Inlet Guide Vanes** and concepts with variable inlet diameter (Benz et al. 2011) can be used.
- Increase impeller flow area for more choke mass flow, less efficiency loss at high mass flows and thus better engine brake capabilities and widening of the compressor map which may avoid the use of multiple turbochargers. **Variable Ported Shroud** concepts may arise from this requirement.

The challenge of developing a variable compressor system to use with an internal combustion engine will not only be to reach one of the aerodynamic, compressor and engine goals but to maintain the performance of a non-variable system that is essential for all the remaining engine goals and restrictions as pointed out in section 2.

Conclusions

Analysis of the engine goals to be reached with a variable geometry compressor shows that for heavy duty engines the main objectives are increasing engine efficiency and the ability to raise low end torque. Support for thermal management and the improvement of the engine brake system are also of importance whereas high altitude power reduction, durability and noise act more as constraints for variable compressor systems that should not worsen. The weighting and ranking of these targets differs for medium duty engines whereby the top rated decrease of fuel consumption and increase of low-end torque keep their top priority position.

Fuel consumption data for two contrasting load cycles is transferred from the engine operating map to the compressor map. This reveals the need to increase compressor efficiency at low mass flow rates for all speeds close to the full load curve. This will be equally beneficial to the enhancement of maximum torque at low engine speeds. The majority of the remaining engine objectives aim for reduction of the rotational speed which can mainly be done by increasing the specific work for a given compressor size.

Aerodynamic analysis as the next step points out that a negative preswirl induced for instance by variable inlet guide vanes is a possible way of manipulating rotor speed. Evaluation of 1D and 3D-CFD calculations shows that a reduction of tangential velocity in the diffuser is not only very beneficial for the efficiency at low mass flow rates but also holds the capability to influence the surge margin and thus helps to accomplish the needed torque at low engine speeds. This way the two top heavy duty engine priorities can be accomplished with only one aerodynamic action.

Manipulating tangential velocity without risking flow separation or back-flow in the diffuser can only be done with the use of guide vanes. The importance of efficiency calls for aerodynamic airfoil vanes (contrary to wedge type vanes that raise static pressure but have poor loss characteristics) with a round or elliptic tip to account for the heavily inhomogeneous flow conditions at impeller outlet. This will also help to minimize readjustments due to varying vane inlet flow angles throughout the compressor map. The static vanes themselves have to maximize the compressor efficiency in the left half of the compressor map whereas the variability has to ensure that the map width does not deteriorate in order to comply with the identified performance restrictions as for instance durability and noise.

References

Benz A, Grigoriadis P, Sens M (2011) Variable Trim Compressor (VTC) – Ein neuer Ansatz für eine variable Verdichtergeometrie. 16. Aufladetechnische Konferenz, Dresden, Germany.

Berenyi S, Raffa C (1979) Variable Area Turbocharger for High Output Diesel Engines. No. 790064. SAE Technical Paper, 1979.

Eckardt D (1975) Instantaneous measurements in the jet-wake discharge flow of a centrifugal compressor impeller. Trans ASME Journ Eng for Power, pp. 337-345

Fraser N, Fleischer T, Thornton J, Rueckauf J (2007) Development of a Fully Variable Compressor Map Enhancer for Automotive Application. SAE International 2007-01-1558

Hamann M, (2012) Experimentelle Parameterstudie zur Optimierung eines Radialverdichters im Hinblick auf Kennfeldbreite und Spitzenwirkungsgrad. Diplomarbeit an der Universität Stuttgart

Hamann M, Chebli E, Müller M, Krampitz A (2014) Enhancing the centrifugal compressor performance map measurements through a developed one-dimensional calculation tool to analyse local flow phenomena. ASME Paper No. GT2014-26720

Herwig H, Kock F (2007) Direct and indirect methods of calculating entropy generation rates in turbulent convective heat transfer problems. Heat Mass Transfer (2007) 43: 207-215

Japikse D (1996) Centrifugal Compressor Design and Performance. Concepts ETI.

Krämer E (2010) Strömungslehre I und II. Universität Stuttgart.

Lang O, Habermann K, Wittler M (2006) Verbesserung des Betriebsverhaltens von Turbomotoren durch Verdichtervariabilitäten. 11. Aufladetechnische Konferenz

Müller M, Sumser S, Feldersbacher P, Rößler K, Hertweck G, Fieweger K, Bauer H (2005) Ist quasidrehzahlstationäre Abgasturboaufladung für PKW-Motoren möglich ? 10. Aufladetechnische Konferenz

Oatway T, Harp J (1973) Investigations of a variable geometry compressor for a diesel engine turbocharger. No. SR-21. THERMO MECHANICAL SYSTEMS CO CANOGA PARK CA, 1973

Schenkel S, Löffler P, Müller W (2004) Einfluss eines beschaufelten verstellbaren Verdichter-Diffusors auf den Aufladegrad von Nfz-Motoren. 9. Aufladetechnische Konferenz

Uchida H, Kashimoto A, Iwakiri Y (2006) Development of wide flow range compressor with variable inlet guide vane. R&D Review of Toyota CRDL Volume 41/3

Wallace F, Whitfield A, Atkey R (1975) Experimental and theoretical performance of a radial flow turbocharger compressor with inlet prewhirl. Proceedings of the Institution of Mechanical Engineers Vol 189 Pages 177-186

Wöhr M, Chebli E, Stiller M, Müller M, Leweux J, Gorbach A, Zellbeck H (2014) Entwicklung eines variablen Verdichters für schwere Nutzfahrzeugmotoren – Bewertung beschaufelter Diffusoren als Basis für eine Variabilität. 19. Aufladetechnische Konferenz

Mazda's future powertrain strategy and development status of new internal combustion engines

Y.Terazawa[1]

[1]Mazda Motor Corporation - 3-1, Shinchi Fuchu-cho, Aki-gun Hiroshima 730-8670 Japan

E-mail: terasawa.y@mazda.co.jp
Telephone: +81(0) 82 565 1393
Fax: +81(0) 82 287 5131

Abstract. Mazda introduced SKYACTIV-G and SKYACTIV-D into the market as the first generation engines that represented the company's environmental strategy focusing on the internal combustion engine. Continuous refinement of them is taking place to maintain their competitive advantage to highly boosted downsized engines. In parallel, the development of next generation engines is being accelerated to achieve hybrid-level fuel economy without help of an electric drive system. To realize such a gasoline engine, HCCI combustion in a wide operating range as well as a technology equivalent to variable compression ratio by further improving combustion are under study. As for the diesel engine, Mazda aims for a 10% reduction in fuel consumption compared to SKYACTIV-D by improving homogeneity of an air-fuel mixture. This paper focuses on the improvement roadmap for Mazda's internal combustion engine including the latest status and the overview of the above-mentioned engine developments.

1. Introduction

Mazda's basic philosophy is to provide all customers who purchase Mazda cars with the joy of driving, excellent environmental and safety performance.

This is based on the belief that the best contribution to the environment is to incorporate superior and affordable technologies into every car model rather than limiting expensive technologies to certain eco cars.

According to Mazda's prediction, the internal combustion engine will be the power source of the majority of cars even in 2030. This indicates that no improvement in the efficiency of the internal combustion engine means no contribution of cars to the environment.

For this reason, Mazda thoroughly pursues and continues to evolve "ideal combustion" focusing on the internal combustion engine. Improving the efficiency of the internal combustion engine is equal to reducing exhaust loss, cooling loss, pumping loss and mechanical loss. Control factors in reducing the losses are compression ratio, specific heat ratio, combustion period, combustion timing, heat transfer to cylinder wall, pressure difference between intake and exhaust gases, and mechanical friction. In short, the quest for the ultimate internal combustion engine involves efforts to bring these factors closer to the ideal state. As shown in Fig.1, Mazda considers that the gasoline engine and the diesel engine should take the same approach to achieve ideal combustion. It is therefore Mazda's policy to evolve these control factors continuously so that both types of engine will step closer to the same ultimate goal.

This paper introduces the gasoline engine and the diesel engine developed in line with this policy, and in addition, it describes the next generation engines focusing on aspects to be evolved and the development status.

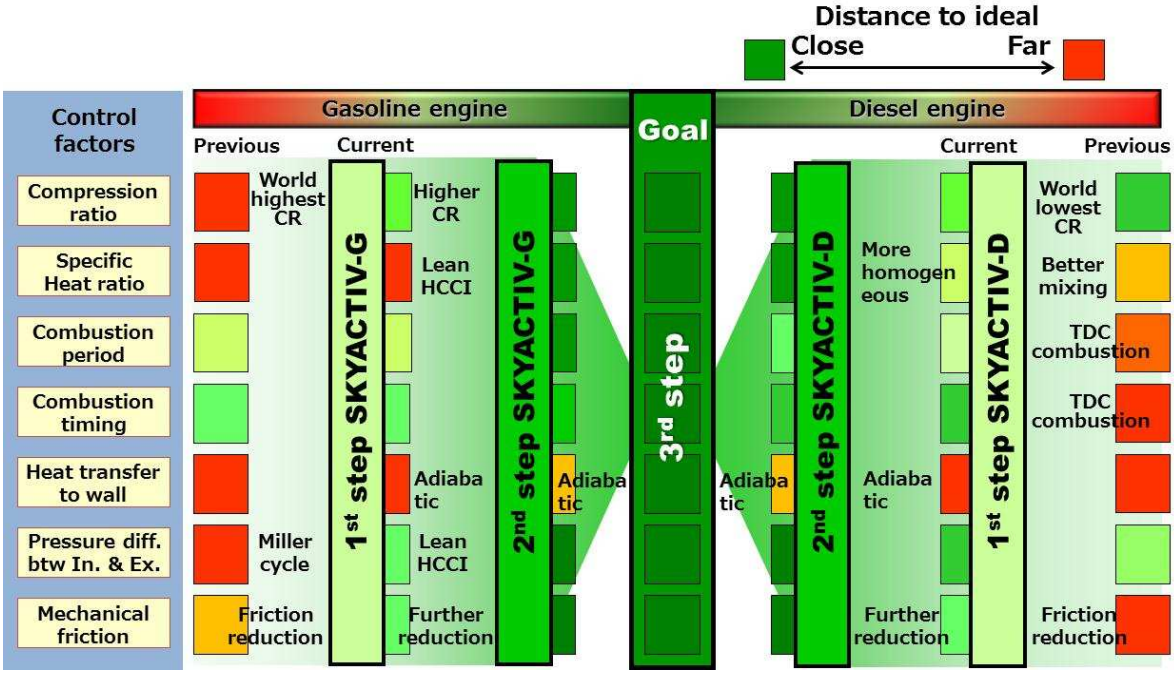

Fig. 1. Roadmap for ultimate internal combustion

2. Development of the first generation SKYACTIV

2.1 First generation SKYACTIV-G

"SKYACTIV" is a generic name for next generation technologies which embody Mazda's concept of the joy of driving, excellent environmental and safety performance. The first generation SKYACTIV was developed in the late 2000s.

The first generation gasoline engine, SKYACTIV-G1, was commercialized in 2011. It is characterized by the world's highest compression ratio of 14 as well as a significant reduction in mechanical friction, which led to a 15% fuel consumption reduction compared to the previous model. To maximize the fuel consumption reducing effect of the high compression ratio, Mazda developed a cavity piston with a devised shape, increased combustion speed by maintaining tumble flow and reduced cooling loss.

In the early phase of the development, Mazda investigated the torque lowering rate at a compression ratio of 15 and observed an unexpectedly small falling rate (Fig.2). The heat release rate in Fig.3 indicates that setting a high compression ratio induced a chemical reaction to occur before ignition. (Mazda calls this low-temperature oxidation reaction.) This finding gave a bright prospect for achieving high torque. In fact, SKYACTIV-G1 achieved 15% higher torque than the previous model. This is due to the reduction in residual gas by utilizing exhaust pulsation of a 4-2-1 long exhaust system as well as a combustion chamber designed to enable rapid combustion.

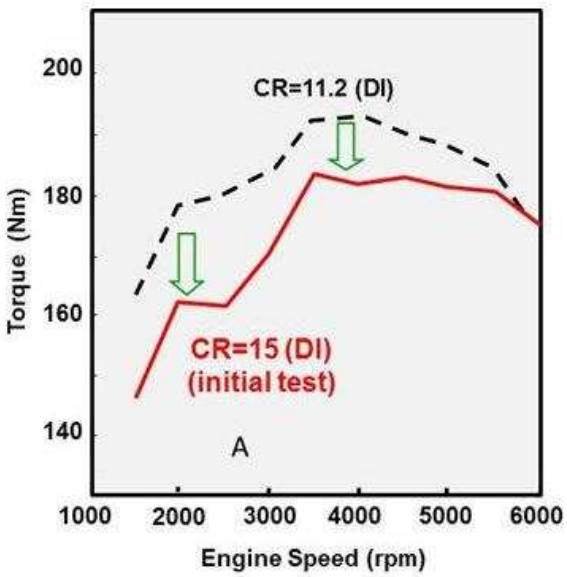

Fig. 2. Torque curve of high compression ratio

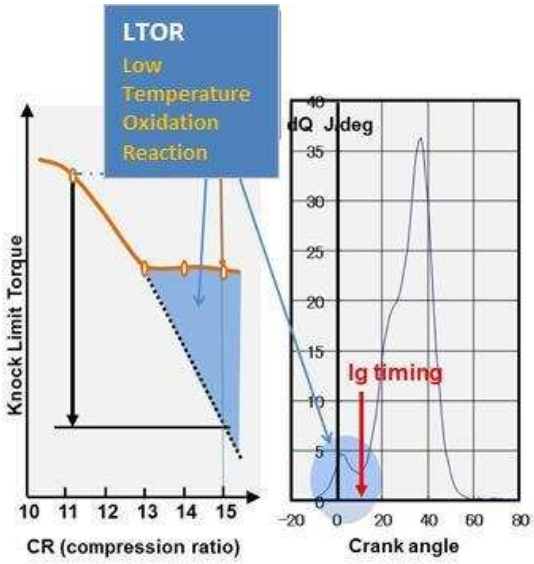

Fig. 3. Low temperature oxidation reaction

2.2 First generation SKYAVTIV-D

The first generation diesel engine, SKYACTIV-D1, was commercialized in 2012. It is characterized by the world's lowest compression ratio of 14. The low compression ratio was a means to improve air-fuel mixing for the realization of TDC combustion, but it also contributed to reduction in mechanical friction. The combination of these positive effects resulted in a 20% fuel consumption reduction.

Conventional engines required a high compression ratio to ensure combustion stability. Ignition of an insufficiently mixed air-fuel mixture in a cylinder led to the generation of soot and NOx. To avoid the issue, the start of combustion had to be delayed by initiating ignition while the piston was descending. In the case of SKYACTIV-D1, high expansion ratio combustion can be initiated at TDC as its low compression ratio allows for sufficient mixing of air and fuel, suppressing the generation of soot and NOx (Fig.4).

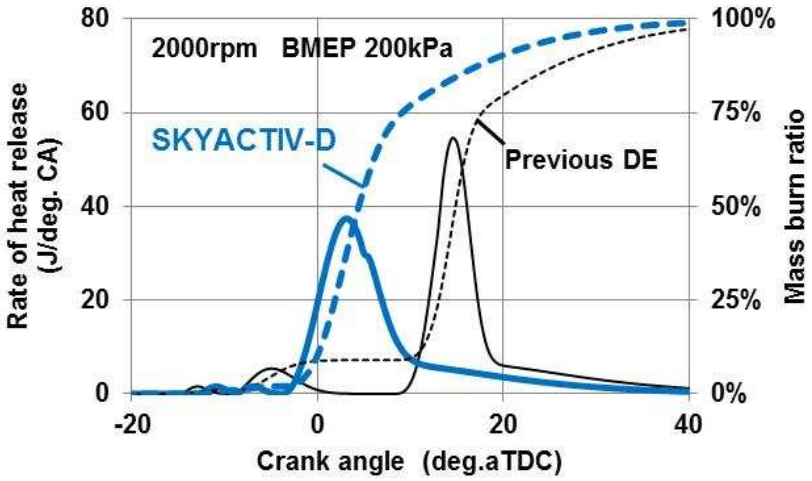

Fig. 4. Combustion timing difference

Lowering a compression ratio is also effective to reduce mechanical friction. A low compression ratio engine requires lower peak firing pressure to produce the same torque as a high compression ratio engine. This makes it possible to design lower-rigidity and lightweight reciprocating and ro-

tating parts, which generate approximately half of diesel engine's mechanical friction. The lower-rigidity reciprocating and rotating parts also enable SKYAVTIV-D1 to realize smooth acceleration up to 5000 rpm. This is higher than the previous model by 1000 rpm.

Deterioration in ignitability, a side effect of lowering a compression ratio, is suppressed by initiating pre-combustion which generates a certain amount of heat production prior to main combustion. In addition, the exhaust valves open twice to increase cylinder temperature especially when ambient temperature is extremely low, multi-hole fuel injectors and precise multiple injections suppress excessive dispersion of a mixture, and a two-stage turbocharger increases boosting efficiency from no load. With these measures, SKYACTIV-D ensures stable combustion.

2.3 Refinement of the first generation SKYACTIV

SKYACTIV G1 and D1 are currently being upgraded aiming to reduce mechanical friction further by controlling coolant flow for rapid warm-up. In the case of the diesel engine, low-pressure EGR will be used to reduce pumping loss so that further reduction in fuel consumption can be achieved.

3 Next generation SKYACTIV

3.1 Next generation SKYAVTIV-G

In parallel to the upgrading activities, Mazda is pursuing the development of the second generation engines aiming to achieve hybrid-level fuel economy based only on the internal combustion engine.

In the case of the gasoline engine, its compression ratio and specific heat ratio should be raised so that thermal efficiency steps closer to the ideal (Fig.5). To estimate thermal efficiency, Mazda performed zero-dimensional analyses on compression ratio, specific heat ratio, combustion start timing, combustion period and heat transfer to cylinder wall. According to the estimate, thermal efficiency at 2000 rpm and light load (pi = 300 kPa) would be brought closer to the ideal by setting a compression ratio at 18, excess air ratio between 3 and 5, and combustion duration within 20 crank angle degrees.

Increasing an excess air ratio to generate a lean mixture leads to lower flame temperature. On the other hand, in-cylinder pressure rises, which increases heat transfer to cylinder wall and consequently increases cooling loss. This indicates that there is an optimum value of excess air ratio. Mazda's estimate shows the optimum value is between 3 and 5 from the viewpoint of heat transfer to cylinder wall. As cooling loss increases with a rise in compression ratio and specific heat ratio, a method to suppress heat transfer to cylinder wall is also necessary for thermal efficiency improvement.

The problem in realizing lean burn by a compression ratio of 18 and a specific heat ratio higher than 3 is that significantly low burning speed of a lean mixture makes it difficult to ensure stable combustion. Mazda is therefore exploring the possibility of HCCI.

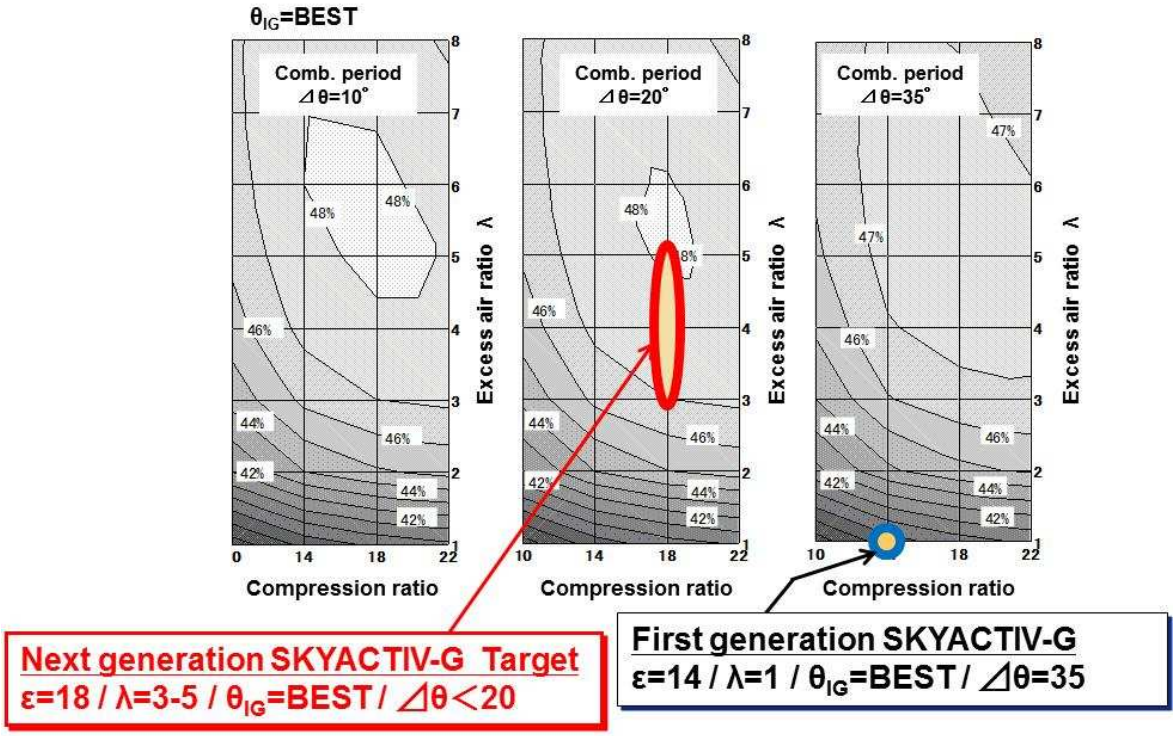

Fig. 5. Target of next generation SKYACTIV-G

The main challenge in HCCI combustion is to expand its limited operating range, which Mazda overcame by increasing the compression ratio and opening the exhaust valves twice.

HCCI combustion requires cylinder temperature suitable for compression ignition. Possible methods to attain the required temperature are to create negative valve overlap (NVO) and to open the exhaust valves twice (the second time in the intake stroke). Mazda set compression ratio as the parameter and calculated Tivc and Ttdc of both methods. The results indicate that opening the exhaust valves twice produces a larger temperature rise along with the increase in compression ratio (Fig.6). On the other hand, cooling loss during NVO becomes larger along with the increase in compression ratio.

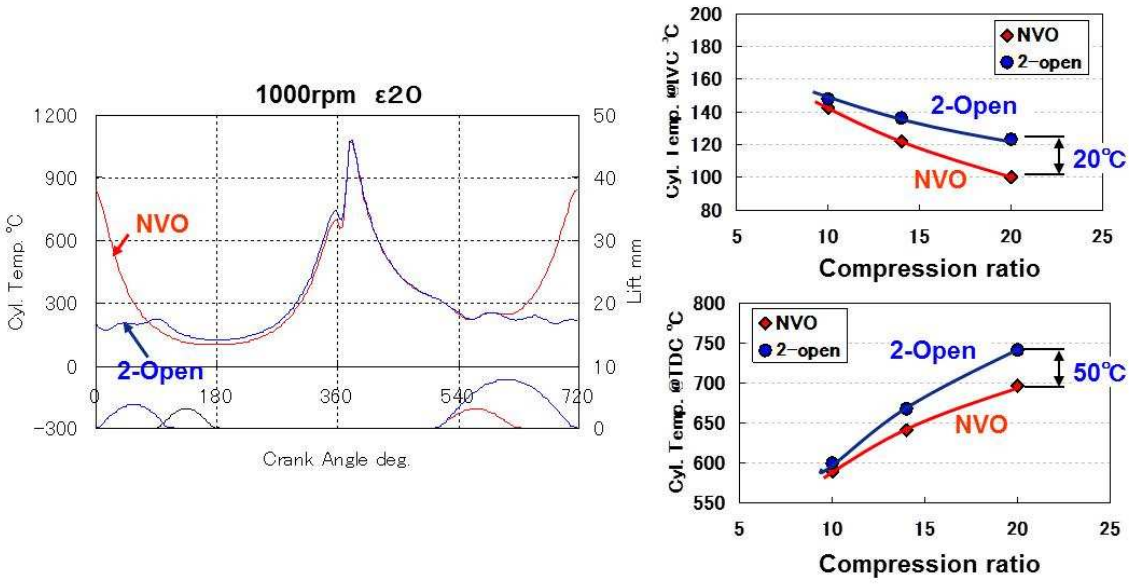

Fig. 6. Cylinder temperature difference between opening exhaust valves twice and NVO

As stated above, increasing a compression ratio contributes to the expansion of HCCI operating range. Figure 7 shows comparison of heat release rates at extremely light load between different compression ratios. Combustion gravity center can be advanced by increasing a compression ratio. Due to small fuel injection quantities, flame temperature is low at extremely light load. It is therefore advantageous to raise cylinder temperature by near-TDC combustion and reduce unburned fuel loss although cooling loss is increased by near-TDC combustion.

Increasing a compression ratio also helps to expand HCCI operating range to a higher load region. The upper limit of the range is defined by combustion sound. However, when suitable in-cylinder conditions are set for compression ignition, it is possible to retard combustion while maintaining appropriate combustion duration without causing misfire or hitting the limit defined by combustion sound (Fig.8).

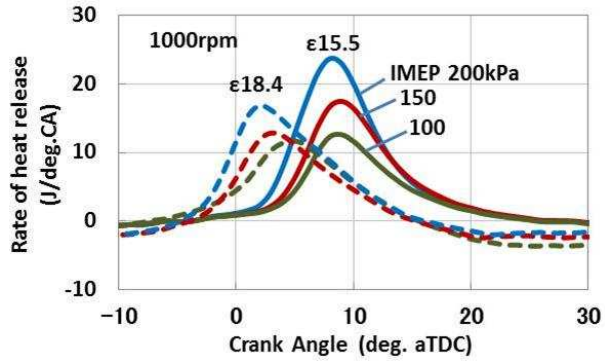

Fig. 7. Effect of compression ratio on HCCI

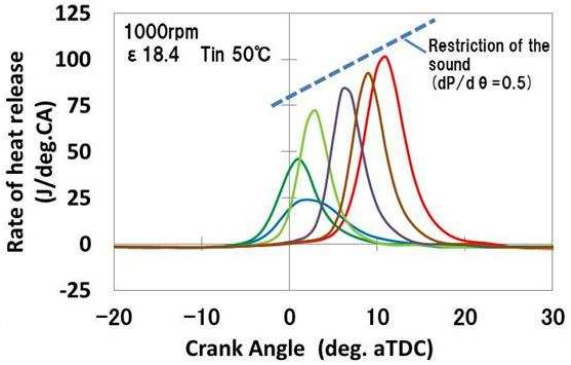

Fig. 8. Rate of heat release of HCCI at different loads

3.2 Next generation SKYAVTIV-D

In the case of the diesel engine, its specific heat ratio and heat transfer to cylinder wall should be improved so that thermal efficiency steps closer to the ideal (Fig.1). Mazda performed zero-dimensional analyses to estimate the effects of improving these factors.

Although the average G/F of the diesel engine is lean, the G/F of a local combustion zone is rich. If the specific heat ratio at middle load is increased by homogenizing such heterogeneous combustion, thermal efficiency improves by approximately 2 points at a maximum. If the average excess air ratio is increased 1.5 times by enhancing boosting efficiency, thermal efficiency improves by approximately 2 points (Fig.9). This indicates that the following two approaches are required to increase a specific heat ratio. One is to improve the average specific heat ratio by raising air content with a turbocharger. The other one is to improve local specific heat ratios by mixing air and fuel well. These approaches are also effective to shorten too long a combustion period at middle load.

At light load, where the average excess air ratio is sufficiently high and combustion periods are sufficiently short, it is effective to reduce cooling loss. If heat transfer to cylinder wall is decreased by half, thermal efficiency improves by approximately 4 points (Fig.10). Effective methods for reducing heat transfer are to reduce flame temperature near cylinder wall by attenuating over-rich areas and to control overexpansion of a mixture so that a compact combustion zone can be formed and the flame can be kept as far away from cylinder wall as possible. Figure 11 shows an example of suppressing spray penetration in a small fuel quantity region at light load. As a result of suppressing the contact between the combustion chamber wall and the flame, cooling loss decreased and thermal efficiency improved by 4%.

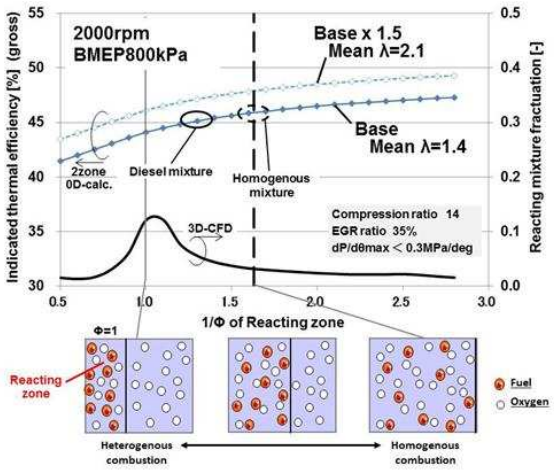

Fig. 9. Thermal efficiency improvement by increasing specific heat ratio at middle load

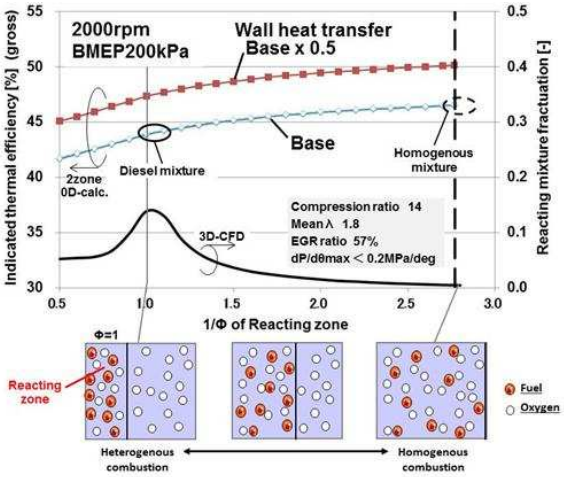

Fig. 10. Thermal efficiency improvement by suppressing heat transfer to cylinder wall at light load

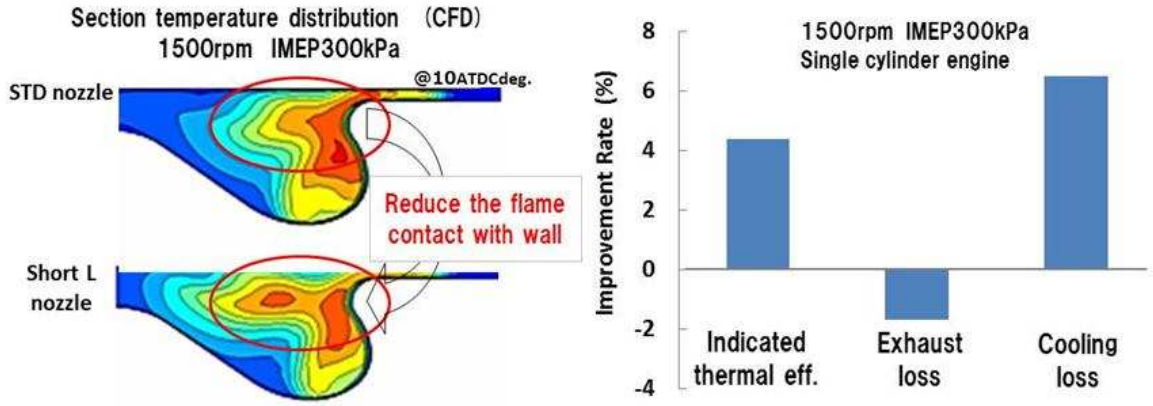

Fig. 11. Example of cooling loss reduction

Conclusions

To improve the efficiency of the internal combustion engine means to reduce various losses. The first generation SKYACTIV gasoline and diesel engines achieved 15 to 20% improvement in fuel consumption with a compression ratio of 14. Thermal efficiency will step closer to the ideal with a compression ratio raised to 18 and an excess air ratio between 3 and 5. However, as raising a compression ratio and a specific heat ratio leads to an increase in cooling loss, this approach should be combined with a method to suppress heat transfer to cylinder wall.

Through the development of the second generation engines, Mazda aims for 10% reduction in diesel fuel consumption compared to SKYACTIV-D1. In the case of the gasoline engine, an even larger reduction is expected.

References

Hidetoshi Kudo, Ichiro Hirose, Tatuhiro Kihara, Masahisa Yamakawa, Mitsuo Hitomi (2011) Mazda SKYACTIV-G 2.0L gasoline engine: Proceeding of 20th Aachen Colloquium Automobile and Engine Technology vol1 P111

Masahisa Yamakawa, Takashi Youso, Tatsuya Fujikawa, Toshiaki Nishimoto, Yoshitaka Wada, Kiyotaka Sato, Hideaki Yokohata (2011) Combustion technology development for a high compression ratio SI engine. SAE paper 2011-01-1871

Mitsuo Hitomi (2013) The future prospect of internal combustion engines: Proceeding of 22nd Aachen Colloquium Automobile and Engine Technology vol1 P5

Takashi Sakono, Eiji Nakai, Motoshi Kataoka, Hiroshi Takamatsu, Yasuyuki Terazawa (2011) Mazda SKYACTIV-D 2.2L diesel engine: Proceeding of 20th Aachen Colloquium Automobile and Engine Technology vol2 P943

An investigation on the performance of the Combined Diesel-Brayton Cycle engine

Hailong HE[1], Weilin ZHUGE[1*], Kaisheng HUANG[1], Yangjun ZHANG[1], Sheng LIU[2]

[1] State Key Laboratory of Automotive Safety and Energy, Tsinghua University, Beijing 100084, China
E-mail: zhugewl@tsinghua.edu.cn
Telephone: +(86) 1062789662
[2] China North Engine Research Institute, Tianjin 300400, China
E-mail: lutliu@163.com
Telephone: +(86) 2258707309

Abstract: Combining the advantages of the Diesel cycle and the Brayton cycle is an effective way to improve the performance of internal combustion engine. In this paper, a Combined Diesel-Brayton Cycle (CDBC) engine modified from a diesel engine was investigated. The Brayton cycle consists of a separate combustor and a power turbine, and uses the same compression system with the Diesel cycle. The turbocharging system of the original diesel engine was redesigned to adapt to the CDBC engine. The performance of the combined cycle engine was simulated with the engine cycle simulation code GT-POWER. Results show that the specific volume power of the combined cycle engine can be improved by 116.5% at the rated operating condition. However, the BSFC increases 37.6%. In addition, the performance of the CDBC engine with different diesel engine intake pressure was studied. It is shown that increasing the intake pressure of the diesel engine can significantly improve the specific volume power and the fuel economy of the CDBC engine.

Keywords: Combined Diesel-Brayton Cycle; Power density; Diesel engine; Turbocharging

Notation

Latin symbols

A	equivalent turbine flow area (m^2)
C_{PT}	discharge coefficient of power turbine
c_p	Specific heat ratio at constant pressure (kJ/kg K)
k	adiabatic exponent
m	air mass flow rate(kg/s)
p	pressure (Pa)
P	power(kW)
R	gas constant(J/kg K)
T	temperature(K)
B	fuel consumption
H_u	diesel fuel calorific value(42500 kJ/kg)

Acronyms

BSFC	brake specific fuel consumption
TT	turbocharger turbine
PT	power turbine
DE	diesel engine
MFP	mass flow rate parameter, $m\sqrt{T_{in}^*}/p_{in}^*$

Greek symbols

π	expansion ratio
η	efficiency

Subscripts and superscripts

*	Stagnation state
1~8	locations from compressor inlet to turbine exit
C	parameters on the combustor branch
D	parameters on the diesel engine branch

1. Introduction

With the development of vehicle and engine, the power density of diesel engine has achieved a high level. However, restricted by thermal load and mechanical load, the power density of diesel engine is difficult to increase substantially. As a representative of internal combustion engine with high power density, gas turbine has the shortcoming of high fuel consumption. The characteristics of diesel engine and gas turbine has formed a good complementary relationship. Thus, combining their advantages has become a new direction of research on high power density engine.

During the past decade, many efforts have been made to combine diesel engine and gas turbine. Scania [3], Volvo [2] and Daimler [5] developed turbo-compound engines that employ a power turbine downstream the turbocharger turbine to recover energy from the exhaust gas. Results have shown that fuel economy of the engine can be improved by 3~5%. However, there is little improvement on the power density of the engine.

A combustion chamber added to a turbo-compound engine which results in a Giesel engine is developed by TMS (Thermo Mechanical Systems Company). The combustion chamber is between the exhaust manifold and turbocharger turbine. It shows that Giesel engine achieves the desired agility and speed without exorbitant weight penalties and has a great improvement of output power. But it is modified from a two-stroke diesel engine which is not widespread used in vehicles.

Turbo-compound engine with bypass and complementary combustion was studied by Xie [9], Wang [10] and Zheng [11] . In this engine, the combustor is in parallel with the cylinders of diesel engine and the power turbine is also in parallel with the turbocharger turbine. Results show that this compound engine also has a great improvement of power and is very flexible.

Some turbo-compound engines called combined cycle engines were investigated, such as Krishna [4], Sanjay [8] and Mohamed [6]. Their investigations showed that combined cycle engine with high thermal efficiency has the advantages of both diesel engine and gas turbine.

In this paper, a Combined Diesel-Brayton Cycle (CDBC) engine was investigated, which was modified from a normal diesel engine. A separate combustor was added in parallel with the cylinders of the diesel engine and a power turbine was placed downstream the turbocharger turbine.

2. The Combined Diesel-Brayton Cycle engine

2.1. Engine configuration

The configuration of the CDBC engine is illustrated in Fig. 1. In the combined cycle, the Brayton cycle consists of a separate combustor and a power turbine (PT), using the same compression system with the Diesel cycle. The combustor is in parallel with the cylinders of the diesel engine (DE) and the power turbine is fitted downstream the turbocharger turbine (TT) to recover heat from the exhaust. This parallel structure, which enables the diesel engine and gas turbine to be run independently, gives the system great flexibility.

As following is a brief description of the engine operation. First of all, ambient air is pressurized to a high pressure in the compressor. A portion of the compressed air goes into the intercooler and then enters the cylinders for Diesel cycle. The other air flows through the valve 2 and get into the combustor for Brayton cycle. This part

of gas burns in the combustor, reaching a high temperature. Then it mixes with the diesel engine exhaust and flows through two turbines successively. At last the turbine exhaust is discharged into the atmosphere.

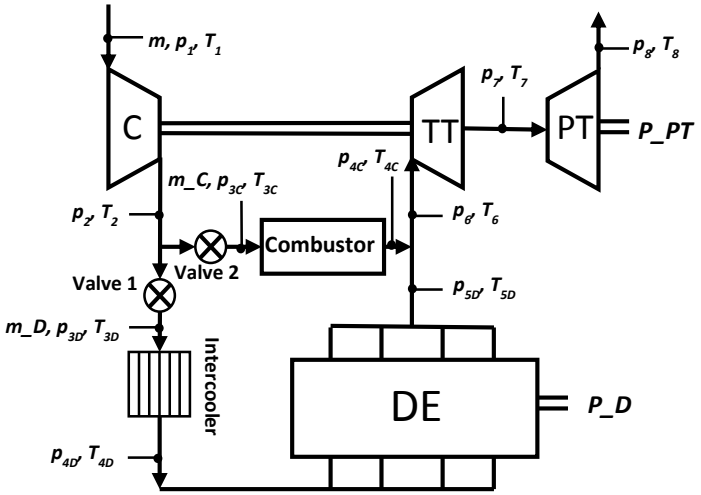

Fig. 1. Configuration of the parallel structure of the CDBC engine.

2.2. Turbocharging system modification

Considering the shunting effect and the characteristics of Brayton cycle, modification of the turbocharging system of the original diesel engine is needed to increase the total flow and pressure ratio of the combined cycle. Consequently, the Brayton cycle could run at a good efficiency and have enough air to output more power.

The turbine and compressor of the turbocharger need to be redesigned to have sufficient flow capacity and pressure ratio required by the combined cycle. The air mass flow rate of each cycle determines the cycle output power, and it also influences the turbocharger operation. The energy flow distribution between the Diesel cycle and the Brayton cycle has great influence on the overall performance of the combined cycle. The combined cycle system parameters at design point condition were determined by optimizing the energy flow distribution between two cycles, as listed in Table 1.

Table 1. Design conditions of the turbocharger turbine.

Parameters	Value
Mass flow rate	1.554 kg/s
Efficiency	80%
Inlet temperature	1233.15 K
Inlet pressure	477 KPa
Outlet pressure	166 KPa
Rotational speed	60000 RPM

Table 2. Design results.

Parameters	Value
Inlet tip radius	85.2 mm
inlet blade height	20 mm
Exit tip radius	72.4 mm
Exit hub radius	29.8 mm
Number of blades	11
Volute radius	128 mm
Volute area	3500 mm^2

A new turbocharger turbine was designed to meet the pressure ratio and air mass flow rate requirement at 2100RPM under full load operating conditions. The design results are listed in Table 2. The turbine performance

was simulated based on the mean-line analysis of the internal gas flow of the turbine.[1][12] The performance map is shown in Fig. 2. According to the similarity law, a new compressor was designed based on an existing compressor to meet with the flow and pressure ratio requirements of the CDBC engine. Its performance map is shown in Fig. 3.

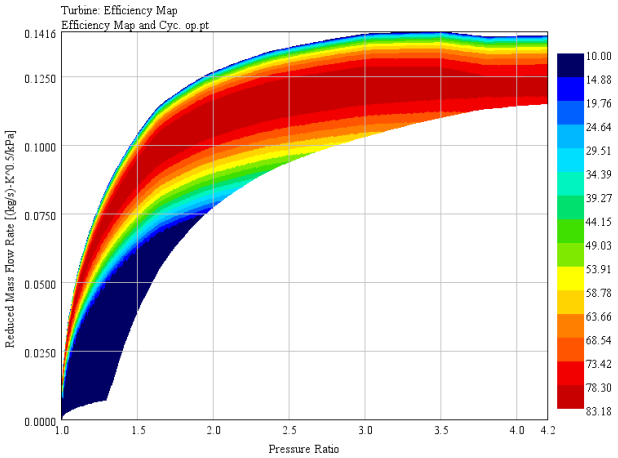

Fig. 2. The performance map of the new TT

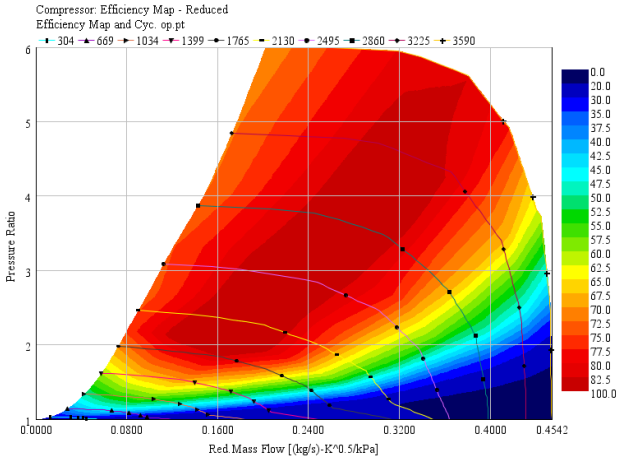

Fig. 3. The performance map of the new compressor

3. Simulation models

A simulation platform was established to investigate the performance of the CDBC engine using 1D diesel cycle simulation model GT-POWER. The combustor model was integrated into the diesel engine model to simulate the combined cycle of Diesel and Brayton. Components including turbocharger, intercooler, cylinders, power turbine and etc., were all modeled in the simulation platform.

3.1. Diesel engine model

A turbocharged diesel engine was considered as the baseline engine for analysis. Table 3 lists the parameter specifications of this diesel engine. The baseline engine was equipped with a turbocharger and an intercooler.

Table 3. Baseline diesel engine characteristics.

Parameters	Value
Cylinder arrangement	4cyl., in-line type
Displacement	7.9 L
Bore /Stroke	132/145 mm/mm
Compression Ratio	17
Connecting Rod Length	262 mm
Maximum Power	200 kW(2100r/min)
Maximum Torque	1200 N·m(1300 r/min)

Table 4. Baseline diesel engine external characteristic simulation data error.

Speed(r/min)	BSFC%	Power%	Mass flow%
2100	0.3192	-0.3192	0.3164
1900	-0.3007	0.3022	0.3143
1700	0.1133	-0.1119	0.2037
1500	-0.0866	0.1709	0.3964
1300	-1.6337	0.5442	1.8296
1200	-1.5272	0.7383	0.8352

The baseline engine model was validated with experimental data under full load conditions. The simulation

results are in good agreement with experimental data, with the maximum simulation error less than 2%, as shown in Table 4, Fig. 4 and Fig. 5.

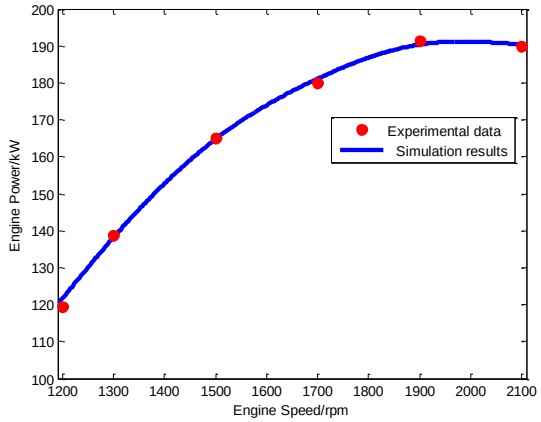

Fig. 4. Predicted baseline engine power curve compared with experimental data.

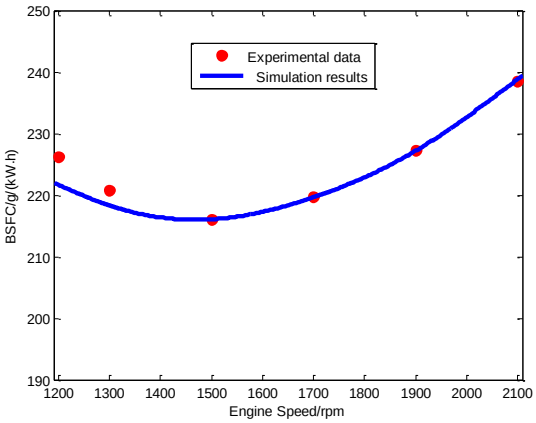

Fig. 5. Predicted baseline engine BSFC curve compared with experimental data.

3.2. Combustor model

In the CDBC engine, the combustor was modeled as multiple pipes, using the similar simulation method with the intercooler, and the outlet temperature can be adjusted to a specific value. In the simulations, the outlet temperature was adjusted to make the temperature of mixed gas before the turbocharger turbine (T_6) equal 1000℃. The fuel consumption is calculated by Eq. (1).

$$B_c \cdot H_u \cdot \eta_c = 3.6 \cdot m\_C \cdot c_p \cdot (T_{4C}^* - T_{3C}^*) \tag{1}$$

Where m_C represents air mass flow rate through the combustor. η_c is assumed as 0.98.

3.3. Power turbine model

In the simulation, the power turbine was modeled by a template named “TurbineSimple” in GT-POWER. It can predict the output power, mass flow rate and outlet temperature using a simple orifice flow model and an imposed efficiency. The turbine upstream and downstream pressures are used to calculate the mass flow rate through the turbine. The output power and the outlet temperature are calculated using Eq. (2) and (3) respectively.[7]

$$P_{PT} = m \cdot c_p \cdot T_7^* \left(1 - \pi_{PT}^{\frac{1-k}{k}}\right) \cdot \eta_{PT} \tag{2}$$

$$T_8^* = T_7^* \left[1 - \left(1 - \pi_{PT}^{\frac{1-k}{k}}\right) \cdot \eta_{PT}\right] \tag{3}$$

There are two major parameters of the power turbine model, which are turbine orifice diameter and turbine efficiency. Turbine efficiency is set to 80%. Turbine orifice diameter determines the value of the turbine equivalent

flow area which is an important parameter to represent the swallowing capacity of a turbine. The air mass flow rate through the PT under non-choked and choked conditions is calculated using Eq. (4) and (5) respectively.

$$m_{PT} = C_{PT} A_{PT} \sqrt{\frac{2k}{k-1} \cdot \frac{p_7^2}{RT_7} \cdot \left[(1/\pi_{PT})^{2/k} - (1/\pi_{PT})^{(k+1)/k} \right]} \tag{4}$$

$$m_{PT} = C_{PT} A_{PT} \sqrt{\frac{kp_7^2}{RT_7} \cdot (\frac{2}{k+1})^{\frac{k+1}{k-1}}} \tag{5}$$

4. Simulation results

4.1. Simulation at the same intake pressure of DE

In this investigation, the diesel engine of the CDBC system has the same cycle fuel injection quantity with the baseline engine, and the intake pressure of DE controlled by valve 1(as shown in Fig. 1) is the same as the baseline diesel engine.

Table 5. Simulation results of the CDBC engine compared with baseline engine.

Performance parameters	Baseline	CDBC
Power of DE (kW)	189.38	174.29
BSFC of DE (g/kW·h)	239.25	259.97
Air mass flow rate of DE (g/s)	402.97	393.78
Air mass flow rate of Combustor (g/s)	-	1093.3
Power of power turbine (kW)	-	261.92
Overall Power (kW)	189.38	436.21
Overall BSFC (g/kW·h)	239.25	329.30
The specific volume power (kW/m^3)	204.96	443.75

Table 5 shows the simulation results of the CDBC engine and baseline engine at the rated operating condition. Results show that the output power of DE decreases about 7.97% and the BSFC of DE increases 8.66%. The reason is that the exhaust back pressure of DE increases about 52% while the intake pressure of DE does not change practically, which causes a lot of pumping losses to worsen the performance of DE.

In the CDBC engine, the power of power turbine reaches 261.92 kW which is much more than the power of DE. In other words, the power generated by Brayton cycle exceeds it from Diesel cycle. Even though the power of DE decreases, the overall power of the CDBC engine has been improved by 130%.

In order to calculate the specific volume power, the increased volume of the CDBC engine should be estimated. In the CDBC engine, a combustor and a power turbine were added to the baseline engine and the original turbocharger was replaced by a new one. According to air mass flow rate of the combustor, its volume was estimated as 0.008 m^3. The volume increment of turbocharger was estimated as 0. 035 m^3, and the volume of power turbine was predicted as 0.016 m^3. Thus, the total volume increment was estimated as 0.059 m^3 while the volume of the baseline engine is known as 0.924 m^3.

Results show that the specific volume power of the combined cycle engine can be improved by 116.5%.

However, the BSFC increases 37.6%, which is caused by pumping losses of the diesel engine, mixing losses of gas from diesel engine and combustor, high fuel consumption of Brayton cycle and so on.

4.2. Simulation at different intake pressure of DE

In the following investigation, the CDBC engine was simulated at different intake pressure of DE. The intake pressure of DE can be controlled by varying the valve opening. Let valve 2 (as shown in Fig. 1) keep the maximum opening and the intake pressure of DE increases with the opening of valve 1 changed to maximum. Different intake pressure of DE results in different air mass flow distribution between two cycles. The air mass flow rate of DE and the combustor are represented by *m_D* and *m_C* respectively. *m_PT* stands for the air mass flow rate through the power turbine, which is also the total air mass flow rate of the CDBC engine. *m_PT* is the sum of *m_D* and *m_C*.

Figure 6 shows the variation of *m_D*, *m_C* and *m_PT* with the intake pressure of DE. It can be seen that increasing the intake pressure increases *m_D* but decreases *m_C*. There is a trade-off about air mass flow rate between the diesel engine and the combustor obviously. In this simulation, the outlet temperature of combustor was set to make T_6 equal 1000℃. Therefore, the inlet condition of TT remains basically unchanged, so is the outlet condition of compressor. As a result, the intake pressure of DE has little effect on *m_PT*.

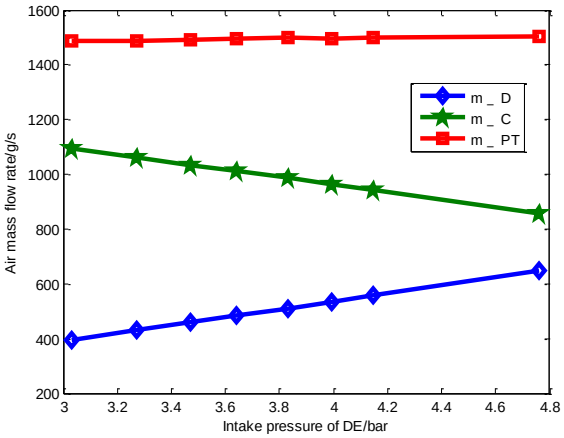

Fig. 6. Variation of air mass flow rate with the intake pressure of DE.

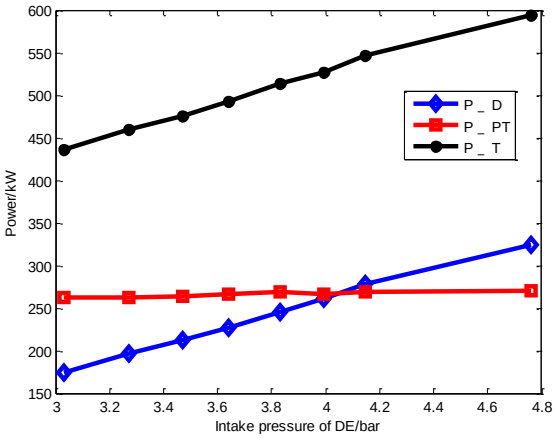

Fig. 7. Variation of power with the intake pressure of DE.

When the air mass flow rate of DE increases and the air-fuel ratio remains the same with the baseline engine, the power of DE (*P_D*) increases with the throttle angle of valve 1. However, it has little effect on the power of power turbine (*P_PT*) because of little variation of *m_PT*. Hence, the total power (*P_T*) increases with the intake pressure, as shown in Fig. 7.

Figure 8 illustrates the variation of BSFC when changing the opening of valve 1. The BSFC of DE and the CDBC engine are represented by BSFC_D and BSFC_T respectively. Obviously, increasing the intake pressure can decrease the pumping losses of diesel engine. Therefore, the fuel economy of diesel engine becomes better and the overall BSFC of the CDBC engine also becomes lower, as shown in Fig. 8.

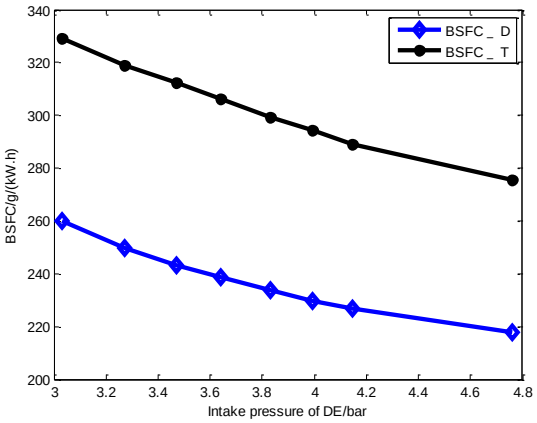

Fig. 8. Variation of BSFC with the intake pressure of DE.

When valve 1 reached the maximum opening, the value of intake pressure of DE was 4.76 bar. The simulation results are shown in Table 6. It can be seen that the output power of DE has a great improvement because of the increased air mass flow rate and less pumping loss. The fuel economy is also getting better. Comparing Table 5 and Table 6, it can be seen that when valve 1 reached the maximum opening the performance of the CDBC engine is much better than the CDBC engine which has the same intake pressure of DE with the baseline engine. But its maximum cylinder pressure was up to 247.4 bar while that of baseline engine was only 151.2 bar, which means high intake pressure of DE results in high mechanical loads. Reducing the compression ratio of DE can be used to solve this problem. The maximum cylinder pressure can be decreased to 177.4bar by reducing the compression ratio from 17 to 13.

Table 6. Simulation results of the CDBC engine compared with baseline engine when the intake pressure is 4.76 bar.

Performance parameters	Baseline	CDBC
Power of DE (kW)	189.38	324.11
BSFC of DE (g/kW·h)	239.25	217.71
Air mass flow rate of DE (g/s)	402.97	649.09
Air mass flow rate of Combustor (g/s)	-	855.99
Power of power turbine (kW)	-	269.78
Overall Power (kW)	189.38	593.89
Overall BSFC (g/kW·h)	239.25	275.62
The specific volume power (kW/m^3)	204.96	604.16

5. Conclusions

The performance of a CDBC engine modified from a Diesel engine was investigated. The Brayton cycle of the engine consists of a separate combustor and a power turbine, and uses the same compression system with the Diesel cycle. The combustor is in parallel with the cylinders of the diesel engine and the power turbine is placed downstream the turbocharger turbine. The turbocharging system of the original diesel engine was redesigned to adapt to the CDBC engine.

Simulation results show that the specific volume power of the CDBC engine could be improved by 116.5% while the BSFC increases 37.6%. Besides, increasing the intake pressure of the diesel engine can significantly improve the performance of the CDBC engine. When the intake pressure reaches 4.76 bar, the specific volume power of the CDBC engine could be improved by 194.8% and the BSFC increases only 15.2%. However, increasing the intake pressure leads to high mechanical loads on the diesel engine, which can be reduced by decreasing the compression ratio of the diesel engine.

References

[1] Dawes W.N. Development of a 3D Navier–Stokes solver for application to all types of turbomachinery. ASME 88-GT-70, 1988.

[2] Greszler A. Diesel turbo-compound technology. ICCT/NE-SCCAF Workshop-Improving the Fuel Economy of Heavy-Duty Fleets II. San Diego, 2008.

[3] Holset Turbochargers. Turbocompounding. HTi magazine, 2004, 2: 6-7.

[4] Krishna S.S, Renald C.J.T. Numerical analysis of a turbo-compounded Diesel-Brayton combined cycle. Continuum Mechanics, Fluids, Heat, (2010), 258-261.

[5] Luo X. Introduction of DD15 Truck Engine——World Engine from Daimler. Commercial vehicle, 2008(4).

[6] Mohamed M.E.A. Energy and Exergy Analysis of a combined Diesel-Engine Gas-Turbine System for Distributed Power Generation. Thermal & Environmental Engineering Volume 5, No. 1 (2013) 31-39

[7] Marcello C, Fabio C, Giorgio R and Wang Y. Model-Based Characterization and Analysis of Diesel Engines with Two-Stage Turbochargers. SAE International, 2010, 2010-01-1220.

[8] Sanjay, Agarwal M, Rajay. Energy an Exergy Analysis of Brayton-Diesel Cycle. Proceedings of the World Congress on Engineering 2009 Vol II.

[9] Xie H, Zhang H, Bai T. Theoretical Study on the Turbo-compound Engine with Bypass and Complementary Combustion. Journal of Engineering Thermophysics, 1983; 4(2): 105-111.

[10] Wang Y, Tian X, Sheng S. Calculation and Analysis of the Diesel Engine with Bypass and Complementary Combustion and Sequential Turbocharging. Transactions of CSICE, 1994; 12(3): 276-282.

[11] Zheng L, Zhao C, Lin L. Second Law Analysis of the Hyperbar Turbocompound Engine cycle. Journal of Engineering Thermophysics, 1989; 10(3): 236-239.

[12] Zhuge W, Zhang Y, Zheng X, Yang M, He Y, Development of an advanced turbocharger simulation method for cycle simulation of turbocharged internal combustion engines. Proceedings of the Institution of Mechanical Engineering Part D-Journal of Automobile Engineering, 223(D5): 661-672, 2009

Optimization of a Radial Turbine Design for Improved Engine-Turbocharger Matching

P. Kapoor[1], A. Javed[2] and A. W. Costall[3]

[1]Delft University of Technology, The Netherlands
E-mail: prakhar.kapoor@hotmail.com

[2]Mitsubishi Turbocharger and Engine Europe BV, The Netherlands
E-mail: ajaved@mtee.eu

[3]Imperial College London, United Kingdom
E-mail: a.costall@imperial.ac.uk

Abstract. Turbocharging the internal combustion engine is considered a promising way to improve the energy efficiency and to reduce exhaust gas emissions. However, matching a turbocharger to the engine involves a complicated balance of various design and performance variables. Turbocharger design is an essential factor that determines the performance of a turbocharged engine. An appropriate matching between the engine requirements and turbocharger performance is, therefore, fundamental and must be performed carefully to obtain the most suitable matching in terms of energy efficiency and transient behaviour. Presently, engine-turbocharger matching is carried out by fitting the engine performance data at various operating conditions over predefined compressor and turbine maps to decide the best combination that fulfils all the engine requirements. Although a favourable match is obtained, there is still room for performance improvement by tweaking the turbine design, thereby achieving an optimal engine-turbocharger matching. This paper describes a novel methodology for engine-turbocharger matching by adapting an off-the-shelf turbine for a smarter matching with an internal combustion engine. The paper presents a 1D meanline model coupled with optimization routines to obtain optimized turbine geometry in compliance with the engine requirements. To begin with, the baseline turbine design has been simulated in the 1D meanline model to determine the basic performance validated against the experimental data. The turbine performance corresponding to the engine operating line is then calculated using a regression analysis. A genetic algorithm is employed to optimize the turbine geometry at a specific engine operating point to achieve improved overall turbine efficiency. Finally, the impact of the modified turbine geometry on engine performance and transient response is simulated in GT-Power, which is a 1D engine simulation tool. The optimized turbine design presents a more suitable alternative for the given turbocharger and is expected to deliver a better engine-turbocharger matching.

Notation

N	*Rotational Speed, rpm*
P	*Power, kW*
Q	*Volumetric Flow rate, m^3/s*
b	*Blade Height, mm*
$\dot{m}$	*Mass flow rate, kg/s*
r	*Radius, mm*
β	*Blade angle, ^{o}*
η	*Isentropic Efficiency, -*
π	*Pressure ratio/Expansion ratio, -*

Subscripts

4	*Rotor inlet*
5	*Rotor Outlet*
b	*Blade*
c	*corrected flow, compressor*
t	*Throat, turbine*

1. Introduction

A turbocharger is a simple compressor-turbine arrangement, employed in automotive internal combustion engines to improve power density – and indirectly (e.g., by downsizing) the thermal efficiency and CO_2 emissions. However, to maximize the substantial performance benefits offered by turbocharging an internal combustion engine, it is essential that the correct match between the engine and turbocharger components is made. Ultimately the correct matching of the turbocharger with an engine becomes extremely important for the successful operation of a turbocharged engine. The overall objective of the matching process is to select a turbocharger that results in the best compromise of the desired engine performance characteristics, which will usually consider the full-load torque and power capability, part-load fuel consumption, and transient response, including a number of other constraints (e.g., speed margin, operation at altitude, turbine back pressure, compressor delivery temperature). The internal combustion engine and the rotating machine of the turbocharger are connected by the air charge and exhaust gas flow. The critical turbocharger components, namely the turbine and compressor, are linked by means of power transferred and shaft speed. The pressure ratios across all the components must be synchronized with each other and with the intake and exhaust pressures. All the above requirements should be dealt with in the matching study. Turbocharger matching can thus be defined as a process of selecting an optimal combination of compressor and turbine, given the target engine performance characteristics and certain constraints.

Currently, to match a turbocharger to an engine, the performance data of the associated components, namely the compressor and turbine maps, are assessed by superimposing the corresponding full-load engine operating line. The compressor that gives adequate surge and choke margin (including operation at altitude) while achieving the best efficiency is the general starting criteria for selection. Corresponding to this compressor, a turbine delivering the power required by the compressor, at maximum efficiency, minimum back pressure and lowest inertia, is selected. Currently, however, the possible variation in turbine geometry is discrete because the selection can only be made from a finite number of pre-existing turbine options – and in this sense the matching is passive. The focus of the present work is to develop a tool that allows the various turbine geometrical parameters to vary continuously while assessing the coupled impact on the engine-turbocharger system – and this we call active matching.

2. 1D Performance Analysis Tool

A 1D meanline model [7] developed at Delft University of Technology (TU Delft) has been adapted for turbocharger application and is used to estimate the performance characteristics of the complete radial turbine stage. The 1D model swiftly computes the radial turbines performance using a small amount of geometric data and input operating conditions. In the design mode, the tool can predict the most suitable geometric configuration corresponding to the performance targets, whereas, in the analysis mode, the tool calculates the performance of the turbine corresponding to a predefined geometry and operating conditions.

The meanline model is based on a quasi-one-dimensional procedure to determine flow conditions through the turbine along a mean streamline. The flow is analyzed along a mean stream surface through various stage components, using numerous empirical fluid dynamics and loss correlations to supply the information not obtainable through the basic theoretical methods [10]. Such models continue to be the most practical and accurate for predicting component performance in radial machines [1].

Figure 1 presents the 1D meanline model scheme used for the radial turbine design and analysis. The scheme has been implemented in Matlab. It involves calculation of flow properties at different stations in a radial turbine beginning with the volute and the vaneless nozzle, continuing to the turbine rotor inlet and finally the rotor outlet. Different empirical correlations given in ref. [2] have been used to estimate the losses in the radial turbine stage and estimate the final turbine isentropic efficiency. These include the correlations to calculate the incidence loss, passage loss (combination of losses due to skin friction and the secondary flows), and the tip-clearance loss in the radial turbine stage.

Initial inputs to the 1D meanline model include the specification of the operating parameters to the turbine, i.e., mass flow rate, inlet temperature and pressure, and the turbocharger operating speed. In addition, the geometric information of the radial turbine stage has to be specified as well.

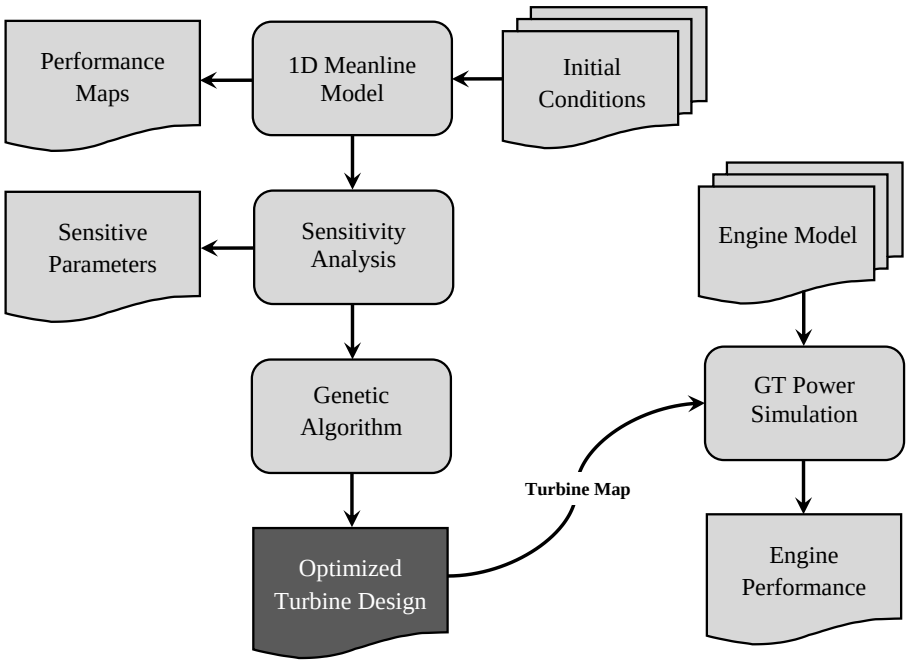

Figure 1 Illustration of methodology employed for improved for engine turbocharger matching

3. Baseline Radial Turbine 1D Performance Evaluation

An off-the-shelf radial turbine has been selected as a test case for the present study. The turbine belongs to a mass-produced turbocharger at Mitsubishi Turbocharger and Engine Europe BV (MTEE). The upcoming sections describe the 1D performance evaluation of the test case radial turbine.

3.1 1D Performance Evaluation and Model Verification

The 1D meanline model has been verified by employing it for predicting the baseline performance of the test case radial turbine. The results obtained from the model have been compared with the available experimental data for 40%, 59%, 75%, 87%, 95% and 100% turbocharger rotational speeds. Figure 2 shows the predicted and measured turbine performances in terms of corrected mass flow parameter and isentropic efficiency. Overall, the performance results obtained from the 1D meanline model agree well with the experimental data. However, for the lower rotational speeds, the 1D meanline tool under predicts the turbine isentropic efficiency. Nevertheless, the 1D meanline model is still very useful as a mean to predict the relative change in isentropic efficiency from the baseline configuration if a design optimization is carried out.

3.2 Sensitivity Analysis

A sensitivity analysis has been performed to identify the critical geometric parameters influencing the turbine performance considerably. The sensitivity analysis will help reduce the computational time for the proposed design optimization by employing the most sensitive of the turbine geometric parameters. The 1D meanline model has been used to perform the sensitivity analysis.

A total of six geometric parameters have been considered - volute throat radius r_t, inlet blade height b_4, inlet radius r_4, exit tip radius r_{5t}, inlet blade angle β_4 and the exit blade angle β_5. The tip-clearance between the rotor and the turbine housing has been maintained constant. All the above mentioned geometric parameters are varied within a specific deviation range from their baseline values and the resulting impact on turbine expansion ratio and isentropic efficiency is calculated using the 1D meanline model. Figure 3 compiles the sensitivity analysis plots showing the impact of various geometric parameters on turbine expansion ratio and isentropic efficiency.

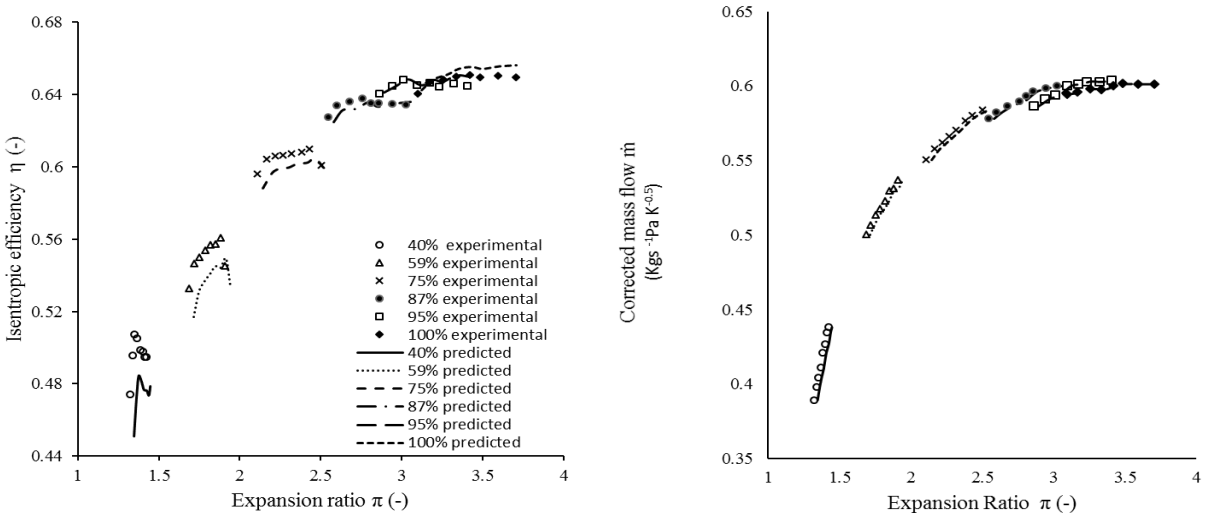

Figure 2 Experimental and simulated turbine performance curves

Deviation in volute throat radius r_t. Figure 3(a) presents the predicted performance variation due to deviations in the volute throat radius r_t. A deviation of ± 0.4 mm is applied to the baseline value. An increase in r_t results in a decrease in the expansion ratio due to the increased flow area. This also reduces the absolute flow velocity, which in turn reduces the flow incidence angle with the rotor blades, leading to a reduction in incidence loss and an increase in turbine efficiency.

Deviation in rotor inlet blade height b_4. Inlet blade height b_4 affects the relative flow angle and the absolute flow velocity and is, therefore, an important geometric parameter influencing the radial turbine performance. At smaller blade height, the frictional losses within the rotor can be expected to increase as a consequence of reduction in its effective hydraulic depth [8], thus causing a decrease in turbine efficiency. Figure 3(b) illustrates the sensitivity of turbine performance to changes in the b_4, where a ± 0.5 mm deviation is applied to the baseline value. The 1D meanline model predicts an increase in the turbine isentropic efficiency with an increase in b_4 and vice versa.

Deviation in rotor exit tip radius r_{5t}. Figure 3(c) shows the influence of deviation in exit tip radius r_{5t} on the performance, where increasing the r_{5t} results in an increase in the turbine isentropic efficiency. This is because the resulting enlarged exit area in the rotor gives a reduced exit Mach number and hence lower associated kinetic energy losses [12]. Therefore, to achieve performance gains from the current geometry, an increase in the baseline value of r_{5t} can be considered.

Deviation in rotor inlet radius r_4. The influence of inlet radius r_4 on the turbine performance is depicted in Fig. 3(d). The plots show that increasing the r_4 increases the isentropic efficiency and decreases the expansion ratio of the turbine. This increase in isentropic efficiency is attributed to a substantial decrease in the blade loading at larger r_4, which causes a reduction in flow separation and hence lower efficiency [11].

Deviation in rotor exit blade angle β_5. Figure 3(e) demonstrates the effect of variation in the exit blade angle β_5 on overall turbine performance. The 1D analysis reveals that a dimensional deviation of $\pm 4^o$ in β_5 does not cause a significant change in the turbine performance. The slight increase in the efficiency with increase in blade angle is attributed to the reduction in the swirl velocity downstream, which results in an optimal flow pattern [7].

Deviation in rotor inlet angle β_4. Figure 3(f) presents the effect of variation in the inlet blade angle β_4 on overall turbine performance. The 1D analysis has shown that a dimensional deviation of $\pm 4^o$ in β_4 from its baseline value of -4^o does not cause a significant variation in the turbine performance.

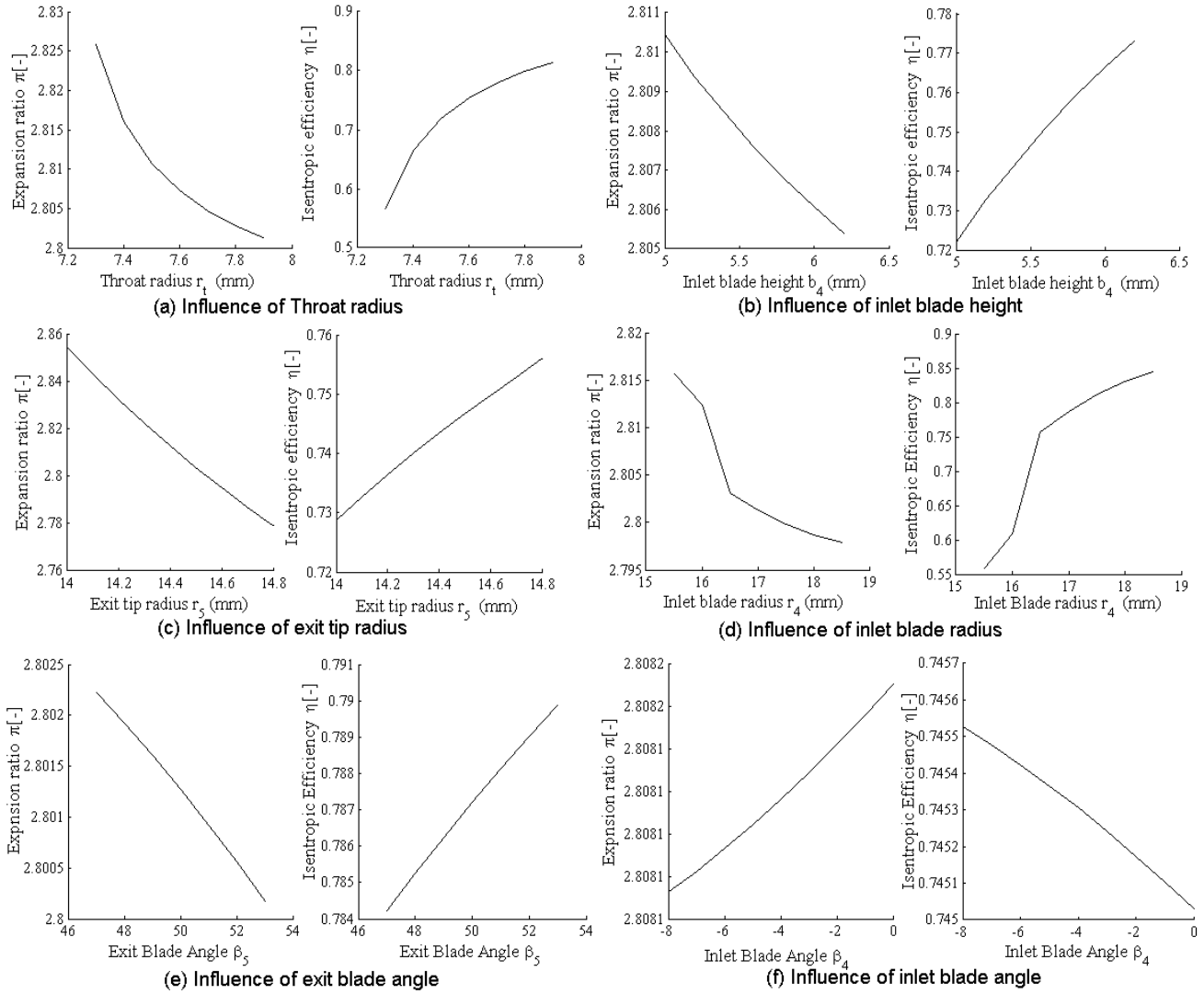

Figure 3 Sensitivities of various geometric parameters

3.3 Sensitivity Ranking of the Geometric Parameters

Figure 4 illustrates the sensitivity ranking of the turbine geometric parameters in terms of their influence on the turbine expansion ratio and isentropic efficiency. Here, the sensitivity of a particular geometric parameter refers to the ratio of the total change in the output performance (expansion ratio or isentropic efficiency) to the applied geometric deviation. It can be observed that the volute throat radius r_t has the most sensitivity, followed by the inlet radius r_4 and the exit tip radius r_{5t}. Hence, these parameters have been selected for future analyses.

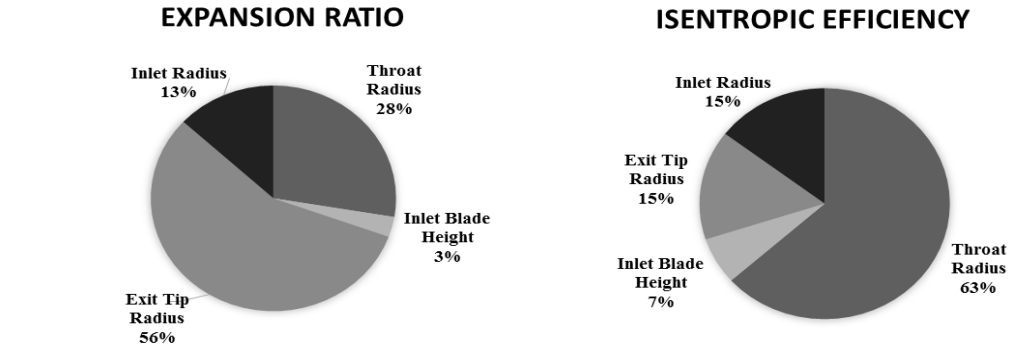

Figure 4 Sensitivity ranking of various turbine geometric parameters

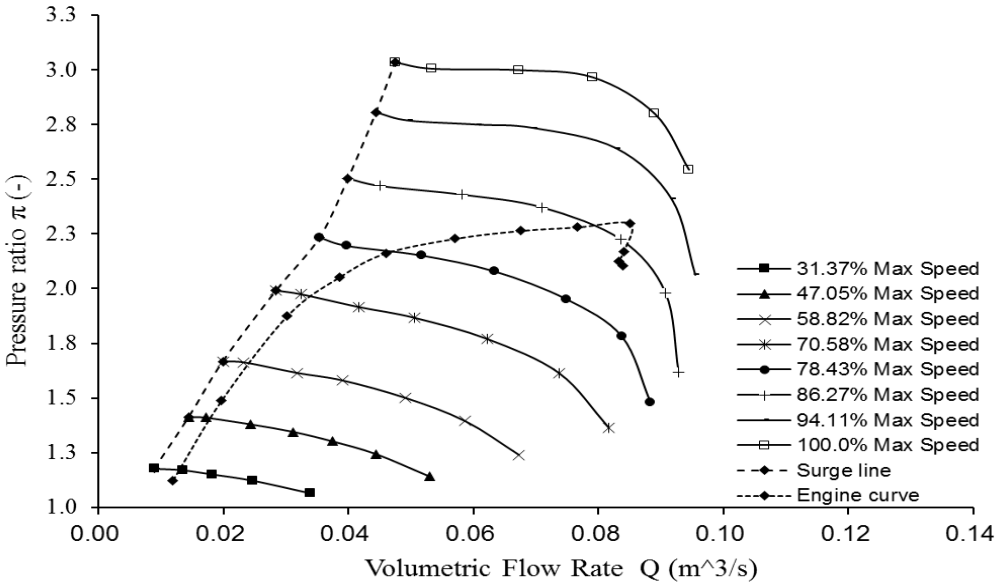

Figure 5 Compressor Map and Engine Operating Line

4. Turbine Performance Corresponding to Engine Operating Points.

To calculate the turbine performance over the known full-load engine operating line, a series of steps are employed. To begin with, the engine operating points are plotted on to the compressor map. This is done in order to determine whether the compressor can meet the boost demand at all engine operating points with adequate surge and choke margins. The mapping of the engine operating points on the compressor map is shown in the Fig. 5, where it can be seen that the compressor does indeed provide adequate performance at all engine operating points. Next, a numerical procedure is employed to determine the turbocharger rotational speed *N* at each point along the engine operating line on the compressor map in order to estimate the required turbine performance for each operating point. Specifically, the intersection of the engine operating line and the compressor speed line is determined, and an estimate for the compressor flow rate Q_c and pressure ratio π_c is made. Using this data as an input, a regression analysis is applied to fit a third-order response surface model in form of Eq. 1 and determine the compressor operating speed at the engine operating points defined in Table 1. Using Eq. 1 and the compressor data, the operating speed and compressor power are determined at the flow rate and pressure ratio corresponding to each engine operating point. These performance variables form the input operating conditions for simulating the turbine performance using the 1D meanline model. The results obtained from the meanline model are depicted in Fig. 6, which form the baseline turbine performance for each engine operating point. This turbine data will be used as a baseline for design optimization of the turbine geometry to obtain better turbine performance and engine-turbocharger matching.

$$N = -3.723\times10^{5} + 6.241\times10^{5}\cdot\pi_c + 0.859\times10^{5}\cdot Q_c - 3.636\times10^{5}\cdot\pi_c^2 - 1.417\times10^{8}\cdot Q_c^2 + 0.743\times10^{5}\cdot\pi_c^3 + 7.4\times10^{8}\cdot Q_c^3 \quad (1)$$

Table 1 Input parameters for regression analysis

π_c [-]	Q_c (m^3/s)	*N* (% of Maximum)
1.171	0.0152	36.36
1.417	0.0215	47.05
1.673	0.0288	58.88
1.989	0.0399	70.58
2.203	0.0559	78.43
2.321	0.0942	86.27
2.219	0.1001	86.27

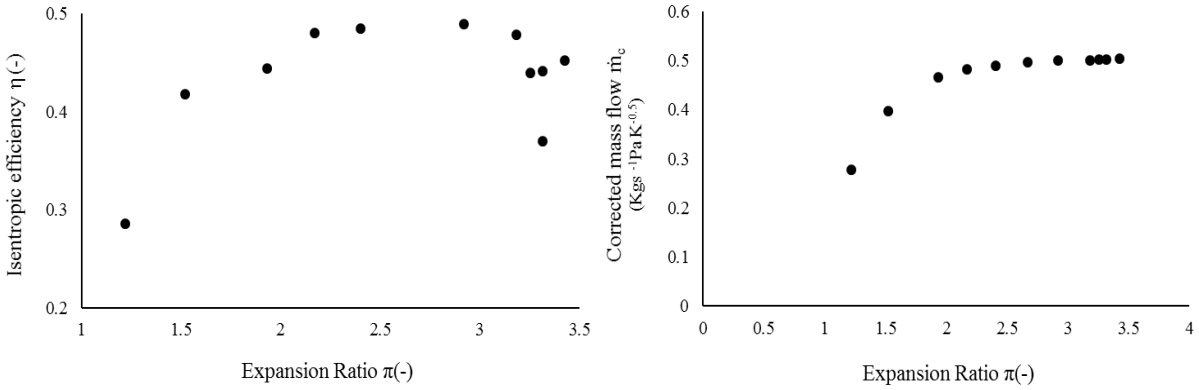

Figure 6 Turbine performance corresponding to engine operating points

5. Turbine Design Optimization

This section of the paper presents the methodology that is employed to optimize the test case radial turbine design for improved engine-turbocharger matching. Genetic algorithm has been applied in Matlab to obtain an optimized turbine geometry that provides a better isentropic efficiency. A genetic algorithm is an adaptive stochastic optimization algorithm involving search and optimization based on the principle of natural selection. For the current work, two optimizations cases have been considered. In the first optimization case, all the turbine geometric parameters are allowed to vary from their baseline values within a specific deviation range as given in Table 2. In the second optimization case, only the turbine rotor has been considered for optimization excluding the volute throat radius r_t. The second optimization case is more practical since the rotor trim changes can be easily made to the existing rotor design during manufacturing (as long as it only requires a removal of material from the rotor casting).

5.1 Case I Optimization - Full Turbine Geometry

The baseline values of the different turbine geometric parameters along with the applied deviation ranges are documented in Table 2. To obtain the optimized turbine geometry, all geometric parameters given in Table 2 have been considered for optimization. A population size of 100 with 800 generations has been employed and the stochastic uniform selection function has been used in the genetic algorithm. A crossover probability of 0.8 has been selected, which determines the blending of parent chromosomes to form the next candidate solutions. Furthermore, a mutation operator is used in the binary strings, which preserves the diversity of offspring. The objective function is set to maximize turbine efficiency and the GA obtains the optimized geometry for the first case after 51 generations. The optimized turbine geometry has been listed in Table 3.

Table 2 Baseline values and deviations applied to various geometric parameters

Geometric Parameter	Lower Limit	Baseline Geometry	Upper limit
Inlet blade height b_4 (mm)	5.0	5.45	6.0
Throat radius r_t (mm)	7.35	7.56	7.77
Inlet radius r_4 (mm)	15.5	17.0	18.5
Exit Blade tip radius r_{5t} (mm)	13.0	14.45	16.0

Table 3 Case I optimized turbine geometry

Inlet blade height b_4 (mm)		5.99
Throat radius r_t	(mm)	7.36
Inlet radius r_4	(mm)	15.77
Exit tip radius r_{5t}	(mm)	17.96

Table 4 Case II optimized turbine rotor geometry

Inlet blade height b_4 (mm)		6.0
Inlet radius r_4	(mm)	15.57
Exit tip radius r_{5t}	(mm)	17.72

5.2 Case II Optimization - Turbine Rotor Geometry

In case II optimization, deviations were applied only to the turbine rotor geometric parameters given in Table 2. Similar settings for the genetic algorithm have been maintained. The optimized turbine rotor geometry is listed in Table 4.

5.3 Optimized Turbine 1D Performance Evaluation

To establish the overall effect of the optimized case I and case II turbine geometries on the turbine performance, the corresponding geometric parameters have been fed back into the 1D meanline model and the turbine performance has been calculated. A comparison has been made against the baseline performance in Figure 7. A considerable gain in isentropic efficiency is obtained at higher turbine rotational speeds for both case I and case II optimizations. The difference between the two optimization cases is only noticeable at higher rotational speeds. At low speed, however, there is little to choose between the baseline and optimized geometries in terms of isentropic efficiency. This low end region of the turbine map has the largest impact on the engine transient response time, since the turbine will likely be operating here at the beginning of a transient event. It is, therefore, important to consider the change in inertia associated with the optimized geometries since this will have an impact on the transient performance of the engine (turbo lag); especially since the isentropic efficiency gain at low turbine speeds is almost negligible.

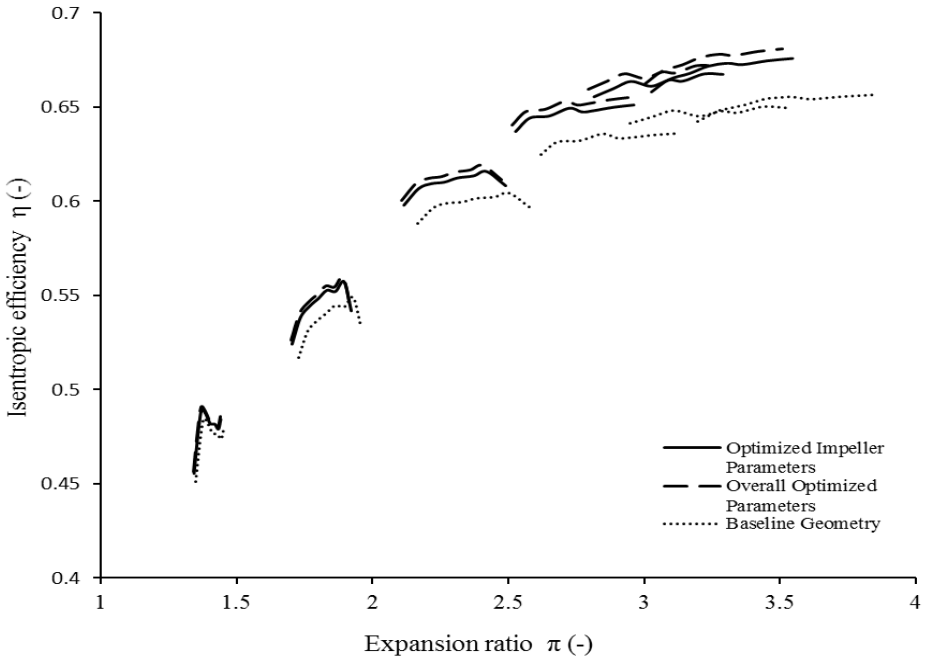

Figure 7 Comparison of performance as a consequence of geometric optimization

Table 5 Estimated values of inertia

Cases	Relative Inertia Change
Baseline	1
Optimized, best inertia	1.107
Optimized, worst inertia	1.161

5.4 Influence of Optimized Turbine Rotor Geometry on Inertia

To estimate the change in the rotor inertia as a consequence of the optimized turbine rotor geometry, solid models of the complete turbine rotors corresponding to baseline and optimized geometry were analyzed using 3D CAD software. This showed that the optimized turbine rotor had larger rotational inertia compared to the baseline. In the worst case (including the full effect of fillets and variable blade thickness) it is estimated that the rotational inertia will increase by 16%. If fillets are ignored, the rise is estimated to be 10%. The relative values of rotor inertia are listed in Table 5.

6 Impact on Engine Performance

The impact of the optimization of turbine geometry on both the steady and transient responses of the engine is analyzed in this section of the paper. Using the estimated values of rotor inertia from Table 5 and the turbine maps corresponding to the baseline and optimized turbine geometries, engine performance is simulated using the commercial 1D engine simulation tool, GT-Power.

6.1 Steady State Analysis

The results obtained from the steady state engine simulation are presented in Fig. 8. It can be observed that for all the optimization cases, the full-load torque and power requirements are being met with reference to the baseline results. Furthermore, the optimized turbine geometry has a positive effect in lowering the brake specific fuel consumption (BSFC) at all engine operating points

6.2 Transient Analysis

The results of the transient engine simulations are shown in Fig. 9, which shows the torque response for a load step applied at two different engine speeds (1000rpm and 3000rpm). It can be observed that despite the improvement in turbine efficiency shown previously, the optimized geometry results in a lower response time because of its more rotor inertia. However, overall difference in time-torque is not significant as typically an increase of 3-5% is observed. In addition to this, an analytic comparison of the variation in the response at different engine speeds is presented in table 6.

Table 6 Predicted engine response

				Time-To-90% Torque [sec]		
Engine Speed [RPM]	TIME [sec]	90% Torque [N-m]	Weight	PREDICTED TURBINE MAP	OPTIMIZED TURBINE MAP (BEST)	OPTIMIZED TURBINE MAP (WORST)
3000	6.0	217.20	1	0.98	1.00	1.01
2500	6.0	223.87	1	1.40	1.43	1.45
2000	9.0	247.72	1	2.29	2.34	2.37
1500	12.0	259.69	1	4.57	4.60	4.67
1250	12.0	179.52	0	6.10	6.24	6.34
1000	12.0	123.52	1	5.99	6.45	6.58
			Weighted average	3.05	3.17	3.22
			Additional lag [s]	-	0.12	0.17
			Additional lag [%]	-	3.9%	5.5%

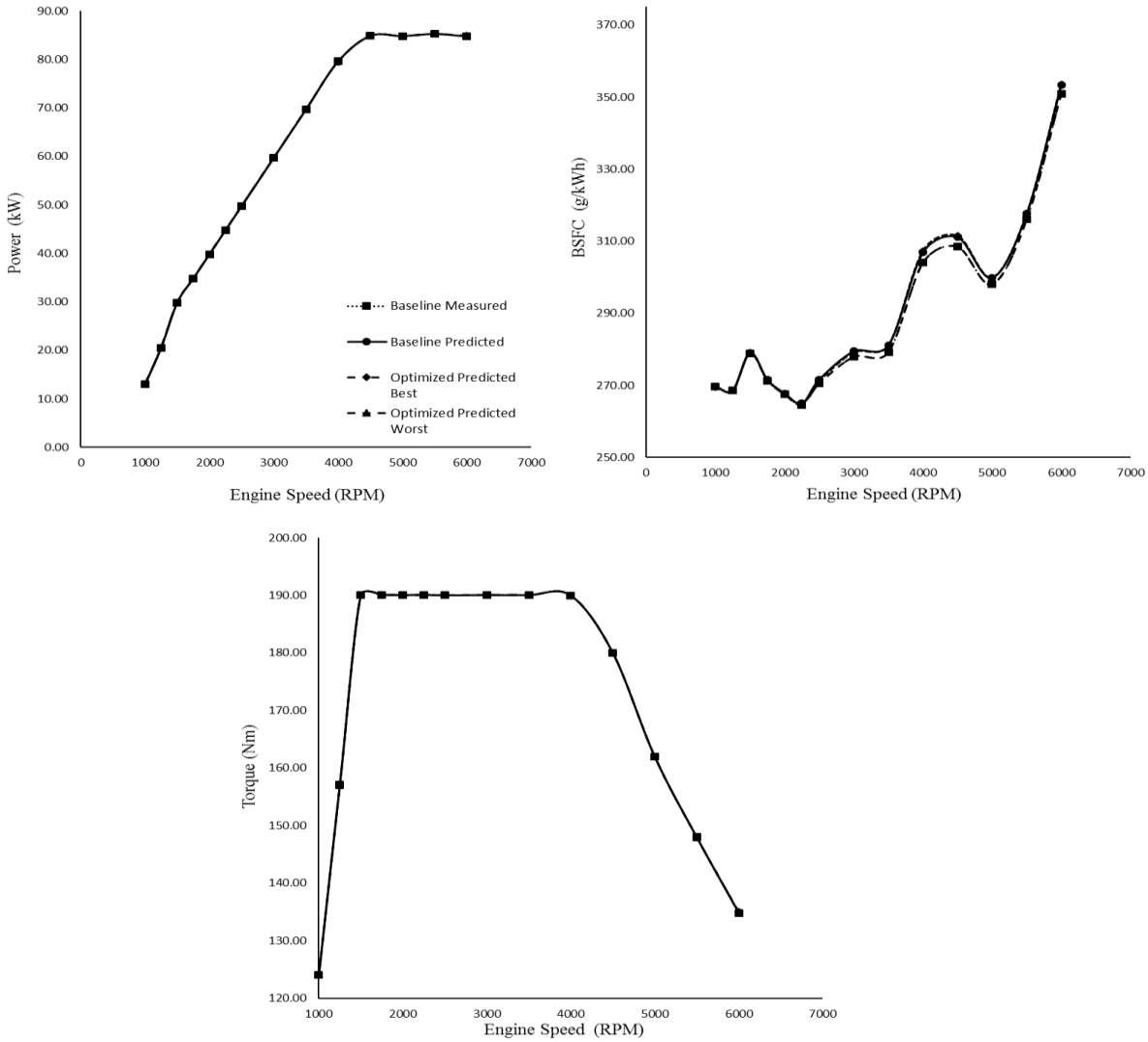

Figure 8 Steady-state analysis

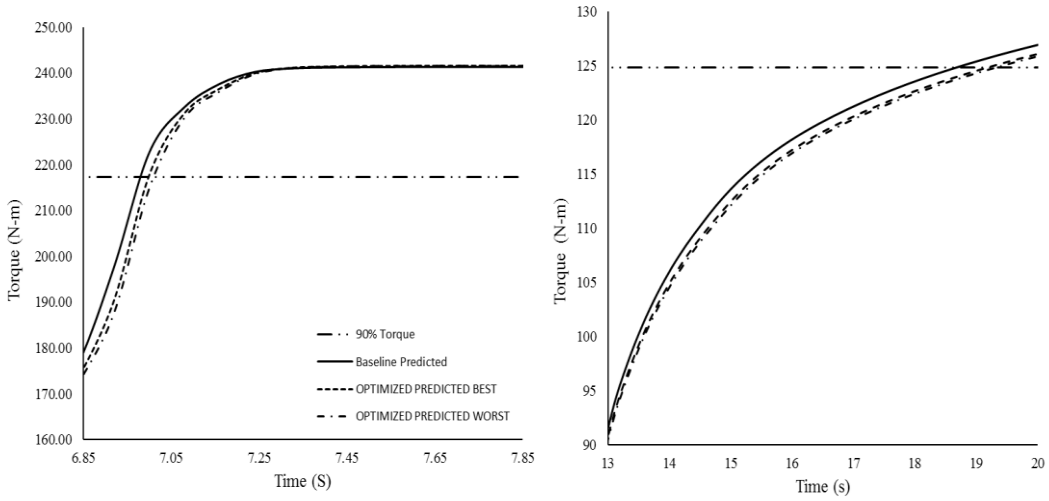

Figure 9 Transient analysis

7 Conclusion

Geometry optimization of radial turbine belonging to a commercial automotive turbocharger has been performed using a genetic algorithm coupled to a 1D meanline radial turbine performance model. After consideration of the sensitivity of turbine performance to various geometric parameters, an efficiency-optimized geometry has been calculated and its impact on engine steady-state and transient performance has been simulated. The analysis reveals that for the cases studied, optimization of the baseline turbine design results in an overall gain in turbine isentropic efficiency by 2-3%. At the same time, the optimization results in an estimated increase in rotor inertia by 10–16%. The predicted effect of the optimized geometry on overall engine performance suggests lower BSFC, and that the increased inertia does not lead to a significant increase in time-to-torque.

The novel matching methodology presented in the paper can act as a smarter tool enabling an active matching of the engine-turbocharger system, in the sense that an adapted geometry can be proposed and implemented rather than relying on predefined turbine designs. Note that for the optimization cases studied in this paper, an efficiency-optimized turbine design can result in an increase in rotor inertia, thereby emphasizing the trade-off between efficiency gain and transient response time of the turbocharger and the engine-turbocharger matching.

References

1. Aungier, R. H. (1995), Mean Streamline Performance Analysis of Centrifugal Compressor. Journal of Turbomachinery, Vol. 117, P. 361-366.
2. Baines, N. C. (1998), A Meanline Prediction Method for Radial Turbine Efficiency, Proceedings of IMechE 6th International Conference on Turbocharging and Air Management Systems, London, UK.
3. Baines, N. C. (2005). Fundamentals of Turbocharging.
4. Barr, L., Spence, S., & McNally , T. (n.d.). A Numerical Study of the performance characteristics of a radial turbine with varying inlet blade angle. Instn. Mech. Engrs. 8th International Conference on Turbochargers and Turbocharging.
5. Boyce, M. P. (n.d.). GasTurbine Engineering Handbook.
6. Cohen, H., Sravanamuttoo, H., & Rogers, G. (2006). Gas Turbine Theory. Delhi: Pearson Education.
7. Eijgelshoven, T. G. (2011). Initial Turbine component optimization study for the MTT microturbine. Delft.
8. Hiett, G. F., & Johnston, I. H. (1963). Experiments Concerning the Aerodynamic Performance of Inward Flow Radial Turbines. Proceedings of the Institution of Mechanical Engineers.
9. Japikse , D. (2009). Turbomachinery Performance Modeling. SAE Technical Paper 2009-01-0307.
10. Javed , A., Olivero, M., Pecnik, R., & van Buijtenen, J. P. (2011). Performance analysis of a microturbine centrifugal compressor from a manufacturing perspective. Proceedings of ASME turbo expo. Vancouver, Canada.
11. Kofskey, M. G., & Haas, J. E. (1973). Effect of reducing rotor blade inlet diameter on performance of 11.66centimeter radial-inflow turbine, NASA Technical Memorandum, NASA TM X-2730, Washington.
12. Muller, L., Alsalihi, Z., & Verstraete, T. (2012). Multidisciplinary optimization of a turbocharger radial turbine. ASME Journal of Turbomachinery, Vol. 135.

Air Loop Characterization and First Potential of an Automotive Two-Stroke HSDI Diesel Engine

C. Ternel[1], G. De Paola[1] and P. Tribotté[2]

[1]IFP Energies nouvelles – 1 et 4 Avenue du Bois Préau 92852 Rueil-Malmaison, France.
E-mail: gaetano.de-paola@ifpen.fr
Telephone: +33 147525357

[2]Renault Powertran Division, 1 avenue du golf 78288 Guyancourt, France
E-mail: pascal.tribotte@renault.fr
Telephone: +33 176854912

Abstract. The target of substantial CO2 reductions in the spirit of the Kyoto Protocol as well as higher engine efficiency requirements has increased research efforts into small Internal Combustion Engines (ICE) with high power density. The two-stroke cycle can be a solution to reach this goal, allowing reductions of engine displacement, size and weight while maintaining good NVH (Noise, vibration and harshness), power and consumption levels. Reducing the number of cylinders, could also help reducing engine cost.
In the frame of the POWERFUL European research project, the combustion system and the complete air loop system were designed for an innovative two-stroke downsized Diesel engine. The main geometrical specifications (displacement, architecture) were chosen at the beginning of the project based on calculations. The engine has two cylinders, 730cc of total displacement, with four valves per cylinder and no ports in the liners.
1D numerical simulation oriented the technical solutions to achieve boost and air management requirements: with respect to the engine behaviour and the power targets, two boosting stages, integrating a Variable-Nozzle Turbine (VNT) turbocharger and a mechanical supercharger, and a Variable Valve Timing (VVT) on both intake and exhaust camshafts were selected.
The combination of all these technologies and the 2 stroke engine requirements introduce new trade-offs, *i.e.* the effects of the overlap and of the boost pressure on the in-cylinder equivalence ratio (ER). The expected improvements can be counterbalanced by the higher engine backpressure worsening the scavenging, or by penalties in fuel consumption when acting only on the mechanical compressor.
In detail, this paper deals with the experimental campaign performed at IFP Energies nouvelles on the twin-cylinder engine, on full and partial load conditions, which investigates the fundamental keys to obtain high two-stroke engine efficiency:

- Effect of the valve overlap and the engine differential pressure (intake / exhaust) on fuel consumption and emissions
- Influence of acoustic waves between intake and exhaust manifold on scavenging, in-cylinder air-fuel ratio (AFR) and trapping ratio.

1. Introduction

The two-stroke Gasoline engine is known to be cheap, compact, light, robust and friendly to use. That is why it is mainly found on light mobile applications such as the small powered vehicles (scooter, jet ski, outboard, snowmobile…) or mobile tools (chain saw, generator…).
The two-stroke Diesel engine appears to have a high potential in specific sectors such as that of huge power (marine propulsion or electric power plant) where some Diesel two-stroke engines called “slow engines” supply more than 100,000 HP with at least 50% of efficiency [5]. Such engines count from five up to fourteen inline cylinders where the piston bore can reach 1 meter and its stroke 2.5 meters; the shaft revolution speed being of around 100 RPM. Their main qualities are the reliability (some electric generators have worked during more than 50 years) and low fuel consumption.

Some aircraft engines also use the Diesel two-stroke cycle, a rather old technology [5] used by Clerget engines in the 1930’s. Nowadays, another example is the Wilksch engine, a three-cylinder supercharged by a compressor, supplying 120 HP, and addressed to light airplanes (such as microlight…). However, today two-stroke engines (Gasoline or Diesel) cannot be found in the automotive industry even if during the 80’s and the 90’s there was a real interest from car manufacturers for the two-stroke Gasoline engine, with many studies and patents published on this subject [3, 9]. Indeed, despite the numerous advantages offered by the two-stroke engine, the tightening of pollutant emis-

sion standards and the good level of consumption reached by four-stroke Diesel engines finally drove the carmakers away. Nowadays, given the trend to reduce the costs coupled with the price increase of Diesel post-processing devices, the question of the use of two-stroke engine for automotive application can now be reopened. Considering hybrid application, or small vehicle using small (and low power) combustion engine, the benefit in terms of cost becomes more advantageous compared to a Euro 6 compatible four-stroke engine.
The present study aims to examine the feasibility of a two-stroke Diesel engine designed for a A/B segment cars, complying with the current pollutant emission and drivability standards.

The framework of this scientific research falls within the need to assess alternative combustion systems to the four-stroke single turbo Diesel engine with the intention of reducing the carbon emission below 95g/km by 2020. In this context the study highlighted that the air system is the key element to achieve ultra-low emission levels with an ultra-downsized Diesel engine for mini and sub-mini vehicle segments.

2. Context and Objectives

In this context of necessary reductions of greenhouse gas and pollutant emissions, the use of small urban and extra-urban vehicles is going to increase in a significant way. The use or the maintaining of Diesel engines (characterized by their high efficiency) on such vehicles represents one of the major keys to achieve those objectives. On the other hand, the cost of the after-treatment systems (particle filter + nitrogen oxide reduction system) needed to comply with Euro 6+ standards becomes so high that the Diesel engine applications on small vehicles may be compromised.

The two-stroke engine presents several advantages in an approach of strongly downsized Diesel engines:

- A two-stroke engine, thanks to its higher specific power density, allows pushing further the downsizing. Due to the double combustion frequency, the number of cylinders can be reduced with very low impact on the NVH, maintaining a high unitary displacement in order to favor the combustion efficiency. Therefore, a downsized two-stroke engine reduces the mass, the bulk and the cost of the powertrain;
- The extension of the operating range of Homogeneous Charge Compression Ignition (HCCI) combustion and the use of Internal Gas Residual (IGR) to reduce the HC and CO emissions associated to such a combustion mode, generating low NOx emissions;
- The control of the scavenging process may improve the management of the exhaust temperature, allowing the use of a lighter and therefore a less expensive de-NOx system.

The goal of the Powerful project was to define the “strict minimum” technology for the target proposed with an objective of breakthrough in terms of NOx emissions, a saving of fuel consumption (~10%) and a decrease of cost compared to a four-stroke engine with similar performance levels.

The combustion system has been developed using a 3D CFD by Renault [11], and optimized through an experimental single cylinder campaign at CMT. In parallel, the air loop system has been designed through a 1D CFD [10].
This paper deals with the multi-cylinder experimental campaign done at IFP Energies nouvelles, in order to characterize the air loop system and the first potential of this small engine.

3. Engine Specification, Power Targets and Studied Configurations

The geometry of the concept engine presented in Table 2 is based on the Renault K9K 1.5 dCi power unit. Required power output was set to 45kW at 3000 rpm while keeping constant torque from 1000 rpm to 3000 rpm (see Fig. 1).

The engine is small, compact and light, with 4 valves (no inlet or exhaust ports) and a variable valve timing (VVT) system. This engine is thus compatible with a four-stroke production line.
The part load operating points were selected based on the NEDC (New European Driving Cycle) with an A/B-segment car (see Table 2 and green points in Fig. 1).

Table 1. Part load points definition

		Point 1	*Point 2*	*Point 3*	*Point 4*	*Point 5*	*Point 6*
Engine Speed	*RPM*	1250	1000	1500	2000	1500	2500
Torque	*Nm*	25	50	50	50	90	130
BMEP	*bar*	2.15	4.3	4.3	4.3	7.7	11.2

Table 2. Engine geometrical data

Bore	76	*mm*
Stroke	80.5	*mm*
No. of cylinders	2	-
Displacement	740	*cc*
Connecting rod length	133.8	*mm*
Compression ratio	17.2	-
No. of valves per cylinder	4	-

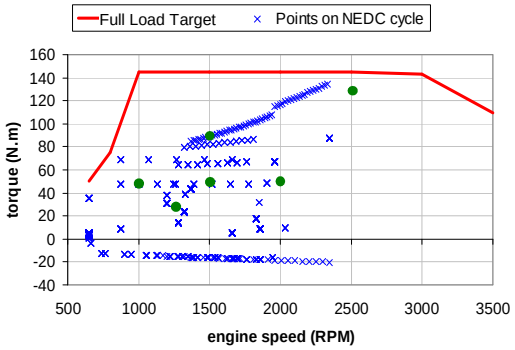

Fig. 1 Full load requirements, NEDC trace and investigated part load points (in green)

The engine is equipped with a two stage boosting air loop (see Fig.2): a Variable-Nozzle Turbine (VNT) turbocharger in the low pressure (LP) stage in series with a supercharger in the high pressure (HP) stage. A concept only equipped with turbochargers with respect to the engine starting capabilities and scavenging sensitivity on the power of the two-stroke engine was abandoned [10]. The EGR circuit is a middle pressure (MP) one, *i.e.* the exhaust gas recirculation (EGR) is introduced between the LP and HP compressor, and is cooled by a water/gas cooler.

Several temperature and pressure sensors are dispatched on the engine (see Fig. 2). The Variable Valve Timing (VVT) system on both intake and exhaust camshafts allows varying the valve opening of 30 Crank Angle Degrees (CAD) from the nominal position, independently. It cannot change the duration of the valve opening, or their lift (see Fig. 3).

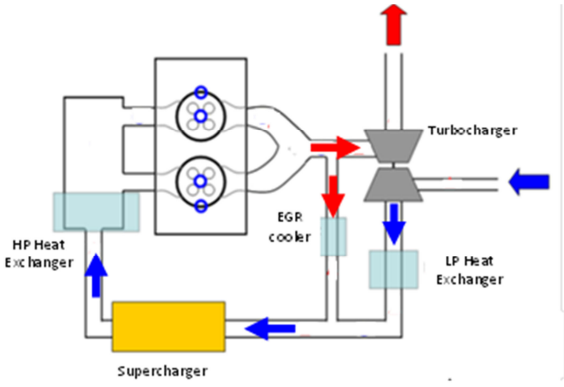

Fig. 2. Engine architecture

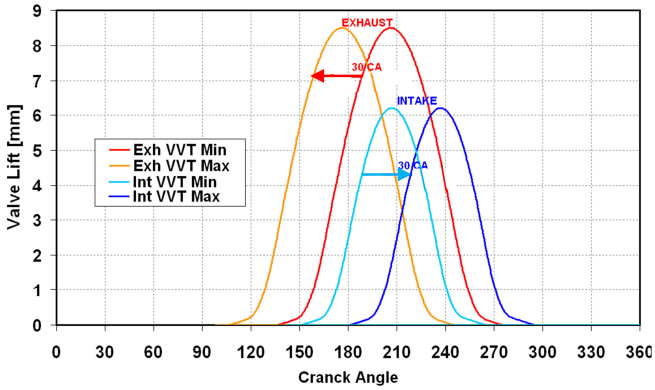

Fig. 3. Valve lift profiles

4. Experimental campaign

4.1 Full Load

The full load tests of the twin-cylinder were performed in this first phase only at 1500 rpm in this first experimental campaign, because the mechanical compressor used here presented some weaknesses at very high loads and engine speeds, (*i.e.* high air mass flow and inlet/outlet mechanical compressor pressure). In future developments, it is planned to test a new evolution of the compressor, able to perform the high loads and engine speeds.

4.1.1 Scavenging optimization at Full Load

The scavenging efficiency of the engine was optimized by varying the valve timing through the VVT actuators, in order to reach the best trade-off between engine permeability and air trapping.

Two-stroke engine requires first and foremost good scavenging efficiency. This is essential to reach low in-cylinder fuel/air equivalence ratio (ER). Because of the large amount of fresh air in the exhaust pipe, it is not possible to use the classical way to estimate the equivalence ratio, generally measured in the exhaust pipe. Consequently, a special methodology exploiting a gas tracer was developed in this study to estimate the in-cylinder fuel/air ER.

In Table 3 are showed the main engine parameters kept constant for scavenging optimization experimental campaign. In detail, the pressure ratio of the supercharger is kept constant at 1.6. The injected fuel quantity is tuned to reach a constant smoke level of 2.5 Filter Smoke Number (FSN), and the start of injection is adapted to have maximal in-cylinder pressure equal to 140 bar. The VNT opening is kept constant to 30%, where 100% is the maximum opening.

Table 3 Engine parameters for Full Load experimental campaign

In-cylinder pressure *bar*	*LP compression ratio* *-*	*Smoke* *FSN*	*VNT nozzle* *%*
140	1.6	2.5	30

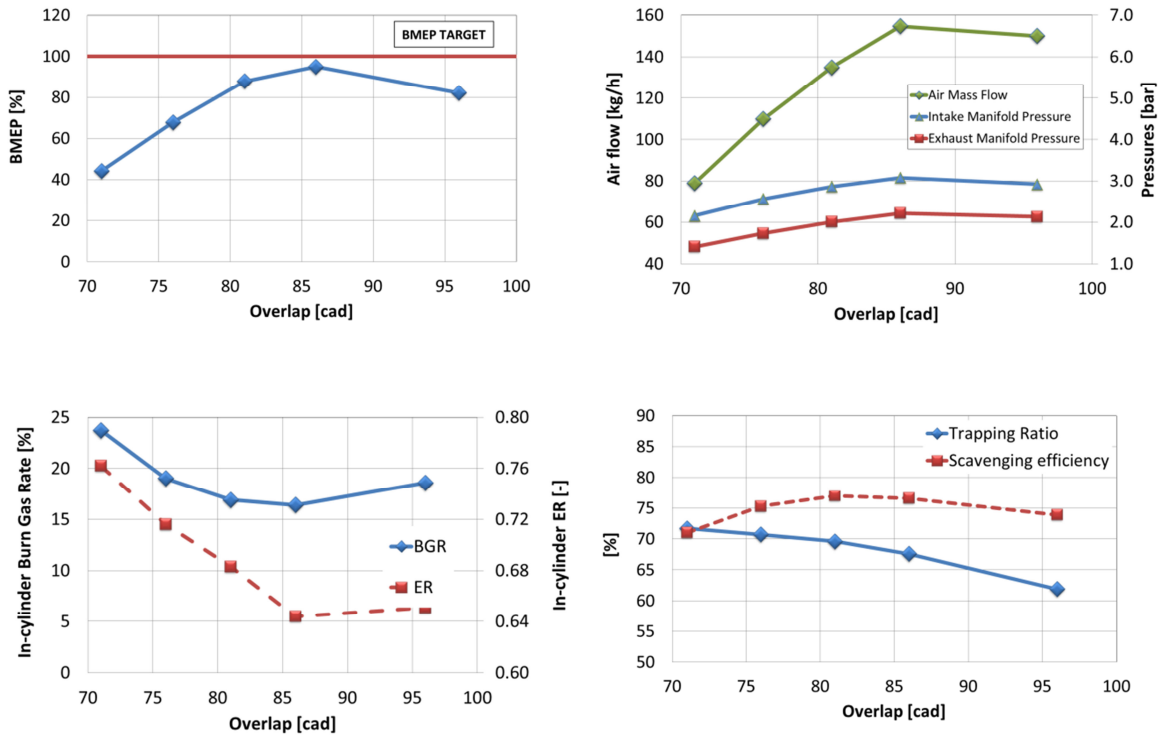

Fig. 4. Effect of Overlap at Full Load at 1500 rpm

The results presented in Fig. 4 show that by increasing the valve overlap, it is possible to get higher air mass flow through the engine. It can also be observed that the in-cylinder ER and the burnt gas rate (BGR, corresponding to the EGR + IGR) trapped in the cylinder after the scavenging, have a minimum for an overlap of 86 CAD, and then worsen at overlap equal to 96 CAD as well as the BMEP. As consequence, the maximum BMEP is obtained with an overlap of 86 CAD.

Further explications of this phenomenon can be found in the analysis of high frequency pressures in the intake and exhaust manifolds (see Fig. 5 and Fig. 6). This happens generally when the intake valves close before the exhaust valves (see Fig. 3): in these conditions some in-cylinder mass (including some fresh air) goes through the exhaust valves, decreasing strongly the scavenging efficiency. The scavenging efficiency (SE) is defined as the ratio of the trapped fresh air to the total mass (fresh air and residual exhaust gases) trapped in the cylinder.

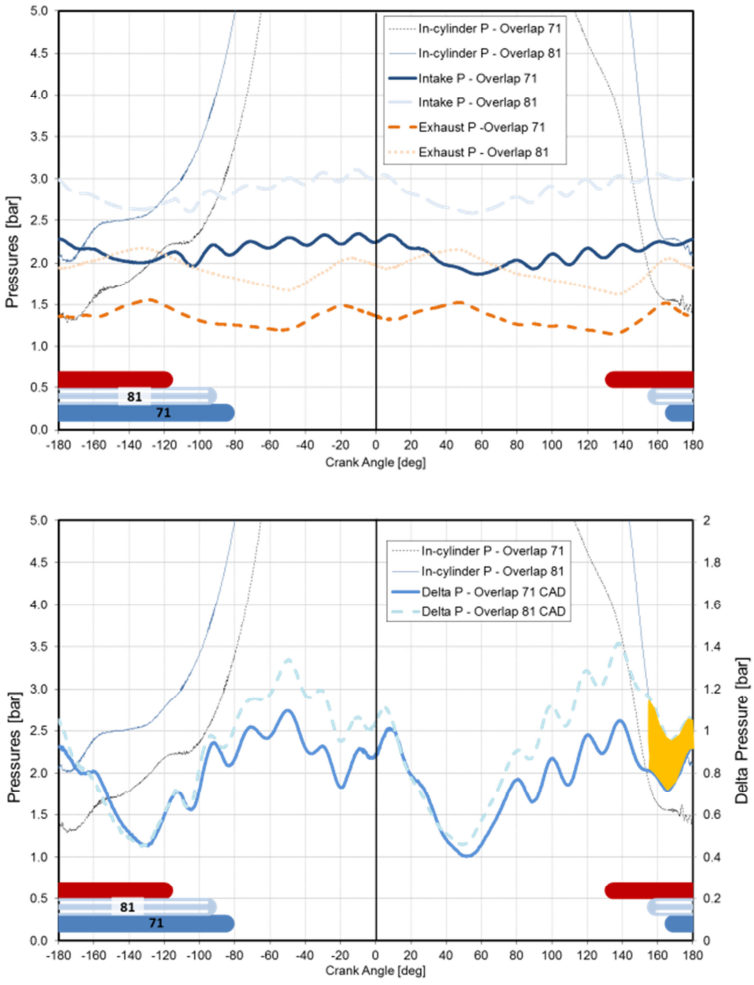

Fig. 5. Effect of Overlap on Scavenging

In Fig. 5 the effect of the overlap increasing on in-cylinder, intake and exhaust pressures can be observed; the reader must notice that the bars in the bottom side indicate the valves timing; the blue bars are for intake, and red ones for exhaust valves. Inside the bars the overlap values in CAD are specified. For these tests, the exhaust valves timing is fixed.

Setting the intake valves opening earliers, the overlap increases from 71 to 81 CAD: in these conditions, the intake valves opening occurs with a more effective instantaneous engine differential pressure (see yellow area in Fig. 5), which has a positive effect on the scavenging efficiency.

The higher engine differential pressure is obtained thanks to higher boost pressure (higher mass, and so energy, flows into the turbine), and even the increasing of the backpressure is counter-balanced (see Fig. 4).

The trapping ratio (TR), defined as the mass of delivered charge that is trapped in the cylinder before combustion divided by the mass of delivered charge supplied to the cylinder (fresh air plus EGR), is higher for lower overlap: the fresh air is trapped easily when a large intake phase occurs with closed exhaust valve, as happens for overlap 71 CAD.

Finally, the overall effect of trapping ratio, scavenging efficiency and in-cylinder ER is better using higher overlaps.

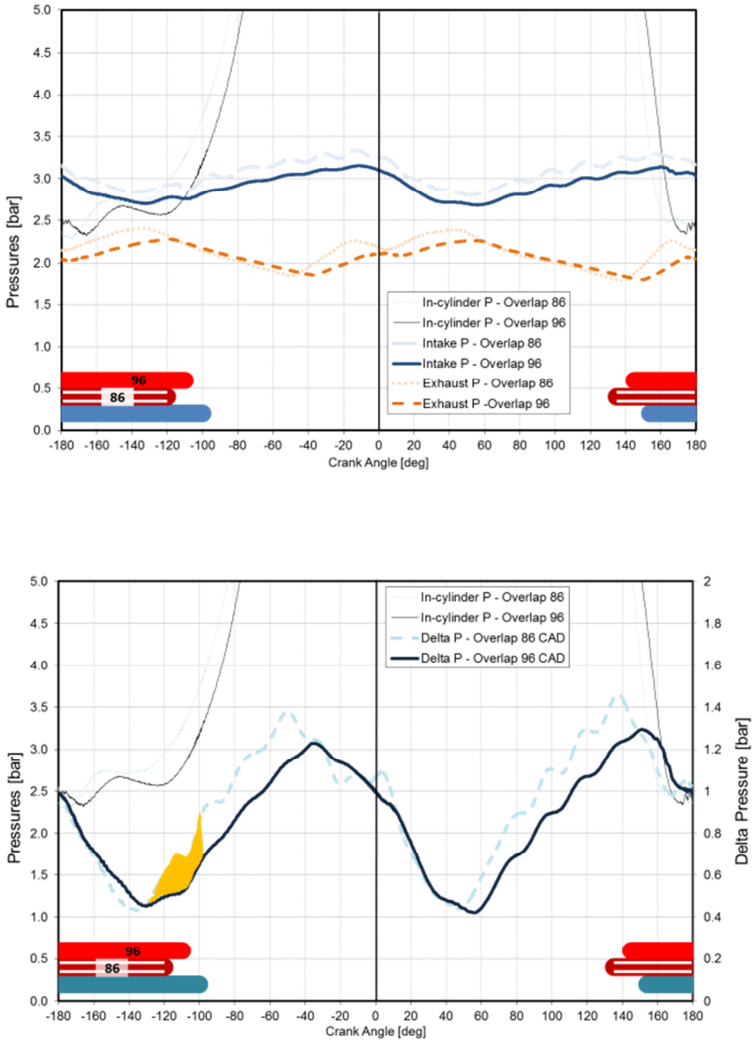

Fig. 6. Effect of high Overlap on Scavenging

In Fig. 6 it can be observed the negative effect of an excessive overlap, obtained by delaying the exhaust valves timing. With 86 CAD overlap, the engine takes advantage of the positive engine pressure differential when the exhaust valve is already closed (around -120 CAD): in this condition, all the fresh air entering in the cylinder is trapped. The effect is also visible on the higher trapping ratio and scavenging efficiency (see Fig. 4).

4.1.2 VNT opening optimization at Full Load

Once the valve lifts optimised, it is then possible to get the optimal performance of the engine by varying the VNT settings. For example, at 1500rpm, the VNT positions were swept from 20% to 60% (where 100% is the maximum opening). Generally, too high opening values do not produce enough work on the turbine shaft, and consequently on the compressor side, and too low values reduce strongly the turbine permeability increasing engine exhaust pressure.

In Table 4 are showed the main engine parameters kept constant for the VNT opening optimization experimental campaign.

Table 4 Engine parameters for Full Load experimental campaign

In-cylinder pressure *bar*	*LP compression ratio* *-*	*Smoke* *FSN*	*Overlap* *%*
140	1.6	2.5	86

Fig. 7 shows the results of a VNT opening sweep: it can be observed that the best performances are obtained for VNT opening equal to 30%, which means not fully closed.

Closing the turbine increases the intake manifold pressure, but also the backpressure. At 20% opening the increased intake manifold pressure does not completely balance the increased engine backpressure, and finally the mean and instantaneous engine differential pressures, which drive the scavenging phenomenon, are lower (see Fig. 7 and Fig. 8).

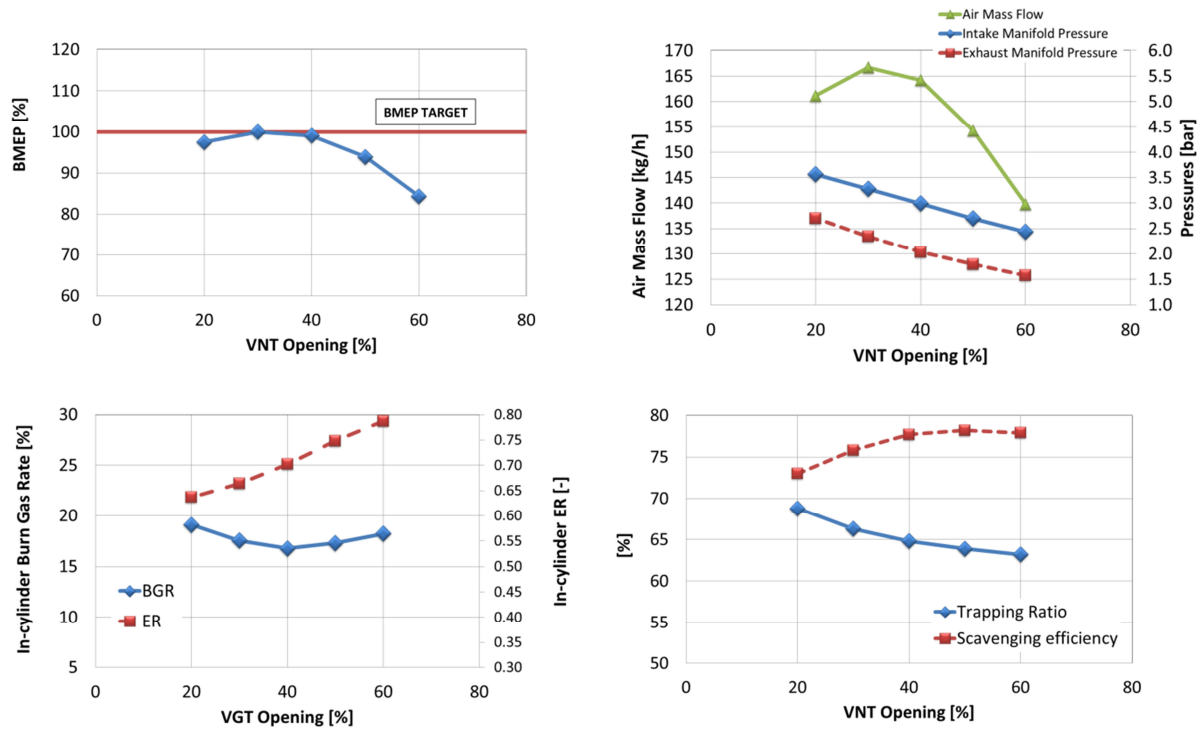

Fig. 7. Effect of VNT opening at 1500 rpm Full Load

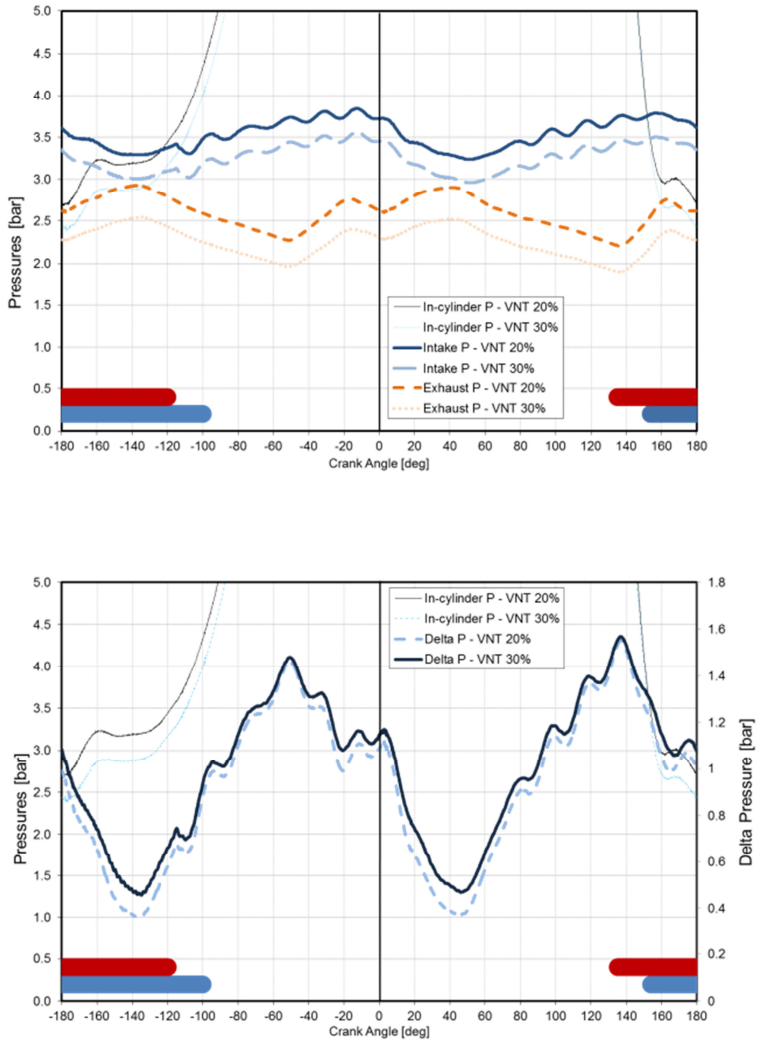

Fig. 8. Effect of VNT opening on instantaneous pressures at 1500rpm Full Load

4.2 Partial Load, 1500 rpm; 7.7 bar BMEP

4.2.1 Scavenging optimization at Partial Load

The first partial load operating point (OP) explored in the experimental campaign was at 1500rpm; 7 bar BMEP; this OP is very significant over the NEDC with an A/B-segment car, corresponding to the main acceleration phases in EUDC (see Fig. 1). In Table 5 are showed the main engine parameters kept constant during the overlap sweeps and Fig. 9 shows the main results.

As expected, the best point in terms of in-cylinder equivalence ratio produces the lower value of smoke. It is obtained when the overlap is tuned at 81 CAD. This is the results of a typical trade-off between long overlap duration to enhance scavenging process, and the limitation of closing the intake valves after the exhaust valves. Fig. 9 shows the high frequency pressures for 61 and 81 CAD of overlap.

At overlap equal to 61 CAD, the intake valves open very late, so that the fresh gases are not sucked by the piston during its expansion stroke. In addition, the intake valves are still widely open when the piston rises. The in-cylinder pressure is higher than intake one (see the yellow area in Fig. 10), and the fresh air cannot enter inside the cylinder and even some backflow toward the intake runners occurs.

The fuel consumption decreases with the overlap, both ISFC and BSFC. The behavior of the ISFC depends on the in-cylinder ER, and is mainly the effect of the combustion process efficiency. On BSFC, we can observe in addition the impact of the mechanical compressor work for compressing the additional fresh air back-flowed toward the intake runners.

Table 5 Engine parameters for Partial Load experimental campaign

Injection Pressure *bar*	*Pilot Injection Quantity* *mg/strk*	*CA50* *CAD*	*EGR* *%*	*VNT* *%*	*LP Pressure Ratio* *-*
1000	1.3	6	0	30	1.6

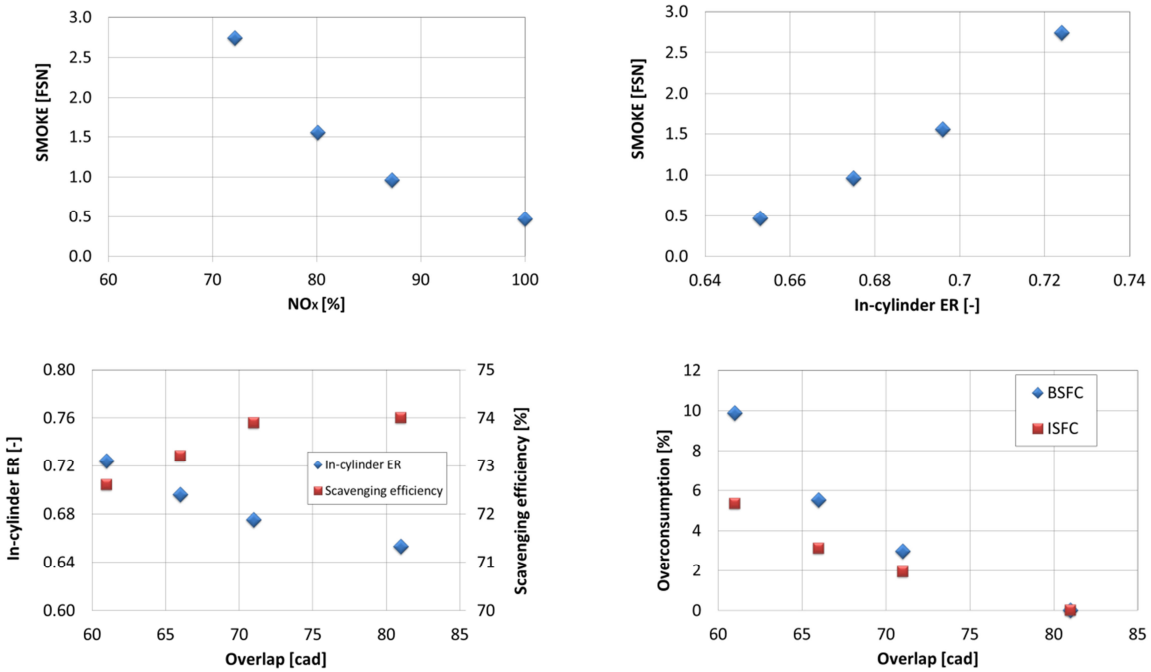

Fig. 9. Effect of Overlap at 1500rpm, 7.7 bar BMEP

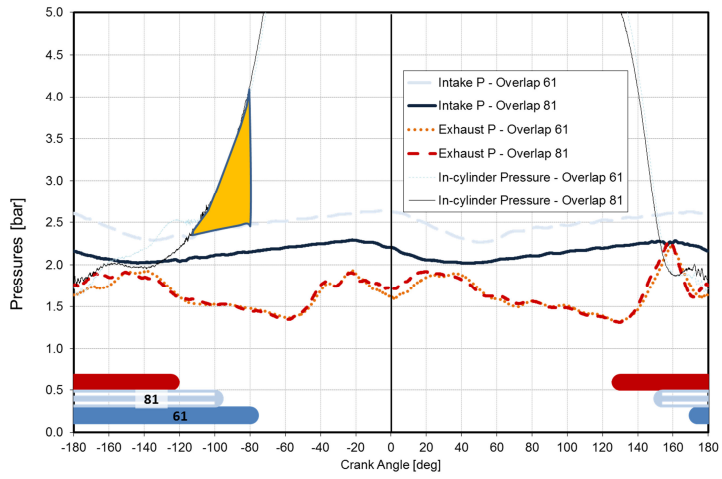

Fig. 10. Effect of Overlap on instantaneous pressures at 1500 rpm; 7.7 bar BMEP

4.2.2 VNT opening optimization at Partial Load

Once the valve lifts optimized, it was then possible to get the optimal performance of the engine by varying VNT settings.

In Table 6 are showed the main engine parameters kept constant for the VNT sweeps; the VNT opening was swept from 20% to 40% (where 100% is the maximum opening).

Table 6 Engine parameters for Partial Load VNT optimization

Injection Pressure *bar*	*Pilot Injection Quantity* *mg/strk*	*CA50* *CAD*	*OVERLAP* *CAD*	*LP Pressure Ratio* *-*
1000	1.3	6	81	1.6

In Fig. 11 it can be observed that at same NOx level (20% of maximum values), the lowest smoke level is achievable with VNT 20%. The best benefits come from the in-cylinder equivalence ratio: at BGR equal to 27% (and therefore very similar NOx emissions), the in-cylinder ER goes from 0.7 for the VNT at 40% to 0.65 for the VNT at 20%.

In Fig. 11 it can be observed that when the intake manifold pressure increases (VNT → 20%), the exhaust pressure increases too but finally the engine pressure differential and the overall effect that can be observed in Fig. 11 are better with to the closest VNT openings.

In the same figure the effect of VNT opening on the fuel consumption is represented as function of the overconsumption with respect to the VNT 20% case (which has the lowest fuel consumptions). The ISFC and BSFC are represented, and the results suggest that the main influence of the VNT opening should be on the ISFC, and very slightly on the BSFC. As for the overlap sweep, ISFC behavior depends mainly on the in-cylinder ER which impacts the combustion process efficiency. In-cylinder ER increases with BGR and decreases with the intake manifold pressure (consequence of the VNT opening → 20%).

5. Future works: Acoustic optimization

In Fig. 6, Fig. 8 and Fig. 10, it can be observed that even if the average exhaust pressure is always lower than the intake manifold pressure, which should allow an appropriate scavenging of the burnt gas by the fresh air, the instantaneous values are often very close to the intake ones. In some conditions the instantaneous engine pressure differential can even drop close to zero, worsening the scavenging by back flowing a part of the in-cylinder trapped air.

In order to lower as much as possible the impact of the exhaust wave on the engine performances, further investigations were planned with both simulation and experimental approach. In detail, a large investigation campaign has been performed with 0D and 3D codes, in order to develop advanced intake and exhaust manifolds for smoothing the wave oscillations.

In the next step of the project, an experimental campaign will be carried out for assessing the hardware modification and its impact on the maximum performances, fuel consumption and emissions.

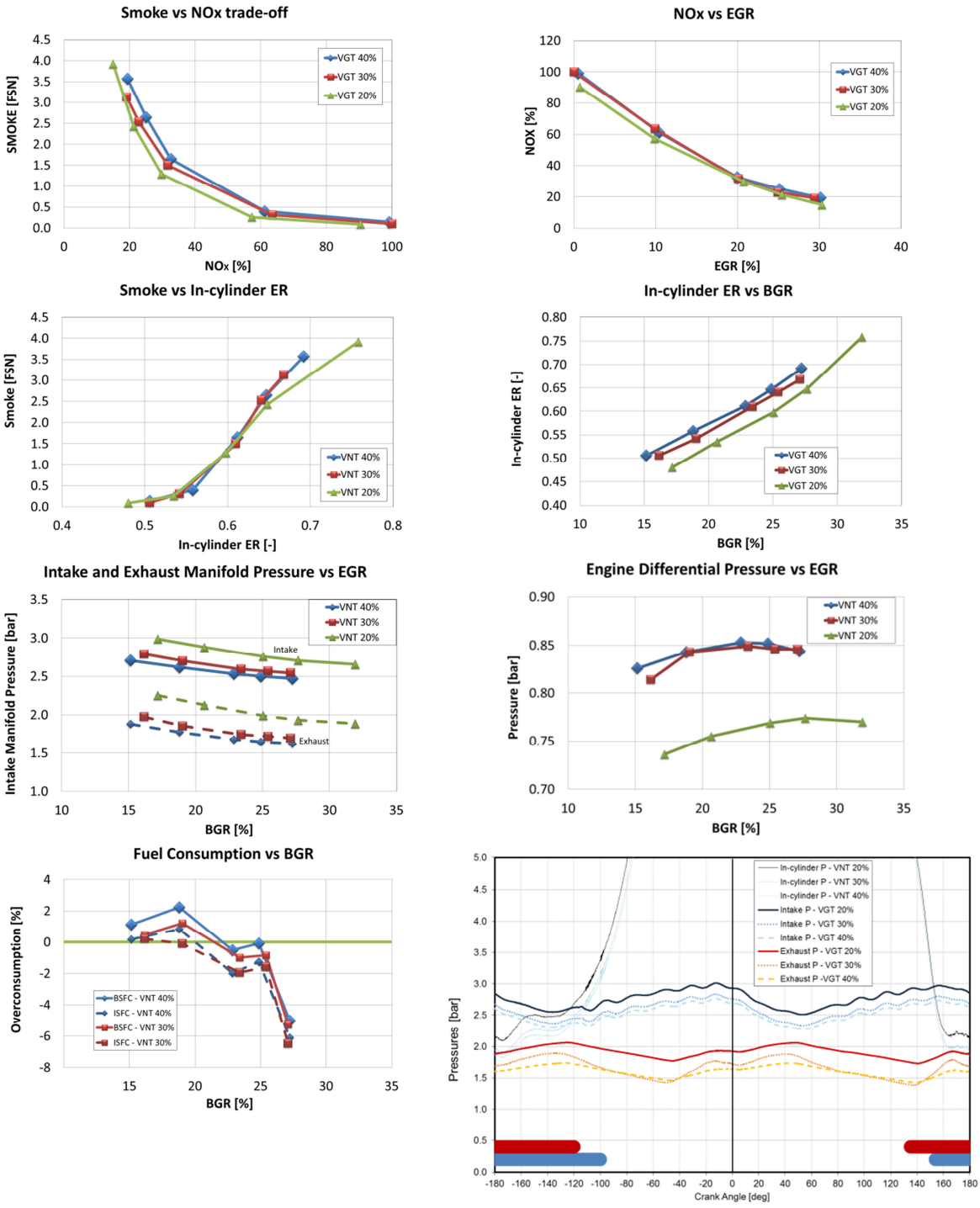

Fig. 11. Effect of VNT Opening at 1500rpm, 7.7 bar BMEP

6. Conclusions

The two-stroke activities inside the POWERFUL European research project aim to develop a full valved Diesel engine and assess its potential for an automotive application, A/B-car segment, complying with the current pollutant emission and drivability standards.

Firstly the two-stroke twin cylinder engine and its air loop were designed in order to address the specific two-stroke sensitive points: scavenging efficiency, in-cylinder ER management etc. [12] Secondly, the engine has been tested at IFP Energies nouvelles, in order to characterise and understand the impacts of the of air loop factors, (*e.g.* overlap, intake and exhaust manifold pressures, EGR etc.), on engine performances, fuel consumption and pollutants emission.

The main results of the second part of the project are that the control of the overlap is essential for the management of the in-cylinder ER. The optimized overlap reduces the intake manifold pressure requirements, lowering the consumption penalties due to the mechanical compressor.

The study also highlighted that the instantaneous engine pressure differential, with respect to the overlap and to the intake and exhaust valves timing, must be controlled and well phased in order to optimise engine scavenging and fresh air filling.

In addition, a strong influence of the exhaust pressure waves was highlighted at the end of this first task, and will be analysed and improved in the next steps of the project.

The final updated engine will be calibrated, exploiting dedicated engine control strategies developed by IFP Energies nouvelles within the framework of the Powerful project, and equip a Renault Twingo demo-car.

References

1. Abthoff J., Duvinage F., Hardt T., Krämer M. & Paule M., *"The 2-Stroke DI-Diesel Engine with Common Rail Injection for Passenger Car Application"*, SAE Technical Paper 981032, 1998, doi:10.4271/981032
2. Blair G.P., *"Design and Simulation of Two-Stroke Engines"*, Society of Automotive Engineers, 1996
3. Cantore G. et al., *"A New Concept for Ultra-Compact Automotive HSDI Diesel Engines"*, SAE Technical Paper 2007-01-1253, 2007, doi:10.4271/2007-01-1253
4. Fleck R., Campbell D.J., *"An Experimental Investigation Into the Potential of Small Two-Stroke Diesel Engines"*, IMechE n°C433/061, 1991
5. Heywood J.B., Sher E., *"The Two-Stroke Cycle Engine, Its Development, Operation, and Design"*, SAE International, 1999.
6. Knoll R., *"AVL Two-Stroke Diesel Engine"*, SAE Technical Paper 981038, 1998, doi:10.4271/981038
7. Laget, O., Ternel, C., Thiriot, J., Charmasson, S. et al., "*Preliminary Design of a Two-Stroke Uniflow Diesel Engine for Passenger Car*," SAE Int. J. Engines 6(1):596-613, 2013, doi:10.4271/2013-01-1719
8. Masuda T., Itoh H. & Ichihara Y., *"Research on the Practical Application of 1 Liter, Semi-DI, 2-Stroke Diesel Engine to Compact Cars"*, SAE Technical Paper 1999-01-1249, 1999, doi:10.4271/1999-01-1249
9. Nomura K., Nakamura N., *"Development of a New Two-Stroke Engine with Poppet-Valves: Toyota S-2 Engine, A New Generation of Two-Stroke Engines for the Future?"* p.53-62, Editions Technip, 1993
10. Pohorelsky R., Pavel B., Macek J., Vallaude PY., Ricaud JC., Obernesser P., Tribotté P.,"*Air System Conception for a Downsized Two-Stroke Diesel Engine"* SAE Technical Paper 2012-01-0831, 2012, doi:10.4271/2012-01-0831
11. Servant, C., Quechon, N., Obernesser, P., "*Two-stroke engine e.g. two-stroke diesel engine, has air deflector located downstream of part of seat in intake valve of intake duct, and directing air flow from intake duct towards lower part of combustion chamber*," Patent Renault FR2931880
12. Wyczalek, F., "Two-Stroke Engine Technology in the 1990's," SAE Technical Paper n°910663
13. http://www.auto-innovations.com/actualite/611.html

Influence of Swirl Ratio on Combustion System Performance of a 0.4L Single-Cylinder Diesel Engine

J. De La Morena[1]*, A. Vassallo[2], R.C. Peterson[3], V. Gopalakrishan[3] and J. Gao[3]

[1]General Motors Powertrain-Europe, Diesel Engine Advanced Engineering, Corso Castelfidardo 34, Torino, Italy

E-mail: joaquin.de_la_morena@gm.com
Telephone: +(39) 011 424 8274

[2]General Motors Powertrain-North America, Engine Combustion & Air Flow, 823 Joslyn Avenue - Pontiac, MI, USA

[3]General Motors Research & Development, Propulsion Systems Research Lab, 30500 Mound Road Warren, MI, USA

* Corresponding author and presenter

Abstract. The influence of swirl ratio on diesel combustion system performance is studied using a fully instrumented four-valve 0.4-L single-cylinder engine. A swirl flap is introduced to control the swirl ratio (as measured by a honeycomb-type flow bench) in the range 2.2 – 3.6. The rated-power of the engine is evaluated at 4000 r/min and 4 levels of swirl ratio: 2.2, 2.5, 2.9 and 3.6. Higher swirl ratio results in lower engine power, and significantly higher smoke emissions. In addition, it reduces the engine power sensitivity to boost pressure. Results indicate the swirl ratio of 2.2 as a threshold beyond which spray penetration and air utilization are impaired at rated power. These results are consistent with 3D-CFD simulations, which show the negative effect of increasing swirl on spray propagation and equivalence ratio distribution. The part-load operation is assessed by Design of Experiments (DOE) techniques at the same 4 discrete swirl ratio values. Three other independent variables are considered: EGR rate, rail pressure and injection timing. A total of 6 part-load keypoints that represent two certification cycles, New European Driving Cycle (NEDC) and World-Wide Harmonized Light-duty Test Procedures (WLTP), are included in this study. The NEDC and WLTP cycles represent engine operating conditions at low/mid speed and load, and mid/high load, respectively. At mid-to-high loads, an optimal swirl ratio of 2.5 has been identified, beyond which air utilization via spray penetration is impaired in a similar way as seen for the rated-power conditions. Below the swirl ratio of 2.5, on the contrary, air utilization weakens due to poor atomization and fuel-charge mixing. Concerning light loads, the optimal swirl ratio increases to 2.9. This swirl ratio achieves good fuel atomization in spite of the lower rail pressures and charge densities typical of these conditions. Factoring in all previous requirements for the combustion system design, a swirl ratio of 2.5 is found to be best balanced for a fixed-swirl engine. Cycle estimations based on the keypoints results show that, at constant emissions levels, the fuel consumption penalty for a 2.5 fixed-swirl engine configuration is only ~1% with respect to an optimized variable-swirl engine. The deterioration in rated power between these 2 solutions is around 1.8 bar in NMEP basis. Considering this, a fixed-swirl ratio configuration is seen as a suitable solution for 4-valve low-power density engines.

Notation

AFR *Air/Fuel Ratio*
BMEP *Brake Mean Effective Pressure*
Boost *Intake Pressure*
CAD *Crank Angle Degree*
COV *Coefficient of Variance*
DFCO *Deceleration Fuel Cut-Off*
DOE *Design of Experiments*
Dwell *Separation between start of energizing for injections*

EI *Emission Index*
FC *Fuel Consumption*
FSN *Filter Smoke Number*
MCE *Multi-Cylinder Engine*
NEDC *New European Driving Cycle*
NMEP *Net Mean Effective Pressure (full cycle)*
NSFC *Net Specific Fuel Consumption*
PCP *Peak Compression Pressure*
PFP *Peak Firing Pressure*
PM *Particulate Matter*
RP *Rail Pressure*
RPM *Revolutions per Minute*
SCE *Single-Cylinder Engine*
SOI *Start of Main Injection*
SR *Swirl Ratio*
TDC *Top Dead Center*
Texh *Exhaust Manifold Temperature*
VGT *Variable Geometry Turbocharger*
WLTP *World-Wide Harmonized Light-duty Test Procedures*

1. Introduction

Swirl motion in direct-injection diesel engines improves combustion performance and emissions. McCracken and Abraham (2002) demonstrate that high swirl ratios enhance air/fuel mixing. Miles (2000) states that higher swirl tends to decrease the ignition delay and improves the final part of the diffusion-controlled heat release rate. This is consistent with the benefit observed in terms of soot emissions and fuel consumption for moderate to high swirl ratios (Catania et al, 2009; Zhu et al. 2003; Cursente et al. 2008; Genzale et al., 2007). Nevertheless, Benajes et al (2004) show that these two parameters deteriorate significantly if the swirl ratio is excessive, due to a negative effect over spray penetration. The optimal swirl ratio depends on the operating condition of the engine, as well as the piston bowl shape and the spray targeting (Shi and Reitz, 2008; Prasad et al., 2011). For rated-power conditions, it is also necessary to match the number of holes of the injector depending on the swirl motion in the combustion chamber (Van den Hueven and Willems, 2006).

In passenger car four-valve diesel engines, two different kinds of intake ports are found: one which generates a low swirl ratio and has a high flow (called helical port), and other one which induces a higher swirl motion (tangential port). One of the methods to vary swirl ratio consists of placing a throttle plate upstream of the helical port (Kawashima et al., 1998). When high flow is required to maximize engine power, this plate operates in its fully open position, giving the maximum amount of flow through the helical port and reducing the mean swirl ratio in the combustion chamber. On the other hand, when high swirl is required to mitigate emissions, the plate closes and most of the air flows through the tangential port. However, the introduction of the throttle plate has a negative effect in terms of cost and calibration complexity.

The current work analyzes the impact of swirl ratio on combustion performance both at full load (rated power) and at part load conditions. For this purpose, a 0.4L single-cylinder engine with the same combustion system as that of the GM 1.6L Eu6 diesel engine is used (Antonioli et al., 2013). At full load conditions, the sensitivities of the power achieved with respect to boost, peak firing pressure and rail pressure are analyzed for four different values of swirl ratio (SR): 2.2, 2.5, 2.9 and 3.6. The experimental results obtained are consistent with the findings from 3D-CFD simulations, which show the effect of increasing swirl-ratio on the spray penetration and equivalence ratio distribution. For part load conditions, a Design of Experiments (DOE) is performed for 6 different operating conditions. The DOE includes swirl ratio, EGR rate, rail pressure and injection timing as independent variables. The results are assessed against a baseline Eu6 calibration in terms of fuel consumption, emissions and

combustion noise. Finally, cycle-based fuel consumption and NOx/soot emissions are estimated for 2 different strategies: a variable-swirl, for which the swirl flap position is adjusted at each keypoint according to the DOE output; and a fixed-swirl, for which all keypoints are run with the flap in the same position.

2. Experimental setup

The experiments were carried out in a fully instrumented 0.40 liter displacement Single-Cylinder Engine (SCE). The main geometrical characteristics of the engine are summarized in Table 1. The injector used for this purpose is solenoid-driven, with 8 holes, a flow number of 340 cc/30s and an included angle of 155 degrees.

Table 1. Engine geometrical parameters

Parameter	Unit	Value
Compression ratio	-	16
Bore	mm	79.7
Stroke	mm	80.1
Connecting rod length	mm	140
Pin offset	mm	0.5
Swirl ratio	-	2.2-3.6

A high cetane diesel fuel, representative of European market, was selected for the experiments. Table 2 includes the most important physical and chemical properties of this fuel.

Table 2. Fuel properties

Parameter	Unit	Method	Value
Density at 15 degC	Kg/m^3	ASTM D4052	854.7
Viscosity at 40 degC	cSt	ASTM D445	3.06
Cetane number	-	ASTM D613	47.1
Lower Heating Value	MJ/kg		42.75
Distillation 0%/IBP	degC	ASTMD86	186.7
Distillation 10%	degC	ASTMD86	222.9
Distillation 50%	degC	ASTMD86	280.8
Distillation 90%	degC	ASTMD86	312.1
Distillation 99%/FBP	degC	ASTMD86	331.6
H/C Molar		Calc. SAE J1829	1.82
Stoichiometric Air-Fuel Ratio (mass)		Calc. SAE J1829	14.53

Figure 1 shows a scheme of the test stand installation. Two high-speed pressure transducers were installed to measure in-cylinder and injection pressures. A Fuel Bench measured the fuel consumption. Air flow rate was controlled and calculated using a critical orifice system. The critical orifice system consisted of a set of convergent nozzles with different diameters. The air flow rate was controlled directly from the supply pressure, making the nozzles work in sonic conditions. After mixing with cooled EGR, the intake air was heated and accumulated in a pressure vessel, where an emissions analyzer sampled CO2. In the exhaust side, the gases accessed a second vessel, insulated and heated in order to minimize the condensation of unburned hydrocarbons. In this vessel, the emissions analyzer sampled the exhaust gases and measured the values corresponding to each exhaust species. After the vessel, the flow divided between the EGR flow and the rest of the exhaust. After the backpressure valve, Smoke and Opacity meters estimated the particulate matter emissions. During the data processing phase, the Filter Smoke Number (FSN) given by the smoke meter was transformed to Emission Index (EI) using the widely employed MIRA correlation (Dodd and Holubecki, 1965). Finally, a standard noise meter, based on instantaneous in-cylinder pressure trace, evaluated the combustion noise.

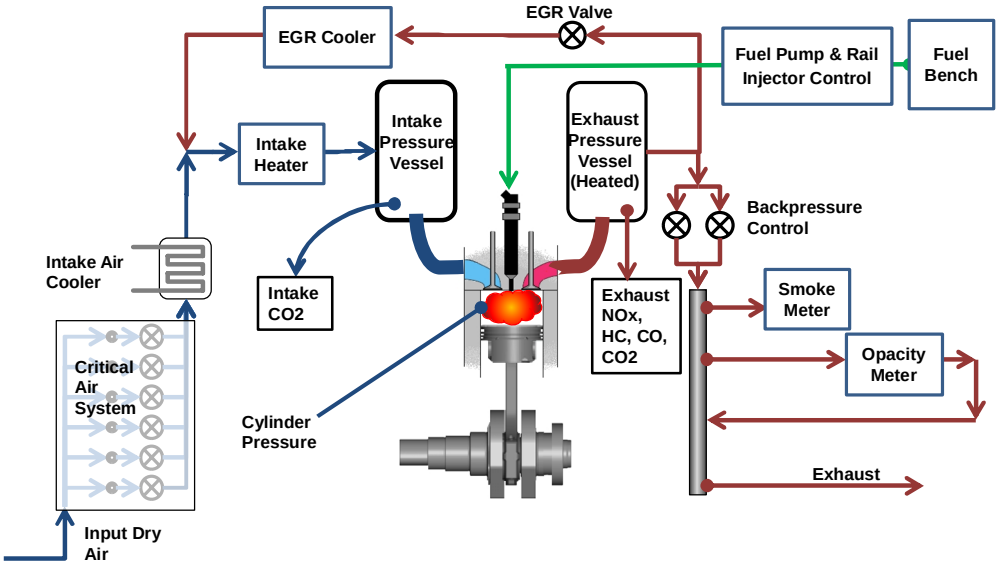

Figure 1. Scheme of Test Cell Installation

3. Experimental methodology

The main objective of the study is to investigate the effect of swirl on engine performance. In order to change the swirl in the combustion chamber, a throttle-plate upstream of the helical intake port was used. This setup enables control of swirl ratio in the range of 2.2 to 3.6 (from fully open to fully closed) with up to ten intermediate throttle positions. The results presented along this study corresponded to four of these positions, with SR values of 2.2, 2.5, 2.9 and 3.6.

The rated power conditions were evaluated at 3750 RPM and 1600-bar injection pressure. Apart from the SR, the following parameters and values were studied:

- Intake pressure: 230 and 250 kPa.
- Peak firing pressure: 140 and 160 bar.

The injection strategy for the rated power assessment consisted of a 2.7 mg/cycle pilot injection followed by a main injection. The dwell time between pilot and main injection, defined as the time between the start of the electrical command of the two injections, was constant at 600 microseconds. The peak firing pressure required for each test determined the timing of the main injection. The quantity of fuel injected in the main event itself was limited based on the Filter Smoke Number limit (FSN<3.0), and exhaust temperature limit. The exhaust temperature limit for variable geometry turbocharger (VGT) is around 810°C in a multi-cylinder engine. However, the measured exhaust temperature in a single cylinder engine is lower than the multi-cylinder due to lower firing frequency. GT-Power calculations compared the turbine inlet temperatures for SCE and MCE architectures in terms of time-averaged and mass-averaged values (Caton, 1962). Considering the results from these simulations, the limiting exhaust temperature for the SCE rated-power conditions selected was 750 degC.

For the part-load conditions, a Design of Experiments (DOE) was employed at six keypoints, representative of two different driving cycles. These operating conditions result from vehicle simulation of a small vehicle (B-segment) application. The keypoints comprehend the conditions for the NEDC and the WLTP, with the exception of the idling area, excluded due to assumed Stop&Start strategy.

The DOE included four independent variables: swirl ratio, EGR rate, rail pressure and Start Of main Injection (SOI). The rail pressure range explored phenomena like spray momentum and penetration, which interacts with the swirl motion in the combustion chamber. The injection timing variation considered possible effects of the swirl ratio on combustion duration. Figure 2 shows all the points included in the DOE in terms of the combinations of the four variables for one particular keypoint: 1500 RPM and 8-bar BMEP. The DOE was made up of a total of 67 points, including 3 repetitions of a centered condition in order to assess engine repeatability and track any potential drift during the execution of the tests, represented in the graph with a triangle.

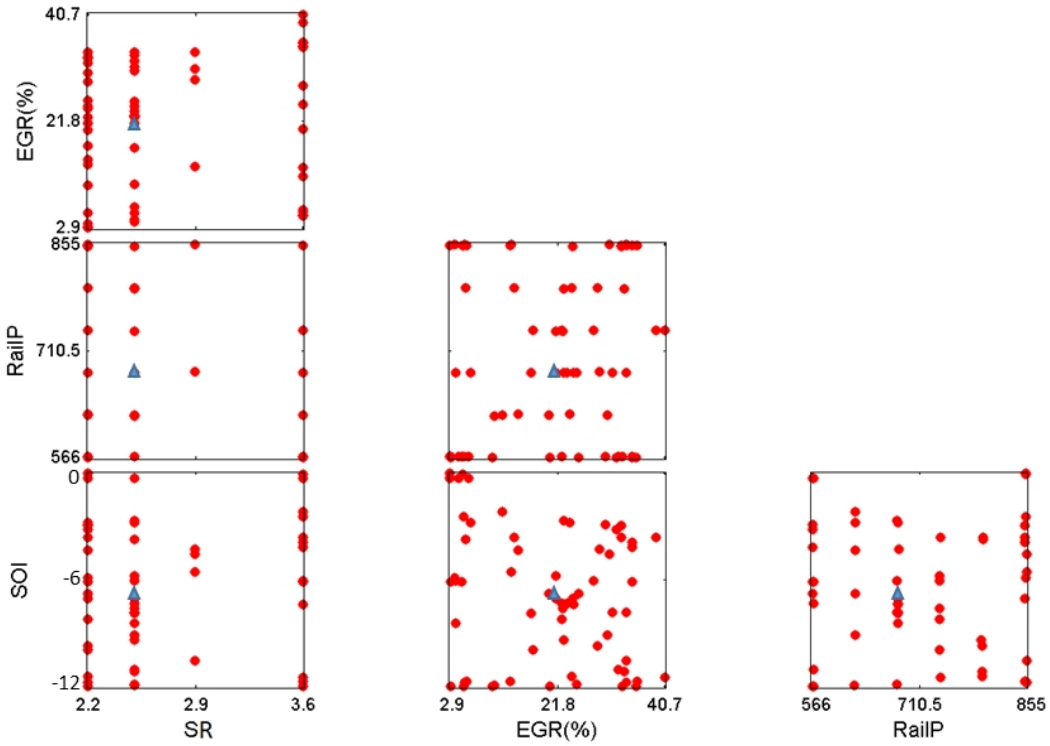

Figure 2. Design of Experiments test plan for keypoint at 1500RPM and 8-bar BMEP. Triangle: repetition point.

The experimental conditions for each keypoint were selected based a multi-cylinder Eu6 representative calibration, which is considered as the baseline for the rest of the study. This baseline calibration features double-pilot injections and EGR rates compatible with ~50% aftertreatment conversion efficiency. For the DOE activity the focus was to extend as much as possible the ranges of EGR rates tested. Preliminary EGR sweeps performed in the SCE helped to identify the maximum EGR for each keypoint, in order to avoid conditions with excessive soot production (smoke number higher than 4 FSN) or combustion instability (Coefficient of Variance of NMEP higher than 6%). Rail Pressure and injection timing (SOI Main) cover a range of around 300 bar and 12 degrees including the values from the baseline calibration. Intake and exhaust pressures were equal to the values achieved on the multi-cylinder engine for the baseline calibration. Regarding the injection strategy, double pilot injection strategy was selected to minimize the combustion noise. Pilot quantities and dwell times were constant for all the keypoints in order to simplify the DOE and reduce the total number of tests. In particular, pilot quantities of 1.5 mg/cyc and dwell times of 0.8ms were used. Table 3 summarizes all the inputs for each keypoint, including in brackets the maximum and minimum EGR rate, Rail Pressure and main injection timing covered during the DOE.

Table 3. Main experimental conditions for DOE on each keypoint

Keypoint [RPMxBMEP]	Boost [kPa]	EGR [%]	Rail P [bar]	Int-Exh ΔP [kPa]	SOI Main [degATDC]
1500x2	103	[0,55]	[250,550]	7	[-12,0]
1500x8	125	[0,40]	[550,850]	7	[-12,0]
2000x5	115	[0,45]	[400,700]	18	[-11,1]
1500x14	165	[0-25]	[600,900]	25	[-14,-2]
2000x12	182	[0-30]	[800,1100]	45	[-14,-2]
2000x16	215	[0-20]	[800,1100]	45	[-16,-4]

After completion of tests, a Stochastic Parameter Mapping (SPM) (Seabrook, 2007) was carried out to generate a robust response surface model (RSM). This model was used to perform emission-constrained minimization of NSFC within the ranges covered in the DOE. The combination of input parameters that minimized the NSFC, while maintaining the emissions equal to or lower than the baseline values, were obtained in order to ensure Eu6 compliance. Finally, the optimal calibration found using this methodology for each operating condition was verified on the single-cylinder engine. This allowed to ensure the accuracy of the RSM to predict the actual engine behavior.

4. Spray combustion simulation: model description

In this study, engine CFD simulations were performed to better understand the interaction between swirl ratio and spray penetration, together with their effect on combustion system performance. A sector-symmetric domain, typically used for 4V diesel combustion studies, helped to improve the simulation speed while maintaining adequate representation of the combustion system. The computations analyzed a 3750 RPM full load condition with two different nominal swirl levels: 2.1 and 3.2. Table 4 shows the corresponding engine operating conditions. For all cases, the injection train includes double-pulse injections (pilot + main) at the injection pressure of 1600 bar, equal to the one used for the engine testing.

The renormalized group (RNG) k-ε model calculated the in-cylinder flow turbulence. Spray droplet breakup was modeled using KH-RT hybrid breakup model. A reduced n-heptane mechanism with 32 species and 65 reactions was used to simulate the chemical characteristics of the diesel combustion process (Kong et al., 2007; Park and Reitz, 2008).

Table 4. Engine Operating Conditions at Rated Power and Boundary Conditions for Combustion Analysis

Engine speed	3750 RPM
Air Fuel Ratio	19.8
Cylinder Pressure at IVC	282 kPa
Cylinder Temperature at IVC	429.2 K
Injection Strategy	Pilot + Main
Injection Pressure	1600 bar
Injector Cone Angle	155°
Sector angle	45°
Piston Bowl Shape	Omega

5. Results

The present section discusses of the main results for rated power (including experiments and simulations) and part load conditions.

5.1 Rated power: experiments

Figure 3 shows the results of the rated-power tests in terms of the swirl ratios tested for the highest and lowest conditions: PFP 160 bar, boost 250 kPa (represented by a circle) and PFP 140 bar, boost 230 kPa (plotted as a square). In all cases, the limiting factor for the fuel quantity was the exhaust temperature. Increasing swirl tended to reduce the NMEP, increase the combustion duration (CA10-90) and the emissions. Comparing the two conditions, the higher PFP and boost produced higher NMEP, longer combustion duration and higher NOx emissions. In the case of the smoke, PFP and boost did not have a significant influence.

The figure also shows that the combustion duration (CA10-90) for the condition with higher boost/PFP was considerably more sensitive to the swirl, in the sense that the increase in combustion

duration with swirl for high boost/PFP was much larger than that for the low boost/PFP case. As swirl and boost pressure increased, spray penetration was reduced due to higher in-cylinder angular momentum and charge density. As a result, the spray did not properly entrain the air in the outer area of the combustion chamber. This leads to a drop in the rate diffusion-controlled combustion and an increase in the duration of combustion (CA10-90).

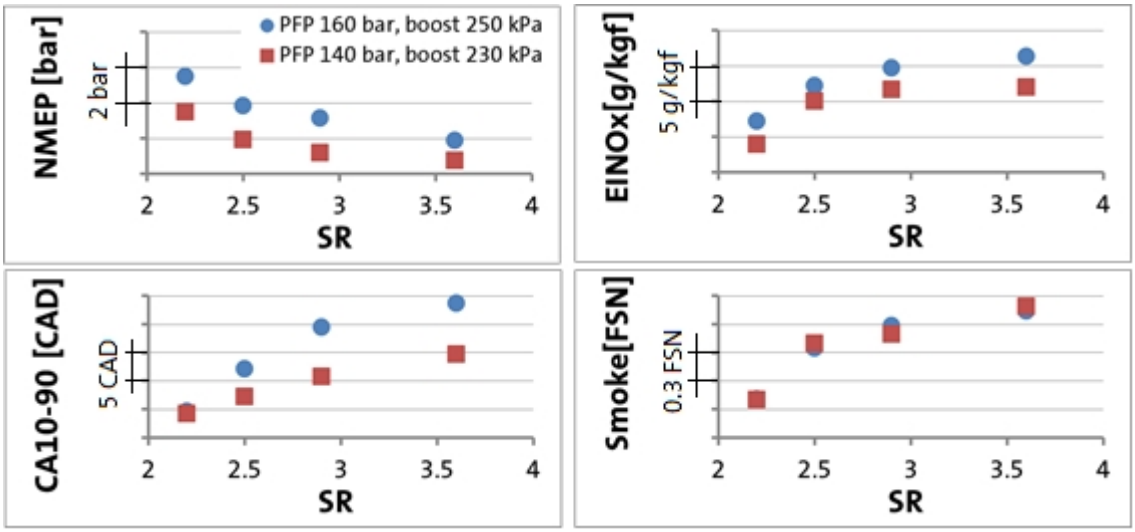

Figure 3. Effect of swirl ratio at full load condition (3750 RPM): NMEP, combustion duration, NOx and smoke emissions

Figure 4 shows the sensitivity of NMEP to boost, expressed as the increase achieved in NMEP for every kPa increment of boost. This sensitivity was calculated separately for the two levels of PFP tested, using the following expression:

$$\frac{\Delta NMEP}{\Delta Boost}(PFP) = \frac{NMEP(Boost = 250kPa, PFP) - NMEP(Boost = 230kPa, PFP)}{250 - 230} \quad (1)$$

In Figure 4, the circles represent this value for the cases at PFP=160 bar, while the squares correspond to the PFP=140 bar. The values for the case of PFP=140 bar were lower, especially for the lowest SR case. This was due to the margin between peak compression pressure (PCP) and PFP. When the PFP limit was low (140 bar), increasing the boost tended to reduce this margin. Therefore, the main injection timing and duration were limited, and the extra air introduced by the higher boost did not give a significant benefit.

In both cases, the higher swirl ratio tended to decrease the sensitivity to boost. The physical explanation for this phenomenon relates to spray penetration. In general, as swirl motion increases, spray penetration reduces, preventing the atomized and partially evaporated fuel from reaching the external part of the combustion chamber. Thus, the extra air introduced by increasing boost was not properly utilized. For the low PFP case, the density in the combustion chamber is moderate, and it was necessary to achieve a very strong swirl (3.6) to observe any significant spray penetration reduction and air utilization impairment. When the PFP increased, the higher in-cylinder density further reduced the spray penetration, the deterioration previously described appeared at much lower swirl ratio (2.5).

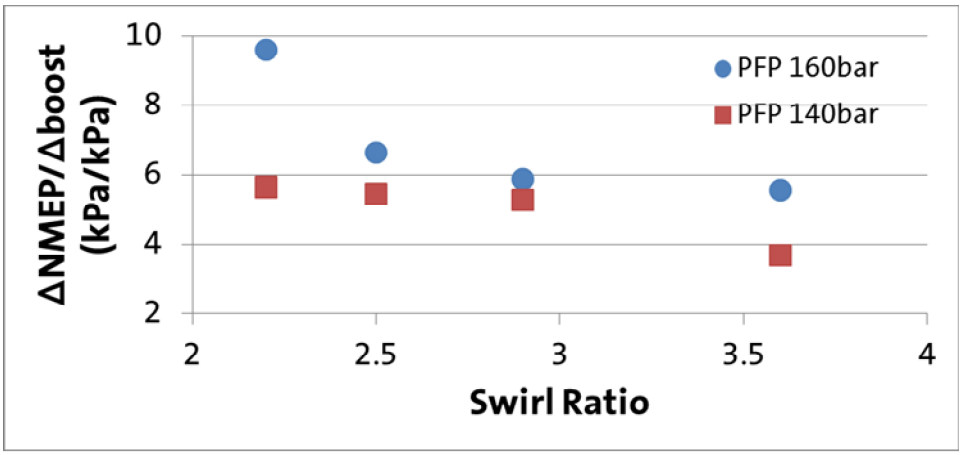

Figure 4. Sensitivity of NMEP to boost for each SR

Figure 5 shows the same kind of analysis for the sensitivity of the NMEP to the peak firing pressure. In this case, the sensitivity is defined as the increase in NMEP for 1 bar increase in PFP, and was calculated independently for the two levels of boost tested, using the following formula:

$$\frac{\Delta NMEP}{\Delta PFP}(Boost) = \frac{NMEP(Boost, PFP = 160\ bar) - NMEP(Boost, PFP = 140\ bar)}{160 - 140} \quad (2)$$

Looking at Figure 5, the sensitivity to the PFP was on average ~1kPa/bar higher for the case of boost 250kPa. This was related to the extra amount of air introduced, which allowed a more efficient combustion process, achieving greater NMEP benefit for the increase of the PFP. Furthermore, increasing the PFP increased the margin between PCP and PFP, which was particularly important for the high boost case due to the higher PCP achieved. Regarding the SR, no significant effect was seen until reaching the case of SR=3.6, where combustion was highly impaired.

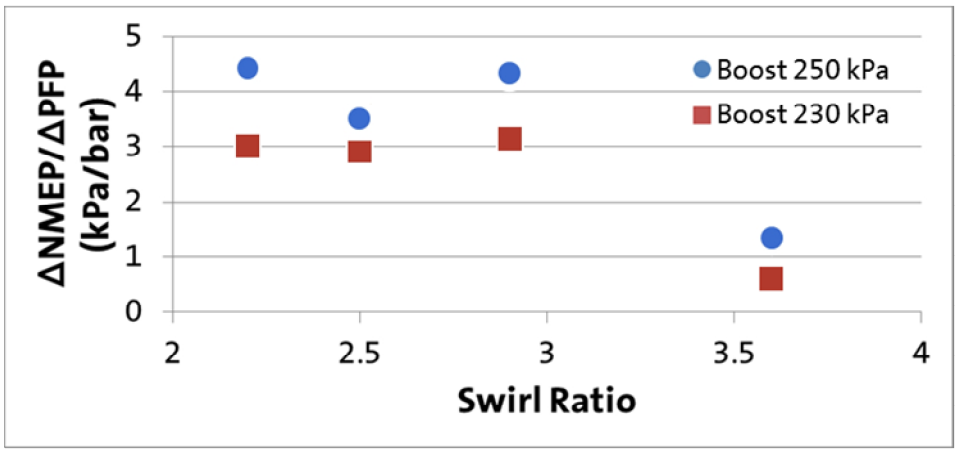

Figure 5. Sensitivity of NMEP to PFP for each SR

5.2 Rated power: simulation

Figure 6 summarizes the results from the 3D-CFD simulations at rated power conditions (3750 RPM). In particular, the figure shows the equivalence ratio distribution at two different moments in the cycle: 15 and 40 degATDC. For the case of 15 degATDC, the velocity vectors corresponding to the spray are overlaid in the figure, to better assess the spray plume motion. The figure shows two different levels of swirl ratio: low (2.1) and high (3.2),

In the low swirl case, the picture at 15 degATDC shows how the spray plume was targeted to the corner that separates the piston bowl and the squish region, enabling fuel distribution through all the combustion chamber and good air utilization. The low equivalence ratio values achieved at 40 degATDC (maximum 1.5) are consistent with the very low smoke emissions previously seen in the engine.

When the swirl increased, the stronger air motion in the combustion chambers acted as a barrier for the spray plume, limiting the spray tip velocity and penetration. The reverse squish flow deflected the spray towards the fire deck, preventing it from efficiently involving the air in the piston bowl. This is also evident looking at the equivalence ratio distribution at 40 degATDC, which shows almost no fuel present inside the bowl, while relatively high equivalence ratio values appeared in other areas of the combustion chamber, and especially in the squish volume.

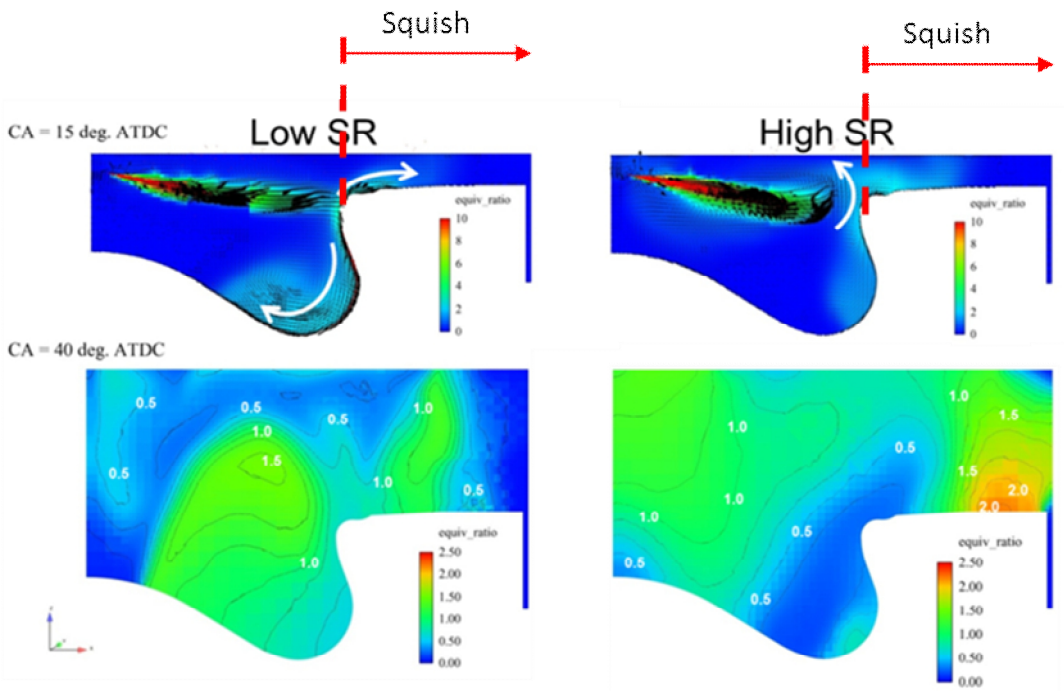

Figure 6. Spray penetration and equivalence ratio distribution for low (2.1) and high (3.2) swirl-ratio at rated-power. Conditions: 3750 RPM, Rail Pressure 1600 bar, AFR 19.8, Pilot+Main injection

The results from the spray simulations are well in-line with the previous findings coming from the single-cylinder engine testing:

- Spray simulations show that, as swirl increases, combustion tends to take place near the squish region. In this situation, the latest part of the combustion process deteriorates, which is consistent with the longer combustion duration observed in the experiments. Additionally, the longer combustion duration would result in higher temperatures near exhaust valve opening, which is consistent with the deterioration in NMEP seen when increasing SR at same exhaust temperature limitation.
- As already discussed in the previous section (Figure 4), the low NMEP sensitivity to the boost pressure observed for high swirl-ratio in the SCE testing is an indication of a poor air utilization situation. This is evident looking at the simulation results, where a significant fraction of the air existing in the combustion chamber is not involved in the combustion process.
- The higher equivalence ratio value achieved at the higher swirl ratio case is the source for the increment in smoke emissions.

5.3 Part load: experiments

Six part-load keypoints were studied using a Design of Experiments methodology. The same set

of swirl ratios used for the rated-power assessment was tested. Additionally, the tests considered variations of EGR rate, rail pressure and injection timing.

5.3.1 1500RPM, 8-bar BMEP

Figure 7 shows the result of the DOE optimization. The objective of this optimization was to minimize fuel consumption. The plots show the main outcomes (NOx and PM emissions, fuel consumption and combustion noise) as a function of EGR rate and swirl ratio using iso-lines. The NSFC and emissions results are presented as a ratio between the model output and baseline calibration results, while the combustion noise is presented as a differential value between model and baseline. For each one of these parameters, the shaded zone represents the conditions where each value is lower than the baseline calibration. Together with these parameters, the figure shows the values of rail pressure and CA50 consistent with each set of results.

Paying attention to the NOx and NSFC contours, the best results occurred at high EGR rates (>35%), and were almost independent of the swirl ratio. Nevertheless, the capability of working at high EGR was limited due to PM constraints for low swirl (SR<2.4), and combustion noise constraints for higher swirl ratios. The optimal rail pressures in this area were higher as SR reduced, in order to compensate the poorer atomization and mixing. In terms of combustion timing, the optimal CA50 were very similar for all SR tested, although slightly lower values were visible for SR<2.6 due to faster spray penetration and combustion.

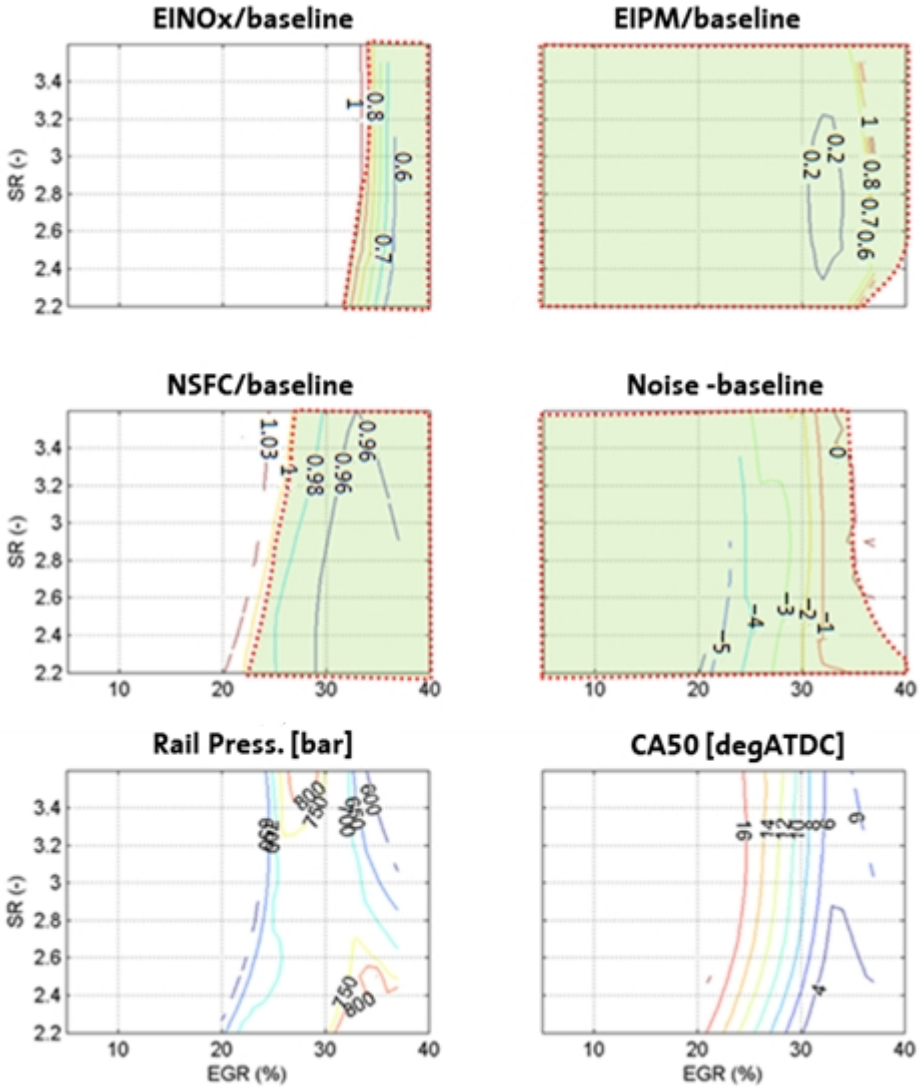

Figure 7. DOE optimization results as a function of EGR rate and swirl for 1500x8

From these results, it is possible to derive an optimized calibration for each one of the swirl ratios used during the study: 2.2, 2.5, 2.9 and 3.6. Figure 8 shows the main output parameters for each of these calibrations compared to the baseline, represented as a dashed line. For the lowest swirl ratio (2.2), the combustion was constrained by particulates, since the EIPM was higher than the baseline. In the case of the SR 3.6 a feasible condition was achieved, but there was no margin in terms of NOx, PM and Noise, making this calibration not robust. The best solution for fuel consumption and emissions/noise appeared at a swirl ratio of 2.5.

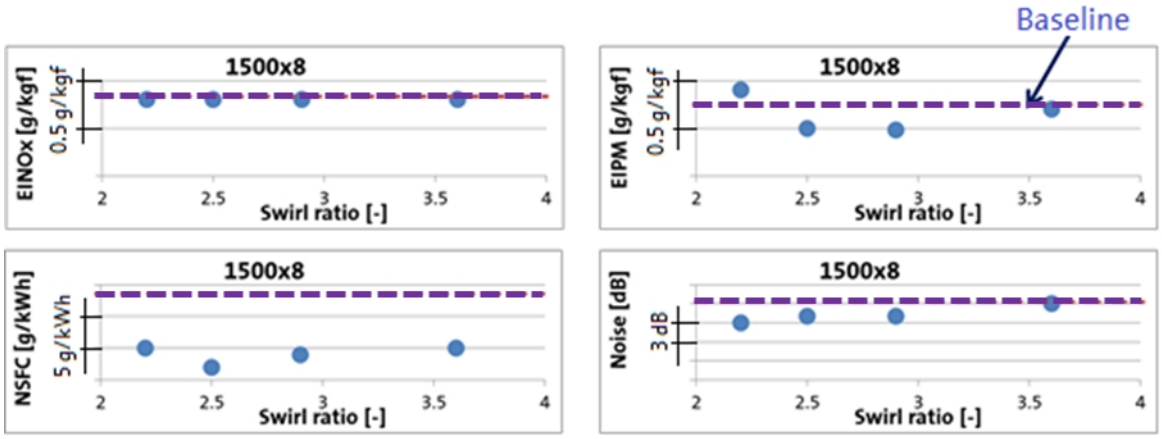

Figure 8. Optimal model output at each swirl ratio for 1500x8 against experimental baseline

To confirm the results of the DOE optimization, the single-cylinder engine was tested at different air-fuel ratios obtained by variable EGR levels around the optimal calibration at SR 2.5 (Figure 9). The dots represent the experimental values obtained during these confirmation tests. The squares show the values achieved from the DOE solution, after the optimization process. The baseline calibration values are marked as a dashed line. There was a very good correlation between the experiments and the optimal values coming from the DOE. According to the EGR tradeoff, any AFR value between 18 and 20 was equal or below the baseline for all the parameters, which indicates a good robustness of the calibration for this keypoint.

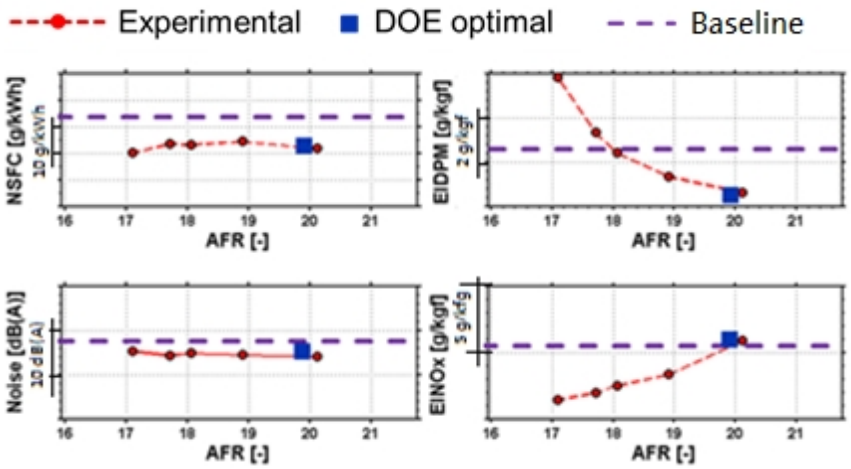

Figure 9. DOE model vs experiments for 1500x8 at SR2.5

5.3.2 1500RPM, 2-bar BMEP

Figure 10 summarizes the result of the optimization process for the 1500x2 keypoint. NOx showed to be mostly dependent on the EGR rate, with a small sensitivity to swirl ratio at low values. In

the case of PM, increasing the SR gave a significant benefit due to the better air/fuel mixing and higher local AFR. Nevertheless, increasing swirl ratio deteriorated fuel consumption and combustion noise. This deterioration related to the need to use higher injection pressures as swirl ratio increased. Higher injection pressures lead to faster fuel injection, accelerating the heat release and increasing combustion noise. Besides, the injection timing was delayed in order to partially compensate for this higher combustion noise, penalizing the fuel consumption.

In this figure, the values of the PM emissions and combustion noise are above the baseline for all the conditions tested. In the case of the PM, it is important to consider that the total particulate matter produced for this low load point in terms of mass is small, giving a small contribution to the total particulate emissions during the certification cycle. For this reason, a calibration with higher PM can be acceptable. Regarding the noise, further investigation regarding the injection train characteristics (number of pilots, pilot masses and dwell times) would be necessary to reduce the values observed.

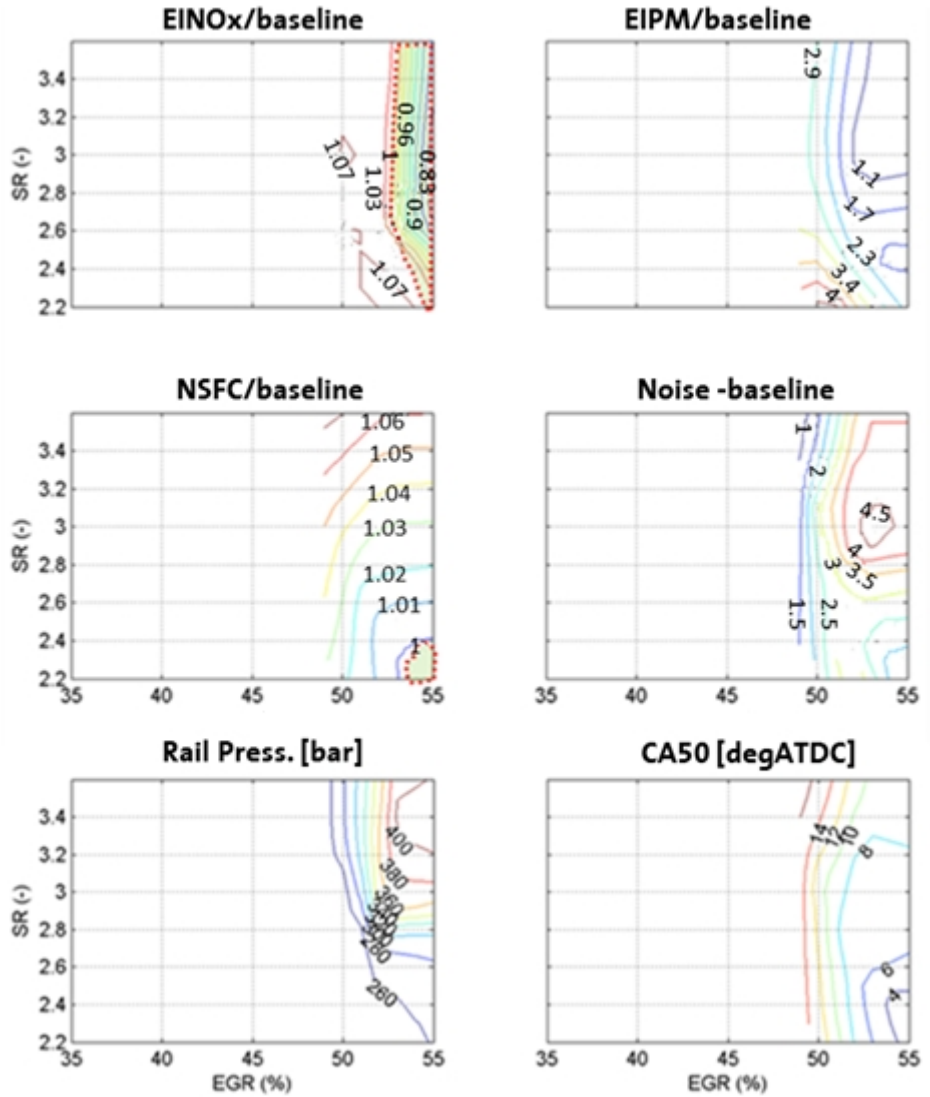

Figure 10. Optimization results as a function of EGR rate and swirl for 1500x2

Figure 11 shows the best output achievable for each one of the swirl ratios used. As already seen in Figure 10, there was no condition able to meet the particulates or the noise baseline values. An increase of the swirl ratio tended to increase also the fuel consumption and the noise. In the case of the soot emissions, an optimal value was achieved for a SR=2.5. The best compromise between all parameters was observed at SR=2.2.

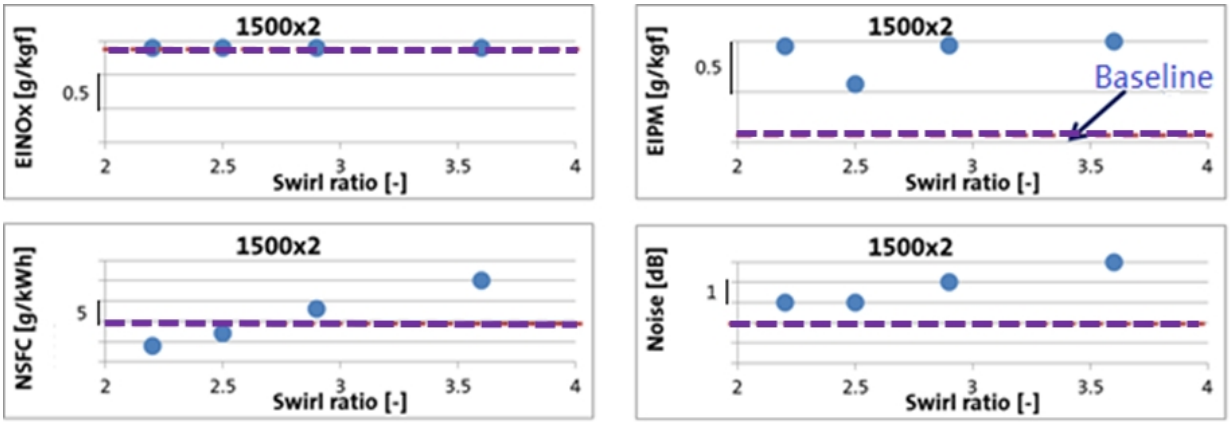

Figure 11. Optimal model output at each swirl ratio for 1500x2 against experimental baseline

Finally, an air-fuel ratio sweep obtained by varying EGR was performed in the engine around the optimal model output for SR=2.2 (Figure 12). Good correlation between the model obtained using the DOE technique and the engine behavior was observed.

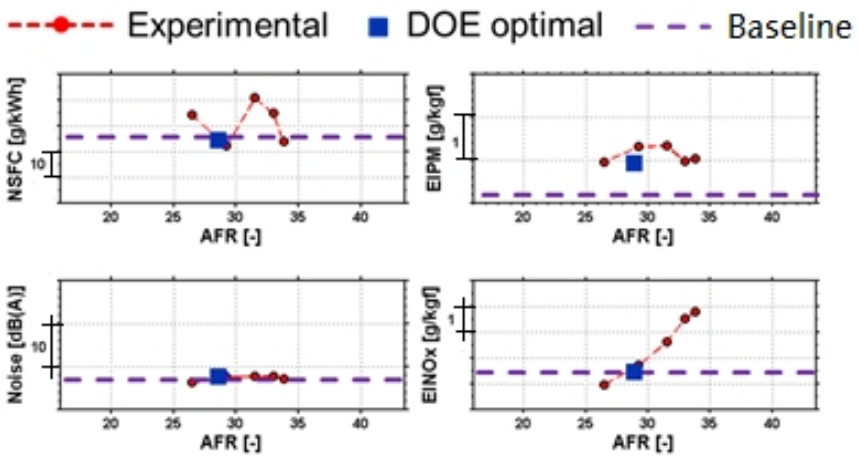

Figure 12. DOE model vs. experiments for 1500x2 at SR2.2

5.3.3 1500RPM, 14-bar BMEP

Figure 13 shows the result of the DOE optimization for the keypoint 1500x14. In this point, only SR values below 3 achieved a NSFC below the baseline calibration. For these swirl values, EGR rates between 14 and 17% were necessary to achieve the NOx and PM emissions baseline levels. The noise was lower than the baseline at all the conditions tested.

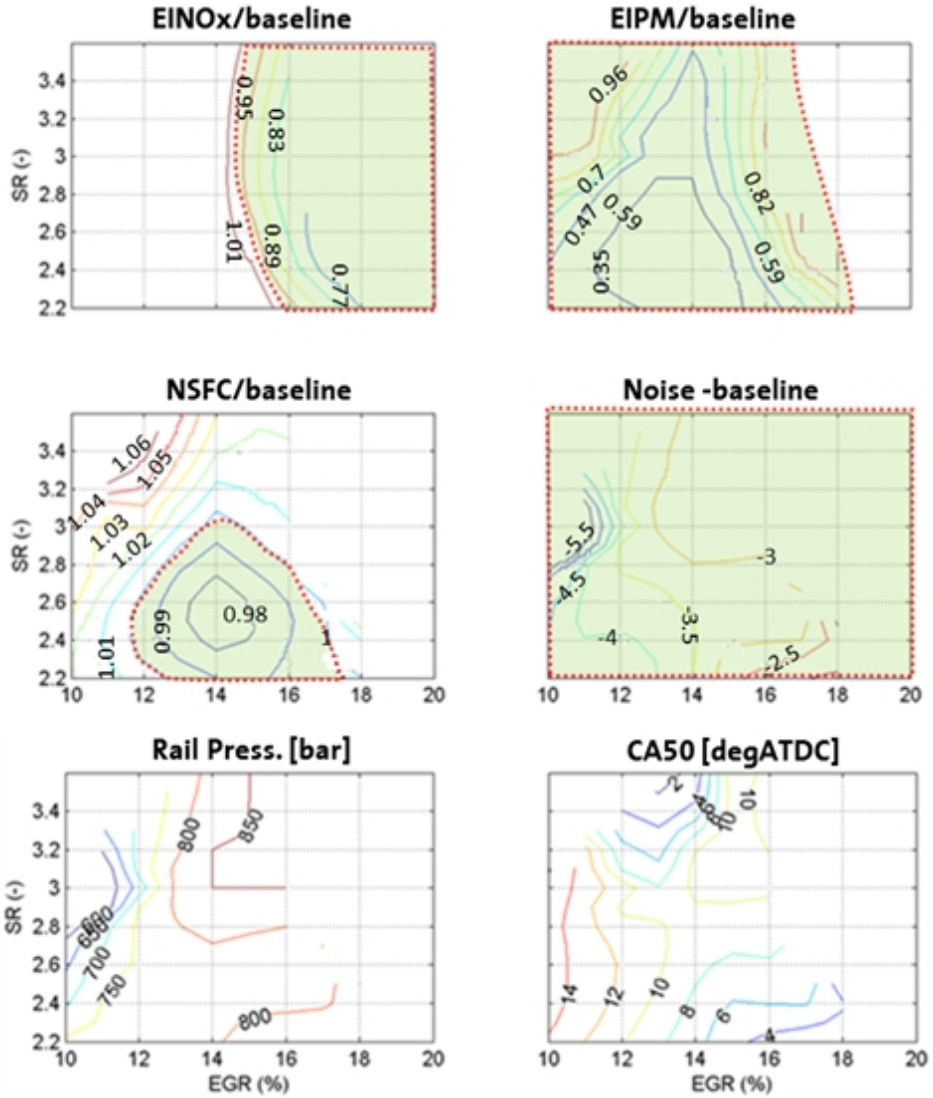

Figure 13. Optimization results as a function of EGR rate and swirl for 1500x14

Figure 14 shows the results of the best DOE calibration achievable for each one of the SR tested. In general, increasing SR tended to increase emissions and fuel consumption, while slightly improving combustion noise. The best SR value for this keypoint was 2.5. As seen for the other keypoints evaluated, the solution given by the surface response model correlates well with the engine data (Figure 15).

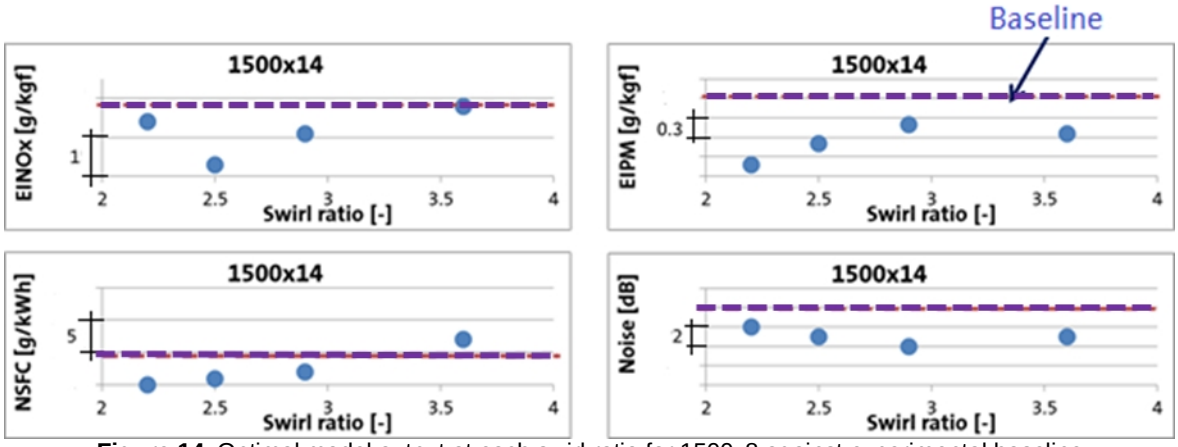

Figure 14. Optimal model output at each swirl ratio for 1500x8 against experimental baseline

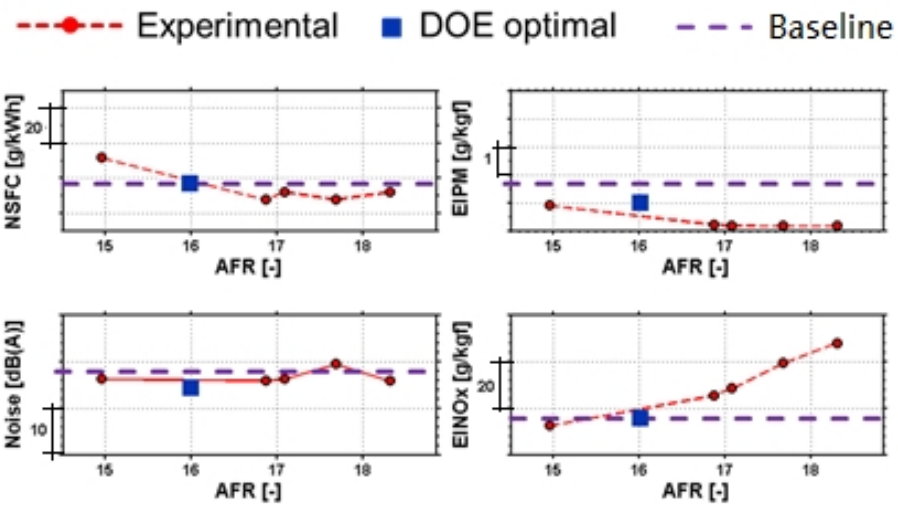

Figure 15. DOE model vs. experiments for 1500x14 for SR 2.5

5.3.4 Overall assessment

Figure 16 shows the result of the optimization for each one of the keypoints and swirl ratios tested relative to the baseline, in the same way seen for the contour plots. For most parameters, there was at least one swirl ratio able to meet the baseline values. The main exceptions were the PM and the combustion noise for 1500x2. Nevertheless, PM values above the baseline can be acceptable in this point due to the low contribution to the total PM mass over the cycle. For the combustion noise, further refinement of the injection train in terms of pilot masses and dwell times would be needed to achieve the baseline calibration output.

These results allowed the evaluation of the optimal SR for each operating condition. The main differences observed between the different swirl ratios corresponded to fuel consumption and PM emissions. For the higher load points (1500x14, 2000x16), increasing swirl ratio tended to deteriorate both parameters due to an over-swirl situation, similar as already explained for the rated power conditions. For the intermediate loads (1500x8, 2000x12), the sensitivity to swirl ratio was relatively low, and mid-to-low SR (2.5) were preferable. In the case of the low load points, the results achieved were completely different for the 1500x2 and 2000x5 cases. While the 2000x5 fuel consumption improved as SR increased due to a benefit in terms of mixing, the 1500x2 case showed the opposite behavior. This was consistent with the very low rail pressures used for this keypoint (275 bar) in order to reduce the combustion noise to values as close as possible to the baseline. The low rail pressures coupled with high swirl ratio produced high interaction between adjacent sprays. If the combustion noise required was relaxed, or an optimized injection train improved the trade-off between rail pressure and combustion noise, it is expected that higher swirl ratios would be beneficial also for the 1500x2 condition.

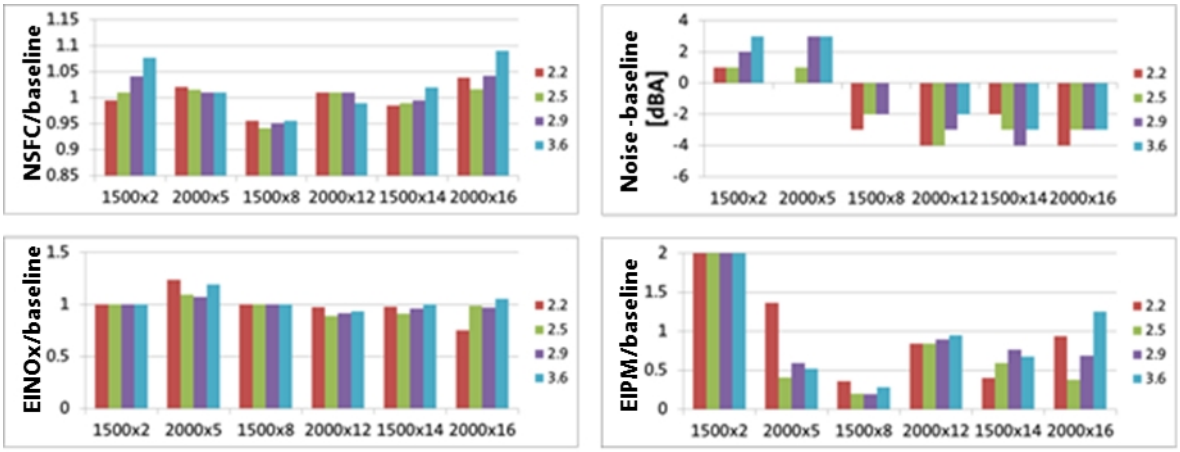

Figure 16. Model results relative to baseline for each keypoint

5.4 Cycle fuel consumption and emissions estimation

The results obtained from the part-load keypoints analysis were used to estimate the fuel consumption and emissions over a certification cycle for a small vehicle application. The first step of the process was to determine the appropriate weighting factors for each one of the keypoints selected. For this purpose, a vehicle simulation was run using the previous boundary conditions for the two certification cycles evaluated in this study: NEDC and WLTP. One of the results of this simulation was the schedule of the different conditions over the cycles in terms of engine speed and load. The weighting factors for each keypoint represented the proportion of the time in the cycle that the engine is operating in the area represented by that keypoint. For this purpose, conditions where the Stop&Start and Deceleration Fuel Cut-Off (DFCO) strategies are applied (i.e., conditions with no net fuel consumption) were not taken into account. It is important to consider that for the NEDC, the 1500x2 keypoint represented a very significant area, while the higher load points (1500x14 and 2000x16) were not even part of the calculation. This limited the accuracy and robustness of the results obtained for this representation of the certification cycle. Another limitation of this procedure is related to the fact that all tests were done under warm engine conditions (90 degC). This means that the effects of the warm-up profile of the engine on both fuel consumption and emissions were disregarded.

Figure 17 shows the results of the fuel consumption over the cycle relative to the values computed using the baseline values for different swirl strategies. The first one represents a variable-swirl solution, in which the calculation was done selecting the optimal SR for each keypoint. The rest of the strategies corresponded to fixed-swirl solutions at the different swirl levels tested along the study. In general, the fuel consumption achieved for all the strategies was close to the estimation with the baseline (within ~3%). For the fixed-swirl cases, fuel consumption deteriorated with swirl ratio, especially for NEDC. Comparing with the variable SR solution, the fixed SR configurations gave between 1% and 4% higher fuel consumption, depending on the SR selected.

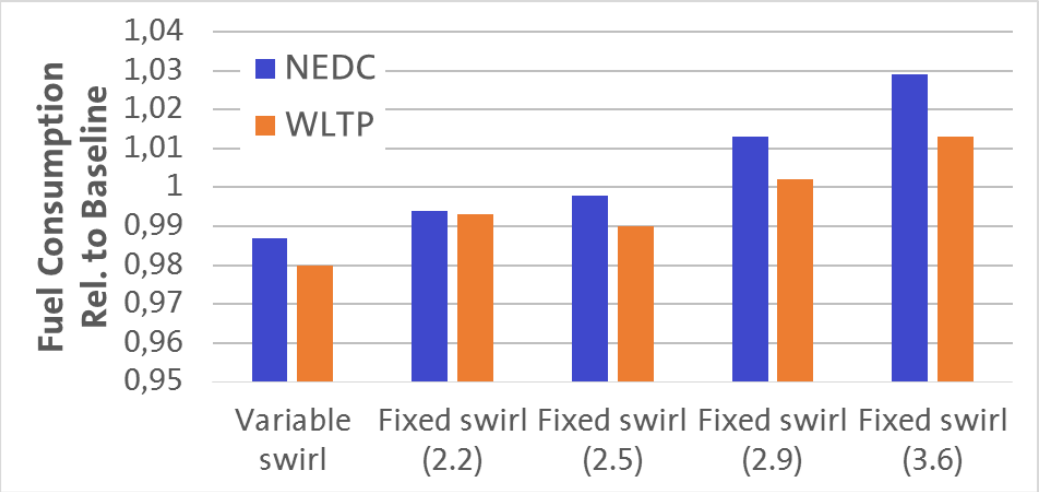

Figure 17. Cycle fuel consumption estimations relative to baseline for different swirl strategies

Figure 18 shows the same kind of analysis for engine-out NOx and PM emissions. Almost all the strategies show values equal or lower to the baseline calibration. For both parameters, the best values were achieved for a fixed-swirl solution at 2.5, even slightly lower than the variable-swirl results. This was because the swirl-ratio selection for each keypoint was aimed to minimize the fuel consumption, with the only restriction for NOx and PM emissions to be equal or lower than the baseline. Comparing the different fixed-swirl configurations, emissions rapidly deteriorated when either increasing or decreasing the SR from the optimal 2.5 value.

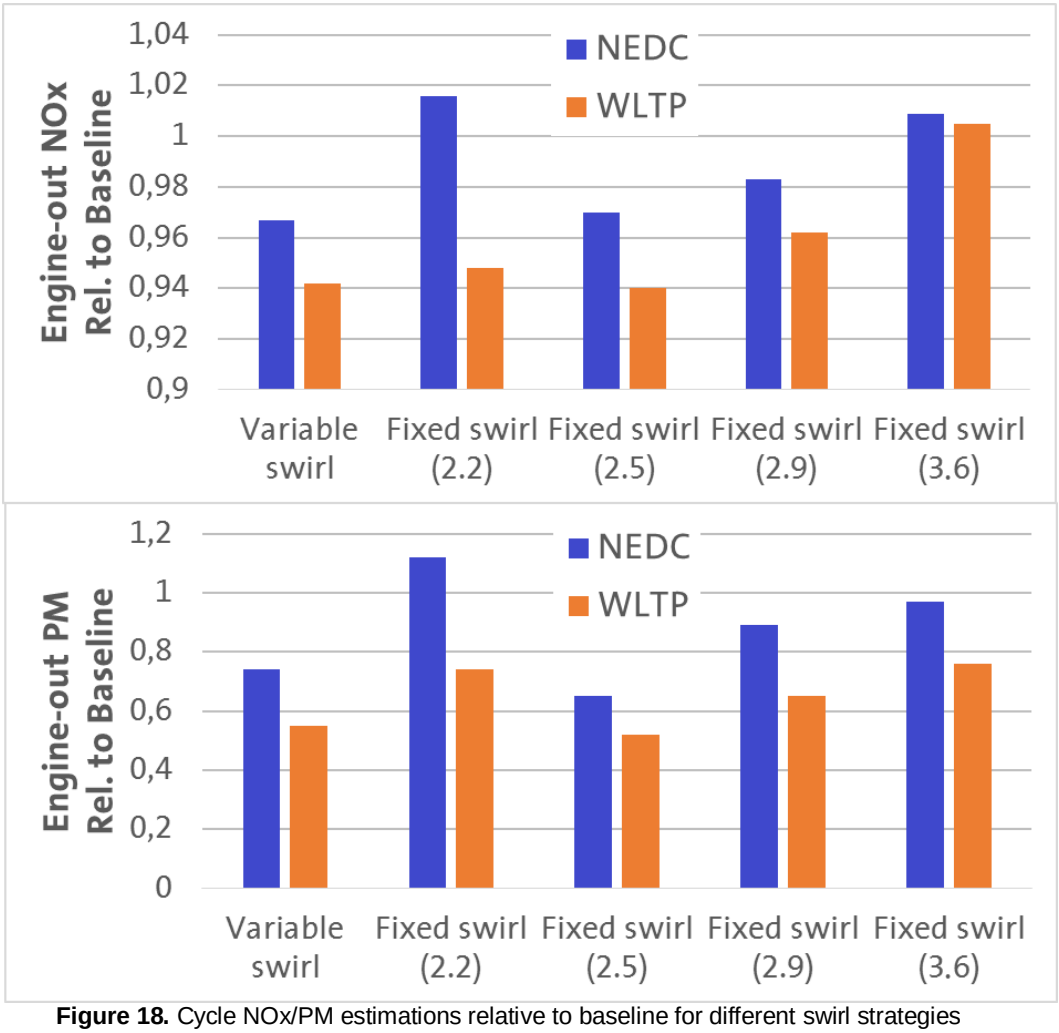

Figure 18. Cycle NOx/PM estimations relative to baseline for different swirl strategies

Considering all these results, the fixed-swirl configuration that gave the best compromise between fuel consumption and emissions was the swirl ratio 2.5. This configuration showed a penalty of around 1% in fuel consumption with respect to a variable-swirl solution for both certification cycles, while maintaining similar engine-out NOx and PM emissions. Nevertheless, according to the results seen during the rated power evaluation, a fixed 2.5 swirl ratio engine would have a decrease in rated-power capability of around 1.8-bar NMEP compared to a variable-swirl engine. Therefore, a fixed 2.5 swirl ratio configuration could be an option to reduce cost and complexity with relatively low fuel consumption penalty, but this solution may be restricted to mid-to-low power density applications.

6. Conclusions

A single-cylinder activity was performed to assess the effect of swirl on combustion performance at rated power and part-load conditions.

At rated power, increasing swirl above SR=2.2 caused lower NMEP, higher emissions and longer combustion duration. The sensitivities of NMEP with respect to boost and PFP showed significant decreases at very high swirl ratios (SR=3.6). Both results were related with a reduction in spray penetration, confirmed by 3D-CFD spray combustion analysis. The simulations showed that the high swirl motion prevented the fuel from reaching the external part of the combustion chamber and properly splitting the spray plume between the bowl and squish regions which reduced the air utilization. Additionally, high local equivalence ratio areas were detected which produced the extra soot observed in the engine tests.

For the part-load conditions, 6 keypoints relevant for two different certification cycles (NEDC and WLTP) were tested. Design of Experiments techniques evaluated the effects of swirl ratio, EGR rate, rail pressure and injection timing. The results of these designs of experiments generated a calibration for each keypoint that minimized fuel consumption while maintaining constraints in emissions and combustion noise to the same levels of a baseline Eu6 calibration. The predictions of the model generated with the DOE technique were validated against new engine data, with good consistency.

The optimal swirl ratio achieved depended on the operating condition. For relatively high loads, high swirl ratio increased both fuel consumption and emissions, again due to spray penetration issues. For low loads, increasing swirl ratio reduced PM emissions due to the enhanced air/fuel mixing. As swirl ratio increased, higher rail pressure needed to optimize the spray penetration caused significantly higher combustion noise.

Finally, cycle-based fuel consumption and engine-out NOx and PM emissions were estimated for a small vehicle application. According to these estimations, using a fixed 2.5 swirl ratio geometry introduced a penalty of around 1% in fuel consumption with respect to a variable-swirl solution, with similar engine-out NOx and PM emissions. In terms of rated power capability, the fixed 2.5 swirl ratio configuration represented a deterioration of around 1.8-bar NMEP. Consequently, a fixed swirl ratio configuration may be only applicable to mid-to-low power density applications.

Acknowledgments

The authors would like to acknowledge Jim Cauley, from General Motors R&D, for the careful and efficient engine operation and data recording, Diego Giusello, from General Motors Powertrain-Europe for providing very valuable input from the vehicle simulations, as well as to thank the entire PSR Diesel team for the precious feedback, which helped to improve the report.

References

Antonioli, P., Boretto, G., Frank, R.M., Golisano, R., Rovatti, G., Scotti, M., and Weßlau, M., 2013, “The first of a new generation of diesel engines from General Motors: the efficient and powerful 1.6 liter Euro6 Midsize Diesel Engine,” 34th Vienna Motoren Symposium, 2013.

Benajes, J. , Molina, S., García, J.M., Riesco, J.M., The effect of swirl on combustion and exhaust emissions in heavy-duty diesel engines, Proceedings of the Institution of Mechanical Engineers, Part D: Journal of Automobile Engineering Volume 218, Issue 10, October 2004, Pages 1141-1148

Catania, A.E., d'Ambrosio, S., et al., Combustion System Optimization of a Low Compression-Ratio PCCI Diesel Engine for Light-Duty Application. SAE Int. J. Engines, 2009. 2(1): p. 1314-1326.

Caton, J. A., Comparisons of Thermocouple, Time-Averaged and Mass-Averaged Exhaust Gas Temperatures for a Spark-Ignited Engine. SAE Paper 820050, 1982.

Cursente, V., Pacaud, P., and Gatellier, B., Reduction of the Compression Ratio on a HSDI Diesel Engine: Combustion Design Evolution for Compliance the Future Emission Standards, SAE Int. J. Fuels Lubr., 2008. 1(1): p. 420-439

Dodd, A. and Holubecki, Z. The Measurement of Diesel Exhaust Smoke. MIRA Report. Number 1965/10. 1965.

Genzale, C.L., Reitz, R.D., and Wickman, D.D, A Computational Investigation into the Effects of Spray Targeting, Bowl Geometry and Swirl Ratio for Low-Temperature Combustion in a Heavy-Duty Diesel Engine, SAE 2007-01-0119

Kawashima, J., Ogawa, H. and Tsuru, Y., Research on a Variable Swirl Intake Port for 4-Valve High-Speed DI Diesel Engines, SAE 982680

Kong, S. C., Kim, H. and Reitz, R. D., Comparisons of diesel PCCI combustion simulations using a representative interactive flamelet model and direct integration of CFD with detailed chemistry, J. Eng. Gas. Turbine Power Vol.129, pp.252-260, 2007

McCracken, M.E. and Abraham, J, Characterization of mixing enhancement in swirl-spray interactions in diesel engines, Combustion Science and Technology Volume 174, Issue 10, October 2002, Pages 93-124

Miles, P.C., The Influence of Swirl on HSDI Diesel Combustion at Moderate Speed and Load, SAE 2000-01-1829

Park, S. W. and Reitz, R.D., Modeling the effect of injector nozzle-hole layout on diesel engine fuel consumption and emissions, Journal of Engineering for Gas Turbines and Power, Vol. 130, p. 032805-1, 2008

Prasad, B.V.V.S.U., Sharma, C.S., Anand, T.N.C., Ravikrishna, R.V, High swirl-inducing piston bowls in small diesel engines for emission reduction, Applied Energy Volume 88, Issue 7, July 2011, Pages 2355-2367

Seabrook, J. Statistical Parametric Mapping (SPM) tools. Shoreham: Ricardo UK Ltd, 2007

Shi, Y. and Reitz, R.D., Optimization study of the effects of bowl geometry, spray targeting, and swirl ratio for a heavy-duty diesel engine operated at low and high load, "International Journal of Engine Research Volume 9, Issue 4, 2008, Pages 325-346

Van den Hueven, B., Willems, W., Combustion System Development for the New Diesel Engines in Light and Medium Commercial Vehicles from Ford and PSA, MTZ Worldwide, 67-9, 2006

Zhu, Y., Zhao, H. and Ladommatos, N., Computational Study of the Effects of Injection Timing, EGR and Swirl Ratio on a HSDI Multi-Injection Diesel Engine Emission and Performance, SAE 2003-01-0346